Transactions of the ASME

Journal of Heat Transfer

Published Quarterly by The American Society of Mechanical Engineers

VOLUME 107 • NUMBER 1 • FEBRUARY 1985

HEAT TRANSFER DIVISION
Chairman, **R. J. SIMONEAU**
Secretary, **F. A. KULACKI**
Senior Technical Editor, **K. T. YANG**
Technical Editor, **I. CATTON**
Technical Editor, **M. EPSTEIN**
Technical Editor, **G. M. FAETH**
Technical Editor, **R. GREIF**
Technical Editor, **P. J. MARTO**
Technical Editor, **R. H. PLETCHER**
Technical Editor, **R. K. SHAH**
Technical Editor, **R. VISKANTA**

BOARD ON COMMUNICATIONS
Chairman and Vice President
K. N. REID, JR.

Members-at-Large
J. T. COKONIS
W. G. GOTTENBERG
D. KOENIG
M. KUTZ
F. LANDIS
R. E. NICKELL
J. ORTLOFF
C. PHILLIPS
H. C. REEDER

President, **G. KOTNICK**
Executive Director,
PAUL ALLMENDINGER
Treasurer,
ROBERT A. BENNETT

PUBLISHING STAFF
Mng. Dir., Publ., **J. J. FREY**
Dep. Mng. Dir., Pub.,
JOS. SANSONE
Managing Editor,
CORNELIA MONAHAN
Production Editor,
VALERIE WINTERS
Editorial Prod. Asst.
MARISOL ANDINO

The Journal of Heat Transfer (ISSN 0022-1481) is published quarterly for $100 per year by The American Society of Mechanical Engineers, 345 East 47th Street, New York, N Y 10017. Second class postage paid at New York, NY and additional mailing offices. POSTMASTER: Send address changes to The Journal of Heat Transfer, c/o THE AMERICAN SOCIETY OF MECHANICAL ENGINEERS, 22 Law Drive, Box 2300, Fairfield, NJ 07007-2300.
CHANGES OF ADDRESS must be received at Society headquarters seven weeks before they are to be effective. Please send old label and new address.
PRICES: To members, $24.00, annually; to nonmembers, $100.00.
Add $6.00 for postage to countries outside the United States and Canada.

STATEMENT from By-Laws. The Society shall not be responsible for statements or opinions advanced in papers or . . . printed in its publications (B7.1, para. 3).
COPYRIGHT © **1985** by the American Society of Mechanical Engineers. Reprints from this publication may be made on condition that full credit be given the TRANSACTIONS OF THE ASME, JOURNAL OF HEAT TRANSFER, and the author, and date of publication be stated.

INDEXED by the Engineering Index, Inc.

ANNOUNCEMENTS

TECHNICAL PAPERS

Downloaded 04 Feb 2011 to 194.85.80.107. Redistribution subject to ASME license or copyright; see http://www.asme.org/terms/Terms_Use.cfm

(Contents continued)

TECHNICAL NOTES

D. B. Moog
Graduate Student.

B. Rubinsky[1]
Associate Professor
Assoc. Mem. ASME

Department of Mechnical Engineering,
University of California,
Berkeley, Calif. 94720

An Analytical Model of Thermal and Vapor Diffusion in Freezing of Wet Coal

An analytical study is presented for the freezing of a semi-infinite domain of wet coal particles with special attention to the role of the airborne water vapor diffusion process. The results indicate that energy transport in this multiphase system can occur by means of thermal diffusion or mass diffusion. The magnitude of the Lewis number can be used to determine the mechanism. For a Lewis number smaller than 1, water vapor will evaporate from the coal particles, condense on the wall, and increase the freezing rate in the system.

Introduction

Transportation of coal in northern regions is significantly affected by the freezing of the coal in winter. The economical problems associated with the adherence of the frozen coal to the car in which it is transported and the difficulty in unloading the coal have generated worldwide interest and research on this phenomena [1-7].

After mining, coal, a porous material, has a significant water content which in certain types of coal can reach up to 45 percent by volume [2]. When loaded into railroad cars under severe weather conditions, the coal begins to freeze. The ice bonds coal particles to each other and to the walls. The frozen coal is usually removed by thawing in special thawing sheds. This process is expensive and time-consuming.

In an attempt to avoid the freezing of coal during transportation "freeze control agents," FCA's are sprayed on the coal before loading [8, 9]. FCA's are either glycol or oil based. They reduce the bonding strength of the ice by changing the solidification process. Unfortunately the FCA's have serious shortcomings in practice. Under severe weather conditions, the FCA can be ineffective [8-10]. The most important shortcoming is their ineffectiveness in preventing coal from adhering to the car sides [8, 11]. Consequently, research in coal freezing should include a focus on why wall adherence is so prevalent and how it might be combatted.

It was suggested [3] that ice accumulates near the car wall as a result of moisture diffusion and convection from the bulk of the car.

The present study proposed to model anaytically the freezing of a semi-infinite domain of wet coal particles with special attention to the role of the airborne water vapor diffusion process. The transport mechanism in this work involves only thermal diffusion, vapor diffusion, and phase change. The convection mechanism was not considered here.

A closed-form solution was obtained to the discussed problem using simplifying assumptions. Interesting results were obtained with respect to the mechanism of heat and mass transfer in this particular media. The analytical results indicate that during freezing the value of a modified Lewis number (Le = α/D) will determine the special thermophysical behavior of the system. It was originally thought that moisture from the bulk of the car would condense on the coal in the lower temperature regions adjacent to the car wall. Although this physical behavior can occur for a situation with a modified Lewis number larger than 1, in this problem, where the modified Lewis number is smaller than 1, moisture will actually evaporate from the moist coal in the vicinity of the car wall (including the frozen region) and condense only on the wall. This will, in effect, increase the freezing rate in the system.

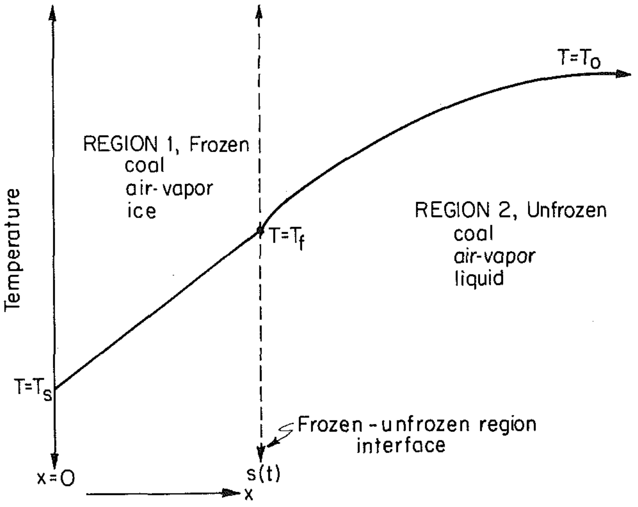

Fig. 1 Schematic of the temperature distribution in the semi-infinite domain

Analysis

The idealized problem is diagramed in Fig. 1. The coal-air-water system is approximated as a semi-infinite conglomerate of porous coal particles saturated with water and surrounded by air saturated with water vapor. The uniform initial temperature for the system is T_o. To initiate the freezing process, the outer surface temperature (at $x = 0$) is dropped to T_s, below freezing, at time $t = 0$ and held constant throughout the freezing process. Freezing of water in the porous coal particles begins immediately at the wall and progresses in the x-direction so that the problem is one-dimensional. The position of the interface between the frozen and unfrozen regions is designated $s(t)$. The air in the system is assumed to be saturated with vapor at all points at all times. This assumption should be easily met by the wet coal particles which have enough water to saturate the air and whose typical dimensions are on the order of several millimeters. Consequently, during the solidification process condensation on or evaporation from the coal particle will occur at all times according to the transient temperature distirbution in the system. Water vapor diffusion will also occur in the air according to the water vapor density gradient. The temperature at a large distance from the wall is the initial temperature T_o. To model this system, several simplifying assumptions were made:

---

[1] To whom correspondence should be addressed

Contributed by the Heat Transfer Division for publication in the JOURNAL OF HEAT TRANSFER. Manuscript received by the Heat Transfer Division January 30, 1984.

1 The medium is homogeneous and isotropic. Specifically, the coal particle sizes are considered small relative to the dimensions of interest.

2 The energy and mass transport mechanisms include evaporation/condensation, diffusion of water vapor, and of energy and freezing. There is, however, no convection of the gas (air/vapor mixture) in the analyzed system.

3 Constant thermophysical properties are assumed for the region with unfrozen water in the coal and for the region with frozen water in the coal. These properties were evaluated by averaging the gas, water/ice, and coal volume fractions in each region. In the averaging process it was assumed that the change in local water content due to evaporation/condensation has a negligible effect on the averaged thermal properties. This assumption will be confirmed by the results of the analysis.

4 The coal water matrix does not impede the water vapor diffusion in the air.

5 Any frozen condensate layer on the wall is thin and does not effect the system behavior including the assumption of a constant wall temperature throughout the freezing process. This assumption is later validated.

6 The air-water vapor mixture is in thermal equilibrium with the coal-water matrix at all points.

Two governing equations describe this system, one for the diffusion of water vapor in air and the other for the thermal diffusion in the system.

The vapor density, in terms of mass per unit system volume, may be written $\epsilon_g \rho_v$, where ϵ_g is the volume fraction of gas in the system and ρ_v is the vapor mass per unit volume of gas. At any point, the rate of change in vapor density equals the diffusion rate to that point minus/plus the local condensational evaporation

$$\frac{\partial \epsilon_g \rho_v}{\partial t} = D_j \frac{\partial^2 \epsilon_g \rho_v}{\partial x^2} - \Gamma_j \qquad j=1,2 \tag{1}$$

where j is one for the frozen region and two for the unfrozen region, while Γ is the mass condensation rate per unit volume (positive for condensation and negative for evaporation).

The change in internal energy at any point is equal to the diffusion rate to that point plus the rate of energy released/absorbed by vapor condensation/evaporation

$$\frac{\partial (\rho c)_j T_j}{\partial t} = k_j \frac{\partial^2 T_j}{\partial x^2} + h_j \bullet \Gamma_j \qquad j=1,2 \tag{2}$$

where h_j is the latent heat of evaporation (in region 1 from ice to vapor and in region 2 from liquid water to vapor).

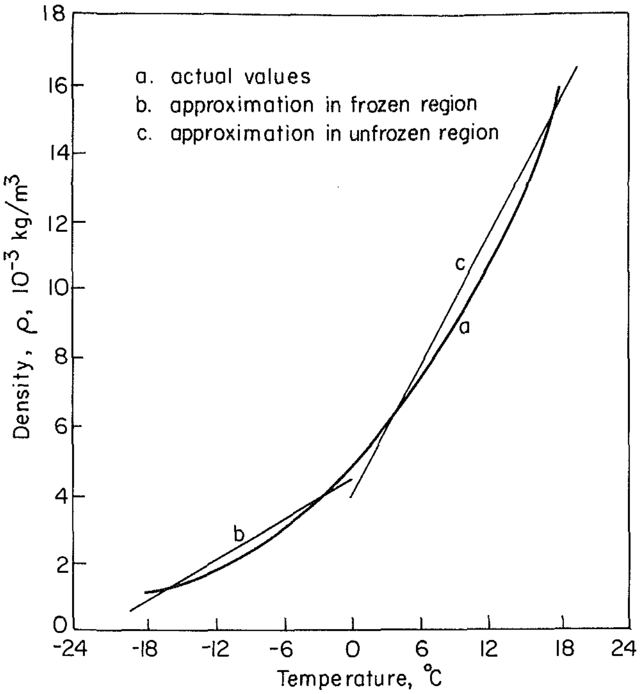

Fig. 2 Vapor density in air at saturation versus temperature

It was indicated previously that this analysis uses a single, constant volume averaged value for the thermal properties in each of the regions of discussion

$$(\rho c)_j = \epsilon_c (\rho c)_c + \epsilon_{L,I} + \epsilon_g (\rho c)_g \qquad j=1,2 \tag{3}$$

and

$$k_j = \epsilon_c k_c + \epsilon_{L,I} (\rho k c)_{L,I} + \epsilon_g k_g \qquad j=1,2$$

where the subscript c indicates coal, I and L indicates water in frozen or unfrozen states, respectively, and g indicates gas (air-vapor mixture). In the actual calculations the thermal properties of the air-vapor mixture were taken to be those of air.

The initial and boundary conditions in this problem are

$$T(0,t) = T_o; T(0,t) = T_s; T(s(t),t) = T_f; T(\infty,t) = T_o \tag{4}$$

The energy balance on the change of phase interface is given by

Nomenclature

a = correlation parameter (equation (7))
b = correlation parameter (equation (7))
c = specific heat, J/kg K
D = vapor diffusivity in air, m^2/s
D_{cn} = condensate thickness, m
h = latent heat of vaporization of ice vapor or water vapor, J/kg
k = thermal conductivity, W/mK
L = latent heat of fusion of water, J/kg
Le = Lewis number (α_j / D_j)
m'' = mass flux of vapor to wall, kg/m^{2s}
m_A'' = accumulated water mass at wall, kg
s = frozen region-unfrozen region interface position, m

t = time, s
T = temperature, K
t_{sx} = time at which the interface reaches distance x, s
x = distance from the wall, (x = 0 at the wall), m
α = thermal diffusivity, m^2/s
β = effective thermal diffusivity (equation (8)) m^2/s
γ = eigenvalue for Neumann solution (equation (12))
Γ = mass condensation rate per unit volume (negative for evaporation) (equations (13) and (14)), kg/m^{3}s
ϵ = volume fraction
ϕ = dimensionless parameter, (equation (26))

Subscripts

c = coal
f = change of phase interface
g = gas
I = ice
j = region (1 = frozen; 2 = unfrozen)
L = liquid water
L,I = either liquid water or ice, depending on region
L/I = water at the change of phase interface
o = initial
s = at the wall
V = vapor (water)
1 = region 1 (frozen)
2 = region 2 (unfrozen)
12 = region 1 value divided by region 2 value

$$k_1\frac{\partial T_1}{\partial x}-k_2\frac{\partial T_2}{\partial x}=\epsilon_L\rho_L\bullet L\bullet\frac{ds(t)}{dt}\ \text{on}\ x=s(t) \tag{5}$$

and with

$$s(0)=0 \tag{6}$$

From thermodynamic relations it is known that the vapor density in air, is uniquely determined at saturation by its temperature. This relation obtained from [12] can be seen plotted in Fig. 2. to facilitate the solution of this problem, a simplifying assumption was made, namely, that in the temperature range corresponding to the temperature in the frozen coal region and in the unfrozen coal region the saturation vapor density is linearly related to the temperature. Figure 2 compares the actual and the approximated vapor densities. The linear curves were obtained by a least-square fit in each of the temperature regions of interest. By this assumption, we write

$$\rho_{vj}=a_j+b_jT_j \qquad j=1,2 \tag{7}$$

where the value for j of 1 corresponds to the frozen region and that of 2 to the unfrozen region. The temperature in our correlation is in °C. This simplifying assumption facilitates a close form solution to the problem; it obviously effects the quantitative accuracy of the results. We consider the results important despite this simplifying assumption because they reveal an interesting physical behavior of the system. A sensitivity study on the effects of this assumption on the results will be presented later in the paper. Substituting equation (7) into equation (1) and combining it with equation (2) yields one single equation whose solution will give the temperature and vapor distribution in the system.

$$\frac{\partial T_j}{\partial t}=\beta_j\frac{\partial^2 T_i}{\partial x^2}; \qquad j=1,2 \tag{8}$$

where

$$\beta_j=\alpha_j\frac{\left(1+\dfrac{\epsilon_g b_j\bullet h_j}{(\rho c)_j}\dfrac{D_j}{\alpha_j}\right)}{\left(1+\dfrac{\epsilon_g b_j h_j}{(\rho c)_j}\right)}$$

The formulation of this problem as given by equation (8) and conditions (4) to (6) is essentially identical to the classic Newman problem. The only alteration is the replacement of thermal diffusivities α_j by new effective diffusivities β_j. The significance of this new diffusivity will be discussed later. Using the Newman similarity solution, we obtain

$$\frac{T_1-T_s}{T_f-T_s}=\frac{\operatorname{erf}\left(\dfrac{x}{2\sqrt{\beta_1 t}}\right)}{\operatorname{erf}\gamma}\ ; \quad 0\le x\le s(t) \tag{9}$$

$$\frac{T_o-T_2}{T_o-T_f}=\frac{\operatorname{erfc}\left(\dfrac{x}{2\sqrt{\beta_2 t}}\right)}{\operatorname{erfc}(\gamma\sqrt{\beta_{12}t})}\ s(t)\le x<\infty \tag{10}$$

where $\beta_{12}=\beta_1/\beta_2$, and

$$s(t)=2\gamma\sqrt{\beta_1 t} \tag{11}$$

where γ is an eigenvalue dependent upon the physical parameters and constants. It is given implicitly by

$$\frac{1}{\gamma\bullet e^{\gamma^2}\bullet\operatorname{erf}(\gamma)}-\frac{\sqrt{\beta_{12}}\bullet(T_o-T_f)}{(k_1/k_2)\bullet(T_f-T_s)\bullet\gamma\bullet\left(e^{\beta_{12}\cdot\gamma^2}\right)\operatorname{erfc}(\gamma\sqrt{\beta_{12}})}$$

$$=\frac{\epsilon_L\bullet L\bullet\sqrt{\pi}}{c_1\bullet(T_f-T_s)} \tag{12}$$

The evaporation/condensation at any point and time may be found by subtituting equations (9) and (10) into equation (2) resulting in

$$\Gamma_1=\frac{(T_f-T_s)k_1x}{2h_1\sqrt{\pi\beta_1t^3}\operatorname{erf}(\gamma)}\left[\frac{1}{\beta_1}-\frac{1}{\alpha_1}\right]\exp\left(-\frac{x^2}{4\beta_1 t}\right) \tag{13}$$

$$\Gamma_2=\frac{(T_o-T_f)x\,k_2}{2h_2\sqrt{\pi\beta_2t^3}\operatorname{erfc}(\gamma\sqrt{\beta_{12}})}\left[\frac{1}{\beta_2}-\frac{1}{\alpha_2}\right]\exp\left(-\frac{x^2}{4\beta_2 t}\right) \tag{14}$$

Setting $\partial\Gamma_i/\partial x=0$, one finds that the maximum Γ is located in the unfrozen region, at $x=\sqrt{2\beta_2 t}$.

Since there is a positive temperature gradient at the wall, there are both heat diffusion through it and vapor diffusion to it. The vapor density gradient at the wall is equal to $\partial\epsilon_g\rho_{v1}/\partial x|_{x=0}$. Therefore, the mass flux of vapor to the wall is given by

$$\dot{m}''=D_1\frac{\epsilon_g\rho_{v1}}{\partial x}\bigg|_{x=0} \tag{15}$$

Since the wall is impermeable, we must assume that the vapor condenses on the wall. At any time, the accumulated condensate has the mass

$$m''_A=\int_o^t D_1\frac{\partial\epsilon_g\rho_{v1}}{\partial x}\bigg|_{x=0}dt \tag{16}$$

Using equations (6) and (16), we obtain

$$m''_A=\frac{2\epsilon_g D_1(T_f-T_s)b_1t^{1/2}}{\sqrt{\pi\beta_1}\operatorname{erf}(\gamma)} \tag{17}$$

Though the condensate would form initially as frost, for evaluation purposes we will consider its density to be that of ice. Since it would displace the gas in the gas/coal system, the condensate layer would have thickness

$$D_{cn}=\frac{m''_A}{\rho_I\epsilon_g}=\frac{2D_1(T_f-T_s)b_1t^{1/2}}{\rho_I\sqrt{\pi\beta_1}\operatorname{erf}(\gamma)} \tag{18}$$

Since the condensate thickness has the same time dependence as the interface advance (equation (11)), the ratio between them is constant over time

$$\frac{D_{cn}}{s(t)}=\frac{D_1(T_f-T_s)b_1}{\rho_I\sqrt{\pi}\,\beta_1\gamma\operatorname{erf}(\gamma)} \tag{19}$$

This equation will allow a better assessment of the initial assumption that the condensate layer is thin relative to the thickness of the frozen region.

A particularly important assumption is that of constant thermal properties in the frozen and unfrozen regions. The evaporation/condensation of water will change the relative amounts of water and gas at any point. To find the change in liquid fraction, one may note that, at any specific point in the unfrozen region, the liquid volume fraction is given by the initial fraction plus/minus the net fraction of condensate/evaporate, added or removed

$$\epsilon_{L2}(x,t)=\epsilon_L(x,0)+\frac{1}{\rho_L}\int_0^t\Gamma_2(x,t)dt \tag{20}$$

where: $\epsilon_L(x,0)$ = initial liquid fraction
Using equation (14), we obtain

$$\epsilon_{L2}=\epsilon_L(x,0)+\frac{(T_0-T_f)k_2\left(\dfrac{1}{\beta_2}-\dfrac{1}{\alpha_2}\right)}{\rho_2h_2\operatorname{erfc}(\gamma\sqrt{\beta_{12}})}\operatorname{erfc}\left(\frac{x}{2\sqrt{\beta_2 t}}\right) \tag{21}$$

The liquid/ice fraction at the interface is of particular importance because it directly multiplies ds/dt in the interface condition, equation (5). Substituting equation (11) for $x=s$, into equation (21) yields

$$\epsilon_{Ll}(s,t)=\epsilon_L(x,0)+\frac{(T_o-T_f)k_2\left(\dfrac{1}{\beta_2}-\dfrac{1}{\alpha_2}\right)}{\rho_L h_2} \tag{22}$$

The water fraction at the interface is here seen to be constant over time.

In the frozen region, the ice fraction at any point is equal to the ice fraction at the interface, plus the net fraction of condensate added since the time at which the interface reached that point. That time may be designated t_{sx}, determinable from equation (11). Then the ice fraction is given by

$$\epsilon_{Il}(x,t)=\epsilon_L(x,t)+\frac{1}{\rho_L}\int_{t_{sx}}^{t}\Gamma_1(x,t)\,dt \tag{23}$$

where t_{sx} = time at which the interface reaches x.

Integrating equation (23), using equations (11) and (22), one obtains

$$\epsilon_{Il}(x,t)=\epsilon_{Ll}(s,t)+\frac{(T_f-T_s)k_1\left(\dfrac{1}{\beta_1}-\dfrac{1}{\alpha_1}\right)}{\rho_I h_1\,\mathrm{erf}(\gamma)}\,\mathrm{erfc}\left(\frac{x}{2\sqrt{\beta_1 t}}\right) \tag{24}$$

As shown in the following computations, the change in liquid/ice fraction is small, and may be ignored in the calculation of thermal properties, having a very small effect. For greatest accuracy, however, the analysis uses equation (22) for the water volume fraction at the interface in equation (12), since it is constant and depends only on physical properties and parameters. It may thus be determined independently, before its used in equation (12).

Results and Discussion

Even before obtaining numerical results, we may observe some important properties of the results, which are represented by equations (9-24).

It was previously noted that there is a vapor flux to the wall, since vapor density is directly proportional to temperature, which must decrease as the wall approached. Equations (13) and (14) provide an answer as to the origin of this vapor. The values of Γ_j are negative when $\beta_j > \alpha_j$, indicating evaporation. The condition $\beta_j > \alpha_j$ is met when and only when $D_j > \alpha_j$ (see equation (8)). This condition is found to be true for both regions. Thus evaporation occurs from both regions at all points and times, since vapor has a greater mass diffusivity in air than the thermal diffusivity of the system.

In this light, the assumption of proportionality to temperature makes the vapor density equivalent to thermal energy, but with a different specific heat and diffusivity. Thus the system has two forms of energy storage: vapor enthalpy and internal energy. Both are proportional to temperature. The system may transfer between the two forms at any point through evaporation or condensation. It favors the transport mode with the highest diffusivity. The system has an overall effective diffusivity for each region β_j, which balances the two (see equation (8)).

Another point of interest is obtained directly from equation (8). One finds that

$$\beta_j=\alpha_j\left(\frac{1+\phi_j/\mathrm{Le}_j}{1+\phi_j}\right)\qquad j=1,2 \tag{25}$$

The Lewis number Le_j is the ratio of diffusivities α_j/D_j and is of fundamental importance in determining the behavior of the system. The dimensionless parameter ϕ is the ratio of energy stored in vapor enthalpy to that stored as internal energy.

$$\phi_j=\frac{\epsilon_g b_j h_j}{(\rho c)_j}\qquad j=1,2 \tag{26}$$

Table 1 Thermophysical properties

		Specific Heat J/kg K	Thermal Conductivity W/mK	Density kg/m^3	Vapor Diffusivity in air, m^2/s	Phase Change Enthalpies J/kg	Slope of Density-Temperature Curve kg/m^3°C
1	coal	1,000	0.17	1,750.0			
2	gas in frozen region	1,003	0.0233	1.341	2.09×10^{-5}	$h_{vs} = 2.836 \times 10^6$	$b_1 = 1.94 \times 10^{-4}$
3	gas in unfrozen region	1,004	0.0248	1.242	2.36×10^{-5}	$h_{ve} = 2.466 \times 10^6$	$b_2 = 6.18 \times 10^{-4}$
4	ice	1,995	2.34	921.0		$h_{se} = 3.334 \times 10^5$	
5	water	4,180	0.602	998.2		$h_{se} = 3.334 \times 10^5$	

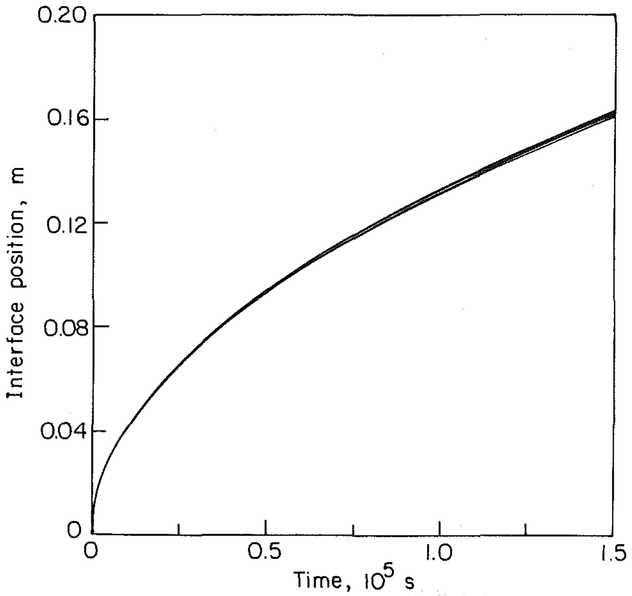

Fig. 3 Interface position versus time

The magnitude of Le_j determines whether evaporation or condensation occurs in region j. For $\mathrm{Le}_j < 1$ evaporation will occur in the system, which yields an increased equivalent thermal diffusivity. However, ϕ also affects the magnitude of the difference between α_j and β_j.

We may also note that for $D_j = \alpha_j$, or $\mathrm{Le}_j = 1$, we obtain $\beta_j = \alpha_j$. The problem is then identical to the Neumann problem, and the presence of vapor has no effect on the temperature distribution beyond its wall flux and accumulation.

The total energy flux at any point and time is

$$(D_j b_j h_j \epsilon_g+\alpha_j(\rho c)_j)\,\frac{dT_j}{dx}\qquad j=1,2 \tag{27}$$

The fraction in vapor enthalpy is

$$\frac{D_j b_j h_j \epsilon_g}{D_j b_j h_j \epsilon_j+\alpha_j(\rho c)_j}=\frac{\phi_j}{\phi_j+\mathrm{Le}_j}\qquad j=1,2 \tag{28}$$

The fraction in internal energy is

$$\frac{\mathrm{Le}_j}{\phi_j+\mathrm{Le}_j}\qquad j=1,2 \tag{29}$$

The ratio of energy flux in vapor enthalpy to that in internal energy is

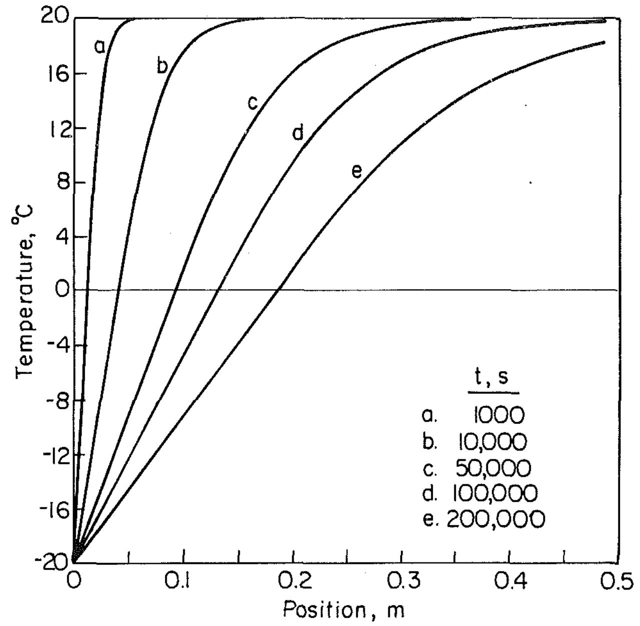

Fig. 4 Temperature distribution at different times

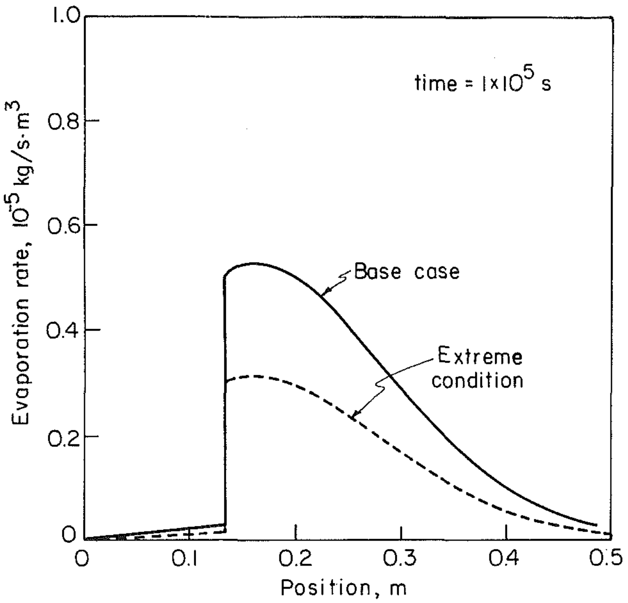

Fig. 6 Evaporation rate profiles

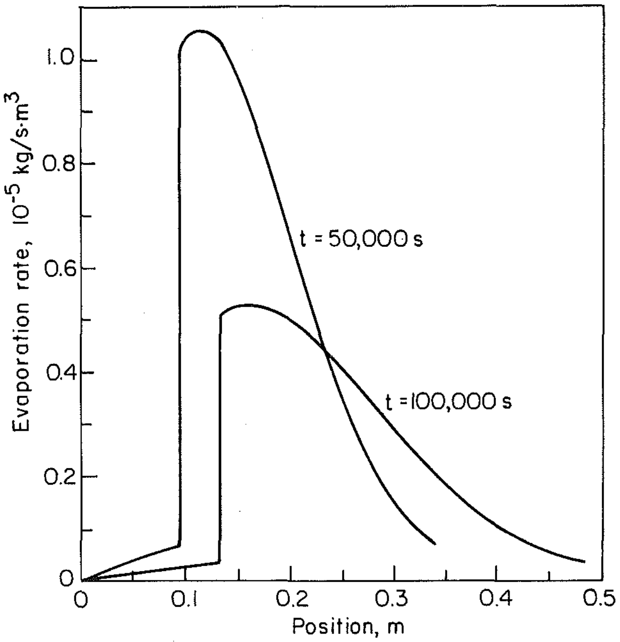

Fig. 5 Evaporation rate profiles

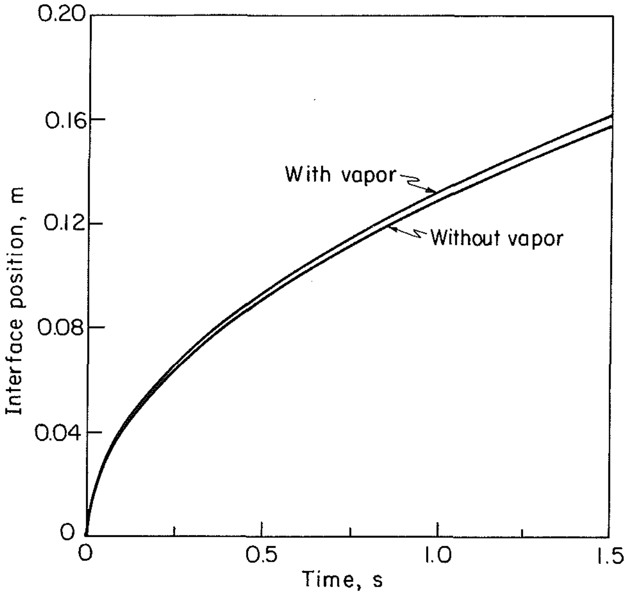

Fig. 7 Comparison of interface position, with or without vapor effect

$$\frac{\phi_j}{\mathrm{Le}_j}=\frac{D_j b_j h_j \epsilon_g}{\alpha_j(\rho c)_j}=\frac{D_j b_j h_j \epsilon_g}{k_j}\qquad j=1,2 \tag{30}$$

Numerical results may now shed more light on the system behavior. Evaluations are made with reference to a base case, which represents a typical case of coal freezing. The base case is defined by the following parameters

$$T_o=20°\mathrm{C}, T_s=-20°\mathrm{C}, T_f=0°\mathrm{C}, \epsilon_g=0.3, \epsilon_c=0.5, \epsilon_{L,l}=0.2$$

With the above constituent fractions, the coal is assumed to be 29 percent water by volume, 19 percent by weight. This water content is near the average range for transported coal, toward the high side (2). The bed has a void (gas) fraction of 30 percent.

The initial and boundary temperatures, T_o and T_s, will not vary greatly (e.g., more than 20°C) for any realistic model of coal freezing. It is reasonable then to use constant thermal property values for each constituent. These values, evaluated at −10°C (region 1) and 10°C (region 2), in order to represent average values for each region, are given in Table 1.

The approximate vapor density/temperature slopes, b_1 and b_2, vary with T_s and T_o, respectively. They represent the slopes of linear least-square correlations of the saturated vapor density over ice or liquid to the local temperature, shown in Fig. 2.

We may now check the accuracy of the approximations. In Fig. 3 the interface position s is solved as a function of time for varying values of b_1 and b_2. Five cases were analyzed. One is for the usual least-squares fit. Four are for cases in which the extreme high or low slope in each region (i.e., at a boundary) is used as b for that region. Figure 3 shows that the freezing rate is insensitive to the extreme variations in b, since the plots are to close to label.

The assumption of constant constituents may be checked by solving for the liquid fraction over time at the wall ($x = 0$ in equation (24)), where water fraction would be lower (neglecting the accumulation of vapor); and at the moving interface, where it is constant (equation (22)). For the base case, it is found that nowhere does the liquid fraction change

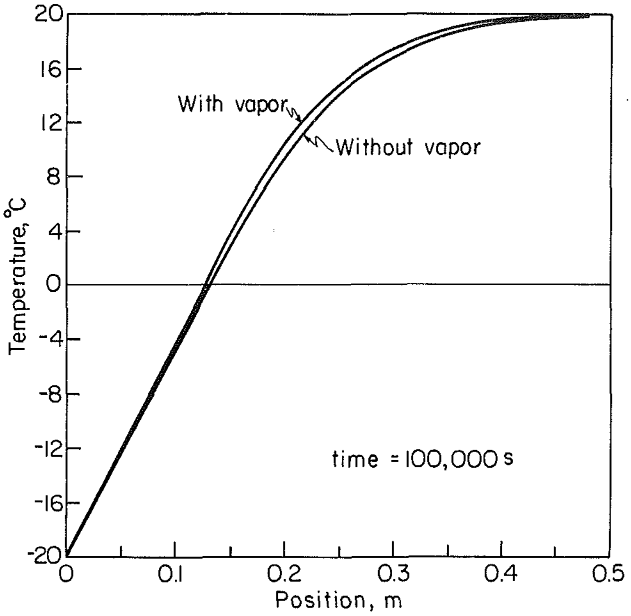

Fig. 8 Temperature distribution with or without vapor effect

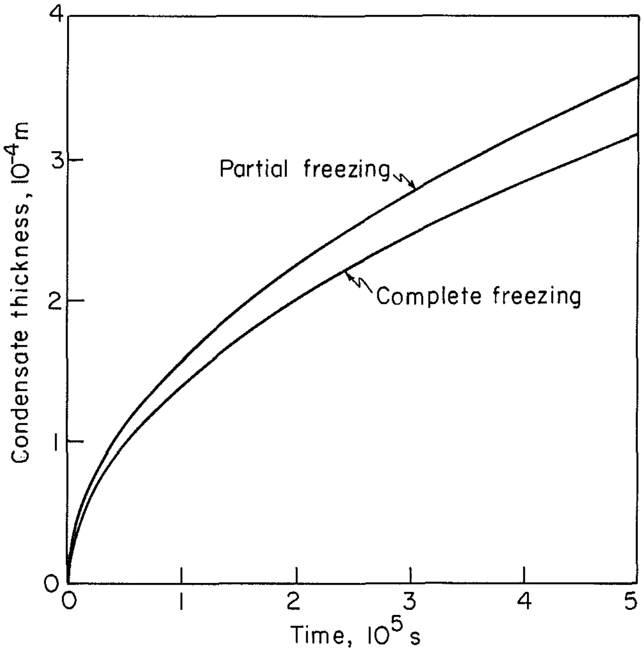

Fig. 9 Condensate thickness on the car wall as a function of time

(i.e., decrease) by more than 0.4 percent. This magnitude of change has no meaningful effect on regional effective property values or the interface condition. Thus the assumption of constant constituents is valid.

Figure 4 shows temperature profiles at different times for the base case. The interface is located at $T = 0°\mathrm{C}$. Like most conduction freezing problems, the temperature profile is virtually linear in the frozen region.

Figure 5 shows profiles for the evaporation rate from the frozen and the unfrozen region. Comparison to plots *c* and *d* in Fig. 3 show that the evaporation rate in the unfrozen regions falls off at the furthest "penetration" of the temperature profile. The large discontinuity at the interface results primarily from the frozen region's higher thermal diffusivity, which makes evaporation relatively less advantageous for energy transport. Essentially all evaporation comes from the unfrozen region rather than the frozen region. The maximum evaporation rate occurs near the interface.

To test the sensitivity of the results to the assumed linear temperature/vapor density correlation, an extreme case was analyzed in which the linear relation in the solid and liquid region was taken to be the same and equal to a line passing tangent to the accurate temperature/vapor density curve at a temperature of 0°C. The results for the evaporation rate, shown in Fig. 6, indicate a significant quantitative difference from the previous result, Fig. 5. The qualitative behavior is, however, similar, and we can conclude that the results will provide a reliable understanding for the physical behavior of this system. It should be noted that this sensitivity test was performed for an extreme case.

Of particular interest is the effect of vapor's presence on the freezing rate, demonstrated for the base case in Fig. 7. Results for a case without vapor transport may be calculated simply by setting $\beta_j = \alpha_j$. Figure 7 shows that the presence of vapor speeds freezing by enhancing heat transfer.

Figure 8 demonstrates the difference in temperature profiles with and without vapor transport.

We are also interested in the condensation of vapor on the wall. As noted, the condensate thickness on the wall is a constant fraction of the interface distance for a given freezing case. The calculated fraction for the base case is very small—equal to 1.064×10^{-3} for ice formation. In view of this result, the assumption of a thin ice layer near the wall appears to be justified even if the density of the frost layer is taken to be smaller by one order of magnitude than that of ice. While vapor contributes to the energy transport, the actual mass transport is very small because of the high enthalpy associated with the water vapor. Calculations indicate that for this base case the condensate layer reaches a thickness of 3 mm in 4 to 6 days. These results seem to indicate that moisture transport by diffusion alone cannot be responsible for the accumulation of ice near the wall of the cars.

Recent experiments by Oosthuizen and Sears [6] have suggested that under certain circumstances the liquid in the coal might not completely freeze. Calculations were performed for a similar problem to that discussed here in which only 10 percent of the water in the coal freezes. The results indicate that in this latter case the ratio D_{cn}/s increases from 1.064×10^{-3} to 1.399×10^{-3}. However, the frozen condensate thickness on the wall is still (as shown in Fig. 9) small, and unlikely to account for wall adherence.

The important question is whether this result rules out the possibility that vapor transport by diffusion to and freezing at the wall contribute to wall adherence of the coal. The foregoing analysis argues strongly that vapor diffusion in response to thermal gradients is unlikely to cause the wall adherence problem. Obviously, for a better understanding of this complex system further work has to be done to investigate the effects of convection in the coal load and those of condensation on the wall.

Conclusions

The preceding analysis provides an exact solution to an approximate model of the coal freezing process. There are four major deviations in the model from an actual case: (*i*) constant wall temperature, (*ii*) semi-infinite medium, (*iii*) isotropy, and (*iv*) absence of any liquid motion or bulk gas motion. The first three deviations probably do not invalidate the qualitative conclusions of this work. However, the presence of fluid motion could greatly change the mechanisms of heat and mass transfer. Thus this model must be considered as representing part of the physics of coal freezing (heat and vapor diffusion), and only tentatively as modeling the whole process.

The physical behavior of the analyzed system is, however, of fundamental interest. The results indicate that energy transport in this multiphase system can occur by means of thermal diffusion or mass diffusion. The magnitude of the

Lewis number can be used to determine the actual mechanism. In this case it was found that for a Lewis number smaller than 1, water vapor will evaporate thoughout the conglomerate of particles and condense only on the wall of the car. This process will increase the solidification rate in the conglomerate of wet coal particles. Calculations have shown, however, that the amount of vapor diffusion to the wall is very small, and probably contributes little to any increased bonding of the frozen coal near the wall. Partial freezing of water in the coal will cause a small increase in vapor accumulation at the wall.

Acknowledgment

We would like to thank Professor D. W. Fuerstenau for the interest he expressed in this study and the continuing support through the Office of Surface Mining with the U.S. Department of the Interior, and the Mining and Mineral Resources and Research Institute at the University of California, Berkeley.

References

1 Colijn, H., "Field Survey of Freezing Problems, "Canadian Institute of Guided Ground Transport, Report 76/12, 1976.

2 *1979 Keystone Coal Industry Manual*, McGraw-Hill, New York, 1979.

3 1980 National Conference and Workshop on Coal Freezing, EPRI, Study Project WS-80-119, December 1980.

4 Yefinov, S. S., and Nikitina, L. M., "Experimental Study of Moisture Transfer in Bulk Coal Subject to Freezing," *Heat Transfer—Soviet Research*, Vol. 10, Mar.-Apr. 1978.

5 Oosthuizen, P. H., "Development of a Computer Model and Experimental Study of Coal Freezing During Rail Transportation," Report 16GT 78110, Canadian Institute of Guided Ground Transport, Kingston, Ontario, 1978.

6 Oosthuizen, P. H., and Sears, D. E., "The Freezing of Moist Coal," ASME Paper 83-HT-22, 1983.

7 Raymond, J. F., and Rubinsky, B., "A Numerical Study of the Thawing Process of a Frozen Coal Particle," ASME JOURNAL OF HEAT TRANSFER, Vol. 205, 1983, pp. 197-200.

8 Holtz, M. A., and Cox, H. B., "Overview in the Use of Freeze Conditioning Agents," *Coal Utilization (Frozen Coal)*, SME-AIME Mining Symposium, Fall Meeting, Minneapolis, Minn., Oct. 1980.

9 Glanville, J. O., and Leighton, H. H., "The Physical Chemistry of Frozen Coal," *Coal Utilization (Frozen Coal)*, 1980.

10 Rosenberg, N. I., "Reducing the Frozen Coal Problem to Manageable Proportions," *Coal Utilization (Frozen Coal)*, 1980.

11 Mitzel, J. D., "Frozen Coal—Problems and Solutions," *Coal Utilization (Frozen Coal)*, 1980.

12 *ASHRAE Handbook, 1981 Fundamentals*, ASHRAE, New York.

B. Dorri

A. F. Emery
Fellow ASME

P. C. Malte
Mem. ASME

Department of Mechanical Engineering,
University of Washington,
Seattle, Wash. 98195

Drying Rate of Wood Particles With Longitudinal Mass Transfer

The drying of small wood particles of shape L:W:t = 3 to 5:2:1 is examined by three numerical models, and results are compared to measurements. (i) *A one-dimensional rectangular model has liquid water concentrated in the center of a particle, and this is removed as an evaporation front propagates into the liquid.* (ii) *The one-dimensional model is also treated by the volume-averaged, or "smeared" approach, for which the moisture at any point is a distribution of liquid and vapor. For the simple rectangular geometry, the frontal and smeared models give similar results.* (iii) *Equivalent spherical particles are analyzed by a smeared model which includes capillarity. Reasonable agreement is obtained between the spherical results and the measurements, though an overprediction in drying rate occurs for slender particles.*

Introduction

The ability to predict the drying rate of small wood particles is of importance to the operation of process dryers and wood waste furnaces used in the forest products industry. It is important to operate process dryers with particle drying rates that lead to minimum dryer energy consumption and capital cost, and that produce high quality dried products. In wood waste furnaces, the rate of drying of the particles influences fuel ignition and particulate emissions.

Over several years, a research program has been conducted to measure and predict the drying rate of small wood particles, and these experimental results are described by Malte et al. [1-3]. Douglas fir sawdusts of three sizes, with average particle lengths of $L = 3.4$, 2.1, and 1.75 mm, have been treated experimentally. The respective volume-equivalent spherical diameters are 2.5, 1.4, and 0.7 mm, and the nominal shapes are $L:W:t = 3:2:1$ for the two largest sizes, and 5:2:1 for the smallest size.

In this paper, the theoretical/numerical modeling of the drying of such sawdust particles is treated, and results are presented for one-dimensional rectangular, or planar models, and for a spherically symmetric model.

The planar models have been developed to compare two distinctly different modeling approaches: (*i*) the frontal, or two-regime approach, in which drying occurs as an evaporation front propagates into the free liquid water, which is assumed to be concentrated in the center of the particle; and (*ii*) the "smeared" approach, in which the initial moisture in the particle is assumed to be a uniform distribution of free and bound water, and water vapor. For small particles, the smeared approach, which corresponds to volume-averaging over the fine structure of the wood (e.g., see [4]), is open to question, though it is numerically less complex. Therefore, we have chosen to compare the frontal and smeared approaches for the simple geometry of a rectangular box particle in which internal heat and mass transfer are restricted to the direction along the particle length.

In order to effectively account for heat transfer in all directions and, therefore, to compare predictions of drying rate to experimental results, the spherical model has been developed. This is based on the smeared approach, and includes the effect of capillarity.

Our theoretical/numerical treatment is restricted to "chunky" wood particles with lengths in the grain direction that are approximately equal to or less than the characteristic trachied length for softwood (3.5 mm, [5]). In this case, the internal transfer of moisture does not meet great resistance, and the controlling internal transfer mechanism is the diffusion of heat. This is not to say, however, that the internal mass transfer can be eliminated from the problem, since the weakening of capillary flow of liquid to the particle surface as drying progresses is the mechanism which "turns on" the internal diffusion of heat.

Experimental Summary

A thorough description of the experimental system and results is given by Malte et al. [1-3]. Wood particles of moisture content M of 2 to 140 percent (dry basis) were carried upward in a tube and dried. The temperature of the conveying, vitiated air was 400 to 750 K. The particles traveled essentially at equilibrium velocity, and were heated predominately by convection. The ratio of drying tube diameter to characteristic particle diameter was 70, and particle-to-particle spacing was about 20 particle diameters.

The gas humidity was low, and thus, was not a significant independent variable, though it was the quantity measured to determine the drying rate. For steady-state operation of the drying tube, gas humidity was measured at intervals along the tube. The increase in gas humidity, in conjunction with knowledge of the inlet gas and wood flow rates, inlet wood moisture content, and the local particle velocity, allowed the local particle bulk moisture content and drying rate dM/dt to be determined. Local gas temperature was also measured.

For each particle size range, the results have been found to agree with the following empirical formula [3]

$$dM/dt = a(1 - \exp(-bM)) \qquad (1)$$

where in the limit of large M, external heat transfer controlled drying, i.e., $dM/dt = a$, is obtained, where $a = a(T)$, and in the limit of small M, internal controlled falling rate drying, i.e., $dM/dt = (ab)M$, is obtained. In this formulation, the parameter a represents the particle heating rate per unit dry mass and b represents the reciprocal of an overall Biot number. The uncertainty in the empirical drying rate is ±30 percent for large M, and ±60 percent for small M.

Physical Model

A small wood particle is a porous capillary structure that contains tracheids and pit openings (Fig. 1). In the present application, the long dimension of the particle, its length, corresponds to the longitudinal or grain direction in Fig. 1. The tangential and radial directions of the wood, as in Fig. 1, are not used explicitly in our study. Rather, the transverse direction refers generally to the direction normal to the grain, and thickness is the minimum transverse dimension of a rectangular particle.

Contributed by the Heat Transfer Division for publication in the JOURNAL OF HEAT TRANSFER. Manuscript received by the Heat Transfer Division August 1, 1983.

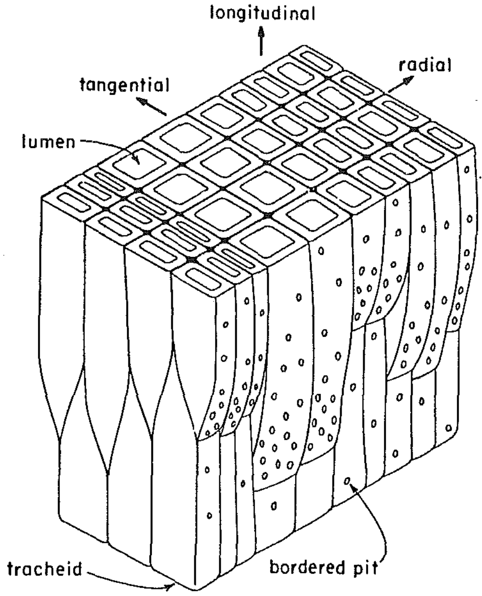

Fig. 1 Wood structure

One process of drying consists of moisture transfer within the particle to its surface, followed by moisture evaporation and removal at the surface due, respectively, to external convective heat and mass transfer. The internal mass transfer in this case is capillary flow of liquid. Gas pressure driven liquid flow can also occur, for example, especially for a thin particle for which internal gas bubbles can become heated while significant liquid still exists in the particle. A second process of drying, which becomes important as the moisture content decreases, consists of (*a*) heat diffusion into the particle, (*b*) local vaporization of free- and bound-liquid water, and (*c*) subsequent mass transfer of the vapor to the particle surface by diffusion and by gas pressure driven flow. A third process of drying, which occurs at low moisture contents, consists of bound water diffusion in the cell walls, though because of the "chunky" particle structures involved, this is not thought to be important in the present application.

The driving force for the internal vapor diffusion and gas pressure driven flow is the diffusion of heat into the particle with a consequent increase in the vapor and total pressures. This heat transfer is complicated by internal convection of heat which can proceed in the opposite direction.

The presence of moisture in the form of vapor, free-liquid, and bound water implies that only certain thermodynamic states exist. In this regard, it is presumed that changes occur slowly enough that local thermodynamic equilibrium exists. If free water is present, the local temperature is the saturation temperature, and if free water is not present, the local temperature is not the saturation temperature, and the desorption isotherms for the wood must be applied locally in order to interrelate the vapor pressure, moisture content, and temperature. In this regard, the wood particle may be divided into two types of regimes. In the first, the free-water regime, the moisture appears as free water in the lumen and as bound water in the cell walls. No water vapor is present, and this regime is associated with the tapered ends of the lumen. In the other regime, the bound water regime, the moisture is present as bound water in the cell walls and as a small mass of water vapor in the lumen. An interface or front separates these two regimes, and this front moves during drying. Within a single particle, any number of regimes and interfaces may exist, though this should be correlated with the number of tapered lumen ends. In the modeling of large pieces of wood, it is possible to volume-average over many regimes, thereby giving a numerical volume element that has associated with it a definite mixture of bound and free water, and water vapor [4]. This "smeared" concept is also used in our particle drying model, and though (for the spherical particle) it gives reasonable agreement with our experimental results, the smeared concept is obviously fundamentally questionable for application to small wood particles.

The physical model used for the capillary flow is the following. Given a local moisture gradient in the particle and the presumed presence of a tapered lumen end, as in the Comstock model [5], the amount of water on each side of the tapered lumen end is assigned. The respective liquid quantities correspond to respective radii of the gas–liquid interfaces on each side of the tapered lumen end. The difference in these radii determines the capillary pressure. Finally, the effective capillary flow is determined by assigning a liquid permeability and a probability of occurrence of a tapered lumen end at a point in the particle. This probability is based on the size of the structure of nominal softwood. Details are provided elsewhere [6].

Nomenclature

a = empirical drying rate parameter, constant-rate drying rate
A = spherical surface area element
b = empirical drying rate parameter, reciprocal of overall Biot number
c = particle center
C = specific heat of wet wood
D = gas-phase binary diffusion coefficient
F = liquid mass flux
h = external convective film coefficient, no subscript denotes heat transfer
k = coefficient of thermal conductivity for wet wood
K = permeability, no subscript denotes gas permeability
L = particle length, long dimension with grain
M = moisture content, mass of water to mass of bone dry wood
P = pressure, no subscript denotes total gas pressure
Q_L = differential heat of sorption of bound water
Q_o = latent heat of vaporization
r = spherical radial direction; also radius of liquid meniscui
R = individual gas constant, no subscript denotes total gas; also radius of lumen
s = position of front
t = time; also particle thickness
T = temperature
V = spherical volume element
W = particle width
x = longitudinal direction
Δr = thickness of spherical shell
γ = surface tension
ϕ = porosity of wood
ρ = mass density, no subscript denotes wet wood

Subscripts

c = capillarity
d = dry wood
F = free water
FS = saturation free-water
m = mass transfer convective film coefficient
p = moisture phase change
sat = saturated vapor
v = water vapor
w = liquid water
∞ = free stream

Superscripts

I = bound-water regime
II = free-water regime

Structural and Numerical Considerations. The one-dimensional rectangular, or planar, particle structure is assumed in order to compare the two-regime approach with the smeared approach. This particle is represented simply as a bundle of tubes (i.e., lumen) of constant diameter running in the grain direction. Since there are no tapered lumen ends in this assumed structure, there is no capillary flow. For the two-regime approach, the liquid, or free water, is assumed to be concentrated in the center of the particle, and the evaporation front progresses into this. The surrounding region is a bound-water regime. This structure is represented by the fixed and moving nodal points shown in Fig. 2. The evaporation front, which may also be regarded as a condensation front, at which discontinuities in the variables or their gradients exist, is necessarily one node. But since the front moves, large changes in the variables are expected whenever it passes a spatially fixed node. In order to reduce these effects, a series of moving nodes, centered about the frontal node is used. This set of nodes always overlaps those spatially fixed nodes which are in the vicinity of the front. Interpolation and extrapolation are used to find the values of the variables at the extremities of the moving array and also at the two stationary nodes located on either side of the frontal node.

Although the moving nodes permit an accurate determination of the interface, they substantially increase the complexity of the solution so that it is very difficult to apply the technique to a multiregime wood particle. The smeared model, with its spatially fixed nodes, is simpler and more efficient. In this case, however, there is a spatially varying amount of free water with a consequent smearing of the interfaces and some loss of definition of the detailed drying process. In order to compare the theoretical/numerical results to the empirical results, a one-dimensional spherical smeared model is used. This allows a better simulation of heat transfer in the wood particle than is provided by the one-dimensional rectangular structure, and it permits capillary flow to be studied.

Mathematical Model

The equations for water mass balance, total material balance, energy balance, desorption isotherms, saturation vapor pressure, Darcy flow, Fickian diffusion, and capillary flow form a set of coupled nonlinear partial differential equations with different parameters and boundary conditions. Below, the equations are shown for the two-regime approach, and for the smeared approach for the spherical particle.

Free-Water Regime. An energy balance in this regime can be expressed by the general transient heat conduction equation

$$\rho^{\mathrm{II}} C^{\mathrm{II}} \frac{\partial T^{\mathrm{II}}}{\partial t} = k^{\mathrm{II}} \frac{\partial^2 T^{\mathrm{II}}}{\partial x^2} \tag{2}$$

The boundary conditions for temperature are expressed

$$x = s: \qquad T^{\mathrm{I}} = T^{\mathrm{II}} \tag{3}$$

$$x = c: \qquad k^{\mathrm{II}} \frac{\partial T^{\mathrm{II}}}{\partial x} = 0 \tag{4}$$

Bound-Water Regime. An energy balance in this regime is written as follows

$$\rho^{\mathrm{I}} C^{\mathrm{I}} \frac{\partial T^{\mathrm{I}}}{\partial t} = k^{\mathrm{I}} \frac{\partial^2 T^{\mathrm{I}}}{\partial x^2} + (Q_o + Q_L)\,\rho_d \frac{\partial M}{\partial t} \tag{5}$$

where heat convection has been neglected because it is found to be of negligible importance. The moisture content in these equations is the local value, not the bulk value as used earlier in the paper.

At the particle surface the boundary condition is

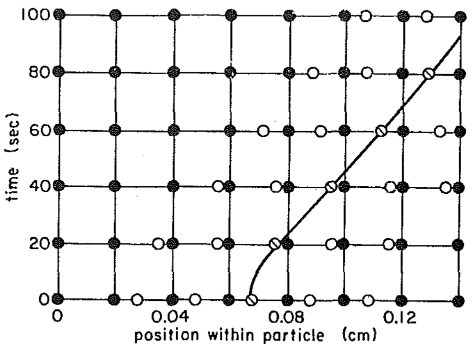

Fig. 2 Nodal system and front position: fixed nodes (●); moving nodes (○); interface nodes (⊘)

$$x = 0: \qquad k^{\mathrm{I}} \frac{\partial T^{\mathrm{I}}}{\partial x} = h(T^{\mathrm{I}} - T_\infty) \tag{6}$$

and at the interface it is:

$$x = s: \qquad k^{\mathrm{I}} \frac{\partial T^{\mathrm{I}}}{\partial x} - k^{\mathrm{II}} \frac{\partial T^{\mathrm{II}}}{\partial x} = \phi \rho_w Q_o \frac{\partial s}{\partial t} \tag{7}$$

where the partial differential term on the right-hand side of the equation represents the velocity of the interface.

The total gas material balance, assuming Darcy flow and perfect gas behavior, is

$$K \frac{\partial}{\partial x}\left[\frac{P}{RT^{\mathrm{I}}} \frac{\partial P}{\partial x}\right] - \frac{1}{\phi} \rho_d \frac{\partial M}{\partial t} = \frac{\partial}{\partial t}\left[\frac{P}{RT^{\mathrm{I}}}\right] \tag{8}$$

It should be noted that since liquid flow is not part of this model, the rate of loss of moisture content is exactly equal to the local vapor generation rate. Furthermore, the permeability K is proportional to the effective cross-sectional flow radius raised to the fourth power and divided by the fluid viscosity. The units of permeability are m^3 (fluid)/m-kPa-s. The boundary conditions are

$$x = 0: \qquad P = P_\infty \tag{9}$$

$$x = s: \qquad -K \frac{P}{RT^{\mathrm{I}}} \frac{\partial P}{\partial x} + \phi \rho_w \frac{\partial s}{\partial t} = 0 \tag{10}$$

Likewise, the material balance for the water vapor, with Fickian diffusion of vapor included, gives the equation

$$\frac{\partial}{\partial x}\left[\frac{1}{R_v T^{\mathrm{I}}}\left(D \frac{\partial P_v}{\partial x} + K P_v \frac{\partial P}{\partial x}\right)\right] - \frac{1}{\phi} \rho_d \frac{\partial M}{\partial t} = \frac{\partial}{\partial t}\left[\frac{P_v}{R_v T^{\mathrm{I}}}\right] \tag{11}$$

The boundary conditions are

$$x = 0: \quad -K \frac{P_v}{R_v T^{\mathrm{I}}} \frac{\partial P}{\partial x} - \frac{D}{R_v T^{\mathrm{I}}} \frac{\partial P_v}{\partial x} = \frac{h_m}{R_v T^{\mathrm{I}}} (P_v - P_\infty) \tag{12}$$

$$x = s: \quad -K \frac{P_v}{R_v T^{\mathrm{I}}} \frac{\partial P}{\partial x} - \frac{D}{R_v T^{\mathrm{I}}} \frac{\partial P_v}{\partial x} + \phi \rho_w \frac{\partial s}{\partial t} = 0 \tag{13}$$

The local desorption isotherms describe the local moisture content in the bound-water regime in terms of the local relative humidity and the local temperature. An equation suggested by Stamm [7] has been fitted to the desorption isotherms for Sitka spruce, with the result that

$$M = 10^{(0.0031 - 0.0022 T^{\mathrm{I}})} (P_v / P_{\mathrm{sat}})^{(0.3131 + 0.0026 T^{\mathrm{I}})} \tag{14}$$

The saturation vapor pressure is computed from the standard thermodynamic information on free water.

At the interface between the two regimes, saturated conditions exist. Also, because the characteristic lumen radius is 10 μm [5], the effect of surface tension on the saturated vapor pressure and latent heat of vaporization is negligibly small [8].

In the equations for the two-regime model, the thermal conductivity is the value for the longitudinal direction of the wood [5]. In this regard, $k = k(M)$, and therefore, for the free-water regime, k is determined as the value corresponding to completely wet conditions.

Likewise, the gas permeability K is for the longitudinal direction [5]. The diffusion coefficient D is the binary, air-water vapor diffusion coefficient [5], and the differential heat of sorption of bound water Q_L is a function of moisture content as is the heat capacity C of the wood [5].

Smeared Models. The equations used to model the rectangular particle by the smeared approach are the same equations as given for the bound water regime, i.e., equations (5, 8, 11, 14) and the saturation vapor pressure relationship. That is, liquid flow due to capillarity is omitted because of the constant diameter flow cross section, and liquid flow due to gas pressure gradients is neglected in order to compare the two-regime and smeared models with the same transport mechanisms. Of course, the boundary conditions are changed to reflect the symmetry at the center of the particle rather than the conditions at the front. For the spherical particle, the smeared model is set up to include transport of heat and vapor by gradient diffusion, and transport of liquid by capillarity. The energy balance, again neglecting convection, now takes the form

$$\frac{\partial}{\partial r}\left[kA\frac{\partial T}{\partial r}\right] = -(Q_o + Q_L)\rho_d \frac{V}{\Delta r}\frac{\partial M_p}{\partial t} + \rho C\frac{V}{\Delta r}\frac{\partial T}{\partial t} \qquad (15)$$

And the vapor material balance is given by the equation

$$\frac{\partial}{\partial r}\left[\frac{D}{R_v T}A\frac{\partial P_v}{\partial r}\right] = \frac{1}{\phi}\frac{V}{\Delta r}\frac{\partial M_p}{\partial t} + \frac{V}{\Delta r}\frac{\partial}{\partial t}\left[\frac{P_v}{R_v T}\right] \qquad (16)$$

In this model, because the moisture content at a location can change due to both vaporization and liquid flow, a distinction must be made between these two phenomena. The subscript p on M_p represents the change (loss) of moisture content, or generation of vapor due to phase change.

Darcy's law is used to represent the capillary flow of liquid. That is, the mass flux (kg/m^2-s) of liquid is written

$$F = -\rho_w K_w \frac{\partial P_c}{\partial x} \qquad (17)$$

where K_w is now the liquid permeability and P_c is the capillary pressure, which is defined in terms of the surface tension and the radius of the meniscui

$$P_c = -\frac{2\gamma}{r} \qquad (18)$$

The radius r is a function of the capillary structure within the particle as well as the amount of the liquid water present in the capillaries. The capillary structures in the wood are the tapered ends of the lumen and the pit pores which are concentrated in the tapered ends. The radius r can be described as

$$r = R\left[\frac{M_F}{M_{FS}}\right]^{1/3} \qquad (19)$$

where M_F is the local free water content, M_{FS} is the saturation free-water content, and R is the radius of the lumen. Substitution into equation (17) gives

$$F = -\frac{2}{3}\rho_w K_w \gamma \frac{M_{FS}^{1/3}}{R}(M_F^{-4/3})\frac{\partial M_F}{\partial x} \qquad (20)$$

If the coefficient of the partial differential is defined to be K_c, the capillary conductivity, then the liquid balance can be written as

$$\frac{\partial}{\partial r}\left[K_c A\frac{\partial M_F}{\partial r}\right] = \frac{V}{\Delta r}\left[\frac{\partial M}{\partial t} - \frac{\partial M_p}{\partial t}\right] \qquad (21)$$

The transport properties for the spherical model are set as follows. The coefficient of thermal conductivity for the wet wood is taken from Siau [5] for the transverse direction. This depends upon the local moisture content and upon the porosity of the wood. The resultant expression is $k = k(M)$. (The longitudinal thermal conductivity used in the rectangular model is 2.5 times the transverse conductivity.) The permeability also follows from Siau [5]: $K = 3.62 \times 10^2\ r^4/\mu$, where μ is the appropriate fluid (gas or liquid) viscosity. For the spherical model, only liquid flow is considered, and the effective radius is determined by equation (19). The value of r can vary between 0.01 and 4 μm, depending upon the wood species. Stamm [7] gives a value of 0.05 μm for Douglas fir, but since longitudinal flow is important in our modeling, a larger effective radius, or pore size, is used, i.e., r = 0, 0.4, and 1.0 μm in our analysis.

Numerical Method. As discussed above, and as indicated in Fig. 2, the two-regime numerical solution involves 8 spatially fixed nodes and 5 moving nodes. The smeared spherical model involves 10 nodes equally spaced along the radius of the sphere. Each model involves discretization of the system of nonlinear partial differential equations using an implicit finite difference technique. The resultant systems of algebraic equations are solved using direct inversion, along with an iterative method to account for the nonlinearities. In the case of the two-regime approach, the position of the interface adds an additional dependent variable to the system.

Results and Discussion

Rectangular Particle. Results are shown for the two-regime frontal model applied to a particle of length 0.28 cm with an initial bulk moisture content of 77 percent (dry basis). The convective film coefficient corresponds to the situation of a (volume-equivalent spherical) particle being heated in a gas stream that has a relative velocity of 2 m per s and a temperature of 600 K. The initial position of the front corresponding to 77 percent moisture content is 0.068 cm from the particle surface (see Fig. 2). The results have been calculated for every 2.1 s and are plotted in Figs. 3 and 4. Only one-half of the particle is shown, since it is symmetric. The instantaneous location of the front is indicated in Fig. 2. During the early stage of drying, small amounts of water vapor diffuse into the particle due to higher vapor generation rate at the surface. This causes some condensation of water on the interface. After the first few seconds, the front begins to move inward with an almost constant speed until the center of the particle is reached. Vapor pressure and total pressure gradients are the driving forces, respectively, for diffusion and flow which remove the water vapor from the particle. Figure 3 shows the local moisture content at six different times. The surface is nearly completely dried in the early stage of the process, and this results in a relatively steep moisture gradient existing between the particle surface and the front until the free water vanishes. In Fig. 4, the corresponding local temperatures are shown, and these plots indicate a continually increasing temperature in the bound-water regime of the particle. The bound-water regime has a substantial temperature gradient but this gradient remains relatively constant until the free water vanishes, implying a nearly constant rate of drying.

Results for the smeared model applied to this particle are shown in Fig. 5. This same particle with the same external conditions has a behavior very similar to that predicted by the two-regime approach (Fig. 3). Figure 5 shows the local moisture content within the particle at six different times. Even though the explicit frontal model is not implemented for this case, the results, nonetheless, indicate the existence of a moving front.

The instantaneous drying rate versus the instantaneous bulk moisture content of the particle is plotted in Fig. 6 for the two-regime and smeared models. Comparable results are

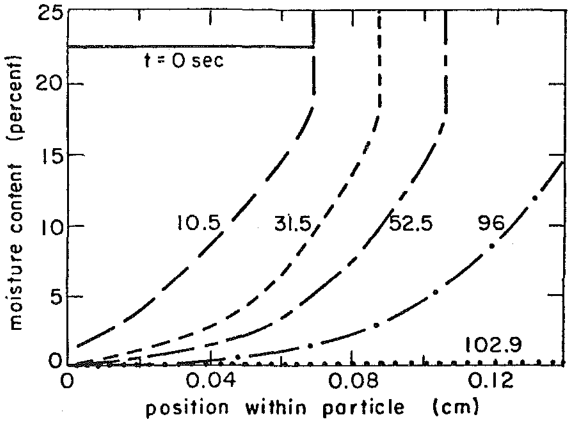

Fig. 3 Moisture profile for frontal model

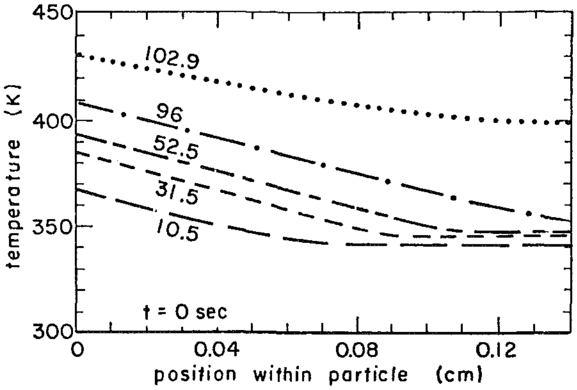

Fig. 4 Temperature profile for frontal model

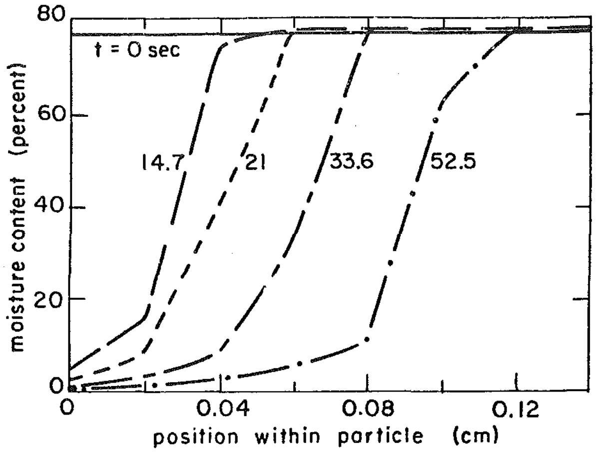

Fig. 5 Moisture profile for smeared model

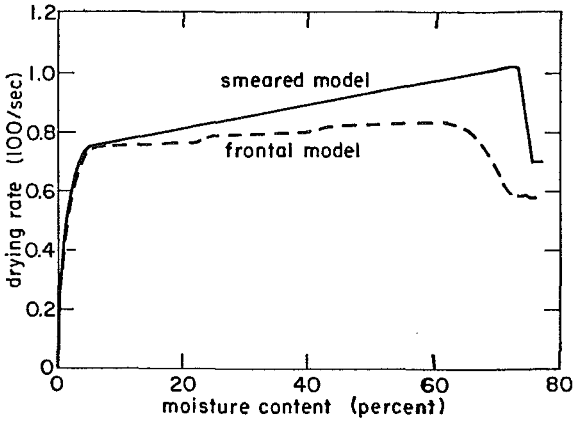

Fig. 6 Drying rate for one-dimensional planar models

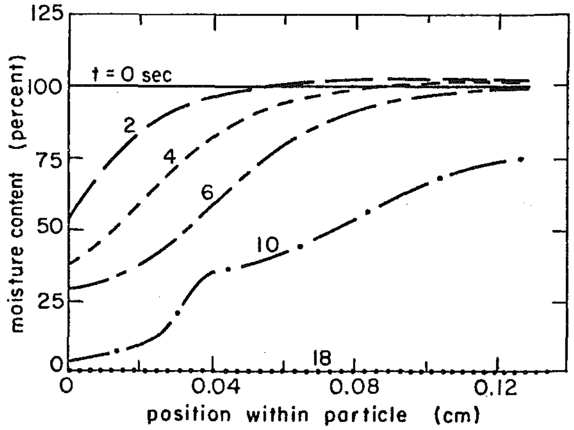

Fig. 7 Moisture profile for spherical model with capillary flow (r = 0.4 μm)

obtained with the two-regime and smeared models, except for a difference during the early stages of drying. The higher drying rate for the smeared model is due to the fact that a proportionately greater amount of moisture exists near the surface of the smeared particle during the early drying stages. This moisture is removed preferentially during startup because of its proximity to the surface, and because the thermal conductivity in this zone during startup is greater in the smeared particle than in the two-regime particle. However, as soon as the surface zone dries, the behavior of the two models is similar.

The results in Fig. 6 indicate three distinct intervals of drying. Initially, because of the high wetness, the drying rate is controlled by the vapor pressure and total pressure inside the particle, which must stabilize before a nearly steady front propagation is reached. Also, at this stage, a relatively high fraction of the input energy is used to increase the temperature of the particle. Following this initial process an interval of nearly constant rate drying is computed, in which case the drying is controlled by the diffusion of heat to the interface. The slight decrease in drying rate with decreasing moisture is due to the greater distance for diffusion from the surface to the front. At low moisture contents, the third interval occurs, and the drying rate decreases greatly because only bound water is vaporized, with the resultant vapor then transported to the particle surface.

Comparison of the results predicted by these two different approaches indicates that the inherent conceptual advantages of the two-regime, frontal model do not yield clearly superior results compared to the smeared model. As a consequence, the smeared model is used for the remainder of the material presented in this paper. Also, it should be noted that in the two regime model the property variations are small, because the material represented at a given node is in one of the two regimes. As a consequence, the iterations needed within each time step to account for the nonlinear effects tend to be few. On the other hand, in the smeared model, the moisture content ranges from zero to a maximum value and the property variations from node to node are substantial. In this case, different degrees of underrelaxation must be used for each of the balance equations, depending upon the time constant associated with each transport process.

Spherical Particle. The type of drying curve noted in Fig. 6, i.e., a nearly constant drying rate until very low moisture contents are reached, followed by a sharp decrease, is not

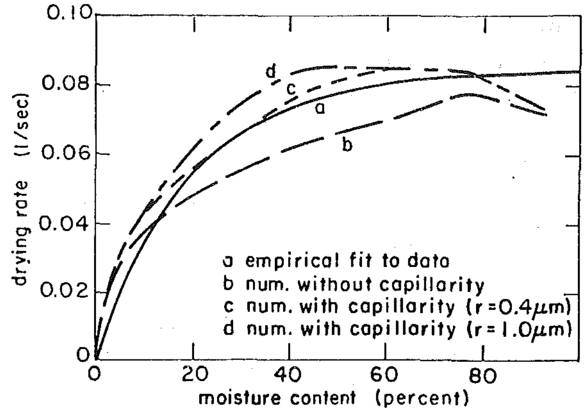

Fig. 8 Influence of capillary flow on drying rate and comparison to data for 2.5-mm-dia particle

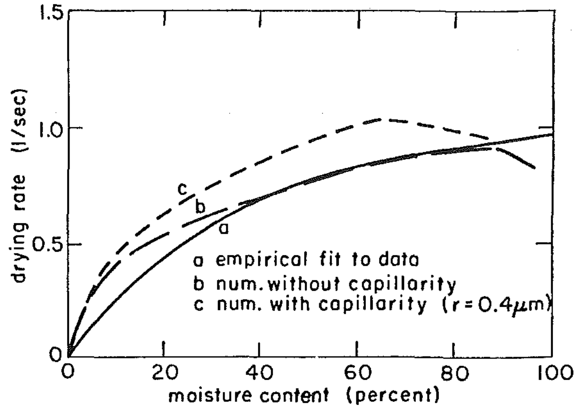

Fig. 9 Influence of capillary flow on drying rate and comparison to data for 0.7-mm-dia particle

observed in the experimental data [1-3]. The experiments (see Figs. 8 and 9) indicate a continual decrease in drying rate as the bulk moisture content decreases from values of intermediate magnitude (i.e., about 60 percent). This behavior can be explained by the presence of capillary flow of liquid in the actual particle. Furthermore, the absolute drying rate predicted for the one-dimensional planar particle is an order of magnitude lower than the measured rate. This difference can be explained by the fact that for the actual particle heat transfer occurs over the total surface area of the particle, not just at the longitudinal ends of the particle as presumed above. In order to overcome these difficulties the spherical smeared model, with capillarity, is used to compare theory with experiment. Results for sawdust particles with volume-equivalent spherical diameters of 2.5 mm (large sawdust) and 0.7 mm (small sawdust), with initial moisture contents of 100 percent (dry basis), and in a convective environment of 515 K capable of producing a maximum drying rate of dM/dt = 0.085 s^{-1} (observed experimentally), are given below.

In Fig. 7, modeling results are shown at different times for moisture distributions in the 2.5-mm-dia particle. Although moisture gradients are noted, they are not as steep as noted for the previous results (Figs. 3 and 5). This smoothing of the moisture gradients is due to the capillary flow of liquid. Some surface evaporation of liquid continues as the particle dries (and the drying rate decreases), and there is less indication of frontal behavior. Although not shown here, the corresponding computed temperatures are constant (at 310 K wet-bulb temperature) in the particle until the 10-s point, at which time some heating (340 K) of the surface occurs. That is, substantial local temperature increases do not occur until the local free water has been removed.

Because of the capillary flow in the model there is a reduction in the tendency to form a front in the particle, at least until the surface moisture falls below the fiber saturation point. The results for 10 s in Fig. 7 do appear to demonstrate a front moving into the wet central region of an otherwise fairly dry particle. These observations do not mean that the comparison in results shown in Fig. 6 for the two-regime and smeared models is invalid. Rather, they mean that bulk frontal behavior is not likely to occur until the capillary flow weakens to the point that the particle surface becomes devoid of free water.

Computations of the drying rate for the 2.5-mm- and 0.7-mm-dia particles are shown, respectively, in Figs. 8 and 9. The experimental information is shown as empirical curves per equation (1). The original data are presented elsewhere [3]. Computed results are shown for no capillary flow, which results in internal moisture distributions similar to those shown in Figs. 3 and 5, and for capillary flow. The liquid permeability corresponds to an effective pit pore radius of 0.4 μm, and in Fig. 8 results are also plotted for an effective radius of 1.0 μm.

The computed results show the following general features: (*a*) a start-up period that is due to the abstraction of the surface supplied energy to heat the wood and the water to the wet-bulb temperature; (*b*) an essentially constant rate drying period when the particle surface is wet and all of the energy is used for drying; and (*c*) a falling rate period where the surface becomes increasingly dry, due to weakening of capillary flow, and the surface temperature increases.

The difference in the drying rates is a measure of the sensitivity of the drying process to the liquid permeability. Since the capillary flow is dependent on the capillary radius to the fourth power, the similarity of the results for effective radii of 0.4 μm and 1.0 μm and the difference between these results and those for no capillary flow suggests the importance of considering that some capillary flow exists. However, more than a threshold capillary flow does not cause a large change in the results. Furthermore, the experimental results indicate that the capillary flow was not great enough to maintain a constant drying rate at bulk moisture contents below approximately 60 percent.

It should be noted that the computed results are normalized to the experimental drying rate at wet conditions, i.e., the constant-rate drying rate. This is done by basing the convective film coefficient h for an assumed spherical particle on the experimental results at wet conditions, and then correcting h analytically as the particle surface temperature increases. Therefore, the predicted shape of the drying rate curves is a good indication of how well the model predicts the experimental behavior.

The results in Fig. 8 indicate that capillary flow must be considered in order to explain the drying of the large sawdust particle. Without capillary flow, the surface dries out too quickly, leading to a reduction in predicted drying rate.

The results for the small particle (Fig. 9) also show sensitivity to capillarity flow, though the sensitivity is not quite as great. However, the agreement between the no-capillarity predictions and the empirical rate is fortuitous. The actual small sawdust particles were more elongated than the larger particles, and thus the assumed spherical geometry is less appropriate. This is the root cause of the overprediction of drying rate with the capillary model. This will be demonstrated in future publication by way of predictions with a cylindrical particle model [6].

Conclusions

Our objective has been to examine two aspects of the modeling of the drying of small wood particles: (*i*) the two-regime, or frontal, approach versus the smeared approach, and (*ii*) the sensitivity of the model to capillary flow of liquid. The conclusions we have formed are the following:

1 Although the two-regime model is intrinsically desirable, the smeared model predicts similar drying behavior, at least for a particle with a simple structure, and is simpler and more efficient to use. The advantages of the smeared model become apparent when multidimensional problems are considered, since in these cases the formulation of the frontal model is significantly more difficult.

2 The inclusion of capillarity in the model substantially changes the local moisture and temperature distributions, though the effect on the drying rate is only modest. Capillarity works against the propagation of an evaporation front into the particle, until the capillary flow becomes sufficiently weak to allow the particle surface moisture to fall below the fiber saturature point.

3 The sensitivity of the predicted drying rate to capillary flow has been examined. However, the sensitivity to other transport and thermodynamic properties is to be reported later with results for the cylindrical smeared model [6], which is the most realistic model geometry.

Acknowledgments

Financial support for this research came through grants from the Weyerhaeuser Company, Tacoma, Washington, and the authors gratefully acknowledge this support.

References

1 Malte, P. C., Robertus, R. J., Strickler, M. D., Cox, R. W., Messinger, G. R., Kennish, W. J., and Schmidt, S. C., "Experiments on the Kinetics and Mechanisms of Drying Small Wood Particles," Report TEL-76-8, Department of Mechanical Engineering, Washington State University, Pullman, Wash., 1976.

2 Malte, P. C., Cox, R. W., Robertus, R. J., Messinger, G. R., and Strickler, M. D., "Wood Particle Drying Rates," *Proc. of Eleventh Symposium on Particle Board*, Washington State University, Pullman, Wash., 1976, pp. 231–257.

3 Malte, P. C., Dorri, B., Emery, A. F., Cox, R. W., and Robertus, R. J., "The Drying of Small Wood Particles," *Drying Technology, an International Journal*, Vol. 1, Marcel Dekker, New York, 1983, pp. 83–116.

4 Spolek, G. A., "A Model of Simultaneous Convective, Diffusive, and Capillary Heat and Mass Transport in Drying Wood," Ph.D. thesis, Department of Mechanical Engineering, Washington State University, Pullman, Wash., 1981.

5 Siau, J., *Flow in Wood*, Syracuse University Press, Syracuse, N.Y., 1971.

6 Dorri, B., "Simultaneous Heat and Mass Transfer Modeling for Small Wood Particle Drying," Ph.D. thesis, Department of Mechanical Engineering, University of Washington, Seattle, Wash., 1983.

7 Stamm, A. J., *Wood and Cellulose Science*, Ronald Press, New York, 1964.

8 Skaar, C., *Water in Wood*, Syracuse University Press, Syracuse, N.Y., 1972.

G. F. Carrier
Pierce Hall,
Harvard University,
Cambridge, Mass. 02138
Hon. Mem. ASME

F. E. Fendell

P. S. Feldman
Engineering Sciences Laboratory,
TRW Space and Technology Group,
Redondo Beach, Calif. 90278

Firestorms

Quantitative criteria are sought for onset of firestorms, severe stationary (nonpropagating) holocausts arising via merger of fires from multiple simultaneous ignitions in a heavily fuel-laden urban environment. Within an hour, surface-level radial inflow from all directions sustains a large-diameter convective column that eventually reaches altitude of about 10 km (e.g., Hamburg, Dresden, Hiroshima). As the firestorm achieves peak intensity (a couple of hours after the ignitions), inflow speeds are inferred to attain 25-50 m/s; typically 12 km^2 are reduced to ashes, before winds relax to ambient levels in six-to-nine hours. Here the firestorm is interpreted to be a mesocyclone (rotating severe local storm). Even with exceedingly large heat release sustained over a concentrated area, in the presence of a very nearly autoconvectively unstable atmospheric stratification, onset of vigorous swirling on the scale of 2 hrs requires more than concentration of circulation associated with the rotation of the earth; rather, a preexisting, if weak, circulation appears necessary for firestorm cyclogenesis.

Introduction

In the aftermath of the atomic bombing of Hiroshima [1, 2], and of the massive incendiary bombing of Hamburg [3-5] and Dresden [6], particularly virulent, long-lived, uncontrolled burning occurred that had few if any recorded precedents. About ½ hr after multiple simultaneous ignitions (in a heavily fuel-laden urban environment), effected either by radiative-precursor heating and blast-wave disruption [2] or by contact with burning magnesium and gelled gasoline dispersed from clustered cannisters [7], the fires merged to form a rather uniformly burning area of many square kilometers. Whereas the ambient winds were less than 4 m/s, the mass fire engendered radially inward winds at street level from all directions; about 2-3 hrs after the initiating bombing, these winds reached a peak intensity of about 20 m/s, with some estimates by professional firefighters of 50 m/s. The radially inward wind apparently precluded spread beyond the initially ignited area, though virtually everything combustible within this region was burned, before the winds subsided to moderate in speed and variable in direction about 6 hrs after initiation. A single huge central convective column, into which the hot product gases flowed, rose to about 10 km. This rare nonpropagating fire, so distinct from more common ambient-wind-aided spreads, is termed a firestorm. The goal of the present investigation is to delineate, from thermohydrodynamic modeling, quantitative criteria for the onset of a firestorm; while some characterization of structure and properties is inevitably entailed, full detailed description of the event at peak intensity is not the prime objective.

In the interpretation given here, the term firestorm is apt. In a conventional meteorological context, *storm* suggests cyclonic wind about a center of low surface pressure, with precipitation from convectively induced advection (i.e., from buoyancy-caused ascent and saturation of warm moist air, with (*i*) radial influx under continuity, and (*ii*) possible attendant spin-up under conservation of angular momentum associated with earth rotation or some locally enhanced level). Hence a firestorm is a "heat cyclone" [8], a mesolow in which the exothermicity of combustion, as distinguished from the condensation of water vapor, induces free convection. Just as firestorms are exceptional fire events, so mesolows (thunderstorms with organized rotation, also referred to as tornado cyclones and supercells) are uncommon relative to the total number of thunderstorms, and are characterized by horizontal scale of several kilometers and life-span of about 6 hrs [9]. Further, just as the mesolow is characterized by towering cumulonimbi ascending through the depth of the troposphere to the tropopause, so the firestorm is characterized by a convective column ascending to exceptionally great height, e.g., 10 km at Hamburg.

The observation at low altitudes of appreciable radial flux from all directions toward the base of the centrally sited convective column corroborates, rather than contradicts, the primarily rotating nature of the bulk of the air motion. Investigation of the near-surface inflow layer near the center of a virgorously rotating air mass over a fixed flat surface shows that strong, purely swirling motion is altered to equally strong, purely radial influx near the ground, though immediately at the ground the no-slip constraint holds [10-12].

The firestorm is the exceptional event in that diffusive mechanisms normally relax spin-up, such that swirling is either modest or nil [13]. Allusions to the parallel between firestorms and tropospheric storms in the general sense of strong convection accompanied by strong surface winds are frequent. However, pertinence of the dynamic characteristics of a *rapidly rotating* air mass above a relatively fixed flat surface plane has been emphasized by Ebert [8], Emmons [14], and Long [15]; Ebert and Emmons suggest that the rotation of the air surrounding the plume suppresses entrainment such that the buoyant plume rises to exceptional altitude, while Emmons and Long note that radial near-surface inflow is consistent with rapid higher-level swirling. Here, quantitative description seeking onset criteria is undertaken. It may be remarked that the well-known propensity for long-range, spotting-type (discontinuous) spread of free-burning fire via firebrands in the event of firewhirls [16, 17] suggests that the spatially confined character of recorded firestorms yet may have exceptions.

Formulation – Outline

A fully established convective column exists over a maintained heat source of known strength (total enthalpy released per time) in an atmosphere of known stratification (temperature as a function of pressure, with relative humidity taken as negligible for circumstances of interest). That is, a conventional entraining, nonrotating plume exists above a fire approximated as a point source of heat, without associated release of momentum per time or mass per time. Ultimately, the point source is placed at a subterranean site, such that the plume width at ground level is ascribed observed values; arbitrarily assuming the plume to be entraining (in an adiabatic atmosphere with ground-level properties) and nonrotating, between subterranean site and ground, is accepted as yielding adequate description at ground level. Of

---

Contributed by the Heat Transfer Division for publication in the JOURNAL OF HEAT TRASNFER. Manuscript received by the Heat Transfer Division September 21, 1983.

course, the plume width at ground level is an approximation, as is the acceptance of finite mass and momentum input at ground level. Indeed, the strength of the heat source is also an estimate, since the fuel loading (average mass of combustible matter per area), exothermicity (heat released per mass of combustible matter, with adjustment, if required, for drying prior to burning), and fire duration are known, but the rate of heat release in time is not known, and in fact the duration is more rigorously an output than an input. Nevertheless, the procedure avoids specifying even more (probably unavailable) detail as input.

A conventional integral-type plume theory yields the vertical structure of this convective column, in particular, the width, upward speed, and density discrepancy from ambient as functions of altitude above the source [18]. Typically, the plume spreads as the speed of ascent slows, ultimately to zero, owing to entrainment of heavier surrounding air into the convective column; even below the altitude of stagnation of ascent, the discrepancy in density between plume air and surrounding air vanishes and reverses, and above the height of zero discrepancy the validity of the entrainment concept is in doubt. In any case, this known solution serves as an initial condition to the questions of interest here: As a function of heat-source strength and dimension, ambient stratification, and ambient circulation, how long would spin-up require and how is the structure of the convective column altered? If spin-up would require more than a couple of hours, relaxation processes not included in the formulation are inferred to enter and to preclude cyclogenesis.

Seeking answers motivates three innovations. The aspect of time development must be added to the description of flow over a maintained source (as distinguished from time dependence associated with the starting plume or buoyant thermal). The plume is taken to respond in a quasi-steady manner to the consequences of spin-up of the surrounding air, which introduces explicit temporal derivatives. Accordingly, conservation of angular momentum enters; conservation of radial momentum must be treated (since existence of appreciable swirl implies existence of a significant radial pressure gradient), in contrast with a simple statement of radially invariant pressure, to which the conservation of radial momentum degenerates for a nonrotating column. Finally, the effective reduction of the entrainment parameter with spin-up of the surrounding air must be quantified [19, 20]; with reduced entrainment, the spreading of the plume with altitude is decreased. There are two further considerations. First, if one concentrates on the strongly buoyant region near the fire, the lateral discrepancy in density (and temperature) between air in the plume and surrounding air warrants inclusion [21]. In the weakly buoyant region further above the fire, the density of air in the plume may be identified with the density of ambient air surrounding the plume (Boussinesq approximation); however, for a firestorm the convective column extends to such heights that the variation of ambient air with altitude warrants retention (modified Boussinesq approximation). Second, observations of intense Australian bushfires indicate several occasions, at peak burning, of clouds above the top of the convection column clearly being drawn down in the column [22]. However, no provision is to be made for evolution to a more intense stage of rotating flow incorporating two-cell structure (i.e, provision for a downdrift, at least near the axis at the top of the column, within an annular upflux).

Formulation – Equations

Consider an axisymmetric treatment in cylindrical polar coordinates (r,θ,z), with corresponding velocity components (u,v,w), of a plume above a maintained enthalpy source of strength E (given), without associated mass-source strength M or momentum-source strength ϕ:

Nomenclature

$B(z,t)$ = radius of preexisting mesoscale vortex, m
$B_o(z)$ = $B(z,0)$, m
$\bar{B}$ = reference acceleration for nonadiabatic atmosphere, m/s^2
$b(z,t)$ = e-folding radial distance for plume variables, m
b_i = "plume radius" at ground level, m
c_p = specific heat capacity at constant pressure for air, m^2/s^2 – K
E = time-averaged strength of maintained heat source, W
$F(z,t)$ = centerline mass flux in plume, kg/s
$G(z,t)$ = centerline axial momentum flux in plume, N
g = gravitational acceleration, m/s^2
$H(z,t)$ = centerline energy flux in plume, W
$J(z,t)$ = "transversely averaged" momentum flux in plume, J
M = strength of maintained mass source, kg/s
$p(r,z,t)$ = pressure, Pa
$q(r,z,t)$ = swirl associated with plume, m/s
R = gas constant for air, m^2/s^2 – K
r = cylindrical radial coordinate, m
$S(z,t)$ = angular momentum per mass derived from earth rotation, m^2/s
$T(r,z,t)$ = temperature, K
t = time, s
$u(r,z,t)$ = radial velocity component, m/s
$V(z)$ = swirl speed of preexisting mesoscale vortex, m/s
$v(r,z,t)$ = azimuthal velocity component, m/s
$W(x,t)$ = centerline axial velocity in plume, m/s
$w(r,z,t)$ = axial velocity component, m/s
z = axial distance above ground, m
z_i = distance from subterranean point source to ground, m
$\alpha(r,z,t)$ = entrainment functional defined in equation (16), taken as in equation (39)
α_o = value of α in absence of rotation, 0.093
$\Gamma_o(z)$ = angular momentum per mass of preexisting mesoscale vortex, m^2/s
γ = $c_p/(c_p-R)$
ϵ = volumetric-flux equivalent of E [see (37)], m^3/s
θ = aximuthal cylindrical-polar coordinate
κ = polytropic exponent characterizing ambient-atmosphere stability [see (38)]
$\rho(r,z,t)$ = density, kg/m^3
$\sigma(z,t)$ = centerline plume pressure deficit, Pa
ϕ = strength of maintained momentum source, N; also, angular momentum per mass rv, m^2/s
ϕ_0 = parameter appearing in entrainment function (39), m^2/s
Ω = component of angular velocity of earth locally perpendicular to surface, s^{-1}

Subscripts

a = ambient
i = initial, i.e., pertaining to $z=0$

$$M \equiv 2\pi \int_0^{b\to 0} \rho w r\, dr = 0, \phi \equiv 2\pi \int_0^{b\to 0} \rho w^2 r\, dr = 0,$$

$$E \equiv 2\pi \int_0^{b\to 0} \rho w c_p T_a \left(\frac{T-T_a}{T_a}\right) r\, dr > 0 \tag{1}$$

The plume radius $b\to 0$ at the source; subscript a refers to ambient conditions, i.e., to conditions outside the plume where (in the absence of rotation) thermodynamic quantities are a known function of altitude z only.

The flow is so subsonic that (not too close to the source) the density, except for the gravitational term in the momentum equation, is well approximated by its ambient value, and variance of the temperature from ambient is linearly related to the variance from ambient of density (only). Here the ambient values vary with altitude because of the tropospheric scale of the phenomena. In the absence of adequate models, no provision for axially distributed chemical exothermicity is included.

The conservations equations for mass, radial momentum, axial momentum, and energy are taken to be described adequately by the following:

$$(\rho r w)_z + (\rho r u)_r = 0 \tag{2}$$

$$(\rho r u w)_z + (\rho r u^2)_r + r p_r - \rho v^2 = 0 \tag{3}$$

$$(\rho r w^2)_z + (\rho r u w)_r + r p_z + \rho r g = 0 \tag{4}$$

$$(\rho w r c_p T)_z + (\rho u r c_p T)_r + \rho r g w = 0 \tag{5}$$

Conservation of angular momentum involves time-derivative, advective, convective, and Coriolis terms, the last being important only when planetary vorticity is a significant source of angular momentum ($\phi \equiv rv$):

$$\rho r \phi_t + (\rho r w \phi)_z + (\rho r u \phi)_r + 2\Omega \rho r^2 u = 0 \tag{6}$$

The following Gaussian description is adopted for the dependent variables:

$$w(r,z,t) = W(z,t) \exp[-r^2/b^2(z,t)] \tag{7}$$

$$p_a(z) - p(r,z,t) = \sigma(z,t) \exp[-r^2/b^2(z,t)] \tag{8}$$

$$g\frac{\rho_a(z) - \rho(r,z,t)}{\rho_a(z)} = f(z,t) \exp[-r^2/b^2(x,t)] \tag{9}$$

$$\phi(r,z,t) = \phi_{1a}(r,z,t) + \phi_{1b}(r,z,t) + \phi_2(r,z,t) \tag{10}$$

where

$$\phi_{1a}(r,z,t) = S(z,t)\{1 - \exp[-r^2/b^2(z,t)]\} \tag{11}$$

$$\phi_{1b}(r,z,t) = \Gamma_o(z)\{1 - \exp[-r^2/B^2(z,t)]\} \tag{12}$$

$$\phi_2(r,z,t) = q(z,t)[r^2/b(z,t)]\exp[-r^2/b^2(z,t)] \tag{13}$$

where ϕ_{1a} is a "response" to the Coriolis term and ϕ_{1b} is a "response" to the initial condition (in which a weak diffuse vortex preexists, the circulation Γ_o of which is invariant over time scales of interest, but the characterizing radius B of which, though initially large so $B >> b$, may decrease appreciably over the time span of interest). The contribution ϕ_2 describes plume-scale redistribution of angular momentum. The functions to be found, W, σ, f, b, B, S, and q, are all anticipated to be positive near the source; f goes to zero and changes sign at a finite distance above the source.

Also the equation of state gives

$$p(r,z,t) = \rho(r,z,t) R T(r,z,t) \Rightarrow p_a(z) = \rho_a(z) R T_a(z) \tag{14}$$

Hydrostatics suffices for the ambient

$$p_{a_z} = -\rho_a g \tag{15}$$

The Taylor entrainment concept is introduced:

$$-\lim_{r\to\infty} (ru) = \alpha b W \tag{16}$$

where, in the absence of swirl, $\alpha = \alpha_o$ ($\equiv 0.093$); in the presence of swirl, α is a functional of the swirl-associated variables.

Integration of (1) over r, from $r=0$ (where $u=0$) to $r\to\infty$ (where (16) holds), by use of (7) and upon setting $\rho(r,z,t) = \rho_a(z)$, gives

$$\frac{d}{dz}(\rho_a W b^2) = 2\alpha \rho_a W b \tag{17}$$

Multiplying (15) by r and subtracting from (4) gives, upon integration over all r and use of (7-9) and setting $\rho\to\rho_a$, $w(r\to\infty,z,t)\to 0$, gives

$$\frac{d}{dz}\left[\left(\frac{\rho_a W^2}{2} - \sigma\right) b^2\right] = \rho_a f b^2 \tag{18}$$

Equation (5) may be rewritten

$$\{\rho w r[c_p(T-T_a)]\}_z + \{\rho u r[c_p(T-T_a)]\}_r$$
$$= \rho w r c_p T_{a_z} - \rho w r g \tag{19}$$

If $\rho\to\rho_a$ in all terms, by (14) and (15), and since $R = (c_p - c_v) = c_v(\gamma - 1)$

$$\{\rho_a w r[c_p(T-T_a)]\}_z + \{\rho_a u r[c_p(T-T_a)]\}_r =$$
$$-\frac{\rho_a w r}{\gamma - 1}\frac{d}{dz}\left[\ln\left(\frac{p_a}{\rho_a{}^\gamma}\right)\right] \tag{20}$$

Integration over r and use of (7), (9), (14), and the Boussinesq relation ($(\partial T/\partial\rho)_p$ is evaluated in the ambient)

$$\frac{T(r,z,t) - T_a(z)}{T_a(z)} = \frac{1}{T_a(z)}\left(\frac{\partial T}{\partial \rho}\right)_p [\rho(r,z,t)$$
$$-\rho_a(z)] \Rightarrow \frac{T-T_a}{T_a} = \frac{\rho_a - \rho}{\rho_a} \tag{21}$$

gives

$$\frac{d}{dz}\left[p_a W b^2\left(\frac{f}{g}\right)\right] = -\frac{2}{\gamma}(p_a W b^2)\frac{d}{dz}\left[\ln\left(\frac{p_a}{\rho_a{}^\gamma}\right)\right] \tag{22}$$

Integration of (3) over r yields zero from the perfect differential, and the axial derivative term yields a contribution of $O(b^3) = O[(\alpha z)^3]$, since, from the selfsimilar solution for a point source in an adiabatic nonrotating ambient, $b \doteq \alpha z$. But $\alpha = o(1)$, and perhaps even smaller under spin up. That is, the plume-scale radial inflow u, small relative to other velocity components in a nonrotating convective column, is reduced still further under spin-up (for heights above the surface-inflow layer), according to experiment [17]. Hence, (3) reverts to the cyclostrophic balance ($\rho \doteq \rho_a$)

$$\int_0^\infty p_r dr = \rho_a \int_0^\infty \frac{v^2}{r} dr \Rightarrow \sigma = \rho_a \int_0^\infty \frac{(\phi_{1a} + \phi_{1b} + \phi_2)^2}{r^3} dr \tag{23}$$

Execution of the integrals yields

$$\frac{\sigma b^2}{\rho_a} = (\ln\ 2)\left[S^2 + \frac{b^2\Gamma_o^2}{B^2} + (qb)S\right] + \frac{(bq)^2}{4}$$
$$+ \ln\left[\left(\frac{B^2+b^2}{B^2}\right)\left(\frac{B^2+b^2}{b^2}\right)^{b^2/B^2}\right] S\Gamma_o$$
$$+ \left[\ln\left(\frac{b^2+B^2}{B^2}\right)\right](qb)\Gamma_o \tag{24}$$

In this context it may be helpful to note

$$I_1 = \int_0^\infty \frac{[1-\exp(-x^2)]^2}{x^2} dx = \ln\ 2$$

$$I_2 = \int_0^\infty \frac{\exp(-x^2)}{x}[1-\exp(-x^2)]dx = \frac{I_1}{2} \tag{25}$$

$$I_3(\Upsilon) = \int_0^\infty \frac{\exp(-\Upsilon x^2)}{x}[1-\exp(-x^2)]dx \Rightarrow$$

$$\frac{dI_3}{d\Upsilon} = \frac{-(1/2)}{(1+\Upsilon)\Upsilon}, I_3(\infty) = 0 \tag{26}$$

$$I_4(A)=\int_0^\infty \frac{1-\exp(-x^2)}{x^3}\,[1-\exp(-Ax^2)]dx \Rightarrow$$

$$\frac{d^2 I_4}{dA^2}=\frac{-(1/2)}{(1+A)A}, I_4(1)=\ln 2, I_4'(1)=I_2 \qquad (27)$$

Plume-associated dependent variables (b,W,f,q) are anticipated to change during firestorm onset more slowly in time than the scale of the preexisting vortex B. Accordingly, it is taken that $\phi_{2_t} << \phi_{1_t}$, where $\phi_1 \equiv (\phi_{1a}+\phi_{1b})$. Substitution of (10–13) in (6) is construed to yield three relations:

$$\rho r\phi_{1b_t}+(\rho ru\phi_{1b})_r=0 \qquad (28)$$

$$[\rho ru(\phi_{1a}+\phi_2)]_r+[\rho wr(\phi_2+\phi_1)]_z \doteq 0 \qquad (29)$$

$$\lim_{r\to\infty} \{\rho r\phi_{1_t}+[\rho ru(\phi_1+\phi_2)]_r+[\rho rw(\phi_1+\phi_2)]_z + 2\Omega r^2 \rho u\}=0 \qquad (30)$$

Integration of (28) over r yields

$$(B^2)_t=-2\alpha bW \qquad (31)$$

while (30) gives contributions from the first and last terms only:

$$S_t=2\Omega\alpha bW \qquad (32)$$

Since $\Omega=2^{1/2}\pi/24\ h^{-1}$ at midlatitudes and $\alpha<O(0.1)$, the growth of swirl from the rotation of the earth is too slow to account for significant vorticity on the scale of two hours; although (32) is tentatively retained, the decrement of B in time from (31) is of more importance to spin-up if Γ_o has nonnegligible value. Finally, integration of (29) over r yields, if $\rho \doteq \rho_a$

$$\frac{d}{dz}\left[\rho_a Wb^2\left(\frac{qb}{4}+\frac{S}{2}+\frac{\Gamma_o b^2}{B^2+b^2}\right)\right]=2\alpha\rho_a bWS \Rightarrow$$

$$\frac{d}{dz}\left[\rho_a b^2 W\left(\frac{qb}{4}+\frac{\Gamma_o b^2}{B^2+b^2}\right)\right]=3\alpha\rho_a bWS+\frac{1}{2}\rho_a Wb^2\frac{dS}{dz} \qquad (33)$$

by transposition, with the aid of (17). Only the product (qb) occurs.

The equations may be brought into canonical form by introduction of the following functionals:

$$F=\rho_a b^2 W, G=\rho_a b^2 W^2, H=p_a Wb^2 f/g,$$

$$J=\rho_a b^2 W\left(\frac{qb}{4}+\frac{\Gamma_o b^2}{B^2+b^2}\right) \qquad (34a)$$

so, for instance,

$$\frac{dF}{dz}=2\alpha(\rho_a G)^{1/2}; \frac{dG}{dz}=2g\left(\frac{\rho_a}{p_a}\right)\frac{HF}{G}+2\frac{d(\sigma b^2)}{dz}$$

$$\frac{dH}{dz}=-\frac{2}{\gamma}\rho_a{}^{\gamma-1}\left[\frac{d}{dz}\left(\frac{p_a}{\rho_a{}^\gamma}\right)\right]F; \frac{dB^2}{dt}=-2\alpha\left(\frac{G}{\rho_a}\right)^{1/2} \qquad (35)$$

$$W=\frac{G}{F}, b=\frac{F}{(\rho_a G)^{1/2}}, \frac{f}{g}=\frac{H}{(p_a/\rho_a)F},$$

$$\frac{b^2}{B^2}=\beta^2, qb=\frac{4J}{F}-\frac{4\Gamma_0\beta^2}{1+\beta^2} \qquad (34b)$$

Use of (7–9), (21), and (34) in (1) gives at the source

$$F=\frac{M}{\pi}=0, G=\frac{2\phi}{\pi}=0, H=\frac{2(\gamma-1)}{\pi\gamma}E \qquad (36)$$

A solution procedure is to adopt two half-steps in a simplistic form of time-splitting. The seven variables b, B, S, W, σ, q, f (or, equivalently, F, G, H, J, S, σ, B) are taken as known in z at a given time. In the first half-step, B, S, and σ are updated via (31), (32), and (24); in (24), updated values of S, B, but not of b, q, are used. In the second half-step, (17), (18), (22), and (33) are used to update F, G, H, J; in (18), the term $d(\sigma b^2)/dz$ is transposed and evaluated using the value of σb^2 from the first half-step. While iteration on q, b in σ could be adopted, this procedure might be dispensed with. At time zero, $B^2>>b^2$, so discarding all effects associated with swirl to obtain a classical initial plume is taken as an adequate approximation.

Nondimensionalization, Ambient Stratification, Entrainment Functional

If, in the translationally invariant set presented above, $z=0$ denotes ground level, then nondimensionalization could be carried out in terms of the quantities $\rho_a(0)$, $T_a(0)$, $d\rho_a(0)/dz$, and E, where it is recalled that $p_a(0)=\rho_a(0)RT_a(0)$; it is convenient to define

$$\epsilon \equiv \frac{E}{\rho_a(0)c_p T_a(0)}, \frac{\text{volume}}{\text{time}};$$

$$\tilde{B}\equiv\rho_a{}^{\gamma-1}(0)\frac{d}{dz}\left[\left(\frac{p_a}{\rho_a{}^\gamma}\right)\right]_{z=0}, \frac{\text{length}}{\text{time}^2} \qquad (37)$$

The quantity $(p_a\rho_a{}^{-\gamma})_z$ is positive in a dry stable atmosphere (the case of prime interest here), zero in a dry neutrally stable atmosphere (a special case, the selfsimilar solution of which in a nonrotating atmosphere is classical), and negative in a dry unstable atmosphere (of no interest here). A length scale is furnished by $\epsilon^{2/5}\tilde{B}^{-1/5}$; a time scale, $\epsilon^{1/5}\tilde{B}^{-3/5}$; a speed scale, $\epsilon^{1/5}\tilde{B}^{2/5}$. However, the neutral-stability, dry-adiabatic-atmosphere case $\tilde{B}=0$ would require special treatment, so the advantages of nondimensionalization are taken to be outweighed by this limitation.

For purposes of a one-parameter characterization of stratification, a so-called polytropic atmosphere [23] is adopted ($1 \gtrsim \kappa > 0$, where κ is given and piecewise constant); i.e., under (14) and (15), adoption of

$$p_a \sim \rho_a{}^{\kappa\gamma} \Rightarrow \frac{dT_a}{dz}=-\frac{g}{c_p}\left(\frac{\kappa\gamma-1}{\kappa(\gamma-1)}\right); \qquad (38a)$$

$$\frac{dH}{dz}=2(1-\kappa)\frac{p_a(0)}{[\rho_a(0)]^2}\left[\frac{\rho_a}{\rho_a(0)}\right]^{\kappa\gamma-2}F\frac{d\rho_a}{dz} \qquad (38b)$$

In fact, $1 \gtrsim \kappa > \gamma^{-1}$, since temperature (aside from possible local inversion layers) decreases with altitude. Since firestorm-prone ambients are typically very dry, discussion of stability on a dry basis is apropos.

In the absence of experimental data beyond the general guidance that entrainment continually decreases as the air surrounding the plume is spun up above some threshold value, only a "schematic" functional is presented [ϕ_o an assigned constant; Υ an assigned function, with $\Upsilon(0)=1$]:

$$\alpha(b,z,t)=\alpha_o\Upsilon\{\phi(b,z,t)U[\phi(b,z,t)-\phi_o]\}, \frac{d\Upsilon}{d\phi}<0 \qquad (39)$$

Boundary and Initial Conditions

At $z=0$ for $t>0$

$$b=b_i, \text{ given}; H=\frac{2(\gamma-1)}{\pi\gamma}E, \text{ given} \qquad (40)$$

One could let b_i vary in time, and could require that only the time average of H at $z=0$ has the cited value; however, these quantities should be nearly constant over the interval for a fluid element to rise the vertical extent of the plume

$$t_{\text{rise}}(t)=\int_0^{z_{\text{top}}}[W(z_1,t)]^{-1}dz_1 \qquad (41)$$

Here, $W(z_{\text{top}},t)\to 0$, and W is anticipated to be but weakly variant in time during firestorm onset. In the absence of specific data, b_i and $H(0,t)$ are held constant.

The initial condition at $t=0$ is taken as

$$S=0, \text{ so } \frac{dS}{dz}=0; B(z,0)=B_o(z) \text{ specified} \tag{42}$$

where the choice for $B_o(z)$ is guided by the fact that $B_o(z)$ plays a role in the preexisting weak vortex that b plays in the current intense plume. Physically, one anticipates (on the basis of data for tropical cyclones and mesocyclones) that the pressure anomaly (i.e., pressure deficit on the centerline, from ambient value at the same altitude) decreases with increasing altitude (except *possibly* at low altitude). Therefore, one anticipates that Γ_o may decrease with altitude and may vanish at finite altitude. It is convenient to introduce

$$V(z)=\frac{\Gamma_o(z)}{B_o(z)} \tag{43}$$

Simplification

As anticipated below (32), spin-up associated with the rotation of the earth is negligible relative to spin-up associated with intensification of a preexisting vortex. (The preexisting circulation seemed to have been caused by fires from prior recent raids at Hamburg, and by orography at Hiroshima.) Hence all terms involving S are ignored. Furthermore, rotation associated with the convective column itself is small during the firestorm-onset interval of prime interest here. Accordingly, all terms involving qb are ignored, and the equation for J is discarded completely. It may be confirmed a posteriori that principal evolution during spin-up is the decrease of the radius B of the preexisting mesoscale vortex. The problem devolves to (35), subject to (40) at $z=0$ (see below) and to (42–43) at $t=0$. Thus, if the axial pressure gradient is retained at all, (24) simplifies to

$$\sigma b^2=(\ln 2)\rho_a\Gamma_0{}^2 b^2/B^2 \tag{44}$$

In fact, it seems reasonable to expect buoyancy to exceed the axial pressure gradient in magnitude during the spin-up interval of interest. Accordingly, during this time interval, b, W, f remain effectively identical to their initial (swirl-free) values given by (35) with the term $d(\sigma b^2)/dz$ discarded. For consistency, one expects $\phi<\phi_o$ in (39), so $\alpha=\alpha_o$.

If ρ_a is taken invariant over the range of altitude z of interest (so p_a is invariant in z from (38a)), if $\alpha=\alpha_o$ and $\kappa=1$, and if $d(\sigma b^2)/dz=0$, then from the first three relations of (35) and from (40) one recovers the known similarity solution [19]

$$b=\frac{6}{5}\alpha_o(z+z_i), W=\frac{5}{6\alpha_o}\left[\frac{18}{5\pi}\left(\frac{\alpha_o\epsilon g}{z+z_i}\right)\right]^{1/3}$$

$$\frac{f}{g}=\left[\frac{1}{3^5 g}\left(\frac{5}{\alpha_o}\right)^4\left(\frac{\epsilon}{\pi}\right)^2\frac{1}{(z+z_i)^5}\right]^{1/3} \tag{45}$$

where

$$b_i=\frac{6}{5}\alpha_o z_i \tag{46}$$

Although the procedure incurs spurious finite values for the mass flux F and the momentum flux G at $z=0$ (investigated below), the above formulae furnish starting values at $z=0$ for the plume solution at all times t during firestorm onset. The conventional procedure of placing an equivalent-strength point heat source at the subterranean site $z=-z_i$, with an adiabatic nonrotating atmosphere holding in $-z_i<z<0$ (where $|z_i|$ is small enough relative to tropospheric scale height that ρ_a is effectively constant), has been taken as acceptable a procedure as any facile alternative for starting the plume solution at $z=0$. Below, the relative insensitivity of results to choice of z_i is established by varying $W(0)$ and $f(0)$. The fact is that, with spin-up, a near-ground-level inflow *is* engendered, and absence of data giving temporal and spatial resolution of the heat release at Hamburg precludes established the adequacy of adopting (46).

Further, because of the convenience of a closed-form expression, for the virtually adiabatic atmosphere holding in the pertinent lower troposphere at Hamburg, for given z_i and ϵ, (45) and (46) are utilized below, over the spin-up interval, in (31). However, the variation of ambient density and pressure with altitude for a not-quite-adiabatic lower troposphere is later examined as a check; in this check, (45) and (46) are used only to start the upward integration in z of (35) under (38), results being sought with the axial pressure gradient term both retained and discarded.

In short, if it is recalled that $\phi=rv$, one anticipates that B decreases from $B_o(z)$ to b as time t increases, such that v increases at radius b from virtually zero at $t=0$ to almost $(2/3)[B_o(z)V(z)]/b(z)$, or $(2/3)\Gamma_o(z)/b(z)$, from (12), (31), and (43) – although, as $B\rightarrow b$, the domain of validity of the theory probably is being overextended. (The model fails as $B\rightarrow b$ because plume circulation qb should not be ignored, and input to the convective column from a rotating near-surface layer is not adequately incorporated.) The issue being investigated is whether the stratification as reflected in κ, (more importantly) the size of the intensely convective region as reflected in the parameter b_i, and (still more importantly) the rate of enthalpy release as reflected in the parameter ϵ are such that spin-up from weak preexisting-vortex swirl to about 15 m/s is achieved on the scale of 2 hrs, as reported at Hamburg.

Thus, in the present interpretation, $\alpha=\alpha_o$ during the early stages of spin-up, such that B is reduced from B_o to b, presumably in about 2 hrs. *Then*, α is reduced significantly in appreciably swirling surroundings, so the plume ascends to exceptional altitude [see (39)]. While *very preliminary* evidence encourages the concept [19], far more data are required. The increase in plume altitude with decrease of α is suggested only very qualitatively below.

Results

Nominal values for problem parameters, believed appropriate for the Hamburg firestorm, are presented in Table 1. The basis for the more critical of these parameter values is now discussed. An area of 12 km² with 157 kg/m² of combustible material was reduced (virtually completely) to ashes in about 6 hrs [24, 25]; for adopted exothermicity of $1.86\cdot10^4$ J/g of combustibles, $E=0(10^{19}$ ergs/s), or, for plausible

Table 1 Nominal values for parameters

$B_o(0)$	=	$8.00\cdot10^5$ cm	α_o	=	$9.30\cdot10^{-2}$
$\tilde{B}$	=	$1.23\cdot10^1$ cm/s^2	$\Gamma_o(0)$	=	$3.20\cdot10^8$ cm^2/s
b_i	=	$5.00\cdot10^4$ cm	ϵ	=	$2.60\cdot10^{12}$ cm^3/s
c_p	=	$1.00\cdot10^7$ cm^2/s^2 – K	κ	=	$\begin{cases}9.90\cdot10^{-1}, z<2.74\cdot10^5 \text{ cm}\\8.30\cdot10^{-1}, z>2.74\cdot10^5 \text{ cm}\end{cases}$
E	=	$9.05\cdot10^{18}$ erg/s			
g	=	$9.80\cdot10^2$ cm/s^2	γ	=	1.40
$p_a(0)$	=	$1.00\cdot10^6$ g/cm – s^2	$\rho_a(0)$	=	$1.16\cdot10^{-3}$ g/cm^3
R	=	$2.87\cdot10^6$ cm^2/s^2 – K	$d\rho_a(0)/dz$	=	$1.17\cdot10^{-9}$ g/cm^4
$T_a(0)$	=	$3.00\cdot10^2$ K			

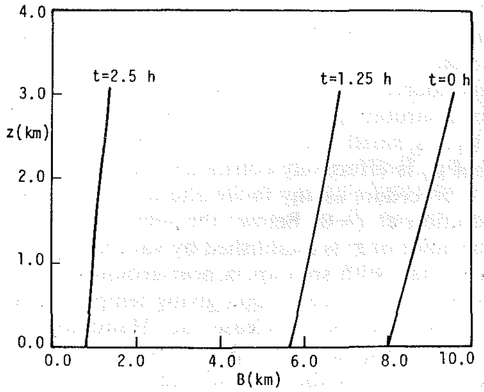

Fig. 1 Profile of the characteristic radius B of the preexisting vortex versus altitude above ground level z, at time t (ignition at $t=0$, with $B(z,0)=B_0(z)$, adopted as a plausible initial profile). The decrement in B owing to convectively induced advection is computed for a constant-density atmosphere; the calculation is carried to the approximate altitude to which the ambient remained very nearly autoconvectively unstable at Hamburg. Here the volumetric flux of the heat source $\epsilon = 2.586\cdot10^{12}$ cm^3/s. As in all succeeding figures, parameter values are those of Table 1 except as explicitly noted.

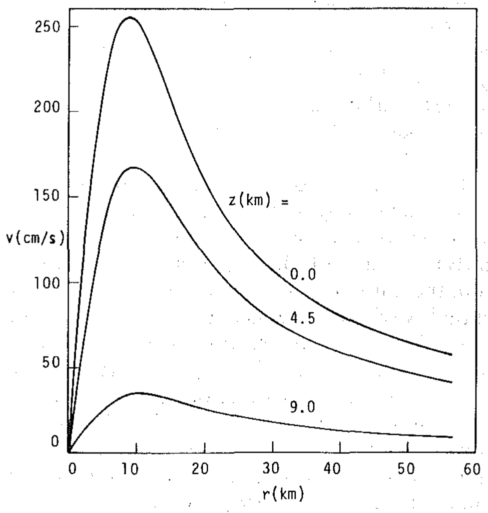

Fig. 2 Swirl speed v, at time $t=0$ at three altitudes z, versus radial distance from the axis of symmetry r, for the result of Fig. 1. (The peak swirl speed occurs at $r \doteq 1.12\ B$, for fixed altitude and time, for the Oseen-type vortex adopted.) Initial swirling is taken quite small. Here $\epsilon = 2.586\cdot10^{12}$ cm^3/s.

ambient reference (ground-level) atmospheric conditions, by (37), $\epsilon = O(3\cdot10^{12}$ cm^3/s). This is an average value for ϵ: enhanced values at earlier time could be afforded by reduced values later. At the Hamburg airport at the time of the firestorm [24], between 0.3 and 3.0 km, $\kappa = 0.96$, and a higher value almost surely held in the Hammerbrook district itself; above 3 km or so, $\kappa = 0.75$. A value of κ somewhat greater than 0.95 near the ground, and somewhat greater than 0.75 at midtropospheric levels, typically is adopted, for the present, two-layer, piecewise-constant polytropic parameterization of atmospheric stability. From data taken at the Hamburg airport, the preexisting vortex is characterized at ground level [8, 24] by $V(0) = 4$ m/s and $B_o(0) = 8$ km, so $\Gamma_o(0) = O(3.2\cdot10^4$ m^2/s); the radius of the strongly convective area at the ground $b_i = 0.5$ km. The other parameter assignments seem standard.

If one approximates the product of the plume-scale dependent variables bW, and entrainment factor α, as constant in time, then (31) yields [recall $B(z,0) = B_o(z)$]

$$B^2(z,t) = B_o{}^2(z) - 2\alpha bWt \tag{47}$$

where, as previously noted, the equation is inappropriate for $B < O(b)$. If for explicitness one adopts $\kappa = 1$, such that the solution for an isopycnic nonrotating atmosphere, (45–46), is employed for all z, so

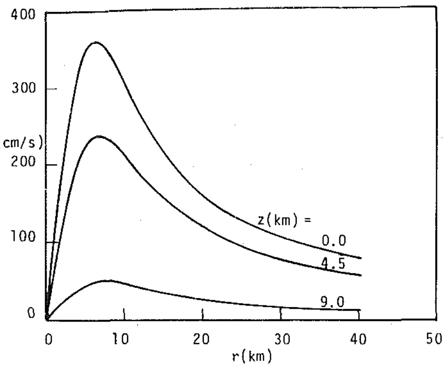

Fig. 3 Swirl speed v at time t = 1.25 hrs, for the case of Figs. 1 and 2. Swirling remains modest.

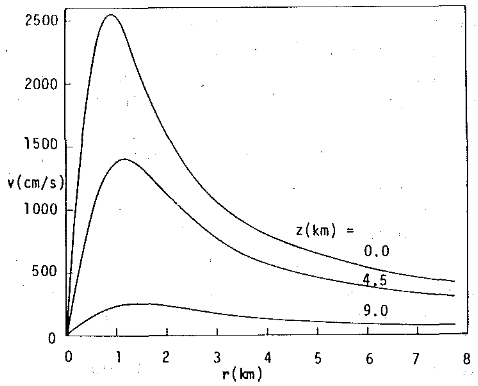

Fig. 4 Swirl speed v at time t = 2.5 hrs, for the case of Figs. 1, 2, and 3. Onset of intense swirling occurs within a span of 1 hr.

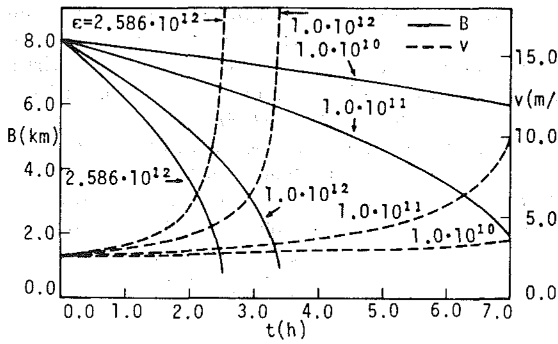

Fig. 5 Ground-level values of the swirl v and the preexisting-vortex radius B versus time t, for the radius of peak swirl ($r \doteq 1.12$ B). Order-of-magnitude decrement of ϵ extends spin-up to such long times that relaxational mechanisms presumably preclude firestorm onset.

$$\alpha bW = \left(\frac{18}{5\pi}\,\alpha_o{}^4\right)^{1/3} [\epsilon g(z+z_i)^2]^{1/3} \tag{48}$$

then, from (10–12) and (45), since $rv = \phi \doteq \phi_{1b}$, at the plume edge $r = b$

$$v(b,z,t) = \frac{B_o(z)\,V(z)}{b(z)}\left\{1 - \exp\left[-\left(\frac{b(z)}{B(z,t)}\right)^2\right]\right\}. \tag{49}$$

One anticipates $B_o(z) \doteq \alpha_o z + B_o(0)$, where

$$v(b,z,t) = O[B_0(z)V(z)/b(z)]$$

for sufficient time t elapsed since ignition for B to decrease from B_o to b over the lower-tropospheric range of z for which

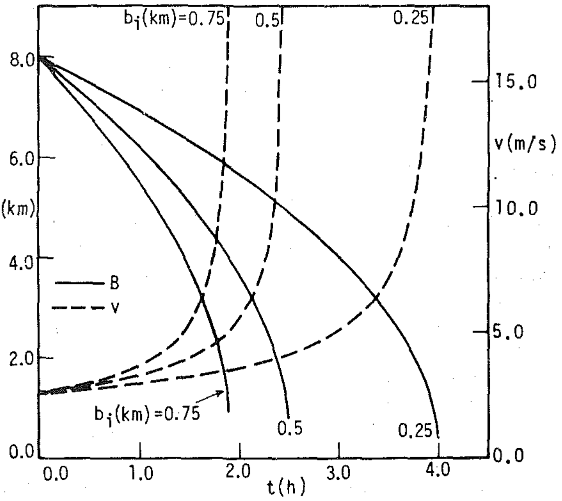

Fig. 6 Ground-level values of the swirl v and the preexisting-vortex radius B versus time t, for the radius of peak swirl ($r \doteq 1.12$ B). Enlarging the radius of convection b_i, shortens the spin-up time. Here $\epsilon = 2.586 \cdot 10^{12}$ cm^3/s.

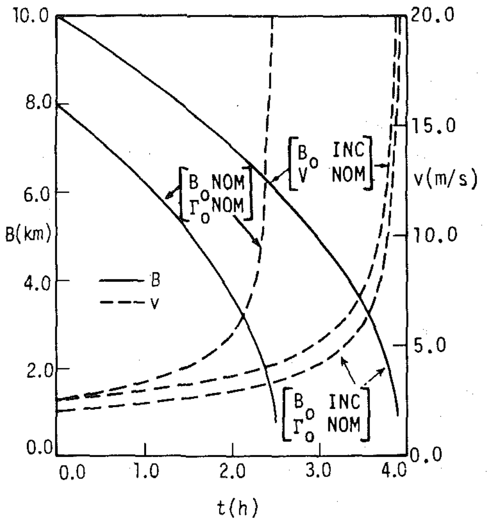

Fig. 7 Ground-level values of the swirl v and the preexisting vortex radius B versus time t, for the radius of peak swirl ($r \doteq 1.12$ B). The initial radius $B_0(z)$ is increased 2 km at all altitudes (denoted B_0 INC). This is presented both with $V(z)$ decreased so Γ_0 is unchanged (denoted Γ_0 NOM), and with $V(z)$ unaltered so Γ_0 is increased at all z (denoted V NOM). Modest increase of B_0 somewhat lengthens spin-up time. Here $\epsilon = 2.586 \cdot 10^{12}$ cm^3/s.

$\Gamma_o > 0$. It is well worth noting from (47) and (48) that the magnitude of swirl is not greatly altered by small changes in B_o, but rather sensitive to changes in ϵ and b_i, and that spin-up, modest at early time, accelerates abruptly. Results are given in Fig. 1-7.

Neglecting the axial pressure gradient in the second of (35) gives b, W, f as functions of z independently of the spin-up, except as reflected in the value assigned α, from (35), (40), and (42). In particular, Figs. 8-10 give the vertical profiles of the plume-scale dependent variables for α_o, $(\alpha_o/10)$, $(\alpha_o/100)$, for several states of atmospheric stability reflected in κ. Two-order-of-magnitude decrement in α from α_o is required for doubling of the the plume altitude, so one infers that the sensitivity of α to $\phi(>\phi_o)$ is substantial. If a modest role holds for the axial pressure gradient, the decrement in time of the characterizing radius B of the preexisting vortex differs under (35) and (46) from the decrement in time

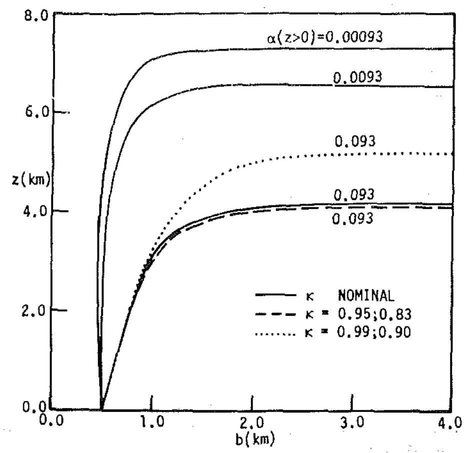

Fig. 8 Plume radius b versus altitude above ground level z. Ground-level values are obtained from (45-46); deviation of the axial pressure gradient from hydrostatic owing to rotation is neglected. Reduction by two orders of magnitude of the entrainment parameter nearly doubles plume height. Also displayed is the effect of altering the ambient stratification [decreasing κ from its value for neutrally buoyant condition ($\kappa = 1$) increases stability, with $\kappa = \gamma^{-1}$ holding for an isothermal layer]. When two values of κ are given for one curve, the first pertains to $z < 2.74$ km and the second, to $z > 2.74$ km. Although other sources give higher values, according to [24] the plume reached only 7 km.

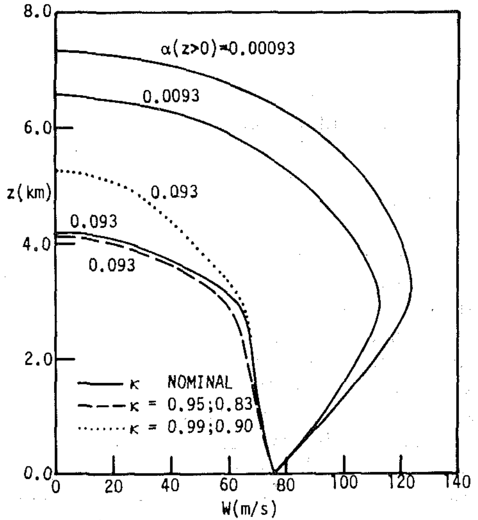

Fig. 9 Vertical component of velocity on the axis of symmetry W versus altitude above ground z, associated with the result of Fig. 8.

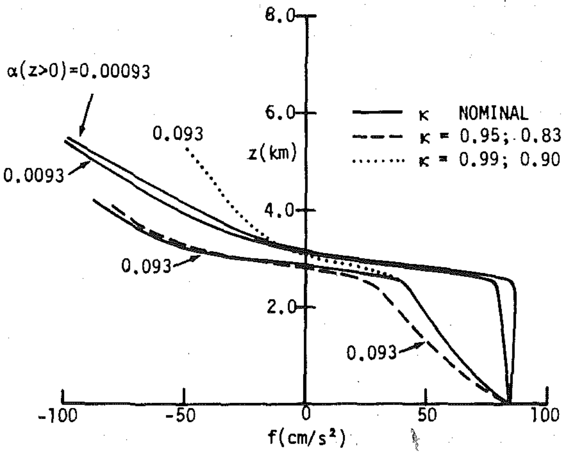

Fig. 10 Centerline density discrepancy from ambient, normalized by the ambient density and multiplied by the magnitude of the gravitational acceleration f versus altitude above ground z, associated with the result of Figs. 8 and 9. Validity of the theory for altitudes for which $f \leq 0$ is problematic.

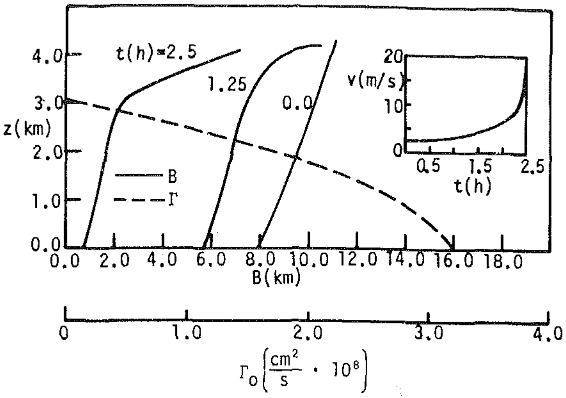

Fig. 11 Preexisting-vortex radius *B* versus altitude above ground *z* at several times since ignition *t*, under nominal parameters (Table 1); also the pre-existing angular momentum Γ_o versus *z*. Also swirl speed *v*(1.12*B*, 0, *t*) versus *t*. Here a variable-density, two-layer, polytropic atmosphere is adopted, whereas a constant-density (neutrally stable) atmosphere is adopted in Fig. 4.

calculated under (48). The distinction derives from the fact that $\kappa \ll 1$ in (35), whereas $\kappa = 1$ under (48); perhaps even more importantly, stratification of the ambient is included appropriately in (35), whereas density is held constant in the oversimplified (but explicit) relation (48). Results are given in Fig. 11.

A point raised earlier just below (46) concerns the spurious ground-level mass and momentum flux incurred by using (45) and (46) to initiate the plume calculation. As a check, ground-level updraft $W(0)$ is decreased by a factor of 4, and simultaneously the ground-level normalized density discrepancy $f(0)$ is increased by a factor of 4, such that the ground-level release of heat per time $H(0)$ is invariant while the mass per time $F(0)$ is reduced by a factor of four [see (34*a*)]. It turns out that for otherwise nominal assignment of values to problem parameters, such alteration of $W(0)$ and $f(0)$ results in a plume of height 5.1 km, as opposed to a height of 4.2 km without such alteration. Thus imprecise ground-level mass and momentum fluxes may not alter overall plume dynamics significantly. While, from (48), such alteration might seem to alter low-tropospheric spin-up, in fact a compensatory radial pressure gradient (not included here) may well enter to restore the influx to the values adopted. This nonhydrostatic-pressure-gradient contribution for strongly buoyant plumes is being investigated, and is to be described in a subsequent publication. Within the weakly buoyant formulation given here, calculations confirm that, uniformly in altitude over the time span for firestorm onset, the axial pressure gradient makes a fairly modest contribution to the balance of inertial and buoyant effects in the conservation of vertical momentum.

Conclusions

Current estimates for firestorm-onset criteria are as follows: "(1) at least 8 pounds of combustible per square foot of fire area, (2) at least half of the structures in the area on fire simultaneously, (3) a wind of less than 8 miles per hour at the time, and (4) a minimum burning area of about half a square mile" [2, pp. 299–300]. On the basis of the study described above, the following alternate criteria are proposed:

1 A localized heat release of order 10^{19} erg/s sustained for at least 2–3 hrs

2 A preexisting weak vortex characterized near ground level by swirl of 4 m/s at radius 8 km, such that preexisting angular momentum (per unit mass) near ground level is $3.2 \cdot 10^4$ m^2/s

3 Absence of a strong ambient crosswind, with less than 4 m/s perhaps being adequate constraint, but with total absence being even more conducive to firestorm onset

4 A very nearly dry-adiabatic lapse rate holding for the lowest few kilometers of the atmosphere.

Lower-tropospheric spin-up to about 20 m/s within 2-3 h seems plausible under such criteria. If the exothermicity of combustibles is taken to be that of dry woody matter consumed readily in forest fires, which is $1.86 \cdot 10^4$ J/g or so, then the requisite fuel loading appears to be about four times the 8 pounds per square foot cited earlier, if an area of 12 km^2 is entailed and the burning continues at high intensity for 6 hrs (as reported at Hamburg). The onset of swirling near the convective-column edge may be abrupt in that it can rise from nearly nil levels to 20 m/s or so within a half hour. The background angular momentum associated with the rotation of the earth is inadequate for spin-up to the cited swirl speed on the scale of 2 hrs or so.

Further work on plumes whose base temperatures are $O(10^3$ K) and which are accompanied by significant swirl is impeded by the current absence of answers to the questions:

1 Is the entrainment rate more properly related to *mass* entrained [i.e., $\rho_a \lim_{r\to\infty} (ru)$] per unit of axial *mass* flux [$bW \cdot \lim_{r\to 0} \rho$], or to *volume* entrained [$\lim_{r\to\infty} (ru)$] per unit of axial *volume* flux (bW)?

2 By how much is the entrainment coefficient reduced by an increase in swirl?

Answers can be furnished experimentally only. In fact, it is clear from already published laboratory experiments on firewhirls [19, 20] that reduction in entrainment with swirl is highly significant.

Acknowledgment

The authors are grateful to technical monitors Mike Frankel and Tom Kennedy for the opportunity to pursue this investigation. This work was supported by the Defense Nuclear Agency under Contract DNA001-83-C-0104. The authors also wish to thank Ann McCollum and Asenatha McCauley for preparation of the manuscript and the figures.

References

1 Bond, H., ed., *Fire and the Air War*, National Fire Protection Association, Boston, Mass., 1946.

2 Glasstone, S., and Dolan, P. J., eds., *The Effect of Nuclear Weapons* (3rd ed.), U.S. Department of Defense and U.S. Department of Energy, Washington, D.C., 1977.

3 Caidin, M., *The Night Hamburg Died*, Ballantine, New York, 1960.

4 Musgrove, G., *Operation Gomorrah—The Hamburg Firestorm Raids*, Jane's, New York, 1981.

5 Middlebrook, M., *The Battle of Hamburg—Allied Bomber Forces against a German City in 1943*, Charles Scribner's Sons, New York, 1981.

6 Irving, D., *The Destruction of Dresden*, Ballantine, New York, 1965.

7 Fisher, G. J. B., *Incendiary Warfare*, McGraw-Hill, New York, 1946.

8 Ebert, C. H. V., "The Meteorological Factor in the Hamburg Fire Storm," *Weatherwise*, Vol. 16, 1963, pp. 70–75.

9 Brandes, E., "Mesocyclone Evolution and Tornadogenesis," *Monthly Weather Review*, Vol. 106, 1978, pp. 995–1011.

10 Carrier, G. F., "Swirling Flow Boundary Layers," *Journal of Fluid Mechanics*, Vol. 49, 1971, pp. 133–144.

11 Burggraf, O. R., Stewartson, K., and Belcher, R., "Boundary Layer Induced by a Potential Vortex," *Physics of Fluids*, Vol. 14, 1971, pp. 1821–1833.

12 Carrier, G. F., and Fendell, F. E., "Analysis of the Near-Ground Wind Field of a Tornado with Steady and Spatially Varying Eddy Viscosity," Wind Field and Trajectory Models for Tornado-Propelled Objects, Report NP-748, Electric Power Research Institute, Palo Alto, Calif., 1978, pp. A-1-A-45.

13 Dergarabedian, P., and Fendell, F., "Parameters Governing the Generation of Free Vortices," *Physics of Fluids*, Vol. 10, 1967, pp. 2293–2299.

14 Emmons, H. W., "Fundamental Problems of the Free Burning Fire,"

Tenth Symposium (International) on Combustion, Combustion Institute, Pittsburgh, Pa., 1965, pp. 951-964.

15 Long, R. R., "Fire Storms," *Fire Research Abstracts and Reviews*, Vol. 9, 1966, pp. 53-68.

16 Graham, H. E., "Fire Whirlwinds," *Bulletin of the American Meteorological Society*, Vol. 36, 1965, pp. 99-103.

17 Lee, S. L., and Hellman, J. M., "Heat and Mass Transfer in Fire Research," *Advances in Heat Transfer*, Vol. 10, Academic, New York, 1974, pp. 219-284.

18 Morton, B. R., Taylor, G., and Turner, J. S., "Turbulent Gravitational Convection from Maintained and Instantaneous Sources," *Proceedings of the Royal Society*, Vol. A234, 1956, pp. 1-23.

19 Emmons, H. W., and Ying, S.-J., "The Fire Whirl," *Eleventh Symposium (International) on Combustion*, Combustion Institute, Pittsburgh, Pa., 1967, pp. 475-488.

20 Ying, S.-J., "The Fire Whirl," Technical Report, Engineering Sciences Laboratory, Division of Engineering and Applied Physics, Harvard University, Cambridge, Mass., 1965.

21 Smith, R. K., "Radiation Effects on Large Fire Plumes," *Eleventh Symposium (International) on Combustion*, Combustion Institute, Pittsburgh, Pa., 1967, pp. 507-515.

22 Taylor, R. J., Evans, S. T., King, N. K., Stephens, E. T., Packham, D. K., and Vines, R. G., "Convective Activity Above a Large-Scale Bushfire," *Journal of Applied Meteorology*, Vol. 12, 1973, pp. 1144-1150.

23 Prandtl, L., and Tietjens, O. G., *Fundamentals of Hydro- and Aeromechanics*, Dover, New York, 1957.

24 Brunswig, H., *Feuersturm uber Hamburg*, Motorbuch, Stuttgart, Germany, 1981.

25 Schubert, R., "Examination of the Building Density and Fuel Loading in the Districts Eimsbüttel and Hammerbrook in the City of Hamburg as of July 1943" (translation), Project MU-6464, Stanford Research Institute, Menlo Park, Calif., 1969.

D. Duffy
Laboratory for Atmospheric Sciences,
NASA/Goddard Space Flight Center,
Greenbelt, Md. 20771

The Temperature Distribution Within a Sphere Placed in a Directed Uniform Heat Flux and Allowed to Radiatively Cool

The temperature field within a sphere is found when the sphere is heated by a directed heat flux and cooled by blackbody radiation. For small heat fluxes, the analytic solution is obtained by transform methods. For large heat fluxes, the solution is computed numerically.

Introduction

The steady-state temperature within a sphere that is heated by a uniform heat flux and cooled by radiation was found by Lord Rayleigh [4] over one hundred years ago. It has been the subject of student exercises in books authored by Byerly [5] and Lebedev et al. [6]. Moon and Spencer [7] have included it as a worked example in their text.

The problem of the transient evolution from an initial temperature T_0 to this steady state has not yet been solved. Recently Werley and Gilligan [8] gave the temporal evolution of the temperature field within a sphere heated by a directed, uniform heat flux. Because they did not include radiation, the temperature field within the sphere grew linearly with time and no steady-state solution existed. This solution has also been given by Cheung et al. [9] in their study of the transient thermal stress within a sphere due to local heating.

These problems differ from those studies of the thermal effect of solar heating on an artifical satellite published by Nichols [10], Hrycak [11], Phythian [12], and Sova and Malmuth [13]. In their papers, the satellite was assumed to be a conducting spherical shell containing an ideal gas. Because the shell is so thin, there is no radial dependence.

Although the solution given by Werley and Gilligan is adequate for small times, eventually radiative effects will become important and the equilibrium solution of Rayleigh will be established. In this paper the work of Werley and Gilligan will be extended and the transient solution will be found when both a directed heat flux and radiation is present. In the case of small heat flux, the analytic solution is found. In the case of strong heat flux, the problem is solved numerically.

Mathematical Equations

Heat conduction within a sphere of uniform conductivity is governed by the nondimensional equation

$$\frac{1}{r^2}\frac{\partial}{\partial r}\left(r^2\frac{\partial T}{\partial r}\right)+\frac{1}{r^2\sin\theta}\frac{\partial}{\partial\theta}\left(\sin\theta\frac{\partial T}{\partial\theta}\right)=\frac{\partial T}{\partial t} \qquad (1)$$

The initial condition is $T(r,\theta,0) = 1$ and the boundary condition at the surface of the sphere ($r=1$) is given by

$$\frac{\partial T}{\partial r}+\alpha(T^4-1)=\beta\cos\theta\mathrm{H}(\cos\theta) \qquad (2)$$

where

$$\alpha=\frac{\sigma T_0{}^4}{(kT_0/a)}=\frac{\text{radiative cooling}}{\text{surface heat flux}}$$

$$\beta=\frac{F}{kT_0/a}=\frac{\text{directed heat flux}}{\text{surface heat flux}}$$

The parameter α gives a measurement of the ratio of radiative cooling to the surface heat flux; β is a measure of the ratio of directed heat flux to the surface heat flux.

Small Heat Flux

If the impinging heat flux is sufficiently small, the departure of T from one will be small and T^4-1 can be linearized to $4(T-1)$. If we define

$$T=1+\beta T' \qquad (3)$$

then the heat equation (1) remains unchanged except for T' replacing T while the initial condition becomes $T'(r,\theta,0) = 0$ and

$$\frac{\partial T'}{\partial r}+4\alpha T'=\cos\theta H(\cos\theta) \qquad (4)$$

Clearly if $T' = 0(1)$, then β must be much less than one for the linearization of black-body radiation to be correct.

Taking the Laplace transform of the heat equation, equation (1) becomes

$$\frac{1}{r^2}\frac{\partial}{\partial r}\left(r^2\frac{\partial\bar{T}'}{\partial r}\right)+\frac{\partial}{r^2\sin\theta}\frac{\partial}{\partial\theta}\left(\sin\theta\frac{\partial\bar{T}'}{\partial\theta}\right)=s\bar{T}' \qquad (5)$$

with

$$\frac{\partial\bar{T}'}{\partial r}+4\alpha\bar{T}'=\frac{\cos\theta}{s}H(\cos\theta)\text{ at }r=1 \qquad (6)$$

because $T'(r,\theta,0) = 0$. The solution to the partial differential equation (5) that is finite throughout the sphere is

$$\bar{T}'(r,\theta,s)=\sum_{n=0}^{\infty}A_n i_n(qr)P_n(\cos\theta) \qquad (7)$$

where $q = s^{1/2}$.

The coefficients A_n are found by substituting equation (7) into the boundary condition (6), giving the formal expression for $\bar{T}'$

$$\bar{T}'(r,\theta,s)=\sum_{n=0}^{\infty}\frac{\left(\frac{2n+1}{2}\right)i_n(qr)P_n(\cos\theta)}{s[qi_n{}'(q)+4\alpha i_n(q)]}\int_0^1\mu P_n(\mu)d\mu \qquad (8)$$

In order to evaluate $T'(r,\theta,t)$ from equation (8), Bromwich's integral in the complex plane is employed. From the power series for $i_n(x)$

$$i_n(x)=\frac{x^n}{1.3.5.\ldots(2n+1)}+0(x^{n+2}) \qquad (9)$$

Contributed by the Heat Transfer Division for publication in the JOURNAL OF HEAT TRANSFER. Manuscript received by the Heat Transfer Division February 24, 1984.

Table 1 The first six roots of the equation (12) for $n = 0, 1, 2$, and 3. The top number is for $\alpha = 0$; the lower, $\alpha = 0.25$.

	x_1	x_2	x_3	x_4	x_5	x_6
$n=0$	0.000 2.043	4.493 5.396	7.725 8.578	10.904 11.737	14.066 14.888	17.221 18.036
$n=1$	2.082 2.744	5.940 6.117	9.206 9.317	12.404 12.486	15.579 15.644	18.743 18.796
$n=2$	3.342 3.870	7.290 7.443	10.614 10.713	13.846 13.921	17.043 17.102	20.222 20.272
$n=3$	4.514 4.973	8.584 8.722	11.973 12.064	15.242 15.314	18.469 18.524	21.667 21.714

it can readily be shown that $s = 0$ is a simple pole provided $\alpha \neq 0$. The terms associated with this pole give the steady-state solution

$$T_s'(r,\theta) = \frac{1}{16\alpha} + \frac{3r\cos\theta}{2(1+4\alpha)}$$

$$- \sum_{n=1}^{\infty} \frac{4n+1}{2} \frac{r^{2n} P_{2n}(\cos\theta)}{2n+4\alpha} \frac{P_{2n}(0)}{(2n+2)(2n-1)} \tag{10}$$

because

$$\int_0^1 x P_n(x) dx = -\frac{P_n(0)}{(n+2)(n-1)} \text{ for } n > 1$$

See [14].

The remaining poles in equation (8) are given by roots to the equation

$$q i_n'(q) + 4\alpha i_n(q) = 0 \tag{11}$$

The only roots to equation (11) occur when $q = -ix$ where x satisfies the equation

$$x j_n'(x) + 4\alpha j_n(x) = 0 \tag{12}$$

where $i = \sqrt{-1}$.

The roots to equation (12) may be obtained either graphically or by a numerical algorithm. The roots for the case of $\alpha = 0$ (no radiation) were found by Werley and Gilligan from the local extrema from tables of spherical Bessel functions. In Table 1, the first six roots for $n = 0, 1, 2$ and 3 for $\alpha = 0$ and 0.25 are listed. These roots were calculated numerically by a simple bisection method. Except for the lowest root, the roots for $\alpha = 0$ and 0.25 are fairly close.

Because the roots of equation (12) depend weakly upon α, this suggests that an approximate formula for them can be found by expanding around the solutions for $\alpha = 0$. If a Taylor expansion is made about the roots to $j_n'(x_0) = 0$, then

$$x(x-x_o) j_n''(x_o) + 4\alpha j_n(x_o) = 0 \tag{13}$$

after neglecting quadratic terms and noting that $j_n'(x_o) = 0$. Using the differential equation for $j_n(x)$, $j_n''(x_o)$ can be eliminated from equation (13) and equation (13) becomes

$$x(x-x_o) - 4\alpha\left(\frac{1}{1-\frac{n(n+1)}{x_o^2}}\right) = 0 \tag{14}$$

or

$$x = \frac{x_o}{2}\left[1 + \sqrt{1 + \frac{16\alpha}{x_o^2 - n(n+1)}}\right] \tag{15}$$

Because $x_o^2 >> n(n+1) \geq 1$ for most of the roots, equation (15) can be used to find roots even for α of order 1. Equation (15) can be further approximated by

$$x = x_0\left[1 + \frac{4\alpha}{x_o^2}\left(1 + \frac{n(n+1)}{x_o^2} + \frac{n^2(n+1)^2}{x_o^4} + \ldots\right)\right] \tag{16}$$

Regardless of the method of calculating α, there are an infinite number of simple poles for each n because each root of equation (12) is unique. Consequently, the transient part of the solution is given by

$$\theta(r,\theta,t) = \frac{1}{2r} \sum_{n=1}^{\infty} \frac{\sin(\beta_n r)}{\sin(\beta_n)} \frac{1}{4\alpha - 16\alpha^2 - \beta_n^2} e^{-\beta_n^2 t}$$

$$+ \cos\theta \sum_{n=1}^{\infty} \frac{j_1(\mu_n r) e^{-\mu_n^2 t}}{(2 - \mu_n^2 + 4\alpha - 16\alpha^2) j_1(\mu_n)}$$

$$- \sum_{m=1}^{\infty} \frac{2m + 1/2}{2m^2 + m - 1} P_{2m}(0) P_{2m}(\cos\theta)$$

$$\left\{\sum_{n=1}^{\infty} \frac{j_{2m}(\gamma_n r) e^{-\gamma_n^2 t}}{j_{2m}(\gamma_n)[2m(2m+1) - \gamma_n^2 + 4\alpha - 16\alpha^2]}\right\} \tag{17}$$

where β_n are roots of

$$\beta_n \cot(\beta_n) = 1 - 4\alpha \tag{18}$$

μ_n the roots of

$$\mu_n^2 \tan(\mu_n) + (2 - 4\alpha)(\mu_n - \tan(\mu_n)) = 0 \tag{19}$$

and γ_n the roots of

$$\gamma_n j_{2m}'(\gamma_n) + 4\alpha j_{2m}(\gamma_n) = 0, \; m = 1,2,3,4 \tag{20}$$

In obtaining the denominator of equation (17) the differential

Nomenclature

a = radius of the sphere
erfc(x) = complimentary error function [1]
F = heat flux
$H(x)$ = Heaviside step function
$i_n(x)$ = modified spherical Bessel function of the first kind [2]
$j_n(x)$ = spherical Bessel function of the first kind [3]
k = thermal conductivity
$P_n(x)$ = Legendre polynomial
t = $\kappa \times \text{time}/a^2$
T = temperature/T_0
T_0 = initial temperture
α = $a\sigma T_0^3/k$
β = Fa/kT_0
κ = thermal diffusivity
μ = $\cos\theta$
σ = Stefan-Boltzmann constant
θ = angle (0 deg at North pole to 180 deg)

equation defining the spherical Bessel function and equation (12) were used.

In Fig. 1, the tempertaure field when (a) $\alpha=0$ and (b) $\alpha=0.025$ at the nondimensional times t = 0.05, 0.5, and 5.0 are presented. For a sphere of pure iron (k = 80.3 W/m K) this α corresponds to a sphere of radius 1.3 m if the initial temperature is 300 K. Terms up to n = 6 and m = 2 were included in the calculation. The solutions are essentially identical for times up to $t=0.1$ and show strong heating at the surface of the sphere where the directed heating is taking place. After the time $t=0.1$, the solutions begin to diverge. In the case of no radiation, the solution increases linearly with time and the temperature variation from pole to pole is of secondary importance. In the case when radiation is present, the solution approaches the steady-state solution given by equation (10).

An alternative method of obtaining our results is to use Green's functions as given by Carslaw and Jaeger [15] in section 14.1. They showed that heat conduction within a solid that is radiating into a medium at temperature $\phi(x,y,z,t)$ can be computed from a surface and time integral if the Green's function for a solid that is radiating into a medium at temperature zero is known. Because equation (4) is identical to the radiative boundary condition for a sphere surrounded by a medium at temperature $\mu H(\mu)/(4\alpha)$, this technique could have been used because the Green's function for a sphere radiating into a medium at temperature zero is given in Carslaw and Jaeger, section 14.6, part II [16]. As a check of our results, this technique was tested and the sum of equation (10) and (17) was obtained.

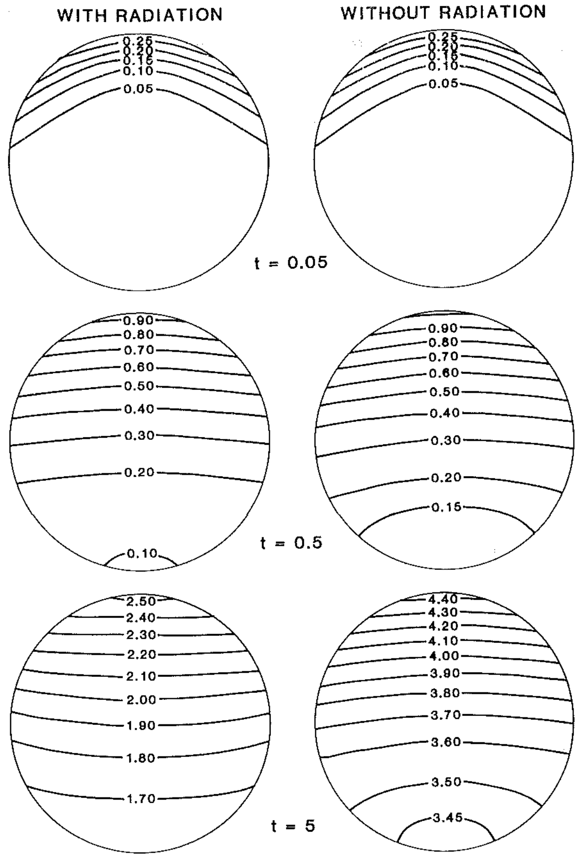

Fig. 1 Nondimensional temperature deviation T' within a sphere at nondimensional times t = 0.05, 0.5, 5.0 with and without radiation for a small directed heat flux.

Solution for Small Time

Although the total solution expressed by equation (10) plus equation (17) is true for all time, it converges very slowly for very small time. Furthermore, calculating the roots to equation (20) and summing equations (10) and (17) for large m is very cumbersome because it involves spherical Bessel functions. However, a rapidly converging series can be found because the inverse of a Laplace transform for small time is given by the limit of $s \to \infty$. The only difficulty is the presence of r in the modified spherical Bessel function of equation (8). For small r, the asymptotic expansion for $i_n(x)$ will not be valid. However, we can circumvent this difficulty because we know that the initial effects of the heating will be confined to the surface of the sphere. Consequently, an expression can be found for radii $r \geq 0(0.1)$, and the rise in temperature near the center can be taken to be negligibly small.

For large arguments, the modified spherical Bessel function of the first kind is given by the asymptotic expression

$$i_n(z) \sim \frac{1}{2z}e^z \tag{21}$$

as $z \to \infty$. See Ref. [2].

Therefore, for finite r,

$$\bar{T}'(r,\theta,s)=\frac{e^{-q(1-r)}}{rs^{3/2}}\left(1+(1-4\alpha)\frac{1}{q}+\ldots\right)$$
$$\sum_{n=0}^{\infty}\frac{2n+1}{2}P_n(\cos\theta)\int_0^1 \mu P_n(\mu)d\mu \tag{22}$$

Inverting the Laplace transforms and recognizing that the expansion in Legendre polynomials is $\mu H(\mu)$, equation (22) becomes

$$T'(r,\theta,t)=\frac{\mu H(\mu)}{r}\left\{\left[2\left(\frac{t}{\pi}\right)^{1/2}\exp\left(-\frac{(1-r)^2}{4t}\right)\right.\right.$$
$$-(1-r)\operatorname{erfc}\left[\frac{(1-r)}{2t^{1/2}}\right]$$
$$+(1-4\alpha)\left[\left(t+\frac{(1-r)^2}{2}\right)\operatorname{erfc}\left(\frac{1-r}{2t^{1/2}}\right)\right.$$
$$\left.\left.-(1-r)\left(\frac{t}{\pi}\right)^{1/2}\exp\left(-\frac{(1-r)^2}{2t}\right)\right]+\ldots\right\} \tag{23}$$

The results given by equation (23) have been compared with the exact solution equation (10) plus equation (17) for α = 0.025. The solutions agreed within 5 percent for times up to 0.05.

Numerical Solution

When the heating becomes sufficiently large so that β is no longer small, the linearization of long-wave radiation becomes invalid unless the radiation is extremely large and equations (1) and (2) must be solved numerically. The most widely used technique for efficiently solving the heat equation in two space dimensions is the alternating direction implicit (ADI) method [17]. I have chosen, however, to use the hopscotch method developed by Gourlay [18]. Gourlay has shown that this hopscotch method is 3 to 4 times faster than a comparable ADI computation and is far easier to code.

This hopscotch method may be ilustrated by considering the one-dimensional heat equation. If n denotes the time level and i the ith grid point, the finite difference grid is as follows:

+	0	+	0	+	0	+	$n+2$ line
0	+	0	+	0	+	0	$n+1$ line
$i-3$	$i-2$	$i-1$	i	$i+1$	$i+2$	$i+3$	n line, all values known

At time step $n+1$, the temperature is first calculated using the classic explicit approximation

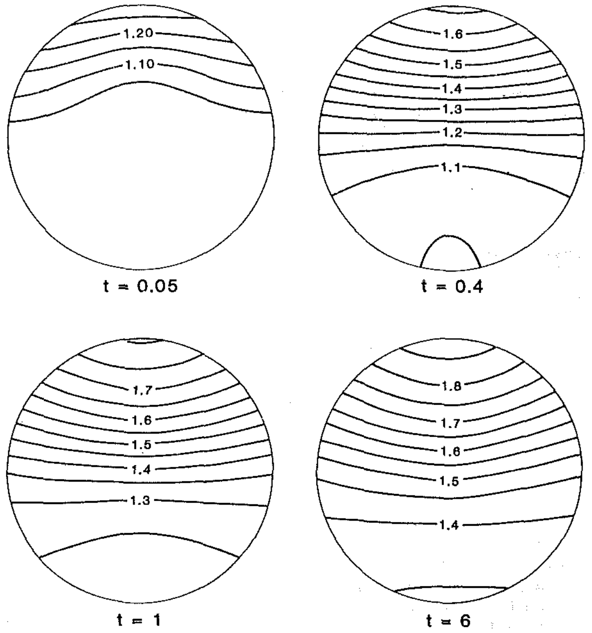

Fig. 2 Nondimensional temperature within a sphere at nondimensional times t = 0.05, 0.4, 1.0, and 6.0 when α = 0.05 and β = 1.0. The interval is every 0.05.

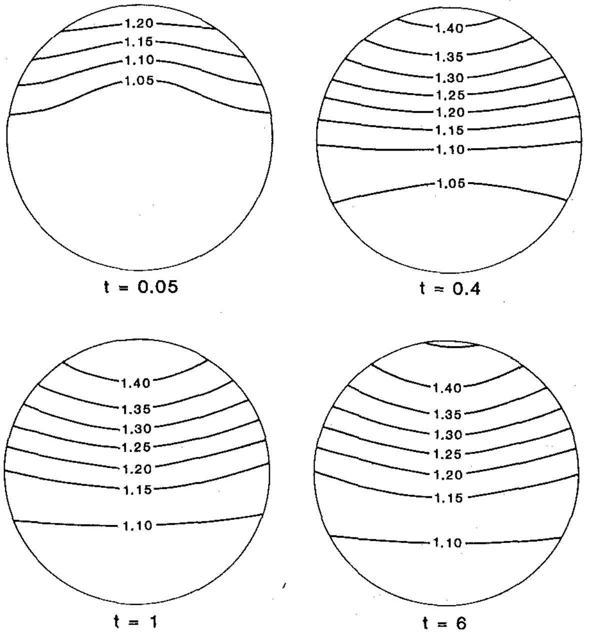

Fig. 3 Nondimensional temperature within a sphere at nondimensional times t = 0.05, 0.4, 1.0, and 6.0 when α = 0.2 and β = 1.0. The interval is every 0.05.

$$\frac{T_i^{n+1}-T_i^n}{\Delta t}=\frac{T_{i+1}^n-2T_i^n+T_{i-1}^n}{(\Delta x)^2} \tag{24}$$

at the points marked by a zero. Then the temperatures at the + points is calculated by the backwards implicit approximation:

$$\frac{T_i^{n+1}-T_i^n}{\Delta t}=\frac{T_{i+1}^{n+1}-2T_i^{n+1}+T_{i-1}^{n+1}}{(\Delta x)^2} \tag{25}$$

Because the tempertaure is already calculated at the 0 points, T_{i+1}^{n+1} and T_{i-1}^{n+1} is already known in the implicit calculation and the overall result is a series of explicit calculations. During the $n+2$ calculation, the roles of each grid point is reversed, as shown in the diagram.

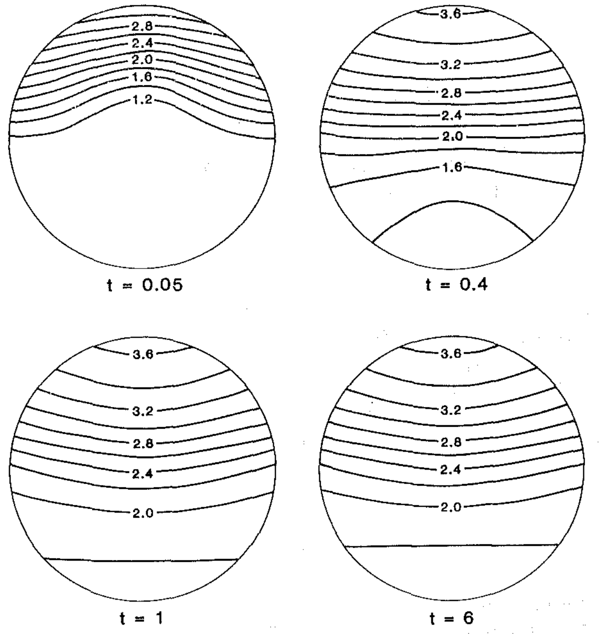

Fig. 4 Nondimensional temperature within a sphere at nondimensional times t = 0.05, 0.4, 1.0, and 6.0 when α = 0.05 and β = 10.0. Interval is every 0.2.

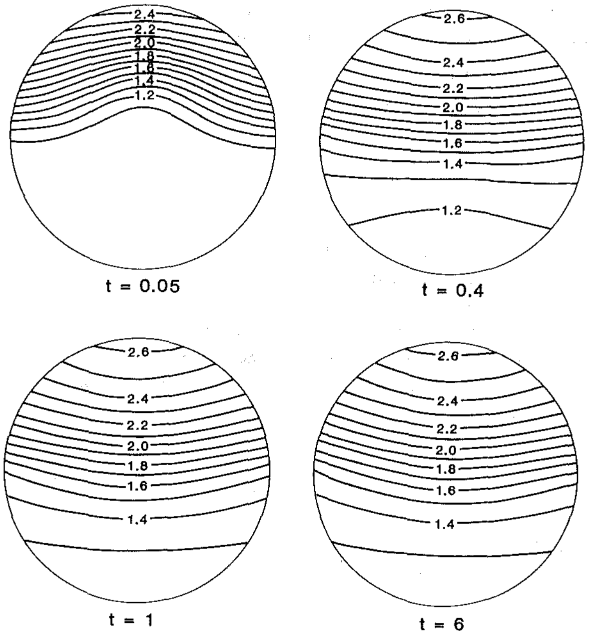

Fig. 5 Nondimensional temperature within a sphere at nondimensional times t = 0.05, 0.4, 1.0, and 6.0 when α = 0.2 and β = 10.0. Interval is every 0.1.

In the case of two space dimensions, our one-dimensional scheme can be extended by introducing the odd-even function

$$\beta_{i,j}^n = \begin{cases} + \text{ if } i+j+n \text{ is odd} \\ 0 \text{ if } i+j+n \text{ is even} \end{cases}$$

At the zero points, the temperature is calculated by the classic explicit approximation. Then, at the + points, the temperature is calculated by the backwards implicit approximation. Once again the overall algorithm is explicit because the values at $T_{i+1,j}^{n+1}$, $T_{i-1,j}^{n+1}$, $T_{i,j+1}^{n+1}$, and $T_{i,j-1}^{n+1}$ in the implicit calculation have been calculated using the classic explicit approximation. However, the scheme is unconditionally stable.

For the numerical solution, the heat equation was rewritten as

$$\frac{\partial^2 T}{\partial r^2}+\frac{2}{r}\frac{\partial T}{\partial T}+\frac{1}{r^2}\frac{\partial^2 T}{\partial \theta^2}+\frac{\cot(\theta)}{r^2}\frac{\partial T}{\partial \theta}=\frac{\partial T}{\partial t} \tag{26}$$

The heat equation (26) has three singularities: at the center of the sphere and at the poles. At the origin, the finite difference form of the heat equation is

$$\frac{\partial T}{\partial t}=\frac{6(T_m-T^{(0)})}{\delta r^2} \tag{27}$$

where T_m is the mean value of temperature over the sphere of radius δr, centered at the origin, and $T^{(0)}$ the temperature at the origin [19]. A backwards implicit method was used to solve for the temperature at the origin.

At the poles, there are singularities because $\sin\theta$ and $\partial T/\partial\theta$ go to zero and the fourth term in equation (26) becomes indeterminant. Applying l'Hospital's rule, equation (26) becomes

$$\frac{\partial^2 T}{\partial r^2}+\frac{2}{r}\frac{\partial^2 T}{\partial r}+\frac{2}{r^2}\frac{\partial^2 T}{\partial \theta^2}=\frac{\partial T}{\partial t} \tag{28}$$

at both poles.

An imaginary row of grid points were introduced just outside the sphere so that centered differences could be used in both the radial and azimuthal directions with a resolution of $\Delta r = 0.05$ and $\Delta\theta = 5$ deg. The heat equation and the surface boundary condition were combined to eliminate the fictitious points. During the backwards implicit step of the integration, the equations along the surface became

$$\frac{\alpha\Delta t(T_{ij}^{n+1})^4}{1+(\Delta r)^2+(\Delta\theta)^2}+T_{ij}^{n+1}=\text{constant} \tag{29}$$

This quartic equation was solved by the iterative scheme

$$y^{n+1}=\text{constant}-\frac{\alpha\Delta t(y^n)^4}{1+(\Delta r)^2+(\Delta\theta)^2} \tag{30}$$

where y^n is the temperature found during the nth iteration and y^{n+1} represents the next iteration. The time step was taken to be $\Delta t = 2\times10^{-4}$.

To check the accuracy of the numerical solution, several experiments were run with a longer time step and coarser resolution. In each experiment either Δr or $\Delta\theta$ or the time step was doubled while the other two parameters remained fixed at their original value. It was found that doubling Δr, $\Delta\theta$ and the time step resulted in differences of 3, 7 and 1 percent, respectively, between the two solutions. Furthermore, it was found that if $\Delta\theta$ was less than Δr, then the temperature given by equation (27) overpredicted the temperature at the center. The amount of overprediction depended upon the ratio of $\Delta r/\Delta\theta$.

In Figs. 2–5, the nondimensional temperature field within the sphere is shown for $t = 0.05$, 0.4, 1.0, and 6.0 when $\alpha = 0.05$ or 0.2 and $\beta = 1.0$ or 10.0. As the amount of radiation increases (larger α), the greater the radiative cooling and the less the temperature rises within the sphere. Similarly, for a fixed radiative cooling, the larger the directed heating (greater β) the larger the temperature derivates from the outside temperature.

The evolution of the temperature field is similar to that in the case of small directed heating. Initially there is a strong temperature gradient near the top of the sphere. As time progresses, the heating spreads throughout the sphere and a steady-state is eventually reached.

Acknowledgments

The manuscript was expertly typed by Ms. Lora Thompson and the figures were done by Mr. Brian Sherbs. Computations were performed at the NASA High-Speed Computer Facility. The author would also like to thank one of the reviewers for pointing out the solution with Green's function.

References

1 Abramowitz, M., and Stegun, I. A., *Handbook of Mathematical Functions*, Dover Publications, New York, 1964, pp. 297–309.

2 Abramowitz, M., and Stegun, I. A., *Handbook of Mathematical Function*, Dover Publications, New York, 1964, pp. 443–445.

3 Abramowitz, M., and Stegun, I. A., *Handbook of Mathematical Functions*, Dover Publications, New York, 1964, pp. 437–441.

4 Rayleigh, Lord, "On the Value of the Integral $\int_0^1 Q_n' \, Q_n \, d\mu$, Q_n, Q_n' Being Laplace's Coefficients of the Orders n,n', with Application to Theory of Radiation," *Phil. Trans. (London)*, Vol. 160, 1870, pp. 579–590.

5 Byerly, W. E., *An Elementary Treatise on Fourier's Series and Spherical, Cylindrical, and Ellipsoidal Harmonics*, Ginn and Co., Boston, 1893, p. 177.

6 Lebedev, N. N., Skalskaya, T. P., and Ulfyand, Y. S., *Worked Problems In Applied Mathematics*, Dover Publishers, New York, 1965, pp. 90–91.

7 Moon, P., and Spencer, D. E.,, *Field Theory for Engineers*, D. van Nostrand, New York, 1961, pp. 221–224.[1]

8 Werley, A., and Gilligan, J. G., "The Temperature Distribution of a Sphere Placed in a Directed Uniform Heat Flux," ASME JOURNAL OF HEAT TRANSFER, Vol. 103, 1981, pp. 399–401.

9 Cheung, J. B., Chen, T. S., and Thirumalai, K., "Transient Thermal Stresses in a Sphere by Local Heating," ASME *Journal of Applied Mechanics*, Vol. 41, 1974, pp. 930–934.

10 Nichols, L., "Surface-Temperature Distribution on Their Walled Bodies Subjected to Solar Radiation in Interplanetary Space," TN D-584, Oct. 1961, NASA.

11 Hyrcak, P., "Influence of Conduction on Spacecraft Skin Temperature," *AIAA Journal*, Vol. 1, No. 11, Nov. 1963, pp. 2619–2621.

12 Phythian, J. E., "Heating of the Cavity Inside a Spherical Shell Satellite," *AIAA Journal*, Vol. 3, No. 1, Jan. 1964, pp. 151–154.

13 Sova, G. J., and Malmuth, N. D., "Asympototic Solutions for Heat Conduction in Radiating Shells Subject to Discontinuous Solar Flux," *AIAA Journal*, Vol. 7, No. 8, 1969, pp. 1631–1633.

14 Gradshteyn and Ryzhik, I. M., *Tables of Integrals, Series, and Products*, Academic Press, New York, 1965, Formula 7.121.

15 Carslaw, H. S., and Jaeger, J. C., *Conduction of Heat in Solids*, Oxford University Press, London, 1959, pp. 353–355.

16 Carslaw, H. S., and Jaeger, J. C., *Conduction of Heat in Solids*, Oxford University Press, London, 1959, p. 382.

17 Peaceman, D. W., and Rachford, H. H., Jr., "The Numerical Solution of Parabolic and El iptic Differential Equations," *SIAM J.*, Vol. 3, 1955, pp. 28–41.

18 Gourlay, A. R., "Hopscotch: A Fast Second-Order Partial Differential Equation Solver," *J. Inst. Math. Appl.*, Vol. 6, 1970, pp. 375–390.

19 Smith, G. D., *Numerical Solution of Partial Differential Equations*, Oxford University Press, London, 1969, pp. 44–45.

---

[1] In their Fig. 8.05, the parameter ϵ is incorrectly stated as 20 W/m^{2}K. It should be 5 W/m^{2}K.

J. R. Dryden
Mem. ASME
The University of Western Ontario,
Faculty of Engineering Science,
London, CANADA
NGA 5B9

M. M. Yovanovich
Mem. ASME
University of Waterloo,
Department of Mechanical Engineering,
Waterloo, CANADA

A. S. Deakin
The University of Western Ontario
Department of Applied Mathematics
London, CANADA

The Effect of Coatings on the Steady-State and Short Time Constriction Resistance for an Arbitrary Axisymmetric Flux

The effect of a coating upon the short-time and steady-state constriction resistance is analyzed for an arbitrary axisymmetric contact spot flux. At very short times the expression obtained for R is identical to the expression for one-dimensional transient heat flow through a two-layer wall. At steady-state, the results of the analysis predict that the effect of the coating are mainly dependent on the relative thermal properties of the coating and substrate. The limiting cases, where the coating thickness approaches either zero or infinity, are discussed.

1 Introduction

When two apparently flat surfaces are pressed into contact it is well known that the actual contacting area is very small. The contacting asperities are widely separated, and if heat is to be passed through the interface there is a thermal constriction. In most cases of practical interest the contacting spots are sufficiently far apart to treat them individually as being an isolated spot on a half-plane. The constriction resistance of a spot of radius a of a half-plane with thermal conductivity k is equal to about $1/(4ka)$.

Often surfaces are coated with material having different mechanical and thermal properties from the substrate. These surface layers although apparently thin may cause large changes in the constriction resistance. In many present-day applications, such as laser annealing and microelectronics, it is important to know quantitatively the effect of a surface coating upon the constriction resistance. Recently, the effect of the coating upon the steady-state constriction resistance, for a particular specified flux, has been analyzed [1]. Here, a more general analysis is undertaken. The effect of the coating upon the short-time and also the steady-state constriction resistance for any axisymmetric flux is analyzed.

Figure 1 shows a half-space of substrate material 2 with a coating of material 1 having thickness δ. There is an axisymmetric flux $f(r)$, prescribed over a circular spot of radius a and outside this spot an adiabatic boundary condition is imposed. Initially the temperatures in materials 1 and 2 are assumed to be zero. The aim of the analysis performed in this paper is to find the effect of the coating upon the short time and steady-state constriction resistance. (On the surface $z=0$, the average temperature of the circular spot, $0<r<a$, is equal to $R \times Q$). The mathematical details are discussed later.

The results of the analysis indicate that when $\mathrm{Fo}_1 < 1/10$ the constriction resistance is controlled by one-dimensional heat flow. The expression obtained for R is identical to that obtained from the analysis of transient heat flow through a two-layer wall. At steady-state

$$R = R_{1c} - \frac{1}{2\pi a k_1}\left[\ln(1-K)\frac{a}{\delta} + C_3\left(\frac{a}{\delta}\right)^3 + C_5\left(\frac{a}{\delta}\right)^5 \ \ldots\right]$$

The coefficients C_3, C_5, . . . depend on $f(r)$. If the coating is thick enough so that the terms involving $(a/\delta)^3$, $(a/\delta)^5$, . . . can be neglected, or if the coating is highly conductive relative to the substrate so that $\ln(1-K)$ is large compared with C_3, C_5 . . ., then

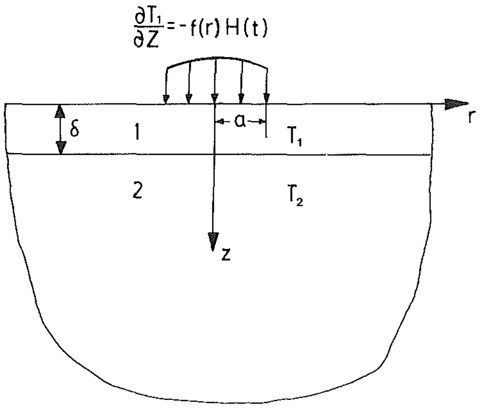

Fig. 1 Half-space with coating of thickness δ and axisymmetric flux $0<r<a$. Coating is material 1 and substrate is material 2.

$$R \approx R_{1c} - \frac{1}{2\pi a k_1}\ln(1-K)\left(\frac{a}{\delta}\right)$$

If the coating is very thin, so that $2/1-K\ \delta/a$ is somewhat less than one, then

$$R = R_{2c} - \frac{1}{\pi a k_1}\frac{2K}{1-K}\frac{2}{1-K}\frac{\delta}{a}[1+0(1)]$$

The higher-order terms of the thin film expansion cannot be found unless $f(r)$ is specified.

2 Problem and Analysis

A half-plane with a coating is to be analyzed to find the effect of the coating upon the constriction resistance. The transient axisymmetric problem is stated below. Referring to Fig. 1, the temperatures $T_1(r, z, t)$ and $T_2(r, z, t)$ must satisfy the heat conduction equation

$$\frac{\partial T_1}{\partial t} = \alpha_1 \nabla^2 T_1 \quad r>0, 0<z<\delta, t>0 \tag{1}$$

$$\frac{\partial T_2}{\partial t} = \alpha_2 \nabla^2 T_2 \quad r>0, z>\delta, t>0 \tag{2}$$

where

$$\nabla^2 = \frac{\partial^2}{\partial r^2} + \frac{1}{r}\frac{\partial}{\partial r} + \frac{\partial^2}{\partial z^2}$$

Initially at $t=0$

$$T_1(r,z,0) = 0 \quad r>0, 0<z<\delta \tag{3}$$

$$T_2(r,z,0) = 0 \quad r>0, z>\delta \tag{4}$$

Contributed by the Heat Transfer Division for publication in the JOURNAL OF HEAT TRANSFER. Manuscript received by the Heat Transfer Division September 29, 1984.

At the interface, $z=\delta$ there is continuity of both temperature and flux

$$T_1(r,\delta,t)=T_2(r,\delta,t) \tag{5a}$$

$$k_1\frac{\partial}{\partial z}T_1(r,\delta,t)=k_2\frac{\partial}{\partial z}T_2(r,\delta,t) \tag{5b}$$

At $z=0$, an axisymmetric heat flow is prescribed

$$\left.\begin{aligned}\frac{\partial T_1}{\partial z}(r,0,t)&= -f(r)H(t) \quad r<a\\ &= 0 \quad r>a\end{aligned}\right\} \tag{6a}$$

where $H(t)$ represents a Heaviside unit function and $f(r)$ is arbitrary except that

$$k_1\int_{r=0}^{a}2\pi rf(r)\,dr=Q \quad (t>0) \tag{6b}$$

At this point the integral I_1 is defined as

$$I_1=\int_{x=0}^{1}f(ax)x\,dx=\frac{Q}{2\pi a^2k_1} \tag{6c}$$

where the integral I_1 follows from (6b) by a simple change of variables.

And finally, as $r^2+z^2\to\infty$

$$T_1(r,z,t)=T_2(r,z,t)=0 \tag{7}$$

A double transformation technique is used. A Laplace transformation and then a Hankel transformation are applied. Using equations (3) and (4), equations (1) and (2) are transformed to

$$\alpha_1\left(\frac{d^2}{dz^2}-\lambda^2\right)w_1=sw_1 \tag{8}$$

$$\alpha_2\left(\frac{d^2}{dz^2}-\lambda^2\right)w_2=sw_2 \tag{9}$$

The solutions to (8) and (9) are

$$w_1=Ae^{\eta_1 z}+Be^{-\eta_1 z} \quad \delta>z>0 \tag{10}$$

$$w_2=Ce^{-\eta_2 z} \quad z>\delta \tag{11}$$

The coefficients A, B, and C are found from the double transforms of equations (5a), (5b), and (6a). After some algebraic manipulation

$$A=\frac{F(\lambda)}{s\eta_1}\,\frac{\phi}{1-\phi} \tag{12}$$

$$B=\frac{F(\lambda)}{s\eta_1}\,\frac{1}{1-\phi} \tag{13}$$

$$C=\frac{F(\lambda)}{s\eta_1}\,\frac{2k_1\eta_1}{k_1\eta_1+k_2\eta_2}\exp(-\delta(\eta_1-\eta_2))\frac{1}{1-\phi} \tag{14}$$

On the plane $z=0$

$$\begin{aligned}w_1&=A+B\\ &=\frac{F(\lambda)}{s\eta_1}\,\frac{1+\phi}{1-\phi}\end{aligned} \tag{15}$$

and since $|\phi|<1$ this can be expanded as

$$w_1=\frac{F(\lambda)}{s\eta_1}\left[1+2\sum_{i+1}^{\infty}\phi^i\right] \tag{16}$$

3 Laplace Transformation of Constriction Resistance

On the plane $z=0$

$$u_1=\int_{\lambda=0}^{\infty}w_1\lambda J_0(\lambda r)\,d\lambda$$

and using the formula for w_1 in (15)

$$u_1=\int_{\lambda=0}^{\infty}\frac{F(\lambda)}{s\eta_1}\,\frac{1+\phi}{1-\phi}\lambda J_0(\lambda r)\,d\lambda \tag{17}$$

The Laplace transformation of the constriction resistance is

$$\begin{aligned}\mathcal{L}[R]&=\frac{1}{\pi a^2}\int_{r=0}^{a}2\pi ru_1\,dr/Q\\ &=\frac{2}{Qa}\int_{\lambda=0}^{\infty}\frac{F(\lambda)}{s\eta_1}\,\frac{1+\phi}{1-\phi}J_1(\lambda a)\,d\lambda\end{aligned} \tag{18}$$

If the following substitutions are made

$$\left.\begin{aligned}&\lambda=\xi/a\\ \text{and}\quad &\mathcal{H}_0[f(r);\xi/a]=a^2\mathcal{H}_0[f(ar);\xi]\end{aligned}\right\} \tag{19}$$

then

$$\mathcal{L}[R]=2/Q\int_{\xi=0}^{\infty}\frac{G(\xi)}{s\eta_1}\,\frac{1+\phi}{1-\phi}J_1(\xi)\,d\xi \tag{20}$$

where

$$G(\xi)=\int_{x=0}^{1}f(ax)xJ_0(\xi x)\,dx \tag{21}$$

Expressions for R which are valid for steady-state ($t=\infty$)

Nomenclature

a = contact spot radius

$C_1 = \ln\left(\frac{2k_2}{k_1+k_2}\right)=\ln(1-K)$

$C_3 = \frac{1}{16}\left(1+2\frac{I_3}{I_1}\right)\sum_{i=1}^{\infty}\frac{K^i}{i^3}$

$C_5 = -\frac{1}{128}\left(1+6\frac{I_3}{I_1}+3\frac{I_5}{I_1}\right)\sum_{i=1}^{\infty}\frac{K^i}{i^5}$

$E(x)$ = complete elliptic integral (see equation (24b))

$f(r)$ = radial distribution of axial flux

$F(\lambda)$ = $\mathcal{H}_0\{f(r);\lambda\}$

$\mathrm{Fo}_1,\mathrm{Fo}_2$ = Fourier numbers α_1t/a^2, α_2t/a^2

$G(\xi)$ = $\mathcal{H}_0\{f(ar);\xi\}$ (see equation (21))

$H(t)$ = Heavy side function

$\mathcal{H}_0\{\psi(x);\lambda\} = \int_{x=0}^{\infty}\psi(x)xJ_0(\lambda x)\,dx$ (Hankel transform of zeroth order)

$I_n = \int_{x=0}^{1}f(ax)x^n\,dx$ (see equation (26))

$J_0(\ ),J_1(\ )$ = Bessel functions

K = $(k_1-k_2)/(k_1+k_2)$

k_1,k_2 = thermal conductivity of materials 1 and 2

$\mathcal{L}\{\psi(x)\} \equiv \int_{x=0}^{\infty}\psi(x)e^{-xs}\,dx$

Q = flux passing through contact spot (see equation (6b))

R = constriction resistance of coated material

R_{1c} = constriction resistance of half space of material 1

R_{2c} = constriction resistance of half space of material 2 and for very short times ($\alpha_1 t/a^2 < 0.1$) are found by considering the behavior of $\mathcal{L}[R]$ as $s \to 0$ and $s \to \infty$.

4 Steady-State Constriction Resistance

In the theory of Laplace transformations it is well known that the limits $s\mathcal{L}[R]$ as $s \to 0$ will yield the steady-state solution, see, for example, Doetsch [2]. Thus from equation (20)

$$R = \frac{2a}{Q} \int_{\xi=0}^{\infty} \frac{1+\phi}{1-\phi} \frac{J_1(\xi)}{\xi} \int_{x=0}^{1} xf(ax) J_0(\xi x) dx d\xi \qquad (22)$$

At steady-state $\phi = K \exp(-\sigma\xi)$ which will always be less than unity. Since $|\phi| < 1$, $(1+\phi)/(1-\phi)$ can be exapnded using the binomial theorem to obtain

$$R = R_{1c} + \frac{4a}{Q} \sum_{i=1}^{\infty} K^i \Omega(\sigma_i) \qquad (23)$$

where

$$R_{1c} = \frac{2a}{Q} \int_{\xi=0}^{\infty} \frac{J_1(\xi)}{\xi} \int_{x=0}^{1} xf(ax) J_0(\xi x) dx d\xi \qquad (24a)$$

and after integrating over $0 < \xi < \infty$

$$R_{1c} = \frac{4a}{\pi Q} \int_{x=0}^{1} f(ax) x E(x) dx \qquad (24b)$$

In equation (23), the term R_{1c} represents the constriction resistance of a spot on a half-space of material 1. The presence of the substrate is accounted for by the summation $i = 1, 2, \ldots \infty$.

Equation (6.626) on page 715 of [3] gives

$$\int_{\xi=0}^{\infty} d\xi e^{-\sigma\xi} J_0(\xi x) \frac{J_1(\xi)}{\xi}$$

$$= \frac{1}{2\sigma} \sum_{m=0}^{\infty} \frac{(2m)!2^{-2m}}{(m!)^2(m+1)} F(-m, -1-m; 1; x^2) \left(-\frac{1}{\sigma^2}\right)^m$$

Using this equation and integrating over $0<x<1$, $\Omega(\sigma_i)$ is found to be

$$\Omega(\sigma_i) = I_1 \left[\frac{1}{2\sigma_i} - \left(\frac{1}{8} + \frac{I_3}{4I_1} \right) \frac{1}{\sigma_i{}^3} + \left(\frac{I_5}{128 I_1} + \frac{I_3}{64 I_1} + \frac{1}{384} \right) \frac{24}{\sigma_i 5} \ldots \right] \qquad (25)$$

where

$$I_n \equiv \int_{x=0}^{1} x^n f(ax) dx \qquad (26)$$

The integral I_1 has been previously defined in equation (6c) and the only restriction on $f(ax)$ is that I_1 be constant. The integrals I_3 and I_5 will have the same units as I_1 since x is dimensionless. The integrals I_n are similar to moments of $f(ax)$ about $x = 0$.

The expansion given in (25) is useful when $\sigma > 1$ and can be used in (23) to give

$$R = R_{1c} - \frac{1}{2\pi a k_1} \left[\ln(1-K) \left(\frac{a}{\delta} \right) + C_3 \left(\frac{a}{\delta} \right)^3 + C_5 \left(\frac{a}{\delta} \right)^5 \ldots \right] \qquad (27)$$

This expression shows the effect of the coating upon the constriction resistance. It is useful for small values of a/δ that correspond to thick coatings. In the next section an asymptotic form that shows the thin film behavior is found.

Effect of a Thin Coating – $\delta/a \to 0$. After integrating by parts equation (22) may be reexpressed as

$$R = R_{2c} - \frac{2a}{Q} \frac{2K}{1-K} \psi(\sigma) \qquad (28a)$$

and

$$\psi(\sigma) = \int_{x=0}^{1} dx f(ax) x \int_{\xi=0}^{\infty} d\xi \frac{J_1(\xi)}{\xi} J_0(\xi x) \left[\frac{1-e^{-\sigma\xi}}{1-Ke^{-\sigma\xi}} \right] \qquad (28b)$$

where $R_{2c} = R_{1c}\ k_1/k_2$. In this section the behavior of the integral given in (28b) is considered as $\sigma \to 0$.

Within the interval $0 < \xi < 1 - K/\sigma$

$$\left[\frac{1-e^{-\sigma\xi}}{1-Ke^{-\sigma\xi}} \right] = \left(\frac{\sigma\xi}{1-K} \right) + 0\left(\left(\frac{\sigma\xi}{1-K} \right)^2 \right)$$

and results I, II, and III are obtained.

I $$\int_{x=0}^{1} dx f(ax) x \int_{\xi=0}^{\frac{1-K}{\sigma}} d\xi \frac{J_1(\xi)}{\xi} J_0(\xi x) \left(\frac{\sigma\xi}{1-K} \right)$$

See Errata Sheet (p 33)

$$= \frac{\sigma}{1-K} I_1 + 0\left(\frac{\sigma}{1-K} \right)$$

(See integral #3 on page 667 of [3].)

II $$\int_{x=0}^{1} dx f(ax) x \int_{\xi=0}^{\left(\frac{1-K}{\sigma}\right)^p} d\xi \frac{J_1(\xi)}{\xi} J_0(\xi x) 0\left(\left(\frac{\sigma\xi}{1-K} \right)^2 \right)$$

$$= 0\left(\left(\frac{\sigma}{1-K} \right)^{2-2p} \right) (0 < p < 1/2)$$

Nomenclature (cont.)

r = radial coordinate
s = transformed time variable
T_1, T_2 = temperature in materials 1 and 2
$\bar{T}$ = average temperature of contact spot
t = time
u_1, u_2 = Laplace transforms of T_1 and T_2
v_1, v_2 = Hankel transforms of T_1 and T_2
w_1, w_2 = double transforms of T_1 and T_2
W = $(\delta/a)/\sqrt{\mathrm{Fo}_1}$
z = axial coordinate

Greek Symbols

α_1, α_2 = thermal diffusivities of materials 1 and 2
γ = $(k_1/\sqrt{\alpha_1} - k_2/\sqrt{\alpha_2})/(k_1/\sqrt{\alpha_1} + k_2/\sqrt{\alpha_2})$
δ = coating thickness
λ = ξ/a
η_1 = $\sqrt{\lambda^2 + s/\alpha_1} = \sqrt{(\xi/a)^2 + s/\alpha_1}$
η_2 = $\sqrt{\lambda^2 + s/\alpha_2} = \sqrt{(\xi/a)^2 + s/\alpha_2}$
$\psi(\sigma)$ = $\int_{x=0}^{1} dx f(ax) x \int_{\xi=0}^{\infty} d\xi \frac{J_1(\xi)}{\xi} J_0(\xi x) \left[\frac{1-e^{-\sigma\xi}}{1-Ke^{-\sigma\xi}} \right]$
ϕ = $\frac{k_1\eta_1 - k_2\eta_2}{k_1\eta_1 + k_2\eta_2} \exp(-2\delta\eta_1)$; $|\phi| < 1$
λ = Hankel transform of radial coordinate
ρ = R/R_{2c}
σ = $2\delta/a$
σ_i = $2i\delta/a$
$\Omega(\sigma)$ = $\int_{x=0}^{1} dx f(ax) x \int_{\xi=0}^{\infty} d\xi e^{-\sigma\xi} \frac{J_1(\xi)}{\xi} J_0(\xi x)$
θ = $\frac{k_2}{k_1} \sqrt{\frac{\alpha_1}{\alpha_2}}$

See
Errata
Sheet

$$\text{III}\quad \int_{x=0}^{1} dxf(ax)x\int_{\xi=\left(\frac{1-K}{\sigma}\right)^p}^{\frac{1-K}{\sigma}} d\xi\,\frac{J_1(\xi)}{\xi}\,J_0(\xi x)0$$

$$\left(\left(\frac{\sigma\xi}{1-K}\right)^2\right)=0\left(\frac{\sigma}{1-K}\right)\xi=\left(\frac{1-K}{\sigma}\right)^p$$

See Lemma 1 on page 304 of Sneddon [4].

For the interval $1-K/\sigma<\xi<\infty$

$$\text{IV}\quad \int_{x=0}^{1} dxf(ax)x\int_{\xi=\frac{1-K}{\sigma}}^{\infty} d\xi\,\frac{J_1(\xi)}{\xi}\,J_0(\xi x)\left[\frac{1-e^{-\sigma\xi}}{1-Ke^{-\sigma\xi}}\right]$$

$$=0\left(\frac{\sigma}{1-K}\right)$$

See Lemma 1 on page 304 of Sneddon [4].

Using the results I, II, III, and IV the asymptotic behavior of $\psi(\sigma)$ is

$$\psi(\sigma)=\frac{\sigma}{1-K}I_1+0\left(\frac{\sigma}{1-K}\right)$$

The only restrictions of $f(ax)$ are that it is piecewise continuous and that the integrated flux is Q. The 0 symbol gives no information about the next series term, which will depend on $f(r)$. At this point all that can be stated is that

$$R\sim R_{2c}-\frac{1}{\pi ak_1}\,\frac{2K}{(1-K)}\,\frac{\delta}{a}\,\frac{2}{1-K}[1+0(1)]\ \text{as}\ \frac{2}{1-K}\,\frac{\delta}{a}\rightarrow 0 \tag{29}$$

Equation (29) compliments (27). In (29) if $\delta/a=0$ then $R=R_{2c}$ as expected. For a small value of $\sigma/(1-K)$ the effect of the coating upon R will be as shown in (29).

5 Effect of Surface Coating on the Constriction Resistance at Short Times

By considering the behavior of $\mathcal{L}[R]$ as $s\rightarrow\infty$, an expression for R is found which is valid for very short times.

If the flux over the contact spot is uniform, then it is expected that for extremely short times the average temperature of the spot would be the same as if there were a continuous planar source distributed on the surface $z=0$. In fact, Beck [5] has shown that for uncoated surfaces this is true. It is shown below that for any axisymmetric flux $(0<r<a)$ the constriction resistance is behaving in this manner.

Equation (20) can be written as

$$\mathcal{L}[R]\ =\ \frac{2}{Q}\int_{\xi=0}^{\xi_1}\frac{G(\xi)}{s\eta_1}\,\frac{1+\phi}{1-\phi}J_1(\xi)d\xi$$

$$+\ \frac{2}{Q}\int_{\xi=\xi_1}^{\infty}\frac{G(\xi)}{s\eta_1}\,\frac{1+\phi}{1-\phi}J_1(\xi)d\xi \tag{30}$$

We can choose ξ_1 large enough so that the second integral is negligible.

For a fixed value of ξ_1 we can take s sufficiently large so that the minimum of $(s/\alpha_1,\ s/\alpha_2)>>\xi_1{}^2/a^2$. Under these conditions

$$\eta_1=\sqrt{s/\alpha_1},\eta_2=\sqrt{s/\alpha_2}$$

and

$$\phi=\gamma\exp[-2\delta\sqrt{s/\alpha_1}]$$

and then (30) can be written as

$$\mathcal{L}[R]=\frac{2}{Q}\,\frac{\sqrt{\alpha_1}}{s^{3/2}}\,\frac{1+\phi}{1-\phi}\int_{\xi=0}^{\xi_1}G(\xi)J_1(\xi)d\xi \tag{31}$$

For large ξ_1 the integral in (31) is equal to $Q/2\pi a^2\,k_1$, so that

$$\mathcal{L}[R]=\frac{\sqrt{\alpha_1}}{k_1\pi a^2}\,\frac{1}{s^{3/2}}\,\frac{1+\phi}{1-\phi}=\frac{\sqrt{\alpha_1}}{k_1\pi a^2 s^{3/2}}\left[1+2\sum_{i=1}^{\infty}\phi^i\right] \tag{32}$$

This can be inverted to give

$$R=\frac{\sqrt{4\alpha_1}}{k_1\pi a^2}\left\{\sqrt{\frac{t}{\pi}}+2\sum_{i=1}^{\infty}\gamma^i\left[\sqrt{\frac{t}{\pi}}\exp\left(-\frac{i^2\delta^2}{\alpha_1 t}\right)\right.\right.$$

$$\left.\left.-\left(\frac{i\delta}{\sqrt{\alpha_1}}\right)\mathrm{erfc}\left(\frac{i\delta}{\sqrt{\alpha_1 t}}\right)\right]\right\} \tag{33}$$

This is identical to the surface temperature on a two-layer wall with a prescribed flux density $\{(Q/\pi a^2)/Q\}$ being imposed on the surface, see Griffith and Horton [6].

Equation (33) can be rewritten

$$R=\frac{2}{k_1\pi a}\sqrt{\frac{\mathrm{Fo}_1}{\pi}}+\frac{4}{k_1\pi a}\sum_{i=1}^{\infty}\gamma^i\left\{\sqrt{\frac{\mathrm{Fo}_1}{\pi}}\exp\left(-\frac{i^2(\delta/a)^2}{\mathrm{Fo}_1}\right)\right.$$

$$\left.-i\left(\frac{\delta}{a}\right)\mathrm{erfc}\left(\frac{i(\delta/a)}{\sqrt{\mathrm{Fo}_1}}\right)\right\} \tag{34}$$

For the case of a uniform flux for $r<a$ on a half-space of material 1, Beck [5] shows that R behaves as the first term in (34) for values of $\mathrm{Fo}_1<0.1$. The effect of the substrate material 2 is represented by the summed quantity. In (34) if $\delta/a=0$, then after some simple algebra it follows that

$$R=R_{2c}=\frac{2}{k_2\pi a}\sqrt{\frac{\mathrm{Fo}_2}{\pi}} \tag{35}$$

On the other hand, if $\{(\delta/a)/\sqrt{\mathrm{Fo}_1}\}$ is greater than about 2

Table 1 Values of R_{1c}, C_1, C_3 and C_5 in equation (27)

$f(r)$	R_{1c}	C_1	C_3 $(\Sigma(1)^i i^{-3}=1.202)$ $(\Sigma(-1)^i i^{-3}=-0.902)$	C_5 $(\Sigma(1)^i i^{-5}=1.037)$ $(\Sigma(-1)^i i^{-5}=-0.972)$
(*i*) Point source at center	$\frac{1}{\pi ak_1}$	$ln(1-k)$	$0.0625\sum_{i=1}^{\infty}\frac{K^i}{i^3}$	$-0.0078\sum_{i=1}^{\infty}\frac{K^i}{i^5}$
(*ii*) $\frac{Q}{k_1\pi a^2}$	$\frac{8}{3\pi^2 ak_1}$	$\ln(1-K)$	$0.1250\sum_{i=1}^{\infty}\frac{K^i}{i^3}$	$-0.0391\sum_{i=1}^{\infty}\frac{K^i}{i^5}$
(*iii*) $\frac{Q}{2k_1\pi a\sqrt{a^2-r^2}}$	$\frac{1}{4ak_1}$	$\ln(1-K)$	$0.1458\sum_{i=1}^{\infty}\frac{K^i}{i^3}$	$-0.0516\sum_{i=1}^{\infty}\frac{K^i}{i^5}$
(*iv*) Ring Source at $r=a$	$\frac{2}{\pi^2 ak_1}$	$\ln(1-K)$	$0.1878\sum_{i=1}^{\infty}\frac{K^i}{i^3}$	$-0.0781\sum_{i=1}^{\infty}\frac{K^i}{i^5}$

$$\operatorname{erfc}\left(\frac{i(\delta/a)}{\sqrt{\mathrm{Fo}_1}}\right) \sim \sqrt{\frac{\mathrm{Fo}_1}{\pi}}\,\frac{1}{i}\left(\frac{a}{\delta}\right)\exp\left(-\frac{i^2(\delta/a)^2}{\mathrm{Fo}_1}\right) \tag{36}$$

then

$$R = R_{1c} = \frac{2}{k_1 \pi a}\sqrt{\frac{\mathrm{Fo}_1}{\pi}} \tag{37}$$

6 Results and Discussion

6.1 Steady-State.

6.1.1 Effect of Coating. If $\delta/a = \infty$ then $R = R_{1c}$. The effect of a coating can be found using equation (27) which is

$$R = R_{1c} - \frac{1}{2\pi a k_1}\left[C_1\left(\frac{a}{\delta}\right) + C_3\left(\frac{a}{\delta}\right)^3 + C_5\left(\frac{a}{\delta}\right)^5 + \ldots\right] \tag{27}$$

The coefficients $C_3, C_5, \ldots$ depend on k_1, k_2 and $f(r)$ while the leading term C_1 is only dependent on k_1 and k_2. In Table 1 values of R_{1c}, C_1, C_3, and C_5 are given for

(*i*) $f(r)$ as a point source at the center of the contact
(*ii*) uniform flux over the contact
(*iii*) flux which causes an isothermal contact spot
(*iv*) $f(r)$ as a ring source located at the periphery $r = a$

Cases (*i*) and (*iv*) represent the two extreme cases. (The values C_3, C_5, etc., corresponding to (*i*) will be smaller than any other flux and the values C_3, C_5, etc. corresponding to (*iv*) will be larger than any other flux.)

From the values in Table 1, it is apparent that if $a/\delta < 1/2$ (say) then the effect of the coating can be predicted from the leading term of the series which is $[-\ln(1-K)/2\pi a k_1(a/\delta)]$. For thinner coatings the terms involving C_3, C_5, etc., which depend on $f(r)$, become increasingly important.

If the coating is highly conductive relative to the substrate, then $K \rightarrow 1$, and there is a logarithmic singularity that arises because of the adiabatic boundary condition at $z = \delta$. In this case, even for large values of a/δ the leading series term will be dominant.

Recently, the steady-state temperature distribution in a large circular plate heated by a disk heat source has been studied by Mehta and Bose [7]. In their analysis they specify uniform flux over $0 < r < a$ with an adiabatic condition outside the spot and at $z = \delta$ they set $T_1 = 0$. These conditions correspond to case (*ii*) with $K = -1$. Their expression for the average contact spot temperature, (their equation (13)), contains a minor error. (The 4 preceding the summation should be replaced with 2.) Their results are valid for $\sigma > 1$.

6.1.2 Effect of a Thin Coating. If $\delta/a = 0$ then $R = R_{2c}$ and for very thin coatings R can be found using equation (29) which is

$$R \sim R_{2c} - \frac{1}{\pi a k_1}\,\frac{4K}{(1-K)^2}\,\frac{\delta}{a} \quad \text{as} \quad \frac{2}{1-K}\,\frac{\delta}{a} \rightarrow 0 \tag{29}$$

To find the higher-order terms in the thin coating expansion, $f(r)$ must be given. For example, if $f(r) = Q/2\pi a k_1\sqrt{a^2 - r^2}$ then $\psi(\sigma)$ in (28*b*) is

$$\psi(\sigma) = \frac{Q}{2\pi a^2 k_1}\left[\frac{\sigma}{1-K} + 0\left(\left(\frac{\sigma}{1-K}\right)^{3/2}\right)\right]$$

and if $f(r) = Q/\pi a^2 k_1$ then $\psi(\sigma)$ is

$$\psi(\sigma) = \frac{Q}{\pi a^2 k_1}\left[\frac{1}{2}\,\frac{\sigma}{1-K} + 0\left(\left(\frac{\sigma}{1-K}\right)^2 \ln\left(\frac{\sigma}{1-K}\right)\right)\right]$$

The higher-order terms in the thin film asymptotic expansion cannot be found unless $f(r)$ is given. This is in contrast to equation (27), which gives the effect of the coating as a power series in (a/δ), the coefficients of which depend on $f(r)$.

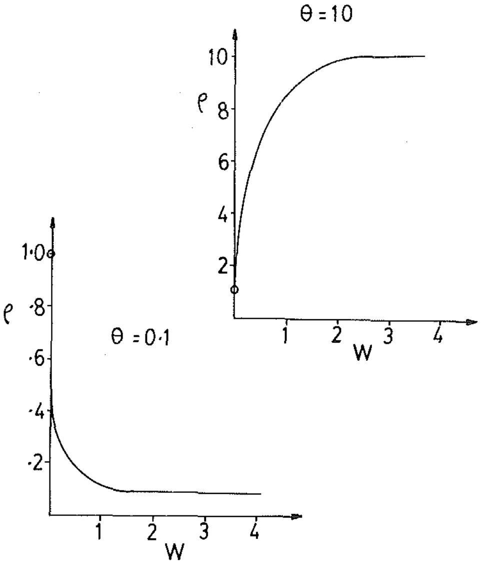

Fig. 2 Short-time values of ρ as a function of $W = (\delta/a)/\sqrt{\mathrm{F0}_1}$ for a resistive layer $k_1/k_2 \simeq \alpha_1/\alpha_2 = 0.01$ $(\theta = 10)$ and for a conductive layer $k_1/k_2 \simeq \alpha_1/\alpha_2 = 100.$ $(\theta = 0.1)$

If there is a thin layer of a poor conductor it is reasonable to expect that the heat flow through the coating will be mainly in the z = direction. The extra resistance due to the coating will be a one-dimensional effect and

$$R_{1-d} = \Delta T_{1-d}/Q = \frac{1}{\pi a}\,\frac{\delta}{a}\left[\frac{1}{k_1} - \frac{1}{k_2}\right].$$

The total constriction resistance is

$$R = R_{2c} + R_{1-d}$$

and if $k_1 << k_2$ then

$$R = R_{2c} + \frac{1}{\pi a k_1}\,\frac{\delta}{a} \tag{38a}$$

This is the same result as predicted by equation (29) and is valid when

$$\frac{2}{1-K}\,\frac{\delta}{a} \approx \frac{\delta}{a} << 1.$$

On the other hand, when there is a thin coating of highly conductive material, then it is reasonable to assume that the temperature within the coating does not vary across its thickness δ. If $T_1(r,\delta,t) = T_2(r,\delta,t)$ and if continuity of flux is mountained, then at steady-state the appropriate boundary condition at $z = \delta \simeq 0$ becomes

$$\frac{\partial^2 T_2}{\partial z^2} - \frac{1}{\delta}\left[\frac{k_2}{k_1}\,\frac{\partial T_2}{\partial z} + f(r)\right] = 0 \text{ at } z = 0$$

This is discussed on pages 23–24 of Carslaw and Jaeger [8]. Using this boundary condition

$$R = R_{2c} - \frac{2a}{Q}\left(\frac{k_1}{k_2}\right)^2\,\frac{\delta}{a}\int_{\xi=0}^{\infty} dx f(ax)x$$

$$\int_{\xi=0}^{\infty} d\xi\,\frac{J_1(\xi)J_0(\xi x)}{\left(1 + \frac{k_1}{k_2}\,\frac{\delta}{a}\,\xi\right)}$$

See
Errata
Sheet

p 3

and from an analysis similar to that in section 4.2

$$R = R_{2c} - \frac{1}{\pi a k_1}\,\frac{k_1}{k_2}\left[\frac{k_1}{k_2}\,\frac{\delta}{a} + 0\left(\frac{k_1}{k_2}\,\frac{\delta}{a}\right)\right] \tag{38b}$$

When $k_1 >> k_2$ equation (29) gives the same result and is valid only when $2/1 - K\,\delta/a \simeq k_1/k_2\,\delta/a << 1$. Apparently as k_1/k_2 becomes large δ/a must be very small if (29) is to be valid.

In summary, the effect of a thin surface coating is given in equation (29). If the surface coating is a poor conductor of heat, then the extra resistance caused by the coating is a one-dimensional effect and is given in equation (38*a*), which is valid when δ/a is somewhat less than 1. On the other hand, if the film is highly conductive, then the flow within the surface layer is in the radial direction and the decrease in the constriction resistance is given in equation (38*b*), which is valid when δ/a is somewhat less than k_2/k_1. This shortcoming is offset by the fact that as k_2/k_1 becomes very small, euation (27) becomes useful for smaller values of δ/a.

6.2 Short Time Constriction Resistance. To investigate the effect of a coating at short time, a dimensionless constriction resistance $\rho = R/R_{2c}$ is defined. Using (34) and (35)

$$\rho = \theta\left[1 + 2\sum_{i=1}^{\infty}\left(\frac{1-\theta}{1+\theta}\right)^{i}\{\exp(-i^2W^2) - \sqrt{\pi}pW\,\mathrm{erfc}(iW)\}\right] \tag{39}$$

where

$$\theta = \frac{k_2}{k_1}\sqrt{\frac{\alpha_1}{\alpha_2}} \text{ and } W = \frac{(\delta/a)}{\sqrt{\mathrm{Fo}_1}}$$

In (39) if $W \rightarrow 0$ then $\rho \rightarrow 1$ and for large values of W (about $W > 2$) $\rho \rightarrow \theta$. In other words, for a given δ/a, at small values of Fo_1 the coating controls ρ and at large values of Fo_1 the substrate dominates.

In Fig. 2 this effect is shown for a resistive layer $\theta = 10$ and a conductive layer $\theta = 1/10$. If we assume that $k_1/k_2 \approx \alpha_1/\alpha_2$, then it can be seen that the effect of the coating on the short time values of ρ are about equal to the square root of the steady-state maximum.

8 Acknowledgment

The paper has been supported by a grant from the Natural Science and Engineering Research Council. We would like to thank Professor Blackwell of The University of Western Ontario for his advice.

References

1 Dryden, J. R., "The Effect of a Surface Coating on the Constriction Resistance of a Spot on an Infinite Half-Plane," ASME JOURNAL OF HEAT TRANSFER, May 1983, pp. 408-410.

2 Doetsch, G., *Introduction to the Theory and Application of the Laplace Transformation*, Springer, New York, 1970, (Theorem 34.3) p. 233.

3 Gradshteyn, I. S., and Ryzhik, I. M., *Table of Integrals, Series and Products*, Academic Press, 1980.

4 Sneddon, I. N., *The Use of Integral Transforms*, McGraw-Hill, 1972.

5 Beck, J. V., "Average Transient Temperature Within a Body Heated by a Disk Heat Source," *Heat Transfer, Thermal Control and Heat Pipes*, Vol. 70, *Progress in Astronautics and Aeronautics, AIAA*, New York, 1980, pp. 3-24.

6 Griffith, M. V., and Horton, G. K., "The Transient Flow of Heat Through a Two-Layer Wall," *Proc. Physc. Soc.*, Vol. 58, 1946, (equation (19)) pp. 481-487.

7 Mehta, R. C., and Bose, T. K., "Temperature Distribution in a Large Circular Plate Heated by a Disk Heat Source," *International Journal of Heat and Mass Transfer*, July 1983, Vol. 26, No. 7, pp. 1093-1095.

8 Carslaw, H. S., and Jaeger, J. C., *Conduction of Heat in Solids*, Oxford Press, 1959, pp. 23-24.

J. Baker-Jarvis

R. Inguva

Department of Physics and Astronomy,
University of Wyoming,
Laramie, Wy. 82071

Heat Conduction in Heterogeneous Materials

A new solution to the heat equation in composite media is derived using a variational principle developed by Ben-Amoz. The model microstructure is fed into the equations via a term for the polar moment of the inclusions in a representative volume. The general solution is presented as an integral in terms of sources and a Green function. The problem of uniqueness is studied to determine appropriate boundary conditions. The solution reduces to the solution of the normal heat equation in the limit of homogeneous media.

1 Introduction

In many problems inclusions and host possess thermal conductivities and heat capacities that vary spatially in a complicated manner. In these problems the effects of the microstructure on the global heat conduction cannot be neglected. The effects of the microstructure should be observable in a certain length and time regime. Slattery [1] has presented a solution to the heat equation in heterogeneous materials by an averaging process. In this theory the effects of the microstructure (contact resistance and dispersion) are included as empirical relations obtained from data. Recently, Ben-Amoz [2] developed an elegant theory incorporating the effects of local or microconduction for media without contact resistance. In this theory a fourth-order equation has been developed by means of a variational technique that generalizes the heat conduction equation. The method developed by Ben-Amoz includes the effects of the inclusions on the temperature profiles by an averaging process. The variational functional for the heat conduction equation is averaged over a representative volume (see Fig. 1) of the composite. The resulting Euler–Lagrange equation then yields an equation of heat conduction that includes some of the effects of the microstructure. The effects of microconduction are manifested in the emergence of characteristic length and time scales (see section 2, 3 of [2]) over which the effects of microconduction are important. Ben-Amoz presents an approximate solution to the homogeneous equation using Laplace transform techniques. The boundary conditions used are complicated and somewhat unphysical. The theory also requires an additional boundary condition on the surfaces, involving the so-called hyperflux, which is the spatial derivative of the heat flux.

In this paper a new, exact solution to the nonhomogeneous problem for finite regions is developed utilizing Green function techniques. This solution has several interesting features to be discussed later. It is shown that an examination of the variational principle yields alternative and simpler boundary conditions in addition to those originally proposed by Ben-Amoz. These are the specification of the temperature and temperature gradient on the boundary surfaces. In section 2 the problem is defined and the boundary conditions presented. Section 3 develops a uniqueness proof for the problem, which yields appropriate boundary conditions for a unique solution. The next section develops the Green function for the problem which satisfies homogeneous boundary conditions. The temperature is expressed in terms of a volume integral over sources and a surface integral. Finally, numerical results are presented for the case of one-dimensional heat flow with Dirichlet and hyperflux boundary conditions. The solution is compared with the solution of Slattery for oil shale materials.

2 Derivation of the Generalized Heat Equation

In this section we review the basic results of Ben-Amoz needed in this work. Consider a medium consisting of inclusions embedded in a matrix material. The medium may be thought of as consisting of a large number of representative volumes of length l. The medium is assumed to be homogeneous on a macroscopic scale so that all representative volumes have the same model microstructure. Two scales over which conduction takes place are recognized. The microscale over which microconduction occurs is parameterized by the local coordinate η_i in a representative volume. The macrobehavior is described by the coordinate z (see Fig. 1). Ben-Amoz derives a heat equation that includes the effects of microconduction on a global scale by expressing the heat equation in variational form and then averaging at each point z over a representative volume. To see this, let the dimensionless microtemperature be described by $T^*(\eta_i, t)$ and the

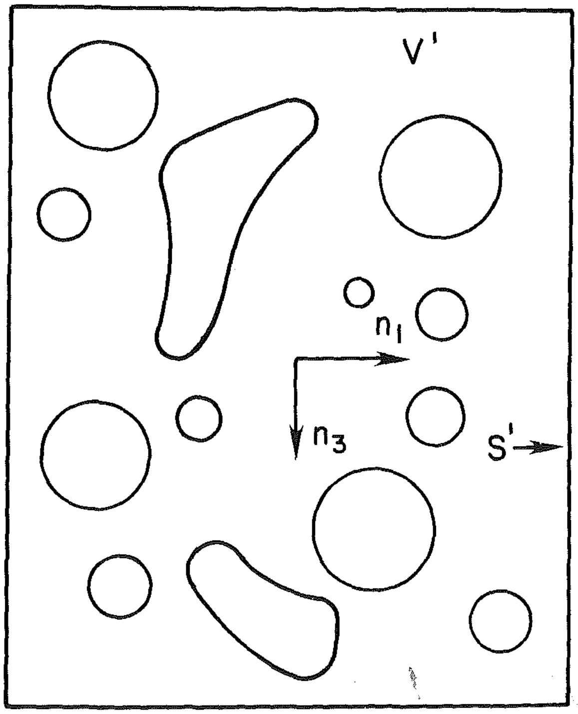

Fig. 1 Representative volume of length l: z is the macrocoordinate for the region to be averaged around and n is the microcoordinate which describes the local microstructure.

Contributed by the Heat Transfer Division for publication in the JOURNAL OF HEAT TRANSFER. Manuscript received by the Heat Transfer Division June 10, 1983.

dimensionless macrotemperature be described by $T(z, t)$ (in general let the starred quantities represent the micro or local variables and be functions of η_i and the unstarred quantities represent the macrovariables). The dimensional temperature $\bar{T}$ is related to the nondimensional temperature T by $T = [\bar{T} - T_{\mathrm{ref}}]/T_{\mathrm{ref}}$, where T_{ref} is the reference temperature. The thermal conductivities are given by K, and K^*, the temperature gradients by q_i, and q_i^*. The heat flux is given by $Q_i = Kq_i$, and $Q_i^* = K^* q_i^*$. The temperature gradients are given by $q_i = \partial T/\partial z_i$ and $q_i^* = \partial T^*/\partial \eta_i$. Since it is convenient to work in nondimensional units, let l be the length scale and t_o be the time scale. With these definitions the following nondimensional variational equation has been obtained by Ben-Amoz for the heat equation in a representative volume (V').

$$\delta I = 0 = \int_{v'} \left[\bar{K} q_i^{v*} \delta q_i^* + \frac{(c_R l^2)}{K_v t_0} \bar{c}^* \frac{\partial T^*}{\partial t} \delta T^*\right] dV' + \int_{s'} \bar{Q}_i^* n_i \delta T^* ds' \tag{1}$$

Here $c_R = (1/(v_f/c_f + v_m/c_m)$ is the reference heat capacity; $\bar{c}^*$ is the heat capacity divided by the reference value; $\bar{K}^v$ is the thermal conductivity divided by the reference thermal conductivity; $K_v = K_f v_f + K_m v_m$ is the reference thermal conductivity and v_f, v_m are volume fractions of inclusions and matrix; and $\bar{Q}$ is the heat flux Q divided by the reference thermal conductivity K_v.

The exact solution to equation (1) would be impossible because of the complicated variations in thermal properties. However, an averaging process is possible. Consider summing equation (1) over all representative volumes. If the number of volumes is large then the sum can be replaced by an integral

$$\delta I = 0 = \int_v \int_{v'} \left[\bar{K} q_i^{v*} \delta q_i^* + (c_R l^2/K_v t_0) \bar{c}^* \frac{\partial T^*}{\partial t} \delta T^*\right] dv dv' + \int_s \int_{s'} \bar{Q}_i^{\,*} n_i \delta T^* ds' ds \tag{2}$$

The surface integrals over all internal surfaces cancel by continuity of flux and temperatures on the interfaces. This leaves a surface integral only on the outer bounding surface. The scale t_o can be fixed by considering the maximum diffusion time over the length of a typical inclusion

$$t_o = \frac{d^2 c_v}{K_R} \tag{3}$$

where d is the length of the largest inclusion in a representative volume and $c_v = v_f c_f + v_m c_m$, $K_R = 1/(v_f/K_f + v_m/K_m)$. The length scale l used to render the spatial coordinates dimensionless is on the order of the dimensions of a representative volume. The length scale l can be fixed in terms of properties of the medium.

$$l = d\left(\frac{K_v c_v}{K_R c_R}\right)^{1/2} \tag{4}$$

The length scale l has the physical interpretation of a region over which the microconduction is important. We can define the dimensionless time and length in terms of the dimensional quantities.

$$t = \frac{\bar{t}}{t_0} \tag{5}$$

$$z_{(i)} = \frac{\bar{z}_{(i)}}{l} \tag{6}$$

In order to evaluate equation (2), a relationship is needed between the starred and unstarred quantities. This relationship is given by a Taylor series expansion of the starred quantities about the point $\eta = 0$ in a representative volume.

$$T^* = T(z,t) + \frac{\partial T}{\partial z_i} \eta_i \tag{7}$$

$$q_i^* = q_i(z,t) + \frac{\partial q_i}{\partial z_j} \eta_j \tag{8}$$

Inserting equations (7) and (8) into equation (2) and performing the integral over V' yields the following quantity (a nondimensional source term $g(r, t)$ has been included for generality).

$$\delta I = 0 = \int_V (\bar{K}^v [T_{,i} \delta T_{,i} + \alpha^2 T_{,iK} \delta T_{,iK}] + a_0 [\dot{T} \delta T + \gamma^2 \dot{T}_{,i} \delta T_{,i}] - g \delta T) dV + \int_S (\bar{Q}_i n_i \delta T + \bar{Q}_{i,j} n_i \delta T_{,j}) dS \tag{9}$$

All the terms with odd powers of η are zero because the integrand is odd over a symmetric interval. Integration by parts yields

$$\delta I = -\int_V [(1 - \alpha^2 \nabla^2) \bar{K}^v \nabla^2 T - a_0 (1 - \gamma^2 \nabla^2) \dot{T} + g] \delta T dV + \int_S [(\bar{Q}_i n_i \delta T + \bar{Q}_{i,i} n_i \delta T_i + (\bar{K}^v (1 - \alpha^2 \nabla^2) T_{,i} + a_0 \gamma^2 \dot{T}_{,i}) n_i \delta T + \alpha^2 \bar{K}^v T_{,ii} \delta T_{,i} n_i] dS = 0 \tag{10}$$

The quantities α^2, γ^2 are material constants given by

$$\alpha^2 = 1/4 [1 - (v_f - 4 I_f)(K^f - K^m)/K_v] \tag{11}$$

$$\gamma^2 = 1/4 [1 - (v_f c_R/c_f - 4 I_f)(c_f - c_m)/c_R]/a_0 \tag{12}$$

also

$$I_f = \int_{V'} r^2 dV_f' \tag{13}$$

$$\bar{K}^v = K/K_v \tag{14}$$

$$a_0 = 1 + v_f v_m (c_f - c_m)^2 / c_f c_m \tag{15}$$

From the volume integral we obtain the equation of microconduction

$$a_0 (1 - \gamma^2 \nabla^2) \frac{\partial T}{\partial t} = (1 - \alpha^2 \nabla^2) \bar{K}^v \nabla^2 T + g(\mathbf{r}, t) \tag{16}$$

From the surface contributions we can extract boundary conditions. We can either specify the temperature and hyperflux on the surface

$$T \text{ and } \bar{\mathbf{Q}}_{i,i} = -\alpha^2 \bar{K}^v \nabla^2 T \text{ [hyperflux on surfaces]} \tag{17a}$$

or we may specify the temperature gradient and heat flux on the surfaces

$$T_{,i} \text{ and } \bar{\mathbf{Q}} \cdot \mathbf{n} = -[\bar{K}^v (1 - \alpha^2 \nabla^2) \nabla T \cdot \mathbf{n} + a_0 \gamma^2 \nabla \dot{T} \cdot \mathbf{n}]. \tag{17b}$$

In the following development we will use the first set of boundary conditions on the surfaces (equation (17*a*)). That is, the specification of temperatures and hyperflux on all surfaces. The initial condition is

$$T(\mathbf{r}, 0) = F(\mathbf{r}) \tag{18}$$

3 Uniqueness Proof

We can show that a solution to equation (16) is unique with the boundary conditions of equations (17). Consider two solutions to equation (16) and take the difference

$$T = \tilde{T}_1 - \tilde{T}_2 \tag{19}$$

Then T satisfies

$$a_0 (1 - \gamma^2 \nabla^2) \frac{\partial \tilde{T}}{\partial t} = (1 - \alpha^2 \nabla^2) \bar{K}^v \nabla^2 \tilde{T} \tag{20}$$

The initial condition and boundary conditions for T are

$$\begin{aligned}&\tilde{T}(\mathbf{r},0)=0,\\ &\tilde{T}(\mathbf{r},t)=0 \qquad \text{(on surfaces)}\\ &\nabla^2\tilde{T}(\mathbf{r},t)=0\end{aligned} \tag{21}$$

Consider the following positive definite quantity

$$\int_V a_0[(1-\gamma^2\nabla^2)\tilde{T}]^2 dV \tag{22}$$

where V is any volume. By use of equation (20) we can write

$$\begin{aligned}1/2\frac{d}{dt}\int_V & a_0((1-\gamma^2\nabla^2)\tilde{T})^2 dV\\ &=\int_V [(1-\alpha^2\nabla^2)\bar{K}^v\nabla^2\tilde{T}][1-\gamma^2\nabla^2]\tilde{T}\,dV\\ &=\bar{K}^v\int_V [(\nabla^2\tilde{T})\tilde{T}-\alpha^2\tilde{T}(\nabla^2\nabla^2\tilde{T})-\gamma^2\nabla^2\tilde{T}\,[\nabla^2\tilde{T}]\\ &+\alpha^2\gamma^2[\nabla^2\nabla^2\tilde{T}]\nabla^2\tilde{T}]dV \qquad (23)\\ &=-\bar{K}^v\int_V [\nabla\tilde{T}\cdot\nabla\tilde{T}+\alpha^2(\nabla^2\tilde{T})^2+\gamma^2(\nabla^2\tilde{T})^2+\\ &+\alpha^2\gamma^2\nabla(\nabla^2\tilde{T})\cdot\nabla(\nabla^2\tilde{T})]dV\end{aligned}$$

where the last quantity is obtained by integration parts and use of equation (20). We now note that the right-hand side of equation (23) must be less than or equal to zero. Since $\tilde{T}(t=0)=0$ so that $(1-\gamma^2\nabla^2)\tilde{T}(t=0)=0$, and since t is always nonnegative, we must have for all t

$$(1-\gamma^2\nabla^2)\tilde{T}=0 \tag{24}$$

The only solution to this with the boundary conditions (equation (21)) is

$$\tilde{T}=0 \tag{25}$$

This completes the uniqueness proof.

4 Green Function

We now develop the associated Green function (see Morse and Feshbach [3]) for equations (16, 17). Let the Green function G satisfy

$$\begin{aligned}-a_0(1-\gamma^2\nabla'^2)\frac{\partial \mathrm{G}}{\partial\tau}(\mathbf{r},\mathbf{r}',t-\tau)&\\ =(1-\alpha^2\nabla'^2)\bar{K}^v\nabla'^2\mathrm{G}(\mathbf{r},\mathbf{r}',t-\tau)&\\ +\delta(\mathbf{r}-\mathbf{r}')\delta(t-\tau)&\end{aligned} \tag{26}$$

The minus sign comes from the fact that G is a function of $t-\tau$. The Green function satisfies the following conditions

$$\begin{aligned}&\mathrm{G}(\mathbf{r},\mathbf{r}',t,\tau)_{|t<\tau}=0\\ &\mathrm{G}(\mathbf{r},\mathbf{r}',t-\tau)\quad \text{(on surface)}=0\\ &\nabla'^2\mathrm{G}(\mathbf{r},\mathbf{r}',t-\tau)\quad \text{(on surface)}=0\end{aligned} \tag{27}$$

The solution to equation (26) can be written in the form

$$\mathrm{G}(\mathbf{r},\mathbf{r}',t-\tau)=\sum_n C_n(t-\tau)u_n(\mathbf{r})u_n(\mathbf{r}') \tag{28}$$

where $\{u_n\}$ are the normalized three dimensional eigenfunctions, satisfying the following equation

$$\nabla^2 u_n=-\lambda^2{}_n u_n \tag{29}$$

with homogeneous Dirichlet boundary conditions. Substitution of equation (29) into equation (28) yields the following equation for C_n

$$\begin{aligned}-a_0(1+\gamma^2\lambda_n{}^2)\frac{dC_n}{d\tau}=-\bar{K}^v\lambda^2{}_n(1+\alpha^2\lambda^2{}_n)C_n&\\ +\delta(t-\tau)&\end{aligned} \tag{30}$$

where we have used $\Sigma_n u_n(r')u_n(r)=\delta(r-r')$. The solution for C_n is

$$C_n=\frac{\theta(t-\tau)}{a_0(1+\gamma^2\lambda^2{}_n)}\exp\left\{\frac{-\bar{K}^v\lambda_n{}^2(1+\alpha^2\lambda_n{}^2)(t-\tau)}{a_0(1+\gamma^2\lambda_n{}^2)}\right\} \tag{31}$$

where $\theta(t-\tau)$ is the unit step function. Substitution of equation (31) into equation (26) yields the Green function.

5 Equation for the Temperature

We wish to obtain $T(r, t)$ in terms of an integral over the volume and surfaces, in terms of the Green function. If we multiply equation (16) by G and equation (26) by T and subtract and integrate over all τ and r we obtain

$$\begin{aligned}\bar{K}^v\int_0^{t^+} d\tau\int_{V'} [\mathrm{G}(1-\alpha^2\nabla'^2)\nabla'^2T-T(1-\alpha^2\nabla'^2)\nabla'^2\mathrm{G}]&\\ +(g\mathrm{G}-\delta(\mathbf{r}-\mathbf{r}')\delta(t-\tau))T]dV'& \qquad (32)\\ =a_0\int_0^{t^+} d\tau\int_{V'}\left[G(1-\gamma^2\nabla'^2)\frac{\partial T}{\partial\tau}+T(1-\gamma^2\nabla'^2)\frac{\partial G}{\partial\tau}\right]dV'&\\ t^+=t+\epsilon \quad (\epsilon<<1)&\end{aligned}$$

Considering the first part of the left side of equation (32), if we integrate by parts and use the boundary conditions of equation (27) on G, we obtain

$$\begin{aligned}\bar{K}^v\int_0^{t^+} d\tau\int_{S'} [-T\nabla'\mathrm{G}\cdot\mathbf{n}+\alpha^2[(\nabla'^2T)\nabla'\mathrm{G}\cdot\mathbf{n}&\\ +T\nabla(\nabla'^2\mathrm{G})\cdot\mathbf{n}]]dS'&\end{aligned} \tag{33}$$

All the other volume integrals either cancel or are zero by boundary conditions. We then obtain the following expression for the right-hand side of equation (32)

$$\begin{aligned}a_0\int_{V'}\left[\Big|_{\tau=0}^{\tau=t^+}(\mathrm{G}T)-\gamma^2\int_0^{t^+}\left(\left(G\nabla'^2\frac{\partial T}{\partial\tau}\right.\right.\right.&\\ \left.\left.\left.+T\left(\nabla'^2\frac{\partial \mathrm{G}}{\partial\tau}\right)\right)d\tau\right)\right]dV'&\end{aligned} \tag{34}$$

Using the conditions $T(t=0)=F(r)$ and $\mathrm{G}(\tau=t^+)=0$ in equation (34) and integrating the other term by parts we obtain the following result

$$\begin{aligned}&-a_0\int_{V'} F(\mathbf{r}')\mathrm{G}dV'+\gamma^2a_0\int_{S'}\int_0^{t^+}\left[(\nabla'\mathrm{G})\cdot n\frac{\partial T}{\partial\tau}\right]dS'd\tau\\ &-\gamma^2a_0\int_0^{t^+}\int_{V'}\left[\left(\nabla'^2\mathrm{G}\frac{\partial T}{\partial\tau}+T\left(\nabla'^2\frac{\partial\mathrm{G}}{\partial\tau}\right)\right)\right]dV'd\tau \qquad (35)\\ &=-a_0\int_{V'} F(\mathbf{r}')\mathrm{G}dV'+\gamma^2a_0\int_{S'}\int_0^{t^+}\frac{\partial T}{\partial\tau}\nabla'\mathrm{G}\cdot\mathbf{n}\,dS'd\tau\\ &+\gamma^2a_0\int_{V'}\nabla'^2\mathrm{G}F(\mathbf{r}')dV'\end{aligned}$$

From equations (32–35), we obtain the following expression for $T(r, t)$

$$\begin{aligned}T(\mathbf{r},t)=\bar{K}^v\int_0^t\int_{S'} [-T\nabla'\mathrm{G}+\alpha^2[(\nabla'^2T)\nabla'\mathrm{G}&\\ +T\nabla'(\nabla'^2\mathrm{G})]]\cdot\mathbf{n}dS'd\tau&\\ +\int_0^t\int_{V'} g\mathrm{G}dV'd\tau-a_0\gamma^2\int_{S'}\int_0^t\frac{\partial T}{\partial\tau}\nabla'\mathrm{G}\cdot\mathbf{n}dS'd\tau&\\ +a_0\int_{V'} F(\mathbf{r}')[1-\gamma^2\nabla'^2]\mathrm{G}(\tau=0)dV'&\end{aligned} \tag{36}$$

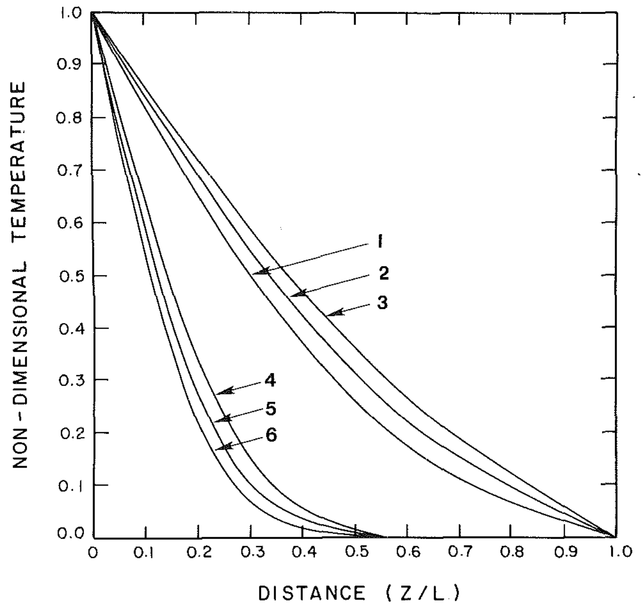

Fig. 2 The solution to Ben-Amoz's equation is plotted in curves (3, 4) subject to boundary conditions $T(r, 0) = 0$, and $T(0, t) = 1$, $T(1, t) = 0$, $\nabla^2 T(0, t) = 0$, $\nabla^2 T(1, t) = 0$. The curves (2, 5) are the solution to normal heat equation $\alpha^2, \gamma^2 = 0$. Curves (1, 6) are Slattery's solutions with K^+ in equation (38) taken for oil shale materials [4]. The profiles are in nondimensional time units of 0.01, 0.05. The volume fraction of inclusions is $v_f = 0.1$. I_f is calculated by assuming all the inclusions are concentrated in a sphere of volume v_f around the origin of each representative volume.

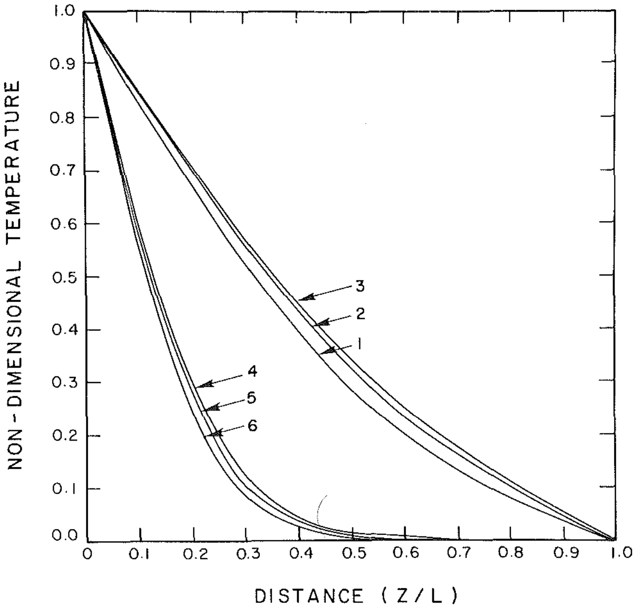

Fig. 4 Same as Fig. 2, but with $\nabla^2 T(1, t) = \nabla^2 T(0, t) = -1$

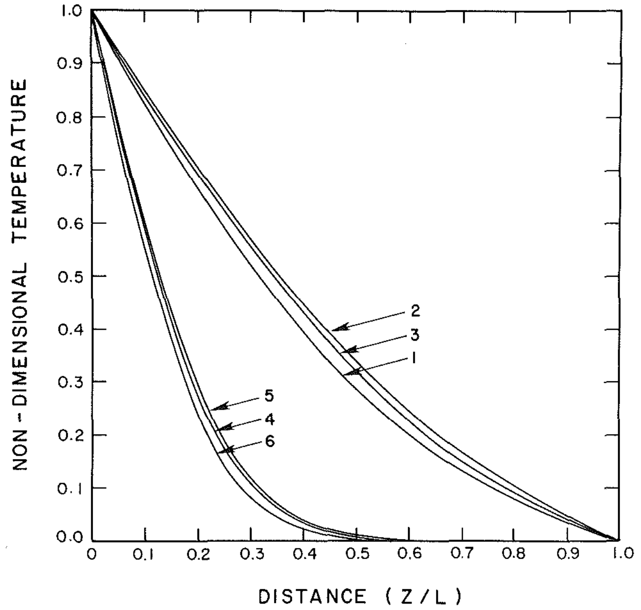

Fig. 3 Same as Fig. 2, but with $v_f = 0.5$

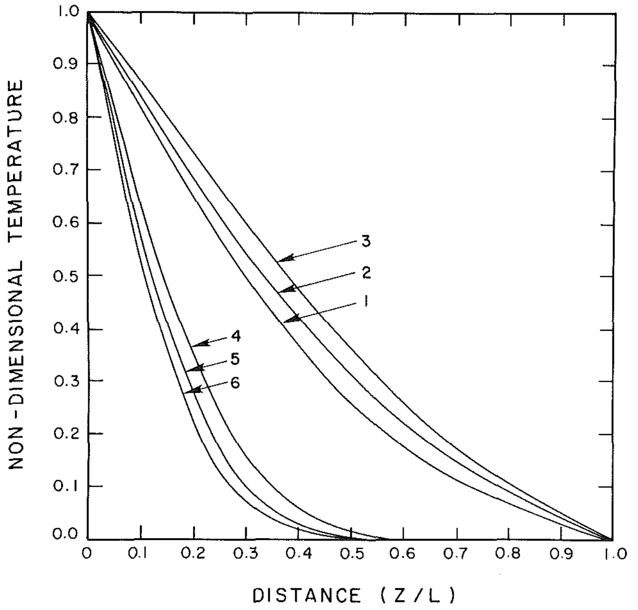

Fig. 5 Same as Fig. 2, but with $v_f = 0.5$

In the limit as $\alpha^2 \to 0$, $\gamma^2 \to 0$, equation (36) reduces to the normal integral equation for heat conduction satisfying Dirichlet boundary conditions.

6 Numerical Results and Discussion

Consider the following problem of heat conduction in one dimension. A slab is assumed to be at $T = 0$ for $t < 0$. For $t \geq 0$ the plane $x = 0$ is maintained at a constant non-dimensional temperature $T = 1$. The plane at $x = 1$ is maintained at $T = 0$. At both boundaries $\nabla^2 T$ is specified. The term I_f (which specifies the model microstructure) is calculated in a simplified form as the moment of inertia of a sphere of volume v_f about the origin of each representative volume. The solution to equation (36) for this case reduces to the following expression

$$T=2 \sum_n \sin n\pi z\left[1-\exp\left[-(n\pi)^2\left[\frac{1}{a_0}\left[\frac{1+\alpha^2(n\pi)^2}{1+\gamma^2(n\pi)^2}\right]t\right]\right]\right. \tag{37}$$

$$\frac{[n\pi+\alpha^2/n\pi)^3-\nabla^2 T(z=0)\alpha^2(n\pi)(-1)^n+\alpha^2\nabla^2 T(z=1)n\pi]}{[(n\pi)^2+(n\pi)^4\alpha^2]}$$

In Fig. 2 the temperature profiles calculated from the modified equation of conduction are compared to the solution to the normal heat equation ($\alpha^2 = 0$, $\gamma^2 = 0$) and the solution of Slattery. In Slattery's theory the effects of the microstructure are input by an effective thermal conductivity in the normal heat equation. This effective thermal conductivity is then used in the solution of the normal heat equation. The effective thermal conductivity is given by

$$K_{\mathrm{eff}} = K_{(1)}n_{(1)} + K_{(2)}n_{(2)} - K^{+} \tag{38}$$

The parameter K^{+} in Slattery's theory can be determined for oil shales from the data of DuBow and Rajeshwar [4]. For all cases the plots are at dimensionless times 0.01 and 0.05. The thermal conductivity of inclusions is 3 W/M°C and of matrix is 0.2 W/M°C. The heat capacity of the inclusions is 3×10^6 J/°C M^3 and heat capacity of the matrix is 1.5×10^6 J/°C M^3. In Fig. 2 the volume fraction of inclusions is 0.1 and the hyperflux is zero. Figure 3 is similar, but with volume fraction of inclusions 0.5. Figures 4, 5 show the solutions when the hyperflux at the endpoints is nonzero for volume fraction of inclusions of 0.1, 0.5.

An examination of the various plots shows that the temperature profiles of the normal and modified heat conduction equations are quite different. The larger volume fraction of inclusions gives a larger difference in the solutions. The effect of the hyperflux condition at the endpoints is to modify the profile slightly. The solution to Slattery's equation in general yields a colder temperature profile. This is probably because the effects of contact resistance have been fed into Slattery's solution by the empirical relationships for the thermal conductivity (equation (38)), whereas in Ben-Amoz's equation no contact resistance is assumed to exist at inclusion interfaces. An interesting feature can be noted when comparing Figs. 2, 3. As the volume fraction of inclusions increases from 0.1 to 0.5, the temperature profiles of the modified heat equation become "warmer" than the solutions to the normal heat equation with effective values for the thermal properties.

Acknowledgments

We wish to acknowledge the continual support and encouragement of Mr. William Little. This work is supported in part by grant from the Dept. of Energy through the Laramie Projects Office, Grant No. DE-AS20-8ILC10783.

References

1 Slattery, J. C., *Momentum, Energy, and Mass Transfer Continua*, McGraw-Hill, New York, 1972.

2 Ben-Amoz, M., "Heat Conduction for Composite Materials," *ZAMP*, Vol. 27, 1976, pp. 335–345.

3 Morse, P. M., and Feshbach, H., *Methods in Theoretical Physics*, McGraw-Hill, New York, 1953.

4 DuBow, J., and Rajeshwar, K., "Thermophysical Properties of Oil Shales," Final Technical Report No. EF-77-5-03-1584 (DOE), 1979.

Studies on Heat Transfer From a Vertical Cylinder, With or Without Fins, Embedded in a Solid Phase Change Medium

B. Kalhori
Graduate Student.

S. Ramadhyani[1]
Assistant Professor.
Assoc. Mem.

Department of Mechanical Engineering,
Tufts University,
Medford, Mass. 02155

An experimental investigation of melting and cyclic melting and freezing around a vertical cylinder is reported. The studies encompass two cases: a plain vertical cylinder, and a vertical cylinder with fins. In the melting studies, the total heat transfer from the cylinder was measured as a function of time. In addition, measurements have been made of the solid-liquid interface shape after various melting times. In these studies, the solid phase was initially isothermal and either at its fusion temperature or subcooled below the fusion point. The experiments reveal the important influence of natural convection in the liquid phase in both unfinned and finned situations. Subcooling of the solid phase is observed to strongly inhibit heat transfer in the unfinned situation. In the experiment on cyclic melting and freezing, subcooling of the solid phase is once again found to have an important effect on the unfinned situation. Heat transfer from the finned cylinder is much less affected by solid-phase subcooling. All the experiments were performed with 99 percent pure n-eicosane paraffin.

1 Introduction

The purpose of this paper is to report an experimental investigation of melting and freezing around a vertical cylindrical surface. Two cases have been considered: a plain vertical cylinder, and a vertical cylinder with fins. The work was motivated by the need for quantitative heat transfer data applicable to these configurations. Such data could be of use in the development of practical thermal energy storage units to be used in conjunction with intermittent energy sources such as the sun. Another possible application of phase-change thermal capacitors would be as emergency heat sinks in the cooling of large electronic systems such as computers.

As will shortly become evident, the problem of phase change around an embedded vertical cylinder is a moving-boundary problem in a complex geometry. An analysis of the problem would involve the solution of the energy equation coupled with the hydrodynamic equations in the liquid phase. This is a challenging task that is amenable only to a numerical solution. Consequently, in addition to providing information of utility in the design of thermal storage units, data from the present study could be useful in validating a numerical solution of the problem.

The qualitative nature of the heat transfer processes involved in melting and freezing have recently been established through a series of experiments by other investigators [1-4]. It has been demonstrated that natural convection in the liquid phase plays a dominant role in melting and to a certain extent influences freezing. The influence of subcooling the solid phase has been qualitatively studied in [5], and it has been shown that melting can be severely inhibited due to solid-phase subcooling.

When the present investigation was begun, only a single, qualitative, experimental investigation of melting around a plain vertical cylinder had appeared in the literature [6]. Subsequently, a comprehensive series of experiments on melting were reported by Kemink and Sparrow [7]. The cases of both subcooled and nonsubcooled solid phase were studied and considerable heat transfer data were obtained in that investigation.

The present studies encompass three different sets of experiments. The same basic apparatus is employed for both unfinned and finned situations. The first set of experiments is aimed at obtaining data for melting around a vertical cylinder embedded in an isothermal solid initially at its fusion temperature. The experimental procedures employed in this investigation are different from those of [7], and the thermal boundary condition at the heated surface is different as well. While a timewise constant heat flux was employed in [7], a spatial and timewise uniform wall temperature was employed in the present work in the belief that this would be more representative of actual working conditions in a thermal storage capacitor. Nevertheless, the present results for the unfinned cylinder are found to agree closely with those of [7] in the convection dominated regime of melting. Thus the present work may be viewed as confirming the work reported in [7]. The authors are unaware of any previous work with which the results of the finned cylinder may be compared.

The data from the first set of experiments serve as a standard of comparison for the subsequent experiments. In the second set of experiments, the solid phase-change medium is initially subcooled below its fusion temperature prior to the onset of melting. In the unfinned situation, the great impact of the thermal capacity of the subcooled solid is demonstrated by these experiments. In addition, measurements of the solid-liquid interface position after various melting times highlight certain qualitative details of the melting process. In the finned situation, initial subcooling of the solid phase is found to have only a small effect on the heat transfer rate.

The third experiment has not so far been reported by other investigators. In this experiment, the actual operation of a thermal storage unit is simulated by repeatedly cycling the phase-change material through freezing and melting. The time periods of each stage are chosen to correspond with the duty cycle of a storage unit used in conjuction with a solar water heater. The heat transfer and temperature distributions in the periodic steady state obtained after a large number of cycles are the objects of this study. Once again, it is shown that the

---

[1] Presently at the School of Mechanical Engineering, Purdue University, West Lafayette, Ind. 47907.

Contributed by the Heat Transfer Division for publication in the JOURNAL OF HEAT TRANSFER. Manuscript received by the Heat Transfer Division October 6, 1983.

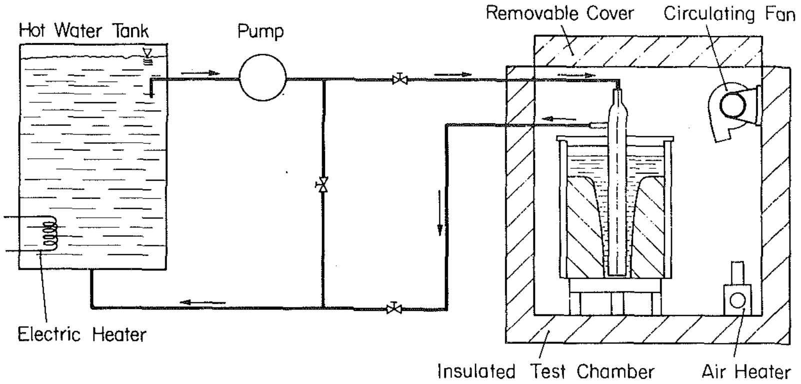

Fig. 1 Schematic depiction of the experimental apparatus

thermal inertia of the solid phase has an important influence on the unfinned situation but a relatively small effect on the finned case.

The phase-change medium used in this study was 99 percent pure n-eicosane (a paraffin) with a measured melting point of 36.6°C. The suppliers of this material are The Humphrey Chemical Co., North Haven, Connecticut.

2 Description of the Apparatus

The experimental apparatus employed in this study is shown schematically in Fig. 1. It consists of an insulated test chamber within which the paraffin canister is situated, and a thermostatically controlled hot water tank. The test chamber is a hollow wooden box surrounded by fibrous insulation on all four sides and the bottom. For accessibility to the phase-change canister, a removable plexiglass sheet is used to cover the top. A thick layer of fibrous insulation is placed above the plexiglass sheet as an additional thermal barrier. A thermostatically controlled heater and circulating fan system is installed at the bottom of the chamber, and an additional circulating fan is installed at the top to minimize air stratification. With this arrangement, the combined spatial- and timewise temperature variations in the box could be controlled within ±1°C.

The hot water tank is an aluminum drum of 30l capacity, surrounded by several layers of insulation. An immersion water heater controlled by a thermostat of ±0.5°C accuracy is installed in the lower part of the tank. A pump and piping system as shown in Fig. 1 allow the hot water to be conveyed to the heating element in the paraffin canister.

2.1 The Phase-Change Canister. The phase-change canister is depicted schematically in Fig. 2. It consists of a thin-walled sheet metal cylindrical tank filled with the phase-change medium (n-eicosame) and insulated by two layers of foam rubber insulation. The wall thickness of the tank is 0.2 mm. An electrical strip heater is wrapped around the upper part of the canister, under the insulation, and is used to help prevent the formation of voids during the freezing that necessarily precedes each melting run. Void formation is prevented by keeping the upper part of the paraffin in the liquid phase while chilling the lower part of the paraffin container. This ensures directional solidification from the bottom to the top of the container. Chilling of the paraffin is effected by means of a cooling ring consisting of a coil of copper tubing sandwiched between two flat aluminum rings. Cold water from the faucet is circulated through the coil.

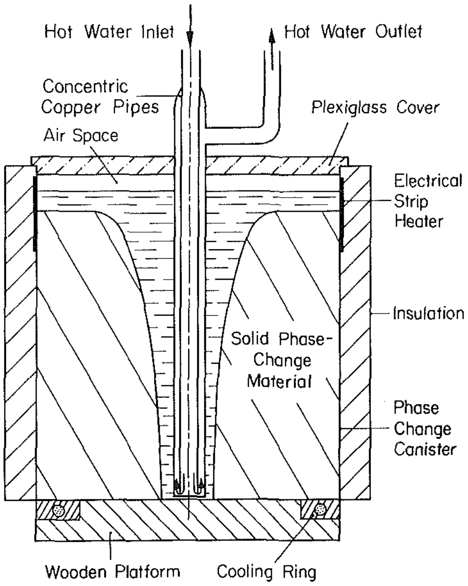

Fig. 2 Cross-sectional view of the phase change canister

In the case of the plain cylinder, the heating element consists of two concentric copper pipes with the outer pipe sealed at the bottom and at the top. Through suitable ports at the top end of the two pipes, hot water from the hot water tank flows downwards through the inner pipe and returns

Nomenclature

c = specific heat of the solid
c_p = specific heat at constant pressure of the liquid
k = thermal conductivity of the liquid
L = length of the heating cylinder
m = mass of melted liquid
m_i = mass of the ith element of the unmelted solid
Nu_L = spatially averaged Nusselt number based on the length of the cylinder
Q = total heat transferred from the cylinder between initiation and termination of melting
q = spatially averaged heat flux from the cylinder
T_{mix} = mixed mean temperature of the liquid
T_{sat} = fusion temperature of the solid
T_{sub} = initial temperature of the subcooled solid
T_w = wall temperature of the cylinder
λ = latent heat of fusion

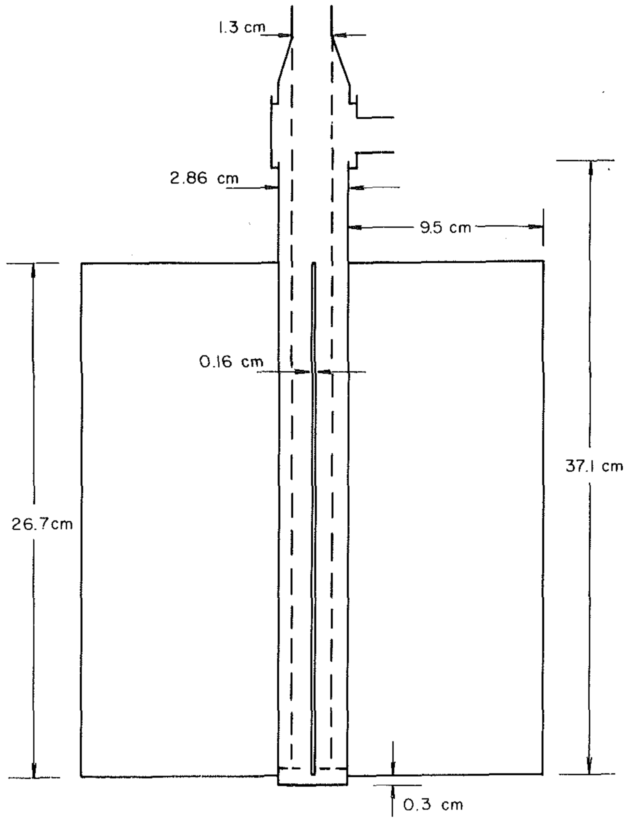

Fig. 3 Schematic depiction of the finned heating element

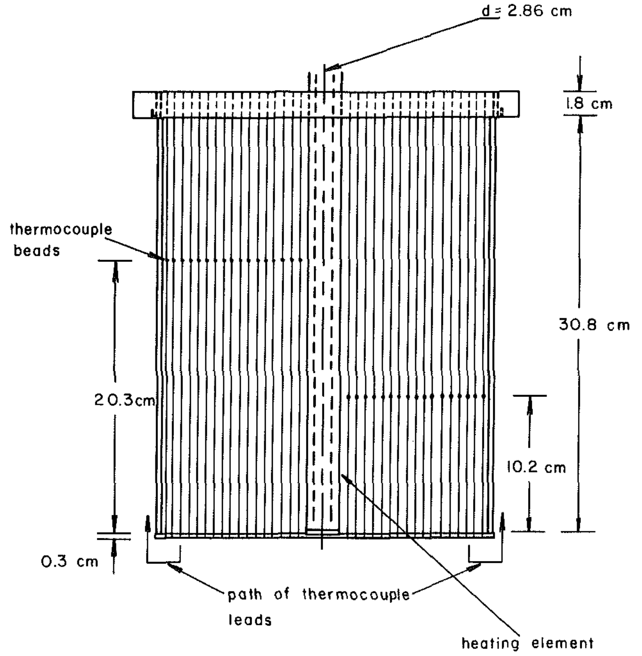

Fig. 4 The arrangement of thermocouples in the phase change canister

upwards through the annulus. Heat transfer to the paraffin occurs from the surface of the outer pipe, which has an o.d. of 28.6 mm and a wall thickness of 1.6 mm. The thermally active length of the heating element (i.e., the length embedded in the paraffin) is 0.3 m. There is a space of 1.8 cm between the top of the paraffin and the cover plate of the paraffin canister, which allows for the expansion of the paraffin during melting.

Figure 3 is a schematic drawing of the finned heating element. Six rectangular copper sheets having the dimensions shown on the figure are inserted into shallow longitudinal grooves machined in the outer diameter and are fixed by soldering to ensure good thermal contact. The surfaces of the tube and the fins are then cleaned with fine emery paper, and any excess solder is removed.

The thermocouples deployed through the paraffin are arranged as shown in Fig. 4. All the thermocouples are made from two matched rolls of 30 gage teflon coated copper and constantan wire. They are threaded through holes between two supporting plexiglass racks, one at the top and the other at the bottom of the canister. Two sets of seventeen thermocouples span the radius of the paraffin container. The two sets of thermocouple junctions are located in two different horizontal planes with a distance of 6.35 mm between neighboring junctions. The free ends of the thermocouples are placed in tension and clamped to ensure the proper location of the beads and to prevent sagging of the wires.

The wall temperature of the paraffin canister is monitored by means of nine thermocouples soldered on the outer surface of the container in a vertical plane. To monitor the heating element, three thermocouples insulated with moisture-resistant teflon coating are soldered to the surface of the heating element at equidistant vertical locations with an angular spacing of 120 deg. These thermocouples pass through the interior of the heating element and are drawn out through an auxiliary port at the top.

2.2 The Data Acquisition System. Two different data acquisition systems were used at different stages in the present work. For the initial experiments involving melting with no subcooling of the solid phase, a Kaye System 8000 data-logger was used. This instrument can be programmed to read and print out the temperatures of upto twenty thermocouples at preselected time intervals. Since complete monitoring of the solid-phase temperature was not necessary in this series of experiments, the 20-channel capability of the data-logger was adequate.

For the subsequent experiments, the paraffin temperatures were measured and recorded with an on-line microcomputer system. The microcomputer system consisted of an Apple II Plus computer with appropriate software and suitable interfacing equipment including a digital/analog converter, amplifier, and eight multiplexer boards with eight channels of input each. The first thermocouple of each multiplexer board was situated in a distilled water-ice bath and served as a cold reference junction for all the other thermocouples connected to the same board. All the other thermocouples on the board read temperatures with respect to the thermocouple junction at the board temperature. By subtracting the e.m.f. registered by the first thermocouple from all the other e.m.f's, the tempertures of the thermocouple beads with respect to the ice bath reference were obtained.

3 Experimental Procedures

As mentioned earlier, three different sets of experiments were undertaken in the present work. In the first set of experiments, the solid was initially at its fusion temperature, while, in the second set, the solid was subcooled prior to the onset of the melting process. In the third experiment, the paraffin was cycled several times through melting and freezing until a periodic steady state was obtained. The heat transfer and temperature distributions in this periodic condition were measured.

3.1 Solid Initially at its Fusion Temperature. In this set of experiments, the paraffin is initially melted completely by circulating hot water through the heating element and, simultaneously, maintaining the temperature in the test chamber above the fusion point. Once the paraffin is completely liquid, directional solidification is initiated by circulating cold water through the cooling coil at the bottom of the paraffin canister and through the central heating element. At the same time, the top section of the canister is maintained at 1 or 2 degrees above the fusion temperature by activating the electrical strip heater. Toward the end of the solidification process, which normally requires about five days, more liquid paraffin is added to level off the slanted solid surface caused by the radially outward freezing, the electrical strip heater is deactivated, and the chilling water circulation is stopped.

In the ensuing equilibration phase, the temperatures of the test chamber and the water circulating through the main heater are maintained at a value slightly below the fusion temperature. Through several days of careful monitoring, the temperature of the entire solid mass is brought up to within 1°C of the fusion point. After equilibration of the paraffin, water from the hot water tank, at a temperature of 11.1°C above the fusion pont, is circulated through the heating element of the phase-change canister. The interior of the test chamber is maintained at the fusion temperture. During the melting, temperature data from several selected thermocouples in the paraffin are constantly recorded by the datalogger. The tempertures of the water bath and the three thermocouples on the heating element are also registered by the datalogger and are found to vary from one another by 0.3°C or less. Thus the heating cylinder is, to a good approximation, at uniform tempertaure. At the end of a preselected melting time, the circulation is stopped and the liquid paraffin is quickly stirred to record its mixed mean temperature. The molten paraffin is then withdrawn from the canister by means of a vacuum system and the mass of the liquid parafin is determined by weighing it in a sensitive balance.

The shape of the melting interface is measured by means of a special depth gauge. The gauge consists of a set of disks with diameters varying in increments of 6.35 mm and a rod with a threaded hole at one end. The disks may be attached to the threaded end of the rod by means of a countersunk screw. The interface shape is obtained by measuring the depths to which the rod may be inserted corresponding to various disk diameters. The disk diameter provides the distance between the heater surface and the sloping interface at the corresponding depth of insertion.

The durations of the melt runs vary between 2 h and 25 hrs. The heat transfer from the surface of the heating element to the paraffin is computed for each data run by summing the energy required for melting the solid and the energy required for elevating the temperature of the liquid above the fusion point. These two energy terms are denoted respectively by Q(latent) and Q(sensible). The total heat transfer may then be expressed as

$$Q(\text{total}) = Q(\text{latent}) + Q(\text{sensible}) \tag{1}$$

where

$$Q(\text{latent}) = m\lambda \tag{2}$$

and

$$Q(\text{sensible}) = mc_p(T_{\text{mix}} - T_{\text{sat}}) \tag{3}$$

Here, m denotes the mass of melted liquid, λ the latent heat of fusion, c_p the specific heat at constant pressure of the liquid, and T_{mix} the mixed mean temperature of the liquid. A test on the repeatability of the experiment showed that the precision in the value of Q(total) was ± 5 percent.

3.2 Solid Initially Subcooled. In this set of experiments, the initial solidification of the paraffin mass is conducted in a fashion similar to the nonsubcooled case. However, the initial temperature of the paraffin is equilibrated at a value significantly below the fusion point by controlling the air temperature within the test chamber. The extent of subcooling is selected to be 20.5°C. Prior to the initiation of melting, the empty space in the test chamber is filled with fiberglass insulation so that the entire surface of the paraffin canister is almost adiabatic.

The total heat transfer from the heating element to the paraffin is obtained by adding three terms: the latent heat required to melt the paraffin, the sensible enthalpy in the liquid region, and the energy required to raise the temperature of the solid mass. The first two terms are identical to equations (2) and (3). The last term is obtained from the readings of the thermocouples embedded in the solid paraffin. In the unfinned situation, the solid is imaginarily divided into several small annular ring elements, and the internal energy change corresponding to the temperature rise of each element is evaluated. The resulting contributions from each element are then summed to yield Q(internal):

$$Q(\text{internal}) = \Sigma cm_i(T_i - T_{\text{sub}}) \tag{4}$$

Here, m_i is the mass of element i, T_i is its tempertaure, c is the specific heat of the solid, and T_{sub} is the subcooled temperature of the solid at the beginning of the melt run. If the solid element has undergone melting, T_i is equal to T_{sat}.

In the finned situation, temperature measurements indicate that the subcooling of the solid phase is rapidly eliminated. Consequently, at the end of a melt run, the unmelted solid is isothermal at T_{sat}. Therefore, in equation (4) T_i is identically equal to T_{sat} in evaluating the internal energy contribution in the finned situation.

3.3 Cyclic Melting and Freezing. In this experiment, the paraffin is repeatedly cycled through freezing and melting until a periodic steady state is obtained. The periodic steady state is that situation in which identical temperature distributions recur from cycle to cycle at corresponding instants of time. In the present experiment, a periodic steady state was found to be established after twelve cycles.

During the freezing stage of each cycle, water from the tank is circulated through the freezing/heating element at a temperature 12.8°C below the fusion point for a period of 15.25 hrs. The water temperature in the tank is held constant by means of an auxiliary cooling system. At the end of the freezing stage, circulation in the element is stopped, and the water in the tank is heated for the melting stage. When the water reaches a temperature of 11.1°C above the fusion point, a process that requires 45 min, the melting stage of the cycle is initiated. The melting process has a time span of 7.25 hrs, and upon termination the water is cooled for the next cycle. The cooling process requires 45 min, so that the total time for one cycle is 24 hrs.

At the end of the melting stage of the final cycle, after the liquid is stirred and the average temperature recorded, the melted paraffin is withdrawn, weighed, and the shape of the melting interface is recorded in the usual manner. In the unfinned situation, the total heat transfer during the melting stage is calculated in the same fashion as in the subcooled case, with one significant difference. In the subcooled case, the internal energy required to raise the temperature of the solid mass is obtained by using a constant value for T_{sub} in equation (4). In the cyclic situation, the tempertaure of the solid mass varies with location due to the temperature fluctuations introduced by the repeated freezing and melting. Therefore, instead of a constant value for T_{sub}, the temperature of each element, before the commencement of the final melting stage, is acquired from the readings of the thermocouples embedded in the solid mass. Therefore, Q(internal) is given by

$$Q(\text{internal}) = \Sigma cm_i(T_i - T_{i,\text{sub}}) \tag{5}$$

In the finned situation, the solid phase is found to be isothermal within 0.5°C at the beginning of the melting stage.

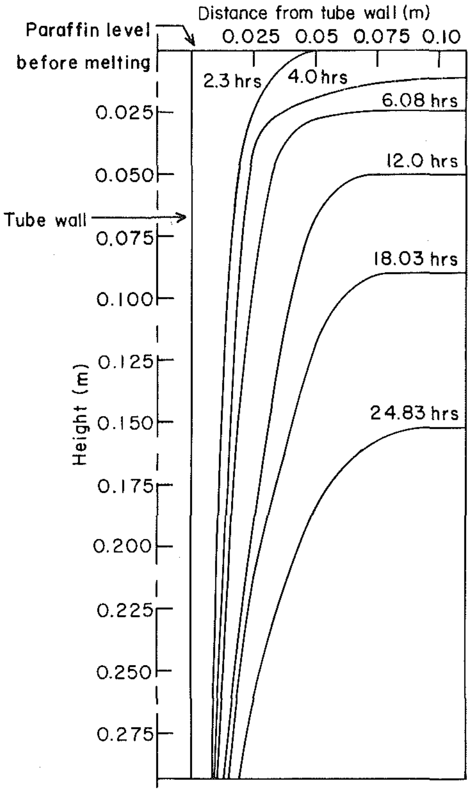

Fig. 5 Solid-liquid interface shapes after various melting times (no subcooling)

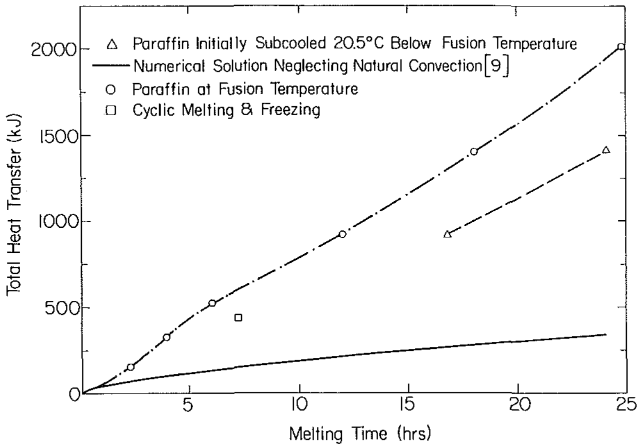

Fig. 6 Total heat transfer from the plain cylinder as a function of time

In addition, at the end of the melting stage, the unmelted solid is isothermal and within 0.5°C of the fusion temperature. Therefore, in equation (5) a measured uniform value of T_{sub} is employed, and T_i is taken as being equal to T_{sat}.

4 Results and Discussions for the Unfinned Situation

4.1 Melting With no Subcooling. Figure 5 is a depiction of the solid-liquid interface shapes at various instants in time after the initiation of melting. These curves are obtained by measuring the interface shapes at four circumferential positions and averaging the readings. The four readings were usually in close agreement, indicating good axisymmetry in the melting. It is observed that initially the thickness of the melted layer around the heater tube is almost uniform from top to bottom. Clearly, the dominant heat transfer mode at early times is conduction. Four hours after the initiation of melting, the interface displays a pronounced curvature at the top, indicating the formation of a natural convection driven eddy. This eddy augments the heat transfer to the melting interface at the very top, but the major portion of the melted layer appears to be uninfluenced by natural convection. The enhanced heat transfer at the top causes a relatively rapid downward recession of the melting interface while the radial melting near the bottom, largely uninfluenced by natural convection, remains slow. The temperature scans taken during this study indicate that the molten paraffin is strongly stratified; tempertaure differences of up to 5°C were observed between the upper and the lower thermocouple locations in the longer melt runs. The Grashof number, computed from the property values cited by Kemink [8] and based on the diameter of the cylinder, is 9×10^4.

Attention is now directed to Fig. 6, in which the total heat transfer from the heating element is plotted against the melting time. Several pieces of data appear in this figure, but the present discussion focuses on the data corresponding to paraffin initially at its fusion temperature (open circles). This line is compared to the line depicting the numerical solution for the case of zero subcooling obtained by neglecting natural convection effects (solid line) [9]. The marked disparity between the two lines confirms that the total heat transfer from the heater is strongly augmented by natural convection in the liquid paraffin.

For melting times greater than 7 hrs, the slope of the total heat transfer curve increases only very gradually with time. This indicates that the heat transfer from the element is principally determined by the thermal resistance of the natural convection boundary layer adjacent to its surface. In the numerical predictions of Sparrow et al. [10], representative temperature profiles depicting the evolution of the heat transfer from a conduction-dominated to a convection-dominated mode are shown. The temperature profiles illustrate that the dominance of natural convection progresses from top to bottom. Once the entire liquid zone is in the convection-dominated mode, a constant heat transfer rate, or a constant slope of the total heat transfer curve, is to be expected. In the present results, the slight increase of slope with time is indicative of the progressive increase of the extent of the convection-dominated region. The other prominent feature of the total heat transfer curve is an inflection point in the neighborhood of 4 hrs. This change in slope is believed to be a consequence of the interaction of the convective flow with the side walls of the paraffin canister.

A spatially averaged Nusselt number may be computed from the slope of the total heat transfer curve at large time. The Nusselt number is defined by the equation

$$\overline{\text{Nu}_L} = \frac{qL}{k(T_w - T_{\text{sat}})} \tag{6}$$

where q is the spatially averaged heat flux from the heating element, L is the length of the heater, and k is the thermal conductivity of the liquid paraffin evaluated at the mean temperature $0.5\ (T_w + T_{\text{sat}})$. The Nusselt number evaluated on the basis of equation (6) is 170. This value may be compared with the data of Kemink and Sparrow [7], who proposed the correlation

$$\overline{\text{Nu}_L} = 0.393\text{Ra}_L^{0.267}$$

In the present investigation, the value of Ra_L is 5.85×10^9 which, when employed in the aforementioned correlation, yields a Nusselt number of 160. Thus the present result agrees within 6 percent with the results of Kemink and Sparrow.

A note on the sizing of a practical thermal storage unit is appropriate at this point. On examining Fig. 5, it is clear that, in the present work, the canister was too large in relation to the diameter of the heater. A very substantial amount of paraffin remains unmelted at the end of a typical charging period of 8 hrs. From the evidence of Fig. 5, certain rough

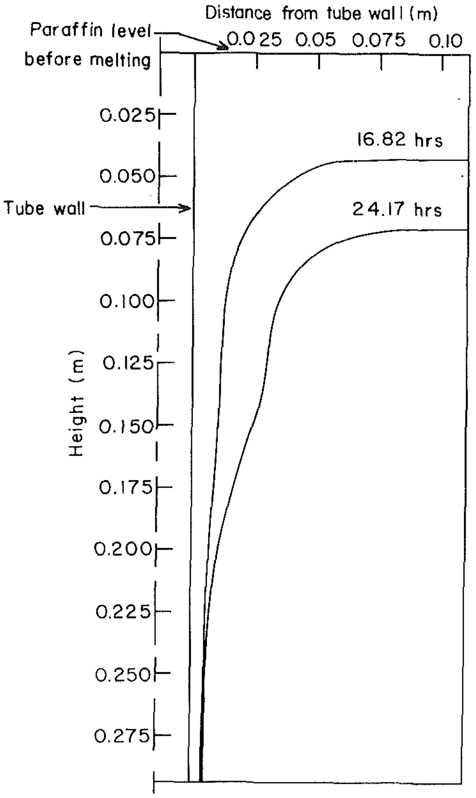

Fig. 7 Solid-liquid interface shapes in the case of subcooled melting; solid phase initially subcooled 20.5°C

guidelines for the sizing of the phase change canister emerge. It is suggested that in a practical thermal storage unit, the height to heater diameter ratio be less than 5, and the ratio of canister diameter to heater diameter be less than 6.

4.2 Melting With Subcooling. In Fig. 6, two data points (triangles) are plotted to show the results of the subcooled melting experiments. Clearly, the total heat transfer in the subcooled cases is substantially lower than in the nonsubcooled cases. This is an interesting result that contradicts the numerical predictions of Sparrow et al. [9]. The numerical solutions predict an increased rate of heat transfer when the solid phase is initially subcooled.

This disparity is resolved by first noting that subcooling of the solid leads to a drastic reduction in the rate of growth of the melt region. This reduction in the rate of melting occurs because the large subcooled solid mass is able to rapidly drain away energy from the melting interface by conduction, thus retarding the growth of the melt region. In the numerical solutions, the effect of natural convection in the liquid was neglected, and a conduction-dominated model was employed. According to this model, a smaller melt layer thickness leads to larger temperature gradients and larger heat fluxes. Therefore, the heat transfer in the subcooled case should be greater than in the nonsubcooled case. However, in the present experiment, natural convection enhances the heat transfer in both the subcooled and the nonsubcooled cases. The heat transfer enhancement is considerably greater in the nonsubcooled case, because the smaller melt layer thickness of the subcooled case tends to inhibit the natural convection. The overall result of these two conflicting effects is that the heat transfer in the nonsubcooled situation is larger.

Figure 7 is a depiction of the interface shapes in subcooled melting. A comparison of these shapes with the ones dipicted in Fig. 5 reveals a drastic reduction in the melting rate, due to subcooling. In addition, it is seen that melting is virtually arrested at the bottom portion of the canister, so that natural convection is free to act only in the upper part. The wavy shape of the interface at 24.17 hrs is an interesting feature of these curves for which the present investigators have no simple explanation. In closing this section, it is emphasized that initial subcooling of the solid can have a great impact on the heat transfer from the cylinder.

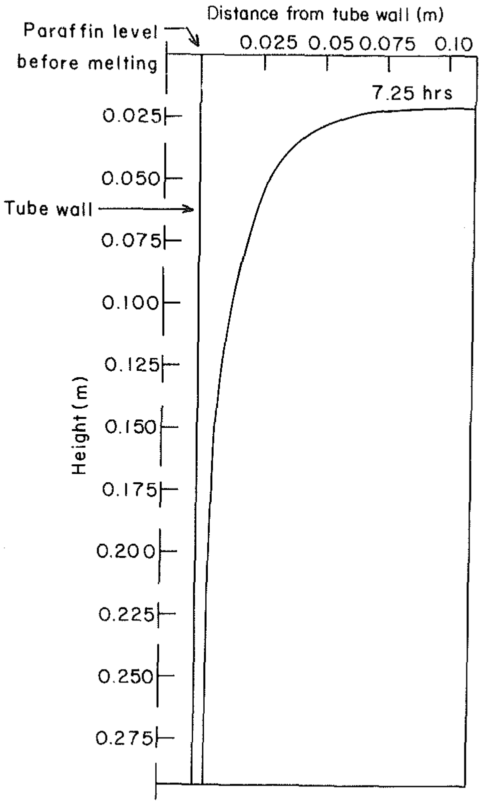

Fig. 8 Solid-liquid interface shape at the end of the melting stage in the case of cyclic melting and freezing

4.3 Cyclic Melting and Freezing. The findings of the preceding sections are useful in understanding the results of the experiment on cyclic melting and freezing. In cyclic melting and freezing, the solid phase necessarily undergoes a certain amount of subcooling. Bearing in mind the important effect of subcooling as demonstrated in the previous section of this report, it is to be expected that the heat transfer in the present situation would also be significantly influenced by the subcooling of the solid.

As discussed earlier, the present investigation is concerned with the periodic steady state in which the amount of heat transferred to the phase-change material during melting is exactly equal to the amount of energy recovered from the phase-change material during freezing. A single data point is plotted in Fig. 6 (square symbol) corresponding to the amount of heat transferred during the melting stage of a typical cycle. Evidently, the amount of heat transferred during the cyclic charging and discharging of the phase-change material is significantly lower than in the case of zero subcooling. This effect could have an important bearing on the design of practical thermal storage units. For efficient operation, a thermal storage unit would have to be designed in such a way as to minimize the influence of subcooling.

One of the motives in performing the cyclic experiment was to determine if multiple layers of solid and liquid phase would occur in the paraffin. The occurrence of several alternating layers of solid and liquid would have interesting consequences relating to the heat transfer in the phase change medium. Visual observations during the experiment showed, however,

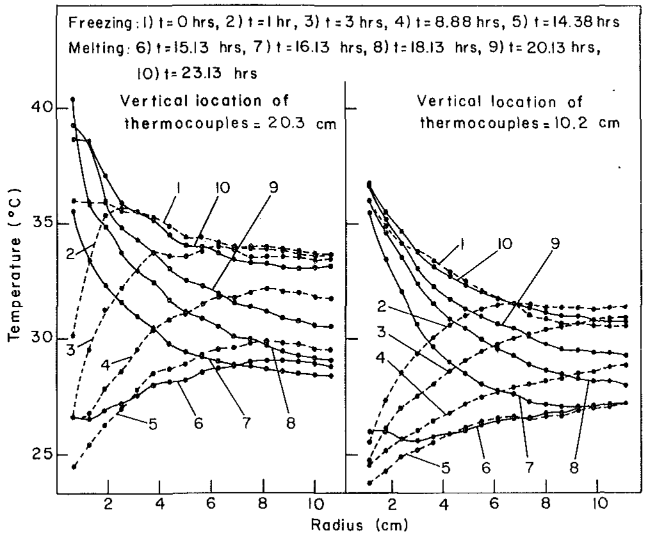

Fig. 9 Temperature distributions in the phase change material during cyclic melting and freezing

that multiple layers of solid and liquid occurred only during the initial transient period consisting of the first three or four cycles. In the periodic steady state, only a narrow annular region of phase-change material around the heating element undergoes melting and freezing. This annular region is surrounded by a mass of solid paraffin that never undergoes phase change, but participates in the heat transfer by conduction.

Figure 8 is a depiction of the interface position at the end of the melting stage of a cycle. It is seen that the interface is smooth and continuous with an almost flat surface at the top. As in the subcooled cases previously described, melting occurs primarily at the top of the paraffin and is virtually arrested along the remainder of the heated tube wall. Figure 9 shows the timewise variation of temperatures in the paraffin mass during a typical cycle. The two halves of the figure contain temperature information from the two vertical locations shown in Fig. 4. The dashed lines correspond to the freezing stage and the solid lines are graphs of temperatures during the melting stage. Inspection of these graphs reveals the significant role of the thermal inertia of the paraffin mass. It is seen that while the surface temperature of the heating tube swings almost 24°C during a cycle, the temperature of the paraffin mass near the canister wall swings only 5°C. Furthermore, the bulk of the paraffin is subcooled as much as 8°C at the end of the freezing stage of the cycle. Calculation of the total heat transfer by the procedure described in sections 3.2 and 3.3 shows that about 30 percent of the total heat transferred from the heating element is utilized in elevating the temperature of the solid paraffin.

One of the concerns in the cyclic operation of such a thermal storage unit is the formation of shrinkage voids that could inhibit heat transfer. Visual observations of the freezing phase of the cycle show that the thin annular liquid layer in the lower region of the canister is quickly bridged by radially outward solidification. Later, a solid crust forms at the top of the liquid paraffin. This crust prevents further observation of the freezing, but it is expected that a shrinkage void is formed just below the crust, extending from an intermediate radius upto the wall of the canister. This void does not influence the melting stage of the cycle, because it is quickly filled with liquid when the melting is initiated.

5 Results and Discussions for the Finned Situation

In this section, the principal results of the investigation with the finned heater will be presented and compared with the results of the unfinned case. Attention is directed to Fig. 10, in which the total heat transfer is plotted as a function of melting time for the three sets of experiments performed in the present study. The open circles are the data points corresponding to the experiments in which the solid paraffin is initially at its melting point. For a melting time up to 2 hr, the heat transfer appears to be conduction dominated. This accounts for the diminishing slope of the curve in this region. For a melting time greater than 2 hr, the slope of the total heat transfer curve increases, i.e., the heat transfer rate increases. This indicates the augmentation of the heat transfer rate by natural convection. For melting times greater than 2½ hours, the slope of the total heat transfer curve diminishes progressively. This is attributed to the fact that the area of the solid–liquid interface begins to diminish as the upper part of the solid is completely melted away. Consequently, the rate of heat transfer to the interface diminishes. This, in turn, leads to a reduction of the rate of heat transfer from the heating element.

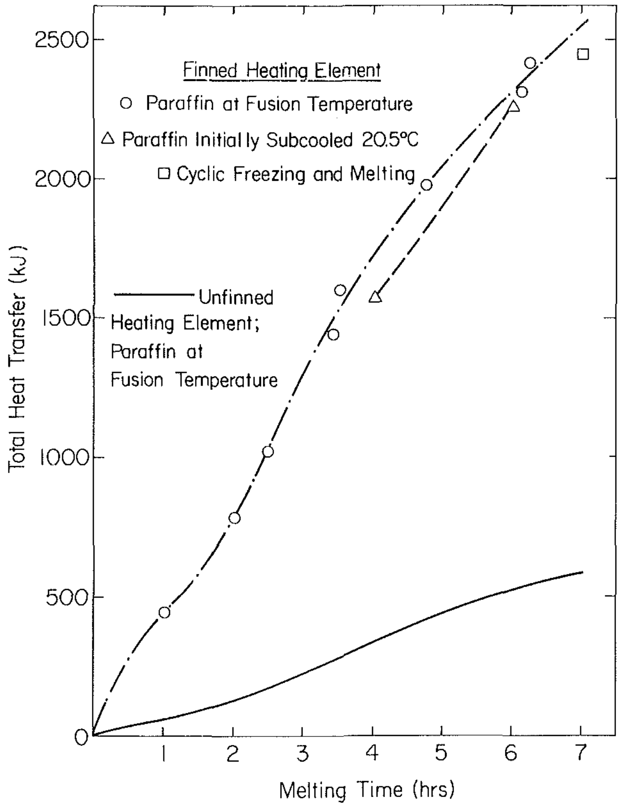

Fig. 10 Total heat transfer from the finned cylinder as a function of time

For comparison, the total heat transfer from the unfinned heating element is plotted on Fig. 10 as the solid line. The general features of this curve are similar to those of the curve corresponding to the finned element. However, there is a significant enhancement in the total heat transfer due to the addition of fins.

The augmentation of the rate of heat transfer is in accordance with expectation. The heat transfer *rate* is obtained by taking the slope of the total heat transfer curve. In the present instance, the average slope of the curve evaluated between 2.5 and 3.5 hrs of melting time yields a heat transfer rate of 140 W. The design of the finned heating element was based on the data obtained for nonsubcooled melting in the unfinned case. In that study, a heat transfer coefficient of 83 W/m^2°C (Nu = 170) was measured at large melting times, i.e., in the convection dominated regime. Based on this heat transfer coefficient, the fins were designed for an efficiency of

60 percent which, in turn, leads to a predicted heat transfer rate of 195 W in the finned situation. The actually achieved heat transfer rate of 140 W is close to, but somewhat short of, the predicted value. The discrepancy may be attributed to a nonuniform distribution of heat transfer coefficient along the length of the fin, with the maximum coefficient at the fin base.

Attention is now directed to the data points corresponding to subcooled melting (triangles) and cyclic melting and freezing (square symbol). It may be observed that these data points are not far removed from the curve for zero subcooling. Evidently, subcooling of the solid phase has only a small effect on the total heat transfer in the finned situation. In comparison, in the unfinned situation a significant reduction in the total heat transfer and melting rate was observed in subcooled melting and cyclic melting and freezing.

In the unfinned situation, the reduction in the total heat transfer was caused by the large subcooled solid mass conducting energy away from the interface. The consequent retardation of the growth of the melt layer lead to an inhibition of the natural convection flow and a reduction in the rate of heat transfer. In the finned situation, heat conduction from the extended fin surfaces is able to rapidly overcome the subcooling of the relatively small pie-shaped regions between the fins. Visual observations show that substantial melt layers are developed within 2 hrs of the initiation of melting. Thus natural convection heat transfer becomes fully effective more quickly than in the unfinned situation.

In the case of cyclic operation, in the unfinned experiments it was found that a large proportion (30 percent) of the total heat transferred during the melting stage of the cycle was utilized in raising the tempreature of the subcooled solid phase. Thus 30 percent of the total heat transferred to the phase change unit was stored as sensible heat of the solid rather than latent heat of fusion. In the finned situation, calculation of the total heat transfer using equations (1-5) shows that about 12 percent of the total heat transferred is utilized in elevating the temperature of the solid paraffin. From the point of view of thermal storage and recovery, it is desirable to minimize the proportion of energy stored as sensible heat of the solid. Judged from this criterion, the performance of the finned configuration is superior to that of the unfinned configuration.

6 Conclusions

In the unfinned situation, the experiments on melting in a solid initially at its fusion temperature are in good agreement with the earlier work by Kemink and Sparrow. The experiments with the finned heater in a nonsubcooled solid demonstrate that the addition of longitudinal fins to the cylindrical surface is an economical and effective way of substantially enhancing the heat transfer rates. Both sets of experiments highlight the pivotal role played by natural convection in the heat transfer process.

When the solid phase is subcooled, it is found that the heat transfer rate from the plain cylinder is significantly reduced in comparison with the nonsubcooled situation. Heat transfer from the finned cylinder is much less affected by subcooling of the solid phase.

The experiments on cyclic freezing and melting once again reveal that heat transfer from the unfinned cylinder is reduced when compared with the nonsubcooled case. The large thermal inertia of the solid paraffin inhibits melting; consequently, a significant fraction of the total heat transferred goes into increasing the sensible heat of the solid. It is observed that in the periodic steady state only a narrow annular region surrounding the cylinder undergoes phase change. Therefore, the plain cylinder is a poor configuration for the design of an actual thermal storage unit.

In comparison, heat transfer from the finned cylinder in cyclic freezing and melting is much less affected by the thermal inertia of the solid phase. In view of its superior heat transfer characteristics, the finned cylinder is a much better choice for the design of a practical thermal storage unit.

Acknowledgment

This work was supported by a Research Initiation Grant RI-A-82-8 from the Engineering Foundation.

References

1 Sparrow, E. M., Schmidt, R. R., and Ramsey, J. W., "Experiments on the Role of Natural Convection in the Melting of Solids," ASME JOURNAL OF HEAT TRANSFER, Vol. 100, 1978, pp. 11-16.

2 Bathelt, A. G., and Viskanta, R., "Heat Transfer at the Solid-Liquid Interface During Melting From a Horizontal Cylinder," *International Journal of Heat and Mass Transfer* , Vol. 23, 1980, pp. 1493-1503.

3 Bathelt, A. G., Viskanta, R., and Leidenfrost, W., "A Experimental Investigation of Natural Convection in the Melted Region Around a Heated Horizontal Cylinder," *Journal of Fluid Mechanics*, Vol. 90, 1979, pp. 227-239.

4 Sparrow, E. M., Ramsey, J. W., and Harris, J. S., "The Transition from Natural Convection-Controlled Freezing to Conduction-Controlled Freezing," ASME JOURNAL OF HEAT TRANSFER, Vol. 103, 1981, pp. 7-12.

5 Abdel-Wahed, R. M., Ramsey, J. W., and Sparrow, E. M., "Photographic Study of Melting About an Embedded Horizontal Heating Cylinder," *International Journal of Heat and Mass Transfer*, Vol. 22, 1979, pp. 171-173.

6 Ramsey, J. W., and Sparrow, E. M., "Melting and Natural Convection Due to a Vertical Embedded Heater," ASME JOURNAL OF HEAT TRANSFER, Vol. 100, 1978, pp. 368-370.

7 Kemink, R. G., and Sparrow, E. M., "Heat Transfer Coefficients for Melting About a Vertical Cylinder With or Without Subcooling and for Open or Closed Containment," *International Journal of Heat and Mass Transfer*, Vol. 24, 1981, pp. 1699-1710.

8 Kemink, R. G., "Melting of a Solid Adjacent to a Heated Vertical Cylinder With or Without Subcooling of the Solid," Ph.D. thesis, Department of Mechanical Engineering, University of Minnesota, Minneapolis, Minn., 1981.

9 Sparrow, E. M., Ramadhyani, S., and Patankar, S. V., "Effect of Subcooling on Cylindrical Melting," ASME JOURNAL OF HEAT TRANSFER, Vol. 100, 1978, pp. 395-402.

10 Sparrow, E. M., Patankar, S. V., and Ramadhyani, S., "Analysis of Melting in the Presence of Natural Convection in the Melt Region," ASME JOURNAL OF HEAT TRANSFER, Vol. 99, 1977, pp. 521-526.

Oscillatory Conductive Heat Transfer for a Fiber in an Ideal Gas

H. L. Kuntz[1]
Senior Consultant,
Hoover Keith and Bruce Inc.,
Houston, Texas 77082

N. D. Perreira
Associate Professor,
Department of Mechanical Engineering,
University of Nevada-Reno,
Reno, Nevada 89557
Assoc. Mem. ASME

A description of the thermal effects created by placing a cylindrical fiber in an inviscid, ideal gas, through which an acoustic wave propagates, is presented. The fibers and the gas have finite heat capacities and thermal conductivities. Expressions for the temperature distribution in the gas and in the material are determined. The temperature distribution is caused by pressure oscillations in the gas which, in turn, are caused by the passage of an acoustic wave. The relative value of a dimensionless parameter is found to be indicative of whether the exact or approximate equations should be used in the solution. This parameter is a function of the thermal conductivities and heat capacities of the fiber and gas, the acoustic frequency, and the fiber diameter.

Introduction

The following study is an analysis of how heat transfer to and from a cylindrical fiber affects the propagation of a sinusoidal acoustic wave in an inviscid, ideal gas of infinite extent. An object exposed to oscillatory heat transfer will have thermal waves generated within the object [1-3]. Thermal waves are also generated in the medium surrounding the object [1]. The propagation of thermal waves is mathematically similar to the propagation of viscous boundary waves generated by a sinusoidally moving object [4]. In the analysis presented below, a differential equation to describe the heat flow to and from cylinders is determined. The most general case, where both the fiber and the gas have finite heat capacities and thermal conductivies, is considered. The effects of oscillatory heat transfer on acoustic wave propagating in air filled tubes have been treated by many researchers [5-8]. Their treatments are quite general; viscous effects are included. In the present analysis we consider a cylindrical fiber immersed in air of an infinite extent. The wavelength of the sinusoidal wave is assumed to be much larger than the fiber diameter and the thermal boundary layer. Convective heat transfer and mixing, caused by acoustic streaming around the fiber, are neglected; the particle displacement amplitude in the gas is taken to be much smaller than the fiber diameter. Acoustic streaming would increase the heat transfer rate and make theoretical analysis extremely difficult. Reference [9] contains a discussion of the nonlinear streaming effects associated with the fairly similar case of oscillating cylinders.

In the present analysis, the solution of the differential equation is obtained and written in two parts, one for the fiber and the other for the gas. In the solutions we define a dimensionless parameter χ. The magnitude of χ influences the manner in which heat is transferred between the gas and the fiber. We examine three cases: first, χ much less than 1; second, χ much greater than 1; and, finally, real fibers in real gases $(0.1<\chi<10)$.

Because heat takes a finite time to diffuse through the gas, a thermal boundary layer is set up around the fiber. In actuality, a viscous boundary layer also surrounds the fiber. In the viscous boundary layer there is a rapid transition from the mainstream particle velocity to zero at the fiber surface. In the thermal boundary layer the transition across the boundary layer is not so simple. This transition is influenced by the complicated boundary conditions at the fiber surface. The boundary conditions depend on the thermal properties of both the fiber and the gas. We shall treat only the thermal boundary layer problem. Solution of the viscous boundary layer problem can be found in the literature [9]. The details of the resultant effect of the thermal boundary layer on the phase speed of sound propagating in the gas surrounding the fibers are the subject of another paper [11]. The primary result of the present analysis is to provide a physically oriented background as to how the heat transfer affects the phase speed. The present analysis shows the extent of the influence of the thermal properties of the fiber. A special case example of the phase-speed calculation is given below.

The solution method presented here is motivated by the work done by Pfreim [12] and restated by Devin [13] on heat transfer effects in oscillating gas bubbles in water. Pfreim and Devin were concerned with how heat transfer to and from gas bubbles affects the damping of sound propagating in water. In this paper the concern is how heat transfer affects the temperature distribution in and around a fiber. Whereas the approaches are similar, the cylindrical coordinate system and objectives of this paper lead to a much different result. The method used here also has some similarities to that presented by Jakob for heat transfer between two semi-finite plates due to periodic temperature fluctuations [1], to the work of Gröber who considered the internal temperature oscillation of cylinders due to convective heat transfer [2].

Kirchhoff [5] analyzed an air-filled tube with a constant temperature wall and Rayleigh [6] used that analysis to model the effects of porous absorbers on sound waves. Henry [10] considered thermal wave traveling into the tube walls, but made the assumption that the walls could be considered as plane surfaces, i.e., the radius was large relative to the boundary layer size. These assumptions are not used in the present analysis. Rott [8] considered thermal waves that travel radially into the cylinder wall. He assumed that the tube has infinitely thick walls, which may be considered as the reverse of the present analysis.

Equation Formulation and General Solutions

Equation Formulation. The derivation is based on the application of the first law of thermodynamics to determine the forced heat transfer equation. Both the control volume and the fiber are assumed to be cylindrical. The control

---

[1] This work constitutes part of the first author's Doctoral Dissertation in Mechanical Engineering from the University of Texas at Austin.

Contributed by the Heat Transfer Division for publication in the JOURNAL OF HEAT TRANSFER. Manuscript received by the Heat Transfer Division September 23, 1982.

volume is assumed to have an arbitrary radius r and coaxially surrounds the fiber.

The first law of thermodynamics applied to an ideal gas and written as a rate equation yields

$$K\left(\frac{\partial^2 T}{\partial_r{}^2}+\frac{1}{r}\,\frac{\partial T}{\partial r}\right)-\rho C_p\,\frac{\partial T}{\partial t}=-\frac{\partial P}{\partial t} \qquad (1)$$

Equation (1) is a general equation applicable to a pressure fluctuation in a gas with angular symmetry when the region of the pressure fluctuation is much larger than the fiber radius a, i.e., $\lambda >> a$. For example, for a 1-mm-radius fiber, equation (1) is valid for frequencies much less than 340 kHz. Analysis of conductive heat transfer in solid materials results in an expression like that of equation (1) except that the pressure variation term is not present. Although the pressure variation in a solid fiber exists, the pressure variation does not result in heat generation; there is no work done on an incompressible fiber. In addition, in order for the boundary conditions to be valid, the wavelength must be much larger than the thermal boundary layer. The equation is valid only for zero velocities and this limits the analysis to small signal sounds. In order for the equation to be valid as an approximation, the particle displacement must be much smalller than the radius of the fiber. In the case of a fiber radius of 6 μm, the sound level at 1KHz must be less than 85 dB.

General Solution. In a gas medium containing a fiber, the equations governing the temperature fluctuations may be obtained by combining the homogeneous and particlar solutions of equation (1). Equations for both the external and internal fiber temperature distributions may be determined. Because the fiber is assumed to be incompressible and no work is done on or by the fiber, the term on the right-hand side of equation (1) is zero internal to the fiber. The same term is nonzero in the gas. Solution of the homogeneous portion of equation (1) can be found in [3].

The forced solution of equation (1) is determined by assuming that the pressure fluctuation is time dependent, such that

$$P(r,t)=P_a e^{j\omega t} \qquad (2a)$$

Since the region of the pressure variation is much larger then fiber radius, $\lambda >> a$, there is no pressure gradient in the vicinity of the fiber, and the pressure, P is assumed to be independent of the radial distance r. On the other hand, the acoustic temperature function depends on the radius. The temperature dependence has the form

$$T(r,t)=T_a(r)\,e^{j\omega t} \qquad (2b)$$

When internal to the fiber $T_a = T_I$ and when external to the fiber $T_a = T_E$.

The total solution of equation (1) for both the external and internal regions of the fiber is written in terms of the modified Bessel function of the second kind of order zero, $K_0 < RZ_j{}^{1/2})$, and the Bessel function of the first kind of order zero, J_0 $(RZ_j{}^{3/2})$. The total solution for the temperature is written in terms of dimensionless variables as

$$T_E(RZ_E)=M_E J_o(RZ_E\,j^{3/2})+N_E K_o(RZ_E\,j^{1/2})+\frac{P_a}{\rho_o C_p} \qquad (3a)$$

and

$$T_I(RZ_I)=M_I J_o(RZ_I\,j^{3/2})+N_I K_o(RZ_I\,j^{1/2}), \qquad (3b)$$

where the unknown coefficients M_E, M_I, N_E, and N_I are determined by the boundary conditions.

The first two boundary conditions are determined by noting that the radial gradient of the temperature oscillations must approach zero at infinity and at the center of the fiber. These two boundary conditions insure finite temperature oscillations at the two locations. In terms of the dimensionless variables these two boundary conditions are written as

$$\left.\frac{\partial T_E(RZ_E)}{\partial R}\right|_{R=\infty}=0 \qquad (4a)$$

and

$$\left.\frac{\partial T_I(RZ_I)}{\partial R}\right|_{R=0}=0. \qquad (4b)$$

The heat flow and temperature at the fiber surface must be continuous. Thus

$$T_I(R)\Big|_{R=1}=T_E(R)\Big|_{R=1} \qquad (4c)$$

and

$$K_I\left.\frac{\partial T_I}{\partial(RZ_I)}\right|_{R=1}\frac{\partial(RZ_I)}{\partial r}=K_E\left.\frac{\partial T_E}{\partial(RZ_E)}\right|_{R=1}\frac{\partial(RZ_E)}{\partial r}. \qquad (4d)$$

The external temperature becomes

$$T_E(R)e^{j\tau}=\frac{P_a}{\rho_{oE}C_{PE}}$$

$$\left[1+\frac{K_o(RZ_E j^{1/2})\,J_o'(Z_I\,j^{3/2})\,.}{\frac{K_E Z_E}{K_I Z_I}K_o'(Z^E\,j^{1/2})J_o(Z_I\,j^{3/2})-K_o(Z_E\,j^{1/2})J_o'(Z_I\,j^{3/2})}\right]^{e^{j\tau}} \qquad (5)$$

Nomenclature

a = fiber radius
C_p = specific heat at constant pressure
C_V = specific heat at constant volume
E = subscript used external to fiber
f = frequency
I = subscript used internal to the fiber
j = $\sqrt{-1}$, imaginary number
$J_o(\cdot)$ = Bessel function of the first kind of order zero
K_I, K_E = thermal conductivity
$K_o(\cdot)$ = Bessel function of the second kind of order zero
M_i, M_E = coefficients dependent on boundary conditions
N_I, N_E = coefficients dependent on boundray conditions
P = linearized acoustic pressure
P_a = magnitude of the acoustic pressure
Q = heat transferred per unit volume
r = radial coordinate, equals zero at the fiber center
r_o = characteristic integration distance
R = r/a, dimensionless distance
R_o = dimensionless characteristic integration distance
t = time
T = linearized acoustic temperature
T_a, T_I, T_E = magnitude of the temperature fluctuation
Z_I, Z_E = $a\sqrt{\omega/\alpha}$, dimensionless frequency
α_I, α_E = thermal diffusivity
ρ = density
ρ_0, ρ_E, ρ_I = ambient density
ω = $2\pi f$, angular frequency
τ = ωt, dimensionless time
χ = a dimensionless parameter defined by equation (7)
λ = acoustic wavelength

while the internal temperature becomes

$$T_I(R)e^{j\tau} = \frac{P_a}{\rho_{oE}C_{PE}}$$

$$\left[\frac{K_o'(Z_E j^{1/2})\,J_o(RZ_I j^{3/2})}{K_o'(Z_E j^{1/2})J_o(Z_i j^{3/2}) - \dfrac{K_I Z_I}{K_E Z_E} K_o(Z_E j^{1/2})J_o'(Z_I j^{3/2})} \right] e^{j\tau} \tag{6}$$

where the prime denotes derivatives with respect to Z_I and Z_E, respectively; the j terms are accounted for in the derivatives of the Bessel functions.

Thermal Boundary Layer

A description of the internal and external thermal boundary layers is obtained by using equations (5) and (6). In the following discussion, the solutions of two limiting cases are presented. These two limiting cases are not only used to model actual situations, but they also are presented to gain insight into the results of the general solution.

Equations (5) and (6) depend on the ratio

$$\chi = \frac{K_E Z_E}{K_I Z_I} \, \frac{K_o'(Z_E j^{1/2})J_o(Z_I j^{3/2})}{K_o(Z_E j^{1/2})J_o'(Z_I j^{3/2})}. \tag{7}$$

The relative values of this dimensionless parameter are indicative of whether we are able to use the special case solutions or the general solution. The thermal constants of equation (7) may be written as

$$\frac{K_E Z_E}{K_I Z_I} = \frac{\sqrt{K_E \rho_E C_E}}{\sqrt{K_I \rho_I C_I}} \tag{8}$$

This expression relates the ability of the heat to flow between the two materials. The part of equation (7) containing the Bessel functions expresses the heat flow ability for the case of a cylindrical solid body in an infinite gas medium when the heat flow is oscillatory.

Special Case, $\chi << 1$. When χ is very small, equation (5) reduces to

$$T_E(R) = \frac{P_a}{\rho_{oE}C_{PE}} \left(1 - \frac{K_o(Z_E R j^{1/2})}{K_o(Z_E j^{1/2})}\right) \tag{9}$$

and equation (6) reduces to

$$T_I(R) = -\frac{P_a}{\rho_{oE}C_{PE}} \, \frac{K_E Z_E}{K_I Z_I} \, \frac{K_o'(Z_E j^{1/2})\,J_o(RZ_I j^{3/2})}{K_o(Z_E j^{1/2})\,J_o'(Z_I j^{3/2})} \simeq 0 \tag{10}$$

Thus the internal temperature variation and fluctuation becomes negligibly small when $\chi << 1$. The solution of the external temperature distribution given by equation (9) would occur, for example, when a fiber with a large heat capacity and conductivity is immersed in a gas of a much smaller heat capacity and conductivity. This special case solution of the more general problem discussed in this paper is presented using a more direct procedure in [3].

The solutions described by the special case of equations (9) and (10) are portrayed graphically as functions of dimensionless variables by first substituting

$$T_{EI} = \frac{P_a}{\rho_{oE}C_{PE}} \tag{11a}$$

and

$$V_E(R) = \frac{T_E(R)}{T_{EI}} \tag{11b}$$

into equations (9) and (10) and evaluating the resulting equations by computer. The magnitude of the dimensionless temperature oscillations within the fluid, $|V_E|$, is plotted for various values of Z_E for the case $\chi << 1$ in Fig. 1. The influence of the fiber's thermal properties in the external temperature oscillations is exhibited by low values of the dimensionless variable V_E. When V_E is small, say less than 0.1, the compressions in the gas approach the isothermal case for a large volume around the cylinder. Only for gases with low values of Z_E will this thermal boundary layer be large. Since V_E varies with frequency, the boundary layer will be largest at low frequencies. When V_E is large, say greater than 0.9, the compressions that occur in the gas approach the adiabatic case; the boundary layer is small. The implication is that large values of Z_E allow only a small region near the fiber surface to have isothermal conditions. The thermal properties of the fiber do not greatly influence the acoustic wave and the fiber's presence may be ignored. On the other hand, small values of Z_E allow large regions to have nonadiabatic conditions. The thermal properties of the fibers in this case greatly influence the acoustic wave by both attenuating the amplitude and by reducing the phase speed around the fiber.

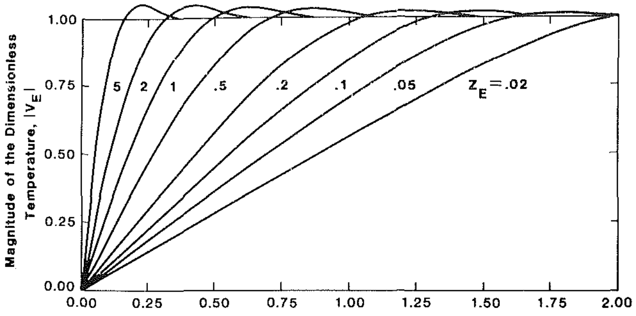

Fig. 1 Magnitude of the dimensionless temperature external to the fiber versus log distance for $\chi << 1$

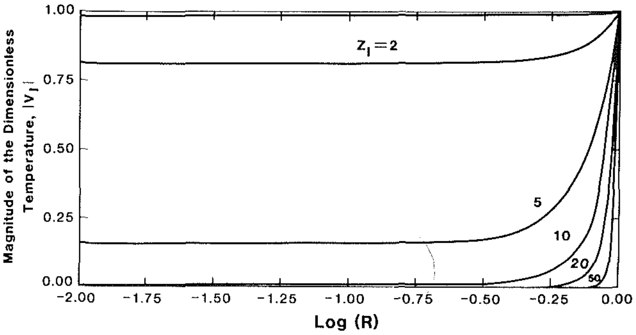

Fig. 2 Magnitude of the dimensionless temperature internal to the fiber versus log distance for $\chi >> 1$

Special Case, $\chi >> 1$. When χ is very large, equation (5) reduces to

$$T_E(R) = T_{EI} \tag{12}$$

and equation (6) becomes

$$T_I(R) = T_{EI} \frac{J_o(Z_I R j^{3/2})}{J_o(Z_I j^{3/2})} \tag{13}$$

Thus, the external temperature approaches a uniform oscillation throughout the medium and the temperature in the fiber has an oscillating gradient. This special case solution can also be found in [3].

The solutions described by the special case equations (12) and (13) can be portrayed graphically as functions of dimensionless variables by evaluating

Table 1 Magnitude of $K_E/K_I{}^*\chi$ for various internal and external dimensionless frequencies

	Z_E / Z_I	EXTERNAL DIMENSIONLESS FREQUENCY									
		.01	.02	.05	.10	.20	.50	1.00	2.00	5.00	10.00
INTERNAL DIMENSIONLESS FREQUENCY	.01	4.2×10^{3}	4.9×10^{3}	6.2×10^{3}	7.8×10^{3}	10.4×10^{3}	17.0×10^{3}	27.2×10^{3}	47.3×10^{3}	10.7×10^{4}	20.7×10^{4}
	.02	1.0×10^{3}	1.2×10^{3}	1.5×10^{3}	2.0×10^{3}	2.6×10^{3}	4.3×10^{3}	6.8×10^{3}	11.8×10^{3}	26.9×10^{3}	51.7×10^{3}
	.05	167	195	250	310	420	680	1.1×10^{3}	1.9×10^{3}	4.3×10^{3}	8.3×10^{3}
	.10	42	49	62	78	104	170	270	470	1.1×10^{3}	2.1×10^{3}
	.20	10	12	16	20	26	43	68	118	270	520
	.50	1.7	2.0	2.5	3.1	4.2	6.8	10.9	18.9	43	83
	1.00	.42	.49	.63	.79	1.06	1.72	2.8	4.8	10.9	21
	2.00	.12	.14	.18	.23	.31	.50	.80	1.39	3.2	6.1
	5.00	.045	.052	.068	.084	.11	.18	.29	.51	1.2	2.2
	10.00	.022	.025	.032	.041	.054	.088	.141	.24	.55	1.1
	20.00	.011	.012	.016	.020	.027	.043	.069	.12	.27	.53
	50.00	4.2×10^{-3}	4.9×10^{-3}	6.3×10^{-3}	7.9×10^{-3}	10.4×10^{-3}	17.1×10^{-3}	27.4×10^{-3}	47.6×10^{-3}	.11	.21

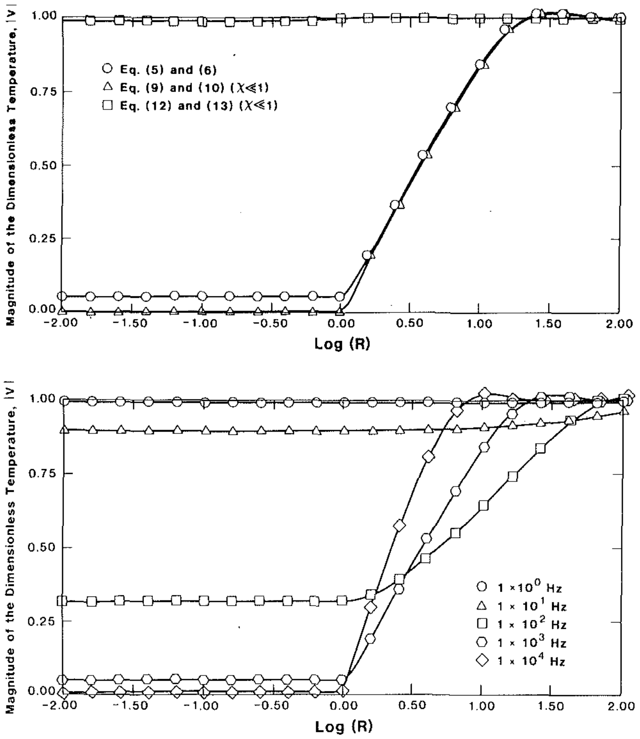

Fig. 3 Magnitude of the dimensionless temperature versus log distance for a 6 μm Kevlar fiber in air: (*a*) results of various models at 1000 Hz; results using the exact equations (5) and (6) at several frequencies

$$V_I(R) = \frac{T_I(R)}{T_{EI}} \tag{14}$$

The magnitude of the temperature variations within the fiber, $|V_I|$, is plotted for various values of Z_I in Fig. 2 for the case $\chi >> 1$. The size of the boundary layers is largest in the low frequency case. For low values of Z_I (metals, low frequencies, smaller diameters), the magnitude of the temperature oscillations across the fiber is fairly constant, thus the fiber acts as a fairly good heat sink. On the other hand, for high values of Z_I (plastics, high frequencies, larger diameters), the thermal wave does not penetrate very far into the fiber and only the heat capacity of the outer surface of the fiber exchanges heat with the gas. At higher frequencies the small thermal boundary layer limits the fiber's ability to exchange heat with the gas. For all cases where $\chi >> 1$, the magnitude of the external temperature oscillation does not vary with R.

General Case. In the most general case where $.1 < \chi < 10$, equations (5) and (6) must be used. These solutions can be portrayed graphically as functions of dimensionless variables by substituting equations (11*b*) and (14) into equations (5) and (6). Figures showing the general temperature distributions are not included; because of the infinite number of possible values for Z_E, Z_I, R, K_E, K_I, and χ only a couple of specific cases are presented. The magnitude of the temperature oscillations obtained from equations (5) and (6), modified to include the results of equations (7), (11*b*), and (14), are represented as

$$V_E(R) = \left[1 + \frac{1}{\chi - 1}\,\frac{K_o(RZ_E j^{1/2})}{K_o(Z_E j^{1/2})}\right] \tag{15a}$$

and

$$V_I(R) = \left[\frac{\chi}{\chi - 1}\,\frac{J_o(RZ_E j^{3/2})}{J_o(Z_I j^{3/2})}\right] \tag{15b}$$

The influence of the internal and external dimensionless frequencies and the ratio of external to internal thermal conductivities on the value of χ is shown in Table 1. Increasing the value of Z_E increases the value of χ, while increasing the values of Z_I or K_E/K_I decreases the value χ. Thus either increasing Z_E/Z_I or increasing K_E/K_I reduces χ and the influence of the fiber on the temperature oscillation in the fluid approaches the first of the two special cases discussed above. In the limiting regions (Z_E, $Z_I \rightarrow 0$ or Z_E, $Z_I \rightarrow \infty$) the individual values of Z_I and Z_E control the characteristics of the functions because Z_I and Z_E are found along in the Bessel functions of χ.

In Fig. 3 the magnitude of the temperature distribution in and around a Kevlar fiber of $a = 6.0$ micrometers immersed in air is presented. In Fig. 3(*a*) the temperature distribution at 1000 Hz was computed using the general expressions that were given in equations (5) and (6). In addition, the errors generated by using the approximate equations (9) and (10) (where it is assumed that $\chi << 1$) and equations (12) and (13) (where it is assumed that $\chi >> 1$) are shown as the differences between the appropriate curves. In Fig. 3(*b*) the magnitude of the temperature distribution is shown for pressure oscillations of 1, 10, 100, 1000, and 10,000 Hz. These figures show that the frequency of the pressure oscillations has a large effect on the temperature distribution. The amplitude of the oscillating temperature varies with the dimensionless radius and thus neither of the limiting solutions should be used. In the case of large fibers, the extent of the thermal boundary layers is over a rather small dimensionless distance and the appropriate equations (10) and (12) may be used.

Phase Speed

Application of the preceding theory to the propagation of

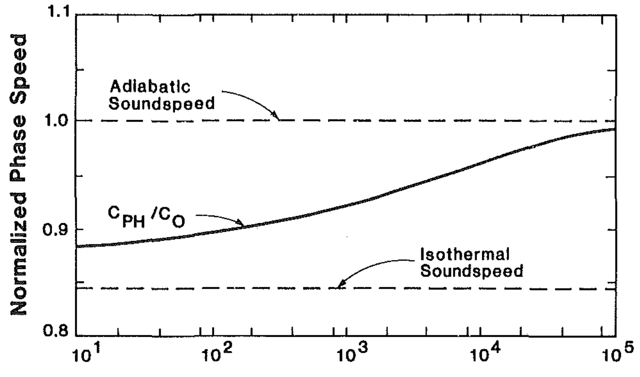

Fig. 4 Magnitude of the dimensionless phase speed in Kevlar of 98 percent porosity ($a = 6^* \mu 10^{-6}$m)

See Errata Sheet (p. 54)

sound in a fibrous material is treated in detail elsewhere [11]. An example of the application is made here with fibers of constant temperature.

Equation (9) may be integrated over a cylindrical surface around a single fiber from the fiber surface to a characteristic distance r_o that accounts for the packing of fibers in a porous material. The integration yields

$$T_E(R_o) = \frac{2P_a}{(r_o{}^2 - a^2)\rho_{oE}C_{pE}} \int_a^{r_o} \left[1 - \frac{K_o(Z_E R j^{1/2})}{K_o(Z_E j^{1/2})}\right] rdr \tag{16}$$

$$= \frac{P_a}{\rho_E C_{pE}} \left\{1 - \frac{2[K_1(Z_E R_o j^{1/2}) - R_o K_1(Z_E j^{1/2})]}{Z_E(R_o{}^2 - 1^2)K_o(Z_E j^{1/2})}\right\}$$

where we let

$$T_E(R_o) = \frac{P_a}{\rho_{oE}C_{pE}} F(R_o) \tag{17}$$

Equation (17) is made nondimensional by multiplying both sides by $C_{pE}/C_o{}^2$ and

$$T_E'(R_o) = P_a' \, F(R_o) \tag{18}$$

The dimensionless, linearized equation of state is

$$\gamma P' - \rho' = (\gamma - 1)T' \tag{19}$$

Since the wavelength of the sound is large relative to the integration radius. $T_e{}'$ of equation (18) may be substituted for T' in equation (19) to obtain

$$P_a'[\gamma - (\gamma - 1)F(R_o)] = \rho' \tag{20}$$

Equation (20) is then rewritten in terms of dimensionless phase speed to yield

$$\frac{P_a'}{\rho'} = \left(\frac{c_{ph}}{c_o}\right)^2 = [\gamma - (\gamma - 1)F(R_o)]^{-1} \tag{21}$$

where C_{ph} is the phase speed of sound in a fibrous porous material.

Figure 4 shows the change of the phase speed of sound in a specific porous material with respect to frequency. At high frequencies, the thermal boundary layers are small and the phase speed approaches the adiabatic sound speed. On the other hand, at low frequencies, the thermal boundary layers are large and the phase speed approaches the isothermal sound speed. Although the effects of the heat transfer on the phase speed are moderate, a certain error is to be expected when approximating the phase speed in fibers materials as either isothermal or adiabatic.

Conclusions

The temperature distribution within and around an infinitly long cylindrical fiber, which is immersed in a fluid that has a sinusoidally varying pressure wave, has been determined. Both the fiber and the gas are assumed to have finite heat capacities and thermal conductivities. The pressure fluctuation is assumed to be uniform in a region much larger than the fiber radius. It was found that the thermal properties of the fiber affect the temperature distribution in a large region of the gas. This varying temperature distribution influences the phase speed of sound propagating in gases which contain heat absorbing materials. Although this particular concept is not new, an expression to determine the influence of the thermal properties of cylindrical fibers on the temperature distribution in the gas is new. The expressions resulting from this paper are used in [11] to obtain the phase speed of sound traveling in a fibrous material.

Acknowledgments

The authors gratefully acknowledge the support of the Acoustics Division of NASA-Lewis Research center and the Office of Naval Research. In addition, the authors thank Dr. D. T. Blackstock, for his early editorial comments, and Mr. Chi-Hwey Chang for programming the solutions of the equations.

References

1 Jakob, M., *Heat Transfer*, Vol. I, ch. 14, John Wiley and Sons, N.Y., 1949.

2 Gröber, "Temperatureverlauf und Wärmeströmungen in Periodish Erwärmten Körpern" (Temperature Variation and Heat Flow in Periodically Heated Bodies), Forschungsarbeiten auf dem Gebrite des Ingenieurwesens, No. 300, 1928, pp. 3-13.

3 Carslaw, H. S., and Jaeger, J. C., *Conduction of Heat in Solids* (2d ed.), Oxford at the Clarendon Press, D. R. Hillman and Sons, Ltd., 1959, p. 193.

4 Lamb, H., *Hydrodynamics* (6th ed.), Dover Pub., N.Y., 1945, p. 622.

5 Kirchhoff, G., "Über den Einfluss der Wärmleitung in einem Gase auf die Schallbewegung," *Annalen der Physik und Chemie (Poggendorf's Annalen)*, Vol. 134, 1868, pp. 177-193.

6 Lord Rayleigh, J. W. S., *Theory of Sound* (2d ed.), Vol. II, The Macmillan Company, New York, 1945.

7 Monkewitz, P. A., "The Linearized Treatment of General Forced Gas Osillations in Tubes," *J. Fluid Mech.*, Vol. 91, 1979, pp. 357-397.

8 Rott, N., "Thermally Driven Acoustic Oscillations. Part II: Stability Limit for Helium," *J. Appl. Math. and Phys.* (ZAMP), Vol. 24, 1973, pp. 54-72.

9 Bertelsen, A., Svordal, A., and Tjøtta, S., "Nonlinear Streaming Effects Associated With Oscillating Cylinders," *J. Fluid Mech.*, Vol. 59, 1973, pp. 493-511.

10 Henry, P. S. H., "The Tube Effect in Sound Velocity Measurements," *Proc. of the Phys. Soc. of Lond,*, Vol. 43, 1931, pp. 340-363.

11 Kuntz, H., and Perrreira, N. D., "Sound Speed in Fibrous Materials," to be submitted to *J. Acoust. Soc. Am.*

12 Pfriem, H., "Zur Thermischer Dämpfung in Kugelsymmetrisch Schwingenden Gasblasen," *Akustische Zeitschrift*, Vol. 5, 1940, pp. 101-212.

13 Devin, C., Jr., "Survey of Thermal, Radiation, and Viscous Damping of Pulsating Air Bubbles in Water," *J. Acoust. Soc. Am.*, Vol. 31, 1959, pp. 1654-1657.

Transient Response of a Coupled Conduction and Convection Heat Transfer Problem

J. C. Friedly
Department of Chemical Engineering,
University of Rochester,
Rochester, N.Y. 14627

Systems of dynamic models involving the coupling of both conduction and convection offer significant theoretical challenges because of the interaction between parabolic and hyperbolic types of responses. Recent results of state space theory for coupled partial differential equation models are applied to conjugate heat transfer problems in an attempt to understand this interaction. Definition of a matrix of Green's functions for such problems permits the transient responses to be resolved directly in terms of the operators' spectral properties when they can be obtained. Application of the theory to a simple conjugate heat transfer problem is worked out in detail. The model consists of the transient energy storage or retrieval in a stationary, single dimensioned matrix through which an energy transport fluid flows. Even though the partial differential operator is nonself-adjoint, it is shown how its spectral properties can be obtained and used in the general solution. Computations are presented on the effect of parameters on the spectral properties and the nature of the solution. Comparison is made with several readily solvable limiting cases of the equations.

Introduction

The interaction between conduction and convection is a common occurrence in a variety of heat transfer problems. Although there has been a considerable amount of work on specific problems of this nature, the general theory does not always encompass the coupling of the fundamentally different types of behavior expected from parabolic and hyperbolic equations, giving rise to nonself-adjoint operators. Linear pure conduction problems can be handled by theory that is well developed. The several approaches leading to solutions of these problems rest on the basis of a self-adjoint partial differential operator. It is well known that a complete orthogonal set of eigenfunctions exists for self-adjoint operators and the spectral properties can be established. Pure convection problems can generally be handled by characteristic methods. However, real problems are virtually never purely convective, with the presence of conduction never totally absent.

Problems involving coupling between conduction and convection have been solved by a variety of means. Some problems can be treated by singular perturbation about the pure convection solution, as in boundary layers or shock fronts, but there are others with such strong coupling that this approach is not feasible. These problems are most frequently solved by numerical means, by difference methods, finite elements, or weighted residual methods. Any such method ultimately reduces the problem from infinite dimensions to finite dimensions, and in effect computes the spectral properties of the reduced operator so obtained. This then is taken as an adequate approximation to the original problem.

The objective of this work is to investigate the fundamental nature of the linear transient heat transfer problem involving coupled conduction and convection. Using recent results in the state space theory of coupled partial differential equations, the conjugate heat transfer problem will be formally solved in terms of a matrix of Green's functions. Then if the eigenvalues and eigenfunctions of the operator and its adjoint can be obtained, the solution can be written formally. Although theory does not guarantee that such a spectral expansion exists for nonself-adjoint operators, it will be shown for a simple heat transfer problem how to obtain the eigenvalues and eigenfunctions. Numerical calculations will then be presented to investigate how these spectral properties depend on the degree of coupling between the conduction and the convection part of the problem.

Theory

We will restrict our attention to the unsteady state behavior of a system of coupled partial differential equations on a finite spatial domain of one dimension. Analogous results can be obtained for higher spatial dimensions, but the principles are more cumbersome to demonstrate. Coupled conduction and convection problems can be described in general by a set of equations of the form [1]

$$\frac{\partial \mathbf{x}}{\partial t} = \frac{\partial}{\partial z}\left(\mathbf{D}\frac{\partial \mathbf{x}}{\partial z}\right) - \mathbf{V}\frac{\partial \mathbf{x}}{\partial z} + \mathbf{A}\mathbf{x} + \mathbf{f} = L\mathbf{x} + \mathbf{f} \qquad (1)$$

The vector of dependent variables $\mathbf{x}$ depends on the matrix of thermal diffusivities $\mathbf{D}$, the matrix of flow velocities $\mathbf{V}$, and the matrix of coefficients $\mathbf{A}$, all of which can be dependent on the spatial position and time, but it will be assumed that they do not depend on the dependent variables or their derivatives. $\mathbf{f}$ is a nonhomogeneous disturbance that may appear in the equation. To accompany equation (1), there will be a set of initial conditions and a set of boundary conditions.

It is well known that the concept of Green's functions [2, 3] can be extended to coupled sets of partial differential equations of the parabolic type. It has been shown recently [4] that the same approach can be used to obtain the solution for problems involving coupling between parabolic and hyperbolic partial differential equations. The Green's function reduces identically to a form of the Riemann function when the operator L is purely hyperbolic. However, the operator L is in general nonself-adjoint for coupled parabolic and hyperbolic problems. In spite of some results for classes of nonself-adjoint operators [5–7], it is still necessary to assume the existence of a complete spectrum of eigenvalues and eigenfunctions to obtain a useful spectral decomposition of the Green's function for these problems.

Assuming that a Green's function for equation (1) exists, the solution for $\mathbf{x}(z',t')$ can be written in the form

---

Contributed by the Heat Transfer Division for publication in the JOURNAL OF HEAT TRANSFER. *Manuscript received by the Heat Transfer Division August 11, 1983.* Paper No. 83-HT-98.

$$\mathbf{x}(z',t') = \int_0^1 \mathbf{G}(z,0;\; z',t')\cdot\mathbf{x}(z,0)dz - \int_0^{t'} \phi(\mathbf{G},\mathbf{x})\Big|_{z=0} dt$$

$$+ \int_0^{t'} \phi(\mathbf{G},\mathbf{x})\Big|_{z=1} dt + \int_0^{t'}\int_0^1 \mathbf{G}\cdot\mathbf{f}dzdt \qquad (2)$$

or in terms of the spectral decomposition of $\mathbf{G}$ with eigenfunctions $\mathbf{e}_j$ of L and $\mathbf{e}_j^*$ of the adjoint operator L^*

$$\mathbf{x}(z',t') = \sum_j e^{\lambda_j t'} \frac{c_j \mathbf{e}_j(z')}{<\mathbf{e}_j^*,\mathbf{e}_j>} \qquad (3)$$

where

$$c_j = <\mathbf{e}_j^*(z),\mathbf{x}(z,0)> + \int_0^{t'} e^{-\lambda_j t}\Big[\phi(\mathbf{e}_j^*,\mathbf{x})\Big|_{z=1}$$

$$-\phi(\mathbf{e}_j^*,\mathbf{x})\Big|_{z=0}\Big]dt + \int_0^{t'} e^{-\lambda_j t} <\mathbf{e}_j^*,\mathbf{f}> dt$$

The equations that define the Green's matrix $\mathbf{G}$, the adjoint operator L^*, and the boundary function ϕ for this problem are included in Appendix A.

Since the operator L is in general nonself-adjoint for coupled parabolic and hyperbolic problems, we will not be able to prove that the solution form of equations (2) or (3) will apply for all conjugate heat transfer problems. Experience suggests that it will be useful in most cases, reducing the problem simply to that of establishing the eigenvalues of L, the corresponding eigenfunctions, and adjoint eigenfunctions. When this can be done, the formal results in equation (3) will apply.

Example

The purpose of this work is to investigate the behavior of conjugate heat transfer problems when the coupling between the conduction and the convection components is significant. The preceding analysis indicates that if a complete spectrum of eigenvalues exists for the partial differential operator L, it is sufficient to see how the coupling affects these spectral properties. Therefore, a specific example of a simple conjugate heat transfer problem will be used to show how the eigenvalues and eigenfunctions can in fact be obtained and how they are affected by the parameters which govern the coupling.

The example chosen for detailed study consists of a one-dimensional matrix of conductive solid that exchanges energy with a fluid flowing past it. The solid temperature is of course described by the parabolic heat conduction equation, but it is coupled with the fluid energy balance. It is assumed that the fluid is nonconducting in the direction of flow, so that its temperature is described by a single hyperbolic equation (when uncoupled from the solid). In dimensionless variables the system is therefore modeled by the coupled equations

$$\begin{aligned}\frac{\partial x_1}{\partial t} &= \frac{\partial^2 x_1}{\partial z^2} + h_1(x_2 - x_1)\\ \frac{\partial x_2}{\partial t} &= -v\frac{\partial x_2}{\partial z} + h_2(x_1 - x_2)\end{aligned} \qquad (4)$$

with no flux boundary conditions for the solid ends and a fixed inlet fluid temperature

$$\begin{aligned}\frac{\partial x_1}{\partial z} &= 0 \quad \text{at } z=0 \text{ and } z=1\\ x_2 &= x_{2_i} \quad \text{at } z=0\\ x_1 = x_{1_0}&,\quad x_2 = x_{2_0} \quad \text{at } t=0\end{aligned} \qquad (5)$$

In these equations the x_i's represent temperatures of the solid and fluid. t is the time made dimensionless by the thermal diffusion time. z is the length made dimensionless by the contact length. v represents the fluid velocity relative to the characteristic velocity of thermal diffusion. The h's are the dimensionless heat transfer coefficients, proportional to the overall heat transfer coefficient but divided by the thermal capacitance of the corresponding phase. The parameters v, h_1, and h_2 will be assumed constant.

Before the exact solution to these equations is investigated, it is instructive to consider several limiting cases which can be solved with relative ease. These solutions are all given in Appendix B. When one or both of the heat transfer coefficients is zero, the two equations are partially decoupled. The well-known eigenfunctions of the parabolic equation alone are $\cos h\sqrt{\lambda_j + h_1}\; z$ with eigenvalues $\lambda_j + h_1 = -j^2\pi^2 = 0, -\pi^2, -4\pi^2 \ldots$. The solution of the hyperbolic equation alone does not possess its own eigenfunction expansion but instead is written in terms of the delay inherent in the hyperbolic equation solution, for example when h_1, x_{2_i}, $x_{2_0} = 0$, $x_2 = \int_0^z e^{(h_2/v)(z_1 - z)}(h_2/v)\quad x_1(z_1, t-(z-z_1)/v)dz_1$. Of course, if $h_2 \neq 0$ the solution for x_2 will contain the eigenvalues of the parabolic equation through the integral of x_1.

Limiting cases are obtained both when the fluid velocity (relative to the diffusion time) is very large and when it is zero.

Nomenclature

$\mathbf{A}$ = matrix of coefficients in equation (1)
a_k = function of s defined in equation (6)
c_j = coefficient in eigenfunction expansion
$\mathbf{D}$ = matrix of thermal diffusivities
d_k = function of s defined in equation (6)
$\mathbf{E}$ = function of z and s in transformed solution equation (6)
$\mathbf{e}_j$ = eigenfunction
$\mathbf{f}$ = nonhomogeneous term in equation (1)
$\mathbf{G}$ = matrix of Green's functions
g = characteristic equation defined in equation (7)
h = heat transfer coefficients in equation (4)
$\mathbf{I}$ = identity matrix
L = linear partial differential operator
m_k = roots of a cubic equation defined for equation (6)
s = Laplace transform parameter
t = time
V = linear space of vector valued functions
$\mathbf{V}$ = matrix of velocities
$\mathbf{v}$ = an element of vector space
v = fluid velocity in equation (4)
$\mathbf{x}$ = state variable vector
z = spatial position
β_j = coefficients in partial fraction expansion
δ = delta function
λ_j = eigenvalue
ϕ = potential function defined in equation (A3)
Ω = state transition operator

Subscripts

0 = initial condition
i = inlet condition

Superscripts

$*$ = adjoint
$'$ = specific point at which solution is to be obtained
$\hat{}$ = Laplace transformed variable

Special Symbols

$<,>$ = inner product

When the fluid velocity is infinitely large the fluid temperature physically should be constant at the inlet value. Then the result for the solid temperature will be analogous to the case above when h_2 is zero. When the fluid velocity is zero, the solid is coupled with another stagant medium through which no conduction occurs. This problem has exactly the same eigenfunctions $\cos j\pi z$ as the $h_2 = 0$ case above, but with somewhat more complicated expressions for the eigenvalues as is shown in Appendix B.

The important results to be aware of from these limiting cases is that when the conduction problem is uncoupled from the convection problem the solution possesses eigenvalues of the form of $-h_1$, $-h-\pi^2$, $-h_1-4\pi^2$, etc. On the other hand, the hyperbolic solution does not have eigenvalues in the forms presented, but can be represented in closed form, albeit integral or discontinuous, solutions.

The spectral properties of the exact linear operator can be obtained in a number of ways. Laplace transforms are convenient for this purpose and will be used here. Assuming that the inlet fluid temperature is zero and that we are looking for the solution to the problem with spatially uniform nonzero initial conditions, equation (4) can be transformed and solved in the form

$$\hat{\mathbf{x}}(z,s) = \frac{[h_2 x_{1_0} + (s+h_1)x_{2_0}]\mathbf{E}(z,s)}{sh_2(s+h_1+h_2)g(s)} \tag{6}$$

where

$$\mathbf{E}(z,s) = \left(\begin{array}{c} (s+h_2)x_{1_0} + h_1 x_{2_0} \\ \hline h_2 x_{1_0} + (s+h_1)x_{2_0} \\ 1 \end{array}\right) g(s)h_2$$

$$+ \sum_{k=1}^{3} \begin{pmatrix} a_k(s) \\ h_2 \end{pmatrix} (-1)^k d_k(s) e^{m_k(s)z}$$

and where $a_k(s) = vm_k + s + h_2$, $d_k(s) = a_l a_n m_l m_n (e^{m_n} - e^{m_l})$ for $l,n \neq k$ and $n > l$, and the m_k's are the roots of the cubic equation

$$vm_k^3 + (s+h_2)m_k^2 - (s+h_1)m_k + h_1 h_2 - (s+h_1)(s+h_2) = 0$$

The characteristic denominator of equation (6) is given simply by

$$g(s) = d_1 - d_2 + d_3 \tag{7}$$

It is recognized that if all singularities of equation (6) are obtained and are distinct, a partial fraction expansion can be written and inverted term by term to obtain the time domain solution of the form

$$\mathbf{x} = \sum_j \beta_j e^{\lambda_j t} \tag{8}$$

where β_j are the residues at the singularities λ_j. Comparing equation (8) with the solution equation (3) suggests that the eigenfunction expansion has been achieved. As should be expected the singularities of equation (6) are the eigenvalues of the operator L with its boundary conditions. It can be shown that neither $s=0$ nor $s+h_1+h_2=0$ are singularities of equation (6) (provided h_1, $h_2 \neq 0$), so the eigenvalues are given by the roots of equation (7), $g(\lambda_j) = 0$. (The special case when two of the m's are identical is a root of equation (7), but also of the numerator of equation (6). It too will not be considered as an eigenvalue.) Furthermore, the eigenfunctions of L are given to within an arbitrary constant factor by inspection

$$e_j = \sum_{k=1}^{3} \begin{pmatrix} a_k(\lambda_j) \\ h_2 \end{pmatrix} (-1)^k d_k(\lambda_j) e^{m_k(\lambda_j)z} \tag{9}$$

These are of course independent of the values of the initial condition disturbances. The eigenfunctions of the adjoint operator can be obtained in much the same manner. They can be written in virtually the same form as equation (9)

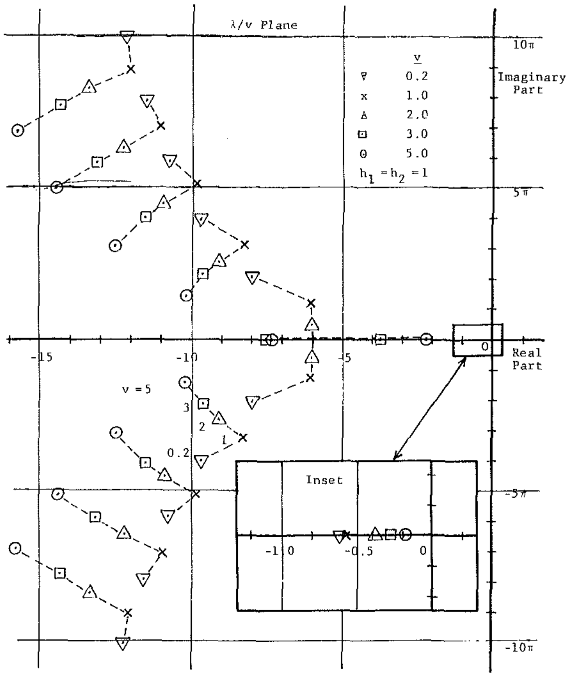

Fig. 1 Root locus for varying velocity v (λ/v plane)

$$e_j^* = \sum_{k=1}^{3} \begin{pmatrix} a_k(\lambda_j) \\ h_1 \end{pmatrix} (-1)^k d_k(\lambda_j) e^{m_k(\lambda_j)z} \tag{10}$$

Results

The eigenvalues of the partial differential operator L for the conjugate heat transfer problem of equations (4) and (5) have been computed numerically. Since the operator is nonself-adjoint, there is no assurance that the roots of g in equation (7) will be real or infinite in number. Therefore, an asymptotic analysis was performed first to discover what form should be expected for the large eigenvalues. Careful expansion of the expressions entering the characteristic equations shows that the solutions for the m's approach the following form as s gets large

$$\begin{aligned} m_1 &\rightarrow -\frac{s+h_2}{v} + 0(1/s) \\ m_{2,3} &\rightarrow \pm(s+h_1)^{1/2} + 0(1/s^{1/2}) \end{aligned} \tag{11}$$

It can be noted that the limiting forms of the arguments of the exponentials in the transfer functions correspond to those normally obtained for hyperbolic systems of equations (m_1) and to those normal for parabolic systems ($m_{2,3}$) [2]. Using these limiting forms in the characteristic equation (7) and solving for the leading order terms for the real and for the imaginary parts of the characteristic large roots yields the form

$$\lambda_j \rightarrow -\sqrt{j\pi v}\, v + ij\pi v \quad \text{as } j \rightarrow \infty \tag{12}$$

This shows that there are an infinite number of discrete large roots and that they are always complex conjugates. The frequency increases in intervals of πv. The real parts are always negative as must be the case for inherently stable systems and their values tend to get closer and closer together as $j \rightarrow \infty$. This is in distinct contrast to the behavior of the eigenvalues of the uncoupled parabolic system in the limiting cases considered above. There the roots are always real and become increasingly separated as $j \rightarrow \infty$. The asymptotic form suggests that as long as there is any degree of coupling between the conductive and convective parts of the system, the

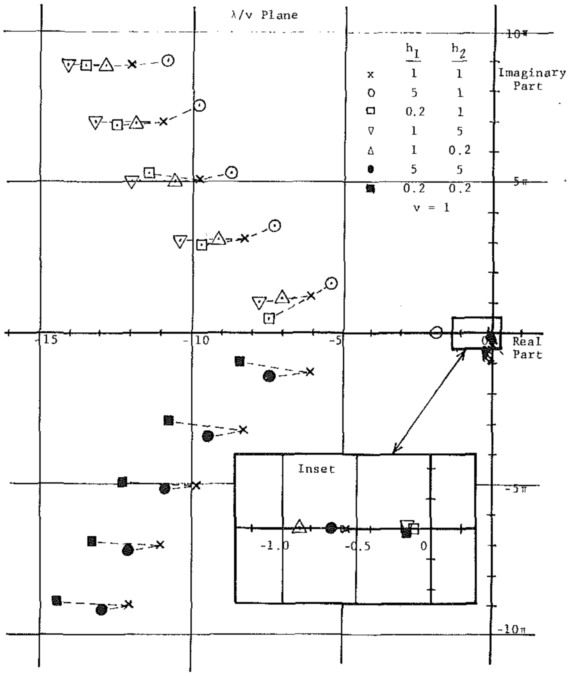

Fig. 2 Root locus for varying heat transfer parameters, h_1 and h_2 (λ/v plane)

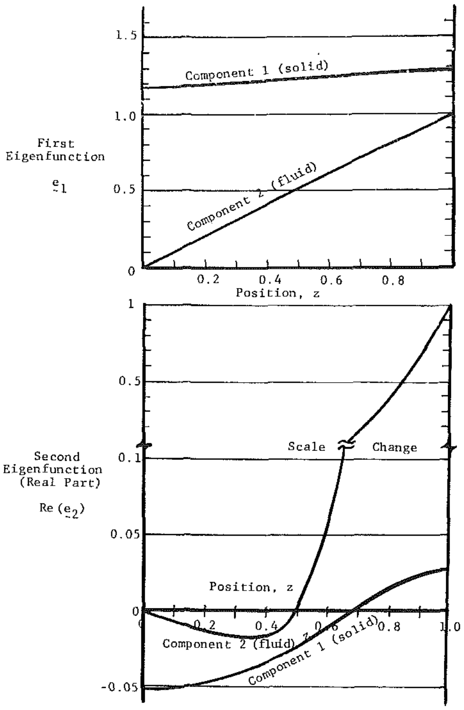

Fig. 3 Eigenfunctions corresponding to the first two eigenvalues when $v=1, h_1=1, h_2=1$

large eigenvalues will not have the character expected from a purely parabolic problem.

The most important roots in determining the dynamic response of any system are not the largest ones but those with the most positive real parts. These can only be obtained by numerical computation for this problem. Since we can anticipate that there will be some complex conjugate roots from the asymptotic analysis, careful numerical search procedures are required to find all possible roots. The Nyquist stability criterion was adapted for this purpose here. For any function of a complex variable $g(s)$, if s is permitted to encircle a region of the complex plane, the mapping of $g(s)$ can be used to determine the difference in the number of roots and singularities of $g(s)$ falling within that region simply by counting the number of times the mapping $g(s)$ encircles the origin. The characteristic function in equation (7) has no singularities so its mapping indicates its roots alone. The procedure used was then to select a real part for s and increase the imaginary part to an asymptotically large value. The mapping of $g(s)$ would then indicate whether there were any roots to the right of that set of s's in the complex plane. A new, more negative real part was then selected and the mapping repeated until an additional root or pair of roots was indicated. It is then relatively easy to iterate to find the exact value of the root, when the $g(s)$ mapping exactly intersects the origin.

Values of the eigenvalues of the partial differential operator L, or roots of equation (7), computed in this way are presented in a root locus plot in Fig. 1. The crosses indicate values of roots computed at specific values of the relative velocity parameter v. Both heat transfer coefficient parameters h_1, h_2 have been taken as unity. The dotted lines are used to indicate the directions of the root locus, not the precise values at intermediate values of v. Both the real and the imaginary axes have been normalized by v as suggested by the asymptotic form of the roots in equation (12). Only the first 11 roots are presented, the remainder being complex conjugate pairs that appear to approach the limiting form in equation (12).

The root locus in Fig. 1 shows that when the velocity is large there are three real roots that tend to dominate the behavior. There is one real root close to the origin and the next two approach $-h_1-\pi^2$ and $-h_1-4\pi^2$. These latter two are clearly associated with those for the purely parabolic limiting case discussed above. The dominant real root occurs for all values of the parameters investigated and appears to be due to the coupling between the conduction and the convection. The higher roots (more negative real parts) are all complex conjugate pairs which tend to approach the limiting form equation (12) fairly rapidly. They occur at intervals of about $j\pi$ in their frequencies and at decreasing intervals in their real parts. Computations for all parameters have never revealed any further real roots to the left of the first appearing pair of complex roots. As the velocity decreases the complex roots tend to move away from the real axis. The two large real roots move together, coalesce and form a pair of complex roots which also move away from the real axis. By about $v=2$ then the parabolic character of the problem has given way to predominately hyperbolic character.

The effect of the heat transfer parameters h_1, h_2 is much less dramatic than that for v. Figure 2 shows the eigenvalues computed for all combinations of h's $=0.2$, 1, and 5, with $v=1$. Again the dotted lines indicate the direction of the root locus, not the precise intermediate values. The effect of varying the h's separately is shown only on the complex eigenvalues above the real axis. The effect of varying the h's simultaneously is shown only below the real axis. In each case the conjugate eigenvalue would of course vary the same way. It is clear from Fig. 2 that the heat transfer parameters in this range do not change the character of the eigenvalues. Decreasing either h from unity tends to make the real parts of the eigenvalues larger in magnitude. Increasing the h's tends to have opposing effects, h_2 making the real part larger. Judging from the result when both h's are increased simultaneously, h_2 tends to have the stronger effect. The dominant real roots varies with the values of the h's but not as directly as would be expected from the uncoupled limiting cases. As should be expected, as h_1 decreases the first pair of complex roots tends to approach the real axis. For sufficiently low h_1 they will coalesce and split into two real roots showing a parabolic character to the coupled problem.

The expression for the eigenfunctions in equation (9) is complex enough so that it is not easy to anticipate the shape of the eigenfunctions. Figure 3 shows the computed eigenfunctions corresponding to the first two eigenvalues when all of parameters are unity. The eigenfunctions have been normalized by setting the maximum value of the second (fluid) component to unity. The first eigenfunction, corresponding to the dominant real root, is quite simple in form. For all practical purposes, the first (solid) component is flat and the second component is linear. The second eigenfunction is of course complex, since the corresponding eigenvalue is complex. Therefore only the real part is shown as the dotted curves in Fig. 3. Both components appear as skewed sinusoids in spatial position. The fluid component is very much more strongly skewed towards the downstream end. Additional computations have shown similar behavior for the successive eigenfunctions, with both the spatial frequency and the skewness tending to increase in succession.

Conclusions

Linear transient conjugate heat transfer problems offer the complications of having nonself-adjoint operators and interaction between parabolic and hyperbolic character in their response. Nevertheless, they can be solved by a straightforward extension of the Green's function approach. Although available theory does not guarantee existence of a spectral decomposition of the Green's function, and thus the solution, the standard formulas apply when it does exist. Therefore there is a significant incentive to obtain the spectral properties of conjugate operators for example problems even when the completeness of the spectrum can not be guaranteed.

The elementary problem of conductive heat transfer in a solid matrix exchanging energy with a convecting fluid has been considered as an example. It is shown how the eigenfunctions of the partial differential operator, as well as of the adjoint operator, can be obtained in a relatively straightforward manner using Laplace transforms. The resulting expressions have terms with the character of hyperbolic problems and terms with parabolic character. The Nyquist stability criterion can be readily adapted to permit computation of the eigenvalues of the system operator directly from the Laplace transform solution. It has been shown that there are an infinite number of eigenvalues for the coupled problem and that the large ones are complex conjugate pairs. The character of the large eigenvalues is definitely dominated by the convection part of the system.

Numerical calculations of the dominate eigenvalues show that the fluid velocity tends to be the controlling parameter in the character of the response. Large values of the fluid velocity give dominant eigenvalues very much like those for a parabolic problem. On the other hand, for moderate and small values of v, the character is very much different, presumably dictated by the convection. Only the dominant eigenvalue remains real for the values of the parameters considered, and this eigenvalue is believed to result from the coupling rather than the parabolic character of the problem. Aside from the dominant eigenvalue, the convenient properties of real, well separated eigenvalues characteristic of parabolic systems no longer prevail. Instead the spectrum consists of complex conjugate pairs of eigenvalues whose real parts tend to become closer together the larger in magnitude they become. The fact that there tend to be a rather larger number of eigenvalues with real parts differing no more than by a factor of about two from the first ones suggests that the convergence of the series in the spectral decomposition of the solution will tend to be rather slow even for larger times. This is the type of behavior to be expected for hyperbolic problems with discontinuities in their solutions, but not altogether expected for this coupled problem. Based on this result, one would expect that methods indirectly approximating a relatively small number of the dominant eigenvalues, such as weighted residual methods, would tend not to be the most effective under these conditions. However, since the dominant eigenvalue is real in all cases considered, and, except for rather small values of v, it tends to be well separated from the remainder of the eigenvalues, a one term approximation of the result may be feasible in many cases. Transients in the deviation away from a final steady state profile are then expected to approach very quickly the shape of the dominant eigenfunction for the problem, which appears to have a very elementary profile.

References

1 Friedly, J. C., *Dynamic Behavior of Processes*, Prentice-Hall, Englewood Cliffs, N. J., 1972.

2 Courant, R., and Hilbert, D., *Methods of Mathematical Physics*, Vol. II, Wiley-Interscience, N.Y., 1962.

3 Kreysig, E., *Introductory Functional Analysis With Applications*, Wiley, N.Y., 1978.

4 Friedly, J. C., "Contributions to a State Space Theory for Linear Partial Differential Equation Models," *Mathematical Modelling in Science and Technology*, edited by X. Avula et al., Pergamon Press, Oxford, 1984, pp. 71-81.

5 Gohberg, I. C., and Krein, M. G., "Introduction to the Theory of Linear Nonself-adjoint Operators," *Translations of Mathematical Monographs*, Vol. 18, American Mathematical Society, Providence, R.I., 1969.

6 Ramkrishna, D., and Amundson, N. R., "Boundary Value Problems in Transport With Mixed and Oblique Derivative Boundary Conditions, Steady State and Transient Solutions," *Chemical Engineering Science*, Vol. 35, 1980, pp. 577-587.

7 Ramkrishna, D., and Amundson, N. R., "Boundary Value Problems in Transport With Mixed and Oblique Derivative Boundary Conditions: I Formulation of Equivalent Integral Equations and II Reduction to First Order Systems," *Chemical Engineering Science*, Vol. 34, 1979, pp. 301-308, 309-318.

APPENDIX A

Definitions of Green's Matrix

The Green's function matrix in equation (2) is defined to satisfy

$$-\frac{\partial \mathbf{G}}{\partial t} = L^*\mathbf{G} + \delta(z-z')\delta(t-t')\mathbf{I} \tag{A1}$$

with boundary conditions at $z=0$ and 1 and a final condition at $t=t'$

$$\phi(\mathbf{G},\mathbf{v}) = \mathbf{G}\cdot\mathbf{D}\frac{\partial \mathbf{v}}{\partial \mathbf{z}} - \mathbf{D}^T\frac{\partial \mathbf{G}}{\partial z}\cdot\mathbf{v} - \mathbf{G}\cdot\mathbf{V}\mathbf{v} = 0$$

$$\mathbf{G}(z,t';z',t') = \mathbf{0}$$

L^* is the operator adjoint to L defined such that the scalar $\mathbf{v}^*\cdot L\mathbf{v} - L^*\mathbf{v}^*\cdot\mathbf{v}$ yields a divergence of a vector in z,t space having ϕ as its z-component. $\mathbf{v}$ is any vector of V the linear function space consisting of all functions satisfying the homogeneous boundary conditions of the same form that apply for equation (1). The adjoint vector space V^* will consist of all functions satisfying the homogeneous boundary conditions $\phi(\mathbf{v}^*,\mathbf{v}) = 0$ at $z=0$ and 1.

If the inner product takes the common form for Cartesian coordinates $<\mathbf{v}^*,\mathbf{v}> = \int_0^1 \mathbf{v}^*\cdot\mathbf{v}\,dz$, the adjoint operator for L of equation (1) becomes

$$L^*\mathbf{v}^* = \frac{\partial}{\partial z}\left(\mathbf{D}^T\frac{\partial \mathbf{v}}{\partial z}\right) + \frac{\partial(\mathbf{V}^T\mathbf{v}^*)}{\partial z} + \mathbf{A}^T\mathbf{v}^* \tag{A2}$$

and the corresponding boundary conditions defining the space on which L^* is defined become at both $z=0$ and 1

$$\phi(\mathbf{v}^*,\mathbf{v}) = \mathbf{v}^*\cdot\mathbf{D}\frac{\partial \mathbf{v}}{\partial z} - \mathbf{D}^T\frac{\partial \mathbf{v}^*}{\partial z}\cdot\mathbf{v} - \mathbf{v}^*\cdot\mathbf{V}\mathbf{v} = 0 \tag{A3}$$

It can be shown [4] that the boundary conditions equation (A3) represent the correct number and are otherwise consistent with the partial derivatives in equation (A1), even when there are coupled parabolic and hyperbolic equations.

APPENDIX B

Solutions for Limiting Cases of Example Problem

The several limiting cases of the example model equation (4) and (5) can be solved exactly. These limiting cases can then be used for comparison with the more generally applicable results presented above. Only sufficient detail of the solution will be presented here to show the form of the solution and obtain the exact values of the eigenvalues that apply. In each case it will be assumed that the inlet fluid temperature is zero and that the initial conditions are both general functions of position.

Case 1: $v \rightarrow \infty$. In this case the solution for x_2 becomes simply that of its inlet value, $x_2 = x_{2_i} = 0$. The solution for x_1 can be obtained by Laplace transforms. The transformed solution takes the form

$$\hat{x}_1 = \frac{\int_0^1 x_{1_0} \cosh\alpha(1-z_1)\cosh\alpha z_1 dz_1 - \int_0^z x_{1_0} \sinh\alpha(z-z_1)\sinh\alpha dz_1}{\alpha \sinh\alpha} \tag{B1}$$

where $\alpha = \sqrt{s+h_1}$, which can be expanded in partial fractions quite readily, since the roots of the denominator can be written $s+h_1 = -j^2\pi^2$ for all nonnegative j. The partial fraction expansion takes the form

$$\hat{x}_1 = \sum_{j=0}^{\infty} \frac{\beta_j}{s+h_1+j^2\pi^2} \tag{B2}$$

where the coefficients $\beta_j = \int_0^1 x_{1_0} \cos j\pi(1-z_1)\cos j\pi z dz_1$. Equation (B2) can be inverted term by term to obtain the form shown in equation (8). The eigenvalues of this limiting case are $\lambda_j = -h_1 - j^2\pi^2 = -h_1, -h_1 - \pi^2, \ldots.$

Case 2: $v = 0$. In this case the transformed temperatures are related by the algebraic relation

$$\hat{x}_2 = \frac{h_2\hat{x}_1 + x_{2_0}}{s+h_2} \tag{B3}$$

Eliminating $\hat{x}_2$ then yields a solution for $\hat{x}_1$ of the same form as in equation (B1) if x_{1_0} and $s+h_1$ in equation (B1) are everywhere replaced by $x_{1_0} + h_1 x_{2_0}/(s+h_2)$ and $s(1+h_1/(s+h_2))$, respectively. The resulting expression can be shown to be finite as $s \rightarrow -h_2$ so the singularities of the transfer function for $\hat{x}_2$ are given by

$$\lambda_j = -\frac{h_1+h_2+j^2\pi^2}{2} \pm \sqrt{\left(\frac{h_1+h_2+j^2\pi^2}{2}\right)^2 - j^2\pi^2 h_2} = 0, -h_1-h_2, -\frac{h_1+h_2+\pi^2}{2} \pm \sqrt{\frac{(h_1+h_2+\pi^2)^2}{2} - \pi^2 h_2}, \ldots \tag{B4}$$

The eigenvalue $\lambda = 0$ results in this limiting case because without a flowing fluid ($v=0$) there is no mechanism to remove the energy and reduce the temperatures to zero. The second eigenvalue is the analog of the first one in Case 1. The eigenvalues in equation (B4) apply for the solution for x_1. Because of equation (B3) these eigenvalues as well as the additional one $\lambda = -h_2$ apply for x_2.

Case 3: $h_1 = 0$. The solution for x_1 is the same as in Case 1, but with $h_1 = 0$. Therefore, the eigenvalues will be $\lambda_j = -j^2\pi^2 = 0, -\pi^2, -4\pi^2$. The solution for x_2 can be written in terms of an integral of the x_1 solution with shifted argument

$$x_2 = \int_0^z e^{\frac{h_2}{v}(z_1 - z)} \left[\frac{h_2}{v} x_1\left(z_1, t - \frac{z-z_1}{v}\right) + \frac{x_{2_0}(z_1)}{v} \delta\left(t - \frac{z-z_1}{v}\right) \right] dz_1 \tag{B5}$$

Therefore, the same eigenvalues will enter the solution for x_2, but in addition the characteristic behavior of hyperbolic equations with shifted arguments and discontinuous solutions appears as well. This behavior does not possess a normal spectral decomposition.

Case 4: $h_2 = 0$. x_2 can be solved explicitly in the form

$$x_2 = \begin{cases} x_{2_0}(z - vt) & , \; z - vt \geq 0 \\ 0 & , \; z - vt < 0 \end{cases} \tag{B6}$$

Coupling this into the equation for x_1 gives a solution exactly like that in Case 1 but with x_2 a known function of both time (transformed) and position in equation (B1). Again the eigenvalues for x_1 are of the form $\lambda_j = -h_1 - j^2\pi^2$ and do not appear in the solution for x_2.

J. O. Ilegbusi

D. B. Spalding
Mem. ASME

Imperial College of Science
and Technology,
London SW7, England

An Improved Version of the *k*-*W* Model of Turbulence

Introduction

In 1968 one of the present authors (DBS) devised a two-equation turbulence model [1] of which the major calculated quantities were k, the turbulence energy, and W, a measure of the vorticity fluctuations. This model was shown in [2] and [3] to yield predictions of two-dimensional turbulent flows that were in tolerable agreement with experimental data.

A similar model was independently proposed by Saffman [4] in 1970. This model, however, differed in the formulation of the productive terms in the transport equations for k and W. Saffman took the production term in the k equation as being proportional to the product of k and the absolute rate of strain, while Spalding used the sum of the products of the local Reynolds stress and the appropriate mean velocity gradient. The production term of the W equations of Saffman was thus proportional to the product of W and the absolute value of the velocity gradient, while Spalding used a term proportional to the product of W/k and the production term in the k equation. Saffman's [4] model was subsequently revised in line with that of Spalding [1] by Wilcox and co-workers [5-7]: and their revisions, as it happens, brought the production term into line with that of [1].

The model of Spalding [1] nevertheless possessed the defect (shared incidently with the k-kl model [8, 9, 10] of requiring a modification of one of its constants for near-wall flows.

This defect was regarded at the time (1970) as sufficient reason for allowing the k-W model (and the k-kl one for that matter) to be overshadowed by the k-ϵ model of Harlow and Nakayama [11], which was then being refined by Jones and Launder [12]: for the k-ϵ model appeared to require no such modification.

However, experience with the k-ϵ model has not been universally favorable; it has come to light that some early users of the k-W model who transferred to k-ϵ have preferred to return, in the interests of agreement with experimental data. An additional reason for returning is that it is vorticity fluctuations, resulting from the breakdown of vorticity sheets into less regular structures, which give turbulent flows their characteristic properties. Any turbulence model that concerns itself with the fluctuations directly can draw more direct support from experimental observations, and from intuition, than can one involving less accessible concepts.

The New Term

The objectionable feature of the earlier version of the k-W model was its inclusion of a term $(k/W)^{1/2}y^{-1}$, which became very important when the distance y from a bounding wall was small. Recently, however, it was recognized by one of the present authors [13] that the gradient of the length scale would serve equally well to characterize the effect of the wall in causing strong eddy-sized variations, but that this would not require the distance from the wall to be evaluated. This suggestion has been investigated by the other author and reported on in a series of CFDU reports [14-16], the main features of which are brought together here.

The investigation concerned itself with flows that are precisely the same as, or very similar to, those used for testing the earlier version of the model in [2] and [3], namely, pipe flow [17], abrupt enlargement of pipe diameter [18], smooth flat plate [19, 20], plate with intense heat transfer [21], boundary layer with longitudinal pressure gradient [22], plate with intense mass transfer [23], plane free turbulent jet [24], plane turbulent mixing layer [25], and round turbulent jet [26].

A term proportional to the length-scale gradient has been employed earlier by Wilcox and co-workers [5, 6]. However, it is not clear from their papers whether it was introduced for the same reason: indeed the new term has been omitted from Wilcox's [7] recent work. In any case, the present authors have determined the constants appearing in the new term, and have demonstrated their appropriateness by comparison with a variety of flow situations.

One of the constants was derived directly from knowledge of the well-known logarithmic velocity profile, and the authors' first guess concerning the second proved to be satisfactory. Next, near-wall boundary conditions for the new model had to be prescribed. This was effected by devising formulae that fitted exactly some well-known experimental conditions, and varied smoothly in between. Third, the model had to be incorporated into a suitable computer program, with which tests could be made of the necessary grid-fineness requirements. Finally, predictions of distributions of velocity, temperature, shear stress, etc., were made by means of the computer program, for comparison with experimental data, and in some cases with k-ϵ predictions.

The main outcome was that agreement with experiment was at least as good as had been reported for any two-equation turbulence model.

Mathematical Formulation

Differential Equations. The turbulence energy k and the vorticity fluctations W are here supposed, as in the original publications, to be governed by conventional "transport" equations. Thus

$$\frac{Dk}{Dt} = \rho^{-1}\left[\operatorname{div}\left(\frac{\mu_t}{\sigma_k}\operatorname{grad} k\right) + S_k\right] \tag{1}$$

$$\frac{DW}{Dt} = \rho^{-1}\left[\operatorname{div}\left(\frac{\mu_t}{\sigma_w}\operatorname{grad} W\right) + S_W\right] \tag{2}$$

wherein the left-hand sides represent time-dependence and bulk-transport terms, and the right-hand sides represent firstly the turbulent-diffusion transport and secondly the "source" (i.e., creation and destruction) terms.

The details of the derivation and modeling of the foregoing equations have been published earlier [27] and will not be repeated here. However, the main features are as follows:

The source term for turbulence energy k is expressed as

$$S_k = G_k - C_D \rho k W^{1/2} \tag{3}$$

wherein the "generation" term on the right is expressed in Cartesian-tensor form through velocity gradients as

---

Contributed by the Heat Transfer Division for publication in the JOURNAL OF HEAT TRANSFER. Manuscript received by the Heat Transfer Division August 29, 1983. Paper No. 83-HT-27.

$$G_k = \mu_t \left(\frac{\partial u_i}{\partial x_j} + \frac{\partial u_j}{\partial x_i} \right) \frac{\partial u_i}{\partial x_j} \tag{4}$$

without any compressible-flow adjustment. The "turbulent viscosity" μ_t is related to k and W by

$$\mu_t = C_\mu \rho k W^{-1/2} \tag{5}$$

The source term for vorticity fluctuations W is expressed as

$$\begin{aligned} S_W = {} & k^{-1} W(C_3 G_k - C_2 \rho k W^{1/2}) \\ & + C_1 \mu_t (|\operatorname{grad} \Omega|)^2 \\ & - C_4 \rho W^{1/2} (|\operatorname{grad} k W^{-1})^{1/2}|)^{C_5} \end{aligned} \tag{6}$$

wherein Ω is the major component of the vorticity of the mean motion.

Of the three terms on the right of this equation, the first parallels S_k, the second is a comparatively small term, and the last is the novelty on which the new k-W model is founded.

Differential equations (1) and (2), along with the auxiliary term and constant-defining equations, constitute the turbulence model that is investigated here.

The Values of the Constants. Nine constants appear in the foregoing equation, namely, σ_k, σ_W, C_D, C_μ, C_1, C_2, C_3, C_4, C_5. Of these, the first seven have been established by earlier work and have been adopted without change. They appear in Table 1.

Of the two remaining constants, C_5 was guessed to equal 2.0, implying that the new term is proportional to the square of the gradient of the turbulence length scale and therefore independent of its sign. The constant C_4 could then be determined by reference to the as-yet-unused von Karman constant κ (taken as 0.435) in the "logarithmic law of the wall," through the relation (Spalding [2])

$$\begin{aligned} (4\sigma_W{}^{-1} + C_1 C_D - C_\mu C_4)\kappa^2 - C_2 C_\mu C_D{}^{-1/2} & \\ + C_3 C_D{}^{1/2} C_\mu{}^{-1/2} = 0 & \end{aligned} \tag{7}$$

From this relation, C_4 is deduced to equal 2.97; and this value is employed in the computations that are to be described.

Boundary Conditions at a Wall.

The Problem. As explained in the original k-W model publication [1], to use the true wall conditions as boundary conditions for k and W would necessitate the solution of the equations through the thin semilaminar region immediately adjacent to the walls. This would be expensive even if a low-Reynolds-number version of the model were employed. Consequently, the practice adopted in the present work is the same as that in the old one: boundary conditions are inserted at the computational grid point lying *nearest* to the wall, not that *at* the wall.

Table 1 Previously established turbulence-model constants

Constant	σ_k	σ_W	C_D	C_μ	C_1	C_2	C_3
Value	1.00	1.00	0.09	1.00	3.50	0.17	1.04

For simple flows along smooth walls, it can be presumed that: (*a*) the velocity profile obeys the logarithmic law; (*b*) the turbulence energy is proportional to the wall shear stress; and (*c*) the length scale is proportional to the distance from the wall.

These three presumptions entail the relations

$$(a) \quad \frac{u}{\sqrt{\tau/\rho}} = \frac{1}{\kappa} \ln\left[E\left(\frac{y\sqrt{\tau\rho}}{\mu}\right)\right] \tag{8}$$

from which the wall shear stress τ can be determined from the velocity u

$$(b) \quad k = (C_\mu C_D)^{-1/2}(\tau/\rho) \tag{9}$$

which enables the energy k to be deduced from τ, and

$$(c) \quad W = \kappa^{-2} C_D{}^{-1/2} \kappa/y^2 \tag{10}$$

which serves as the third boundary condition, viz, that for W.

More elaborate expressions are needed when the wall is not smooth, when heat and mass transfer are effective, when pressure gradients are present, and when turbulence diffusion from the bulk of the fluid is more important than that generated by wall shear. Some of these will be described below.

Heat Transfer. Heat-transfer predictions have been made and compared with experimental data. The smooth-wall, boundary-condition formula employed is [16]

$$(T - T_W) = (\dot{q}/c)\,(u/\sqrt{\tau/\rho} + P)/\sqrt{\tau\rho} \tag{11}$$

wherein the function P depends upon the laminar Prandtl number in accordance with the empirical function

$$P = 9.0\left(\frac{\sigma_h}{0.9} - 1\right)\left(\frac{0.9}{\sigma_h}\right)^{1/4} \tag{12}$$

When the heat-transfer rate is intense, as is true in some of the

Nomenclature

A = Van Driest constant ($\equiv 26.0$)
B = constant in the grid-expansion formula (equation (15))
C_f = skin-friction coefficient
C = specific heat at constant pressure
d_0 = small pipe diameter
D = large pipe diameter
E = constant in near-wall description of velocity profile ($\simeq 9.0$)
h = nozzle-slot height
H_{12} = boundary-layer shape factor
k = turbulence kinetic energy
l = length scale of turbulence fluctuation ($\equiv k^{1/2}/W^{1/2}$)
m = mass transfer rate per unit area through plate surface
Nu = Nusselt number
P = Jayatillaka function
q = heat transfer rate per unit area
r = radial coordinate
$r_{1/2}$ = jet half-radius
Re = Reynolds number
Re_0 = Reynolds number based on small pipe diameter
Re_x = Reynolds number based on distance from plate leading edge
R_2 = momentum thickness Reynolds number
St = Stanton number
T = temperature (K)
T_G = temperature of the main stream
T_W = temperature at the wall
U = axial velocity component
U_G = free stream velocity
U_0 = maximum velocity excess
U^* = friction velocity
V = cross-stream velocity component
W = time-mean square vorticity fluctuation
x = streamwise coordinate
y = cross-stream coordinate
y_P = distance of near-wall node P from wall
$y_{1/2}$ = jet half-width
δ = boundary layer thickness
δ_1 = displacement thickness
δ_2 = momentum thickness
κ = von Karman constant ($\equiv 0.435$)
ρ = density
Γ = exchange coefficient
τ = shear stress
σ = Prandtl number
μ = absolute viscosity
ν = kinematic viscosity
Ω = magnitude of vorticity
ϕ = scalar quantity

cases considered below, the density ρ and Prandtl number σ_h have been given values appropriate to the temperature at the near-wall grid point.

The Effect of Longitudinal Pressure Gradient. When pressure varies significantly in the direction of flow, the shear stress τ varies significantly between wall and the near-wall grid point. The value inserted on the right-hand sides of the above equations has therefore been calculated as a mean τ [28]. Thus

$$\tau=\tau_w+(y/2)\partial P/\partial x \tag{13}$$

wherein τ_w is the shear stress at the wall.

The Effect of Mass Transfer. The presence of mass transfer poses a similar problem, which is solved in a similar way. In this case the value of τ inserted into the right-hand sides of the equations is given by

$$\tau=\tau_w+mu\kappa\sqrt{\tau_w/\rho}/(u+\kappa\sqrt{\tau_w/\rho}) \tag{14}$$

For strong suction, the heat-transfer resistance of the near-wall region is without influence. To account for this, and to accord with physical realism, the practice adopted has been to take as the value of $(T-T_w)/q$ the *smaller* of that given by the preceding formulae, on the one-hand, and cm^{-1} on the other.

Turbulence Diffusion. When diffusion of turbulence from the main flow to the near-wall grid point outweighs the generation of turbulence there from shear effects, as happens in the vicinity of the "reattachment" of a separated flow, equation (9) gives too low a value of κ.

In such cases, the practice adopted has been that described in respect to the k-ϵ model in [29]. This has two aspects, namely: (*a*) the τ appearing on the right-hand sides of the boundary condition equation is replaced by $(C_\mu C_D)^{1/2}k\rho$; and (*b*) k itself is calculated from the balance of turbulence-energy generation, dissipation, diffusion, and convection in the computational cell surrounding the near-wall grid point. When diffusion of turbulence is unimportant, this practice produces the same results as would the direct use of equation (9).

Solution Procedure. The differential equations for k and W, together with those governing the velocity components u and v and the temperature T, have been solved by means of the PHOENICS computer program [30]. This embodies a finite-domain formulation of the equations, and a procedure for solving these, which both derive from [31], and are too well-known to require description here.

The version of PHOENICS adopted, it should be mentioned, was equipped with the k-ϵ turbulence model but not the k-W one. It was therefore necessary to make use of the facilities provided by PHOENICS for the attachment of user-generated coding sequences. These facilities proved to be satisfactory.

Finite-domain solutions of differential-equation systems are influenced by the number of grid nodes employed, unless this number is large enough for "grid-independent" solutions to have been obtained, and the only way to determine how large is this necessary number is to perform the calculation several times with differing numbers of grid nodes.

This practice has been adopted in the present work. Here it will be simply asserted that the solutions to be described below can all be regarded as grid-independent. The documentation of this assertion is contained in the Ph.D. thesis of one of the present authors [32].

Comparison With Experiment

Fully Developed Turbulent Pipe Flow. The fully developed turbulent flow in a smooth pipe of Laufer [17] is considered. The calculation assumes axial symmetry and is performed with 18 nonuniformly-spaced radial grid divisions and a forward-step size of 30 percent of the radius. Table 2 shows, respectively, the predicted values of the mean velocity, the ratio of shear stress to kinetic energy and the normalized kinetic energy at various radial positions for a Reynolds number of 5×10^5; also displayed are the experimental data of Laufer [17]. The agreements are generally satisfactory both near to and far from the wall.

The comparison is directly relevant to the novel feature of the new k-W model, for if the C_4-term were not correctly describing the W-source, good agreement would definitely not have been obtained.

Flow and Heat Transfer Downstream of a Pipe Expansion. The experimental situation considered is that of Zemanick and Dougall [18] for an air flow in a pipe with expansion ratio of 0.544. The computational task is to predict the heat-transfer-coefficient distribution. The calculation is started at the expansion and ended 12 diameters (of the larger pipe) downstream of it. Axial symmetry is assumed.

The entering fluid is assumed to have uniform axial velocity, turbulence intensity (3 percent), and enthalpy. W is deduced from the values of k and the distribution of μ_T for a fully developed pipe flow.

At the downstream boundary of the integration domain, the fluid is assumed to leave without a radial velocity component. The enthalpy at all walls is prescribed by way of constant heat flux. The step wall is always taken as adiabatic.

The calculation requires 22 × 22 nonuniformly spaced grids for sufficient accuracy. Most of the nodes are located at the high-shear regions at the pipe junction and near the wall. Figures 1 and 2 compare predictions with data for the 0.54 diameter ratio of Zemanick and Dougall [18].

The agreements are generally satisfactory, the measured locations and magnitudes of the maximum heat-transfer coefficients being approximately reproduced in the calculations. The variation of the maximum Nusselt number shown in Fig. 2 suggests that the predicted behavior exhibits a slightly smaller sensitivity to Reynolds number than does the measurement.

Table 2 Flow parameter distributions across a pipe at Re = 5.10^5 (data of Laufer [17])

$(R-r)/R$	U/U_G		$\tau/2\rho K$		$2K/U_*^2$	
	Measured	Computed	Measured	Computed	Measured	Computed
0						
0.1	0.77	0.78	0.13	0.135	7.54	7.52
0.2	0.84	0.845	0.145	0.145	6.08	6.00
0.3	0.89	0.895	0.15	0.15	5.15	5.15
0.4	0.92	0.92	0.146	0.145	4.46	4.46
0.5	0.94	0.95	0.144	0.138	3.79	3.81
0.6	0.97	0.97	0.135	0.127	3.16	3.25
0.7	0.985	0.986	0.118	0.112	2.70	2.75
0.8	0.997	0.997	0.087	0.086	2.32	2.40
0.9	1.00	1.00	0.053	0.055	2.10	2.16
1.0	1.00	1.00				

Smooth Flat Plate With Uniform Properties. Two flow situations are considered, namely, those of Klebanoff [19] and of Wieghardt as processed for the AFOSR-IFP Stanford conference by Coles and Hirst [20]. Both are for turbulent boundary layers on smooth flat plates exposed to uniform fluid streams. In contrast to the "elliptic" flow of the last section, those of the present and subsequent sections are "parabolic," by which is meant that influences travel in only one (downstream) direction.

The grid in each of the cases considered is made to expand with the boundary-layer growth so that the cross-stream width of the grid is proportional to $x^{0.8}$, where x is the longitudinal distance. The initial grid width is taken as 0.01 meter. Grid-independent solutions are obtained with 18 nonuniform, cross-stream grid points, a forward-step size of 30 percent of the grid width and five hydrodynamic iterations at each forward step.

Predictions are compared with the data of Klebanoff [19] in Table 3, which gives the normalized mean velocity, the kinetic energy of turbulence, and the shear stress against normalized distance from the wall. The boundary-layer thickness δ is here and elsewhere defined as the distance from the wall which the mean velocity attains is free-stream value.

Predictions of the local skin-friction coefficient C_f, of the boundary layer shape factor H_{12}, and of the momentum thickness δ_2 at various distances along the plate are compared with the data of Wieghardt [20] in Table 4.

The agreement in both cases is satisfactory, indeed probably within the margin of experimental error over most of the range.

Smooth Flat Plate With Intense Heat Transfer. The ability of the new k-W model to predict wall flows with heat transfer and nonuniform properties has been tested against the data for the cooled flat plate collected by Chi and Spalding [21], for which the absolute temperature ratios (mainstream to plate) ranged from 1.5 to 2.7. The expanding-grid system previously mentioned is again employed, with the width of the grid taken as proportional to $x^{0.8}$. Systematic grid refinement shows that 30 cross-stream grid nodes and a forward-step size of 10 percent of the grid width provide sufficient "grid independence."

Figure 3 compares the Stanton number with some of the data collected by Chi and Spalding [21], and with the overall best-fit correlation proposed by those authors. The maximum difference between the new predictions and the correlation is 7 percent. This may be regarded as satisfactory, in view of the scatter in the data.

Smooth Flat Plate With Longitudinal Pressure Gradient. Predictions have been made for the experiment of Bradshaw [22], in which a severe adverse pressure gradient was imposed. A forward-step size of 10 percent of the grid width is used, with 36 cross-stream intervals. The grid-expansion rate employed is deduced, from the measured velocity and boundary layer parameters δ_1, δ_2, and δ at different streamwise locations, to be proportional to $x^{0.9}$.

Table 5 shows typical predictions of shape factor, skin friction, and momentum thickness at various longitudinal distances x along the plate, while Table 6 presents profiles across the boundary layer at the fully developed region. Also shown in both tables are the data of Bradshaw [22].

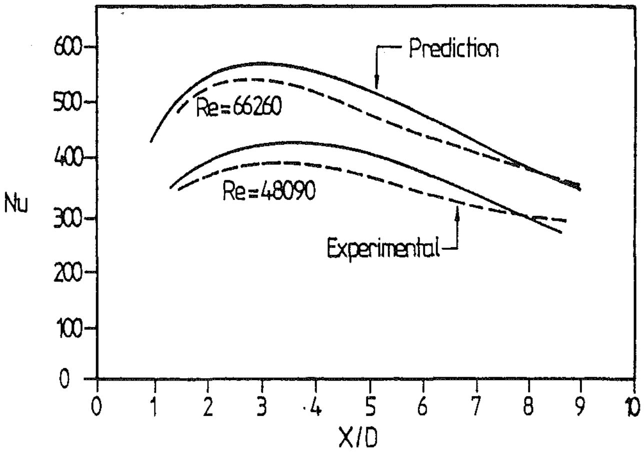

Fig. 1 Nusselt number distribution for $d_0/D = 0.54$ (pipe-expansion data of Zemanick and Dougall [18])

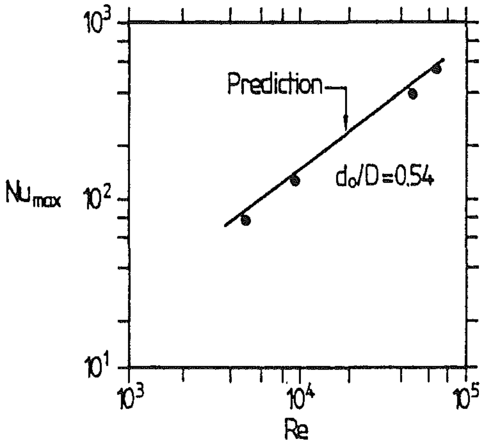

Fig. 2 Variation of maximum Nusselt number with Reynolds number: $d_0/D = 0.54$ (pipe-expansion data of Zemanick and Dougall [18])

Table 3 Comparisons of predicted and Klebanoff's [19] experimental values for the flat plate

y/δ	U/U_G		$10^3 \cdot k/U_G{}^2$		$10^3 \cdot \tau/\rho U_G{}^2$	
	Measured	Computed	Measured	Computed	Measured	Computed
0.2	0.77	0.78	4.4	4.25	1.32	1.30
0.4	0.86	0.87	3.4	3.2	1.05	1.01
0.6	0.93	0.93	2.25	2.24	0.70	0.67
0.8	0.98	0.98	1.0	1.0	0.31	0.33

Table 4 Comparison of predicted and Wieghardt's [19] experimental values for the flat plate

X(m)	H_{12}		$10^3 \cdot C_f$		$10^{-3} \cdot R_2$	
	Measured	Computed	Measured	Computed	Measured	Computed
1	1.4	1.35	3.1	3.1	4.2	4.2
2	1.38	1.33	2.75	2.75	7.5	7.5
3	1.32	1.30	2.6	2.6	0.5	10.5
4	1.30	1.28	2.45	2.5	13.5	13.5
5	1.28	1.28	2.4	2.45	15.5	15.5

The measure of agreement is considered satisfactory except for the turbulence energy profile in Table 6. There is no obvious reason for the latter discrepancy.

Smooth Flat Plate With Mass Transfer Through the Surface. Predictions have been made for the experimental situation of Moffat and Kays [23], which is for heat transfer from a flat plate having a porous surface through which air can be sucked from, or blown into, the boundary layer.

The calculation is started at the leading edge of the plate. There the profiles of turbulence energy and length scale (and hence of W) are calculated from the procedure employed by Ng and Spalding [9], who assumed a polynomial distribution of k. Uniform streamwise velocity, enthalpy, and pressure are specified at the free stream in correspondence with the measured values.

The grid employed has a forward-step size of 10 percent of the width, and 36 cross-stream grid nodes for blowing and 30 for suction. The relation for the growth of the grid width is

$$y_G = Bx^e \tag{15}$$

in which y_G is the vertical height of the free-stream grid line above the plate, x the longitudinal distance, and B and e are constants. Values of e of 0.8 and 1.2 are used for cases with suction and blowing, respectively.

Figure 4 shows the predicted and measured variation with the length Reynolds number of the Stanton number for the problem considered. The results show that agreement is satisfactory even at strong suction rates. The latter success is a result of the use of a sublayer resistance factor that ensures the asymptotic limit (St $\rightarrow \dot{m}/\rho_G U_G$) is approached for these cases. For strong blowing, the experimental Stanton number tends to zero; this behavior is quite adequately predicted, as shown in the figure.

Plane Jet. As a further test of universality, the new k-W model has been applied to a plane jet issuing into slow-moving surroundings [24]. The problem is to predict the rate of spread

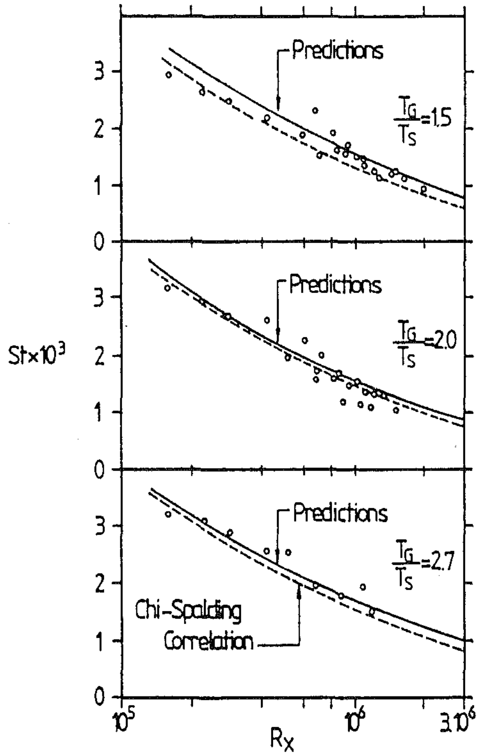

Fig. 3 Predicted and measured Stanton number with the length Reynolds number on a flat plate with intense heat transfer (data of Chi and Spalding [21])

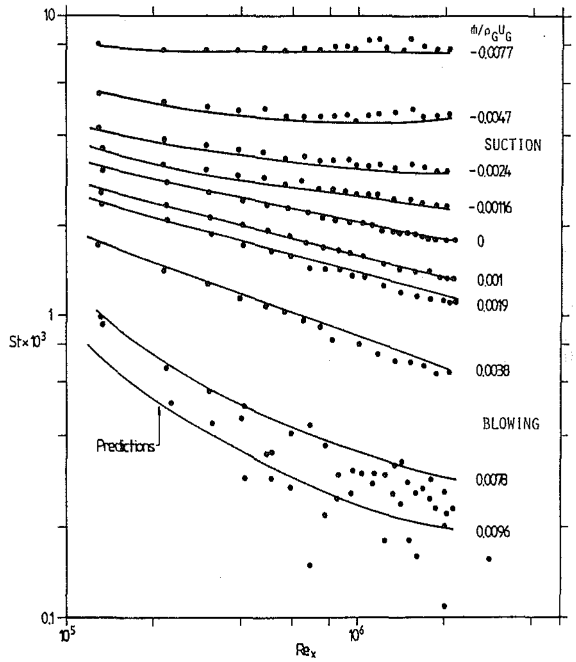

Fig. 4 Predicted and measured variation with the length Reynolds number of the Stanton number for heat transfer to a porous flat plate with low temperature ratio and various degrees of suction and blowing (data of Moffat and Kays [23])

Table 5 Longitudinal distributions of flow parameters for flow with longitudinal pressure gradient (data of Bradshaw [22])

X(m)	H_{12}		$10^3 \cdot C_f$		$10^3 \cdot \delta_2$	
	Measured	Computed	Measured	Computed	Measured	Computed
0.58	1.65	1.65	1.42	1.42	5.0	5.0
1.19	1.59	1.58	1.38	1.40	10.54	11.3
1.65	1.56	1.54	1.39	1.42	13.6	15.0
2.10	1.57	1.55	1.32	1.34	17.6	18.2

Table 6 Flow-parameter distributions across a flow along a flat plate with longitudinal pressure gradient (data of Bradshaw [22])

y/δ	U/U_G		$10^3 \cdot k/U_G^2$		$10^3 \cdot \tau/\rho U_G^2$	
	Measured	Computed	Measured	Computed	Measured	Computed
0.2	0.60	0.63	10.3	9.70	2.45	2.5
0.4	0.73	0.75	12.3	10.2	3.2	3.25
0.6	0.85	0.86	10.5	8.8	2.75	2.97
0.8	0.94	0.95	5.0	4.8	1.25	1.38

of the jet and the similarity profiles of the velocity, turbulence energy, and shear stress.

Plane symmetry is assumed, so the calculation is performed only over one half of the jet. The inlet plane is located at the jet exit. There the outer boundary of the domain is located in the free stream at $y/h = 1$, where h is the height of the nozzle. The vertical height of the outer boundary, y_L, is made to change with downstream distance so that the flow domain covers only the region in which jet properties vary. The location of y_L is defined through

$$y_L = y_0 + fx \tag{16}$$

in which y_0 is the value of y_L at inlet, and f is the rate of spread of the outer boundary taken as 0.145. This value is deduced from the half-width spreading rate of the plane jet as presented by Rodi [33]. Thirty lateral grid nodes and a forward step-size of 10 percent of the grid width are used.

Figure 5 shows the predicted rate of jet spread, while Table 7 shows the normalized maximum shear stress and maximum turbulence kinetic energy at the self-similar region, compared with the measurements.

The predictions are in fair agreement with measurements except for the turbulence energy; the maximum predicted energy is some 7 percent above the measurements. However, the predicted and measured profile shapes are very similar.

Plane Mixing Layer. The new k-W model has been applied to a plane mixing-layer formed by a fluid emerging steadily from a rectangular-shaped nozzle into a reservoir of the same fluid at rest. The problem is to predict the rate of spread and the profiles of fluid variables across the layer.

The domain of calculation is made to cover essentially the mixing region. The inlet plane is placed near the nozzle exit where the inner and outer boundaries are located respectively in the fast- and slow-moving fluids.

The cross-stream width of the grid, y_L, is expanded with downstream distance x according to equation (16); the constant of proportionality f is taken as 0.33. A grid having 50 cross-stream nodes and a forward-step size of 1 percent of the grid width is employed. Most of the nodes are placed within the high-shear region where the velocity gradient is steep.

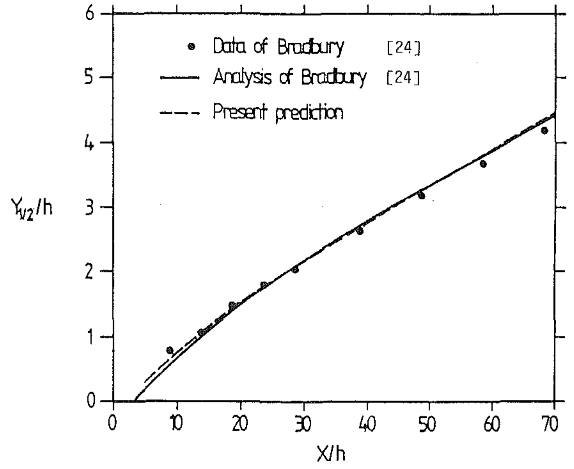

Fig. 5 Variation of plane-jet width (data of Bradbury [24])

At inlet, uniform turbulence intensity of 0.09 percent and length scale of 0.2 y_L are specified within the layer, while nearly-zero values of variables are prescribed in the stagnant fluid outside. An arbitrary velocity profile is specified within the mixing layer. At the free-stream boundaries, the imposed conditions are: constant pressure; zero k and W; and the velocities corresponding to the stream values.

In Table 8 are shown the predicted rate of spread; the maximum shear stress $\tau_{\max}$, and the maximum specific turbulence energy $k_{\max}$ for the fully developed plane mixing layer. Also shown are the experimental values representing averages of the data of Wygnanski and Fiedler [25]. The rate of spread is defined by $(y_{0.9} - y_{0.1})/x$, where $y_{0.9} - y_{0.1}$ represents the cross-stream distance between points, where the fluid velocity has values equal to 0.9 times and 0.1 times the velocity at the edge of the layer, and x is the distance from the virtual origin of the mixing layer. The shear stress and energy are normalized by reference to the square of the maximum velocity.

It can be seen that the predictions agree fairly well with the measured values. It should be noted that the ratio of $\tau_{\max}$ to $\rho k_{\max}$ is equal approximately to 0.3, i.e., to $C_D^{1/2}$.

Round Jet. The new k-W model has further been applied to a round jet. The details of the calculation parallel those of the plane jet. However, as is true of all other two-equation turbulence models, it has been found that one of of the "constants" of the turbulence model has to be changed to give realistic results. In the present case, C_3 has been changed to 1.42.

In Table 9 the predicted rate of spread, normalized maximum turbulence-energy, and shear stress are compared with the experimental data of Wygnanski and Fiedler [26] and of Rodi [33]. The latter set of data has been included for comparison because the latter author reported in a review that his measurements of turbulence energy and shear stress were more reliable than those of Wygnanski and Fiedler because of his more accurate method of analyzing the hot-wire signals.

The predicted turbulence energy is closer to the profile of Rodi. At the jet axis, however, it is still underpredicted by about 20 percent.

The predicted shear stress appears satisfactorily in agreement with the measured profile of Rodi, the maximum value occurring at $r/r_{1/2} \cong 0.77$.

Comparison With k-ϵ Predictions. Some results of predictions with the present model have been compared with those of the k-ϵ model. Typical of these are the predictions of

Table 7 Comparison of measured and computed relative maximum shear stress and turbulence energy across a plane jet. Data of Bradbury [23].

Quantity	$\tau_{\max}/\rho U_D^2$	$K_{\max}/U_D^2$
Measured	.024	.078
Computed	.024	.083

Table 8 The turbulent mixing layer

Quantity	Rate of spread $(y_{0.9}-y_{0.1})/x$	Relative maximum shear stress $\tau_{\max}/\rho U_{\max}^2$	Relative maximum specific energy $k_{\max}/U_{\max}^2$
Computed value	0.16	0.0109	0.0335
Experimental value	0.16	0.0091	0.034

Table 9 Comparison of measured and computed rate of spread, relative maximum kinetic energy, and shear stress across a round jet

Quantity	$dr_{1/2}dx$	$K_{\max}/U_D^2$	$\tau_{\max}/\rho U_D^2$
Measured Wygnanski & Fiedler [26]	.086	.101	.0165
Measured Rodi [33]	.086	.095	.0186
Computed	.088	.075	.0188

turbulent flow downstream of a backward-facing step reported in [34] by the present authors. The results with both models are also compared with the data of Kim et al. [35]. The main conclusions from the work are:

(*i*) The reverse flow is well simulated with the k-W model. The peak value is underpredicted by up to 40 percent with the k-ϵ model.

(*ii*) In the outer region of the separated flow, the results with both models are comparable.

(*iii*) The k-ϵ model generally predicts a slower recovery of the flow than the k-W model.

(*iv*) The pressure distribution results are comparable.

(*v*) The predicted locations of the peak shear stresses are 0.91 and 0.94 of the step height, respectively, for the k-ϵ and k-W models. The measured value is quoted as being 0.9 step height.

(*vi*) The maximum differences between predicted and measured peak shear stresses are -17 percent and $+21$ percent, respectively for the k-ϵ and k-W models.

(*vii*) The predicted shear-stress distributions across the duct show that the k-W results have more gradual return to the mainstream levels than the k-ϵ ones.

Conclusion

It has been demonstrated that the new version of the k-W model of turbulence can predict rather well a wide range of fluid-dynamic and heat-transfer phenomena. The one disadvantage from which its predecessor suffered (the near-wall modification of constants) has been successfully removed.

On present evidence the new k-W model can therefore be accepted once more as a candidate, if a two-equation turbulence model is required, not least because of the strong physical appeal of the vorticity-fluctuation idea.

Acknowledgments

One of the authors (JOI) acknowledges the financial support accorded to him by the Commonwealth Universities Commission during the performance of this work. Both authors wish to express their thanks to Mrs. C. Webb and Mrs. F. Oliver for the preparation of the successive typescripts.

References

1 Spalding, D. B., "The Prediction of Two-Dimensional, Steady, Turbulent Elliptic Flows," *International Seminar on Heat and Mass Transfer with Separated Regions*, Herceg Novi, Yugoslavia, September 1-13, 1969, reprinted in IC CFDU Report No. CFD/82/17.

2 Spalding, D. B., "A Two-Equation Model of Turbulence," VDI-Forsch Heft 549, 1972.

3 Gibson, M. M., and Spalding, D. B., "Two-Equation Model of Turbulence Applied to the Prediction of Heat and Mass Transfer in Wall Boundary Layers," ASME Paper No. 72-HT-15, 1972.

4 Saffman, P. G., "A Model of Inhomogeneous Turbulent Flow," *Proc. Royal Society*, London, Series A, Vol. 317, 1970, pp. 417-433.

5 Wilcox, D. C., and Traci, R. M., "A Complete Model of Turbulence," AIAA Paper No. 76-351, 1976.

6 Wilcox, D. C., and Rubesin, M. W., "Progress in Turbulence Modeling for Complex Flow Fields Including Effects of Compressibility," NASA Technical Paper 1517, 1980.

7 Wilcox, D. C., "A Complete Model of Turbulence Revisited," AIAA 22nd Aerospace Sciences Meeting, Reno, Nevada, Jan. 9-12, 1984.

8 Rodi, W., and Spalding D. B., "A Two-Parameter Model of Turbulence and Its Application to Free Jets," *Warme und Stoffubertragung*, Vol. 3, 1970, p. 85.

9 Ng, K. H., and Spalding, D. B., "Predictions of Two-Dimensional Boundary Layers on Smooth Walls With a Two-Equation Model of Turbulence," Imperial College, London, MED, Technical Note No. BL/TN/A/25, 1970.

10 Ng, K. H., and Spalding, D. B., "Some Applications of a Model of Turbulence to Boundary Layers Near Walls," *Phys. Fluids*, Vol. 15, 1972, p. 20.

11 Harlow, F. H., and Nakayama, P. I., "Turbulent Transport Equations," *Phys. Fluids*, Vol. 10, 1967, pp. 2323-32.

12 Jones, W. P., and Launder, B. E., "The Prediction of Laminarisation With A Two-Equation Model of Turbulence," *International Journal of Heat and Mass Transfer*, Vol. 15, 1972, p. 301.

13 Spalding, D. B., "A Modification to the k-W Model," CFDU, Imperial College, London, File Note, February 1982.

14 Ilegbusi, J. O., and Spalding, D. B., "Application of a New Version of the k-W Model of Turbulence to Equilibrium Boundary-Layer Flow Over a Flat Plate With (*i*) Intense Heat Transfer and (*ii*) Streamwise Adverse Pressure Gradients," CFDU, Imperial College, London, Report No. CFD/82/14, 1982.

15 Ilegbusi, J. O., and Spalding, D. B., "Application of a New Version of the k-W Model of Turbulence to Equilibrium Boundary Layer With Mass Transfer," CFDU, Imperial College, London, Report No. CFD/82/15, 1982.

16 Ilegbusi, J. O., and Spalding, D. B., "Prediction of Steady Turbulent Flow and Heat Transfer Downstream of a Circular-Pipe Expansion With a New k-W Model of Turbulence," CFDU, Imperial College, London, Report No. CFD/83/2, 1983.

17 Laufer, J., "The Structure of Turbulence in Fully Developed Pipe Flow," NACA, Report 1174, Washington, D.C., 1954.

18 Zemanick, P. P., and Dougall, R. S., "Local Heat Transfer Downstream of Abrupt Circular Channel Expansion," ASME JOURNAL OF HEAT TRANSFER, Vol. 92, 1970, p. 53.

19 Klebanoff, P. S., "Characteristics of Turbulence in a Boundary Layer With Zero Pressure Gradient," NACA Report 1247, Washington, D.C., 1954.

20 Coles, D., and Hirst, E. A., *Proceedings of the AFOSR-IFP Stanford Conference on Turbulent Boundary Layer Prediction—2: Compiled Data*, Dept. of Mech. Engg., Stanford University, 1969.

21 Chi, S. W., and Spalding, D. B., "Influence of Temperature Rate on Heat Transfer to a Flat Plate Through a Turbulent Boundary Layer in Air," *Proc. 3rd Int. Heat Transfer Conference*, Chicago, Vol. 2, AIChE, New York, 1966, pp. 41-49.

22 Bradshaw, P., "The Turbulence Structure of Equilibrium Boundary Layers," Nat. Phys. Lab. (NPL) Aero Report No. 1184, 1965.

23 Moffat, R. J., and Kays, W. M., "The Turbulent Boundary Layer on a Porous Plate: Experimental Heat Transfer with Uniform Blowing and Suction," *International Journal of Heat and Mass Transfer*, Vol. 11, 1968, pp. 1547-66.

24 Bradbury, L. J. S., "The Structure of Self-Preserving Turbulent Plane Jet," *Journal of Fluid Mechanics*, Vol. 23, pt. 1, 1965, pp. 31-64.

25 Wygnanski, I., and Fiedler, H., "The Two-Dimensional Mixing Region," *Journal of Fluid Mechanics*, Vol. 41, pt. 2, 1970, pp. 327-362.

26 Wygnanski, I., and Fiedler, H., "Some Measurements in the Self-Preserving Jet," *Journal of Fluid Mechanics*, Vol. 38, pt. 3, pp. 577-612.

27 Spalding, D. B., "Concentration Fluctuations in a Round Turbulent Free Jet," *Chemical Engineering Science*, Vol. 26, 1971, pp. 95-107.

28 Spalding, D. B., *GENMIX: A General Computer Program for Two-Dimensional Parabolic Phenomena*, Pergamon Press Ltd., Headington Hill Hall, Oxford, 1977.

29 Launder, B. E., and Spalding, D. B., "The Numerical Computation of Turbulent Flows," *Comp. Methods in Applied Mech. and Engg.*, Vol. 3, 1974, pp. 269-89.

30 Spalding, D. B., "A General-Purpose Computer Program for Multidimensional One- and Two-Phase Flow," Lehigh IMACS Conference, July 1981, *Mathematics and Computers in Simulation*, Vol. XIII, 1981, pp. 267-276.

31 Patankar, S. V., and Spalding, D. B., "A Calculation Procedure for Heat, Mass and Momentum Transfer in Three-Dimensional Parabolic Flows," *International Journal of Heat and Mass Transfer*, Vol. 15, 1972, pp. 1787-1806.

32 Ilegbusi, J. O., "A Revised Two-Equation Model of Turbulence," Ph.D. thesis, University of London, 1983.

33 Rodi, W., "The Prediction of Free Turbulent Boundary Layers by Use of a Two-Equation Model of Turbulence," Ph.D. thesis, University of London, 1972.

34 Ilegbusi, J. O., and Spalding, D. B., "Steady Turbulent Flow in a Backward-Facing Step," 4th Symposium on Turbulent Shear Flows, Karlsruhe, FRG, Sept. 12-14, 1983.

35 Kim, J., Kline, S. J., and Johnston, J. P., "Investigation of Separation and Reattachment of a Turbulent Shear Layer: Flow Over a Backward-Facing Step," Report MD-37, Department of Mechanical Engineering, Stanford University, 1978.

A. M. Gooray
Xerox Corporation,
Rochester, N.Y. 14644

C. B. Watkins
Mem. ASME

Win Aung
Fellow ASME
Department of Mechanical Engineering,
Howard University,
Washington, D.C. 20059

Turbulent Heat Transfer Computations for Rearward-Facing Steps and Sudden Pipe Expansions

Results of numerical calculations for heat transfer in turbulent recirculating flow over two-dimensional, rearward-facing steps and sudden pipe expansions are presented. The turbulence models used in the calculation are the standard $k-\epsilon$ model and the low-Reynolds number version of this model. The $k-\epsilon$ models have been improved to account for the effects of streamline curvature and pressure-strain (scalar) interactions including wall damping. A sequence of two computational passes is performed to obtain optimal results over the entire flow field. The presented results consist of computed distributions of heat transfer coefficents for several Reynolds numbers, emphasizing the low-to-moderate Reynolds number regime. The heat transfer results also include correlations of Nusselt numnber for both side and bottom walls. The computed heat transfer results and typical computed fluid dynamic results are compared with available experimental data.

Introduction

The presence of a recirculating wall layer greatly influences the process of energy transfer in separated flow beyond a rearward-facing step or sudden pipe expansion. It has been demonstrated experimentally [1, 2] that within the recirculating region the heat transfer coefficient is considerably larger than that of an attached flow. This increase in heat transfer, in principle, can be attributed to the increase in streamwise turbulent kinetic energy in the mixing layer.

Convective recirculating heat transfer flows have been recently reviewed by Aung and Watkins [3] and by Aung [4]. Reliable experimental data are essential for the development and testing of turbulence models used for the numerical prediction of recirculating heat transfer. However, such data are limited. Aung and Goldstein [2] reported what is apparently the only existing low-speed turbulent heat transfer data for the rearward-facing step. Mean temperature profiles and heat transfer coefficients are presented for the entire flow field. Other important work includes that of Seban et al. [1], who studied the heat transfer over the rearward-facing step for high-speed flows. For the pipe expansion, Zemanick and Dougall [5] reported rather complete turbulent heat transfer measurements for the entire flow field. Recently, Sparrow and O'Brien [6] presented heat transfer data for the heated side wall in a pipe expansion geometry. Unfortunately, none of these experimental studies contain measurements of the hydrodynamic flow field in conjunction with the heat transfer data.

Due to the scarcity of available data, correlations of experimental recirculating turbulent heat transfer data are very rare indeed. A noteworthy exception is the attempt of Lamb [7] to develop a correlation for the rearward-facing step in supersonic flow.

Only a handful of researchers have attempted modeling recirculating flows for the rearward-facing step or pipe expansion. In most of the recent work, the $k-\epsilon$ model was used [8, 9]. Oliver [10] studied heat tranfer over the rearward-facing step and compared his results with the experiments of Seban [1] for high-speed flows. His predictions overestimate the heat transfer data in the entire flow field, particularly in the reattachment region. Gooray et al. [11] applied the standard $k-\epsilon$ model in a partially successful attempt to replicate the heat transfer coefficients obtained experimentally by Aung and Goldstein [2]. Chieng and Launder [12] studied the pipe expansion geometry, by using both the standard $k-\epsilon$ model and the low-Reynolds number version of the model. They compared heat transfer coefficients with the data of Zemanick and Dougall [5] (The calculations presented in [12] have recently been revised and exhibit improved agreement [13].) More recently, Amano [14] extended the Chieng and Launder [13] near-wall procedure and reexamined the pipe expansion geometry. To obtain accurate results in both recirculatin and redevelopment regions, Gooray et al. [15] devised a two-pass procedure combining standard and low-Reynolds number $k-\epsilon$ models, and recently developed improvements for these basic models [16-18], which can be incorporated into the two-pass procedure. The standard model of [15] was "sensitized" to include the effects of streamline curvature in the recirculating region. The recent improvements sensitize both models to account for the effects of pressure-strain (scalar) interactions, including wall damping corrections. The resulting method is utilized for the calculations presented herein. The purpose of the present paper then, is to present the results obtained by applying the method to both rearward-facing steps and sudden pipe expansions, emphasizing the low to moderate Reynolds-number regime.

Computational Model

In the present paper only a brief outline of the mathematial model and computational procedures are given. Full details are given in other papers [16-18]. The usual time-independent mean momentum and energy equations for two-dimensional or axisymmetric turbulent flow written in terms of effective viscosity and effective thermal diffusivity [19] are used in the computations where the effective viscosity and diffusivity are taken as the sum of molecular and turbulent values as follows

$$\mu_{\text{eff}} = \mu + \mu_t;\ \mu_t \text{ is the turbulent viscosity} \qquad (1)$$

$$\Gamma_{\text{eff}} = \frac{\mu}{\mathrm{Pr}} + \frac{\mu_t}{\mathrm{Pr}_t};\ \mathrm{Pr}_t \text{ is the turbulent Prandtl number} \qquad (2)$$

A modified version of the $k-\epsilon$ viscosity approximation is used in the present study for calculation of the turbulent

---

Contributed by the Heat Transfer Division for publication in the JOURNAL OF HEAT TRANSFER. Manuscript received by the Heat Transfer Division April 11, 1983. Paper No. 83-HT-30.

quantities. The turbulent viscosity is computed from the relation

$$\mu_t = C_\mu \rho k^2/\epsilon \tag{3}$$

The transport of turbulent kinetic energy, k is expressed by [19]

$$\rho\frac{\partial}{\partial x}(uk) + \rho\frac{\partial}{\partial y}(vk) = \frac{1}{y^j}\left\{\frac{\partial}{\partial x}\left[y^j\left(\vdots\,\mu + \vdots\,\frac{\mu_t}{\sigma_k}\right)\frac{\partial k}{\partial x}\right]\right.$$
$$\left.+\frac{\partial}{\partial y}\left[y^j\left(\vdots\,\mu + \vdots\,\frac{\mu_t}{\sigma_k}\right)\frac{\partial k}{\partial y}\right]\right\} + \mu_t G - \rho\epsilon\,\vdots\, -2\mu\left(\frac{\partial k^{1/2}}{\partial y}\right)^2\vdots \tag{4}$$

The transport of the rate of dissipation of this energy, ϵ can similarly be expressed by [19]

$$\rho\frac{\partial}{\partial x}(u\epsilon) + \rho\frac{\partial}{\partial y}(v\epsilon) = \frac{1}{y^j}\left\{\frac{\partial}{\partial x}\left[y^j\left(\vdots\,\mu + \vdots\,\frac{\mu_t}{\sigma_\epsilon}\right)\frac{\partial \epsilon}{\partial x}\right]\right.$$
$$\left.+\frac{\partial}{\partial y}\left[y^j\left(\vdots\,\mu + \vdots\,\frac{\mu_t}{\sigma_\epsilon}\right)\frac{\partial \epsilon}{\partial y}\right]\right\} + \frac{\epsilon}{k}C_{\epsilon 1}\,\mu_t G$$
$$-C_{\epsilon 2}\rho\frac{\epsilon^2}{k}\,\vdots\, f_2\,\vdots\,\vdots\, +2\frac{\mu\,\mu_t}{\rho}\left(\frac{\partial^2 u}{\partial y^2}\right)^2\vdots \tag{5}$$

In the preceding equation, $j = 0$ applies to the rearward-facing step and $j = 1$ applies to the pipe expansion where

$$G \equiv 2\left[\left(\frac{\partial u}{\partial x}\right)^2 + \left(\frac{\partial v}{\partial y}\right)^2 + j\left(\frac{v}{y^j}\right)^2\right] + \left(\frac{\partial u}{\partial y} + \frac{\partial v}{\partial x}\right)^2 \tag{6}$$

The C and σ's are constants of the $k-\epsilon$ models used. All constants used in the present calculations are given in Table 1. It should be noted that the values for C_{s1} and C_{s2} differ from those most often used for thin shear calculations. The present values are those used in the duct flow computations of Launder and Ying [20]; these values gave better results than the conventional shear layer constants. The low-turbulent Reynolds number function f_2 is

$$f_2 = 1.0 - 0.222\exp[-R_t^2/36];\ R_t = \frac{\rho k^2}{\epsilon\mu} \tag{7}$$

In the generalized equations presented above, terms appearing within the broken lines are omitted when using the standard (high-Reynolds number) version of the model.

The basic improvements incorporated into the $k-\epsilon$ mode for the present calculations consist of functional relationships derived for the coefficients C_μ and Pr_t, usually assumed constant, through the use of algebraic stress closure relations. These improvements sensitize the turbulence model to the effects of streamline curvature as in the work of Leschziner and Rodi [21] and to pressure-strain (scalar) interactions, including wall damping. An explicit correction term for rotational strain in the equation was not found to be necessary. The lengthy mathematical details for obtaining the functions and the historical motivation for this approach are given by Gooray [16].

Table 1 Values of empirical coefficients used in turbulence model

Coefficients	Variable modeled	Value
C_μ	Turbulent viscosity	functionalized
σ_k	Turbulent kinetic energy	1.0
σ_ϵ $C_{\epsilon 1}$ $C_{\epsilon 2}$	Dissipation rate of turbulent energy	1.3 1.44 1.92
C_{s1} C_{s2} C_{s1w} C_{s2w}	Pressure strain effects	2.6 0.22 0.75 0.3
$C_{\theta 1}$ $C_{\theta 2}$ $C_{\theta 1w}$	Pressure scalar effects	3.0 0.33 0.5
C_w	Wall damping contributions	2.44

The derivation procedure first involves obtaining algebraic stress closure approximations for the Reynolds stress and scalar flux terms in streamline coordinates. Terms accounting for pressure-strain and pressure-scalar interaction, including the effects of wall damping are retained. The resulting set of algebraic equations is solved for the individual stress and scalar flux components to obtain relationships for these variables in terms of mean local rate of strain and mean temperature gradient, respectively. These relationships are then compared with the Boussinesq approximations for the Reynolds stresses and scalar fluxes to obtain new relationships for C_μ and Pr_t as functions of mean gradient and turbulent quantities.

The resulting functions, in streamline coordinates, where $dy/dx = \tan^{-1}(v/u)$ appropriate for the recirculation region are

Nomenclature

d = upstream pipe diameter
D = donwstream pipe diameter
H = step or expansion height
k = turbulent kinetic energy
n = coordinate normal to streamline
Nu = Nusselt number based on step height for back step and down-stream diameter for pipe expansion
P = production rate of turbulent kinetic energy
Pr = molecular Prandtl number
Pr_t = turbulent Prandtl number
R_c = radius of curvature for streamline
R_t = turbulent Reynolds number ($= k^2/\epsilon\nu$)
Re = Reynolds number based on mean inlet velocity and step height for back step or downstream pipe diameter for pipe expansion
r = in cylindrical coordinates, $y = r$
T = mean temperature
u = mean velocity in the streamwise or x-direction
U_0 = free-stream mean velocity
v = near velocity in the normal or y-direction
x = distance along the main flow direction (see Fig. 1)
x_R = reattachment distance
$\bar{x}$ = distance from reattachment ($= x - x_R$)
y = distance normal to x-direction (see Fig. 1)

Greek Symbols

Γ = molecular thermal diffusivity
Γ_{eff} = laminar plus turbulent thermal diffusivity
Γ_t = turbulent thermal diffusivity
δ_T = thermal boundary layer thickness
δ_u = momentum boundary layer thickness
ϵ = dissipation rate of turbulent energy
μ = molecular viscosity
μ_{eff} = laminar plus turbulent viscosity
μ_t = turbulent viscosity
ρ = density

Subscripts

H = value of quantity just upstream of step
s = value of quantity tangential to streamline
w = wall values
$\bar{x}$ = value of parameter based on distance measured from reattachment

$$C_{\mu} = -\frac{2}{3}\Lambda'\left(\Lambda\frac{P}{\epsilon} - 1\right)S_4 \tag{8}$$

$$\mathrm{Pr}_t = C_{\mu}\, S_{T1}/S_{T2} \tag{9}$$

where

$$S_{T1} = 1 + 2\left(\phi'_T\,\frac{k}{\epsilon}\right)^2 \frac{u_s}{R_c}\left(\frac{\partial u_s}{\partial n} + \frac{u_s}{R_c}\right) \tag{10}$$

$$S_{T2} = -\frac{2\phi_T}{\epsilon}\left\{C_{\mu}\frac{k^2}{\epsilon}\left(\frac{\partial u_s}{\partial n} - \frac{u_s}{R_c}\right)\left[\frac{u_s}{R_c}(2\Lambda' + \phi'_T) + \Lambda'' S_2\right] + \frac{1}{3}\epsilon\left(\Lambda'\,\frac{P}{\epsilon} - 1\right)\right] \tag{11}$$

$$S_4 = 1 + \frac{k^2}{\epsilon^2}\left[8\,\Lambda'^2\,\frac{u_s}{R_c}\,S_1 + 4\,\Lambda''\,S_2\left(3\,\Lambda'\,\frac{u_s}{R_c} + \Lambda''\,\frac{\partial u_s}{\partial n} + \Lambda''\,S_2\right)\right] \tag{12}$$

$$S_1 = \partial u_s/\partial n + u_s/R_c; \quad S_2 = \partial u_s/\partial n + 3\,u_s/R_c \tag{13}$$

In the foregoing relations the subscript s refers to the component tangential to a streamline, while the coordinate n is directed along the normal, and R_c is the radius of streamline curvature. Also the following definitions apply

$$P = \mu_t G/\rho \tag{14}$$

$$\phi_T = C_{\theta 1} + C_{\theta 1 w} f + \frac{1}{2}(P/\epsilon - 1) \tag{15}$$

$$\phi'_T = \phi_T(1 - C_{\theta 2}) \tag{16}$$

$$\Lambda' = (1 - C_{S2})/(P/\epsilon - 1 + C_{S1} - C_{S1w} f) \tag{17}$$

$$\Lambda'' = C_{S2w} f\,\Lambda'/(1 - C_{S2}) \tag{18}$$

The function $f(x,y)$ has been modeled so as to approach the proper asymptotic limit away from the corner region of Fig. 1. Acceptable results were obtained from a function of the form

$$f(x,y) = \frac{1}{C_w}\,\frac{k^{3/2}}{\epsilon}\left\{\left[\frac{1}{(D/2 - y)}\right]^{1/m} + \left[\frac{1}{x}\right]^{1/m}\right\}^m \tag{19}$$

Because this formula does not accurately simulate wall influences near the corner, a range of small integer values of m were investigated. The results of these test calculations were little disturbed by the choice of m, and therefore, a value of $m = 2$ was abritrarly chosen for subsequent calculations. In equation (19) the $1/x$ term is omitted for $y < d/2$. Again the constants used in the foregoing relations are given in Table 1. Equation (8) reduces to the more restrictive formulation of Leschziner and Rodi [21] if equilibrium of turbulence energy is assumed, $P/\epsilon = 1$, and if "wall damping" corrections in the pressure-strain terms are ignored. Derivation of equation (8) involves neglect of some terms.

As mentioned in the previous section, earlier work by the authors [15] pointed out that to obtain an optimum $k-\epsilon$ solution for heat transfer over the entire flow field a sequence of two calculations can be performed. In applying this method here, the first calculation consists of a single computational pass in which the reattachment point is estimated from a fully converged solution using the improved standard $k-\epsilon$ model. The standard wall functions are applied at wall surfaces.

After the reattachment point is estimated, the calculation is repeated once with the improved standard $k-\epsilon$ model employed upstream of the reattachment point, and the improved low-Reynolds number version of the model applied downstream of this point. The justifcation for this simple attempt at "zonal modeling" of the flow field is that the low-Reynolds number equations were initially developed and tested for a thin shear flow [19] and would, therefore, seem to be more applicable to the redeveloping region. In implementing this procedure during the second calculation, the low-Reynolds number terms in equations (4) and (5) are simply omitted upstream of reattachment. The calculation downstream of reattachment proceeds to the wall without use of wall functions.

In the present calculations the computed reattachment length from the second-pass was at most 5 percent greater than the first-pass computed value, although the heat transfer results improve significantly. Recycling the second-pass calculation with the previously computed value does not significantly improve the heat transfer results nor the reattachment length.

The functional relationships derived for C_{μ} and Pr_t, appropriate for the redevelopment region and consisting of relations similar to equations (8–19) for the standard model, but written in Cartesian coordinates with all terms retained, are

$$C_{\mu} = \frac{\Lambda''}{Ak}\,\frac{1}{C_l}\left[F\left(\frac{A}{\beta} + \frac{C}{A}\right) + \frac{2}{3}k\,B\left(\frac{1}{\beta A} + \frac{C}{a}\right) + \frac{A}{\alpha}\left(F + \frac{2}{3}k\,B\right)\right] \tag{20}$$

$$\mathrm{Pr}_t = \frac{C_{\mu}\left[\left(1 + \frac{k}{\epsilon}\,\phi'_T\,\frac{\partial v}{\partial y}\right)\left(1 + \frac{k}{\epsilon}\,\phi'_T\,\frac{\partial u}{\partial x}\right) + \frac{k}{\epsilon}\,\phi'_T\,\frac{\partial u}{\partial y}\right]}{\phi_T\left(1 + \frac{k}{\epsilon}\,\phi'_T\,\frac{\partial u}{\partial x}\,\frac{\overline{v'^2}}{k}\right)} \tag{21}$$

In the foregoing equations

$$C_l = \left[\frac{k}{\epsilon}\,\frac{v}{y}\left(\frac{1 - C_{s2} + C_{s2w} f}{\frac{P}{\epsilon} + C_{s1} - C_{s1w} f}\right)\right]^j \tag{22}$$

$$\frac{\overline{v'^2}}{k} = -\frac{1}{\beta k}\left[F + \beta C + \frac{2}{3}kB(1 + \beta C)\right] \tag{23}$$

$$A = -\frac{\Lambda''}{\Lambda' + \Lambda''}; \quad B = \frac{\Lambda' P}{\epsilon} - 1; \quad C = \frac{1 - \beta}{A\alpha\beta} \tag{24}$$

$$E = C_l - \frac{1}{2}\,\frac{2k\Lambda''}{\epsilon A}\,\frac{\partial u}{\partial y}\left[\frac{A(\alpha + \beta)}{\alpha\beta} + \frac{1 - \beta}{A\alpha\beta}\right] \tag{25}$$

$$F = \frac{1}{3}k\frac{B}{E}\left(\frac{\partial u}{\partial y}\right)^2\left(\frac{2k\Lambda''}{\epsilon A}\right)^2\left(\frac{1 + A}{\alpha\beta} + \frac{1 - \beta}{A\alpha\beta}\right) \tag{26}$$

$$\alpha = 1 + 2\,\frac{\Lambda' k}{\epsilon}\,\frac{\partial u}{\partial x}; \quad \beta = 1 - \frac{2k}{\epsilon}\Lambda''\,\frac{\partial u}{\partial y} \tag{27}$$

The compuatational procedures used in the present study are described in detail by Gooray et al. [16, 18]. The boundary conditions applied are also discussed in these references. Initial upstream profiles used were either obtained from measurements in the experiments simulated or were approximated as shown in Table 2. The computer code used for the calculations was a modified version of the TEACH-T program described by Gosman [25]. The program was modified to include a temperature field solution routine and to replace hybrid differencing of the convective terms by more accurate quadratic differencing procedures [26]. Some modification was also made to the iterative scheme to insure convergence of the quadratic procedure.

Results and Discussion

The results presented herein were obtained by applying the turbulent modeling and computational procedures described

Table 2 Summary of approach conditions for test cases

Geometry	Experimenters	δ_u/H	δ_T/H	k	ϵ	u and T
Back-step	Aung and Goldstein [2]	Simulated [6]	1.0	Klebanoff fit [22]	Klebanoff fit [22]	T, known; u; Abbott and Kline fit [23]
Pipe expansion	Zemanick and Dougall [5]	Fully developed	Fully developed	Laufer fit [24]	Laufer fit [24]	Fully developed profiles
Pipe expansion	Sparrow and O'Brien [6]	Fully developed	Fully developed	Laufer fit [24]	Laufer fit [24]	Fully developed profiles

Table 3 Summary of predicted reattachment lengths

		Predictions of reattachment length, x_R/H			
			C_μ functionalized		
Geometry	Experimental values of x_R/H	$C_\mu = 0.09$	Pass 1	Pass 2	Pass 3
Rearward-facing step	4.5–5.0 Aung and Goldstein [2]	4.5	5.8	6.1	6.1
Pipe expansion	6–9 Zemanick and Dougall [5]	6.4	8.4	8.6	8.7
Rearward-facing step	5.7–6.0 Moss and Baker [27]	4.9	6.0	x_R/H data available for one pass only	
Rearward-facing step	7.97 Eaton and Johnson [28]	5.1	7.5	x_R/H data available for one pass only	

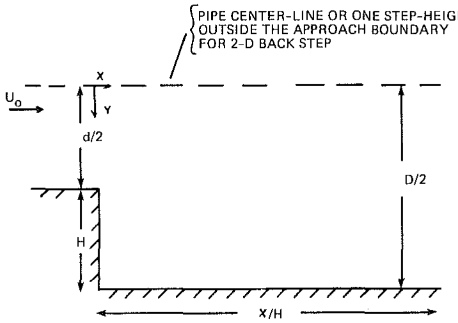

Fig. 1 Geometrical representation of two-dimensional rearward-facing step and sudden pipe expansion

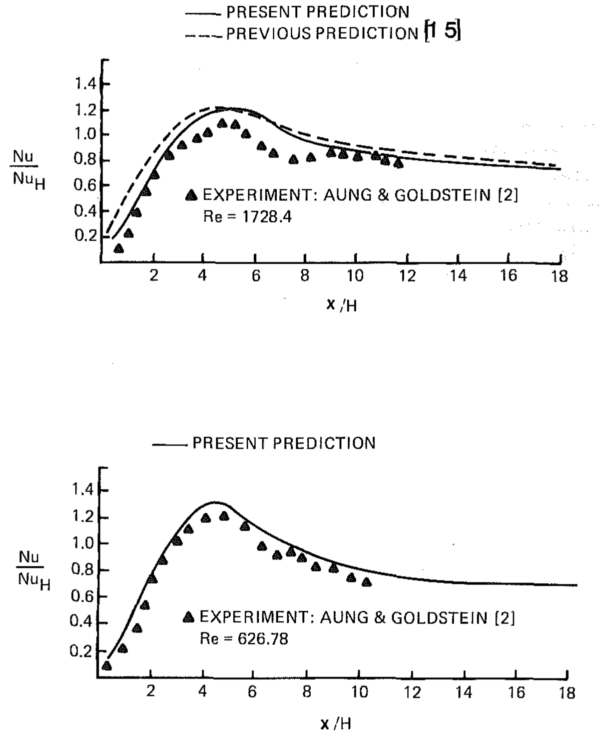

Fig. 2 Streamwise variation of Nusselt number downstream of step for two-pass procedure

to the two-dimensional back-step and pipe expansion geometries. Comparisons are made with the experimental heat transfer data of Aung and Goldstein [2], Zemanick and Dougall [5] and Sparrow and O'Brien [6], and with experimental fluid dynamic data [27, 28].

Figure 1 shows schematically the two-dimensional back-step and sudden pipe expansion geometries considered in this study. The point $y = 0$, for the back-step is at a location well outside the approach boundary layer; for the pipe expansion it is located at the symmetry axis. A variable finite-difference grid was superimposed on this geometry with extreme care taken to insure grid independent heat transfer coefficients [16, 18]. Accurate results were obtained on a variable grid with 28 to 32 grid lines in the y-direction. Convergence for one pass is obtained after about 250 iterations with central processor times on an IBM 3033 averaging about four minutes.

It is important to emphasize that the results presented herein, obtained by applying the sensitized two-pass procedure to the experiments of Aung and Goldstein [2] and Zemanick and Dougall [5], are a significant improvement over results for these experiments previously presented by the authors in [15]. In the previous work, although the standard $k-\epsilon$ model of the two-pass procedure was improved to account for the effect of streamline curvature in the recirculating region, pressure-strain (scalar) interactions with wall damping corrections were not included as they are in the present work, for both standard and low-Reynolds number models.

The effect of this new pressure-strain sensitization is illustrated in the upper portion of Fig. 2, which compares the streamwise distribution of computed rearward step, bottom-wall heat transfer coefficients obtained by applying the two-pass procedure with streamline curvature only [15], and the present two-pass model sensitized with both streamline curvature and pressure-strain interaction with wall damping, to one Reynolds number case of the Aung and Goldstein data [2]. The improvement due to adding pressure-strain in-

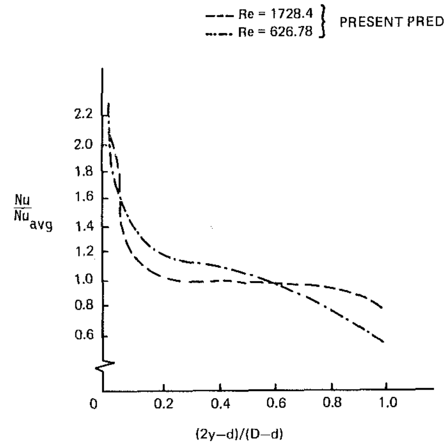

Fig. 3 Cross-stream variation of Nusselt number on the downstream face of the rearward-facing step

teraction is obvious. The lower portion of Fig. 2 shows the even better agreement of the present computations with experiment for another case of the Aung and Goldstein data [2]. Including the pressure-strain terms in the standard version of the model, also results in improved predictions of the hydrodynamic reattachment lengths, which contributes to the improved agreement of the two-pass procedure heat transfer results with experiment. Table 3 summarizes the reattachment lengths computed using the present procedure with experiment and with computations performed using the standard $k-\epsilon$ model with no refinements. Note that the turbulent reattachment lengths are typically somewhat smaller than the observed experimental results for laminar flow, which are characteristically 8-9 step heights downstream of reattachment [29]. The effect of mulitple passes on computed reattachment length for two cases are also shown in the table.

Figure 3 shows the computed side-wall heat transfer coefficient for the rearward step for the two Reynolds numbers for which bottom wall results are shown in Fig. 2. The Nusselt number is normalized by its average value and the horizontal axis is normalized to vary from 0 to 1, the former corresponding to a point adjacent to the opening and the latter to a point where the side wall meets the horizontal wall. The highest heat transfer occurs on the portion of the side wall adjacent to the main flow and the lowest occurs in the corner region. No experimental data are available for comparison.

Results related to correlations of heat transfer coefficents have been obtained for the rearward-step geometry by computing heat transfer distribution for several Reynolds numbers. The Reynolds number range covered was from 500 to 10,000. All calculations were performed by assuming, at the step, an untripped turbulent boundary layer having a heated starting length. Also the same momentum thickness for the incident boundary layer is assigned for all Reynolds numbers. This is not too damaging an assumption becauue the heat transfer coefficients beyond the step are fairly independent of approach boundary layer thicknesses [16, 17]. Equations (28) and (29) below represent the approximate dependence of the maximum bottom and average side-wall Nusselt numbers with Reynolds numbers, respectively.

$$(\mathrm{Nu}_{\mathrm{bottom}})_{\max} = 0.107\ \mathrm{Re}^{0.68} \tag{28}$$

$$(\mathrm{Nu}_{\mathrm{side}})_{\mathrm{avg}} = 0.0839\ \mathrm{Re}^{0.55} \tag{29}$$

The power law behavior for the maximum Nusselt number of equation (28) is used in an attempt to correlate the distribution of heat transfer coefficients for design purposes. This result is presented in Fig. 4. Also plotted on the figure are the experimental data of Aung and Goldstein [2]. The

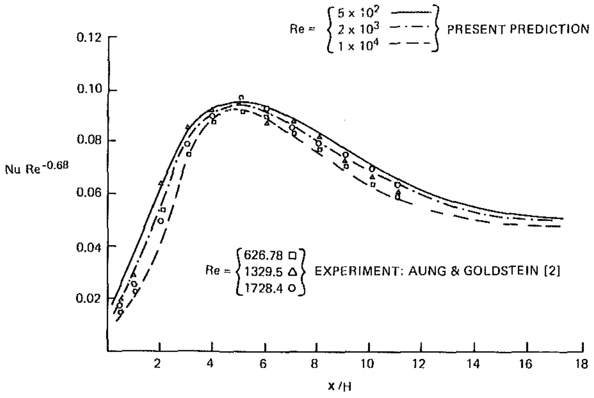

Fig. 4 Streamwise Nusselt number for rearward-facing step normalized through its maximum Reynolds number dependence

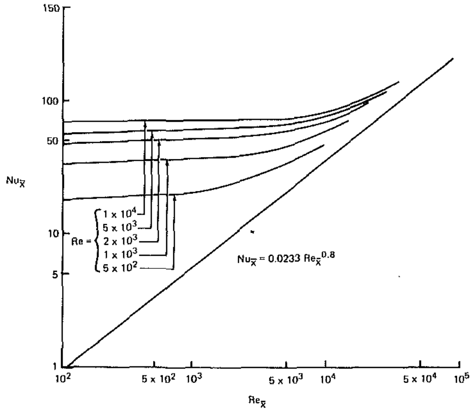

Fig. 5 Boundary layer Nusselt number growth beyond reattachment for the rearward-facing step

deviation of the data from the computed curves is probably partially due to the slight influence of the difference in approach boundary layer thicknesses on heat transfer coefficients. Equations (28) and (29) and Fig. 4 can be used with some confidence to predict rearward-facing step heat transfer coefficients with accuracy sufficient for most design purposes, within the range of Reynolds number considered. The overvalue of the local heat transfer downstream of reattachment, as shown in Figs. 2 and 4 is rather surprising initially but may be explained by the increased heat transfer caused by the high turbulent kinetic energy present in the reattaching shear layer.

Figure 5 is a logarithmic plot of Nusselt number, $\mathrm{Nu}_{\bar{x}}$ based on distance, $\bar{x}$, downstream of reattachment versus Reynolds number, $\mathrm{Re}_{\bar{x}}$, for five computed cases of flow over a rearward facing step. The flat plate turbulent boundary layer theory relation is also shown for comparison. The computed results all tend to the 0.8 power growth law of the flat plate relation sufficiently far downstream of the step. Here this occurs between 10 and 12 step heights downstream of the step. The reattachment point for these cases is approximately six step heights downstream of the step. These results demonstrate the fact that the flat plate boundary layer theory based on distance downstream of reattachment cannot be used to predict heat transfer in the redeveloping boundary layer region. Even at significant distances downstream where the same power law behavior is followed, it will always tend to underestimate the heat transfer rate. In the present results, the computed numerical results exceed flat plate theory by factors ranging from 1.3 to 1.6.

Computed heat transfer results for two pipe expansion cases are plotted in Fig. 6, together with the experimental data

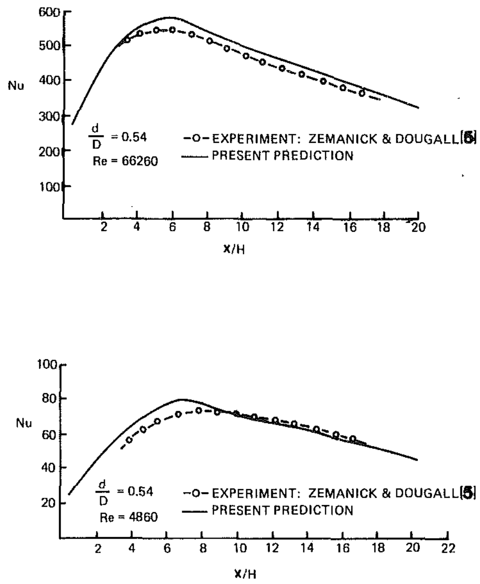

Fig. 6 Streamwise variation of Nusselt number downstream of sudden pipe expansion for two-pass procedure

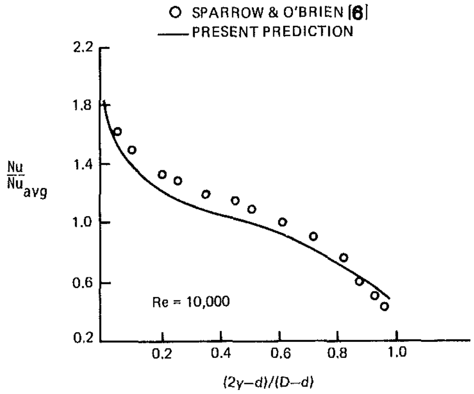

Fig. 7 Cross-stream variation of Nusselt number on the downstream face of the pipe expansion

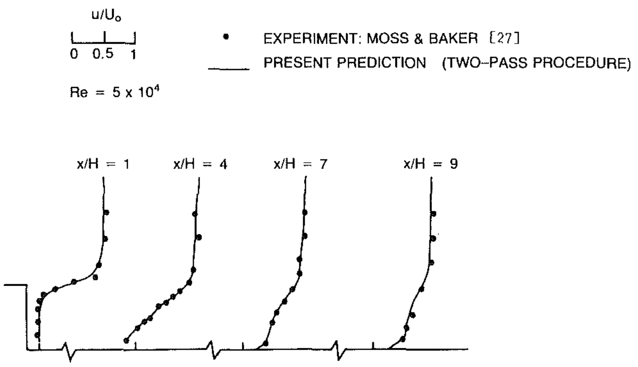

Fig. 8 ***Streamwise mean velocity downstream of a step***

of Zemanick and Dougall [5] for comparison. To a good approximation, the maximum (peak) Nusselt number dependence on Reynolds number for the pipe expansion from the numerical calculations based on a single expansion ratio can be represented by the following expression

$$(\mathrm{Nu}_{\mathrm{bottom}})_{\max} = c\mathrm{Re}^{0.75}, \quad c = 0.145 \tag{30}$$

The predictions exhibit a slightly greater sensitivity to Reynolds number than do the measuremnts [16]. However, this slight difference is insignificant when considering the range of Reynolds number studied (Re = 4860 to Re = 66260).

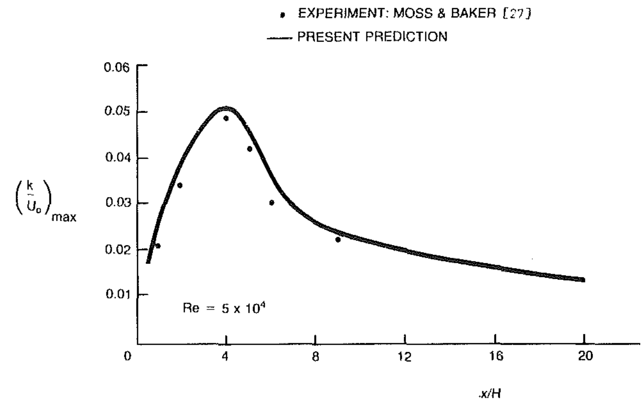

Fig. 9 Streamwise variation of cross-stream maximum in turbulent kinetic energy for step

The difference in the power law behavior of equations (30) and (28) is not surprising, since, despite the similarity in reattachment lengths, the flow in the backward step is free to expand in the negative y-direction and, unlike the axisymmetric pipe flow, there is no upper bound on the large scale turbulence.

Figure 7 shows predicted side wall results of heat transfer coefficients for one Reynolds number out of the three for which computations were performed for the downstream face of a pipe expansion. Comparison is made with the experimental data of Sparrow and O'Brien [6]. Agreement with the experiment is even better for larger Reynolds numbers than the case shown. The computed dependence of the average Nusselt number on Reynolds number for the side wall, i.e., the growth law, is essentially the same as that of the experimental data, where the predicted growth law is represented by the following expression.

$$(\mathrm{Nu}_{\mathrm{side}})_{\mathrm{avg}} = c\mathrm{Re}^{0.69}, \quad c = 0.057 \tag{31}$$

The encouraging ability of the present procedures to predict fluid-dynamic phenomena as well as heat transfer phenomena is illustrated in Figs. 8 and 9, which are typical comparisons between computed and measured predictions of fluid dynamic variables. These figures compare predictions of the streamwise variations in mean streamwise velocity and maximum turbulent kinetic energy for the rearward-facing step experiments of Moss and Baker [27], with data from these experiments. The maximum turbulent kinetic energy in Fig. 9 is the value obtained by traversing the flow in the cross-stream (y) direction. Further comparisons for fluid dynamic variables are given in [17].

Conclusions

Turbulent heat transfer in separated flow regions is a very complicated process; the calculation of the local heat transfer coefficients downstream of rearward-facing steps and sudden pipe expansions is still far from being routine. In the present study, computations have been carried out only for a few cases; therefore, no definitive answers concerning the details of the associated transfer processes can be drawn at this time. Nonetheless, the good correlation of the local heat transfer coefficients, as exemplified by Fig. 4, shows promise for the success of this type of approach in generalizing the information obtained.

The present study shows the two-pass, improved $k-\epsilon$ procedure is capable of providing an insight into the complex phenomena attending turbulent separated and reattaching flow with heat transfer. For engineering calculations involving rearward-facing steps, sudden pipe expansions, and related geometries the present method seems to be a viable alternative to the more complex higher-order schemes. The model developed has potential for future refinement, for example, by employing recently developed wall function modifications [13, 14] to the calculation for the recirculation region. However, due to the inherent limitations of $k-\epsilon$ representations of turbulence, it is uncertain at this time if it can also be successfully applied to other geometries of engineering interest, and further research is needed.

Acknowledgment

In carrying out this research, the first two authors (AMG and CBW) received partial support from the Office of Naval Research under Contract N0014-80-C-0545, Work Unit No. NR 094-444.

References

1 Seban, R. A., Emery, A., and Levy, A., "Heat Transfer to Separated and Reattached Subsonic Turbulent Flows Obtained Downstream of a Surface Step," *J. Aerospace Sci.*, Vol. 26, No. 12, 1959, pp. 809-814.

2 Aung, W., and Goldstein, R. J., "Heat Transfer in Turbulent Separated Flow Downstream of a Rearward-Facing Step," *Israel J. of Tech.*, Vol. 10, 1972, pp. 35-41.

3 Aung, W., and Watkins, C. B., "Heat Transfer Mechanisms in Separated Forced Convection," *Proceedings of the NATO Institute on Turbulent Forced Convection in Channels and Rod Bundles*, Hemisphere Publications, Washington, D.C., 1979.

4 Aung, W., "Separated Forced Convection," *Proc. ASME/JSME Thermal Eng. Joint Conf.*, March 20-24, 1983, Honolulu, Hawaii.

5 Zemanick, P. P., and Dougall, R. S., "Local Heat Transfer Downstream of Abrupt Circular Channel Expansion," ASME Journal of Heat Transfer, Vol. 92. 1970, p. 53.

6 Sparrow, E. M., and O'Brien, "Heat Transfer Coefficients on the Downstream Face of an Abrupt Enlargement or Inlet Constriction in a Pipe," ASME Journal of Heat Transfer, Vol. 102, 1980, pp. 408-414.

7 Lamb, J. P., "Convective Heat Transfer Correlations for Planar, Separated Flows," ASME Journal of Heat Transfer, Vol. 102, 1980, p. 351.

8 Taylor, C., et al., "F.E.M. and the Two-Equation Model of Turbulence," *Proc. 2nd Int. Conf., Num. Methods in Laminar and Turbulent Flow*, Venice, Italy, 1981, published by University College of Swansea, Swansea, U.K., 1981.

9 Kwon, O. K., and Pletcher, R. H., "Prediction of the Incompressible Flow Over a Rearward-Facing Step," Technical Report HTL-26, CFD-4, Engrg. Res. Inst., Iowa State Univ., Ames, Iowa, Aug. 1981.

10 Oliver, A. J., "The Prediction of Turbulent Flow and Heat Transfer Over Rearward Facing Steps," *Computer Methods in Fluid Mechanics*, London,

11 Gooray, A. M., Watkins, C. B., and Aung, W., "Numerical Calculations of Turbulent Heat Transfer Downstream of a Rearward-Facing Step," *Proc. 2nd Int. Conf. Num. Methods in Laminar and Turbulent Flow*, Venice, Italy, 1981, published by University College of Swansea, Swansea, U.K., 1981.

12 Chieng, C. C., and Launder, B. E., "On the Calculation of Turbulent Heat Transport Downstream from an Abrupt Pipe Expansion," *Numer. Heat Transfer*, Vol. 3, 1980, pp. 189-207.

13 Johnson, R. W., and Launder, B. E., "Discussion of On the Calculation of Turbulent Heat Transport Downstream from an Abrupt Pipe Expansion *Numer. Heat Transfer*, Vol. 5, 1982, p. 493.

14 Amano, R. S., "On the Calculation of Turbulent Heat and Mass Transport Downstream from an Abrupt Pipe Expansion," AIAA Paper 82-1269, AIAA/SAE/ASME 18th Joint Propulsion Conference, June 1982.

15 Gooray, A. M., Watkins, C. B., and Aung, W., "$k-\epsilon$ Calculations of Heat Transfer in Redeveloping Turbulent Boundary Layers Downstream of Reattachment," ASME Paper 82-HT-77, AIAA/ASME Fluids, Plasma, Thermophysical and Heat Transfer Conference, St. Louis, Missouri, June 1982.

16 Gooray, A. M., "Numerical Calculations of Turbulent Recirculating Heat Transfer Beyond Two-Dimensional Back-Steps and Sudden Pipe Expansions," Ph.D. dissertation, Department of Mechanical Engineering, Howard University, Washington, D.C., May 1982; see also by Watkins, C. B., and Gooray, A. M., same title, Final Report ONR Contract Number N0014-80C-0545, Howard University, Aug. 1982.

17 Gooray, A. M., Watkins, C. B., and Aung, W., "Improvements to the $k-\epsilon$ Model for Calculation of Turbulent Separated Forced Convection," *Proc. of Fourth Symposium on Turbulent Shear Flows*, University of Karlsruhe, F.R., Germany, Sept. 1983.

18 Gooray, A. M., Watkins, C. B., and Aung, W., "A Two-Pass Procedure for the Calculation of Heat Transfer in Recirculating Turbulent Flow," to appear in *Numer. Heat Transfer*.

19 Jones, W. P., and Launder, B. E., "The Prediction of Laminarization with a Two-Equation Model of Turbulence," *Int. J. Heat Mass Transfer*, Vol. 15, 1972, pp. 301-313.

20 Launder, B. E., and Ying, W. M., "Prediction of Flow and Heat Transfer in Ducts of Square-Cross-Section," *Proc. Inst. Mech. Eng.*, Vol. 187, 1973, p. 455.

21 Leschziner, M. A., and Rodi, W., "Calculation of Annular and Twin Parallel Jets Using Various Discretization Schemes and Turbulence-Model Variation," ASME *J. Fluids Eng.*, Vol. 103, 1981, pp. 352-360.

22 Klebanoff, P. S., "Characteristics of Turbulence in a Boundary Layer with Zero Pressure Gradient," NACA TN-3178, 1958.

23 Abbot, D. E., and Kline, S. J., "Experimental Investigation of Subsonic Turbulent Flow over Single and Double Backward Facing Steps," ASME *J. Basic Engrg.*, Vol. D84, 1962, pp. 317-325.

24 Laufer, J., "The Structure of Turbulence in Fully Developed Pipe Flow," NACA Report No. 1174, 1954, p. 18.

25 Gosman, A. D., "The TEACH-T Computer Program-Structure," *Flow Heat and Mass Transfer in Turbulent Recirculating Flows-Prediction and Measurements*, Notes from seminar presented at McGill University, Canada, 1976.

26 Leonard, B. P., "A Stable and Accurate Convective Modeling Procedure Based on Quadratic Upstream Interpolation," *Comput. Methods Appl. Mech. Eng.*, Vol. 19, 1979, pp. 59-98.

27 Moss, W. D., and Baker, S., "Re-Circulating Flows Associated with Two-Dimensional Steps," *The Aeronautical Q.*, Vol. 31, pt. 3, 1980.

28 Eaton, J. K., and Johnston, J. P., "Turbulent Flow Reattachment: An Experimental Study of the Flow and Structure Behind a Backward-Facing Step," Report MD-39, Department of Mechanical Engineering, Stanford University, 1980.

29 Aung, W., "On Experimental Study of Laminar Heat Transfer Downstream of Backstep," to appear in ASME Journal of Heat Transfer.

A Method to Solve Conjugate Heat Transfer Problems: The Case of Fully Developed Laminar Flow in a Pipe

G. S. Barozzi
Associate Professor.

G. Pagliarini
Researcher.

Instituto di Fisica Tecnica,
Facolta di Ingegneria,
Universita di Bologna,
I-40136 Bologna, Italy

A simple, fast, and rather general procedure combining the superposition principle with a finite element method is proposed to deal with conjugate heat transfer problems. The method is employed to consider the wall conduction effect on heat transfer to fully developed laminar flow through a pipe whose exterior boundary is uniformly heated along a finite length. Results are given for two values of each of the four parameters determining the relative importance of axial conduction: the Peclet number of the fluid, the wall to fluid conductivity ratio, and the dimensionless thickness and length of the heated section of the pipe.

Introduction

Axial heat conduction along the walls bounding the fluid is usually overlooked in the design and analysis of heat transfer devices as well as in the interpretation of experimental data. Nevertheless, in actual practice, the temperature and heat flux distributions on the boundary depend not only on the thermal properties and the flow characteristics of the fluid, but also on the properties of the wall. This is especially true in regions of large temperature gradients such as the neighborhood of the leading edge in the flow over a heated body or the thermal entrance region in a duct. Such situations where heat conduction in the solid interacts with convective heat transfer are referred to as conjugate problems.

This paper is concerned with coupled conduction and laminar convection in ducts. The subject has received recent theoretical consideration, the most relevant literature having been collected by Shah and London [1] in their fundamental monograph on laminar heat transfer in internal flow. Even with the addition of a new contribution, the number of conjugate problems treated is still limited.

The influence of wall conduction on convection in pipes and channels has been studied by Chu and Bankoff [2] with slug flow, and by Povarnitsyn and Yurlova [3], Aleksashenko [4], Luikov et al. [5] for Poiseuille flow. These contributions have a more theoretical than practical relevance as the assumption of infinite or semi-infinite domain limits the usefulness of the results to extremely long ducts. The coupled effect of wall and fluid axial conduction in laminar pipe-flow has recently been considered by Faghri and Sparrow [6] and Zariffeh et al. [7] using finite difference and by Campo and Rangel [8] analytically. Once more the pipe was supposed to extend indefinitely both in the positive and negative directions, while assuming one-dimensional wall temperature distribution. Wall conduction was found to produce a significant preheating of the fluid, easily overcoming the effect of axial fluid conduction.

The case of a short heat transfer section is of more practical interest.

Davis and Gill [9] have been concerned with heat transfer from a thick block of conducting material to a plane Poiseuille-Couette flow. The theoretical predictions compare well with the experimental evidence of Davis and Cooper [10], showing the effect of heat conduction on the measurements was noticeable.

Fully developed laminar flow in a plane channel with a short heating section has been considered by Shelyag [11] and by Mori et al. [12]. The case of duct-flow was investigated by Mori et al. [13], both for the condition of uniform heat flux, and of constant temperature at the outer surface of the heat conducting wall. Results in [12, 13] are of great value since they allow the effects of the wall to fluid conductivity ratio and wall thickness to be clearly demonstrated. Experimental data for a parallel plate channel with constant temperature boundary condition are also presented in [12] and show very good agreement with theoretical predictions. The study was then extended to consider internal heat generation in the fluid [14-16] and parallel plate heat exchangers [17].

Davis and Venkatesh [18] also studied heat transfer to Poiseuille flow in a pipe with a heat conducting section, as an example of their new general formulation of the solution of conjugate boundary value problems. Computations, however, were not performed.

Conjugate problems of convective heat transfer with internal turbulent flow have been tackled by Kuznetzov and Belousov [19] and by Sakakibara and Endoh [20]. Shulman et al. [21] have been concerned with non-Newtonian fluids.

In the aforementioned analytical methods, solutions to the energy equation are sought in the solid and fluid regions. Matching conditions are then imposed at the interface so as to ensure the continuity of heat flux and temperature there. All analyses take advantage of the linearity of the energy equation. Only constant property problems have therefore been investigated.

The presence of discontinuities as well as the variability of transport properties can more easily be accomodated by numerical methods.

Purely numerical solutions of conjugate heat transfer problems exist in the literature: natural convection from a vertical flat plate and the flow over a heated cylinder have been respectively considered by Zinnes [22] and by Sunden [23]. Lock and Ko [24], Sparrow and Faghri [25], and Sparrow and Prakash [26] have dealt with thermal interaction of two convective systems coupled through a thin wall. The energy equation was iteratively solved in the two streams by a finite difference method in [25, 26]. It is relevant to this paper that the convection equation has been used there for interface coupling.

Use of the armonic mean of transport properties on the two sides of an interface has been suggested by Patankar [27] to treat the points of discontinuity with finite difference methods. The fully developed heat transfer in a square duct with finite wall thickness was presented as an example. The

---

Contributed by the Heat Transfer Division for publication in the JOURNAL OF HEAT TRANSFER. Manuscript received by the Heat Transfer Division, January 5, 1984.

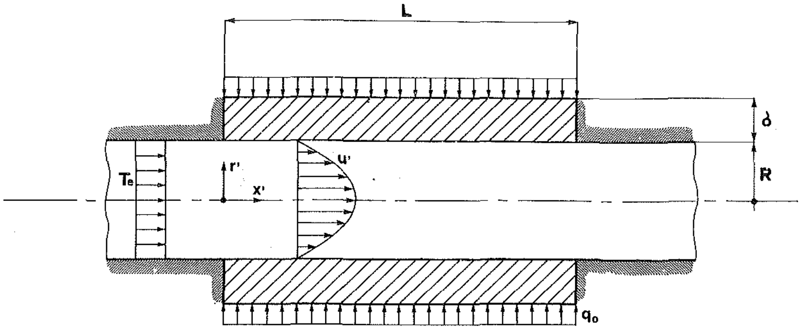

Fig. 1 Schematic diagram of the problem and coordinate system

method is quite general and also allows fluid flow and heat transfer calculation in arbitrary geometries to be performed [28].

In this paper a simple and fast procedure is presented to deal with a rather wide class of conjugate heat transfer problems. The method combines a finite element treatment of the energy equation in the solid wall and the application of the Duhamel theorem at the interface. The heat transfer coefficient is iteratively specified there. Determination of the temperature field in the fluid is therefore avoided in the computational procedure.

The features of the method are demonstrated by the analysis of coupled conduction and convection in laminar flow of a fluid through a pipe. A uniform heat flux condition is imposed at the outer surface of the heated section. The influence of Peclet number and the nondimensional pipe length is particularly stressed in the presentation of results so as to complete Mori's et al. analysis [13].

Basic Equations and Design Parameters

The physical problem examined is sketched in Fig. 1. It concerns steady flow of a constant property fluid through a circular duct whose exterior wall is uniformly heated along a finite length. The end sections of the heating zone are thermally insulated, and the flow is assumed laminar and fully developed. Heat generation and dissipation, and axial heat conduction are assumed to be negligible in the fluid.

The following nondimensional quantities are defined

$$r=r'/R,\ x^*=x'/2R\mathrm{Pe},\ L^*=L/2R\mathrm{Pe},\ \Delta=\delta/2R,$$

$$\mathrm{Pe}=2RU\rho_f c_f/k_f,\ K=k_s/k_f,\ u=u'/U=2(1-r^2),$$

$$\Theta_f=\frac{T_f-T_e}{q_{w,o}R/k_f},\ \Theta_s=\frac{T_s-T_e}{q_{w,o}R/k_f}$$

Here $q_{w,o}$ designates the nominal heat flux, i.e, the mean value of the heat flux at the inner surface of the tube, $q_w(x')$.

The governing equations and auxiliary boundary conditions are: for the fluid region $(0 \leq x^* \leq L^*; 0 \leq r \leq 1)$

$$u\frac{\partial\Theta_f}{\partial x^*}=4\left(\frac{\partial^2\Theta_f}{\partial r^2}+\frac{1}{r}\frac{\partial\Theta_f}{\partial r}\right) \tag{1}$$

$$\Theta_f(0,r)=0$$

$$\frac{\partial\Theta_f}{\partial r}(x^*,0)=0 \tag{2}$$

for the solid region $(0 \leq x^* \leq L^*; 1 \leq r \leq 1+2\Delta)$

$$4\left(\frac{\partial^2\Theta_s}{\partial r^2}+\frac{1}{r}\frac{\partial\Theta_s}{\partial r}\right)+\frac{1}{\mathrm{Pe}^2}\frac{\partial^2\Theta_s}{\partial x^{*2}}=0 \tag{3}$$

Nomenclature

[ ] = matrix
{ } = column vector
c = specific heat
h = convective heat transfer coefficient
Ⓗ = thermal boundary condition referring to constant wall heat flux
I = functional
k = thermal conductivity
K = wall to fluid conductivity ratio
L = length of the heated section of the duct
L^* = nondimensional length of the heated section of the duct
N_i = shape function
Nu_x = local Nusselt number
$\mathrm{Nu}_{x,H}$ = local Nusselt number for the thermal boundary condition Ⓗ
$\mathrm{Nu}_{x,T}$ = local Nusselt number for the thermal boundary condition Ⓣ
Pe = Peclet number
q = heat transfer rate per unit of heat transfer area
q^* = nondimensional heat transfer rate per unit of heat transfer area
r = nondimensional radial coordinate
r' = radial coordinate
R = inner radius of the duct
S = surface for which boundary conditions are specified
T = temperature
Ⓣ = thermal boundary condition referring to constant wall temperature
u = nondimensional fluid axial velocity
u' = fluid axial velocity
U = fluid mean axial velocity
V = volume of the solid region
x' = axial coordinate
x^* = nondimensional axial coordinate

Greek Symbols

δ = thickness of the tube wall
Δ = nondimensional thickness of the tube wall
$\Delta\mathrm{Nu}_x$ = difference between Nu_x and $\mathrm{Nu}_{x,T}$
Θ = nondimensional temperature
ξ = dummy variable of the pipe length
ρ = density

Subscripts

e = initial value at the entrance of the duct
f = fluid
fb = fluid bulk
s = solid
x = local value
w = fluid-solid interface
o = nominal value

Superscripts

e = element

$$\frac{\partial \Theta_s}{\partial x^*}(0,r) = \frac{\partial \Theta_s}{\partial x^*}(L^*,r) = 0$$

$$\frac{\partial \Theta_s}{\partial r}(x^*,1+2\Delta) = \frac{1}{K(1+2\Delta)} \tag{4}$$

The following compatibility conditions complete the statement of the problem:

$$\Theta_s(x^*,1) = \Theta_f(x^*,1)$$

$$\frac{\partial \Theta_f}{\partial r}(x^*,1) = K\frac{\partial \Theta_s}{\partial r}(x^*,1) \tag{5}$$

The interfacial temperature Θ_w, distribution of the nondimensional heat flux q_w^*, fluid bulk temperature Θ_{fb}, and the local Nusselt number Nu_x, are of main interest for the designer. They are defined as follows

$$\Theta_w = \Theta_s(x^*,1) = \Theta_f(x^*,1) \tag{6}$$

$$q_w^* = \frac{q_w}{q_{w,o}} = K\frac{\partial \Theta_s}{\partial r}(x^*,1) \tag{7}$$

$$\Theta_{fb} = \int_0^1 \Theta_f urdr \Big/ \int_0^1 urdr \tag{8}$$

$$\mathrm{Nu}_x = 2Rh_x/k_f = 2q_w^*/(\Theta_w - \Theta_{fb}) \tag{9}$$

The bulk temperature and the heat power supplied through the wall are also correlated by the integral energy balance equation

$$\Theta_{fb} = 8\int_0^{x^*} q_w^*(\xi)d\xi \tag{10}$$

Analysis

Conjugate boundary value problems such as the one expressed by equations (1-5) generally require the energy equation to be solved separately over the solid and fluid regions. Nevertheless, provided that the distribution of the design parameters defined by (6-9) are of primary interest, the direct solution of equations (1) and (2) may be avoided. The problem is then reduced to the solution of the energy equation in the solid phase. In principle, this may be achieved by setting up an iterative procedure in which equation (3) is solved by an analytical or numerical method. As a starting step, a guessed temperature distribution at $r=1$ is chosen to complete the set of conditions at the wall boundaries. After $\Theta_s(x^*,r)$ has been obtained, the heat flux $q_w^*(x^*)$ and the bulk temperature of the fluid $\Theta_{fb}(x^*)$ are computed by equations (7) and (10), respectively. New values of the interfacial temperature must then be generated to start a new run. This may be obtained by applying Duhamel's theorem [29] at the solid-fluid boundary to give

$$\Theta_w(x^*) - \Theta_{fb}(x^*) = \frac{2q_w^*(0)}{Nu_{x,H}(x^*)} + 2\int_0^{x^*} \frac{dq_w^*(\xi)}{d\xi}\,\frac{d\xi}{\mathrm{Nu}_{x,H}(x^*-\xi)} \tag{11}$$

Here $\mathrm{Nu}_{x,H}$ is the local value of the Nusselt number for the limiting case, here denoted as Ⓗ, where a uniform heat flux is imposed at the inner surface of the tube. Very accurate formulas for $\mathrm{Nu}_{x,H}$ have been presented by Shah and London ([1], pp. 125—126).

The foregoing procedure is conceptually straightforward and simple. Nevertheless it has proven to be impractical, at least when the finite element method is used to deal with the energy equation in the solid phase. The direct imposition of Θ_w results in an extremely rigid constraint, as very small irregularities in the axial temperature gradient may lead to a physically unreliable situation where heat should be supplied by the fluid to the wall at some locations of the interface. This causes the onset of instabilities leading to divergence. To prevent these difficulties, the computation should be started with a guessed distribution of Θ_w almost equal to the exact one, following to some extent the original method suggested by Karvinen [30, 31], dealing with boundary layer flow over a thin heat generating plate. In practice, however, prediction of the correct values of Θ_w represents a difficult task owing to the rather wide range of variability of this quantity, and instabilities easily appear in the neighbourhood of the origin, where $\partial\Theta_s/\partial x^*$ takes on comparatively large values.

It has been recognized that the observed effect is due to uncoupling between the fluid and wall temperature inherent in the choice of the Dirichlet condition at $r=1$. This may then be fruitfully replaced by the convection equation

$$\frac{\partial \Theta_s}{\partial r}(x^*,1) = \frac{\Theta_w - \Theta_{fb}}{2K}\mathrm{Nu}_x \tag{12}$$

which states that the heat flux conducted at the interface is balanced by convection to the fluid. Thus, rather than updating Θ_w each iteration, we now update Θ_{fb} and Nu_x. The calculation procedure may now be synthesized as follows.

The values of $\mathrm{Nu}_{x,H}$ as given in [1] and the corresponding linear distribution of the fluid bulk temperature are inserted in equation (12) to initialize the process. The finite element method is employed to approximate the solution of equation (3), and equations (7) and (10) give q_w^* and Θ_{fb}, respectively. The difference $\Theta_w - \Theta_{fb}$ is determined from equation (11) and, once the values of Nu_x have been computed according to the definition equation (9), a new iteration is started from equation (12), the procedure stopping when the prescribed level of convergency is reached. This structure has proven to be advantageous as not only are instabilities eliminated and convergence always achieved, but also the number of the iterations needed is strongly reduced as, in terms of the Nusselt number, the initial guess never differs widely from the final result. In fact, according to the results of Mori et al., the Nusselt number is bounded by the results of case Ⓗ and that of uniform temperature imposed at the inner surface of the tube, here denoted by Ⓣ.

It is therefore confirmed that the heat transfer coefficient is an effective vehicle for transmitting thermal information through an interface during the iteration process. This conclusion had already been reached by Sparrow et al. [25, 26]. It is verified here in the case where analytical solutions are employed for the convective heat transfer field and a finite element method for the heat conduction.

A variational formulation of the problem specified by equation (3) with boundary conditions (4) and (12) is based on the proper functional

$$I = \int_V \left[4\left(\frac{\partial \Theta_s}{\partial r}\right)^2 + \frac{1}{\mathrm{Pe}^2}\left(\frac{\partial \Theta_s}{\partial x^*}\right)^2\right]dV - \int_{S_1} \frac{8}{K(1+2\Delta)}\Theta_s dS + \int_{S_2} 2\frac{\mathrm{Nu}_x}{K}(\Theta_s - \Theta_{fb})^2 dS \tag{13}$$

The first integral is over the entire volume of the solid region; S_1 and S_2 refer to those parts of the boundary surface for which conditions (4) and (12) are respectively specified. In the finite element approximation, a linear temperature variation is assumed inside each element, as given by

$$\Theta_s = N_1\Theta_{s1} + N_2\Theta_{s2} + N_3\Theta_{s3} \tag{14}$$

In the above Θ_{si} is the temperature value at the ith nodal point, and N_i are shape functions depending linearly on the spatial variables. I of equation (13) is minimized over the whole region, taking into account the temperature distribution, as given by equation (14). This leads to a system of algebraic linear equations of the same number as the unknown nodal temperatures. These may be expressed as

$$[K]\cdot\{\Theta_s\} = \{\mathbf{H}\} \tag{15}$$

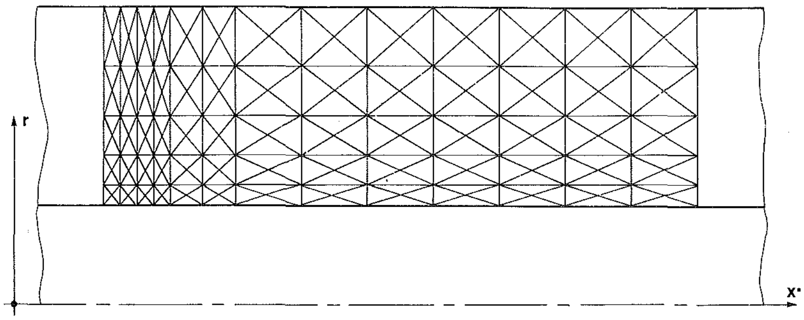

Fig. 2 Finite element subdivision of the pipe wall

Typical terms of matrix $[K]$ and vector $\{\mathbf{H}\}$ are

$$k_{ij}=\sum\int_{V^e}\left(8\frac{\partial N_i}{\partial r}\frac{\partial N_j}{\partial r}+\frac{2}{\mathrm{Pe}^2}\frac{\partial N_i}{\partial x^*}\frac{\partial N_j}{\partial x^*}\right)dV^e$$

$$+\sum\int_{S^e}4\frac{\mathrm{Nu}_x}{K}N_iN_jdS^e \qquad (16)$$

$$h_i=-\sum\int_{S_1^e}\frac{8}{K(1+2\Delta)}N_idS^e+\sum\int_{S_2^e}4\frac{\mathrm{Nu}_x}{K}N_i\Theta_fdS^e \qquad (17)$$

The summation in the above expresses the contribution of the elements to which the ith nodal point belongs. V^e is the volume of a single element, and S_1^e, S_2^e those parts of its boundary surface to which condition (4) or (12) respectively refer. More details of the numerical procedure can be found in [32].

A schematic view of the finite element subdivision by linear triangular elements is given in Fig. 2. The axial spacing is increased logarithmically with x^* in order to achieve greater accuracy near the tube entrance. The nondimensional length of the first element is equal to 1.10^{-6}. Every decade includes 260 elements; moreover from $L^*/2$ to L^* the pipe wall is subdivided into 400 elements so that a very fine mesh results near the end section.

In the numerical solution of the energy equation and the determination of Θ_w, a problem is represented by the condition prescribed for $x^*\rightarrow 0$, as physical arguments and results from the literature suggest that both the Nusselt number and the heat flux go to infinity. Mori et al. [13] found that Nu_x approaches $\mathrm{Nu}_{x,T}$, the Nusselt number referring to case Ⓣ, for $x^*\rightarrow 0$, and this agrees with the boundary condition equation (4) stating that the inner wall of the pipe is isothermal at least in a narrow zone near the entrance. Therefore, for computational purposes, Nu_x was taken equal to the mean value of $\mathrm{Nu}_{x,T}$ at the boundary of the first element, and the value obtained numerically at $x^* = 0$ has been assigned to $q_w^*(0)$ in equation (11). The former approximation does not seem to affect the results as Nu_x always approaches $\mathrm{Nu}_{x,T}$ well above 1.10^{-6} in all the cases considered. The influence of the latter assumption can be checked by performing computations for a limiting case approximating the Ⓣ condition at the inner surface of the wall and comparing the resultant values of $q_w^*(x^*)$ with data from the literature [1]. This test has shown that the deviation from the theoretical results sharply falls from 30 percent at $x^* = 1.10^{-6}$ to $\simeq$ 2 percent at $x^* = 1.10^{-5}$. The accuracy of the solution has also been checked by solving for two of the runs presented in [13]. The predicted values of Nu_x and Θ_w are indistinguishable from Mori's graphs.

In conclusion, the results are believed to be accurate to within 2 percent at least for $x^* > 1.10^{-5}$.

The convergency level has been fixed equal to 0.5 percent for all the quantities and less than eight iterations were needed to achieve convergency in all the cases examined. Computations were performed on the CDC 7600 Computer at the University of Bologna.

Results and Discussion

Following Faghri and Sparrow's [6] observations, the local Nusselt number is not a convenient design parameter in the present problems as it includes three unknowns, namely, q_w^*, Θ_w, and Θ_{fb}. Indeed, it is these three quantities which are of basic interest, and hence they will be presented. Nevertheless, the Nusselt number distributions are also given as they do contain some interesting information as well.

The inspection of equations (1-5) reveals that the solution of the conjugate boundary value problem depends on four independent groups, namely the wall to fluid conductivity ratio K, the nondimensional length of the heating section L^*, the Peclet number Pe, and the dimensionless thickness of the wall Δ.

Computations have been performed for combinations of the following conditions: Δ = 0.1 or 1, L^* = 0.002, 0.02, or 0.2 (i.e. $L/2R$ = 10 or 100), Pe = 500 or 5000, K = 50 or 500. Results had been presented in [13] for one value of the pipe length (L^* = 0.05) and the Peclet number (Pe = 500), K ranging from 1 to 5000 and Δ from 0.001 to 0.5.

From the graphs in Figs. 3(*a*,*b*), where the interfacial temperature Θ_w is plotted versus the downstream distance x^*, the presence of an isothermal region in the nearness of the thermal inlet section is easily recognized owing to the logarithmic scale used for the abscissa. A nonzero value of Θ_w is got at $x^* = 0$. Even if not consistent with the results for the limiting case Ⓗ, this is physically understandable. In fact, the bulk fluid temperature has a nonzero derivative at $x^* = 0$, then in the case $\Theta_w(0) = 0$, the wall to fluid temperature difference would be reversed in the neighborhood of the leading edge and heat would be transferred from the fluid to the wall in that region. Several theoretical results [9, 12, 13, 31, 33] referring to the uniform heat flux condition at the outer face of the heat transfer section, similarly show a wall to fluid temperature jump at $x^* = 0$. The wall temperature is also uniform in the neighborhood of the end section even if this is less clearly seen.

As expected, an almost isothermal situation is reached all along the heated section for the higher values of K and Δ and the lower values of L^* and Pe. It is observed that plots referring to the same value of L^* have a common point of intersection whose position falls in the second half of the heated portion of the pipe and is shifted towards the end section for increasing values of L^*. It may be worth pointing out that the ordinate of this point gives the values of the interfacial temperature in the limiting conditions where Θ_w becomes uniform. For instance from Fig. 3(*a*,*b*) this limiting value of the wall temperature is seen to be 0.17, 0.43, and 1.8 for L^* = 0.002, 0.02, and 0.2, respectively. Moreover points of intersection fall on the graph of $\Theta_{w,H}$, the wall temperature distribution for case Ⓗ.

The trend of $q^*(x^*)$ in Figs. 4(*a*) and 4(*b*) is also interesting.

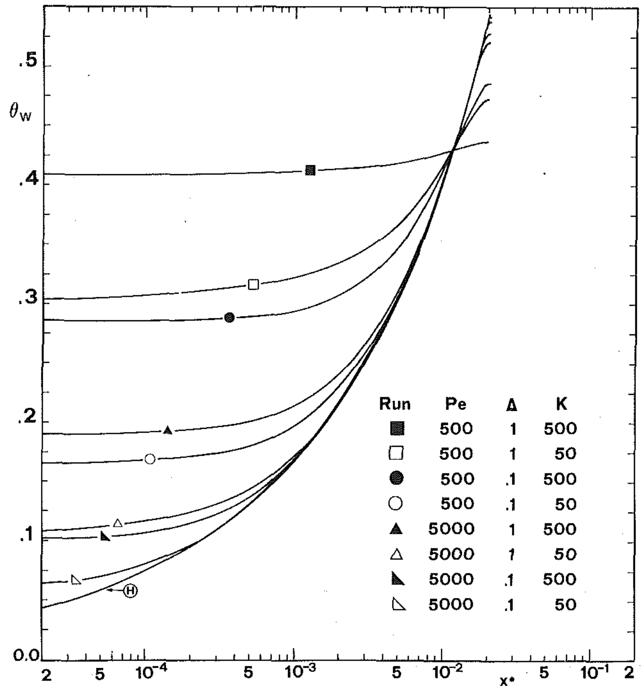

Fig. 3(*a*) Axial distribution of the interfacial temperature, $L^* = 2.10^{-2}$

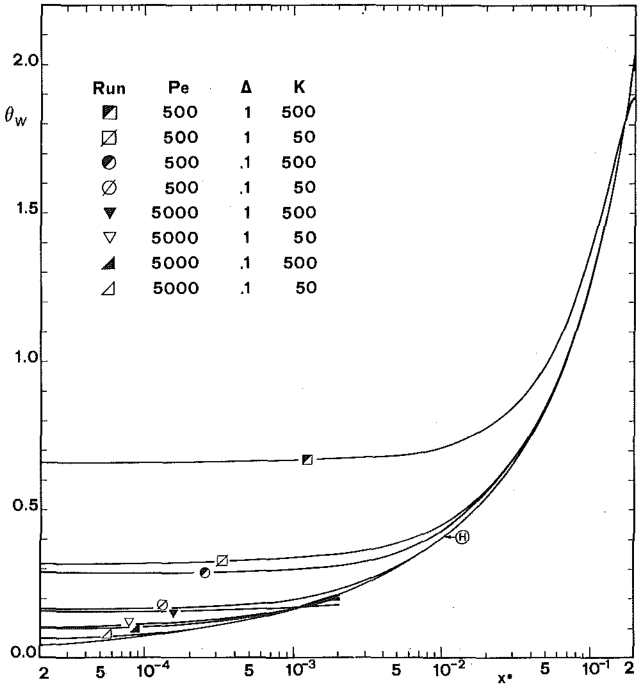

Fig. 3(*b*) Axial distribution of the interfacial temperature, $L^* = 2.10^{-3}$ and 2.10^{-1}

In the initial part of the heating section the heat flux supplied to the fluid is seen to decrease from very high values in the neighborhood of the entrance, towards the nominal value $q_w^* = 1$. Further downstream, the heat flux can vary in two different ways. The first is for it to reach a minimum and then increase towards the reference line $q_w^* = 1$, which, however, is never reached. It may be easily recognized that this trend is typical of the limiting case where the temperature distribution inside the wall is one-dimensional. The wall may be defined as thermally thin in these cases. Alternatively the heat flux can decrease monotonically from 0 to L^*, in which case, the axial component of the temperature gradient is seen to decrease sharply from the outer to the inner surface of the wall so that the minimum is no longer found. This behavior may be assumed to define the wall as thermally thick.

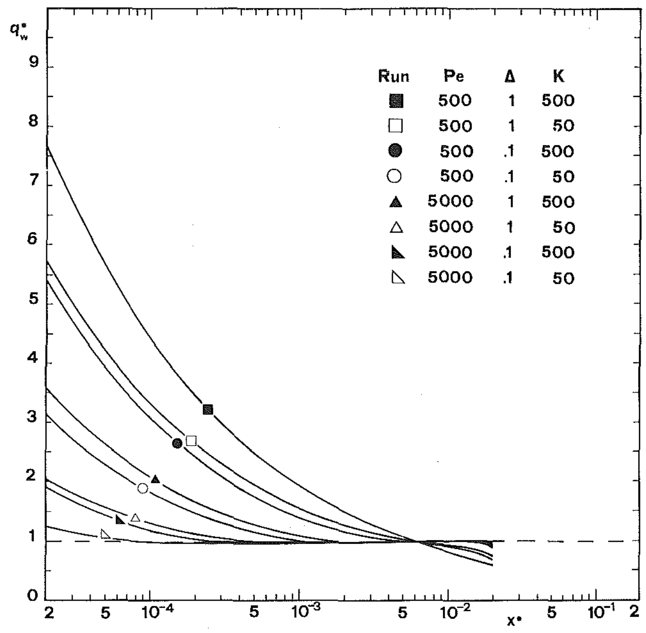

Fig. 4(*a*) Axial distribution of the nondimensional heat flux, $L^* = 2.10^{-2}$

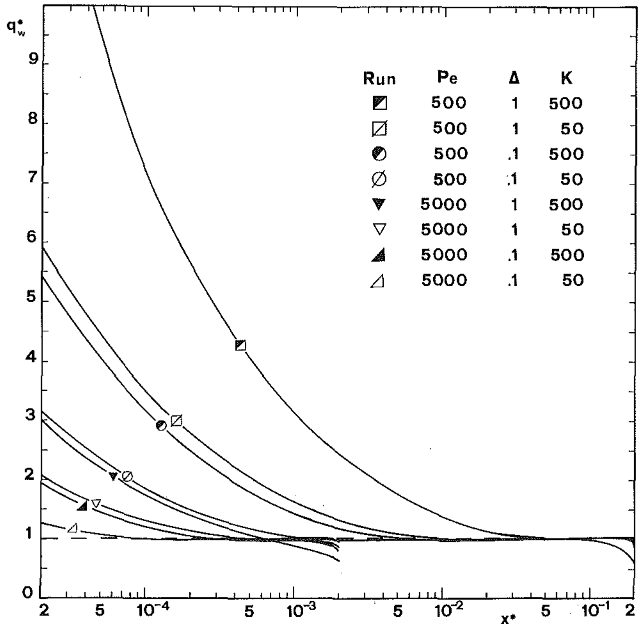

Fig. 4(*b*) Axial distribution of the nondimensional heat flux, $L^* = 2.10^{-3}$ and 2.10^{-1}

The distinction has practical relevance as disregarding heat conduction along the wall leads to very large errors in the heat flux distribution all over the pipe length for thick-walled tubes, while a single narrow zone near the entrance, where the heat flux is underpredicted, is found for thermally thin tubes. The present results can then be helpful in forecasting the extent of the wall conductivity effects on heat transfer for practical applications.

Redistribution of heat flux produced by conduction along the wall affects the enthalpy content of the fluid at any axial position. The extent of such an effect can be characterized by the ratio of Θ_{fb} to the bulk fluid temperature in the absence of axial conduction

$$\Theta_{fb,H} = 8x^* \tag{18}$$

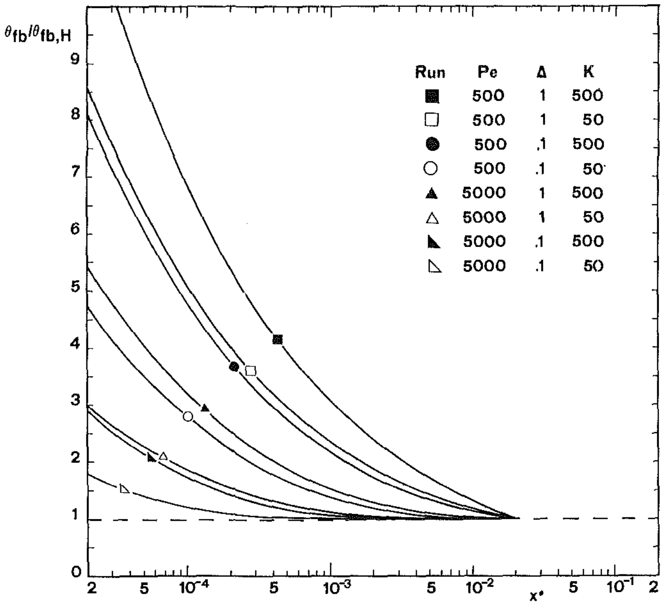

Fig. 5(*a*) Axial distribution of the fluid bulk temperature ($\theta_{fb,H} = 8x^*$), $L^* = 2.10^{-2}$

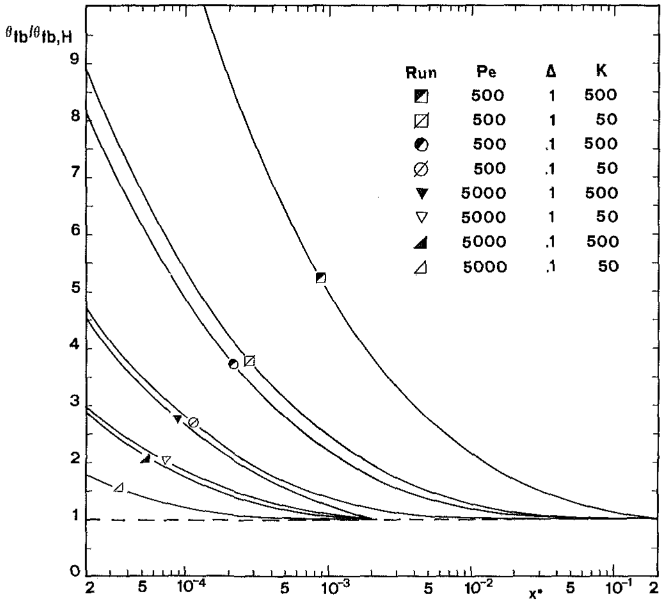

Fig. 5(*b*) Axial distribution of the fluid bulk temperature ($\theta_{fb,H} = 8x^*$), $L^* = 2.10^{-3}$ and 2.10^{-1}

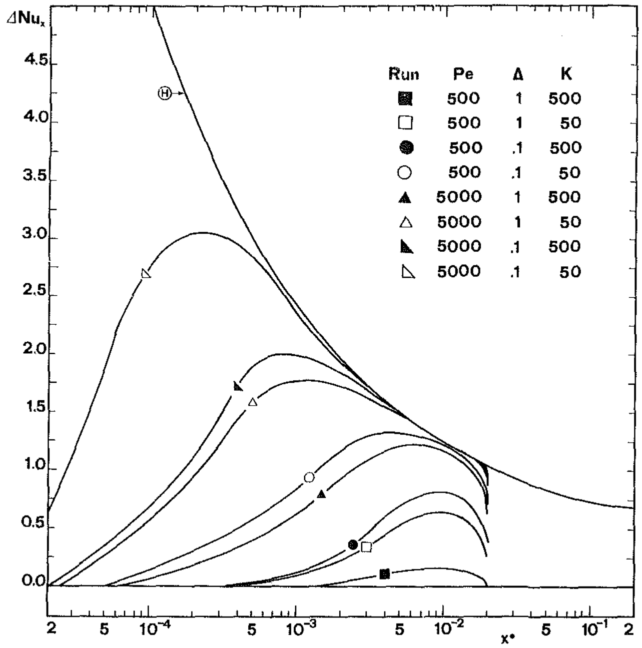

Fig. 6(*a*) Axial distribution of the difference ($Nu_x - Nu_{x,T}$), $L^* = 2.10^{-2}$

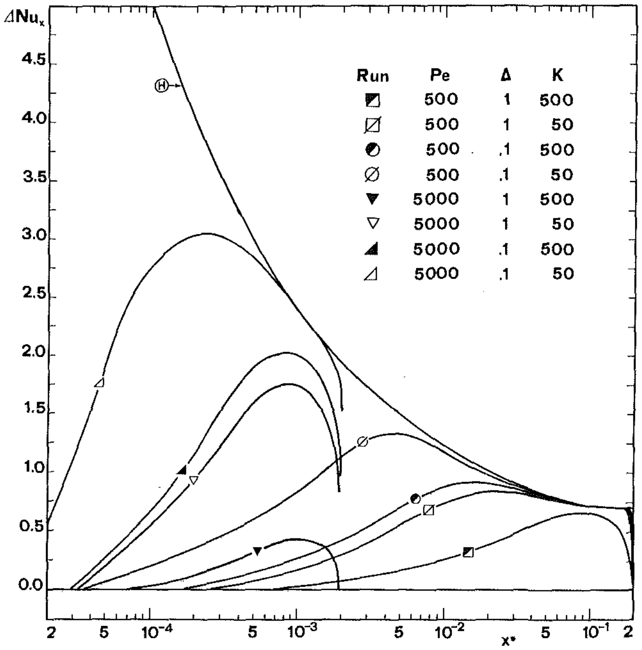

Fig. 6(*b*) Axial distribution of the difference ($Nu_x - Nu_{x,T}$), $L^* = 2.10^{-3}$ and 2.10^{-1}

The ratio $\Theta_{fb}/\Theta_{fb,H}$ is plotted versus x^* in Figs. 5(*a*) and 5(*b*).

The difference ΔNu_x between the actual values of the Nusselt number Nu_x and $Nu_{x,T}$ is presented in Figs. 6(*a*) and 6(*b*). All the plots of ΔNu_x depart from zero at some axial position whose downstream distance increases as the influence of conduction in the wall becomes more pronounced. The graphs show a common tendency towards the reference line Ⓗ , which is reached in a comparatively short distance with thermally thin tubes, while Nu_x always remains lower than $Nu_{x,H}$ when the wall is thermally thick. In all cases Nu_x is seen to decrease sharply near the end section. This effect is linked to the decrease of q_w^* observed in Figs. 3(*a*) and 3(*b*) in the same area and must be ascribed to the adiabatic condition imposed at $x^* = L^*$.

As far as relevance of the nondimensional parameters involved in the problem is concerned, the Peclet number as found over the range of values considered in this paper, has a decidedly higher influence on heat transfer than the wall to fluid conductivity ratio or the wall thickness parameter. In fact, increasing Pe 10 times produces a much stronger reduction in the effects of axial heat conduction than a corresponding reduction of K or Δ. At constant Pe and L^*, it is slightly more effective to modify Δ than to change K. Finally, to increase the length of the heated section, all other conditions remaining equal, produces a considerable reduction in the influence of axial conduction, as would be expected.

Concluding Remarks

The solution of coupled heat transfer problems generally requires a large amount of computational work both with analytical and numerical methods. In this paper a simple fast solution technique is presented to deal with a rather wide class of boundary-value conjugate problems. The strength of the procedure lies in the use of the superposition of known solutions at the solid-fluid interface. A convection equation is adopted for interface coupling. Two main advantages are got: (*i*) the Nusselt number distribution for a step change in the wall temperature or heat flux is the only datum needed from the literature. Results not only from analytical solutions but also from numerical methods can therefore be employed; (*ii*) the solution to the energy equation is avoided in the course of iterations, so that a considerable reduction of the computation time is achieved.

A finite element method is used to handle the energy equation in the solid phase, and hence, internal heat generation, the presence of inhomogeneous materials in the wall, as well as different thermal and geometrical conditions at the exterior boundaries can all be easily accomodated.

The method holding as long as the superposition principle applies, nonlinearities – such as that due to temperature dependent properties – are not allowed in the fluid phase. They can nonetheless be present in the energy equation for the solid or in the thermal condition at the outer boundary surface of the wall.

Simultaneously developing flow problems could also be dealt with, in principle. However use of Duhamel theorem may become very cumbersome in such a case.

Heat transfer to fully developed laminar flow through a duct is analysed in some depth. The effects of axial heat conduction along the wall on the heat flux, the interfacial temperature, the bulk temperature of fluid, and the Nusselt number are discussed. Results of previous investigation [13] are extended pointing out the influence of the Peclet number and the nondimensional pipe length. Unlike in [13] no unstable solution has been got at the lower values of the latter parameter.

From a practical point of view, it has been shown that axial conduction in the wall lowers the Nusselt number with respect to the theoretical predictions in the absence of axial conduction and causes redistribution of the heat flux supplied to the fluid. The latter effect is much more relevant than the former as the extent of the deviation of the Nusselt number values from case Ⓗ are of the order of 10 percent, while the heat flux may differ from the nominal value by 100 percent or more, near the inlet section. Furthermore sensible variations of the heat flux are present even where the Nusselt number closely approximates the theoretical values for the case Ⓗ. Therefore, axial heat conduction along the wall may in general not be overlooked, even if in some situations, where the wall may be defined as "thermally thin," a rough approximation may be obtained if the uniform heat flux condition is assumed at the interface.

References

1 Shah, R. K., and London, A. L., *Laminar Flow Forced Convection in Ducts*, Academic Press, New York, 1978.

2 Chu, S. C., and Bankoff, S. G., "Heat Transfer to Slug Flows with Finite Wall Thickness," *Applied Scientific Research*, Section A, Vol. 14, 1965, pp. 379–395.

3 Povarnitsyn, M. S., and Yurlova, E. V., "Calculation of the Temperature Field in a Plane Channel with Nonuniform Heating of Thermally Conducting Walls," *Journal of Engineering Physics*, Vol. 10, 1966, pp. 82–85.

4 Aleksashenko, V. A., "Conjugate Stationary Problem of Heat Transfer with a Moving Fluid in a Semi-Infinite Tube allowing for Viscous Dissipation," *Journal of Engineering Physics*, Vol. 14, 1968, pp. 55–58.

5 Luikov, A. V., Aleksashenko, V. A., and Aleksashenko, A. A., "Analytical Methods of Solution of Conjugated Problems in Convective Heat Transfer," *International Journal of Heat and Mass Transfer*, Vol. 14, 1971, pp. 1047–1056.

6 Faghri, M., and Sparrow, E. M., "Simultaneous Wall and Fluid Axial Conduction in Laminar Pipe-Flow Heat Transfer," ASME JOURNAL OF HEAT TRANSFER, Vol. 102, 1980, pp. 58–63.

7 Zariffeh, E. K., Soliman, H. M., and Trupp, A. C., "The Combined Effects of Wall and Fluid Axial Conduction on Laminar Heat Transfer in Circular Tubes," Paper FC-23, *Proceedings, Seventh Heat Transfer Conference*, Vol. IV, 1982, pp. 131–136.

8 Campo, A., and Rangel, R., "Lumped-system Analysis for the Simultaneous Wall and Fluid Axial Conduction in Laminar Pipe-flow Heat Transfer," *Physico Chemical Hydrodynamics*, Vol. 4, 1983, pp. 163–173.

9 Davis, E. J., and Gill, W. N., "The Effects of Axial Conduction in the Wall on Heat Transfer with Laminar Flow," *International Journal of Heat and Mass Transfer*, vol. 13, 1970, pp. 459–470.

10 Davis, E. J., and Cooper, T. J., "Thermal Entrance Effects in Stratified Gas-Liquid Flow: Experimental Investigation," *Chemical Engineering Science*, Vol. 24, 1969, pp. 509–520.

11 Shelyag, V. R., "Calculation of Temperature Fields in a Laminar Gas Flow in Flat Slot Channels," *Journal of Engineering Physics*, Vol. 12, 1967, pp. 227–234.

12 Mori, S., Shinke, T., Sakakibara, M., and Tanimoto, A., "Steady Heat Transfer to Laminar Flow between Parallel Plates with Conduction in Wall," *Heat Transfer, Japanese Research*, Vol. 5, n. 4, 1976, pp. 17–25.

13 Mori, S., Sakakibara, M., and Tanimoto, A., "Steady Heat Transfer to Laminar Flow in Circular Tube with Conduction in the Tube Wall," *Heat Transfer, Japanese Research*, Vol. 3, no. 2, 1974, pp. 37–46.

14 Mori, S., Inoue, T., and Tanimoto, A., "Heat Transfer to Laminar Flow with Temperature—Dependent Heat Generation," *The Canadian Journal of Chemical Engineering*, Vol. 55, 1977, pp. 138–144.

15 Mori, S., Inoue, T., and Tanimoto, A., "Heat Transfer to Laminar Flow between Parallel Plates with Interfacial Heat Generation," *Journal of Chemical Engineering of Japan*, Vol. 11, 1978, pp. 83–88.

16 Mori, S., Kawamura, Y., and Tanimoto, A., "Conjugated Heat Transfer to Laminar Flow with Internal Heat Source in a Parallel Plate Channel," *The Canadian Journal of Chemical Engineering*, Vol. 57, 1979, pp. 698–703.

17 Mori, S., Kataya, M., and Tanimoto, A., "Performance of Counterflow, Parallel Plate Heat Exchangers under Laminar Flow Conditions," *Heat Transfer Engineering*, Vol. 2, 1980, pp. 28–38.

18 Davis, E. J., and Venkatesh, S., "The Solution of Conjugated Multiphase Heat and Mass Transfer Problems," *Chemical Engineering Science*, Vol. 34, 1979, pp. 775–787.

19 Kuznetzov, Yu. N., and Belousov, V. P., "Unsteady Turbulent Conjugated Heat Transfer in Tubes," Paper FC 9.3, *Proceedings, Fifth Heat Transfer Conference*, Vol. II, 1974, pp. 349–352.

20 Sakakibara, M., and Endoh, K., "Effect of Conduction in Wall on Heat Transfer with Turbulent Flow between Parallel Plates," *International Journal of Heat and Mass Transfer*, Vol. 20, 1977, pp. 507–516.

21 Shulman, Z. P., Zaltsgendler, E. A., and Gleb, V. K., "Conjugated Problem of Convective Heat Transfer in Recuperative Heat Exchangers with a Non-Newtonian Heat Carrier," Paper HX-31, *Proceedings, Sixth Heat Transfer Conference*, Vol. IV, 1978, pp. 367–372.

22 Zinnes, A. E., "The Coupling of Conduction with Laminar Natural Convection from a Vertical Flat Plate with Arbitrary Surface Heating," ASME JOURNAL OF HEAT TRANSFER, Vol. 92, 1970, pp. 528–535.

23 Sunden, B., "Conjugated Heat Transfer from Circular Cylinders in Low Reynolds Number Flow," *International Journal of Heat and Mass Transfer*, Vol. 23, 1980, pp. 1359–1367.

24 Lock, G. S. H., and Ko, R. S., "Coupling through a Wall between two Free Convective Systems," *International Journal of Heat and Mass Transfer*, Vol. 16, 1973, pp. 2087–2096.

25 Sparrow, E. M., and Faghri, M., "Fluid-to-Fluid Conjugate Heat Transfer for a Vertical Pipe—Internal Forced Convection and External Natural Convection," ASME JOURNAL OF HEAT TRANSFER, Vol. 102, 1980, pp. 402–407.

26 Sparrow, E. M., and Prakash, C., "Interaction between Internal Natural Convection in an Enclosure and an External Natural Convection Boundary-Layer Flow," *International Journal of Heat and Mass Transfer*, Vol. 24, 1981, pp. 895–907.

27 Patankar, S. V., "A Numerical Method for Conduction in Composite Materials, Flow in Irregular Geometries and Conjugate Heat Transfer," Paper CO-14, *Proceedings, Sixth International Heat Transfer Conference*, Vol. III, 1978, pp. 297–302.

28 Sparrow, E. M., and Chukaev, A., "Forced-Convection Heat Transfer in a Duct Having Spanwise-Periodic Rectangular Protuberances," *Numerical Heat Transfer*, Vol. 3, 1980, pp. 149–167.

29 Wylie, C. R., *Advanced Engineering Mathematics*, McGraw-Hill Kogakusha, Tokyo, 1975.

30 Karvinen, R., "Note on Conjugated Heat Transfer in a Flat Plate," *Letters in Heat and Mass Transfer*, Vol. 5, 1978, pp. 197–202.

31 Karvinen, R., "Some New Results for Conjugated Heat Transfer in a Flat Plate," *International Journal of Heat and Mass Transfer*, Vol. 21, 1978, pp. 1261–1264.

32 Pagliarini, G., "Il metodo degli elementi finiti nel calcolo dei ponti termici delle strutture edilizie. L'uso di elementi con modello di temperatura del secon do ordine," *Condizionamento dell'Aria, Riscaldamento, Refrigerazione*, Vol. 25, 1981, pp. 199–208.

33 Rotem, Z., "The Effect of Thermal Conduction of the Wall upon Convection from a Surface in a Laminar Boundary Layer," *International Journal of Heat and Mass Transfer*, Vol. 10, 1967, pp. 461–466.

Analysis of Laminar Flow and Heat Transfer in the Entrance Region of an Internally Finned Circular Duct

C. Prakash

Ye-Di Liu[1]

Department of Mechanical Engineering,
Aeronautical Engineering
and Mechanics,
Rensselaer Polytechnic Institute,
Troy, N.Y. 12181

Steady, laminar, forced convection flow and heat transfer in the entrance region of an internally finned circular duct has been analyzed by numerically integrating the governing partial differential equations. The fins are radial, continuous, and of zero thickness. Two types of thermal boundary conditions are considered: (i) a uniform heat input per unit axial length with peripherally uniform temperature at any cross-section, and (ii) uniform temperature both axially and peripherally. Results exhibit the expected high-pressure gradients and heat transfer coefficients in the entrance region, approaching, asymptotically, the fully developed values at large axial distance. Results are presented for 8, 16, and 24 fins, and for the fin height to duct radius ratio 0.3, 0.6, and 1. The Prandtl number is kept as .707 corresponding to air.

Introduction

For the purpose of heat transfer augmentation, internal fins are often employed in circular tubes. Such internally finned tubes find application in many compact heat exchange devices [1] and have been the subject of many research investigations [2-14]. For laminar forced convection, the available results have been summarized by Shah and London [15]. A survey of [15] revealed only fully developed results, with no results for the hydrodynamic or thermal entry region. It is known, however, that the entrance region can be very important because of the very large pressure gradients and heat transfer coefficients there; for example, for an isothermal duct, a major fraction of the total heat transfer occurs in just the entrance region. It is this recognition that provided the motivation for the present investigation.

Analysis

The Problem Definition. The problem being investigated is schematically sketched in Fig. 1. It concerns the prediction of steady, forced, laminar flow and heat transfer in an internally finned circular tube of diameter D (radius $= a = D/2$). The fluid is assumed to be incompressible and of constant properties, and viscous dissipation and compression work are assumed to be negligible in the energy equation. The fins are continuous, of zero thickness, and uniformly placed on the inside of the duct. h represents the height of the fins and is clearly limited to $0 \leq h \leq a$. The fluid enters the duct with a uniform inlet velocity $\bar{w}$ and a uniform temperature T_i.

Two types of thermal boundary conditions are considered: (*i*) a uniform heat input per unit axial length with a uniform temperature at any cross section. This is the $H1$ boundary condition as per the nomenclature used by Shah and London [15]; (*ii*) Uniform temperature both axially and peripherally. This is called the T boundary condition in [15]. Implicit in these boundary conditions is the assumption that the fins are made of a highly conducting material and are 100 percent efficient.

Mathematical Formulation. The problem under investigation is a three-dimensional boundary layer problem. In the present analysis we treat the flow to be "parabolic." Thus, as in any boundary layer analysis, the flow is assumed to have a predominant direction, the axial (z) direction in Fig. 1, along which the diffusion of mass, momentum, and energy can be neglected. Also, along the main flow direction, downstream pressure has no effect on the conditions upstream. This latter assumption is implicit in the two-dimensional boundary layer analysis also, and the matter has been discussed at length by Patankar and Spalding [16]. The parabolic assumption implies that the pressure p can be written as $p = \bar{p} + p'$ where $\bar{p}$ is the average pressure over the duct cross section, and p' is the small pressure variation governing the flow distribution in the cross-stream plane. The

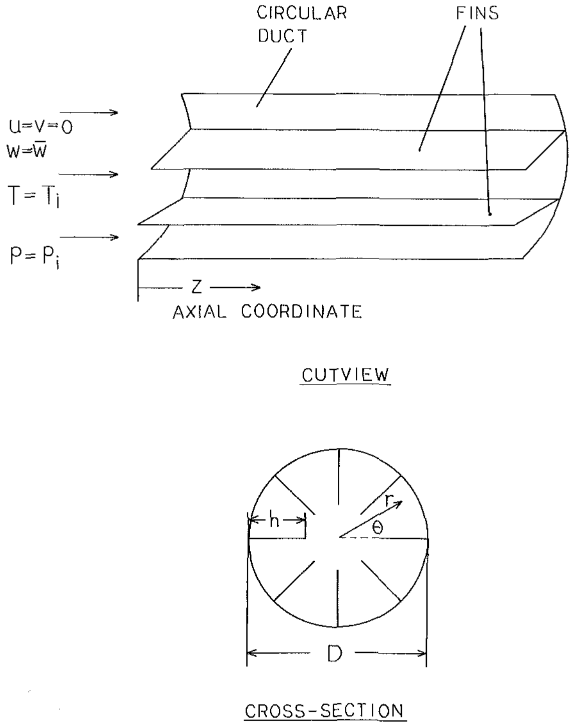

Fig. 1 An internally finned circular duct

---

[1] Visiting scholar from the People's Republic of China.

Contributed by the Heat Transfer Division for publication in the JOURNAL OF HEAT TRANSFER. Manuscript received by the Heat Transfer Division May 19, 1983.

velocity component in the main flow direction is driven by the gradients of $\bar{p}$ (i.e., the term $d\bar{p}/dz$), while for the cross-stream flow the gradients of p' enter into the momentum equations. As a result, the problem can be solved by employing a marching-type procedure which involves solution of a series of two-dimensional elliptic problems in the cross-stream plane.

Consider the r, θ, z polar cylindrical coordinate shown in Fig. 1. Let v, u, and w represent the velocity components along the r-, θ-, and z-coordinates respectively, and let T represent the temperature. The parabolized Navier–Stokes equations governing the flow are given as:

continuity:

$$\frac{1}{r}\frac{\partial}{\partial r}(rv)+\frac{1}{r}\frac{\partial u}{\partial \theta}+\frac{\partial w}{\partial z}=0 \tag{1}$$

r-momentum:

$$v\frac{\partial v}{\partial r}+\frac{u}{r}\frac{\partial v}{\partial \theta}+w\frac{\partial v}{\partial z}=-\frac{1}{\rho}\frac{\partial p'}{\partial r}+\nu\left[\frac{1}{r}\frac{\partial}{\partial r}\left(r\frac{\partial v}{\partial r}\right)+\frac{1}{r^2}\frac{\partial^2 v}{\partial \theta^2}\right]+\frac{u^2}{r}-\nu\left[\frac{v}{r^2}+\frac{2}{r^2}\frac{\partial u}{\partial \theta}\right] \tag{2}$$

θ-momentum:

$$v\frac{\partial u}{\partial r}+\frac{u}{r}\frac{\partial u}{\partial \theta}+w\frac{\partial u}{\partial z}=-\frac{1}{\rho r}\frac{\partial p'}{\partial \theta}+\nu\left[\frac{1}{r}\frac{\partial}{\partial r}\left(r\frac{\partial u}{\partial r}\right)+\frac{1}{r^2}\frac{\partial^2 u}{\partial \theta^2}\right]-\frac{uv}{r}+\nu\left[\frac{2}{r^2}\frac{\partial v}{\partial \theta}-\frac{u}{r^2}\right] \tag{3}$$

z-momentum:

$$v\frac{\partial w}{\partial r}+\frac{u}{r}\frac{\partial w}{\partial \theta}+w\frac{\partial w}{\partial z}=-\frac{1}{\rho}\frac{d\bar{p}}{dz}+\nu\left[\frac{1}{r}\frac{\partial}{\partial r}\left(r\frac{\partial w}{\partial r}\right)+\frac{1}{r^2}\frac{\partial^2 w}{\partial \theta^2}\right] \tag{4}$$

energy:

$$v\frac{\partial T}{\partial r}+\frac{u}{r}\frac{\partial T}{\partial \theta}+w\frac{\partial T}{\partial z}=\frac{k}{\rho c_p}\left[\frac{1}{r}\frac{\partial}{\partial r}\left(r\frac{\partial T}{\partial r}\right)+\frac{1}{r^2}\frac{\partial^2 T}{\partial \theta^2}\right] \tag{5}$$

overall mass conservation:

$$\iint_{\text{duct}} \rho w dA=\dot{m}=\text{ same for all } z \tag{6}$$

Because diffusion has been neglected in the main flow direction, there is no term of the type $\partial^2/\partial z^2$ on the right-hand side of equations (2–5). Equations (2–4) determine the velocity components, and the cross-stream pressure p' is determined by the continuity constraint expressed by equation (1). The axial pressure gradient $d\bar{p}/dz$ is determined by the statement of overall mass conservation, equation (6), and the temperature is determined by equation (5). Different symbols are described in the Nomenclature.

The boundary conditions supplementing these equations are given as follows:

at the inlet of the duct ($z=0$)

$$\begin{aligned} &u=v=0\\ &w=\bar{w};\ \text{uniform}\\ &T=T_i;\ \text{uniform}\\ &\bar{p}=p_i;\ \text{uniform}\end{aligned} \tag{7}$$

at the fin surface or base tube

$$\begin{aligned} &u=v=w=0\\ &T=T_w\end{aligned} \tag{8}$$

Nomenclature

a = radius of the circular duct ($=D/2$)
c_p = specific heat of the fluid
D = diameter of the circular duct ($=2a$)
D_h = equivalent hydraulic diameter
f = friction factor
h = fin height
k = thermal conductivity of the fluid
K = incremental pressure drop, equation (17)
L_h = hydrodynamic entrance length
L_t = thermal entrance length
$\dot{m}$ = mass flow rate through the duct
N = number of fins
Nu = Nusselt number
Pr = Prandtl number
p = pressure
p' = pressure driving the cross-stream flow
$\bar{p}$ = cross-section average pressure at any axial location
p_i = pressure at the inlet plane
Δp = $p_i-\bar{p}$, the pressure drop
Q = total heat transfer up to z
Q' = heat input per unit axial length for the $H1$ boundary condition
Re = Reynolds number
r = radial coordinate
T = temperature
T_w = uniform duct and fin temperature for the T boundary condition; local duct and fin temperature at any cross-section for the $H1$ boundary condition
T_b = mean or bulk temperature at any axial location
T_i = uniform temperature of the fluid at the inlet
ΔT_{lm} = log-mean temperature difference for the T boundary condition
u = angular velocity component
v = radial velocity component
w = axial velocity component
$\bar{w}$ = uniform axial velocity at the inlet plane = the average axial velocity at any section
z = axial distance
Θ = dimensionless temperature
θ = angular coordinate
ρ = density of the fluid
μ = coefficient of viscosity of the fluid
ν = kinematic viscosity

Subscripts

f.d. = corresponding to the fully developed conditions
$H1$ = corresponding to the case of uniform heat input per unit axial length with a peripherally uniform temperature at any cross-section – the $H1$ boundary condition
h = based on the equivalent hydraulic diameter; the exception is L_h where h is to identify it as the hydrodynamic entrance length
T = corresponding to the case of a uniform temperature both axially and peripherally – the T boundary condition

Superscripts

$-$ = average value

Solution Methodology. For the case of isothermal fins and base tube, the temperature T_w is known and there is no difficulty.

For the second type of thermal boundary condition, involving a uniform heat input per unit axial length, the temperature T_w is unknown and is a function of z. Instead, what is known is the bulk temperature of the fluid, which can be obtained by a heat balance as

$$T_b = T_i + \frac{Q' z}{\dot{m} c_p} \tag{9}$$

Q' being the heat input per unit axial length. The procedure that was employed to handle this boundary condition involved adjusting the wall temperature iteratively till the computed bulk temperature agreed with the exact bulk temperature given by equation (9). Thus, suppose computations are being performed at a cross-stream plane located at some axial coordinate z. Let $T_w{}^k$ be the wall temperature at z at the kth iteration, leading to a computed bulk temperature $T_b{}^k$. For the next iteration, T_w was adjusted by the equation.

$$T_w{}^{k+1} = (T_w{}^k)\,\frac{T_b}{T_b{}^k} \tag{10}$$

where T_b is the desired bulk temperature given by equation (9). When the iterations converge, $T_b = T_b{}^k$ and $T_w{}^{k+1} = T_w{}^k$. About four to five iterations were found to be enough to get the convergence of wall temperature to four significant digits. These iterations do not pose any special demand on the computational procedure because iterations have to be performed at each marching step, anyway, to account for nonlinearity in the flow equations.

Dimensionless Formulation. Define the Reynolds number Re and Prandtl number Pr as

$$\mathrm{Re} = \frac{\bar{w} D}{\nu} \tag{11}$$

$$\mathrm{Pr} = \frac{\mu c_p}{k} \tag{12}$$

The problem can be nondimensionalized by introducing the following dimensionless variables.

$$R = r/D;\ Z = z/(D.\mathrm{Re});\ V = vD/\nu;\ U = uD/\nu;$$
$$W = w/\bar{w};\ \bar{P} = \bar{p}/(\rho \bar{w}^2);$$
$$P' = p' D^2/(\rho \nu^2);\ \Theta_T = (T - T_i)/(T_w - T_i);$$
$$\Theta_{H1} = (T - T_i)/(Q'/k)$$

where Θ_T and Θ_{H1} represent dimensionless temperatures for the T and $H1$ boundary conditions, respectively. In dimensionless form, the problem is characterized by the following parameters

(*i*) N, the number of fins
(*ii*) h/a (or h/D) representing the dimensionless fin height
(*iii*) Pr, the Prandtl number

Computations were made for N = 8, 16, and 24; h/a = 0.3, 0.6, and 1; and the Prandtl number was kept fixed as .707 corresponding to air.

Fully Developed Region. Sufficiently far downstream from the inlet plane, the flow becomes fully developed. This region is characterized by no cross-stream flow, i.e., $u = v = 0$; the axial velocity w is independent of z; the pressure decreases linearly with z; and the friction factor, Nusselt numbers, etc., attain constant values that are independent of z. The results in the fully developed region can be obtained in two ways: one can either carry out the marching solution very far downstream, or one can solve the fully developed flow equations separately. These equations are obtained from equations (1-5) by setting $u = 0$, $v = 0$, w independent of z, etc. This yields two Poisson equations (one for w and one for T), which can be solved by any two-dimensional Poisson equation solver. In the present investigation, we followed the second approach. That is, fully developed results were obtained by solving the appropriate two-dimensional Poisson equations separately.

Computational Procedure. The governing differential equations were integrated using the control volume based, fully implicit, finite difference method of Patankar and Spalding [16]. The fully developed results were obtained by using the two-dimensional counterpart of this algorithm. For numerical solution, the dimensionless equations were employed. Because of symmetry, we only need to consider flow in an angular sector of angle π/N, extending from a fin to midway between the next fin. A 17 × 23 (angular × radial) grid was employed in the cross-stream plane. Both the developing and fully developed results were obtained, though separately, but using identical grid layout. The fully developed results were obtained first. Then the results in the developing region were computed, and the solution was marched far enough so that the local friction factors and Nusselt numbers, etc., were within 1 percent of their fully developed values. This length was covered in about 100 marching steps. A typical estimate of the dimensionless entrance length (to be defined later) is $\simeq 0.1$. The first dimensionless step size was taken as 10^{-3} times this value, i.e., $= 10^{-4}$. Starting with this value, subsequent step sizes were gradually increased using the relation $\Delta z = (1.1)$ (previous Δz). At each marching step, sufficient number of iterations (usually about 6) were performed to ensure that the local values of the friction factor, Nusselt numbers, velocity at some sample points, etc., had converged to four significant digits.

Hydraulic Diameter. For internal flows, the equivalent hydraulic diameter D_h is often used as the characteristic length. It is defined as

$$D_h = \frac{4(\text{cross-sectional area})}{\text{wetted perimeter}} = \frac{\pi D^2}{(\pi D + 2Nh)} \tag{13}$$

and the Reynolds number based on D_h is defined as

$$\mathrm{Re}_h = \frac{\bar{w} D_h}{\nu} \tag{14}$$

Use of D_h and Re_h has been known to facilitate the development of correlations. In the present paper, both (D_h, Re_h) and (D, Re) are used depending on the suitability; some results are presented both ways.

Hydrodynamic Results

Let $(d\bar{p}/dz)$ be the local pressure gradient at some axial location. In dimensionless form, it can be expressed as a *local friction factor f* defined as

$$f = \frac{(-d\bar{p}/dz) D/4}{(\rho \bar{w}^2)/2} \tag{15}$$

Using D_h as the characteristic length, the local friction factor f_h is defined as

$$f_h = \frac{(-d\bar{p}/dz) D_h/4}{(\rho \bar{w}^2)/2} \tag{16}$$

Once the flow gets fully developed, the friction factor becomes inversely proportional to the Reynolds number – i.e., $f\mathrm{Re}$ (or $f_h \mathrm{Re}_h$) becomes independent of z.

Let $\bar{p}(z)$ be the pressure at some axial location z. The pressure drop from inlet up to z is $\Delta p = p_i - \bar{p}(z)$, where p_i is the pressure at the inlet plane. This pressure drop can be expressed as

Table 1 Friction factor for fully developed flow

$(f_h\,\mathrm{Re}_h)_{\mathrm{f.d.}}$

	h/a \ N	8	16	24
(*a*)	0	15.96		
	0.3	8.960	6.131	4.245
	0.6	15.24	12.65	9.397
	1	13.66	12.86	12.51

$(f\mathrm{Re})_{\mathrm{f.d.}}$

	h/a \ N	8	16	24
(*b*)	0	15.96		
	0.3	27.88	39.18	46.00
	0.6	97.37	208.1	293.0
	1	171.8	477.4	933.8

Table 2 Incremental pressure drop in the entrance region; values extrapolated from Fig. 3

h/a \ N	8	16	24
0	1.25		
0.3	2.44	4.11	5.40
0.6	2.85	10.7	23.5
1	1.58	1.79	1.93

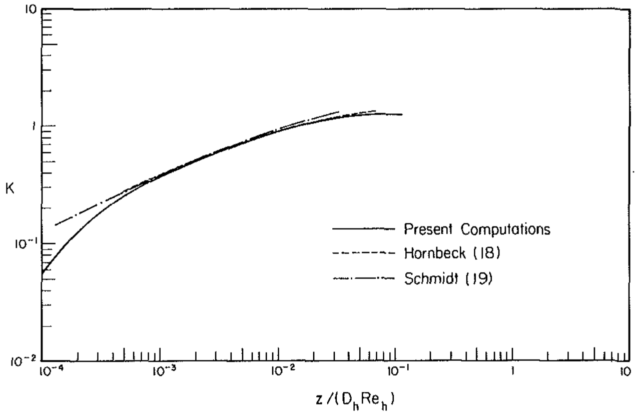

Fig. 2 Incremental pressure drop in the entrance region of a circular duct

$$\frac{\Delta p(z)}{(\rho\bar{w}^2/2)} = \frac{[\Delta p(z)]_{\mathrm{f.d.}}}{(\rho\bar{w}^2/2)} + K(z) \tag{17}$$

where $[\Delta p(z)]_{\mathrm{f.d.}}$ is the pressure drop that would have occurred if the flow were fully developed all the way from the inlet, and $K(z)$ is the incremental or extra pressure drop due entrance region effects. It is easy to see

$$\frac{\Delta p(z)}{(\rho\bar{w}^2/2)} = (f\mathrm{Re})_{\mathrm{f.d.}}\left(\frac{4z}{D\mathrm{Re}}\right) + K(z)$$

$$= (f_h\mathrm{Re}_h)_{\mathrm{f.d.}}\left(\frac{4z}{D_h\mathrm{Re}_h}\right) + K(z) \tag{18}$$

where $(f\mathrm{Re})_{\mathrm{f.d.}}$ and $(f_h\mathrm{Re}_h)_{\mathrm{f.d.}}$ are the fully developed values of $(f\mathrm{Re})$ and $(f_h\mathrm{Re}_h)$, respectively. The main hydrodynamic quantities of interest, therefore, are the friction factor for the fully developed flow and the incremental pressure drop K as a function of the axial distance z. Knowing these, the pressure drop up to any axial distance can be calculated.

Friction Factor for Fully Developed Flow. The fully developed friction factors as obtained in the present study are given in Table 1. Both $(f\mathrm{Re})_{\mathrm{f.d.}}$ and $(f_h\mathrm{Re}_h)_{\mathrm{f.d.}}$ are given for convenience.

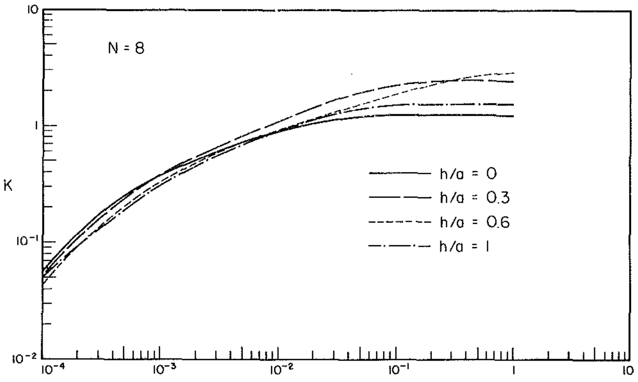

Fig. 3(*a*) Incremental pressure drop for a finned duct: $N = 8$

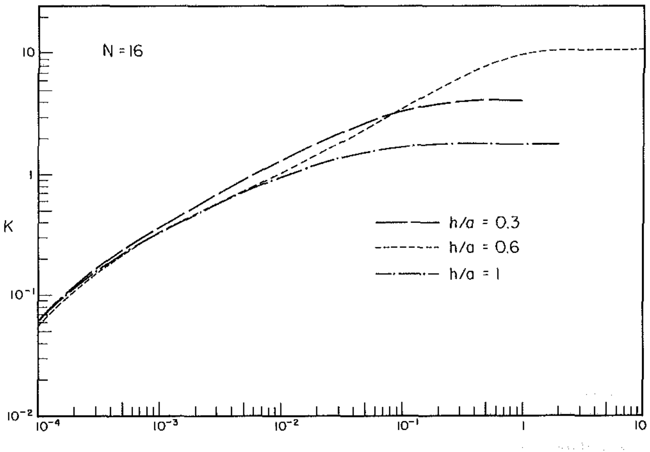

Fig. 3(*b*) Incremental pressure drop for a finned duct: $N = 16$

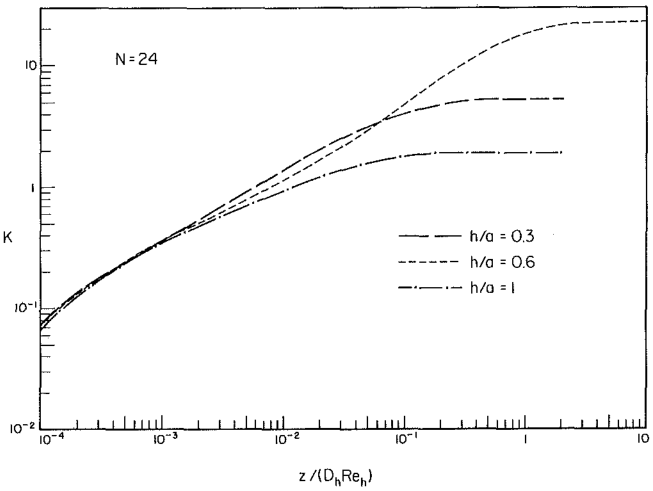

Fig. 3(*c*) Incremental pressure drop for a finned duct: $N = 24$

To examine the adequacy of the grid employed, the fully developed friction factors of Table 1 were compared with those obtained using a fine 32 × 42 grid. The results of the 32 × 42 grid were found to be slightly higher: for $h/a = 0.3$, the agreement was within 3.5 percent; for $h/a = 0.6$, the agreement was within 5 percent; and for $h/a = 1$, the agreement was within 1 percent.

Hu and Chang [10] have analyzed the fully developed flow analytically, and the numerical values of $f\mathrm{Re}$ obtained by them have been listed by Shah and London [15]. From Table 127 of [15], the $f\mathrm{Re}$ values of Hu and Chang were found to be slightly higher than those obtained presently: both, as compared with the fine 32 × 42 grid results, and the results of Table 1. For $h/a = 0.6$, the results of Hu and Chang are within 2 percent of 32 × 42 grid results, and within 6 percent of the results of Table 1.

The $h/a = 1$ case corresponds to a circular sector duct and has been analyzed, among others, by Chiranjivi and Vidyanidhi [17]. A discussion of their work has been presented by Shah and London [15], and the fRe values have been listed in Table 76 of [15]. These values are also slightly higher than those obtained presently; the agreement is within 1 percent for the 32 × 42 grid, and within 2 percent of the results of Table 1.

Fully developed flow has also been analyzed numerically by Masliyah and Nandakumar [11], and more extended version of their results has been presented by Shah and London [15]. From Table 127 of [15], the fRe values obtained by Masliyah and Nandakumar were found to be consistently higher: not only compared with those computed presently, but also with the analytical results of Hu and Chang [10]. For $h/a = 0.6$, the values of Masliyah are greater by about 10–15 percent. For $h/a = 1$ the agreement is better, the difference being ~ 2 percent.

Variation of Incremental Pressure Drop in the Entrance Region. In Fig. 2, the variation of incremental pressure drop K in the entrance region of a finless circular tube is presented. A comparison is made with the results of Hornbeck [18] who numerically solved the linearized form of the momentum equations, and with the results of Schmidt [19] who solved the complete Navier–Stokes equations. As can be seen, the agreement is quite good. The noticeable difference is limited to a very small region near the inlet ($z/D_h \text{ Re}_h < 4 \times 10^{-4}$), which was covered in the first four steps of the present marching solution.

Variation of the incremental pressure drop in the entrance region of a finned duct is presented in Figs. (3a–c). Plotted against the dimensionless axial distance $z/D_h \text{ Re}_h$, the results for different N and h/a cases fall close to each other in the near entrance region. As expected, K increases with z, approaching, asymptotically, a constant value at large axial distance.

Total Incremental Pressure Drop $K(\infty)$. The asymptotic value that K approaches for large z is called $K(\infty)$, and it represents the total incremental pressure drop due to the entrance effects. The value of $K(\infty)$, as obtained by graphically extrapolating the results of Figs. 3(a–c), are summarized in Table 2.

Bender [20] obtained $K(\infty) = 1.25$ theoretically for a circular duct. This value agrees with Table 2, and it approximates a mean of the experimental values and a mean of the numerical values derived from Table 10 of [15].

For $h/a = 1$, the circular sector duct case, Sparrow and Haji-Sheikh [21] obtained $K(\infty) = 1.657$, 2.0, and 2.235 corresponding to $N = 8$, 16, and 24, respectively. The agreement is favorable with values listed in Table 2. Some difference occurs because the analysis of [21] is approximate and does not account for the effect of secondary flows in the cross-stream plane.

Results of Table 2 indicate that for a given fin height, the incremental pressure drop increases with the number of fins. For a given number of fins, the incremental pressure drop first increases and then decreases with increasing fin height.

Estimate of the Hydrodynamic Entrance Length. Conventionally [15], the hydrodynamic entrance length L_h is defined as the distance it takes for the axial velocity at the centerline to reach 99 percent of its fully developed value. According to this definition, the present computations gave a value of $L_h/(D_h\text{Re}_h) = .054$ for a circular duct. Using a linearized analysis, Hornbeck [18] obtained $L_h/D_h\text{Re}_h = .056$.

Table 3 Estimate of the hydrodynamic entrance length L_h

$L_h/(D_h \text{ Re}_h)$

	h/a \ N	8	16	24
(a)	0	.0415		
	0.3	.138	.280	.452
	0.6	.205	.888	1.94
	1	.0659	.0871	.102

$L_h/(D \text{ Re})$

	h/a \ N	8	16	24
(b)	0	.0415		
	0.3	.0443	.0438	.0417
	0.6	.0320	.0540	.0622
	1	.00524	.00235	.00136

The definition of L_h given above cannot be extended to an internally finned duct because the maximum axial velocity does not, in general, occur at the duct centerline. Therefore, some other procedure for defining L_h is necessary. We propose the following definition: The hydrodynamic entrance length L_h is the distance it takes for the local friction factor to be equal to 1.05 times its fully developed value. That is, we define L_h as the distance it takes for the local friction factor to fall to 5 percent of its fully developed value. This definition is consistent with the conventional definition of thermal entry length to be discussed later.

Variation of L_h so defined is presented in Table 3. In Table 3(a), the values of the dimensionless group $L_h/(D_h\text{Re}_h)$ are listed. A more meaningful dimensionless representation would be $L_h/(D\text{Re})$ from which the effect of N and h on L_h for fixed mass flow rate can be easily discerned. This dimensionless group is listed in Table 3(b).

Suppose the tube diameter D and the mass flow rate through the duct, i.e., Re, are kept fixed. Then increasing N or h reduces the extent to which the boundary layers must grow for the flow to become fully developed. However, increasing N or h also increases the core flow velocity implying thinner boundary layers. In addition, N and h have a strong effect on the strength of the secondary cross-stream flow which can take a long axial length to decay. The effect of N and h on L_h for fixed D and Re is therefore mixed as is displayed by the results of Table 3(b).

Thermal Results: Uniform Heat Input per Unit Axial Length – the $H1$ Boundary Condition

Let $T_w(z)$ be the peripherally uniform temperature of the base tube and the fins at an axial location z. The local bulk temperature $T_b(z)$ is given by equation (9). The local Nusselt number can be defined as

$$\text{Nu}_{h,H1} = \frac{Q'/(\pi D + 2Nh)}{(T_w - T_b)} \frac{D_h}{k} \tag{19}$$

or, basing everything on the tube diameter D, as

$$\text{Nu}_{H1} = \frac{Q'/(\pi D)}{(T_w - T_b)} \frac{D}{k} \tag{20}$$

$\text{Nu}_{h,H1}$ accounts for the total (tube + fin) surface area for computing the heat flux and uses the hydraulic daimeter D_h as the characteristic length. The subscript h is to indicate the use of D_h, and the subscript $H1$ identifies the thermal boundary condition. The Nusselt number Nu_{H1} as defined by equation (20) uses an average heat flux based on the base tube area and uses the duct diameter D as the characteristic length. The

Table 4 Fully developed Nusselt number for the $H1$ boundary condition

$(\mathrm{Nu}_{h,H1})_{\mathrm{f.d.}}$

	h/a \ N	8	16	24
(a)	0	4.371		
	0.3	1.686	.7992	.4457
	0.6	2.701	.8097	.2936
	1	3.306	2.868	2.680

$(\mathrm{Nu}_{H1})_{\mathrm{f.d.}}$

	h/a \ N	8	16	24
(b)	0	4.371		
	0.3	5.245	5.107	4.830
	0.6	17.26	13.32	9.154
	1	41.58	106.5	200.0

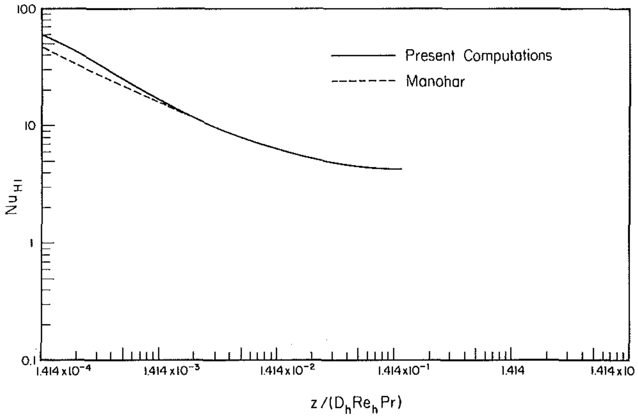

Fig. 4 Local Nusselt number for a circular duct: $H1$ boundary condition

effect of N and h on the heat transfer performance can be discerned more easily and directly from Nu_{H1}.

Nusselt Number for Fully Developed Flow. The fully developed Nusselt number values are listed in Table 4.

As mentioned before, to examine the adequacy of the grid used, fully developed results were also computed on a very fine 32 × 42 grid. For $h/a = 0.3$ and $h/a = 0.6$ the fine grid values were slightly higher than the values listed in Table 4: for $h/a = 0.3$ the agreement was within 1 percent and for $h/a = 0.6$ the agreement was within 5 percent. For the case of $h/a = 1$, the fine grid values were slightly lower and the agreement was within 1 percent.

For $h/a = 1$, which corresponds to a circular sector duct, the present thermal boundary condition has been considered by Haji-Sheikh [22]. From Table 76 of Shah and London [15], the values of Sparrow and Sheikh were found to be slightly lower than those listed in Table 4 but the agreement was within 2 percent.

The $H1$ boundary condition for fully developed flow was also considered by Masliyah and Nandakumar [11]. Using Table 1 of [11] or Table 128 of [15], the Nusselt number values of Masliyah and Nandakumar were found to be higher by about 20 percent for the $h/a = 0.6$ case. It must be recalled here that the $f\mathrm{Re}$ results of Masliyah and Nandakumar are also higher by about the same margin: not only compared with present computations but also with the analytical results of Hu and Chang [10]. For the $h/a = 1$ case, the results of Masliyah and Nandakumar are slightly lower than those computed presently but the agreement is within 5 percent.

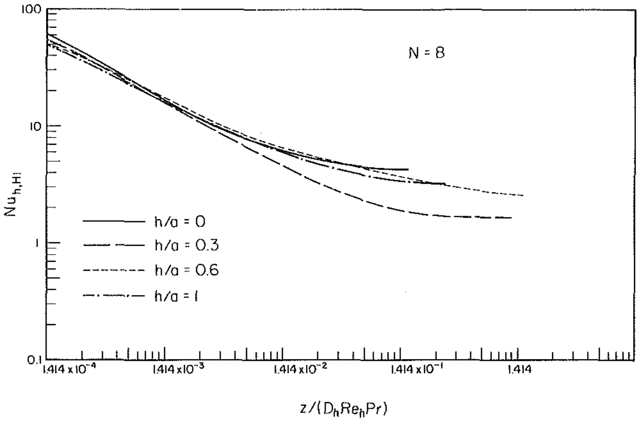

Fig. 5(a) Local Nusselt number for a finned duct with $H1$ boundary condition: $N = 8$

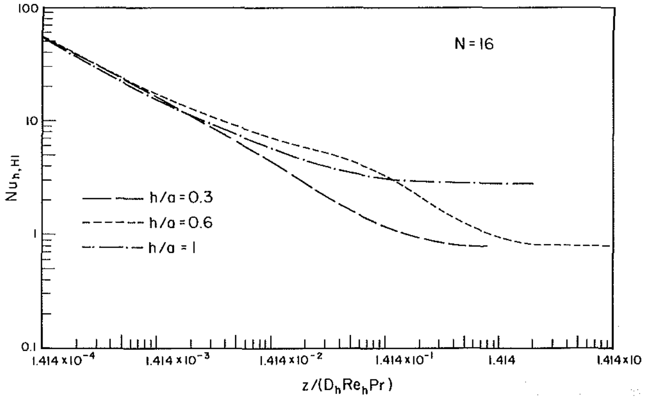

Fig. 5(b) Local Nusselt number for a finned duct with $H1$ boundary condition: $N = 16$

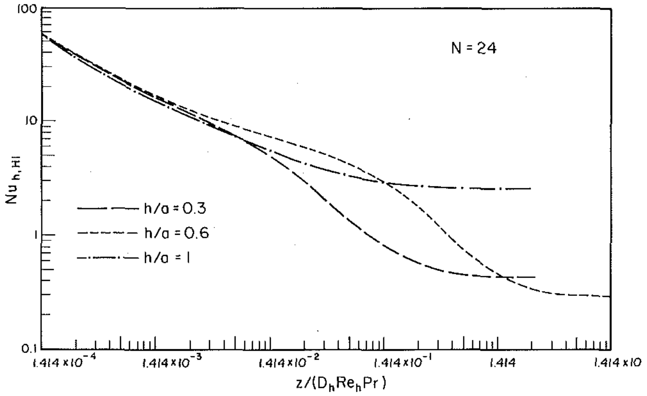

Fig. 5(c) Local Nusselt number for a finned duct with $H1$ boundary condition: $N = 24$

Variation of the Local Nusselt Number in the Entrance Region. In Fig. 4, variation of the local Nusselt number in the entrance region of a circular duct is displayed. A comparison is made with the results of Manohar [23] as presented in Table 22 of Shah and London [15]. For z/D_h Re_h Pr $> 6 \times 10^{-4}$ (a distance covered by the first four steps of the present marching solution) the agreement is quite good.

For the finned duct, the variation of the local Nusselt number is displayed in Figs. 5(a–c). As expected, the Nusselt number is very large in the entrance region. It decreases with increasing axial distance approaching, asymptotically, the fully developed values. Use of the equivalent hydraulic diameter D_h as the characteristic length seems appropriate for

Table 5 Estimate of the thermal entrance length for the $H1$ boundary condition

$L_{t,H1}/(D_h \, \mathrm{Re}_h \, \mathrm{Pr})$

	h/a \ N	8	16	24
(a)	0	.0572		
	0.3	.205	.417	.669
	0.6	.542	1.99	3.61
	1	.0974	.141	.170

$L_{t,H1}/(D \, \mathrm{Re} \, \mathrm{Pr})$

	h/a \ N	8	16	24
(b)	0	.0572		
	0.3	.0658	.0653	.0618
	0.6	.0848	.121	.116
	1	.00774	.00379	.00227

Table 6 Fully developed Nusselt number for the T boundary condition

$(\mathrm{Nu}_{h,T})_{\mathrm{f.d.}}$

	h/a \ N	8	16	24
(a)	0	3.658		
	0.3	1.321	.6249	.3562
	0.6	1.374	.3979	.1704
	1	2.643	2.170	1.925

$(\mathrm{Nu}_T)_{\mathrm{f.d.}}$

	h/a \ N	8	16	24
(b)	0	3.658		
	0.3	4.110	3.993	3.859
	0.6	8.779	6.545	5.313
	1	33.25	80.55	143.7

for the near entrance region results because the curves for different h/a and N cases lie quite close together.

Estimate of the Thermal Entrance Length. The thermal entrance length L_t is defined [15] as the length required for the local Nusselt number to equal 1.05 times its fully developed value. This definition was used in the present study also.

Table 5 lists the estimated thermal entrance length values for the $H1$ thermal boundary condition. Using an approximate analysis with linearized momentum equations, Hornbeck [24] obtained (L_t/D Re Pr) = .053 for a circular tube, which agrees well with the value listed in Table 5.

For fixed tube diameter D and Re (i.e., mass flow rate) L_t shows a mixed dependence on N and h/a. This, as already discussed, is a consequence of the secondary flow effects: increasing N and h/a can increase or decrease the strength of the secondary flow, and the distance required for this flow to decay. This, in turn, effects the development of different variables to their fully developed values.

Thermal Results: Isothermal Duct and Fins – The T Boundary Condition

The T boundary condition corresponds to a uniform temperature T_w both axially and peripherally. The bulk temperature $T_b(z)$ at an axial location z is given by

$$T_b(z) = \frac{1}{\dot{m} c_p} \int_A c_p \rho w T \, dA \tag{21}$$

and the heat transfer $Q(z)$ up to a distance z is equal to

$$Q(z) = \dot{m} c_p (T_b - T_i) \tag{22}$$

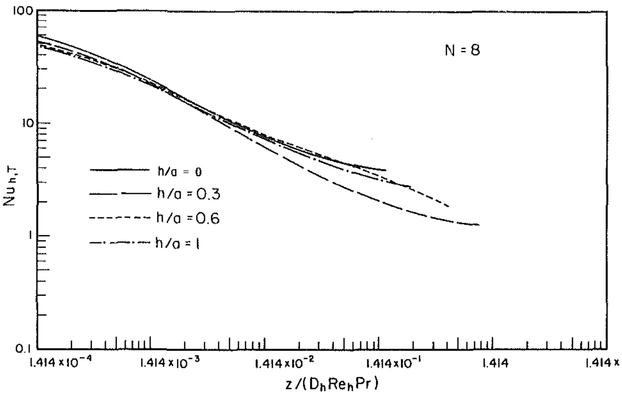

Fig. 6(*a*) Average Nusselt number for a finned duct with the T boundary condition: $N = 8$

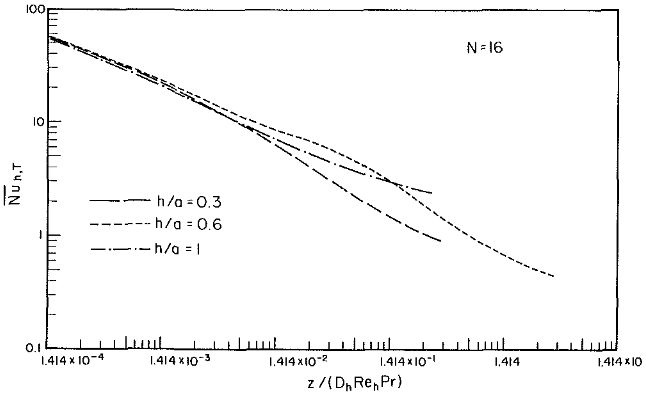

Fig. 6(*b*) Average Nusselt number for a finned duct with the T boundary condition: $N = 16$

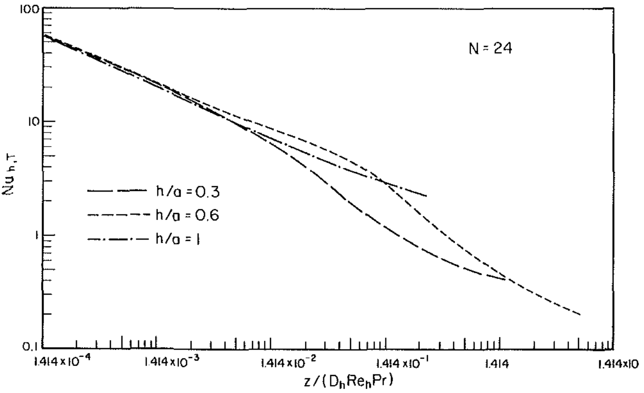

Fig. 6(*c*) Average Nusselt number for a finned duct with the T boundary condition: $N = 24$

Defining the log-mean temperature difference ΔT_{lm} as

$$\Delta T_{\mathrm{lm}} = \frac{(T_w - T_i) - (T_w - T_b)}{\ln[(T_w - T_i)/(T_w - T_b)]} \tag{23}$$

The average Nusselt number up to the axial location z can be defined as

$$\overline{\mathrm{Nu}}_{h,T} = \frac{Q/[(\pi D + 2Nh)z]}{\Delta T_{\mathrm{lm}}} \frac{D_h}{k} \tag{24}$$

or, basing everything on the base tube diameter D, as

$$\overline{\mathrm{Nu}}_T = \frac{Q/(\pi D z)}{\Delta T_{\mathrm{lm}}} \frac{D}{k} \tag{25}$$

In equations (24) and (25), the overbar represents average. The subscript h in (24) designates that D_h is used as the

Table 7 Estimate of the thermal entrance length for the T boundary condition

$L_{t,T}/(D_h\ \mathrm{Re}_h\ \mathrm{Pr})$

	N h/a	8	16	24
(*a*)	0	.0421		
	0.3	.122	.193	.280
	0.6	.351	.675	.360
	1	.0722	.125	.184

$L_{t,T}/(D\ \mathrm{Re}\ \mathrm{Pr})$

	N h/a	8	16	24
(*b*)	0	.0421		
	0.3	.0392	.0301	.0258
	0.6	.0549	.0411	.0116
	1	.00574	.00336	.00246

characteristic length, and the subscript T in (24) and (25) identifies the T boundary condition.

Let dQ/dz be the rate of increase of Q with the axial distance. The local Nusselt numbers can be defined as

$$\mathrm{Nu}_{h,T}=\frac{(dQ/dz)/(\pi D+2Nh)}{(T_w-T_b)}\ \frac{D_h}{k} \tag{26}$$

or

$$\mathrm{Nu}_T=\frac{(dQ/dz)/(\pi D)}{(T_w-T_b)}\ \frac{D}{k} \tag{27}$$

Fully Developed Nusselt Number. The fully developed values of the Nusselt number are presented in Table 6. Once again, to check the adequacy of the grid, a comparison was made with the 32 × 42 fine grid results. For $h/a = 0.3$ and 0.6, the 32 × 42 grid results are slightly higher: the agreement is within 1 percent for $h/a = 0.3$ and within 3 percent for $h/a = 0.6$. For $h/a = 1$, the fine grid results were about 1 percent lower.

Variation of the Nusselt Number in the Entrance Region. Variation of the average Nusselt number in the entrance region is presented in Fig. 6. As expected, the Nusselt number is large near the inlet, and decreases asymptotically to the fully developed value. Once again, the equivalent hydraulic diameter is a suitable characteristic length for representing results in the near entry region.

Estimate of the Thermal Entrance Length. Estimate values of the thermal entrance length L_t, defined as the distance required for the local Nusselt number to drop to 1.05 times the fully developed value, are presented in Table 7. Based on the results of Table 21 of [15] an estimate of $L_{t,T}/(D\ \mathrm{Re}\ \mathrm{Pr})$ is = .037 for a circular duct. Once again, the effect of N and h on L_t for a fixed mass flow rate is found to be quite mixed.

Concluding Remarks

Steady, laminar, forced convection flow and heat transfer in the entrance region of an internally finned circular duct is analyzed by numerically integrating the governing partial differential equations. The fins are radial, continuous, and of zero thickness. Results, exhibit the expected large pressure gradients and heat transfer coefficients in the entrance region, approaching, asymptotically, the fully developed values at large axial distance.

References

1 Bergles, A. E., "Survey and Evaluation of Techniques to Augment Convective Heat and Mass Transfer," *Progress in Heat and Mass Transfer*, Vol. 1, Pergamon Press, Oxford, 1969, pp. 331-424.

2 Carnavos, T. C., "Cooling Air in Turbulent Flow with Internally Finned Tubes," AIChE Paper No. 4, 17th National Heat Transfer Conference, Aug. 1977.

3 Russell, J. R., and Carnavos, T. C., "An Experimental Study: Cooling Air in Turbulent Flow with Internally Finned Tubes," AIChE Paper No. 28, 16th National Heat Transfer Conference, Aug. 1976.

4 Watkinson, A. P., Miletti, D. L., and Kubanek, G. R., "Heat Transfer and Pressure Drop of Internally Finned Tubes in Laminar Oil Flow," ASME Paper No. 75-HT-41, 1975.

5 Watkinson, A. P., Miletti, D. L., and Kubanek, G. R., "Heat Transfer and Pressure Drop of Forge-Fin Tubes in Turbulent Air Flow," ASHRAE Paper No. 2347, ASHRAE Semi-Annual Meeting, 1975.

6 Watkinson, A. P., Miletti, D. L., and Tarassoff, P., "Turbulent Heat Transfer and Pressure Drop in Internally Finned Tubes," *AIChE Symposium Series*, Vol. 69, No. 131, 1973, pp. 94-103.

7 Bergles, A. E., Brown Jr., G. S., and Snider, W. D., "Heat Transfer Performance of Internally Finned Tubes," ASME Paper No. 71-HT-31, 1971.

8 Hilding, W. E., and Coogen Jr., C. H., "Heat Transfer and Pressure Loss Measurements in Internally Finned Tubes," *Proceedings, Symposium on Air-Cooled Heat Exchangers*, ASME, New York, 1964, pp. 57-85.

9 Patankar, S. V., Ivanovic, M., and Sparrow, E. M., "Analysis of Turbulent Flow and Heat Transfer in Internally Finned Tubes and Annuli," ASME JOURNAL OF HEAT TRANSFER, Vol. 101, 1979, pp. 29-37.

10 Hu, M. H., and Chang, Y. P., "Optimization of Finned Tubes for Heat Transfer in Laminar Flow," ASME JOURNAL OF HEAT TRANSFER, Vol. 95, 1973, pp. 332-338.

11 Masliyah, J. H., and Nandakumar, K., "Heat Transfer in Internally Finned Tubes," ASME JOURNAL OF HEAT TRANSFER, Vol. 98, 1976, pp. 257-261.

12 Prakash, C., and Patankar, S. V., "Combined Free and Forced Convection in Vertical Tubes with Radial Internal Fins," ASME JOURNAL OF HEAT TRANSFER, Vol. 103, 1981, pp. 566-572.

13 Soliman, H. M., Chau, T. S., and Trupp, A. C., "Analysis of Laminar Heat Transfer in Internally Finned Tubes with Uniform Outside Wall Temperature," ASME JOURNAL OF HEAT TRANSFER, Vol. 102, 1980, pp. 598-604.

14 Eckert, E. R. G., Irvine, T. F., and Yen, J. T., "Local Laminar Heat Transfer in Wedge-Shaped Passages," ASME *Transactions*, Vol. 80, 1958, pp. 1433-1438.

15 Shah, R. K., and London, A. L., *Laminar Flow Forced Convection in Ducts*, Academic Press, Inc., New York, 1978.

16 Patankar, S. V., and Spalding, D. B., "A Calculation Procedure for Heat, Mass and Momentum Transfer in Three-Dimensional Parabolic Flows," *International Journal of Heat and Mass Transfer*, Vol. 15, 1972, pp. 1787-1806.

17 Chiranjivi, C., and Vidyanidhi, V., "Heat Transfer in Wedge-Shaped Ducts," *Indian Chem. Eng.*, Vol. 15, 1973, pp. 49-51.

18 Hornbeck, R. W., "Laminar Flow in the Entrance Region of a Pipe," *Appl. Sci. Res.*, Sect. A, Col. 13, 1964, pp. 224-232.

19 Schmidt, F. W., cross-reference from [15].

20 Bender, E., "Druckverlust bei laminarer Stromung im Rohreinlauf," *Chem. - Ing. - Tech.*, Vol. 14, 1969, pp. 682-686.

21 Sparrow, E. M., and Haji-Sheikh, A., "Laminar Heat Transfer and Pressure Drop in Isosceles Triangular, Right Triangular and Circular Sector Ducts," ASME JOURNAL OF HEAT TRANSFER, Vol. 87, 1965, pp. 426-427.

22 Haji-Sheikh, A., cross-reference from [15].

23 Manohar, R., cross reference from [15].

24 Hornbeck, R. W., "An All-Numerical Method for Heat Transfer in the Inlet of a Tube," ASME Paper 65-WA/HT-36, 1965.

Thermal Conditions in Irradiated, Slowly Moving Liquid Layers

W. G. Houf[1]

F. P. Incropera
Fellow ASME

R. Viskanta
Fellow ASME

Heat Transfer Laboratory,
School of Mechanical Engineering,
Purdue University,
W. Lafayette, Ind.

Vertical temperature distributions have been measured in slowly moving, horizontal liquid layers that were irradiated from above. Radiation was concentrated in the spectral range from 350 to 5000 nm, and the low wavelength ($\lambda < 1300$ nm) values of the liquid and substrate radiative properties were varied. Due to the effects of infrared radiation absorption, thermal conditions within the liquid did not exhibit a strong dependence on radiative properties. Conditions were characterized by a stably stratified upper layer, a core region of nearly uniform temperature, and a thin bottom layer of large, unstable temperature gradient. Satisfactory agreement was obtained between the measurements and predictions based on three-dimensional, laminar flow and one-dimensional, radiative transfer models. A weak secondary flow, which involves longitudinal vortices and/or ascending-descending thermals, was predicted by the model and was responsible for maintaining the nearly isothermal core conditions.

Introduction

In recent years there has been considerable interest in the response of horizontal liquid layers to irradiation at a free surface. Applications include ocean thermal energy conversion systems, solar ponds, central receivers, and absorbing liquid solar collectors. The radiation field within the liquid can strongly influence hydrodynamic and thermal conditions, which, in turn, influence system performance. The response to radiation is influenced by several factors, which include the spectral and directional distributions of the incident radiation, refraction and reflection at the air–liquid interface, scattering and absorption within the liquid, and multiple reflections between an opaque bottom substrate and the air–liquid interface. Pertinent radiative properties are the index of refraction, the scattering and absorption coefficients, and the phase function of the liquid, as well as the substrate reflectivity. Radiative effects influence hydrodynamic and thermal conditions within the liquid, which also depend on heat exchange at the air interface and conduction and advection in the liquid. Conditions are strongly influenced by whether radiation deposition is concentrated near the air interface or at the bottom substrate. Elevated temperatures due to deposition at the interface increase heat loss to the surroundings and contribute to thermal stratification of the liquid. In contrast, deposition at the bottom causes thermal destabilization and buoyancy-driven secondary flows.

The facility to deal with radiative transfer in absorbing-scattering liquids is well in hand. Prediction methods that are well suited for the strongly anisotropic scattering distributions associated with liquid suspensions have been reviewed [1], and considerable success has been realized in applying one of these methods (discrete ordinates) to liquids bounded by an air interface and an opaque substrate [2–4]. Techniques have been developed for measuring scattering and absorbing properties, and detailed measurements have been made for a wide range of liquid suspensions [5–8]. Using measured properties with predictions based on the discrete ordinate method, good agreement has been obtained between experimental and theoretical results for the radiation field in aqueous suspensions [9, 10].

Although there have been several studies of the thermal response of liquids to irradiation from above, little has been done to establish the combined influence of radiation deposition, forced convection, and free convection. Combined conduction and radiation in thermally stratified, quiescent liquids has been considered, with good agreement obtained between measured and predicted results for the vertical temperature distribution [11, 12]. The study of moving liquids has been limited to fully developed flows with negligible buoyancy [13, 14]. It is well known that, if a horizontal flow is heated from below, buoyancy-driven secondary flows are induced and the resulting flow field is three-dimensional [15, 16]. Such flows may be established due to radiation deposition at the bottom substrate and are therefore strongly coupled to the thermal and radiative fields. Less than satisfactory agreement has been obtained between temperature measurements in an open channel flow and predictions based on a simplified model of radiative, hydrodynamic, and thermal conditions [14].

The purpose of this study was to obtain an improved understanding of the effects of radiation on thermal conditions in a horizontal, slowly moving liquid layer. Experiments were performed for an open channel flow irradiated from above, and measurements of the vertical temperature distribution were made at different longitudinal stations. Experiments were performed for a range of liquid layer heights and flow rates, for liquids characterized by large and small values of the scattering albedo, and for large and small values of the substrate reflectivity. Attempts were made to predict and interpret the measurements by using a three-dimensional, laminar flow model, which considers buoyancy, with a one-dimensional radiation model, which accounts for absorption, anisotropic scattering, and surface reflection.

Experimental Methods

Flow Channel. Experiments were performed in an open channel (Fig. 1) consisting of a test section of length 0.99 m and width 0.30 m. The channel was constructed of plexiglass, except for a 9.5-mm-thick aluminum plate at the bottom of the test section. The plate was coated with optical white (3M 101-A10) or ultraflat black (Krylon 1602) paints to achieve high reflection or absorption, respectively. For the liquid layer heights and velocities of interest ($10 \leq H \leq 20$ mm, $5 \leq w_m \leq 20$ mm/s), hydrodynamic conditions were fully developed at the test section inlet.

Vertical temperature distributions in the irradiated liquid were measured by thermocouple probes attached to a longitudinal support at 222 mm intervals. Measurements were made at the midplane ($x = W/2$), and the support was vertically traversed at a rate of 0.20 mm/s. A potentiometer was used to indicate thermocouple position, and thermocouple

---

[1] Presently at Sandia National Laboratory, Livermore, Calif. 94550.

Contributed by the Heat Transfer Division for publication in the JOURNAL OF HEAT TRANSFER. Manuscript received by the Heat Transfer Division November 2, 1983.

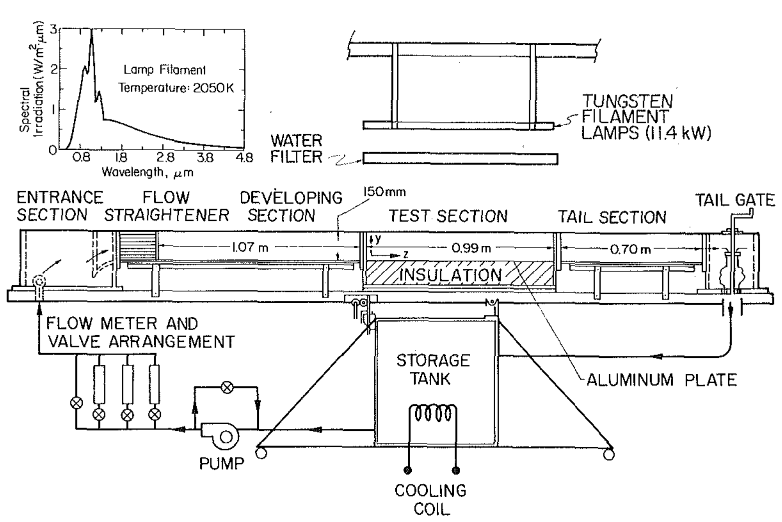

Fig. 1 Schematic of test facility and spectral distribution of irradiation (insert)

and potentiometer outputs were recorded at 5s intervals on a datalogger (Esterline Angus, Model PD2064). Stationary thermocouple probes were also used with an x-y recorder to determine temperature fluctuations. All thermocouples were calibrated to 0.1°C using a standard resistance thermometer with a constant temperature bath.

Radiation Source. The test section was irradiated by an overhead array of four tungsten filament, tubular quartz lamps, housed within parabolic reflectors. To reduce the amount of infrared radiation, a thin (15-mm), double-skinned, water-cooled Lexan filter was installed 0.30 m below the lamp housing. The spectral transmittance of the filter was measured and found to be approximately 0.80 in the visible portion of the spectrum and approximately 0 for $\lambda > 1500$ nm. Reflecting panels (not shown) were extended vertically from the ends and sides of the test section, permitting some radiation from the lamps to be reflected around the filters and onto the test section. With the panels and filter in place, the irradiation varied by less than 5 percent and 15 percent, respectively, over the length and width of the test section. Reflecting surfaces were also attached to the sidewalls of the test section in order to better approximate the existence of one-dimensional radiation transfer. The combined effects of the Lexan filter and reflecting walls also aided in the production of a diffuse irradiation field at the air-liquid interface.

The spectral distribution of the irradiation at the air-liquid interface was determined by using an Eppley radiometer (Model 8-48) to separately measure the total filtered and unfiltered radiation fluxes for the spectral region from 280 to 2800 nm. To obtain spectral distributions for this band, the unfiltered flux was multiplied by the ratio of the spectral blackbody emitted flux to the total blackbody emitted flux for the 280–2800 nm band, and the filtered flux was multiplied by the product of this ratio and the spectral transmittance of the filter. The blackbody function was evaluated at the lamp filament temperature, which was measured using an optical pyrometer (Leads and Northrup, Model 184 1820). The blackbody function was also used to determine the unfiltered spectral flux component for $\lambda > 2800$ nm. The spectral distribution of the irradiation was obtained by summing the filtered and unfiltered spectral fluxes.

In this study the lamps were operated at a filament temperature of 2050 K, and the corresponding spectral irradiation is shown in the insert of Fig. 1. The total irradiation is approximately 2300 W/m^2, approximately 55 percent of which is in the semitransparent region from 300 to 1400 nm. Approximately 14 percent of the radiation is beyond 2800 nm.

Radiation Properties. To consider a range of liquid radiative properties, experiments were performed for aqueous suspensions of India ink (Higgins 813) and talc (Fisher Scientific Co.), as well as for tap water. Concentrations of 0.13 percent by mass for the talc and 0.013 percent by volume for the ink were used for the suspensions. In terms of low wavelength spectral response ($\lambda < 1000$ nm), the ink and talc are representative of highly absorbing and scattering suspensions, respectively. Their spectral extinction (β_λ) and absorption (κ_λ) coefficients were measured over the spectral range $350 \leq \lambda \leq 2500$ nm by using a Shimadzu (Model MPS-50L) multipurpose spectrophotometer [8, 17]. The scattering

Nomenclature

c_p = specific heat
F = net radiation flux
F^-, F^+ = backward and forward flux components
G = irradiation
g = gravitational acceleration
H = liquid layer height
I = radiation intensity
k = thermal conductivity
$\bar{P}$ = cross-stream average pressure
p = pressure perturbation or phase function
Q = volumetric radiation absorption rate
T = temperature
T_o = reference temperature
u,v,w = spanwise, vertical and streamwise velocities
W = liquid layer width
w_m = mean streamwise velocity
x,y,z = spanwise, vertical, and streamwise directions
β = thermal expansion coefficient or radiative extinction coefficient
κ = absorption coefficient
λ = wavelength
ξ = scattering angle
μ = viscosity
σ = scattering coefficient
ω = scattering albedo
ρ = density
ρ_b = reflectivity of bottom substrate
θ = polar angle
τ = optical depth, $\beta(H-y)$
τ_H = optical thickness, βH

coefficient ($\sigma_\lambda = \beta_\lambda - \kappa_\lambda$) and scattering albedo ($\omega_\lambda = \sigma_\lambda/\beta_\lambda$) were inferred from the measurements. For the talc, β_λ and κ_λ were independent of wavelength for $\lambda < 1000$ nm, with $\beta_\lambda \approx 0.1$ 1/mm and $\omega_\lambda \approx 0.8$. For $\lambda > 1000$ nm, β_λ and κ_λ increased sharply and converged, such that $\omega_\lambda \approx 0$ for $\lambda > 1300$ nm. Similar trends characterized the ink, although the low wavelength behavior was restricted to $\lambda < 700$ nm, with $\beta_\lambda \approx 0.01$ 1/mm and $\omega_\lambda \approx 0.3$, and the high wavelength behavior ($\omega_\lambda \approx 0$) corresponded to $\lambda > 1000$ nm. For both suspensions, the single scattering phase function p_λ was determined by using a rotating fiber optic probe to measure radiation scattered from a He-Ne ($\lambda = 632.8$ nm) laser beam [7, 8, 17]. The phase function is known to be independent of wavelength [18, 19], and for both suspensions, it is strongly peaked in the forward direction.

Since the measurement techniques could discern no difference between the absorption and extinction coefficients of tap and distilled water, the properties were assumed to be equivalent and results were obtained from the literature [20–22]. The coefficients increase with increasing wavelength from a minimum of approximately 3×10^{-5} 1/mm at 350 nm.

The spectral reflectivity of the white substrate was measured for the range $300 \leq \lambda \leq 5000$ nm [23]. It is approximately 0.85 in the visible spectrum and approximately 0 for $\lambda > 1400$ nm. The reflectivity of the black substrate is assumed to be approximately 0.01 throughout the spectrum [24].

Theoretical Methods

Governing Equations. The model considers horizontal flow in an open channel that is uniformly irradiated from above (Fig. 2). Assuming steady, laminar flow, the continuity, momentum, and energy equations are

$$\frac{\partial u}{\partial x} + \frac{\partial v}{\partial y} + \frac{\partial w}{\partial z} = 0 \qquad (1)$$

$$\rho u \frac{\partial u}{\partial x} + \rho v \frac{\partial u}{\partial y} + \rho w \frac{\partial u}{\partial z} = -\frac{\partial p}{\partial x} + \mu \left| \frac{\partial^2 u}{\partial x^2} + \frac{\partial^2 u}{\partial y^2} \right| \qquad (2)$$

$$\rho u \frac{\partial v}{\partial x} + \rho v \frac{\partial v}{\partial y} + \rho w \frac{\partial v}{\partial z} = -\frac{\partial p}{\partial y} + \rho g \beta (T - T_o) + \mu \left| \frac{\partial^2 v}{\partial x^2} + \frac{\partial^2 v}{\partial y^2} \right| \qquad (3)$$

$$\rho u \frac{\partial w}{\partial x} + \rho v \frac{\partial w}{\partial y} + \rho w \frac{\partial w}{\partial z} = -\frac{d\bar{P}}{dz} + \mu \left| \frac{\partial^2 w}{\partial x^2} + \frac{\partial^2 w}{\partial y^2} \right| \qquad (4)$$

$$\rho u \frac{\partial T}{\partial x} + \rho v \frac{\partial T}{\partial y} + \rho w \frac{\partial T}{\partial z} = \frac{k}{c_p} \left| \frac{\partial^2 T}{\partial x^2} + \frac{\partial^2 T}{\partial y^2} \right| + \frac{1}{c_p} \frac{\partial F}{\partial y} \qquad (5)$$

Streamwise diffusion terms are neglected, and the pressure is expressed as the sum of an average over the channel cross section $\bar{P}(z)$ and a perturbation about this average $p(x, y, z)$. It is assumed that $\partial p/\partial z << \partial \bar{P}/\partial z$ and that all properties are constant, except for the density in the buoyancy term of the vertical momentum equation, which is obtained from the Boussinesq approximation.

Taking advantage of symmetry about the midplane, equations (1–5) were solved for the domain $0 \leq x \leq W/2$, $0 \leq y \leq H$, and $z \geq 0$. Zero-slip and impermeable wall conditions were prescribed for u, v, and w at the sidewall ($x = 0$) and bottom ($y = 0$), while zero shear and impermeable surface conditions were prescribed at the air interface ($y = H$). Invoking symmetry, the spanwise terms u, $\partial v/\partial x$, and $\partial w/\partial x$ were equated to zero at $x = W/2$. With an adiabatic sidewall and symmetry about the midplane, $\partial T/\partial x$ was set equal to zero at $x = 0$ and $x = W/2$. At $y = 0$, the rate of radiation absorption at the substrate was equated to the rate of heat transfer by conduction in the liquid; at $y = H$, conduction in the liquid was equated to net heat exchange with the surroundings by radiation, convection, and evaporation. The radiative loss term was evaluated by considering the liquid free surface to be opaque to longwave thermal radiation and by considering the net exchange between the opaque surface and large surroundings [11]. The convective and evaporative losses were evaluated from semiempirical relations [30]. Inlet conditions ($z = 0$) were prescribed in accordance with the experiments.

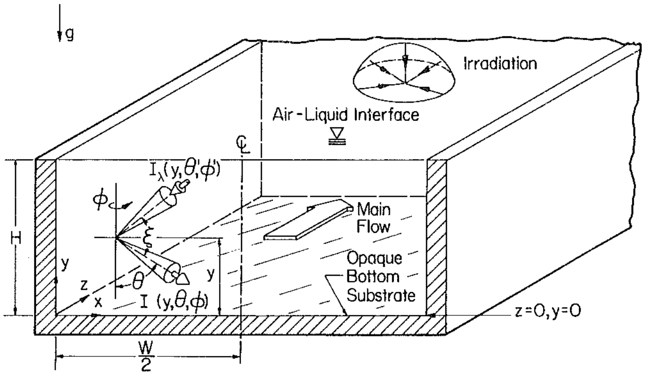

Fig. 2 Coordinate system for three-dimensional flow model

To evaluate the radiation deposition term of equation (5), as well as the rate of radiation absorption by the substrate, the liquid was assumed to be a plane-parallel, nonemitting, absorbing-scattering medium and the radiation field was determined by solving the one-dimensional, radiative transfer equation

$$\cos\theta \frac{dI_\lambda}{d\tau_\lambda} = -I_\lambda + \frac{\omega_\lambda}{2} \int_0^\pi I_\lambda p_\lambda(\theta', \theta) \sin\theta' d\theta' \qquad (6)$$

Equation (6) was solved for $I_\lambda(\theta, y)$, subject to conditions at the air and substrate interfaces which account for refraction and/or reflection effects. The bottom substrate was modeled as an opaque diffuse reflector, while the air–liquid interface was treated by Fresnel's equations [17]. The solution was obtained for prescribed spectral and directional distributions of the irradiation and spectral distributions of the liquid and substrate radiative properties. Positive, $F_\lambda^+(y)$, and negative, $F_\lambda^-(y)$, components of the spectral flux were then obtained by integrating the results over $0 \leq \theta \leq \pi/2$ and $\pi/2 \leq \theta \leq \pi$. The total, net radiation flux $F(y)$ was obtained by integrating $[F_\lambda^+(y) + F_\lambda^-(y)]$ over wavelength.

Solution Methods. Equation (6), which is uncoupled from the flow equations, (1–5), was solved by the method of discrete ordinates [2–4]. The solution involves dividing the radiation field into M discrete streams, expanding the phase function in a series of Legendre polynomials, and replacing the scattering integral on the right-hand side of (6) by a Lobatto quadrature formula. The equation of transfer reduces to a system of M simultaneous, linear differential equations corresponding to M discrete values of θ_i, which was solved by an eigenvalue method. The radiation field was calculated by dividing the spectral irradiation into 100 nm bands for a semitransparent range from 300 to 2000 nm and assigning constant values of the irradiation and the optical properties to each band. The total flux and volumetric absorption were obtained by summing results for each band. For $\lambda > 2000$ nm, the liquid interface was assumed to be opaque.

A variant of the finite diffference scheme of Patankar and Spalding [25] was used to solve equations (1–5). A staggered grid was used with a hybrid difference scheme, and velocity and temperature fields were computed in a stepwise manner along the z-direction. Using a marching-step and grid-space halving technique to study convergence and stability of the numerical scheme, a 32×12 grid was found to be sufficient for the x-y plane. Validation of the numerical scheme was also achieved by successfully predicting measured velocity and temperature distributions for closed channel flows [26, 27].

Results

Although experiments were performed for varying liquid layer velocities and heights in the ranges $5 \leq w_m \leq 20$ mm/s and $10 \leq H \leq 20$ mm, trends and comparisons were found to be independent of w_m and H. Accordingly, results will only be presented for $w_m = 10.3$ mm/s and $H = 20$ mm. The irradiation was maintained at 2300 W/m^2 (± 50W/m^2), while the substrate reflectivity and the nature of the liquid were varied. Conditions were modeled by assuming the flow to be uniform at the outlet of the straightener and to develop hydrodynamically for a distance of 1.13 m, which corresponds to $z/H = 2.55$ and the first temperature measurement station. The complete (radiative-thermal-hydraulic) model solution was then initiated by assuming the temperature distribution to be uniform in the spanwise direction and to equal the measured vertical distribution for the first station.

Predicted radiant flux and absorption distributions are shown in Fig. 3 for tap water with highly absorbing and reflecting substrates. Due largely to the strong influence of long wavelength components of the irradiation, volumetric absorption in the upper layers is independent of the substrate condition and is approximately two orders of magnitude larger than absorption in the lower layers. Although it is small, volumetric absorption in the lower layers is affected by the bottom reflectivity and is approximately twice as large for the white substrate as for the black substrate. Use of the white substrate reduces the net radiant flux in the lower layers, as well as the rate of radiation absorption by the substrate. For the white and black surfaces, the absorbed flux is approximately 160 and 675 W/m^2, respectively.

In Fig. 4(a) midplane vertical temperature distributions measured for tap water with a black bottom are compared with predicted midplane and spanwise average distributions at selected longitudinal stations. The results are plotted as a reduced temperature, where the reference temperature is $T_o = 25°$C. The data are characterized by a thin surface layer of nearly uniform temperature ($0.9 < y/H \leq 1.0$), a stably stratified zone ($0.6 < y/H < 0.9$), a nearly isothermal core ($0.1 < y/H < 0.6$), and a thin conduction layer adjoining the substrate. The surface layer is due to the destabilizing effect of surface heat loss, while development of the stratified zone is due to longwave radiation absorption and heat conduction in the downward direction. The thin conduction layer originates from radiation absorption at the substrate and is characterized by an unstable temperature gradient of approximately 1°C/mm. Buoyancy forces associated with this gradient can induce a secondary flow which contributes to mixing in the core and maintenance of a nearly uniform temperature.

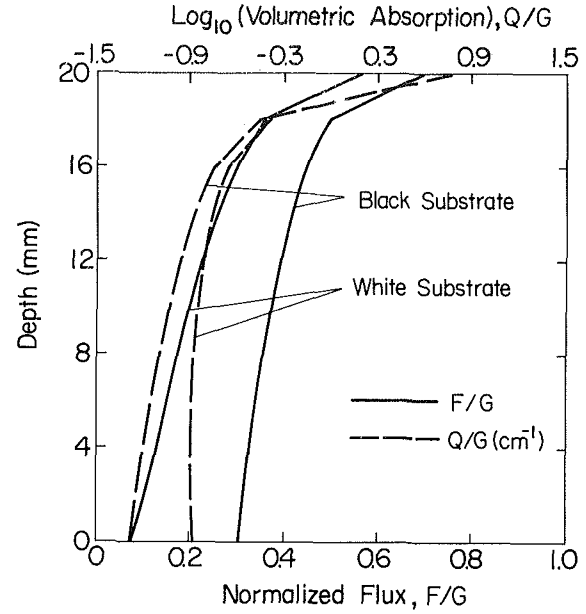

Fig. 3 Net radiation flux and volumetric absorption for tap water

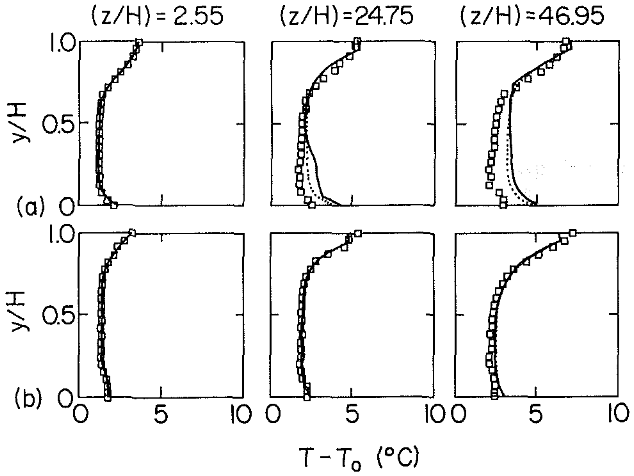

Fig. 4 Comparison of predicted and measured temperature distributions for tap water (solid and dashed curves correspond to midplane and spanwise average predictions, respectively): (a) black substrate, (b) white substrate

The flow was visualized by injecting dye at various core locations. Although the dye formed streaks that aligned themselves approximately with the mainflow, small cross-stream (vertical and spanwise) deviations were observed in the streaklines. These deviations are attributed to a secondary flow that is characterized by velocities approximately an order of magnitude less than the longitudinal velocity. Temperature fluctuations were also measured with stationary thermocouple probes. The amplitude and frequency of the fluctuations were approximately $\pm 0.2°$C and 0.03 Hz in the lower fluid layers and $\pm 0.08°$C and 0.10 Hz in the core. The flow visualization and temperature measurements suggest that core mixing can be attributed to buoyancy induced laminar advection, rather than to turbulence.

All trends associated with the data of Fig. 4(a) are predicted by the model, although the amount of heating in the lower and intermediate layers ($0 < y/H < 0.5$) is overpredicted. The disagreement is most likely due to prediction, not experimental, errors and may result from uncertainties in knowledge of the magnitude and/or spectral distribution of the irradiation, the liquid radiative properties, and the substrate reflectivity. The fact that, with increasing z/H, the disagreement propagates upward from the substrate, while good agreement is maintained in the stratified surface layer, suggests that bottom heating is being overpredicted. Such a result may be due to overpredicting the forward flux at the substrate and/or to underestimating the substrate reflectivity. In particular, the reflectivity of $\rho_b = 0.01$ obtained from the literature [24] may be unrealistically low. Although plate conduction effects could cause predicted plate temperatures to exceed measured values, spanwise, vertical, and longitudinal temperature gradients inferred from thermocouples imbedded in the plate suggest that the effects are small.

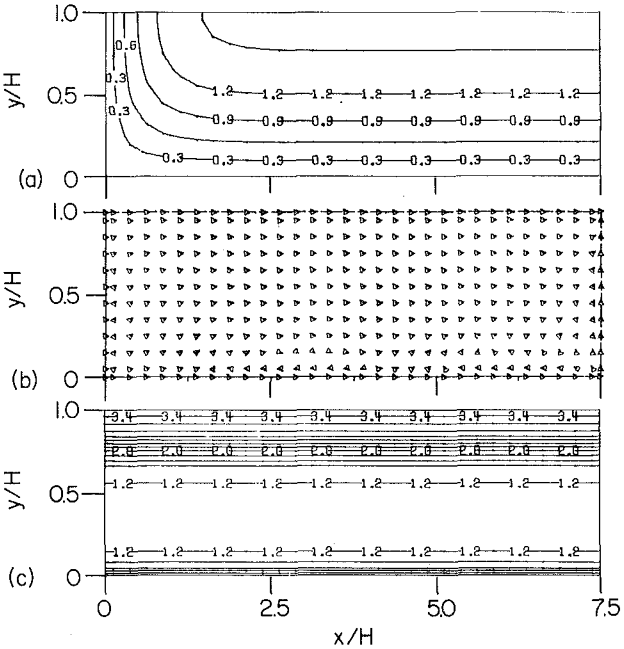

Fig. 5 Prediction of (*a*) longitudinal velocity contours, w/w_m, (*b*) cross-stream velocity vectors, and (c) isotherms, $T - T_o$(°C), at z/H = 2.55 for tap water and a black substrate

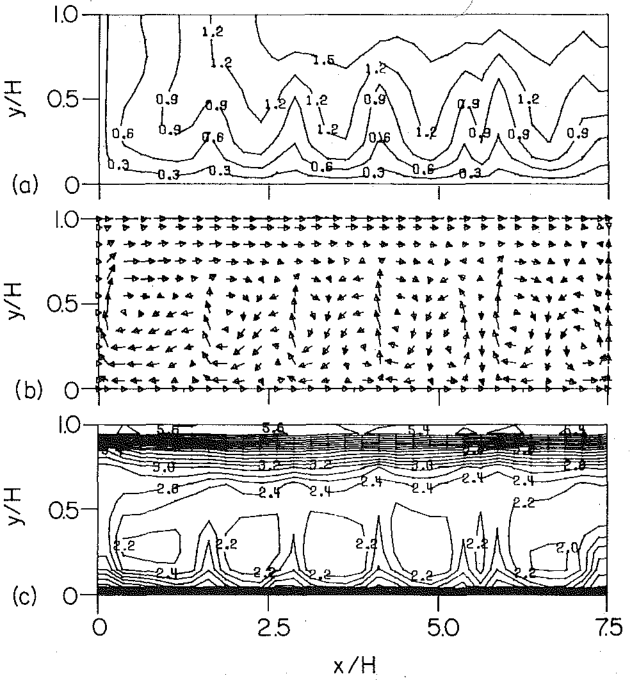

Fig. 6 Prediction of (*a*) longitudinal velocity contours, w/w_m, (*b*) cross-stream velocity vectors, and (c) isotherms, $T - T_o$(°C), at z/H = 24.75 for tap water and a black substrate

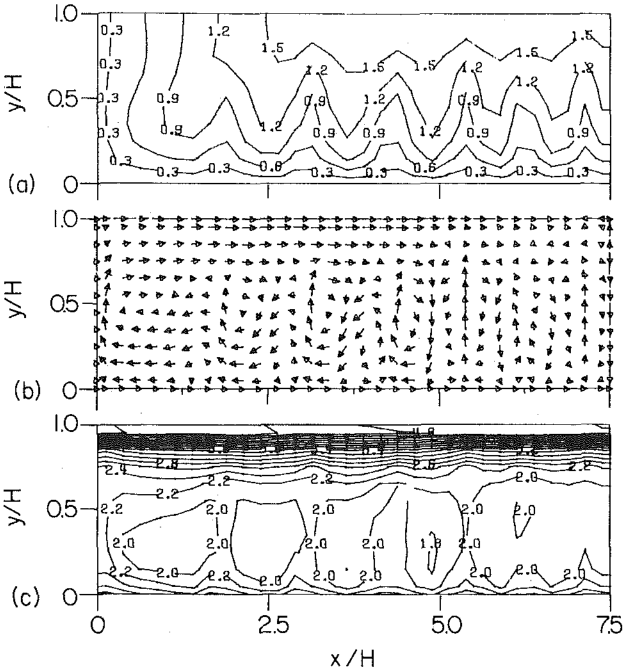

Fig. 7 Prediction of (*a*) longitudinal velocity contours, w/w_m, (*b*) cross-stream velocity vectors, and (c) isotherms, $T - T_o$(°C), at z/H = 24.75 for tap water and a white substrate

Cross-stream velocity and temperature fields computed for the conditions of Fig. 4(*a*) are shown in Figs. 5 and 6. The contours of (*a*) reveal lines of constant longitudinal velocity, normalized with respect to the mean velocity, and the arrows of (*b*) reveal the magnitude and direction of the cross-stream velocity vectors. The contours of (*c*) reveal lines of constant temperature. At z/H = 2.55 (Fig. 5) the cross-stream velocities are negligible (< 0.1 mm/s), and the longitudinal velocity contours are smooth, with low velocities existing near the sidewall and substrate (due to bondary layer development) and large velocities existing in the core and upper layers. The isotherms, which are plotted at 0.2°C intervals, are horizontal, revealing weakly stable and unstable conditions in the upper and lower layers, respectively.

At z/H = 24.75, Fig. 6, irradiation has significantly increased the stabilizing and destabilizing temperature gradients. The thermal structure (Fig. 6(*c*)) consists of the thin surface layer of uniform temperature, a stably stratified layer, a well-mixed core of nearly uniform temperature, and a thin bottom layer ($0 < y/H < 0.1$) in which the unstable temperature gradients are concentrated. The dark horizontal band in the bottom layer is due to the high contour density associated with a predicted temperature gradient of approximately 1.5°C/mm. Transport in this layer is dominated by conduction, and the layer acts to thermally destabilize the flow. The instability induces a secondary flow, which, at $z = H$ = 24.75, is characterized by a longitudinal vortex in the outer region ($x/H < 1.3$) and by ascending thermals at $x/H \approx 1.6$, 2.7, 4.0, 5.6, and 7.5 (Fig. 6(*b*)). Maximum cross-stream velocities are approximately 1 mm/s, and the thermals provide for spikes in the longitudinal velocity and temperature contours (Figs. 6(*a*) and 6(*c*)). Unable to penetrate the upper stratified layer, the thermals spread laterally and begin a descending motion as they cool. The overall secondary flow pattern resembles the system of longitudinal vortices that has been observed in channel flows heated from below [28, 29]. Although the cross-stream velocities are small, buoyant convective mixing is sufficient to produce a nearly uniform (±0.2°C) core temperature. With increasing z/H, the basic structure of the hydrodynamic and temperature fields remains the same, although the spanwise extent of the outer vortex increases.

For the tap water and the white substrate, there is excellent agreement between the measured and predicted midplane temperatures (Fig. 4(*b*)). Both results reveal the development of a surface stratified layer and maintenance of a core region of nearly uniform temperature. Although bottom heating is not as significant as for the black substrate, the strength of the resulting secondary flow is sufficient to maintain a uniform core temperature. As shown in Fig. 7, although the unstable temperature gradient associated with the bottom conduction layer is small, a secondary flow is maintained. Since the only

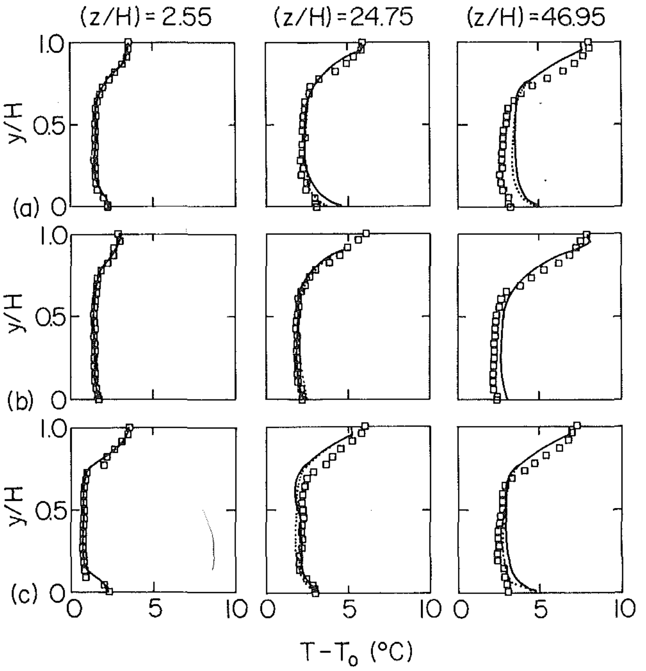

Fig. 8 Comparison of predicted and measured temperature distributions for (*a*) talc suspension with black substrate, (*b*) talc suspension with white substrate, and (*c*) ink suspension with black substrate

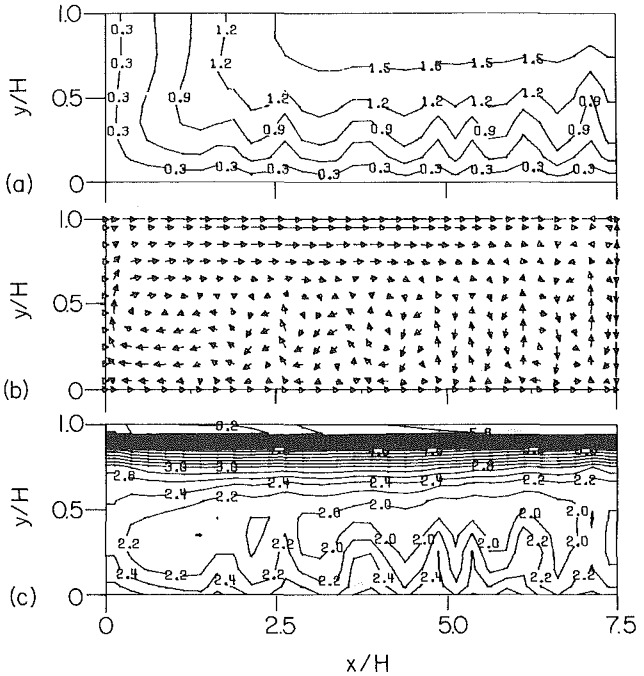

Fig. 10 Prediction of (*a*) longitudinal velocity contours, w/w_m, (*b*) cross-stream velocity vectors, and (*c*) isotherms, $T - T_0$(°C), at z/H = 24.75 for talc suspension and a white substrate

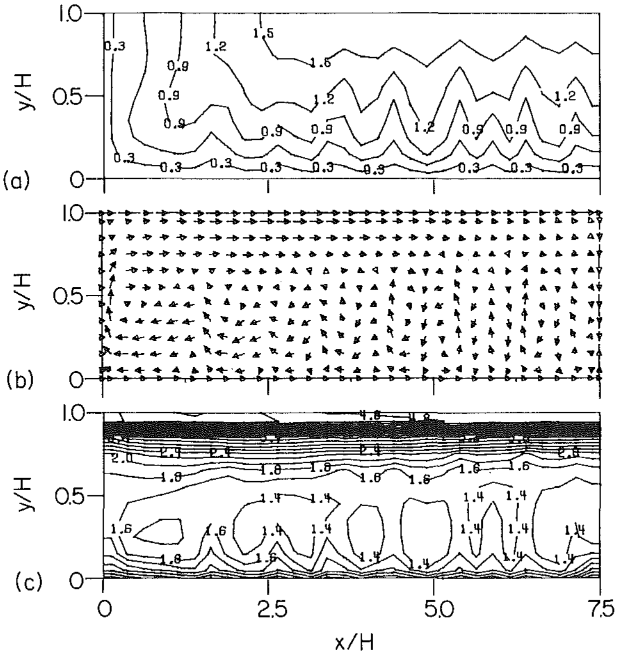

Fig. 9 Prediction of (*a*) longitudinal velocity contours, w/w_m, (*b*) cross-stream velocity vectors, and (*c*) isotherms, $T - T_0$(°C), at z/H = 24.75 for talc suspension and a black substrate

difference between the experimental conditions of Figs. 4(*a*) and 4(*b*) is in the value of ρ_b, the agreement of Fig. 4(*b*) reinforces the suspicion that the discrepancy of Fig. 4(*a*) is due to use of an unrealistically low value of ρ_b in the predictions.

Temperature distributions obtained for the talc suspension with black and white substrates are shown in Figs. 8(*a*) and 8(*b*), respectively. Due to the strong influence of the longwave radiation, volumetric radiation absorption in the upper layers is approximately independent of the substrate condition and virtually identical to results for the tap water. In the lower layers, volumetric absorption is approximately two times larger for the white bottom, and for both substrates it is approximately 25 percent larger in the talc than in the water. Due to the effect of enhanced backscattering and volumetric absorption, radiation absorption by the black and white substrates, respectively, is approximately 15 and 45 percent smaller for the talc than for the water. The net effect of these differences is to yield predicted and measured temperatures that are slightly larger in the talc than in the water. However, in the talc, as well as the water, thermal conditions are dominated by a stratified surface layer and a nearly isothermal core. For the black substrate (Fig. 8(*a*)), agreement between predicted and measured temperatures is good in the early stages of development ($z/H < 25$) but deteriorates in the core and lower layers with increasing z/H. Differences are again attributed to overprediction of absorbed radiation at the bottom, which contributes to bottom layer heating via conduction from the substrate. As for the tap water, agreement between predictions and measurements for the white substrate (Fig. 8(*b*)) is good, although the data are now slightly overpredicted in the core and lower layers.

Predictions of the cross-stream velocity and temperature fields for the talc suspension at z/H = 24.75 are shown in Figs. 9 and 10 for the black and white substrates, respectively. In both cases the secondary flow consists of a longitudinal vortex near the sidewall and ascending-descending thermals at larger values of x/H. Although destabilizing temperature gradients in the conduction layer are substantially smaller than for the tap water, buoyancy-driven convection is sufficient to maintain nearly isothermal core conditions. In the case of the white substrate, however, it appears that this condition is marginal. Further reduction in bottom heating, due, for example, to an increase in β or ρ_b, would likely eliminate the secondary flow. Thermal conditions would then be dominated by stable stratification throughout the layer.

Temperature distributions for the ink suspension with a black bottom are shown in Fig. 8(*c*). Over much of the liquid, volumetric absorption is approximately 15 percent larger than in the tap water, while radiation absorption at the substrate is approximately the same. Despite slight underprediction of the data in the stratified layer and overprediction in the core and bottom layer, the general agreement is good. As shown in Fig.

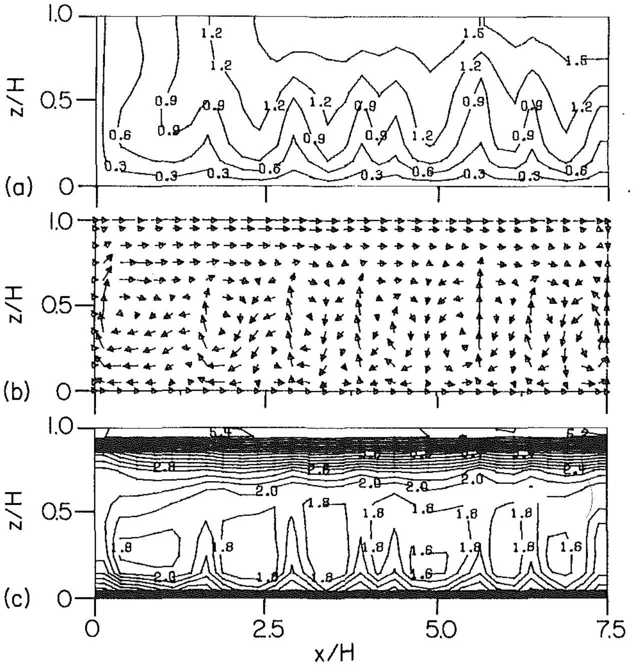

Fig. 11 Prediction of (*a*) longitudinal velocity contours, w/w_m, (*b*) cross-stream velocity vectors, and (*c*) isotherms, $T - T_0$(°C), at z/H = 24.75 for ink and a black substrate

11, trends predicted for the cross-stream velocity and temperature fields are consistent with those for the tap water and talc.

Summary

Experiments have been performed in which horizontal liquid layers of variable height and velocity were irradiated in the spectral range $350 \leq \lambda \leq 5000$ nm. Liquid and substrate radiative properties associated with visible and near infrared portions of the spectrum were varied, and experimental conditions were predicted by using a three-dimensional laminar flow model with a one-dimensional radiation transfer model.

For the prescribed experimental conditions, the thermal structure of the irradiated liquid was not influenced strongly by the liquid or substrate properties. This structure consisted primarily of an upper, stably stratified layer, a large core of nearly uniform temperature, and a thin bottom layer of large, unstable temperature gradient. Uniformity of the core temperature was maintained by buoyancy-driven secondary flows originating from the bottom layer. Vertical motion was suppressed by the upper, stable layer, and the flows were characterized by longitudinal vortices and/or ascending-descending thermals. The strength of the secondary flow decreased with increasing substrate reflectivity, although, even for the highly reflecting surface of this study, the flow was sufficient to maintain an isothermal core. Agreement between measured and predicted temperature distributions was generally good, with the largest discrepancy occurring in lower fluid layers for the highly absorbing substrate.

Due to the large amount of irradiation in the infrared region of the spectrum, the effect of the radiative properties was not strong. An increase in the source temperature is needed to make thermal effects more sensitive to these properties and to provide a more severe test of the radiative-thermal-hydraulic model.

Acknowledgments

Support of this work by the National Science Foundation under Grant No. MEA-8009034 is gratefully acknowledged.

References

1 Grant, I. P., and Hunt, G. E., "Solution of Radiative Transfer Problems in Planetary Atmospheres," *Icarus*, Vol. 9, 1968, pp. 526-534.

2 Viskanta, R., and Toor, J. S., "Effect of Multiple Scattering on Radiant Transfer in Waters," *Journal Geophysical Research*, Vol. 78, 1973, pp. 3538-3551.

3 Daniel, K. J., Laurendeau, N. M., and Incropera, F. P., "Prediction of Radiation Absorption and Scattering in Turbid Waters," ASME JOURNAL OF HEAT TRANSFER, Vol. 101, 1979, pp. 496-501.

4 Houf, W. G., and Incropera, F. P., "An Assessment of Techniques for Predicting Radiative Transfer in Aqueous Media," *Journal Quantitative Spectroscopy and Radiative Transfer*, Vol. 23, 1980, pp. 101-115.

5 Drotning, W. D., "Optical Properties of Solar Absorbing Oxide Particles Suspended in a Molten Salt Heat Transfer Fluid," *Solar Energy*, Vol. 20, 1978, pp. 313-320.

6 Timofeeva, V. A., "Optics of Turbid Waters," *Optical Aspects of Oceanography*, edited by N. G. Jerlov and E. S. Nielsen, Academic Press, 1974, pp. 177-219.

7 Incropera, F. P., and Privoznik, K. G., "Radiative Property Measurements of Selected Water Suspensions," *Water Resources Research*, Vol. 15, 1979, pp. 85-89.

8 Wagner, T. R., Houf, W. G., and Incropera, F. P., "Radiative Property Measurements for India Ink Suspensions," *Solar Energy*, Vol. 25, 1980, pp. 549-554.

9 Wagner, T. R., Incropera, F. P., and Houf, W. G., "Visible Radiation Transfer in a Black Liquid Suspension," ASME JOURNAL OF HEAT TRANSFER, Vol. 102, 1980, pp. 709-714.

10 Incropera, F. P., Wagner, T. R., and Houf, W. G., "Comparison of Radiation Field Predictions and Measurements in a Shallow Water Layer," *Water Resources Research*, Vol. 17, 1981, pp. 142-148.

11 Snider, D. M., and Viskanta, R., "Radiation Induced Thermal Stratification in Surface Layers of Stagnant Water," ASME JOURNAL OF HEAT TRANSFER, Vol. 97, 1975, pp. 35-40.

12 Arai, N., Kato, Y., Hasatani, M., and Sugiyama, S., "Unsteady Heat Transfer in Optically Thick Semitransparent Liquid Radiantly Heated," *Heat Transfer Japanese Research*, Vol. 8, 1980, pp. 94-106.

13 Kurosaki, Y., and Viskanta, R., "Heat Transfer in a Solar Radiation Absorbing Fluid Flowing over a Substrate," *Thermal Storage and Heat Transfer in Solar Energy Systems*, edited by F. Krieth, ASME, New York, 1978, pp. 13-21.

14 Hasatani, M., Arai, N., Bando, Y., and Nakamura, H., "Collection of Radiation by Semitransparent Fluid Layer in an Open Channel," *Heat Transfer Japanese Research*, Vol. 11, 1982, pp. 17-30.

15 Hwang, G. J., and Cheng, K. C., "Convective Instability in Thermal Entrance Region of a Horizontal Parallel Plate Channel Heated from Below," ASME JOURNAL OF HEAT TRANSFER, Vol. 95, 1973, pp. 72-77.

16 Kamotani, Y., and Ostrach, S., "Effects of Thermal Instability on Thermally Developing Laminar Channel Flow," ASME JOURNAL OF HEAT TRANSFER, Vol. 98, 1976, pp. 62-66.

17 Houf, W. G., "Effect of Radiation Transfer on Thermal and Hydrodynamic Conditions in Shallow, Slowly Moving Liquid Layers," Ph.D. thesis, Purdue University, W. Lafayette, Ind., 1982.

18 Duntley, S. Q., "Light in the Sea," *Journal Optical Society of America*, Vol. 53, 1963, pp. 214-233.

19 Daniel, K. J., and Incropera, F. P., "Optical Property Measurements in Suspensions of Unicellular Algae," TR HTL-4, Purdue University, W. Lafayette, Ind., 1977.

20 Curcio, J. A., and Petty, C. C., "Near Infrared Absorption Spectrum of Water," *Journal Optical Society of America*, Vol. 14, 1951, pp. 302-304.

21 Sullivan, S. A., "Experimental Study of Absorption in Distilled Water," *Journal Optical Society of America*, Vol. 53, 1963, pp. 962-968.

22 Hass, M., and Davisson, J. W., "Absorption Coefficient of Pure Water 488 and 541.5 nm," *Journal Optical Society of America*, Vol. 67, 1967, pp. 622-624.

23 Wynn, R., private communication, Wright-Patterson Air Force Base, Dayton, Ohio.

24 Touloukian, Y. S., DeWitt, D. P., and Hernicz, R. S., *Thermophysical Properties of Matter*, Vol. 9, IFI Plenum, New York, 1972.

25 Patankar, S. V., and Spalding, D. B., "Calculation Procedure for Heat, Mass and Momentum Transfer in Three-Dimensional, Parabolic Flows," *International Journal of Heat and Mass Transfer*, Vol. 15, 1972, pp. 1787-1806.

26 Goldstein, R. J., and Kreid, D. K., "Measurement of Laminar Flow Development in a Square Duct using a Laser-Doppler Flowmeter," ASME *Journal of Applied Mechanics*, Vol. 34, 1967, pp. 813-818.

27 Mercer, W. E., Pearce, W. M., and Hitchcock, J. E., "Laminar Forced Convection in Entrance Region between Parallel Plates," ASME JOURNAL OF HEAT TRANSFER, Vol. 89, 1967, pp. 251-257.

28 Gilpin, R. R., Imura, H., and Cheng, K. C., "Experiments on the Onset of Longitudinal Vortices in Horizontal Blasius Flow Heated from Below," ASME JOURNAL OF HEAT TRANSFER, Vol. 98, 1976, pp. 71-77.

29 Kamotani, Y., Ostrach, S., and Miao, H., "Convective Heat Transfer in Thermal Entrance Regions by Means of Thermal Instability," ASME JOURNAL OF HEAT TRANSFER, Vol. 101, 1979, pp. 222-226.

30 Ginzburg, A. I., and Fedorov, K. N., "Cooling of Water at a Surface for Free and Forced Convection," *Ocean Physics* (USSR), Vol. 14, 1978, pp. 57-62.

Heat Rejection to the Surface Layer of a Solar Pond

Y. Jaluria
Mem. ASME

C. K. Cha[1]
Mechanical Engineering Department
Rutgers University
Piscataway, NJ 08854

An analytical and numerical study of the thermal and fluid flow effects of heat rejection to the surface layer of a salt-gradient solar pond, by means of a recirculating thermal discharge, is carried out. The use of solar ponds for power generation involves heat rejection, for which the surface zone may be employed. However, it is very important to determine the effect of the discharge of hot fluid on the temperature field in the surface zone and on the stability of the nonconvective zone, which lies between the surface and storage zones. Of particular interest is the dependence of this flow on the inflow conditions, on heat loss at the surface and on the inflow-outflow configuration. The downward penetration of the flow is strongly governed by the buoyancy effects, and the study considers both the transient and the steady-state circumstances. The effect of the surface energy loss and of the conductive heat gained from below the surface zone is also studied. The flow is found to be strongly dependent on the inflow and outflow conditions and on the surface heat loss. The disturbance to the nonconvective zone is also studied. The basic physical processes involved are considered in detail, and the relevance of the results obtained in the design of the corresponding recirculating flow is outlined.

Introduction

Salt-gradient solar ponds have received considerable attention in the recent years for collection and long-term storage of solar energy [1-3]. The salinity at the bottom of the water body is greater than that at the surface and the gradient is large enough to give rise to a stable stratification, with the fluid density increasing downward, despite the destabilizing effect of the temperature, which also increases downward. A salt-gradient solar pond normally consists of three zones; a relatively shallow convective surface layer, a nonconvective gradient zone, and a homogeneous and convective storage zone. Figure 1 shows the typical depths of these zones and the shape of the temperature and salinity profiles that arise. The two distributions are similar, giving rise to essentially uniform conditions in the convective surface and storage zones. Further details on the operation of a solar pond may be obtained from [1-5].

Solar ponds have considerable promise for power generation. Since the surface layer of the pond is at a temperature close to the ambient temperature, it may be employed for heat rejection from a power plant operating on the energy extracted from the solar pond. However, the recirculating flow used for the heat rejection process will increase the temperature of the surface layer and cause additional disturbance to the nonconvective gradient zone [6]. Therefore, it is important to determine the effect of the thermal field due to the recirculating flow for heat rejection on the performance of the salt-gradient solar pond. This problem has not received much attention in the literature, though considerable information does exist on the similar problem of heat rejection from power plants to natural water bodies, such as lakes, rivers, and the sea [7-10]. The main differences lies in the considerable disparity in the depths of the water body in the two cases and the concerns that motivate the study. Natural water bodies are generally much deeper and often thermally stratified over much of the year. As a consequence, a vertical separation of the inflow and outflow channels is usually employed. In a solar pond, the flow must be restricted to a region near the surface to avoid destabilizing the nonconvective zone and attempt has to be made to spread out the flow over the entire surface area for effective energy loss to the environment. Therefore, the problem mainly involves horizontal convection and diffusion, with energy loss to the environment, rather than vertical transport, which is generally of greater concern in heat rejection to natural water bodies. Also, the increase in the temperature and depth of the surface layer must be kept at a minimum, since each centimeter increase in depth decreases the operating temperature of the pond by about 0.5°C, and the temperature increase results in an increase in surface evaporation, which necessitates further replenishment of water [6, 11].

This paper considers the mixed convection recirculating flow in the surface zone in order to answer some of the questions raised above. A detailed analytical and numerical study of the flow and temperature fields is carried out, considering wide ranges of the governing parameters, boundary conditions and inflow-outflow configuration. The inflow and outflow channels are assumed to be long so that

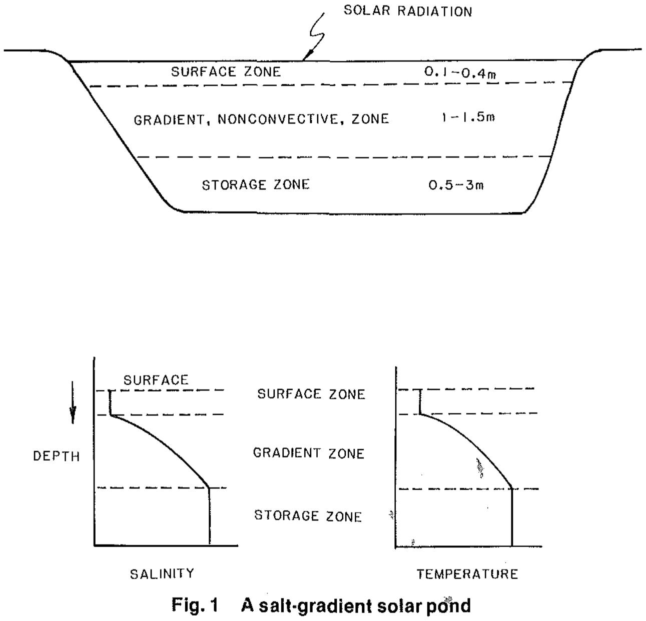

Fig. 1 A salt-gradient solar pond

---

[1] Present address: Foster Wheeler Development Corp., Livingston, N.J. 07039

Contributed by the Heat Transfer Division for publication in the JOURNAL OF HEAT TRANSFER. Manuscript received by the Heat Transfer Division April 22, 1983. Paper No. 83-HT-77.

the flow may be taken as two-dimensional. Because of the temperature gradient, the effect on the flow due to the heat input into the surface zone from the gradient zone is also considered. Of particular interest are the decay of temperature away from the inflow, the downward penetration of the flow, and the stability of the nonconvecting gradient zone. The temperature rise in the surface layer due to heat rejection is determined, and the effect of the flow on the depth of the layer is considered in terms of entrainment from the gradient zone. The study mainly considers the steady-state circumstance that would arise under constant ambient conditions and constant heat rejection to the surface layer. Such a quasi-steady approach is satisfactory for the small depths that are of interest in solar ponds. However, the transient behavior, following the onset of the recirculating flow, may also be of interest in some cases and may be obtained by the procedure outlined in this paper. No concentration differences are considered in the present work, since the surface layer has an essentially uniform salt concentration in practice [1-3], and since the recirculating flow is withdrawn from and discharged into the surface zone only, without significant disturbance to the gradient zone.

The basic nature of the resulting mixed convection flow is studied and the effect of the physical variables, such as boundary conditions, aspect ratio of the enclosure and the flow configuration, on the flow is determined. The underlying physical processes are considered in terms of the results obtained and related to earlier work on mixed convection flow. The study, therefore, brings out several important features of combined natural and forced convection flow in enclosures, particularly with respect to the inflow conditions, which determine the buoyancy effects. The basic mechanisms are also related to the flow in actual solar ponds. The results obtained indicate how various physical variables may be chosen to minimize the effect of the flow on the stability of the gradient zone. With a proper design of the flow system, the surface layer of a salt-gradient solar pond may, therefore, be employed for heat rejection from a power plant operating on the energy extracted from the pond, without significantly affecting its performance and efficiency.

Analysis

As previously outlined, the main concerns pertaining to heat rejection in the surface layer of a salt-gradient solar pond are the surface temperature increase and the consequent increase in evaporation, increase in the depth of the layer, effect of flow on the stability of the nonconvective zone, and the increase in temperature at the outflow. The last consideration is an important one, since an increase in the outflow temperature leads to an increase in the cooling water temperature for the power plant and a consequent decrease in thermal efficiency of power generation. The outflow needs to be located where the temperature increase is negligible.

We will first study the energy exchange between the surface layer and the environment. Considerable information exists on the underlying physical processes, and empirical correlations are available for the determination of energy transfer by the dominant modes, which are solar heating, evaporation, convection and back-radiation. Under steady-state conditions, the total energy gained from the solar flux, conduction from the gradient layer, and energy rejected by the power plant is lost by evaporation, back-radiation and convection. Therefore

$$H_T = H_e + H_c + H_{br} - H_s = H_d + H_p \qquad (1)$$

Nomenclature

B = atmospheric radiation factor in equation (3)

Bi = Biot number for surface heat loss defined in equation (15)

Bi_d = Biot number for conduction heat input from gradient zone defined in equation (15)

d = height of inflow and outflow channels, m

g = gravitational acceleration, $\mathrm{m/s^2}$

Gr = Grashof number defined in equation (15)

h = heat transfer coefficient defined in equation (5)

h_o = depth of a stratified fluid layer, m

H = depth of surface layer, m

$H_{br}, H_c, H_d, H_e, H_p, H_s, H_T$ = heat flux due to back radiation, convection, conduction from below, evaporation, heat rejection, solar energy and total heat loss, respectively, $\mathrm{W/m^2}$

k = thermal conductivity of the fluid, W/mk

P = atmospheric pressure, kPa

p = local pressure, $\mathrm{N/m^2}$

p_a = partial vapor pressure in the ambient medium, kPa

p_s = partial vapor pressure at surface, kPa

Pr = Prandtl number

Re = Reynolds number defined in equation (15)

Ri = local Richardson number defined in equation (16)

Ri_o = overall Richardson number defined in equation (17)

$T, T_a, T_b, T_e, T_i, T_p, T_S$ = local, ambient, outlet, equilibrium, initial, solar pond surface and natural water body surface temperature, respectively, K

u = horizontal velocity component, m/s

U = nondimensional horizontal velocity defined in equation (10)

U_o = inlet velocity, m/s

U_m = mean velocity of a stratified layer, m/s

v = vertical velocity component, m/s

V = nondimensional vertical velocity defined in equation (10)

V_e = ambient air speed, m/s

x = horizontal coordinate distance, m

X = nondimensional horizontal coordinate distance

y = vertical coordinate distance, m

Y = nondimensional vertical coordinate distance

α = thermal diffusivity, $\mathrm{m^2/s}$

β = coefficient of thermal expansion, $\mathrm{K^{-1}}$

ν = kinematic viscosity, $\mathrm{m^2/s}$

ρ = local density, $\mathrm{kg/m^3}$

ρ_o = reference density, $\mathrm{kg/m^3}$

$\Delta\rho$ = density difference across a stratified layer, $\mathrm{kg/m^3}$

ω' = vorticity, $\mathrm{m^2/s}$

ω = dimensionless vorticity defined in equation (10)

ψ' = stream function, $\mathrm{s^{-1}}$

ψ = dimensionless stream function defined in equation (10)

σ = Stefan-Boltzman constant, $\mathrm{W/m^2K^4}$

τ' = time, s

τ = dimensionless time defined in equation (10)

θ = dimensionless temperature defined in equation (10) where H_T is the total energy lost per unit area at the surface and H_e, H_c, H_{br}, H_s, H_d, and H_p are the corresponding heat fluxes due to evaporation, convective loss, back-radiation, solar energy input, conduction into the surface layer from below, and heat rejection. Employing the results from various studies [12-14], the following correlations, in S.I. units, are obtained [6]

$$H_e = 21.7\ V_e (p_s - p_a) \tag{2}$$

$$H_{br} = 0.97\sigma (T_s{}^4 - BT_a{}^4) \tag{3}$$

$$H_c = 0.0041\ V_e P (T_s - T_a) \tag{4}$$

The solar flux may be obtained for a given location [15], H_d from the measured temperature profile in the gradient zone and H_p from the thermal efficiency of a given power plant operating on the extracted energy.

If the total surface heat loss H_T is plotted against the surface temperature T_s for given ambient conditions, the temperature at $H_T = 0$ is the equilibrium temperature T_e for a natural water body, and the surface attains this temperature at steady state. The surface temperature of a solar pond is higher because of H_d and may be denoted by T_p, where $H_d = H_T(T_p) - H_T(T_e)$. If heat rejection to the pond also exists, the surface temperature must rise further to reject the additional energy to the atmosphere. Therefore, the increase in the average surface temperature due to heat rejection may be determined. A frequently employed expression for surface energy exchange is derived from equations (1-4) and is given by [7]

$$H_T = h(T_s - T_e) \tag{5}$$

where the heat transfer coefficient h may be determined from the gradient of the H_T versus T_s plot at the equilibrium temperature. Therefore, both h and T_e may be computed at various times during the year. Clearly, this approach is a quasi-steady one, and it has been found to be quite satisfactory for the study of thermal processes in natural water bodies.

The flow field generated in the surface zone by the recirculating flow for heat rejection may now be considered. Considering the geometry and coordinate system of Fig. 2, the heated fluid loses thermal energy to the atmosphere as it moves from the inflow to the outflow. The flow region is bounded by the interface with the gradient zone at the bottom and with the free surface at the top. The governing equations for the laminar, unsteady two-dimensional flow are the continuity, momentum, and energy conservation equations. Employing the Boussinesq approximations, these may be written as [16]

$$\frac{\partial u}{\partial x} + \frac{\partial v}{\partial y} = 0 \tag{6}$$

$$\frac{\partial u}{\partial \tau'} + u\frac{\partial u}{\partial x} + v\frac{\partial u}{\partial y} = -\frac{1}{\rho}\frac{\partial p}{\partial x} + \nu\left(\frac{\partial^2 u}{\partial x^2} + \frac{\partial^2 u}{\partial y^2}\right) \tag{7}$$

$$\frac{\partial v}{\partial \tau'} + u\frac{\partial v}{\partial x} + v\frac{\partial v}{\partial y} = -\frac{1}{\rho}\frac{\partial p}{\partial y} + \nu\left(\frac{\partial^2 v}{\partial x^2} + \frac{\partial^2 v}{\partial y^2}\right) - g\beta(T - T_i) \tag{8}$$

$$\frac{\partial T}{\partial \tau'} + u\frac{\partial T}{\partial x} + v\frac{\partial T}{\partial y} = \alpha\left(\frac{\partial^2 T}{\partial x^2} + \frac{\partial^2 T}{\partial y^2}\right) \tag{9}$$

For turbulent flow, both ν and α are replaced by the corresponding sums of molecular and eddy components. The laminar flow assumption is appropriate for small solar ponds and for laboratory systems [11]. The two-dimensional approximation also implies long inflow and outflow channels, which spread out the flow over the entire width of the pond, and thus reduce the velocities. The results obtained indicate the general trends, which would also be expected to apply qualitatively for larger ponds with high wind-induced turbulence levels, as characterized by large eddy viscosity and diffusivity [17, 18].

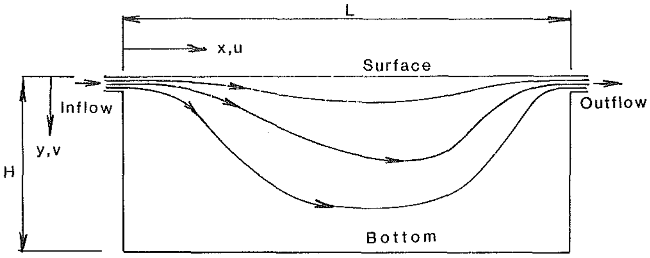

Fig. 2 Coodinate system for a flow configuration under consideration

The foregoing equations may be written in the conservative vorticity-stream function formulation, with the following nondimensionalization

$$X = x/d,\ Y = y/d,\ U = u/U_o,\ V = v/U_o,$$
$$U = \partial\psi/\partial Y,\ V = -\partial\psi/\partial X,\ \omega = \omega'/(U_o/d),$$
$$\tau = \tau' U_o/d,\ \psi = \psi'/U_o d,\ \theta = \frac{T - T_i}{T_o - T_i},\ \omega' = \frac{\partial v}{\partial x} - \frac{\partial u}{\partial y} \tag{10}$$

as [19]

$$\frac{\partial \omega}{\partial \tau} + \frac{\partial}{\partial X}(U\omega) + \frac{\partial}{\partial Y}(V\omega) = \frac{1}{\mathrm{Re}}\left(\frac{\partial^2 \omega}{\partial X^2} + \frac{\partial^2 \omega}{\partial Y^2}\right) - \frac{\mathrm{Gr}}{\mathrm{Re}^2}\frac{\partial \theta}{\partial X} \tag{11}$$

$$\omega = -\left(\frac{\partial^2 \psi}{\partial X^2} + \frac{\partial^2 \psi}{\partial Y^2}\right) \tag{12}$$

$$\frac{\partial T}{\partial \tau} + \frac{\partial}{\partial X}(U\theta) + \frac{\partial}{\partial Y}(V\theta) = \frac{1}{\mathrm{Re\,Pr}}\left(\frac{\partial^2 \theta}{\partial X^2} + \frac{\partial^2 \theta}{\partial Y^2}\right) \tag{13}$$

The corresponding initial and boundary conditions in terms of velocity and temperature are

$$\tau = 0,\ U = V = \theta = 0,\ \text{for } 0 \le X \le L/d,\ 0 \le Y \le H/d,$$
$$\tau > 0,\ U = V = \frac{\partial \theta}{\partial X} = 0,\ \text{for } X = 0,\ (H/d - 1) \le Y \le H/d$$
$$X = L/d,\ (H/d - 1) \le Y \le H/d \tag{14}$$
$$\partial U/\partial Y = 0,\ \partial\theta/\partial Y = \mathrm{Bi}\,\theta,\ \text{at } Y = 0$$
$$\frac{\partial U}{\partial Y} = 0,\ \frac{\partial \theta}{\partial Y} = \frac{H_d d}{k(T_o - T_i)},\ \text{at } Y = H/d$$
$$U = 1,\ V = 0,\ \theta = 1,\ \text{for } X = 0,\ 0 < Y < 1$$
$$U = 1,\ V = 0,\ \frac{\partial \theta}{\partial X} = 0,\ \text{for } X = L/d,\ 0 < Y < 1 \tag{14}$$

The boundary conditions in terms of ω and ψ may be obtained from these [6]. The outflow temperature T_b is obtained from the solution of these equations, and the inflow temperature T_o is specified. The governing parameters that arise are the Reynolds number Re, the Prandtl number Pr, the Grashof number Gr, the Biot number Bi, a similar parameter Bi_d, which characterizes the conduction heat gain from the nonconvective zone, and the geometry parameters H/d and L/d. Thus

$$\mathrm{Re} = U_o d/\nu,\ \mathrm{Gr} = g\beta(T_o - T_i)d^3/\nu^2,\ \mathrm{Pr} = \nu/\alpha$$
$$\mathrm{Bi} = hd/k,\ \mathrm{Bi}_d = \frac{H_d d}{k(T_o - T_i)} \tag{15}$$

A solution of these time-dependent elliptic equations, with the corresponding boundary conditions, yields the flow and temperature fields.

The effect of the recirculating flow on the stability of the nonconvective zone must also be considered, since a disturbance to and an entrainment of fluid from this layer may increase the depth of the surface layer. The flow has a destabilizing effect, which tends to overturn the stably stratified region. If the flow velocity at the interface is high enough, it will overturn the gradient region to some depth, thereby increasing the depth of the surface layer. A comparison between the stabilizing density gradient and the destabilizing effect of the shear flow yields the local Richardson number Ri, where

$$\mathrm{Ri}=\frac{g}{\rho}\frac{\partial \rho}{\partial y}\Big/\left(\frac{\partial u}{\partial y}\right)^2 \tag{16}$$

The stratification is stable if Ri is larger than a certain amount, obtained as 0.25 for a linear velocity distribution [20]. For the flow of a stratified fluid layer, an overall Richardson number Ri_o may be defined as

$$\mathrm{Ri}_o=g\frac{\Delta\rho}{\rho_o}h_o/U_m{}^2 \tag{17}$$

where U_m is the mean velocity in the layer, h_o its depth, $\Delta\rho$ the density difference across the layer and ρ_o a reference density. Entrainment into such a flow has been measured in several studies, and it has been found that if $\mathrm{Ri}_o \gtrsim 0.85$, the entrainment into the flow is negligible [21, 22]. Therefore, for larger values of Ri_o the entrainment into the flow from the nonconvective zone is negligible, indicating an essentially unaltered depth of the surface. These considerations are again discussed when numerical results are presented.

The governing equations, equations (11–13), were solved numerically, employing the Alternating Direction Implicit (ADI) method of Peaceman and Rachford [23]. The elliptic stream function equation was solved by successive overrelaxation, though cyclic reduction was also employed for some runs at later stages of the study. The solution was obtained with increasing time, at various values of the governing parameters, till steady-state was reached. Various other inflow-outflow locations and other boundary conditions were also considered. The grid spacing and the criterion for convergence at each time step and at the steady-state were varied to ensure a negligible dependence of the results on the values chosen. Further details on the numerical procedure may be obtained from [19, 23–27]. Results were obtained over wide ranges of the governing parameters and boundary conditions. Some of the characteristic results are outlined and discussed in the next section. Re values up to around 1000 were considered, to simulate laminar flow at the inflow channel. This corresponds to values as high as around 10^5 for Reynolds number Re_H based on the total depth of the surface layer, a definition which has also been employed in earlier studies of recirculating flows [25]. The value of $\mathrm{Gr}/\mathrm{Re}^2$ was varied from 0 to 1.0, which corresponds to the range encountered in actual practice. All the results are shown for $L/H=10$, though other values were considered, and the corresponding trends are outlined. The parameter d/H was taken at a typical value of 0.1, since a variation in its value did not substantially affect the basic characteristics of interest in the flow.

It must be noted that both the interfaces of the surface zone are taken as horizontal with a zero shear condition imposed on the flow. In the presence of significant wind shear, the velocity gradient at the air–water interface may be obtained from the computed shearing stress due to wind [25]. Similarly, at the interface with the gradient zone, the shear due to the recirculating flow generates a circulating flow in the region below the interface. A consideration of this effect, therefore, involves a study of the flow field in the entire pond, including double-diffusion due to salt and temperature differences. In order to simplify the analysis, the no-shear condition is taken as a limiting case of negligible effect of the stably stratified gradient zone on the flow. In practice, of course, a finite nonzero shear is exerted on the flow at the interface. The study also considered the other limiting case of zero-velocity, so that maximum shear is exerted on the flow. It was found that the two velocity boundary conditions yielded results that were quite close, except near the interface, for the flow configurations and parametric ranges considered here. The slip condition is obviously closer to the actual situation, because the interface is with the same fluid, which is stably stratified. For a more accurate representation, all three regions must be considered with appropriate flow and shear continuity at the interfaces.

Before proceeding to the presentation of the numerical results, some of the assumptions made to obtain the mathematical model just outlined need to be discussed in greater detail, particularly with respect to their validity in an actual system. In practice, the flow would be three-dimensional near the inflow and outflow channels. However, since it is necessary to spread the flow out horizontally for effective heat transfer to the environment and for lower velocity levels, in order to minimize the disturbance to the gradient zone, the diffusers need to be suitably designed to obtain an essentially two-dimensional flow in much of the enclosed region. Buoyancy effects also contribute to a horizontal temperature homogeniety, as observed in several earlier studies [5, 7, 17]. In fact, simple one-dimensional, vertical models have also been found to be satisfactory for deep, stratified lakes due to horizontal uniformity of temperature observed in practice. The expressions for the surface energy transport, equations (1–5), are also based on several of these studies, which have employed actual ambient conditions to predict the thermal behavior of natural lakes and ponds [7, 17]. Consequently, the basic mechanisms underlying heat transfer processes at the surface are numerically simulated by means of the results obtained from earlier studies on similar problems.

The stability of the gradient zone should rigorously be considered in terms of the stable salt stratification in the zone and the destabilizing shear flow in the surface layer. However, this is a very complicated problem because of the double-diffusive nature of the transport mechanisms. A fairly good approximation of the disturbance to this zone may be obtained by considering the entrainment into the shear flow from below the surface zone. Earlier work on stratified shear flows provides information on the Richardson number at which this entrainment, and hence the disturbance to the nonconvective region, becomes negligible [21, 22]. Since these results have received corroboration from both analysis and experimentation, the results are employed in the present work to consider the destabilization of the gradient zone due to the flow in the surface layer. Unfortunately, not much experimental work has been done on recirculating mixed convection flows in enclosures to allow a detailed comparison of the present results with experiment. However, comparison can be made with earlier analytical and numerical work and with some available experimental data. A good agreement between the results from the present study and those from earlier work was obtained [28], lending further support to the mathematical model and to the numerical study carried out. A recent experimental study on a similar flow configuration [29] has also indicated good agreement with the numerical results obtained here. Some of the characteristic trends are presented in the next section.

Results and Discussion

The surface heat loss as a function of the surface temperature at various values of the windspeed V_e is shown in Fig. 3. The temperature at which the heat loss is zero is the equilibrium temperature T_e for a natural water body. The surface temperature for a solar pond is obtained by equating the heat loss to the energy gained H_d by the surface layer due to conduction from the gradient zone. Thus a typical value for

H_d of 64 W/m^2 [6] gives a surface temperature T_s about 3.6 K higher than T_e at $V_e = 8$ km/hr. The heat transfer coefficient h may also be obtained from the slope of the curves at the corresponding surface temperature. A value of 20 W/m^2 K was obtained at $V_e = 10$ km/hr, and this value increases with V_e as expected. The curves in Fig. 3 are shown at an ambient air temperature of 30°C, relative humidity 20 percent and B of 0.8, corresponding to typical ambient conditions in North America in the summer. Similar curves may be obtained at different ambient conditions. The values of h and T_p from this and similar computations were employed in the determination of the corresponding heat loss parameters in the study of the recirculation.

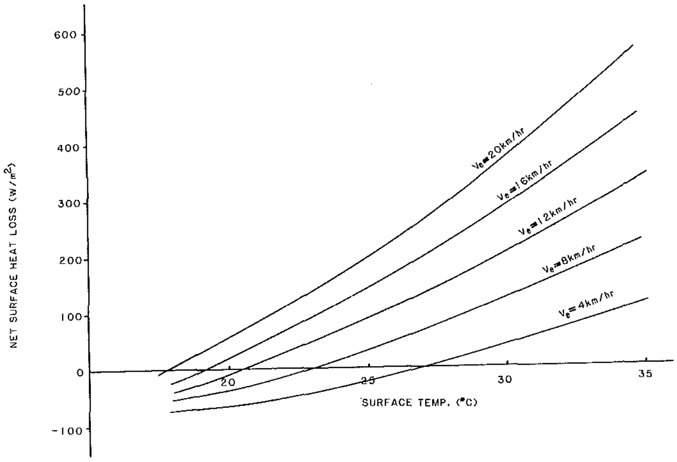

Fig. 3 Total surface heat loss as a function of the average surface temperature at various windspeeds

Figure 4 shows the steady-state streamlines at Re = 100, $L/H = 10$, Bi = 1.0, and Bi$_d$ = 0.12 for three values of Gr/Re^2, 0.001, 0.01, and 0.1. As the mixed convection parameter Gr/Re^2 increases, the buoyancy effect increases and pushes the streamlines upwards, as expected. This results in a narrower flow region near the surface and consequently larger flow velocities. This, in turn, causes a circulating flow in the lower region of the layer, the strength of the circulation increasing as Gr/Re^2 increases and gives rise to larger shear in the upper region. It is also seen that the flow is essentially developed over most of the length of the layer, indicating negligible change in the velocity profile along x. For larger aspect ratios L/H, 100 and 1000, this effect was found to be even more pronounced. Thus, over much of the flow region, U varies only with Y, and V is zero. The profile is also strongly dependent on Gr/Re^2. Therefore, for given Re and Gr/Re^2, a developed flow analysis, similar to that in channel flow, may be expected to yield results close to those obtained by a solution of the full equations. This is an interesting feature and was found to arise shortly after the onset of the flow and to change very gradually with time. The flow is established very rapidly, and as the thermal field moves outward from the inlet, the flow varies slowly due to the buoyancy coupling in the momentum equation. The steady-state is, therefore, largely determined by the thermal field, as also found in [24]. As is physically expected, the parameters Bi and Bi$_d$ determine the temperature level in the surface layer, and the effect on the flow field, over the range considered, was found to be small.

The isotherms corresponding to foregoing flow circumstances are shown in Fig. 5. The thermal field is narrower and more concentrated near the surface at the larger value of Gr/Re^2. In addition, the temperature θ at the outlet is higher

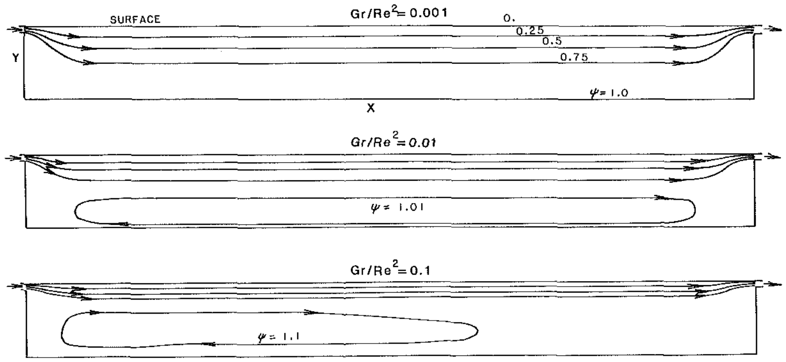

Fig. 4 Steady-state streamlines at Re = 100, Bi = 1.0 and Bi$_d$ = 0.12 at three values of the parameter Gr/Re^2

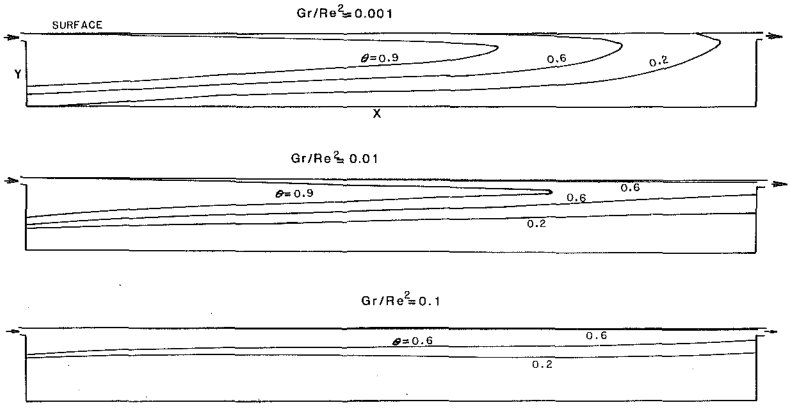

Fig. 5 Steady-state isotherms at Re = 100, Bi = 1.0 and Bi$_d$ = 0.12

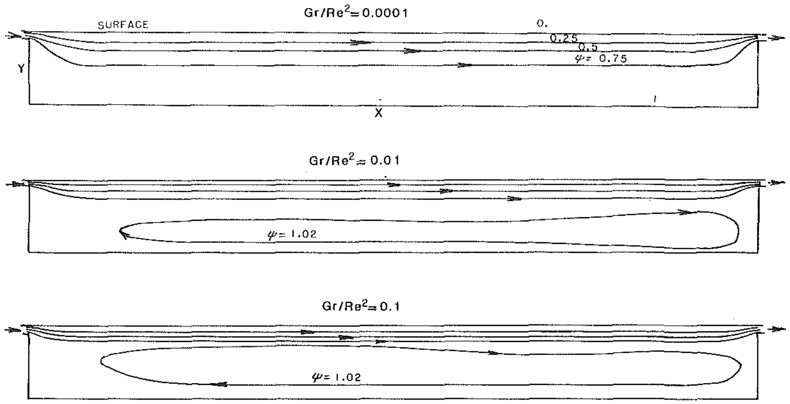

Fig. 6 Steady-state streamlines at $Re = 1000$, $Bi = 1.0$, $Bi_d = 0.12$

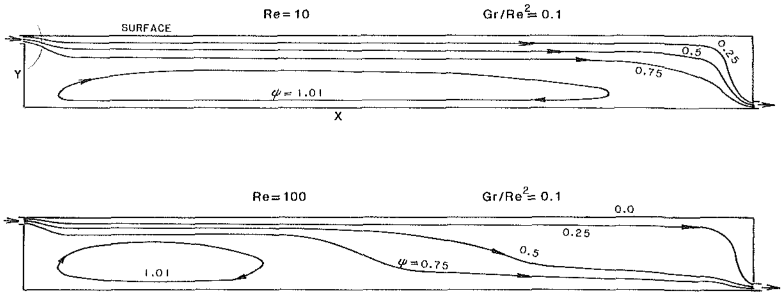

Fig. 7 Steady-state streamlines for the outflow at the bottom at $Re = 10$ and 100 for $Gr/Re^2 = 0.1$, $Bi = 1.0$ and $Bi_d = 0.0$

at the larger Gr/Re^2. The first effect is an expected one and agrees with the results of the preceding figure. Also the narrowing of the flow region implies larger flow velocities, which allow less time for heat loss at the surface, as the flow moves from the inlet to the outlet. This results in the observed greater penetration of the isotherms away from the inlet. The temperature in the lower region of the surface layer does not change appreciably from its initial value, particularly at the larger Gr/Re^2. This also indicates a small thermal effect on the gradient zone because of the heat rejection process. The effect of increasing the Reynolds number is seen by comparing these results with those at $Re = 1000$, shown in Fig. 6. At a given value of Gr/Re^2, an increase in Re results in a narrowing of the flow region for this flow configuration, a trend expected from a similar behavior in boundary layer flows, such as jets [16, 21]. This, in turn, leads to a larger outlet temperature with an increase in Re, for a given value of Gr/Re^2.

Figure 7 shows the results for a different flow configuration at $L/H = 10$, with the outflow at the bottom on the opposite side. Due to thermal buoyancy, the flow stays near the top surface over much of the flow region and then moves downward toward the outlet. At the larger Re, the downward movement of the flow starts at a much smaller distance from the inlet. In the absence of buoyancy, the flow is expected to spread out essentially evenly in the surface layer due to the pressure difference generated by the flow. It is evident from the two cases shown that the mixed convection flow being studied depends strongly on the Reynolds number in addition to the parameter Gr/Re^2. Therefore, a larger Re, which indicates a larger inflow of momentum, and hence a larger pressure effect, results in a greater spread of the flow. Due to the spreading of the flow at the larger Re, the flow velocities far from the inlet are smaller, resulting in a weaker circulation in the region below the main flow. Similar trends were observed at larger aspect ratios and for different values of the governing parameters. Good agreement was observed with experimental results for an aspect ratio of 1.0 [28].

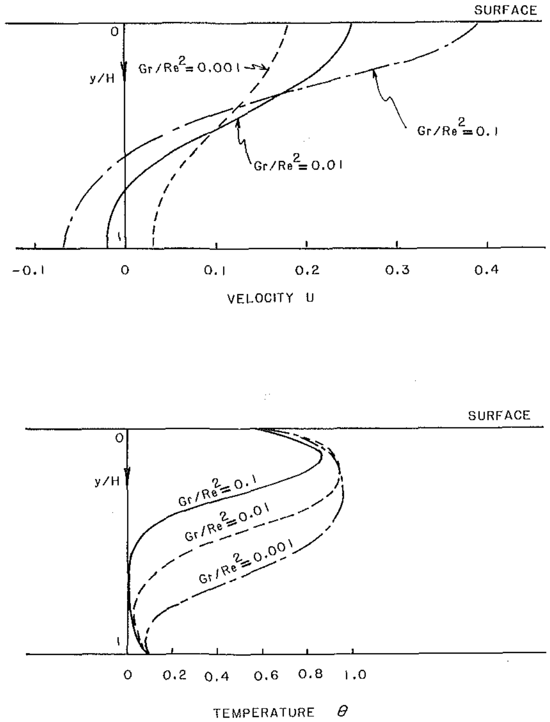

Fig. 8 Velocity and temperature profiles for the flow circumstance of Fig. 4 at various values of Gr/Re^2

The foregoing trends are also evident in the temperature and velocity profiles, shown in Fig. 8 for the flow configuration of Fig. 2 at the midplane of the surface layer at various values of the parameter Gr/Re^2. As seen before, an increasing buoyancy effect, indicated by the value of Gr/Re^2, results in a narrowing of the flow region near the surface, an increase in flow velocities in this region, and a stronger cir-

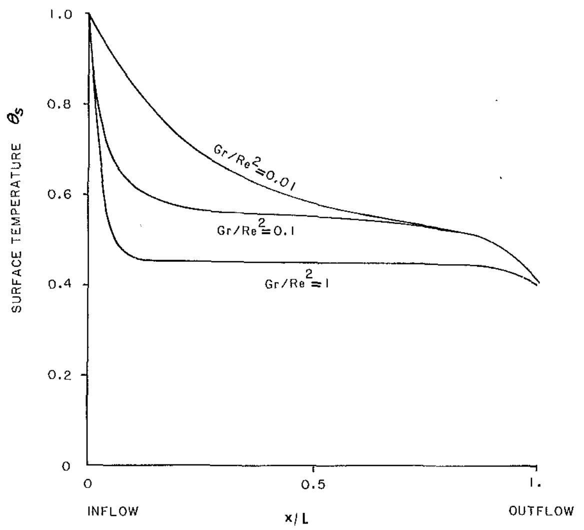

Fig. 9 Surface temperature variation along the length of the pond for the flow circumstance of Fig. 4

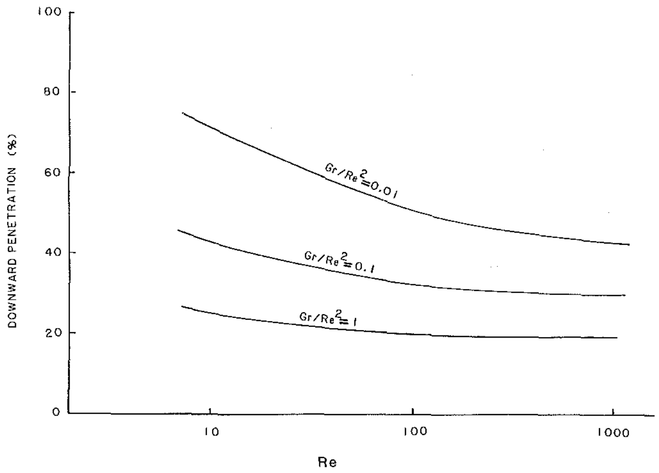

Fig. 10 Dependence of the downward penetration of the flow, as percentage of the total depth, on the inflow conditions

culating flow below the region. The variation of the Richardson number with the depth y may be determined from these graphs. A value of 14.0 was obtained at $Gr/Re^2=0.1$ in the region between the upper main flow and the circulating flow at the bottom of the layer, indicating a strong stable stratification. Similarly, the value of the overall Richardson number Ri_o may be obtained for the flow in the surface layer above the nonconvective zone, considering the typical density variation in the latter [3, 6]. For the velocities at the interface, shown in Fig. 8, it was found that the gradient zone is very stable to the flow and that the entrainment into the flow from the nonconvective layer is also negligible. For the flow configuration of Fig. 7, the interface near the outlet was found to be disturbed, with $Re<0.85$, as expected. However, by moving the outlet only a few centimeters away from the interface, the flow velocities at the interface became small enough to result in a negligible disturbance to the interface. Several other flow configurations were studied, and it was found that the configuration of Fig. 2 results in a negligible disturbance to the interface for layer depths larger than about 0.2 m. Other boundary conditions for the velocity field, at the lower boundary, were also considered, since the actual circumstance requires a shear continuity condition. The imposition of a no-slip condition did not affect the flow in the upper region significantly, though the flow in the lower region is changed substantially, as expected. Similarly, the temperature profiles are affected at the lower boundary by a change in Bi_d.

The variation of the surface temperature along the length of the solar pond is shown in Fig. 9 for three values of Gr/Re^2. A larger value of Gr/Re^2 was seen earlier to give rise to larger flow velocities near the surface, and thus result in a small temperature drop from the inlet to the outlet. Figure 9 shows only the surface temperature, the outflow temperature T_b being an average of fluid temperatures at the outlet, as shown in Fig. 5. It is seen that a large temperature drop occurs at the inlet, followed by a gradual decrease towards the outlet. At the outlet, again, a sharp drop occurs as the cold water from below mixes with the hotter upper region fluid. The initial sharp drop is expected because of the entrainment of cold fluid at the inlet and larger heat loss to the environment because of higher temperature. Because of larger velocities at the higher Gr/Re^2, following inflow, a greater entrainment is expected, which is reflected in a sharper temperature drop at the inlet. The entrainment decreases, due to Ri_o increasing downstream, and a larger velocity level at the higher Gr/Re^2 leads to a more gradual temperature decrease. The results would obviously also depend strongly on the heat loss parameter Bi. The downward penetration of the flow, in terms of the $\psi=0.9$ streamline, is shown in Fig. 10 as percentage of the total depth. This figure, therefore, indicates quantitatively the trends outlined earlier. It could provide inputs for the selection of the inlet conditions for the desired minimum flow penetration and consequent minimum disturbance to the nonconvective zone.

In summary, the surface layer of a salt-gradient solar pond may be employed for heat rejection from a power plant operating on the energy extracted from the pond, and thus avoid the need to provide an additional water body for heat rejection. However, the inflow-outflow locations and the inflow conditions must be chosen with care, employing results such as those presented here, so as to avoid significant disturbances to the gradient zone and to keep the overall effect on the thermal field in the solar pond small.

Conclusions

An analytical and numerical study of the convective flow in the surface layer of a salt-gradient solar pond due to a recirculating flow for heat rejection has been carried out. The temperature and velocity fields are studied in detail for a wide range of inlet and surface heat loss conditions. Various flow configurations are considered and the effect of buoyancy on the flow field investigated. The results obtained indicate a strong dependence of the flow on the mixed convection parameter Gr/Re^2. The temperature field is also strongly affected by the thermal boundary conditions at the surface and at the interface with the gradient zone. For large aspect ratios, which are of interest in practice, the flow is found to be essentially developed over much of the flow region, indicating the possibility of developing simple, approximate analytical models for the study of these systems for design. The gradient zone is found to be very stable and to be only slightly disturbed by the flow, if the inflow and outflow are located close to the surface. For other flow configurations, more care is needed to avoid significant disturbance to the nonconvective zone.

The study has considered two-dimensional laminar flow, which applies in several cases of practical interest. Though not reported here, turbulent flow, employing a simple eddy viscosity model, was also studied and the basic trends, features and conclusions obtained here were found to apply in that case as well. The two-dimensional approximation is both relevant and important, since the spreading out of the flow over the surface layer results in much lower velocities than those that would arise for a three-dimensional flow due to a different design for inlet and outlet channels. This indicates the need for the design of a system that allows a close approximation to a two-dimensional flow. The study also considers the surface heat loss mechanisms and indicates the determination of the increase in the average surface temperature due to heat rejection. The underlying physical processes are discussed in terms of the numerical results obtained and their effect on a practical heat rejection system outlined.

Acknowledgments

The authors acknowledge the support of the Department of Mechanical and Aerospace Engineering, Rutgers University, for this work and the several discussions with F. Zangrando on this problem.

References

1 Tabor, H., "Solar Ponds," *Solar Energy*, Vol. 7, 1963, pp. 189–194; also, "Nonconvecting Solar Ponds," *Phil. Trans. Royal Soc. London*, Vol. A295, 1980, pp. 423–433.

2 Elata, C., and Levin, O., "Hydraulics of the Solar Pond," *Proc. 11th Cong. Int. Assoc. Hyd. Res.*, Leningrad, USSR, 1965.

3 Nielsen, C. E., "Nonconvective Salt-Gradient Solar Ponds," *Solar Energy Handbook*, ed. by W. C. Dickinson and P. N. Cheremisinoff, Marcel Dekker, N.Y., 1979.

4 Zangrando, F., and Bryant, H. C., "Heat Extraction from a Salt-Gradient Solar Pond," *Proc. Int. Conf. Alt. Energy Sources*, Vol. 6, Miami Beach, Hemisphere, pp. 2935–2967.

5 Harris, M. J., and Wittenberg, L. J., "Heat Extraction from a Large Salt-Gradient Solar Pond," Rep. TP-245-430, *Proc. Solar Heating Cooling Systems Conf.*, Colorado Springs, 1979.

6 Jaluria, Y., "Heat Rejection and Energy Extraction Within Solar Ponds," Tech. Rep. SERI/RR-252-1393, Solar Energy Research Institute, Colo., 1982.

7 Moore, F. K., and Jaluria, Y., "Thermal Effects of Power Plants on Lakes," ASME JOURNAL OF HEAT TRANSFER, Vol. 94, 1972, pp. 163–168.

8 Jaluria, Y., "Thermal Effects of Energy Discharge to a Lake," *Proc. Int. Conf. Num. Meth. Thermal Problems*, Pineridge Press, Swansea, U.K., 1979, pp. 317–328.

9 Wada, A., "A Study on Phenomena of Flow and Thermal Diffusion Caused by Outfall Cooling Water," *Proc. 10th Conf. Coastal Engg.*, Vol. 2, 1967, pp. 1389–1411.

10 Jirka, G. H., Abraham, G., and Harleman, D. R. F., "An Assessment of Techniques for Hydrothermal Prediction," Rep. No. B250509, U.S. Nat. Tech. Inf. Ser., 1975.

11 Zangrando, F., "Heat and Mass Extraction from Solar Ponds: Analysis and Development of a Laboratory Facility," Tech. Rep. SERI/TR-252-1569, Solar Energy Research Institute, Colorado, 1982.

12 Raphael, J. M., "Prediction of Temperature in Rivers and Reservoirs," *ASCE J. Power Div.*, Vol. 88, 1962, pp. 157–181.

13 Edinger, J. E., Duttweiler, D. W., and Geyer, J. C., "The Response of Water Temperatures to Meteorological Conditions," *Water Resources Res.*, Vol. 5, 1968, pp. 1137–1143.

14 Wada, A., "Studies on Prediction of Recirculation of Cooling Water in a Bay," *Proc. 11th Conf. Coastal Engg.*, London, England, pp. 1453–1471.

15 Duffie, J. A, and Beckman, W. A., *Solar Energy Thermal Processes*, Wiley, N.Y., 1974.

16 Jaluria, Y., *Natural Convection Heat and Mass Transfer*, Pergamon Press, Oxford, U.K., 1980.

17 Sundaram, T. R., and Rehm, R. G., "Effects of Thermal Discharges on the Stratification Cycle of Lakes," *AIAA Journal*, Vol. 10, 1972, pp. 204–210.

18 Meyer, K. A., "A One-Dimensional Model of the Dynamic Layer Behavior in a Salt-Gradient Solar Pond," Los Alamos Lab., Rep. No. LA-UR-81-987, 1981.

19 Patankar, S. V., *Numerical Methods in Heat Transfer and Fluid Flow*, Hemisphere, Washington, D.C., 1980.

20 Miles, J. W., "On the Stability of Heterogeneous Shear Flows," *J. Fluid Mech.*, Vol. 10, 1961, pp. 496–508.

21 Koh, R. C. Y., "Two-Dimensional Surface Warm Jets," *ASCE J. Hyd. Div.*, Vol. 97, 1971, pp. 819–836.

22 Turner, J. S., *Buoyancy Effects in Fluids*, Cambridge Univ. Press, U.K., 1973.

23 Peaceman, D. W., and Rachford, H. H., "The Numerical Solution of Parabolic and Elliptic Differential Equations," *J. Soc. Ind. Appl. Math*, Vol. 3, 1955, pp. 28–41.

24 Jaluria, Y., and Gupta, S. K., "A Numerical Study of Mixed Convection in Enclosures," *Int. J. Energy Res.*, Vol. 7, 1983, pp. 201–210.

25 Oberkampf, W. L., and Crow, L. I., "Numerical Study of the Velocity and Temperature Fields in a Flow Through a Reservoir," ASME JOURNAL OF HEAT TRANSFER, Vol. 98, 1976, pp. 353–359.

26 Roache, P. J., *Computational Fluid Dynamics*, Hermosa Publishers, Albuquerque, N.M., 1982.

27 Cha, C. K., and Jaluria, Y., "Recirculating Mixed Convection Flow for Energy Extraction," ASME Paper No. 83-HT-75; *Int. Journal of Heat and Mass Transfer*, Vol. 27, 1984, pp. 1801–1812.

28 Cha, C. K., "An Analytical and Numerical Investigation of Recirculating Mixed Convection Flow in an Enclosure," Ph.D. thesis, Rutgers University, 1983.

29 Jaluria, Y., and O'Mara, B. T., "Thermal Field in a Water Body Due to a Buoyant Two-Dimensional Surface Water Jet," ASME Paper No. 84-HT-68, 1984.

K. L. Tzuoo[1]

T. S. Chen
Mem. ASME

B. F. Armaly
Mem. ASME

Department of Mechanical and
Aerospace Engineering,
University of Missouri-Rolla,
Rolla, Mo. 65401

Wave Instability of Natural Convection Flow on Inclined Surfaces

Wave instability of nautral convection boundary layer flow adjacent to inclined surfaces is analyzed by a linear theory. The effects of the nonparallelism of the main flow and thermal fields are taken into account in the analysis. Neutral stability results for Prandtl numbers of 0.7 and 7.0 are presented for upward-facing heated surfaces, for angles of inclination ranging from 0 to 90 deg. These results are compared with available analytical wave instability results for small angles of inclination. They are also compared with analytical vortex instability results and with available experimental data.

Introduction

Natural convection flows over vertical, inclined, and horizontal flat plates have been studied extensively (see, for example, [1-5] and those cited therein). The stability of these flows has also been investigated rather extensively from the standpoint of either the wave mode or the vortex mode of disturbances. Typical examples of the work can be found in [4-10]. It has been concluded from these studies that (*i*) both wave and vortex modes of instability exist in natural convection flow over inclined, upward-facing heated plates, (*ii*) the susceptibility of such a flow to both wave and vortex modes of instability increases as the angle of inclination from the vertical increases, and (*iii*) the first onset of the instability of flow is due to the wave mode or vortex mode of disturbances, depending on whether the angles of inclination from the vertical are smaller or larger than a certain critical value.

In contrast to the vortex instability analysis from which results are available for all angles of inclination [5], the analysis on wave instability of inclined, natural convection flow has been limited to a range of inclination angles close to the vertical [9] and to a very small range of angles close to the horizontal [10], with no results for the range of angles between the two. Furthermore, a large discrepancy in the trends of the critical Grashof numbers between the two wave instability analyses exists. The cause for such a discrepancy warrants a thorough investigation, and this has motivated the present study.

It should be noted that the problem treated here is different from that described in [11]. In that study the effect of buoyancy force on the wave instability of forced flow over inclined surfaces was examined; that is, the analysis was carried out for the forced-convection dominated situation, and critical Grashof and Reynolds numbers were presented for buoyancy force intensity, $\mathrm{Gr}_x/\mathrm{Re}_x{}^2$, between 0 and 1.0. The present study, on the other hand, is directed at pure natural convection; that is, for $\mathrm{Re}_x = 0$ or $\mathrm{Gr}_x/\mathrm{Re}_x{}^2 = \infty$. Thus, even though the formulation of the instability problem is similar between the two studies, the main flow problems considered are physically different. Another point that needs to be mentioned here is that there are large discrepancies in the experimental data on the critical Grashof or Rayleigh numbers for inclined natural convection flows [6, 12-14]. The predicted critical Grashof numbers based on the linear theory from the present analysis will be compared with experimental data.

Analysis

Consider a semi-infinite flat plate that is situated at an angle of inclination γ from the horizontal in a queiscent ambient fluid at temperature T_∞. The surface of the plate is maintained at a uniform temperature T_w, with its heated surface facing upward. The main flow and thermal fields for this configuration must be known before the flow instability analysis can be performed. In a recent study [5], such a main flow was described by the following system of equations

$$f''' + 3ff'' - f'^2 + \frac{2}{5}\left[\eta\theta + \int_\eta^\infty \theta d\eta + \frac{3}{2}\xi\int_\eta^\infty \frac{\partial\theta}{\partial\xi} d\eta\right] + \xi\theta$$

$$= 3\xi\left[f'\frac{\partial f'}{\partial\xi} - f''\frac{\partial f}{\partial\xi}\right] \tag{1}$$

$$\frac{1}{\mathrm{Pr}}\theta'' + 3f\theta' = 3\xi\left[f'\frac{\partial\theta}{\partial\xi} - \theta'\frac{\partial f}{\partial\xi}\right] \tag{2}$$

$$\begin{gathered} f(\xi,0) = f'(\xi,0) = 0,\ \theta(\xi,0) = 1 \\ f'(\xi,\infty) = \theta(\xi,\infty) = 0 \end{gathered} \tag{3}$$

in which the dimensionless coordinates (ξ, η), the reduced stream function $f(\xi, \eta)$, and the dimensionless temperature $\theta(\xi, \eta)$ are defined respectively by

$$\eta = \frac{y}{x}G, \quad \xi = G\tan\gamma \tag{4}$$

$$f(\xi,\eta) = \frac{\psi(x,y)}{5\nu G}, \quad \theta(\xi,\eta) = \frac{T - T_\infty}{T_w - T_\infty} \tag{5}$$

with

$$G = [(\mathrm{Gr}_x \cos\gamma)/5]^{1/5} \tag{6}$$

and the primes denotes partial differentiation with respect to η. Also Pr is the Prandtl number, $\psi(x, y)$ is the stream function, ν is the kinematic viscosity, (x, y) are the streamwise and normal coordinates, and Gr_x is the local Grashof number.

The formulation of the stability problem as based on linear theory parallels that described in [11], and its details are omitted here. The resulting equations for the amplitude functions, ϕ for the stream function of disturbances and s for the temperature disturbances, assume the following dimensionless form

$$(f' - c)(D^2\phi - \alpha^2\phi) - f'''\phi - \frac{i}{5\alpha G}\left[\left(2\eta f' - 3f - 3\xi\frac{\partial f}{\partial\xi}\right)\right.$$

---

[1] Presently a Ph. D. candidate at the Department of Mechanical Engineering, Standford University, Stanford, Calif. 94305

Contributed by the Heat Transfer Division and presented at the 1983 ASME/JSME Thermal Engineering Joint Conference, Honolulu, Hawaii, March, 1983. Manuscript received by the Heat Transfer Division August 25, 1983.

$$\cdot (D^3\phi - \alpha^2 D\phi) - \left(2\eta f''' + f'' - 3\xi \frac{\partial f''}{\partial \xi}\right) D\phi \Big]$$

$$+ \frac{i}{5\alpha} \tan\gamma\, Ds + \frac{1}{5} s$$

$$= - \frac{i}{5\alpha G} (D^4\phi - 2\alpha^2 D^2\phi + \alpha^4\phi) \tag{7}$$

$$(f' - c)s - \frac{i}{5\alpha G}\left(2\eta f' - 3f - 3\xi \frac{\partial f}{\partial \xi}\right) Ds - \theta'\phi$$

$$+ \frac{i}{5\alpha G}\left(2\eta\theta' - 3\xi \frac{\partial \theta}{\partial \xi}\right) D\phi$$

$$= - \frac{i}{5\alpha \mathrm{Pr} G} (D^2 s - \alpha^2 s) \tag{8}$$

with the boundary conditions

$$D\phi = \phi = s = 0 \quad \text{at } \eta = 0 \quad \text{and } \eta = \infty \tag{9}$$

In arriving at equations (7-9), all lengths, velocities, and temperatures have been normalized by a reference length L, a reference velocity U, and a reference temperature difference ΔT defined, respectively, by

$$L = \frac{x}{G}, \quad U = \frac{5\nu}{x} G^2, \quad \Delta T = T_w - T_\infty \tag{10}$$

In equations (7-9), the wave number of the disturbances α is a positive real number and the wave velocity c is a complex number. The real part of c, c_r, represents the phase speed of the wave propagation and its imaginary part c_i determines the amplification ($c_i > 0$), neutrality ($c_i = 0$), or damping ($c_i < 0$) of the disturbances with respect to time. Thus the disturbances are considered to be of plane waves of a temporal mode expressible as

$$\{\phi(y), s(y)\} \exp[i\alpha(x - ct)] \tag{11}$$

The main flow is stable, neutrally stable, or unstable according to whether $c_i < 0$, $c_i = 0$, or $c_i > 0$.

The system of equations (1-3) and (7-9) are valid for all angles γ except for γ = 90 deg (i.e., for a vertical flat plate). When γ = 0 deg (i.e., a horizontal flat plate), ξ reduces to 0 and the boundary layers of the main flow/thermal fields become similar such that the terms containing ξ and $\xi\, \partial/\partial\xi$ vanish from these equations.

To provide a system of flow instability equations that are valid for plates at and close to the vertical orientation, a separate analysis was carried out. This gives rise to the following system of equations

$$(f' - c)(D^2\phi - \alpha^2\phi)$$

$$- f'''\phi - \frac{i}{4\alpha G}\Big[\left(\eta f' - 3f + 3\xi \frac{\partial f}{\partial \xi}\right)(D^3\phi - \alpha^2 D\phi)$$

$$- \left(\eta f''' - f'' + 3\xi \frac{\partial f''}{\partial \xi}\right) D\phi\Big] + \frac{i}{4\alpha G} Ds + \frac{1}{4G} \cot\gamma\, s$$

$$= - \frac{i}{4\alpha G}(D^4\phi - 2\alpha^2 D^2\phi + \alpha^4\phi) \tag{12}$$

$$(f' - c)s - \frac{i}{4\alpha G}\left(\eta f' - 3f + 3\xi \frac{\partial f}{\partial \xi}\right) Ds - \theta'\phi$$

$$+ \frac{i}{4\alpha G}\left(\eta\theta' + 3\xi \frac{\partial \theta}{\partial \xi}\right) D\phi$$

$$= - \frac{i}{4\alpha \mathrm{Pr} G}(D^2 s - \alpha^2 s) \tag{13}$$

with the boundary conditions

$$D\phi = \phi = s = 0 \quad \text{at} \quad \eta = 0 \quad \text{and} \quad \eta = \infty \tag{14}$$

The reference quantities for length, velocity, and temperature difference for equations (12-14) are respectively

$$L = \frac{x}{G}, \quad U = \frac{4\nu}{x} G^2, \quad \Delta T = T_w - T_\infty \tag{15}$$

and G now is given by

$$G = [(\mathrm{Gr}_x \sin\gamma)/4]^{1/4} \tag{16}$$

The main flow quantities f, θ and their (ξ, η) derivatives appearing in equations (12) and (13) are now obtained from the system of equations [3]

$$f''' + 3ff'' - 2f'^2 + \theta + \xi\left[\eta\theta + \int_\eta^\infty \theta\, d\eta - 3\xi \int_\eta^\infty \frac{\partial\theta}{\partial\xi} d\eta\right]$$

$$= 3\xi\left(f'' \frac{\partial f}{\partial \xi} - f' \frac{\partial f'}{\partial \xi}\right) \tag{17}$$

$$\frac{1}{\mathrm{Pr}} \theta'' + 3f\theta' = 3\xi\left(\theta' \frac{\partial f}{\partial \xi} - f' \frac{\partial \theta}{\partial \xi}\right) \tag{18}$$

$$f(\xi,0) = f'(\xi,0) = 0, \quad \theta(\xi,0) = 1$$
$$f'(\xi,\infty) = \theta(\xi,\infty) = 0 \tag{19}$$

in which

$$\eta = \frac{y}{x} G, \quad \xi = \frac{1}{4G} \cot\gamma \tag{20}$$

Nomenclature

c = dimensionless wave velocity
c_r = real part of c
c_i = imaginary part of c
D^n = differential operator, $d^n/d\eta^n$
f = reduced stream function defined by equation (5) or (21)
g = gravitational acceleration
G = dimensionless parameter defined by equations (6) or (16)
Gr_x = local Grashof number, $g\beta(T_w - T_\infty)x^3/\nu^2$
L = reference length defined by equation (10) or (15)
Pr = Prandtl number
s = dimensionless temperature disturbance amplitude function
T = mainflow temperature
T_w = wall temperature
T_∞ = free-stream temperature
t = time
U = reference velocity defined by equation (10) or (15)
x = axial coordinate
y = normal coordinate

Greek Symbols

α = dimensionless wavenumber based on L
β = volumetric coefficient of thermal expansion
γ = angle of inclination from the horizontal
η = pseudosimilarity variable defined by equation (4) or (20)
θ = dimensionless temperature
ν = kinematic viscosity
ξ = buoyancy parameter defined by equation (4) or (20)
ϕ = dimensionless flow disturbance amplitude function
ψ = stream function of mainflow

$$f(\xi,\eta)=\frac{\psi(x,y)}{4\nu G},\quad \theta(\xi,\eta)=\frac{T-T_\infty}{T_w-T_\infty} \tag{21}$$

It is noted that the system of equations (12-14) and (17-19) are not valid at $\gamma = 0$ deg (i.e., for a horizontal plate), but are good for 0 deg $< \gamma \leq 90$ deg; that is, they can be applied to plates that are vertical or inclined from the vertical. When $\gamma = 90$ deg, ξ reduces to 0, the boundary layers of the main flow/thermal fields become similar, and equations (17) and (18) transform to those for the classical problem of natural convection flow along a vertical flat plate [1].

With the availability of equations (7-9) for 0 deg $\leq \gamma < 90$ deg and equations (12-14) for 0 deg $< \gamma \leq 90$ deg, along with their respective main flow equations (1-3) and (17-19), the wave instability for inclined natural convection flow can be analyzed for the entire range of inclination angles between $\gamma = 0$ deg to $\gamma = 90$ deg. In the present study, equations (7-9) were employed for 0 deg $\leq \gamma < 90$ deg and equations (12-14) for $\gamma = 90$ deg. It needs to be pointed out here that in equations (7), (8), and (12), (13), the terms arising from the normal velocity component and the axial temperature gradient of the main flow/thermal field are included. These terms vanish in a striclty parallel flow model, and are often neglected in the instability analyses of boundary layer flows.

Equations (7-9) for 0 deg $\leq \gamma < 90$ deg and (12-14) for 0 deg $< \gamma \leq 90$ deg, along with a normalizing condition (say, $D^2\phi = 1$ at $\eta = 0$) constitute an eigenvalue problem of the form

$$E(\alpha,G,c_r,c_i,\xi,\gamma,\mathrm{Pr})=0 \tag{22}$$

For prescribed values of ξ, γ, and Pr, solution of equation (22) provides a relationship among α, G, c_r, and c_i. In particular, in the mapping of a neutral stability curve (i.e., the α versus G curve for which $c_i = 0$), the values of c_r and α that satisfy equation (22) were sought as the eigenvalues for preassigned values of $c_i = 0$ and $G = \xi/\tan\gamma$ or $G = \cot\gamma/4\xi$.

Results and Discussion

Equations (1-3) were solved by a finite-difference scheme similar to, but modified from that described in [15] to provide the main flow quantities $f(\xi,\eta)$ and $\theta(\xi,\eta)$ and their derivaties that were needed in the numerical solution of equations (7-9) for 0 deg $\leq \gamma < 90$ deg. The main flow for the case of $\gamma = 90$ deg was obtained by solving equations (17-19) with $\xi = 0$ numerically by a fourth-order, Runge-Kutta integration scheme. The equations describing the wave instability problem, equations (7-9) and equations (12-14), were also solved respectively for 0 deg $\leq \gamma < 90$ deg and $\gamma = 90$ deg by the Runge-Kutta numerical integration scheme. The eigenvalues α and c_r for prescribed values of c_i and G were obtained by employing a Newton-Raphson iterative technique. To suppress the growth of the truncation errors that are inherent in the numerical integration of the stability equations, the Gram-Schmidt orthogonalization procedure similar to that described in [16] was employed. The details of the numerical integration and solution of the eigenvalve problem parallel those given elsewhere [11] and are omitted here.

Neutral stability results, such as neutral stability curves and critical wave and Grashof numbers, were obtained for Prandtl numbers of 0.7 and 7 over a range of inclination angles γ from 0 to 90 deg. The α and c_r values obtained from solutions of equations (7-9) for given values of $G = (\mathrm{Gr}_x \cos\gamma/5)^{1/5}$, Pr, and $c_i = 0$ are based on a reference length L and a reference velocity U as given by equation (10), whereas the α and c_r values obtained from equations (12-14) for given values of $G = (\mathrm{Gr}_x \sin\gamma/4)^{1/4}$, Pr, and $c_i = 0$ are based on the L and U values defined by equation (15). To illustrate the neutral stability curves for all γ values between 0 and 90 deg, a commmon reference length and reference velocity must be defined. In the present study, the common reference quantities are taken as

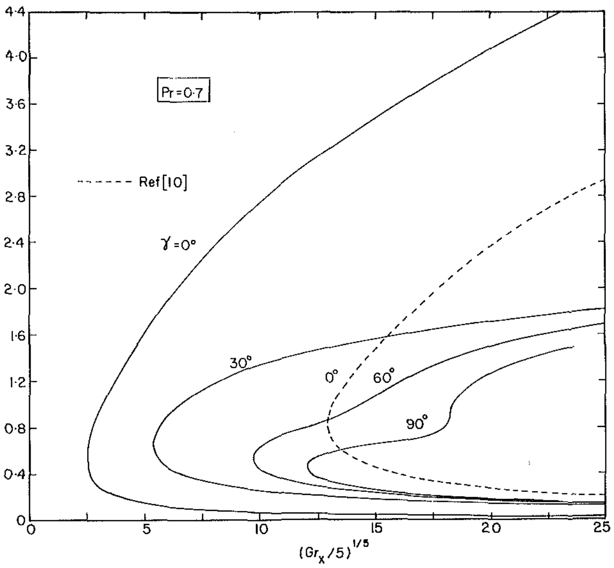

Fig. 1 Representative neutral stability curves, Pr = 0.7

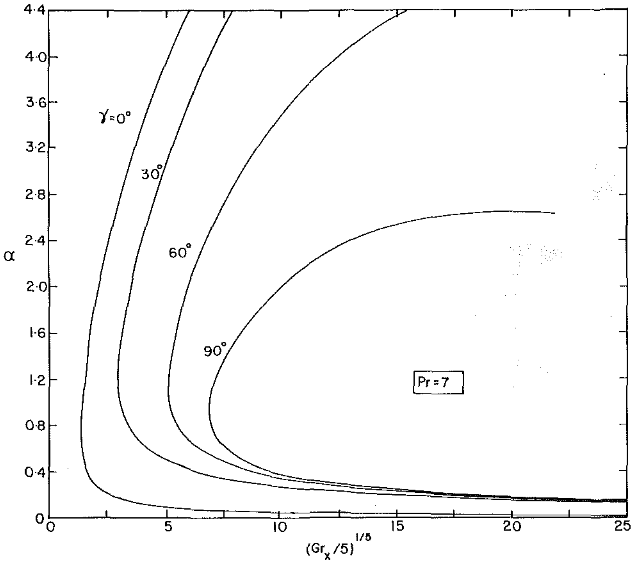

Fig. 2 Representative neutral stability curves, Pr = 7

$$L=x/(\mathrm{Gr}_x/5)^{1/5},\ U=(5\nu/x)\,(\mathrm{Gr}_x/5)^{2/5} \tag{23}$$

If one denotes the wave number and wavespeed in equations (7) and (8) as α_H and c_H, then the corresponding expressions based on L and U in equation (23) assume the form

$$\alpha=\alpha_H(\cos\gamma)^{1/5},\ c=c_H(\cos\gamma)^{2/5} \tag{24}$$

Similarly, if the wave number and wave velocity in equations (12) and (13) are denoted by α_v and c_v, the corresponding expressions based on L and U in equation (23) become

$$\alpha=(5^{1/5}/4^{1/4})(\sin\gamma)^{1/4}\,\alpha_v\,\mathrm{Gr}_x^{1/20} \tag{25}$$
$$c=(2/5^{3/5})(\sin\gamma)^{1/2}\,c_v\,Gr_x^{1/10}$$

Figures 1 and 2 show the neutral stability curves, α versus $(\mathrm{Gr}_x/5)^{1/5}$, respectively, for Pr = 0.7 and 7, for four representative angles $\gamma = 0$ deg (horizontal plate), 30, 60, and 90 deg (vertical plate), in which the wave number α is based on $L = x/(\mathrm{Gr}_x/5)^{1/5}$. It is seen for these figures that for both Pr = 0.7 and 7, the neutral stability curve shifts to the right as

Table 1 Critical Grashof numbers, wave numbers, and phase speeds

	Pr = 0.7			Pr = 7.0		
γ	Gr_x^*	α^*	c_r^*	Gr_x^*	α^*	c_r^*
0°	510	0.530	0.170	24	0.780	0.096
15°	2,642	0.606	0.220	154	1.023	0.114
30°	21,950	0.651	0.318	1,136	1,205	0.157
45°	140,660	0.597	0.466	5,573	1.250	0.212
60°	419,210	0.531	0.609	17,550	1.158	0.269
75°	840,170	0.488	0.717	41,550	1.045	0.317
90°	1,245,030	0.453	0.775	80,210	0.927	0.351

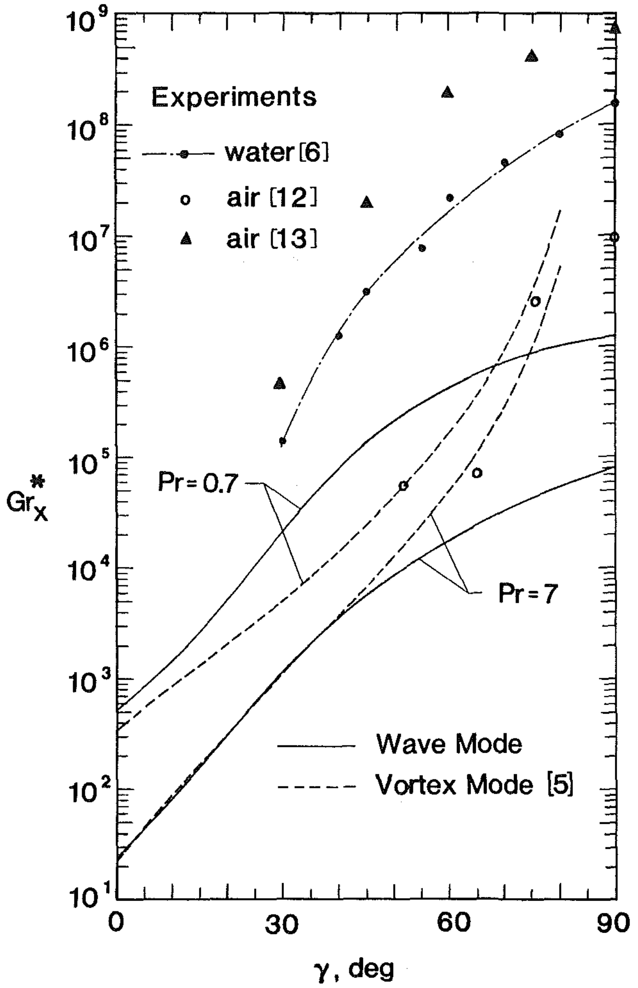

Fig. 3 Critical Grashof number versus angle of inclination from the horizontal

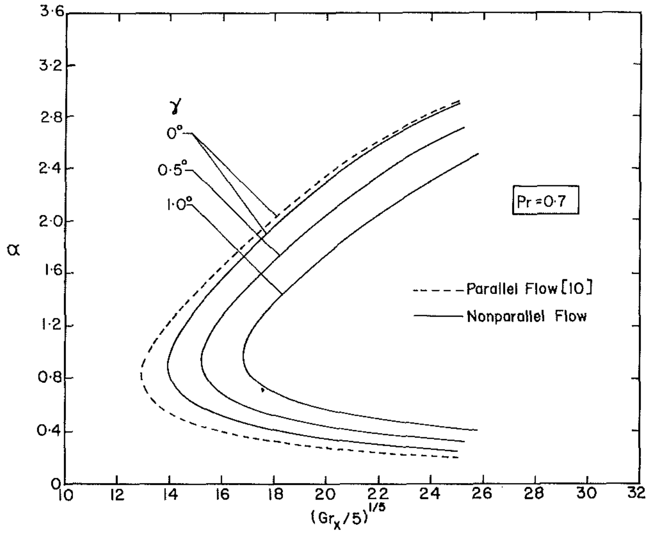

Fig. 4 Representative neutral stability curves for 0 deg ≤ γ ≤ 1 deg based on a different mode of solution, Pr = 0.7

the angle of inclination γ increases from the horizontal. That is, natural convection flow on inclined, heated, upward-facing plates becomes more stable to the wave mode of disturbances as the plate is tilted toward a vertical position. The least stable condition occurs at $\gamma = 0$ deg (i.e., for a horizontal plate) and the most stable situation exists at $\gamma = 90$ deg (i.e., for a vertial plate). Also the range of wave numbers for the instability of the flow is seen to decrease with increasing angle of inclination γ. A comparison between Fig. 1 and Fig. 2 reveals that fluids with Pr = 7 (such as water) are more susceptible to the wave mode of instability than fluids with Pr = 0.7 (such as air).

The minimum critical Grashof number Gr_x^* and the corresponding wave number α^* and phase speed c_r^* were also determined for various angles of inclination. They are listed in Table 1. It is noted that α^* and c_r^* are based on the reference length L and velocity U given by equation (23). The variation of the critical Grashof number $\mathrm{Gr}_x{}^*$ with angle of inclination γ for the two Prandtl numbers are illustrated in Fig. 3. Included in the figure also are the vortex instability results from [5] and the experimental results from [6, 12, 13]. The critical Grashof numbers from the present wave instability analysis are in good agreement with those reported in [9] for 45 deg ≤ γ ≤ 90 deg for Pr = 0.733 and Pr = 6.7. The analysis of [10] for Pr = 0.7, on the other hand, predicted critical Grashof number Gr_x^* of about 1.8×10^6 for $\gamma = 0$ deg, 7.5×10^6 for $\gamma = 1.67$ deg, and 3.1×10^7 for $\gamma = 2.51$ deg, as compared to $\mathrm{Gr}_x^* = 510$ for $\gamma = 0$ deg from the present analysis. The discrepancy between the two sets of analytical results has been determined to result from different modes of eigenvalues in the solution. The present solution is a continuation of the least stable model of solution from $\gamma = 90$ deg to $\gamma = 0$ deg, whereas the results of [10] are based on a mode of solution other than the least stable one. Indeed, the results of [10] for $\gamma = 0$ deg from a different mode were reproduced in the present study, under the parallel mainflow assumption, as shown with a dashed line in Fig. 1 and Fig. 4. The other three solid lines in Fig. 4 are the neutral stability curves for $\gamma = 0$ deg, 0.5 deg, and 1 deg, based on the mode of solution given in [10] under nonparallel mainflow assumption, that were obtained in the present investigation. Thus it may be concluded that the present analysis not only resolves the discrepancy in the trends of results between the two previous analytical studies on wave instability [9, 10], but also provides for the first time the correct minimum critical Grashof numbers for all inclination angles γ between 0 and 90 deg from the linear wave instability theory.

A comparison between the Gr_x^* versus γ curves from the wave mode and the vortex mode of disturbances in Fig. 3 reveals that the first onset of instability of the flow shifts from the vortex mode to the wave mode at a certain inclination angle γ as the plate is tilted from the horizontal to the vertical orientation. The shifting of instability mode occurs at $\gamma = 68$ deg for $\mathrm{Pr} = 0.7$ and 40 deg for $\mathrm{Pr} = 7$, which is in qualitative agreement with the experimental observations in water [6]. Also, as can be seen from Fig. 3, the critical Grashof numbers from experiments in water by Lloyd and Sparrow [6] are about two to three orders of magnitude larger than those for $\mathrm{Pr} = 7$ predicted by the linear theory, whereas the critical Grashof numbers from experiments in air by Tritton [12] are in good agreement with the prediction for $\mathrm{Pr} = 0.7$ except at γ close to 90 deg. The experimental results of Lock et al. [13] for air, on the other hand, are over two orders of magnitude larger than the predicted values except at $\gamma = 30$ deg. The trends of the Gr_x^* versus γ curves between theory and experiments, however, are similar. The large discrepancy between the analytical and experimental results is rather disturbing. It may be due to a certain degree of randomness in the observed critical Grashof numbers obtained by the various investigators [6, 12, 13] using different techniques. Indeed, during the course of experiments, instability of the flow in the boundary layers may not be detected or observed right at its incipient location until further downstream where the disturbances have grown sufficiently large. This is in contrast to the linear theory in which the disturbances are assumed to be infinitesimally small. For instance, since the Grashof number Gr_x is proportional to x^3, if the natural disturbances were not detected or observed until a downstream location 2.15 times the distance from the original incipient location, the observed critical Grashof number would be larger by an order of magnitude. The fiber anemometer used by Tritton [12] may have been more sensitive in detecting the flow instability than the electrochemical flow visualization used by Lloyd and Sparrow [6] or the Schlieren pictures and thermocouple probes used by Lock et al. [13], and this may have accounted for the lower critical Grashof numbers he has obtained. To verify this conjecture, further experimental studies using more senstive measuring devices may be in order. On the other hand, a flow instability analysis based on a more rigorous linear, nonparallel flow model, in which the axial dependence of the amplitude function as well as the wave number is accounted for, may also shed light on the discrepancy between the critical Grashof number results from the present analysis and the available experimental data.

Conclusion

Wave instability of natural convection flow on inclined, upward-facing heated plates has been investigated for angles of inclination ranging from the horizontal to the vertical orientation. Neutral stability curves and critical Grashof and wave numbers have been obtained for fluids with Prandtl numbers of 0.7 and 7.0. It has been found that the stability of the flow subject to the wave mode of disturbances increases as the angle of inclination from the horizontal increases. A comparison between the wave instability results and the vortex instability results indicates that the first onset of the flow instability shifts from the vortex mode to the wave mode at a certain angle of inclination as the plate is tilted from the horizontal toward the vertical orientation. The existence of a large discrepancy in the critical Grashof numbers between experiments and predictions warrants further investigations.

Acknowledgment

The present study ws supported in part by a grant from the National Science Foundation (NSF CME 79-19459).

References

1 Ostrach, S., "An Analysis of Laminar Free-Convection Flow and Heat Transfer About a Flat Plate Parallel to the Direction of the Generating Body Force," *NACA*, TN 2635, 1952.

2 Pera, L., and Gebhart, B., "Natural Convection Boundary Layer Flow over Horizontal and Slightly Inclined Surfaces," *International Journal of Heat and Mass Transfer*, Vol. 16, 1973, pp. 1131-1146.

3 Hasan, M. M., and Eichhorn, R., "Local Nonsimilarity Solution of Free Convection Flow and Heat Transfer from an Inclined Isothermal Plate," ASME JOURNAL OF HEAT TRANSFER, Vol. 101, 1979, pp. 642-647.

4 Gebhart, B., "Buoyancy Induced Fluid Motions Characteristic of Applications in Technology—The 1978 Freeman Scholar Lecture," ASME *Journal of Fluids Engineering*, Vol. 101, 1979, pp. 5-28.

5 Chen, T. S., and Tzuoo, K. L., "Vortex Instability of Free Convection Flow over Horizontal and Inclined Surfaces," ASME JOURNAL OF HEAT TRANSFER, Vol. 104, 1982, pp. 637-643.

6 Lloyd, J. R., and Sparrow, E. M., "On the Instability of Natural Convection Flow on Inclined Plates," *Journal of Fluid Mechanics*, Vol. 42, 1970, pp. 465-470.

7 Hwang, G. J., and Cheng, K. C., "Thermal Instability of Laminar Natural Convection Flow on Inclined Isothermal Plates," *Canadian Journal of Chemical Engineering*, Vol. 51, 1973, pp. 659-666.

8 Haaland, S. E., and Sparrow, E. M., "Vortex Instability of Natural Convection Flow on Inclined Surfaces," *International Journal of Heat and Mass Transfer*, Vol. 16, 1973, pp. 2355-2367.

9 Haaland, S. E., and Sparrow, E. M., "Wave Instability of Natural Convection on Inclined Surfaces Accounting for Nonparallelism of the Basic Flow," ASME JOURNAL OF HEAT TRANSFER, Vol. 96, 1973, pp. 405-407.

10 Pera, L., and Gebhart, B., "On the Stability of Natural Convection Boundary Layer Flow over Horizontal and Slightly Inclined Surfaces," *International Journal of Heat and Mass Transfer*, Vol. 16, 1973, pp. 1147-1163.

11 Chen, T. S., and Moutsoglou, A., "Wave Instability of Mixed Convection Flow on Inclined Surfaces," *Numerical Heat Transfer*, Vol. 2, 1979, pp. 497-509.

12 Tritton, D. J., "Transition to Turbulence in the Free Convection Boundary Layers on an Inclined Heated Plate," *Journal of Fluid Mechanics*, Vol. 16, 1963, pp. 417-435.

13 Lock, G. S. H., Gort, C., and Pond, G. R., "A Study of Instability in Free Convection from an Inclined Plate," *Applied Scientific Research*, Vol. 18, 1967, pp. 171-182.

14 Vliet, G. C., "Natural Convection Local Heat Transfer on Constant-Heat-Flux Inclined Surfaces," JOURNAL OF HEAT TRASNFER, Vol. 91, 1969, pp. 511-516.

15 Cebeci, T., and Bradshaw, P., *Momentum Transfer in Boundary Layers*, ch. 7, Hemipshere, Washington, D.C., 1977.

16 Wazzan, A. R., Okamura, T. T., and Smith, H. M. O., "Stability of Laminar Boundary Layer at Separation," *Physics of Fluids*, Vol. 190, 1967, pp. 2540-2545.

On the Stability and Flow Reversal of Pressure-Driven Flow in an Asymmetrically Heated U-Shaped Tube

Kun-Ying Zhou[1]

H. H. Bau
Assoc. Mem. ASME

Department of Mechanical Engineering
and Applied Mechanics,
University of Pennsylvania,
Philadelphia, Pa. 19104

Experimental and theoretical results are reported about the stability of pressure-driven flow in a vertical U-shaped loop to whose descending leg heat is supplied. The stability of the flow depends on a nondimensional number B, which represents the ratio between the buoyancy and the pressure heads. As long as $B<B_{cr}$, the flow is stable and the buoyancy assists the pressure in driving the flow. When $B>B_{cr}$, the flow ceases to be stable, the flow rate oscillates with increasing amplitude and then the flow reverses direction. The end result consists of stable ascending flow in the heated section. That is, the flow is driven by the buoyancy force and opposed by the pressure head. Two types of loops are considered: one containing single-phase fluid; and the other, saturated porous media (packed bed). A marginal stability curve is constructed using linear stability analysis. Finite difference numerical simulation suggests that the same curve is also valid for finite amplitude disturbances. The theoretical results are compared with experimental data.

1 Introduction

Asymmetrically heated, pressure-driven flow in a U-shaped loop is examined in this paper. We focus on a situation in which the buoyancy and pressure forces are of comparable magnitude.

Loops of this kind are often used to model geohydrothermal phenomena [1-3] such as hot springs. Thermal convection loops, in general, are also of interest for many technological applications. Witness their use in solar heaters, nuclear reactor core cooling systems, geothermal energy production systems, and process industries [4].

Prior studies [5-15] have tended to emphasize loops in which fluid motion is driven by buoyancy alone. These loops can be classified as closed loops [5-11] in which the fluid circulates continuously in a piping network, or as open loops [12-15] in which the feed fluid is supplied externally. Consideration has also been given to closed loops with throughflow [14-15], wherein some of the fluid circulates continuously and some of it is externally supplied. Further classification can be made according to whether the heating/cooling is supplied symmetrically [5-10, 12, 14-15], to the ascending fluid [11] or to the descending fluid [13].

Aspects which have been examined in previous works include the steady-state performance [6, 7, 10-12] and the stability of the steady-state motion [5, 7, 8, 10, 12-15]. Both experiments [7, 10] and analyses [5, 7, 8, 14, 15] reveal that under certain conditions the flow ceases to be stable. In the case of closed loops with symmetrical or slightly asymmetrical heating, the flow rate oscillates, and the flow occasionally reverses direction. When the descending fluid is heated [13] the flow rate oscillates with increasing amplitude until the flow direction reverses. Once the flow reverses direction, stable flow is observed along with an upward motion in the heater. In both cases, the unstable behavior may be attributed to the phase lag between the heating process and the generation of the buoyancy force.

From the foregoing, it is clear that very little has been done to examine the stability characteristics of pressure-driven flow in a loop with asymmetric heating. This is the topic of our present paper. We employed an experimental apparatus like that shown in Fig. 1. Fluid motion was driven by a pressure head, heat was supplied to the descending leg, and the ascending leg was insulated. We used in the loop both liquid and liquid saturated porous medium (packed bed). We shall refer to these two cases as the "water loop" and the "porous loop," respectively.

Additionally, we construct a simple one-dimensional model to describe the fluid motion in the loop (section 3). The stability of the motion is investigated using linear stability analysis and a numerical simulation (section 4). Finally, the theoretical and experimental results are compared in section 6.

2 The Experimental Apparatus

The experimental apparatus is described schematically in Fig. 1. The apparatus consists of a vertical U-shaped tube whose ends are connected to constant head tanks. The relative height (h) of the tanks can be varied.

By feeding the upper tank continuously with degassed, distilled water, we imposed a pressure difference between the

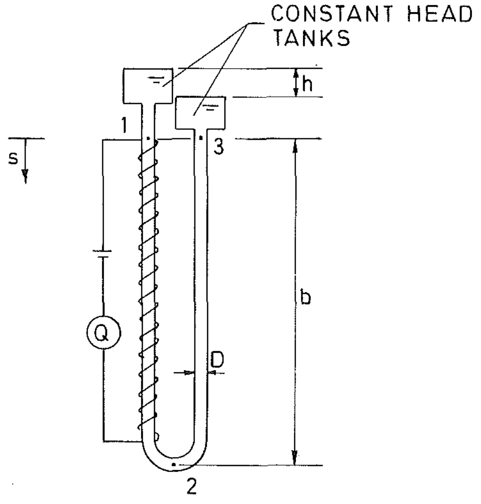

Fig. 1 The experimental apparatus

---

[1] Visiting Scholar, Beijing Institute of Chemical Technology, Beijing, China

Contributed by the Heat Transfer Division for publication in the JOURNAL OF HEAT TRANSFER. Manuscript received by the Heat Transfer Division January 20, 1984.

two ends of the U, which in turn created pressure driven flow in the U-shaped apparatus. The flow rate was obtained by measuring directly the amount of liquid drained from the lower tank.

Temperatures within the loop were measured with 36 gauge copper-constantan thermocouples located at the center of the pipe at stations 1, 2, and 3 in Fig. 1.

Heating was accomplished by wrapping the descending leg with nichrome wire. The heating was distributed uniformly along the vertical leg. The U-shaped loop was insulated with a layer of foil-covered fiberglass insulation. The input heat flow ranged from 0-550 W. We obtained the heat input from the heater resistance and the voltage input on the one hand and from the energy gain of the fluid in the descending leg

$$\rho C_p \frac{\pi D^2}{4} \hat{u}_s (\hat{T}_2 - \hat{T}_1)_s$$

on the other hand. The deviation was always smaller than 5 percent. We also took into consideration possible heat losses in the ascending leg. The average heat transfer coefficient (U) was estimated from the temperature drop between stations 2 and 3 (Fig. 1).

Two different loops were used in our experiments. The first had a height of $b = 1.5$ m and a diameter of $D = 8$ mm. In the other, $b = 0.95$ m and $D = 15.8$ mm (5/8 in.). The first loop contained distilled water, while the second loop was filled with saturated, closely packed, uniformly-sized, 4-mm glass beads. In both cases the working fluid was distilled water.

3 The Mathematical Model

A simple, theoretical model of the experimental loop is formulated in this section. The model consists of two straight tubes of internal diameter D, height b, and overall length $2b$. As was the case in many previous works [5-15], one-dimensional, time-dependent balances of mass, momentum, and energy are employed. Properties are assumed to be constant with the exception of density in the buoyancy term (the Oberbeck-Boussinesq approximation [18]). The equations are written in a form suitable for a loop filled with liquid or a liquid-saturated porous medium. The velocities and temperatures appearing in the balances are cross-sectionally averaged values.

For an incompressible (Boussinesq) fluid, the continuity equation implies that the velocity ($\hat{u}$) is constant within the loop and a function only of time ($\hat{t}$)

$$\hat{u} = \hat{u}(\hat{t}), \tag{1}$$

In the foregoing equation we neglected terms of order $\beta(\hat{T}_2 - \hat{T}_1)$ where β is the thermal expansion coefficient appearing in the state equation

$$\rho = \rho_1 [1 - \beta(\hat{T} - \hat{T}_1)]. \tag{2}$$

To be more specific, our analysis is correct only for $\beta(\hat{T}_2 - \hat{T}_1) << 1$.

In the above, superscript carets denote the dimensional form of variables which will later be made nondimensional.

A momentum balance at any axial location $\hat{s}$ along the loop yields

$$\frac{1}{\phi} \frac{d\hat{u}}{d\hat{t}} + \tau_w \frac{4}{\rho_1 D} + \frac{\rho}{\rho_1} g \cos\theta = -\frac{1}{\rho_1} \frac{\partial \hat{P}}{\partial \hat{s}} \tag{3}$$

where the various terms are respectively due to inertia, friction, body and pressure forces. Integration of equation (3) from inlet to outlet along the loop yields an integral balance

$$\frac{1}{\phi} \frac{d\hat{u}}{d\hat{t}} + f \frac{\hat{u}^2}{2D} = \frac{g\beta}{2b} \int_{\hat{s}_1}^{\hat{s}_3} \hat{T} \cos\theta d\hat{s} + \frac{\Delta \hat{P}}{2\rho_1 b} \tag{4}$$

where

$$f \frac{\rho_1 \hat{u}^2}{8} = \frac{1}{2b} \int_{\hat{s}_1}^{\hat{s}_3} \tau_w d\hat{s}, \text{ and } \Delta\hat{P} = \hat{P}_1 - \hat{P}_2 \tag{5}$$

The significance of the various symbols is given in the Nomenclature.

The friction factor f in (4) and (5) is expressed in the form

$$f = \frac{a}{\mathrm{Re}^n} \tag{6}$$

where a and n are constants and Re in the Reynolds number. For example, for the case of laminar isothermal flow in a tube, $a = 64$, $n = 1$; for flow in porous media (packed bed), $a = 2D^2/\lambda$ and $n = 1$. The foregoing correlations neglect secondary flows due to curvature and buoyancy.

One drawback of the proposed model is that the friction law (equation (6)) has to be supplied either from a numerical solution of the three-dimensional equations of motion or from experimental data. In this paper we assume that the friction law is given.

A local heat balance on the loop, neglecting axial conduction, compression work, and viscous heating, yields

$$r \frac{\partial \hat{T}}{\partial \hat{t}} + \hat{u} \frac{\partial \hat{T}}{\partial \hat{s}} = \begin{cases} \dfrac{4\hat{Q}}{\pi D^2 \rho_1 C_{p_f} b} & \text{(in section 12, } 0 \le \hat{s} \le b, \text{ Fig. 1)} \\ \dfrac{-4U(\hat{T} - \hat{T}_1)}{\rho_1 C_{p_f} D} & \text{(in section 23, } b \le \hat{s} \le 2b, \text{ Fig. 1)} \end{cases} \tag{7}$$

Nomenclature

A = nondimensional coefficient (equation (14))
a = numerical coefficient in the friction factor correlation
B = nondimensional group = $\dfrac{\rho_1 g\beta b(\hat{T}_2 - \hat{T}_1)_s}{2\Delta P}$
b = loop height (Fig. 1)
C_p = specific heat
D = tube inside diameter
d = the diameter of the glass beads
f = friction factor ($= a/\mathrm{Re}^n$)
k = thermal conductivity of the fluid
Gr = Grashof number $\left(= \dfrac{g\beta D^3 Q}{\pi k \nu^2 b}\right)$
h = height difference between the two tanks (Fig. 1)
H = nondimensional heat transfer coefficient
I = inertia term
n = exponent in the friction law
P = pressure
Q = heating rate at the descender
Re = Reynolds number (uD/ν)
r = specific heat ratio (equation (7))
s = a coordinate along the loop
T = temperature
t = time
u = velocity in the loop
U = overall heat transfer coefficient in the ascender

Subscripts

1,2,3 = locations in the loop (Fig. 1)
cr = critical value
f = fluid
m = solid matrix
s = steady state

Superscripts

$\hat{}$ = dimensional quantities
$'$ = perturbation

Greek letters

β = volume thermal expansion
θ = angle between fluid velocity vector and the vertical
λ = permeability
ν = kinematic viscosity
ρ = density
ϕ = porosity
τ_w = wall shear stress
ω = growth rate of the disturbance

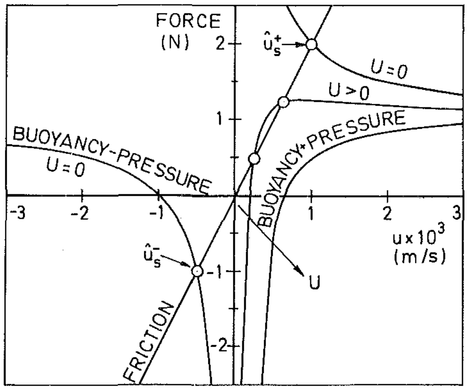

Fig. 2 Multiple steady-state solutions for the velocity are obtained when buoyancy ± pressure balances the friction force

where

$$r = \frac{\phi \rho_1 C_{p_f} + (1-\phi)\rho_m C_{p_m}}{\rho_1 C_{p_f}}.$$

Subscripts f and m respectively denote the fluid and solid matrix appearing in the porous loop. For the porous loop, $\phi = 0.44$ and $r = 0.72$. For the water loop, $\phi = 1$ and $r = 1$. The entrance condition at $\hat{s} = 0$ is $\hat{T} = \hat{T}_1$. The steady-state equations are obtained by eliminating the time derivatives from equations (4) and (7). The steady-state temperature distribution $(\hat{T} - \hat{T}_1)_s$ is

$$(\hat{T} - \hat{T}_1)_s = \begin{cases} \dfrac{4\hat{Q}}{\pi D^2 \rho_1 C_{p_f} \hat{u}_s} \dfrac{\hat{s}}{b} & 0 \le \hat{s} \le b \\ \dfrac{4\hat{Q}}{\pi D^2 \rho_1 C_{p_f} \hat{u}_s} \exp\left\{ -H \dfrac{(\hat{s} - b)}{b} \right\} & b \le \hat{s} \le 2b \end{cases} \tag{8}$$

where

$$H = \frac{4}{\rho_1 C_{p_f}} \frac{U}{\hat{u}_s} \frac{b}{D}$$

The steady-state velocity $(\hat{u}_s)$ is obtained from the transcendental equation

$$\frac{a\nu^n}{2D^{1+n}} \hat{u}_s^{2-n} = \frac{\Delta\hat{P}}{2\rho_1 b} + \frac{2g\beta\hat{Q}}{\pi D^2 \rho_1 C_{p_f} \hat{u}_s} \left[\frac{1 - e^{-H}}{H} - \frac{1}{2} \right] \tag{9}$$

Recall that $\hat{u}_s$ is also imbedded in H.

We depict in Fig. 2 the friction pressure and buoyancy forces as functions of the velocity $(\hat{u}_s)$ for laminar flow $(n = 1)$. Clearly, the steady-state solution corresponds to a situation in which the aforementioned forces balance each other. In cases where there are no heat losses at the ascending leg $(U = H = 0)$, equation (9) becomes

$$\frac{a\nu}{2D^2} \hat{u}_s^2 = \frac{\Delta\hat{P}}{2\rho_1 b} \hat{u}_s + \frac{g\beta\hat{Q}}{\pi D^2 \rho_1 C_{p_f}} \tag{10}$$

In this case, there are two possible steady-state solutions, denoted $\hat{u}_s^+$ and $\hat{u}_s^-$ in Fig. 2, which correspond, respectively, to descending and ascending flows in the heating section. In the case of counterclockwise circulation $(\hat{u}_s^+)$ both the pressure and buoyancy assist the flow; while in the case of clockwise circulation $(\hat{u}_s^-)$ the flow is driven by buoyancy and opposed by the pressure. Note that the model predicts possible flow in the clockwise direction regardless of the size of the pressure head. That is, the model permits limitless increase in the heater temperature till an appropriate balance is achieved. This, of course, is not realistic; but, since we are concerned mainly with relatively small pressure heads, this is not a serious limitation.

When we take into consideration possible heat loss from the nonheated leg $(U > 0)$, we observe that according to the magnitude of U there are two, one or no possible steady solutions with counterclockwise circulation. In these three cases the pressure always assists the flow. The same may not be true with regard to the buoyancy. High values of U may imply negative buoyancy. In conclusion, we note that the system accepts multiple steady-state solutions; and this naturally brings up the question of stability which we shall address in the next section.

We next introduce nondimensional variables, scaling the velocity with the counterclockwise steady-state velocity $(\hat{u}_s)$, the temperature with the steady-state temperature $(\hat{T}_2 - \hat{T}_1)_s$ and the length with the height b. The foregoing nondimensional scheme has been chosen so as to facilitate easy comparison with experimental data. The nondimensional momentum and energy equations are transformed into the following

$$I \frac{du}{dt} + A u^{2-n} = 1 + 2B \int_{s_1}^{s_3} T \cos\theta \, ds \tag{11}$$

$$r \frac{\partial T}{\partial t} + u \frac{\partial T}{\partial s} = \begin{cases} 1 & \text{(in section 12, } 0 \le s \le 1) \\ -HT & \text{(in section 23, } 1 \le s \le 2) \end{cases} \tag{12}$$

where

$$I = \frac{2}{\phi} \frac{\rho_1 \hat{u}_s^2}{\Delta\hat{P}}, \quad A = \frac{(\rho_1 \hat{u}_s^2) b}{\Delta\hat{P} D} \frac{a}{\mathrm{Re}_s^n},$$

and

$$B = \frac{\rho_1 \beta g b (\hat{T}_2 - \hat{T}_1)_s}{2\Delta\hat{P}} \tag{13}$$

and the corresponding boundary condition at $s = 0$ is $T = 0$.

Note that B is actually the ratio between the buoyancy and the pressure forces. I, B, and H are independent parameters, whereas A is not

$$A = 1 + 2B \left(\frac{1 - e^{-H}}{H} - \frac{1}{2} \right) \tag{14}$$

Equation (14) is obtained from the nondimensional steady-state momentum equation by using the fact that $u_s = 1$.

The steady-state solution in nondimensional form becomes

$$u_s = 1$$

$$T_s = \begin{cases} s & 0 \le s \le 1 \\ \exp\{-H(s-1)\} & 1 \le s \le 2 \end{cases} \tag{15}$$

In section 5, we shall investigate the conditions for which this steady-state solution is stable.

4 Experimental Results

We imposed a driving pressure head in the system by changing the relative height between the two constant head tanks. Then we gradually increased the heat supply to the descending leg. After each increase in the heat flux, sufficient time was allowed to permit a steady state to be achieved and the net effect of the heating was to accelerate the flow in the loop. This is not unexpected, since the increase in the heating rate contributes to the buoyancy and thus results in an increase in the driving force. To demonstrate this, we depict in Fig. 3 the observed increase in the Reynolds number and the temperature $(\hat{T}_2 - \hat{T}_1)_s$ as functions of the heating rate $(\hat{Q})$. For comparison, we also depict the predicted values of Re and $(\hat{T}_2 - \hat{T}_1)_s$ (solid lines), assuming laminar friction law $(f = 64/\mathrm{Re}, n = 1)$. The deviation of the actual data and the predictions indicates the inadequacy of the laminar friction law for this type of flow.

Once the heating rate exceeded some critical value, steady

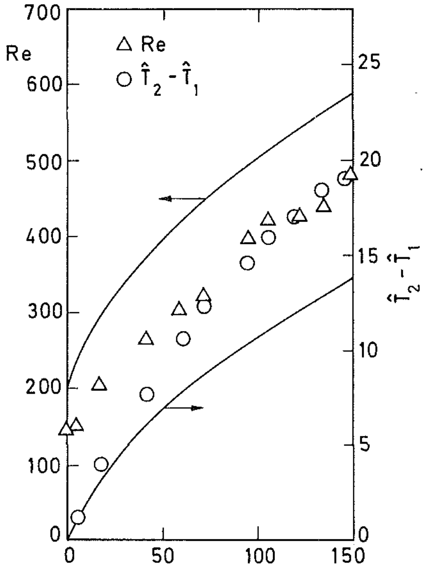

Fig. 3 Experimentally measured Reynolds number, Re (△) and temperature difference ($\hat{T}_2-\hat{T}_1$) (○) in the water loop as a function of the heating rate $\hat{Q}$. The solid lines are theoretical predictions based on a laminar friction law.

state could not be achieved. Instead, the flow rate and the temperature difference ($\hat{T}_2-\hat{T}_1$) started to oscillate with ever increasing amplitude. An example of this oscillatory behavior is depicted in Fig. 4. The period of the oscillations was about twice the flow time through the loop. The oscillations amplified until the flow reversed direction. The reversed flow corresponded to ascending motion in the heated section. Typical time intervals which elapsed from the time the oscillations were first observed until the flow reversal occurred were 0.5–9 hrs and 4–20 hrs for the water and porous loops, respectively. Once flow reversal occurred, stable flow was observed in the loop. (Of course, we switched the water supply to the other tank so as to maintain a constant pressure difference.)

The experimental path is also depicted in Fig. 5 (dashed line), where transition from one triangle to another is a result of an increase in the heat input. The open triangles represent stable runs, while the solid triangle represents the unstable situation, including the type of oscillations depicted in Fig. 4.

Clearly, oscillations develop when a critical value of the B number is attained. Values of B that correspond to the last stable run are documented in Table 1. Also shown in the table are the Reynolds (Re) number, the ratio of the Grashof number of the Reynolds number (Gr/Re), and the heat transfer coefficient H. The experimental error in calculating H, I, and B_{cr} is estimated to be smaller than 20 percent.

5 Stability Analysis

We use linear stability analysis to establish the conditions for which the steady flow predicted in the previous section is stable for small disturbances. Later we also carry out a numerical simulation through which we establish that the same stability conditions apply for finite disturbances as well.

Briefly, we perturb the steady-state solutions by introducing a small disturbance (u' and T'). The linearized perturbation equations are

$$I\frac{du'}{dt}+A(2-n)u_s^{1-n}u'=2B\int_{s_1}^{s_3}T'\cos\theta ds \tag{16}$$

$$r\frac{\partial T'}{\partial t}+u_s\frac{\partial T'}{\partial s}+u'\frac{\partial T_s}{\partial s}=\begin{cases}0 & 0\le s\le 1\\ -HT' & 1\le s\le 2\end{cases} \tag{17}$$

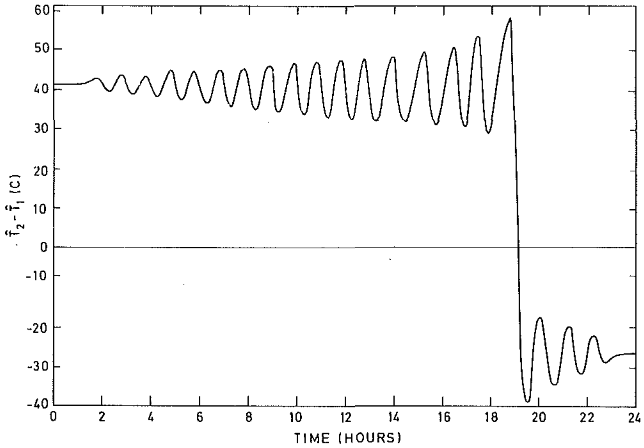

Fig. 4 Experimentally observed oscillations and a flow reversal in the porous loop. The temperature difference $\hat{T}_2-\hat{T}_1$ is depicted as a function of the time ($\hat{t}$)

and the corresponding entrance condition at $s=0$ is $T'=0$.

Equations (16,17) are linear and therefore admit solutions in which the dependent variables are proportional to exp ($\omega t/r$). In general, the growth rate ω is a complex variable. If the real part of ω, $\text{Re}(\omega)>0$, we say that the disturbance grows exponentially and the steady-state solution is unstable. On the other hand, if $\text{Re}(\omega)<0$ the disturbance decays and the steady-state solution is stable.

The characteristic equation for the growth rate (ω) is

$$F(\omega)=\frac{I}{2r}+\frac{(2-n)}{2}\frac{A}{\omega}-\frac{B}{\omega^3}(e^{-\omega}+\omega-1)+\frac{B}{\omega^2}(e^{-H}-1)$$
$$+\frac{B}{\omega^2(\omega+H)}(e^{-(\omega+H)}-1)(e^{-\omega}-H-1)=0 \tag{18}$$

In order to investigate the root locus of equation (18), we use the Nyquist technique [16]. The procedure is described in detail in [13] and therefore will not be repeated here. The growth rate ω is a complex number. Thus the disturbances grow in an oscillatory fashion. This is in accord with our experimental observations (Fig. 4).

The resulting marginal stability curves are plotted in Fig. 5 for $H=0$ and different values of the power $n=0.7$, 0.8, 1.0, 1.2. Recall n is the power in the friction law (equation (6)). We investigate the effect of the friction law on the stability of the loop, since in our case it is expected that the power law will deviate significantly from the conventional correlation ($n=1$). As is evident from Fig. 5, the stability curves are very sensitive to the value of the power (n) used in the friction law.

In Fig. 6, we present the effect of the heat losses in the ascending leg on the stability of the loop. We plot the marginal stability curve for $n=1$ and $H=0.$, 0.5, 0.5, and 1.0. We note that an increase in the heat losses has a destabilizing effect because the increase reduces the contribution of the buoyancy in driving the flow.

The linear stability theory, although powerful, is limited in the sense that it can only predict sufficient conditions for instability. It does not predict the stability limit for finite amplitude disturbances nor does it describe the subsequent development of the instability. In order to gain this additional information, we use numerical simulation. Calculations are undertaken for a friction law corresponding to laminar flow ($n=1$).

Finite differences are used to approximate (11) and (12). Forward time and backward space are used for (12). The momentum equation (11) is simulated using a backward time difference and Simpson's rule for the buoyancy integral. For $n=1$, the momentum and energy equations can be solved explicitly. To assure numerical stability and to reduce the

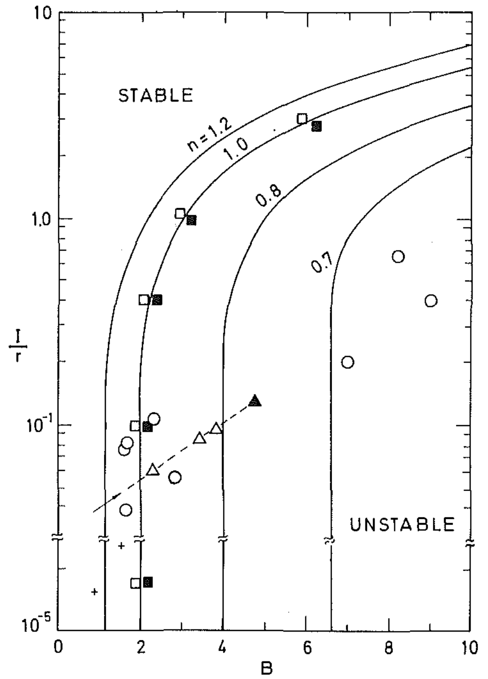

Fig. 5 The marginal stability curves predicted by the linear stability theory (solid lines) for various values of the friction power ($n = 1.2$, 1., 0.8, 0.7) are compared to numerical and experimental observations. The stable and unstable numerical experiments for $n = 1$ are denoted by open and solid squares, respectively. The last stable experimental run before oscillations are observed is denoted by (○) and (+) for the water and porous loops, respectively. The triangles represent the history of one experiment, where transition from one triangle to another is a result of an increase in the heating rate. Open and solid triangles denote stable and unstable runs, respectively.

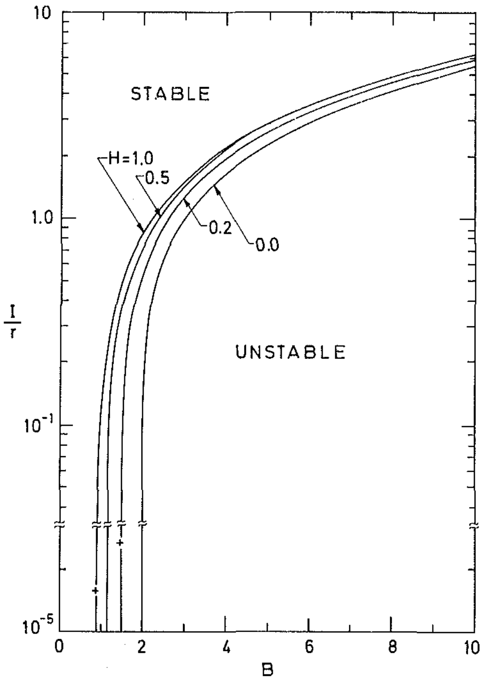

Fig. 6 Marginal stability curves as predicted linear stability analysis for $n = 1$ and $H = 0.$, 0.2, 0.5, and 1.0

truncation error, we set $u\Delta t/r\Delta s = 1$, where Δt and Δs are respectively the time and spatial steps. In our calculations, we use $\Delta s = 1/20$, $1/40$. A velocity disturbance of 5 percent was used in the unstable cases; and disturbances as large as 30 percent, for the stable cases.

The instability the numerical simulation predicts resembles very closely what we observe experimentally (Fig. 4). The development of the instability includes oscillations in the flow rate and in the temperature difference ($T_2 - T_1$). In unstable cases, the amplitude of the disturbance keeps growing until eventually the flow reverses direction. Once a flow reversal occurs, stable flow is observed in the loop with upward motion in the heater section. In stable cases, the amplitude of the oscillations decays exponentially.

We document the results of the numerical simulation in Fig. 5, where stable and unstable runs are denoted by open and solid squares. Clearly, the numerical simulation agrees very well with the linear theory's predictions.

6 Results and Discussion

In this paper, we consider the stability of pressure-driven flow in a U-shaped tube with heating of the descending fluid. The experimental evidence suggests that, as long as the ratio of buoyancy and pressure heads (B) does not exceed some critical value (B_{cr}), the flow is stable. Once this critical value is exceeded, the flow ceases to be stable. The disturbances amplify in an oscillatory fashion until eventually flow reversal occurs and a new steady state is established in which the flow is driven by the buoyancy force and opposed by the pressure head.

The one-dimensional model, constructed in section 3, yields results which are in good qualitative agreement with the experimental observations. For example, results of the numerical simulation with regard to the disturbance amplification (not shown here) resemble very closely those observed experimentally (Fig. 4). Thus there is every reason to believe that the mathematical model adequately described the physical phenomena involved.

Next, we compare the theoretical predictions for the stability characteristics of the loop with the experimental evidence. In Fig. 5, the solid lines depict the marginal stability curves obtained using linear stability analysis for various powers (n) in the friction law. The abscissa is the ratio between buoyancy and pressure heads (B) while the ordinate is the loop inertia (I/r). Conditions on the left and on the right of the solid curves are stable and unstable, respectively. For $n = 1$, we confirm the validity of the linear stability analysis using a finite difference numerical simulation. The open and solid rectangles represent stable and unstable runs, respectively. Clearly, the analytical and numerical predictions are in excellent agreement. Note that the marginal stability curves are very sensitive to the value of n.

The triangles in Fig. 5 represent the history of one experiment. As the B number increases, we move from the stable (open triangles) to the unstable (solid triangle) situation, in accord with the theoretically predicted trends. We also depict in Fig. 5 the conditions that correspond to the last stable run. The circles and pluses correspond to the water and porous loops, respectively. Unfortunately, we are not able to carry out a quantitative comparison between the experimental data and the theoretical predictions, since we do not know the value of n. We could not procure n in our experiments due to the extremely low pressure heads encountered. Nevertheless, our work and the work of others [7, 12] suggest that the magnitude of n may vary considerably from one experimental run to another. Also, the high values of the ratio Gr/Re (>1000) encountered in our experiments suggest that the velocity profiles deviate significantly from the laminar parabolic profile (see, for example [17]). Thus for the water loop the value of n may significantly differ from one. In the porous loop, on the other hand, it is more likely that n is approximately 1. In this case our experimental data (pluses in Fig. 5) fall below the theoretical predictions. We attribute this discrepancy to the effect of heat losses in the ascender.

The effect of the heat losses in the ascender is examined in

Table 1 Experimentally determined values of Q, ΔP, B, Re, H, I, and Gr/Re at the onset of unstable flow in the water and porous loops

Q (w)	ΔP (N/m^2)	Re	H	I	B_{cr}	Gr/Re
			Water loop			
48	9.76	170	.14	5.6×10^{-2}	2.8	871
70	23.34	267	.14	3.8×10^{-2}	1.7	1470
72	9.75	243	.23	9.4×10^{-2}	3.8	1325
109	7.78	348	.18	2.0×10^{-1}	7.0	2028
157	25.37	548	.13	1.0×10^{-1}	2.3	2577
158	38.74	573	.15	7.7×10^{-2}	1.6	2664
158	35.87	548	.15	8.0×10^{-2}	1.6	2448
178	7.75	516	.11	6.5×10^{-1}	8.2	3086
281	9.66	899	.22	3.3×10^{-1}	9.0	2955
			Porous loop			
11.3	45.82	8.8	1.1	1.58×10^{-5}	0.9	
19.8	38.96	10.9	1.1	2.61×10^{-5}	1.5	

Fig. 6, where the theoretical stability curves (solid lines) are depicted for various values of the heat losses and for friction law $n=1$. The heat losses have a destabilizing effect, and as H increases, the marginal stability curves shift to the left. The heat loss effects are especially significant for the porous loop and almost negligible in the water loop (Table 1). Thus, in Fig. 6, we depict our experimental data for the porous loop only. We note that one experimental point is in good agreement with the theoretical prediction while the other is not. We suspect that again this is due to the fact that with an increasing heating rate (Table 1) the value of n deviates from one. We note, however, that both Figs. 5 and 6 predict that the inertia (I/r) has a stabilizing effect. The larger the value of I, the larger is B_{cr}. The same trend is exhibited by the experimental data.

The physical mechanism which causes the disturbance amplification is similar to the one identified by Bau and Torrance [13] in their investigation of asymmetrically heated loops (without a driving pressure head). This mechanism is essentially based on the fact that there is a time lag between the heating process and the resulting buoyant force. In order to clarify the ideas involved, let us consider the following situation.

Suppose a positive thermal anomaly occurs in the descending leg. Such an anomaly causes a decrease in the total buoyancy. This tends to decelerate the flow. As a result, the anomaly tends to move more slowly through the descending leg, receives additional heating, and can be amplified. If the flow is not actually brought to rest the warmer then usual fluid will reach the ascending leg. As the warmer fluid rises in the ascending leg, the total buoyancy will increase. The resulting acceleration causes the fluid to proceed through the heated, descending leg more rapidly than normal. Consequently, the fluid in the descending leg becomes cooler than usual. This, in turn, results in a higher overall buoyancy force, and the disturbance is amplified again.

The result is a continuing sequence of thermal anomalies of alternating sign. This explains the oscillatory behavior of the flow once instability occurs and the fact that the period of the oscillations is about twice the transit time through the loop. When the oscillations amplify, the disturbance grows in time until the flow is momentarily brought to rest and a flow reversal occurs. The reversal flow is stable because the heating and the buoyancy generation processes in the heater are now in phase.

The amplification of disturbances is counteracted by the action of the friction force. Consequently, disturbances will not always amplify. This is the reason for the strong dependence of B_{cr} on the friction law. Additionally, the inertia plays an important role in stabilizing the flow, as is evident from Fig. 5 and Table 1.

References

1 Elder, J. W., "Heat and Mass Transfer in the Earth: Hydrothermal Systems," Bull. N. Z. Dept. Scient. Ind. Res. 169, 1966.

2 Lowell, R. P., "Circulation in Fractures, Hot Springs, and Convective Heat Transport on Mid Ocean Crests," *Geophys. J. R. Astr. Soc.*, Vol. 40, 1975, pp. 351–365.

3 Torrance, K. E., "Open Loop Thermosyphons with Geological Applications," ASME JOURNAL OF HEAT TRANSFER, Vol. 101, 1979, pp. 677–683.

4 Japkise, D., "Advances in Thermosyphon Technology," *Ad. in Heat Transfer*, edited by T. F. Irvine and J. P. Hartnett, Vol. 9, Academic Press, New York, 1973, pp. 1–111.

5 Welander, P., "On the Oscillatory Instability of a Differentially Heated Fluid Loop," *J. Fluid Mech.*, Vol. 29, 1967, pp. 17–30.

6 Yu, D. L., "Heat Transfer in Communicating Channels Under Conditions of Free Convection," *Thermal Eng.*, Vol. 16, 1969, pp. 94–97.

7 Creveling, H. F., de Paz, J. F., Baladi, I. Y., and Schoenhals, R. J., "Stability Characteristics of a Free Convection Loop," *J. Fluid Mech.*, Vol. 67, 1975, pp. 65–84.

8 Greif, R., Zvirin, Y., and Mertol, A., "The Transient and Stability Behavior of a Natural Convection Loop," ASME JOURNAL OF HEAT TRANSFER, Vol. 101, 1979, pp. 684–688.

9 Zvirin, Y., and Greif, R., "Transient Behavior of Natural Circulation Loops: Two Vertical Branches With Point Heat Source and Sink," *International Journal of Heat and Mass Transfer*, Vol. 22, 1979, pp. 499–504.

10 Damerell, P. S., and Schoenhals, R., "Flow in a Toroidal Thermosyphon With Angular Displacement of Heated and Cooled Sections," ASME JOURNAL OF HEAT TRANSFER, Vol. 101, 1979, pp. 672–676.

11 Alstad, C. D., Isbin, H. S., Amundson, N. R., and Silvers, J. P., "Transient Behavior of Single-Phase Natural Circulation Loop Systems," *AIChE Journal*, Vol. 1, 1957, pp. 417–425.

12 Bau, H. H., and Torrance, K. E., "Transient and Steady Behavior of an Open, Symmetrically Heated, Free Convection Loop," *International Journal of Heat and Mass Transfer*, Vol. 24, 1981, pp. 597–609.

13 Bau, H. H., and Torrance, K. E., "On the Stability and Flow Reversal of an Asymmetrically Heated Open Convection Loop," *J. Fluid Mech.*, Vol. 109, 1981, pp. 417–433.

14 Zvirin, Y., "The Effects of a Throughflow on the Steady State and Stability of a Natural Circulation Loop," *19th National Heat Transfer Conference*, Orlando, Fla., 1980.

15 Mertol, A., Greif, R., and Zvirin, Y., "The Transient, Steady State and Stability Behavior of an Open Thermosyphon," *International Journal of Heat and Mass Transfer*, Vol. 24, pp. 621–633.

16 Carrier, G. F., Krook, M., and Pearson, C. E., *Functions of Complex Variable—Theory and Techniques*, 1966, McGraw Hill.

17 Scheele, G. F., and Hanratty, T. J., "Effects of Natural Convection on Stability of Flow in a Vertical Pipe," *J. Fluid Mech.*, Vol. 14, 1962, pp. 244–256.

18 Tritton, D. J., *Physical Fluid Mechanics*, Von Nostrand Reinhold, 1977, pp. 151–161.

Buoyancy Induced Flow in a Vertical Internally Finned Circular Duct

C. Prakash
Assistant Professor.
Assoc. Mem. ASME

Ye-Di Liu[1]

Department of Mechanical Engineering,
Aeronautical Engineering and Mechanics,
Rensselaer Polytechnic Institute,
Troy, N.Y. 12181

Laminar buoyancy induced flow in a vertical internally finned circular tube has been analyzed by numerically integrating the governing partial differential equations. The temperature of the duct is greater than that of the surrounding fluid; hence the density of the fluid inside the duct is less than that of the fluid on the outside, which creates a hydrostatic pressure head across the duct that induces the flow (chimney effect). Results show that despite reduction in the induced flow rate due to increased friction, a finned tube can yield significant heat transfer enhancement compared to a finless tube of the same height. Depending on the parameters, the degree of enhancement can be comparable to the factor by which the heat transfer area increases due to the presence of the fins.

Introduction

For the purpose of heat transfer augmentation, internal fins are often employed in circular tubes. Such internally finned tubes find applications in many compact heat exchange devices [1], and have been the subject of many research investigations [2–12]. These studies are directed towards the determination of heat transfer enhancement that can be achieved by employing the fins, and the price one must pay in terms of the increased pressure drop or pumping power. All of these investigations are for forced convection – the only exception is the work presented in [12] which deals with combined forced and free convection.

The work presented in this paper is different than all earlier investigations in that it deals with purely buoyancy induced flow – the so-called chimney flow. Such a flow is induced by the hydrostatic pressure head across the duct which gets created due to the difference in the density of the fluid inside and outside the duct. The induced flow rate attains a value such that the frictional losses in the duct equal the buoyancy created pressure head. Unlike for forced convection, in the buoyancy induced flow there is no guarantee a priori that the presence of fins will give rise to heat transfer enhancement – for, the presence of fins not only increases the induced pressure head but also the total friction which reduces the induced flow rate. Whether or not enhancement is attained depends upon these two competing factors. However, when the fins do result in heat transfer enhancement, such an enhancement comes free since no price has to be paid in terms of increased pumping power, etc. It is these interesting features of this problem which provided motivation for the present investigation.

There have been rather few investigations of purely buoyancy induced flows. Pertinant to the present problem is the numerical study of Davis and Perona [13] for a finless circular tube. Investigations on some other duct geometries may be found in [14–19].

Analysis

The Problem Definition. The problem being investigated is schematically sketched in Fig. 1. It concerns the prediction of laminar buoyancy induced flow in an internally finned circular tube of radius a. The fins are continuous, radial, and uniformly placed on the inside of the duct. Here h represents the height of the fins and H represents the vertical height of the duct. The entire assembly, i.e., the base tube and the fins, is taken to be isothermal with a uniform temperature T_w, which is greater than the temperature T_∞ of the surrounding fluid. This is the so-called Ⓣ boundary condition in [20] and has applications in condensers, evaporators, etc. At the duct inlet, the induced flow is assumed to have a uniform velocity $w = w_o$ and uniform temperature $T = T_\infty$ corresponding to the surrounding fluid.

The thickness of the fins is assumed to be zero. At the same time, the fins are taken to be made of a highly conducting material and to be 100 percent efficient. This assumption is implicit in our regarding the temperature T to be equal to T_w everywhere on the base tube and the fins. Thus we are considering the limiting case of "thin but highly conducting fins." Such a treatment examines the effect of a "sufficiently thin" fin on the velocity distribution in the duct, and the efficacy of such a flow field in being able to remove heat from a "highly conducting" fin surface. The zero fin thickness assumption has often been made in the past; in chapter 16 of the text by Shah and London [20], the rationale of this assumption has been discussed, and a review is given of works that make this assumption while analyzing internally finned circular, square, hexagonal ducts, etc. For the circular duct case, the assumption has been made, amongst others, by Hu and Chang [10]; Mashiyah and Nandakumar [11]; and Patankar, Ivanovic, and Sparrow [12].

The fluid is assumed to be incompressible, except for the calculation of the buoyancy term in the vertical direction, which is computed using the Boussinesq-type equation of state. All other fluid properties are assumed constant. Viscous dissipation and compression work terms are assumed negligible in the energy equation.

Mathematical Formulation. Unlike most of the earlier studies [13–19], which deal with two-dimensional situations, the problem under investigation is of the three-dimensional, boundary-layer type. This added dimensionality, arising due to the fins, makes the computational task a lot more formidable. In the present analysis we treat the flow to be "parabolic" – thus, as in any boundary layer analysis, the flow is assumed to have a predominant direction, the vertical z-direction in Fig. 1, along which the diffusion of mass, momentum, or energy can be neglected. Also, along the main flow direction, downstream pressure is assumed to have no effect on the conditions upstream. This latter assumption is implicit in the two-dimensional boundary layer analysis also, and the matter has been discussed at length in [21]. The parabolic assumption implies that the pressure p can be

---

[1] Visiting Scholar from the People's Republic of China.

Contributed by the Heat Transfer Division for publication in the JOURNAL OF HEAT TRANSFER. Manuscript received by the Heat Transfer Division May 3, 1983.

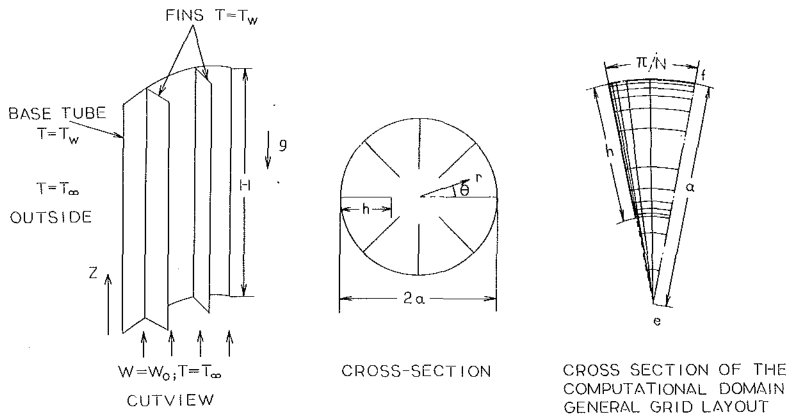

Fig. 1 An internally finned circular duct

written as $p = \bar{p}(z) + p'(r,\theta)$, where $\bar{p}$ is the average pressure over the duct cross section and p' is the small pressure variation governing the flow distribution in the cross-stream plane. The velocity component in the main flow direction is driven by the gradient of $\bar{p}$ (i.e., the term $d\bar{p}/dz$), while for the cross-stream flow the gradients of p' enter into the momentum equations. As a result the problem can be solved by employing a marching-type computational procedure which involves solution of a series of two-dimensional elliptic problems in the cross-stream plane.

Consider the r, θ, z cylindrical coordinate shown in Fig. 1, and let v, u, and w represent the velocity components along these coordinates, respectively. Let T represent the temperature. The parabolized equations governing the flow are given as

Continuity:

$$\frac{1}{r}\frac{\partial}{\partial r}(rv) + \frac{1}{r}\frac{\partial u}{\partial \theta} + \frac{\partial w}{\partial z} = 0 \tag{1}$$

r-momentum:

$$v\frac{\partial v}{\partial r} + \frac{u}{r}\frac{\partial v}{\partial \theta} + w\frac{\partial v}{\partial z} = -\frac{1}{\rho}\frac{\partial p'}{\partial r} + \nu\left[\frac{1}{r}\frac{\partial}{\partial r}\left(r\frac{\partial v}{\partial r}\right) + \frac{1}{r^2}\frac{\partial^2 v}{\partial \theta^2}\right] + \frac{u^2}{r} - \nu\left[\frac{v}{r^2} + \frac{2}{r^2}\frac{\partial u}{\partial \theta}\right] \tag{2}$$

θ-momentum:

$$v\frac{\partial u}{\partial r} + \frac{u}{r}\frac{\partial u}{\partial \theta} + w\frac{\partial u}{\partial z} = -\frac{1}{\rho r}\frac{\partial p'}{\partial \theta} + \nu\left[\frac{1}{r}\frac{\partial}{\partial r}\left(r\frac{\partial u}{\partial r}\right) + \frac{1}{r^2}\frac{\partial^2 u}{\partial \theta^2}\right] - \frac{uv}{r} + \nu\left[\frac{2}{r^2}\frac{\partial v}{\partial \theta} - \frac{u}{r^2}\right] \tag{3}$$

z-momentum:

$$v\frac{\partial w}{\partial r} + \frac{u}{r}\frac{\partial w}{\partial \theta} + w\frac{\partial w}{\partial z} = -\frac{1}{\rho}\frac{d\bar{p}}{dz} - g + \nu\left[\frac{1}{r}\frac{\partial}{\partial r}\left(r\frac{\partial w}{\partial r}\right) + \frac{1}{r^2}\frac{\partial^2 w}{\partial \theta^2}\right] \tag{4}$$

Energy:

$$v\frac{\partial T}{\partial r} + \frac{u}{r}\frac{\partial T}{\partial \theta} + \omega\frac{\partial T}{\partial z} = \frac{k}{\rho c_p}\left[\frac{1}{r}\frac{\partial}{\partial r}\left(r\frac{\partial T}{\partial r}\right) + \frac{1}{r^2}\frac{\partial^2 T}{\partial \theta^2}\right] \tag{5}$$

Overall mass conservation:

$$\iint_{\text{duct}} \rho w dA = \dot{m} = \text{same for all } z \tag{6}$$

As for any boundary layer flow, these equations neglect diffusion in the main flow (z)-direction and hence there is no term of the type $\partial^2/\partial z^2$ on the right-hand side. Equations (2-4) determine the velocity components, and the cross-stream pressure p' is determined by the continuity constraint

Nomenclature

a = tube radius
c_p = specific heat of the fluid
D_h = equivalent hydraulic diameter, equation (21)
Gr = Grashof number, equation (17)
g = acceleration due to gravity
H = tube height
h = fin height
k = thermal conductivity of the fluid
$\dot{m}$ = mass flow rate through the duct
N = number of fins
Pr = Prandtl number, equation (18)
p = pressure
p' = pressure driving the cross-stream flow
$\bar{p}$ = cross-section average pressure at any axial location
p_∞ = ambient pressure outside the tube
$\tilde{p}$ = difference between $\bar{p}$ and p_∞, equation (9)
Q = total heat transferred by the tube
Ra = Rayleigh number, equation (20)
Ra$_h$ = Rayleigh number based on the equivalent hydraulic diameter D_h, equation (22)
r = radial coordinate
T = temperature
T_m = mean temperature of the fluid
T_w = temperature of the tube and fins
T_∞ = ambient temperature outside the tube
u = angular velocity component
v = radial velocity component
w = axial velocity component
w_o = axial velocity at the inlet
z = axial coordinate
α = thermal diffusivity of the fluid
β = coefficient of thermal expansion
θ = angular coordinate
Ω = volumetric flow rate through the duct
ρ = density of the fluid
ρ_∞ = density of the ambient fluid
μ = coefficient of viscosity of the fluid
ν = kinematic viscosity

expressed by equation (1). The axial pressure gradient $d\bar{p}/dz$ is determined by the statement of overall mass conservation, equation (6), and temperature is determined by equation (5).

Equations (1-6) are for an incompressible fluid and this assumption is to be made all along *except* for the buoyancy terms in the axial momentum equation (equation (4)). The buoyancy effects are contained in the first two terms on the right-hand side of equation (4), and in these the dependence of density on temperature is to be acknowledged. For this purpose we use the Boussinesq model with β, the coefficient of thermal expansion, assumed constant. The details can be worked out as follows.

Let p_∞ represent the ambient pressure outside the duct. Assuming quiescent fluid on the outside, p_∞ is given by

$$p_\infty = -\rho_\infty g z + c \tag{7}$$

where ρ_∞ is the density of the ambient fluid and c is a constant. Let $\bar{\bar{p}}$ represent the difference between the cross-section average pressure $\bar{p}$ inside the duct and the ambient pressure p_∞ at the same location z, i.e.,

$$\bar{\bar{p}} = \bar{p} - p_\infty \tag{8}$$

so that

$$\bar{p} = \bar{\bar{p}} + p_\infty \tag{9}$$

From equations (7) and (9) we get

$$\frac{d\bar{p}}{dz} = \frac{d\bar{\bar{p}}}{dz} + \frac{dp_\infty}{dz} = \frac{d\bar{\bar{p}}}{dz} - \rho_\infty g \tag{10}$$

which gives

$$-\frac{1}{\rho}\frac{d\bar{p}}{dz} - g = -\frac{1}{\rho}\frac{d\bar{\bar{p}}}{dz} + \frac{(\rho_\infty - \rho)}{\rho} g \tag{11}$$

And, using the Boussinesq-type equation of state, we can write equation (11) as

$$-\frac{1}{\rho}\frac{d\bar{p}}{dz} - g = -\frac{1}{\rho}\frac{d\bar{\bar{p}}}{dz} + \beta g (T - T_\infty) \tag{12}$$

where β represents the coefficient of thermal expansion of the fluid. Using equation (12), the axial momentum equation reads

$$v\frac{\partial w}{\partial r} + \frac{u}{r}\frac{\partial w}{\partial \theta} + w\frac{\partial w}{\partial z} = -\frac{1}{\rho}\frac{d\bar{\bar{p}}}{dz} + \beta g (T - T_\infty) + \nu\left[\frac{1}{r}\frac{\partial w}{\partial r}\left(r\frac{\partial w}{\partial r}\right) + \frac{1}{r^2}\frac{\partial^2 w}{\partial \theta^2}\right] \tag{13}$$

The problem is now governed by equations (1), (2), (3), (13), and (5), and $\bar{\bar{p}}$ is now the cross-stream average pressure determined by equation (6).

The boundary conditions supplementing these differential equations are given as follows

At the fin surface or base tube:

$$\begin{aligned} u &= v = w = 0 \\ T &= T_w \end{aligned} \tag{14}$$

At the inlet of the duct ($z = 0$):

$$\begin{aligned} u &= v = \bar{\bar{p}} = 0 \\ w &= w_0 \\ T &= T_\infty \end{aligned} \tag{15}$$

At the duct exit ($z = H$):

$$\bar{\bar{p}} = 0 \tag{16}$$

Solution Methodology. The conditions $w = w_0$ at $z = 0$ and $\bar{\bar{p}} = 0$ at $z = H$ are not two independent conditions. This is so because everything else remaining fixed, there is a one-to-one relation between w_o and H. Thus for a given height H, w_o will attain such a value that the condition $\bar{\bar{p}} = 0$ at $z = H$ is satisfied. Determining w_o in this manner is both difficult and unnecessary. Instead, the convenient procedure is to assign some value to w_o, carry out the computation, and keep examining $\bar{\bar{p}}$ obtained at each marching step. As soon as $\bar{\bar{p}}$ becomes zero again, we say that this value of z is the height H for the chosen w_o. To obtain an estimate of the range of w_o that will yield H in some desired range, some preliminary computations can be made on coarse grid. Subsequently, computations can be made on a finer grid. Also, by computing the bulk temperature at the exit station (where $\bar{\bar{p}} = 0$) the total amount of heat transferred to the fluid can be determined. This quantity, which is the primary quantity of concern to us, can then be plotted as a function of the assembly height H.

Marching along the flow, $\bar{\bar{p}}$ initially decreases due to large friction close to the entry. It goes through a minimum and then starts increasing due to the buoyancy terms becoming dominant. It becomes zero again at the $z = H$, where the fluid exits from the duct.

Dimensionless Formulation. Define the Grashof number Gr and Prandtl number Pr as

$$\mathrm{Gr} = \frac{g\beta(T_w - T_\infty)a^3}{\nu^2} \tag{17}$$

$$\mathrm{Pr} = \mu c_p / k \tag{18}$$

The problem can be nondimensionalized by introducing the following dimensionless variables

$$R = r/a; Z = z/(a \bullet \mathrm{Gr}); V = va/\nu; U = ua/\nu; W = wa/(\nu \bullet \mathrm{Gr});$$
$$p' = p'/\rho(\nu/\alpha)^2; \bar{\bar{P}} = \bar{\bar{p}}\alpha^2/(\rho\nu^2\mathrm{Gr}^2); \Theta = (T - T_\infty)/(T_w - T_\infty) \tag{19}$$

In dimensionless form, the problem is characterized by the following parameters:

(*i*) N, the number of fins
(*ii*) h/a representing the fin height
(*iii*) Pr, the Prandtl number
(*iv*) $H/(a \bullet \mathrm{Gr})$, representing the height of the assembly

Computations were made for $N = 8$, 16, and 24; $h/a = 0.3$, 0.6, and 1; a range of values of $H/(a \bullet \mathrm{Gr})$; and $\mathrm{Pr} = .7$ corresponding to air.

Computational Procedure. The governing differential equations were integrated using the control volume based finite difference procedure of Patankar and Spalding [21]. For this problem, the control volumes are parallelepiped with sectorial cross-sections. A fully implicit formulation is applied in the marching (z)-direction. In the cross-stream plane, the equations are discretized by using the exponential differencing scheme. At each marching step we have an elliptic problem in the cross-stream plane that is solved by the SIMPLER-type algorithm [22]. Thus the cross-stream velocities are computed using the available p' field, which is then corrected by imposing the continuity constraint. The nominally linear equations are solved by using a tridiagonal matrix algorithm (TDMA). For computing the axial pressure gradient ($d\bar{\bar{p}}/dz$) using the requirement of overall mass conservation, the procedure suggested by Raithby and Schneider [23] is employed.

Because of symmetry, we only need to compute flow is a cross section of angular width π/N. The computational domain is shown in Fig. 1. A 15 × 15 nonuniform grid was used in the cross-stream plane. The grid points are packed closer to the base tube, the fin surface, and the fin tip. The general grid deployment pattern is shown in Fig. 1—the picture has been drawn just to give an idea of the grid layout and is not to scale. In the marching direction, the step size Δz was carefully monitored with Δz being very small in the entry region. Typically, about 50 steps were employed for any single case. To choose Δz, we need to have an estimate of H for

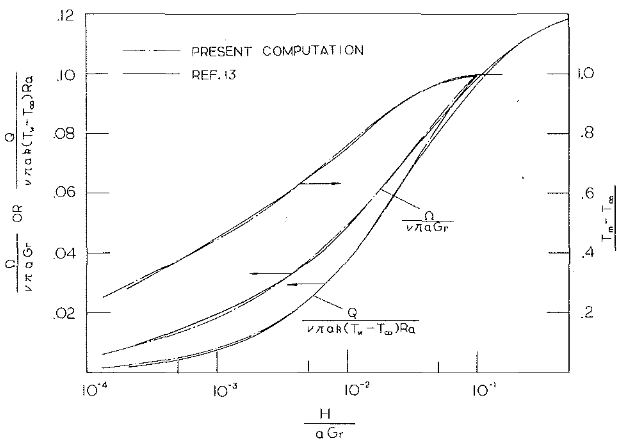

Fig. 2 Comparison of the present computations with the results of Davis and Perona [13] for a finless circular tube

some desired flow rate. Such an estimate was obtained by first solving the problem on a rather coarse grid. At each marching step, a sufficient number of iterations (usually about three) were performed to ensure convergence of the nonlinear flow equations. Grid refinement studies for some typical cases ensure that the computed results should be accurate to less than 1 percent.

Results

The only two quantities of interest here are the total heat transferred to the fluid Q and the volumetric flow rate Ω of the induced flow. Results will be presented for the variation of these quantities with the height of the duct H.

As a check on our computed results, a comparison is made with the results of Davis and Perona [13] in Fig. 2 for the case of a finless circular duct. The agreement affirms the reasonable adequacy of the grid size.

Figures 3(a, b, c) show the variation of Q and Ω in the finned duct. These figures correspond, respectively, to 8, 16, and 24 fins in the duct. Within each figure, different curves correspond to different fin heights. The curve with $h/a = 0$ corresponds to a finless circular tube and is common to all three figures. The new symbol introduced in Figs. 3(a-c) is the Rayleigh number Ra defined from

$$\mathrm{Ra} = \mathrm{Gr}\ \mathrm{Pr} = \frac{g\beta(T_w - T_\infty)a^3}{\nu\alpha} \tag{20}$$

α being the thermal diffusivity of the fluid. Since the characteristic length entering into the definition of Gr and Ra is the tube radius a, the effect of adding the fins can be easily discerned.

As the duct height H increases, it increases the pressure head available for driving the flow, and also increases the friction in the path of the fluid. Whether or not the induced flow rate increases will depend on these two competing factors. As can be seen from Figs. 3(a-c), for small values of H the first factor wins and the flow rate increases with H. The total heat transferred Q also increases with H because of the increased flow rate and the increased heat transfer area. For large H, the two competing factors tend to cancel each other's effect and Ω tends to become independent of H. The total heat transferred Q also tends to taper off because of the flow rate becoming independent of H, and because for large H the flow tends toward thermal saturation (i.e., $T = T_w$ everywhere in the fluid) beyond a certain distance from the entrance. The value of H beyond which this happens decreases with increasing number of fins and the fin height as expected.

From Figs. 3(a-c) it can be seen that adding the fins decreases the flow rate and increases the total heat transfer Q. The decrease in flow rate is rather small, but the increase in heat transfer is very significant. Everything else being fixed, Ω decreases and Q increases with the fin height h/a over most of the range of duct height H. For very large H, however, fins with smaller h/a can show more heat transfer compared to fins of greater h/a because of thermal saturation of flow in the later.

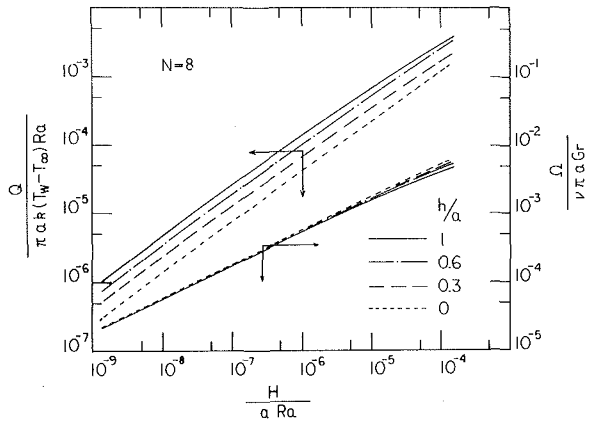

Fig. 3(a) Variation of total heat transferred and induced flow rate with height of the duct: $N = 8$

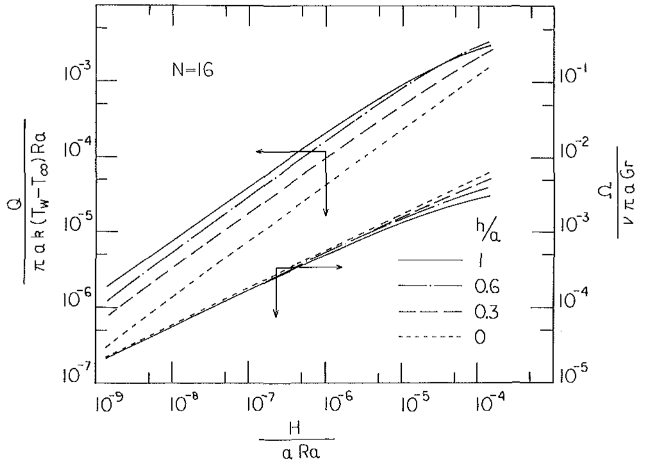

Fig. 3(b) Variation of total heat transferred and induced flow rate with height of the duct: $N = 16$

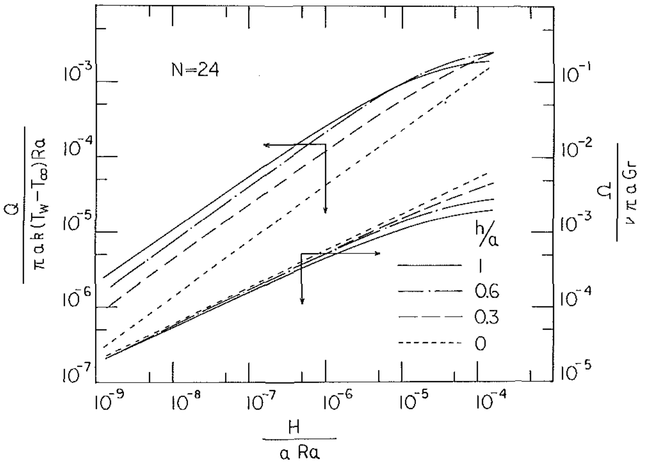

Fig. 3(c) Variation of total heat transferred and induced flow rate with height of the duct: $N = 24$

To examine the effect of number of fins for a fixed fin height, the variation of Q with duct height H is replotted in Figs. 4(a-c). Everything else remaining fixed, the total heat transfer increases with the number of fins. The exception to

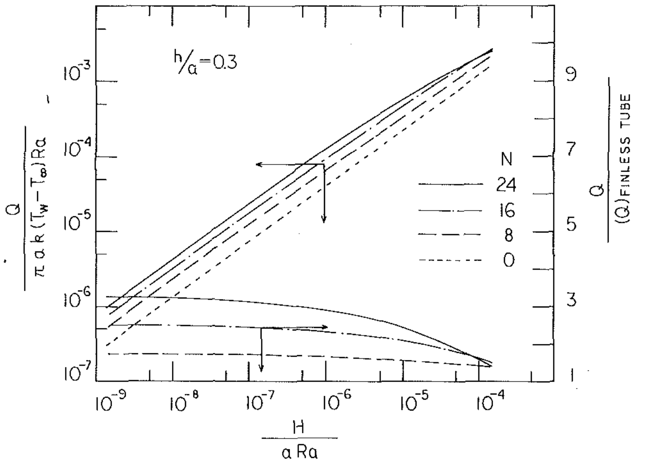

Fig. 4(*a*) **Total heat transferred by a finned tube and the ratio with the heat transferred by a finless tube: *h*/*a* = 0.3**

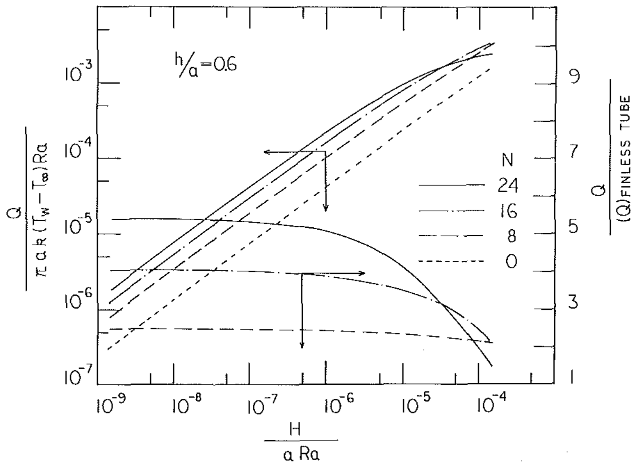

Fig. 4(*b*) **Total heat transferred by a finned tube and the ratio with the heat transferred by a finless tube: *h*/*a* = 0.6**

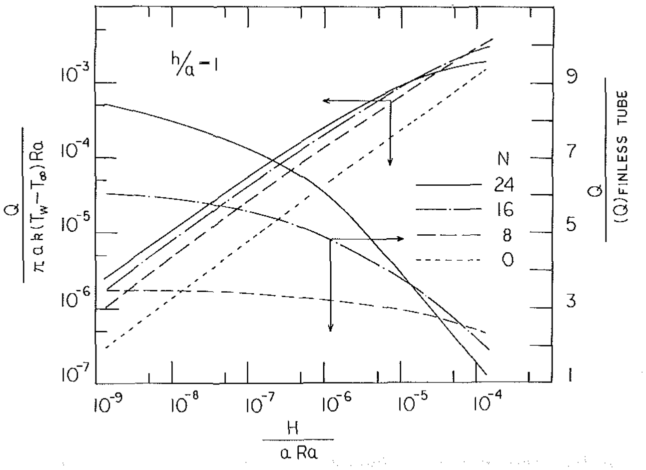

Fig. 4(*c*) **Total heat transferred by a finned tube and the ratio with the heat transferred by a finless tube: *h*/*a* = 1**

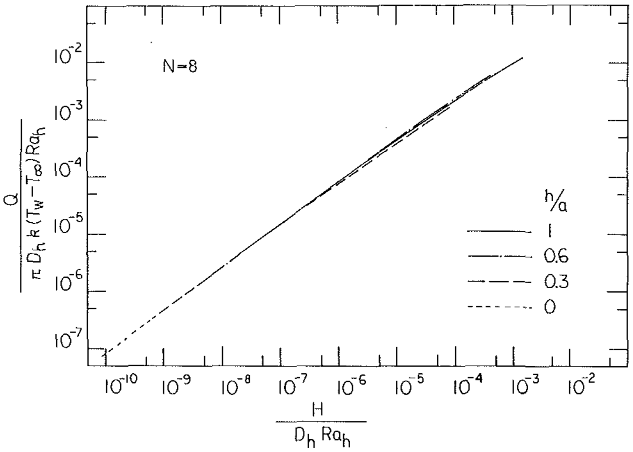

Fig. 5(*a*) **Heat transfer results using the equivalent hydraulic diameter as the characteristic length: *N* = 8**

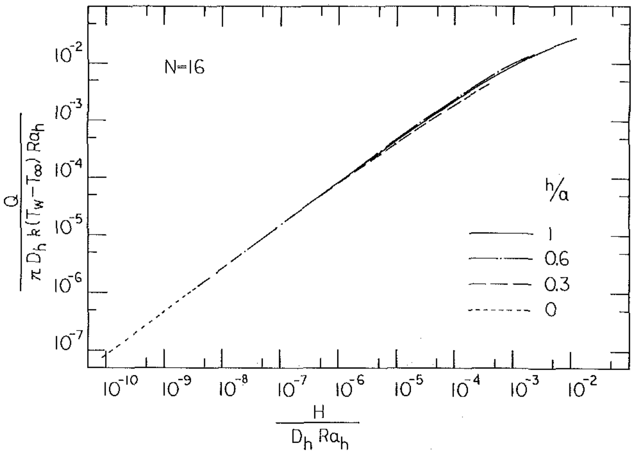

Fig. 5(*b*) **Heat transfer results using the equivalent hydraulic diameter as the characteristic length: *N* = 16**

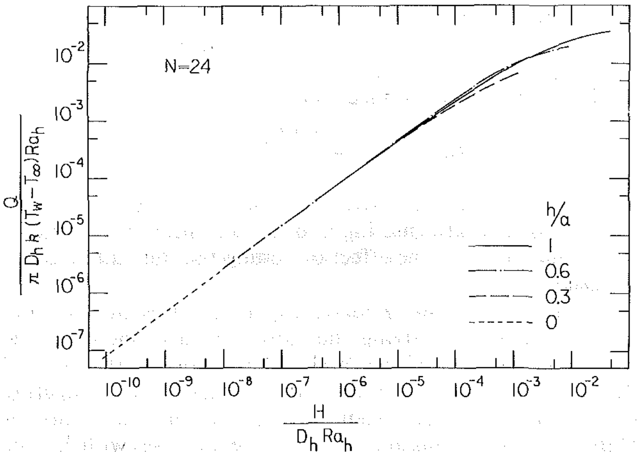

Fig. 5(*c*) **Heat transfer results using the equivalent hydraulic diameter as the characteristic length: *N* = 24**

this statement are the conditions for large H where the flow for the case of large N gets thermally saturated.

For a given height H of the duct, by what factor does the heat transfer increase in a finned tube compared to a finless tube? How does this compare with the factor by which heat transfer area increases in a finned tube? The answer to these questions is provided by the curves for $Q/(Q)_{\text{finless tube}}$ in Figs. 4(*a*–*c*) and Table 1 giving the area ratios. As can be seen from Figs. 4(*a*–*c*) a finned duct can transfer about one to eight times as much heat as a finless duct of the same height. This ratio compares well with the ratio of heat transfer area between a finned and a finless duct. It is interesting that we get such high heat transfer augmentation factors in this buoyancy induced flow despite the reduction in the induced flow rate. For large H when the flow starts getting thermally saturated, the heat transfer augmentation factors decrease as expected.

So far we have used the tube radius a as the characteristic length. It is conventional to use the hydraulic diameter D_h if one is seeking a correlation. Here D_h is defined from

Table 1 The ratio of heat transfer area for finned and a finless duct of same radius a and height H

h/a	N=8	16	24
0.3	1.764	2.528	3.292
0.6	2.528	4.056	5.583
1.	3.547	6.092	8.639

$$D_h = \frac{4(\text{cross-sectional area})}{\text{wetted perimeter}} \tag{21}$$

Using D_h as the characteristic length, and a Rayleigh number based on D_h defined as

$$\text{Ra}_h = \frac{g\beta(T_w - T_\infty)D_h^3}{\nu\alpha} \tag{22}$$

the heat transfer results are presented in Figs. 5(a–c). As can be seen, the curves corresponding to different (h/a) are all very close to each other if plotted in this manner. Also, if these figures were placed over each other, it will be found that all curves are very close to each other no matter what N or h/a. The following correlation can be derived from Figs. 4(a–c)

$$\left.\begin{aligned} \frac{Q}{\pi D_h k(T_w - T_\infty)\text{Ra}_h} &= 1.68\left\{\frac{H}{D_h \text{Ra}_h}\right\}^{0.72} \\ \text{for } 10^{-10} \le \frac{H}{D_h \text{Ra}_h} &\le 10^{-3} \end{aligned}\right\}$$

Figure 6 has been prepared to get a perspective of the velocity distribution. In this figure, the variation of axial velocity along the line e–f (Fig. 1) has been presented. Different curves correspond to different axial locations. The velocity is zero at $r/a = 1$ (the base tube) and increases as one moves away from it. The velocity then starts decreasing again because decreasing r/a means nearing the fin surface. Near the center, the velocity is somewhat uniform. It must be noted, however, that Fig. 6 is only a representative example – for other combinations of parameters, somewhat different, but generally similar, distributions will arise.

Concluding Remarks

Laminar, buoyancy induced flow in a vertical, internally finned circular tube is analyzed by numerically integrating the governing partial differential equations. The fins are continuous, of zero thickness, and isothermal. Results show that despite a reduction in the induced flow rate due to increased friction, a finned tube can yield significant heat transfer enhancement compared to a finless tube of the same height.

References

1 Bergles, A. E., "Survey and Evaluation of Techniques to Augment Convective Heat and Mass Transfer," *Progress in Heat and Mass Transfer*, Vol. 1, Pergamon Press, Oxford, 1969, pp. 331–424.

2 Carnavos, T. C., "Cooling Air in Turbulent Flow with Internally Finned Tubes," AIChE Paper No. 4, 17th National Heat Transfer Conference, Aug. 1977.

3 Russell, J. R., and Carnavos, T. C., "An Experimental Study: Cooling Air in Turbulent Flow with Internally Finned Tubes," AIChE Paper No. 28, 16th National Heat Transfer Conference, Aug. 1976.

4 Watkinson, A. P., Miletti, D. L., and Kubanek, G. R., "Heat Transfer and Pressure Drop of Internally Finned Tubes in Laminar Oil Flow," ASME Paper No. 75-HT-41, 1975.

5 Watkinson, A. P., Miletti, D. L., and Kubanek, G. R., "Heat Transfer and Pressure Drop of Forge-Fin Tubes in Turbulent Air Flow," ASHRAE Paper No. 2347, ASHRAE Semi-Annual Meeting, 1975.

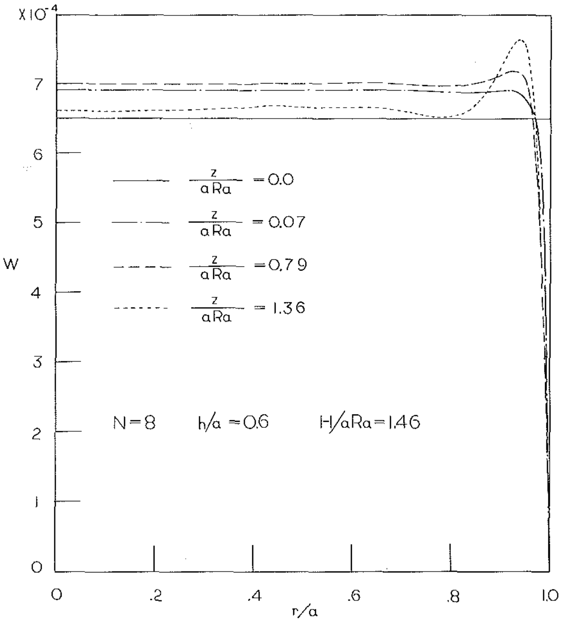

Fig. 6 Variation of axial velocity along the line e–f (Fig. 1) at different axial locations: $N = 8$, $h/a = 0.6$

6 Watkinson, A. P., Miletti, D. L., and Tarassoff, P., "Turbulent Heat Transfer and Pressure Drop in Internally Finned Tubes," *AIChE Symposium Series*, Vol. 69, No. 131, 1973, pp. 94–103.

7 Bergles, A. E., Brown, G. S., Jr., and Snider, W. D., "Heat Transfer Performance of Internally Finned Tubes," ASME Paper No. 71-HT-31, 1971.

8 Hilding, W. E., and Coogen, C. H., Jr., "Heat Transfer and Pressure Loss Measurements in Internally Finned Tubes," Symposium on Air-Cooled Heat Exchangers, ASME, New York, 1964, pp. 57–85.

9 Patankar, S. V., Ivanović M., and Sparrow, E. M., "Analysis of Turbulent Flow and Heat Transfer in Internally Finned Tubes and Annuli," ASME JOURNAL OF HEAT TRANSFER, Vol. 101, 1979, pp. 29–37.

10 Hu, M. H., and Chang, Y. P., "Optimization of Finned Tubes for Heat Transfer in Laminar Flow," ASME JOURNAL OF HEAT TRANSFER, Vol. 95, 1973, pp. 332–338.

11 Masliyah, J. H., and Nandakumar, K., "Heat Transfer in Internally Finned Tubes," *ASME Journal of Heat Transfer*, Vol. 98, 1976, pp. 257–261.

12 Prakash, C., and Patankar, S. V., "Combined Free and Forced Convection in Vertical Tubes with Radial Internal Fins," ASME JOURNAL OF HEAT TRANSFER, Vol. 103, 1981, pp. 566–572.

13 Davis, L. P., and Perona, J. J., "Development of Free Convection Flow of a Gas in a Heated Vertical Open Tube," *International Journal of Heat and Mass Transfer*, Vol. 14, 1971, pp. 889–903.

14 Bodoia, J. R., and Osterlle, J. F., "The Development of Free Convection Between Heated Vertical Plates," ASME JOURNAL OF HEAT TRANSFER, Vol. 84, 1962, pp. 40–44.

15 Aung, W., Fletcher, L. S., and Sernas, V., "Developing Laminar Free Convection Between Vertical Flat Plates with Asymmetric Heating," *International Journal of Heating and Mass Transfer*, Vol. 15, 1972, pp. 2293–2308.

16 Aung, W., "Fully Developed Laminar Free Convection Between Vertical Plates Heated Asymmetrically," *International Journal of Heat and Mass Transfer*, Vol. 15, 1972, pp. 1577–1580.

17 Carpenter, J. R., Briggs, D. G., and Sernas, V., "Combined Radiation and Developing Laminar Free Convection Between Vertical Flat Plates with Asymmetric Heating," ASME JOURNAL OF HEAT TRANSFER, Vol. 98, 1976, pp. 95–100.

18 Sparrow, E. M., and Prakash, C., "Enhancement of Natural Convection Heat Transfer by a Staggered Array of Discrete Vertical Plates," ASME JOURNAL OF HEAT TRANSFER, Vol. 102, 1980, pp. 215–220.

19 Sparrow, E. M., and Bahrami, P. A., "Experiments on Natural Convection from Vertical Parallel Plates with Either Open or Closed Edges," ASME JOURNAL OF HEAT TRANSFER, Vol. 102, 1980, pp. 221–227.

20 Shah, R. K., and London, A. L., *Laminar Flow Forced Convection in Ducts*, Advance in Heat Transfer, Academic Press, New York, 1978.

21 Patankar, S. V., and Spalding, D. B., "A Calculation Procedure for Heat, Mass and Momentum Transfer in Three-Dimensional Parabolic Flows," *International Journal of Heat and Mass Transfer*, Vol. 15, 1972, pp. 1787–1806.

22 Patankar, S. V., *Numerical Heat Transfer and Fluid Flow*, McGraw-Hill, New York, 1980.

23 Raithby, G. D., and Schneider, G. E., "Numerical Solution of Problems in Incompressible Fluid Flow: Treatment of the Velocity-Pressure Coupling," *Numerical Heat Transfer*, Vol. 2, 1979, pp. 417–440.

Experimental, Variable Properties Natural Convection From a Large, Vertical, Flat Surface

D. L. Siebers
Sandia National Laboratories,
Livermore, Calif.
Assoc. Mem. ASME

R. F. Moffatt
Dept. of Mech. Engineering,
Stanford University,
Stanford, Calif.
Mem. ASME

R. G. Schwind
Nielsen Engineering and Research Inc.,
Mountain View, Calif.
Mem. ASME

Natural convection heat transfer from a vertical, 3.02 m high by 2.95 m long, electrically heat surface in air was studied. The air was at the ambient temperature and the atmospheric pressure, and the surface temperature was varied from 60 C to 520 C. These conditions resulted in Grashof numbers up to 2 × 10^{12} and surface-to-ambient temperature ratios up to 2.7. Convective heat transfer coefficients were measured at 105 locations on the surface by an energy balance. Boundary layer mean temperature profiles were measured with a thermocouple. Results show that: (1) the turbulent natural convection heat transfer data are correlated by the expression

$$Nu_y = 0.098\,\mathrm{Gr}_y^{1/3}\left(\frac{T_w}{T_\infty}\right)^{-0.14}$$

when all properties are evaluated at T_∞; (2) variable properties do not have a significant effect on laminar natural convection heat transfer; (3) the transition Grashof number decreases with increasing temperature; and (4) the boundary layer mean temperaturue profiles for turbulent natural convection can be represented by a "universal" temperature profile.

Introduction

An experimental study of the effects of variable properties on natural convection from a large, vertical, flat, electrically heated surface has been conducted. The vertical surface was placed in air at the ambient temperature and atmospheric pressure and heated to temperatures between 60 and 520°C. These conditions resulted in Gr_y up to 2 × 10^{12}, and T_w/T_∞ ranging from 1.1 to 2.7. The objective of this paper is to present the effects of variable properties noted in the experiment on the natural convection heat transfer from the surface, on the location of transition from laminar to turbulent flow in the natural convection boundary layer, and on the natural convection turbulent boundary layer temperature profile. In addition, comparison of the turbulent boundary layer temperature profiles to others in the literature indicate the existence of a "universal" temperature profile for turbulent natural convection. This work was part of a larger effort to examine a range of heat transfer conditions, varying from natural convection, to mixed convection driven by orthogonal buoyant and inertia forces, to forced convection, all from the same vertical surface [1].

Interest in variable properties effects on natural convection stems from the desire to predict more accurately the heat loss by convection heat transfer from the external-type receivers used in large-scale solar central receiver power plants. Convective heat loss from receivers can occur in a natural, mixed, or forced convection mode. In the natural convection mode, the convective heat transfer from an external-type receiver, essentially a large vertical, high-temperature surface, is complicated by variable properties effects as a result of the high operating temperatures. There is little information in the literature concerning variable properties effects on natural convection, particularly in the turbulent flow regime.

Literature Review

The effects of variable properties on laminar natural convection in liquids have been reviewed in two recent articles [2, 3]. Variable properties effects on laminar natural convection in gases have been examined experimentally and analytically by several authors [4–7]. The general consensus is that the effects of property variations on *laminar* natural convection are small in gases for the T_w/T_∞ range studied to date (0.25–4.0). Reference temperature methods are recommended by most authors to account for the small variable properties effects. One author, Hara [4], demonstrated analytically that when all properties were evaluated at T_∞, the following relationship would account for variable properties effects in air

$$\mathrm{Nu} = \mathrm{Nu}_{cp}\left[1 - 0.055\left(\frac{T_w - T_\infty}{T_\infty}\right)\right] \tag{1}$$

For those authors recommending a reference temperature method, definitions of T_{ref} ranged from a film temperature [6, 7] to that given in [5]

$$T_{\mathrm{ref}} = T_w - 0.38(T_w - T_\infty) \tag{2}$$

In most reference temperature methods, β is evaluated at T_∞. One exception is Clausing [7], who recommends that β be evaluated at T_f. This recomendations was based on experimental laminar heat transfer data taken at cryogenic temperatures, where T_w/T_∞ ranged from 1.0 to 2.6.

Variable properties effects on *turbulent* natural convection in gases have also been examined by several authors [6–8]. The numerical predictions of Siebers [8] for natural convection from a vertical surface in the T_w/T_∞ range of 1.0 to 3.0 with T_∞ at 20°C showed that evaluating the properties, including β, at T_f did not correlate the turbulent natural convection heat transfer predictions in terms of Nu and Gr. Pirovano et al. [6] correlated their turbulent natural convection experimental results in air in the T_w/T_∞ range of 1.0 to 1.5, with a T_{ref} heavily weighted toward T_∞ and with β evaluated at T_∞. Pirovano et al. defined T_{ref} as

$$T_{\mathrm{ref}} = \mathrm{T}_\infty + 0.2(T_w - T_\infty) \tag{3}$$

If Siebers [8] had used the recommendations of Pirovano et al. to correlate his numerical predictions of turbulent natural convection heat transfer, the results, when expressed in terms of Nu and Gr, would have agreed closely with the experimental results of Pirovano et al. Clausing [7] used T_f with

---

Contributed by the Heat Transfer Division for publication in the JOURNAL OF HEAT TRANSFER. Manuscript received by the Heat Transfer Division May 23, 1983.

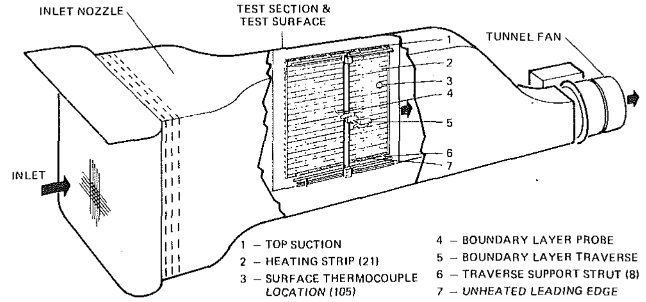

Fig. 1 Schematic of the apparatus, including the wind tunnel, the test surface, and the boundary layer traverse (+'s represent heat transfer coefficient measurement locations)

an additional large temperature-dependent correction to correlate the turbulent natural convection data obtained at cryogenic temperatures. He did note, however, that using T_∞ as the reference temperature for evaluating the properties significantly reduced the size of the temperature-dependent correction needed to correlate the data. Most basic heat transfer textbooks generally recommend a T_{ref} given by equation (2) or T_f with β evaluated either at T_∞ or at T_{ref} to account for variable properties effects in both laminar and turbulent flow.

The review of the literature shows that here are conflicting recommendations on how to account for variable properties effects on turbulent natural convection heat transfer in gases. These recommendations range from using a T_{ref} weighted toward T_w, given by equation (2), to a T_{ref} weighted toward T_∞, given by equation (3). Basic heat transfer textbooks generally recommended a T_{ref} given by equation (2) or T_f to account for variable properties effects on turbulent natural convection heat transfer in gases, but recent experimental and numerical works [6-8] point to a T_{ref} weighted toward T_∞ with β evaluated at T_∞. The differences in these various recommendations are significant when there are large temperature differences across the boundary layer.

Apparatus and Instrumentation

The following is a brief discussion of the apparatus and instrumentation. Further details can be found in [1]. Much of the apparatus was designed for the mixed- and forced-convection experiments and is described here only to completely describe the environment for the natural convection experiments.

An open-return, draw-through wind tunnel, 18 m long with a 4.8 m wide by 4.3 m high inlet, was built for these experiments (Fig. 1). The inlet nozzle to the test section has a two-dimensional 3:1 contraction. The heat transfer test surface, 3.02 m high by 2.95 m long, is mounted in a sidewall of the test section. The test section is 4.3 m high, 1.2 m wide, and 4.3 m long. The walls of the test section facing the heat transfer surface are water cooled to the ambient temperature. A small amount of boundary layer suction along the top of the test surface is used to ingest most of the hot, inner region of the boundary layer that leaves the top of the test surface, thereby preventing stratification in the tunnel. The suction rate was adjusted using velocity measurements and smoke flow visualization. The bottom leading edge is defined as the horizontal line where heating starts. Below this line are another 6 cm of smooth unheated surface; the struts that support the boundary layer traverse 30 cm off of the test surface extend through this unheated surface. Figure 1 shows the boundary layer traverse centrally located over the test surface. The traverse was used in some tests to take boundary layer mean velocity, temperature, and flow angle profiles. The traverse could move a boundary layer probe vertically or horizontally over the test surface, rotate a probe about an axis normal to the test surface, or move a probe normal to the test surface. The struts supporting the traverse had no effect on the vertical boundary layer flow in the natural convection mode.

The test surface consisted of 21 horizontal strips of 304 stainless steel foil stretched tightly over a slightly crowned surface of high-temperature insulating material 5.38 cm thick (Fig. 1). The strips were heated electrically using a-c current. Each strip was made from a 14.43-cm-wide by 0.13-mm-thick piece stainless steel foil. Along the entire length of both edges of each strip, 0.32 cm of the 14.43 cm width was tightly folded under, creating a strip with a net width of 13.79 cm. The 21 strips were mounted horizontally with a 0.64 cm wide gap between them to assure electric isolation of the strips from one another even with thermal expansion of the strips when heated. Folding the edges of the strips under was done for two reasons: first, it helped keep the strips flat on the surface [1] and, second, it provided additional electric power dissipation (4 percent of the total strip power dissipation) along the gaps between strips to exactly compensate for the unheated gap area (4 percent of the total area).

Surface temperatures on the test surface were measured at 105 locations, each equipped with a rosette of three ther-

Nomenclature

g = gravitational constant, m/s^2
Gr_y = Grashof number, $g\beta(T_w - T_\infty)y^3/\nu^2$
h = convective heat transfer coefficient, W/m^{2}C
ID = test indentification number
k = thermal conductivity, W/mC
n = exponent on the variable properties correction
Nu_y = Nusselt number, hy/k
Nu'_y = $\text{Nu}_y(T_w/T_\infty)^n$, n = 0.14 for turbulent flow, n = 0.04 for laminar flow
Pr = Prandtl number, ν/α
q = heat flux, W/m^2
T = temperature, °C
T_0 = temperature scalar for the outer region of the boundary layer (24), $(q_w/\rho c_p)^{2/3}(g\beta\delta)^{-1/3}$
y = vertical direction, m
z = distance normal to the wall, cm

Greek

α = thermal diffusivity, m^2/s
β = coefficient of volumetric expansion, K^{-1}
θ = dimensionless temperature,

$$\left(\frac{T_w - T}{T_w - T_\infty}\right)$$

δ = Length scalar for the outer region of the boundary layer
δ_t = thermal boundary layer thickness,

$$\int_0^\infty \left(\frac{T - T_\infty}{T_w - T_\infty}\right) dz$$

η_t = length scalar for the inner region of the boundary layer (24), $(\alpha^2/g\beta(T_w - T_\infty))^{1/3}$
η'_t = modified length scalar for the inner region of the boundary layer,

$$\eta_t\left(\frac{k_w}{k_\infty}\right)\left(\frac{T_w}{T_\infty}\right)^{0.14}$$

Subscripts

c = conduction heat transfer
cp = constant properties solution
e = electric power
f = film temperature
r = radiation heat transfer
ref = reference temperature
w = wall or surface temperature
∞ = ambient condition

mocouple junctions arranged equally spaced on the circumference of a 7.5-cm-dia circle. The three thermocouple junctions of a rosette were connected electrically in parallel so that the average temperature at the three junction locations was sensed. The thermocouple rosettes were located underneath the stainless steel heating strips, electrically insulated from the strips by a thin layer of mica. The 105 thermocouple rosettes on the test surface formed a staggered array with a 10 vertical columns, as shown by the "+'s" in Fig. 1. Columns 1, 3, 5, etc., had 11 measuring stations, open on each of heating strips 1, 3, 5, etc.; Columns 2, 4, 6, etc., had 10 measuring stations, located on heating strips 2, 4, 6, etc.

An extensive program of analysis and bench testing was conducted on prototypes of the electrically heated test surface. The analysis and tests verified that the surface thermocouples installation would measure T_w (in°C) within ±1 percent, even though the thermocouples were not welded to the strips [1].

The natural convection data were taken only on calm nights since the tunnel was outside. A hatch in the roof of the tunnel was open and the top-edge suction was operated to mimimize stratification in the test section. Flow visualization with smoke showed that the air in the test section was essentially at rest. Except for the boundary layer on the heated test surface, there was no discernible flow. The stratfication in the test section for the natural convection tests was small, ranging from less than 1°C from top to bottom of the test surface for low-temperature tests to 10°C over the top half of the test surface at a T_w of 520°C. (The bottom half showed no stratification for any tests.) For tests where stratification occurred over the top half of the test surface, the local T_∞ at a given elevation was used in the data reduction.

Heat transfer coefficients were calculated at each of the 105 surface temperature measurement locations on the test surface on the basis of an energy balance

$$h = \frac{q_e - q_r - q_c}{(T_w - T_\infty)} \tag{4}$$

where

q_e = electrical power dissipated
q_r = net radiation heat transfer from the front of the test surface
q_c = conduction heat transfer through the back of the test surface

The data reduction was done on a minicomputer system which acquired and then reduced the data on-line. For natural convection tests, q_r ranged from 14 percent for the lowest T_w cases to 44 percent of the electrical power dissipated for the highest T_w cases, while q_c was typically 8 to 14 percent of the electrical power dissipated.

The electric power dissipated per unit area at a temperature measurement point on a given heating strip, q_e, was equal to the average electric power dissipated per unit area for that strip. This resulted from the uniformity of the electric power dissipation by each heating strip, which in turn resulted from the uniformity of temperature (i.e., uniformity of resistivity) on each horizontal heating strip for the natural convection mode of heat transfer and the uniformity of the heating strip thickness, ±1 percent. The average electric power dissipated per unit area on a heating strip was determined from the product of the measured RMS voltage drop across the length of a heating strip and the measured RMS current through a heating strip, divided by the surface area of the strip (including the folded under edges) between the voltage measurement points. The small effect of thermal expansion on the surface area of a heating strip, which caused a 1 percent increase in surface area for the highest temperature case, was taken into account. The uniformity of electric power dissipation for all the 105 surface temperature measurement points was ±2.5 percent.

Several checks were made on the uniformity of and the measurement of the electric power dissipated [1]. One important check confirmed the accuracy of the voltage and the current measurements used to determine q_e. In this check, the resistivity of the stainless steel as a function of temperature determined from the strip dimensions and from the strip voltage and current measurements made during actual heat transfer tests was compared with direct measurements of the resistivity of a sample of the 304 stainless steel heated in an oven and with resistivities reported in the literature for 304 stainless steel. The independently measured resistivities agreed within 1 percent over the temperature range of the experiment. There was also similar good agreement between the measured resistivities and those reported in the literature.

The radiation heat transfer from the surface to the tunnel walls q_r, was determined from a three zone, diffuse, gray body radiation heat transfer model. The zones in the model were (*i*) the tunnel walls surrounding the test surface (which were water cooled), (*ii*) the local spot on the surface where h was being measured, and (*iii*) the remainder of the test surface. Shape factors between the zones were: 0, 1, or an area ratio in the case of the tunnel wall to test surface shape factor. The temperature boundary conditions for the three zones were respectively (*i*) the average tunnel wall temperature determined from the measurement of the tunnel wall temperature at 35 locations with thermocouples, (*ii*) the local surface temperature measurement on the test surface where h was being measured, and (*iii*) the average test surface temperature measurement calculated from all 105 surface temperature measurements. The tunnel wall temperature rarely exceeded 40°C at any spot, since it was water cooled. As a result, the average tunnel wall temperature was always near ambient and not an important factor in determining q_r in equation (4).

The emittance of the stainless steel test surface was determined from measurements of the normal, spectral reflectance of the 304 stainless steel in the 2.0 to 25.0 micron wavelength range at up to 70 wavelengths with a paraboloid reflectometer. These measurements were integrated over the appropriate Planckian blackbody distribution for each temperature considered and subtracted from one to give the normal, total emittance. The hemispherical, total emittance was then obtained from the relationship that exists between the hemispherical, total and normal, total emittances of smooth metal surfaces found in [9]. These measurements of hemispherical, total emittance agreed very well with previous measurements of emittance for the same material by other researchers [10, 11] and with the theory for smooth metal surfaces found in [9]. Also, the measured temperature dependence agreed with the temperature dependence given by the smooth metal surface theory. The measuerments show the emissivity is 0.13 ± 0.01 at ambient temperatures and 0.22 ± 0.01 at the peak temperatures of the experiment. No detectable effect of material aging during testing was recorded for test conditions reported in this paper. Measurements of the emissivity over the temperature range of the experiment were made on samples of the stainless steel from before, during, and after testing.

The conduction through the insulation on the back of the test surface q_c was determined at each of the 105 surface temperature measurement points by applying a one-dimensional conduction model between two locations through the 5.38 cm depth on the insulation. The two locations were (*i*) the surface temperature measurement point and (*ii*) a point directly behind the surface temperature measurement point where a thermocouple was located between the two layers of insulation that made up the insulated back of the test surface. Variation of the thermal conductivity of the insulation with temperature was accounted for in the one-dimensional model. A numerical, three-dimensional conduction analyis of the insulation showed that the one-dimensional conduction model

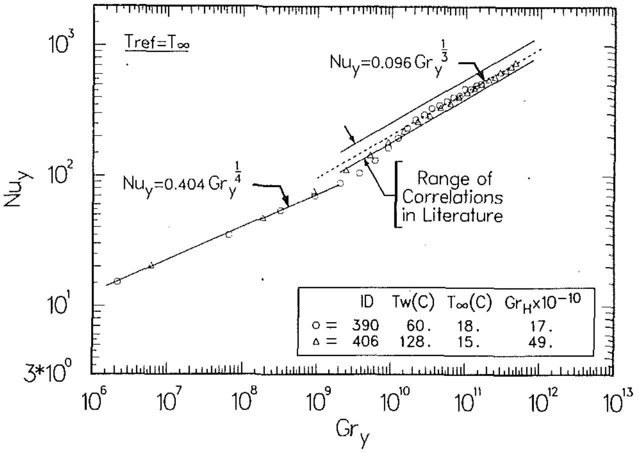

Fig. 2 Natural convection baseline results—Nusselt number versus Grashof number

was accurate to within 1 percent for areas of the 3 m by 3 m test surface 8 cm away from its edges. The calculated one-dimensional conduction loss through the insulation for the thermocouple locations on the top and the bottom heating strips, which were within 8 cm of an edge of the test surface (10 of the 105 locations), was increased by 5 percent, based on the results of the numerical, three-dimensional conduction analysis.

The values of h obtained by equation (4) are reliable within ± 6 percent for the baseline cases and the low-T_w cases and within ± 10 percent for the high-T_w cases. The uncertainties were calculated following the method of Kline and McClintock [12], using observed values for the individual uncertainties in the input terms. The uncertainty analysis was an important part of the experimental planning process and served as the principal criterion for choosing among alternative measurement techniques and for setting the standards for acceptable accuracy on the individual measurements.

Boundary layer mean temperature profiles were taken with a 0.052 mm type-K thermocouple probe [1]. Natural convection velocity profiles, taken with a pressure probe, were used in making a correction to the thermocouple readings. The correction accounted for errors caused by radiation between the thermocouple, the hot test surface, and the cold tunnel walls, as well as conduction heat transfer down the thermocouple stem. The model used for the radiation correction is similar to the three-zone model used for the radiation correction in equation (4), except that a fourth zone has been added to the model to represent the thermocouple. The corrections made were small. The boundary layer mean temperature data are reliable within the larger of $\pm 2°\mathrm{C}$ or ± 4 percent based on the same method of uncertainty analysis that was used to determine the uncertainty of h. The measurement of distance normal to the test surface for the boundary layer profiles was accurate to within ± 0.12 mm.

Apparatus and Instrumentation Qualification

To qualify the apparatus and instrumentation, baseline (i.e., low wall-to-ambient temperature difference) heat transfer tests were taken in both the forced and natural convection modes and compared with accepted flat-plate, uniform heat flux, constant properties correlations appearing in the literature. Also, baseline boundary layer profiles of temperature and velocity were taken for forced convection and compared with accepted profiles appearing in the literature for flow on a flat, uniform heat flux surface. The forced convection baseline results are presented in [1]. The forced convection heat transfer results show excellent agreement with the accepted forced-convection heat transfer correlations for both laminar and turbulent flow on a flat, uniform heat flux surface. The transition from laminar to turbulent flow occurs at Reynolds numbers noted by the others in the literature. The forced convection baseline boundary layer velocity and temperature profiles show similar good agreement with accepted forced convection profiles for both laminar and turbulent flow on a flat, uniform heat flux surface.

The natural convection baseline heat transfer results are shown in Fig. 2. Two natural convection baseline heat transfer tests were taken with T_w equal to 60°C and 128°C and T_∞ equal to 15°C and 18°C, respectively. The baseline results are plotted in Nu_y versus Gr_y coordinates in Fig. 2 with fluid properties evaluated at a T_{ref} equal to T_∞. (The choice of T_{ref} for these low-temperature difference tests has very little effect on the data in Fig. 2). The 21 points shown for each test are each the average of the five data points along a horizontal heating strip (see Fig. 1). The RMS variation of the five data points along a heating strip was 4 percent or less.

The solid line in the laminar flow region in Fig. 2 ($\mathrm{Gr}_y < 10^9$) represents accepted constant properties natural convection correlation for laminar flow on a vertical, uniform heat flux surface in air [13]

$$\mathrm{Nu}_y = 0.404\mathrm{Gr}_y^{1/4} \tag{5}$$

In the turbulent flow region ($\mathrm{Gr}_y > 10^{10}$), three lines are shown. The two solid lines represent the range of correlations in the literature for turbulent natural convection from a vertical surface. The dashed line is a "best-fit" line through the data in the literature, represented by

$$\mathrm{Nu}_y = 0.096\mathrm{Gr}_y^{1/3} \tag{6}$$

Equation (6) is the correlation recommended by Churchill and Chu [14] for turbulent natural convection from a vertical surface with the coefficient 0.096 evaluated for a Pr of 0.71. The equation is based on their survey of the then current data (1975). The data at that time included only low-temperature difference data with minor variable properties effects.

Figure 2 shows three main points. First, the agreement between baseline laminar data and the accepted constant properties correlation is good. Second, the baseline turbulent data lie within the range of correlations appearing in the literature and agree very well with the "best-fit" correlation of Churchill and Chu. Third, the transition location for the baseline data agrees with other data in the literature that show transition between a Gr_y of 10^9 and 10^{10}. This close agreement between baseline data and the data in the literature qualifies the apparatus and instrumentation. In addition, the close agreement shows that the small horizontal gaps between the 21 heating strips have little, if any, effect on the results. The lack of effect was expected, since the total area of the gaps was small compared to the heated area of the test surface, a small amount of additional heating to make up for the unheated gaps was provided along the gap edges by the folded under strip edges, and the depth of the step created by the gap ($\approx$ 0.13 mm) was small compared to the boundary layer thickness, which was as large as 15 cm.

In addition to the baseline tests, a comparison was made between the heat transfer coefficient as determined by equation (4) at a given location on the surface and one which could be determined from a boundary layer temperature profile measured at that same location by the following relationship

$$h = \frac{d\theta}{dz} \tag{7}$$

This comparison was possible for 43 cases. These were cases which had boundary layer temperature profiles with temperature measurements well into the viscous sublayer of the turbulent boundary layer or the inner region of the laminar boundary layer ($\theta < 0.2$), where equation (7) is valid. Two of the cases were natural convection profiles, and 41 were forced

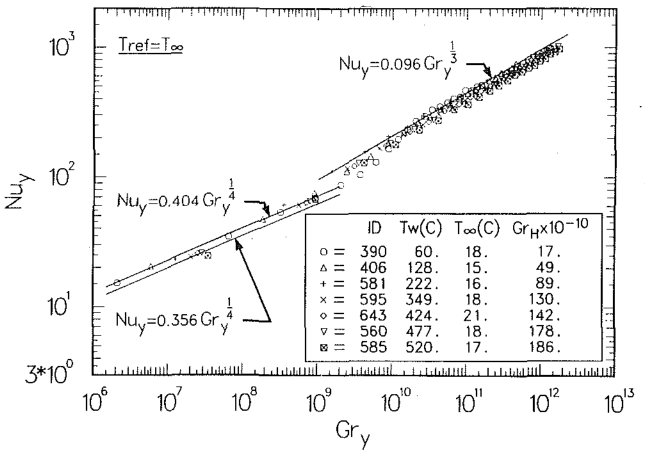

Fig. 3 Effect of variable properties on natural convection from a vertical surface in air

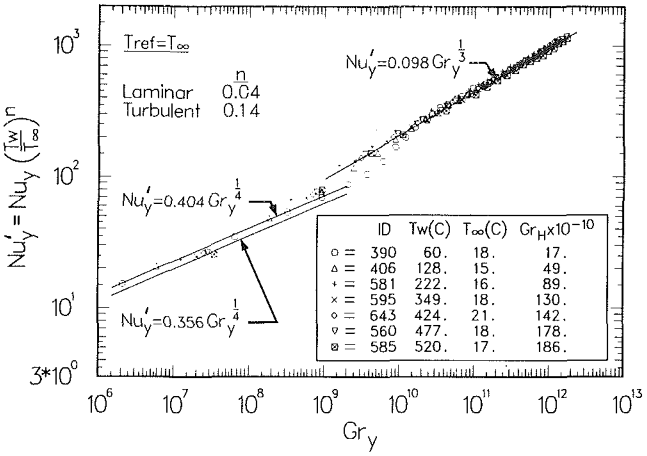

Fig. 4 Correlation of variable properties effects on natural convection from a vertical surface in air

or mixed convection profiles taken as part of the forced and mixed convection experiments also conducted with this apparatus. The profiles were for the T_w in the 200°C to 580°C range. The average ratio of the measurement of h from equation (4) to the measurement of h from equation (7) for the 43 cases was 1.008 with a standard deviation of 14 percent. The closeness of this ratio to 1.0 is a check on the consistency of the independently measured surface heat transfer data and boundary layer temperature profiles over the entire temperature range of the experiment. Other consistency checks are presented in [1].

Results and Discussion

Heat Transfer. Variable properties effects on natural convection heat transfer from an electrically heated, vertical, 3.02-m-high by 2.95-m-long surface were studied. The ambient temperature was approximately 20°C. Average values of T_w that were considered were 60, 128, 222, 349, 424, 477, and 520°C. These temperatures resulted in T_w/T_∞ ratios from 1.1 to 2.7. Figure 3 shows the heat transfer results in terms of Nu_y and Gr_y with all properties, including β, evaluated at T_∞ for each test. The 21 data points shown in Fig. 3 for each surface temperature were obtained in the same manner as those for the baseline cases shown in Fig. 2. For all tests except test ID 585, the test surface was at steady-state conditions. Test 585, which had to be stopped before steady state was reached, has a transient energy storage correction equal to -5 percent of electric power dissipated. This correction accounted for energy being stored in the insulation. The correction was based on measurements of the insulation temperature taken over a 10-min interval and was made along with the radiation and conduction corrections in equation (4).

In the turbulent region ($\mathrm{Gr}_y > 10^{10}$) in Fig. 3, the data shows two important points. First, there is a small decrease in Nu_y for a given Gr_y as T_w increases, when properties are evaluated at T_∞. Second, each data set for each temperature remains parallel to the low-temperature difference correlation given by equation (6) from Churchill and Chu; the second point in most visible for test 585. This latter point means that Nu_y remains dependent on $\mathrm{Gr}_y^{1/3}$ in the turbulent flow region with increasing temperature difference across the boundary layer, or in other words, the heat transfer coefficient remains uniform in the turbulent region. Only the coefficient in equation (6) is changing with increasing temperature. It decreases from the 0.096 value for a small temperature difference across the boundary layer to a value of 0.08 for the 520 C test, a decrease of 15 percent. This decresse does not imply that the turbulent natural convective heat transfer coefficient at a fixed location is lower for higher T_w. It only indicates that, as a result of property variations across the boundary layer, the heat transfer coefficent is less than would be predicted by the low-temperature difference constant-properties correlation with all properties evaluated at T_∞.

In the laminar region ($\mathrm{Gr}_y < 5 \times 10^8$) in Fig. 3, there is a small decrease in Nu_y for a given Gr_y as T_w increases. The decrease in Nu_y with increasing T_w is most clearly shown by the lower Gr_y data point for each T_w. As T_w increases, the lowest Gr_y data point for each T_w lies progressively farther below the uniform heat flux correlation given by equation (5), the upper line in the laminar region.

The decrease in Nu_y with increasing T_w in the laminar region is not totally due to variable properties effects as was the case in turbulent flow. The decrease in Nu_y is partly due to a change in the heat transfer boundary condition on the test surface as T_w increases. At low temperatures, the surface has a uniform heat flux, as described earlier. At high temperatures, the surface approaches a uniform temperature as a result of the radiation heat transfer from the surface. For the highest temperature case, 520°C, the test surface is within 2 percent of a uniform temperature surface in the laminar and transition regions. The correlation for uniform surface temperature is the lower line in the laminar region in Fig. 3 [15]. A combination of variable properties effects and a change in boundary condition are indicated by the fact that the highest temperature laminar data point lies about 8 percent below the uniform surface temperature relationship.

Unlike the situation in the laminar region, a change in boundary condition does not occur in the turbulent region. A vertical surface with a turbulent natural convection flow over it is simultaneously a uniform temperature and a uniform heat flux surface (i.e., h is spatially uniform for a given T_w). Churchill and Chu's uniform temperature and uniform heat flux correlations based on "best fits" of data in the literature are only different by 2 percent for a Pr of 0.71. The difference is well within the uncertainty of the data available.

When all the properties are evaluated at T_∞, the variable properties effects noted in Fig. 3 for *turbulent* natural convection in air are accounted for by the following relationship

$$\mathrm{Nu}_y = 0.098\mathrm{Gr}_y^{1/3}\left(\frac{T_w}{T_\infty}\right)^{-0.14} \tag{8}$$

This equation is based on a "best fit" of the natural convection data in Fig. 3, where the 1/3 power on Gr was assumed as a result of the lack of dependence of h on y (shown by each set of the heat transfer coefficient data for each T_w). The coefficient in equation (8) is 2 percent higher than that in the baseline equation, equation (6), and a temperature ratio correction has been added to account for the effects of variable properties. Figure 4 (where the Nusselt number, Nu_y', is defined so that it includes the temperature ratio correction

Table 1 A comparison of recommendations for evaluating variable properties effects on turbulent natural convection (T_∞ = 20°C).

Ref. →	[6]	[7]	[16]	[17]	[18]
T_{ref} →	Eq. (3)	T_f	T_f	T_f	Eq. (2)
β →	$1/T_\infty$	$1/T_f$	$1/T_\infty$	$1/T_f$	$1/T_\infty$
T_w (°C) ↓	h/h predicted by Eq. (8)				
300	1.03	1.30	0.95	0.82	0.90
600	1.04	1.17	0.90	0.71	0.87
900	1.06	1.10	0.88	0.65	0.82

term in the definition of Nusselt number) shows that equation (8) accounts for the small systematic decreases in Nu_y with increasing temperature, which appeared in Fig. 3. The turbulent data collapse to within ±6 percent of the correlation given by equation (8). This percentage is within the uncertainty band on the heat transfer data.

The variable properties effects on turbulent natural convection could also have been accounted for by evaluating all the properties, except β in Gr_y, at a T_{ref} defined as:

$$T_{\mathrm{ref}} = 0.3T_w + 0.7T_\infty \tag{9}$$

The term β should still be evaluated at T_∞.

The correlation for the *laminar* natural convection heat transfer data, with all properties for air evaluated at T_∞, is

$$\mathrm{Nu}_y = a\mathrm{Gr}_y^{1/4}\left(\frac{T_w}{T_\infty}\right)^{-0.04} \tag{10}$$

The term a equals 0.404 for a uniform heat flux surface and 0.356 for a uniform temperature surface, the values reported in the literature. Equation (10) agrees with numerical predictions made by Siebers [8] for $T_w/T_\infty < 3.0$, with the more detailed laminar data for $T_w/T_\infty < 1.5$ from the experiments of Pirovano et al. and with various analyses for air [4, 5]. Equation (10) demonstrates that variable porperties effects on laminar natural convection heat transfer are small. The difference in h calculated from equation (10) with and without the T_w/T_∞ corrections at a T_w/T_∞ of 3.0 would only be 4 percent.

The effects of variable properties on laminar natural convection heat transfer can also be accurately accounted for by evaluating all properties except β in Gr_y at T_f, as noted by Sparrow and Gregg [5] and Pirovano et al. The term β should still be evaluated at T_∞, as in turbulent flow.

The trends noted in the turbulent natural convection region are new. No experiments were found in the literature for high-temperature flows on a vertical surface with large temperature differences across the boundary layer. The highest temperature experiment with turbulent flow in gases was by Pirovano et al. with temperatures up to 150°C and $T_w/T_\infty <$ 1.5. The one experiment that had large temperature variations across a turbulent boundary layer was at cryogenic temperatures. Clausing, who conducted this experiment, noted different trends.

Table 1 shows a comparison of the effects of variable properties on turbulent natural convection heat transfer from a vertical surface in air predicted by various recommended methods to account for those effects. In the table, the effects predicted by five recommendations appearing in the literature [6, 7, 16, 17, 18] are compared with the effects predicted by the method proposed in this paper. The present work recommends evaluating all properties in the constant properties heat transfer relationship at T_∞ and making the wall-to-ambient temperature ratio correction, $(T_w/T_\infty)^{-0.14}$, shown in equation (8).

For each of the five methods from the literature, the table gives the T_{ref} at which properties are evaluated, the temperature used to determine β, and the ratio of h predicted by that method to h predicted by equation (8) for three different values of T_w (300, 600, and 900°C) and a T_∞ of 20°C. The first two methods listed [6, 7] are recent recommendations reported in the literature based on experimental data. The next three [16, 17, 18] are recomendations reported in most basic heat transfer textbooks. All of the methods except Clausing's, the second method, are reference temperature methods. Clausing evaluates all properties, including β, at T_f and makes a large correction based on T_w/T_∞ to account for variable properties effects. The correction is given in Fig. 1 of [7].

The constant properties Nusselt-Grashof number correlation to which all the recommended methods presented in Table 1 are applied is given by equation (8) without the $(T_w/T_\infty)^{-0.14}$ term. The correlation represented by equation (8) without the temperature ratio term is not significantly different than the constant properties correlations used in each of the references in Table 1. The only difference is in the coefficient (0.098 in equation (8)) in each correlation. Applying all methods to one constant properties correlation allows the different methods of handling variable properties to be compared, without introducing the small differences in the coefficient of the constant properties relationship that is recommended in each work. Effectively, this means that Table 1 compares with relative trend in the variable properties effects predicted by each method for increasing T_w with that predicted by equation (8).

Table 1 shows that the first method, from Pirovano et al. (the most closely related experiment to the work described in this paper), predicts substantially the same variable properties effect as equation (8) for all temperatures. This reference temperature method uses a T_{ref} heavily weighted toward T_∞, given by equation (3), with β evaluated at T_∞. It is based on an experiment with values of T_w up to 150°C. The second method in the table, the method recommended by Clausing based on data taken at cryogenic temperatures, predicts 30 percent higher heat transfer at 300°C, but only 10 percent higher at 900°C. This trend indicates that his method predicts a different variable properties effect on turbulent natural convection with increasing T_w than equation (8) does. The last three methods in Table 1—the textbook methods—predict progressively lower heat transfer coefficents with increasing T_w. This trend is particulary true for the fourth method, where β is evalauted at T_f along with the rest of the properties.

The disagreement between the methods recommended in this work and the last three methods is most likely explained by the fact that these recommendations are based on forced convection experience or on a laminar flow natural convection analysis by Sparrow and Gregg [5]. No turbulent natural convection data with significant variable properties effects are available. Recommendations based on forced convection experience should not be expected to work a priori for turbulent natural convection. Similary, recommendations based on Sparrow and Gregg's laminar flow analysis should not be expected to work a priori for turbulent natural convection since, first, the analysis was for laminar natural convection heat transfer and, second, the variable properties effects on which they based their conclusions in that analysis were only a few percent for the realistic gas models and temperature ranges studied (330 K $< T <$ 1000 K, $T_w/T_\infty <$ 3.0). For example, if an h for air predicted using T_f as the reference temperature in the laminar heat transfer relationship, equation (5), is compared to an h predicted with the same relationship using Sparrow and Gregg's recommended reference temperature, given by equation (2), there would be less than a 1 percent difference for T_w at 600°C and T_∞ at 20°C ($T_w/T_\infty \approx 3.0$). The reasons for the disagreement with the results of Clausing are not clear at this point. One possibility is that variable properties effects on

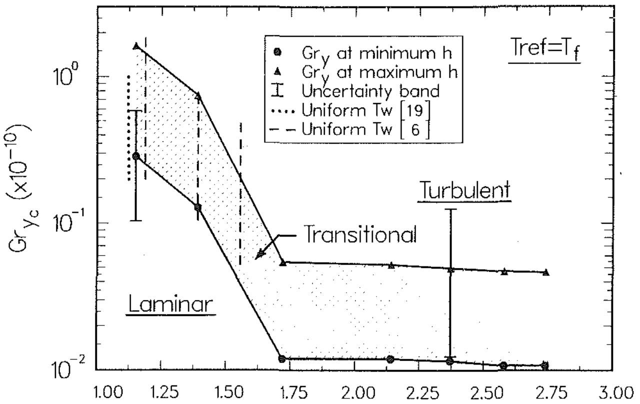

Fig. 5 Effect of wall temperature on the transition Grashof number in natural convection from a vertical surface in air

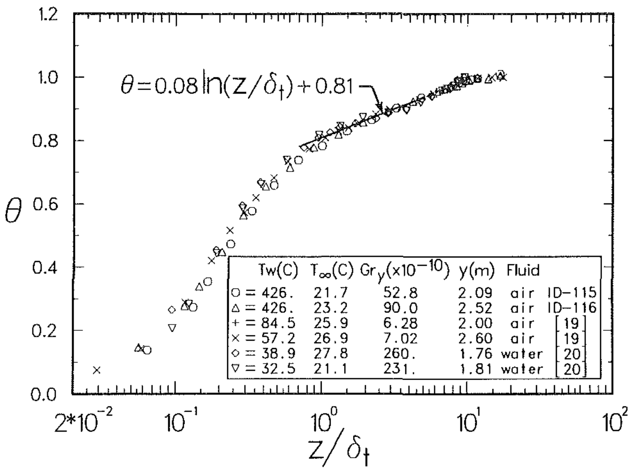

Fig. 6 Temperature profiles in a turbulent natural convection boundary layer on a vertical surface

turbulent natural convection are different for different fluids in significantly different temperature ranges.

Transition. Figure 5 shows the effect of T_w on the natural convection transition from laminar to turbulent flow for fixed T_∞. The figure is a plot of the $\log_{10}$ of the Grashof number based on y_c versus T_w/T_∞. The length y_c is the location of either the minimum h or the maximum h. The location of the minimum h is the point where h begins to deviate from the laminar h value. The location of the maximum h is the first point at which h equals its fully turbulent value, which is a constant. The resolution in determining these locations is plus or minus the width of one heating strip. Uncertainty bands based on this resolution are shown in Fig. 5. The upper value for Gr_{y_c} at each T_w/T_∞ corresponds to the location of maximum h; the lower value corresponds to the minimum h location. The zone between the minimum and maximum h is defined here as the "transition zone" (the crosshatched area). All properties in this figure are evaluated at T_f with the exception of β, which is evaluated at T_∞. Film temperature was used largely because transition starts in the laminar boundary layer where one way to correlate heat transfer data is to evaluate properties at T_f, as discussed earlier. The solid lines connecting the data points from this experiment are for visual reference only.

Figure 5 shows that T_w has a significant effect on the stability of the boundary layer for a fixed T_∞. As T_w/T_∞ increases, the Grashof number at which transition occurs, Gr_{y_c}, decreases significantly up to a T_w/T_∞ of 1.75. Furthermore, the size of the transition zone, in terms of the difference between Gr_{y_c} at the minimum and maximum h locations, decreases up to a T_w/T_∞ of 1.75. This decrease in size is also true in terms of vertical distance. However, the ratio of Grashof numbers at the minimum and maximum h locations remains fixed at approximately 5.0. These results agree closely with the results of Pirovano et al. for T_w/T_∞ up to 1.5. The very low-temperature ratio case agrees with the results of Cheesewright [19].

Beyond a T_w/T_∞ of 1.75, transition zone size and location in terms of Gr_{y_e} appear fixed. This apparent trend is believed due to a loss of resolution in locating the transition zone. By $T_w/T_\infty = 1.75$, the transition zone has moved down to the first three heating strips on the test surface (see Fig. 1) and is occurring over a very short distance ($\approx$ 1 strip). On the basis of the resolution of the transition zone location, accurate location of the transition zone is impossible when T_w/T_∞ exceeds 1.75. It is only clear that the transition zone does not move upward on the surface for $T_w/T_\infty > 1.75$.

Temperature Profiles. Boundary layer mean temperature profiles were taken for turbulent natural convection for a T_w equal to 420°C. The corrections to the temperature measurements accounting for errors caused by radiation heat transfer and conduction heat transfer (discussed earlier) were small, ranging from +10°C near the wall to −2°C at the outer edge of the boundary layer. In the following figures, the uncertainty in z, ± 0.12 mm, results in a ± 15 percent uncertainty in the nondimensional distances used in the figures for the point closest to the wall for each profile from this experiment. This uncertainty is inversely proportional to the distance from the wall.

The temperature profiles are shown in Fig. 6, which is a plot of dimensionless temperature θ versus distance normal to the wall z divided by δ_t. Also shown are turbulent boundary layer temperature profiles from other works for which tabular data were available to plot. Two of the profiles shown were taken in air by Cheesewright and two were taken in water by Chokouhmand [20]. For Cheesewright's profiles, T_w equals 84.5 and 57.2°C. For Chokouhmand's profiles, T_w equals 38.9 and 32.5°C. The high-temperature profiles from this experiment compare well with the profiles for air and water at lower temperatures taken by Cheesewright and Chokouhmand, respectively. The close comparison of Cheesewright's low-temperatrure profiles for air with the high-temperature profiles from this experiment indicates that there is very little effect of variable properties on the turbulent natural convection temperature profile shape. All of the profiles in Fig. 6 show a "viscous" sublayer or "linear" region near the wall, $z/\delta_t < 0.2$, and a "logarithmic" region in the outer region of the boundary layer, $z/\delta_t > 1.0$. The temperature distribution in the "logarithmic" region is given by

$$\theta = 0.08\ln(z/\delta_t) + 0.81 \tag{11}$$

Equation (11) is represented by the solid line in Fig. 6.

Comparisons were also made with turbulent boundary layer temperature profiles from other experiments for which tabular data was not readily available for plotting [21–23]. In the outer region, the "logarithmic" region, the data from the experiments of Warner and Arpaci [21], Vliet and Liu [22], and Fujii [23] agree very well with the data in Fig. 6. In the inner region, for $z/\delta_t < 0.6$, the temperature profiles from these same references agree in terms of their shape, but there is more scatter than is indicated by the data in Fig. 6, approximately ± 40 percent at z/δ_t equal to 0.1 The reasons for the scatter are not clear. One possible reason is a Pr number effect. The experiments cover a Pr number range of 0.7 to 33.

The agreement of the turbulent profiles from the various experiments strongly suggests the existence of a "universal" temperature profile for turbulent natural convection. Existence of a universal profile has not been clearly

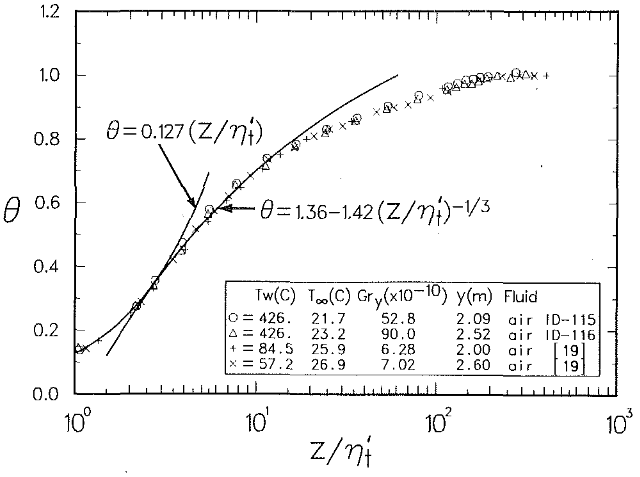

Fig. 7 Temperature profiles in a turbulent natural convection boundary layer on a vertical surface in air

established experimentally but has been theorized most recently by George and Capp [24]. George and Capp proposed dividing the boundary layer into an inner and outer region. The inner region was assumed to be a constant heat flux layer consisting of a "viscous" sublayer and a "buoyant" sublayer. The "buoyant" sublayer is between the "viscous" and "logarithmic" regions pointed out in Fig. 6. The form of the equations derived by George and Capp for the "viscous" and "buoyant" sublayers for a uniform temperature surface are, respectively

$$\theta = C_1 (z/\eta_t) \tag{12}$$

$$\theta = C_2 + C_3 (z/\eta_t)^{-1/3} \tag{13}$$

In these equations, the definition of θ is one minus that used by George and Capp, and the terms C_1, C_2, and C_3 are functions of Pr. Based on the experimental data available, George and Capp determined C_1, C_2, and C_3 to be 0.1, 1.35, and -1.45, respectively, for air.

George and Capp theorized that the temperature profile in the outer region of the boundary layer was dependent only on z/δ, where δ is a length scale for the outer region of the boundary layer. Their theory showed that there should be no Pr number dependence in the outer region. George and Capp expressed the equation for the outer region as

$$\frac{T-T_\infty}{T_0} = C_4 f\left(\frac{z}{\delta}\right) \tag{14}$$

where δ was undefined. No specific form for the equation was given by their theory. An empirical fit to data is required to obtain the equation for the outer region.

Figure 6 suggests a logarithmic form for the "universal" temperature profile in the outer region of the boundary layer. Deviations of the data from equation (11) are within the uncertainty of the data available. Figure 6 also suggests δ_t as a length scale and $T_w - T_\infty$ as a scalar for temperature in the outer region as a result of the close agreement of the various sets of data over a large range of Pr.

Using δ_t as an outer region length scale is contrary to the recommendation of George and Capp, who stated that since δ_t had "no dynamical significance," it should not be used as a length scale for the outer or inner regions. It is worth noting however, that when the Boussinesq approximation is made, the integral $\int_0^\infty (T-T_\infty)\,dz$ appears in the integral form of the momentum equation for natural convection. The integral appears in a source term in the integral momentum equation, representing the buoyant force term in the differential momentum equation. The appearance of the integral suggests strong dynamical significance for δ_t, since dividing the integral by $T_w - T_\infty$ gives δ_t.

The important points shown by Fig. 6 and equation (11) are: (*i*) there are no significant variable properties effects on the temperature profile shape, (*ii*) the temperature in the outer region appears logarithmically dependent on z, (*ii*) δ_t appears to be a good length scale for the outer region, and (*iv*) the profile appears to be independent of Pr in the outer region as suggested by George and Capp in their theory. This last point appears true for the Pr range of 0.7 to 33 based on [21-23].

The temperature profiles for air from both this experiment and Cheesewright's experiment (the same cases as shown in Fig. 6) are presented in Fig. 7 in terms of the inner region coordinate, z/η_t'. The term η_t' is a modified form of the inner region length scale of George and Capp. The modification, which is based on equation (8), accounts for a small shift in profile locations in these coordinates caused by variable properties effects. Also shown in this plot are the following equations

$$\theta = 0.127(z/\eta_t') \tag{15}$$

$$\theta = 1.36 - 1.42(z/\eta_t')^{-1/3} \tag{16}$$

These equations are equations (12) and (13) with coefficients modified to fit the data in Fig. 7. The coefficients in the equations are only slightly different than those derived by George and Capp on the basis of the data available to them. The figure shows that the form of the equations for a "universal" temperature profile derived by George and Capp for the inner region of the boundary layer agree very well with the data for air. The coefficients are Pr-dependent, though, since the water data of Chokouhmand, if shown, would be significantly to the right of the air data.

As a final note, equations (7) and (15) can be used to determine a heat transfer relationship for turbulent natural convection in air in a straightforward fashion

$$\mathrm{Nu}_y = 0.10\,\mathrm{Gr}_y^{1/3}\left(\frac{T_w}{T_\infty}\right)^{-0.14} \tag{17}$$

This heat transfer relationship and the heat transfer relationship given by equation (8), determined from the independently measured boundary layer temperature profiles and surface heat transfer data, respectively, agree within 2 percent. The consistency of the independently measured boundary layer temperature profiles and the surface heat transfer data is a very good check on the experimental technique and the variable properties effects noted in this experiment.

Conclusions

An experimental study of variable properties natural convection heat transfer in air was conducted on a large (3.02 m high by 2.95 m long), electrically heated, vertical surface. The wall temperature was varied from 60 to 520°C. The ambient temperature was approximately 20°C. Surface heat transfer coefficients were measured at 105 locations on the surface. Boundary layer mean temperature profiles were also taken. Turbulent natural convection heat transfer results show that variable properties effects on turbulent natural convection heat transfer can be correlated using the low-temperature difference correlation, if properties are evaluated at T_∞ and a small wall-to-ambient temperature ratio correction is added. This correlation is given by

$$\mathrm{Nu}_y = 0.098\,\mathrm{Gr}_y^{1/3}\left(\frac{T_w}{T_\infty}\right)^{-0.14}$$

The correlation fits the turbulent heat transfer data taken to within ±6 percent. The laminar variable properties heat transfer results show, as demonstrated by others, that the laminar variable properties effects for gases are small. The results also show that the location and extent of transition from laminar to turbulent flow are significantly affected by T_w for a fixed T_∞. As T_w/T_∞ changes from 1.1 to 1.75, the transition Gr decreases from about 7×10^9 to 3×10^8 when the properties in Gr are evaluated at a film temperature.

Boundary layer mean temperature profiles indicate that a "universal" temperature profile exists for turbulent natural convection. The "universal" profile for the inner region of the boundary layer for air, which includes the effects of variable properties on the profile location, is given by the following equations

$$\text{Viscous sublayer:} \quad \theta = 0.127(z/\eta_i')$$

$$\text{Buoyant sublayer:} \quad \theta = 1.36 - 1.42(z/\eta_i')^{-1/3}$$

The forms of the equations were taken from George and Capp. The constants in the equations, which are Pr-dependent, were determined from mean temperature profiles taken in air. The outer region of the "universal" temperature profile, based on temperature profiles from this work and temperature profiles taken in air and water from other works, has a logarithmic form.

Acknolwedgments

The authors would like to acknowledge the financial support of the Department of Energy, acting through Sandia National Laboratories, Livermore, California. In particular, we would like to thank Dr. Robert Gallagher for his attentive overview of the program and Dr. John Kraabel for his close and effective technical monitoring. This work was supported by the U.S. Department of Energy under Contract DE-AC04-76DP00789.

References

1 Siebers, D. L., "Experimental Mixed Convection Heat Transfer from a Large, Vertical Surface in a Horizontal Flow," Ph.D. thesis, Department of Mechanical Engineering, Stanford University, 1983; available as Sandia National Laboratories Report No., SAND83-8225, Sandia National Laboratories, Livermore, Calif., 1983.

2 Carey, V. P. , and Mollendorf, J. C., "Variable Viscosity Effects in Several Natural Convection Flows," *IJHT*, Vol. 23, 1980, pp. 95–108.

3 Shaukatullah, H., and Gebhart, B., "The Effect of Variable Properties on Laminar Natural Convection Boundary-Layer Flow Over a Vertical Isothermal Surface in Water," *Numerical Heat Transfer*, Vol. 2, 1979, pp. 215–232.

4 Hara, T., "Heat Transfer by Laminar Natural Convection About a Vertical Flat Plate with Large Temperature Difference," *Bull. JSME*, Vol. 1, No. 3, 1958, pp. 251–254.

5 Sparrow, E. M., and Gregg, J. L., "The Variable Fluid-Property Problem in Natural Convection," ASME *Transactions*, Vol. 80, 1958, pp. 869–886.

6 Pirovano, A., Viannay, S., and Jannot, M., "Convection Naturelle En Regime Turbulent Le Long D'Une Plaque Plane Verticale," Paper No. NC-1.8, 1970, *Proceedings of the 4th International Heat Transfer Conference*, Paris-Versailles, France, pp. 1–12.

7 Clausing, A. M., "Natural Convection Correlations for Vertical Surfaces Including Influences of Variable Properties," ASME JOURNAL OF HEAT TRANSFER, Vol. 105, 1983, pp. 138–143.

8 Siebers, D. L., "Natural Convection Heat Transfer From an External Receiver," Sandia National Laboratories Report No. SAND78-8276, Sandia National Laboratories, Livermore, Calif., 1978.

9 Siegel, R., and Howell, J. R., *Thermal Radiation Heat Transfer*, McGraw-Hill, New York, 1972, p. 116.

10 Edwards, D. K., and Catton, I., "Radiation Characteristics of Rough and Oxidized Metals," Advances in Thermophysical Properties at Extreme Temperatures and Pressures," edited by Serge Gratch, ASME, 1965, pp. 189–199.

11 Edwards, D. K., and deVolo, N. B., "Useful Approximations for Spectral and Total Emissivity of Smooth Bare Metals," *Advances in Thermophysical Properties at Extreme Temperatures and Pressures*, edited by Serge Gratch, ASME, 1965, pp. 174–188.

12 Kline, S. J., and McClintock, F. A., "Describing Uncertainties in Single Sample Experiments," *Mechanical Engineering*, Vol. 75, 1953, pp. 3–8.

13 Sparrow, E. M., and Gregg, J. L., "Laminar Free Convection from a Vertical Plate with Uniform Surface Heat Flux," ASME *Transactions*, Vol. 78, 1956, pp. 435–440.

14 Churchill, S. W., and Chu, H. H. S., "Correlating Equations for Laminar and Turbulent Natural Convection From a Vertical Plate," *IJHT*, Vol. 18, 1975, pp. 1323–1328.

15 Ostrach, S., "An Analysis of Laminar Free-Convection Flow and Heat Transfer About a Flat Plate Parallel to the Direction of the Generating Body Force," NACA TR 1111, 1953.

16 Kays, W. M., and Crawford, M. E., *Convective Heat and Mass Transfer*, (2d ed.), McGraw-Hill, New York, 1980.

17 McAdams, W. H., *Heat Transmission*, (3d ed.), McGraw-Hill, New York, 1954, p. 258.

18 Gebhart, B., *Heat Transfer*, (2d ed.), McGraw-Hill, New York, 1975.

19 Cheesewright, R., "Turbulent Natural Convection From a Vertical Plane Surface," ASME JOURNAL OF HEAT TRANSFER, Vol. 90, 1968, pp. 1–8.

20 Chokouhmand, H., "Convection Naturelle Dans L'eau Le Long D'Une Plaque Verticale Chaufee a Densite de Flux Constante," Ph.D. thesis, A L'Universite Et Marie Curie, Paris, Rapport CEA-R-4867, 1976.

21 Warner, C. Y., and Arpaci, V. S., "An Experimental Investigation of Turbulent Natural Convection in Air at Low Pressure Along a Vertical Heated Flat Plate," *IJHT*, Vol. 11, 1968, pp. 397–406.

22 Vliet, G. C., and Liu, C. K., "An Experimental Study of Turbulent Natural Convection Boundary Layers," ASME JOURNAL OF HEAT TRANSFER, Vol. 91, 1969, pp. 517–531.

23 Fugii, T., "Experimental Studies of Free Convection Heat Transfer," *Bulletin JSME*, Vol. 2, No. 8, 1959, pp. 555–558.

24 George, W. K., and Capp, S. P., "A Theory for Natural Convection Turbulent Boundary Layers Next to Heated Vertical Surfaces," *IJHT*, Vol. 22, 1979, pp. 813–826.

Z. Y. Zhong

K. T. Yang
Fellow ASME.

Department of Aerospace and
Mechanical Engineering,
University of Notre Dame,
Notre Dame, Ind. 46556

J. R. Lloyd
Department of Mechanical Engineering,
Michigan State University,
East Lansing, Mich. 48824
Mem. ASME

Variable Property Effects in Laminar Natural Convection in a Square Enclosure

A numerical, finite-difference study has been carried out to determine the effects of variable properties on the temperature and velocity fields and the heat transfer rate in a differentially heated, two-dimensional square enclosure. Calculations have been done for a Rayleigh number range up to 10^6, and temperature difference ratios $\theta_0 = (T_H - T_C)/T_C$ of 0.2, 0.5, 1.0, and 2.0, where T_H and T_C are the hot and cold wall temperatures, respectively. Specific issues that have been addressed are the limits of validity of the Boussinesq approximation, the proper use of a reference temperature, variable property correlation of the heat transfer rate, and the limits of conduction-dominated regions.

Introduction

Natural convection flow in enclosures and cavities has received considerable attention in the recent heat transfer literature, due largely to its direct relevance in a variety of applications, ranging from growth of crystals, solar collector performance, fire and smoke spread in rooms and compartments, to large-scale geophysical phenomena. Comprehensive reviews of this literature have been given by Ostrach [1] and Catton [2], and more recently again by Ostrach [3] in terms of the full range of aspect ratios of the cavities. Furthermore, there is also a growing interest in square or unity aspect ratio cavities. In such cases, the scaling problem associated with either small- or large-aspect ratios becomes less critical [3]; the simpler enclosure geometry permits studies including other effects such as internal baffles [4, 5] and thermal radiation [6], and the solutions provide validations of both small-aspect ratio and large-aspect ratio solutions as the aspect ratio approaches unity [7]. In addition, the square cavity geometry has been utilized as the benchmark case for evaluating accuracy of various numerical calculations [8, 9].

While the recent studies have contributed greatly to an understanding of the physical processes occurring in natural convection phenomena in enclosures, the basic issue of variable properties still remains unresolved. One good example is the almost universal adoption of the Boussinesq approximation in theoretical natural convection calculations. It is generally known that this approximation is valid for small temperature differences. However, when the calculated results are compared with experiments, an uncertainty always arises as to whether the temperature differences in the experiments are sufficiently small to validate the Boussinesq approximation used in the calculations. Definitive quantitative indications of the limit of the validity of Boussinesq approximation are still lacking, and there is a critical need to determine this limit [10], as also evidenced by the consensus in the recent Natural Convection Workshop [11]. Another somewhat related aspect of this variable property issue is the effect of variable transport properties such as specific heat, viscosity, and thermal conductivity on the heat transfer and fluid flow behavior in laminar natural convection inside cavities. In experimental studies, the common practice is to correlate the heat transfer results with constant properties evaluated at a reference temperature. Unfortunately, there is no consensus as to what this reference temperature should be, since the hot wall, cold wall, and average wall temperature have all been used [12, 3, 4]. This creates a severe difficulty in comparing results of different investigators.

Seveal variable-property analyses for enclosure flows are available in the literature. MacGregor and Emery [13] utilized the Boussinesq approximation together with variable viscosity and thermal conductivity in their study, which is particularly pertinent to liquids. Rubel and Landis [14] linearized the governing equations based on a small parameter of temperature difference ratio and obtained a first-order solution in a limited Rayleigh number range. Polezhaev [15] obtained a numerical solution of the full variable-property problem over a Grashof number range between 5×10^3 and 10^6, but at a specific hot wall temperature that is 1.5 times that of the cold wall temperature on the absolute scale. It is, however, interesting to note that the heat transfer results are given with densities evaluated at the hot wall temperature, while all other properties including the volumetric coefficient of expansion are determined at the cold wall temperature. The more recent numerical studies of Leonardi and Reizes [16, 17, 18] employed a stream function–vorticity analysis of a constant-volume enclosure. While the constant-volume enclosure calculation results in increasing pressures, it is primarily important only during the transient stages, and if the variable properties are handled accordingly, it should lead to little difficulty in interpreting the results. References [17] and [18] also addressed the reference temperature issue in correlating the heat transfer data. The authors of these studies devised a modified Rayleigh number, involving several reference temperatures, that was cumbersome to employ and difficult to interpret on a physical basis. To settle this issue of variable properties, including determining the limit of validity of the Boussinesq approximation in buoyant enclosure flows, it is necessary to carry out a systematic variable-property study over a range of temperature ratios and Rayleigh numbers. In the present study, an analysis based on numerical finite difference calculations has been carried out for a square enclosure problem utilizing air as the medium.

Mathematical Formulation and Numerical Computations

The standard, two-dimensional enclosure of a square cross section consists of two adiabatic, horizontal walls and two vertical, isothermal walls that are differentially heated (Fig. 1). The medium inside the enclosure is air. The governing differential equations for laminar natural convection under full variable property conditions in the standard tensor notation are given by

---

Contributed by the Heat Transfer Division and presented at the 21st National Heat Transfer Conference, Seattle, Washington, July 24–27, 1983.

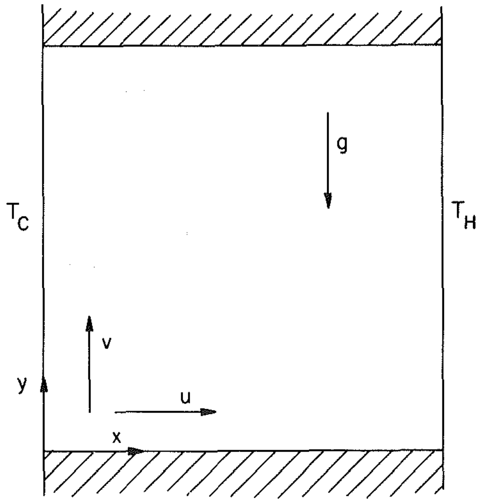

Fig. 1 Enclosure geometry

$$\rho_t+(\rho u_i)_{,i}=0 \tag{1}$$

$$(\rho u_i)_t+(\rho u_i u_j)_{,j}=-p_{,i}-\rho g_i+\sigma_{ij,j} \tag{2}$$

$$(\rho h)_t+(\rho u_i h)_{,j}=(kT_{,i})_{,i}+\mu\Phi-pu_{i,i} \tag{3}$$

where ρ is the fluid density, u_i the velocity vector, p the static pressure, g the gravitational acceleration, σ the stress tensor, h the fluid enthalpy, k the thermal conductivity, μ the dynamic viscosity, and Φ the dissipation function. Also the subscript t denotes derivatives with respect to time. Furthermore, the stress tensor, enthalpy, and dissipation function can be written as

$$\sigma_{ij}=\mu\Big((u_{i,j}+u_{j,i}-\frac{2}{3}\delta_{ij}u_{k,k}\Big) \tag{4}$$

$$h=\int_{T_R}^{T}c_p(T)dT \tag{5}$$

$$\Phi=2(u_{i,i}^2)+[u_{i,j}(1-\delta_{ij})]^2-\frac{2}{3}(u_{i,i})^2 \tag{6}$$

where c_p is the specific heat, δ_{ij} the Kronecker's delta, and T_R a constant reference temperature. In order to close the foregoing equations, additional relations are required. The density of air may be adequately represented in the temperature range of 300–900 K by the perfect gas law

$$p=\rho RT \tag{7}$$

while the following transport properties as given by Hilsenrath et al. [16] are used in the present study

$$\mu=\frac{14.58\times10^{-5}T^{3/2}}{110.4+T}\ \text{kg/s-m} \tag{8}$$

$$k=\frac{2.6482\times10^{-6}T^{1/2}}{1+245.4\times10^{-(12/T)}/T}\ \text{W/m-K} \tag{9}$$

$$c_p=0.2383-0.7915\times10^{-5}T+0.4834\times10^{-7}T^2\,\text{kJ/kg-K} \tag{10}$$

It is noted that in equations (1), (4), and (6) the repeated indices convention is utilized. Furthermore, it is desirable to eliminate the enthalpy as a dependent variable by introducing a mean specific heat c_{pm} such that

$$h=c_{pm}(T-T_R)\quad\text{and}\quad c_{pm}=\frac{1}{T-T_R}\int_{T_R}^{T}c_p dT \tag{11}$$

As a result, the energy equation (3) can be transformed into a more convenient form:

$$(\rho c_{pm}T)_t+(\rho u_i c_{pm}T)_{,i}=(kT_{,i})_{,i}+\mu\Phi-pu_{i,i} \tag{12}$$

Also the momentum equation (2) can be rewritten to incorporate a driving force based on a difference between the local fluid density and the fluid density corresponding to the fluid hydrostatic equilibrium condition, which is given by

$$-\rho_e g_i-p_{e,i}=0 \tag{13}$$

Finally, the boundary conditions (Figure 1) can be simply stated as

$$\begin{array}{llll} x=0 & u=0 & v=0 & T=T_C \\ x=H & u=0 & v=0 & T=T_H \\ y=0 & u=0 & v=0 & \dfrac{\partial T}{\partial y}=0 \\ y=H & u=0 & v=0 & \dfrac{\partial T}{\partial y}=0 \end{array} \tag{14}$$

It is customary that the governing equations and boundary conditions are nondimensional before numerical calculations are carried out. In the present study, all length quantities are normalized with respect to H, the cavity dimension, and the velocities to a constant reference velocity U_0, which is arbitrarily chosen. This velocity scaling is done deliberately in view of the fact that natural convection enclosure flow is a multiple-scale problem in which various scales operate in different regions in the flow, as also discussed recently by Ostrach [3]. Pressure p is normalized by $\rho_R U_0^2$, and temperature by T_R. Finally all transport properties are nondimensionalized by their own reference values based on T_R, which is consistently taken to be the cold wall temperature T_C. As a result, the overall rate of heat transfer represented by a Nusselt number Nu is defined by

$$\text{Nu}=\frac{-\int_0^H\left(k\dfrac{\partial T}{\partial x}\right)_w dy}{k_C(T_H-T_C)} \tag{15}$$

Nomenclature

c_p = specific heat
g = gravitational acceleration
H = enclosure height or width
h = enthalpy
k = thermal conductivity
Nu = Nusselt number
p = static pressure
R = gas constant
Ra = Rayleigh number
T = temperature
U_o = arbitrary reference velocity
u_i = general velocity components
u,v = velocity components in the x- and y-directions, respectively
x,y = enclosure coordinates
α = thermal diffusivity
δ_{ij} = Kronecker's delta
θ_o = $(T_H-T_C)/T_C$
μ = dynamic viscosity
ν = kinematic viscosity
ρ = density
σ = stress tensor
Θ = dissipation function

Subscripts

C = cold wall conditions
e = hydrostatic equilibrium conditions
H = hot wall conditions
i,j,k = tensor indices
m = average conditions
R = reference temperature conditions
t = time derivatives
w = cold or hot wall conditions
∞ = free-stream conditions

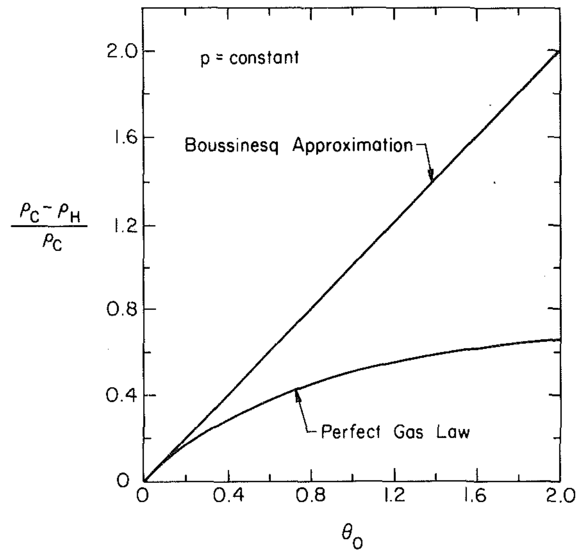

Fig. 2 Driving force for natural convection

where the subscript w, which refers to either the hot wall or the cold wall conditions. The resulting Nusselt number can be expressed as a function of a Rayleigh number Ra and a temperature difference ratio θ_0 defined respectively by

$$\mathrm{Ra} = \frac{\rho_C H^3 (T_H - T_C)}{\alpha_C v_C T_C} \quad \theta_o = \frac{T_H - T_C}{T_C} \tag{16}$$

where α and ν are the fluid thermal diffusivity and kinematic viscosity, respectively.

The governing differential equations, after being nondimensionalized, have been solved numerically by an upwind, finite difference, semi-implicit scheme based on primitive variables and staggered cells for the velocity components, similar to that used in our previous studies for square enclosures with internal baffles [5] and with surface and gaseous radiation [6]. Details of the numerical procedure and the guiding stability criteria will not be repeated here. However, it is perhaps pertinent to mention several validation studies of this numerical procedure based on a uniform 36 × 36 mesh in the calculation domain. It has found that calculation errors increase both with increasing Ra and θ_o. However, even at Ra = 10^6 and θ_o = 2.0, the maximum net mass flux along x, which should be zero in the exact solution, is only about 2 percent of the entire circulating mass flux in the cavity, and the maximum deviation of the net energy flux along x, which consists of both conduction and convection components, from the mean wall heat flux is about 5 percent. Excellent agreement has been obtained between the present result based on the Boussinesq approximation and the "best" data from the recent Venice competition [8], deviations only occuring in the third digits of the Nusselt number comparisons in the Rayleigh number range from 10^3 to 10^6. Furthermore, results of the present calculations for sufficiently low Rayleigh numbers do approach those of the one-dimensional conduction solution under variable thermal conductivity conditions. Finally, the calculation procedure has also been modified to accommodate the constant volume enclosure problem and applied to a specific case calculated by Leonardi and Reizes [17]. Despite the entirely different calculation approaches used for this case, the agreement at a Rayleigh number of 10^4 is quite satisfactory, and there is an indication that our present calculation may be more accurate based on the net energy flux considerations along x. The readers are referred to [20] for details of these validation studies.

Detailed numerical calculations in the present study have been carried out over the Rayleigh number range up to 10^6 and a θ_o range from 0.2 to 2.0. The reference and cold wall temperature is taken to be at 288 K. Results are presented in the following sections in terms of the Boussinesq approximation limits, the reference temperature issue, and the variable property effects.

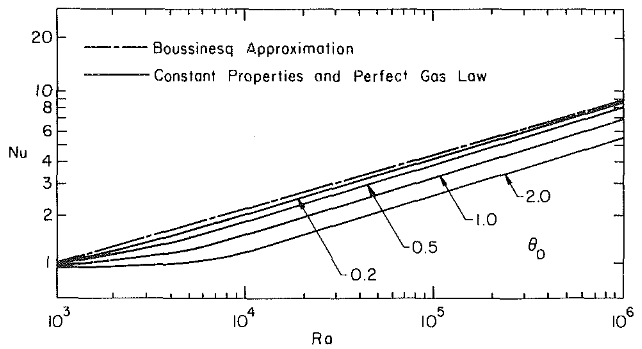

Fig. 3 Nusselt numbers for variable density and constant transport properties

Limits of Boussinesq Approximation

The easiest way to consider the validity limits of the Boussinesq approximation is to examine the driving force under both perfect gas and Boussinesq approximation conditions. For the present enclosure flow problem, the driving force may be represented approximately by the quantity $(\rho_C - \rho_H)/\rho_C$, which, under the same pressure conditions, can be shown to be simply θ_o for the Boussinesq approximation case and $\theta_o/(1+\theta_o)$ for the full compressibility or perfect gas condition. As an alternative and less explicit discussion of this point, [17] plots the density as a function of temperature and shows how the perfect gas law density differs from that calculated in the Boussinesq calculation under the constant pressure assumption. The relations developed in the present study are plotted in Fig. 2. It is seen that the driving force curves both have the same slope at $\theta_o = 0$ and that the Boussinesq approximation is always higher throughout the θ_o range. Also the Boussinesq approximation curve increases without bound, while that for the perfect gas curve has an asymptotic value of 1.0, indicating that the driving force remains finite regardless how large θ_o is. Based either on Fig. 2 alone or on the discussion in [17], it is seen that the Boussinesq approximation should be adequate for $\theta_o \leq 0.10$. This, however, must be substantiated by more detailed calculations.

To settle this issue, numerical finite difference calculations have been carried out for the case of constant properties (based on T_c), except density, which is evaluated by the perfect gas law, for a range of Ra up to 10^6 and θ_o of 0.2, 0.5, 1.0, and 2.0. The results for the overall Nusselt number, taken to be the average of those based on hot wall and cold wall calculations, are shown in Fig. 3. Data for the Boussinesq approximation case are taken from [8]. Based on the driving force considerations, it is not surprising to see that the Nusselt number is always smaller than that for the Boussinesq approximation case, the deviations being larger for increasing values of θ_o. It can also be seen that the Boussinesq approximation still yields adequate heat transfer results even at $\theta_o = 0.2$, indicating that its validity is certainly justifiable for $\theta_o \leq 0.10$, especially in view of the degree of scattering of experimental data now existing in the literature [4]. On the other hand, there are larger differences in the flow field, as shown in Fig. 4 for $\theta_o = 0.2$ and Ra = 10^6, in which the data for the Boussinesq approximation are again those from [8]. This behavior, however, is expected in view of the fact that in any natural convection phenomenon, the flow field is always sensitive to small temperature differences. It is also of interest to note that the vertical velocity components for the perfect

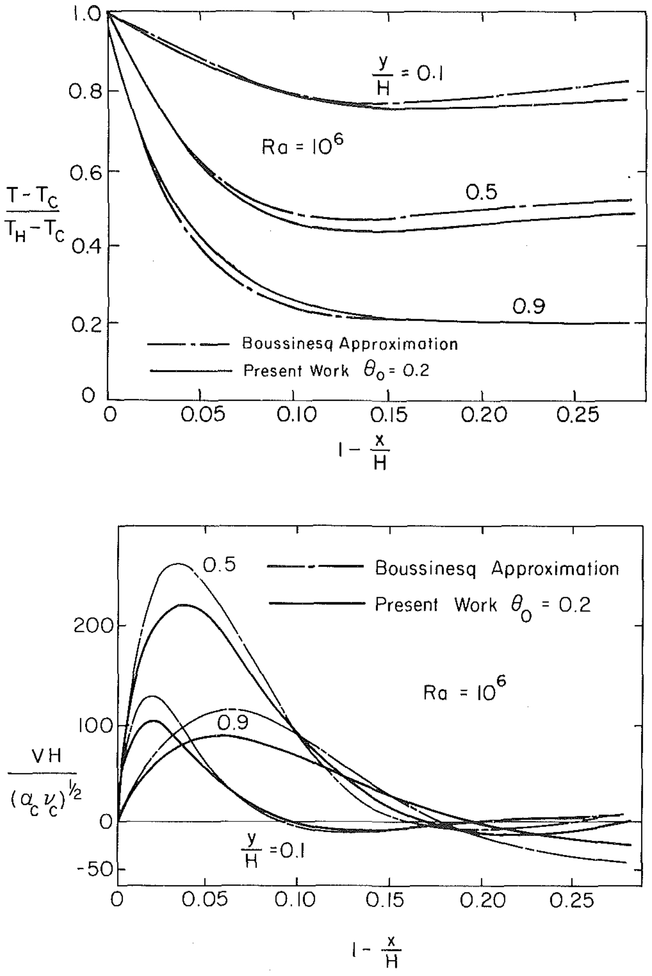

Fig. 4 Effects of variable density on the temperature and flow fields for θ_o = 0.2 and Ra = 10^6

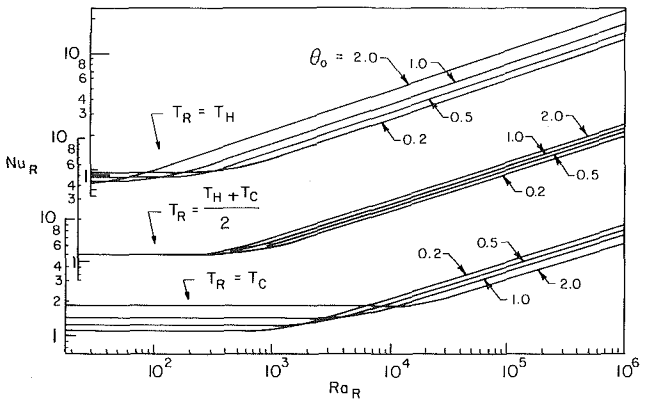

Fig. 5 Nusselt number correlations with different reference temperature

gas case close to the hot wall are always smaller than those for the Boussinesq approximation case at all levels in the cavity.

On the basis of the present study, it may be concluded that the Boussinesq approximation for the enclosure flow problem is certainly valid when $\theta_o \leq 0.10$. Furthermore, even at θ_o = 0.2 and Ra = 10^6, the Boussinesq approximation still predicts the correct Nusselt number within 2 percent, even though the vertical velocity components may be overestimated by as much as 20 percent by the Boussinesq approximation. The present results also allow us to develop a useful correlation for the determination of a limiting value of θ_o under which the heat transfer data can be predicted adequately by the Boussinesq approximation to within 5 percent, and this correlation is given by

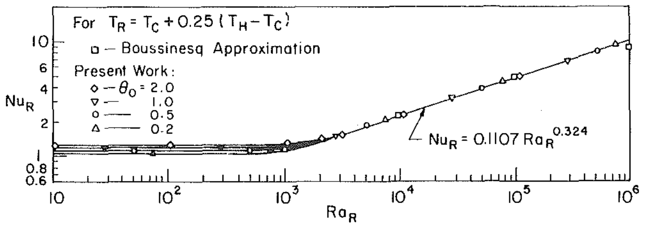

Fig. 6 Nusselt number correlation with $T_R = T_C + 0.25(T_H - T_C)$

$$\theta_{o,\text{limit}} = 0.0244\,\text{Ra}^{0.243} \tag{17}$$

The Reference Temperature Issue

The full variable property equations including the use of perfect gas law for the density have been solved numerically in the present study for Ra numbers up to 10^6 and θ_o values of 0.2, 0.5, 1.0, and 2.0. The results relative to the reference temperature issue are presented first, which are then followed by the general variable property effects to be presented in the next section. The reference temperature issue is always of major concern to an experimentalist in presenting the correlations of experimental data. The use of a reference temperature allows him or her to present the data in the simplest correlated form. However, the difficulty is that there is usually no rational basis to choose a proper reference temperature. In the case of the natural convection enclosure flow problem, the hot wall temperature, the cold wall temperature, and the average of the wall temperatures have all been used as the reference temperature, and there is no clear consensus in the literature at this time. The variable property results of the present analysis covering a substantial temperature difference range provide a good basis to determine whether the use of a reference temperature is even feasible for the enclosure flow problem.

Figure 5 shows three sets of Nusselt number data using T_H, T_C, and $(T_H + T_C)/2$ as the reference temperatures for evaluating all properties in the correlations. It is evident that none of the three correlates the heat transfer data well in the full range of θ_o calculated. However, it may be noticed that the trends of θ_o effects are completely reversed in going from the case of $T_R = T_H$ to the case of $T_R = T_C$, and that the case of $T_R = (T_H + T_C)/2$ represents the best among the three cases. This immediately suggests that a specific reference temperature may be found that will collapse all the θ_o curves into a single curve. Such an excercise has been successfully carried out and the result is shown in Fig. 6 for a reference temperature T_R given by

$$T_R = T_C + 0.25(T_H - T_C) \tag{18}$$

The correlated Nusselt number can be written as

$$\text{Nu}_R = 0.1107\,\text{Ra}_R^{0.324} \tag{19}$$

in the convection-dominated region, $3\times10^3 \leq \text{Ra}_R \leq 10^6$. This correlation is of considerable value to the experimentalists working in this field.

The most interesting part of this result is that this reference temperature is closer to the cold wall temperature, and it is very different from that for the vertical plate boundary layer phenomenon as given by Sparrow and Gregg [21]

$$T_R = T_\infty + 0.62(T_w - T_\infty) \tag{20}$$

where T_∞ is the undisturbed temperature outside the boundary layer. The primary reason for this difference is that in the boundary layer case the entrainment from the undisturbed field is not substantial, and the field inside the boundary layer is essentially heated by the hot wall, resulting

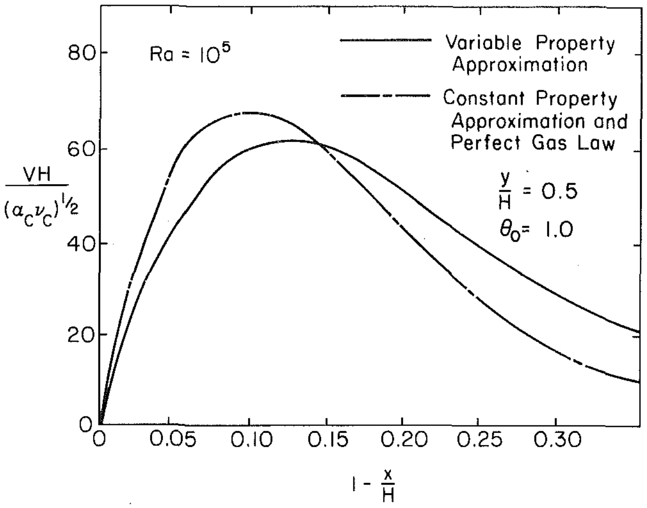

Fig. 7 Effect of variable properties on the flow field for θ_o = 1.0 and $Ra = 10^5$

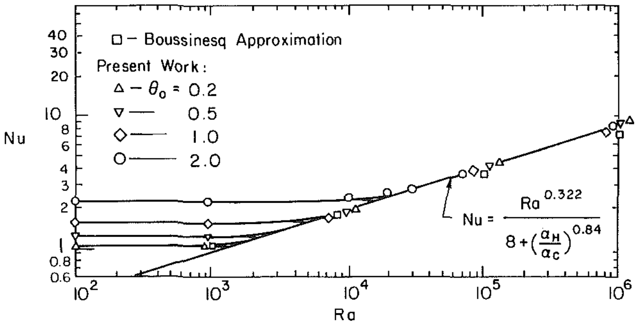

Fig. 8 Variable-property Nusselt number correlation

in a reference temperature close to the wall temperature. On the other hand, the circulation inside the cavity in the present enclosure flow problem constantly feeds a substantial amount of cold fluid into the hot wall region, thus reducing the reference temperature. The variable property effects evidentally also play an important role here. Figure 6 also shows that the Boussinesq approximation results do deviate from this reference temperature correlation at high Rayleigh numbers, but not by very much. This gives an indication of the validity of the reference temperature in equation (18) for the entire range of Θ_o up to θ_o = 2.0. While the reference temperature is a good concept for data correlation, it is somewhat artifical in that there is no assurance that the same reference temperature is valid for all enclosure flow situations.

Variable Property Effects in Natural Convection Enclosure Flows

The same results of the full variable-property calculations can now be used to determine the effects of variable properties on the velocity and temperature fluids in the enclosure flow problem. Figure 7 shows a typical comparison of the vertical velocity profiles between the constant property and variable property cases at the midheight of the cavity away from the hot wall at Ra = 10^5 and θ_o = 1.0. It is seen that the effect of variable property is to reduce the velocity in the wall region, but to increase it in the core region. Also the maximum vertical velocity is reduced. These behaviors are accentuated for larger θ_o values, and essentially are due to the higher viscocity values at higher temperature levels, which tend to slow down the velocities in the hot wall region. The variable properties effect the temperature field in two opposing ways: the reduced velocity in the hot wall region tends to reduce the heat transfer at the hot wall, but on the other hand, the increased thermal conductivity tends to increase it. The dominating effect of the increased thermal conductivity also manifests itself in that the start of the convection-dominated regime is delayed to higher Ra for the variable property case. This becomes more pronounced when θ_o is increased. These results are consistent with observations made in [16, 17, 18].

There is also an alternative way in correlating the variable property results as shown in Fig. 9 without using the artificial reference temperature given in equation (18). The correlation for the convection region may be given by

$$\mathrm{Nu} = \frac{\mathrm{Ra}^{0.322}}{8 + \left(\frac{\alpha_H}{\alpha_C}\right)^{0.84}} \qquad \mathrm{Ra}_{\mathrm{limit}} \leq \mathrm{Ra} \leq 10^6 \tag{21}$$

where $\mathrm{Ra}_{\mathrm{limit}}$ is the limiting Ra number below which conduction dominates. This is given by

$$\mathrm{Ra}_{\mathrm{limit}} = 780(1 + \theta_o)^{2.7} \tag{22}$$

Finally, it is seen in Fig. 8 that the conduction regions for different θ_o values are dominated by one-dimensional conduction with variable thermal conductivities. The transition regions between conduction-dominated and convection-dominated regions for all θ_o are relatively small, and therefore no significant error would occur if these transition regions are ignored.

Concluding Remarks

In the present study, the full variable-property governing differential equations are solved by a numerical finite difference scheme to determine the variable property effects on the heat transfer and flow behavior for natural convection flow in a square enclosure for a range of Rayleigh numbers and wall temperature differences. The following conclusions can be made:

1 The Boussinesq approximation is generally valid for $\theta_o \leq 0.1$. Up to a θ_o value of 0.2, the Boussinesq approximation still predicts the overall heat transfer rate adequately, but overpredicts the maximum vertical velocity as much as 20 percent.

2 It is possible to correlate the heat transfer data for the full range of θ_o considered by using a specific reference temperature, which is closer to the cold wall temperature. This behavior is very different from that of the vertical plate boundary layer phenomenon.

3 The variable property effects slow down the vertical velocities in the hot wall region, but increase these velocities in the core. The effect of increased thermal conductivity in the hot wall region more than offsets the effect of reduced vertical velocities to result in increased rate of heat transfer for given θ_o and Ra.

4 The full variable property results can be correlated by introducing a ratio of thermal diffusivities into the usual Nu-Ra correlation for the full θ_o range. This correlation may be more preferable in view of the fact that no artificial reference temperature is used.

5 For the full θ_o range considered, the transition regions from the conduction-dominated region to the convection-dominated region are all very limited in extent, and can be ignored without significant errors.

It is important to note that the present study treats the pure laminar natural convection phenomena. In the realistic physical cases, thermal radiation effects may become significant for elevated θ_o values, as already discussed in the study of square enclosures with internal partitions [5]. A companion study is now underway to treat the corresponding natural convection-radiation interaction problem for tilted square enclosures with variable properties.

Acknowledgement

The authors gratefully acknowledge support for this study by the National Science Foundation under grant CME-79-18682 and by the University of Notre Dame Computing Center. The authors also wish to thank Dr. A. M. Kanury for his valuable discussions.

References

1 Ostrach, S., "Natural Convection in Enclosures," *Advances in Heat Transfer*, edited by J. P. Hartnett and T. F. Irvine, Vol. 8, 1972, pp. 161-227.

2 Catton, I., "Natural Convection in Enclosures," *Proceedings of the Sixth International Heat Transfer Conference*, Vol. 6, 1978, pp. 13-31.

3 Ostrach, S., "Natural Convection Heat Transfer in Cavities and Cells," *Proceedings of the Seventh International Heat Transfer Conference*, Vol. 1, 1982, pp. 365-379.

4 Bajorek, S. M., and Lloyd, J. R., "Experimental Investigation of Natural Convection in Partitioned Enclosures," ASME JOURNAL OF HEAT TRANSFER, Vol. 104, No. 3, 1982, pp. 527-532.

5 Chang, L. C., Lloyd, J. R., and Yang, K. T., "A Finite Difference Study of Natural Convection in Complex Enclosures," *Proceedings of the Seventh International Heat Transfer Conference*, Vol. 2, 1982, pp. 183-188.

6 Chang, L. C., Yang, K. T., and Lloyd, J. R., "Radiation-Convection Interaction in Two-Dimensional Complex Enclosures," ASME JOURNAL OF HEAT TRANSFER, Vol. 105, No. 1, 1983, pp. 89-95.

7 Bejan, A., "A Synthesis of Analytical Results for Natural Convection Heat Transfer Across Rectangular Enclosures," *International Journal of Heat and Mass Transfer*, Vol. 23, No. 5, 1980, pp. 723-726.

8 de Vahl Davis, G., and Jones, I. P., "Natural Convection in a Square Cavity: A Comparison Exercise," Report 1982/FMT/3, ISSN 0157-5104, School of Mechanical and Industrial Engineering, The University of New South Wales, 1982.

9 Quon, C., "Effects of Grid Distribution on the Computation of High Rayleigh Number Convection in a Differentially Heated Cavity," *Numerical Properties and Methodologies in Heat Transfer*, edited by T. M. Shih, Hemisphere Publishing Corporation, New York, 1983, pp. 261-282.

10 Gray, D. D., and Giorgini,A., "The Validity of the Boussinesq Approximation for Liquids and Gases," *International Journal of Heat and Mass Transfer*, Vol. 19, 1976, pp. 545-551.

11 Yang, K. T., and Lloyd, J. R., (eds), *Proceedings of Workshop on Natural Convection*, National Science Foundaton and University of Notre Dame, 1983.

12 Eckert, E. R. G., and Carlson, W. O., "Natural Convection in an Air Layer Enclosed Between Two Vertical Plates with Different Temperatures," *International Journal of Heat and Mass Transfer*, Vol. 2, 1961, pp. 106-120.

13 MacGregor, R. K., and Emery, A. F., "Free Convection Through Vertical Plane Layers-Moderate and High Prandtl Number Fluids," ASME JOURNAL OF HEAT TRANSFER, Vol. 91, 1969, pp. 391-403.

14 Rubel, A. R., and Landis, F., "Laminar Natural Convection in a Rectangular Enclosure with Moderately Large Temperature Differences," *Proceedings of the Fourth International Heat Transfer Conference*, Paper No. NC 2.10, 1970, pp. 1-12.

15 Polezhaev, V. I., "Numerical Solution of a System of Two-Dimensional Unsteady Navier-Stokes Equations for a Compressible Gas in a Closed Region," *Fluid Dynamics*, Vol. 2, 1967, pp. 70-74.

16 Leonardi, E., and Reizes, J. A., "Natural Convection in Compressible Fluids with Variable Properties," *Numerical Methods in Thermal Problems*, Vol. 1, edited by R. W. Lewis and K. Morgan, Pineridge press, Swansea, 1979, pp. 297-306.

17 Leonardi, E., and Reizes, J. A., "Convective Flows in Closed Cavities with Variable Fluid Properties," *Numerical Methods in Heat Transfer*, edited by R. W. Lewis, K. Morgan, and O. C. Zinkiewicz, John Wiley & Sons, New York, 1981, pp. 387-412.

18 Leonardi, E., and Reizes, J. A., "Natural Convection Heat Transfer for Variable Property Fluids Using the Boussinesq Approximation," *Numerical Methods in Thermal Problems*, Vol. 2, edited by R. W. Lewis, K. Morgan, and B. A. Schregler, Pineridge Press, Swansea, 1981, pp. 978-989.

19 Hilsenrath, J., et al., *Tables of Thermodynamic and Transport Properties of Air, Argon, Carbon Dioxide, Carbon Monoxide, Hydrogen, Nitrogen, Oxygen, and Steam*, Pergamon Press, New York, 1960.

20 Zhong, Z. Y., "Variable-Property Natural Convection and Its Interaction with Thermal Radiation in Tilted Square Enclosures," Ph.D. thesis, University of Notre Dame, 1983.

21 Sparrow, E. M., and Gregg, J. L., "The Variable Fluid-Property Problem in Free Convection," ASME *Transactions*, Vol. 80, 1958, pp. 879-886.

D. M. Kim

R. Viskanta
Fellow ASME

Heat Transfer Laboratory,
School of Mechanical
Engineering,
Purdue University,
West Lafayette, Ind. 47907

Effect of Wall Heat Conduction on Natural Convection Heat Transfer in a Square Enclosure

This paper presents numerical and experimental results for buoyancy-induced flow in a two-dimensional, fluid-filled enclosure. Rectangular cavities formed by finite conductance walls of different void fractions and aspect ratios are considered. Parametric heat transfer calculations have been performed and results are presented and discussed. Local and average Nusselt numbers along the cavity walls are reported for a range of parameters of physical interest. The temperatures in the walls were measured with thermocouples, and the temperature distributions in the air-filled cavity were determined using a Mach-Zehnder interferometer. Good agreement has been obtained between the measured and the predicted temperatures in both the solid wall and in the fluid using the mathematical model. Wall heat conduction reduces the average temperature differences across the cavity, partially stabilizes the flow, and decreases natural convection heat transfer.

Introduction

Natural convection heat transfer in cavities has been of considerable research interest. However, most of the studies have neglected the interaction between convection in the fluid filled cavity and conduction in the walls surrounding the cavity by using idealized boundary conditions such as those corresponding to prescribed heat flux or temperatures at the heated (cooled) walls, and adiabatic or perfectly conducting on the connecting walls. This type of treatment is completely justified in many problems. However, there are some physical situations where heat conduction in the material forming the enclosure walls must also be considered. Examples of such situations include cellular and porous materials as well as cellular structures (walls, cement blocks, cellular cavities, sandwich structures, etc.) [1].

Numerous experimental and numerical studies dealing with natural convection in enclosures have been reported in the literature. Excellent reviews are available [2–4] and there is no need to repeat them. By assuming that walls are either isothermal or have a constant heat flux boundary condition imposed on them, most of the literature on natural convection heat transfer in cells and cavities avoids an accounting for wall heat conduction and radiation exchange between the walls. In the case of an adiabatic wall, a linearly varying wall temperature has been imposed. Heat conduction in an insulated wall (on the outside) causes the temperature distribution to deviate from that of the truly adiabatic case, and thus precludes the possibility of obtaining experimentally a truly adiabatic boundary condition in some fluids such as air. In all enclosures, thermal boundary conditions (wall conductance) can lead to a stabilizing or destabilizing of the flow and corresponding large changes in the heat transfer coefficient. Natural convection in the cavity can also induce conduction heat transfer in the surrounding walls [5].

It has been recognized [4, 5] that thermal boundary conditions (wall conductance) on all the enclosure boundaries have an important bearing on natural convection heat transfer in the cavity. The effect of confining, rigid boundaries on the initiation of natural convection in a cavity has also been recognized for some time [6]. However, the problems have received relatively little theoretical [7–9] investigation. Natural convection in a two-dimensional enclosure surrounded by one-dimensional conducting and radiating walls has been analyzed numerically [7]. The effects of cell wall thickness and thermal conductivity on natural convection heat transfer within inclined rectangular cavities have been examined in order to gain an understanding of the efficiency of cellular structures in reducing convection heat losses in flat-plate solar collectors [8, 9]. Natural convection in a rectangular enclosure subjected to comparable horizontal and vertical temperature differences has been analyzed [10], and the effects of finite wall heat conductance on natural convection in a two-dimensional rectangular cavity within a cellular structure has been studied by solving numerically the model equations [10]. No experimental studies of the problem considered in the paper have been identified in the open literature, but two recent, remotely related experiments which are concerned with finite wall conductance effects on natural convection heat transfer in cavities should be mentioned [9, 12].

The intent of this paper is to report on a computational and experimental study of natural convection in a two-dimensional rectangular enclosure having finite wall conductances. A mathematical model is formulated, and a numerical procedure has been developed to solve the model equations. Parametric studies have been conducted and the numerical results are reported in tabular and graphical form for a range of parameters of physical interest. The measured temperatures in the walls and in the cavity are compared with the numerical calculations for the purpose of validating the model and gaining improved understanding of thermal boundary conditions on heat transfer in the solid-cavity system.

Analysis

Physical Model and Assumptions. The physical model and coordinate system of the problem are illustrated schematically in Fig. 1. The two-dimensional, rectangular cavity is formed by walls having finite conductance. The vertical and the horizontal walls can be of different thickness but are assumed to be of the same material. Initially, the walls of the enclosure and the fluid inside the cavity are assumed to be at a constant uniform temperature, and the fluid is taken to be stagnant. The horizontal walls forming the enclosure are assumed to be insulated on the outside. At time $t>0$, constant but different temperatures are suddenly imposed on the outside of the two vertical walls and maintained until steady-state conditions are reached.

Contributed by the Heat Transfer Division for publication in the JOURNAL OF HEAT TRANSFER. Manuscript received by the Heat Transfer Division September 16, 1983.

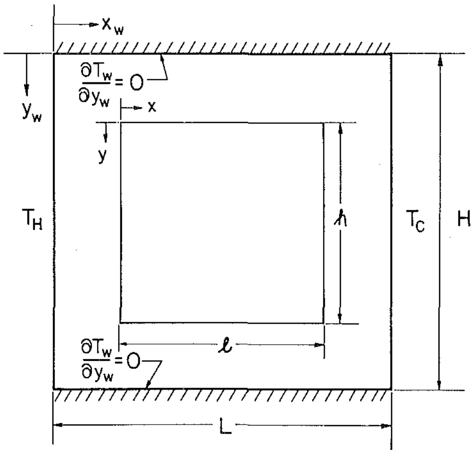

Fig. 1 Physical model of the system

It is assumed in the analysis that the thermophysical properties of the walls and of the fluid are independent of temperature, and the flow is laminar. The fluid is Newtonian, incompressible, and the Boussinesq approximation is valid. The fluid motion and heat transfer in the cavity are assumed to be two-dimensional. Radiation heat exchange between the walls is neglected in comparison to convection, and the fluid is assumed to be radiatively nonparticipating. A detailed analysis that accounts for radiation interchange among cavity walls has been recently described [14].

Model Equations. For the sake of brevity, the conservation equations are written in dimensionless form from the start.

The transient heat conduction equation in the wall is

$$\frac{\partial \theta_w}{\partial \tau}=\alpha^*\left(\frac{l}{L}\right)^2\left[\frac{\partial^2\theta_w}{\partial \xi_w^2}+\left(\frac{L}{H}\right)^2\frac{\partial^2\theta_w}{\partial \eta_w^2}\right] \tag{1}$$

The conservation equations of mass, momentum and energy for the fluid can be expressed in standard form by introducing the concepts of stream function and vorticity. The dimensionless vorticity, energy, and stream function equations become, respectively,

$$\frac{\partial\Omega}{\partial\tau}+\left[\frac{\partial(U\Omega)}{\partial\xi}+\frac{1}{A}\frac{\partial(V\Omega)}{\partial\eta}\right]=$$

$$\Pr\left(\frac{\partial^2\Omega}{\partial\xi^2}+\frac{1}{A^2}\frac{\partial^2\Omega}{\partial\eta^2}\right)+\mathrm{Ra}^*\Pr\frac{\partial\theta}{\partial\xi} \tag{2}$$

$$\frac{\partial\theta}{\partial\tau}+\frac{\partial(U\theta)}{\partial\xi}+\frac{1}{A}\frac{\partial(V\theta)}{\partial\eta}=\frac{\partial^2\theta}{\partial\xi^2}+\frac{1}{A^2}\frac{\partial^2\theta}{\partial\eta^2} \tag{3}$$

$$\Omega=-\left[\frac{\partial^2\Psi}{\partial\xi^2}+\frac{1}{A^2}\frac{\partial^2\Psi}{\partial\eta^2}\right] \tag{4}$$

The temperature boundary conditions on the outside walls of the enclosure are

$$\theta_w(0,\eta_w,\tau_w)=\theta_H \tag{5}$$

$$\theta_w(1,\eta_w,\tau_w)=\theta_C \tag{6}$$

and

$$\left.\frac{\partial\theta_w}{\partial\eta_w}\right|_{\eta_w=0}=\left.\frac{\partial\theta_w}{\partial\eta_w}\right|_{\eta_w=l}=0 \tag{7}$$

The temperature boundary conditions at the interior walls (solid–fluid interface) of the enclosure are

$$\theta_w(\xi,\eta,\tau)_w=\theta(\xi,\eta,\tau)_w \tag{8}$$

and

$$\left.\frac{\partial\theta}{\partial\zeta}\right|_w=k^*\left.\frac{\partial\theta_w}{\partial\zeta}\right|_w \tag{9}$$

The boundary conditions on the velocity at the surface bounding the cavity are

$$U(\xi,\eta,\tau)_w=\Psi(\xi,\eta,\tau)_w=\frac{\partial\Psi}{\partial\eta}(\xi,\eta,\tau)_w=0 \tag{10}$$

$$V(\xi,\eta,\tau)_w=\Psi(\xi,\eta,\tau)_w=\frac{\partial\Psi}{\partial\xi}(\xi,\eta,\tau)_w=0 \tag{11}$$

The initial temperature and velocity boundary conditions are taken as

Nomenclature

A = aspect ratio of cavity, h/l, see Fig. 1
Fo = Fourier number, $\alpha t/l^2$
H = height of solid wall, seee Fig. 1
h = local heat transfer coefficient, $-k\left.\frac{\partial T}{\partial n}\right|_w/(T-T_{\mathrm{ref}})$
h = height of cavity, see Fig. 1
k = thermal conductivity
k^* = thermal conductivity ratio, k_w/k
L = width of solid wall, see Fig. 1
l = width of cavity, see Fig. 1
Nu = local Nusselt number, hl/k
$\overline{\mathrm{Nu}}$ = average Nusselt number
Pr = Prandtl number, ν/α
Q^* = dimensionless, heat transfer rate, $\int_0^H q(x)dx/Hk_w(T_H-T_C)$
Ra = Rayleigh number, $g\beta l^3(T_H-T_C)/\nu\alpha$
Ra* = Rayleigh number, $g\beta l^4(T_H-T_C)/\nu\alpha L$
T = temperature
t = time
U = dimensionless velocity in the x-direction, u/U_o
U_0 = reference velocity, α/l
u = fluid velocity in the x-direction
V = dimensionless velocity in the y-direction, v/U_o
v = fluid velocity in the y-direction
x = coordinate, see Fig. 1
y = coordinate, see Fig. 1
α = thermal diffusivity
α^* = thermal diffusivity ratio, α_w/α
β = thermal expansion coefficient
ζ = dimensionless coordinate, ξ or η
η = dimensionless y-coordinate, y/h
η_w = dimensionless y-coordinate, y/H
θ = dimensionless temperature, $(T-T_C)/(T_H-T_C)$
ξ = dimensionless x-coordinate, x/l
ξ_w = dimensionless x-coordinate, x/L
τ = dimensionless time (Fo), $\alpha t/l^2$
ϕ = void fraction, hl/HL
Ψ = dimensionless stream function, $\psi l/U_0$
ψ = stream function
Ω = dimensionless vorticity, $\omega l/U_0$
ω = vorticity

Subscripts

b = bottom of cavity
C = cold side of the wall
c = cold side of cavity
H = hot side of the wall
h = hot side of the cavity
i = inside to the cavity
t = top of cavity
w = solid wall

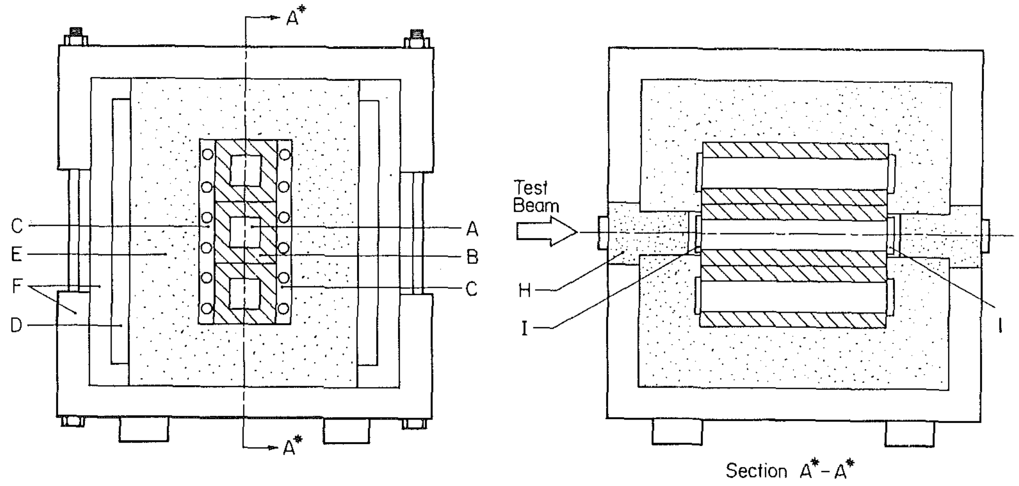

Fig. 2 Schematic diagram of the test apparatus: A – test region (air); B – test region (solid); C – heat exchanger; D – air gap; E – insulation; F – flanges; G – optical quality glass windows, and H – removable insulation

$$\theta_w(\xi,\eta,0)=\theta(\xi,\eta,0)=\theta_i(\xi,\eta,0) \tag{12}$$

$$U(\xi,\eta,0)=V(\xi,\eta,0)=0 \tag{13}$$

$$\Omega(\xi,\eta,0)=0 \tag{14}$$

We note that in addition to such customary dimensionless parameters as the Rayleigh number (Ra), the Prandtl number (Pr) and the aspect ratio of the cavity ($A=h/l$), the following dimensionless groups arise: (*i*) the thermal diffusivity ratio α^*, (*ii*) the thermal conductivity ratio k^*, (*iii*) the aspect ratio H/L of the wall, and (*iv*) the void fraction ϕ. Even though they do not appear explicitly in the dimensionless model equations, the arrangement of the cavity with respect to the wall and the void fraction ϕ are additional factors that influence the temperature distributions in wall and the fluid as well as the heat across the system.

Analytical solutions of the model equations (1-4) are not feasible, and approximate methods available are not sufficiently flexible. Therefore, a numerical solution procedure has been adopted. The ADI method [12] has been employed for the numerical solution of the system of transient elliptic equations. For this purpose the stream function equation, equation (4), was also rewritten in a transient form and solved using the ADI method until steady-state was reached. The results reported here were obtained using a 26 × 26 grid. The grid in the fluid was nonuniform for the purpose of resolving the boundary layers. The details of the method of solution are given elsewhere [14, 15].

The accuracy of the numerical algorithm used was checked by comparison of the benchmark solutions for the limiting case of isothermal vertical wall cavity [16]. For example, for $\mathrm{Ra}=10^6$ the average Nusselt numbers calculated differed from the benchmark solutions by less than 1.5 percent. Numerical experiments were performed for different grids showed that the number of nodes chosen was a reasonable compromise between computational effort and accuracy [14, 15]. There was less than 0.022 percent difference in the average Nusselt numbers calculated using a 13 × 13 and 21 × 21 grids in the fluid filled cavity for $\mathrm{Ra}^*=10^6$.

Experiments

Test Cell and Instrumentation. A schematic diagram of the test cell used for the experiments is shown in Fig. 2. Because of the symmetry in the geometry and boundary conditions of the test material, the test cell is formed by combining three identical rectangular structures. The central part of the test solid was used for the measurements, and the two sides of the test material served to minimize edge effects, such as heat gains or losses, by the test material. The inside dimensions of each cavity test material are 3.6 cm by 3.6 cm and the outside dimensions are 6 cm by 6 cm. A low aspect ratio enclosure was purposely chosen because the boundary conditions on the horizontal connecting walls take on a much greater importance than do the connecting walls in high aspect ratio enclosures. The length of a test cell along the optical path is 19 cm. A larger test cell would have been desirable to minimize the edge effects. Unfortunately, a width and height limit in the direction of the optical path is imposed by the available interferometer optics. A Mach-Zehnder interferometer of typical rectangular design having 25-cm-dia optics was employed as a diagnostic tool for measuring the temperature distribution in a cavity filled with air at atmospheric pressure.

Lexan was chosen as the wall material because it is readily machinable, has low thermal conductivity, has well-established thermophysical properties, and is moderate in cost. A moderate Biot number is required in order to investigate conduction induced convection in a cavity. If the thermal conductivity is too high, the Biot number becomes too small and conduction becomes the dominant heat transfer mode in the system. This is one of the most important reasons why Lexan was chosen as a test material instead of others. The thermophysical properties of Lexan at a temperature of 25°C are the following [17]:

Thermal conductivity = 0.201 W/m-°C
Specific heat = 1256.0 J/kg-°C
Specific Gravity = 1.2

The interior surfaces of the cavity were carefully sprayed with several coats of 3M Nextell Black Velvet paint to give a surface emissivity greater than 0.98.

The outside walls of the test cell were maintained at uniform but different temperatures. Multiple-pass heat exchangers, through which a working fluid at a desired temperature can be circulated by a constant temperature bath and maintain the surfaces at a uniform temperature, were designed and attached to the walls of the test cell to provide constant temperature boundaries. Optical quality glass windows, with dimensions 4.0 cm by 4.0 cm and 0.9 cm thick, were installed at the front and back faces of the test cell for interferometric measurements. The entire test cell (top, bottom, sidewalls, and ends) were covered by two layers of

Styrofoam insulation in order to minimize heat gains or losses from the surroundings. The ends of the test cell were covered with removable insulation to facilitate photographic and optical observations.

The thermal boundary conditions imposed on the outside walls of the test cell were established by circulating a temperature-controlled working fluid from a constant temperature bath. Two temperature baths were used in the experiments. This temperature bath was capable of maintaining a preset temperature to within 0.1°C at a maximum flow rate (4.0 L/min).

Eleven calibrated, copper-constantan thermocouples were used for measuring temperatures at different locations in the solid. All of the thermocouples were placed at the center of the midplane of the solid. They were read with an automatic scanning multichannel datalogger with a printer capable of resolving 0.1°C and a calibrated accuracy of 0.1°C.

The temperature distribution in the fluid (air) filling the cavity was measured using a Mach-Zehnder interferometer. A 10-mW He-Ne laser served as the light source for the interferometer. The primary reason for using a laser source was that it eliminated the need for compensation of the optical path in the reference leg of the interferometer.

Test Procedure and Data Reduction. The test cell was fixed in the test position and centered in the test beam of the interferometer. A 35-mm camera was used to photograph the interference fringe pattern reflected from the parabolic mirror and focused at the center of the test cell. Kodak technical film (TP 135-36) was used to obtain clear and sharp photographs of the interference fringe images.

The test was initiated by supplying the heat exchanger with a working fluid to impose isothermal boundary conditions on the outside walls of the cell. A photograph of the interference fringe patterns was taken every 10 min (to record the fringe patterns during those experiments for which transient record was desired) by removing the insulation covering the windows to facilitate photographing of the patterns. The insulation was immediately replaced after photography. At the same time, the temperatures in the solid were recorded using the datalogger. The experiments continued until steady-state conditions were reached. Steady state was assumed to exist when the temperatures at the solid-fluid interface did not change.

The interference fringe data were interpreted using the procedure described in the literature [18]. The temperature at a reference point was measured with a thermocouple. Then, for each reference fringe pattern evaluated, the fringe shifts were calculated for the temperature about the reference temperature. For a more convenient and accurate reduction of data, a computer program was written to determine the temperature at every fringe shift for the measured reference temperature.

Results and Discussion

Numerical Results.

Dimensionless Parameters. There are a large number of independent parameters Ra*, Pr, A, H/L, ϕ, k^*, α^*) governing the problem, and it is not feasible to obtain solutions for the complete range of interest. Extensive numerical results, however, have been obtained for combined conduction and laminar natural convection in rectangular cavities with all four walls having finite conductances for a range of parameters of physical interest [15], including different aspect ratio cavities. It is possible to include here only results for a square enclosure. The results for the flow and temperature fields, the local Nusselt numbers, the average Nusselt numbers, and total heat transfer through the systems are calculated for Prandtl number range from 0.01 to 100 over a Rayleigh number Ra* range from 10^4 to 10^7. The emphasis of the discussion is on heat transfer rather than on stability or flow. The results reported in the paper have been generated using a total of 26 × 26 grids for the wall with a 16 × 16 grid in the fluid.

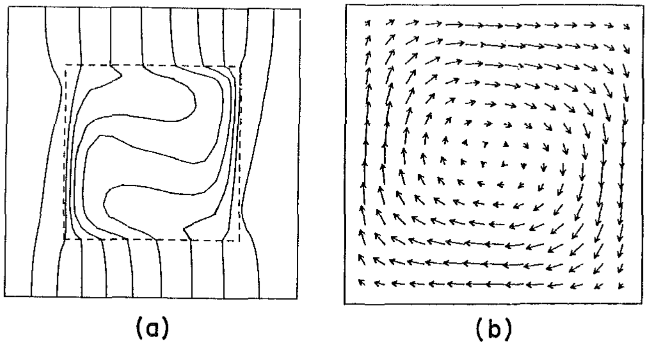

Fig. 3 The contours of isotherms ($\Delta\theta = 0.1$) (*a*), and velocity vectors (*b*): $Ra^* = 10^6$, $Pr = 0.71$, $A = 1.0$, $L/H = 1.0$, $\phi = 0.25$, $k^* = 10.0$, and $\alpha^* = 0.005$

Isotherms and Velocity Vectors. Figure 3 illustrates the contours of the isotherms and of the velocity vectors for the Rayleigh number $Ra^* = 10^6$. The dimensionless constant temperature lines in both the solid (wall) and the fluid are given in Fig. 3(*a*) for temperature difference $\Delta\theta = 0.1$. The bounding surfaces of the fluid filled cavity are indicated with a dashed line. The dimensionless velocity vectors plotted in Fig. 3(*b*) were obtained by linear interpolation of numerical results. The arrows denote the direction and magnitude of the resolved U and V velocity components at each grid point.

Near the adiabatic horizontal outside walls the temperature decreases almost linearly with the distance from the hot (left) vertical wall to the cold (right) vertical wall (Fig. 3). However, natural convection causes the fluid in the cavity to take up a temperature profile different from the linear one. At smaller Ra* (not shown) the departure from linearity is smaller than at a higher Ra* [15]. For small Rayleigh numbers, both the fluid and the wall take up an almost linear temperature profile, and therefore there is little heat transfer between the wall and the fluid. The adiabatic condition imposed on the outside horizontal walls appears to be locally violated, since there is heat flow from the fluid to the wall at the top horizontal wall and heat flow from the wall to the fluid at the bottom horizontal wall. There is heat flow from the wall to the fluid in the left quarter of the cavity and heat flow from the fluid to the wall in the rest of the cavity (Fig. 3(*a*)). This is due to the fact that as the warm fluid sweeps the hot vertical wall it becomes heated. As the fluid flows along the upper wall it continues to be heated until at some point it begins to release some of its energy to the wall. On the other hand, the upper boundary of the horizontal wall "tries" to maintain a linear temperature distribution. The fluid flowing down along the cold vertical wall continues to release some of its energy. As the bottom horizontal wall is swept by the cold fluid, the direction of heat transfer is still from the fluid to the wall; however, further along the wall the direction of heat flow is reversed. The location (along the horizontal walls) where the direction of heat flow is reversed depends on the Rayleigh and Prandtl numbers as well as the other dimensionless parameters (A, L/H, ϕ, and k^*) [15]. As the void fraction increases, natural convection in the cavity becomes more intense for otherwise identical conditions and parameters.

Isotherms for the thermal conductivity ratio between $k^* = 1$ and $k^* = 100$ have been calculated [15]. For large thermal conductivity ratios k^*, heat transfer rate is higher through the wall then the fluid due to larger temperature gradient at the

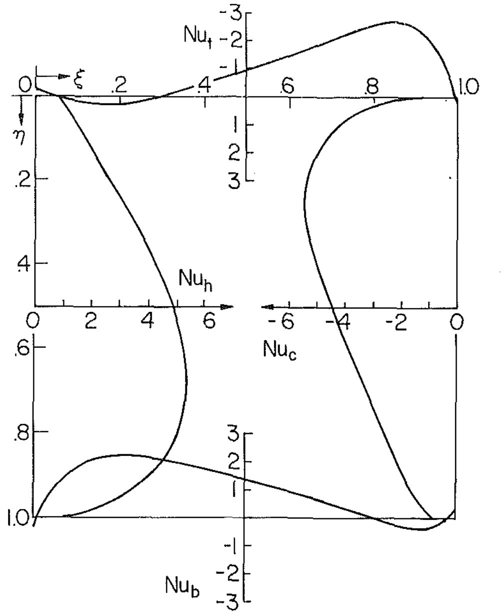

Fig. 4 Local Nusselt number distribution along the four walls: $Ra^* = 10^6$, $Pr = 0.71$, $L/H = 1.0$, $A = 1.0$, $\phi = 0.36$, $k^* = 10.0$, and $\alpha^* = 0.005$

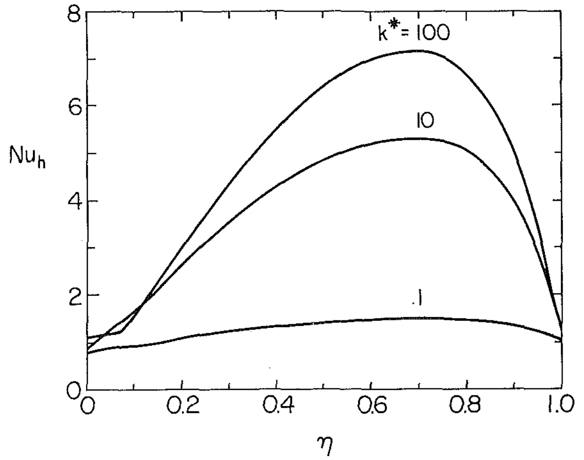

Fig. 5 Effect of the thermal conductivity ratio k^* on local Nusselt number at the hot wall: $Ra^* = 10^6$, $Pr = 0.71$, $A = 1.0$, $L/H = 1.0$, $\phi = 0.36$, and $\alpha^* = 0.01$

Table 1 Average Nusselt number along the four walls of a square cavity; $Pr = 0.71$, $A = 1.0$, $H/L = 1.0$, $\phi = 0.36$, $k^* = 10.0$, and $\alpha^* = 0.005$

	Average Nusselt number			
Ra^*	$\overline{Nu}_h$	$\overline{Nu}_c$	$\overline{Nu}_t$	$\overline{Nu}_b$
10^4	1.310	1.311	0.219	0.220
10^5	2.195	2.184	0.651	0.647
10^6	3.801	3.781	1.017	1.057
10^7	5.517	5.701	−1.139	1.555

top and the bottom of the square solid than the left-hand side of the solid-fluid interface. In other words, the fluid in the cavity behaves as a thermal insulator for a large thermal conductivity ratio, but for a small thermal conductivity ratio enclosure, heat transfer through the solid is lower than the fluid. As the thermal conductivity ratio increases, the value of the stream function at the midpoint of the cavity ($\Psi_o = 19.02$) with $k^* = 100$ becomes much larger than the one for the stream function ($\Psi_o = 10.97$) with $k^* = 1$, and the flow patterns (not shown) change significantly. The horizontal and the vertical velocity component in the cavity increase significantly with the increase in the thermal conductivity ratio [15].

The velocity vectors (Fig. 3(*b*)) clearly show that the velocity boundary layer thickness on the hot inside wall increases in the same way as on the cold wall. The growth is different and is largely due to the change in buoyancy effect. As expected, the velocity boundary layers are thickest in the corners of the cavity where the direction of flow is changed. Some representative results for the numerical value of the streamlines at the midpoint (Ψ_o) and the maximum horizontal ($U_{\max}$) and vertical ($V_{\max}$) velocity components are available [15]. As the void fraction increases, the value of the midpoint stream function ($\Psi_o = 18.56$) with $\phi = 0.5$ becomes larger than that of the stream function ($\Psi_o = 15.32$) with $\phi = 0.25$, but the flow patterns remain similar for the Rayleigh number $Ra^* = 10^6$ [15].

Local Nusselt Number. Because the rectangular cavity has four conducting walls, the local Nusselt number should be defined for all four walls. Figure 4 illustrates the local Nusselt number variations along the cavity walls. Because of the definitions adopted, the local Nusselt number is positive if heat flows from the wall to the fluid, and it is negative if heat flows from the fluid to the wall. At the connecting horizontal walls, the local Nusselt number may be positive or negative, depending on the position along the walls. This indicates that for conjugate (combined conduction-convection) problems the Nusselt number may not be the most desirable heat transfer parameter for correlating results and data. For the problem considered, the Nusselt number not only depends on the geometry of the cavity and the relevant conventional parameters (Ra, Pr, and A), but also on the thermophysical properties of the wall materials, the porosity, and the orientation of the cavity within the solid wall.

The maximum in the local Nusselt number at the hot inside (vertical) wall Nu_h occurs in the lower half of the cavity (Fig. 4). The results are consistent in trends with those reported in the literature [19]. As can be seen from the figure, the local Nusselt number attains the highest value near $\eta = 0.7$. This is caused by the cold fluid, which descended from the cold wall, moved along the lower surface, and impinged on the hot wall near its base. There is heat flow from the fluid to the wall at the top horizontal wall and heat flow from the wall to the fluid at the bottom horizontal wall as shown in Fig. 4. The location of the maximum local Nusselt number at the hot vertical wall is shifted down to the lower half of the cavity as the Rayleigh number is decreased. It is interesting to note the changes in the heat flow direction at the horizontal connecting walls. The location (along the horizontal wall) where the direction of heat flow is reversed depends on the Rayleigh number, the Prandtl number, and other parameters (ϕ, A, L/H, and k^*).

The local Nusselt number depends strongly on the void fraction of the solid wall. For example, the local Nusselt numbers with $\phi = 0.5$ are almost twice as large as those with $\phi = 0.25$ for the same Rayleigh number [15]. This is due to the larger temperature differences between the hot and the cold inside walls with an increase in the void fraction. It should be emphasized that the value of the Rayleigh number Ra^* is based on the outside wall temperature difference and the assumption of linear temperature variation across the system.

The local Nusselt numbers Nu_h are plotted in Fig. 5 against the dimensionless height η for three different values of the thermal conductivity ratio k^*. The maximum in Nu_h occurs in the lower half of the cavity ($\eta = 0.70$). For $k^* = 1.0$, the local Nusselt number is practically constant over 90 percent of the cavity height.

Average Nusselt Number. The results for the average Nusselt numbers have been calculated over a range of Rayleigh numbers and are presented in Table 1. As the

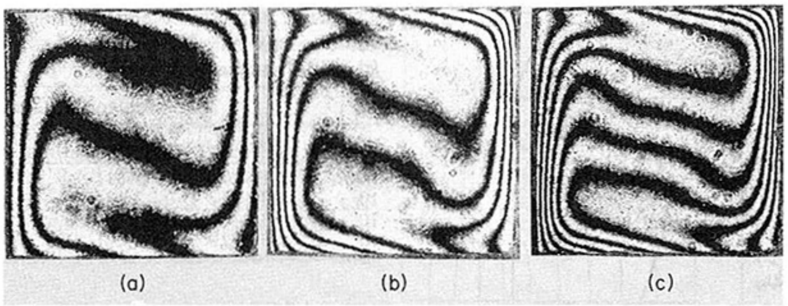
(a) (b) (c)

Fig. 6 Steady-state interference fringe patterns, $\mathrm{Pr} = 0.71$, $A = 1.0$, $L/H = 1.0$, $\phi = 0.36$: (a) $\mathrm{Ra}^* = 6.4 \times 10^5$, (b) $\mathrm{Ra}^* = 1.01 \times 10^6$, and (c) $\mathrm{Ra}^* = 1.28 \times 10^6$

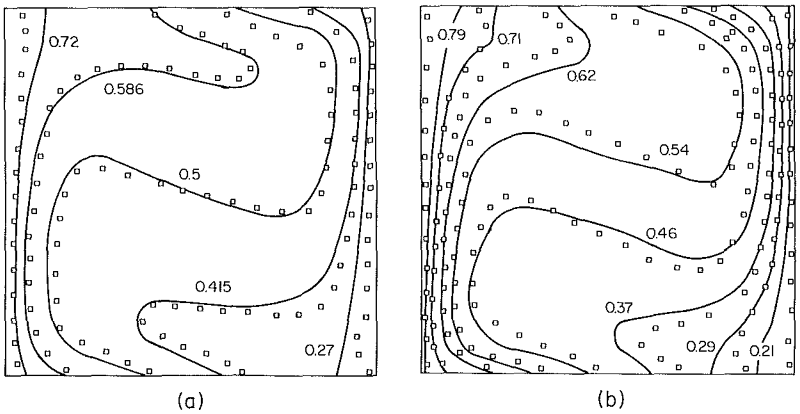

(a) (b)

Fig. 7 Comparison between measured and predicted temperatures: (a) $\mathrm{Ra}^* = 0.64 \times 10^6$, and (b) $\mathrm{Ra}^* = 1.01 \times 10^6$

Rayleigh and the Prandtl numbers increase, the average Nusselt number on the four walls of the cavity also increases. Although the average Nusselt numbers at the top and the bottom walls are quite small, the local Nusselt numbers can be quite large, as shown in Fig. 4. In other words, the total heat transfer across the top and bottom walls is small (see Table 1), since average Nusselt number is very small at the top and the bottom of the cavity, but the local heat transfer through the top and the bottom walls is large.

The effects of Prandtl number on average Nusselt number at the heated wall were calculated for various Prandtl numbers [15]. The Nusselt number becomes more sensitive to the Prandtl number as the Rayleigh number increases as indicated in Table 2. However, the Nusselt number is not sensitive to the Prandtl number over a range from 0.71 to 100 for higher Rayleigh number ($\mathrm{Ra}^* > 10^6$). It should be noted that, even though the modified Rayleigh number is low, natural convection is significant for Prandtl number of 100.

The average Nusselt numbers at the hot wall have been calculated over a range of Rayleigh numbers and void fractions. The results show that as both Rayleigh number and the void fraction increase, the average Nusselt numbers on the hot wall of the cavity also increase. An empirical correlation of the average Nusselt number for a rectangular cavity surrounded by conducting wall has been obtained from a least-squares fit of the numerical results

$$\overline{\mathrm{Nu}} = 0.410\phi^{0.93}(k^*)^{0.138}(\mathrm{Ra}^*)^{0.2}, \qquad 0.3 < \mathrm{Pr} < 50 \tag{15}$$

$$\overline{\mathrm{Nu}} = 0.485\phi^{0.93}(k^*)^{0.138}(\mathrm{Ra}^*)^{0.2}, \qquad 50 < \mathrm{Pr} < 100 \tag{16}$$

These equations are based on the following range of parameters:

$$A = 1.0, 10^5 < \mathrm{Ra}^* < 10^7, 0.25 < \phi < 0.6 \text{ and } 3 < k^* < 100.$$

A comparison of average Nusselt numbers between the correlations, equations (15) and (16), for finite conductance walls and the correlations for the limiting case of isothermal cavity with perfectly conducting and perfectly insulated horizontal walls is of interest. The empirical correlations for the perfectly conducting and perfectly insulated walls reported in the literature [20] for an air filled cavity ($\mathrm{Pr} = 0.71$) are

$$\overline{\mathrm{Nu}} = 0.13\mathrm{Ra}^{0.28} \quad \text{for } 10^4 < \mathrm{Ra} < 10^5 \tag{17}$$

and

$$\overline{\mathrm{Nu}} = 0.138\mathrm{Ra}^{0.31} \quad \text{for } 10^4 < \mathrm{Ra} < 10^5 \tag{18}$$

respectively. The average Nusselt numbers (with $\mathrm{Ra}^* = 0.6 \times 10^5$ and $k^* = 100$) calculated from equation (15) for void fraction of 0.36 is 2.70, and for void fraction of 0.5 it is 3.67. These two Nusselt numbers are compared with the average values of 3.26 and 4.36, which are evaluated from the equations (17) and (18), respectively, for Rayleigh number of $\mathrm{Ra} = 10^5$. The average Nusselt numbers for the two systems are not directly comparable, since the Rayleigh numbers are not based on the same temperature difference across the cavity.

As the thermal conductivity ratio k^* increases, the average Nusselt number increases (see Table 3). However, the value is not sensitive to the thermal diffusivity ratio α^*. The effect of α^* should not be significant on the steady-state results, since the ratio is only important for transient conditions in the energy equation for the solid. The thermal conductivity ratio k^* appears in the solid–fluid interface boundary conditions that control the solutions of the governing equations. Therefore, the local and the average Nusselt numbers are much more sensitive to the thermal conductivity ratio than to the thermal diffusivity ratio.

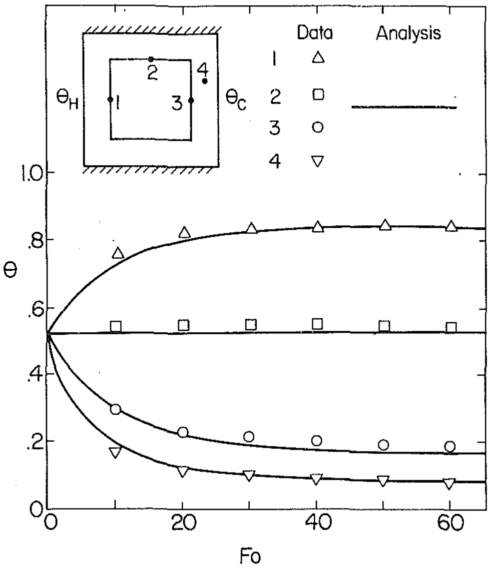

Fig. 8 Comparison of the measured and predicted solid temperatures in the wall, $Ra^* = 0.64 \times 10^6$

Comparison of Experimental Data With Predictions. A number of experiments have been performed with an air-filled cavity for the orientations of the heating and cooling from the sides of the cell, and it will be possible to describe here only the results for some typical conditions. In all of the experiments, the cold outside wall was maintained at a temperature of −5°C. The temperature difference imposed across the cell ranged from $\Delta T = 34°C$ to $\Delta T = 68°C$. The maximum temperature in the test cell was limited by the material (Lexan), radiation heat exchange among walls and heat loss considerations. The experimental parameters for the Lexan-air ($Pr = 0.71$) system studied were the following: $A = 1.0$, $H/L = 1.0$, $\phi = 0.36$, $k^* = 7.4$, and $\alpha^* = 0.008$.

Before performing the experiments an energy balance was established on the test cell. The details are given elsewhere [15]. Suffice it only to mention that the energy balance on the system was closed to within about 1.5 percent. At larger temperature differences, the measured and predicted heat losses agreed with each other to within less than 1 percent and accounted for about 7 percent of the total energy input to the system.

Photographs of the interference fringe patterns at steady-state conditions are illustrated in Fig. 6 for three experimental runs. The number of fringes increases with the temperature difference across the wall, but the shape of the fringes remained the same. It is appropriate to mention that during preliminary experimentation the image of the cavity and the fringe shift patterns were carefully monitored on a frosted glass screen placed between the test cell and the camera in order to detect motions in the fringe field which would indicate instabilities in the fluid. At no time during the transient and after steady-state thermal conditions had been reached were instabilities, quasi-periodic, or periodic oscillations detected. The Rayleigh numbers were apparently too low for unstable or oscillatory flow to develop.

Figure 7 show comparisons of the predicted and the measured steady-state temperatures in air. The squares denote the experimental data points, and the solid lines denote isotherms predicted by the model. The results show relatively uniform temperatures near the cavity center and clearly illustrate that two thermal boundary layers are formed near the vertical walls. The interference fringes are spaced almost equally along the top and the bottom connecting walls forming the cavity due to adiabatic conditions imposed on the outside horizontal walls. In other words, a horizontal wall tries to maintain a linear temperature distribution due to heat conduction in the wall. The temperature gradients clearly indicate that there is heat flow from the fluid to most parts of the upper wall. The interference fringe patterns at the right (cold) wall indicate a behavior which is opposite to that at the left (hot) wall.

The numerical results presented are based on a model that has neglected radiation heat exchange between surfaces. The agreement between the analysis and data is excellent throughout most of the cavity (Fig. 7(*a*)). This good agreement is in part due to a relatively small temperature difference imposed across the cell and a relatively low absolute temperature of the system so that heat losses (gains) to the ambient environment are relatively small. Although the agreement between the data and predictions is good, the analysis could not predict accurately the data at the isotherms 0.21 and 0.79 (Fig. 7(*b*)). The discrepancy between the data and predictions could be due to experimental errors, three-dimensional effects, uncertainties in thermophysical properties of the solid, truncation error in the numerical model and/or radiation heat exchange among the walls of the cavity, particularly for larger temperature difference across the system. Uncertainties in the knowledge of the vorticity boundary conditions at the solid-liquid interface and insufficiently fine grid for handling the nonlinearities of the variables (stream function, vorticity) at higher Rayleigh numbers may also contribute to the discrepancy.

The accuracy of the interferometrically measured temperature distributions is difficult to ascertain precisely. The uncertainty is primarily due to the imperfection of the insulation at the ends of the test cell. The actual temperatures are estimated to be as much as 1°C to 2.5°C lower than those determined for the temperature difference of 34°C to 68°C imposed across the system, respectively.

Figure 8 gives a comparison between the measured and numerically predicted temperatures at some selected locations in the solid wall for one of the experiments as a function of the Fourier number Fo. The symbols indicated on the inset of the figure represent the data at the particular location, and the solid lines denote numerical predictions. The agreement between the data and predictions is excellent and could in part be due to a relatively low temperature ($T = 31.8°C$) at the warm sidewall (point 1). The maximum deviation between the predicted and measured temperatures at steady-state is approximately 6.0 percent at point 3.

At higher temperatures and temperature differences imposed across the test cell, the discrepancy between data and predictions increased because of the neglect of radiation heat

Table 2 Effect of Prandtl number on the average Nusselt number at the hot vertical wall; $A = 1.0$, $H/L = 1.0$, $\phi = 0.36$, $k^* = 10.0$ and $\alpha^* = 0.005$

	Average Nusselt number			
	Rayleigh number, Ra*			
Pr	10^4	10^5	10^6	10^7
0.01	1.176	1.291	2.130	3.300
0.1	1.252	1.661	3.092	4.580
0.71	1.310	2.195	3.801	5.517
10	1.329	2.303	4.154	5.957
100	3.180	3.325	4.312	6.262

Table 3 Effect of thermal conductivity ratio k^* on total dimensionless heat transfer and average Nusselt number; $Ra^* = 10^6$, $Pr = 0.71$, $A = 1.0$, $H/L = 1.0$, $\phi = 0.36$, and $\alpha^* = 0.005$

k^*	1.00	5.00	10.0	50.0	100.0
$\overline{Nu}_h$	1.253	3.119	3.801	4.696	4.821

exchange between the surfaces and increased heat losses from the test cell [15]. Radiation exchange among surfaces forming the fluid filled cavity has been accounted for in a detailed manner [14]. The results show that inclusion of radiation exchange between surfaces for higher absolute temperatures of the system decreases the discrepancy between data and predictions at some locations and increases at the others.

Local Nusselt numbers have not been determined and compared with predictions, because there is a question of uniqueness. For the conjugate problem considered in the paper, the local Nusselt number depends not only on the location of the cavity in the enclosure, conductance of the wall, the void fraction, and the imposed boundary conditions, but also on the fluid and the geometry of the cavity.

Conclusions

The experimental and numerical study performed shows a very significant effect of wall conduction on the convective heat transfer in an enclosure of aspect ratio of unity. Heat conduction in the walls of the cavity can lead to simultaneous stabilization and destabilization of the natural convection flow, depending on the location in the cavity. Natural convection induces heat transfer in the connecting horizontal walls of the cavity.

Very good agreement has been obtained between the predictions based on the mathematical model and the experimental data for the temperatures in the solid, and less favorable, but still good agreement, for the temperature distributions in the fluid.

For the particular system configuration, wall conductance and fluid combinations considered, heat conduction in the walls not only reduces the average temperature difference across the cavity but also produces partial stabilization of the flow and decreases natural convection heat transfer. The extent of thermal stratification in the fluid induced by heat conduction in the walls needs to be quantified.

The local and the average Nusselt numbers may not be desirable concepts or parameters for correlating experimental data or analytical results in conjugate heat transfer problems of the type considered here, since they depend not only on the fluid and flow in the cavity but also on the interaction of heat conduction in the wall and convection in the cavity.

References

1 Jakob, M., *Heat Transfer*, Vol. I, John Wiley & Sons, New York, 1949, pp. 82–107.

2 Catton, I., "Natural Convection in Enclosures," *Heat Transfer—1978*, Vol. 6, National Research Council of Canada, Ottawa, 1978, pp. 13–30.

3 Ostrach, S., "Natural Convection Heat Transfer in Cavities and Cells," *Heat Transfer—1982*, Vol. 1, Hemisphere Publishing Corp., Washington, D.C. 1982, pp. 365–379.

4 Catton, I., Bejan, A., Greif, R., and Hollands, K. G. T., "Natural Convection in Enclosures," *Proceedings of a Workshop on Natural Convection*, July 18–21, 1982, Breckenridge, Colo., edited by K. T. Yang and J. R. Lloyd, University of Notre Dame, Notre Dame, Ind., 1983, pp. 24–35.

5 ElSherbiny, S. M., Hollands, K. G. T., Raithby, G. D., "Effect of Thermal Boundary Conditions on Natural Convection in Vertical and Inclined Air Layers," ASME JOURNAL OF HEAT TRANSFER, Vol. 104, 1982, pp. 515–520.

6 Catton, I., "The Effect of Insulating Vertical Walls on the Onset of Motion in a Fluid Heated from Below," *International Journal of Heat and Mass Transfer*, Vol. 15, 1972, pp. 665–672.

7 Larson, D. W., and Viskanta, R., "Transient Combined Laminar Free Convection and Radiation in a Rectangular Enclosure," *Journal of Fluid Mechanics*, Vol. 78, 1976, pp. 68–85.

8 Koutsoheras, W., and Charters, W. W. S., "Natural Convection Phenomena in Inclined Cells with Finite Walls- A Numerical Solution," *Solar Energy*, Vol. 19, 1977, pp. 433–438.

9 Meyer, B. A., Mitchell, J. W., and El-Wakil, M. M., "The Effect of Thermal Wall Properties on Natural Convection in Inclined Rectangular Cells," ASME JOURNAL OF HEAT TRANSFER, Vol. 104, 1982, pp. 111–117.

10 Shiralkar, G. S., and Tien, C. L., "A Numerical Study of the Effect of a Vertical Temperature Difference Imposed on a Horizontal Enclosure," *Numerical Heat Transfer*, Vol. 5, 1982, pp. 185–197.

11 Kim, D. M., and Viskanta, R., "Heat Transfer by Combined Wall Conduction and Natural Convection Through a Rectangular Solid with a Cavity," *Proceedings of the ASME/JSME Joint Thermal Engineering Conference*, edited by Y. Mori, W.-J. Yang, ASME, New York, 1983, Vol. 1, pp. 313–322.

12 Krane, R. J., and Jessee, J., "Some Detailed Field Measurements for a Natural Convection Flow in a Vertical Square Enclosure," *Proceedings of the ASME/JSME Joint Thermal Engineering Conference*, Vol. 1, edited by Y. Mori and W.-J. Yang, ASME, New York, 1983, pp. 323–329.

13 Peaceman, D. W., and Rachford, H. H., Jr., "The Numerical Solution of Parabolic and Elliptic Differential Equations," *Journal of the Society of Industrial Applied Mathematics*, Vol. 3, 1955, pp. 28–41.

14 Kim, D. M., and Viskanta, R., "Effect of Wall Conduction and Radiation on Natural Convection in a Rectangular Cavity," *Numerical Heat Transfer* (in press).

15 Kim, D. M., "Heat Transfer by Combined Wall Heat Conduction, Convection, and Radiation through a Solid with a Cavity," Ph.D thesis, Purdue University, West Lafayette, Ind. 1983.

16 Davis, DeVahl, G., and Jones, I. P., "Natural Convection in a Square Cavity, a Comparison Exercise," *International Journal of Numerical Methods in Fluids*, Vol. 3, 1983, pp. 227–248.

17 Stedfeld, R., *Material Engineering/Materials Selector*, edited by R. Stedfield, Penton/IPC Publications, Cleveland, Ohio, 1979.

18 Hauf, W., and Grigull, U., "Optical Methods in Heat Transfer," *Advances in Heat Transfer*, Vol. 6, edited by J. P. Hartnett and T. F. Irvine, Jr., Academic Press, New York, 1970, pp. 133–366.

19 Bajorek, S. M., and Lloyd, J. R., "Experimental Investigation of Natural Convection in Partitioned Enclosures," ASME JOURNAL OF HEAT TRANSFER, Vol. 104, No. 3, 1982, pp. 527–532.

20 Roux, B., Grondin, J. C., Bontoux, P., and Gilly, B., "On a High-Order Accurate Method for the Numerical Study of Natural Convection in a Vertical Square Cavity," *Numerical Heat Transfer*, Vol. 1, 1978, pp. 331–349.

Natural Convection in Porous Media Bounded by Short Concentric Vertical Cylinders

V. Prasad
Assoc. Mem. ASME
Department of Mechanical Engineering,
Columbia University,
New York, N.Y. 10027

F. A. Kulacki
Mem. ASME
Department of Mechanical and Aerospace Engineering,
University of Delaware,
Newark, Del. 19716

Free-convective heat transfer in short cylindrical annuli filled with saturated porous media has been studied numerically and experimentally. For an annulus whose inner wall is heated at constant temperature and outer wall is isothermally cooled, the top and bottom being insulated, heat transfer results have been obtained numerically for $0.9 \geq A \geq 0.3$, $1 < \kappa \leq 11$ and Rayleigh number, Ra^* up to 10^4, where A is the aspect (height-to-gap width) ratio and κ is the radius ratio. Introduction of curvature effects diminishes the multicellular flow behavior observed in the case of shallow cavity, and hence, the higher the radius ratio, the lower is the aspect ratio required for multicellular flow to exist. Heat transfer rates for isothermal heating have also been determined experimentally for $A = 1$ and $\kappa = 5.338$, using water and glass beads (3 and 6 mm dia) as the porous media. The experimental values of Nusselt number agree well with the numerical predictions for Ra^* up to 4000. Agreement between the measured temperatures at various locations and the numerically established temperature field is also quite reasonable.

Introduction

Convective heat transfer in differentially heated vertical enclosures filled with saturated porous media is a topic of many recent investigations, owing to its importance in various technological applications. Consequently, several investigators have presented analytical, numerical, and experimental results for the rectangular cavity with vertical walls at constant temperature, the horizontal walls being insulated. A detailed review of these works has recently been presented by Prasad [1]. The effect of heating by applying a uniform heat flux as opposed to isothermal heating has also been studied by Prasad and Kulacki [2] for a rectangular cavity.

Natural convection in cylindrical annuli filled with saturated porous media has only been investigated very recently. The present available reports are due to Prasad and Kulacki [3], Reda [4], Havstad and Burns [5], and Hickox and Gartling [6]. Hickox and Gartling have considered a case when the inner wall is heated at a constant temperature and the outer wall is isothermally cooled, the top and bottom being insulated. Using a finite element technique and an approximate method, they have obtained heat transfer results for tall annulus ($A \geq 2$) and low Rayleigh numbers, Ra^* up to 100. Havstad and Burns [5] have used three different methods to investigate the problem: finite difference numerical method, perturbation technique, and an approximate analysis, which is essentially the same as that reported by Hickox and Gartling [6]. The work of Havstad and Burns [5] is again applicable for only low Rayleigh number heat transfer. Though they considered a wide range of radius ratio, $1 \leq \kappa \leq 10$, the aspect ratio range of their results are limited, $A \geq 0.555$. They have also presented a correlation for the heat transfer rates for $A \geq 1$. Our work [3] on the cylindrical annuli considers the same thermal boundary conditions but for the larger ranges of Rayleigh number and radius ratio, Ra^* up to 10^4 and $1 \leq \kappa \leq 26$. Using finite difference numerical method, the temperature and flow field have been studied for the height-to-gap width ratio, $1 \leq A \leq 20$, and consequently, the heat transfer rates have been obtained for the above ranges of Ra^*, A, and κ. This paper [3] also presents heat transfer correlations and flow regime criteria for various ranges of the aspect and radius ratios.

The only experimental study reported thus far is due to Reda [4], who has conducted experiments with constant heat flux on the inner wall for $\kappa = 23$, $A = 4.25$, and $Ra^* < 80$. His major results are that the inner surface temperature increases with distance from the bottom of the annulus, even at relatively low Rayleigh number of 10 or less, and that the temperature distribution across the gap is progressively below that for conduction as the power input to the inner cylinder was increased.

The purpose of the present work is to consider the problem for relatively lower aspect ratios and study the effects of curvature on temperature field and flow structure, particularly in the light of multicellular flow behavior reported for shallow cavity [7]. By using a suitable finite difference numerical method, the problem has been investigated when the aspect ratio is reduced below unity, and the heat transfer results have been obtained for $0.3 \leq A < 1$. Also an experimental study has been conducted for the heat transfer in a square vertical annulus filled with a saturated porous medium for the isothermally heated inner wall. To produce the saturated porous media, water and glass beads have been used. For a radius ratio of 5.338, the heat transfer results have been obtained for $45 < Ra^* < 4000$ by using the glass beads of 3 mm and 6 mm diameter. Temperatures at various locations in the medium have also been recorded and compared with the numerical predictions.

Formulation and Numerical Method

For axisymmetric steady natural convection in a porous media where Darcy's law holds, the governing equations for mass, momentum, and energy are:

$$\frac{\partial (ru)}{\partial r} + \frac{\partial (rv)}{\partial z} = 0 \qquad (1)$$

$$\frac{\partial p}{\partial r} + \frac{\mu}{K} u = 0 \qquad (2)$$

$$\frac{\partial p}{\partial z} + \rho g + \frac{\mu}{K} v = 0 \qquad (3)$$

Contributed by the Heat Transfer Division for publication in the JOURNAL OF HEAT TRANSFER. Manuscript received by the Heat Transfer Division September 2, 1983.

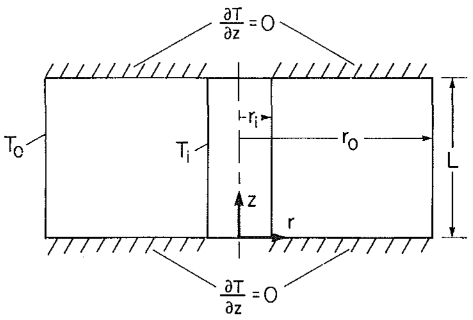

Fig. 1 Vertical shallow annulus, coordinate system and thermal boundary conditions ($T_i > T_o$)

$$u\frac{\partial T}{\partial r}+v\frac{\partial T}{\partial z}=\alpha\left[\frac{1}{r}\frac{\partial}{\partial r}\left(r\frac{\partial T}{\partial r}\right)+\frac{\partial^2 T}{\partial z^2}\right] \tag{4}$$

$$\rho=\rho_r[1-\beta(T-T_r)] \tag{5}$$

Here it has been assumed that the fluid properties are constant, except for the density variation in producing the buoyancy force. Additional viscous drag (Brinkman's model) and inertia terms are neglected because their magnitudes are of small order compared to other terms for low Darcy numbers and low particle Reynolds numbers. Thus velocity slip at the bounding surfaces is permitted.

Using dimensionless variables, equations (1-5) can be transformed to the stream function form

$$A^2\frac{\partial}{\partial R}\left[\frac{1}{(\gamma R+1)}\frac{\partial\psi}{\partial R}\right]+\frac{\partial}{\partial Z}\left[\frac{1}{(\gamma R+1)}\frac{\partial\psi}{\partial Z}\right]=\mathrm{Ra}^*A\frac{\partial\theta}{\partial R} \tag{6}$$

$$\frac{\partial\psi}{\partial R}\frac{\partial\theta}{\partial Z}-\frac{\partial\psi}{\partial Z}\frac{\partial\theta}{\partial R}=\frac{\partial}{\partial R}\left[(\gamma R+1)\frac{\partial\theta}{\partial R}\right]+\frac{1}{A^2}\frac{\partial}{\partial Z}\left[(\gamma R+1)\frac{\partial\theta}{\partial Z}\right] \tag{7}$$

where Ra* is the Rayleigh number based on the gap-width; A is the aspect ratio L/D; and γ is the radius ratio parameter $\kappa-1$.

The relevant hydrodynamic boundary conditions for the impermeable boundaries and the thermal boundary conditions are (Fig. 1)

$$\psi=0,\quad \theta=1\quad \text{at } R=0 \tag{8}$$

$$\psi=0,\quad \theta=0\quad \text{at } R=1 \tag{9}$$

$$\psi=0,\quad \frac{\partial\theta}{\partial Z}=0\quad \text{at } Z=0 \text{ and } Z=1 \tag{10}$$

Finite difference equations are derived from equations (6) and (7) by integration over finite area elements, following a procedure developed by Gosman et al. [8]. The successive-substitution formulae, derived in this way by employing the upwind differences [9] for the convective terms in the energy equation, satisfy the convergence criterion and are quite stable for many circumstances [8]. For solving the system of algebraic equations thus obtained, a point iterative method is used which makes use of the new values as soon as they are available. For low Rayleigh numbers, overrelaxation of the temperature helped in obtaining a faster convergence, and for high Ra*, underrelaxation of the stream function was found useful. The overrelaxation parameter used was varied between 1.95 and 1, whereas a suitable value of the underrelaxation parameter was between 0.5 and 1.

For the present work, a mesh of 41 × 21 was used for $A=0.3$, whereas for $A\geq 0.5$, a mesh of 31 × 31 was employed. These mesh sizes gave an average Nusselt number within 3 percent of the asymptotic value predicted by calculations with much finer mesh. In each case, varying grids were used in both $r-$ and z-directions for $\mathrm{Ra}^*>500$, whereas for lower Rayleigh numbers uniform grids were employed. The iterative convergence criterion ϕ used for the present computations was 5×10^{-4} for both ψ and θ and was satisfied at all grid points in the domain. Nusselt numbers obtained for the trial cases by using $\phi=10^{-5}$ indicated that the present value of ϕ provided a convergence accuracy of 0.25 percent or less. A detailed account of the effects of mesh sizes, relaxation parameters, convergence criterion, the upwind differencing, etc., on the accuracy and the computational costs is presented in [1, 3].

Nomenclature

A = aspect ratio L/D
c = specific heat of fluid at constant pressure, J/kg − K
d = diameter of glass beads, m
D = gap width of porous annulus, $r_o - r_i$, m
g = acceleration due to gravity, m/s^2
h = average heat transfer coefficient on inner wall, W/m^2-K
K = permeability of porous medium, m^2
k_m = thermal conductivity of the saturated porous medium, W/m-K
L = height of porous annulus, m
Nu = average Nusselt number, hD/k_m
p = pressure, Pa
Ra* = Rayleigh number, $(g\beta KD\Delta T)/(\nu\alpha)$
T = temperature, K
ΔT = temperature difference across annulus, $T_i - T_o$, K
u = Fluid velocity in r-direction, $-\frac{\alpha}{D}\frac{1}{(\gamma R+1)}\frac{\partial\psi}{\partial Z}$
v = fluid velocity in z-direction, $\frac{\alpha L}{D^2}\frac{1}{(\gamma R+1)}\frac{\partial\psi}{\partial R}$
r,z = cylindrical coordinates, m
R = dimensionless distance on r-axis, $(r-r_i)/D$
Z = dimensionless distance on z-axis, z/L

Greek Symbols

α = thermal diffusivity of porous medium, $k_m/\rho c$, m^2/s
β = isobaric coefficient of thermal expansion of fluid, K^{-1}
γ = radius ratio parameter, $D/r_i = \kappa - 1$
ϵ = porosity
θ = dimensionless temperature, $(T-T_o)/(T_i-T_o)$
μ = dynamic viscosity of fluid, kg/m − s
ν = kinematic viscosity of fluid, m^2/s
κ = radius ratio, r_o/r_i
ρ = density of fluid, kg/m^3
ρ_s = density of glass balls, kg/m^3
ψ = dimensionless stream function, $(D/\alpha r_i L)\psi'$
ψ^1 = stream function
ϕ = convergence criterion

Subscripts

f = fluid
i = inner wall (heated)
L = based upon annulus height, L
o = outer wall (cooled)
r = reference point for equation (5)
s = solid

Numerical Results

Results for a shallow vertical annulus have been obtained for the Rayleigh number up to 10^4 and the radius ratio up to 11. The aspect ratio has been varied below unity. As the inaccuracy in the computation grows very fast as the radius ratio is increased for very low aspect ratios, the present results are limited only up to $A = 0.3$.

Velocity Fields. Effects of increase in the radius ratio for a shallow annulus is very similar to what have been observed for the square and tall annuli [3, 5]. An introduction of the curvature effects shifts the streamlines toward the top edge of the cold (outer) wall, resulting in high velocities in that region. Any increase in radius ratio further strengthens this behavior and results into a thick cold layer at the bottom. Also the vertical velocity near the hot wall is smaller (in magnitude) as compared to that on the cold wall, and the horizontal velocity in the upper region is higher than that in the lower region (Figs. 2 and 3; also compare with the streamlines for shallow cavity presented in [7]). For the given radius ratio and Rayleigh numbers, the velocities are much lower for low aspect ratio. As is expected, the width of the core increases as the aspect ratio decreases.

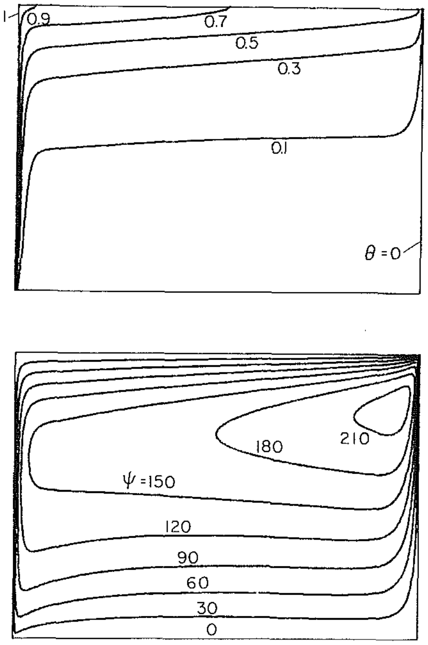

Fig. 2 Isotherms and streamlines for a vertical shallow annulus, for $A = 0.7$, $\kappa = 6$, and $Ra^* = 1000$: (a) Isotherms, $\Delta\theta = 0.1$; (b) Streamlines, $\Delta\psi = 10$

The effects of the curvature are more pronounced on the multicellular behavior of the flow. For any fixed values of A and Ra^*, the multicellular flow behavior of the rectangular cavity diminishes as the radius ratio increases beyond unity. As already reported, the multicellular flow structure is observed for any aspect ratio below unity in the case of rectangular cavity [7], but for shallow annuli the flow structure is purely unicellular for $A \geq 0.5$ and $\kappa \geq 2$.

As the radius ratio is reduced below 0.5, the multicellular flow patterns appear. For $A = 0.3$, the multicellular behavior does not diminish till $\kappa = 2$. When Ra^* is increased beyond 100, secondary cells are observed at two locations for $A = 0.3$ and $\kappa = 2$ (Figs. 3(*a*) and 3(*b*)). The cell near the cold wall is much stronger as compared to the cell near the hot wall. This is contrary to what has been observed for the shallow cavity – equally strong hot and cold cells. This is mainly due to the cold cell being a part of the main circulatory flow. Any increase in the radius ratio delays the start of the multicellular flow behavior (in terms of Ra^*), and, as such, for $A = 0.3$ and $\kappa = 6$ the flow is unicellular even at $Ra^* = 10{,}000$ (Fig. 3(*c*)). Qualitatively, a similar stabilizing effect of radius ratio has been reported by Lee, Korpela, and Horne [10], on the multicellular flow structure in a tall vertical annulus filled with a Newtonian fluid. It is expected that at lower aspect ratios, the multicellular behavior will stay longer in terms of the radius ratio.

Temperature Field. An increase in the radius ratio shifts the isotherms toward the hot wall. This results into a thinner thermal boundary layer on the hot wall and a thicker thermal boundary layer on the cold wall. The thickness of the cold layer at the bottom, also, increases with an increase in κ (Figs. 2 and 3; also compare with the isotherms for shallow cavity presented in [7]).

As observed for the square and tall annuli [3], the temperature drop near the hot wall is much more pronounced as compared to that near the cold wall (Fig. 4). This follows from the conduction temperature profile for an annulus. In the core, the temperature variation is almost linear, but the slope decreases as the radius ratio increases and/or the aspect ratio decreases. This clearly indicates that the fraction of total heat transferred by conduction through the core increases as the aspect ratio is reduced or the radius ratio is increased.

Heat Transfer Results. Heat transfer rates in terms of average Nusselt number on the inner wall are presented in Figs. 5(*a*-*d*), for the aspect ratios 0.9, 0.7, 0.5, and 0.3, respectively. In each case, the Nusselt number approaches the

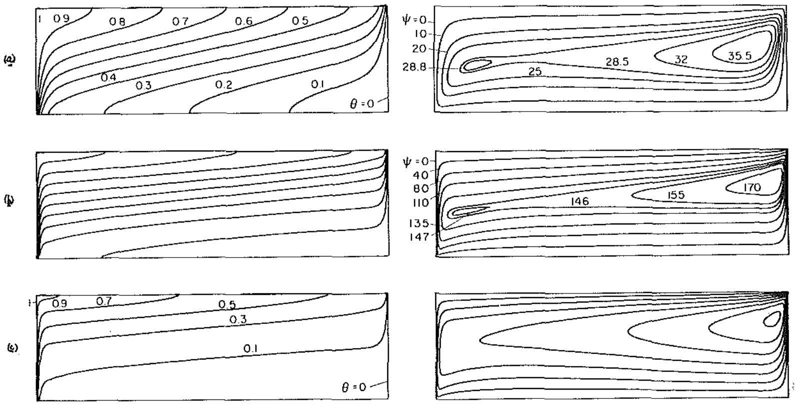

Fig. 3 Isotherms and streamlines for a vertical shallow annulus, for $A = 0.3$: (a) $Ra^* = 1000$, $\kappa = 2$; (b) $Ra^* = 10{,}000$, $\kappa = 2$; and (c) $Ra^* = 10{,}000$, $\kappa = 6$ ($\Delta\psi = 50$)

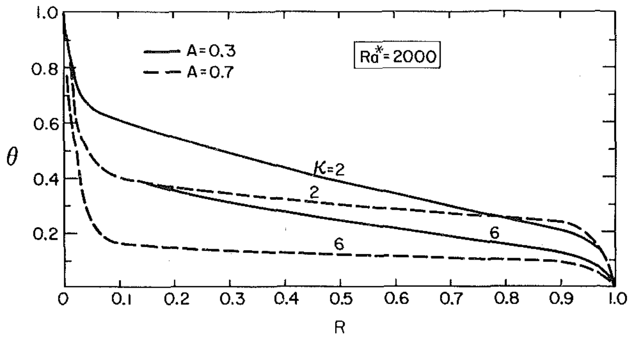

Fig. 4 Temperature distribution at midheight for $A = 0.7$ and 0.3, and $\kappa = 2$ and 6

pure conduction value, in the conduction regime. As usual this conduction regime is always followed by the asymptotic and the boundary layer flow regimes. The start of boundary layer regime is invariably delayed as the radius ratio is increased – very similar to what is observed for the tall annulus [3]. The decrease in height-to-gap width ratio further delays the boundary layer behavior, as observed for the shallow cavity case [7]. The combination of these two effects results in a longer delay for the boundary layer behavior to start in the present case. Consequently, the conduction and the asymptotic flow regimes get extended much more for the shallow annulus.

As usual the slope of ln (Nu_i) versus ln (Ra^*) curve is always higher in the asymptotic flow regime compared to that in the boundary layer regime (Figs. 5(*a–d*)). For the asymptotic flow, the slope of this curve decreases as the radius ratio is increased. So is the case when the heat transfer is dominated by the boundary layer effects. These indicate that the heat transfer rate always increases as the radius ratio is increased, but the rate of increase is maximum for the pure conduction and decreases as the Rayleigh is increased. Depending upon the aspect ratio and Rayleigh number, a situation comes when the enhancement in the Nusselt number is very small (compare the curves for $\mathrm{Ra}^* = 100$ and 2000 in Fig. 6).

For $\mathrm{Ra}^* = 2000$ and $A = 0.7$, the slope of the curve near $\kappa = 10$ is seen to be very small (Fig. 6). This is mainly due to the annulus results approaching the solution for a heated cylinder (at temperature T_i) embedded in a saturated porous medium at T_o. Owing to large end effects in the case of shallow annuli, very high values of Ra* and/or κ are required for the two results to be closer. For $A = 0.5$, the Nusselt number in the present case is 11 percent lower than that for the heated cylinder (obtained from Minkowycz and Cheng [11]) when $\kappa = 11$ and $\mathrm{Ra}^* = 10{,}000$. The deviation is larger at lower aspect ratios for any given Ra* and κ.

The effect of aspect ratio is not straightforward. For low Rayleigh numbers, an increase in aspect ratio increases the Nusselt number, irrespective of the value of κ. As the Rayleigh number increases, this rate of increase diminishes. Consequently, a situation arises when a change in the aspect ratio does not affect the Nusselt number, as an example, $\mathrm{Ra}^* = 500$. $\kappa = 11$ and $0.5 < A < 0.7$ (Fig. 6). Beyond this the Nusselt number starts decreasing with an increase in A. The Rayleigh number at which this happens, strongly depends upon the radius ratio. A similar dependence on aspect ratio was observed for the tall annuli [3, 5]. If we consider the Nusselt number based on the height of the annulus Nu_L the heat transfer rate always increases with an increase in the aspect ratio, for any given height of the annulus.

The Nusselt numbers obtained by using the present method are compared with the results of Havstad and Burns [5] in Table 1, for all values of Ra*and κ considered by them when the aspect ratio is less than unity. The present values of Nusselt number agree within 7 percent of the values reported

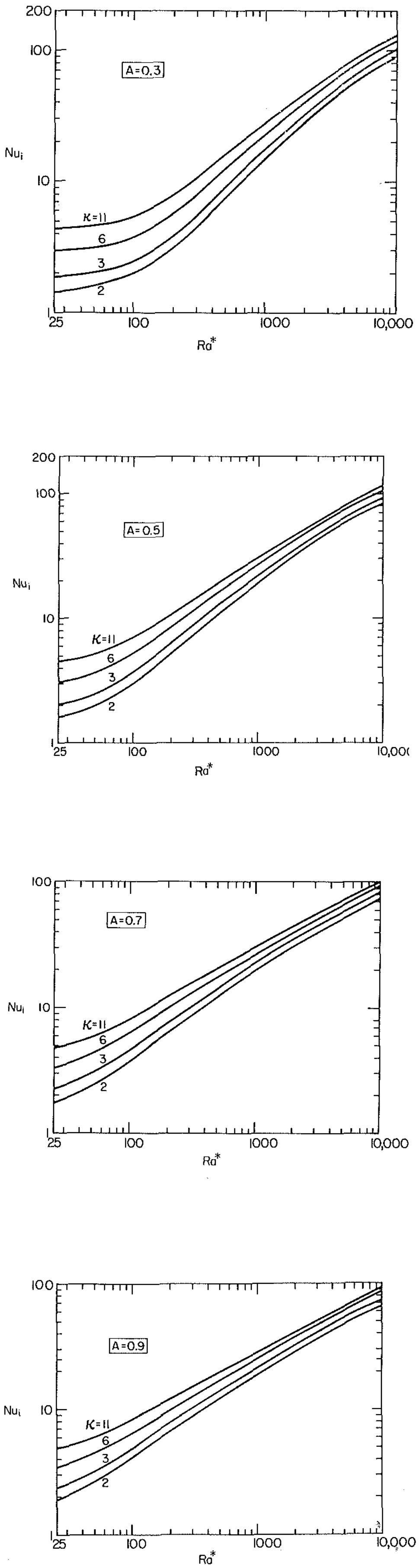

Fig. 5 Variation in heat transfer rates for $\kappa = 2,3,6$ and 11: (*a*) $A = 0.9$; (*b*) $A = 0.7$; (c) $A = 0.5$; and (d) $A = 0.3$

Table 1 Numerical results of Havstad and Burns [5] compared with present values of Nusselt number

κ	2.5				3.333				5				10			
A	0.8333				0.7143				0.555				0.555			
Ra*	90	60	30	21	105	70	35	24.5	120	80	40	28	135	90	45	31.5
Havstad & Burns	4.593	3.443	2.323	2.031	5.448	4.064	2.733	2.388	6.627	4.973	3.392	2.981	8.898	6.875	4.905	4.368
Present	4.271	3.273	2.275	2.007	5.071	3.876	2.691	2.374	6.242	4.801	3.384	3.005	8.673	6.794	5.009	4.534

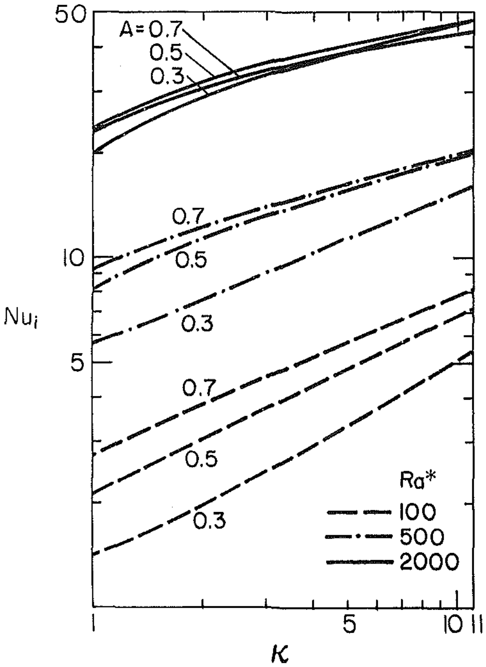

Fig. 6 Curvature effects on heat transfer rates for Ra* = 100, 500, and 2000

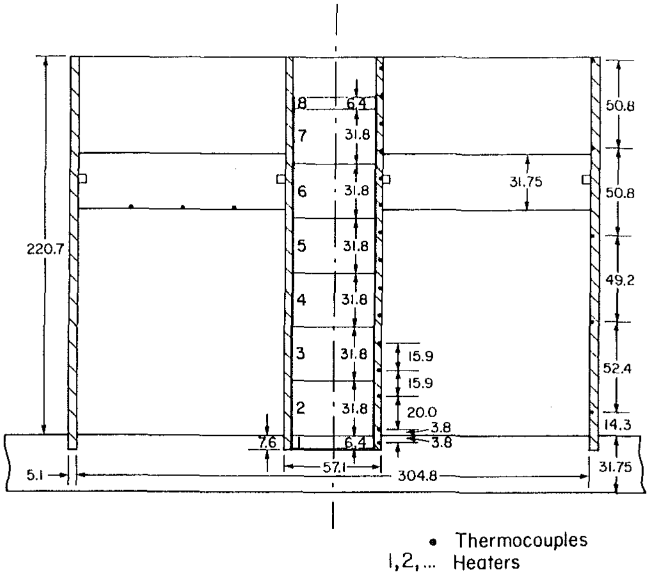

Fig. 7 Heaters and thermocouples arrangement for the experimental apparatus (all dimensions are in mm)

by Havstad and Burns. No other direct or indirect comparison is possible, since the numerial work of Hickox and Gartling [6] and experimental results of Reda [4] are applicable only for tall annuli.

Experimental Apparatus and Procedure

To model an annulus with inner wall heated at a constant temperature and the outer wall isothermally cooled, an experimental apparatus was designed and fabricated in the following way. First, the inner cylinder was constructed out of a brass cylinder, a glass-epoxy cylinder, and a hardwood rod. A hardwood rod of diameter 38.1 mm was shrink-fitted into a glass-epoxy cylinder of o.d. 54 mm, and 228.3 mm long. The o.d. of the glass-epoxy cylinder was reduced to 50.9 mm and eight Thermofoil heaters were wrapped on it. Out of these, six heaters, nos. 2 to 7 (see Fig. 7) were silicone rubber insulated thermofoil heaters (31.8 mm × 160 mm, 41.3 ohms), and were cemented on the cylinder with silicone-rubber cement. The other two heaters were Kaptan insulated (6.86 mm × 139.7 mm, 40.7 ohms) and were attached, one each on both ends (as shown in Fig. 7) with the help of stretch tape. The purpose of these two heaters was to guard against the end losses, particularly the axial conduction. All the heaters were wrapped as close to each other as possible and their leads were taken to the bottom of the glass-epoxy cylinder through a slot made in it.

The glass-epoxy cylinder with heaters mounted on it was then fitted into a brass cylinder of an equal length but o.d. of 57.1 mm. Before doing this, the brass cylinder was machined to make 2.5-mm-deep slots to run the thermocouple wires out. To reduce the error in temperature measurment, the thermocouple wires were run sideways before taking them to the bottom end (see [1]). This type of arrangement was preferred because the thermocouple attached to the wall either with cement or tape disturbs the flow field and indicates a temperature between the wall surface temperature and the temperature of the exposed surface. Fifteen thermocouples made out of 30 AWG Teflon insulated copper-constantan solid wires were cemented at locations shown in Fig. 7. The slots on the brass cylinder were then filled with the copper cement and sanded to have a smooth surface.

The thermocouples of the experimental apparatus were connected to a Doric datalogger, Model Digitrend 220. It had 80 working channels and was able to read temperatures to ±0.1°C.

A brass cylinder of 304.8 mm i.d. and 5.1 mm thick was used as the outer cylinder. Five thermocouples were attached to it by drilling the holes of 2.5 mm dia in its wall (Fig. 7). A copper tube of 12.7 mm dia was soldered to this cylinder to circulate cooling water, which was supplied by a Corola constant temperature circulator. This circulator had a control accuracy of ±0.1°C.

For the base plate and the top cover, 31.75-mm-thick phenolite laminated plastic sheet was used. The thermal conductivity of the material is very low ($k = 0.293$ W/m°C), whereas it has excellent mechanical properties and can be continuously operated at a temperature up to 120°C. The inner and outer cylinders were attached to the base plate as shown in Fig. 7. All the heater leads and thermocouple wires were taken out through the holes drilled in the plate. The top cover plate was provided with two O-rings, one each on the inner and outer side walls. Three thermocouples were cemented to its inner surface at radially equidistant locations (Fig. 7).

To provide and control the power in each heater a power panel with an independent circuit for each heater was constructed. Each circuit was provided with a variac to control the power input to the heater present in that circuit. To have a better control of power, all the variacs were connected to a voltage regulator through another step-down variac [1].

Temperatures within the porous medium were measured with copper-constantan grounded thermocouple probes with an inconel sheath of 3.2 mm diameter. These probes were positioned to within ±0.5 mm through holes in the top plate and were held in place by fitting at the top of the annular gap (see [1] for additional details).

To obtain a saturated porous medium, the annular gap was filled up to the required height with solid balls and distilled water. The balls were stirred so that they settled down in a random manner. A transparent epoxy plate was used to level the porous medium. Finally, the liquid was added in excess and the top plate was placed and pushed to the position where it rested on the balls, allowing extra water to come out. The foregoing procedure to fill the annulus was expected to result in avoiding the air voids.

Power was supplied to the first six heaters for the present experiments ($A=1$). Heater no. 1 worked as a guard against the bottom end losses, whereas heater no., 6 was used as a compensator for the top end losses. Every 2 to 3 hrs, the temperature distribution on the inner wall was checked to make sure that the inner surface was maintained at a constant temperature. Power in the heaters was changed depending upon the temperature being higher or lower in that region. Several adjustments of the power in heaters was required before the uniformity in the temperatures on the inner surface could be achieved within a reasonable accuracy. The steady state was obtained before recording the temperatures and power for any run. In general, 10 to 30 hrs time was required to get one set of readings. For the present experiment, the maximum variation on the hot wall from a mean value was 3.2 percent whereas on the cooled wall it was 5.3 percent.

To estimate the conduction loss through the top plate, temperatures at various locations on the upper surface of the top plate were recorded with the help of a digital thermometer.

By using a measured amount (weight) of glass beads to fill the annulus to the required height, the porosity of the medium ϵ was obtained by calculating the volume of glass beads and its total volume. The permeability of the working medium was then calculated by using the Kozeny-Carman equation [12]

$$K=\frac{d^2}{180}\,\frac{\epsilon^3}{(1-\epsilon)^2} \tag{11}$$

where d is the average diameter of glass beads. For the glass beads of 3 mm and 6 mm dia, ($\rho_s = 2537$ kg/m^3), the porosity ϵ was obtained as 0.3514 and 0.3698, respectively.

The thermal conductivity of the medium was calculated by using a correlation presented by Yagi, Kunii, and Wakao [13] for a stagnant porous medium saturated with liquid. The comparison between the measured thermal conductivity and the estimated values (using the correlation), presented by Katto and Masuoka [14] shows that the correlation predicts reasonable values for k_m. Moreover, the correlation was obtained based upon the radial heat transfer in saturated porous media, and is, thus, expected to predict quite reasonable values for k_m in the present case. This prediction was about 4 percent less than the value of k_m obtained by using the following relation

$$k_m=\epsilon k_f+(1-\epsilon)k_s \tag{12}$$

It may be noted that several investigators have used equation (12) to predict the stagnant thermal conductivity of the water-glass porous medium. The thermal conductivity of glass beads (borosilicate) has been taken as 0.9 W/m°C (20°C) to 0.92 W/m°C(50°C) based upon the composition supplied by the manufacturer.

Heat transfer data were collected by power input varying between 7 to 122 W, which produced a temperature difference up to 35.9°C for 3 mm beads, and 5 to 256 W for ΔT up to 34.5°C for 6 mm beads. The losses were estimated by calculating the conduction through the top plate and power inputs to the guard heaters (nos. 1 and 6), which used to compensate the axial losses through the top and bottom ends of the inner cylinder. No losses were deducted for the conduction through the bottom plate, since a thick cold layer is maintained in the lower region of the annulus, and hence, the temperature difference between the inner and outer surfaces of the base plate is not appreciable (see isotherms, Figs. 2 and 3). The estimate of losses was also checked by calculating the convection from the exposed surfaces [1].

Rayleigh number was calculated based upon the fluid properties and thermal conductivity of the medium at the mean temperature of the medium, i.e., $(T_i+T_o)/2$. Since deionized distilled water was used for the experiments and the properties of water are well established, the sources of error in Rayleigh number calculation was only due to errors involved in the measurement of T and in the prediction of k_m and K. Similarly, the accuracy of Nusselt number depended on the power and temperature measurements, and k_m. The temperatures could be measured only up to the first decimal place owing to the data logger limitation. A temperature correction based upon the power input was applied to the temperature readings, since the thermocouples were located a little away from the surfaces. Based on the conduction through the solid wall, this correlation was 0.1°C for 100 W on each surface. The maximum value of the correction was about 1.5 percent of the temperature difference ΔT. Altogether, the Rayleigh number and the Nusselt number reported here are expected to be within 5 percent of their real values. A detailed analysis of error and losses is presented in [1].

Experimental Results

Temperature distributions in the R-direction were measured at five different heights, $Z=0$, 0.25, 0.5, 0.75, and 1, in order to examine the behavior of heat transmission through the vertical annular porous layer. Figure 8 shows the typical nondimensional temperature at three radial locations, $R=0.25$, 0.5 and 0.75, along with the numerically obtained temperature profiles at those heights. The experimental Rayleigh numbers selected for these plots are close to the numerical values. In Fig. 8(*a*), the temperatures obtained for 3 mm dia glass beads and water experiments, have been compared with the numerical prediction for $\mathrm{Ra}^*=111$. For $0<Z<1$, the recorded temperatures θ are within 9 percent of the numerical results. At $Z=1$, the recorded temperatures are lower by 14 percent, which is mainly due to the conduction loss through the top plate.

In Fig. 8(*b*) the recorded temperatures for both 3 mm and 6 mm dia glass balls and water experiments are compared with numerical temperature distributions, for $\mathrm{Ra}^*\simeq 500$. Mostly the agreement is quite good. The maximum difference between the temperatures for 3 mm and 6 mm dia glass balls experiment is 6 percent. The largest difference between the numerical prediction and experimental value is 13 percent and exists for experiments with 3 mm balls.

The recorded temperatures for $\mathrm{Ra}^*=1998$ have been compared with numerical temperature distributions for $\mathrm{Ra}^*=2000$ in Fig. 8(*c*). Again, in this case the agreement is quite reasonable. The maximum difference between the two values is 16.5 percent. Some more temperature plots presented in [1] exhibit similar behavior as observed in Figs. 8(*a–c*). The temperatures reported by Seki, Fukusako, and Inaba [5] for vertical cavity filled with porous media show that when the

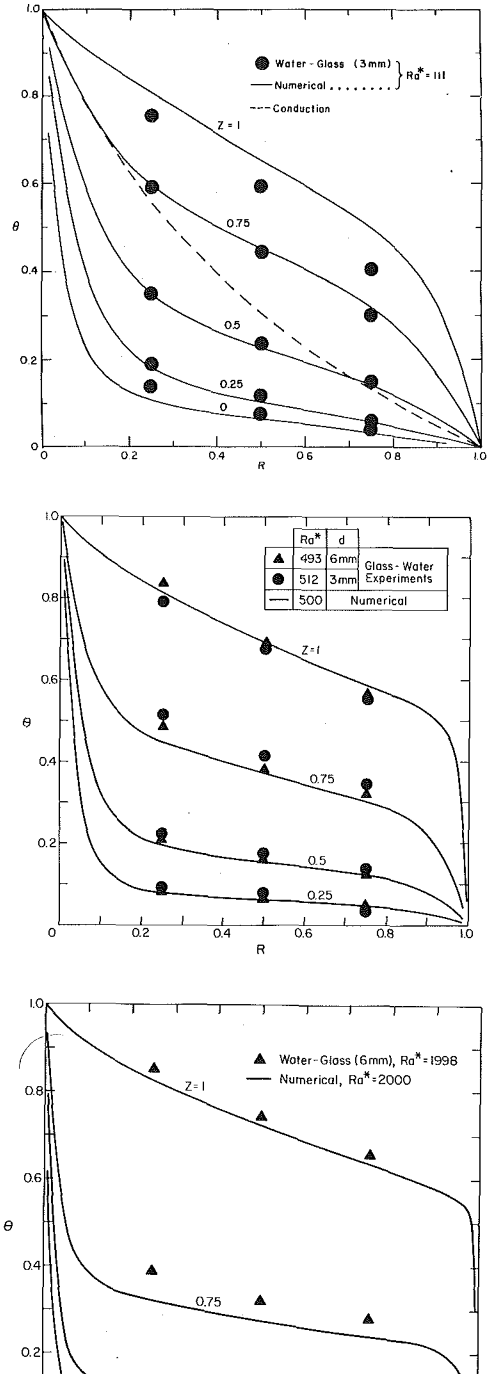

Fig. 8 Experimentally measured temperatures at various locations compared with the temperature distribution obtained numerically for $A = 1$, $\kappa = 5.338$: (a) $Ra^* = 111$, (b) $Ra^* = 500$, and (c) $Ra^* = 2000$.

temperature difference across the cavity ΔT is increased, the recorded temperatures deviate greatly from the numerical prediction. For glass-water experiments, they have reported that θ at the cavity center is 42 percent higher than the numerical value, when ΔT is 40.7°C, whereas for $\Delta T = 10.3$°C, the difference is only 7 percent. No such large deviation between the experimental and numerical values of θ is observed in the present case, for any increase in ΔT. It may be noted that for 6 mm glass beads experiments, ΔT for $Ra^* = 493$ and 1998 are 8.6°C and 36.04°C, respectively.

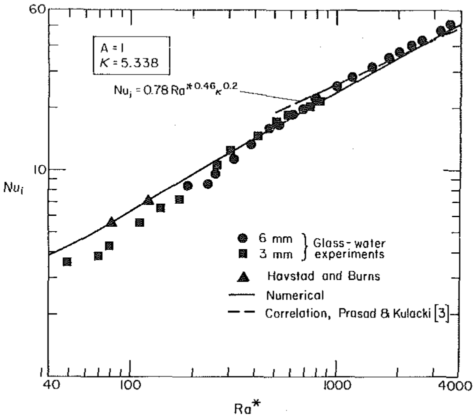

Fig. 9 Experimentally obtained Nusselt number compared with the numerical prediction for $A = 1$ and $\kappa = 5.338$ (water-glass experiments)

Optically measured temperature fields by Klarsfeld [16] show that the temperatures at the cavity center are a little lower for $A = 2.25$ and are higher by a maximum of 8 percent for $A = 4.5$, for the range of Rayleigh number reported by him.

The average Nusselt numbers on the inner wall are presented in Fig. 9 for the Rayleigh number varying between 49 and 3582, and have been compared with the numerical results. Some of the Havstad and Burns values for Nu_i [5] are also plotted for the present aspect and radius ratios. Since their correlations are valid only for $L/r_0 \geq 1$ (present value is 0.813), the plotted values of Nu_i have been approximated from their numerical results.

For $Ra^* < 300$, the experimental values for Nusselt number are less than those obtained numerically either by us or by Havstad and Burns [5], and for $Ra^* > 700$, they are a little higher. The maximum deviation in the upper range of Ra^* is 5 percent from the numerical predictions. In the lower range, the maximum difference between the two values is 25 percent (for $Ra^* = 70$), but mostly they are within 16 percent of the theoretical values. One of the reasons for the experimental values being lower may be the conduction losses through the top and bottom plates, and hence, the absence of perfectly insulated horizontal boundaries. This results in a modified nonlinear temperature distribution on the top and bottom surfaces (see Fig. 8(*a*)). As has been reported by Raithby and Wong [17], the linear temperature profile horizontal boundary conditions result in lower values of Nusselt number as compared to zero heat flux boundary conditions for air-filled vertical cavity. The differences has been reported to be maximum at $A = 1$, and reduces as A increases.

As the Rayleigh number increases the temperature distribution on the upper boundary of the medium gets closer to the temperature profiles predicted for perfectly insulated boundary conditions (see Figs. 8(*b*) and 8(*c*)). Hence the effects of conduction loss through the top plate diminish, and a better agreement between the experimental and numerical results are observed.

The correlation obtained for the numerical results, in the present case is

$$Nu_i = 0.485 \ Ra^{*0.564}, \quad 200 \leq Ra^* \leq 5000 \tag{13}$$

which is very close to the Nusselt number expression

$$Nu_i = 0.448 \ Ra^{*0.581}, \quad Ra^* > 450 \tag{14}$$

obtained from the experimental data only. Equation (14) correlates the experimental values of Nusselt number within 3.7 percent.

In Fig. 10, the present experimental results are also compared with the generalized correlation for $A = 1$ presented in [3], i.e.,

$$Nu_i = 0.78 \ Ra^{*0.46} \kappa^{0.20}, \quad Ra^* > 500, \ \kappa \geq 5. \tag{15}$$

For $500 < Ra^* < 600$, the difference between the Nusselt number predicted by equation (15) is up to 18 percent, but as Ra^* increases, this difference is reduced, and is within 6 percent for $Ra^* > 900$. It may be noted that the foregoing correlation is based upon the numerical results for several radius ratios ($\kappa > 5$), and represents the average values of exponents for Ra^* and κ [3]. As has already been discussed, the slope of Nu_i versus κ curve on log-log plot changes with change in Ra^* or κ (see the discussions on numerical results, also [3]).

In the overlapping range of Rayleigh numbers for 3 mm and 6 mm glass beads data, it is observed that the Nusselt numbers for 6 mm beads are mostly lower than that for 3 mm beads, though the difference is not large. A similar behavior is exhibited by the experimental data of Schneider [18], Buretta and Berman [19], and Combarnous [20] for various sizes of balls. In fact, Buretta and Berman's [19] results for 14 mm beads deviate by as much as 16 percent compared to that for 6 mm beads. This is mainly due to the wall channeling effects of fluid, which grow stronger and stronger as the size of the solid particles is increased resulting in higher porosity and permeability on the walls for any given size of the enclosure.

In the absence of strong channeling effects, a close agreement between the experimental and numerical values of Nusselt number has been obtained for Ra^* up to 4000 in the present case. Not only that, the experimentally measured temperatures at these Rayleigh numbers are also reasonably close to the theoretical prediction. This clearly indicates that the formulation based on the Darcy's law can be applied to the physical modeling of porous layer at least up to the highest value of Rayleigh number reported here. This value is four times more than what Seki et al. [15] have reported based upon the deviation of the experimental values of Nusselt number from the theoretical prediction. The lower values of Nusselt number (at high Ra^*) reported by Seki et al. and other ionvestigators is mainly due to wall channeling effects, since those data are usually obtained with large balls. It may be interesting to know the size of the balls for which channeling effects start dominating the heat transfer rates. It is speculated that for horizontal and vertical layers it would depend on the width of the layers, and for annular layer it would also depend on the diameter of the inner cylinder.

Conclusions

Numerical results obtained for natural convection in a vertical shallow annulus filled with a saturated porous medium indicate the following:

1 An increase in the radius ratio shifts the isotherms toward the hot wall. This results in a thinner boundary layer on the hot wall and a thicker thermal boundary layer on the cold wall. Also the thickness of the cold layer at the bottom increases with an increase in κ.

2 The multicellular flow behavior observed in the case of shallow rectangular cavity, diminishes as the radius ratio is increased. The higher the radius ratio, the lower is the aspect ratio required to introduce multicellular flow structure.

3 As the radius ratio is increased or the aspect ratio is decreased, the conduction and asymptotic flow regimes get extended (in terms of Ra^*), and, as such, the boundary layer flow regime starts at much higher Rayleigh numbers.

4 The slope of the $\ln(Nu_i)$ versus $\ln(\kappa)$ curve changes as the radius ratio increases, the highest slope being at $\kappa = 1$. The higher the values of Ra^*, A, and κ, the smaller is this slope.

5 The sink temperature for the boundary layer on the inner wall decreases with an increase in the radius ratio. This brings the annulus results close to the heat transfer results for a heated vertical cylinder embedded in saturated porous media, whereas the end effects diminish this behavior. Hence, the lower the aspect ratio, the higher are the values required for Ra^* and κ, for the two results to be closer.

To verify the numerical results, experiments have been conducted for the porous media produced by water saturated glass beads of 3 mm and 6 mm diameters, for $\kappa = 5.338$, $A = 1$, and $49 < Ra^* < 3582$. The agreement between the recorded temperatures for the medium and the numerical values of θ is quite reasonable for the entire range of Rayleigh number. Heat transfer results agree to within 5 percent of the numerical prediction for $Ra^* > 700$. In the lower range of Ra^*, the experimentally obtained Nusselt numbers are lower than the numerical values. The heat transfer rates obtained by using the correlation of Prasad and Kulacki [3] also agree well with the experimental results. The present agreement between theoretical and experimental Nusselt numbers and the temperatures clearly indicate that the formulation based on Darcy's law holds good for the natural convection in porous media, even for high Rayleigh numbers, provided the heat transfer rates are not dominated by the wall channeling of fluid.

References

1 Prasad, V., *Natural Convection in Porous Media—An Experimental and Numerical Study for Vertical Annular and Rectangulr Enclosures*, Ph.D. dissertation, University of Delaware, 1983.

2 Prasad, V., and Kulacki, F. A., "Natural Convection in a Rectangular Porous Cavity with Constant Heat Flux on One Vertical Wall," ASME JOURNAL OF HEAT TRANSFER, Vol. 106, 1984, pp. 152–157; also in *Heat Transfer in Porous Media*, ASME HTD Vol. 22, 1982.

3 Prasad, V., and Kulacki, F. A., "Natural Convection in a Vertical Porous Annulus," *International Journal of Heat and Mass Transfer*, Vol. 27, 1984, pp. 207–219.

4 Reda, D. C., "Natural Convection Experiments in a Liquid Saturated Porous Medium Bounded by Vertical Coaxial Cylinders," ASME JOURNAL OF HEAT TRANSFER, Vol. 105, 1983, pp. 795–802.

5 Havstad, M. A., and Burns, P. J., "Convective Heat Transfer in Vertical Cylindrical Annuli Filled with a Porous Medium," *International Journal of Heat and Mass Transfer*, Vol. 25, 1982, pp. 1755–1766.

6 Hickox, C. E., and Gartling, D. K., "A Numerical Study of Natural Convection in a Vertical Annular Porous Layer," ASME Paper No. 82-HT-68, 1982.

7 Prasad, V., and Kulacki, F. A., "Convective Heat Transfer in a Rectangular Porous Cavity—Effect of Aspect Ratio on Flow Structure and Heat Transfer," ASME JOURNAL OF HEAT TRANSFER, Vol. 106, 1984, pp. 158–165.

8 Gosman, A. D., Pun, W. M., Runchal, A. K., Spalding, D. B., and Wolfshtein, M., *Heat and Mass Transfer in Recirculating Flows*, Academic Press, 1969.

9 Roache, P. J., *Computational Fluid Dynamics*, Hermosa, Albuquerque, N.M., 1976.

10 Lee, Y., Korpela, S. A., and Horne, R. N., "Structure of Multi-Cellular Natural Convection in a Tall Vertical Annulus," *Proceedings, 7th International Heat Transfer Conference*, Vol. 2, edited by U. Grigul, et al., Hemisphere Publishing Corp., Washington, D.C., 1982, pp. 221–226.

11 Minkowycz, W. J., and Cheng, P., "Free Convection about a Vertical Cylinder Embedded in a Porous Medium," *International Journal of Heat and Mass Transfer*, Vol. 19, 1976, pp. 805–813.

12 Bear, J., *Dynamics of Fluids in Porous Media*, Elsevier, New York, 1972.

13 Yagi, S., Kunii, D., and Wakao, N., "Radially Effective Thermal Conductivities in Packed Beds," *International Developments in Heat Transfer*, ASME, 1961, pp. 742–749.

14 Katto, Y., and Masuoka, T., "Criterion for the Onset of Convective Flow in a Fluid in a Porous Medium," *International Journal of Heat and Mass Transfer*, Vol. 10, 1967, pp. 297–309.

15 Seki, N., Fukusako, S., and Inaba, H., "Heat Transfer in a Confined Rectangular Cavity Packed with Porous Media," *International Journal of Heat and Mass Transfer*, Vol. 21, 1978, pp. 985–989.

16 Klarsfeld, S. M., "Champs de temperature associes aux mouvements de convection naturelle dans un milieu poreux limite," *Revue Generale de Thermique*, Vol. 9, 1970, pp. 1403–1424.

17 Raithby, G. D., and Wong, H. H., "Heat Transfer by Natural Convection Across Vertical Layers," *Numerical Heat Transfer*, Vol. 4, 1981, pp. 447–457.

18 Schneider, K.-J., "Investigation of the Influence of Free Thermal Convection on Heat Transfer through Granular Material," Paper No. II-4, *Proceedings, Progress in Refrigeration Science and Technology*, 11th International Congress on Refrigeration, 1963, pp. 247–254.

19 Buretta, R. J., and Berman, A. S., "Convective Heat Transfer in a Liquid-Saturated Porous Layer," *Journal of Applied Mechanics*, Vol. 98, 1976, pp. 249–253.

20 Combarnous, M., "Convection Naturelle et Convection Mixte dans une Couche Poreuse Horizontale," *Revue General Thermique*, Vol. 9, 1970, pp. 1335–1355.

Laser-Induced Thermophoresis and Particulate Deposition Efficiency

T. F. Morse

C. Y. Wang
Division of Engineering,
Brown University,
Providence, R.I.

J. W. Cipolla, Jr.
Department of Mechanical Engineering,
Northeastern University,
Boston, Mass.

The interaction of laser radiation and an absorbing aerosol in a tube flow has been considered. The aerosol is produced by external heating of reactants as in the MCVD (Modified Chemical Vapor Deposition) process to produce submicron size particles in the manufacture of optical fiber preforms. These particles are deposited by thermophoretic forces on the inner wall of the tube as they are convected by a Poiseuille velocity profile. Axial laser radiation in the tube interacts with the absorbing particles, and the laser heating of the gas induces additional thermophoretic forces that markedly increase the efficiency of particulate deposition. A particle concentration dependent absorption coefficient that appears in the energy equation couples the energy equation to the equation of particle conservation, so that a nonlinear set of coupled partial integro-differential equations must be solved. Numerical solutions for aerosol particle trajectories, and thus deposition efficiencies, have been obtained. It is shown that laser enhanced thermophoresis markedly improves the deposition efficiency.

Introduction

Laser heating of an absorbing aerosol affects the motion of aerosol particles in a tube or channel flow. The purpose of this work is to analyze numerically the equations describing the motion of such particles in a tube in which the walls may be heated with an arbitrary distribution of temperature, and in which axial laser radiation interacts with the aerosol particles (see Fig. 1). This interaction induces additional thermophoretic motion through the presence of a particle density dependent source term in the energy equation. It is assumed that the aerosol is produced uniformly by a chemical reaction that goes to completion when the gas temperature reaches a certain value. These approximations model the circumstances in which silicon dioxide and germanium dioxide particles are formed by reacting silicon and germanium tetrachloride with oxygen in the MCVD process employed in the fabrication of preforms from which optical fibers are drawn. Subsequent motion of the aerosol particles is determined by the longitudinal velocity component of the background gas, which has an assumed Poiseuille distribution (buoyancy effects are neglected in this work), and the thermophoretic velocity of the aerosol particles that is obtained by a solution of the coupled energy and particle conservation equations. Such approximations and geometry have been the focus of several recent studies [1-4].

The new aspect of our research is the inclusion of axial laser heating that influences markedly the thermophoretic motion of the particles [5-7]. This corresponds to the addition of a volumetric laser heating term in the energy equation, that, even in the case of constant physical properties, does not permit the independent solution of the temperature and the particle concentration fields. Thus the laser heating is determined by particle absorption, and the absorption of energy induces significant thermophoretic motion in the aerosol by the local indirect heating of the background gas. The submicron particles become heated on a time scale that is much faster than any fluid mechanical or diffusion time of the system [5].

From some simple analytic considerations of the fundamental equations, it has been shown that the presence of any laser intensity far downstream, in an asymptotic sense, is adequate to insure that all particles will reach the wall of the tube, insuring a deposition efficiency of 100 percent [5]. Our numerical calculations also confirm this result, and indicate how rapidly this asymptote is reached. In the present study, we have examined the combined effects of the distribution of temperature as a result of localized wall heating, and the distribution of laser intensity on the particle deposition as a function of length.

The Fundamental Equations

We consider a fully developed laminar flow in a tube, with a heated region that may vary in extent. A laser beam propagates axially along the tube and interacts with the aerosol, which is produced uniformly at a critical reaction temperature (see Fig. 1). In the absence of radiation, which couples the energy equation and the equation for particle continuity, the equations describing the thermal behavior of our system have been studied by numerous authors [1-4]. It is noted that the solutions for heat transfer in a tube with a Poiseuille velocity distribution have been known for many years, and recent treatments have centered upon more efficient methods of obtaining eigenvalues for what is a classic Sturm-Liouville problem [8-10]. Numerical solutions however, with a graphic display of physical quantities of interest, seem to convey information in a clearer fashion, particularly if the concern is with aerosol particle trajectories. For the case in which it is assumed that at a given temperature the aerosol is uniformly produced, deposition efficiency may be easily found by following the path line for a given particle until it hits the wall boundary. Conservation of particles then

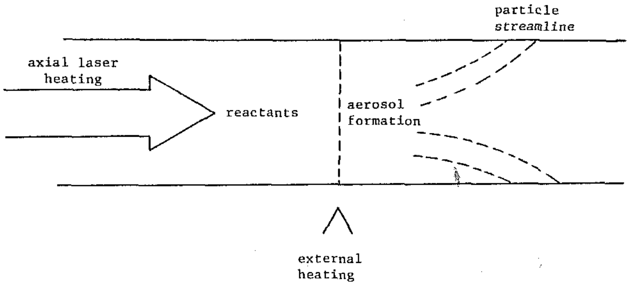

Fig. 1 Schematic of laser-enhanced MCVD

Contributed by the Heat Transfer Division for publication in the JOURNAL OF HEAT TRANSFER. Manuscript received by the Heat Transfer Division May 5, 1983.

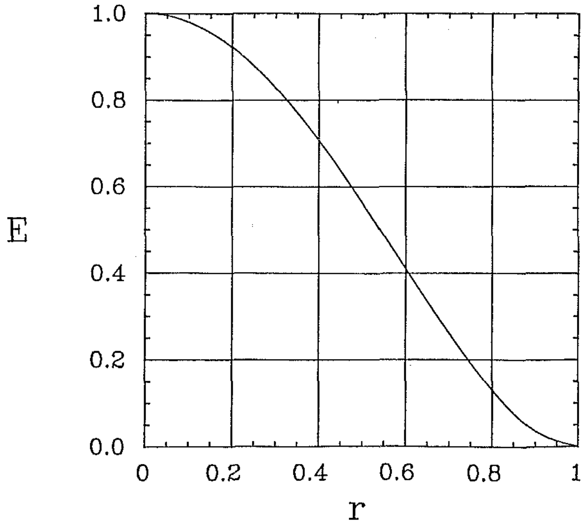

Fig. 2 Particle deposition efficiency versus dimensionless radius, $E = 1 - 2r^2 + r^4$, where r is the initial radial position of the particle path line

yields the efficiency curve shown in Fig. 2. It is more convenient to consider solutions that produce the particle trajectories rather than solve for the spatial dependence of particle concentration.

The equations that are of importance in describing the aerosol motion are the energy equation, the momentum equation, and the equation for conservation of aerosol particles. In this work, as in that of previous authors interested in aerosol deposition, we have neglected any buoyancy effects that may be associated with heating of the gas from either an external source, or from laser heating. A simple assessment of buoyancy effects caused by laser heating is presented elsewhere [7]. Thus we assume that the velocity distribution is a fully developed parabolic Poiseuille profile. This leaves the energy equation to be solved in conjunction with the equation for conservation of particles. It should be understood, however, that our assumptions merely approximate the true situation in optical fiber preform construction and that relatively complicated secondary flows may exist [11]. The energy equation is written as follows:

$$\rho c_p U \frac{\partial T}{\partial Z'} = \frac{k'}{r'} \frac{\partial}{\partial r'}\left(r' \frac{\partial T}{\partial r'}\right) + Q'(r',z') \qquad (1)$$

The gas density, specific heat, and thermal conductivity are given by ρ, c_p, and k', respectively. If we now make equation (1) dimensionless with $z' = r_o z\mathrm{Pe}$, $r = r'/r_o$, $\theta = T/(T_{(\max)} - T_{(\min)})$, and set $U = 2U_m(1-r^2)$, then

$$(1-r^2)\frac{\partial \theta}{\partial z} = \frac{\partial^2 \theta}{\partial r^2} + \frac{1}{r}\frac{\partial \theta}{\partial r} + Q \qquad (2)$$

where $Q = Q' r_o^2 / k'(T_{\max} - T_{\min})$, and axial conduction has been neglected in comparison with axial convection. The laser heating term Q must be obtained from the equation of radiative transfer. If scattering and emission are neglected, then the only contribution to the intensity is that due to the monochromatic and uni-directional incident beam.

$$Q' = \kappa I_o \exp\left(-\beta^2 r^2 - \int_o^{z'} \kappa dz''\right) \qquad (3)$$

The maximum laser intensity is I_o, and β is a parameter describing the radial decay of the Gaussian profile. The absorption coefficient κ is proportional to the local particle concentration c, and the subscript o refers to reference conditions at the location at which the aerosol is initially formed. Thus the laser intensity has an axial variation that depends on an integral over the spatially dependent particle concentration. This particle concentration must be obtained from a solution of the equation for aerosol transport, i.e., the particle continuity equation. Again a Poiseuille velocity distribution is assumed, and the equation for particle transport is written below

$$\mathbf{U} \cdot \nabla C + \nabla \cdot (-D \nabla C + C \mathbf{V}_T) = 0 \qquad (4)$$

The Brownian diffusion coefficient is given by D, and the thermophoretic velocity may be written as

$$\mathbf{V}_T = -K \frac{\nu}{T} \nabla T \qquad (5)$$

The kinematic viscosity is ν, and K is the thermophoretic coefficient. A semiempirical approximation for K valid for all Knudsen numbers has been proposed by Talbot et al. [12]. It will be taken to be a constant whose magnitude is close to 1. In the cases we will consider, except in a small region near the wall, the thermophoretic velocity will dominate any diffusion effects (large Schmidt number), and $D/\nu << 1$. In dimensionless form, with $\phi = c/c_o$, this equation may be written as follows, where we have neglected axial thermophoresis in the large Pe limit.

Nomenclature

c = particle concentration (m^{-3})
c_o = reference particle concentration
c_p = specific heat at constant pressure (kJ/kg K)
D = particle diffusion coefficient (m^2/s)
h = difference in the radial direction
I_o = laser intensity (W/m^2)
k' = thermal conductivity of gas (W/m K)
k = difference in the axial direction
K = thermophoretic coefficient
L = flame width scale
Pr = Prandtl number = (ν/α)
Pe = Peclet number = $(2r_o U_m/\alpha)$
Q = volume heat flux = $Q' r_o^2/k(T_{(\max)} - T_{(\min)})$
Q' = volumetric heat flux (W/m^3)
r = dimensionless radial coordinate ($= r'/r_o$)
r' = radial coordinate
r_o = tube radius (m)
Sc = Schmidt number
T = fluid temperature (K)
T_{in} = inlet gas temperature (K)
$T_{(\max)}$ = maximum temperature at the boundary (K)
$T_{(\min)}$ = minimum temperature at the boundary (K)
U = axial velocity (m/s)
U_m = mean velocity (m/s)
V_T = thermophoretic velocity (radial direction), equation (5)
w = ratio = k/h^2
z = dimensionless axial coordinate = $z'/(r_o\mathrm{Pe})$
z' = axial coordinate
α = thermal diffusivity (m^2/s)
β = dimensionless laser parameter = $(\beta' r_o)$
β' = laser parameter
κ = absorption coefficient (1/cm)
κ_o = absorption coefficient when $c = c_o$
λ = wavelength of laser beam
μ = dynamic viscosity (kg/m s)
ν = kinematic viscosity (m^2/s)
ρ = density (kg/m^3)
ϕ = dimensionless particle concentration = (c/c_o)
θ = dimensionless temperature = $T/(T_{(\max)} - T_{(\min)})$

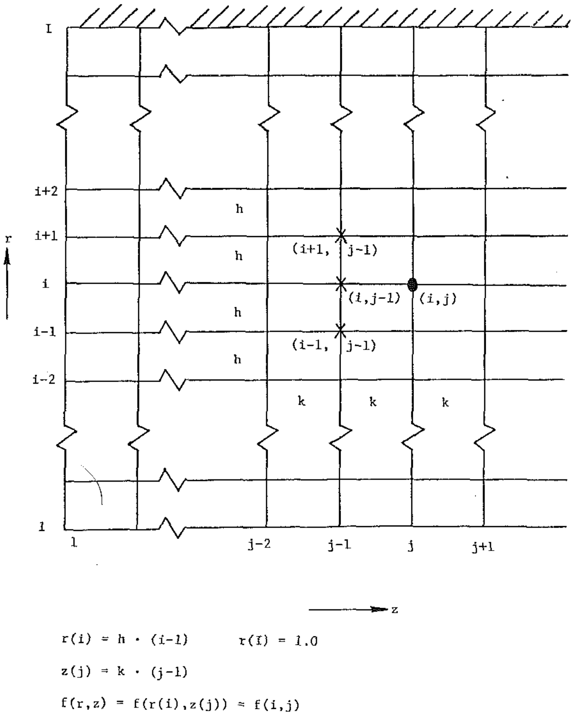

Fig. 3 Designation of mesh points for numerical calculation

$$(1-r^2)\frac{\partial\phi}{\partial z}=\frac{\mathrm{Pr}K}{r}\,\frac{\partial}{\partial r}\left(r\frac{\phi}{\theta}\,\frac{\partial\theta}{\partial r}\right)\tag{6}$$

Since the absorption coefficient is proportional to particle concentration, it may be expressed as $\kappa=\kappa_o\phi$, where κ_o is the constant absorption coefficient for the initial concentration c_o. Thus equations (2), (3), (6) represent a coupled nonlinear set of integro-differential equations that must be solved with appropriate boundary conditions.

We shall consider two sets of boundary conditions. First, as an analog to the classic Graetz problem, we shall assume at $z=0$ a constant inlet temperature, a constant inlet particle concentration, and a laser intensity as a specified function of radius (Gaussian). The wall boundary conditions will be such that the wall temperature is held at a lower constant temperature than the inlet temperature. The second set of boundary conditions more closely approximates the actual physical situation in optical fiber production, and we assume a wall temperature distribution taken from experiment, that approximates the effects of the heating of the tube [3]. The aerosol particle concentration is taken to be zero until the point at which the local temperature in the tube becomes equal to the reaction temperature (which we may set as a parameter), and the reaction goes instantly to completion to produce the aerosol. This appears to be a valid assumption at the low flow rates considered [2].

We have considered radiative absorption by the particles only and have neglected scattering. This will be the case for submicron size particles interacting with radiation in the 9-10 micron range. This is the Rayleigh regime, in which scattering is of lesser importance than absorption (for particles with a nonzero component of the imaginary part of the refractive index) [13-15]. For aerosols associated with optical fiber preforms, the particles have a Gaussian distribution peaked sharply about .3 microns, with over 95 percent of the mass of particles occurring with diameters less than .5 microns [16-17]. The interaction of these particles with 10.6 micron radiation would therefore occur in the Rayleigh limit. We have also neglected reradiation of the particles, which, at higher temperatures, may be significant. This effect will be considered in a future work.

Discussion of the Numerical Solution

A finite difference technique has been used to solve for both the temperature and the concentration from equations (2), (3), and (6). The notation and grid employed are shown in Fig. 3. The energy equation is a parabolic partial differential equation in the absence of the inhomogeneous term, and may be solved by an explicit method [18]. With the concentration dependent inhomogeneous term present, we have chosen to solve it iteratively in conjunction with the concentration equation. The difference form of the energy equation (2) is given as follows:

$$\begin{aligned}\theta(i,j+1)=\theta(i,j)+w/(1-r^2)\Big\{&\theta(i+1,j)\\ &-2\theta(i,j)+\theta(i-1,j)+1/2(i-1)[\theta(i+1,j)\\ &-\theta(i-1,j)]\Big\}+k/(1-r^2)Q(i,j)\end{aligned}\tag{7}$$

where $w=k/h^2$.

The concentration equation and boundary conditions have been approximated as follows:

$$\begin{aligned}&\phi(i,j+1)=\phi(i,j)\left\{1+\frac{k}{1-r^2}\,\frac{\mathrm{Pr}K}{\mathrm{Pe}}\left(\frac{G_1}{r}+G_2\right)\right\}\\ &\quad+\frac{k}{1-r^2}\,\frac{\mathrm{Pr}K}{\mathrm{Pe}}\,\frac{G_1}{2h}[\phi(i+1,j)-\phi(i-1,j)]\quad 1<i<I\\ &\phi(1,j+1)=\phi(2,j+1)\\ &\phi(I,j+1)=\phi(I-1,j+1)\Big/\left(1+h+\frac{G_2}{G_1}h\right);\\ &\qquad G_1=\frac{\partial}{\partial r}\ln\theta,\quad G_2=\frac{\partial G_1}{\partial r}\end{aligned}\tag{8}$$

When θ and ϕ are known at $z(j)$, we can march downstream to find values at $z(j+1)$. The energy equation is first solved for θ by evaluating Q at $z(j)$. Subsequently, θ is substituted into the concentration equation to solve for ϕ. If we substitute this back into the energy equation, we can find a second iterate for the temperature. The foregoing iteration procedures are repeated until values from two subsequent runs are in substantial agreement. The drawback of this marching process, as is known, is that there is an upper limit on k, as defined in Fig. 3. When k is greater than a critical value, we will encounter instabilities. In addition, there is a lower limit, imposed by the problem itself, on h associated with the term $(1-r^2)^{-1}$ in equation (6). The values of h and k used in the computation are 0.1 and 0.001, respectively.

The numerical results have been checked in several limiting cases. For the case of zero laser intensity, the energy equation reduces to a solution of the Graetz problem, and our numerical procedure reproduces the correct temperature field in this limit [8]. For the uniform inlet temperature and constant wall temperature (with PrK = 1), the asymptotic deposition efficiency may be found analytically [19-21]. Our numerical calculations for deposition for zero laser intensity asymptotically approach the analytical result (for PrK = 1) of [21]. For PrK = 0.63, which corresponds to a case of interest and for which no analytical result is available, our numerical results (Fig. 13) are not inconsistent with the results of Walker et al. [2].

Laser Heating and Particle Trajectories

In this section, we wish to examine some specific examples in which laser radiation has a significant influence on the aerosol particle trajectories. Table 1 gives the gas properties used in our calculation.

Table 1 Table of properties

Average temperature for gas properties, $T_{av} = 1100$ K
Kinematic viscosity, $\nu = 1.386 \times 10^{-4} \mathrm{m}^2/\mathrm{s}$
Thermal conductivity, $k' = 0.073$ W/mK
Thermal diffusivity, $\alpha = 1.97 \times 10^{-4} \mathrm{m}^2/\mathrm{s}$
Prandtl number = 0.70
Mean velocity, $U_m = 0.2$ m/s
Tube radius, $r_0 = 0.7$ cm
Peclet number = 14.2
Absorption coefficient, $\kappa_o = 0.1 \ \mathrm{cm}^{-1}$
Thermophoretic coefficient, $K = 0.9$

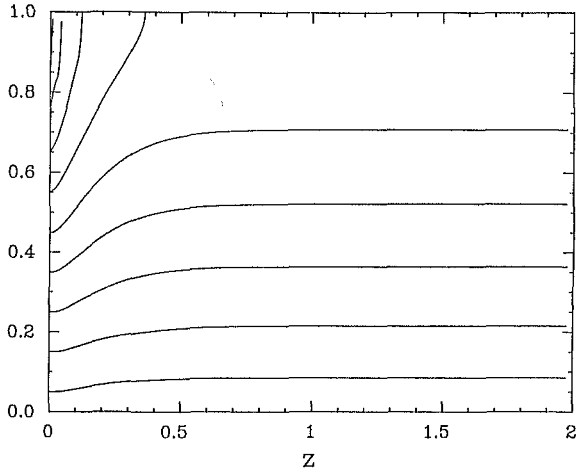

Fig. 4 Particle trajectories for $T_{in} = 1500$ K, $T_w = 500$ K, $I_o = 0$ W/cm^2

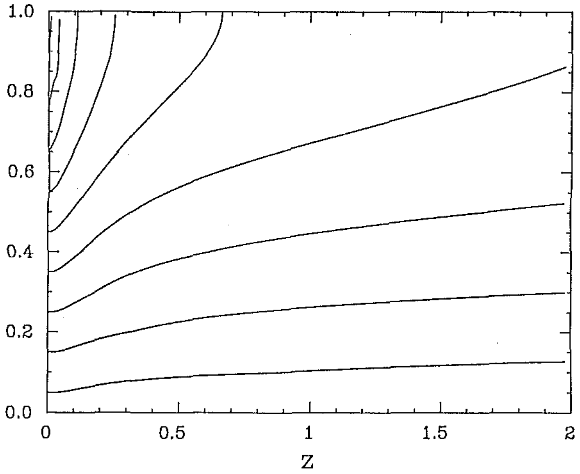

Fig. 5 Particle trajectories for $T_{in} = 1500$ K, $T_w = 500$ K, $I_o = 20$ W/cm^2, $\beta = 1.0$

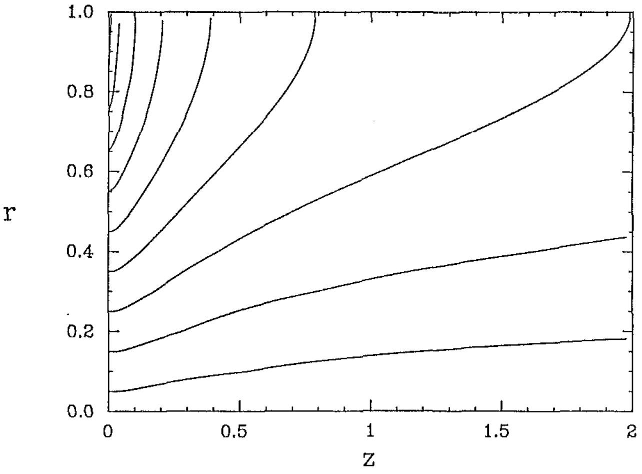

Fig. 6 Particle trajectories for $T_{in} = 1500$ K, $T_w = 500$ K, $I_o = 60$ W/cm^2, $\beta = 1.0$

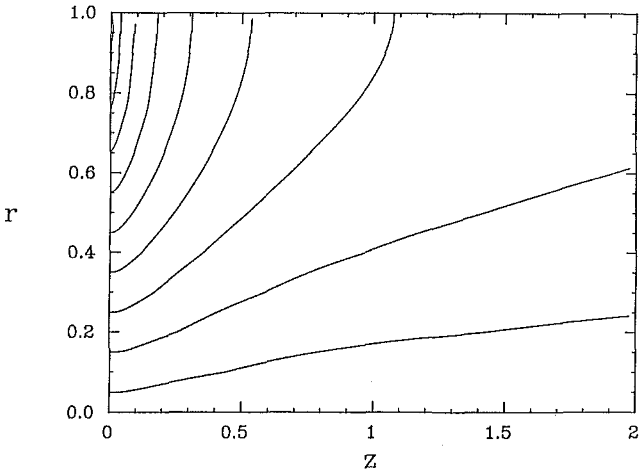

Fig. 7 Particle trajectories for $T_{in} = 1500$ K, $T_w = 500$ K, $I_o = 120$ W/cm^2, $\beta = 1.0$

In Fig. 4, for these conditions, we see the solution of the coupled energy and particle equations for the case in which the inlet conditions are specified at 1500 K, the wall temperature is held at 500 K, and the aerosol concentration is such that at the inlet, the absorption coefficient, κ_o is given as 0.1 cm^{-1}. This appears to be a typical value for the absorption of 10-micron carbon dioxide radiation by silicon dioxide particles in the MCVD process [5]. The value of the thermophoretic coefficient $K = 0.9$ is somewhat too high, but it tends to correct for other simplifying assumptions that have been made with respect to fixing thermal properties at an average temperature of 1100 K. From Fig. 4, we see that only particles entering the tube at radii between 0.55 and 1.0 will eventually impact the tube wall. From Fig. 2, this corresponds to an efficiency of 48 percent. If we follow the trajectory of a particle that originates at radial position r, and impacts the wall at some position z, the efficiency E represents the ratio of particles that hit the wall (up to that position z) to those that enter the tube. That is, the efficiency is the fraction of the particle flux that enters the tube in the annular region between r and 1. All other particles will be convected out the end of the tube. This is a consequence of the decrease in temperature as the aerosol flows away from the heated zone, and the decrease in the temperature gradient that drives particles to the wall. We note that in Fig. 4, for the particles starting from $r = 0.45$, that even at a dimensionless $z = 0.5$, an asymptote has been reached. In dimensional terms, for Pe = 14.2, this corresponds to 7.1 tube radii. Since the Graetz solution indicates an exponential relaxation of the gas temperature to the wall temperature, the early occurrence of the horizontal particle trajectories is not unexpected. We now consider the same initial conditions, with the addition of axial laser radiation. In Figs. 4–7 we see the effect of increasing laser intensity. The laser parameter β (see equation (3)) is taken to be 1.0. This is a measure of the half-width of the Gaussian laser profile, and indicates how quickly the laser intensity decreases from its maximum value at the centerline of the tube. The maximum temperature reached in this series of figures is slightly less than 1900 K, with 120 W/cm^2 of laser radiation (see Fig. 7). This corresponds to an additional 400 K of heating associated with the axial laser.

As the laser intensity increases, the streamlines are inclined more sharply toward the wall. For a tube sufficiently long, all of the streamlines will impact upon the wall, even with an

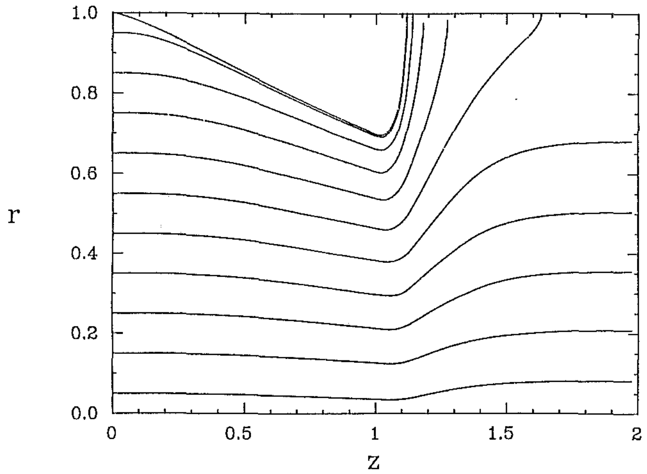

Fig. 8 Particle trajectories for $T_{in} = 1100$ K, "burner heated wall," $\beta = 1.0, I_0 = 0$ W/cm^2

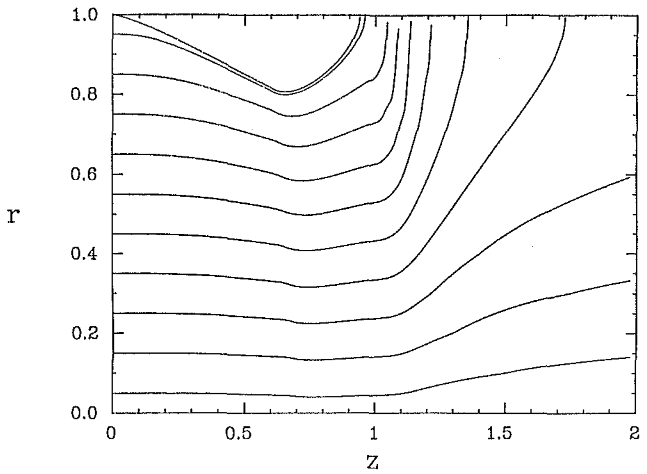

Fig. 10 Particle trajectories for $T_{in} = 1100$ K, "burner heated wall," $\beta = 1.0, I_0 = 60$ W/cm^2

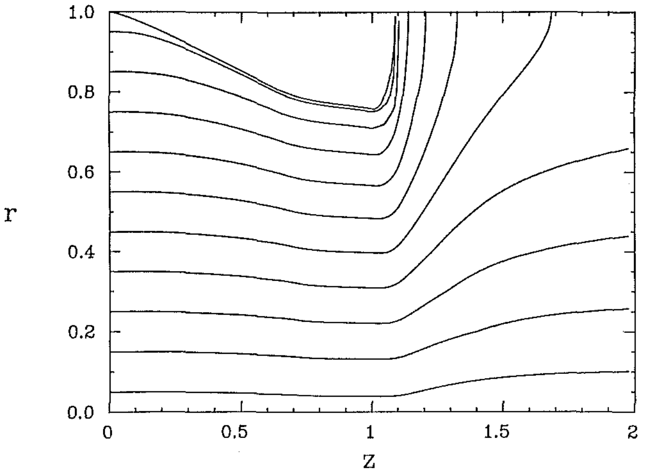

Fig. 9 Particle trajectories for $T_{in} = 1100$ K, "burner heated wall," $\beta = 1.0, I_0 = 20$ W/cm^2

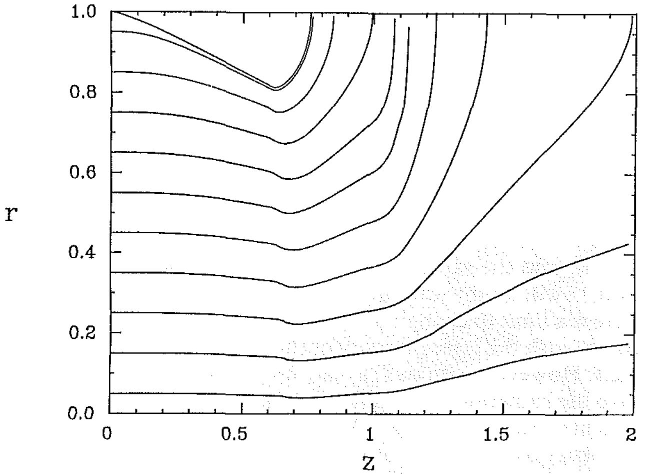

Fig. 11 Particle trajectories for $T_{in} = 1100$ K, "burner heated wall," $\beta = 1.0, I_0 = 120$ W/cm^2

arbitrarily small intensity. Consider now the effects of laser enhanced thermophoresis with a wall temperature distribution that approximates conventional methods of external heating [3]. We assume that from $z=0$ to $z=L_1$, that the wall temperature is given as follows:

$$T = T_{in} + (T_{max} - T_{in})z^2/L_1^2 \qquad (9)$$

where $T_{(in)}$ is the inlet temperature at $z=0$, and $T_{(max)}$ is the maximum wall temperature. From $z=L_1$ to L_2 we assume a linear decrease of temperature given by

$$T = T_{max} - (T_{max} - T_{min})(z - L_1)/L_2 \qquad (10)$$

Both z and L are scaled by the Peclet number. For $z > L_2$, it is assumed that the wall temperature is a constant and equal to $T_{(min)}$, taken to be 500 K. With an inlet temperature of 1100 K, a maximum temperature of 2000 K, $L_1 = 1.0$, (14 tube radii), and $L_2 = 0.1$, (1.4 tube radii), with the mean flow velocity again equal to 0.2 m/s, we arrive at Fig. 8. The laser heating is absent, and this figure corresponds closely to the results of [3]. As the laser intensity is increased to 20 W/cm^2, with $\beta = 1.0$, we see, in Fig. 9, how the particle trajectories incline toward the wall, and the deposition efficiency, at a given axial position, increases (see Fig. 2). Figures 10 and 11 show similar results for 60 and 120 W/cm^2, respectively. The maximum temperatures reached as a consequence of laser heating are 1900 K for 20 W/cm^2, 2300 K for 60 W/cm^2, and 2750 K for 120 W/cm^2, for Figs. 9-11. These latter temperatures are extremely high, and occur as a consequence of the wall heating forcing particles toward the center, or region of maximum laser intensity. The aerosol concentration increases above that of the concentration when initially formed, and the absorption coefficient increases proportionally.

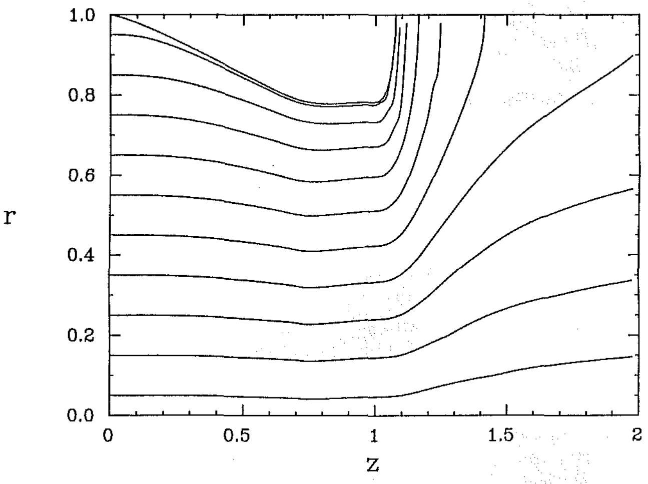

Fig. 12 Particle trajectories for $T_{in} = 1100$ K, "burner heated wall," $\beta = 2.0, I_0 = 60$ W/cm^2

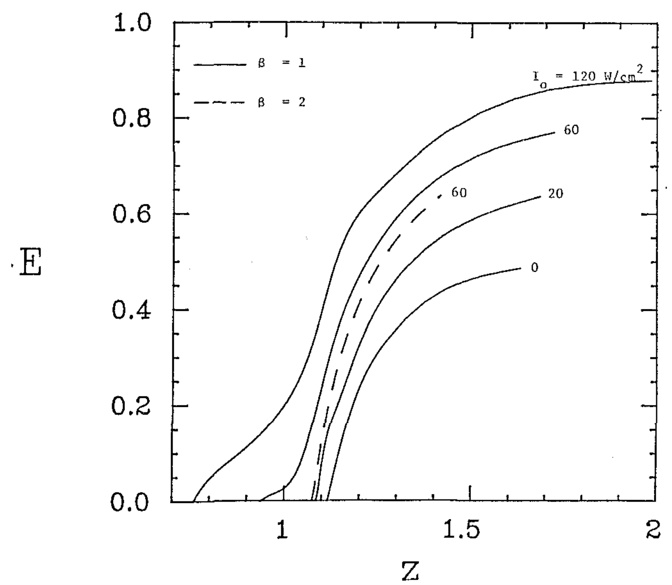

Fig. 13 Deposition efficiency versus length

Figure 12 illustrates the results of increasing β, the Gaussian beam parameter. If β is increased from 1.0 to 2.0, all other quantities held constant, we see that the particle trajectories are less influenced by the laser radiation. For $\beta=1.0$, and for $I_o=60$ W/cm^2, the particles starting at $r=0.35$ will hit the wall at $z=1.8$, as shown in Fig. 10. For $\beta=2.0$, and the same laser intensity, the particles starting at $r=0.35$ will hit the wall further downstream at $z=2.2$. Clearly there is a limit to changing the width of the radiation, since we do not wish the laser intensity at the wall to heat the tube wall itself. However, with this caveat, it is always more efficient to have the radiation as broadly distributed across the tube as is possible. Finally, in Fig. 13, we show a curve of deposition efficiency as a function of length and laser intensity. We have shown particle trajectories starting from $z=0$, since, in terms of the dimensionless z presented in the curves, the reaction temperature of 1300 K occurs no later than $z=.03$. Thus we see significant gains to be achieved in the MCVD process by enhancement of thermophoretic deposition with axial laser radiation.

Conclusions

An aerosol tube flow with heat transfer or temperature boundary conditions is an appropriate model for examining the deposition of particles in the MCVD process associated with the manufacture of optical fiber performs. The efficiency of this process is of the order of 50 percent. In an effort to increase this, we have considered the addition of axial laser radiation that is absorbed by the aerosol particles formed. The background gas is assumed to be transparent to the laser radiation. The laser beam has a Gaussian distribution in intensity, so that there is greater heating in the central core of the beam, and thus thermophoretic forces are more important in this central core than in the wings of the intensity distribution. Any such distribution far downstream from the region in which the aerosol is formed will insure that all particles are deposited. In a numerical analysis of the energy and particle continuity equations, for parameters pertinent to the MCVD process, we have shown the effects of increasing laser radiation on deposition efficiency, and on the length needed to achieve this deposition. An experimental program is also in progress to study the effects of laser radiation on two-phase flow, in the presence of an absorbing aerosol.

Acknowledgments

This work was sponsored by a grant from the National Science Foundation, through the Heat Transfer Program, Division of Mechanical Engineering and Applied Mechanics. The numerical calculations presented in this work were carried out on the Brown University Division of Engineering VAX 11-780 computer. The acquisition of this computer was made possible by grants from the National Science Foundation (Grant ENG78-19378), the General Electric Company, and the Digital Equipment Corporation.

References

1 Simpkins, P. G., Greenberg-Kosinski, S., and MacChesney, J. B., "Thermophoresis: The Mass Transfer Mechanism in Modified Chemical Vapor Deposition," *Journal of Applied Physics*, Vol. 50, 1979, pp. 5676–5681.

2 Walker, K. L., Geyling, F. T., and Nagel, S. R., "Thermophoretic Deposition of Small Particles in the Modified Chemical Vapor Deposition (MCVD) Process," *Journal of American Ceramic Society*, Vol. 63, 1980, pp. 552–558.

3 Walker, K. L., Homsy, G. M., and Geyling, F. T., "Thermophoretic Deposition of Small Particles in Laminar Tube Flow," *Journal of Colloid and Interface Science*, Vol. 69, 1979, pp. 138–147.

4 *Western Electric Engineer*, Winter 1980.

5 Morse, T. F., and Cipolla, Jr., J. W., "Laser Modification of Thermophoretic Deposition," *Journal of Colloid and Interface Science*, Vol. 97, 1984, pp. 137–148.

6 Cipolla, Jr., J. W., and Morse, T. F., "Heat Transfer and Thermophoresis in an Absorbing Aerosol," ASME Paper No. 83-HT-55, presented at 21 National Heat Transfer Conference, Seattle, Wash., July 1983.

7 Wang, C. Y., Morse, T. F., and Cipolla, J. W., Jr., "Laser Induced Natural Convection and Thermophoresis," ASME JOURNAL OF HEAT TRANSFER, Vol. 107, 1985, pp. 161–167.

8 Graetz, L., "Ueber die Waermeleitungsfahigkeit von Fluessigkeiten," *Annalen der Physik. Chem.*, Vol. 25, 1885, pp. 337–357.

9 Sellars, J. R., Tribus, M., and Klein, J. S., "Heat Transfer to Laminar Flow in a Round Tube or Flat Conduit, the Graetz Problem Extended," ASME *Trans*, Vol. 78, 1956, pp. 441–448.

10 Shah, R. K., and London, A. L., *Advances in Heat Transfer, Supplement 1*, 1978.

11 Walker, K. L., National Meeting of the Society of Engineering Science, Brown University, Sept. 1981.

12 Talbot, L., Cheng, R. K., Schefer, R. W., and Willis, D. R., "Thermophoresis of Particles in a Heated Boundary Layer," *Journal of Fluid Mechanics*, Vol. 101, 1981, pp. 737–758.

13 Mie, G., "Beitrage zur Optik Trueber Medien, Spezial Kolloidalen Metalloesungen," *Annalen der Physik*, vierte Folge, Band 25, 1908, pp. 377–445.

14 van de Hulst, H. C., *Light Scattering by Small Particles*, John Wiley & Sons, New York, 1957.

15 Kerker, M., *The Scattering of Light and other Electromagnetic Radiation*, Academic Press, 1969.

16 Nagel, S., private communication, Bell Laboratories.

17 Scherer, G., private communication, Corning Glass Works.

18 Gerald, C. F., *Applied Numerical Analysis*, (2d ed.), Addison Wesley, 1978, pp. 390–432.

19 Weinberg, M. C., and Subramanian, R. S., "Thermophoretic Deposition in a Tube with a Variable Wall Temperature," *Journal of Colloid and Interface Science*, Vol. 87, 1982, pp. 579–580.

20 Weinberg, M. C., "Thermophoretic Efficiency in Modified Chemical Vapor Deposition Process," *Journal of American Ceramic Society*, Vol. 65, 1982, pp. 81–87.

21 Weinberg, M. C., "Calculation of Thermophoretic Deposition Efficiency of Particles in Tubes," *Journal of Colloid and Interface Science*, Vol. 84, 1981, pp. 550–551.

C. Y. Wang

T. F. Morse

Division of Engineering,
Brown University,
Providence, R.I.

J. W. Cipolla, Jr.

Department of Mechanical Engineering,
Northeastern University,
Boston, Mass.

Laser-Induced Natural Convection and Thermophoresis

The influence of axial laser volumetric heating and forced convection on the motion of aerosol particles in a vertical tube has been studied using the Boussinesq approximation. For constant wall temperature, an asymptotic case provides simple temperature and velocity profiles that determine the convection and thermophoretic motion of small aerosol particles. Laser heating induces upward buoyant motion near the tube center, and when forced convection is downward, there may be an inflection in the velocity profile. For constant laser heating (a small absorption limit), a velocity profile may be found that will minimize the distance over which particles are deposited on the wall. Such an observation may have some bearing on the manufacture of preforms from which optical fibers are drawn.

Introduction

It has been demonstrated both experimentally and theoretically that laser radiation may interact with an absorbing aerosol in such a manner as to induce thermophoretic motion of the aerosol particles [1-3]. When the aerosol particles absorb the impinging laser radiation, they become heated. On a time scale (tens of microseconds) determined by thermal diffusivity and aerosol particle size, they exchange energy with gas in their immediate vicinity. In both the continuum and free molecule regimes, it may be shown that there is but negligible temperature slip, and so a particle finds itself immersed in the surrounding gas that it has heated. A distribution in the laser intensity that interacts with the aerosol-gas mixture will become mirrored in the temperature distribution, and as a consequence of the thermophoretic forces, the aerosol particles will move away from the region of maximum laser intensity. Qualitative experiments have been performed to illustrate the above phenomenon. Figure 1(*a*) presents an end on view of a vertical tube filled with dense titanium dioxide aerosol, and Fig. 1(*b*) shows the interaction of this aerosol with a carbon dioxide laser of approximately 10 W. The "hole," which is devoid of aerosol particles, corresponds to the beam size. Immediately after turning on the beam, buoyant effects were observed. As the particles thermophoretically moved away from the beam, these effects decreased, and finally, the beam propagated with no attenuation, since the background gas was transparent to the impinging radiation. The aerosol concentration is determined (in this large Schmidt number case) by a balance between diffusion and thermophoresis that leaves the central region (in steady state) devoid of particles. Consequently, there are steep concentration gradients at the edge of the beam.

The problem of laser-induced buoyant convection has been examined in a series of articles by Vest and coauthors [4-6]. In the present theoretical work, we wish to add forced convection to laser-induced buoyant motion to assess the effects of convective, buoyant, and thermophoretic forces on particle trajectories. As our model problem, we consider a vertical tube, with a constant wall temperature, irradiated axially by a laser whose intensity is constant along the centerline of the tube. This may be regarded as an approximation in which absorption is small enough so that beam attenuation, in lowest order, may be neglected. With these assumptions, velocity and temperature become independent of axial position. In examining natural convection between parallel plates and concentric cylinders, Lipkea and Springer [7] have shown that if the aspect ratio (length/width) is large, then for constant wall temperature the flow field will be independent of axial distance except for an entrance and exit length X_p, determined by $(X_p/2R) = \mathrm{Ra}/4400$, where Ra is the Rayleigh number and R the tube radius. For the cases considered below, it is believed that the gross effects of the combination of laser heating and forced convection on aerosol trajectories can be captured with these assumptions. We restrict our attention to the case of constant tube wall temperature, for which simple solutions for the velocity and temperature profiles may be obtained. Although the solutions for the

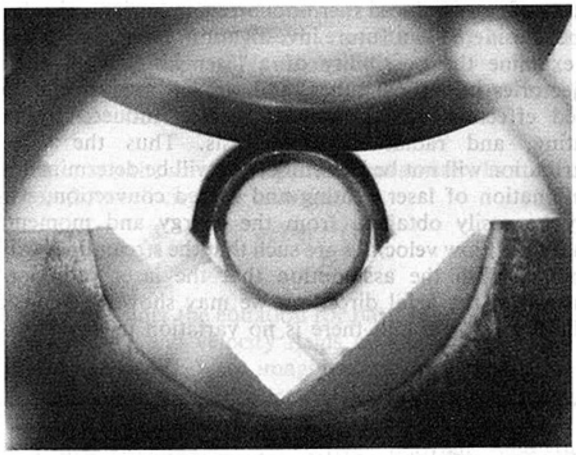

Fig. 1(*a*) End view of aerosol-filled vertical tube, laser off

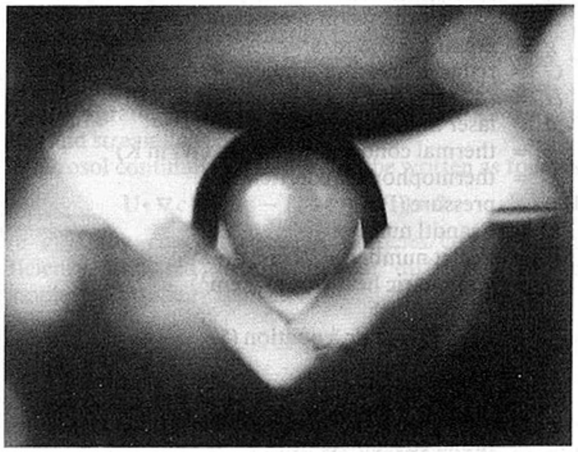

Fig. 1(*b*) End view of aerosol-filled vertical tube, laser on ("laser-induced thermophoretic hole")

Contributed by the Heat Transfer Division for publication in the JOURNAL OF HEAT TRANSFER. Manuscript received by the Heat Transfer Division May 5, 1983.

temperature and velocity fields are known [6, 8–15], for more general cases of forced and free convection, the manner in which such profiles effect the thermophoretic and convective motion of aerosol particles has not been previously studied. Thus we examine a simple asymptotic case (entrance and end effects are neglected) to determine the effects of laser-induced buoyancy on aerosol particle trajectories. Particle trajectories may be obtained directly from kinematic considerations.

The interest in such a model problem is derived from its relation to the thermophoretic deposition of aerosol particles in the manufacture of optical fibers. This process has been described in detail elsewhere [16–18]. With the neglect of buoyancy, this problem is essentially the classic Graetz problem [19–21]. The typical efficiency of such processes (mass of aerosol deposited on the wall/mass of aerosol produced) is of the order of 50 percent [22–23]. Thus part of the motivation for this study is to determine how laser radiation induces buoyancy, and affects thermophoretic deposition. In Fig. 2, we show a vertical tube in which a chemical reaction is initiated at a specific axial location. Previous work on thermophoretic deposition in tubes has assumed that there is a Poiseuille velocity distribution, which allows the solution of the energy and continuity equations independently (for the case of constant gas-aerosol properties). However, it is clear that the heating of the reactants will induce vertical convective forces that modify the subsequent thermophoresis and hence, the aerosol particle trajectories that will determine deposition efficiency. In a horizontal, rotating tube, the situation is more complex, since the thermophoretic and gravitational forces are parallel. The effects of laser induced thermophoresis in horizontal tubes is to be considered in a future investigation. Here, we wish only to examine the possibility of a laser influencing particle trajectories in vertical tubes, and we will analyze the combined effects of axial buoyant motion induced by laser heating, and radial thermophoresis. Thus the velocity distribution will not be Poiseuille, but will be determined by a combination of laser heating and forced convection, which may be easily obtained from the energy and momentum equations. Flow velocities are such that the streamlines will be laminar. With the assumption that the laser radiation is constant in the axial direction, we may show, for constant wall temperature, that there is no variation in any physical quantities along this direction. This allows particularly simple solutions for temperature and velocity to be obtained.

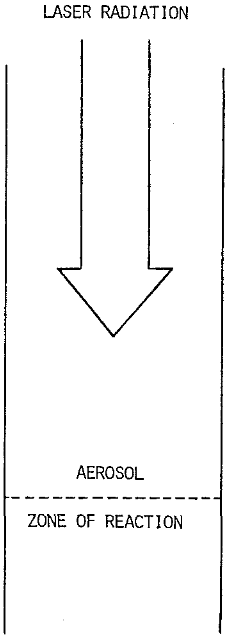

Fig. 2 Laser heating in vertical tube

The Fundamental Equations

The energy equation for the flow under consideration may be written as follows:

$$\rho \mathbf{U} \cdot \nabla (c_p T) = k \nabla^2 T - \nabla \cdot \mathbf{q}_R \qquad (1)$$

Dimensional analysis demonstrates that axial conduction may be neglected in comparison with radial conduction for large Peclet number. The divergence of the radiative heat flux vector $\mathbf{q}_R$, is associated with the effects of laser heating, and its solution, in general, must be obtained from the equation of radiative transfer. For small particles (the Rayleigh limit) or for the case in which the background gas is not severely

Nomenclature

A = $-(\rho_w \beta g r^2/6k)\ (Q/(d\pi/dz'))$ equation (14)
c = particle concentration (particles/cm^3)
C = dimensionless axial pressure parameter equation (10)
c_p = specific heat at constant pressure (kJ/kg K)
D = particle diffusion coefficient (m^2/s)
g = gravity = 9.8 m/s^2
G = reduced pressure gradient = $-(d\pi/dz')$ (Pa/m)
H = $(\rho_w \beta g r_o^4/\mu k)\ (Q/U_m)$ equation (10)
I = laser intensity (W/cm^2)
k = thermal conductivity of gas (W/m K)
K = thermophoretic coefficient
p = pressure (Pa)
Pr = Prandtl number
Pe = Peclet number = $2U_m r_o c_p/k$
Q = volumetric heat flux (W/cm^3)
Q_o = $2\int_o^{r_o} Q(r)\, r\, dr$, equation (5)
$\mathbf{q}_R$ = radiative heat flux vector (W/m^2)
r = dimensionless radial coordinate ($= r'/r_o$)
r' = radial coordinate (m)
r_i = initial position of a specific particle at $z = 0$ (m)
r_o = tube radius (m)
Sc = Schmidt number
T = fluid temperature (K)
T_w = wall temperature
U = axial velocity (m/s)
U_m = mean velocity (m/s)
V_T = thermophoretic velocity (in radial direction), equation (17) (m/s)
w = dimensionless axial velocity = (U/U_m)
X_p = entrance length (m)
z = dimensionless axial coordinate = $z'/(r_o \mathrm{Pe})$
z' = axial coordinate (m)
β = volumetric coefficient of thermal expansion of fluid (K^{-1})
κ = absorption coefficient (m^{-1})
λ = wavelength of laser beam (m)
μ = dynamic viscosity (kg/m.s)
ν = kinematic viscosity (m^2/s)
π = reduced pressure = $(p + \rho_w g z)$ (Pa)
ρ = density (kg/m^3)
ρ_w = density of fluid at wall temperature (kg/m^3)
Φ = $4k\theta(r)/(Q_o r_o^2)$
ϕ = dimensionless particle concentration ($= c/c_o$)
θ = temperature difference between fluid and the tube wall (K)

heated, it is possible to restrict the analysis and consider only absorption of the axial laser beam. Thus

$$\nabla \cdot \mathbf{q}_R \equiv -Q = -\kappa I(r')\exp\left(-\int_o^{z'} \kappa dz''\right) \tag{2}$$

The absorption coefficient given by κ, $I(r')$ is the radial distribution of laser intensity at the wavelength λ. The absorption coefficient κ in equation (2) is taken to be constant and is not dependent on the particle density but on a component of the background gas. This assumption decouples the energy and momentum equations from the equation of particle transport and makes it possible to solve for the velocity and temperature profiles independently of the particle concentration equation (for the case of constant physical properties). Further, since our main purpose here is to gain insight into the effects of laser-induced buoyancy on particle trajectories, we shall avoid some of the complications of the complete problem by consideration of a situation in which temperature and velocity do not vary axially (vertically) along the tube, whose wall temperature is constant. This is consistent with our assumption of no axial variation in laser intensity, and the consequences of this assumption have been previously dicussed here (see also [7]). It is believed that with these restrictions we still may obtain a valid first approximation to the influence of buoyancy-induced laser heating on particle trajectories. The assumption of laser intensity independent of axial position corresponds to a small absorption coefficient. The intensity, however, may be an arbitrary function of radial position, although our results emphasize the case of laser intensity independent of radius.

With these restrictions, the energy equation reflects a balance between laser heating and radial conduction and may be written as

$$k\frac{1}{r'}\frac{d}{dr'}\left(r'\frac{dT}{dr'}\right) = -Q(r') \tag{3}$$

where Q is given by equation (2), neglecting axial attenuation. With the boundary conditions that $T(r' = r_o) = T_w$, we obtain

$$\theta(r') \equiv T(r') - T_w = -\frac{1}{k}\int_{r'}^{r_o}\frac{ds'}{s'}\int_o^{s'} sQ(s)ds \tag{4}$$

For constant laser intensity, and, therefore, constant energy deposition Q_o, a simple integration yields the following:

$$\Phi \equiv \frac{4k\theta(r)}{Q_o {r_o}^2} = (1-r^2) \tag{5}$$

In equation (5), we have normalized r' by r_o, and r is dimensionless.

The momentum equation is given as

$$\rho\mathbf{U}\cdot\nabla\mathbf{U} + \nabla p - \rho\mathbf{g} = \mu\nabla^2\mathbf{U} \tag{6}$$

The velocity at the surface of the vertical tube must be equal to zero, and, for the asymptotic case considered here, we neglect end effects, as well as axial variations in the velocity and temperature fields. We let $p = \pi(z') - \rho_w g z'$, and $-d\pi/dz'$ = constant, the gradient associated with forced convection. With $U(r')$ as the axial velocity, we may write the momentum equation in the Boussinesq approximation as follows:

$$-\frac{d\pi}{dz'} + \frac{\mu}{r'}\frac{d}{dr'}\left(r'\frac{dU}{dr'}\right) + g(\rho_w - \rho) = 0 \tag{7}$$

For a small temperature difference

$$\rho_w - \rho = -\rho_w\beta(T_w - T) \tag{8}$$

where $\beta = -(1/\rho)(d\rho/dT)_p$. Thus the momentum equation in dimensionless form may be written as follows, where $w = U/U_m$, and U_m is the mean flow velocity.

$$\frac{1}{r}\frac{d}{dr}\left(r\frac{dw}{dr}\right) = -8C - \frac{1}{4}H\Phi \tag{9}$$

The parameter C, a pressure parameter, and H, a laser heating parameter, are defined below.

$$C \equiv -\frac{{r_o}^2}{8\mu U_m}\frac{d\pi}{dz'}, \quad H = \frac{\rho_w\beta g {r_o}^4 Q_o}{\mu k U_m} \tag{10}$$

Using the no-slip boundary condition, equation (9) may be integrated to yield the following.

$$w = 2C(1-r^2) - \frac{H}{4}\int_r^1\frac{ds'}{s'}\int_o^{s'}\Phi(s)s\,ds \tag{11}$$

The further integration of equation (11) over the tube area is equal to 1. This yields a relation between C and H in terms of the mean velocity.

$$C = 1 + \frac{H}{2}\int_o^1 r\left[\int_r^1\frac{ds'}{s'}\int_o^{s'}\Phi(s)s\,ds\right]dr \tag{12}$$

For the case in which the intensity is uniform and $\Phi = 1 - r^2$, we find that $C = 1 - H/48$, and the radial distribution of axial velocity is given as a simple quartic

$$w = 2(1-r^2) + \frac{H}{16}\left(\frac{r^4}{4} - \frac{r^2}{3} + \frac{1}{12}\right) \tag{13}$$

There is a Poiseuille component to this solution as well as a component associated with an integral over the laser heating term from the solution of the energy equation. These solutions correspond essentially to limiting cases obtained previously by other authors (see [8–15]). We also note that H is a simple funtion of the ratio of laser heating to the pressure gradient associated with forced convection. By eliminating U_m from the definition of H, we obtain

$$H = 48A/(1+A), A = -\frac{\rho_w\beta g {r_o}^2 Q_o}{6k(d\pi/dz)} \tag{14}$$

where A is now the single independent parameter. In addition, the mean flow velocity may be written as

$$U_m = \frac{\rho_w\beta g {r_o}^4 Q_o}{\mu k H} \tag{15}$$

We now consider the equation for particle trajectories. For the temperature and velocity fields obtained analytically in equations (5) and (13), we imagine that we place a uniform distribution of aerosol particles of fixed concentration across the tube at $z = 0$, and subsequently numerically solve for their motion under combined convective, buoyant, and thermophoretic forces, as described below. Although the problem we have posed is artificial, we believe that critical elements of the true behavior of particle trajectories under the influence of vertical laser heating will be captured. The aerosol particles, typically less than a micron in diameter, are of such a size that gravitational settling is not a factor. Since there is a thermophoretic force on the particles associated with the temperature gradient, it is clear that particle path lines will not follow fluid streamlines.

The aerosol continuity equation may be written as follows.

$$\mathbf{U}\cdot\nabla c + \nabla\cdot(-D\nabla c + c\mathbf{V}_T) = 0 \tag{16}$$

where c is the concentration in particles/cm^3, D is the coefficient associated with Brownian diffusion, and the thermophoretic velocity is given by

$$\mathbf{V}_T = -K\frac{\nu}{T}\nabla T \tag{17}$$

The thermophoretic coefficient K is dependent on a host of parameters (see Talbot et al. [24]). In the following calculations, K shall be taken to be constant, and of order one. For the submicron aerosol particles considered here, the Schmidt number, the ratio of viscous to diffusive forces, is

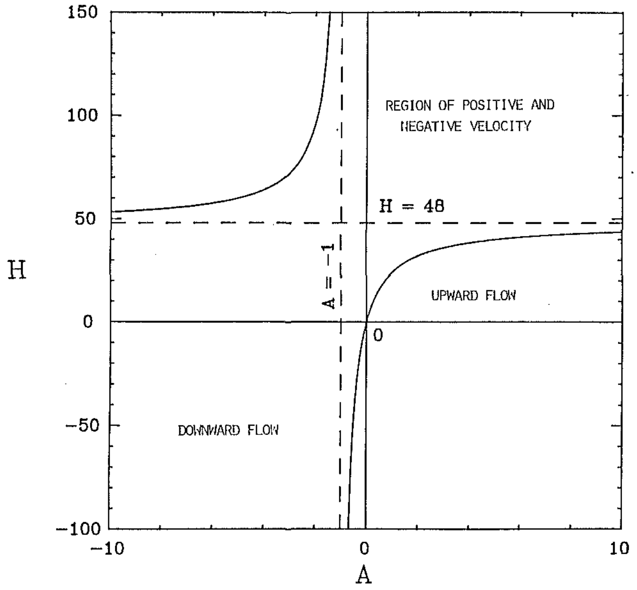

Fig. 3 Flow regions

very large, of the order of several thousand. This permits the neglect of diffusion in the particle continuity equation (except in a very thin boundary region near the wall, see [17]). However, it is not even necessary to solve equation (16) for the concentration: particle trajectories provide the physical information we seek. If $U(r')$ is the axial component of particle velocity, and $V_T(r')$ is the radial, or thermophoretic component of velocity, then particle trajectories may be obtained from solely kinematic considerations

$$\left.\frac{dz'}{dr'}\right|_{\text{pathline}} = \frac{U(r')}{V_T(r')} \tag{18}$$

Integrating along a particle path-line, we obtain the following

$$z' = \int_{r_i'}^{r'} \frac{U(s)}{V_T(s)}\, ds \tag{19}$$

where r_i' is the initial radial position of a particle at $z' = 0$. Thus specifying the radial position r_i' of a particle at $z' = 0$ provides us with the trajectory followed to reach any position downstream.

From equation (19) we may also determine other information that is pertinent to particle deposition. For example, the distance travelled by a particle that is initially at position r_i' before it hits the wall, z_m', may be obtained by setting $r' = r_o$ in equation (19). This equation describes the particle trajectories in the simple model flow considered here. In the next section, results have been obtained for the case of laser intensity independent of radius. A Gaussian distribution of radial intensity produces results qualitatively similar to those for constant radial intensity if the half-width of the Gaussian is of the order of the tube radius.

Discussion of Specific Particle Trajectories

In this section we wish to consider the influence of laser heating on particle trajectories, and we will examine several specific examples whose parameters encompass a range of conditions that might be found in situations pertinent to the fabrication of optical fiber preforms. As shown in equation (13), we see that the velocity profile, normalized by U_m, is governed by the single parameter H. The mean velocity U_m however, depends upon Q and $H(Q, d\pi/dz)$. In Fig. 3, we present a plot of A, (see equation (14)), that depends upon radiation as well as upon the pressure gradient. For $A > 0$, H is positive, and the velocity is everywhere positive. As A increases, H asymptotically increases to a value of 48. We note that the sign of A is governed by the sign of the negative pressure gradient $-(d\pi/dz)$. When A is positive, forced convection is upward, when A is negative, forced convection is downward. Therefore, for $A > 0$, forced convection and the buoyancy induced flow are in the same direction, and no flow reversal can exist. In the region $-1 < A < 0$, the velocity profile is such that there may be negative flow, and at $A = -1$, the net upflow balances the net downflow, so that the total average velocity is zero. In Fig. 3, the dotted vertical line represents a balance between forced convection and laser-induced buoyancy. In this region $-1 < A < 0$, we see the most interesting particle trajectories due to thermophoretic, and convective forces.

To obtain an order of magnitude estimate of the thermophoretic force, consider the following. The thermophoretic velocity is maximum at the tube wall since the temperature gradient has its maximum there. Using equation (17) with the physical properties given below and assuming an energy deposition of $Q_o = 1\ \mathrm{W/cm^3}$ in equation (5), we find the maximum thermophoretic velocity, $V_{Tm} = 1$ cm/s. Substituting this velocity in the Stokes drag formula for a particle of .1 micron diameter provides an estimate of the thermophoretic force $F_T = O(10^{-12}\mathrm{N})$, which is approximately 400 times the particle weight.

We wish now to examine the influence of laser radiation on particle trajectories by modification not only of the temperature profile, but the fluid velocity profile as well. In optical fiber preforms, the first section over which the particles are deposited contributes to an undesired "taper" in the deposition layers. A significant portion of this initial deposition length must be discarded. Thus it is desirable to modify particle trajectories in such a manner as to minimize the distance along the wall over which they are deposited. In Figs. (4–10), the lower curves represent the fluid velocity profiles as a function of radius. The upper curves represent particle trajectories that are the result of the combined fluid mechanical drag forces and thermophoretic forces on particles that start at a given radius at $z = 0$. The values of the physical constants for these calculations are shown in Table 1. Consider first a typical example that is shown in Fig. 4 for $A > 0$ and note that the upward component of velocity will be further increased by the laser heating. This will speed up those particles in the center and will increase the distance downstream at which they are deposited. Since our interest is to separate the effects of laser heating from the wall temperatures needed to produce the chemical reaction that causes aerosol formation, the wall temperature are taken to be only 500 K. In Fig. 4, since $A > 0$ and forced convection is upward, we see particle trajectories that correspond to a laser volumetric heat input of $0.1\ \mathrm{W/cm^3}$. Physical properties are given in Table 1 [25]. The value of the absorption coefficient is of the order of what might be expected in the MCVD process for carbon dioxide radiation. The average flow velocity is taken to be 0.1 m/s, and this profile is also presented in Fig. 4. For this example, the temperature at the centerline is 62 K higher than the wall temperature. In the region of Fig. 3 for $A > 0$, all profiles and trajectories will be qualitatively similar to those shown in Fig. 4.

In the next series of examples, we choose a mean flow velocity of 0.2 m/s in the downward direction. In Fig. 5, we see the effect of laser heating on the particle trajectories and on the velocity distribution. Although the mean flow is negative, the laser heating has caused the velocity at the centerline to increase toward zero. The heating corresponds to an absorption of $0.5\ \mathrm{W/cm^3}$, and a temperature increase of 309 K. In Fig. 6, we increase the laser heating to $0.75\ \mathrm{W/cm^3}$, with a temperature increase of 464 K. This causes the particles at $z = 0$, $r = 0.05$ to hit the wall at $z = -0.4$, which

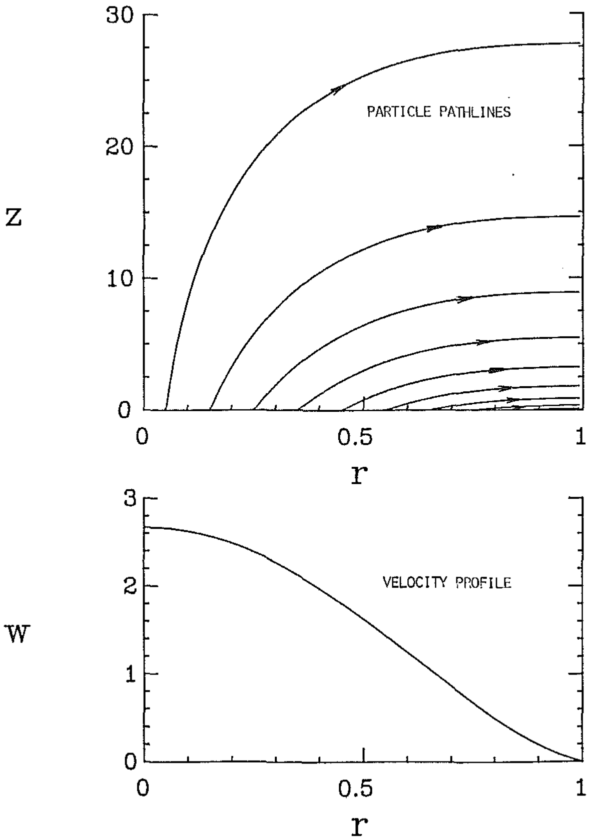

Fig. 4 Particle pathlines and velocity profile for $u_m = +0.1$ m/s, $Q = 0.10$ W/cm^3

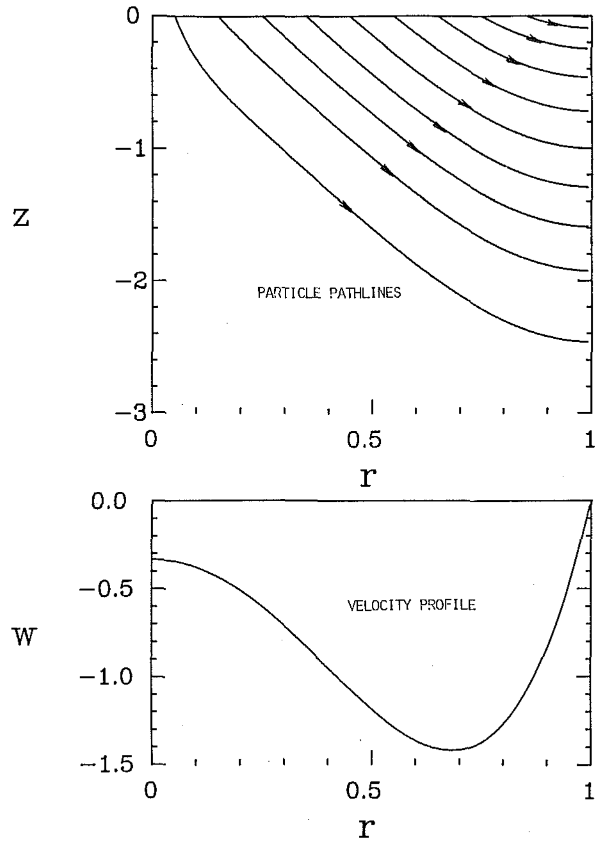

Fig. 5 Particle pathlines and velocity profile for $u_m = -0.2$ m/s, $Q = 0.50$ W/cm^3

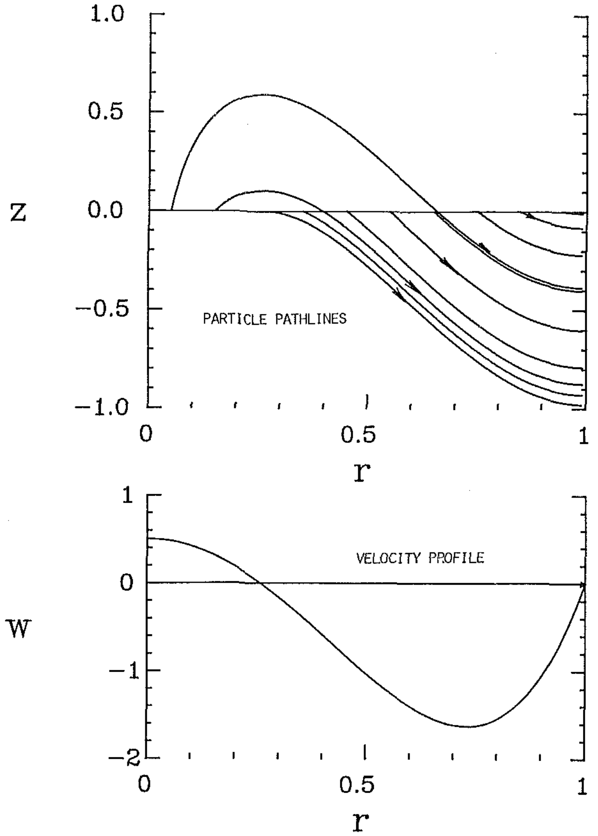

Fig. 6 Particle pathlines and velocity profile for $u_m = -0.2$ m/s, $Q = 0.75$ W/cm^3

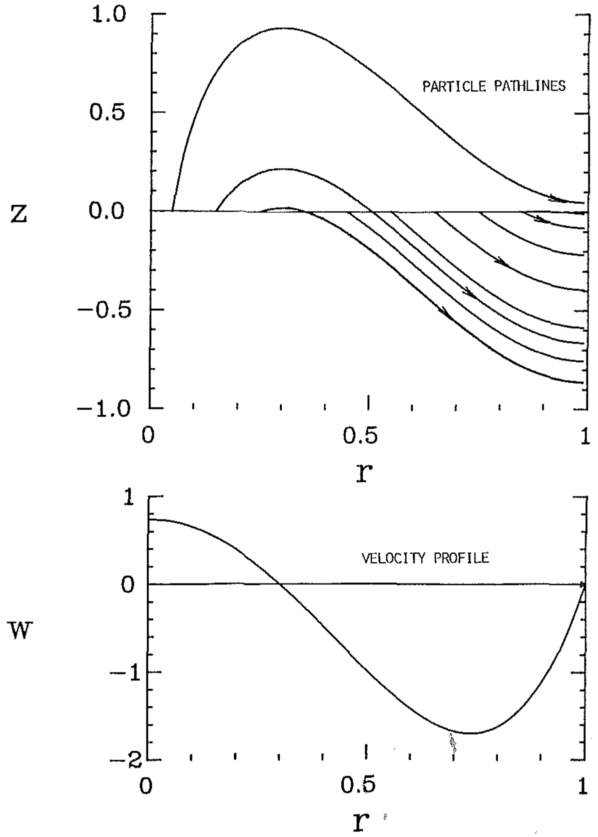

Fig. 7 Particle pathlines and velocity profile for $u_m = -0.2$ m/s, $Q = 0.82$ W/cm^3

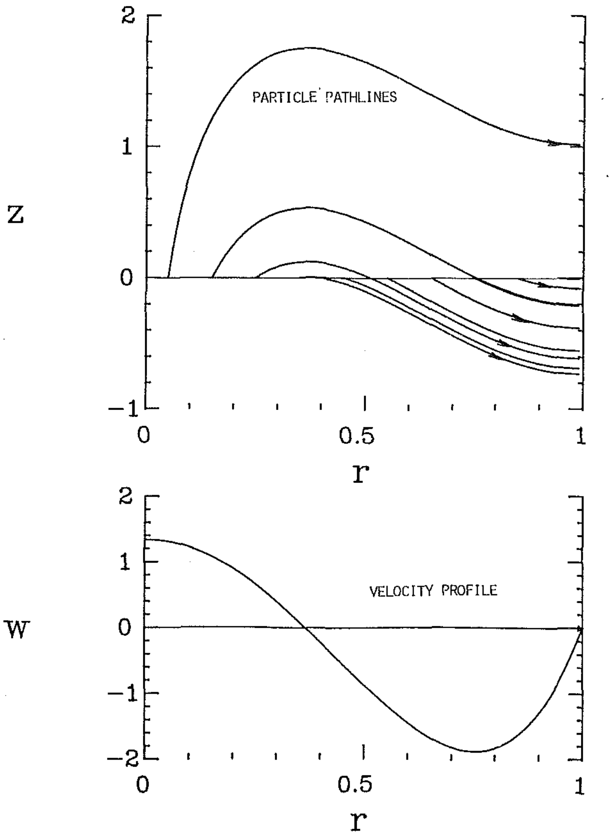

Fig. 8 Particle pathlines and velocity profile for $u_m = -0.2$ m/s, Q = 1.00 W/cm^3

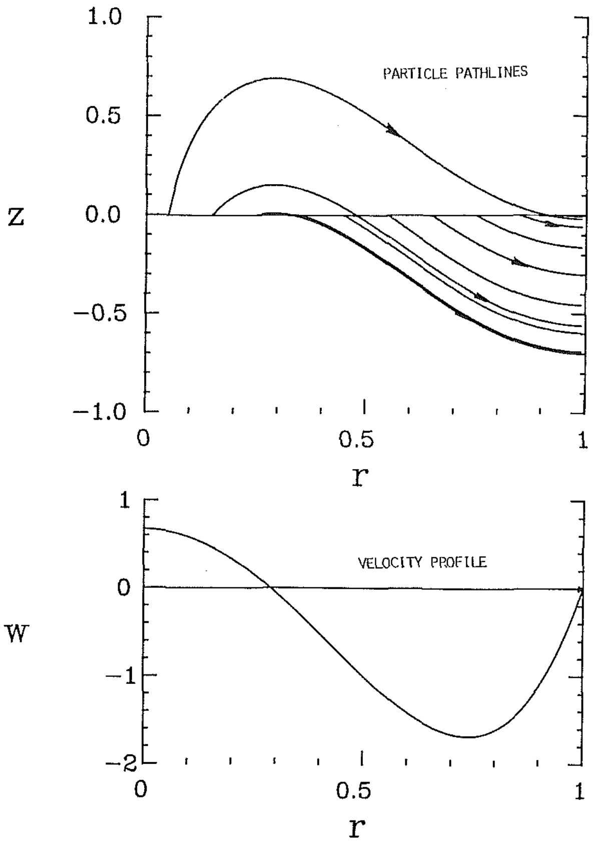

Fig. 10 Particle pathlines and velocity profile for $u_m = -0.3$ m/s, Q = 1.20 W/cm^3

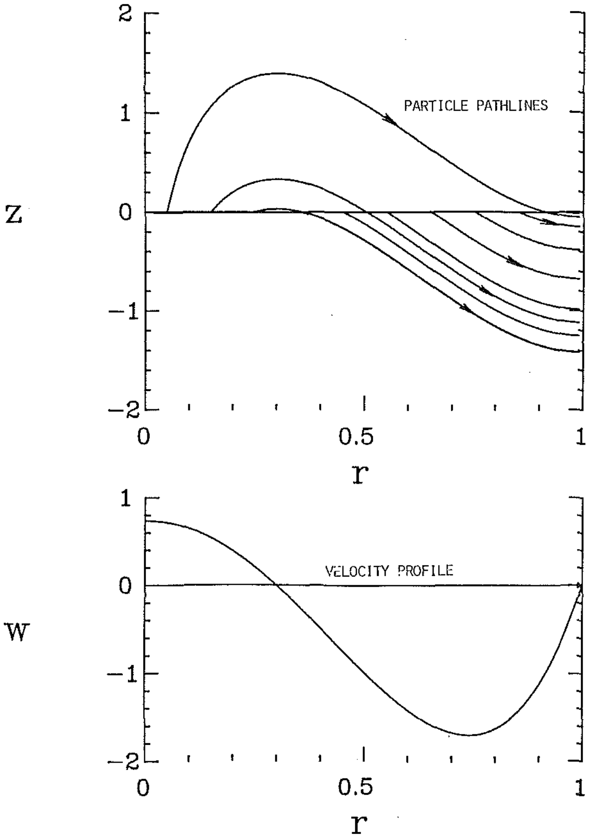

Fig. 9 Particle pathlines and velocity profile for $u_m = -0.1$ m/s, Q = 0.41 W/cm^3

Table 1 Physical constants

viscosity, $\mu = 2.67 \times 10^{-5}$ kg/ms
thermal conductivity, $k = 0.04038$ W/mK
wall temperature, $T_w = 500$ K
thermal expansion coefficient, $\beta = 1/T_w$
gas density at wall, $\rho_w = 0.7048$ kg/m^3
PrK = 1
absorption coefficient, $\kappa = 0.1\text{cm}^{-1}$

corresponds to a deposition efficiency of 99 percent. If the volumetric heating is further increased to $Q = 0.82$ W/cm^3, which corresponds to a temperature increase of 508 K at the centerline, then we have particle pathlines emanating from $r = 0.05$ striking the wall near $z = 0$. This is shown in Fig. 7. The thermophoretic force is always directed toward the wall, and the particles closer than 0.28 to the centerline initially move upward in the positive direction and are then swept downward by the reverse flow associated with the positive impressed pressure gradient near the wall. We note that the particle pathline starting from $r = 0.05$ hits the wall near $z = 0$, where the $r = 1$ particle is created. For this configuration, the length of the wall over which deposition occurs will be a minimum. The value of H for this configuration is -525. This velocity profile is also shown in Fig. 7. Further heating will cause the particles starting from $r = 0.05$ to hit at a higher value of z. This is shown in Fig. 8, with the corresponding velocity profile.

Finally, we note the following. If the mean flow U_m is changed by altering the pressure gradient, it is possible to change the volumetric heating in such a manner as to insure that the condition for minimum deposition length will be satisfied, as in Fig. 7. In Figs. 9 and 10, we see minimum deposition length trajectories for laser heating of 0.41 and 1.2 W/cm^3, respectively. From Figs. 7, 9, and 10, we see that this length depends only upon H (or A). We note that increasing Q

and the net downward flow (for $H = -525$), the length over which deposition occurs is reduced, since the thermophoretic component of velocity increases faster than the net convective velocity.

Conclusions

We have examined an idealized case of flow in a vertical tube that is a combination of forced and natural convection, and for which the tube wall temperature is held to be constant. The natural convection is induced by a volumetric heat source associated with laser absorption. For the situation in which the laser heating may be regarded as constant (a small absorption limit), particularly simple solutions, obtained previously by other authors, may be used to provide the temperature and velocity distributions in which particles move under the influence of thermophoretic and convective forces. The motivation for this research, in part, stems from a desire to study the thermophoretic motion of particles in the manufacture of optical fiber preforms. In these processes, it is desired to move a maximum number of particles to the walls in as short a distance as possible. Laser heating of either the particles or a component of the background gas can accomplish a significant increase in deposition efficiency, see Morse and Cipolla [1-3]. In this present work we have studied the effects of radiation-induced buoyancy on the velocity and temperature distributions, and, consequently on the particle trajectories. A universal velocity profile has been found that will minimize the length over which 99 percent of the particles will be deposited on the wall. The specific results presented here are pertinent to the case in which the laser radiation would be independent of radial position. We have also obtained solutions for the situation in which there is a Gaussian radial variation in the laser profile, and these do not differ qualitatively from results presented here. A conclusion reached in the studies that assume a Gaussian profile, and supported by other calculations [1-3], indicates that a broad distribution of laser intensity that interacts with a maximum number of aerosol particles has the greatest influence on the particle trajectories. It is realized that since these results do not consider three-dimensional aspects of the flow, they are only qualitative and the assumption of no variation in the axial direction is not truly valid. The effects of these assumptions are under current investigations. Additional studies, both experimental and theoretical, that will couple laser heating with external heating to influence particle trajectories, are also in progress.

Acknowledgments

This work was supported by a grant from the National Science Foundation, through the Heat Transfer Program, Division of Mechanical Engineering and Applied Mechanics. The computations reported in this work were carried out on the Brown University Division of Engineering VAX-11/780 computer. The acquisition of this computer was made possible by grants from the National Science Foundation (Grant ENG78-19378), the General Electric Foundation, and the Digital Equipment Corporation.

References

1 Morse, T. F., and Cipolla, J. W., Jr., "Laser Modification of Thermophoretic Deposition," *Journal of Colloid and Interface Science*, Vol. 97, 1984, pp. 137-148.

2 Cipolla, J. W., Jr., and Morse, T. F., "Heat Transfer and Thermophoresis in an Absorbing Aerosol," ASME Paper No. 83-HT-55, presented at 21 National Heat Transfer Conference, Seattle, Wash., July 1983.

3 Morse, T. F., Wang, C. Y., and Cipolla, J. W., Jr., "Laser Induced Thermophoresis and Particulate Deposition Efficiency," ASME JOURNAL OF HEAT TRANSFER, Vol. 107, No. 1, Feb. 1985, pp. 155-160.

4 Boyd, R. D., and Vest, C. M., "Laminar Natural Convection Above a Horizontal Laser Beam," *International Journal of Heat and Mass Transfer*, Vol. 24, 1981, pp. 685-694.

5 Boyd, R. D., and Vest, C. M., "Onset of Convection Due to Horizontal Laser Beams," *Applied Physics Letters*, Vol. 26, 1975, pp. 287-288.

6 Vest, C. M., "Analysis of Laser-Induced Convection in Unconfined Fluids and in Vertical Cylinders," *The Physics of Fluids*, Vol. 17, 1974, pp. 1945-1950.

7 Lipkea, W. H., and Springer, G. S., "Heat Transfer Through Gases Contained Between Two Vertical Cylinders at Different Temperatures," *International Journal of Heat and Mass Transfer*, Vol. 11, 1968, pp. 1341-1350.

8 Morton, B. R., "Laminar Convection in Uniformly Heated Vertical Pipes," *Journal of Fluid Mechanics*, Vol. 8, 1960, pp. 227-240.

9 Poppendick, H. V., "Forced-Convection Heat Transfer in Pipes with Volume Heat Sources Within the Fluids," *Nuclear Engineering, Part I, Chemical Engineering Progress Symposium Series*, Vol. 50, American Institute of Chemical Engineers, New York, pp. 93-94.

10 Tao, L. N., "On Combined Free and Forced Convection in Channels," ASME JOURNAL OF HEAT TRANSFER, Vol. 82, 1960, pp. 233-238.

11 Tao, L. N., "Heat Transfer of Combined Free and Forced Convection in Circular and Sector Tubes," *Applied Science Research*, Vol. 9, 1960, pp. 357-368.

12 Eckert, E. R. G., and Diaguila, A. J., "Convective Heat Transfer for Mixed, Free, and Forced Flow Through Tubes," ASME *Transactions*, Vol. 76, 1954, pp. 497-504.

13 Jackson, T. W., Harrison, W. B., and Boteler, W. C., "Combined Free and Forced Convection in a Constant-Temperature Vertical Tube," ASME *Transactions*, Vol. 80, 1958, pp. 739-745.

14 Hallman, T. M., "Combined Forced and Free-Laminar Heat Transfer in Vertical Tubes with Uniform Internal Heat Generation," ASME *Transactions*, Vol. 78, 1956, pp. 1831-1844.

15 Ostrach, S., "Natural Convection in Enclosures," *Advances in Heat Transfer*, Vol. 8, 1972, pp. 161-227.

16 Simpkins, P. G., Greenberg-Kosinski, G. S., and MacChesney, J. B., "Thermophoresis: The Mass Transfer Mechanism in Modified Chemical Vapor Deposition," *Journal of Applied Physics*, Vol. 50, 1979, pp. 5676-5681.

17 Walker, K. L., Geyling, F. T., and Nagel, S. R., "Thermophoretic Deposition of Small Particles in the Modified Chemical Vapor Deposition (MCVD) Process," *Journal of American Ceramic Society*, Vol. 63, 1980, pp. 552-558.

18 Walker, K. L., Homsy, G. M., and Geyling, F. T., "Thermophoretic Deposition of Small Particles in Laminar Tube Flow," *Journal of Colloid and Interface Science*, Vol. 69, 1979, pp. 138-147.

19 Graetz, L., "Ueber die Waermeleitungsfahigkeit von Fluessigkeiten," *Annalen der Physik. Chem.*, Vol. 25, 1885, pp. 337-357.

20 Sellars, J. R., Tribus, M., and Klein, J. S., "Heat Transfer to Laminar Flow in a Round Tube or Flat Conduit, the Graetz Problem Extended," ASME *Transactions*, Vol. 78, 1956, pp. 441-448.

21 Shah, R. K., and London, A. L., *Advances in Heat Transfer, Supplement 1*, 1978.

22 Weinberg, M., and Subramanian, R. S., "Thermophoretic Deposition in a Tube with Variable Wall Temperature," *Journal of Colloid and Interface Science*, Vol. 87, No. 2, 1982, pp. 579-580.

23 Weinberg, M., "Thermophoretic Efficiency in the Modified Chemical Vapor Deposition Process," *Journal of American Ceramic Society*, Vol. 65, 1982, pp. 81-87.

24 Talbot, L., Cheng, R. K., Schefer, R. W., and Willis, D. R., "Thermophoresis of Particles in a Heated Boundary Layer," *Journal of Fluid Mechanics*, Vol. 101, 1981, pp. 737-758.

25 Eckert, E. R. G., and Drake, R. M., *Analysis of Heat and Mass Transfer*, McGraw-Hill, New York, 1972.

E. A. Ibrahim
Graduate Student.

R. L. Judd
Professor.
Mem. ASME

Department of Mechanical Engineering,
McMaster University,
Hamilton, Ontario L8S 4L7

An Experimental Investigation of the Effect of Subcooling on Bubble Growth and Waiting Time in Nucleate Boiling

The effect of subcooling on bubble waiting time and growth time for water boiling on a copper surface was examined in conjunction with measurements obtained over a range of subcooling from 0 to 15°C and three different levels of heat flux 166, 228, and 291 kW/m^2. The growth-time data was successfully correlated with a model that combined the bubble growth theory of Mikic, Rohsenow, and Griffith with the bubble departure diameter relationship of Staniszewski, thereby establishing confidence in the measuring procedure. The waiting time data agreed with the predictions of the Han and Griffith waiting time theory at lower levels of subcooling but then showed a behavior contrary to that predicted for higher levels of subcooling.

Introduction

It is now widely accepted that in the process of nucleate pool boiling vapor bubbles form at specific locations on the heat transfer surface. These nucleation centers, called active sites, have been demonstrated conclusively [1-4] to be tiny pits, scratches, and other imperfections in the heating surface. The rate of heat transfer in nucleate boiling depends upon the number of active sites per unit area and the bubble emission frequency at each of the active sites [5]. Successful prediction of the bubble departure frequency requires precise knowledge of bubble initiation, growth and departure, the three major processes involved in bubble formation identified by Hsu and Graham [6]. Theoretical analysis of the frequency of bubble departure is associated with the determination of waiting time, the time between the last bubble departure and appearance of the next bubble on the surface and with the determination of bubble growth time, the time elapsed before departure occurs.

Ellion [7] demonstrated that the initial growth rate of vapor bubbles remained substantially independent of subcooling. The average growth rate, however, decreased slightly for lower liquid temperature and for constant pressure, and the bubble attained a smaller maximum radius as the liquid bulk temperature was decreased. This behavior follows directly from the fact that a lower bulk temperature decreases the growth time by removing the superheat from the liquid film surrounding the bubble more rapidly. Consequently, the bubble radius at which condensation and evaporation are equal decreases for lower bulk temperature. Gunther and Kreith [8] reported that with an increase of subcooling, bubble detachment ceased after which the large amount of vapor departing from the surface was replaced by an even distribution of very small hemispherical bubbles of short life cycle which did not detach from the surface. Cochran and Aydelott [9] observed that bubble population decreased as the bulk temperature increased with a trend towards larger bubbles. Shoukri and Judd [10] tested three different bubble growth models and were able to demonstrate that although bubble growth time is almost independent of subcooling and cavity radius, its dependence on wall superheat is quite significant.

Since it is generally accepted that the effect of subcooling on bubble growth time is smaller than its effect on bubble waiting time, therefore the effect of subcooling on bubble life time can be incorporated in its effect on bubble waiting time, especially at lower levels of subcooling. Gunther and Kreith [8] demonstrated that bubble lifetime, which is the reciprocal of bubble emission frequency, decreased as liquid subcooling increased. This result was confirmed by Ellion [7] and Cochran and Aydelott [9]. However, Judd [11] observed just the opposite effect and reported experimental data that indicated bubble life increased as liquid subcooling increased. Shoukri and Judd [10] advanced a theoretical model that predicted a decrease of bubble emission frequency with decreasing surface superheat, increasing liquid subcooling, and increasing nucleation cavity size. Analytically derived waiting time equations by Hsu [12], Han and Griffith [13] and Hatton and Hall [14] predict an increase of bubble waiting time as the liquid subcooling increases. More recently, however, Ali and Judd [15] in an analytical and experimental investigation of bubble waiting time showed that it was possible for bubble waiting time to decrease as liquid subcooling increased. They argued that in addition to conduction, there is a convective component of heat transfer operating in the local thermal boundary layer that hastens the restoration of the energy content of the liquid before the initiation of the next bubble as suggested earlier by Best, Burow, and Beer [16].

From the previous survey, it can be seen that there is considerable conflict in the published literature concerning the effect of subcooling on bubble life time. It is the main purpose of the present work to help clarify the situation by providing additional experimental measurements of the bubble growth and waiting time at different levels of subcooling and heat flux for water boiling on a copper surface.

Experimental Apparatus and Procedure

At the beginning of the research, an experimental apparatus, constructed by Wiebe [17] and modified by Sultan [18], existed that was adequate for the requirements of the investigation, and so it was adapted for the present purpose. A sectional view is shown in Fig. 1. No particular attention was given to the boiling surface finish except that just prior to obtaining the data reported in this paper, the surface was once more cleaned with a soft cloth moistened with liquid silver

---

Contributed by the Heat Transfer Division for publication in the JOURNAL OF HEAT TRANSFER. Manuscript received by the Heat Transfer Division June 24, 1983.

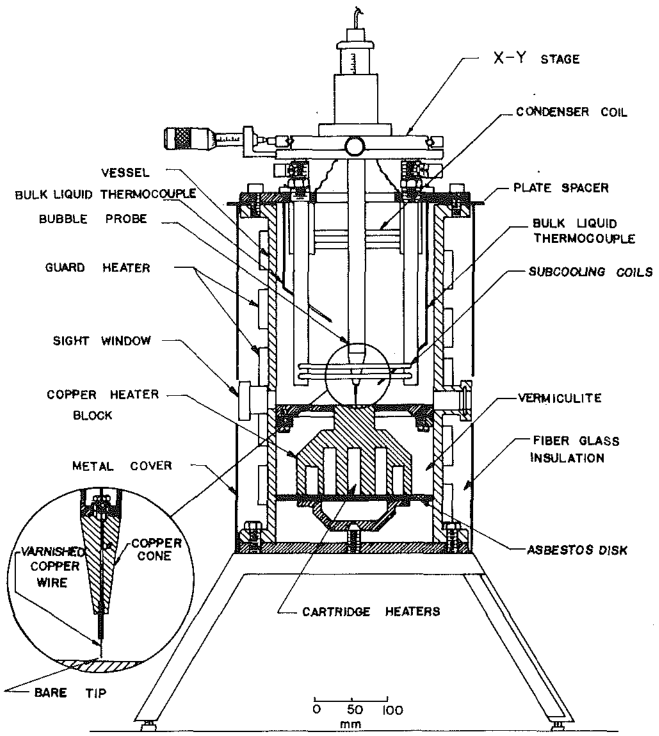

Fig. 1 Experimental apparatus

polish after which the residue was rinsed away with a stream of methanol from a squeeze bottle.

Prior to obtaining test results, the vessel was filled to an approximate depth of 150 mm with dionized distilled water. A heat flux setting of approximately 500 kW/m^2 was established to heat up the boiler assembly quickly and a warm-up time of approximately 2 hrs was allowed to elapse in order to ensure that the nucleation sites were properly activated and that the water was thoroughly degassed after which the power input was reduced to the desired level. One hour was allowed for the system to regain steady-state conditions after each subsequent change in heat flux or subcooling. The attainment of thermal equilibrium was indicated by invariant measurements of the numerous thermocouples that were located at different places in the boiler assembly. Once conditions had attained steady state, these measurements were sampled and the wattmeter and barometer readings were recorded. Subsequent to the test, the heat dissipated at the heater surface q was determined by deducting the total system heat losses calculated according to the method devised by Wiebe [17] from the wattmeter reading, and the temperature differences θ_w and θ_{sat} were determined by subtracting the measured bulk liquid temperature T_∞ from the surface temperature T_w, obtained by extrapolating the temperature gradient in the neck of the heater block to the surface and from the saturation temperature T_{sat} corresponding to the barometric pressure measurement P_{sat}, respectively. Based upon the results of calibration experiments performed in earlier studies using this apparatus, the uncertainty associated with any of these computed values was estimated to be less than 5 percent.

The bubble detection probe assembly used to locate the active nucleation sites was mounted on a vertical positioning mechanism to control the vertical distance between probe tip and the heating surface. An "X-Y stage" provided with two micrometers capable of reading $\pm 2.5 \times 10^{-3}$ mm was fixed to the cover plate on four supports. The stage provided a controlled and accurate travel of the bubble probe in two normal directions. The detection probe output voltage gave an indication of the conductance of the water or vapor in the 0.5 mm gap between the probe tip and the heating surface.

In order to place the probe on an active site, the X-Y stage was deployed. The Y micrometer was moved very slowly until significant activity in the signal was observed on the oscilloscope screen. Both X and Y micrometers were moved very small increments in both directions until the strongest signal was found, at which time the readings of X and Y micrometers were deemed to represent the position of the particular active site.

Each deflection of the oscilloscope beam represented a bubble emitted at that time. The bubble growth period began when the signal voltage started changing and terminated when the voltage signal returned to its initial value after which the cycle repeated itself. As the signals from the probes were transmitted to the oscilloscope, they were also transmitted to a DECLAB 11/03 digital computer. The computer was used to analyze the signal so as to determine bubble growth and waiting time in two different ways, an analogue-to-digital conversion procedure and a time interval measuring technique.

In the analogue-to-digital conversion procedure, the computer converted continuous data to discrete numbers through a digitization process at the rate of 5000 samples/s. A 10,000 value data sample was stored in the digital computer memory for subsequent analysis to calculate the growth time and the waiting time for each bubble detected within a 2 s

Nomenclature

A = parameter used in equation (1),

$$A=\left[\frac{\pi}{7}\,\frac{\rho_v h_{fg}(T_w-T_{\text{sat}})}{\rho_l\;T_{\text{sat}}}\right]^{1/2}$$

B = parameter used in equation (1),

$$B=\left[\frac{12}{\pi}\,\alpha_l\right]^{1/2}\text{Ja}$$

C = specific heat
g = gravitational acceleration
g_c = conversion factor
h_{fg} = latent heat of vaporization
Ja = Jakob number
$\text{Ja}=\rho_l C_l(T_w-T_\infty)/\rho_v h_{fg}$
k = thermal conductivity
P = pressure
q = heat transfer rate
q/A = heat flux
Q = heat transfer
R = bubble radius
R_d = bubble radius at departure
r_c = nucleation cavity radius
T = temperature
t = time
t_g = growth time
t_w = waiting time
X = parameter used in equation (5),

$$X=0.203\beta\sqrt{2\sigma g_c/g(\rho_l-\rho_v)}$$

Y = parameter used in equation (3),

$$Y=2\sqrt{3/\pi}\;\text{Ja}\sqrt{\alpha_l}$$

Z = position of vapor–liquid interface
α = thermal diffusivity
β = contact angle (radians)
δ = thermal layer thickness
ρ = density
σ = surface tension
θ = temperature difference $\theta=(T-T_\infty)$

Subscripts

l = liquid
sat = saturation
v = vapor
w = wall
∞ = bulk

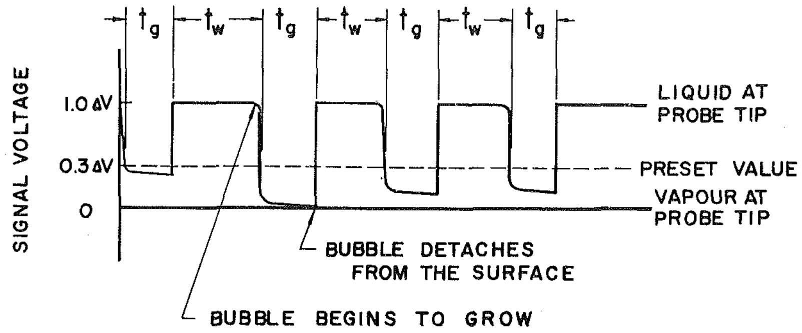

Fig. 2 Schematic representation of analogue-to-digital conversion procedure for measuring waiting time and growth time intervals

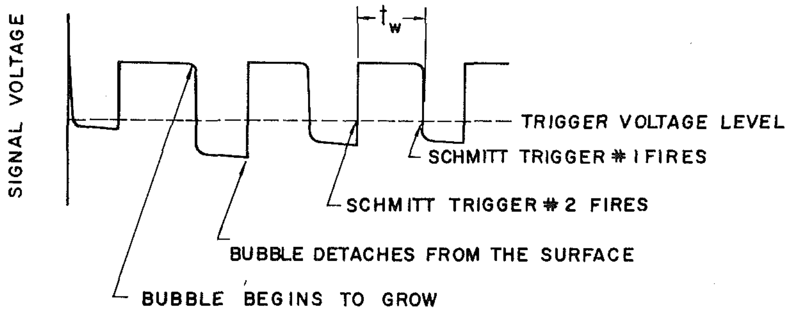

Fig. 3 Schematic representation of Schmitt trigger time interval measuring technique for measuring waiting time

period. The difference between the maximum and minimum values of the signal voltage was then computed and a preset value of 30 percent of that difference above the minimum voltage level was selected to differentiate between the bubble growth and waiting periods. Thus, a signal lower than the preset value was considered as a growth time signal whereas a signal higher than the preset value was considered a waiting time signal as depicted in Fig. 2. On that basis, the computer calculated the growth and waiting time for each bubble detected as well as the mean value of bubble growth and waiting times for the sample.

It was necessary to obtain multiple data samples to determine the mean bubble growth and waiting times since both varied in a random fashion. Hence, after the computer had carried out the averaging process ten times, a sampling criterion was imposed that depended on estimating the confidence interval for the true mean value of the waiting time in order to determine the number of additional samples required to obtain a satisfactory estimate. Each time a new sample after the first ten samples was analysed, a new confidence interval was determined in order that sampling could be stopped when the confidence interval was less than 5 percent of the current value of the sample mean of the bubble waiting time. The 5 percent limit on the confidence interval was applied to the waiting time only, since the fluctuations of the growth time were much less than those of the waiting time, which meant that the confidence interval for the growth time was even smaller.

The second method of analysis involved the use of two Schmitt triggers, devices incorporated in the real time clock of the minicomputer that could be used to start or stop the operation of a programmable clock/counter combination which determined time intervals or counted events. The Schmitt trigger device could be adjusted by a preselected "trigger" voltage, such that a pulse was transmitted to the clock/counter combination each time that the signal voltage passed it. This pulse caused the clock/counter combination to start or stop depending on its initial state. The process by which a Schmitt trigger senses an external event and interrupts the clock/counter combination is termed "Schmitt trigger firing."

Both Schmitt triggers were set to the same trigger voltage. If Schmitt trigger #2 were set to fire when the signal voltage rose above the trigger voltage level causing the clock/counter combination to start and if Schmitt trigger #1 were set to fire when the signal voltage fell below the trigger voltage level causing the clock/counter combination to stop, the bubble waiting time would be measured as depicted schematically in Fig. 3. If the previous Schmitt trigger settings were reversed, the clock/counter combination would measure the bubble growth time.

The Schmitt trigger analysis was only used to check the results of the analogue-to-digital conversion procedure, since the latter proved to be more accurate than the former during tests that were performed prior to the experimental investigation using frequency generators with predetermined waves of various form. The lower accuracy of the Schmitt trigger procedure can be attributed to the fact that the Schmitt trigger level could only be adjusted within a bandwidth of approximately 0.3 V which made it difficult to preset the two Schmitt triggers to exactly the same trigger voltage level.

A detailed description of the experimental apparatus, test conditions, test procedure, uncertainty analysis, and the full range of thermometric, growth time and waiting time data is presented in [19].

Results and Discussion

Figures 4, 5, and 6 show typical experimental results for bubble growth and waiting times for three of seven arbitrarily chosen active sites investigated in the present work. It is observed that the bubble growth time appears to be almost invariant, independent of liquid subcooling up to a certain degree of subcooling after which the bubble growth time curves change their slope showing a decrease in bubble growth time as the liquid subcooling increases further. This trend is

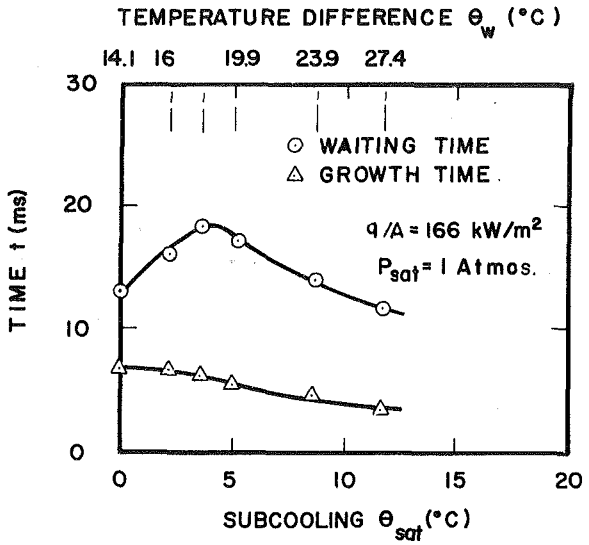

Fig. 4 Low heat flux waiting and growth time results for Site C

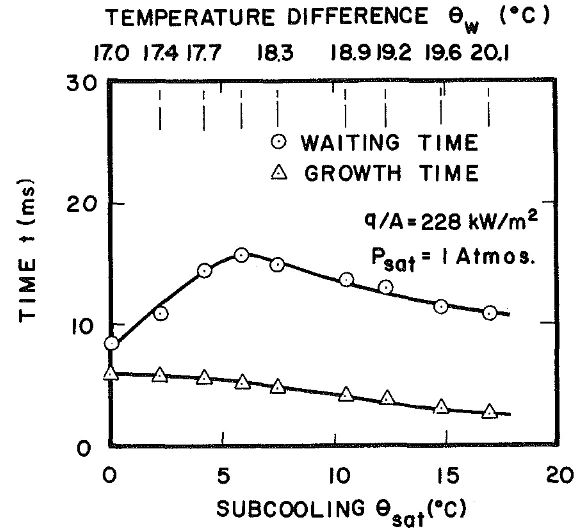

Fig. 5 Intermediate heat flux waiting and growth time results for Site E

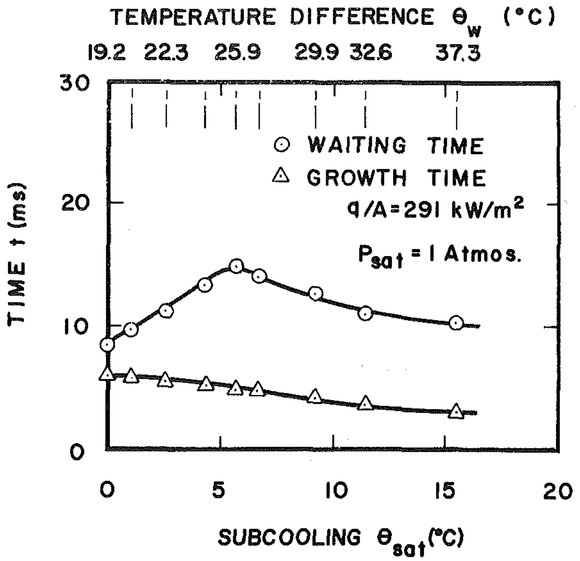

Fig. 6 High heat flux waiting and growth time results for Site G

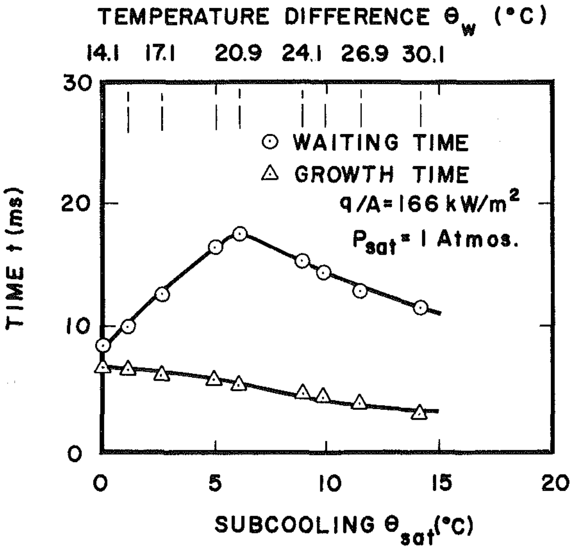

Fig. 7 Low heat flux waiting and growth time results for Site E

consistent with that observed by Ellion [7], Gunther and Kreith [8], and Cochran and Aydelott [9], although the subcooling ranges in which the experiments were performed are different.

The waiting time results show that the bubble waiting time increases as the liquid subcooling increases initially and then decreases with increasing subcooling. It is worth noting that the degree of liquid subcooling at the inflection point is almost invariant, independent of the heat flux or the active site investigated. This observation suggests that a change in the mechanism of heat transfer is responsible, since the reversal of bubble waiting with increasing subcooling occurs at the same degree of subcooling. Also, it is important to note that both the bubble growth time and waiting time curves change slope and start decreasing at the same degree of subcooling, which suggests an interrelation between bubble growth and waiting time phenomena. Such an interrelation was suggested earlier in the bubble growth model of Mikic and Rohsenow [20].

All bubble waiting time theories that assume a one-dimensional transient conduction mechanism for the transfer of heat from the heating surface to the bulk liquid predict that the waiting time increases as the liquid subcooling increases (see for example, Hsu [12] and Han and Griffith [13]). Such predictions agree with the experimental results of the present work up to about 6°C of subcooling, after which the discrepancy between transient conduction theory and the present experimental results is obvious. The only waiting time analysis, to the authors' knowledge, that predicts different behavior is that of Ali and Judd [15]. This paper shows that it is possible for the bubble waiting time to decrease as the liquid subcooling increases because of the influence of a convective heat transfer mechanism. According to the present work, this would hold true only after 6°C of subcooling had been attained. As a consequence of the previous discussion, it is concluded that the mechanism of heat transfer involving transient conduction from the heating surface to the bulk liquid prevails only up to a certain degree of subcooling, after which for higher degrees of subcooling another mechanism such as convection heat transfer becomes more important.

The experimental results also show that at the same level of heat flux, the bubble growth time doesn't change particularly from one active site to another while the bubble waiting time changes significantly as can be seen by comparing Fig. 7 with Fig. 4. This observation implies that while the bubble growth time is independent of cavity radius, the bubble waiting time is very much dependent upon it. It is also observed that for any active site, both bubble waiting time and growth time decrease as the level of heat flux increases, as can be seen by comparing Fig. 5 with Fig. 7.

Correlation of Experimental Results

Mikic, Rohsenow, and Griffith [21] derived a simple general relation for bubble growth rates in a nonuniform temperature field that is valid for both inertia-controlled and heat-diffusion-controlled growth. This relation can be written in dimensionless form as

$$\frac{dR^+}{dt^+}=\left[t^+ +1-\theta^+\left(\frac{t^+}{t^+ +t_w^+}\right)^{1/2}\right]^{1/2}-(t^+)^{1/2} \qquad (1)$$

where $R^+ = AR/B^2$, $t^+ = A^2t/B^2$, and $\theta^+ = (T_w - T_\infty)/(T_w - T_{\text{sat}})$. For cases where $t^+ >> 1$ integration of equation (1) yields the Mikic and Rohsenow [20] bubble growth relationship

$$R(t)=2\sqrt{3/\pi}\,\text{Ja}\sqrt{\alpha_l t}\left\{1-\frac{(T_w-T_\infty)}{(T_w-T_{\text{sat}})}\left[\left(1+\frac{t_w}{t}\right)^{1/2}-\left(\frac{t_w}{t}\right)^{1/2}\right]\right\} \qquad (2)$$

For water boiling at atmospheric pressure over a surface with a wall superheat of 20°C, $A^2/B^2 = 14926$ 1/s so that even for the first ms of the bubble growth history, $t^+ = 14.926 >> 1$, thereby satisfying the condition that makes equation (2) valid. The rate of bubble growth may then be obtained by differentiation of equation (2)

$$\frac{dR}{dt}=\frac{Y}{2\sqrt{t}}\left[1-\frac{\theta_w}{\theta_w-\theta_{\text{sat}}}\,\frac{1}{\left(1+\frac{t_w}{t}\right)^{1/2}}\right] \qquad (3)$$

where $Y = 2\sqrt{3/\pi}\,\text{Ja}\sqrt{\alpha_l}$, $\theta_w = (T_w - T_\infty)$ and $\theta_{\text{sat}} = (T_{\text{sat}} - T_\infty)$. Staniszewski [22] presented an empirical equation for bubble departure size of the form

$$R_d=0.203\beta\sqrt{2\sigma g_c/g(\rho_l-\rho_v)}\left(1+17.72\,\frac{dR}{dt}\right) \qquad (4)$$

where the constants have been converted to SI units from the equivalent values in Imperial units.

The bubble departure radius can be obtained by substituting equation (3) with $t = t_g$ into equation (4) giving

$$R_d=X\left\{1+\frac{8.86Y}{\sqrt{t_g}}\left[1-\frac{\theta_w}{\theta_w-\theta_{\text{sat}}}\,\frac{1}{\left(1+\frac{t_w}{t_g}\right)^{1/2}}\right]\right\} \qquad (5)$$

where

$$X=0.203\beta\sqrt{2\sigma g_c/g(\rho_l-\rho_v)}$$

and

$$Y=2\sqrt{3/\pi}\,\text{Ja}\sqrt{\alpha_l}$$

as before.

Setting equation (5) equal to equation (2) with $t = t_g$ for water boiling on a copper surface at atmospheric pressure yields

$$149.9\left\{1-\frac{\theta_w}{\theta_w-\theta_{\text{sat}}}\left[\left(1+\frac{t_w}{t_g}\right)^{1/2}-\left(\frac{t_w}{t_g}\right)^{1/2}\right]\right\}t_g$$

$$-\frac{46.8}{\theta_w-\theta_{\text{sat}}}\sqrt{t_g}+\frac{\theta_w}{\theta_w-\theta_{\text{sat}}}\,\frac{1}{\left(1+\frac{t_w}{t_g}\right)^{1/2}}=1 \qquad (6)$$

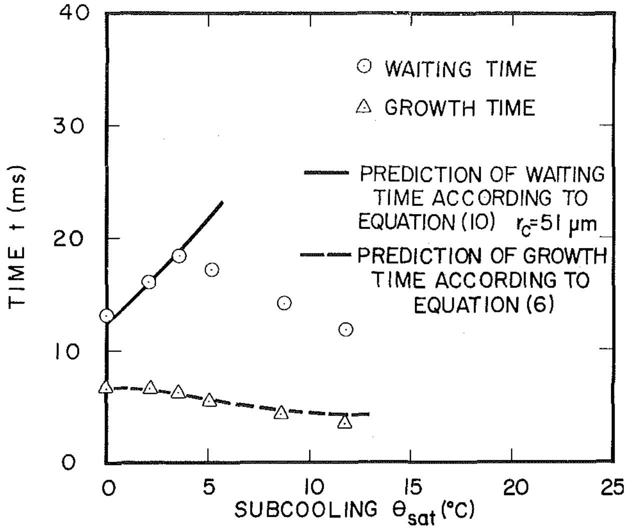

Fig. 8 Waiting and growth time correlations for Site C at 166 kW/m^2

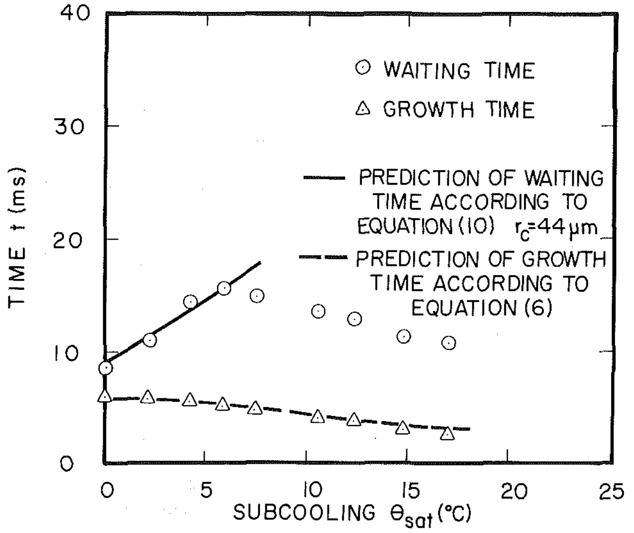

Fig. 9 Waiting and growth time correlations for Site E at 228 kW/m^2

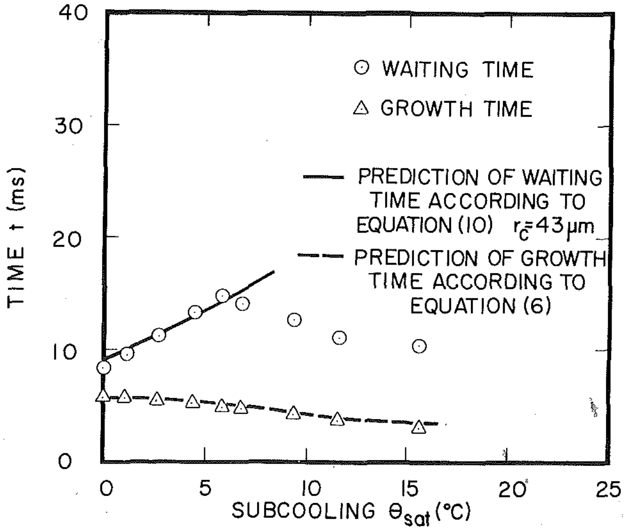

Fig. 10 Waiting and growth time correlations for Site G at 291 kW/m^2

Remarkable agreement was observed between the growth time predictions given by the solution of equation (6) and the experimental results as shown in Fig. 8, 9, and 10. The success of the growth model is attributed to the fact that it combines a bubble growth equation, which incorporates bubble growth in a nonuniform temperature field, with a bubble departure radius equation, which incorporates the dynamic effects in bubble growth. The favorable agreement established confidence in the measuring procedure, especially since the theory used to correlate the growth time results was dependent upon the waiting time data as well.

The portion of the bubble waiting time results that increase as the liquid subcooling increases were correlated using the Han and Griffith [13] one-dimensional transient conduction model. Han and Griffith treated the liquid as a semi-infinite medium so that the usual transient conduction theory is applicable and hence the thickness of the transient thermal layer is given by

$$\delta = \sqrt{\pi \alpha_l t} \tag{7}$$

The criterion for bubble initiation from a nucleation site of radius r_c according to Han and Griffth can be written as

$$T_{\mathrm{sat}} + \frac{2\sigma T_{\mathrm{sat}}}{r_c \rho_v h_{fg}} = T_w - (T_w - T_\infty)\frac{3 r_c}{2\delta} \tag{8}$$

which leads to the relationship

$$\delta = 3/2\left[\frac{(T_w - T_\infty)}{T_w - T_{\mathrm{sat}}[1 + (2\sigma/r_c \rho_v h_{fg})]}\right] r_c \tag{9}$$

When δ is expressed in terms of the waiting period using equation (7), then

$$t_w = \frac{9}{4\pi\alpha_l}\left\{\left[\frac{(T_w - T_\infty)}{T_w - T_{\mathrm{sat}}[1 + (2\sigma/r_c \rho_v h_{fg})]}\right] r_c\right\}^2 \tag{10}$$

In order to use equation (10) to predict the bubble waiting time for a specific nucleation site it is necessary to know the radius at the cavity mouth for this site, but no measurements were made of the active site radii in the present investigation. However, equation (10) may still be used; if for all the waiting time measurements at a specific site equation (10) should predict a unique value of r_c, then this value of r_c must represent the cavity radius and equation (10) would then express the relationship of the bubble waiting time with the other variables involved. A Newton-Raphson iteration technique was used to solve equation (10) for r_c after having substituted the appropriate fluid property values and all the different experimental values of waiting time, surface superheat, and liquid subcooling for a particular active nucleation site. The calculation procedure described above yielded values of r_c corresponding to each bubble waiting time measurement at a particular active site; these values were found to scatter around an average value by less than 10 percent of this value. Consequently, this average value of r_c was used in equation (10) to represent the cavity radius r_c, and the bubble waiting time was predicted as a function of subcooling. The agreement between waiting time experimental results and calculations using Han and Griffiths [13] waiting time theory incorporated in equation (10) is favorable as can be seen from Figs. 8, 9, and 10.

The theory of Singh, Mikic, and Rohsenow [23], which relates bubble waiting time to surface superheat and cavity radius, is potentially capable of explaining the waiting time results reported here. In [24], the same authors proposed a model for the stability of cylindrical nucleation cavities in which the criterion for stability was related to the conditions governing a reversal in the movement of the vapor–liquid interface within the cavity under the influence of inertia, viscous, and thermodynamic effects. By incorporating a relationship to predict the rate of heat transfer to the vapor-liquid interface, they were able to predict the time that would elapse from the moment that the interface began to penetrate the cavity after the departure of a bubble to the moment that the interface returned to the mouth of the cavity once again just prior to bubble emission. The essence of the theory was the relationship

$$Q(t_w)/\rho_v h_{fg} = \pi r_c^2 Z + 2/3 \pi r_c^3 \tag{11}$$

that was solved in [23] for water under saturated boiling conditions ($\theta_{sat} = 0$) to determine the waiting time t_w in terms of the penetration distance Z, the cavity radius r_c, and the superheat ($\theta_w - \theta_{\mathrm{sat}}$) which is implicit in the theoretical solution for $Q(t_w)$, the amount of heat transferred to the vapor–liquid interface in the time interval $0 \le t \le t_w$. Should increasing subcooling cause $Q(t_w)$ to increase at a greater rate than Z, then t_w would decrease with increasing θ_{sat} as noted. However, the authors only evaluated their theory for saturated boiling conditions and in as much as their theory is implicit, it is a difficult matter to extend it to accommodate subcooled boiling conditions. Furthermore, in the present experiment the superheat ($\theta_w - \theta_{\mathrm{sat}}$) was always larger than $2\sigma T_{\mathrm{sat}}/\rho_v h_{fg} r_c$, and the contact angle β would have been on the order of 60 deg so that in accordance with the nucleation cavity stability theory for saturated boiling of water, the vapor–liquid interface would have penetrated the nucleation cavity no more than one cavity radius distance. Consequently, in our analysis a more simplistic approach to formulating nucleation theory, involving transient heating of a semi-infinite fluid above a stationary nucleus sitting at the mouth of a nucleation cavity, was assumed to establish the criterion for bubble emission. The approach to formulating nucleation theory described above may yet be able to correlate the waiting time results over the entire subcooling range, but considerable subsequent development will be required.

Concluding Remarks

The experimental results suggest that conventional nucleation theory is not adequate for predicting bubble waiting time at high degrees of subcooling. It appears that bubble nucleation is governed by some other mechanism, and it is thought that in addition to conduction a convective component acts to transfer heat in the wake of the departing bubbles. The authors intend to carry out further research in order to determine the mechanism governing heat transfer in subcooled nucleate boiling and to advance a comprehensive theory that will explain the effect of subcooling on bubble waiting time.

References

1 Griffith, P., and Wallis, J. D., "The Role of Surface Conditions in Nucleate Boiling," *Chemical Engineering Progress Symposium Series*, Vol. 55, 1959, pp. 49–63.

2 Clark, H. B., Strenge, P. S., and Westwater, J. W., "Active Sites for Nucleate Boiling," *Chemical Engineering Progress Symposium Series*, Vol. 55, 1959, pp. 103–110.

3 Nix, G. H., Vachon, R. I., and Hall, D. M., "A Scanning Electron Microscopy Study of Pool Boiling Surfaces," *Proceedings of the Fourth International Heat Transfer Conference*, Paris-Versailles, 1970.

4 Nail, J. P., Vachon, R. I., and Morehouse, J., "An ASME Study of Nucleation Sites in Pool Boiling from 304 Stainless Steel," ASME JOURNAL OF HEAT TRANSFER, May 1974, pp. 132–137.

5 Rohsenow, W., "A Method for Correlating Heat Transfer Data for Surface Boiling of Liquids," ASME *Trans.*, Aug. 1952, pp. 969–976.

6 Hsu, Y. Y., and Graham, R. W., "An Analytical and Experimental Study of the Thermal Boundary Layer and Ebullition Cycle in Nucleate Boiling," NASA TN D-594, 1961.

7 Ellion, M. E., "Study of the Mechanism of Boiling Heat Transfer," Jet Propulsion Laboratory Memorandum 20-88, California Institute of Technology, 1954.

8 Gunther, F. G., and Kreith, F., "Photographic Study of Bubble Formation in Heat Transfer to Subcooled Water," Progress Report No. 4-120, Jet Propulsion Laboratory, California Institute of Technology.

9 Cochran, T. H., and Aydelott, J. C., "Effect of Subcooling and Gravity Level on Boiling in the Discrete Bubble Region," NASA TN D-3449, 1966.

10 Shoukri, M., and Judd, R. L., "Nucleation Site Activation in Saturated Boiling," ASME JOURNAL OF HEAT TRANSFER, Vol. 97, No. 1, 1975.

11 Judd, R. L., "Influence of Acceleration in Subcooled Nucleate Boiling," Ph.D. thesis, University of Michigan, 1968.

12 Hsu, Y. Y., "On the Size Range of Active Nucleation Cavities on a Heating Surface," ASME JOURNAL OF HEAT TRANSFER, Aug. 1962, pp. 207-216.

13 Han, C., and Griffith, P., "The Mechanism of Heat Transfer in Nucleate Pool Boiling," *International Journal of Heat and Mass Transfer*, 8, 1965, pp. 887-903.

14 Hatton, A. P., and Hall, I. S., "Photographic Study of Boiling on Prepared Surfaces," *Proceedings of the Third International Heat Transfer Conference*, Chicago, 1966, pp. 24-37.

15 Ali, A., and Judd, R. L., "An Analytical and Experimental Investigation of Bubble Waiting Time in Nucleate Boiling," ASME JOURNAL OF HEAT TRANSFER, Nov. 1981, pp. 673-678.

16 Best, R., Burow, P., and Beer, H., "Die Warmeubertragung beim Sieden under dem Einfluss Hydrodynamischer Vorgange," *International Journal of Heat and Mass Transfer*, Vol. 18, 1975, pp. 1037-1047.

17 Wiebe, J. R., "Temperature Profiles in Subcooled Nucleate Boiling," M. Eng. thesis, Mechanical Engineering Department, McMaster University, Canada, 1970.

18 Sultan, M., "Spatial Distribution of Active Sites and Bubble Flux Density," M. Eng. thesis, McMaster University, Canada, 1977.

19 Ibrahim, E. A., "An Experimental Investigation of the Effect of Subcooling on Bubble Growth and Waiting Time in Nucleate Boiling," M. Eng. thesis, McMaster University, Canada, 1983.

20 Mikic, B. B., and Rohsenow, W. M., "Bubble Growth Rates in Nonuniform Temperature Field," *Progress in Heat and Mass Transfer*, 1969, pp. 283-293.

21 Mikic, B. B., Rohsenow, W. M., and Giffith, P., "On Bubble Growth Rates," *International Journal of Heat and Mass Transfer*, 13, 1970, pp. 657-665.

22 Staniszewski, B. E., "Nucleate Boiling Bubble Growth and Departure," MIT Technical Report No. 16, Division of Sponsored Research, Cambridge, Mass., 1959.

23 Singh, A., Mikic, B. B., and Rohsenow, W. M., "Effect of Superheat and Cavity Site on Bubble Departure in Boiling," ASME JOURNAL OF HEAT TRANSFER, Vol. 99, No. 2, 1977, pp. 246-249.

24 Singh, A., Mikic, B. B., and Rohsenow, W. M., "Active Sites in Boiling," ASME JOURNAL OF HEAT TRANSFER, Vol. 98, No. 3, 1976, pp. 401-406.

R. Taleyarkhan

M. Podowksi

R. T. Lahey, Jr.
Fellow ASME

Rensselaer Polytechnic Institute,
Department of Nuclear Engineering,
Troy, N.Y. 12181

An Instability Analysis of Ventilated Channels

A mathematical model has been developed for the linear stability analyses of a system of ventilated parallel boiling channels. The model accomodates phasic slip, nonuniform power distribution, local losses, heater wall dynamics, channel-to-channel (radial) power skews, discrete or continuous ventilation between the channels, turbulent mixing between the channels, various donor-cell options for the lateral transport of energy and momentum, and a transverse momentum equation. A special matrix reduction algorithm was developed to efficiently solve the system of linearized, Laplace-transformed, nodal equations. A parametric study revealed that phasic slip, axial power distribution, heater wall dynamics, local losses, lateral ventilation, and radial power skew can have a significant effect on the stability characteristics of the system [5]. *Comparisons were made with the available experimental data, and good agreement was achieved.*

Introduction

Boiling flow instabilities must be considered in the design and analyses of many devices used in chemical processes and energy production. Sufficiently large excursions and/or oscillations from the steady state can affect the efficiency of the process, erode thermal margins, and may cause physical damage to mechanical components. As an example, flow instabilities are of particular concern in Boiling Water Nuclear Reactor (BWR) cores.

Comprehensive reviews of the status of the current analytical capabilities, and data base, have been conducted by Lahey & Drew [1]. The most common thermal-hydraulic instability mechanism is that due to density-wave oscillations. A good physical description of this phenomenon has been given previously [2]. Briefly, this type of instability is caused by the lag associated with the movement of density-waves which travel at the so-called kinematic wave speed. An analysis of this instability mechanism can be performed using standard feedback control techniques [2].

Most previous experimental and theoretical studies of density-wave oscillations have been conducted for one-dimensional flows, in single or unventilated parallel channels. Experimental studies on density-wave oscillations in a system of heated parallel channels, ventilated at discrete axial locations, have been performed by Veziroglu et al. [3]. No previous theoretical studies, to quantify ventilated channel instability mechanisms, have been reported.

The purpose of this study is to theoretically analyze density-wave instabilities in heated ventilated channels. The interconnections between the channels can be continuous, as between rod-bundle subchannels, or at discrete locations.

Because of the nonlinearity of the two-phase flow conservation equations, a stability analysis is very difficult. Indeed, there are no general solution techniques with which to analyze the stability of nonlinear partial differential equations. Solutions can be obtained numerically in the time domain [4]; however, this approach is normally quite expensive. Moreover it is often difficult to prevent numerical instabilities, and the spatial smearing of the kinematic wave fronts.

Frequency domain techniques involve linearization and Laplace transformation of the conservation equations. The linear stability threshold of a boiling system can be accurately predicted with this relatively inexpensive method. Hence, this technique was adopted for the present study.

A nodal approach has been used to arrive at the characteristic equation of the system. The nodal equations were evaluated using a special matrix reduction scheme [5, 6], which produces accurate results with a minimum of computational effort.

Location of the roots of the characteristic equations in the complex plane determines the system's stability behavior. Any root having a positive real part implies that particular operating state is linearly unstable. Several techniques are available for the determination of the various roots. We have chosen to use a modified Nyquist criterion [5].

Analytic Modeling

The objective of this study was to investigate density-wave oscillations in certain "benchmark" system geometries, shown in Fig. 1. As can be seen, any channel can have at most two interconnections. The sign convention followed was that any quantity transported between channel i, and the neighboring channels, $i-1$ and $i+1$, was positive from channel i to $i+1$ (or $i-1$ to i), and negative from $i+1$ to i (or i to $i-1$).

Assumptions

The assumptions made in deriving the conservation equations were the same as normally made in subchannel analysis [2, 4, 5]. Additionally, subcooled boiling was neglected, and system pressure is considered to be time invariant.

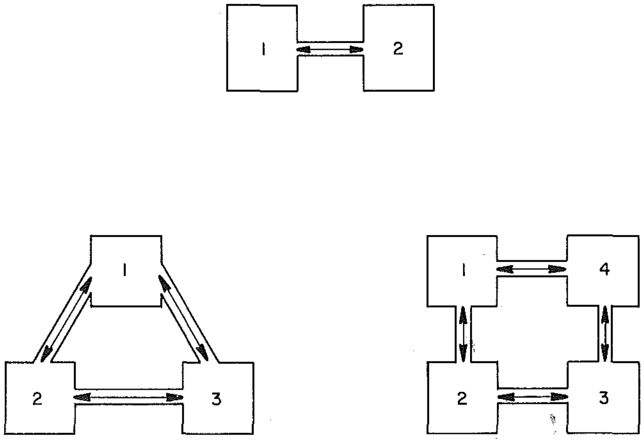

Fig. 1 Schematic diagram (top-view) for two, three and four ventilated channels

---

Contributed by the Heat Transfer Division and presented at the ASME Winter Annual Meeting, Phoenix, Arizona, November 14–19, 1982. Manuscript received by the Heat Transfer Division August 4, 1983. Paper No. 82-WA/HT-3.

Nodalized Conservation Equations. The flow field to be discretized is shown in Fig. 2, for a representative two channel case. As seen, it consists of a single-phase region, and a two-phase region for each ventilated channel. The two regions are separated by the boiling boundary ($z=\lambda_i$), defined as that location where the liquid enthalpy reaches its saturation value.

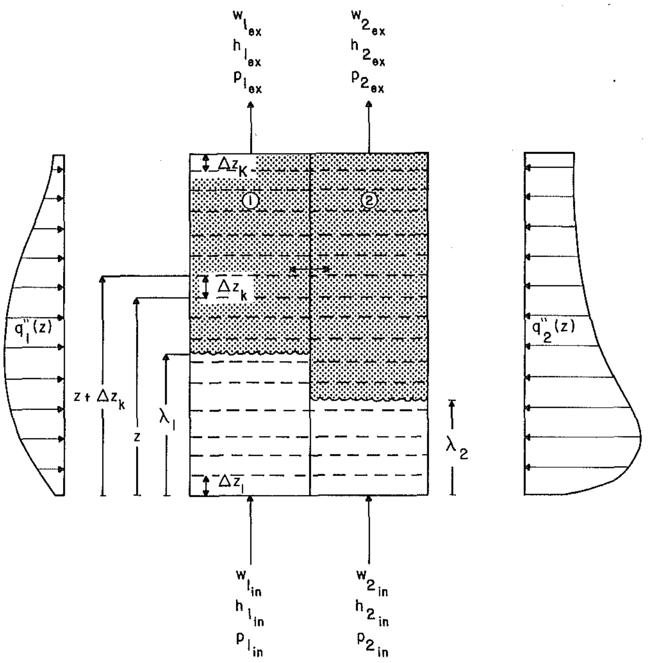

Fig. 2 Nodalization of a ventilated two-channel system

Each of the two regions is nodalized as shown in Fig. 2 by the dotted lines. Of particular interest are the nodes having a moving boundary within the node itself (i.e., at $z=\lambda$), or at its extremities (i.e., z or $z+\Delta z_k$). All possible moving boundary node configurations are shown in Fig. 3. These configurations occur when we set up new nodes in all channels at the location of each boiling boundary λ_i. Figure 4 gives an illustration of this method for a two subchannel case, where the thermal-hydraulic conditions of both adjacent channels are close, but not identical. Setting up nodal boundaries in both channels at locations λ_i and λ_{i+1}, we effectively increase the number of nodes within each ventilated channel between z and $z+\Delta z_k$, from one to three. In this case, the new node between λ_i and λ_{i+1} has upper (λ_i) and lower (λ_{i+1}) boundaries that are functions of time, and this must be taken into account when we derive the nodal conservation equations.

The various moving boundary node configurations can be differentiated by the use of Kronecker delta functions as

$$\delta_{m1,1} \triangleq \begin{cases} 1, & \text{when the node has no moving boundaries within it (Figs. 3(}b\text{), 3(}c\text{), 3(}d\text{))} \\ 0, & \text{otherwise} \end{cases}$$

$$\delta_{m2,1} \triangleq \begin{cases} 1, & \text{when the node has fixed boundaries, with a moving boundary within it (Fig. 3(}a\text{)} \\ 0, & \text{otherwise} \end{cases}$$

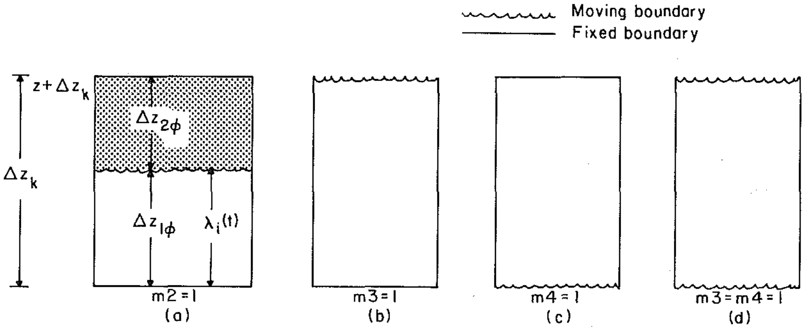

m2 = 1 (a) m3 = 1 (b) m4 = 1 (c) m3 = m4 = 1 (d)

Fig. 3 Possible moving boundary node configuration

Nomenclature

A_{x-s} = cross-sectional flow area
D_H = hydraulic diameter
f = Darcy-Weisbach friction factor
F_D = coefficient of the momentum flux term due to diversion crossflow in the nodal axial momentum equation
F_T = coefficient of the momentum flux interchange between adjacent channels due to turbulence in nodal axial momentum equation
$<F>$ = cross-section average of a function F
g_c = $32.17\ \mathrm{lb_m\text{-}ft/lb_f - s^2} = 1.0\ \mathrm{kg\text{-}m/N\text{-}s^2}$
g = gravitational acceleration
Δh_{sub} = $h_f - h_{\text{in}}$, inlet subcooling
h_{fg} = latent heat of evaporation
h_{cm} = center-of-mass enthalpy $\triangleq [\rho_l h_l(1 - <\alpha> + \rho_g h_g <\alpha>]$
h = two-phase enthalpy $\triangleq [h_l(1 - <x>) + h_g <x>]$
K = local loss coefficient
l = transverse control volume length
M = mass
p = static pressure
P_H = heater perimeter
q = heat rate
q' = heat transfer per unit axial length due to diversion cross flow
q'' = heat flux
q'_m = heat transfer per unit length due to turbulent mixing
s = Laplace transform parameter
S_g = gap width
t = time
T = temperature
U_p = $w/(\rho' A_{x-s})$ = velocity of the center-of-momentum
w_m = lateral mass flow rate due to turbulent mixing
w = mass flow rate
w' = diversion crossflow per unit axial length
x = flow quality
z = axial location

Greek Symbols

α = void fraction
β = mixing Stanton number
$\gamma(t)$ = temporal part of the internal heat generation rate

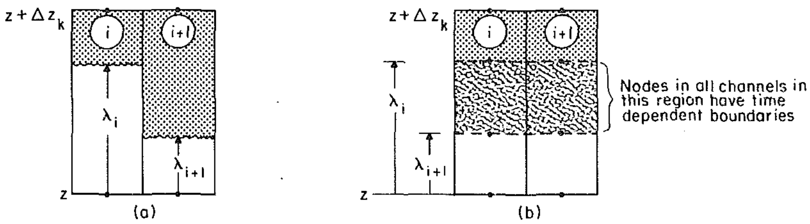

Fig. 4 **Illustration of a node having time-dependent upper and lower boundaries**

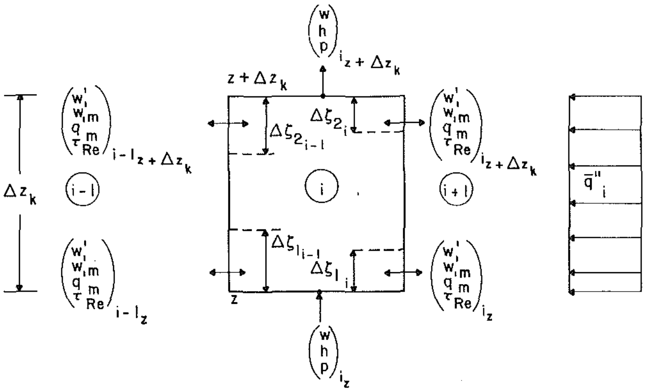

Fig. 5 **Typical node between axial locations z and $z+\Delta z_k$, for channel i communicating with two neighboring channels**

$$\delta_{m3,1} \triangleq \begin{cases} 1, & \text{when the node has the lower boundary fixed, but the upper boundary is a function of time (Fig. 3(}b\text{))} \\ 0, & \text{otherwise} \end{cases}$$

$$\delta_{m4,1} \triangleq \begin{cases} 1, & \text{when the node has the upper boundary fixed, but the lower boundary is a function of time (Fig. 3(}c\text{))} \\ 0, & \text{otherwise} \end{cases}$$

It should be noted that the case shown in Fig. 3(*d*) can be treated as a superposition of the cases shown in Figs. 3(*b*) and 3(*c*).

The subchannel conservation equations [5] can be integrated over an arbitrary node k, shown in Fig. 5. This node has (for generality) discrete ventilation paths. The discrete ventilation length at the lower (z) and upper ($z+\Delta z_k$) extremities of the node are referred to as $\Delta\zeta_1$ and $\Delta\zeta_2$, respectively. Using the rule of Leibnitz for the moving boundary nodes, we obtain [5]:

Nodal Mass Conservation

$$w_{i_{z+\Delta z_k}} + [\Delta\zeta_{1_i} \; w'_{i_z} + \Delta\zeta_{2_i} \; w'_{i_{z+\Delta z_k}} + \Delta\zeta_{1_i} w'_{m_{i_z}}$$

$$+ \Delta\zeta_{2_i} w'_{m_{i_{z+\Delta z_k}}}] - w_{i_z} - [\Delta\zeta_{1_{i-1}} w'_{i-1_z} + \Delta\zeta_{2_{i-1}} w'_{i-1_{z+\Delta z_k}}$$

$$+ \Delta\zeta_{i-1} w'_{m_{i-1_z}} + \Delta\zeta_{2_{i-1}} w'_{m_{i-1_{z+\Delta z_k}}}]$$

$$+ \delta_{m1,1} \Delta z_k A_{x-s_i} \frac{d}{dt} < \bar{\rho}_i > + \delta_{m2,1} \Big\{ A_{x-s} \frac{d}{dt} [\rho_f \Delta z_{1\phi_i}$$

$$+ < \bar{\rho}_{2_i} > \Delta z_{2\phi_i}] \Big\} + \delta_{m3,1} [< \bar{\rho}_i >$$

$$- < \rho_i (z + \Delta z_k) >] A_{x-s_i} \frac{dz}{dt} \Big|_{z+\Delta z_k}$$

$$- \delta_{m4,1} [< \bar{\rho}_i > - < \rho_i (z) >] A_{x-s_i} \frac{dz}{dt} \Big|_{z} = 0 \qquad (1)$$

Nodal Energy Conservation

$$(wh)_{i_{z+\Delta z_k}} + \{ \Delta\zeta_{1_i} [q'_{i_z} [q'_{i_z} + q'_{m_{i_z}}] + \Delta\zeta_{2_i} [q'_{i_{z+\Delta z_k}}$$

$$+ q'_{m_{i_{z+\Delta z_k}}}]\} - (wh)_{i_z} - \{ \Delta\zeta_{1_{i-1}} [q'_{i-1_z} + q'_{m_{i-1_z}}]$$

Nomenclature (cont.)

ρ_k = density of phase-k
$<\rho>$ = two-phase density $\triangleq \rho_l(1 - <\alpha>) + \rho_g <\alpha>)$
ρ' = momentum density $\triangleq 1 \Big/ \left[\frac{(1 - <x>^2)}{\rho_l(1 - <\alpha>)} + \frac{<x>^2}{\rho_g <\alpha>} \right]$
μ = dynamic viscosity
ϵ = eddy diffusity
ϕ^2_{lo} = two-phase friction multiplier
Φ = two-phase local loss multiplier
κ = multiplier to assess importance of two-phase turbulence (equal-volume-exchange model)
λ = nonboiling length (i.e., the boiling boundary)
ω = angular frequency
Δ = difference
τ = stress
δ = perturbation
δ_{ij} = $\begin{Bmatrix} 1, \text{if } i=j \\ 0, \text{if } i \neq j \end{Bmatrix}$, the Kronecker delta function
ζ = length related to discrete ventilation path

Subscripts

ex = exit
f = saturated liquid
fg = difference between saturated vapor and liquid properties
g = saturated vapor
H = heater
HT = heat transfer
in = inlet
k = node number
l = liquid (subcooled) phase
sat = saturation
T = total
v = vapor phase
xs = cross section
w = wall
1ϕ = single phase
2ϕ = two phase
m = turbulent mixing
$\hat{}$ = Laplace transformed quantity

$$+\Delta\zeta_{2_{i-1}}[q'_{i-1_{z+\Delta z_k}}+q'_{m_{i-1_{z+\Delta z_k}}}]\}-q''_{i_k}P_{H_i}\Delta z_k$$

$$+\delta_{m1,1}\Delta z_k A_{x-s_i}\frac{d}{dt}\overline{(<\rho_i>h_{cm_i})}$$

$$+\delta_{m2,1}A_{x-s_i}\left[\frac{d}{dt}(\rho_f\bar{h}_{1_i}\Delta z_{1\phi_i}+\overline{<\rho_{2_i}>h}_{cm_i}\Delta z_{2\phi_i})\right]$$

$$+\delta_{m3,1}[\overline{<\rho_i>h_{cm_i}}-<\rho_i(z+\Delta z_k)>]A_{x-s_i}\frac{dz}{dt}\bigg|_{z+\Delta z_k}$$

$$-\delta_{m4,1}[\overline{<\rho_i>h_{cm_i}}-<\rho_i(z)>h_{cm_i}(z)]A_{x-s_i}\frac{dz}{dt}\bigg|_{z}=0 \quad (2)$$

where

$$(\bar{\ })\triangleq\frac{1}{\Delta z_k}\int_z^{z+\Delta z_k}(\ )dZ$$

Nodal Axial Momentum Conservation

$$(wU_p)_{i_{z+\Delta z_k}}+\{F_D S_{g_i}[\Delta\zeta_{1_i}\tau_{i_z}+\Delta\zeta_{2_i}\tau_{i_{z+\Delta z}}]$$

$$+F_T S_{g_i}[\tau_{\mathrm{Re}_{i_z}}+\tau_{\mathrm{Re}_{i_{z+\Delta z_k}}}]\}-(wU_p)_{i_z}$$

$$-\{F_D S_{g_{i-1}}[\Delta\zeta_{1_{i-1}}\tau_{i-1_z}+\Delta\zeta_{2_{i-1}}\tau_{i-1_{z+\Delta z_k}}]$$

$$+F_T S_{g_{i-1}}[\Delta\zeta_{1_{i-1}}\tau_{\mathrm{Re}_{i-1}}+\Delta\zeta_{2_{i-1}}\tau_{\mathrm{Re}_{i-1_{z+\Delta z_k}}}]\}$$

$$+\delta_{m1,1}\Delta z_k\frac{d}{dt}(\bar{w}_i)+\delta_{m2,1}\frac{d}{dt}(\Delta z_{1\phi_i}\bar{w}_{1_i}+\Delta z_{2\phi_i}\bar{w}_{2_i})$$

$$+\delta_{m3,1}(\bar{w}_i-w_{i_{z+\Delta z_k}})-\delta_{m4,1}(\bar{w}_i-w_{i_z})\frac{dz}{dt}\bigg|_z$$

$$=g_c A_{x-s_i}(p_{i_z}-p_{i_{z+\Delta z_k}})-\delta_{m1,1})-\delta_{m1,1}(g\sin\theta_i A_{x-s_i}\Delta z_k$$

$$<\bar{\rho}_i>+\frac{f_i\Delta z_k}{2\rho_f A_{x-s_i}D_{H_i}}\overline{w_i^2\phi_{lo_i}^2})-\delta_{m2,1}\Big\{g\sin\theta_i A_{x-s_i}(\Delta z_{1\phi_i}\rho_f$$

$$+\Delta z_{2\phi_i}<\bar{\rho}_{2_i}>)+\frac{f_i}{2\rho_f A_{x-s_i}D_{H_i}}[\Delta z_{1\phi_i}(\overline{w_i^2})_1$$

$$+\Delta z_{2\phi_i}(\overline{w_i^2\phi_{lo_i}^2})_2]\Big\} \quad (3)$$

Nodal Transverse Momentum Conservation

$$\frac{d}{dt}[w_i'l]_{z+\Delta z_k}+\frac{l_I}{\Delta z_k}\{w'_{i_{z+\Delta z_k}}[k_i^*U_{p_{i_{z+\Delta z_k}}}$$

$$+(1-k_i^*)U_{p_{i+1_{z+\Delta z_k}}}]-w'_{i_z}[k_i^*U_{p_{i_z}}+(1-k_i^*)U_{p_{i+1_z}}]\}$$

$$=-\frac{K_{G_i}}{2S_{g_i}\rho_f}\{|w_i'|w_i'[k_i^*\Phi_i+(1-k_i^*)\Phi_{i+1}\}_{z+\Delta z_k}$$

$$+S_{g_i}g_c(p_i-p_{i+1})_{z+\Delta z_k} \quad (4)$$

The terms w', w'_m, q', q'_m, τ', and τ'_m in equations (1–3) represent, respectively, the mass, energy, and momentum transfer in the lateral direction due to diversion crossflow (w') and turbulence. For lateral transfers between channels i and $i+1$, these quantities can be expressed as [2, 4]:

Turbulent Mass Transfer (per unit axial length)

$$w'_{m_i}=(1-\delta_{k,1})\kappa\frac{\epsilon_i}{l_{p_i}}(\rho_f-\rho_g)(\alpha_{i+1}-\alpha_i)S_{g_i} \quad (5)$$

Energy Transfer (per unit axial length) Due to Diversion Crossflow

$$q_i'=w_i'[k_i^*h_i+(1-k_i^*)h_{i+1}] \quad (6)$$

Energy Transfer (per unit axial length) Due to Turbulence

$$q'_{m_i}=\delta_{k,1}\beta_i S_{g_i}\left(\frac{w_i+w_{i+1}}{A_{x-s_i}+A_{x-s_{i+1}}}\right)(h_i-h_{i+1})$$

$$+(1-\delta_{k,1})\frac{\epsilon_i}{l_{p_i}}S_{g_i}(\rho_f h_f-\rho_g h_g)(\alpha_{i+1}-\alpha_i) \quad (7)$$

Momentum Flux Due to Diversion Crossflow

$$\tau_i=w_i'[k_i^*U_{p_i}+(1-k_i^*)U_{p_{i+1}}]/S_{g_i} \quad (8)$$

Momentum Flux Due to Turbulence (Reynolds stress)

$$\tau_{\mathrm{Re}_i}=\frac{\delta_{k,1}\beta_i(w_i+w_{i+1})}{g_c(A_{x-s_i}+A_{x-s_{i+1}})}(U_{p_i}-U_{p_{i+1}})$$

$$+(1-\delta_{k,1})\frac{\epsilon_i}{l_{p_i}g_c}\left(\frac{w_{i+1}}{A_{x-s_{i+1}}}-\frac{w_i}{A_{x-s_i}}\right) \quad (9)$$

where

$$\delta_{k,1}\triangleq\begin{cases}1, k=1, \text{ equal mass exchange model used [4]}\\ 0,\ k\neq 1, \text{ equal volume exchange model used [2]}\end{cases}$$

$$k_i^*=\begin{cases}1.0, \text{ donor-cell method used, and } w_i'>0\\ 0.0, \text{ donor-cell method used, and } w_i'<0\\ 0.5, \text{ average-of-channels method used}\end{cases}$$

The remaining notation is either conventional or defined in the Nomenclature section. During volume-for-volume interchange between the adjacent channels, mass transfer occurs only if one, or both, of the two adjacent ventilated channels have a two-phase fluid flowing through. Note, an equal-mass-exchange model, such as used in COBRA [4], always gives no net mass transfer due to turbulence.

In the transverse momentum equation, the lengths l and l_I are effective over which transverse momentum storage and inertia effects are important. A potential flow analysis [5] indicates that l and l_I should be proportional to the gap width (S_g).

Equations (1-9) represent the nodalized system of equations for a general node with moving boundaries. For a node having no moving boundaries, the nodalized system of equations are obtained from equations (1–9) by setting $m1=1$ and $m2, m3, m4=0$.

Further assumptions were necessary to evaluate the node-averaged quantitites, $<\bar{\rho}>$, $\bar{h}$, $\overline{<\rho>h_{cm}}$ and $\overline{w^2\phi_{lo}^2}$. Assuming a uniform heat flux over the length of any node (q_k''), and relatively small lateral transports, we have,

$$\bar{h}\simeq(h_z+h_{z+\Delta z_k})/2 \quad (10)$$

and

$$\bar{w}\simeq(w_z+w_{z+\Delta z_k})/2 \quad (11)$$

The node-average void fraction ($\bar{\alpha}$) was obtained using equations (10) and (11). Thus the quantities $<\bar{\rho}>$ and $\overline{<\rho>h_{cm}}$ were evaluated.

Finally for small crossflow rates, $\overline{w^2\phi_{lo}^2}$ can be approximated by

$$\overline{w^2\phi_{lo}^2}\simeq\bar{w}^2\bar{\phi}_{lo}^2 \quad (12)$$

where the node-averaged, two-phase friction multiplier $(\overline{\phi_{lo}^2})$ is evaluated at the node-average enthalpy $\bar{h}$.

Linearization and Laplace Transformation of the Nodal

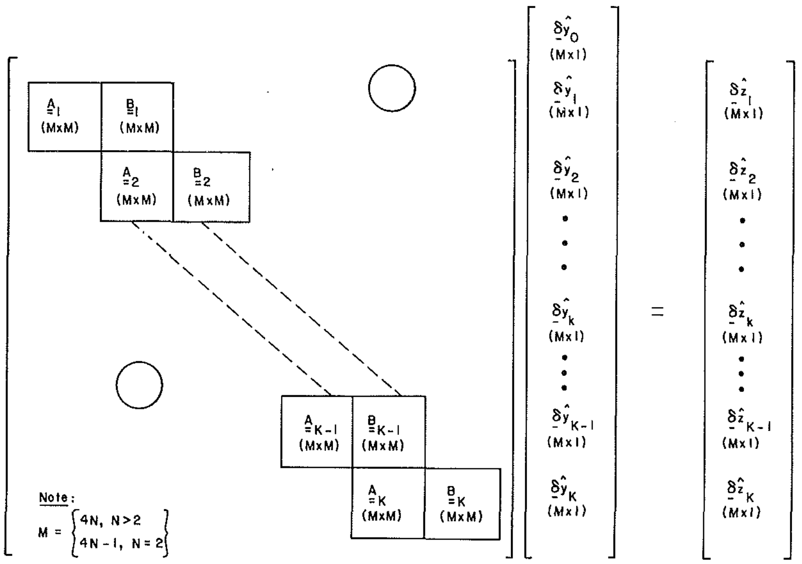

Fig. 6 System of nodalized conservation equations in matrix form for flow in an *N* ventilated channel system

Equations. The nodal conservation equations, equations (1-9), were linearized using classical first-order perturbation techniques [2]. The resulting set of equations were then Laplace-transformed to convert the system from the time domain to the frequency domain. In particular, by perturbating and Laplace-transforming equations (1-9), one obtains for an arbitrary node k, between axial locations z and $z+\Delta z_k$, the following set of algebraic equations [5]

$$\sum_{j\epsilon D_1}\left[A^{(l)}_{w_{j_z}}(s)\,\hat{\delta}w_{j_z}+A^{(l)}_{h_{j_z}}(s)\,\hat{\delta}h_{j_z}+A^{(l)}_{w_{j_{z+\Delta z_k}}}(s)\,\hat{\delta}w_{j_{z+\Delta z_k}}\right.$$

$$\left.+A^{(l)}_{h_{j_{z+\Delta z_k}}}(s)\,\bar{\delta}h_{j_{z+\Delta z_k}}\right]$$

$$+\sum_{j\epsilon D_2}\left[A^{(l)}_{w_{j_z}}(s)\,\hat{\delta}w'_{j_z}+A^{(l)}_{w_{j_{z+\Delta z_k}}}\,\hat{\delta}w'_{z+\Delta z_k}\right]$$

$$+\sum_{j\epsilon D_3}\left[A^{(l)}_{p_{j_z}}(s)\,\hat{\delta}p_{j_z}+A^{(l)}_{p_{j_{z+\Delta z_k}}}(s)\,\hat{\delta}p_{j_{z+\Delta z_k}}\right]+A^{(l)}_{\lambda_i}(s)\,\hat{\delta}\lambda_i$$

$$+A^{(l)}_{z}(s)\,\hat{\delta}z+A^{(l)}_{z+\Delta z_k}(s)\,\hat{\delta}(z+\Delta z_k)+A^{(l)}_{q_i}(s)\,\hat{\delta}q''_i=0$$

$$\begin{bmatrix} i=1,2,\ .\ .\ .\ ,N \\ l=1,2,3,4 \\ k=1,2,3,\ .\ .\ .\ ,K \end{bmatrix} \tag{13}$$

where

K = the total number of axial nodes along any channel
N = the total number of channels
D_1, D_2, D_3 are set indicators, defined by

$$D_1 \triangleq \begin{cases} i-1,\ i,\ i+1, \text{ for } i=2,\ .\ .\ .\ N-1 \\ n-1,\ N,\ 1, \text{ for } i=N \\ N,1,2, \text{ for } i=1 \end{cases}$$

$$D_2 \triangleq \begin{cases} i-1,\ i, \text{ for } i=2,\ N \\ N,\ 1, \text{ for } i=1 \end{cases}$$

$$D_3 \triangleq \begin{cases} i,\ i+1, \text{ for } i=1,\ N-1 \\ N,\ 1, \text{ for } i=N \end{cases}$$

The coefficients $A(s)$ of equation (13) have been tabulated elsewhere [5].

The perturbed and Laplace transformed nodal mass and energy conservation equations for the single-phase region of the node in Fig. 3(*a*) yields a relation of the form

$$\hat{\delta}\lambda_i=f\Big(\hat{\delta}w_{i_z},\ \hat{\delta}w_{i-1_z},\ \hat{\delta}w_{i+1_z},\ \hat{\delta}h_{i_z},\ \hat{\delta}h_{i-1_z},$$

$$\hat{\delta}h_{i+1_z},\ \hat{\delta}w'_{i_z},\ \hat{\delta}w'_{i-1_z},\ \hat{\delta}q''_{i_z}\Big) \tag{14}$$

Finally, the nodal heat flux perturbation $\hat{\delta}q''$, in equations (13) and (14), is related to the dynamics of the heater wall. Heater wall dynamics have been found to have a potentially significant effect on system stability [5, 7]. Hence good mathematical modelling for $\hat{\delta}q''$, is imperative, both in the single-phase and two-phase regions.

In the single-phase region one can use either an exact analytical approach [2] or a nodal scheme [5]. We choose to employ the nodal approach, which unlike analytical modeling, allows for radial variation of heater properties (e.g., density and specific heat) and internal heat generation. Details of this process have been reported elsewhere [5, 7]. Using this procedure, we obtain

$$\hat{\delta}q''_i=Z_{1_i}(s)\,\hat{\delta}w_i+Z_{2_i}(s)\,\hat{\delta}h_i+Z_{3_i}(s)\hat{\delta}q'''_i \tag{15}$$

where the complex coefficients, $Z(s)$, have been tabulated for various heater geometries [5]. Equations (13), (14), and (15) can now be combined to yield the generic set of linearized, Laplace-transformed, nodal equations, which can be conveniently cast in matrix form as

$$\underline{\underline{\mathrm{A}}}_k\,\hat{\delta}\mathbf{y}_{k-1}+\underline{\underline{B}}_k\,\hat{\delta}\mathbf{y}_k=\hat{\delta}\mathbf{z}_k$$

where,

$$\hat{\delta}\mathbf{y}_k=\left[\hat{\delta}\mathbf{w}_{z+\Delta z_k},\ \hat{\delta}h_{k+\Delta z_k},\ \hat{\delta}w'_{k+\Delta z_k},\ \hat{\delta}p_{k+\Delta z_k}\right]^T \tag{16}$$

$\underline{\underline{A}}_k$ and $\underline{\underline{B}}_k$ consist of submatrices corresponding to the coefficients of the subvectors $\hat{\delta}\mathbf{w}$, $\hat{\mathbf{h}}$, $\hat{\delta}\mathbf{w}'$ and $\hat{\delta}\mathbf{p}$, at the inlet and exit of node-k. Each subvector consists of N components,

$$\hat{\delta}w=[\hat{\delta}w_1,\hat{\delta}w_2,\ .\ .\ .\ ,\ \hat{\delta}w_N]^T.$$

Equation (16) written for all nodes $k=1,\ .\ .\ .\ ,K$ forms the matrix system, shown in Fig. 6.

The System Transfer Function. One can note a "chain effect" in the matrix system in Fig. 6. That is, the nodal exit

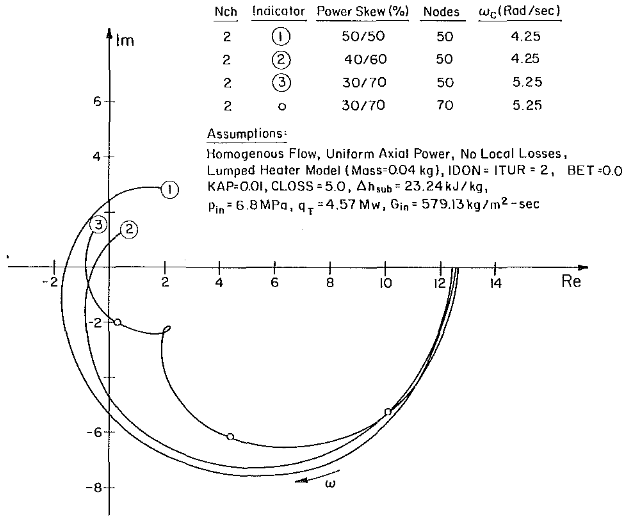

Fig. 7 MAZDA-4F verification run (the effect of power skewing and nodal convergence, with inlet subcooling)

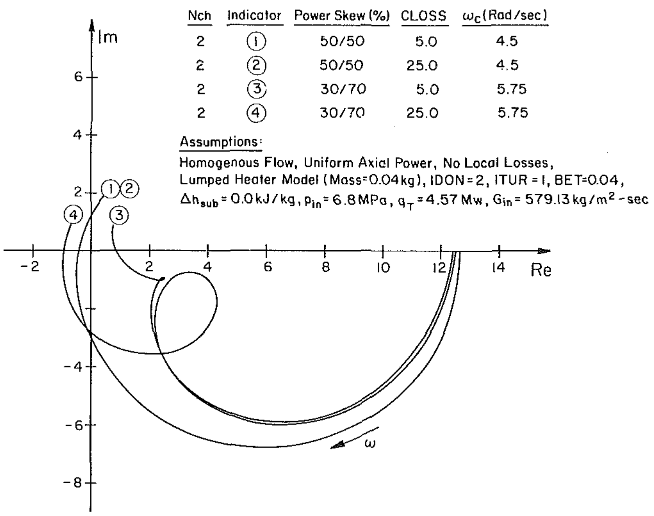

Fig. 8 MAZDA-4F verification runs (the effect of transverse loss coefficient)

variables for node k become the inlet variables for node $k+1$. Taking advantage of this property and using a specially developed matrix reduction scheme [5, 6], one obtains the system's exit vector, $\delta\hat{\mathbf{y}}_K$, in terms of the system's inlet vector, $\delta\hat{\mathbf{y}}_o$, and the nodal internal generation vectors $\delta\hat{\mathbf{z}}_k$ ($k=1,2,3,\ldots,K$). The resultant form is given by,

$$\delta\hat{\mathbf{y}}_K = \left[\sum_{k=K}^{1}(-\underline{\underline{B}}_k^{-1}\underline{\underline{A}}_k)\right]\delta\hat{\mathbf{y}}_o + \sum_{k=1}^{K}\Big\{\delta_{k,K}\underline{\underline{B}}_K^{-1} + (1-\delta_{k,K})\left[\sum_{k'=K}^{k+1}(-\underline{\underline{B}}_{k'}^{-1}\underline{\underline{A}}_{k'})\right]\underline{\underline{B}}_k^{-1}\Big\}\delta\hat{\mathbf{z}}_k \tag{17}$$

where $\delta_{k,K}$ is the Kronecker delta function defined as

$$\delta_{k,K} \triangleq \begin{cases} 1, & k=K \\ 0, & \text{otherwise} \end{cases}$$

Equation (17) enables one to obtain expressions relating the system exit vectors, $\delta\hat{\mathbf{p}}_{ex}$, $\delta\hat{\mathbf{h}}_{ex}$, $\delta\hat{\mathbf{w}}'_{ex}$ and $\delta\hat{w}_{ex}$ in terms of the system inlet vectors $\delta\hat{\mathbf{p}}_{\text{in}}$, $\delta\hat{\mathbf{h}}_{\text{in}}$, $\delta\hat{w}'_{\text{in}}$, $\delta\hat{\mathbf{w}}_{\text{in}}$, and the nodal internal heat generation vectors, $\delta\hat{z}_k$.

As an example, by setting $\delta\hat{\mathbf{w}}'_{\text{in}}$, $\delta\hat{\mathbf{h}}_{\text{in}}$ and $\delta\hat{\mathbf{z}}_k$ ($k=1,\ldots,K$), to zero, in equation (17) we can obtain

$$\delta\hat{\mathbf{p}}_{ex} - \underline{\underline{H}}_1(s)\delta\hat{\mathbf{p}}_{\text{in}} = \underline{\underline{H}}_2(s)\,\delta\hat{\mathbf{w}}_{\text{in}} \tag{18}$$

where $\underline{\underline{H}}_1(s)$ and $\underline{\underline{H}}_2(s)$ are $N \times N$ square matrices.

Further, assuming all channels have a common upper and lower plena, and assuming incompressibility of the liquid in the lower plenum, we can write

$$\delta\hat{p}_{i_{ex}} = \delta\hat{p}_{ex} \quad (i=1,2,\ldots,N) \tag{19}$$

$$\delta\hat{p}_{i_{\text{in}}} = \delta\hat{p}_{\text{in}} \quad (i=1,2,\ldots,N) \tag{20}$$

$$\delta\hat{w}_T = \sum_{i=1}^{N}\delta\hat{w}_{i_{\text{in}}} \tag{21}$$

where p_{in}, p_{ex}, and w_T are the common inlet plenum pressure, exit plenum pressure, and the total mass flow rate entering the lower plenum, respectively.

Multiplying equation (18) by $[\underline{\underline{H}}_2(s)]^{-1}$ we obtain

$$[\underline{\underline{H}}_2(s)]^{-1}\delta\hat{p}_{ex} - [\underline{\underline{H}}_2(s)]^{-1}[\underline{\underline{H}}_1(s)]\delta\hat{\mathbf{p}}_{\text{in}} = \delta\hat{w}_{\text{in}} \tag{22}$$

Summing up all elements of equation (22) and using equations (19), (20) and (21), we obtain

$$\hat{\delta}\Delta p_T = G(s)\,\hat{\delta}w_T \tag{23}$$

where Δp_T is the plenum-to-plenum pressure drop, which is assumed to be the same for all channels, and $G(s)=0$ is the characteristic equation of the system.

Equation (23) has been used to investigate parallel channel stability margins for various operating conditions and system geometry.

The analytical model described above was encoded as a digital computer code, MAZDA-4F [5]. This code has been compared with exact analytical results [2], and good agreement was achieved. The steady-state parameters were evaluated using the code MAZDA-4S [5], which is based on classical subchannel techniques [4].

Results

A linear stability analysis of boiling parallel channels was performed using the Nyquist criterion.

For the present purpose, an encirclement of the Nyquist locus around the origin will indicate a linearly unstable operating state, otherwise the operating state is linearly stable. A parametric study was conducted to investigate the sensitivity of the various models and options incorporated into MAZDA-4F, using operating conditions similar to those for a BWR/4. A typical BWR/4 rod bundle was partitioned into two subchannels. These subchannels communicated continuously along the axial direction. The power skew (i.e., the radial distribution of bundle power) between the two channels, and other pertinent operating data, are given in Figs. 7 and 8, respectively.

A detailed study of nodalization, convergence characteristics, and comparisons with exact analytical results [2] was done [5]. It was found that 50 axial nodes were sufficient to obtain good agreement with the exact results (<1 percent relative error between exact results [2] and MAZDA-4F predictions).

Parametric Study. In the parametric study, a dissimilarity between the two channels was introduced by radial power skewing. Figures 7 and 8 show the effect of power skewing and K_g, transverse loss coefficient CLOSS. As can be seen, both parameters have a significant impact on the system stability behavior. Note that increasing K_g is destabilizing, since this lessens the coupling between the two channels.

Comparison With Experiment. The results from the mathematical model were compared with the steam/water data of Veziroglu et al. [3]. Briefly, the experimental test section, shown schematically in Fig. 9, consisted of two

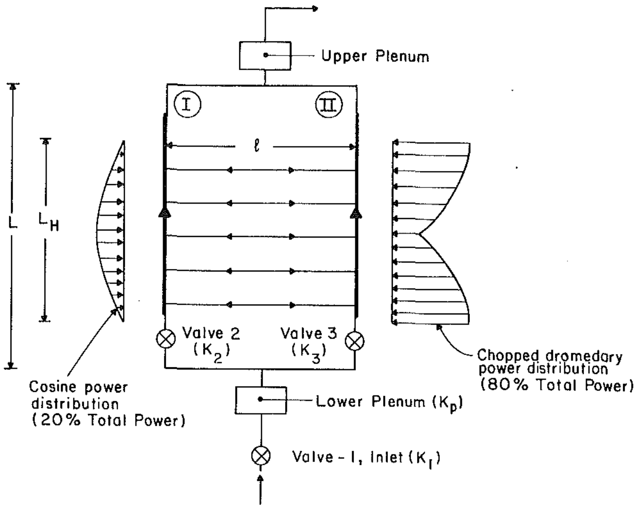

Fig. 9 Schematic representation of experimental test section of Veziroglu et al. [3]

electrically heated tubes that were ventilated at five discrete locations. The steady-state flow distribution was evaluated using the MAZDA-4S code [5], a code similar to the COBRA code. A key input to the problem is the transverse loss coefficient (CLOSS), which unfortunately was not measured by the experimenters. Thus the lowest value of CLOSS, which gave a convergent steady-state solution, was used in MAZDA-4F, the frequency domain code, for stability evaluation. Fortunately, the predicted stability results were not very sensitive to the steady-state flow distribution.

The data indicated that systems with power skewing were more unstable than ones without power skewing. Numerous MAZDA-4F runs were made to generate the linear stability boundary. The results are shown by the triangles in Fig. 10. Also shown is the measured stability boundary. The agreement between MAZDA-4F predictions and the experimental data is good.

Summary and Conclusions

This study has focused on the mathematical modeling and analysis of density-wave oscillations in ventilated boiling channels. It has been shown that radial variations in power distribution and transverse loss coefficient can have a significant effect on the predicted stability margins. This implies that to achieve an accurate prediction of stability margin, considerable care must be taken in determining these parameters.

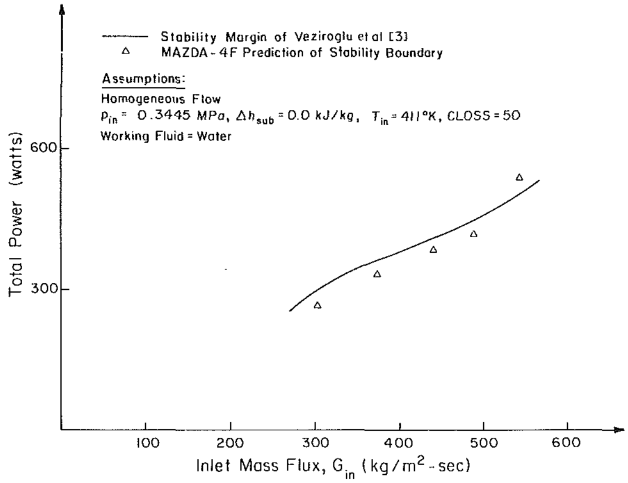

Fig. 10 Stability boundary with experimental data

Comparison was made with the available experimental data. The basic trends were confirmed, and good agreement was obtained between the stability boundary predictions of MAZDA-4F and the experimental results.

Acknowledgments

The authors wish to acknowledge the financial support given this work by the USNRC.

References

1 Lahey, R. T., Jr., and Drew, D., "An Assessment of the Literature Related *to LWR Instability Modes*," NUREG/CR-144 (1980).

2 Lahey, R. T., Jr., and Moody, F. J., "The Thermal-Hydraulics of a Boiling Water Nuclear Reactor," ANS Monograph, 1977.

3 Veziroglu, T. N., and Lee, S. S., "Sustained and Transient Boiling Flow Instabilities in a Cross-Connected Parallel Channel Upflow System," AEC Oak Ridge National Laboratory Subcontract No. 2975, Final Report, 1971.

4 Rowe, D. S. et al., "COBRA-IV-I: An Interim Version of COBRA for Thermal-Hydraulic Analysis of Rod Bundle Nuclear Fuel Elements and Cores," BNWL-1962, PNWL, 1976.

5 Taleyarkhan, R. P., Podowski, M., and Lahey, R. T., Jr., "An Analysis of Density-Wave Oscillations in Ventilated Channels," NUREG/CR-2972, 1983.

6 Taleyarkhan, R. P., Podowski, M., and Lahey, R. T., Jr., "The Development of a Nodal Method for the Stability Analysis of Ventilated Boiling Channels," 2nd International Topical Meeting on Nuclear Reactor Thermal-Hydraulics, Santa Barbara, Calif. 1983.

7 Taleyarkhan, R., Podowski, M., Lahey, R. T., Jr., "The Effect of Heater Wall Dynamics on Density-Wave Oscillations in a Boiling Channel," *Proceedings of the 7th International Heat Transfer Conference*, Munich, 1982.

P. C. Wayner, Jr.

C. Y. Tung[1]

M. Tirumala

J. H. Yang[2]

Department of Chemical Engineering
and Environmental Engineering,
Rensselaer Polytechnic Institute,
Troy, N.Y. 12181

Experimental Study of Evaporation in the Contact Line Region of a Thin Film of Hexane

The transport processes in the contact line region (junction of evaporating thin liquid film, vapor, and substrate) of stationary steady-state evaporating thin films of hexane with various bulk compositions were studied experimentally. The substrate temperature distribution and liquid film thickness profile were measured, analyzed, and compared with previous results on other systems. The results demonstrate that small changes in the bulk composition significantly alter the characteristics of the transport processes in the contact line region. The curvature gradient at the liquid-vapor interface is a strong function of evaporation rate and composition. Concentration and temperature gradients give interfacial shear stresses and flow patterns that enhance contact line stability.

1 Introduction

In a recent set of publications, the use of a scanning microphotometer to determine the heat transfer characteristics of a stationary evaporating film in the film thickness range $\delta < 10^{-5}$ m was described [1, 2]. Decane and a mixture of 98 percent decane plus 2 percent tetradecane by weight were discussed. Herein experimental results obtained using research grade hexane, technical grade hexane, and a mixture of 98 percent hexane plus 2 percent octane are presented and compared with our previous results. The experimental results demonstrate that significant differences in the transport characteristics result from small changes in the bulk composition. These current results are part of a systematic study of the effect of bulk composition on the stability and heat transfer characteristics of evaporating thin films in the contact line region. We note that the size of the evaporating thin film for the film thickness range $\delta < 9 \times 10^{-6}$ m has increased in each subsequent experiment by the judicious choice of a fluid mixture. The transport processes are also found to be more complex. For example, the film profiles discussed in [1, 2] were steady; however, the film profiles for the hexane/octane system discussed herein oscillated.

It has been proposed that since the chemical potential of a curved film is a function of the film profile, considerable information concerning the heat transfer characteristics of an evaporating film can be obtained by studying the effect of evaporation rate on the profile of a stationary evaporating film [1-3]. As a result of this approach, we can now discuss three different systems that can be characterized by the location of the maximum film curvature. These three systems are shown schematically in Fig. 1, in which the abscissa scale is 100 X the ordinate scale. System I represents an evaporating finite apparent isothermal contact angle system, $\beta_{ai} > 0$, in which the maximum curvature occurs at the contact line where a monolayer is present. The modifier apparent is used to emphasize the fact that we do not observe the contact angle (which has molecular dimensions) per se. A recent theoretical study of the thickness profile of an isothermal film with a finite apparent contact angle discussed the physicochemical basis for having the maximum curvature at the contact line [4]. The results of an experimental and theoretical study of an evaporating ethanol meniscus that had a finite apparent angle were presented in [3, 5]. In this case, the analyses indicated that the maximum curvature was located at the contact line and that fluid flows towards the contact line as a result of a curvature gradient. System II represents a relatively pure evaporating thin film, which has an apparent isothermal contact angle equal to zero (spreading system). Theory would indicate that the maximum curvature should occur at a film thickness of the order of $10^{-7} - 10^{-8}$ m, the region where capillarity and disjoining pressure are approximately equal. However, the experimental results indicate that the maximum curvature occurred at a thickness of approximately 10^{-6} m [1]. We feel that the reason for this difference is the presence of impurities in the bulk fluid. In any case, maximum curvature occurs at a location where the thickness is considerably larger than expected in a pure fluid. Fluid flows as a result of gradients in the "disjoining pressure," curvature, and surface tension in the region below this approximate thickness and as a result of a curvature gradient and surface tension gradient in the region above this thickness. The "disjoining pressure" concept describes the relative effects of cohesion and adhesion. Reference [2] was primarily concerned with the microscopic details of System III A, which represents a spreading system in which the transport processes were altered as a result of the controlled addition of a second component with a different vapor pressure. The second component

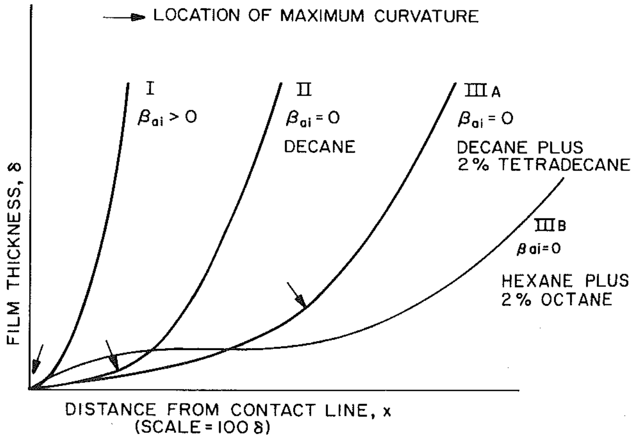

Fig. 1 Evaporating film thickness profiles

---

[1] Present address: General Motors Research Laboratories, Warren, Mich. 48090

[2] Present address: Department of Chemical Engineering, Chonnam National University, Republic of Korea

Contributed by the Heat Transfer Division for publication in the JOURNAL OF HEAT TRANSFER. Manuscript received by the Heat Transfer Division August 29, 1983.

significantly altered the cause of fluid flow and the location of maximum curvature. For example, the addition of a small amount of tetradecane to decane (98 percent decane/2 percent tetradecane moved the location of maximum curvature to $\delta \approx 4 \times 10^{-6}$ m [2]. Some of the new results presented herein concern System III B: a bulk composition of 98 percent hexane and 2 percent octane by weight. In this case the maximum curvature occurs at $\delta > 9 \times 10^{-6}$ m for some of the heat fluxes, and the length of the film before this point can be relatively larger for high rates of evaporation. In some of the experiments, the film length was considerably longer than that shown in Fig. 1. Based on these observations, we feel that the contact line region of an evaporating thin film looks like an evaporating extended meniscus in which the location of the maximum curvature and the heat transfer characteristics can be varied by system selection. Preliminary analyses of the experimental data indicate that a surface shear stress resulting from the effect of concentration and temperature on the surface tension controls the location of maximum curvature [6]. As demonstrated herein by equation (10), the curvature gradient of the evaporating liquid film can be easily altered for a given flow rate by a surface shear stress.

There is voluminous literature concerning the effect of interfacial phenomena on heat and mass transfer in thin liquid films. The review of this literature is of course beyond the scope of this paper. However, easy entry into this literature is accomplished through various review papers (e.g., [7-9]. Of particular relevance to our experimental technique is the pioneering work by Sharp, who used the interference of monochromatic light to visualize an evaporating liquid film at the base of bubbles during nucleate boiling [10]. While these studies demonstrated the usefulness of interferometry to elucidate transport processes in boiling, the transient nature of the phenomena studied included many uncertainties not present in the current study. This work has been extended by Jawurek [11] and by Voutsinos and Judd [12]. Yang and Nouri used laser shawdowgraphy to study surface tension effects in evaporating drops on a flat surface [13]. In other demonstrations of the usefulness of optical techniques to study the effect of surface shear, fluid flow in a climbing liquid film has been investigated by various researchers using interferometry (e.g., [14, 15]). Using a micrometer to measure the thickness of thicker films, Orell and Bankoff studied the formation of a dry spot in a nonboiling evaporating film on a horizontal surface [16]. Various authors have used the reflection of light from a liquid surface to enhance our understanding of fluid motion during vacuum evaporation and extraction (e.g., [17-19]). As demonstrated in these references and herein, optical observations of the film profile greatly enhance our understanding of the underlying fluid flow field. The literature that includes the effect of conduction in the substrate on the evaporating meniscus is limited to a few papers (see, e.g., [20, 21]).

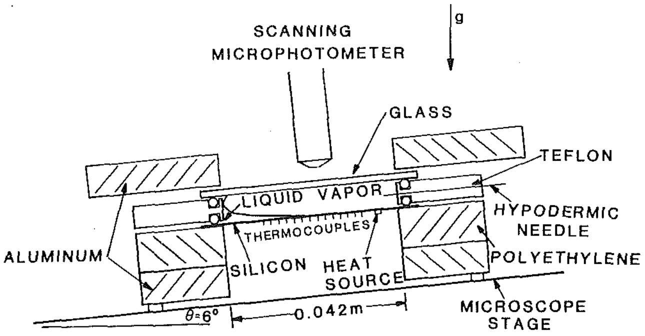

Fig. 2 Cross section of heat transfer cell along centerline

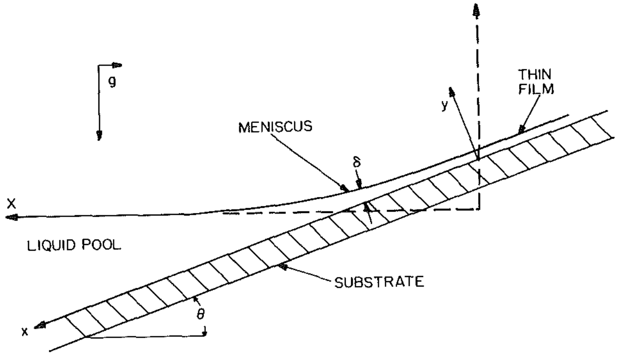

Fig. 3 Extended meniscus on flat plate

2 Experimental Design and Procedures

The experimental design and procedures are essentially those given in [1, 2, 6] and will only be briefly described here. As shown in Fig. 2, a meniscus was formed on an inclined flat plate by injecting a small amount of fluid through a hypodermic needle into a cell that was closed to the atmosphere except through the needle opening. An expanded view of the meniscus is given in Fig. 3. For the results presented herein on the hexane-octane system, the substrate was a 3.81×10^{-4} m thick, 0.059 m × 0.050 m, rectangular plate cut from a single crystal silicon wafter (N-type, phosphorous dopent) that had been lapped and chemically polished to a mirror finish. The other data were taken using plates which were 3.55×10^{-4} m thick [6]. This is a standard electronics material, used for making solid-state devices and is extremely well characterized and smooth. For uniformity, the wafers were initially cleaned and dipped in hydrofluoric acid to remove the original oxide surface layer. It is known that a passivating layer of SiO_2 approximately 3 - 4 $\times 10^{-9}$ m thick grows on a silicon surface in the atmosphere at room temperature. Further growth at an appreciable rate is severly

Nomenclature

B = constant in dispersion term
g = acceleration due to gravity
K = curvature
K' = dK/dx
n = index of refraction
P = pressure, power
q = heat flux
T = temperature
t = thickness of substrate
u = velocity in x-direction
β = contact angle
Γ = mass flow rate per unit length of contact line
δ = film thickness
δ' = $d\delta/dx$
Δx = region of interest
θ = angle
λ = thermal conductivity
μ = viscosity
ν = kinematic viscosity
ρ = density
ϕ = angle of refraction
σ = surface tension
σ' = $d\sigma/dx$
τ = shear stress

Subscripts

l = liquid
p = pressure
T = based on thermocouples
v = vapor
x = distance parallel to substrate
y = distance perpendicular to substrate
τ = shear stress

limited below 600°C by the slow diffusion of oxygen through the SiO_2 film. Therefore, our "silicon surfaces" were in fact a silicon base with a 3 - 4 × 10^{-9} m coating of SiO_2. The rectangular side of the (100) surface-oriented silicon substrate was cut parallel to the [110] direction of its face centered cubic lattice.

The heat source was a rectangular, platinum, d-c resistance heater approximately 2 × 10^{-3} m by 4 × 10^{-2} m in size that was formed by brushing on the underneath surface a platinum liquid film. The film was subsequently baked for 10 min at 600°C to form a solid and connected to a d-c power supply. The distance between the centerline of the platinum film and the first thermocouple was 6 × 10^{-3} m. The power into and out of the zone of evaporation was obtained from the measured temperature distribution, which was obtained using thermocouples. The location of the rest of the thermocouples, which were glued to the underside of the substrate, are given in Fig. 13, which is discussed below. Twelve chromel-alumel thermocouples with an approximate bead diameter of 3 × 10^{-4} m were made from the same spool of wire with a diameter of 10^{-4} m and positioned along the centerline of substrate for this purpose. The contact line was usually positioned so that five thermocouples were located above it and seven below it. However, insufficient fluid sometimes resulted in a lower relative position of the contact line. Since the substrate width to thickness ratio is greater than 100 and since the thermal conductivity of the silicon substrate is very large ($\lambda = 120$ Wm/K), the temperature distribution is one-dimensional except in the vicinity of the contact line, where the evaporation rate should be very large.

The plate was inclined relative to gravity at an angle of approximately 6 deg by placing it on the scanning stage of a tilted Leitz MPV-2 microscope/photometer. As shown in the photographs discussed in section 5, an optical interference pattern representing the thickness profile was readily observed through the microscope using monochromatic light. The MPV-2 microphotometer has a variable-speed automatic scanning stage and a variable diaphram which allowed the reflectivity of a small rectangular area set parallel to the fringes to be measured using green light (548 nm) and recorded on a strip chart recorder. Except for the hexane-octane data, this was used to obtain the liquid-film thickness profile data presented herein. Due to waviness in the evaporating hexane-octane films, instantaneous photographs of the interference patterns were obtained and analyzed for this system. At higher heat fluxes, all the systems oscillated. In addition to the meniscus profile, the temperature distribution in the x-direction was measured using thermocouples attached to the underside of the substrate.

3 Fluid Flow in an Evaporating Film

Neglecting inertia terms and the y-component of velocity, the following simplified Navier-Stokes equation can be written for the velocity in the evaporating thin film shown in Figs. 2 and 3

$$\frac{d^2u}{dy^2} = \frac{1}{\mu}\frac{dP_l}{dx} - \frac{g}{\nu}\sin\theta \tag{1}$$

Equation (1) can be solved for the velocity distribution using the following boundary conditions

$$y = 0 \quad u = 0 \tag{2}$$

$$y = \delta \quad \tau_{yx} = \frac{d\sigma}{dx} \tag{3}$$

The second boundary condition has a significant effect on the velocity distribution in the experiments because of large gradients in concentration and temperature, and therefore the interfacial tension. Using equations (1-3), we obtain

$$u = \left(\frac{1}{\mu}\frac{dP_l}{dx} - \frac{g}{\nu}\sin\theta\right)\left(\frac{y^2}{2} - \delta y\right) + \frac{y}{\mu}\frac{d\sigma}{dx} \tag{4}$$

Using equation (5) for the pressure ($-\sigma K - B\delta^4$ accounts for the normal pressure difference at the liquid-vapor interface) in equation (4) and integrating across the liquid film leads to equation (7) for the mass flow rate in the liquid film, $\Gamma(x)$.

$$P_l = P_v - \sigma K - B\delta^{-4} + \rho g(\delta - y)\cos\theta \tag{5}$$

in which

$$K = \frac{d^2\delta}{dx^2}\left[1 + \left(\frac{d\delta}{dx}\right)^2\right]^{-1.5} \tag{6}$$

and $B\delta^{-4}$ accounts for the disjoining pressure.

$$\Gamma(x) = \Gamma_p(x) + \Gamma_\tau(x) \tag{7}$$

In this equation, the following effects due to pressure and surface shear stress are delineated

$$\Gamma_p(x) = \frac{\delta^3}{3\nu}\left(\sigma\frac{dK}{dx} - \frac{4B}{\delta^5}\frac{d\delta}{dx} + \rho g\sin\theta - \rho g\frac{d\delta}{dx}\cos\theta\right) \tag{8}$$

$$\Gamma_\tau(x) = \frac{\delta^2}{3\nu}\frac{d\sigma}{dx}(K\delta + 1.5) \tag{9}$$

Experimentally, K' and δ' can be obtained from $\delta(x)$, whereas σ' cannot be measured and is modeled.

Due to large variations in the size of the individual terms in equations (8) and (9), general statements concerning their relative importance in all regions are impossible to make. However, we can note the following. Since δ is of the order 10^{-6} m, the product $K\delta$ is neglegible compared to 1.5. Although $\sigma K'$ varies considerably, and in some cases even equals zero at some locations when $\delta > 10^{-6}$ m (see Fig. 12)), it usually is of order 10^4–10^5, which is large relative to $\rho g \sin\theta$ and $\rho g \delta' \cos\theta$. The disjoining pressure term, $4B\delta^{-5}\delta'$, depends on thickness and slope. Since B is of the order 10^{-28} N.m^2 for pure Si and 8.6 × 10^{-30} N.m^2 for pure SiO_2 [1], this term quickly becomes substantial below δ^{-7}, when δ' increases due to flow. An additional complication arises since B would vary (probably decrease) with contamination. Taking $B = 10^{29}$, $\delta = 10^{-6}$, $\delta' = 10^{-2}$ gives $4B\delta^{-5}\delta' = 0.4$. Therefore, except at very low flow rates, the two most important terms in the flow rate in the region $\gtrsim 10^{-6}$ m are

$$\Gamma(x) = \frac{\delta^3\sigma}{3\nu}\frac{dK}{dx} + \frac{\delta^2}{2\nu}\frac{d\sigma}{dx} \tag{10}$$

As a result, the curvature gradient is coupled to the surface tension gradient, which is a function of the concentration and temperature gradients. In our experiments the temperature increases in the direction of flow. Since the surface tension decreases with an increase in temperature, temperature induced surface shear stress would hinder fluid flow towards the contact line. On the other hand, the concentration of the component with the higher surface tension (lower vapor pressure in our studies) increases in the direction of flow. Therefore, a surface tension gradient due to a concentration gradient in our studies would enhance flow toward the contact line. Models to evaluate these effects are currently under study. As representative examples, the expected velocity profiles for two systems based on these concepts are presented in Fig. 4. The enhanced flow due to a shear stress would cause the evaporating film to elongate if the concentration effect is larger than the temperature effect on surface tension. Numerical results based on this model are presented in [22, 6].

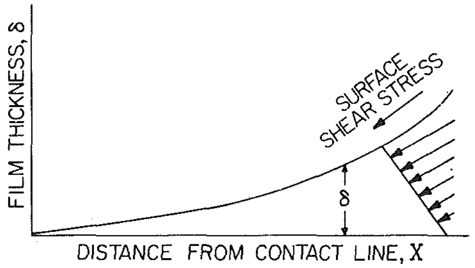

a) CHARACTERISTIC VELOCITY PROFILE FOR MIXTURE 98% HEXANE/2% OCTANE

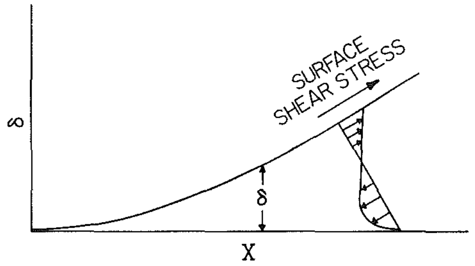

b) CHARACTERISTIC VELOCITY PROFILE FOR RESEARCH GRADE HEXANE

Fig. 4 Characteristic velocity profiles

4 Temperature Distribution and Integral Evaporation Rate

Since the substrate width to thickness ratio is greater than 100 and since the thermal conductivity of the silicon substrate is very large ($\lambda = 120$ Wm/K), the following one-dimenisonal conduction model can be used to calculate the heat flux down the plate q_x except in the vicinity of the contact line, where the evaporation rate should be very large.

$$q_x = -\lambda \frac{dT}{dx} \tag{11}$$

Due to the size of the thermocouples ($\approx 3 \times 10^{-4}$ m) compared to a (presumed) small region ($\Delta x \approx 3 \times 10^{-4}$ m) of very large heat flux q_y near the contact line, the temperature data can give only the following integral measurement of the heat flow rate per unit length of interline for the region Δx

$$P_T = \int_x^{x+\Delta x} q_y dx = t(q_x|_x - q_x|_{x+\Delta x}) \tag{12}$$

The region Δx, which is larger than the beforementioned 3×10^{-4} m, can include regions of high and low heat fluxes. We note that condensation over a portion of the region is also possible because the liquid–vapor interfacial temperature is nonuniform. Since various models for q_y can fit the integral data, our q_y models based on only the temperature data are not definitive at present without extensive modeling with the coupled transport equations. Therefore, the true heat flux cannot be obtained from only these results. However, they do fix the relative size of the integral heat loss for comparative purposes and give useful although incomplete information concerning the details of the evaporation process. In some of our previous papers and herein we minimize the length Δx fitting two straight lines to the temperature data above and below the contact line and calculate the integral heat flow rate P_T($\Delta x \approx 5$ mm in [2, 6]). On the other hand, a polynomial representation of the temperature data can be used to obtain a relatively low heat flux over a relatively larger area. Taking $x = 2$ mm and $(x + \Delta x) = 17$ mm in equation (12) gives P_{T2}, which was used in [23]. Microsize thermistors are needed to measure the temperature field. We note that the relatively pure system studied in [1] appeared to behave well; i.e., the results based on simple heat flow and fluid flow models agreed. However, the mixtures studied herein and in [2] appear to be much more complicated.

5 Film Profile

Herein, the interference phenomena associated with light reflected from a tapered film was used to determine the thickness profile of the meniscus as a function of heating. Alternating constructive and destructive interference occur when coherent light is reflected from the two interfaces of the thin film and recombine. Destructive interference occurs when the optical paths of the two reflected beams is such that they are out of phase by π. In our case, $n_v < n_l < n_s$; therefore, there is a phase shift equal to π at each interface. The relevant equation for the film thickness associated with the minima is

$$\delta = \frac{(2L+1)\lambda}{4n_l \cos \phi_r} \qquad L = 0,1,2,3 \ldots \tag{13}$$

In the reported data, $\cos \phi_r$ monotonously decreased with an increase in thickness, had a minimum value of approximately 0.998, and was neglected. Equation (13) was used with the measured values of the relative locations of the minima and known values of L, n_l, and λ to determine the profile ($\delta = f(x)$). For green light with decane the thickness of the liquid at the first and second destructive fringes ($L = 0,1$) are 9.70×10^{-8} m and 2.91×10^{-7} m.

6 Experimental Results

In our experiments, the following fluid systems, of various degrees of purity, were used

(*a*) "Pure" decane as received with 98 percent minimum purity (we note that the nominal percentage of 98 overstates the impurity effect in these experiments relative to the next fluid because the impurities in this fluid have relatively close boiling points)

(*b*) 98 percent "pure" decane plus 2 percent tetradecane by weight (the purity of the tetradecane was 99 percent minimum as received)

(*c*) "Pure" decane plus various weight percentages of nonanoic acid

(*d*) Research-grade hexane as received with 99.95 percent minimum purity

(*e*) Technical grade hexane as received with 96 percent minimum purity

(*f*) 98 percent research grade hexane plus 2 percent octane by weight (the purity of the octane was 98 percent minimum)

Photographs of the interference patterns observed in an evaporating decane film and an evaporating decane–tetradecane film are presented in Fig. (5). The difference in the fringe spacing is dramatic. Even though P_T in the decane-tetradecane film was 38 percent higher, the fringes were further apart. Therefore, the curvature in the contact line region was significantly less with the mixture. This demonstrates that the physicochemical processes in the contact line region were different. A large lens formed just above the evaporating film at heat transfer rates above approximately $P_T = 11$W/m with the mixture. It appeared that this large lens was continuously fed through an ultra thin film ($\delta < 2 \times 10^{-8}$ m for $P_T = 14.5$ W/m) from the evaporating thin film below it. Approximately 15 percent of the width of the large lens can be seen in the photograph. Obviously, the lens contained fluid with a significantly different composition and vapor pressure. The relative volatility for this system is large, and a large concentration gradient develops. This gives a surface tension gradient that enhances flow towards the contact line. Since the

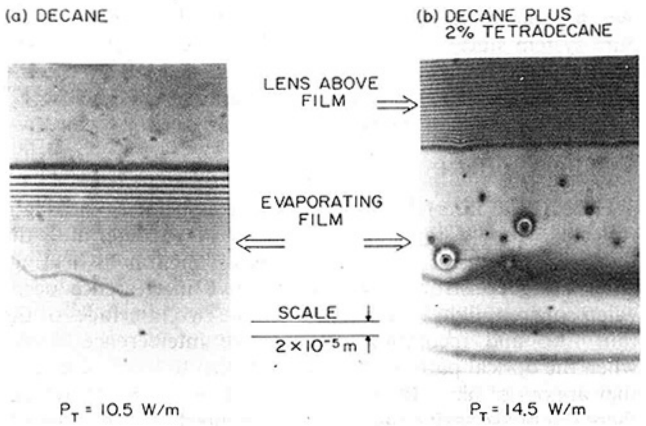

Fig. 5 Interference fringes in the contact line region

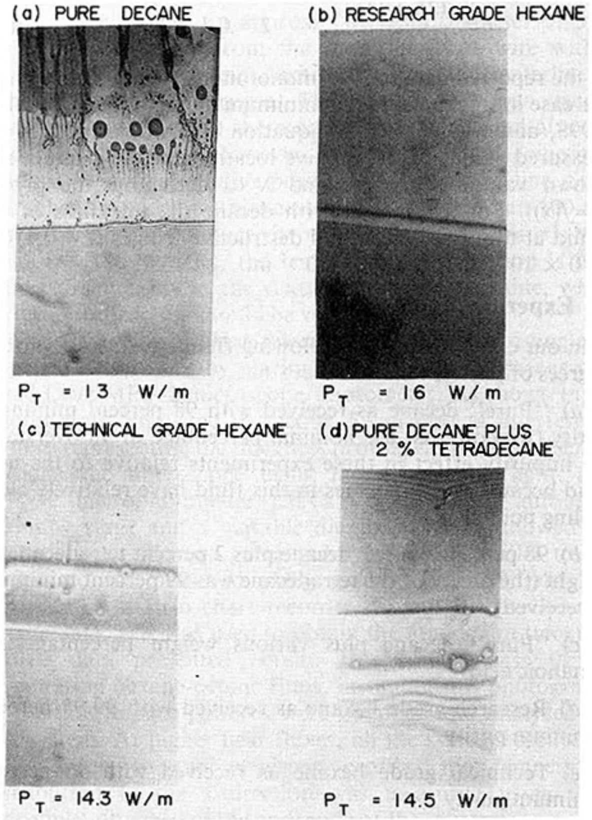

Fig. 6 Comparison of interference fringes in evaporating contact line region of different fluid systems

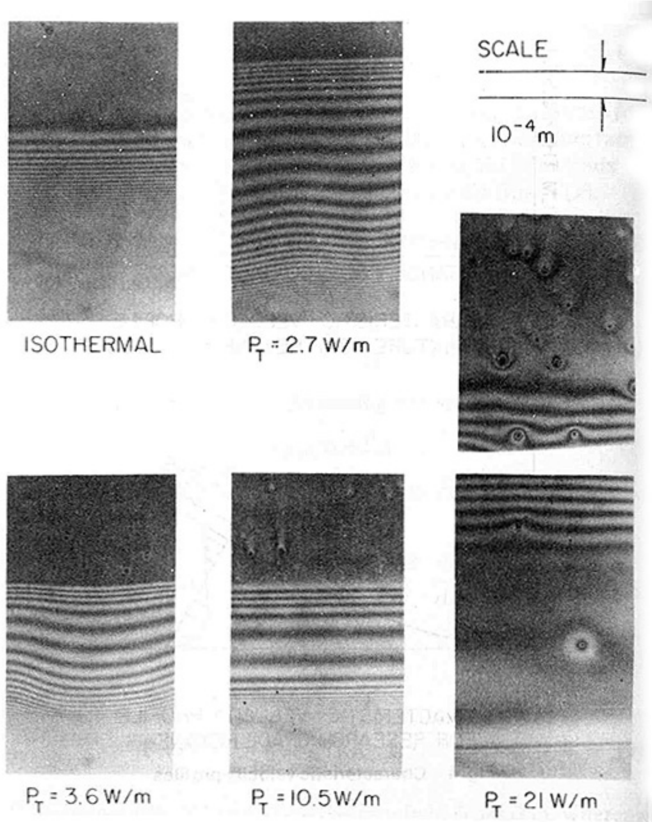

Fig. 7 Photographs of fringe patterns for various heat transfer rates: 98 percent hexane/2 percent octane

contact line temperature is approximately 66°C [2], the vapor pressure is low and a large lens forms. With the decane system, only relatively small lenses (outside the view of the photograph) formed above the evaporating thin film. These small lenses migrated up the plate while evaporating. Small specks of micron size dust can be seen in the photograph of the decane-tetradecane system. Experimentally, unless extreme care is taken, dust particles tend to accumulate when the cell is opened, drained, "cleaned," and refilled over a period of time. Most of the dust can be removed by cleaning the plate with hydrofluoric acid. Although these dust particles affect the local fringe pattern, they do not appear to change the average macroscopic phenomena. Due to the small area over which the reflectivity was measured, the regions in the vicinity of the dust could be avoided when the photometer was used to record the film profile. Additional data on the decane and decane/tetradecane systems are presented in [1, 2]. In Fig. 6, photographs of the fringe patterns observed for various fluid systems at approximately the same value of P_T are shown. As indicated by the interference patterns, the systems behaved differently. A decrease in purity increased the spacing between the fringes. Therefore, the slope and curvature in the contact line region were smaller for the less pure system. Based on equation (10), we presume that a surface shear stress augmented the curvature gradients as a cause of flow.

In Fig. 7, photographs of the fringe pattern for various heat transfer rates in the evaporating thin film are shown for the 98 percent hexane/2 percent octane system. We note that these are dramatically different from those obtained with decane in [1]. In the decane studies, the "width" of the spaces between the fringes decreased in an orderly fashion with an increase in heat flux. (We note, however, that there was a relatively small change in "wetting" at a heat transfer rate of $P_T \approx 1$W/m with decane.) With the 98 percent hexane/2 percent octane system, waviness was present at relatively low values of P_T. Therefore, for this system only the photographs and thermocouples could be used to obtain data. Experimentally, we could not fit the whole region at higher fluxes in one photograph. Therefore, two photographs are shown in Fig. 7 for $P_T = 21$W/m. Fluid flow in the contact line region was more apparent with this system. Clear photographs were not obtained at higher heat fluxes because the oscillating motion was very intense and a nonuniform film of condensate on the glass port interfered with our view. The system was "stable" up to heat flow rates of $P_T \approx 32$ W/m; that is, surges of liquid continually rewetted the surface. The film disappeared at a higher heat flow rate. Video tapes of all our experiments have been made for future use.

The measured profiles of the evaporating thin film for various values of the integral evaporation rate P_T are presented in Fig. 8-11. Since the slopes are small, the horizontal and vertical scales are different. In order to separate the details near the interline, the liquid thickness at

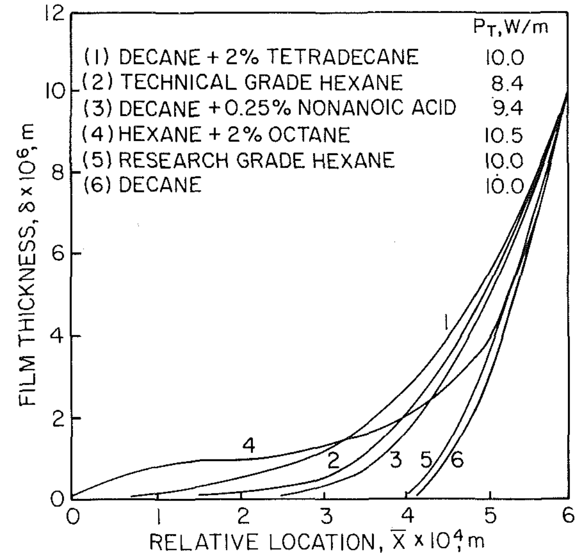

Fig. 8 Evaporating film thickness profiles: comparison of various systems at approximately equal P_t

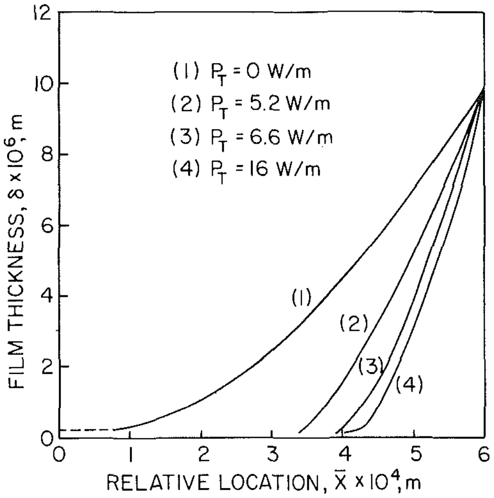

Fig. 9 Evaporating film thickness profiles: research grade hexane

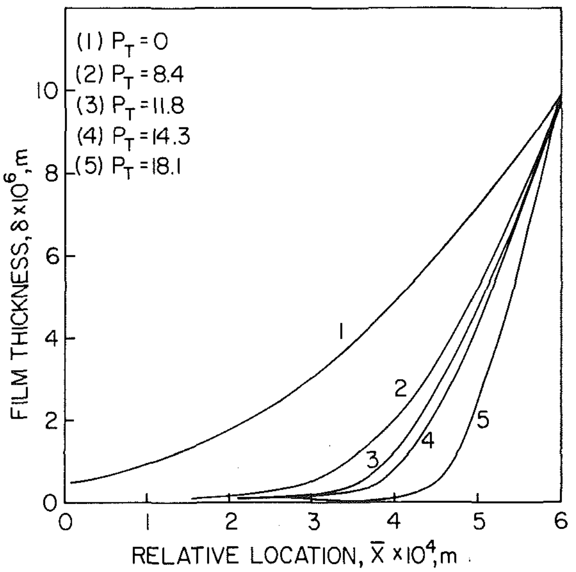

Fig. 10 Evaporating film thickness profiles: technical grade hexane

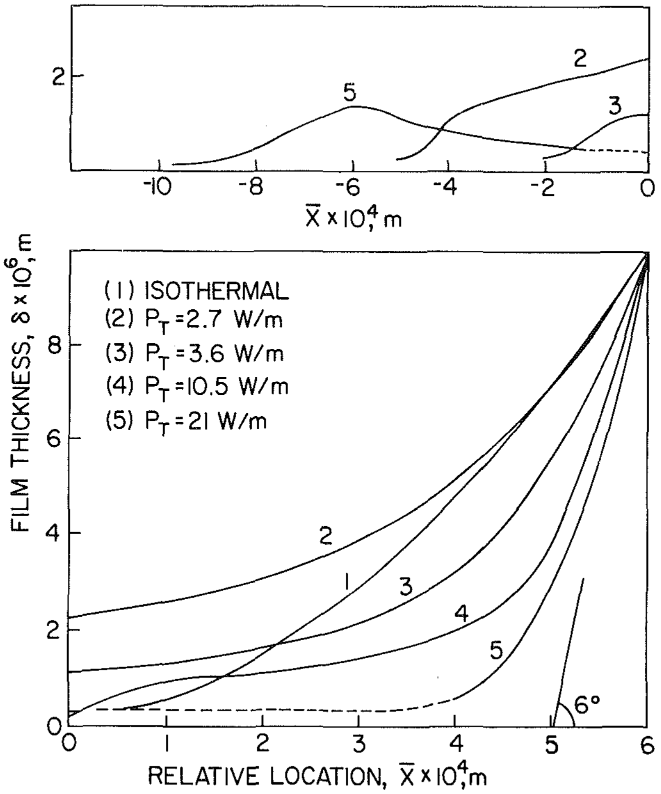

Fig. 11 Evaporating film thickness profiles: 98 percent hexane/2 percent octane

the 50th dark interference fringe, ($\delta = 9.617 \times 10^{-6}$ m for decane) is arbitrarily located at $x = 6 \times 10^{-4}$ m for those cases in which this point can be identified. For a well-behaved system like decane, 50 destructive interference fringes were used to obtain the profile, and a deviation in δ of 100Å was obviously inconsistent [1]. At the other extreme, the profiles for the hexane/octane system were obtained from the photographs presented in Fig. 7. Therefore, they are relatively crude and are snapshots of a oscillatory phenomenon. However, they are representative. As indicated by the interference patterns, the systems behaved differently. The profiles for the mixtures are spread out relative to those for the purer systems. The relative location of the fringes for research grade hexane compared to "pure" decane are misleading, since the lower viscosity of hexane leads to a smaller change in the profile at the same heat flux. We note that lenses were not present above the contact line with research grade hexane whereas they were with the "pure" decane. In Fig. 9 the measured profiles for research grade hexane are presented. These can be compared with those presented in Fig. (10) for technical grade hexane. A comparison of the profiles demonstrated that the initial portion of the evaporating thin film is stretched out for the fluid with the lower purity. We note that, for the isothermal case, a thin film of liquid with varying thickness extended all the way up the plate above the meniscus.

The data presented in Fig. 11 for hexane-2 percent octane indicate that the transport processes are much more complex with this mixture. Depending on the integral evaporation rate, different types of flow patterns developed: even at $P_T \approx 2.7$ W/m, small oscillations were apparent at the contact line, and the fringes were wavy; at $P_T = 10.5$ W/m, surging of the liquid in the contact line region was observed; at $P_T = 21$ W/m, the surging oscillation film was more stretched out; and at $P_T > 32.3$ W/m, the film disappeared. We note that since the design of the heat transfer cell allowed the vapor to

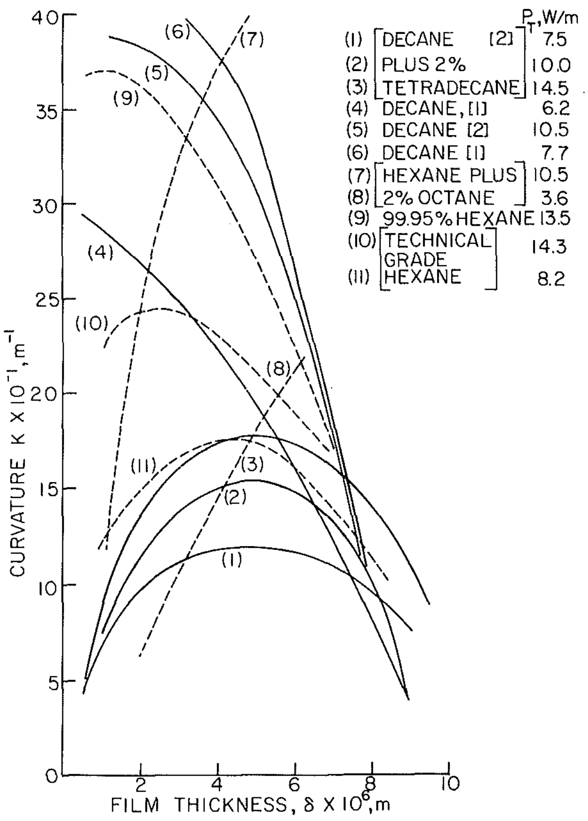

Fig. 12 Interface curvature versus film thickness

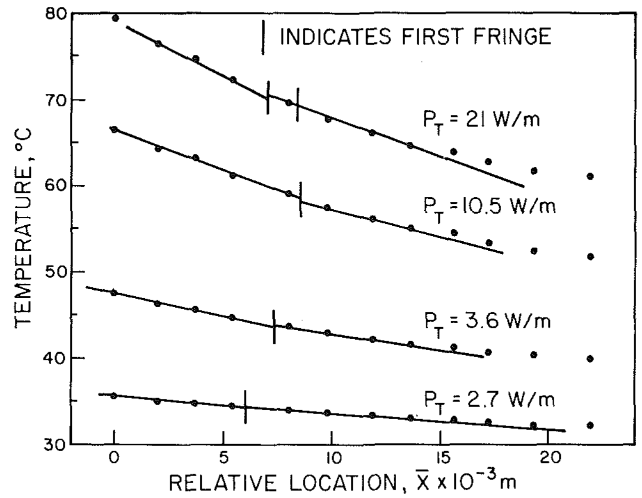

Fig. 13 Temperature distribution on underside of substrate: 98 percent hexane/2 percent octane ($\bar{x} = 0$ is 6×10^{-3} m from the centerline of the heat source)

escape at this vapor pressure, this is not a unique point of instability. For curve (5) the shape of the profile represented by the dashed line is one interpretation of the photograph.

In order to evaluate the hypothesis that flow of the evaporating fluid resulted from a change in the film profile, the data were fitted with polynomials of the mth degree, $2 \leq m \leq 7$. The degree was varied to obtain a best fit to the data using a least-squares criterion. Except for the hexane/octane data, the data could be fitted with a polynomial to within 0.1 percent. In Fig. 12 the curvatures obtained using the polynomial representation of the data are presented as a function of the film thickness δ. With a "well-behaved" fluid like "pure" decane, the data are extremely accurate at low heat fluxes. The sensitivity of the curvature to the data, the order of the polynomial, and to the length of the region included are discussed in [6]. Sufficient accuracy is retained to say that there is a significant curvature gradient for fluid flow and that it is a function of heat flux and composition. For comparison, results for decane (curves 4, 5 & 6), decane plus tetradecane (curves 1, 2 & 3), research grade hexane (curve 9) technical grade hexane (curves 10 & 11), and hexane plus octane (curves 7 & 8) systems are presented. Again the results for these systems are dramatically different. The maximum curvature occurs at a larger thickness for the mixture. This indicates that either an additional mechanism for fluid flow resulting from a concentration gradient was present (e.g., a surface shear stress) or that the evaporation rate was substantially reduced in the thinner portion of the film due to the lower vapor pressure associated with the higher boiling fraction. We note that more motion and, apparently, more fluid flow was observed through the microscope with the hexane plus octane system. Therefore, we believe that significant surface shear induced flow was present. Of course, some reduction in evaporation due to the change in composition with distillation is also occurring.

Representative temperature profiles for the hexane/octane system measured using the thermocouples attached to the bottom surface of the substrate are given in Fig. 13 for different power levels. The profiles are sufficiently nonlinear to warrant fitting them with a polynomial. We feel though that these polynomials would not be definitive because of their insensitivity to the microscopic phenomena around the first fringe. Straight lines used to calculate P_T are shown. For $P_T = 21$W/m two first fringes are indicated because the region between the two vertical lines could be viewed as a lens with a low heat flux. On the other hand, we note that observations through the microscope indicate substantial fluid flow. Obviously, the transport phenomena in this small region can be very complex and additional studies are needed to further refine these observations and analyses. However, the foregoing results do describe some of the dynamic characteristics of a stationary evaporating thin film with surging flow that depends on interfacial phenomena.

7 Conclusions

1 Effective experimental and theoretical techniques to study the transport processes in the contact line region of a stationary evaporating thin film are being developed.

2 The curvature gradient is a strong function of evaporation rate and composition.

3 The characteristics of the transport processes are a strong function of small changes in the bulk composition of the evaporating fluid.

4 It appears that concentration and temperature gradients give interfacial shear stresses and recirculation flow patterns that enhance contact line stability.

5 In general, the results demonstrate that the evaporative heat transfer characteristics of the contact line region can be significantly altered by the addition of a small percentage of a second component. The proper use of this additional variable in devices that rely on evaporation from a stationary thin film should lead to improved control and enhanced performance.

8 Acknowledgment

This material is based upon work supported by the National Science Foundation under Grant Nos. MEA78-28039 and MEA82-13690 and the U.S. Army Research Office under DAAG29-79-C-0204 and DAAG29-83-K-0058. Any opinions, findings, and conclusions or recommendations expressed in this publication are those of the authors and do not necessarily reflect the views of the U.S. Army Research

Office or the National Science Foundation. Some of the results presented herein were presented at the AIAA 18th Thermophysics Conference, June 1-3, 1983, Montreal and at the AIChE 75th Annual Meeting, November 14-18, 1982, Los Angeles Ca.

9 References

1 Cook, R., Tung, C. Y., and Wayner, P. C. Jr., "Use of Scanning Microphotometer to Determine the Evaporative Heat Transfer Characteristics of the Contact Line Region," ASME JOURNAL OF HEAT TRANSFER, Vol. 103, 1981, pp. 325-330.

2 Tung, C. Y., Muralidhar, T., and Wayner, P. C. Jr., "Experimental Study of Evaporation in the Contact Line Region of a Mixture of Decane and 2% Tetradecane," Vol. 4, *Proceedings of the 7th International Heat Transfer Conference*. Munich, Sept. 6-10, 1982, pp. 101-106.

3 Renk, F. J., and Wayner, P. C., Jr., "An Evaporating Ethanol Meniscus, Part I: Experimental Studies, ASME JOURNAL OF HEAT TRANSFER," Vol. 101, 1979, pp. 55-58.

4 Wayner, P. C., Jr., "Interfacial Profile in the Contact Line Region of a Finite Contact Angle System," *J. Colloid Interface Sci.*, Vol. 77, 1980, pp. 495-500.

5 Renk, F. J., and Wayner, P. C., Jr., "An Evaporation Ethanol Meniscus, Part II Analytical Studies," ASME JOURNAL OF HEAT TRANSFER, Vol. 101, 1979, pp. 59-62.

6 Tung, C. Y., "Evaporative Heat Transfer in the Contact Line of a Mixture," Ph.D thesis, Rensselaer Polytechnic Institute, Troy, N.Y., Aug. 1982.

7 Berg, J. C., Acrivos, A., and Boudart, M., "Evaporative Convection," *Advances in Chemical Engineering*, Vol. 6, Academic Press, New York, 1966, pp. 61-123.

8 Ostrach, S., "Motion Induced by Capillarity," *Physiochemical Hydrodynamics II*, Advance Publications, Ltd., London, 1977, pp. 571-589.

9 Kenning, D. B. R., "Interfacial Phenomena in Heat and Mass Transfer," personal copy of review paper at 7th International Heat Transfer Conference, Munich, FRG, Sept. 6-10, 1982.

10 Sharp, R. R., "The Nature of Liquid Film Evaporation During Nucleate Boiling," NASA-TN-D1997, 1964.

11 Jawurek, H. H., "Simultaneous Determination of Microlayer Geometry and Bubble Growth in Nucleate Boiling," *International Journal of Heat and Mass Transfer*, Vol. 12, 1969, pp. 843-848.

12 Voutsinos, C. M., and Judd, R. L., "Laser Interferometric Investigation of the Microlayer Evaporation Phenomena," ASME JOURNAL OF HEAT TRANSFER, Vol. 97, 1975, pp. 88-93.

13 Yang, W. J., and Nouri, A., "Interfacial Turbulence in Minute Drops Evaporating on a Flat Plate," Letters in Heat and Mass Transfer, Vol. 8, 1981, pp. 115-125.

14 Ludviksson, V., and Lighfoot, E. N., "The Dynamics of Thin Liquid Films in the Presence of Surface Tension Gradients," *AIChE Journal*, Vol. 17, 1971, pp. 1166-1173.

15 Bascom, W. D., Cottington, R. L., and Singleterry, C. R., "Dynamics Surface Phenomena in the Spontaneous Spreading of Oils on Solids," *Advances in Chemistry Series*, Vol. 43, 1964, pp. 355-379.

16 Orell, A., and Bankoff, S. G., "Formation of a Dry Spot in a Horizontal Liquid Film Heated From Below," *International Journal of Heat and Mass Transfer*, Vol. 14, 1971, pp. 1835-1842.

17 Hickman, K. C. D., "Surface Behavior in the Pot Still," *Ind. Eng. Chem.*, Vol. 44, 1952, pp. 1892-1902.

18 Palmer, H. J., and Maheshri, J. C., "Enhanced Intefacial Heat Transfer by Differential Vapor Recoil," *International Journal of Heat and Mass Transfer*, Vol. 24, 1981, pp. 117-123.

19 Orell, A., and Westwater, J. W., "Natural Convection Cells Accompanying Liquid-Liquid Extraction," *Chem. Eng. Sci.*, Vol. 16, 1961, p. 127.

20 Edwards, D. K., Balakrishnan, A., and Catton, I., "Power-Law Solutions for Evaporation from a Finned Surface," ASME JOURNAL OF HEAT TRANSFER, Vol. 96c, 1974, pp. 423-425.

21 Holm, F. W., and Goplen, S. P., "Heat Transfer in the Meniscus Thin-Film Transition Region," ASME JOURNAL OF HEAT TRANSFER, Vol. 101, 1979, pp. 543-547.

22 Tung, C. Y., and Wayner, P. C., Jr., "Effect of Surface Shear on Fluid Flow in an Evaporating Meniscus of a Mixture of Alkanes," presented and published at 5th International Heat Pipe Conference, Tsukuba, Japan, May 14-17, 1984.

23 Wayner, P. C., Jr., Tirumala, M., Tung, C. Y., and Yang, J. H., "Fluid Flow in the Contact Line Region of a Mixture of Alkanes: 98% Hexane - 2% Octane," AIAA 18th Thermophysics Conference, Montreal, Canada, June 1-3, 1983.

Natural Convection/Radiation Heat Transfer From Highly Populated Pin Fin Arrays

E. M. Sparrow
Fellow ASME

S. B. Vemuri
Department of Mechanical Engineering,
University of Minnesota,
Minneapolis, Minn. 55455

Experiments were performed to determine the combined-mode natural convection/radiation heat transfer characteristics of highly populated arrays of rodlike cylindrical fins (i.e., pin fins). The fins were oriented with their axes horizontal and were attached to a vertical heated baseplate. The investigated parameters included the number of fins in the array, the fin length and diameter, the baseplate-to-ambient temperature difference, and the presence or absence of adjacent shrouding surfaces. Finning was found to be highly enhancing (up to a sixfold increase in heat transfer), and even the longest fins were highly efficient. When the number of fins was increased for fixed values of the other parameters, the heat transfer increased at first, attained a maximum, and then decreased. Arrays having different diameter fins yielded about the same performance when the surface area of the fin-baseplate assembly was held fixed. Shrouding surfaces positioned close to the array decreased the rate of heat transfer. Calculations showed that the contribution of radiation was substantial and was greatest for more populous arrays, for longer fins, and at small temperature differences.

Introduction

Natural convection, coupled with radiation, is frequently employed for the cooling of low-power-level electronic equipment (e.g., computer components, instrumentation, etc.). Owing to the relatively low heat transfer coefficients that are characteristic of natural convection in air and of low-temperature-difference radiation, fins are often used to enhance the convective–radiative cooling capabilities. In view of the importance of convective–radiative fins in significant technological applications, the sparsity of information about their heat transfer characteristics is quite remarkable.

The available literature is limited to a single fin configuration—an array of parallel plates, with one edge of each plate attached to a vertical wall or to a horizontal wall. Only natural convection was considered, despite the fact (to be documented later) that radiation may make significant contributions. The relevant publications may be subdivided into two groups: (*a*) reports of basic, experimentally determined heat transfer results [1-3] and (*b*) reports of modeling efforts aimed at deducing optimal fin spacing, thickness, length, and inclination [4-7]. The modeling work was based on less-than-certain assumptions, and furthermore, use was made of natural convection heat transfer data [1] for a pair of vertical, parallel plates open to the ambient along all edges (in contrast to actual fins, which are blocked along one edge due to the attachment wall).

The present work is a wide-ranging investigation of the convective-radiative heat transfer characteristics of arrays of pin fins (i.e., circular rods), a fin configuration markedly different from that dealt with in the literature. The fins were oriented with their axes horizontal and were attached to a vertical heated baseplate. Emphasis is placed on highly populated arrays and, in particular, on the response of the heat transfer to the number of fins in the array. All told, 18 different array geometeries were investigated. In the main body of the experiments, the respective arrays were situated in expansive surroundings such that there were no impediments to the buoyancy-induced flow of air into or out of the array. To investigate the possible effects of more complex surroundings, supplementary experiments were performed with shrouds positioned adjacent to the array.

In the presentation of results, basic heat transfer data, in dimensionless form, are provided that are suitable for design. In addition, the results are employed to determine the optimal number of fins which yields the maximum rate of heat transfer for a baseplate of given size.

To provide perspective for the results, calculations were performed to determine the magnitude of the radiation contribution to the overall rate of heat transfer. The radiation analysis is highly complex owing to the geometry of the array. A somewhat simplified model which provides realistic results was employed in the present analysis.

The Experiments

Apparatus Overview. The description of the experimental apparatus is facilitated by reference to Fig. 1, which displays schematic front and side views of a representative fin array. The fins are circular rods of diameter D and exposed length L, which are positioned in a staggered, equilateral triangular array on a square, heated baseplate of side dimension S. As indicated in the figure, the baseplate is vertical and the fins are horizontal. The dashed line abcd seen in the side-view diagram is a fictive control surface used in the radiation analysis and should otherwise be ignored.

The fins are seated in holes that span the thickness of the

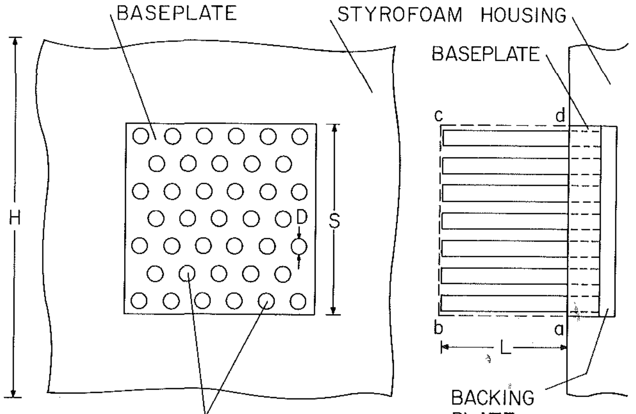

Fig. 1. Schematic front and side views of a representative fin array

---

Contributed by the Heat Transfer Division for publication in the JOURNAL OF HEAT TRANSFER. Manuscript received by the Heat Transfer Division December 14, 1983.

Table 1 Fin-array characteristics

D(cm)	No. of fins	L/D
0.635	18	4,8,12
	27	4,8,12
	39	4,8,12
	52	4,8,12
	68	4,8,12
0.3175	77	8,16,24

baseplate such that the ends of the fins are flush with the rear face of the plate (side-view diagram of Fig. 1). Intimate thermal contact between the fins and the baseplate was achieved by a press fit, with the fin diameter exceeding the hole diameter by 0.00254 cm.

The baseplate of the fin-baseplate assembly was inset in a block of closed-pore polystyrene insulation (styrofoam). For this purpose, a rectangular cavity was cut in the front face of the insulation, with the depth of the cavity chosen so that the exposed surface of the baseplate was flush with the exposed face of the insulation (side view, Fig. 1). The selected insulation material was smooth surfaced, but to ensure hydrodynamic smoothness, the insulation was covered with plasticized, self-adhering contact paper.

The use of the insulation housing virtually eliminated extraneous heat losses by conduction. As an additional defense against extraneous losses, the entire apparatus (fin-baseplate assembly and styrofoam housing) was suspended by nylon lines rather than being supported by rigid structural members.

The radiation properties of the fin-baseplate assembly were established by black-anodizing all surfaces of the assembly. The resulting emissivity, measured with a Gier-Dunkle heated-cavity reflectometer, was 0.82.

Baseplate. In keeping with the objective of determining the fin configuration that yields the maximum rate of heat transfer for a given baseplate surface area ($= S^2$), the same baseplate dimensions were employed for all fin-baseplate assemblies, namely, $S = 7.62$ cm and a thickness of 1.27 cm. The baseplates were made of aluminum because of its high thermal conductivity (to promote temperature uniformity) and for the ease with which it can be coated (i.e., black-anodized) to yield a timewise-invariant, high value of the radiative emissivity ϵ.

Heating of the baseplate was accomplished by electrical resistance wire placed in an array of shallow parallel grooves (½ mm deep) milled into the rear face of the plate. A large number of narrow grooves (~ 50) was employed in order to attain nearly continuous spatial heating. The anodic coating applied to the aluminum prevented possible shorts between the thinly clad heating wire and the baseplate. Once the wire had been laid in the grooves, a temperature-resistant clay was worked around it in order to fill any air gaps. Then, to further secure and protect the wire, a Teflon backing plate was placed over the rear face of the baseplate (Fig. 1, side view) and taped in position.

The baseplate was equipped with six, fine-gage thermocouples deployed so as to detect possible longitudinal (vertical) and transverse (horizontal) temperature variations. The thermocouples were led into the plate through small diameter holes drilled into its vertical edge faces. The baseplate was virtually isothermal, with temperature nonuniformities, relative to the mean, typically less than 1 percent of the baseplate-to-ambient temperature difference.

Fins. The fins were of aluminum and were cut from rod stock selected for straightness and for uniformity of dimensions. Aluminum was used for the fin material for the same reasons that were already cited for its choice as the baseplate material. The geometrical specifications of the fin arrays are listed in Table 1. As seen there, the majority of the experiments were performed using fins having a diameter $D = 0.635$ cm. These were employed to fabricate arrays consisting of 18, 27, 39, 52, and 68 fins, ranging from sparsely populated arrays to densely populated arrays. The choice of these specific numbers (e.g., 39 rather than another nearby number) was made to accommodate the requirement that all arrays be geometrically similar, that is, that all were staggered, with equilateral triangular centers.

For each array population, the exposed fin length L was varied from $12D$ to $8D$ to $4D$, in that order. This variation was accomplished by first fabricating the $L/D = 12$ array for a given population. Then, once the experiments were completed for that case, the fin length was reduced to $8D$ by milling away the unneeded material. Bending of the fins during the milling operation was prevented by filling the interfin spaces with a rigid plastic which was pourable when heated. A further reduction in fin length from $8D$ to $4D$ was made when the $8D$-experiments were completed. The fin tips exposed by the milling were coated with a black paint whose emissivity closely matched that of the black anodic coating.

To explore the generality of the results obtained with the 0.635-cm-dia fins, supplementary experiments were performed with fins of smaller diameter, namely, 0.3175 cm, as specified by the last entry of Table 1. The three investigated lengths L of the thinner fins were identical to those of the thicker fins, with corresponding larger values of L/D ($= 8$, 16, 24). The heat transfer surface area (fins plus baseplate) for the 77-fin, thinner-fin array was virtually identical to that for the 39-fin, thicker-fin array at each of the three fin lengths (area deviations in the one percent range). Indeed, the choice of 77 fins for the thinner-fin arrays was made to achieve area equality with the corresponding 39-fin, thicker-fin arrays.

Thermocouples were installed to measure fin tip temperatures. The sites for the installation of these thermocouples were selected to provide information representative of the various zones of the array (e.g., lowest tier of fins, lower corner, central region, etc.). As many as 10 tip

Nomenclature

A_{cyl} = area of cylindrical surface of fin
$A_{f,b}$ = surface area of fins and baseplate
D = fin diameter
F = angle factor
g = acceleration of gravity
H = side of square face of insulating housing
h = heat transfer coefficient, $Q/S^2(T_b - T_\infty)$
h' = heat transfer coefficient based on exposed surface area, $Q/A_{f,b}(T_b - T_\infty)$
k = thermal conductivity
L = fin length
N = number of fins in array
N_{opt} = value of N corresponding to maximum heat transfer
Nu = Nusselt number, hS/k
Nu′ = Nusselt number, $h'S/k$
Pr = Prandtl number
Q = combined-mode heat transfer rate
Q_R = radiation heat transfer rate
Ra = Rayleigh number, $[g\beta(T_b - T_\infty)S^3/\nu^2]$Pr
S = side dimension of baseplate
T_b = baseplate temperature
T_{tip} = fin tip temperature
T_∞ = ambient temperature
β = coefficient of thermal expansion
ϵ = emissivity
θ^4 = shifted temperature, $(T_b{}^4 - T_\infty{}^4)$
ν = kinematic viscosity
σ = Stefan-Boltzmann constant

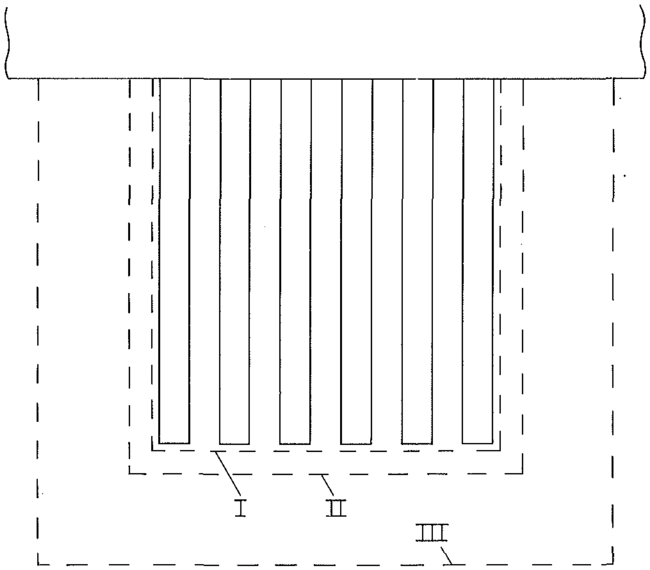

Fig. 2 Shrouding configurations

thermocouples were employed in a given array. Each thermocouple was seated in a shallow (~ 0.5 cm deep), small-diameter hole drilled into the fin tip and fixed in place by copper oxide cement.

Thermal/Fluid Environment. As noted earlier, the fin-baseplate assembly was partially inset into an insulating block. The front face of the block served to frame the exposed face of the baseplate (Fig. 1, front view), with which it was coplanar. The frame was an H by H square, where $H = 27.94$ cm, and the frame width $\frac{1}{2}(H - S) = 10.16$ cm. In the direction normal to the plane of the front view in Fig. 1, the thickness of the insulation was also 10.16 cm.

In the majority of the experiments, all sides and the front face of the fin array were fully open to the ambient, so that air could move freely into or out of the array. In recognition of the fact that in practice, obstructions (e.g., walls, structure, other equipment) may either impede or channel the airflow, supplementary experiments were undertaken in the presence of shrouds.

The investigated shrouding arrangements will be described by making reference to Fig. 2. This figure is a top view looking down on the fin array and the insulation block from above. The 6 fins pictured there are those of the top row of the 39-fin array that has already been illustrated in Fig. 1. These fins are 0.635 cm in diameter and $12D$ in length. All of the shroud-related experiments were performed with this array.

For conciseness, Fig. 2 portrays three different shrouding configurations. However, when envisioning any one configuation, the others should be regarded as being absent. Thus, if attention is being focused on configuration I, the lines representing II and III should be blanked out.

Each shroud configuration defines a vertical channel of axial length S that is open at the top and the bottom but that is closed on all four sides. Of the four side walls, three were formed by the shroud represented by the U-shaped dashed line corresponding to either I, II, or III in Fig. 2. The exposed face of the baseplate served as the fourth side wall. Figure 2 is to scale and, as such, it truly portrays the clearance between the array and the walls of the channel.

The shrouding surfaces were made of styrofoam that was faced with white, plasticized, self-adhering contact paper to ensure hydrodynamic smoothness. The emissivity of the contact paper was measured to be 0.855 by means of a Gier-Dunkle heated-cavity reflectometer.

Supplementary experiments were performed to determine how the heat transfer was affected by the short-range radiant interchange in the small-clearance channels. Initially, it was planned to cover the shroud surfaces of configurations I and II with aluminum foil. However, the clearance for configuration I was too narrow to permit the retrofit installation of the foil (i.e., subsequent to the experiments with the contact-paper-covered shrouds). Therefore, the aluminum foil facing was employed only for configuration II.

The laboratory in which the experiments were performed is uniquely suited to natural convection experiments, owing to its thermal stability and its isolation from external disturbances. The walls, ceiling, and floor of the laboratory are backed by 45 cm of cork, and there are no ducts, grilles, or vents through which air may pass into or out of it. It is located in a deep basement, away from external walls, and is buffered by a surrounding, never-used room. Various high heat capacity objects situated within the laboratory add to its thermal stability. Furthermore, the power supply, digital voltmeter, and barometer were located in a surrounding room.

During a given day, the ambient temperature in the laboratory was stable to 0.03°C. Stratification over a 30-cm height ranged from 0 to 0.03°C, depending on the baseplate-to-ambient temperature difference. The latter extended from 2 to 70°C. The ambient temperature was measured by two shielded thermocouples situated just to the side of the apparatus.

About twelve hours were allowed for the attainment of steady state after a change of input power. Reproducibility was in the 0-2 percent range.

Heat Transfer Results

From the standpoint of practice, the quantity of main interest is the combined-mode (convection and radiation) rate of heat transfer from the fin-baseplate assembly. The subdivision of the combined-mode transfer into its convective and radiative components is an extremely complex undertaking, and the requisite modeling task necessarily requires simplifying assumptions. In view of this complexity and of the fact that it is the combined-mode results that are really needed in practice, the presentation of the convective-radiative subdivision will be postponed until later. For now, full attention will be given to the results for the combined-mode heat transfer.

For the combined-mode heat transfer presentation, the first order of business is the definition of the dimensionless groups used to characterize the results. Then the basic heat transfer results will be presented. These results will then be employed to deduce the optimal number of fins, i.e., the number of fins which yields the maximum rate of heat transfer from the fin-baseplate assembly. After that, the effect of shrouding surfaces on the heat transfer rate will be considered. The last topic of this section is the fin tip temperatures.

Dimensionless Groups. The heat transfer coefficient and Nusselt number to be defined here are intended to be direct reflections of the rate of heat transfer from the fin-baseplate assembly per unit baseplate-to-ambient temperature difference. In particular, areas and lengths in h and Nu which change with the geometry of the assembly will be avoided. Rather, geometrical factors which are constant will be employed. In this way, changes in h and Nu from configuration to configuration will truly indicate changes in the heat transfer rate.

With Q denoting the rate of heat transfer from the fin-baseplate assembly, h and Nu are defined as

$$h = Q/S^2(T_b - T_\infty) \tag{1}$$

$$\mathrm{Nu} = hS/k = Q/Sk(T_b - T_\infty) \tag{2}$$

where T_b and T_∞ respectively denote the baseplate and the ambient temperatures. Note that because S is common to all

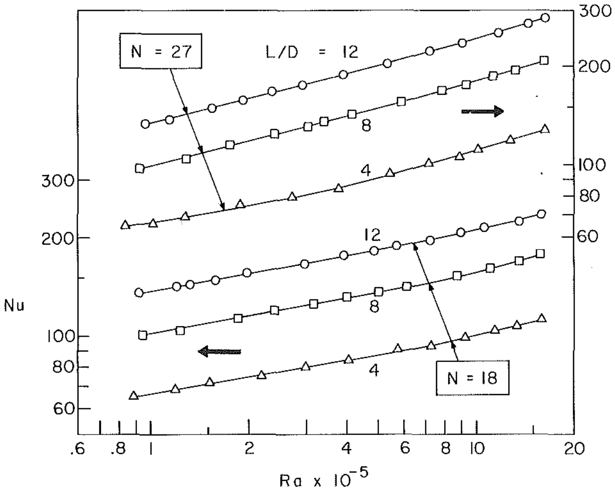

Fig. 3 Heat transfer results for fin-baseplate assemblies with 18- and 27-fin arrays

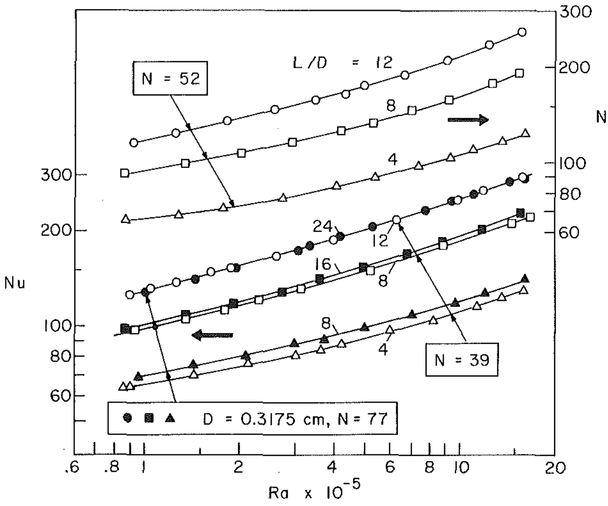

Fig. 4 Heat transfer results for fin-baseplate assemblies with 39- and 52-fin arrays and with an array of 77, 0.3175-cm-dia fins

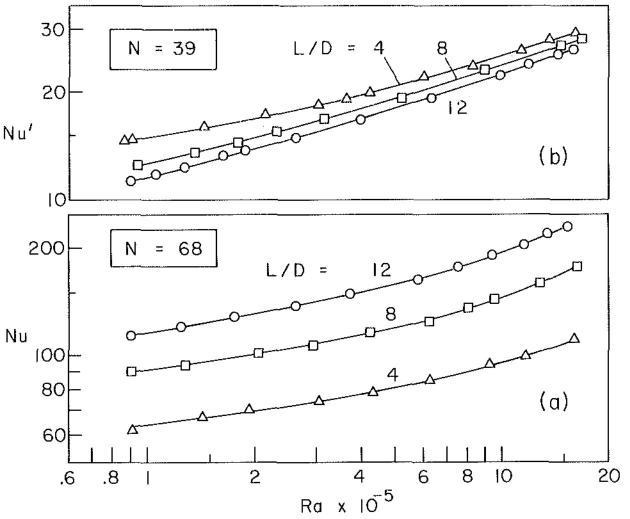

Fig. 5 (a) Heat transfer results for fin-baseplate assemblies with a 68-fin array; (b) heat transfer per unit area for fin-baseplate assemblies with a 39-fin array

the investigated configurations, variations in h and Nu reflect variations in $Q/(T_b - T_\infty)$.

A secondary definition involving the exposed surface area $A_{f,b}$ of the fins and the baseplate will be employed in a more limited presentation of results. Thus

$$h' = Q/A_{f,b}(T_b - T_\infty), \quad \mathrm{Nu}' = h'S/k \tag{3}$$

These definitions reflect the rate of heat transfer per unit surface area, with all portions of the surface being given equal weight (i.e., no accounting of fin efficiency less than unity).

In the execution of the experiments, the independent variable was the temperature difference $(T_b - T_\infty)$. Since T_∞ was essentially constant throughout the entire investigation (25 ± 1°C), this temperature difference also serves as a measure of the baseplate temperature T_b. A dimensionless version of the temperature difference will be expressed via the Rayleigh number

$$\mathrm{Ra} = [g\beta(T_b - T_\infty)S^3/\nu^2]\mathrm{Pr} \tag{4}$$

where, once again, the characteristic length is the fixed baseplate dimension S. Note that the thermophysical properties appearing in Ra, Nu, and Nu′ were evaluated at the reference temperature $\frac{1}{2}(T_b + T_\infty)$.

The radiative transfer is fixed by the emissivity of the exposed surfaces, their geometry, and by T_b and T_∞ (already represented via Ra). As noted earlier, the surfaces had been black-anodized and their emissivity measured to be 0.82. This value is typical both of black-anodized and of painted surfaces. Furthermore, because of the cavity effect (the assembly may be regarded as a partially enclosed cavity), the radiative transfer should be insensitive to small deviations of the emissivity from that of the present apparatus. The geometry of the array is described by the number of fins N and by the specification that they be deployed in an equilateral triangular pattern.

Basic Heat Transfer Results. The combined-mode heat transfer results, expressed via the Nusselt number of equation (2), are presented in Figs. 3, 4, and 5(*a*) as a function of the Rayleigh number. To provide continuity, curves have been passed through the experimental data. In each figure, the results for a given fin population N are grouped together: $N = 18$ and 27 in Fig. 3, $N = 39$ and 52 in Fig. 4, and $N = 68$ in Fig. 5(*a*). For each fixed population, there are three sets of data respectively corresponding to the three fin lengths $L/D = 4$, 8, and 12.

The aforementioned results are for a fin diameter $D = 0.635$ cm. For comparison, results corresponding to a diameter of 0.3175 cm are plotted with black data symbols in Fig. 4—in that part of the figure where the data for 39-fin, larger-diameter arrays are also plotted (open symbols). For corresponding fin lengths (i.e., $L/D = 4$ and 8; 8 and 16; 12 and 24), the exposed surface areas of the different-diameter arrays differ only by about 1 percent (larger area for the 39-fin array).

For all cases, the rate of heat transfer from the fin-baseplate assembly increases with fin length (i.e., with increasing fin surface area). Although this trend is expected, it is significant that the increases continue to be substantial as L/D is varied from 4 to 8 to 12. This indicates that the fin efficiency is high (i.e., relatively uniform fin temperature), which will be substantiated when the fin tip temperatures are presented.

Another indication of the extent of the heat transfer enhancement may be obtained by comparing the Nusselt numbers in Figs. 3, 4, and 5(*a*) with those for an unfinned baseplate. From the Churchill-Chu correlation [8] for Ra = 10^5 and 10^6, Nu = 9.81 and 16.9 , respectively, while the older but still widely used McAdams correlation [9] gives Nu values of 10.5 and 18. 7. These Nusselt numbers are for pure natural convection. For the $L/D = 4$ arrays (shortest fins), the present Nusselt numbers are about 65 and 95–110, respectively for Ra = 10^5 and 10^6. The corresponding numbers for the $L/D = 12$ fins are 115–135 and 200–250. Thus, compared with pure natural convection at an unfinned

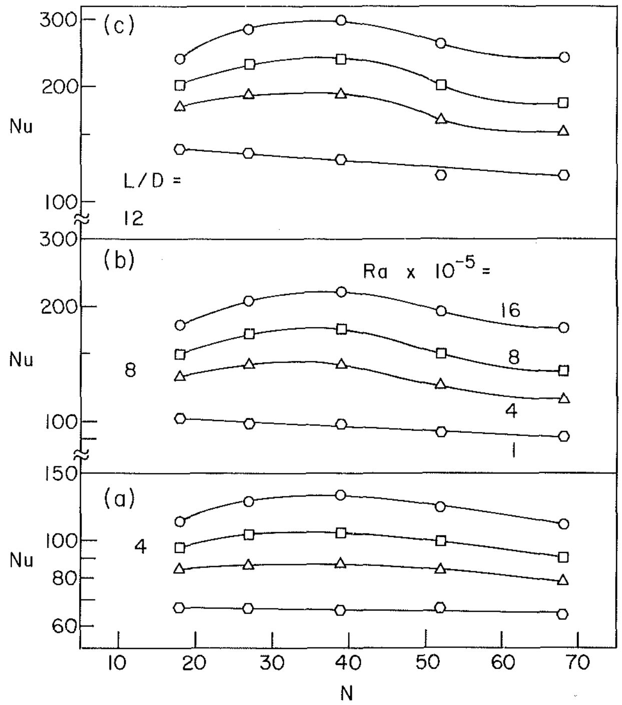

Fig. 6 Demonstration of optimal fin population which yields the maximum rate of heat transfer

baseplate, the $L/D = 12$ finned assembly yields heat transfer enhancements well in excess of an order of magnitude.

Part of the enhancement is, of course, due to the action of radiation. In round numbers, the radiation at the unfinned baseplate may be of the same magnitude as the natural convection. The remaining portion of the enhancement, perhaps a factor of six for the $L/D = 12$ fins, is due to the increased heat transfer surface area.

On the basis of the foregoing, it appears that finning is a highly effective enhancement technique. It remains to explore whether there is an optimal number of fins which maximizes the rate of heat transfer. Such an exploration is most effectively made with crossplots of Figs. 3, 4, and 5(*a*), which will be presented shortly.

Aside from the enhancement and the effect of L/D, another interesting feature of Figs. 3, 4, and 5(*a*) is the tendency of the Nu, Ra distributions to increase in slope with increasing Rayleigh number. To rationalize this finding, it may be noted that the relative contributions of radiation and natural convection vary with $(T_b - T_\infty)$, i.e., with Rayleigh number, with radiation growing in relative importance as $(T_b - T_\infty)$ *decreases*. Also, by using the binomial expansion, it can be shown that the radiation heat transfer Q_R is nearly proportional to $(T_b - T_\infty)$ at small values of $(T_b - T_\infty)$, so that $Q_R/(T_b - T_\infty)$ is virtually independent of $(T_b - T_\infty)$, i.e., of the Rayleigh number. On the other hand, it is well known that natural convection heat transfer varies nonlinearly with the participating temperature difference. From the foregoing facts, it follows that the Nu, Ra distribution should be flatter in the range where radiation is of greater importance, i.e., at the smaller Ra.

Attention may now be turned to the comparison between the different-diameter, equal-surface-area assemblies in Fig. 4. For the longest fins, the Nusselt numbers for the two cases are in exact agreement. For shorter fins, the data tend to spread, but even for the shortest fins the spread is confined to about 8 percent. This finding suggests that as a first approximation, the present results can be employed for arrays having different diameter fins from those used here, provided that the surface areas of the assemblies are the same. With regard to the reason for the aforementioned spread in the data for the shorter fins, it is conjectured that the dropoff of the radiation contribution with decreasing fin length is more rapid for the less populous array (i.e., for the 39-fin array versus the 77-fin array).

Although less applicable to design, it is of interest to compare the various fin arrays on the basis of heat transfer per unit exposed surface area (at a given $(T_b - T_\infty)$). This information is conveyed by the Nusselt number Nu′ of equation (3). A complete presentation of Nu′ results is made in [10]. Here, only results for the $N = 39$ array will be given, and Fig. 5(*b*) has been prepared for this purpose.

From the figure, it is seen that the heat transfer per unit exposed surface area decreases with increasing fin length and that the decrease is most pronounced at smaller Ra (i.e., where radiation plays a larger role). Whereas a portion of the decrease may be attributed to a larger temperature drop along the fin, a decrease would still occur even if the fins were perfectly isothermal. This is because in the presence of longer fins, radiation emitted from zones internal to the array is more screened from the environment, thus diminishing the radiative heat transfer capabilities of those zones. This rationalization is supported by the fact that for smaller N, where the screening is diminished, Nu′ becomes less dependent on L/D [10].

Optional Fin Population. The issue now to be addressed is whether for a given baseplate and for fins of a given length and diameter, there is a particular population size that maximizes the rate of heat transfer from the fin-baseplate assembly at a given value of $(T_b - T_\infty)$. This issue is explored in Fig. 6, in which parts (*a*), (*b*), and (*c*) respectively convey results for $L/D = 4$, 8, and 12 ($D = 0.635$ cm for all cases). In each part of the figure, Nu is plotted versus the fin population N at each of four fixed Rayleigh numbers (i.e., temperature differences) that span the investigated range. The points plotted in Fig. 6 were read from Figs. 3, 4, and 5(*a*).

Inspection of Fig. 6 indicates that, except at the lowest Rayleigh number, the Nusselt number distributions for the other cases all achieve a maximum in the investigated range of N ($18 \leq N \leq 68$), thereby defining an optimum fin population N_{opt}. The respective maxima are rather flat, so that fin population numbers near N_{opt} yield heat transfer rates that are insignificantly different from the maximum. Because of this, a single value of N_{opt} can be used for all cases that display a maximum in Fig. 6. That value of N_{opt} may be taken to be 35, although any number between 30 and 40 would be almost as good.

The fact that there is an optimum fin population (actually, an optimum range) is of practical relevance. Its existence can be explained by considering the N-dependence of the radiative and convective contributions to the rate of heat transfer. The radiation increases monotonically with N—rather rapidly at small N and slowly at large N. On the other hand, the convection, which at first increases with N, drops off at larger N. This is because the flow cannot penetrate the narrow interfin spaces when the fin population is large. It is the dropoff in the convection which is responsible for the maxima in the Nu versus N distributions.

With regard to the lowest Rayleigh number ($\text{Ra} = 10^5$), N_{opt} occurs somewhere between $N = 0$ and $N = 18$ (the lowest N value investigated here). This can be inferred from the fact that the combined convective-radiative Nusselt number for $N = 0$ (baseplate only) is about 25, while those for $N = 18$ are 67, 102, and 137 for the respective L/D in Fig. 6.

Effect of Shrouding. The investigated shrouding configurations have already been illustrated in Fig. 2 and described in the related text. As noted there, the shrouding experiments were performed using the $N = 39$, $L/D = 12$, $D = 0.635$ cm array.

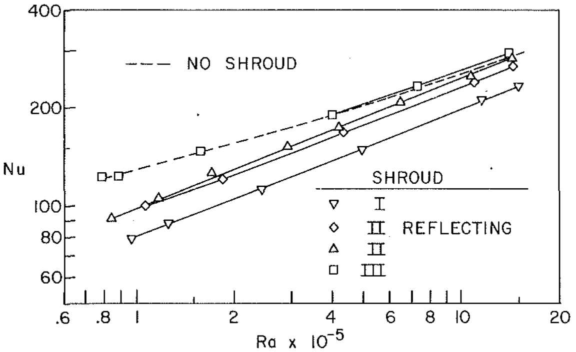

Fig. 7 Effect of various shrouding configurations on heat transfer for a given array (N = 39, L/D = 12, D = 0.635 cm)

Figure 7 conveys the Nusselt number results for the shrouded case. Also shown for reference purposes is a dashed line depicting the no-shroud results. From an overview of the figure, it is seen that shrouding reduces the Nusselt number when the clearance gap between the shroud and the array is small (configurations I and II). However, for intermediate clearances such as that for configuration III, the shroud has virtually no effect on the heat transfer, so that the deleterious effects of shrouding can be easily avoided.

To rationalize the reductions in heat transfer due to closely positioned shrouds, it may be noted that the radiative component will definitely be reduced because the equilibrium temperature of the shroud surfaces exceeds T_∞. Convection may be either enhanced or reduced by shrouding—the enhancement resulting from the extra buoyancy induced by the elevated temperature of the shroud surfaces and the reduction stemming from the blocking action of the shroud walls. Since the radiative and convective components cannot be readily separated for the shrouded configurations, it is uncertain whether shroud-convection interactions add to or counteract the shroud-related reductions in radiation.

It may be noted that with increasing Rayleigh number, the Nusselt number for the low-emissivity (i.e., reflecting) shrouding configuration II tends to fall below that for the same configuration with a high surface emissivity. This is because the shroud-surface equilibrium temperatures are lower for the former. These lower temperatures provide lesser shroud-induced buoyancy, which, in turn, reduces the shroud-assisted convection. This effect asserts itself more strongly at higher Rayleigh numbers, where convection plays a greater role.

Fin Tip Temperatures. The symmetry of the measured fin tip temperatures at geometrically symmetric locations and the general regularity of the tip temperatures throughout the array served to affirm the absence of local nonuniformities due to contact resistance at the fin-baseplate interfaces.

The baseplate-to-tip temperature drop has been cast in dimensionless form via the ratio

$$(T_{\mathrm{tip}}-T_b)/(T_\infty-T_b) \tag{5}$$

which compares the drop to the baseplate-to-ambient temperature difference. A sampling of the measured results for the dimensionless fin temperature drop is presented in Table 2, with a fuller listing available in [10]. In the table, for each designated N, Ra, and L/d, a range is given for $(T_{\mathrm{tip}} - T_b)/(T_\infty - T_b)$. This range corresponds to the maximum and minimum tip temperatures in the array.

The table confirms the expected increase in the fin temperature drop with increasing L/D. However, the expectation of a smaller drop for more populous arrays (i.e., more fins to carry the load) bears some elaboration. As seen in the table, the smaller number in the respective entries behaves according to expectation, but the larger number is quite insensitive to N for a given L/D. To rationalize this finding, it should be noted that the largest temperature drop is sustained at the most outboard fins of the lowermost tier. The heat transfer at those fins (and, in fact, at the entire lowermost tier) is not very dependent on the number of fins in the array. The smallest drop occurs at fins internal to the array, centered with respect to the side edges and at (or just above) the midheight of the baseplate. The temperature drops of such fins are quite responsive to the number of fins.

Table 2 Fin temperature drops, $(T_{\mathrm{tip}} - T_b)/(T_\infty - T_b)$

		L/D		
N	Ra	4	8	12
18	low	0.02-0.03	0.04-0.07	0.07-0.13
	mid	0.02-0.03	0.06-0.08	0.10-0.15
	high	0.03-0.04	0.08-0.10	0.16-0.19
52	low	0 -0.02	0.01-0.06	0.01-0.10
	mid	0.01-0.03	0.02-0.08	0.02-0.14
	high	0.01-0.04	0.03-0.11	0.03-0.19

In general, the minimum fin temperature drop listed in each table entry is more representative of the array as a whole than is the maximum fin temperature drop. As expected, the spread between the maximum and minimum drops is greatest for highly populated arrays and decreases as the number of fins decreases.

Radiation and Convection Components

An analytical scheme for determining the radiation heat transfer Q_R from the fin-baseplate assembly will now be outlined. Once Q_R has been found, the convective component can be obtained by differencing the measured combined-mode heat transfer Q with Q_R.

Two simplifying assumptions are necessary in order to make the analysis tractable (albeit still highly complex). They are: (*a*) all surfaces of the fin-baseplate assembly are black and (*b*) the fins are isothermal at temperature T_b. As noted earlier, the measured emissivity was 0.82 and this, taken together with cavity effect, should yield near blackbody performance. The isothermal fin assumption is well approximated for high-N arrays (aside from the lowermost tier of fins) and for short fins (for all N). Even with these assumptions, the analysis is still far too complicated to be presented here in detail. An outline-type presentation will be made, with complete details available in [10].

The first step in the analysis is to shift the temperature scale to eliminate the need to consider radiation arriving at the assembly from the surroundings (i.e., from extensive surroundings, without shrouds). This is accomplished by defining $\theta^4 = (T_b{}^4 - T_\infty{}^4)$. In terms of θ^4, the net radiation heat transfer from the assembly is equal to the radiation streaming out of the assembly into the surroundings.

To systematize the accounting of this outstreaming radiation, it is advantageous to envision a fictive boxlike envelope placed over the assembly as indicated schematically by abcd in the side view of Fig. 1. If e denotes the envelope and i = 1, 2, . . . , M denote the various surfaces which constitute the assembly, then

$$Q_R = \sigma\theta^4 \sum_{i=1}^{M} A_i F_{i-e} \tag{6}$$

where F_{i-e} denotes the angle factor between i and e. The participating surfaces include the cylindrical portions of the fins, the tips of the fins, and the baseplate. The highly complex geometry of the assembly makes the determination of the F_{i-e} very difficult.

Four basic angle factors were employed in evaluating equation (6), either directly or via angle factor algebra. The geometries corresponding to these angle factors are:

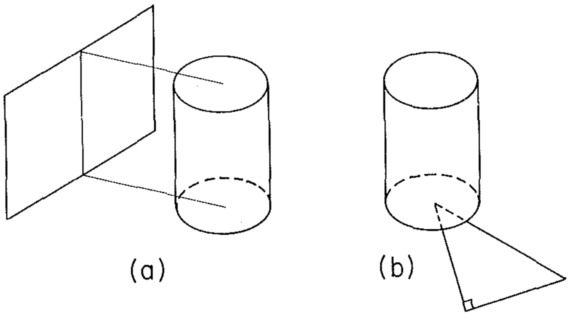

Fig. 8 Geometries whose angle factors were used in the calculation of radiation heat transfer

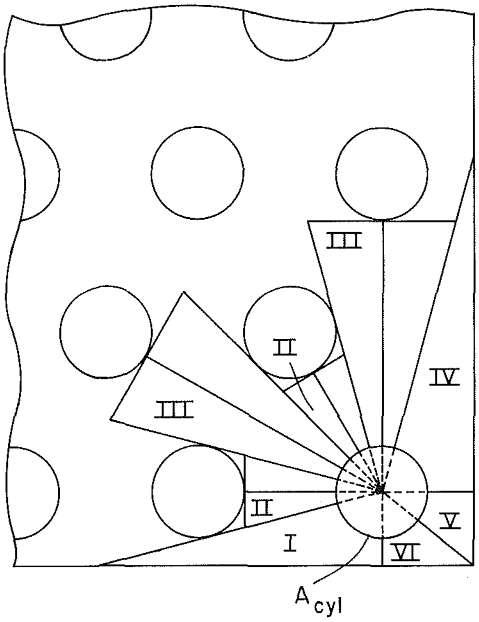

Fig. 9 Illustration of the radiation calculation

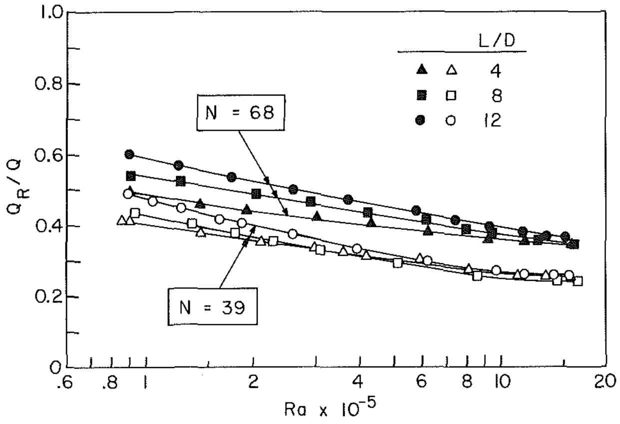

Fig. 10 Ratio of the radiation heat transfer to the combined-mode (convection plus radiation) heat transfer

1 A pair of parallel rectangles situated one above the other
2 A pair of rectangles which share a common edge and whose planes meet at an angle ϕ
3 A cylinder and a parallel rectangle shown in diagram (*a*) of Fig. 8
4 A cylinder and a right triangle that lies in the baseplane of the cylinder, illustrated in diagram (*b*) of Fig. 8

Among these, information for 1 to 3 is available in [11] (configurations 1, 2, and 4 of Appendix A), while 4 is dealt with in [12]. Whereas the angle factor for 1 is described by an algebraic equation, those for 2 to 4 involve integrals which had to be evaluated numerically as a function of various geometrical parameters.

The angle factor for 1 was employed in determining the radiation from the baseplate to the tip-adjacent face of the envelope (bc in Fig. 1). In this regard, the baseplate was subdivided into a set of rectangles which fit between the "feet" of the fins. To determine the radiation from the baseplate to the side faces of the envelope (e.g., face ab in Fig. 1), the baseplate was subdivided into diagonal lanes which were bounded by the fins. The angle factor for 2, employed in conjuction with angle factor algebra, enabled the radiation from the lanes to the envelope side faces to be calculated.

With regard to the fins, the radiation emitted at the tips streams outward through the tip-adjacent face of the envelope; this radiation is readily calculated. For the cylindrical surface of the respective fins, separate consideration has to be given to the radiation which streams outward through the side faces and through the tip-adjacent face of the envelope. For the former, the angle factor for 3, supplemented by angle factor algebra, was used for the calculation, while the angle factor for 4 was used for the latter.

To illustrate the methodology, attention may be focused on determining the radiation passing from the cylindrical surface of a fin through the tip-adjacent face of the envelope. For concreteness, the most outboard fin of the lower tier may be considered, and this fin and the neighboring portion of the array and the baseplate are shown in an enlarged front view of Fig. 9. As seen in the figure, the fin in question is surrounded by a group of right triangles, with the vertex of each triangle coinciding with the axis of fin. These triangles may be envisioned as lying in the tip-adjacent face of the envelope.

The angle factor between the fin and any one of the triangles is that of 4 in the foregoing list (see also Fig. 8(*b*)). Then, to this level of approximation, the contribution to Q_R is

$$\sigma\theta^4 A_{\text{cyl}}[F_{\text{cyl}-\text{I}} + 4F_{\text{cyl}-\text{II}} + 4F_{\text{cyl}-\text{III}} + F_{\text{cyl}-\text{IV}} + F_{\text{cyl}-\text{V}} + F_{\text{cyl}-\text{VI}}] \tag{7}$$

where the angle factors were obtained by numerical integration [10]. Expressions similar to equation (7) have to be written at each fin in the array, and to these are added all of the other contributions discussed in the foregoing paragraphs. Clearly, the evaluation of Q_R is a formidable undertaking.

Representative results from the radiation calculations are shown in Fig. 10, where the computed values of Q_R are plotted in ratio with the measured combined-mode rates of heat transfer Q. The results are for the $N = 39$ and 68 fin arrays. Inspection of the figure reveals that the relative importance of the radiation component is enhanced for more populous arrays, for longer fins, and at small temperature differences (small Ra). At the extreme, for the largest N, largest L/D, and smallest Ra, $Q_R/Q \simeq 0.6$. On the other hand, at the largest investigated Ra, $Q_R/Q \simeq 0.25$ and 0.35, respectively for $N = 39$ and 68. Thus, for these arrays, radiation always plays a significant role.

Concluding Remarks

The present experiments are, seemingly, the first investigation of the natural convection/radiation heat transfer characteristics of highly populated pin fin arrays. The fins are oriented with their axes horizontal and were attached to a heated vertical baseplate. During the course of the experients, the number of fins was varied, as were their length and diameter; the temperature difference between the baseplate and the ambient was also varied parametrically. The majority of the experiments were performed in expansive surroundings, but supplementary studies were made with baffles situated in close proximity to the array.

Finning was found to be highly enhancing compared to an unfinned convecting-radiating baseplate, and even the longest of the investigated fins were highly efficient, yielding a sixfold enhancement. When the number of fins was increased for fixed values of the other geometric and thermal parameters, the heat transfer increased at first, attained a maximum, and then decreased. The performance of arrays of different diameter fins was found to be nearly identical when the surface area of the fin-baseplate assembly was held fixed.

The contribution of radiation was especially important for more populous arrays, for longer fins, and at small temperture differences. For the optimum fin population, the radiation contribution ranged from 45 to 25 percent of the combined convective-radiative heat transfer over the investigated range of temperature differences.

The presence of shrouds positioned in close proximity to the fin array decreased the rate of heat transfer.

References

1 Elenbaas, W., "Heat Dissipation of Parallel Plates by Natural Convection," *Physica*, Vol. 9, 1942, pp. 1-28.

2 Starner, K. E., and McManus, H. N., Jr., "An Experimental Investigation of Free Convection Heat Transfer from Rectangular Fin Arrays," ASME JOURNAL OF HEAT TRANSFER, Vol. 85, 1963, pp. 273-278.

3 Welling, J. R., and Wooldridge, C. B., "Free Convection Heat Transfer Coefficients from Rectangular Vertical Fins," ASME JOURNAL OF HEAT TRANSFER, Vol., 87, 1965, pp. 439-444.

4 Fitzroy, N. D., "Optimum Spacing of Fins Cooled by Free Convection," ASME JOURNAL OF HEAT TRANSFER, Vol. 93, 1971, pp. 462-463.

5 Levy, E. K., "Optimum Plate Spacings for Laminar Natural Convection Heat Transfer from Parallel Vertical Isothermal Flat Plates," ASME JOURNAL OF HEAT TRANSFER, Vol. 93, 1971, pp. 463-465.

6 Pnueli, D., "Optimization of Inclined Convective Fins," ASME JOURNAL OF HEAT TRANSFER, Vol. 96, 1974, pp. 545-547.

7 Bar-Cohen, A., "Fin Thickness for an Optimized Natural Convection Array of Rectangular Fins," ASME JOURNAL OF HEAT TRANSFER, Vol. 101, 1979, pp. 564-566.

8 Churchill, S. W., and Chu, H. H. S., "Correlating Equations for Laminar and Turbulent Free Convection from a Vertical Plate," *International Journal of Heat and Mass Transfer*, Vol. 18, 1975, pp. 1323-1329.

9 McAdams, W. H., *Heat Transmission* (3d ed.), McGraw-Hill, New York, 1954.

10 Vemuri, S. B., "Natural Convection and Radiation Heat Transfer from Highly Populated Pin Fin Arrays," Ph.D. thesis, Department of Mechanical Engineering, University of Minnesota, Minneapolis, Minn., 1984.

11 Sparrow, E. M., and Cess, R. D., *Radiation Heat Transfer*, Hemisphere, Washington, 1978.

12 Tripp, W., Hwang, C. L., and Crank R. E., "Radiation Shape Factors for Plane Surfaces and Spheres, Circles, or Cylinders," Special Report 16, Kansas State University Bulletin, Vol. 46, No. 4, Apr. 1962.

Heat Transfer and Pressure Drop of Typical Air Cooler Finned Tubes

P. W. Eckels
Research and Development Laboratories,
Westinghouse Electric Corporation,
Pittsburgh, Pa. 15235
Mem. ASME

T. J. Rabas
Combustion Turbine Systems Division,
Westinghouse Electric Corporation,
Concordville, Pa. 19331
Mem. ASME

The heat transfer and pressure drop performance of heat exchangers fabricated from helically wrapped finned tubes with an equilateral triangular pitch arrangement are reported for one through five rows. Two finned tube types were tested, one with a "T" foot and the other with an overlapped "L" foot. The dimensions of both finned tubes were similar and were typical of those used in air-cooling applications. The tube diameter was 25.4 mm; the fin height was 15.87 mm; the fin number was 0.41/mm; and the fin-tip clearance was 6.35 mm. The fin base thickness was 0.38 mm and was tapered to half the base thickness at the fin outside diameter. No difference in the thermal performance of the two finned tube types could be detected. Both the heat transfer coefficient and pressure drop were found to increase with the number of tube rows. These results were then compared to other published data.

Introduction

The application of extended surface to tubes by wrapping a fin strip on the outside is a well-known method of making compact heat exchangers. When wide strips are helically wrapped on a tube, there is a strong tendency for the strip to buckle. To forestall buckling, two things are done: the fin strip is rolled thinner at its outer edge so a natural spiral is formed and a stabilizing foot is formed at the base in the fin strip. The foot becomes a collar around the tube to improve contact and protect the tube in some environments. Figure 1 shows a cross section of the two types of finned tubes that were tested. A McElroy machine was used to wrap the "L" foot finned tubes and an Industrial Blast Coil (IBC) machine was used to wrap the "T" foot finned tubes.

A comparison of the performance of finned tubes based only on geometrical considerations is not complete. The contact conductance can be different even at normal operating temperatures for the two tube types because of the wrapping tension. In addition, the manufacturing method can lead to different fin shapes and can produce a different roughness on the fin surfaces and at the root of the finned tube. Recently, Hashizume [1] compared the performance of three finned tube types with identical geometry except for the fins. The first finned tube was the helical type; the second was made from ring-shaped plates; and the third was made the same as the second but was segmented. The pressure drop of the helical finned tubes was about 10 percent greater than the second and the third type. Surprisingly, the pressure drop was not increased with the segmented fins. The heat transfer coefficients from the helical finned tubes were greater than that of the ring-shaped plate finned tubes; however, they were less than that of the segmented finned tubes. The first purpose of this paper is, then, to determine if any performance differences existed between the geometrically similar "T" and "L" finned tubes shown in Fig. 1.

Because it is common practice to build air-cooled heat exchangers with less than six tube rows in the flow direction, the second purpose of this paper is to determine the row number effect on the heat transfer and the pressure drop for this commonly used finned tube geometry and pitch arrangement.

The effect of row number on the heat transfer and pressure drop of finned tube banks is not completely understood. Schmidt [2] stated that the heat transfer coefficient for the first tube row is the best and that of the second row is the worst. From the second row, the heat transfer coefficient increases to a constant value. Both the data of Ward and Young [3] and Brauer [4] showed that the heat transfer coefficient increased with row number to the third row and then remained constant. However, the row number effect was Reynolds-number-dependent, the difference between the first couple rows and the rest of the bundle diminished as the Reynolds number decreased. Mirkovic [5] and Neal and Hitchcock [6] observed that the heat transfer coefficient increased until the fifth or sixth row. Very recently, Granolio and Cuti [7] showed that the row effect on the heat transfer

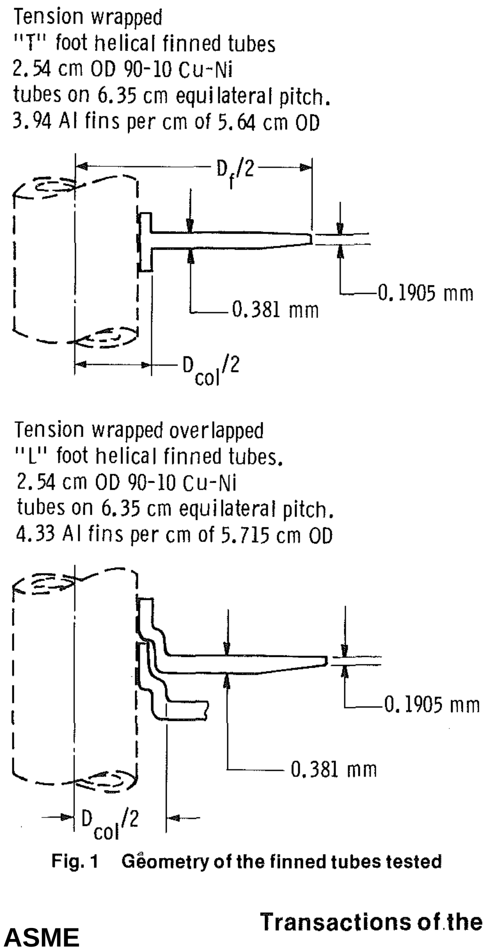
Tension wrapped
"T" foot helical finned tubes
2.54 cm OD 90-10 Cu-Ni
tubes on 6.35 cm equilateral pitch.
3.94 Al fins per cm of 5.64 cm OD

Tension wrapped overlapped
"L" foot helical finned tubes.
2.54 cm OD 90-10 Cu-Ni
tubes on 6.35 cm equilateral pitch.
4.33 Al fins per cm of 5.715 cm OD

Fig. 1 Geometry of the finned tubes tested

Contributed by the Heat Transfer Division and presented at the 1983 ASME/JSME Joint Thermal Engineering Conference, Honolulu, Hawaii, March 1984. Manuscript received by the Heat Transfer Division March 14, 1983.

Table 1 Finned tube and heat exchanger data

Face Dimension, m × m	0.914 × 0.318	0.914 × 0.318
Tubes		
Type	Helical, Tension Wrapped Overlapped "L" Foot	Helical, Tension Wrapped "T" Foot
Number of Rows	1, 2, 3, 4, 5	4
Tubes Per Row	5	5
Pitch	Staggered	Staggered
Transverse Pitch, cm	6.35	6.35
Longitudinal Pitch, cm	5.499	5.499
Tube OD, cm	2.534	2.534
Tube ID, cm	2.324	2.324
Material	90-10 CuNi	90-10 CuNi
Row Orientation	Horizontal	Horizontal
Number Circuits	1	1
Circuitry	Counterflow	Counterflow
Fins		
Material	Al	Al
Fin OD, cm	5.715	5.639
Fin Density, cm^{-1}	4.33	3.937
Fin Thickness at Base, mm	0.381	0.381
Fin Thickness at Tip, mm	0.1905	0.1905
Collar	Overlapped, Full	Full
Collar Area Per Length of Tube, m^2/m	0.0705	0.0694
Fin Area Per Length of Tube, m^2/m	1.731	1.544
Total Surface Area Per Length of Tube, m^2/m	1.802	1.613
Area Face/Area Min.	1.943	1.902
D_h/D_{col}	0.148	0.174
f'/f	0.0726	0.0828

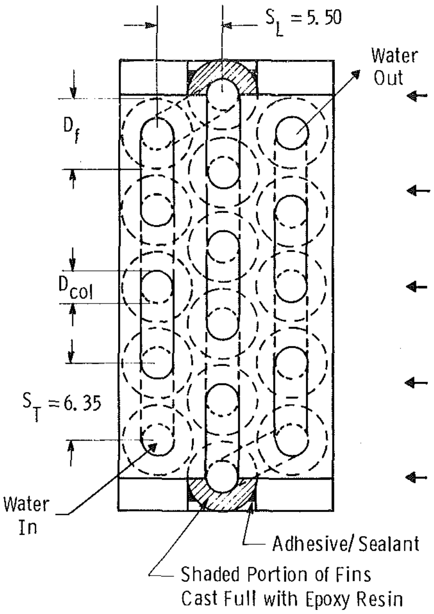

Fig. 2 Construction details of the three-row heat exchanger; dimensions in cm

coefficient is different for induced and forced draft. For induced draft, the heat transfer coefficient increased with row number and is again dependent on the Reynolds number. For forced draft, the heat transfer coefficient increases from a one- to two-row exchanger and then decreases and again is Reynolds-number-dependent. However, the row effect correlation recommended by Weierman [8] does not consider the Reynolds number as a correlating parameter. It is apparent that additional data dealing with the effect of the number of tube rows on heat transfer and pressure drop of finned tube banks will be a valuable contribution to resolving this existing uncertainty.

Finned Tube and Heat Exchanger Description

Table 1 records the dimensions of the finned tubes and of the resulting heat exchangers tested. Note that only a four-row tube bank was constructed with the "T" foot finned tubes made by the IBC machine. Special precautions were taken to prevent unwrapping of the fins on the short tube lengths. The quality of the finned tubes was judged from the appearance, tightness, and rigidity to be excellent.

The heat exchangers contained thermally active half-tubes for side sealing to improve the accuracy of these experiments. The importance of the side sealing was previously demonstrated [9] for low-finned tube bundles. The authors believe that this is the first time data were obtained in this manner. To develop a thermally active half-tube, a tube with a heat impervious wall at the centerline is required. The easiest way to accomplish this is to cast half of the tube in epoxy. A pipe with an inside diameter equal to the fin diameter was cut along the centerline to make a semicircular trough which was filled with epoxy. A finned tube with both ends covered was gently lowered into the trough. After the epoxy cured, the tube was removed, cleaned, and fitted into the tube sheet as shown in Fig. 2. Estimates were made on the departure of this tube's heat transfer from an ideal half-tube. The resulting error in the heat transfer is less than 0.1 percent when considering the following effects: the fin efficiency increase due to two-dimensional conduction from the uncooled fin areas, heat conduction through the epoxy to the air side, and the boundary layer formation on the epoxy wall. About a 2 percent deviation would be expected with thermally inactive half-tubes.

The heating fluid is water which passes through the exchanger in a single circuit. The single-exchanger circuit is arranged as shown in Fig. 2. Sufficient mass flow of water is maintained to keep the crossflow correction factor, based on tube side stream mixed and air side unmixed, less than 3 percent. Since this factor is not formulated for the exact

Nomenclature

A = flow area, m^2
A_s = heat exchange surface area, m^2
C_p = fluid specific heat, J/kg − °C
D = diameter, m
D_h = hydraulic diameter, $D_h = 4A_{min}L/A_s$, m
f = fanning friction factor, equation (4)
f' = friction factor, equation (9)
G = mass velocity, kg/m^2-s
h = bundle average heat transfer coefficient, W/m^2-°C
$h(i)$ = individual heat transfer coefficient of row i, W/m^2 − °C
j = Colburn factor, equation (3)
l = fin height, $(D_f - D_{col})/2$, m
L = heat exchanger streamwise length, m
N_f = number of fins per unit length, fin density, 1/m
N_r = number of tube rows in the flow direction
ΔP = air side pressure drop, Pa
Pr = Prandtl number
Re = Reynolds number based on collar diameter, equation (7)
S_L = longitudinal tube pitch, m
S_T = transverse tube pitch, m
t = fin thickness, m
V = face velocity, m/s
ρ = fluid density, kg/m^3
μ = dynamic viscosity, Pa•s

Subscripts

o = reference to standard conditions, $\rho_o = 1.20\ kg/m^3$
col = collar reference
f = fin reference
face = face
i = index
max = maximum
min = minimum

geometry of these tests but is a conservative estimate and since the tube circuit approaches true counterflow, it is not used to correct the data.

Data Acquisition and Reduction

A general description of the recirculating temperature and humidity controlled wind tunnel in which the heat exchangers are tested has been presented [10]. The handling, fabrication, and data reduction procedures are outlined in that reference. Because the fins are tapered from midradius to the tip, the fin efficiency is determined as that for a circular triangular cross-section fin using the thickness at the base as the characteristic thickness. This is in accordance with ARI Standard 410 [11]. Since the minimum fin efficiency in these tests is 86 percent, the error due to use of the base thickness rather than the actual thickness profile is less than 0.25 percent.

Equations (1-7) define the parameters used in the data presentation. Standard[1] face velocity and pressure drop are computed by the following equations

$$V_o = \rho V/\rho_o \tag{1}$$

$$\Delta P_o = \rho \Delta P/\rho_o \tag{2}$$

The Colburn and friction factors are defined according to the following equations

$$j = h/(G_{\max} C_p)\mathrm{Pr}^{2/3} \tag{3}$$

$$f = \Delta P_o \rho_o/(2N_r G_{\max}{}^2) \tag{4}$$

In equations (3) and (4), $G_{\max}$ is given as

$$G_{\max} = \rho_o V_o A_{\text{face}}/A_{\min} \tag{5}$$

The face area ratio $A_{\text{face}}/A_{\min}$ is given by the equation

$$A_{\text{face}}/A_{\min} = S_T/(S_T - D_{\text{col}} - 1.75 N_f l t_f) \tag{6}$$

The Colburn and friction factors are plotted as a function of the Reynolds number. The Reynolds number definition used for this presentation is

$$\mathrm{Re} = G_{\max} D_{\text{col}}/\mu \tag{7}$$

where D_{col} is the collar or root diameter of the finned tube.

The j, f, and Re parameters of equations (3), (4), and (7) are related to those defined by Kays and London [12] (designated here by a single quotation mark) as follows

$$j'/j = 1 \tag{8}$$

$$f'/f = D_h/(N_r \cdot L) \tag{9}$$

$$\mathrm{Re}'/\mathrm{Re} = D_h/D_{\text{col}} \tag{10}$$

The values of f'/f and Re'/Re are given in Table 1 for the reader's convenience.

Results

The results of the testing and comparisons with existing data are presented in this portion of the paper. The performance of the two finned tube types is presented first and then the row number effects are addressed. In this test series every effort was made to minimize error so that differences in contact conductance could be detected. The following heat balance errors were achieved: mean = 1.21 percent, RMS = 0.66 percent, and standard deviation from the mean = 3.45 percent. Because the average of air-and water-side heat rates are used to determine the heat flux, these data represent the tube bundle performance to within ±5 percent at a 99 percent confidence level.

"T" and "L" Foot Comparison

Figure 3 compares the heat transfer and pressure drop performance of the "L" and "T" foot finned tube bundles having four tube rows. Note that the heat transfer performance for each tube type is almost identical. The "L" foot finned tube bundle appears to have higher pressure drop. The usual method of data presentation for pressure drop does not account for the greater wetted surface area of the "L" foot tubes (10 percent higher fin density than for the "T" foot, larger fin diameter, and larger collar diameter). If the friction factors are based on the hydraulic diameter definition, the f' versus Re' curves for the "T" and "L" foot fins are identical.

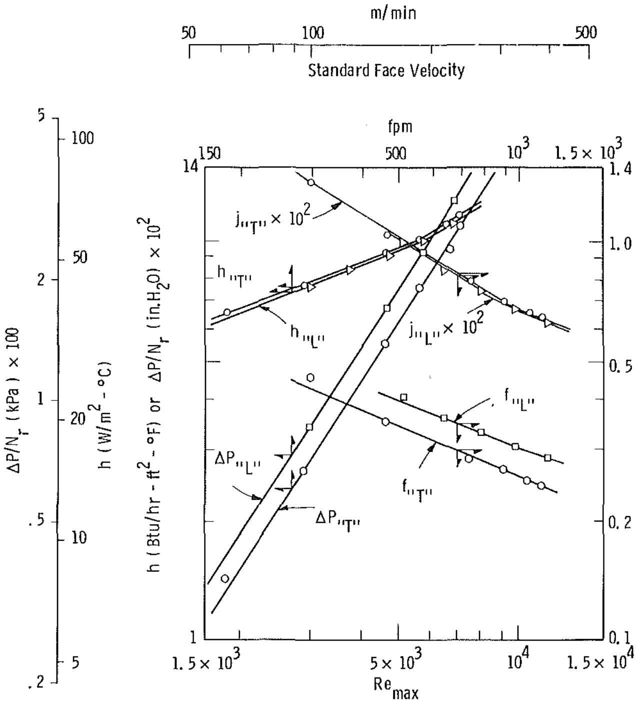

Fig. 3 Comparison of the heat transfer and pressure drop performance of "L" and "T" foot tubes in the four row exchangers

The parallelism of the j and h curves in Fig. 3 is an indication that the contact conductance of the "L" and "T" foot tubes is nearly equal. Poor contact, like tubeside fouling, causes a reduction in the apparent h at higher velocities (greater j versus Re slope). The slope is altered because the contact resistance becomes a greater percent of the overall thermal resistance as velocity increases.

Figures 4 and 5 compare the heat transfer performance and the pressure drop performance respectively with data obtained from HTRI [13] and with two commonly used predictive methods. Table 2 compares the "T" foot, the "L" foot, and the HTRI finned tube geometries. Note that the only significant difference is that the HTRI data was obtained for an embedded fin attachment (tension wound in a groove with the groove subsequently rolled or peened closed). Excellent agreement existed in the past between the data obtained from these two test facilities for comparable finned tube heat exchangers. Noteworthy was the agreement of the heat transfer and pressure drop results presented in [10] and [16].

The first predictive method was recently developed by Weierman [8] and the second method is the Briggs and Young [14] heat transfer correlation and the Robinson and Briggs [15] pressure drop correlation. The second set of correlations was recommended by Webb [17] to predict the performance of finned tube banks.

Figure 4 shows that there is good agreement between the HTRI and the present heat transfer data. For both data sets, the exponents on the Reynolds number are about the same

---

[1] Standard air density is 1.20 kg/m^3

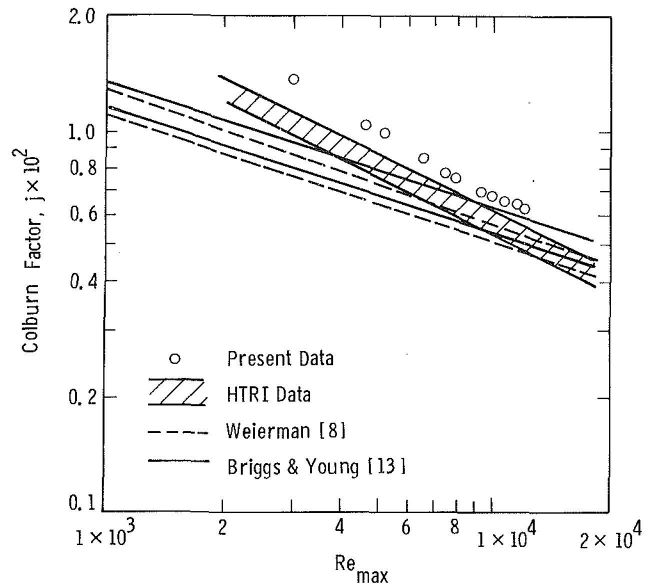

Fig. 4 Colburn factor comparison of typical air-cooler tubes – a four-row equilateral pitch tube bundle

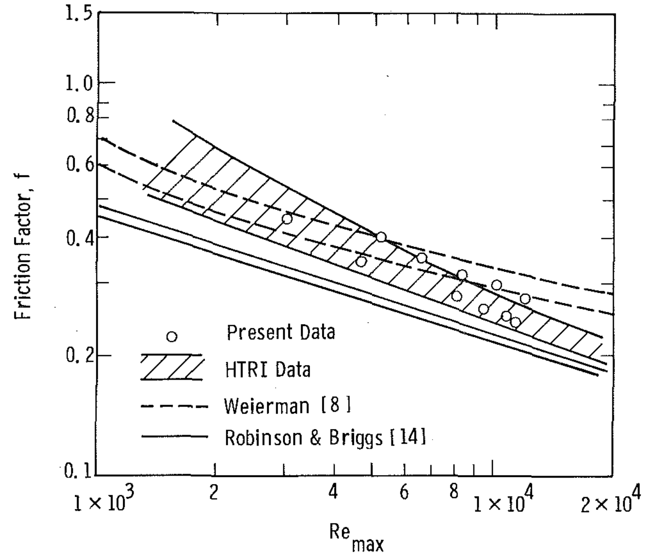

Fig. 5 Friction factor comparison of typical air-cooler tubes – a four-row equilateral pitch tube bundle

and equal to about –0.4. The present data are, however, about 15 percent higher. There are several reasons for this relatively small deviation. The HTRI data was obtained from tube banks containing embedded fins. The fin profile and roughness on the fins and at the fin roots are not necessarily the same. Also, the new heat transfer data could be higher because of the thermally active half-tubes.

Figure 4 shows that both correlation methods underpredict these data sets, especially in the lower Reynolds number range. The exponents of the Reynolds number are –0.35 and –0.319 for the Weierman and the Briggs and Young correlations, respectively. These exponents would have to be larger to be in better agreement with the present data at lower Reynolds numbers. As previously mentioned, differences in contact conductance, i.e., fin attachment, can influence the j versus Re exponent and may, in part, be responsible for the various exponents. Two lines were used to bound the results of both prediction methods. The upper line represents the predictions of the HTRI finned tube with the smaller fin count (0.354 fins/mm) and the lower line represents the predictions of the HTRI finned tube with the higher fin count (0.433 fins/mm). The Colburn factor predictions for the "L" and "T" foot finned tube geometries fell between the two limits but the present data did not.

Table 2 Finned tube geometry comparison – 4 rows

Foot type	D_f mm	D_{col} mm	t_f mm	N_f 1/mm	S_T mm	S_L mm
"T"	56.39	26.11	0.38	0.394	63.50	54.99
"L"	57.15	26.87	0.38	0.433	63.50	54.99
Gr	55.88	25.40	0.43	0.354	63.50	54.99
Gr	56.64	25.40	0.43	0.433	63.40	54.99

Figure 5 compares the new friction factor results with the HTRI data and the correlations of Weierman [8] and Robinson and Briggs [15]. Note that there is good agreement between the two data sets. The Weierman correlation adequately predicts these data except for the higher Reynolds number range, whereas the Robinson and Briggs correlation predicts a somewhat lower pressure drop for the entire Reynolds number range. Again, two lines are used to display the highest and lowest friction factor predictions for the four finned tube geometries shown in Table 2.

Effect of the Number of Rows

Table 1 shows that five heat exchangers were constructed with the overlapped "L" foot finned tubes. Each of these heat exchangers were identical except for the number of tube rows which varied from one through five. Figure 6 presents the heat transfer and pressure drop results for all five exchangers. Note that the pressure drop and heat transfer vary with the number of rows in a manner that is consistent with the analogy between heat and momentum transfer, i.e., both the friction factor and the Colburn factor increase with row number until about the third row.

These heat transfer and pressure drop data are next compared to similar results published in the open literature. The heat transfer row effect is considered first and then the pressure drop row effect is addressed.

Comparison of the Effect of Row Number On Heat Transfer. Two presentation formats are used to display the effect of the row number on the heat transfer performance of finned tube heat exchangers. The first method presents the bundle heat transfer coefficient for different row numbers and the second method presents the individual heat transfer coefficients of each row of a single finned tube heat exchanger.

There does not exist a "clean" procedure to relate the individual outside heat transfer coefficients for each row to the bundle average value. For the particular case of no temperature drop of the tubeside fluid (condensing or boiling), it can only be shown that the bundle overall heat transfer coefficient is equal to the arithmetic average of the overall heat transfer coefficients for each row. Therefore, even when the outside heat transfer resistance is dominant, the bundle outside heat transfer coefficient is not equal to the average of the outside heat transfer coefficients of each row of the bundle because of the row-to-row fin efficiency variation. It is evident, then, that the bundle row effect heat transfer data should not be compared to other bundle heat transfer data that has been computed from individual row heat transfer data by simple averaging techniques. The heat transfer results presented in Fig. 6 are for finned tube bundles with different numbers of tube rows, the first method.

Table 3 compares the present normalized bundle heat transfer coefficient variation with row number with similar results from six additional sources and with the row number correlation of Weierman [8]. For most cases, the row

Table 3 Comparison of normalized bundle heat transfer coefficients for various row numbers[a]

Source	D_{col}	D_f	N_f	S_T	Draft	Re or V_{max}	Row Number								
							1	2	3	4	5	6	7	8	10
Mirkovic [5]	25.4 50.8	44.4 69.9	0.236 0.236	109.0 100.0	Induced	NA	0.71	0.80	0.87	0.91	0.94	0.98	0.99	1.00	1.01
Cox and Jallouk [18]	16.0	36.5	0.303	44.5	Induced	NA	0.70	0.78	0.83	0.86	0.89	0.90	0.91	0.93	
Gianolio and Cuti [7]	25.4	58.0	0.433	60.3	Forced	4.0	1.13	1.29	1.20	1.09	–	1.00			
						6.0	1.02	1.17	1.13	1.05	–	1.00			
						8.0	0.94	1.08	1.10	1.02	–	1.00			
					Induced	4.0	0.78	0.88	0.93	0.95	–	0.98			
						6.0	0.73	0.86	0.91	0.94	–	0.98			
						8.0	0.70	0.83	0.89	0.93	–	0.98			
Ward and Young [3]	29.1	58.5	0.315	61.9	Induced	1.5	0.85	0.92	0.95	0.96	0.97	0.97	0.98	0.98	0.99
						2.5	0.81	0.88	0.92	0.94	0.95	0.96	0.96	0.97	0.98
						5.1	0.74	0.83	0.88	0.92	0.93	0.95	0.95	0.96	0.97
Jameson [19]	15.9	28.5	0.343	39.6	Induced	NA	–	0.85	–	0.92	–	–	–	1.00	
	19.1	37.2	0.356	40.3			–	0.86	–	0.97	–	–	–	1.00	
	19.1	37.2	0.356	51.3			–	0.86	–	0.97	–	–	–	1.00	
Rabas, Eckels and *Sabatino* [20]	31.8	38.7	0.393	42.9	Induced	5000	–	–	0.98	–	–	1.08	–	1.00	
						10000	–	–	0.93	–	–	1.05	–	1.00	
						20000	–	–	0.92	–	–	1.03	–	1.00	
			0.709			5000	–	–	1.35	–	–	1.14	–	1.00	
						10000	–	–	1.14	–	–	1.14	–	1.00	
						20000	–	–	1.07	–	–	1.12	–	1.00	
			0.984			5000	–	–	1.23	–	–	1.07	–	1.00	
						10000	–	–	1.10	–	–	1.07	–	1.00	
						20000	–	–	1.00	–	–	1.07	–	1.00	
Present Data	25.3	57.2	0.433	63.5	Induced	5000	0.80	0.93	0.99	0.97	1.00				
						10000	0.76	0.92	0.97	0.95	1.00				
Weierman [8]	NA				NA	NA	0.71	0.82	0.92	0.97	1.00	1.00	1.00	1.00	1.00

[a] All dimensions in mm, V_{max} in m/s

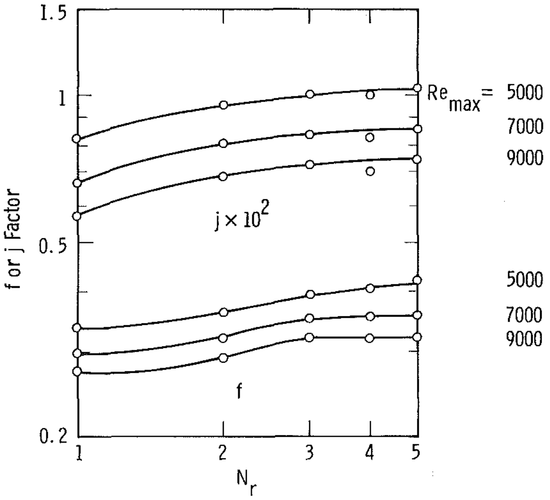

Fig. 6 Nondimensional "friction" and heat transfer as a function of number of rows for various Reynolds numbers ("L" foot tubes)

correction values presented in this table are normalized with the value for the largest (most tube rows) heat exchanger which were tested. Mirkovic [5] extrapolated his findings past an eight row exchanger, the largest which he tested. Ward and Young [3] presented their results in the format h_i/h_∞ even though they only had individual row heat transfer coefficient data for the first eight rows. Their bundle heat transfer coefficient variation with row number was considered for this comparison because it is often used for sizing air-cooled heat exchangers even though it was obtained by averaging the outside individual heat transfer coefficients of individual rows, a procedure which, according to the previous paragraph, can include some small error.

The finned tube geometry and pitch values are also presented in Table 3. Note that not all of these geometries are characteristic of typical air-cooler finned tubes. The data of Cox and Jallouk [18] and Jameson [19] are for smaller tube diameters and the data of Rabas et al. [20] are for low-finned tube banks. These data sets are included in order to establish trends and aid in the understanding of finned tube heat transfer row effects. An equilateral or near equilateral tube pitch arrangement was used, however, for all the data sets.

A column in Table 3 shows either the Reynolds number based on the root diameter or the maximum velocity. The authors were unable to find the mean air temperatures for the tests of Gianolio and Cuti [7] and Ward and Young [3]. As a result, a common comparison based on the Reynolds number – the correct independent variable – was not possible. The Reynolds number is equal to about 7000 for V_{max} equal to 5 m/s, the bulk-average air temperature equal to 50°C, and the root diameter equal to 25.4 mm.

Another column labeled "draft" is included in Table 3. For typical air-coolers, there is no difficulty in distinguishing between induced and forced draft. For wind tunnels, however, the distinction between induced and forced draft is not as clear. The data of Ward and Young was obtained with induced draft because the blower was located after the bundle (air was drawn through the bundle). All the other data sets were obtained by blowing or forcing the air through the bundles which were located within the wind tunnel facilities. However, the forced draft operation in a wind tunnel test is not the same as forced draft operation of a typical air-cooled heat exchanger. In wind tunnels, extreme care is taken to establish very uniform approach velocity distributions and to reduce the approach turbulence intensity levels. Wind tunnel test results even for a blowing condition should, then, more closely represent those of a typical induced draft air-cooled heat exchanger. There is only one data set in Table 3 labeled as forced draft, the data of Gianolio and Cuti [7], which was obtained from a typical air-cooled heat exchanger operated in a forced-draft mode.

Table 3 shows that the present row effect heat transfer coefficient data compares favorably with the results for typical air-cooler finned tubes. Noteworthy is the agreement with the recent induced draft data of Gianolio and Cuti [7].

Table 3 will next be used to address the following row number effects on the outside heat transfer coefficients: Reynolds number, fin root or collar diameter, tube pitch, fin density, and draft and turbulence intensity level.

Reynolds Number. A characteristic common to all data sets is that the smallest row correction values always exist for the highest Reynolds number (or maximum velocity) regardless of the type of draft. However, the statement that the row number effect on the heat transfer coefficient decreases with a decreasing Reynolds number is not true. Note that the variation of the bundle outside heat transfer coefficient for different row numbers is greatest with the small Reynolds number with forced draft and with the high fin density results of Rabas et al. [20]. Table 3 demonstrates that the Reynolds number is a necessary correlating parameter of finned tube bundle heat transfer row effects, a point not considered in the correlation of Weierman [8].

Tube, Fin Root or Collar Diameter. The same row correction results are recommended for use by Mirkovic [5] regardless of the tube or collar diameter. Note that his results were obtained from two different bundles, the root diameter in each varied by about a factor of two. The data of Jameson [19] also somewhat supports the statement that the row number effect is independent of the tube, fin root, or collar diameter.

Tube Pitch. No difference could be detected in the outside heat transfer coefficient data of Jameson [19] for two different equilateral pitch arrangements.

Fin Density. The row number effect on the outside heat transfer coefficients for different fin densities is very interesting. Note that when only the fin density is increased, a point is reached where the heat transfer coefficients begin to decrease rather than increase with row number. Most likely there is less penetration of the air between the fins and more air is forced into the bypass stream between the fin tips with the higher fin density. It has been demonstrated [4, 10, 16] that the heat transfer coefficient decreases with row number for an in-line tube bundle arrangement. Maybe the reason for the reduction of the heat transfer coefficient with row number for the high fin density tube bundles with a staggered arrangement is the existence of a large bypass stream between the fin tips, a situation that does exist for an in-line arrangement.

Draft and Turbulence Intensity. The forced draft row number effects obtained by Gianolio and Cuti [7] show two very interesting points. Note that the change in the bundle average heat transfer coefficient is concentrated to only the first couple rows and approaches unity sooner than that for induced draft. Also note the very large variation with row number for the lowest Reynolds number data set. These two findings are different from typical induced draft results for air-cooler tubes.

A characteristic of forced draft is a higher level of turbulence in the approaching air stream. Zozulya et al. [21] studied the variation of the outside individual row heat transfer coefficients for finned tube banks with different turbulence levels in the approach stream. Table 4, taken from [21], shows that the individual heat transfer coefficient variation with row number decreases when the turbulent intensity or level is increased. Most likely, then, the reason why the row effects do not persist as far into the bundle with forced draft is that a high level of turbulence already exists in the approaching air stream. Also, these data indicate that very high levels of turbulence must exist after the first couple of rows in a finned tube bank.

Table 4 $h_i/h_{4\text{th row}}$

Row	Turbulence levels 2.5–3%	10–12%	14–16%	22–25%
1	0.65	0.72	0.84	0.94
2	0.82	0.84	0.85	0.94
3	0.95	0.95	0.97	1.00
4	1.00	1.00	1.00	1.00

Another characteristic of forced draft is a component of velocity parallel to the tube axis. The reduction of this component after entering the bundle can explain the highest heat transfer coefficient values at the second or third row which then decrease with row number. The large variation for the first couple of rows, particularly the lowest Reynolds number with forced draft, may, therefore, be the result of the velocity component parallel to the tubes and not the higher level of turbulence. Table 4 shows that the individual heat transfer coefficients always increased with increasing row number regardless of the turbulence level.

Some test data of the individual row outside heat transfer coefficient variation with row number exist in the open literature. The recent data of Hashizume [1] showed that the individual row heat transfer coefficients increased to the third row and then remained about the same. Hashizume did not convert this individual row heat transfer data to bundle outside heat transfer coefficient variations with row number, the more useful but possibly the more questionable format.

Comparison of the Effect of Row Number on Pressure Drop. For typical air-cooler finned tubes, the authors were not able to find other data displaying the tube bundle pressure drop variation with row number. It was not possible, then, to compare the present data to other published results. There are, however, some finned tube bundle pressure drop test results that display the effect of the row number for other types of finned tubes. The data obtained by Brauer [4], Jameson [19], Weierman [22], and Rabas et al. [20] will be briefly discussed. These data sources do add some credibility to the present data and suggest that more data and analysis are required to fully understand the row number pressure drop effect. For some unknown reason, there appears to be far less interest in the effect of row number on the bundle pressure drop performance than on the bundle heat transfer performance.

Brauer [4] showed that the friction factor decreased with row number. In the lower Reynolds number range, the friction factor for a one-row bundle was about 1.3 times greater than a two-row bundle; however, there was very little difference in the friction factors between a two-row and a four-row bundle. In the higher Reynolds number range, a gradual decrease of the bundle friction factor from a one-row bundle to a four-row bundle occurred. The one-row friction factor was still 1.3 times greater than the bundle friction factor for a four-row exchanger. The particular finned tube geometry used for this test was somewhat similar to typical air-cooler types except for the fin thickness (about twice as great) and fin density (about one-third less fins). These results of Brauer again demonstrate that the row number effect on the bundle friction factor should contain the Reynolds number as a correlating parameter.

Jameson [19] presented bundle pressure drop results for different numbers of staggered tube rows, two tube diameters (12.7 mm and 19.0 mm), and five different fin-tip clearances. For the larger tube diameter, the pressure drop per row increased with the row number for the smallest fin-tip clearance and decreased with row number for the largest fin-tip clearance. For the smaller tube diameter, the pressure drop per row did not show any consistent trend regardless of the fin-clearance or transverse pitch. The data of Jameson suggest that the transverse pitch and maybe even the tube or collar diameter are necessary correlating parameters.

Weierman [22] showed that there was very little variation in the friction factor for one to seven tube rows for a staggered bank of large diameter heat recovery tubes (50.8 mm). He also showed that the row effect was independent of the velocity for these tubes, a finding not in agreement with the results of Brauer (tube diameter equal to 25.4 mm).

Rabas et al. [20] presented the variation of the friction factor for three, six, and eight row tube banks containing identical low-finned tubes except for the fin density. The details of these bundles are shown in Table 3. For the lowest fin density (same as air-cooler tubes), the friction factor increased with the bundle row number; however, the amount of increase diminished with increasing Reynolds number. As the fin density increased, the friction factor began to decrease with the bundle row number. For the highest fin density, the friction factor decreased with row number regardless of the Reynolds number. Again, the manner in which the fin density increase changes the effect of the row number on the bundle friction factor can be explained with the bypassing argument. When the fin density is increased, more air flows in the bypass lanes between the fin tips as occurs in an inline tube bundle. It has been established that the bundle friction factor substantially decreases with an increase in row number for in-line arrangements regardless of the tube diameter [4, 22].

Finally, Weierman [8] presented a correction to the bundle pressure drop that depends on the number of tube rows. This correction factor would indicate either an increase or decrease depending on the longitudinal/transverse tube pitch ratio. For a typical equilateral pitch arrangement, the pressure drop decreased with an increase in the number of tube rows, which is not in agreement with the present data. Also, this row correction did not consider the Reynolds number as a correlating parameter.

Conclusion

Data are presented that show the heat transfer performance of typical air-cooler tubes with an "L" foot and "T" foot are almost identical, but also that the heat transfer performance of both was greater than other air-cooler tubes with similar tube geometry. The best agreement exists between the present data and that for an imbedded type fin, but the greater Colburn factor of the "L" and "T" foot tubes may not be solely attributable to the fin attachment method. Other differences in the tube bundle and apparatus, such as thermally active half-tubes and air-side flow conditioning, may be a consideration.

Good agreement exists between the friction factor data of the "T", "L," and imbedded foot finned tubes. Some difference exists between the pressure drop data of the "T" and "L" foot tubes in the present data, but when wetted surface area differences are accounted for, the friction factors are also nearly identical.

Data are presented that show both the bundle heat transfer and pressure drop increasing with an increase in the number of tube rows. The increase in the bundle heat transfer performance is consistent with other findings for typical air-cooler tubes in an induced draft mode of operation. The increase in the bundle pressure drop with row number is not necessarily consistent with other published results. However, it is demonstrated that friction factor can increase or decrease with row number and depends on the tube diameter, tube pitch, fin number, and Reynolds number.

Acknowledgment

The approval of the Tennessee Valley Authority to publish this data is acknowledged with appreciation.

References

1 Hashizume, K., "Heat Transfer and Pressure Drop of Finned Tubes in Cross Flow," *Heat Transfer Engineering*, Vol. 3, No. 2, Oct.-Dec. 1981, pp. 15-20.

2 Schmidt, T. E., "Heat Transmission and Pressure Drop In Banks of Finned Tubes and in Laminated Coolers," *Proceedings of the Institution of Mechanical Engineers and ASME*, II, London, 1951, pp. 186-188.

3 Ward, D. J., and Young, E. H., "Heat Transfer and Pressure Drop of Air in Forced Convection Across Triangular Pitch Banks of Finned Tubes," *Chemical Engineering Progress Symposium*, No. 41, Vol. 59, 1963, pp. 37-44.

4 Brauer, H., "Warmeubertragung und Stromungswiderstand bei Fluchtend und Versetztargeordneten Rippenrohren," Dechema Monographic, Band 40, 1962, pp. 41-76.

5 Mirkovic, Z., "Heat Transfer and Flow Resistance Correlation of Helically Finned Tubes in Cross Flow of Staggered Tube Banks," *Heat Exchangers: Design and Theory Source Book*, edited by N. H. Afgan and E. U. Schlunder, 1974, pp. 559-584.

6 Neal, S. B., and Hitchcock, J. A., "A Study of the Heat Transfer Processes in Banks of Finned Tubes in Cross Flow, Using a Large Scale Model Technique," *Proceedings of the Third International Heat Transfer Conference*, Vol. 3, 1966, pp. 209-298.

7 Gianolio, E., and Cuti, F., "Heat Transfer Coefficients and Pressure Drops for Air Coolers With Different Numbers of Rows Under Induced and Forced Draft," *Heat Transfer Engineering*, Vol. 3, No. 1, July-Sept. 1981, pp. 38-48.

8 Weierman, C., "Correlations Ease The Selection of Finned Tubes," *Oil and Gas Journal*, Sept. 1976, pp. 136-139.

9 Eckels, P. W., and Rabas, T. J., "A Finned Tube Heat Exchanger Side Seal Study," *Advances In Enhanced Heat Transfer—1981*, Milwaukee, Wis., Aug. 25, 1981, pp. 43-49.

10 Rabas, T. J., and Eckels, P. W., "Heat Transfer and Pressure Drop Performance of Segmented Extended Surface Tube Bundles," ASME Paper No. 75-HT-45, Aug. 1975.

11 Air Conditioning and Refrigeration Institute Standard 410-72, 1815 N. Fort Meyer Drive, Arlington, Va. 22209.

12 Kays, W. M., and London, A. I., *Compact Heat Exchangers*, (2nd ed.), McGraw-Hill, New York, 1964.

13 Heat Transfer Research, Inc., *Extended Surface Data Book*, July 1978, HTRI Confidential: For the use of members only. Data represented here as a band with the approval of HTRI.

14 Briggs, D. E., and Young, E. H., "Convection Heat Transfer and Pressure Drop of Air Flowing Across Triangular Pitch Banks of Finned Tubes," *Chemical Engineering Progress Symposium Series*, Vol. 59, No. 41, 1963, pp. 1-10.

15 Robinson, K. K., and Briggs, D. E., "Pressure Drop of Air Flowing Across Triangular Pitch Banks of Finned Tubes," *Chemical Engineering Progress Symposium Series*, Vol. 62, No. 64, 1964, pp. 177-182.

16 Weierman, C., Taborek, J. and Marner, W. J., "Comparison of the Performance of In-Line and Staggered Banks of Tubes with Segmented Fins," *AIChE Symposium Series*, Vol. 74, No. 174, 1978, pp. 39-46.

17 Webb, R. L., "Air-Side Heat Transfer in Finned Tube Heat Exchangers," *Heat Transfer Engineering*, Vol. 1, No. 3, Jan.-Mar. 1980, pp. 33-49.

18 Cox, B., and Jallouk, P. A., "Experimental Determination of the Performance Characteristics of Eight Compact Heat Transfer Surfaces," Report No. K-1832, Union Carbide Corp., Oak Ridge Gaseous Diffusion Plant, Prepared for U.S. Atomic Energy Commission, Dec. 1972.

19 Jameson, B. L., "Tube Spacing in Finned Tube Banks," ASME *Transactions*, Vol. 67, Nov. 1945, pp. 633-642.

20 Rabas, T. J., Eckels, P. W., and Sabatino, R. A., "The Effect of Fin Density on the Heat Transfer and Pressure Drop Performance of Low-Finned Tube Banks," *Chemical Engineering Communications*, Vol. 10, No. 1-3, 1981, pp. 127-147.

21 Zozulya, N. V., Vorobyev, Y. P., and Khavin, A. A., "Effect of Flow Turbulization on Heat Transfer in a Finned Tube Bundle," *Heat Transfer Soviet Research*, Vol. 5, No. 1, 1973, pp. 154-156.

22 Weierman, C., "Pressure Drop Data for Heavy-Duty Finned Tubes," *Chemical Engineering Progress*, Vol. 73, No. 2, 1977, pp. 69-72.

Heat Transfer and Pressure Drop Performance of Finned Tube Bundles

P. W. Eckels
Research and Development Laboratories,
Westinghouse Electric Corporation,
Pittsburgh, Pa. 15235
Mem. ASME

T. J. Rabas
Combustion Turbine Systems Division,
Westinghouse Electric Corporation,
Concordville, Pa. 19331
Mem. ASME

The heat transfer and pressure drop performance of two types of finned tubes used in the air-conditioning industry are reported for 14 different bundle configurations. Twelve of these configurations contained a new type of finned tube called K-Y and two contained a more conventional pin fin. A unique characteristic of all these configurations is zero or negative fin-tip clearances. A comparison of the performance of these air-conditioning type finned tubes with negative fin-tip clearance is then made with the performance of typical air-cooled heat exchanger tubes used in the process and power industries. Both the heat transferred and the pressure drop are substantially higher with the air-conditioning configurations; the heat transfer coefficient is superior even to plain tubes. The very high heat transfer performance is more the result of the negative fin-tip clearance than the fin shape or type.

Introduction

Air-cooled heat exchangers used in the process and power industries commonly use tubes with solid helical fins, low fin densities ($N_f \cong 0.4$ fins/mm or lower), large tube diameters ($d_{\mathrm{col}} \cong 25$ mm), and positive fin-tip clearances. Air-cooled heat exchangers used in the air-conditioning industry commonly use tubes with pin fins, high fin densities ($N_f \cong 0.75$ fins/mm), small tube diameters ($d_{\mathrm{col}} \cong 10$ mm), and negative fin-tip clearance. The major reasons for these differences are capital cost, reliability, and performance characteristics. The purpose of this paper is to address the performance or the heat transfer and pressure drop characteristics of these two finned tube types. This paper will not address the other major reasons because of commercial considerations.

A very extensive data base and reliable heat transfer and pressure drop correlations exist for the commonly used air-cooler tubes; however, the writers are not aware of any published data or correlations for the finned tubes used in the air-conditioning industry. Although the performance of rigid segmented, helically wrapped, high-finned tube banks have been reported [1-4], the many variables involved tend to impede correlation attempts. In addition, positive fin-tip clearance (no fin overlap) was always considered for these tests. One purpose of this paper is to present a comprehensive and structured data base for the air-conditioner type finned tubes. The second purpose is to compare the performance of the air-conditioner and air-cooled finned tube types.

The first part of this paper describes some finned tubes which are commonly used for air-conditioning applications. Next, the heat exchangers or coils constructed with these various tube types are described. The data acquisition and reduction methods, the data, and the comparisons are then presented.

Air-Conditioning Finned Tubes

One particular type of finned tube used in the air-conditioning industry is described by Abbott et al. [5]. Although no performance data are given, dimensions of the fin are presented in [5]. The fin has a pin or spline shape,[1] is made from aluminum, and is attached by an adhesive. A new fin configuration, having attributes particularly suited to the construction of air-cooled condensers by the air-conditioning industry was recently developed and called K-Y. The fin material, bonding, and fin outside diameter are somewhat similar to the pin type fin.

Figure 1 shows the K-Y finned tube. Note that the fin shape is like a series of "Y"s joined at both the fin tip and base when looking along the tube axis. The sequential operations in the preparation of the rectangular aluminum fin strip are high-speed rotary lancing of the fin pattern into the strip, flattening and straightening of the fin strip, forming of the fin strip into a "U", lightly upsetting the base of the "U" to form a foot that spaces apart the fin rows, and finally tension wrapping and opening the footed fin on an epoxy coated tube. The results of these operations are shown in Fig. 2. The finned tube is then available in long lengths and heat exchangers are

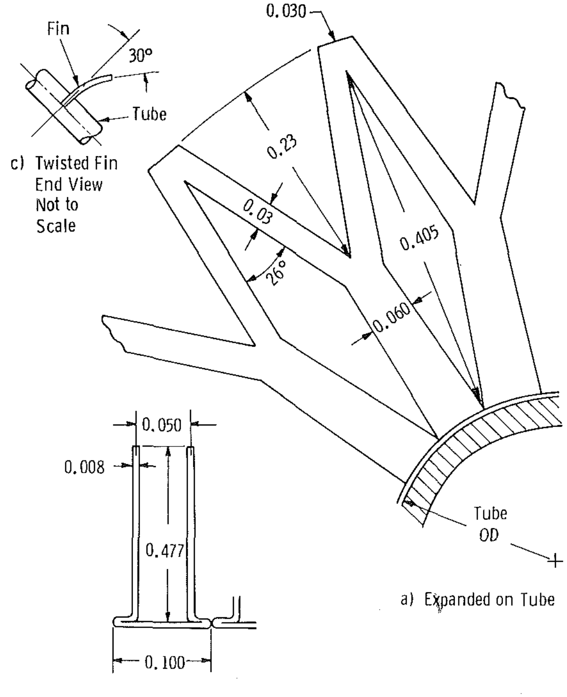

c) Twisted Fin End View Not to Scale

a) Expanded on Tube

b) Cross Section

Fig. 1 The K-Y heat transfer surface (all dimensions in inches)

---

[1] Also referred to as spine fin in [5]

Contributed by the Heat Transfer Division and presented at the 1983 ASME/JSME Joint Thermal Engineering Conference, Honolulu, Hawaii, March 1984. Manuscript received by the Heat Transfer Division March 14, 1984.

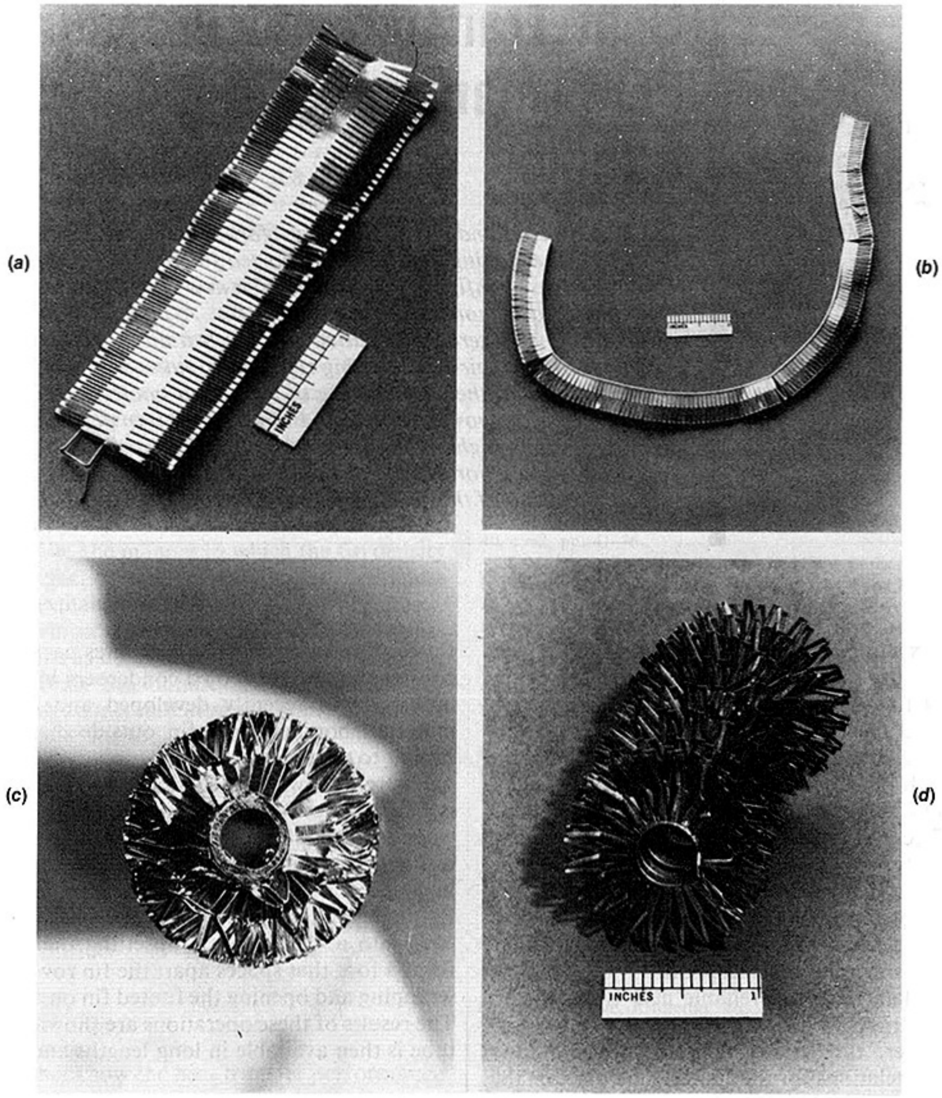

Fig. 2 Steps in the fabrication of K-Y finned tubes: (*a*) aluminum strip is rotary lanced; (*b*) lanced strip is folded and foot is formed; (*c*) footed strip is wrapped on an epoxy coated tube; (*d*) free standing fins removed from tube

Nomenclature

A = flow area
Bo = Biot number, $h\delta/k_e$
C_p = fluid specific heat
C_i = integration constants
d = diameter
f = fanning friction factor for tube collar diameter, equation (4)
f' = friction factor, Table 2 and equation (9)
F = K-Y fin base half-width
G = mass velocity
h = heat transfer coefficient
H = K-Y fin height of the full-width section
j = Colburn factor, equation (3)
k = thermal conductivity
K = fin height of the half-width section
l = fin height, $(d_f - d_{\mathrm{col}})/2$
L' = length of the heat exchanger in the flow direction
L_i = fin height to location i
M = $(h/(kt_f))^{1/2}$
M_i = fin parameters for various portions of fin
N_f = number of fins per unit of tube length, fin density
N_r = number of tube rows in the flow direction
O = fin tip connection height
Pr = Prandtl number
ΔP = air side pressure drop
q = total heat transferred
Re = Reynolds number based on collar diameter, equation (7)
S_T = transverse tube pitch
s = fin spacing
t_f = fin thickness
T = temperature
V = face velocity
W = fin width
X = Cartesian coordinate
ρ = fluid density
η = fin efficiency
μ = dynamic viscosity
δ = epoxy thickness

Subscripts

a = ambient
c = cross sectional
col = collar of tube
e = epoxy
f = fin reference
face = face
i = number of K-Y fin part
max = maximum
min = minimum
o = reference to standard conditions
w = wall

Table 1 Description of the finned tubes

Tube Number	1	2	3	4	5	6	7
Tube OD, mm	9.53	9.53	9.53	9.53	9.53	12.7	12.7
Tube ID, mm	8.71	8.71	8.71	8.71	8.71	11.1	11.9
Tube Material	Al	Al	Al	Al	Al	Al	Cu
Fin OD, mm	33	33	33	33	33	36.3	34.9
Fin Density, 1/mm	.787	.787	.787	.551	.669	.760	.787
Fin Thickness, mm	.203	.203	.203	.203	.203	.203	.203
Fin Type	K-Y	K-Y	K-Y	K-Y	K-Y	K-Y	Pin
Fin Material	3003-H25Al	3003-H25Al	3003-H25Al	3003-H25Al	3003-H25Al	3003-H25Al	Al
Fin Application	Manual	Machine	Machine	Machine	Machine	Manual	Machine
Fin Twist	None	None	30°	None	None	None	None
Collar Area/Length, m^2/m	.0262	.0262	.0262	.0183	.0223	.0348	.0346
Fin Surface Area/Length, m^2/m	.6693	.6693	.6693	.4647	.5647	.862	.900
Total Area/Length, m^2/m	.6955	.6955	.6955	.4830	.5870	.8968	.9346

Table 2 Description of the heat exchangers (coils)

Coil No.	Tube No.	Transverse Row No N_r	Tubes Per Row	Circuit No.	Row Orientation	$\frac{S_T}{d_f}$	$\frac{A_{Face}}{A_{Min}}$	$\frac{D_h}{d_{col}}$ *	$\frac{f'}{f}$ *
1	2	1	10	2	Horizontal	.91	1.84	.312	.0939
2	2	1	10	2	Horizontal	.91	1.84	.312	.0939
3	2	1	10	2	Horizontal	.91	1.84	.312	.0939
4	1	1	10	2	Horizontal	.91	1.84	.312	.0939
5	4	1	10	2	Horizontal	.91	1.84	.449	.1350
6	5	1	10	2	Horizontal	.91	1.84	.369	.1110
7	2	2△	10	2	Horizontal	.91	1.84	.279	.0939
8	2	2□	10	2	Horizontal	.91	1.84	.298	.0939
9	6	1	9	1	Horizontal	.92	2.02	.204	.0737
10	7	1	27	1	Vertical	.95	1.99	.190	.0713
11	7	1	33	1	Vertical	.77	2.59	.118	.0444
12	2	1	10	2	Horizontal	1.0	1.69	.373	.1120
13	2	1	10	2	Horizontal	.86	1.91	.284	.0854
14	3	1	10	2	Horizontal	.91	1.84	.312	.0939

* D_h and f' are equivalent hydraulic diameter and friction factor as defined by Kays and London [6]

made by serpentining the finned tubes into single or multirow refrigerant circuits.

A description of the seven finned tube types studied is presented in Table 1. Six were variations of the K-Y type and one was of the pin type. The K-Y tubes were obtained by the above described sequential procedure. The tubes of the segmented rectangular pin-fin type [5] were cut from a new three ton heat pump using appropriate care. For the K-Y type, note that two different tube diameters and three different fin counts for the smaller tube diameter were considered. Two fin twist angles were considered, since the twist can be controlled by varying the speed of the lancing operation. Both manual and mechanical fin applications were considered because the flatness of the fin varies with machine finning. The fins on the larger diameter K-Y finned tube (tube number 6) could only be manually tension wrapped. Comparison of data for both K-Y fin application methods on the smaller diameter tubes assures relevance of the data for tube number 6, the larger diameter K-Y finned tube.

Heat Exchanger Description

Table 2 describes the details of the 14 different heat exchanger coils tested. A typical heat exchanger is constructed with heavy wood side walls which are necessary to hold the tubes in their overlapped fin-tip position. More side or lateral support is required for the K-Y fin, since it is more rigid due to fin tip joining. Tube sheets are made from two overlapping sheet metal pieces that grip the fin and tube in wedge-shaped slots. The tube sheet is sealed with self-leveling silicone adhesive (GE-734) and insulated to prevent spurious heat leaks. Fittings, when required, are epoxy bonded to the tubes to prevent thermal damage to the fin-tube bond. Clamping the fin to the tube also prevents damage to the bond by unwinding. The pin fin tubes are kept in their original relative positions to maintain the initial fin compression of manufacture and the slight curvature of the tube. The tube pitch variation is obtained by compressing the tubes further together. Return bends are epoxy bonded into the pin fin tubes.

The heated water flows in two parallel circuits which are formed with four and six tube passes. Equal flow is maintained by the relatively high pressure drop of the flexible hoses, fittings, and mixers on each circuit. The exchanger circuits are arranged in cross-counter flow. Sufficient mass flow of water is maintained to keep the crossflow correction factor, based on tube-side stream mixed and the air-side unmixed, less than 3 percent. A typical value would be 1.5 percent but since this factor is not formulated for the exact geometry of these test coils the correction factor was not used. Additional error could be introduced by correcting the data for crossflow temperature difference if internal heat conduction occurs through the fins.

Data Acquisition and Reduction

The heat exchanger test facility has been previously described [2]. The heat exchanger handling, fabrication, and data reduction procedures were also outlined in that reference. The model for the data reduction and the presentation of the results are essentially the same except for the contact conductance and fin efficiency.

The contact conductance is determined by the following technique. An average thickness of the adhesive is determined from a large sample of photomicrographs of finned tube sections. The contact conductance is then computed by dividing the thermal conductivity of the adhesive by its thickness. The K-Y fin is bonded with an aluminum-loaded, high-conductivity epoxy, while the pin fin appears to be bonded with a less viscous phenolic varnish. The thickness of the viscous epoxy layer of the K-Y fin type is greater because it cannot be squeezed from under the fin by the tension winding. One interesting aspect of this evaluation is that the conductances for the two finned tubes are about the same, the higher thermal conductivity of the epoxy merely offsets its greater thickness. The conductance for each is 1.97 W/cm^2 – °C (3460 Btu/hr-ft^2-°F) and is included in the series of thermal resistances of the tube wall, water-side coefficient, and fin collar according to [2].

The fin efficiency of the pin fin is that of a straight rectangular fin [2]. A new fin efficiency calculation for the K-Y finned tube was developed because of the several cross-sectional area changes. The K-Y fin was divided into six parts, and the one-dimensional conduction equation was solved for each. Ten equations for the ten unknown constants were obtained using the end and intermediate boundary conditions. A matrix inversion computer program was then used to obtain the necessary constants needed in the final fin efficiency equation. The appendix delineates the methodology of K-Y fin efficiency evaluation.

Equations (1-7) define the parameters used in the data presentation. Standard[2] face velocity and pressure drop are computed by the following equations

$$V_o = \rho V / \rho_o \tag{1}$$

$$\Delta P_o = \rho \Delta P / \rho_o \tag{2}$$

The Colburn and friction factors are defined according to the following equations

$$j = h / (G_{\max} C_p) \mathrm{Pr}^{2/3} \tag{3}$$

$$f = \Delta P_o \rho_o / (2 N_r G_{\max}{}^2) \tag{4}$$

In equations (3) and (4), $G_{\max}$ is given as

$$G_{\max} = \rho_o V_o A_{\text{face}} / A_{\min} \tag{5}$$

The face area ratio, $A_{\text{face}}/A_{\min}$, is given by the equation

$$A_{\text{face}}/A_{\min} = S_T / (S_T - d_{\text{col}} - 2N_f l t_f) \tag{6}$$

The Colburn and friction factors are plotted as a function of the Reynolds number. The Reynolds number definition used for this presentation is

$$\mathrm{Re} = G_{\max} d_{\text{col}} / \mu \tag{7}$$

where d_{col} is the collar or root diameter of the finned tube.

The parameters j, f, and Re of equations (3), (4), and (7) are related to those defined by Kays and London [6] (designated here with a single quotation mark) as follows

$$j'/j = 1 \tag{8}$$

$$f'/f = D_h / (L' \cdot N_r) \tag{9}$$

$$\mathrm{Re}'/\mathrm{Re} = D_h / d_{\text{col}} \tag{10}$$

The values of f'/f and Re$'$/Re are given in Table 2 for the reader's convenience.

Results

This section of the paper presents the results of the testing of all the exchangers described in Table 2. The particular heat exchanger matrix shown in Table 2 was structured to obtain information concerning the following effects: (*i*) manufacturing repeatability, (*ii*) fin density, (*iii*) row number, (*iv*) tube diameter, (*v*) tube pitch, (*vi*) fin shape, and (*vii*) fin twist.

A comparison of the results illustrating each of these effects follows in respective order.

Manufacturing Repeatability. Figure 3 shows the heat transfer and pressure drop performance of four nominally identical heat exchangers. The fins were machine applied on the tubes in coils 1, 2, and 3, and manually attached on the tube in coil 4. The purpose of this comparison is to determine the variations introduced by the manufacturing process between exchangers with the same specifications. Note the similar performance of the three coils with machine wound finned tubes, and coil 4 with manually wound finned tubes. The pressure drop is slightly lower for coil 4 most likely because the manually wound fin strip is "thumped" absolutely flat during the lancing operation.

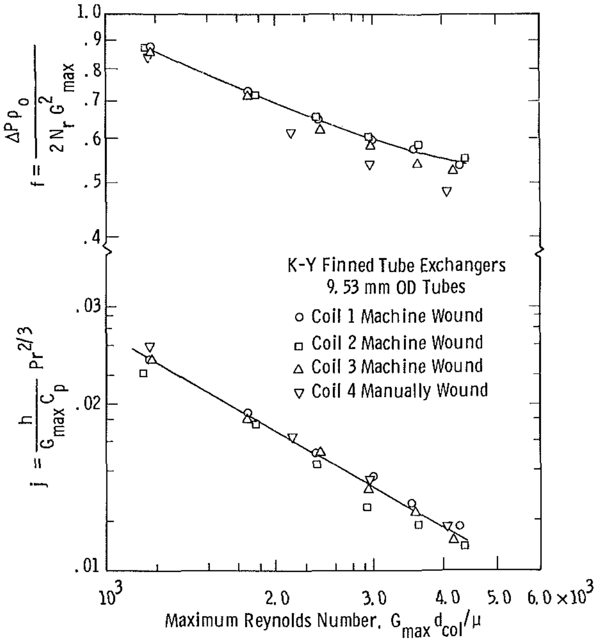

Fig. 3 Colburn and friction factors versus maximum air side Reynolds number for three nominally identical K-Y heat exchangers and a manually wound control exchanger

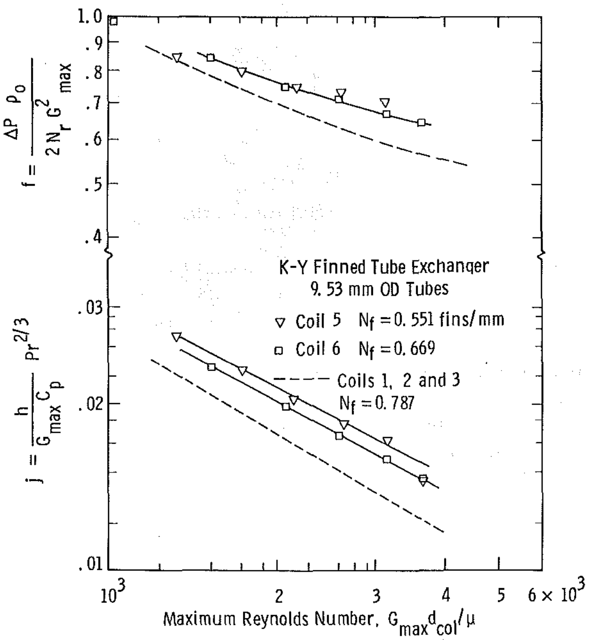

Fig. 4 Colburn and friction factors versus maximum air side Reynolds number for varying fin density

Fin Density. Figure 4 compares the average performance of the first four coils with the performance of coils 5 and 6, which are identical except for the fin density (fins per unit

---

[2] Standard density of air ρ_o is 1.20 kg/m^3.

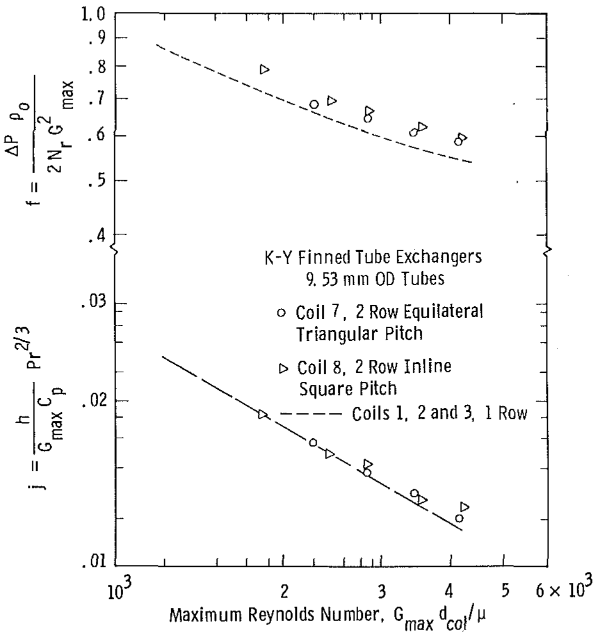

Fig. 5 Colburn and friction factors versus maximum air side Reynolds number for one- and two-row coils with in-line and staggered pitch

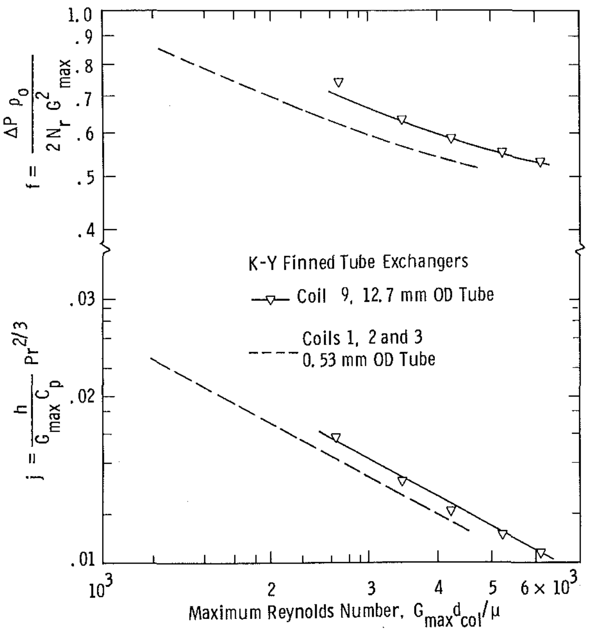

Fig. 6 Colburn and friction factors versus maximum air side Reynolds number for varying tube diameter

length). Figure 4 shows that both *j* and *f* decrease with increasing fin density. The decrease in *f* with increasing fin density appears to be unique to negative fin-tip clearance. For positive fin-tip clearance, Rabas et al. [7] showed that *f* always increases with increasing fin density for low-finned tubes. An increase of *f* with fin density would be predicted by the pressure drop correlation developed by Vampola [8], which is commonly used for high-finned tubes. This figure shows, then, a very interesting fin density effect. One argument which might explain the lower pressure drop is that more alignment of the fins in the air stream is obtained by increasing the fin count.

Since there is no pressure drop penalty and just a minimal heat transfer penalty with increasing fin density, as many fins per unit length as practical are used. It can be shown that an increase in the total heat transferred and the increase in the pressure drop with the fin density are in about a one-to-one ratio, certainly an unusual condition.

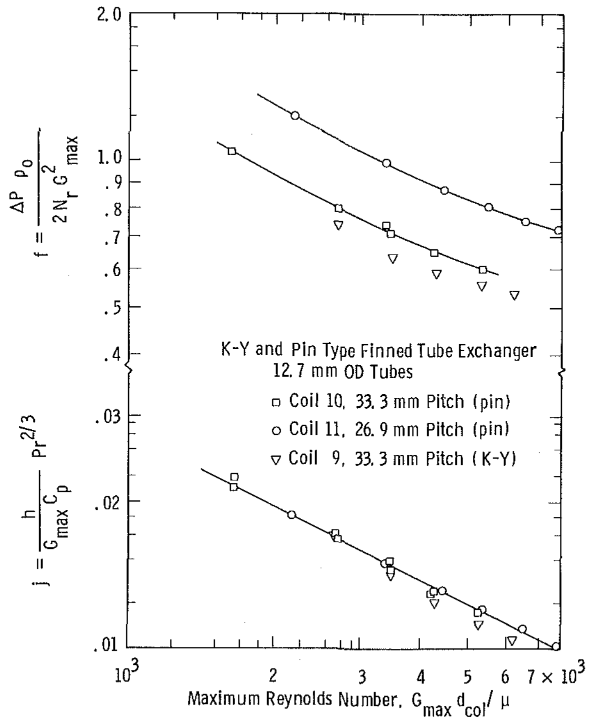

Fig. 7 Colburn and friction factors versus maximum air side Reynolds number of different types of fins

Row Number. Figure 5 shows the effect of a second row for both a staggered arrangement (coil 7) and an in-line arrangement (coil 8). The data are compared with the single row results obtained with the same finned tube (tube number 2 in Table 1). Two points are worth noting. There appears to be almost no transverse alignment effect on the coil heat transfer and pressure drop performance. With overlapped fin tips, no channeling between the fin tips is possible. This might explain why the heat transfer and pressure drop performance of coils 7 and 8 are almost identical. The second point worth noting is that *f* and *j* do slightly increase with the addition of the second row. In Fig. 5, the slightly greater *j* and *f* factor of the in-line tubes compared to the triangular pitch may be due to manufacturing variations.

Tube Diameter. Figure 6 shows the effect of varying the tube diameter by comparing the performance of coil 9, which contains the larger diameter K-Y finned tube (tube number 6 in Table 1), with the average performance of coils 1, 2, and 3 (tube number 2 in Table 1). Both exchanger types have essentially the same geometrical characteristics; the only significant difference is the tube diameter. Even the fin overlap is the same. Figure 6 shows that both *j* and *f* increase by about 20 percent with an increase of the tube diameter of 33 percent.

Fin-Type. Figure 7 presents a comparison of the heat transfer and pressure drop performance of coil 9 (the K-Y fin) and coils 10 and 11 (the pin fin). Table 2 shows that the tube and fin characteristics are very similar (tube numbers 6 and 7) except for the fin type. Table 2 shows that the pitch/fin diameter ratio of the K-Y coil is between the values used for coils 10 and 11. However, it is much closer to that used for coil 10. For comparison purposes, then, more significance should be given to the performance of coil 10 than coil 11. Also the K-Y finned tubes in coil 9 were manually wound. As

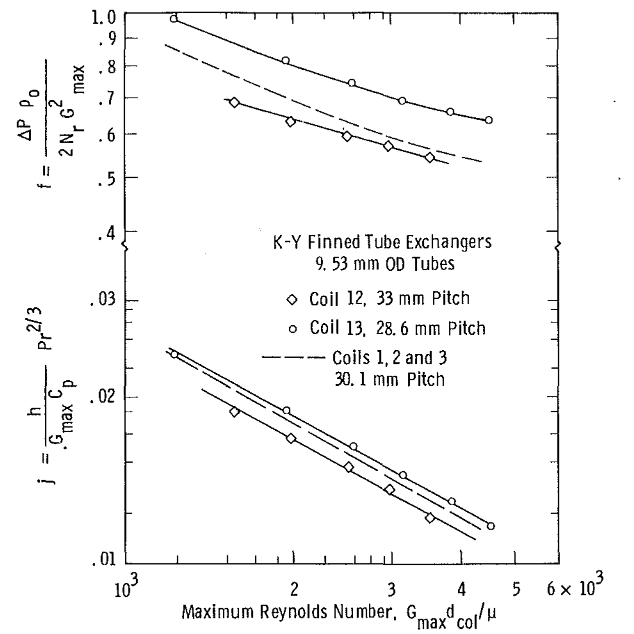

Fig. 8 Colburn and friction factors versus maximum air side Reynolds number with varying tube pitch

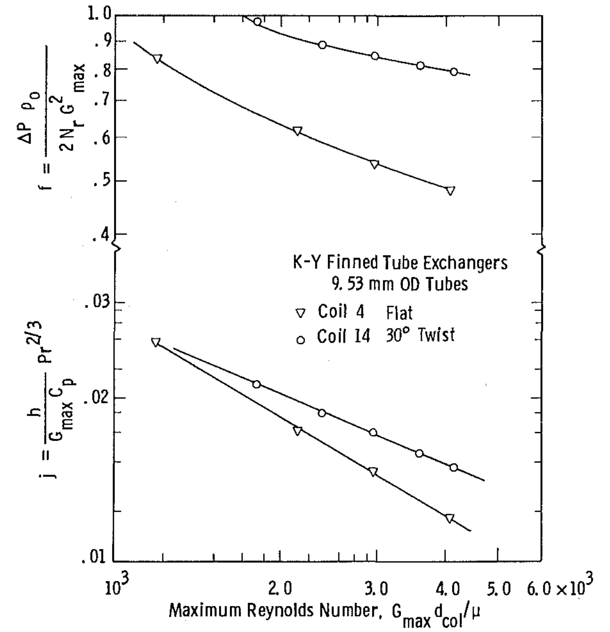

Fig. 9 Colburn and friction factors versus maximum air side Reynolds number of 30 deg twisted K-Y fins compared to that of flattened (0 deg twist) K-Y fins

a result, this exchanger is expected to exhibit a somewhat reduced pressure drop as previously displayed in Fig. 3.

Figure 7 shows that j is almost the same for all three coils. The heat transfer performance of the K-Y exchanger is the lowest but the pressure drop also is the lowest, both by about 10 percent when surface area is considered. Based on these limited tests, it appears that the fin type does not have a major effect on the performance of the exchangers with a negative fin-tip clearance.

Tube Pitch. The performance of the pin fin exchangers with two different fin overlaps was already displayed in Fig. 7. Figure 8 also shows the effect of varying transverse pitch for three K-Y exchangers (coils 12, 13, and the average of coils 1, 2, and 3). These figures show that both the heat transfer and pressure drop increase with a reduction of the transverse pitch for both fin types. It appears that the heat transfer is more sensitive and pressure drop less sensitive to the tube pitch for the K-Y fin when compared to the pin fin. For both fin types, the friction factor increases at a substantially faster rate than the Colburn factor and the largest rate of increase for both occurs simultaneously with the largest fin overlap.

The tube pitch can be much smaller with the pin-fin shape because the fins are less rigid and are not held in circumferential alignment by the fin-tip joining. This feature of the pin fin does not appear to be advantageous, since f increases significantly while, according to Fig. 7, j is nearly constant with a significant change in the tube pitch.

Fin Twist. The effect of the fin twist, as defined by Fig. 1, is shown in Fig. 9; the heat transfer and pressure drop performance of coil 14, which contains the number 3 finned tubes, is compared to the performance of coil 4, which contains the number 1 finned tubes. The tube bundles are identical except the number 3 tubes have a 30 deg fin twist and the number 1 tubes have flat fins that were manually attached. The twist was introduced by lancing the K-Y pattern at an exceptionally high rotary speed. The high speed put a curve in the fin like an air foil with a 30 deg turning angle.

The fin twist increases both the heat transfer and pressure drop. Both probably increase because of the turbulent mixing of the thermal wake. There is approximately a 20 percent increase in the heat transfer and 50 percent increase in the pressure drop. This rather dramatic impact of the fin twist on the performance with negative fin tip is somewhat surprising. These variations are comparable to those obtained by some Russian studies [9, 10, 11] on air-cooled finned tube bundles with positive fin-tip clearances. The fin twist forces some of the bypassing air to flow between the fins, in particular, closer to the roots of the finned tubes. With negative fin-tip clearance, no bypass paths between the fin-tips exist and therefore, the significant effect of the twist is a very interesting finding.

Comparison With Conventional Configurations

In the previous section, the heat transfer and pressure drop performance for various K-Y and pin finned tube configurations were compared. In this section, the performance of these two finned tube types are compared to conventional plain tube and solid-annular finned tube bundle configurations. The conditions selected for the comparison bundles are as follows:

Tube type	Plain	Solid-annular
Pitch arrangement	Equilateral	Equilateral
Transverse row number	$N_r = 8$	$N_r = 8$
Pitch	$S_T = 1.25 d_f$	$S_T = d_f$
Fin thickness	-	$t_f = .203$ mm

Also, the same fin and tube diameters are used for the solid-annular fin tube bundles. The data base developed at the University of Delaware [12] was used for the plain tube heat transfer and pressure drop predictions. The solid-annular fin prediction methods used for this comparison were the Briggs and Young high-fin heat transfer correlation [13] and the Robinson and Briggs pressure drop correlation [14].

Figure 10 compares the Colburn factor for six different configurations. The heat transfer performance of coils 1, 5, and 10, are characterized by curves 4, 5, and 6, respectively, in this figure. Note that the heat transfer performance of the K-Y and pin coils are about the same as the plain tube bundle and substantially better than the performance of the solid-annular finned tube bundles. There are two reasons for the improved performance.

The small fin width and thickness improves the heat transfer coefficient by frequently interrupting the thermal

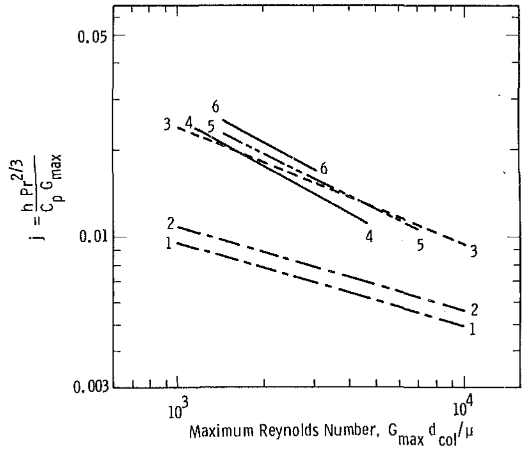

Curve No.	Description	S_T/d_f	d_f/d_{col}	N_f
1	Solid Annular Fin	1.0	3.47	0.787 mm^{-1}
2	Solid Annular Fin	1.0	3.47	0.551
3	Plain Tubes	1.25	1.0	–
4	K-Y Fin	0.91	3.47	0.787
5	Pin	0.95	2.75	0.787
6	K-Y Fin	0.91	3.47	0.551

Fig. 10 **Colburn factor comparison of several tube surfaces**

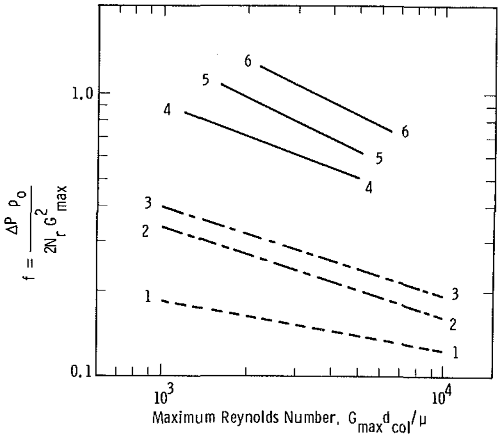

Curve No.	Description	S_T/d_f	d_f/d_{col}	N_f
1	Plain Tube	1.25	1.00	–
2	Solid Annular Fin	1.00	3.47	0.551 to 0.787 mm^{-1}
3	Solid Annular Fin	1.00	2.86	0.551 to 0.787
4	K-Y Fin	0.91	3.47	0.787
5	Pin Fin	0.95	2.75	0.787
6	Pin Fin	0.77	2.75	0.787

Fig. 11 **Friction factor comparison of several tube surfaces**

boundary layer on the fin. However, the negative fin-tip clearance is primarily responsible for the very good thermal performance when compared to heat recovery tubes, because it results in a nearly uniform distribution of heat transfer surface within the heat exchanger volume. Support for that hypothesis comes from comparison of the thermal performance of solid and cut finned tube bundles typical of heat recovery applications that have heat transfer coefficients that are not vastly different [3], usually less than about 50 percent. Also, since the K-Y and pin fin shapes have almost the same thermal performance (Fig. 7), the differences in the K-Y and pin fin shapes cannot be solely responsible for the very high heat transfer performance per unit of surface area.

Consider next a comparison of the pressure drop of the K-Y and pin-fin configurations with conventional plain and solid-annular finned tube bundles. Figure 11 shows that the friction factor is substantially less with the conventional configurations. The higher pressure drops for the negative fin-tip spacing configurations are no surprise since the fluid does not have a bypass gap between the fin tips.

This comparison shows that the thermal performances of the K-Y and pin configurations with negative fin-tip clearances are far greater than conventional extended surface tube bundle configurations. However, there is a substantial pressure drop penalty. The higher pressure drop per tube row is somewhat offset because the number or rows can be reduced.

Conclusions

From the data presented in this paper, several conclusions can be drawn about the performance of the finned tube types used in the air-conditioning industry. Because of the use of negative fin-tip clearances, the performance of these heat exchangers is different from conventional air-cooled heat exchangers.

The fin type, row number, and the tube pitch arrangement are not important variables. Both the heat transfer and pressure drop increase with an increase of the tube diameter and fin twist whereas only the heat transfer increases with an increase of the fin density. The heat transfer is almost independent of the fin overlap whereas the pressure drop is strongly dependent on the overlap. Very high heat transfer coefficients are obtained with these surfaces, even higher than plain tubes. However, the pressure drop is about five times greater than plain tubes.

Acknowledgment

The authors wish to thank the Mitsubishi Electric Corporation for their encouragement in publishing this data.

References

1 Worley, N. G., and Ross, W., "Heat Transfer and Pressure Loss Characteristics of Crossflow Tubular Arrangements with Studded Surfaces," *Proceedings of the Symposium on the Use of Secondary Surfaces for Heat Transfer With Clean Gases, Paper 2, Institution of Mechanical Engineers*, 1960, pp. 15-26.

2 Rabas, T. J., and Eckels, P. W., "Heat Transfer and Pressure Drop Performance of Segmented Extended Surface Tube Bundles," ASME Paper 75-HT-45, Aug. 1975.

3 Weierman, C., Taborek, J., and Marner, W. J., "Comparison of the Performance of Inline and Staggered Banks of Tubes with Segmented Fins," *AIChE Symposium Series*, Vol. 74, No. 174, 1978, pp. 39-46.

4 Schryber, E. A., "Heat Transfer Coefficients and Other Data on Individual Serrated-Finned Surfaces," ASME *Transactions*, Vol. 67, 1945, pp. 683-686.

5 Abbott, R. W., Norris, R. H., and Spofford, W. A., "Compact Heat Exchangers for General Electric Products—Sixty Years of Advances in Design and in Manufacturing Technologies," *Compact Heat Exchangers, HTD*, Vol. 10, edited by R. K. Shah, ASME Publication, Nov. 1980, pp. 37-55.

6 Kays, W. M., and London, A. L., *Compact Heat Exchangers* (2nd ed.), McGraw-Hill, 1964.

7 Rabas, T. J., Eckels, P. W., and Sabatino, R. A., "The Effect of Fin Density on the Heat Transfer and Pressure Drop Performance of Low-Finned Tube Banks," *Chemical Engineering Communications*, Vol. 10, No. 1-3, 1981, pp. 127-147.

8 Vampola, I., "Generalization of the Laws Governing Heat Transfer and Pressure Drop During Transfer Flow of Gases in Finned Tube Banks," *Heat and Mass Transfer*, Vol. 1 (Convective Heat Exchange in a Homogeneous Medium) NASA TTF-431, pp. 224-231.

9 Kuntysh, V. B., and Iokhvedov, F. M., "Effect of the Relative Interfin Distance on the Thermal Efficiency, Convective Heat Transfer in Finned-Tube Bundles and on Augmenting of Heat Transfer," *Heat Transfer—Soviet Research*, Vol. 3, No. 2, Mar. 1971, pp. 50-61.

10 Antuf'ev, V. M., and Gusev, E. K., "Intensification of Heat Transfer of Crossflow Finned Surfaces," *Teploeneregetika*, Vol. 15, No. 7, 1968, pp. 53-57.

11 Kokorev, B. I., Vishnevskii, V. G., Semenov, S. M., and Plaksin, Y. V., "Results of Investigating Heat Transfer Tubes with Slit Transverse Fins," *Teploeneregetika*, Vol. 25, No. 2, 1978, pp. 33-35.

12 Bell, K. J., "Final Report of the Cooperative Research Program on Shell and Tube Heat Exchangers," Bulletin No. 5, University of Delaware Experimental Station, 1963.

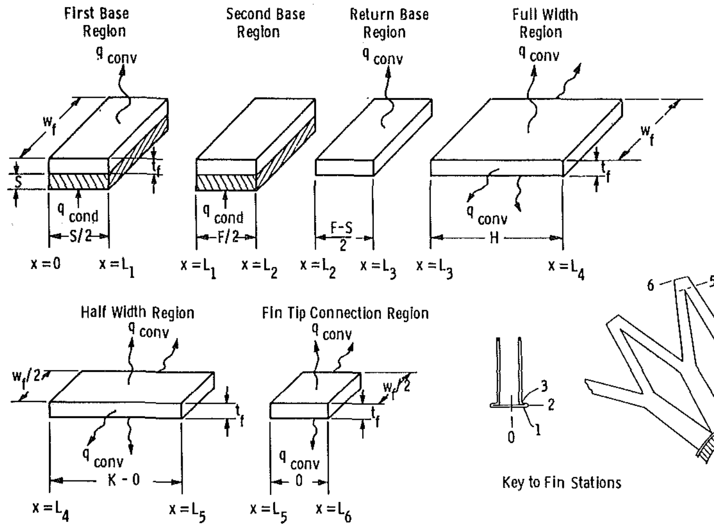

Fig. 12 Heat transfer model for the K-Y fin efficiency analysis

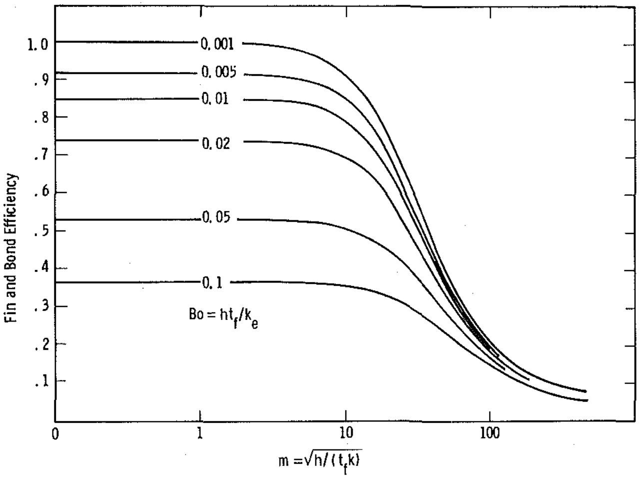

Fig. 13 Fin and bond efficiency for a hemmed K-Y finned tube

13 Briggs, D. E., and Young, E. H., "Convection Heat Transfer and Pressure Drop of Air Flowing Across Triangular Pitch Banks of Finned Tubes," *Chemical Engineering Progress Symposium*, Series No. 41, Vol. 59, 1963, pp. 1-10.

14 Robinson, K.K., and Briggs, D. E., "Pressure Drop of Air Flowing Across Triangular Pitch Banks of Finned Tubes," *Chemical Engineering Progress Symposium*, Series No. 64, Vol. 62, 1966, pp. 177-184.

15 Keller, H. H., and Somers, E. V., "Heat Transfer From an Annular Fin of Constant Thickness," ASME JOURNAL OF HEAT TRANSER, Vol. 81, 1959, pp. 151-156.

APPENDIX

The combined fin and bond efficiency expression for the K-Y extended surface is developed in this appendix. The assumptions used to develop this expression are as follows: steady state, isotropic material, no heat source, one-dimensional heat flow, and uniform outside heat transfer coefficients. Keller and Somers [15] showed that the one-dimensional heat flow assumption leads to very acceptable results if the fin thickness is small when compared to the fin height. The K-Y surface meets this requirement. It is common practice to neglect the variation of the convective heat transfer coefficient and to deal only with the mean value. Since only the mean heat transfer coefficients are isolated for various types of extended surfaces, the same approach shall be adopted for this analysis.

The heat transfer model used for the hemmed K-Y finned surface is shown in Fig. 12. Now there are six regions which must be considered: two base or foot regions, the return foot, and the remaining fin height sections. The assumption is made that no heat is transferred at the overlapping portion of the fin or at the hemmed portion. The energy equations and boundary conditions for the six regions for this case are as follows:

Base—Part 1

$$\frac{d^2T_1}{dx^2} + \frac{k_e}{k\delta t_f}(T_w - T_1) + \frac{h}{kt_f}(T_a - T_1) = 0 \tag{11}$$

$$\left.\frac{dT_1}{dx}\right|_{x=0} = 0, \quad \left.\frac{dT_1}{dx}\right|_{x=L} = \left.\frac{dT_2}{dx}\right|_{x=L},$$

$$\left.T_1\right|_{x=L_1} = \left.T_2\right|_{x=L_1} \tag{12}$$

Hemmed Base—Part 2

$$\frac{d^2T_2}{dx} + \frac{k_e}{k\delta t_f}(T_w - T_2) = 0 \tag{13}$$

$$\left.T_2\right|_{x=L_1} = \left.T_1\right|_{x=L_1}, \quad \left.\frac{dT_2}{dx}\right|_{x=L_1} = \left.\frac{dT_1}{dx}\right|_{x=L_1},$$

$$\left.T_2\right|_{x=L_2} = \left.T_3\right|_{x=L_2}, \quad \left.\frac{dT_2}{dx}\right|_{x=L_3} = \left.\frac{dT_3}{dx}\right|_{x=L_3} \tag{14}$$

Return Foot—Part 3

$$\frac{d^2T_3}{dx^2} + \frac{h}{kt_f}(T_a - T_3) = 0 \tag{15}$$

$$\left.T_3\right|_{x=L_2} = \left.T_2\right|_{x=L_2}, \quad \left.\frac{dT_3}{dx}\right|_{x=L_2} = \left.\frac{dT_2}{dx}\right|_{x=L_2},$$

$$\left.T_3\right|_{x=L_3} = \left.T_4\right|_{x=L_3}, \quad \left.\frac{dT_3}{dx}\right|_{x=L_3} = \left.\frac{dT_4}{dx}\right|_{x=L_3} \tag{16}$$

Full Width Fin—Part 4

$$\frac{d^2T_4}{dx^2} + \left[\frac{2h}{kt_f}\left(\frac{W_f + t_f}{W_f}\right)\right](T_a - T_4) = 0 \tag{17}$$

$$T_4\Big|_{x=L_3}=T_3\Big|_{x=L_3},\quad \frac{dT_4}{dx}\Big|_{x=L_3}=\frac{dT_3}{dx}\Big|_{x=L_3},$$

$$T_4\Big|_{x=L_4}=T_5\Big|_{x=L_4},\quad 2\frac{dT_4}{dx}\Big|_{x=L_4}=\frac{dT_5}{dx}\Big|_{x=L_4} \tag{18}$$

Half Width Fin—Part 5

$$\frac{d^2T_5}{dx^2}+\left\{\frac{4h}{kt_f}\left(\frac{W_f+t_f}{W_f}\right)\right\}(T_a-T_5)=0 \tag{19}$$

$$T_5\Big|_{x=L_4}=T_4\Big|_{x=L_4},\quad \frac{dT_5}{dx}\Big|_{x=L_4}=2\frac{dT}{dx}\Big|_{x=L_4},$$

$$T_5\Big|_{x=L_5}=T_6\Big|_{x=L_5},\quad \frac{dT_5}{dx}\Big|_{x=L_5}=\frac{dT_6}{dx}\Big|_{x=L_5} \tag{20}$$

Fin Tip Connection—Part 6

$$\frac{d^2T_5}{dx^2}+\left\{\frac{2h}{kt_f}\left(\frac{W_f+t_f}{W_f}\right)\right\}(T_a-T_6)=0 \tag{21}$$

$$T_6\Big|_{x=L_5}=T_5\Big|_{x=L_5},\quad \frac{dT_6}{dx}\Big|_{x=L_5}=\frac{dT_5}{dx}\Big|_{x=L_5},$$

$$\frac{dT_6}{dx}\Big|_{x=L_6} \tag{22}$$

The solutions to these six differential equations are:

$$\frac{T_1-T_a}{T_w-T_a}=\frac{1}{\mathrm{Bo}+1}+C_2\cosh(m_1x) \tag{23}$$

$$\frac{T_2-T_a}{T_w-T_a}=1+C_3\sinh\left(\frac{mx}{\sqrt{\mathrm{Bo}}}\right)+C_4\cosh\left(\frac{mx}{\sqrt{\mathrm{Bo}}}\right) \tag{24}$$

$$\frac{T_3-T_a}{T_w-T_a}=C_5\sinh(m_1x)+C_6\cosh(m_1x) \tag{25}$$

$$\frac{T_4-T_a}{T_w-T_a}=C_7\sinh(m_2x)+C_8\cosh(m_2x) \tag{26}$$

$$\frac{T_5-T_a}{T_w-T_a}=C_9\sinh(m_3x)+C_{10}\cosh(m_3x) \tag{27}$$

$$\frac{T_6-T_a}{T_w-T_a}=C_{12}\{-\tanh(m_4L_6)\sinh(m_4x)+\cosh(m_4x)\} \tag{28}$$

where C_1 and C_{11} were determined with the zero heat flux boundary conditions. The dimensionless constants in the above solutions are as follows:

$$\mathrm{Bo}=\frac{hk_e}{\delta},\quad m=\sqrt{\frac{h}{kt_f}},\quad m_1=\sqrt{m^2\left(1+\frac{1}{\mathrm{Bo}}\right)},$$

$$m_2=\sqrt{2m\left(\frac{W_f+t_f}{W_f}\right)},\quad m_3=\sqrt{4m^2\left(\frac{SW_f+t_f}{W_f}\right)},$$

$$m_4=\sqrt{2m^2\left(\frac{W_f+t_f}{W_f}\right)}$$

The two boundary conditions at the five locations L_1, L_2, L_3, L_4, and L_5, yield ten equations that are necessary to evaluate the ten unknown coefficients. These coefficients were evaluated numerically with a matrix inversion computer program rather than with closed form algebraic expressions.

The combined fin and bond efficiency is now determined with the temperature distributions. The total heat transferred into the fin is

$$q=\int_0^{L}\frac{W_fk_e}{\delta}(T_w-T_1)dx+\int_{L_1}^{L_2}\frac{W_fk_e}{\delta}(T_w-T_2)dx \tag{29}$$

$$=\frac{W_fk_e}{\delta}(T_w-T_a)\left[\int_0^{L_1}\left\{1-\frac{1}{\mathrm{Bo}+1}-C_2\cosh(m_1x)\right\}dx\right.$$

$$\left.-\int_{L_1}^{L_2}\left\{C_3\sinh\left(\frac{mx}{\sqrt{\mathrm{Bo}}}\right)+C_4\cosh\left(\frac{mx}{\sqrt{\mathrm{Bo}}}\right)\right\}dx\right]$$

Since $\eta=q/q_{\max}$ where $q_{\max}=hA_{\mathrm{col}}(T_w-T_a)$, the combined efficiency expression is

$$\eta=W_fL_1\left[\frac{1}{1+\mathrm{Bo}}-C_2\frac{\sinh(m_1L_1)}{m_1L_1\mathrm{Bo}}-\frac{C_3}{mL_1\sqrt{\mathrm{Bo}}}\right.$$

$$\left\{\cosh\frac{(mL_2)}{\sqrt{\mathrm{Bo}}}-\cosh\left(\frac{mL_1}{\sqrt{\mathrm{Bo}}}\right)-\frac{C_4}{mL_1\sqrt{\mathrm{Bo}}}\left\{\sinh\left(\frac{mL_2}{\sqrt{\mathrm{Bo}}}\right)\right.\right.$$

$$\left.\left.\left.-\sinh\left(\frac{mL_1}{\sqrt{\mathrm{Bo}}}\right)\right\}\right\}\right] \tag{30}$$

A plot of the combined fin efficiency is presented in Fig. 13 for a particular selection of K-Y geometry. The calculation procedure used to develop this figure was also used in the data reduction presented in the body of this paper.

The Application of the Galerkin Method to the Solution of the Symmetric and Balanced Counterflow Regenerator Problem

B. S. Baclic
Department of Chemical Engineering,
University of Leeds,
Leeds LS2 9JT., England

The Galerkin method is applied to solve the symmetric and balanced counterflow thermal regenerator problem. In this approach, the integral equation, expressing the reversal condition in periodic equilibrium of regenerator matrix, is transformed into a set of algebraic equations for the determination of the expansion coefficients associated with the representation of the matrix temperature distribution at the start of cold period in a power series in the space variable. The method is easy and straightforward to apply and leads to the explict analytical expressions for expansion coefficients. As explicit analytical formula for regenerator effectiveness is derived and the corresponding numerical values are computed. An excellent agreement is found between the present results and those reported in the literature by different numerical methods. The convergence towards the exact results by carrying out the computations to higher order terms, as well as the extension of this method to the more general counterflow regenerator problem is discussed.

Introduction

Currently, interest in storage-type heat exchangers, generally referred to as regenerators, have been renewed due to their applications to heat recovery, heat storage, and general energy related problems. For these, mainly gas-to-gas heat transfer applications, a variety of new problems have arisen and have been thoughtfully investigated in the field. However, an important obstacle, often stressed in various texts on regenerators, and standing in the open literature for more than five decades, still remains: no closed-form solutions are available to the mathematical model of counterflow thermal regenerator. The author's striving to fill this gap has led to some preliminary results that are given in the present paper. It is intended as a complement to the ways of solving in closed-form the problem of symmetric and balanced counterflow regenerator.

Despite the simplicity of the differential equations under classical assumptions, their solution has proved to be challenging, and performances of counterflow regenerator have been widely investigated numerically with the aid of computing machines as well as analytically. The state-of-the-art and survey texts on this subject appeared in the books by Hausen [1] and Schmidt and Willmott [2], and the work of Razelos [3].

For the design purposes, a regenerator is usually considered to have attained regular periodic flow conditions. The solution to the governing differential equations presented in terms of the regenerator effectiveness as a function of the pertinent dimensionless groups. The specific form of these dimensionless groups is to some extent optional, and two most common forms are the effectiveness number of transfer units ($\epsilon - N_{\mathrm{tu},0}$) method [4, 5] (generally used for rotary regenerators) and reduced length-reduced period ($\Lambda - \Pi$) method [1] (generally used for fixed-matrix regenerators). These methods are equivalent as shown by Shah [6].

The theoretical analysis in this paper is based on classical assumptions that are identical for rotary and fixed-matrix regenerators [6], meaning that the results obtained are equally valid for both types of regenerators. The basic mathematical model for description of counterflow regenerator is said to be "classical" if the governing differential equations are essentially the same as those originally considered by Nusselt [7]. Classical idealizations for the regenerators periodic flow theory have been summarized by Shah [6] and will not be repeated here.

The regenerator effectiveness, as the ratio of actual heat transfer rate to the maximal possible heat transfer rate under the same conditions, is simply the dimensionless time average cold fluid outlet temperature [6]. This is true under the condition that the cold steam is weaker, i.e., has the lower heat capacity rate, and that the dimensionless temperatures are defined as

$$\theta_i \equiv \theta_i(\xi,\eta) = \frac{t_i(x,\tau) - t_{c,\mathrm{in}}}{t_{h,\mathrm{in}} - t_{c,\mathrm{in}}}, \quad i = h,m,c \tag{1}$$

Here the hot fluid (h), matrix (m), and cold fluid (c) temperatures depend upon space variable x (measured from the hot fluid entrance) and time τ; while the inlet temperature $t_{h,\mathrm{in}}$, of hot gas during the hot gas flow period, and the inlet temperature $t_{c,\mathrm{in}}$, of cold gas during cold gas flow period, are both constants. Applying the energy balance, the regenerator effectiveness can be expressed in terms of a space average of the difference in dimensionless matrix temperatures at the ends of hot gas flow periods and cold gas flow periods, as

$$\epsilon = \frac{\Lambda_c/\Lambda_h}{\Pi_c} \int_0^{\Lambda_h} \{\theta_m[\xi,(n-1)(\Pi_h+\Pi_c)+\Pi_h] - \theta_m[\xi,n(\Pi_h+\Pi_c)]\}\,d\xi \tag{2}$$

where n is some integer large enough to ensure that the matrix has reached the cyclic equilibrium.

However, the period equilibrium conditions for the regenerator matrix state that the spatial temperature distribution at the end of hot period should coincide with that at the beginning of the cold period, and vice versa. Just so, in the search for analytical solution, one comes to the origin of all mathematical troubles since the stumbling block for obtaining a closed-form solution lies upon the reversal conditions. Namely, these reversal conditions yield two coupled integral equations that are still unsolved in closed-form.

For a symmetric and balanced regenerator ($\Lambda_h = \Lambda_c = \Lambda$ and $\Pi_h = \Pi_c = \Pi$) the temperatures performance of the matrix in

---

Contributed by the Heat Transfer Division and presented at the ASME Winter Annual Meeting, Boston, Massachusetts, November, 13-18, 1983. Manuscript received by the Heat Transfer Division January 25, 1984. Paper No. 83-WA/HT-89.

the hot period is exactly symmmetric to that in the cold period at cyclic equilibrium. In these particular circumstances, the reversal condition can be written as

$$\theta_m(\xi, 2n\Pi) = 1 - \theta_m(\Lambda - \xi, (2n-1)\Pi) \tag{3}$$

so that the effectivness relation, equation (2), reduces to

$$\epsilon = \frac{1}{\Pi}\int_0^{\Lambda} \{\theta_m[\xi, (2n-1)\Pi] - \theta_m(\xi, 2n\Pi)\} d\xi \tag{4}$$

or

$$\epsilon = \frac{1}{\Pi}\int_0^{\Lambda} \{\theta_w(\xi) + \theta_w(\Lambda-\xi) - 1\} d\xi \tag{5}$$

where the matrix temperature distribution $\theta_w(\xi) \equiv \theta_m[\xi, (2n-1)\Pi]$ at the start of the cold period is a solution of the integral equation

$$\theta_w(\Lambda-\xi) + e^{-\Pi}\theta_w(\xi) + \int_0^{\xi} \theta_w(u) e^{-(\Pi+\xi-u)} [\Pi/(\xi-u)]^{1/2} I_1(2\sqrt{\Pi(\xi-u)})\, du - 1 = 0 \tag{6}$$

Many analytical studies have been made to determine this function as summarized by Hausen [1] and the references given there. The attempts for finding an explicit relation $\epsilon = \epsilon(\Lambda, \Pi)$ from equation (5) have been futile ever since Nusselt. The reason for this lies in the structure of the integral equation (6), which is still unsolved in a form suitable for analytical evaluation of integral defining ϵ in equation (5).

However, a number of approximate but accurate solutions to the counterflow regenerator problem have been obtained by various researchers by employing different mathematical techniques. Thus in use are Lambertson's [8] tabular data for regenerator effectiveness obtained by a finite difference method and empirically correlated by Kays and London [4]; Hausen's ([1], Fig. 13-16) effectiveness chart $\epsilon = \epsilon(\Lambda)$ for various Π's; and the "closed" methods for numerical simulation of regenerator for each combination of Λ and Π values, see for example the works of Sandner [9] and Willmott and Duggan [10]. The approximate procedure proposed by Razelos, as presented by Shah [6], extends the correlated tubular data for balanced-symmetric regenerators to unbalanced cases.

Despite the apparent availability of the variety of methods discussed above, there is a need for a development of efficient methods for solving the equations for counterflow regenerator with sufficient accuracy and with little computer time in order to handle the problems that are more realistic. This paper reports on some preliminary results of the promising use of the Galerkin method that utilizes a power series expansion as a trial solution to the problem. The method is simple and straightforward to apply, and it is very efficient and accurate with an obvious advantage of obtaining explicit analytical expressions for expansion coefficients of the trial solution.

Analysis of the Problem by Methods of Weighted Residuals

We consider the problem of determining the regenerator matrix temperature distribution $\theta_w(\xi)$ at the moment of flow reversal, i.e., we are faced with the problem of solving integral equation (6) in a form suitable for obtaining an explicit analytical expression $\epsilon = \epsilon(\Lambda, \Pi)$ from equation (5). The aim is taken to this problem from the standpoint of the methods of weighted residual [11], so that we define accordingly the following terms. An approximation of the unknown function $\theta_w(\xi)$ in the form of expansion

$$\tilde{\theta}_w(\xi) = \sum_{j=0}^{N} b_j \psi_j(\xi) \tag{7}$$

is said to be a trial solution with unknown expansion coefficients b_j, while the members of a set of specified functions $\psi_j(\xi)$ $(j = 0, 1, 2, \ldots, N)$ of space variable ξ, are referred to as trial functions.

In order to apply any of the methods of weighted residuals, one has to pay attention to the integral equation (6) for the matrix temperature distribution $\theta_w(\xi)$, written as

$$L\{\theta_w(\xi)\} \equiv \theta_w(\Lambda-\xi) + e^{-\Pi}\theta_w(\xi) + \int_0^{\xi} \theta_w(u) K(\xi-u)\, du - 1 = 0 \tag{8}$$

with the kernel

$$K(\xi-u) \equiv \exp[-(\Pi+\xi-u)]\sqrt{\Pi/(\xi-u)}\, I_1(2\sqrt{\Pi(\xi-u)}) \tag{9}$$

Introducing the trial solution $\tilde{\theta}_w(\xi)$ into the integral equation (8), one finds a residual

$$L\{\tilde{\theta}_w(\xi)\} \equiv R(\xi) \quad \text{in} \quad 0 \leq \xi \leq \Lambda \tag{10}$$

Nomenclature

A = heat transfer area, m^2
$A_j(\xi_k)$ = integrals defined by equation (12)
a_{jk} = constants defined by equations (29)
B_j = constants defined by equation (27)
b_j = expansion coefficients in a trial solution
C = flow stream heat capacity rate, W/K
C_r = total heat capacity rate of a regenerator, W/K ($C_r = M_m c_m v_r$ for rotary regenerators, $C_r = M_m c_m / P_t$ for fixed-matrix regenerators)
c_k = constants defined by equation (23)
c_m = specific heat of the matrix material, J/kg K
h = heat transfer coefficient, W/m^{2}K
$I_n(\bullet)$ = modified Bessel function of nth (integer) order
K = kernel of the integral equation, defined by equation (9)
M_m = mass of all matrices of a regenerator, kg
N = order of the trial solution
$N_{tu,0}$ = modified number of transfer units, dimensionless
n = an integer
P_c = cold gas flow period, s
P_h = hot gas flow period, s
$P_t = P_c + P_h$ = total period, s
p = Laplace transform variable
$R(\xi)$ = residual of the integral equation
r_{jk} = elements of the matrix of the set of algebraic equations
t = temperature, °C
u = dummy variable
$V_i(x,y)$ = special functions defined by equation (21)
v_r = rotational speed for a rotary regenerator, s^{-1}
$w_k(\bullet)$ = weighting function
x = coordinate along the flow direction, m (also dummy variable in V_i functions)
$Y(\xi)$ = $\theta_w(\xi) + \theta_w(\Lambda-\xi) - 1$
y = dummy variable in V_i functions
α_{jk} = constants defined by equation (24)

In the method of weighted residuals, the constants b_j are chosen in such a way that the residual is forced to be zero in an average sense, namely, the weighted integrals of the residual are set to zero

$$\int_0^\Lambda R(\xi)\, w_K d\xi = 0, \qquad k=0, 1, 2, \dots, N \tag{11}$$

The weighted functions can be chosen in many ways and each choice corresponds to a different criterion of methods of weighted residuals. In this section, just two of those methods will be discussed: the collocation method and the Galerkin method.

In the collocation method, the weighting functions are chosen to be the displaced Dirac delta functions $w_k = \delta(\xi - \xi_k)$, which has the property that $R(\xi_k) = 0$. Thus the residual is zero at $N+1$ specified collocation points ξ_k. As N increases the residual is zero at more and more points and presumably approaches zero everywhere.

The collocation method has been already used for solving counterflow regenerator problem. Typical works of this kind are those by Nahavandi and Weinstein [12] an Willmott and Duggan [10]. While equidistant collocation points have been used in [12], Willmott and Duggan [10] have selected the Chebyshev points as collocation points for obtaining a system of linear algebraic equations. The latter is a good idea for physical reasons, since the nonlinearities of temperature distribution near the regenerator matrix entrances are weighted in the best sense. But, mathematically speaking, the idea is not new; in solving the problems that possess symmetry, Lanczos [13] has proved that a use of the roots of Chebyshev polynomials as the collocation points tends to minimise the largest value of the residual.

Both works [10] and [12] have utilized power series expansion in space variable for $\tilde{\theta}_w(\xi)$, i.e., trial functions have been chosen of the form $\psi_j(\xi) = \xi^j$ $(j=0, 1, 2, \dots, N)$. In these methods, such an expansion was suitable to reduce the problem to the solution of a set of $N+1$ algebraic equations for the expansion coefficients associated with the representation of the matrix temperature distribution at the moment of flow reversal. However, this collocation procedure, being very sensitive on the chosen number of points for various Λ's and Π's, has a serious drawback, since an a priori fixed N leads to the reliable results only for certain ranges of parameters Λ and Π. Usually N should be increased for greater values of Λ and Π, as shown by Willmott and Duggan [10], in spite of the fact that they selected the collocation points in an optimal sense. As discussed in [10], the advantage of the expansion used lies in the fact that the convergence of the solution is nevertheless fast. But, Willmott and Duggan [10] have also stressed that there are still two major problems left in the closed methods. These are:

(*i*) Numerical evaluation of the integrals

$$A_j(\xi_k) = \int_0^{\xi_k} u^j K(\xi_k - u)\, du \qquad j,k=0, 1, 2, \dots, N \tag{12}$$

that requires an excessive computing time, and

(*ii*) Very large matrix elements

$$r_{jk} = (\Lambda - \xi_k)^j + e^{-\Pi}\xi_k^j + A_j(\xi_k) \qquad j,k=0, 1, 2, \dots . N \tag{13}$$

that lead to the difficulties in solving the system of linear algebraic equations.

Both these problems can be easily eliminated as follows: the first one can be eliminated by analytical means. The integrals of equation (12) may be regarded as a convolution of the functions $f(\xi_k) = \xi_k^j$ and $g(\xi_k) = K(\xi_k)$, given by equation (9), so that the application of the Laplace transform with repect to the variable $\xi_k \to p$ yields

$$\bar{A}_j(p) = \{\exp[-\Pi p/(p+1)] - e^{-\Pi}\} j!/p^{j+1} \tag{14}$$

The inversion theorem gives

$$A_j(\xi_k) = j!\, V_{j+1}(\Pi, \xi_k) - e^{-\Pi}\xi_k^j \tag{15}$$

where the functions $V_{j+1}(\Pi, \xi_k)$ are given by equation (21) for $m=j+1$, $x=\Pi$ and $y=\xi_k$. Thus, there is no need for numerical evaluation of the integrals of equation (12).

Now, inserting (15) in equation (13) one finds

$$r_{jk} = (\Lambda - \xi_k)^j + j!\, V_{j+1}(\Pi, \xi_k) \qquad j,k=0, 1, 2, \dots, N \tag{16}$$

so that the set of equations to be solved for unknown coefficients b_j in the trial solution (7) is of the form

$$\sum_{j=0}^{N} r_{jk} b_j = 1 \qquad k=0, 1, 2, \dots, N \tag{17}$$

whereby a way for reducing the order of magnitude of the matrix elements r_{jk} is self-evident. One should start with trial functions $\psi_j(\xi) = \xi^j/j!$ $(j=0, 1, 2, \dots . N)$ instead of ξ^j in equation (7), and will obtain a system of algebraic equations

Nomenclature (cont.)

β_i = constants defined by the last of the equations (32)
$\delta(\bullet)$ = Dirac function
ϵ = $(t_{c,\text{out,ave}} - t_{c,\text{in}})/(t_{h,\text{in}} - t_{c,\text{in}})$ regenerator effectiveness, dimensionless
θ = temperature defined by equation (1), dimensionless
$\theta_w(\xi)$ = matrix temperature distribution at the start of cold period, dimensionless
Λ = hA/C reduced length for a regenerator, dimensionless ($\Lambda = 2N_{tu,0}$ for symmetric regenerator, $\Lambda_h = (hA)_h/C_h$, $\Lambda_c = (hA)_c/C_c$ in general case)
Λ_m = mean reduced length defined by equation (34), dimensionless
ξ = dimensionless coordinate along hot fluid flow direction ($0 \le \xi \le \Lambda_h$)
Π = hA/C_r reduced period for a regenerator, dimensionless ($\Pi_c = (hA)_c P_t/M_m c_m$; $\Pi_h = (hA)_h P_t/M_m c_m$)
Π_m = mean reduced period defined by equation (33), dimensionless
τ = time variable, s
ϕ = parameter defined by equation (36)
$\psi(\xi)$ = trial function

Subscripts:

ave. = average
c = cold fluid
h = hot fluid
i,j,k,m = dummy subscripts (counters)
in = inlet to the regenerator
m = wall (regenerator matrix)
out = outlet to the regenerator
w = wall

Superscripts:

$\sim$ = approximation
$-$ = Laplace transform

for new b_j's with a matrix whose elements will be $r_{jk}^* = r_{jk}/j!$ instead of r_{jk} given by equations (16). By these means, the second problem stated above can be overcome and matrix inversion will not cause troubles with increasing the number of collocations points associated with higher order approximations.

Our intention was just to point out the possible improvements of available collocation methods for solving counterflow regenerator problem and this method will not be discussed further.

In one of the best known approximate methods (the Galerkin method), the weighting functions w_k in equation (11) are chosen to be the trial functions ψ_k, which are linearly independent members of a complete set of functions. Thus the trial solution expanded in terms of such a set is inherently capable of representing exact solution, provided enough terms are used. Consequently, in the limit $N \to \infty$, the Galerkin method forces the residual to be zero by making it orthogonal to each member of a complete set of functions. A dicussion of theory and application of this method is given in several references [11], [14], [15].

The Galerkin method has not been used previously for solving the regenerator problem. The author's impression is that the reasons for this are nearly the same as those leading to the impediments associated with the application of the collocation method. Namely, when a method of weighted residual is used up to now, the coefficients of the resulting set of algebraic equations should be calculated by numerical integration. The use of the Galerkin method, however, leads (similarly as discussed above for collocation method) to a power series expansion in the space variable, which makes it possible to determine explicit analytical expressions for the expansion coefficients of *any order*. This is shown in next section.

Solution by the Galerkin Method

We now consider a power series representation in space variable ξ of the function $\theta_w(\xi)$ as

$$\tilde{\theta}_w(\xi) = \sum_{j=0}^{N} b_j \frac{\xi^j}{j!} \tag{18}$$

where b_j are the unknown expansion coefficients which are yet to be determined. The Galerkin method can now be applied to the integral equation (8) as

$$\int_0^\Lambda R(\xi)\frac{\xi^k}{k!}\,d\xi = 0 \qquad k = 0, 1, 2, \ldots, N \tag{19}$$

which yields $N+1$ algebraic equations for the determination of the expansion coefficients for each j. Since the trial solution equation (18), when introduced into integral equation (8), gives a residual of the form

$$R(\xi) = \sum_{j=0}^{N} b_j[(\Lambda-\xi)^j/j! + V_{j+1}(\Pi,\xi)] - 1 \tag{20}$$

where the special functions V_m $(m = 1, 2, \ldots)$ are of the form

$$V_m(x,y) = \exp[-(x+y)] \sum_{n=m-1}^{\infty} \binom{n}{m-1} (y/x)^{n/2} I_n(2\sqrt{xy}),$$
$$m \geq 1, \tag{21}$$

the resulting set of algebraic equations (19) can be written more compactly as

$$\sum_{j=0}^{N} \alpha_{jk} b_j = c_k, \qquad k = 0, 1, 2, \ldots, N \tag{22}$$

where

$$c_k = \Lambda^{k+1}/(k+1)! \tag{23}$$

$$\alpha_{jk} = \Lambda^{k+j+1}/(k+j+1)! + \sum_{m=0}^{k} (-1)^m \frac{\Lambda^{k-m}}{(k-m)!} V_{j+m+2}(\Pi,\Lambda) \tag{24}$$

For trial solution, equation (18), the effectiveness expression, equation (5), becomes

$$\epsilon = \frac{\Lambda}{\Pi}\left\{2\sum_{j=0}^{N} b_j \frac{\Lambda^j}{(j+1)!} - 1\right\} \tag{25}$$

which suggests a more concise notation

$$\epsilon = \frac{\Lambda}{\Pi}\left\{2\sum_{j=0}^{N} B_j - 1\right\} \tag{26}$$

where

$$B_j \equiv b_j \Lambda^j/(j+1)! \tag{27}$$

Thus, in order to find $\epsilon = \epsilon(\Lambda,\Pi)$, one has, instead of looking for the unknown b_j's, to find the constants B_j defined by equation (27). These can be obtained, upon rearranging the algebraic set of equations (22–24), by solving the set of equations of the form

$$\sum_{j=0}^{N} a_{jk} B_j = 1 \qquad k = 0, 1, 2, \ldots, N \tag{28}$$

where

$$a_{jk} = \frac{(k+1)!(j+1)!}{(k+j+1)!}\left\{1 + (k+j+1)! \sum_{m=0}^{k} \frac{(-1)^m}{(k-m)!} V_{j+m+2}(\Pi,\Lambda)/\Lambda^{j+m+1}\right\} \tag{29}$$

Once the expansion coefficients are determined from equations (28) and hence the function $\tilde{\theta}_w(\xi)$ is available, the regenerator effectiveness is readily obtained in the terms of reduced length (Λ) and reduced period (Π).

When a decision on the choice of the order (N) of the approximation polynominal (18) is to be made, the following property of the function in the integral of equation (5) that defines the regenerator effectiveness should be noticed; this property was somehow overlooked by previous investigators. For a symmetrical and balanced regenerator, the temperature difference of the matrix temperatures at the start of cold and hot periods, as function of coordinate along the matrix $Y(\xi) \equiv \theta_w(\xi) + \theta_w(\Lambda - \xi) - 1$, must be symmetrical around the midlength of matrix, i.e., at $\xi = \Lambda/2$ this function has a maximum

$$\left.\frac{dY(\xi)}{d\xi}\right|_{\xi=\Lambda/2} = 0; \quad \left.\frac{d^2Y(\xi)}{d\xi^2}\right|_{\xi=\Lambda/2} < 0 \tag{30}$$

From this reason, a necessity of choosing $N=2$ as a minimal order of trial polynominal is clear. In the next section, it is shown that $N=2$ is a sufficient order of the trial solution if practically accurate results for regenerator effectiveness are desired and if the Galerkin method is applied.

When very precise results are required, higher approximations must be calculated. These are easily done with equations (28) using a computer. As N increases, the residual usually becomes smaller and the solution corresponds to the exact solution to certain decimal places. This can be then used to demonstrate the convergence of the solution.

We now illustrate the convergence of this method by carrying out the computations to higher order terms. The coefficients B_j ($j = 0, 1, 2, \ldots, N$) obtained from the algebraic set of equations (28–29), as well as the

Table 1 Convergence of $\epsilon=\epsilon(\Lambda,\Pi)$, equation (26), for $\Lambda=15.5$ and $\Lambda/\Pi=1.2$ by increasing the order (N) of the trial polynomial

N	$B_j\,(j=0,1,2,\ldots,N)$ from equations (28-29)	$\epsilon=\dfrac{\Lambda}{\Pi}\left(2\sum_{j=0}^{N}B_j-1\right)$
0	$B_0=0.809\ 276\ 019\ 5$	0.742 262
1	$B_0=0.561\ 969\ 923\ 2$ $B_1=0.276\ 424\ 484\ 3$	0.812 147
2	$B_0=0.435\ 547\ 798\ 1$ $B_1=0.664\ 625\ 137\ 8$ $B_2=-0.258\ 664\ 489\ 5$	0.819 620
3	$B_0=0.440\ 223\ 332\ 9$ $B_1=0.637\ 613\ 667\ 7$ $B_2=-0.214\ 318\ 138\ 7$ $B_3=-0.022\ 007\ 656\ 35$	0.819 627
4	$B_0=0.457\ 031\ 783\ 5$ $B_1=0.469\ 170\ 961\ 7$ $B_2=0.293\ 239\ 547\ 1$ $B_3=-0.616\ 020\ 641\ 4$ $B_4=0.238\ 121\ 928\ 6$	0.819 705
5	$B_0=0.456\ 897\ 260\ 8$ $B_1=0.471\ 204\ 919\ 3$ $B_2=0.283\ 735\ 258\ 0$ $B_3=-0.597\ 013\ 774\ 4$ $B_4=0.221\ 022\ 734\ 1$ $B_5=0.005\ 697\ 183\ 336$	0.819 705

corresponding values of regenerator effectiveness are presented in Table 1 for values of N up to 5 in the case of, arbitrarily chosen, reduced length $\Lambda = 15.5$ and length to period ratio $\Lambda/\Pi = 1.2$. In this case the values of $\beta_i = V_i(\Pi,\Lambda)/\Lambda^{i-1}$, appearing in equation (29), where $V_i(\Pi,\Lambda)$ are given by equation (21), are

$\beta_2=2.356\ 723\ 494$ E-01
$\beta_3=5.275\ 368\ 548$ E-02
$\beta_4=9.199\ 735\ 974$ E-03
$\beta_5=1.330\ 204\ 520$ E-03
$\beta_6=1.653\ 815\ 095$ E-04
$\beta_7=1.810\ 841\ 161$ E-05
$\beta_8=1.776\ 155\ 902$ E-06
$\beta_9=1.580\ 573\ 420$ E-07
$\beta_{10}=1.288\ 787\ 691$ E-08
$\beta_{11}=9.705\ 761\ 425$ E-10
$\beta_{12}=6.795\ 024\ 736$ E-11

These values are given here just for reference.

Explicit Formula for the Symmetric-Balanced Counterflow Regenerator Effectiveness

The matrix of the set of algebraic equations (28) for $N=2$ is 3×3 and can be easily inverted by hand calculations. Thus an explicit analytical formula for symmetrical well-balanced counterflow regenerator effectiveness is obtainable. Next the final result of this procedure is given.

The effectiveness is given by

$$\epsilon=\frac{\Lambda}{\Pi}\,\frac{1+7\beta_2-24\{B-2[R_1-A_1-90(N_1+2E)]\}}{1+9\beta_2-24\{B-6[R-A-20(N-3E)]\}} \tag{31}$$

where

$$\begin{aligned}
B&=3\beta_3-13\beta_4+30(\beta_5-\beta_6)\\
R&=\beta_2[3\beta_4-5(3\beta_5-4\beta_6)]\\
A&=\beta_3[3\beta_3-5(3\beta_4+4\beta_5-12\beta_6)]\\
N&=\beta_4[2\beta_4-3(\beta_5+\beta_6)]+3\beta_5^2\\
E&=\beta_2\beta_4\beta_6-\beta_2\beta_5^2-\beta_3^2\beta_6+2\beta_3\beta_4\beta_5-\beta_4^3\\
N_1&=\beta_4[\beta_4-2(\beta_5+\beta_6)]+2\beta_5^2\\
A_1&=\beta_3[\beta_3-15(\beta_4+4\beta_5-12\beta_6)]\\
R_1&=\beta_2[\beta_4-15(\beta_5-2\beta_6)]\\
\beta_i&=V_i(\Pi,\Lambda)/\Lambda^{i-1},\quad i=2,3,\ldots,6
\end{aligned} \tag{32}$$

To calculate $\epsilon(\Lambda,\Pi)$ from the formula (31), one needs to evaluate just five different special functions $V_i(\Pi,\Lambda)$ ($i=2,3,4,5,6$) as defined by equation (21). These function can readily be calculated, even without the evaluation of modified Bessel functions, by an algorithm similar to one for $V_1(x,y)$ presented in [16]. Since $V_2(\Pi,\Lambda)$ to $V_6(\Pi,\Lambda)$ are functions of the Newmann series type, differing just in coefficients, they can also be calculated (even simultaneously in the same routine) from the unique sequence of scaled modified Bessel functions $\exp(-2\sqrt{\Pi\Lambda})I_n(2\sqrt{\Pi\Lambda})$, $n=1, 2, \ldots$, generated by some available subprograms, say [17]. In any case, a very fast computation will be an advantage of the solution presented, confirming thus, the well-known fact that the application of the Galerkin method being designed for solution by computer, competes directly and often favorably with the finite difference methods. It is worth noting that the total CPU time, for generating the complete set of results presented in Table 2, was 25 s on the Amdahl V/7 computer.

Regenerator effectiveness as computed from equation (31) is presented in Table 2 for a wide range of Λ and Π/Λ.[1] Exact asymptotic values of ϵ for $\Lambda\rightarrow\infty$ and $\Pi/\Lambda\rightarrow 0$ (when $\epsilon=\Lambda/(2+\Lambda)$ holds) are included also in this table. By comparing the results that formula (31) yields with the corresponding from the literature [8], [9], [10], and [19], obtained by various methods, one cannot detect a significant difference for the entire range of parameters in Table 2. It is easy to verify from Table 1 that the values of ϵ's obtained for $N=2$ and $N=5$, respectively, differ in just 0.01 percent. So we conclude that the results for such as poor approximation as $N=2$ are sufficiently accurate for practical purposes.

Extention of the Results to Unbalanced Regenerators.

The Razelos method of extending symmetric regenerator results to unbalanced cases is now used to calculate the effectiveness of an unbalanced regenerator. This procedure can be summarized as follows. For the known values of Π_h, Π_c, Λ_h, and Λ_c calculate mean reduced period Π_m, and mean reduced length Λ_m, as follows

$$\Pi_m=2(\Pi_h^{-1}+\Pi_c^{-1})^{-1} \tag{33}$$

---

[1] Note that the parameter in the corresponding Table of the early version of *this paper* [18] *was* Λ/Π, *a choice not as suitable as* Λ/A *to cover the entire* region of practical interest.

Table 2 Regenerator effectiveness $\epsilon = \epsilon(\Lambda, \Pi)$ as calculated from equation (31)

Λ \ Π/Λ	0.0	0.1	0.2	0.3	0.4	0.5	0.6	0.7	0.8	0.9	1.0
1.0	1/3	0.3332	0.3329	0.3323	0.3315	0.3304	0.3292	0.3277	0.3260	0.3241	0.3221
1.5	3/7	0.4283	0.4276	0.4264	0.4248	0.4227	0.4202	0.4173	0.4139	0.4102	0.4061
2.0	1/2	0.4996	0.4986	0.4968	0.4943	0.4912	0.4874	0.4830	0.4780	0.4725	0.4665
2.5	5/9	0.5551	0.5537	0.5513	0.5481	0.5440	0.5391	0.5333	0.5269	0.5197	0.5120
3.0	3/5	0.5994	0.5977	0.5949	0.5910	0.5861	0.5802	0.5733	0.5655	0.5570	0.5477
3.5	7/11	0.6357	0.6338	0.6305	0.6261	0.6204	0.6137	0.6058	0.5970	0.5872	0.5766
4.0	2/3	0.6659	0.6638	0.6602	0.6553	0.6490	0.6416	0.6329	0.6232	0.6124	0.6006
4.5	9/13	0.6915	0.6892	0.6853	0.6800	0.6732	0.6652	0.6559	0.6454	0.6337	0.6210
5.0	5/7	0.7134	0.7109	0.7068	0.7011	0.6940	0.6855	0.6756	0.6645	0.6521	0.6385
5.5	11/15	0.7324	0.7298	0.7255	0.7195	0.7121	0.7032	0.6928	0.6811	0.6681	0.6537
6.0	3/4	0.7491	0.7463	0.7418	0.7356	0.7279	0.7187	0.7080	0.6958	0.6822	0.6672
6.5	13/17	0.7637	0.7609	0.7562	0.7498	0.7419	0.7324	0.7215	0.7089	0.6948	0.6792
7.0	7/9	0.7768	0.7738	0.7690	0.7625	0.7544	0.7447	0.7335	0.7206	0.7061	0.6900
7.5	15/19	0.7884	0.7854	0.7804	0.7738	0.7656	0.7558	0.7444	0.7313	0.7164	0.6997
8.0	4/5	0.7989	0.7958	0.7908	0.7840	0.7757	0.7658	0.7543	0.7409	0.7257	0.7086
8.5	17/21	0.8084	0.8052	0.8001	0.7933	0.7849	0.7749	0.7633	0.7497	0.7342	0.7167
9.0	9/11	0.8171	0.8138	0.8086	0.8017	0.7933	0.7833	0.7715	0.7578	0.7421	0.7242
9.5	19/23	0.8250	0.8216	0.8164	0.8094	0.8010	0.7909	0.7791	0.7653	0.7493	0.7311
10.0	5/6	0.8322	0.8288	0.8235	0.8165	0.8080	0.7980	0.7862	0.7722	0.7560	0.7375
10.5	21/25	0.8388	0.8354	0.8300	0.8230	0.8146	0.8046	0.7927	0.7787	0.7623	0.7435
11.0	11/13	0.8450	0.8415	0.8361	0.8290	0.8206	0.8106	0.7988	0.7847	0.7681	0.7491
11.5	23/27	0.8506	0.8471	0.8417	0.8346	0.8262	0.8163	0.8044	0.7903	0.7736	0.7543
12.0	6/7	0.8559	0.8524	0.8469	0.8398	0.8315	0.8216	0.8098	0.7956	0.7788	0.7592
12.5	25/29	0.8608	0.8573	0.8517	0.8447	0.8364	0.8266	0.8147	0.8005	0.7836	0.7638
13.0	13/15	0.8654	0.8618	0.8562	0.8492	0.8410	0.8312	0.8194	0.8052	0.7882	0.7682
13.5	27/31	0.8697	0.8661	0.8605	0.8535	0.8453	0.8356	0.8239	0.8096	0.7925	0.7723
14.0	7/8	0.8737	0.8701	0.8644	0.8575	0.8494	0.8397	0.8280	0.8138	0.7966	0.7762
14.5	29/33	0.8775	0.8738	0.8682	0.8612	0.8532	0.8436	0.8320	0.8177	0.8004	0.7799
15.0	15/17	0.8811	0.8773	0.8717	0.8648	0.8568	0.8473	0.8358	0.8215	0.8041	0.7834
15.5	31/35	0.8844	0.8807	0.8750	0.8681	0.8602	0.8508	0.8393	0.8251	0.8076	0.7868
16.0	8/9	0.8876	0.8838	0.8781	0.8713	0.8635	0.8542	0.8427	0.8285	0.8110	0.7900
17.0	17/19	0.8934	0.8896	0.8839	0.8771	0.8695	0.8604	0.8490	0.8348	0.8172	0.7959
18.0	9/10	0.8987	0.8948	0.8891	0.8824	0.8749	0.8660	0.8548	0.8406	0.8229	0.8014
19.0	19/21	0.9034	0.8995	0.8938	0.8872	0.8799	0.8711	0.8601	0.8459	0.8282	0.8065
20.0	10/11	0.9077	0.9038	0.8981	0.8916	0.8844	0.8758	0.8649	0.8509	0.8331	0.8111
25	25/27	0.9245	0.9205	0.9148	0.9087	0.9024	0.8947	0.8844	0.8707	0.8528	0.8302
30	15/16	0.9360	0.9319	0.9263	0.9207	0.9151	0.9081	0.8984	0.8851	0.8673	0.8442
35	35/37	0.9445	0.9403	0.9347	0.9295	0.9246	0.9182	0.9090	0.8961	0.8785	0.8552
40	20/21	0.9509	0.9467	0.9411	0.9363	0.9320	0.9261	0.9174	0.9048	0.8875	0.8640
45	45/47	0.9559	0.9517	0.9462	0.9417	0.9379	0.9325	0.9241	0.9119	0.8948	0.8713
50	25/26	0.9600	0.9557	0.9503	0.9461	0.9427	0.9378	0.9297	0.9177	0.9009	0.8775
60	30/31	0.9662	0.9619	0.9565	0.9529	0.9502	0.9459	0.9383	0.9269	0.9106	0.8874
70	35/36	0.9707	0.9663	0.9611	0.9578	0.9558	0.9519	0.9447	0.9337	0.9180	0.8951
80	40/41	0.9740	0.9697	0.9645	0.9616	0.9600	0.9565	0.9497	0.9390	0.9239	0.9014
90	45/46	0.9767	0.9723	0.9672	0.9646	0.9634	0.9602	0.9536	0.9432	0.9286	0.9065
100	50/51	0.9788	0.9744	0.9693	0.9670	0.9662	0.9632	0.9568	0.9467	0.9325	0.9109
150	75/76	0.9852	0.9808	0.9759	0.9744	0.9747	0.9726	0.9667	0.9574	0.9452	0.9258
200	100/101	0.9885	0.9840	0.9792	0.9782	0.9791	0.9774	0.9719	0.9629	0.9520	0.9348
300	150/151	0.9917	0.9873	0.9826	0.9821	0.9837	0.9824	0.9772	0.9686	0.9592	0.9456
400	200/201	0.9934	0.9889	0.9843	0.9841	0.9860	0.9850	0.9799	0.9714	0.9629	0.9522
500	250/251	0.9944	0.9899	0.9853	0.9853	0.9874	0.9865	0.9815	0.9731	0.9651	0.9568
600	300/301	0.9950	0.9905	0.9860	0.9861	0.9884	0.9876	0.9826	0.9743	0.9665	0.9602
800	400/401	0.9959	0.9914	0.9869	0.9871	0.9896	0.9889	0.9840	0.9758	0.9682	0.9650
1000	500/501	0.9964	0.9919	0.9874	0.9877	0.9903	0.9897	0.9848	0.9766	0.9692	0.9684
2000	1000/1001	0.9974	0.9928	0.9884	0.9890	0.9917	0.9912	0.9865	0.9784	0.9711	0.9770
∞	1.0000	1.0000	1.0000	1.0000	1.0000	1.0000	1.0000	1.0000	1.0000	1.0000	1.0000

$$\Lambda_m = 2\Pi_m[(\Pi/\Lambda)_h + (\Pi/\Lambda)_c]^{-1} \tag{34}$$

With these values of Π_m and Λ_m, obtain the value $\epsilon_r = \epsilon_r(\Lambda_m, \Pi_m)$ from Table 2 or from the equation (31). Subsequently, calculate ϵ from

$$\epsilon = \frac{1 - \exp[\phi\epsilon_r/(1-\epsilon_r)]}{1 - [(\Lambda/\Pi)_h/(\Lambda/\Pi)_c]\exp[\phi\epsilon_r/(1-\epsilon_r)]} \tag{35}$$

where

$$\phi = [(\Lambda/\Pi)_h^2 - (\Lambda/\Pi)_c^2]/2(\Lambda/\Pi)_h(\Lambda/\Pi)_c. \tag{36}$$

A specimen calculation for $\Lambda_h = 18$, $\Lambda_c = 15.5$, $\Pi_h = 16$ and $(\Lambda/\Pi)_c = 1.2$ yields $\Pi_m = 4960/347$ and $\Lambda_m = 5760/347$ from equations (33) and (34), respectively. From Table 2, by linear interpolation,[2] one obtains $\epsilon_r = 0.8215$, since $(\Pi/\Lambda)_m = 31/36$ for this case; while $\phi = -0.0645833$ from equation (36). With these values, $\delta = 0.847047$ from equation (35). The exact value of the effectiveness for this example ($\epsilon = 0.847311$)[3] is just 0.03 percent higher than the result obtained above by approximate procedure.

Concluding Remarks

The present method provides a very simple and straighforward solution to the symmetric and balanced counterflow regenerator problem compared to the collocation technique and various other approximate methods. Over the range of parameters considered in this paper, the convergence of the

---

[2] $\epsilon = 0.8220$ from equation (31) meaning that the error due to interpolation is 0.06 percent.

[3] This value is considered as exact, since it was obtained by carrying out the computations to higher order terms by applying the Galerkin method to unsymmetric and unbalanced regenerator problem [20]. The convergence towards the exact solution was as follows: $\epsilon(2) = 0.847277$; $\epsilon(3) = 0.847233$; $\epsilon(4) = 0.847311$; $\epsilon(5) = 0.847311$, where N in $\epsilon(N)$, ($N = 2, 3, 4, 5$) means that the orders of the trial polynominals, representing matrix temperature distributions at the start of hot gas flow period and the start of cold gas flow period, are both taken to be the same and equal two, three, four, and five. In other words six, eight, ten, and twelve unknown expansion coefficients were determined respectively by the Galerkin method.

Λ \ π/Λ	1.1	1.2	1.3	1.4	1.5	1.6	1.7	1.8	1.9	2.0
1.0	0.3198	0.3174	0.3148	0.3121	0.3092	0.3062	0.3030	0.2998	0.2964	0.2930
1.5	0.4017	0.3971	0.3921	0.3869	0.3815	0.3758	0.3701	0.3641	0.3581	0.3520
2.0	0.4600	0.4531	0.4459	0.4383	0.4305	0.4225	0.4143	0.4060	0.3975	0.3891
2.5	0.5036	0.4948	0.4856	0.4759	0.4660	0.4558	0.4455	0.4351	0.4246	0.4141
3.0	0.5377	0.5272	0.5162	0.5047	0.4929	0.4809	0.4687	0.4564	0.4442	0.4320
3.5	0.5653	0.5532	0.5406	0.5275	0.5141	0.5004	0.4865	0.4727	0.4589	0.4452
4.0	0.5880	0.5747	0.5606	0.5461	0.5312	0.5160	0.5007	0.4854	0.4702	0.4552
4.5	0.6073	0.5927	0.5774	0.5616	0.5453	0.5288	0.5122	0.4956	0.4792	0.4630
5.0	0.6238	0.6082	0.5917	0.5747	0.5572	0.5394	0.5216	0.5039	0.4864	0.4692
5.5	0.6382	0.6216	0.6041	0.5860	0.5673	0.5484	0.5295	0.5107	0.4922	0.4742
6.0	0.6509	0.6334	0.6150	0.5958	0.5761	0.5561	0.5362	0.5164	0.4971	0.4782
6.5	0.6622	0.6439	0.6245	0.6044	0.5837	0.5628	0.5419	0.5212	0.5011	0.4816
7.0	0.6723	0.6532	0.6330	0.6120	0.5904	0.5686	0.5468	0.5253	0.5045	0.4843
7.5	0.6814	0.6617	0.6407	0.6188	0.5963	0.5736	0.5510	0.5289	0.5073	0.4866
8.0	0.6898	0.6693	0.6476	0.6249	0.6016	0.5781	0.5548	0.5319	0.5097	0.4885
8.5	0.6974	0.6763	0.6538	0.6304	0.6063	0.5821	0.5580	0.5345	0.5118	0.4901
9.0	0.7044	0.6827	0.6596	0.6354	0.6106	0.5856	0.5609	0.5368	0.5136	0.4914
9.5	0.7108	0.6886	0.6648	0.6399	0.6144	0.5888	0.5634	0.5388	0.5151	0.4926
10.0	0.7168	0.6940	0.6696	0.6441	0.6179	0.5916	0.5657	0.5405	0.5164	0.4936
10.5	0.7223	0.6991	0.6741	0.6479	0.6211	0.5942	0.5677	0.5421	0.5176	0.4944
11.0	0.7275	0.7038	0.6782	0.6514	0.6240	0.5965	0.5695	0.5434	0.5186	0.4951
11.5	0.7324	0.7082	0.6821	0.6547	0.6266	0.5986	0.5711	0.5446	0.5194	0.4957
12.0	0.7369	0.7123	0.6856	0.6577	0.6291	0.6005	0.5726	0.5457	0.5202	0.4963
12.5	0.7412	0.7161	0.6890	0.6605	0.6313	0.6023	0.5739	0.5467	0.5209	0.4967
13.0	0.7453	0.7197	0.6921	0.6631	0.6334	0.6039	0.5751	0.5475	0.5215	0.4971
13.5	0.7491	0.7232	0.6951	0.6655	0.6353	0.6053	0.5761	0.5483	0.5220	0.4975
14.0	0.7527	0.7264	0.6978	0.6678	0.6371	0.6067	0.5771	0.5489	0.5225	0.4978
14.5	0.7561	0.7294	0.7004	0.6699	0.6388	0.6079	0.5780	0.5496	0.5229	0.4981
15.0	0.7594	0.7323	0.7029	0.6719	0.6403	0.6090	0.5788	0.5501	0.5232	0.4983
15.5	0.7625	0.7351	0.7052	0.6738	0.6418	0.6101	0.5795	0.5506	0.5235	0.4985
16.0	0.7654	0.7377	0.7074	0.6755	0.6431	0.6111	0.5802	0.5510	0.5238	0.4987
17.0	0.7709	0.7426	0.7115	0.6788	0.6455	0.6128	0.5814	0.5518	0.5243	0.4990
18.0	0.7760	0.7470	0.7152	0.6816	0.6476	0.6143	0.5824	0.5524	0.5247	0.4992
19.0	0.7806	0.7510	0.7185	0.6842	0.6495	0.6155	0.5832	0.5529	0.5250	0.4994
20.0	0.7849	0.7548	0.7215	0.6865	0.6511	0.6166	0.5839	0.5534	0.5252	0.4995
25	0.8024	0.7697	0.7334	0.6952	0.6571	0.6204	0.5861	0.5546	0.5259	0.4998
30	0.8152	0.7805	0.7416	0.7008	0.6605	0.6224	0.5872	0.5551	0.5262	0.4999
35	0.8251	0.7886	0.7474	0.7045	0.6626	0.6234	0.5877	0.5554	0.5263	0.5000
40	0.8331	0.7950	0.7518	0.7071	0.6640	0.6241	0.5879	0.5555	0.5263	0.5000
45	0.8397	0.8001	0.7551	0.7089	0.6648	0.6244	0.5881	0.5555	0.5263	0.5000
50	0.8453	0.8043	0.7577	0.7103	0.6654	0.6246	0.5881	0.5555	0.5263	0.5000
60	0.8542	0.8107	0.7614	0.7119	0.6661	0.6249	0.5882	0.5556	0.5263	0.5000
70	0.8610	0.8154	0.7637	0.7129	0.6664	0.6249	0.5882	0.5556	0.5263	0.5000
80	0.8665	0.8188	0.7653	0.7134	0.6665	0.6250	0.5882	0.5556	0.5263	0.5000
90	0.8710	0.8215	0.7664	0.7138	0.6666	0.6250	0.5882	0.5556	0.5263	0.5000
100	0.8747	0.8236	0.7672	0.7140	0.6666	0.6250	0.5882	0.5556	0.5263	0.5000
150	0.8870	0.8293	0.7688	0.7142	0.6667	0.6250	0.5882	0.5556	0.5263	0.5000
200	0.8937	0.8315	0.7691	0.7143	0.6667	0.6250	0.5882	0.5556	0.5263	0.5000
300	0.9008	0.8329	0.7692	0.7143	0.6667	0.6250	0.5882	0.5556	0.5263	0.5000
400	0.9042	0.8332	0.7692	0.7143	0.6667	0.6250	0.5882	0.5556	0.5263	0.5000
500	0.9060	0.8333	0.7692	0.7143	0.6667	0.6250	0.5882	0.5556	0.5263	0.5000
600	0.9071	0.8333	0.7692	0.7143	0.6667	0.6250	0.5882	0.5556	0.5263	0.5000
800	0.9082	0.8333	0.7692	0.7143	0.6667	0.6250	0.5882	0.5556	0.5263	0.5000
1000	0.9087	0.8333	0.7692	0.7143	0.6667	0.6250	0.5882	0.5556	0.5263	0.5000
2000	0.9091	0.8333	0.7692	0.7143	0.6667	0.6250	0.5882	0.5556	0.5263	0.5000
∞	10/11	5/6	10/13	5/7	2/3	5/8	10/17	5/9	10/19	1/2

solution if found to be extremely fast, even the lowest ($N=2$) order solution yields results which are sufficiently close to the values that are computed with other techniques. A detailed tabulation of the regenerator effectiveness is presented in Table 2. The use of the Galerkin method has a promise in solving the general counterflow regenerator problem in closed form. The results of such an analysis will be reported elsewhere [20].

Acknowledgments

Great thanks are due to Dr. R. K. Shah of Harrison Radiator Division, General Motors Corporation, Lockport, N.Y. for editing the manuscript of this paper. The author wishes to thank Dr. A. J. Willmott, Department of Computer Science, University of York, U.K., for his valuable and constructive comments in reviewing this paper. The author is indebted to the SERC for funding as a Senior Visiting Fellow at the University of Leeds during his leave from the University of Novi Sad, Yugoslavia. Leeds University computational facilities are gratefully acknowledged.

References

1 Hausen, H., *Heat Transfer in Counterflow, Parallel Flow, and Cross Flow* (2d ed.), translated from the German by M. S. Sayer; translation edited by A. J. Willmott, McGraw-Hill, New York, 1983.

2 Schmidt, F. W., and Willmott, A. J., *Thermal Energy Storage and Regneration*, McGraw-Hill, New York, 1981.

3 Razelos, P., "History and Advancement of Regenerator Thermal Design Theory," *Compact Heat Exchangers—History, Technological Advancement and Mechanical Design Problems*, edited by R. K. Shah, C. F. McDonald, and C. P. Howard, HTD-Vol. 10, Book No. G00183, ASME, New York, 1980, pp. 91-100.

4 Kays, W. M., and London, A. L., *Compact Heat Exchangers* (2d ed.), McGraw-Hill, New York, 1964.

5 Coppage, J. E., and London, A. L., "The Periodic Flow Regenerator—A Summary of Design Theory," ASME *Transactions*, Vol. 75, 1953, pp. 779-787.

6 Shah, R. K., "Thermal Design Theory of Regenerators," *Heat Exchangers: Thermal-Hydraulic Fundamentals and Design*, edited by S. Kakaç, A. E. Bergles and F. Mayinger, Hemisphere Publishing, McGraw-Hill, Washington, D.C., 1981, pp. 721-763.

7 Nusselt, W., Der Beharrungszustand im Winderhitzer, *Zeitschrift des Vereines deutscher Ingenieure*, Vol. 72, 1928, pp. 1052-1054.

8 Lamberton, T. J., "Performance Factors of Periodic-Flow Heat Exchanger," ASME *Transactions*, Vol. 80, 1958, pp. 586-592.

9 Sander, H., *Beitrag zur linearen Theorie des Regenerators*, Dr.-Ing. Diss., TU München, 1971.

10 Willmott, A. J., and Duggan, R. C., "Refined Closed Methods for the Contra-Flow Thermal Regenerator Problem," *Int. J. Heat Mass Transfer*, Vol. 23, 1980, pp. 655-662.

11 Finlayson, B. A., *The Method of Weighted Residuals and Variational Principles*, Academic Press, New York, 1972.

12 Nahavandi, A. H., and Weinstein, A. S., "A Solution to the Periodic Flow Regenerative Heat Exchanger Problem," *Applied Scientific Research*, Vol. 10, 1961, pp. 335-348.

13 Lanczos, C., "Trigonometric Interpolation of Empirical and Analytical Functions," *Journal of Mathematical Physics*, Vol. 17, 1938, pp. 123-199.

14 Kantorovich, L. V., and Krylov, V. I., *Approximate Methods of Higher Analysis*, Wiley Interscience, New York, 1958.

15 Özisik, M. N., *Heat Conduction*, John Wiley and Sons, New York, 1980.

16 Baclic, B. S., Gvozdenac, D. D., and Dragutinovic, G. D., "Easy Way to Calculate the Breakthrough Curves in Adsorption and Ion Exchange," Paper F2.6 presented at the 7th International Congress of Chemical Equipment Design and Automation, Praha-Czechoslovakia, Aug. 31-Sept. 4, 1981.

17 Amos, D. E., Daniel, S. L., and Weston, M. K., "CDC 6600 Subroutines IBESS and JBESS for Bessel Functions $I_\nu(x)$ and $J_\nu(x)$, $x \geq 0$, $\nu \geq 0$," *ACM Transactions on Mathematical Software*, Vol. 3, No. 1, Mar. 1977, pp. 93-95.

18 Baclic, B. S., "A Closed-Form Solution for the Symmetric and Balanced Counterflow Regenerator: Application of the Galerkin Method," ASME Paper No. 83-WA/HT-89.

19 Romie, F. E., "Periodic Thermal Storage: The Regenerator," ASME JOURNAL OF HEAT TRANSFER, Vol. 101, 1979, pp. 726-731.

20 Baclic, B. S., and Dragutinovic, G. D., "The Galerkin Method for Solving Counterflow Thermal Regenerator Problem," submitted for publication in the JOURNAL OF HEAT TRANSFER.

Prediction of Heat and Mass Regenerator Performance Using Nonlinear Analogy Method: Part 1—Basis

P. J. Banks
Division of Energy Technology,
Commonwealth Scientific and
Industrial Research Organization,
Highett, Victoria 3190, Australia

Coupled heat and mass transfer between fluid streams by a regenerator with a sorbent matrix may be predicted by the superposition of two independent regenerators, in each of which transfer is driven by a combined potential, analogous to temperature in a similar regenerator transferring heat alone. An air-conditioning regenerator for energy recovery or dehumidification with convective transfer controlling is considered. The combined potentials and associated specific capacities are examined, and the nature of the analogy explored, in view of the dependence of matrix sorption properties on state. Approximate nonlinear expressions for the combined potentials, applicable to air-conditioning regenerators, are derived and utilized.

1 Introduction

Regenerators are used to transfer heat and water vapor between two air streams to provide energy recovery and dehumidification in air-conditioning systems.

The prediction of the transfer performance of regenerators transferring heat alone is difficult even when the governing equations are linear, because of the periodic boundary conditions, and finite difference solutions by computer have been used [1]. Such prediction for a regenerator tranferring both heat and water vapor is much more difficult, because the transfer is coupled and nonlinear. Coupling results from the heat release on water vapor sorption into the porous regenerator matrix, which effects transfer between the air streams, while coupling and nonlinearity result from the variation of the sorption properties of matrix materials with state.

An approximate method for predicting the performance of a heat and mass regenerator by analogy from that of a similar regenerator transferring heat alone was presented by the author and colleagues [2–4], and subsequently finite difference solutions of the governing equaitons were obtained [4, 5]. The analogy method retains advantages compared to these solutions. First, it provides better understanding of operation [6]. Second, it enables performance prediction in terms of parameters and their relationships analogous to those well known for a regenerator transferring heat alone, thus facilitating design and development. Third, it is much more rapidly computed or can utilize design charts.

The analogy method has been used in the design of air-conditioning regenerators [7] and to model the regenerative dehumidifier in a computer simulation of a solar desiccant air-conditioning system for a building in a particular location [8]. The simulation is run for a long period of time with actual weather data to evaluate the viability of the system for the building and location. The computing time of a finite difference model of the dehumidifier would be excessive, and for this reason Kettleborough [9] used empirical fits to finite difference results. The reduction of computing time by direct solution after linearization has been suggested [10].

In the analogy method of performance prediction for an air-conditioning regenerator, the regenerator is represented by the superposition of two regenerators, in each of which transfer is driven by a combined potential F_i, $i=1$ or 2, analogous to temperature for heat transfer alone. The storage capacity in the matrix of each superposed regenerator is described by a combined specific capacity ratio γ_i, $i=1$ or 2, analogous to matrix to air specific heat ratio for heat transfer alone. The F_i and γ_i depend on temperature, air specific humidity, and the thermodynamic properties of matrix and air, [11, 12]. These properties include the sorption properties of the matrix which vary with state. Therefore, the F_i depend nonlinearly on state and the γ_i are not constant, whereas in the analogous heat transfer regenerators specific heat ratio is constant.

Regenerator performance prediction by the analogy method involves first the evaluation of the F_i change efficiencies of each of the two superposed regenerators, and second the determination of exit air states from these efficiencies. The first step uses average values of the γ_i in combined matrix to air stream capacity-rate ratios, and the second step the dependence of the F_i on air state. The analogy method as first presented was linear, using averaged properties to give linear F_i and constant γ_i, [2]. The method was then developed to take better account of property variations [3, 4], giving a form of nonlinear analogy method. The present paper examines the requirement and basis for nonlinear analogy methods, and describes a new form of such method. The paper is presented in two parts.

In this part, the basis for nonlinear analogy methods is explored, by deriving and examining the F_i and γ_i for heat and mass transfer in air flow through a porous matrix of water vapor sorbent material (silica gel in particular). Approximate nonlinear expressions for the F_i as functions of t and w are obtained. In Part 2, the expressions are used to explore the requirement for a nonlinear analogy method and to provide a new form of such method which is then compared with the linear and nonlinear methods presented previously.

Attention is confined to air-conditioning regenerators in which convective transfer is controlling, so that the overall transfer coefficients for heat and water vapor may be assumed equal [6], as in [2, 3]. The general case of unequal transfer coefficients requires further study, which is in progress.

An analogy method using forms of the nonlinear F_i expressions derived here has been used to provide a model of a regenerative dehumidifier in a computer simulation of a solar desiccant air-conditioning system by the Solar Energy Laboratory of the University of Wisconsin-Madison [13], at

---

Contributed by the Heat Transfer Division for publication in the JOURNAL OF HEAT TRANSFER. Manuscript received by the Heat Transfer Division January 24, 1983.

the author's suggestion, as described in [6]. Such a method and the earlier method used by the Laboratory [3, 8] have been evaluated particularly for such use [14], and a surprising result from this evaluation is explained in Part 2 of this paper.

Recently, Close [15] has derived nonlinear F_i expressions that are included in the multitude of alternative F_i expressions described in section 2.6 of this part of the paper. From the criteria given in that section for choice of F_i expression in applying the analogy method, it may be deduced that the F_i expressions derived by Close are unsuitable for this purpose. This conclusion follows because the expressions appear inconvenient, and the results given in section 5.2 of Part 2 of this paper indicate that the highly nonlinear nature of the F_2 expression would given excessive error in prediction. Close has usefully applied his expressions to show the dependence of the γ_i on his F_i ([15], Fig. 8).

The nonlinear analogy between coupled heat and mass transfer and heat transfer alone in a regenerator matrix is derived and discussed in section 2. This section clarifies and extends the previous presentations [11, 2, 3], and in section 2.10 new general relations for the F_i slopes and the γ_i are given. In section 3, approximate nonlinear F_i expressions applicable to air-conditioning regenerators are derived.

2 The Nonlinear Analogy

2.1 Model. The porous water vapor sorbent regenerator matrix is assumed to be composed of homogeneous material and to be of uniform and constant porosity, and the air streams to flow through it with uniform and constant velocity and pressure [11].

Adiabatic transfer of heat and water vapor between air streams and matrix is considered. The sorption of water vapor by the matrix is assumed to be reversible, so that air and matrix states in thermodynamic equilibrium are related uniquely. General relations are considered

$$h = h(t,w) \tag{1a}$$

$$H = H(t,W) \tag{1b}$$

$$W = W(t,w) \tag{1c}$$

Equation (1c) is significantly nonlinear as a result of the variation of matrix sorption properties with state.

Nonsorbent carrier material in the matrix that provides periodic thermal storage is considered to be lumped with the sorbent material in determining the thermal and sorption properties of the matrix.

Nonequilibrium operation is considered, with temperature as the driving potential for heat transfer and air specific humidity that for water vapor transfer. Air and matrix states at a location in the matrix are assumed uniform, and distinguished by subscripts f and m. Convective transfer is considered to be controlling, so that the overall transfer coefficients for heat and water vapor, J_t and J_w, may be assumed equal [6].

Transfer in the air flow direction by diffusion, molecular or apparent resulting from flow or matrix nonuniformities, is neglected.

2.2 Governing Equations. The conservation and transfer rate equations for the model of an element of the matrix are [11, 2, 3]

$$v\frac{\partial h_f}{\partial x} + \frac{\partial h_f}{\partial \theta} + \mu\frac{\partial H_m}{\partial \theta} = 0 \tag{2a}$$

$$v\frac{\partial w_f}{\partial x} + \frac{\partial w_f}{\partial \theta} + \mu\frac{\partial W_m}{\partial \theta} = 0 \tag{2b}$$

$$\mu\frac{\partial H_m}{\partial \theta} = J_t(t_f - t_m) + J_w\left(\frac{\partial h_m}{\partial w_m}\right)_{t_m}(w_f - w_m) \tag{3a}$$

$$\mu\frac{\partial W_m}{\partial \theta} = J_w(w_f - w_m) \tag{3b}$$

Using the equilibrium state relations (equations (1)), equations (2) and (3) may be expanded and combined to give

$$\left(v\frac{\partial t_f}{\partial x} + \frac{\partial t_f}{\partial \theta}\right)(1 - d_t) + \mu\sigma_m\frac{\partial t_m}{\partial \theta} - \mu\lambda_m\alpha_{hm}(1 - d_w)\frac{\partial W_m}{\partial \theta} = 0 \tag{4a}$$

$$v\frac{\partial w_f}{\partial x} + \frac{\partial w_f}{\partial \theta} + \mu\frac{\partial W_m}{\partial \theta} = 0 \tag{4b}$$

$$\mu\sigma_m\frac{\partial t_m}{\partial \theta} - \mu\lambda_m\alpha_{hm}\frac{\partial W_m}{\partial \theta} = J_t(t_f - t_m) \tag{5a}$$

Nomenclature

a = adiabatic saturation temperature of moist air
c_f = $(\partial h/\partial t)_w$, specific heat of fluid (moist air); c_{fw} of water vapor and c_{fd} of dry air
c_i = positive constant in equations (37) or (39), $i = 1$, 2, defined by equations (40) for equations (39)
c_m = $(\partial H/\partial t)_W$, specific heat of moist matrix; c_{mw} of water and c_{md} of dry matrix
d_i = parameter, $i = 1, 2$, equations (18b)
d_{it},d_{iw} = parameters, $i = 1, 2$, equations (11b,c)
d_t,d_w = parameters, equations (6), (8)
D_i = parameter, $i = 1, 2$, equations (11a)
e_{it},e_{iw} = parameters, $i = 1, 2$, equations (12b,c)
E_i = parameter, $i = 1, 2$, equations (12a)
f_i = separable component of α_i, $i = 1, 2$, equations (16)
F_i = combined potential, $i = 1$, 2, satisfies an equation (9)
g_i = separable component of α_i, $i = 1, 2$, equations (16)
G_i = parameter, $i = 1, 2$, equations (12d)
h = enthalpy of moist air, per unit mass of dry air
h_w = $(\partial H/\partial W)_t - ((\partial h/\partial w)_t - h_v)$, isothermal differential heat of wetting of matrix with water, per unit mass of water
h_v = latent heat of vaporization of water, per unit mass; h_{vo}, value for $t = 0$
H = enthalpy of moist porous matrix, per unit mass of dry matrix
J = overall transfer coefficient between air flow and matrix, per unit specific capacity of dry air in matrix
K = constant in equation (38)
L = length of matrix in air flow direction
m,n = constant exponents in equation (38)
N = ratio of molecular weights of water vapor and dry air
p = partial pressure of water vapor in moist air
p_s = value of p when moist air saturated with water vapor
p_t = pressure of moist air
Q = $1 - (h_w/h_v)$, ratio of latent heats of sorption and

$$\mu \frac{\partial W_m}{\partial \theta} = J_w(w_f - w_m) \tag{5b}$$

with

$$1 - d_t = \left(\frac{\partial h_f}{\partial t_f}\right)_{w_f} \Big/ \left(\frac{\partial h_m}{\partial t_m}\right)_{w_m} \tag{6a}$$

$$1 - d_w = \left(\frac{\partial h_f}{\partial w_f}\right)_{t_f} \Big/ \left(\frac{\partial h_m}{\partial w_m}\right)_{t_m} \tag{6b}$$

The parameters d_t and d_w reflect the nonlinearity of equation (1*a*), which for air-conditioning application is given by

$$h = c_{fd}t + (c_{fw}t + h_{vo})w \tag{7}$$

with $c_{fd} = 1.00$ kJ/(kg.K), $c_{fw} = 1.80$ kJ/(kg.K), and $h_{vo} = 2503$ kJ/kg. From equations (6) and (7)

$$d_t \; = \; c_{fw}(w_m - w_f)/(c_{fd} + c_{fw}w) \tag{8a}$$

$$d_w \; = \; c_{fw}(t_m - t_f)/(c_{fw}t + h_{vo}) \tag{8b}$$

These parameters are of order 10^{-2} or less for air-conditioning applications and may be neglected.

2.3 Transformed Equations. The pair of equations for heat transfer alone are apparent from equations (4*a*) and (5*a*). Equations (4) and (5) may be transformed into two pairs of equations each of similar form in terms of a combined potential F_i, that satisfies an equation

$$\left(\frac{\partial F_i}{\partial w}\right)_t = \alpha_i \left(\frac{\partial F_i}{\partial t}\right)_w, \quad i = 1,2 \tag{9}$$

and of a combined specific capacity ratio γ_i. The parameters $\alpha_i(t,w)$ and $\gamma_i(t,w)$ determine regenerator operation with thermodynamic equilibrium between air and matrix at every location [11, 12, 6] and are specified by relations given in section 2.10. The transformation is accomplished by multiplying equations (4*a*) and (5*a*) by $(\partial F_{im}/\partial t_m)_{w_m}$, and equations (4*b*) and (5*b*) by $(\partial F_{im}/\partial w_m)_{t_m}$, then adding and using equations (8*a*), (8*c*) and (17) from [11] to give

$$v \frac{\partial F_{if}}{\partial x} + \frac{\partial F_{if}}{\partial \theta} + \mu\gamma_{im}(1 + d_{iw}) \frac{\partial F_{im}}{\partial \theta} = D_i, \quad i = 1,2 \tag{10a}$$

$$\mu\gamma_{im}(1 + e_{iw}) \frac{\partial F_{im}}{\partial \theta} = J_w(F_{if} - F_{im})$$

$$+ J_t E_i + (J_t - J_w)G_i, \quad i = 1,2 \tag{10b}$$

with

$$D_i = \frac{(d_{it} - d_{iw})}{(1 + d_{it})} \left(\frac{\partial F_{if}}{\partial t_f}\right)_{w_f} \left(v \frac{\partial t_f}{\partial x} + \frac{\partial t_f}{\partial \theta}\right) \tag{11a}$$

$$1 + d_{it} = \left(\frac{\partial F_{if}}{\partial t_f}\right)_{w_f} \Big/ \left(\frac{\partial F_{im}}{\partial t_m}\right)_{w_m} \tag{11b}$$

$$1 + d_{iw} = \left(\frac{\partial F_{if}}{\partial w_f}\right)_{t_f} \Big/ \left(\frac{\partial F_{im}}{\partial w_m}\right)_{t_m} \tag{11c}$$

$$E_i = \frac{(e_{iw} - e_{it})}{(1 + e_{it})} \left(\frac{\partial F_i}{\partial t}\right)_{fm} (t_f - t_m) \tag{12a}$$

$$1 + e_{it} = \left(\frac{\partial F_i}{\partial t}\right)_{fm} \Big/ \left(\frac{\partial F_{im}}{\partial t_m}\right)_{w_m} \tag{12b}$$

$$1 + e_{iw} = \left(\frac{\partial F_i}{\partial w}\right)_{fm} \Big/ \left(\frac{\partial F_{im}}{\partial w_m}\right)_{t_m} \tag{12c}$$

$$G_i = (1 + e_{iw})\left(\frac{\partial F_i}{\partial t}\right)_{fm} (t_f - t_m) \tag{12d}$$

and the partial derivatives with *fm* subscript defined by

$$F_{if} - F_{im} = \left(\frac{\partial F_i}{\partial t}\right)_{fm} (t_f - t_m) + \left(\frac{\partial F_i}{\partial w}\right)_{fm} (w_f - w_m) \tag{12e}$$

It is assumed that $J_t = J_w$, therefore the third term on the right-hand side of each equation (10*b*) equals zero.

The parameters d_{iw}, D_i, e_{iw}, and E_i are determined by the nonlinearity of the function $F_i(t,w)$ over the range between fluid and matrix states. These parameters need to be assumed negligible, and this *f-m* linearization is now discussed.

2.4 *f-m* Linearization. The neglect of the parameters d_{iw}, D_i, e_{iw}, and E_i in equations (10) will cause error in prediction by the analogy method that increases with the magnitude of the parameters. Consideration of this effect is facilitated by an approximation.

Expressing $(F_{if} - F_{im})$, and the fluid to matrix difference in each partial derivative of F_i, by the first two terms of Taylor series one obtains from equations (11) and (12)

Nomenclature (cont.)

condensation of water on matrix
r = p/p_s, relative humidity
R = gas constant for water vapor
t = temperature
T = absolute temperature; T_r, reference value
u_i = arbitrary function, $i = 1$, 2, equations (17*b*)
v = velocity of air flow through passages in porous matrix
v_i = expression, $i = 1, 2$, equations (17*a*)
w = specific humidity of moist air, mass ratio to dry air
W = sorbed water content of porous matrix, mass ratio to dry matrix
x = distance in air flow direction
Y = $-\lambda\alpha_h/\alpha_W$
Z_α = parameter, equation (24)
Z_γ = parameter, equation (26)
α_a = $-(\partial t/\partial w)_a$
α_h = $-(\partial t/\partial w)_h$
α_i = combined potential slope $i = 1$, 2, equations (14) and (23); α_{ic}, constant value
α_r = $-(\partial t/\partial w)_r$
α_W = $-(\partial t/\partial w)_W$
β = $(\partial W/\partial w)_t$, sorbability of matrix for vapor from air
γ_i = combined specific capacity ratio, $i = 1$, 2, equations (20) and (25); γ_i', function of F_i alone, equations (22)
θ = time
λ = $1 - ((\partial H/\partial W)_t/(\partial h/\partial w)_t)$
λ_i = factor, $i = 1$, 2, equations (22)
Λ = JL/v, number of transfer units in air stream
μ = ratio of masses in porous matrix of dry matrix and dry air
σ = $(\partial H/\partial h)_{W,w} = c_m/c_f$, matrix to air specific heat ratio

Subscripts

e = entry state of air stream
f = air stream
fm = defined by equations (12*e*)
m = matrix, mean at a location, distance x
n = initial value
t = heat transfer
w = water vapor transfer
x = average exit state of air stream

Superscripts

$'$ = first derivative
$''$ = second derivative
$-$ = average value

$$d_{it} = \frac{\left(\dfrac{\partial^2 F_{im}}{\partial t_m^2}\right)_{w_m}}{\left(\dfrac{\partial F_{im}}{\partial t_m}\right)_{w_m}}(t_f - t_m) + \frac{\left(\dfrac{\partial^2 F_{im}}{\partial t_m \partial w_m}\right)}{\left(\dfrac{\partial F_{im}}{\partial t_m}\right)_{w_m}}(w_f - w_m) \quad (13a)$$

$$d_{iw} = \frac{\left(\dfrac{\partial^2 F_{im}}{\partial w_m^2}\right)_{t_m}}{\left(\dfrac{\partial F_{im}}{\partial w_m}\right)_{t_m}}(w_f - w_m) + \frac{\left(\dfrac{\partial^2 F_{im}}{\partial t_m \partial w_m}\right)}{\left(\dfrac{\partial F_{im}}{\partial w_m}\right)_{t_m}}(t_f - t_m) \quad (13b)$$

$$e_{it} = \tfrac{1}{2} d_{it} \text{ and } e_{iw} = \tfrac{1}{2} d_{iw} \qquad (13c)$$

The approximation of using two-term Taylor series may be regarded as fitting procedure that simplifies the parameters.

It follows from equations (11*a*), (12*a*), and (13) that the error in prediction resulting from *f-m* linearization depends on the magnitudes and difference of the parameters d_{it} and d_{iw}. These parameters are expressed for a useful nonlinear form of the function $F_i(t,w)$ in section 2.7, and their minimization explored.

2.5 Analogous Equations. Equations (10) with *f-m* linearization and $J_t = J_w$ are identical to the equations for heat transfer alone with temperature t replaced by the combined potential F_i, and matrix to air specific heat ratio σ replaced by the combined specific capacity ratio γ_i. The parameters F_i and γ_i are thus named because of this analogy. The parameters and the nature of the analogy are examined in sections 2.6 to 2.9.

2.6 Combined Potentials. With thermodynamic equilibrium between fluid and matrix at every location, regenerator operation is described by equations (9) and the limiting form of equations (10*a*) ([11], equations (10)), which are the characteristic equations for the hyperbolic system ([16], section 8.2). The combined potentials F_i are the characteristic parameters of the system and the functions $F_i(t,w)$ are not defined. Equations (9) give

$$-\left(\frac{\partial t}{\partial w}\right)_{F_i} = \alpha_i(t,w), \quad i = 1,2 \qquad (14a)$$

which are in fact the ordinary differential equations

$$-\frac{dt}{dw} = \alpha_i(t,w), \text{ at constant } F_i, \ i = 1,2 \qquad (14b)$$

The parameters α_i are functions of the partial derivatives of the equilibrium state relations, equations (1), [11] and section 2.10. For given equilibrium relations, curves of constant F_i on a t-w plot, or psychrometric chart, may be obtained by numerical integration of equations (14), as described by Close and Banks [12]. Such curves for silica gel are shown in Fig. 1.

If air and matrix properties are averaged over the state range of interest, giving linear equilibrium relations and constant α_i values, α_{ic}, then equations (14) may be integrated analytically to give the linear F_i expressions [2]

$$F_i = t + \alpha_{ic} w, \quad i = 1,2 \qquad (15)$$

The left-hand side of each equations (15) could have been an arbitrary function of F_i, and the identity function was chosen [2]. This function is linear and so gives zero error from *f-m* linearization. A more complex linear function is not required, since predictions by the analogy method are not altered by multiplying an F_i expression by a constant value, or adding a constant value to the expression. The reason is that only ratios of differences in F_i values are used [2, 3] and Part 2).

It is apparent from Fig. 1 that for silica gel at moderate temperatures, $t < 50°\mathrm{C}$, F_1 can be represented by a linear expression, but not F_2. This result occurs because the form of the F_2 curves reflects that of the saturation line, as shown by equations (23*b*) and (32), so that the result applies to all sorbents. Over the whole temperature range shown in Fig. 1, a nonlinear expression is seen to be needed for F_1 as well as F_2.

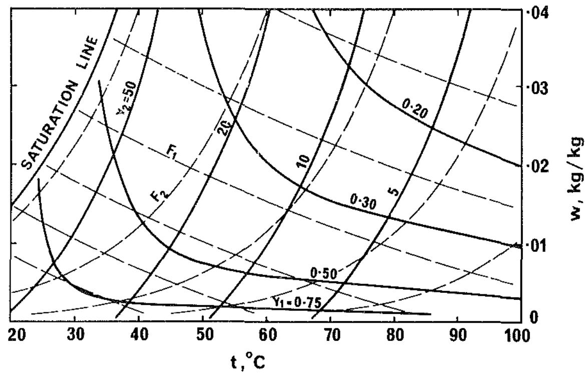

Fig. 1 Curves of constant F_i and γ_i for silica gel on a psychrometric chart [14]

Nonlinear F_i expressions are found by solution of equations (14*b*) with α_i not constant. Each equation (14*b*) has a one-parameter family of solutions with F_i the parameter, which correspond to a set of curves on a t-w plot, as illustrated by Fig. 1, ([17], section 1.4). The set of values for F_i on the curves may be chosen to be the values of t, w, or any function of t and w, at the points of intersection of the curves with any other curve. Thus there is a multitude of alternative sets of values for F_i on a set of curves of constant F_i on a t-w plot. Each set corresponds to an alternative expression for F_i as a function of t and w. The choice of F_i expression in applying the analogy method is based on two criteria, namely convenience and the need to minimize error in prediction resulting from *f-m* linearization. This choice is now explored for a useful nonlinear form of F_i expression.

2.7 F_i Expressions for Separable α_i. Nonlinear F_i expressions may be obtained using the exact solutions of equations (14*b*) that exist for particular forms of dependence of α_i on t and w ([17], section 2.1). The separable form

$$\alpha_i(t,w) = \frac{f_i(w)}{g_i(t)}, \quad i = 1, 2 \qquad (16)$$

is shown in Section 3 to represent the properties of the sorbent matrix material in an air-conditioning regenerator. Equations (14*b*) with (16) may be integrated analytically to give

$$v_i = \int g_i(t)\,dt + \int f_i(w)\,dw, \quad i = 1, 2 \qquad (17a)$$

with v_i constant on a line of constant F_i, so that F_i expressions are given by

$$F_i = u_i(v_i), \quad i = 1, 2 \qquad (17b)$$

where u_i are arbitrary functions.

The parameters v_i are the Riemann invariants ([16], section 8.10) of the characteristic equations (9) for separable α_i.

The choice of functions u_i affects the error in prediction by the analogy method resulting from *f-m* linearization, which is determined by the parameters d_{it} and d_{iw}, section 2.4. Equations (13*a*, *b*) and (17) give

$$d_{it} = d_{iw} = d_i, \quad i = 1, 2 \qquad (18a)$$

where

$$d_i = \left(\frac{u''_{im}}{u'_{im}} g_{im} + \frac{g'_{im}}{g_{im}}\right)(t_f - t_m)$$

$$+ \left(\frac{u''_{im}}{u'_{im}} f_{im} + \frac{f'_{im}}{f_{im}}\right)(w_f - w_m), \quad i = 1, 2 \qquad (18b)$$

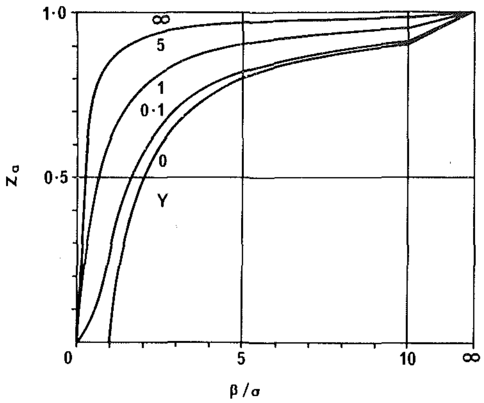

Fig. 2 Parameter dependence of Z_α

It follows from equation (11*a*) that $D_i = 0$, and from equations (12*a*) and (13*c*) that $E_i = 0$.

Therefore with separable α_i, the error in prediction from *f-m* linearization for an F_i regenerator is determined by the magnitude of the parameter d_i at every location in the matrix. From equations (17*a*) and (18*b*), d_i depends on the nonlinearity of u_i and v_i, together with the difference between fluid and matrix states.

An average *f-m* state difference in a regenerator can be obtained by combining equation (4*a*) with (5*a*), and (4*b*) with (5*b*), neglecting d_t and d_w, Section 2.2, and air storage as justified in Part 2, then integrating between air stream entry (*e*) and exit (*x*), to give

$$\overline{(t_f - t_m)} = -(t_{fx} - t_{fe})/\Lambda_t \qquad (19a)$$

$$\overline{(w_f - w_m)} = -(w_{fx} - w_{fe})/\Lambda_w \qquad (19b)$$

where Λ is the number of transfer units in an airstream for heat or water vapor transfer. It is apparent that the average *f-m* state difference, and thus the error from *f-m* linearization, increases with the overall state change in an airstream and decreases with increase in the number of transfer units.

The nonlinearities of u_i and v_i are combined in the coefficient of the state difference in each term of equation (18*b*) for d_i. Therefore, the nonlinearity of u_i may be chosen to minimize either of the coefficients at a particular state, or to minimize the error in prediction for an F_i regenerator resulting from the parameter d_i being not negligible everywhere in the matrix. However, the required variational method may so complicate the analogy method that its advantage over finite difference solution is lost.

In Part 2 of this paper, the errors in analogy method predictions for a silica gel dehumidifier obtained using linear and nonlinear u_i functions are determined. The convenient identity function is found to give the least error. This function is chosen in presenting F_i expressions suited to such a dehumidifier and other air-conditioning regenerators in section 3.2.

2.8 Combined Specific Capacity Ratios. The γ_i are given by [11]

$$\gamma_i = \left(\frac{\partial H}{\partial h}\right)_{F_{3-i}} = \left(\frac{\partial W}{\partial w}\right)_{F_{3-i}}, \quad i = 1, 2 \qquad (20)$$

These equations express the conservation of energy and water vapor in changes of F_i at constant F_{3-i}.

Relations for the γ_i that may be derived from equations (20) are given in section 2.10. Curves of constant γ_i for silica gel are shown on a psychrometric chart in Fig. 1. γ_i is seen to depend on F_i, and to some extent on F_{3-i}. This dependence is clearly show by Close ([15], Fig. 8), provided that the highly nonlinear nature of the F_2 expression used is taken into account.

In general, γ_i depends on F_i, making equations (10) nonlinear. Also in general, γ_i depends on F_{3-i} and both combined potentials change simultaneously, so that equations (10) for $i = 1$ are coupled to those for $i = 2$. The coupling corresponds to lack of conservation of the combined transferred substance for which F_i may be regarded as the driving potential. This lack is made apparent by defining γ_i^i as a function of F_i alone and expressing equations (10*a*) after *f-m* linearization as

$$v\frac{\partial F_{if}}{\partial x} + \frac{\partial F_{if}}{\partial \theta} + \mu\gamma_{im}^i \frac{\partial F_{im}}{\partial \theta} = \mu\lambda_i \frac{\partial F_{im}}{\partial \theta}, \quad i = 1, 2 \qquad (21)$$

with

$$\lambda_i = (\gamma_{im}^i - \gamma_{im}) = -\int_{F_{(3-i)n}}^{F_{(3-i)m}} \left(\frac{\partial \gamma_i}{\partial F_{3-i}}\right)_{F_{im}} dF_{3-i}, \quad i = 1, 2 \qquad (22)$$

where $F_{(3-i)n}$ is the initial value of $F_{(3-i)m}$.

The right-hand side of each equation (21) corresponds to addition or removal of the transferred substance, depending on the direction of change in F_{3-i}. This direction is opposite in the two fluid streams through a regenerator, so that for each component regenerator with F_i the driving potential there is addition of the transferred substance in one fluid stream and removal in the other. Therefore, the effect of lack of conservation on the performance of an F_i regenerator is expected to be of opposite sign in the two fluid streams. This expectation is confirmed by numerical results for a regenerative dehumidifier presented in Part 2 of this paper.

2.9 Application of Analogy. The prediction of the performance of a heat and mass regenerator by analogy from that of a heat transfer-alone regenerator is accomplished in two steps. First, the performance of each component F_i regenerator is determined by the analogy. Second, exit air states are obtained by superposing the F_i regenerators.

In the analogous heat transfer-alone regenerator, specific heat ratio is constant and heat is conserved. Therefore, from section 2.8, in the first step effective average γ_i values need to be evaluated and correction for lack of conservation applied.

The first step yields regenerator exit air states in terms of the F_i, so that expressions $F_i(t,w)$ are required in the second step. The optimum choice of such expressions has been explored in section 2.7 for $\alpha_i(t,w)$ of separable form. This form is now shown to be applicable to air-conditioning regenerators, and suitable F_i expressions are derived.

2.10 Expressions for α_i *and* γ_i. The combined potential slopes α_i, equations (14), are given by the relations, deduced from ([11], equations (6*b*)),

$$\alpha_1 = \lambda\alpha_h / Z_\alpha \qquad (23a)$$

$$\alpha_2 = \alpha_W Z_\alpha \qquad (23b)$$

with

$$\frac{Y}{Z_\alpha} = \frac{1}{2}\left(\left(\frac{\sigma}{\beta} + Y - 1\right) + \left(\left(\frac{\sigma}{\beta} + Y - 1\right)^2 + 4Y\right)^{1/2}\right) \qquad (24)$$

and

$$Y = -\lambda\alpha_h/\alpha_W$$

The F_i slopes are seen to be related to *h* and *W* slopes by the factor Z_α, the parameter dependence of which is depicted in Fig. 2 over the full range of parameter values. The application of Le Châtelier's principle shows that σ, β, and Y are always positive in sign ([11], section 5.1).

It is apparent from Fig. 2 that for $\beta/\sigma > 10$ and $Y > 1$, Z_α is close to unity, and for $\beta/\sigma > 1$ and $Y > 1$, Z_α is fairly constant. Therefore, the main variation in the α_i expressions must result from the quantities $\lambda\alpha_h$ and α_W in these parameter ranges. These quantities and the parameters are formulated in section 3 treating air as a perfect gas mixture, in order to explore the applicability of separable α_i to air-conditioning regenerators.

The combined specific capacity ratios γ_i are given by relations of similar form to those for the α_i, deduced from ([11], equations (6) and (8)),

$$\gamma_1 = \sigma/Z_\gamma \tag{25a}$$

$$\gamma_2 = \beta Z_\gamma \tag{25b}$$

with

$$Z_\gamma = 1 + \frac{Y}{Z_\alpha} \tag{26}$$

3 Applicability of Separable α_i

3.1 Air Treated as a Perfect Gas Mixture. Treating moist air as a mixture of independent perfect gases

$$\frac{p}{p_t} = \frac{w}{N + w} \tag{27}$$

Also, the assumption of constant p_t, section 2.1, results in a form of the Clausius-Clapeyron equation ([18], equation (6.25)),

$$\frac{d\ \ln p_s}{dT} = \frac{h_v}{RT^2} \tag{28}$$

being applicable to condensation of water vapor from the mixture, and a similar equation to sorption of the vapor by the matrix

$$\left(\frac{\partial \ln p}{\partial T}\right)_W = \frac{(h_v - h_w)}{RT^2} \tag{29}$$

Using equations (27) to (29), it may be derived from ([11], equation (23)) that

$$\beta = \left(\frac{\partial W}{\partial r}\right)_t \frac{N}{(N+w)^2} \frac{p_t}{p_s} \tag{30}$$

from ([11], equation (26)) that

$$\lambda\alpha_h = Q\alpha_a = Qh_v/c_f \tag{31}$$

and from ([11], equation (25)) that

$$\alpha_W = \alpha_r/Q \tag{32}$$

The following expression for α_r may be derived from equations (27) and (28)

$$\alpha_r = -\frac{R}{h_v} \frac{N}{(N+w)} \frac{T^2}{w} \tag{33}$$

The specific heats of air and matrix may be expressed as

$$c_f = c_{fd} + w(c_{mw} + dh_v/dt) \tag{34a}$$

and

$$c_m = c_{md} + Wc_{mw} + \frac{dh_v}{dt} \int_0^W \left(\frac{h_w}{h_v}\right) dW \tag{34b}$$

describing the expression for specific heat ratio $\sigma = c_m/c_f$.

Using equations (31) to (33), the parameter Y may be expressed by

$$Y = \frac{Q^2\alpha_a}{\alpha_r} = \frac{h_v^2}{R} \frac{(N+w)}{Nc_f} \frac{Q^2 w}{T^2} \tag{35}$$

and the expressions for α_i, equations (23), become

$$\alpha_1 = \frac{Qh_v}{c_f Z_\alpha} \tag{36a}$$

$$\alpha_2 = -\frac{RNZ_\alpha}{Qh_v(N+w)} \frac{T^2}{w} \tag{36b}$$

Some of the factors in these α_i expressions depend on t or w alone, and the remainder are fairly constant in some circumstances. Hence approximate forms of the expressions that are separable, like equations (16), may be obtained in these circumstances. Such forms for air-conditioning regenerators are now explored. The sorbent regenerator matrix material is considered to be silica gel as a typical example.

3.2 Air-Conditioning Regenerators. In air-conditioning regenerators, the air stream water vapor content is small, enabling $(N + w)$ and c_f to be considered constant, and the latent heat h_v is very nearly constant. The latent heat ratio Q is closely constant and near unity, except at very low matrix water contents, corresponding usually to high temperatures. Hence, from equations (36), for these regenerators the possibility of forming separable α_i depends mainly on the form of Z_α, which has been shown to be close to unity for $\beta/\sigma > 10$ and fairly constant for $\beta/\sigma > 1$, with $Y > 1$, Fig. 2.

For moderate temperatures, $t < 50°\text{C}$, and normal air water contents, $w \sim 0.010$ kg/kg, substitution in equation (35) gives $Y \sim 1$, and substitution in equations (30) and (34) gives $\beta/\sigma \sim 10$ for silica gel as sorbent. Therefore, for silica gel with these air states, Z_α is close to unity and the α_i are given by the expressions

$$\alpha_1 = c_1 \quad \text{and} \quad \alpha_2 = -c_2/w \tag{37}$$

where c_1 and c_2 are positive constants. Nelson and Mitchell [19] suggested α_i of this form for silica gel after computing α_i values over a wider range of air states, using the data and program of Close and Banks [12]. This suggestion stimulated the investigation described in section 3.1 of this paper, and that of the variation with temperature of the α_i for silica gel mentioned below.

The sorbability β decreases rapidly with increase in temperature, because of its dependence on the saturation vapor pressure p_s, equation (30). This is particularly the case for silica gel, for which $(\partial W/\partial r)_t$ does not increase significantly with decrease in r at constant t. The specific heat ratio decreases with increase in t because of reduction in W, equations (34), but this decrease in gradual. Therefore, for silica gel at $t > 50°\text{C}$, $\beta/\sigma < 10$ and Z_α is only fairly constant, Fig. 2. If the matrix is composed partly of a nonsorbent carrier material, then the effective value of β/σ will be reduced, and the temperature above which variation in Z_α needs to be considered will be reduced.

Equations (37) include the main effect of w on the α_i but not that of t. The effect of t is present in equations (36) directly for α_2, but also enters significantly via Z_α and Q. The effect of w may also enter via these parameters. The effects of t and w via the parameters can be included by forming an expression of separable form, like equation (16), for Z_α/Q. Since the parameters are fairly constant, a simple expression with form like equation (36b) is used namely

$$\frac{Z_\alpha}{Q} = K\frac{w^n}{T^m} \tag{38}$$

where K, n, and m are constants. Equation (38) represents a linearization of the relation between the logarithms of Z_α/Q, w, and T over the state range of interest. With this equation, equations (36) become

$$\alpha_1 = c_1 \frac{T^m}{w^n} \quad \text{and} \quad \alpha_2 = -\frac{c_2 T^{2-m}}{T_r{}^2 w^{1-n}} \tag{39}$$

where

$$c_1 = \frac{h_v}{Kc_f} \quad \text{and} \quad c_2 = \frac{RNKT_r{}^2}{h_v(N+w)} \tag{40}$$

are considered constant.

Confirmation of the applicability of equations (39) was obtained from an investigation of the variation with t and w of the α_i for silica gel computed using the data and program of Close and Banks [12].

Equations (39) provide thermodynamically compatible expressions for the α_i that are consistent with the properties of air and matrix in air-conditioning regenerators and that are separable, enabling F_i expressions to be obtained.

From equations (16) and (39)

$$f_1 = c_1 w^{-n}, \quad g_1 = T^{-m} \tag{41a}$$

and

$$f_2 = -c_2 w^{n-1}, \quad g_2 = T_r{}^2 T^{m-2} \tag{41b}$$

Integration gives, following equations (17) with u_i chosen to be the identity function, for $n = m = 0$ and a small temperature range

$$F_1 = t + c_1 w \tag{42a}$$

and

$$F_2 = t - c_2 \ln w \tag{42b}$$

for $n = 0$ and $m \neq 1$,

$$F_1 = \frac{T^{1-m}}{(1-m)} + c_1 w \tag{43a}$$

and

$$F_2 = T_r{}^2 \frac{T^{m-1}}{(m-1)} - c_2 \ln w \tag{43b}$$

and for $n \neq 0$, 1 and $m \neq 1$,

$$F_1 = \frac{T^{1-m}}{(1-m)} + \frac{c_1}{(1-n)} w^{1-n} \tag{44a}$$

and

$$F_2 = T_r{}^2 \frac{T^{m-1}}{(m-1)} - \frac{c_2}{n} w^n \tag{44b}$$

Curves of constant F_i for silica gel on a psychrometric chart have been computed for general α_i expressions using equations (14), (23), and (24) [12, 14], and fitted with approximate expressions of the form just given [20, 14]. The fits were considered close if within about 0.1°C in t and 0.0001 kg/kg in w at every state within the range considered.

Working in collaboration with the author, Beckman [20] found close fits using equations (42) for $t < 50°\mathrm{C}$ and $w < 0.02$ kg/kg, and using equations (43) for $50°\mathrm{C} < t < 150°\mathrm{C}$ and $w < 0.03$ kg/kg, with $m = 3$ for $50°\mathrm{C} < t < 100°\mathrm{C}$ and $m = 8$ for $100°\mathrm{C} < t < 150°\mathrm{C}$. These results show that the effect of t via Z_α/Q, equation (38), increases with increase in t, as expected from the rapid decrease in β/σ with increase in t for silica gel and Fig. 2.

Expressions like equations (44) are used by Jurinak and Banks [14]. These expressions differ from equations (44) in having different values of the exponent n in each equation. Close fits are obtained for $20°\mathrm{C} < t < 90°\mathrm{C}$ and $w < 0.03$ kg/kg. In both fitted expressions, $m = 2.490$, showing a significant effect of t via Z_α/Q, equation (38). For F_1, $n = 0.138$, and for F_2, $n = 0.080$, showing only a small effect of w via Z_α/Q. The discrepancy between the values of n is consistent with the effect of w via c_f and $(N + w)$ that is neglected in equations (44). The author suggests that the use of $n = 0.1$ in both F_i expressions would not significantly affect the accuracy of the fits.

These fits confirm that equations (42–44) can represent to close accuracy the sorption properties of a silica gel matrix in an air-conditioning regenerator, with the constants in equations (41) chosen to suit the air state range of operation. The derivation and discussion above show that this conclusion applies also for other sorbent matrix materials, and for matrices in which the thermal capacity of nonsorbent carrier material needs to be considered.

For some matrices and air state ranges equation (38) may not be sufficiently accurate. For such an application, a suitable form of nonlinear F_i expression for fitting to actual F_i curves may be derived by replacing each equation (16) by a more complex relation for which an exact solution of each equation (14b) exists [17].

4 Conclusions

The description by analogy to heat transfer alone of coupled heat and mass transfer between a fluid stream and a sorbent regenerator matrix has been studied in the case of equal overall transfer coefficients for heat and mass. The parameters F_i and γ_i determining transfer in each superposed regenerator in the description are examined in view of the dependence of matrix sorption properties on state.

Each combined specific capacity ratio γ_i is seen to depend on its associated combined potential F_i, making the governing equations of each superposed F_i regenerator nonlinear, and on the other combined potential F_{3-i}, resulting in lack of conservation in each regenerator. Therefore, prediction by the analogy method of the performance of an F_i regenerator, utilizing results for a heat transfer-alone regenerator with specific heat ratio constant, requires the use of an average γ_i value and correction for lack of conservation. Suitable procedures are considered in Part 2 of this paper.

It is shown that there is a multitude of alternative sets of values for each combined potential F_i on a set of curves of constant F_i on a t–w plot, and a multitude of corresponding nonlinear expressions for F_i as a function of t and w. The criteria for choice of expression are seen to be convenience and minimum error in prediction by the analogy method resulting from the linearization of the expression between fluid and matrix states, required for the analogy to apply.

Exploration of the minimization of this error was facilitated by the use of a form of combined potential slope α_i with separable dependence on t and w. Consideration of the parameter dependence of α_i for the sorbent matrix in an air-conditioning regenerator showed a separable form to be applicable, and this form was used to derive approximate nonlinear F_i expressions, which are utilized in Part 2 of this paper.

Acknowledgments

The author is grateful to Dr. A. N. Stokes of the CSIRO Division of Mathematics and Statistics, to Dr. J. J. Jurinak and Prof. J. W. Mitchell of the University of Wisconsin-Madison, and to his colleagues R. V. Dunkle, Dr. D. J. Close, and Dr. J. G. van Leersum, for helpful discussions.

References

1 Kays, W. M., and London, A. L., "Heat Transfer in Periodic-flow-type Exchangers," *Compact Heat Exchangers*, 2nd ed., McGraw-Hill, New York, 1964, pp. 27–30.

2 Banks, P. J., Close D. J., and Maclaine-cross, I. L., "Coupled Heat and Mass Transfer in Fluid Through Porous Media—an Analogy with Heat Transfer," Paper CT 3.1, *Heat Transfer 1970* (Proceedings of the Fourth International Heat Transfer Conference, Versailles, Sept. 1970), Vol. VII, Elsevier, Amsterdam, 1970, pp. 1–10.

3 Maclaine-cross, I. L., and Banks, P. J., "Coupled Heat and Mass Transfer in Regenerators - Prediction Using an Analogy with Heat Transfer," *International Journal of Heat and Mass Transfer*, Vol. 15, No. 6, June 1972, pp. 1225–1242.

4 Maclaine-cross, I. L., "A Theory of Combined Heat and Mass Transfer in Regenerators, Ph.D thesis, Department of Mechanical Engineering, Monash University, Australia, 1974.

5 Holmberg, R. B., "Combined Heat and Mass Transfer in Regenerators with Hygroscopic Materials," ASME JOURNAL OF HEAT TRANSFER, Vol. 101, No. 2, May 1979, pp. 205–210.

6 Banks, P. J., "Prediction of Heat and Water Vapour Exchanger Performance from that of a Similar Heat Exchanger," *Compact Heat Ex-*

changers—History, Technological Advancement and Mechanical Design Problems, HTD-Vol. 10, edited by R. K. Shah, C. F. McDonald, and C. P. Howard, ASME Winter Annual Meeting, Nov. 1980, ASME, New York, 1980, pp. 57-64.

7 Dunkle, R. V., Banks, P. J., and Maclaine-cross, I. L., "Wound Parallel Plate Exchangers for Air-Conditioning Applications," *Compact Heat Exchangers—History, Technological Advancement and Mechanical Design Problems*, HTD-Vol. 10, edited by R. K. Shah, C. F. McDonald and C. P. Howard, ASME Winter Annual Meeting, Nov. 1980, ASME, New York, 1980, pp. 65-71.

8 Nelson, J. S., Beckman, W. A., Mitchell, J. W., and Close, D. J., "Simulations of the Performance of Open Cycle Desiccant Systems Using Solar Energy," *Solar Energy*, Vol. 21, No. 4, Apr. 1978, pp. 273-278.

9 Kettleborough, C. F., "Solar Assisted Desiccant Dehumidification and Cooling with an Indirect Evaporative Cooler," ASME Paper 80-WA/Sol-29, ASME Winter Annual Meeting, Nov. 1980.

10 Mathiprakasam, B., and Lavan, Z., "Performance Predictions for Adiabatic Desiccant Dehumidifiers Using Linear Solutions," ASME *Journal of Solar Energy Engineering*, Vol. 102, No. 1, Feb. 1980, pp. 73-79.

11 Banks, P. J., "Coupled Equilibrium Heat and Single Adsorbate Transfer in Fluid Flow Through a Porous Medium—I Characteristic Potentials and Specific Capacity Ratios," *Chemical Engineering Science*, Vol. 27, No. 5, May 1972, pp. 1143-1155.

12 Close, D. J., and Banks, P. J., "Coupled Equilibrium Heat and Single Adsorbate Transfer in Fluid Through a Porous Medium—II Predictions for a Silica Gel Air-Drier Using Characteristic Charts," *Chemical Engineering Science*, Vol. 27, No. 5, May 1972, pp. 1157-1169.

13 Jurinak, J. J., and Beckman, W. A., "A Comparison of the Performance of Open Cycle Air Conditioners Utilizing Rotary Desiccant Dehumidifiers," *Proceedings of 1980 Annual Meetings of American Section, International Solar Energy Society*, Phoenix, June 1980, pp. 215-219.

14 Jurinak, J. J., and Banks, P. J., "A Numerical Evaluation of Two Analogy Solutions for a Rotary Silica Gel Dehumidifier," *Heat Transfer in Porous Media*, HTD-Vol. 22, edited by J. V. Beck and L.-S. Yao, ASME Winter Annual Meeting, Nov. 1982, ASME, New York, 1982, pp. 57-68.

15 Close, D. J., "Characteristic Potentials for Coupled Heat and Mass Transfer Processes," *International Journal of Heat and Mass Transfer*, Vol. 26, No. 7, July 1983, pp. 1098-1102.

16 Aris, R., and Amundson, N. R., *Mathematical Methods in Chemical Engineering, Vol. 2, First-Order Partial Differential Equations with Applications*, Prentice-Hall, Englewood Cliffs, N.J., 1973.

17 Ince, E. L., *Ordinary Differential Equations*, Dover, New York, 1956.

18 Denbigh, K. G., *The Principles of Chemical Equilibrium*, 2nd ed., Cambridge University Press, 1966.

19 Nelson, J. S., and Mitchell, J. W., personal communication, Solar Energy Laboratory, University of Wisconsin-Madison, Feb. 1977.

20 Beckman, W. A., unpublished work at CSIRO, Solar Energy Laboratory, University of Wisconsin—Madison, Nov. 1977.

P. J. Banks
Division of Energy Technology,
Commonwealth Scientific and
Industrial Research Organization,
Highett, Victoria 3190, Australia

Prediction of Heat and Mass Regenerator Performance Using Nonlinear Analogy Method: Part 2—Comparison of Methods

The prediction of heat and mass regenerator performance by analogy from that of a similar regenerator transferring heat alone is studied in view of the dependence of matrix sorption properties on state. Air-conditioning regenerators with convective transfer controlling are considered. For an energy recovery regenerator, the previous linear analogy method is shown to be satisfactory, while a nonlinear method is required for a regenerative dehumidifier. A nonlinear method using approximate nonlinear expressions for the combined potentials is described and is compared with the previous nonlinear method that is shown to be partly linear. The sources of error in the methods are explored for a silica gel dehumidifier, and ways of improvement are indicated.

1 Introduction

There are advantages in predicting the performance of a heat and mass regenerator by analogy from that of a regenerator transferring heat alone, particularly an air-conditioning regenerator operated to provide energy recovery or dehumidification [1, 2].

In the analogy method of performance prediction for an air-conditioning regenerator, the regenerator is represented by the superposition of two regenerators, in each of which transfer is driven by a combined potential F_i, $i = 1$ or 2, analogous to temperature for heat transfer alone. The storage capacity in the matrix of each superposed regenerator is described by a combined specific capacity ratio γ_i, $i = 1$ or 2, analogous to matrix to air specific heat ratio for heat transfer alone. The F_i and γ_i depend on temperature, air specific humidity and the thermodynamic properties of matrix and air, [3, 4, 2]. These properties include the sorption properties of the matrix which vary with state significantly. Therefore, the F_i depend nonlinearly on state and the γ_i are not constant, whereas in the analogous heat transfer regenerators specific heat ratio is constant.

Regenerator performance prediction by the analogy method involves first the evaluation of the F_i change efficiencies of each of the two superposed regenerators, and second the determination of exit air states from these efficiencies. The first step uses average values of the γ_i in combined matrix to air stream capacity-rate ratios, and the second step the dependence of the F_i on air state. The analogy method as first presented was linear, using averaged properties to give linear F_i and constant γ_i [5]. The method was then developed to take better account of property variations [6, 7], giving a form of nonlinear analogy method.

In Part 1 of this paper [2], the basis for nonlinear analogy methods has been discussed, and approximate nonlinear expressions for the F_i as functions of t and w derived and shown to be applicable to air-conditioning regenerators. In this part, the expressions are used to explore the requirement for a nonlinear analogy method, and to provide a new form of such method, which is then compared with the linear and nonlinear methods presented previously.

Attention is confined to air-conditioning regenerators in which convective transfer is controlling, so that the overall transfer coefficients for heat and water vapor may be assumed equal [1], as in [5, 6]. The general case of unequal transfer coefficients requires further study, which is in progress.

The accuracy of analogy method predictions is determined by comparison with results from the computer program by Maclaine-cross [7], which gives a finite difference solution of the governing equations. Maclaine-cross [7] used the program to determine the accuracy of previous analogy method developments.

The second step of the nonlinear method presented here has been used to provide a model of a regenerative dehumidifier in a computer simulation of a solar desiccant air-conditioning system by the Solar Energy Laboratory of the University of Wisconsin-Madison [8], at the author's suggestion, as described in [1]. The method presented here and the earlier method used by the Laboratory [6, 9] have been evaluated particularly for such use [10], and a surprising result from this evaluation is explained in the present paper.

Section 2 considers the second step of the analogy method, which utilizes F_i expressions and thus results from Part 1 [2]. Section 2.1 introduces briefly concepts not described in Part 1; section 2.2 summarizes results from Part 1 and provides necessary definitions, while sections 2.3 to 2.6 discuss the information conveyed in Table 1, which is entirely new.

Section 3 considers the first step of the analogy method, and section 4 describes the analogy methods suited to particular modes of regenerator operation. These sections clarify and extend the previous presentations [6, 1], and together with section 2 provide the basis for the study of analogy methods for dehumidifier operation in sections 5 and 6.

2 Exit Air State Determination

2.1 Performance Description. In applying the analogy method to regenerators, it is convenient to describe transfer performance by efficiencies of change in the potentials driving transfer, rather than by transfer rates as fractions of maximum possible values, termed effectivenesses [11]. Thus the F_i efficiencies for period j are defined by the equations

$$\eta_{ij} = \frac{F_{ix} - F_{ie}}{F_{io} - F_{ie}}, \qquad i, j = 1,2 \tag{1}$$

and the temperature and specific humidity efficiencies by

$$\eta_{tj} = \frac{t_x - t_e}{t_o - t_e} \quad \text{and} \quad \eta_{wj} = \frac{w_x - w_e}{w_o - w_e}, \qquad j = 1,2 \tag{2}$$

Contributed by the Heat Transfer Division for publication in the JOURNAL OF HEAT TRANSFER. Manuscript received by the Heat Transfer Division January 24, 1983.

Table 1 Efficiency relations for constant, separable, and general α_i, $i = 1$, 2, with parameter values defined below.

$$\eta_{tj} = \frac{(t_x - t_e)}{(t_o - t_e)} = \frac{\left(1 - \dfrac{\alpha_{1a}}{\alpha_{eo}}\right)}{\phi_1 \psi_1 \left(1 - \dfrac{\alpha_{1b}}{\alpha_{2b}}\right)} \eta_{1j} + \frac{\left(1 - \dfrac{\alpha_{2a}}{\alpha_{eo}}\right)}{\phi_2 \psi_2 \left(1 - \dfrac{\alpha_{2d}}{\alpha_{1d}}\right)} \eta_{2j}$$

$$\frac{\eta_{wj}}{\alpha_{eo}} = \frac{(w_e - w_x)}{(t_o - t_e)} = \frac{-\left(1 - \dfrac{\alpha_{1a}}{\alpha_{eo}}\right)}{\phi_1 \psi_1 (\alpha_{1b} - \alpha_{2b})} \eta_{1j} + \frac{\left(1 - \dfrac{\alpha_{2a}}{\alpha_{eo}}\right)}{\phi_2 \psi_2 (\alpha_{1d} - \alpha_{2d})} \eta_{2j}$$

Case	Constant α_i	Separable α_i		General α_i
	$\alpha_i = \alpha_{ic}$	$\alpha_i = f_i(w)/g_i(t)$		$\alpha_i = \alpha_i(t,w)$
		Exact relations	Inexact relations from equations (10)	
α_{ia}	α_{ic}	f_{ieo}/g_{ieo}	f_{ieo}/g_{ieo}	α_{en}, $i=1$ α_{no}, $i=2$
α_{ib}	α_{ic}	f_{iex}/g_{iex}	f_{ino}/g_{ino}	
α_{id}	α_{ic}	f_{iex}/g_{iex}	f_{ien}/g_{ien}	
ϕ_1	1	g_{1ex}/g_{1eo}	g_{1no}/g_{1eo}	1
ϕ_2	1	g_{2ex}/g_{2eo}	g_{2en}/g_{2eo}	1
ψ_1	1	u'_{1ex}/u'_{1eo}	u'_{1no}/u'_{1eo}	1
ψ_2	1	u'_{2ex}/u'_{2eo}	u'_{2en}/u'_{2eo}	1

Exit air state is necessarily an average value because regenerator operation depends on storage in the matrix, which causes a time variation in the state of air leaving a matrix element.

The superposition of two F_i regenerators to represent a heat and mass regenerator is illustrated in Fig. 1. Entry and exit air states for an air-conditioning regenerator are shown on a psychrometric chart for energy recovery and dehumidifier operation. The two modes of operation are seen to be characterized by different values of the F_i efficiencies η_i.

Inspection of equations (1) and (2) shows that the determination of exit air states from the F_i efficiencies is equivalent to the derivation of relationships between η_t and η_w and the η_i. Such a derivation requires tractable expressions for the F_i in terms of t and w.

2.2 F_i Expressions. The combined potentials satisfy the equations [3]

$$-\left(\frac{\partial t}{\partial w}\right)_{F_i} = \alpha_i(t,w), \qquad i = 1,2 \tag{3}$$

These equations may be integrated numerically to obtain curves of constant F_i for particular thermal and sorption properties [4], and such curves for silica gel are shown in Fig. 2.

A multitude of alternative sets of values for F_i may be put on a set of F_i curves, each set corresponding to an expression for F_i as a function of t and w, [2]. Equations (3) may be solved analytically to obtain F_i expressions for particular forms of α_i expression.

In the linear analogy method [5], thermal and sorption properties are averaged over the state range of operation, giving constant α_i values, α_{ic}, and linear F_i expressions

$$F_i = t + \alpha_{ic} w, \qquad i = 1,2 \tag{4}$$

Nomenclature

a = adiabatic saturation temperature of moist air

c_f = specific heat of fluid (air)

c_i = constant in equations (8*a*), $i = 1, 2$

c_m = specific heat of matrix

f_i = separable component of α_i, $i = 1, 2$, equations (5)

F_i = combined potential, $i = 1$, 2, satisfies an equation (3); particular forms, equations (4), (6), and (8)

g_i = separable component of α_i, $i = 1, 2$, equations (5)

J = overall transfer coefficient between air flow and matrix, per unit specific capacity of dry air in matrix; $J_t = J_w = J$ assumed

L = length of matrix in air flow direction

m_i, n_i = constant exponents in equation (8), $i = 1, 2$

t = temperature

T = absolute temperature

u_i = arbitrary function, $i = 1, 2$, equations (6); $u'_i = du_i/dv_i$

v = velocity of air flow through passages in porous matrix

v_i = expressions, $i = 1$, 2, equations (7)

w = specific humidity of moist air, mass ratio to dry air

x = distance in air flow direction

α_{eo} = $-(t_e - t_o)/(w_e - w_o)$; similarly for α_{en} and α_{no}

α_i = combined potential slope, $i = 1$, 2, equations (3) and ([2], equations (23)); with subscripts a, b, d, see Table 1

γ_i = combined specific capacity ratio, $i = 1$, 2, ([2], equations (20) and (25)); $\bar{\gamma}_{ijs}$, $\bar{\gamma}_{ijd}$ and $\bar{\gamma}_{ijr}$, average values for period j in single-blow, dehumidifier, and energy recovery modes of operation, respectively, equations (12), (14), and (16), respectively; $\bar{\gamma}_{1jda}$ and $\bar{\gamma}_{1jdb}$, approximations to $\bar{\gamma}_{1jd}$, equations (17)

Γ = matrix to air stream specific capacity-rate ratio, Table 2

δ = prefix to quantity denoting value predicted by analogy

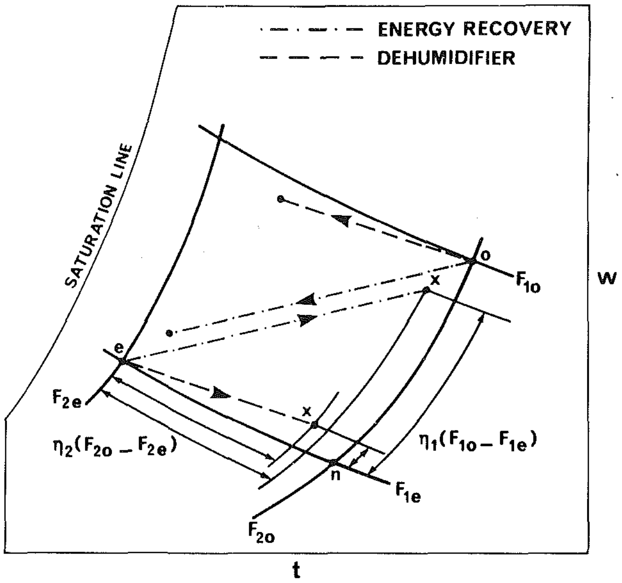

Fig. 1 The superposition of two F_i regenerators to represent energy recovery and dehumidifier modes of operation of an air-conditioning regenerator. Curves of constant F_i through the entry states of the air streams (e and o) enclose the mean air state paths through the regenerator for both modes of operation. The exit state of one air stream (x) is specified by F_i efficiencies η_i for both modes.

In Part 1 of this paper [2], it is shown that α_i expressions of separable form are applicable to air-conditioning regenerators. In general form, such expressions

$$\alpha_i(t,w) = \frac{f_i(w)}{g_i(t)}, \qquad i=1,2 \qquad (5)$$

give [2]

$$F_i = u_i(v_i), \qquad i=1,2 \qquad (6)$$

where u_i are arbitrary functions and

$$v_i = \int g_i(t)dt + \int f_i(w)dw, \qquad i=1,2 \qquad (7)$$

The arbitrary functions may be chosen to minimize the error in prediction by the analogy method resulting from the linearization of each F_i expression between fluid and matrix states, required in transforming the governing equations to analogous form, [2].

It is shown in section 5.2 that the convenient identity function is close to optimum for a silica gel dehumidifier.

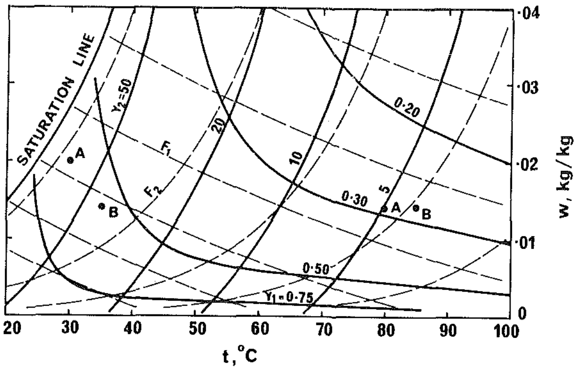

Fig. 2 Psychrometric chart showing curves of constant F_i and γ_i for silica gel [10] and entry air state pairs A and B used in predictions presented in section 5

Forms of equations (7) applicable to air-conditioning regenerators [2] were curve fitted to computed curves of constant F_i for silica gel on a t-w plot, and the identity function assumed, giving the nonlinear F_i expressions ([10], Table 2)

$$F_i = T^{m_i} + c_i w^{n_i}, \qquad i=1,2 \qquad (8a)$$

with $-m_1 = m_2 \cong 1.5$ and $(1-n_1) \cong n_2 \cong 0.1$ (8b)

The exponents are rounded to one decimal place to indicate the order of nonlinearity of the expressions. The constant coefficient of the temperature function is omitted, as for linear F_i, equations (4), since multiplication of an F_i expression by a constant value does not alter predictions by the analogy method using it ([2], section 2.6).

The F_i expressions for constant and separable α_i are now used to derive relationships between η_t, η_w, and η_i.

2.3 Constant α_i. With thermal and sorption properties averaged over the state range of operation, the linear F_i expressions given by equations (4) apply. These equations together with equations (1) and (2) yield the efficiency relations given in Table 1, with α_{ia}, α_{ib}, and α_{id} equal to α_{ic} and $\phi_i = \psi_i = 1$, as specified below the relations. These relations are seen to depend on the constant values α_{ic} and on α_{eo}, the slope of a line joining the regenerator entry air states on a t-w plot. The application of Le Châtelier's principle shows that $\alpha_1 > 0 > \alpha_2$ ([3], section 5.1), therefore the denominators of the coefficients of η_{ij} in the relations are always positive.

Nomenclature (cont.)

method minus value obtained from finite difference solution
η = efficiency of change for a period of potential driving transfer in regenerator matrix; η_{ij}, equations (1); η_{tj} and η_{wj}, equations (2)
θ = time
κ = $L/v\tau$, air carryover ratio
Λ = number of transfer units in a period, Table 2
μ = rato of masses in porous matrix of dry matrix and dry air
Π = Λ/Γ
σ = c_m/c_f, matrix to air specific heat ratio; $\bar{\sigma}$, average between entry temperatures of air streams
τ = period of time that matrix spends in an air stream
ϕ_i,ψ_i = factors, i = 1, 2, Table 1

Subscripts

c = constant value
e = entry state of air stream in period j, Fig. 1
f = air stream
i = F_i regenerator, i = 1, 2
j = period j, j = 1, 2
m = matrix, mean at a location, distance x
M = midstate on t-w plot between states e and 0
n = state at intersection of F_1 curve through e and F_2 curve through o, Fig. 1
o = entry state of other air stream in period j, Fig. 1
t = heat transfer
w = water vapor transfer
x = average exit state of air stream in period j, Fig. 1
eo,en / ex,no = to f_i, g_i, and u_i', denote average value over range between states specified by subscripts; to α, see for example definition of α_{eo}

Superscripts

c = conservation enforced in analogous heat regenerator
u = without conservation enforced in analogous heat regenerator
$*$ = period j value divided by period (3-j) value, j = 1, 2

The use of constant α_i values though α_i varies has been found satisfactory for energy recovery regenerator operation [7, 1], as explained in section 2.4.

2.4 Separable α_i. For thermal and sorption properties such that the dependence of α_i on t and w is separable, the F_i expressions given by equations (6) and (7) apply. From these equations, a difference in combined potential F_i between two air states may be expressed in terms of average values between the states of the separable components of the combined potenital slope α_i and of the derivative of the arbitrary function u_i. For example, the numerator of equations (1) may be written

$$F_{ix} - F_{ie} = u'_{iex}\left((t_x - t_e) g_{iex} + (w_x - w_e) f_{iex} \right) \tag{9}$$

Thus equations (1), (2), (6), and (7) yield the efficiency relations given in Table 1, with α_{ia}, α_{ib}, α_{id}, and ϕ_i formed from average values of f_i and g_i, and ψ_i formed from average values of u'_i, as specified below the relations under the heading "Exact Relations." These α_i values are termed average values.

The efficiency relations for separable α_i are seen to have the same form as those for constant α_i, with two different average values of each α_i replacing the constant values. These averages are taken between the entry states of the two air streams (subscript *eo*), and throughout the matrix in the air stream for which the efficiencies apply (subscript *ex*). The former average is used in the numerators of the coefficients of η_{ij} in the efficiency relations, and the latter in the denominators. Factors ϕ_i, equal to the ratio of the two averages for the temperature dependent components of the α_i, and factors ψ_i formed from the two averages for u'_i, also appear in the relations.

For energy recovery regenerator operation with high performance, states o and x are close together, Fig. 1, so that the two averages of each parameter are nearly identical. Therefore such operation may be treated as if the α_i are constant with values obtained at the midstate between the entry states of the air streams, as shown by computation [7, 1].

2.5 General α_i. General α_i expressions may be approximated by separable α_i expressions over the state range of operation, enabling F_i expressions to be formulated and fitted to the actual F_i curves on a t–w plot, section 2.2 and [2]. Errors in these curve fits result in errors in exit air state determination using the F_i expressions. This method of determination is proposed as an alternative for a regenerative dehumidifier to that presented by Maclaine-cross and Banks [6], which is discussed in section 2.6. The errors resulting from both methods are compared for a silica gel dehumidifier in section 5.3.

2.6 Intersection Point Method. For general α_i, Maclaine-cross and Banks [6] recommended an approximate method for determining the exit state of an air stream that utilizes the relevant intersection point of the F_i curves through the entry states of both air streams in a way indicated by Fig. 1. Thus, from ([6], equation (13)), the following generally inexact equations may be written

$$t_x - t_e = \eta_{1j}(t_o - t_n) + \eta_{2j}(t_n - t_e), \qquad j = 1,2 \tag{10a}$$

and

$$w_x - w_e = \eta_{1j}(w_o - w_n) + \eta_{2j}(w_n - w_e), \qquad j = 1,2 \tag{10b}$$

Equations (10) correspond to using constant α_i values obtained from the entry states of the air streams and the intersection point n, Fig. 1, as specified under the heading "General α_i" in Table 1. Therefore equations (10) correspond to using particular linear F_i expressions.

The accuracy of equations (10) for general α_i is indicated by that for separable α_i, which is shown by the efficiency relations given in Table 1, with α_{ia}, α_{ib}, α_{id}, ϕ_i, and ψ_i formed as specified below the relations under the heading "Inexact Relations from equations (10)." Equations (6) and (7) were used to specify the F_i line intersection point n in terms of average f_i, g_i, and u'_i values, enabling efficiency relations to be determined using equations (10). These relations may be compared with the exact efficiency relations for separable α_i given in Table 1, by comparing subscripts in the definitions given below the relations.

The relations differ in the denominators of the coefficients of η_{ij}, where α_i averages throughout the matrix in the exact relation are replaced by an average along an F_2 line for η_1, and an F_1 line for η_2, in the relation by the intersection point method. The importance of these differences depends on the mode of regenerator operation, as indicated by the relative positions of states e, n, o, and x on Fig. 1.

The differences are greatest for energy recovery operation, for which the intersection point method has been found unsatisfactory [7].

For dehumidifier operation with high performance, state x is close to state n, and the main difference lies in the denominator of the coefficient of η_{1j}. However, for such operation η_{1j} is small so that the effect of the difference is small. It is therefore understandable that Maclaine-cross [7] found the intersection point method satisfactory for such operation. It follows that the accuracy of the intersection point method increases as the exit air state approaches the intersection point.

3 Determination of η_i

3.1 Parameters. In a regenerator transferring heat alone, with fluid and matrix specific heats constant, the temperature efficiency η_t for a period depends on the number of heat transfer units Λ_t and the heat capacity-rate ratio Γ_t for each period [11, 6], neglecting the effect of heat storage in the air contained in the air flow passages through the regenerator matrix [12, 13]. This effect may be included approximately by modifying Λ_t and Γ_t [12].

In a heat transfer alone regenerator, the effect of air heat storage is to increase η_t by an amount less than or equal to the air carryover ratio κ, [13] and further studies by the author. For a silica gel dehumidifier, the matrix to contained air mass ratio μ is greater than 100 while in optimum operation $\mu\kappa$ is about 0.2 [10], hence κ is less than 0.2 percent, and the effect of air heat storage is negligible in each superposed analogous heat transfer-alone regenerator.

Thus for the analogy method, the temperature efficiency of an analogous heat transfer-alone regenerator is considered to have the parameter dependence shown in Table 2. The ratios Γ_t^* and Π_t^* describe the unbalance and asymmetry, respectively, of the regenerator. In the definition of Γ_{tj}, the mass ratio μ is the same for both periods, in accord with the model [2], and the specific heat ratio is constant with value σ_c. The parameter definitions given in Table 2 apply to both rotary and fixed-matrix regenerators. The parameters for rotary regenerators of Kays and London [11] may be related to those used here if fluid stream j is considered to have the minimum thermal capacity rate. Then $C^* = 1/\Gamma_t^*$, $C_r^* = \Gamma_{tj}$, $\bar{C}_r^* = \mu\,\sigma_c$, $N_{tu,o} = \Lambda_{tj}/(1 + \Pi_t^*)$, $(hA)^* = \Pi_t^*$ and $\epsilon = \eta_{tj}$.

The parameters for the corresponding F_i regenerator are also given in Table 2. In the number of transfer units of a period for this regenerator Λ_{ij}, the transfer coefficient equals that in the analogous heat regenerator, because $J_t = J_w$ ([2], section 2.3). Since γ_i depends on F_i, an average value is used in defining the capacity-rate ratio Γ_{ij}. This step corresponds to assuming that dependence of σ on t in the analogous heat regenerator is accounted for by using $\sigma_c = \bar{\sigma}$, an average value between the entry air states, and the accuracy of this assumption is described in section 3.2. The determination of

Table 2 Parameter dependence of efficiencies for period j, $j = 1, 2$

Regenerator:	Analogous heat (σ constant)	Combined heat and mass ($J_t = J_w$)
Potential:	t	$F_i,\ i=1,2$
Efficiency:	$\eta_{tj} = \Gamma_t^* \eta_{t(3-j)}$	$\eta_{ij} = \Gamma_i^* \eta_{i(3-j)}$ using Γ_i^{*c}
Parameters:	$\Lambda_{tj} = J_{tj} L / v_j$	$\Lambda_{ij} = J_{tj} L / v_j$
	$\Gamma_{tj} = \mu\ \kappa_j \sigma_c$	$\Gamma_{ij} = \mu\ \kappa_j \bar{\gamma}_{ij}$
	$\Gamma_t^* = 1/\tau^* v^*$	$\Gamma_i^{*u} = 1/\tau^* v^*$
		$\Gamma_i^{*c} = \bar{\gamma}_i^* / \tau^* v^*$
	$\Pi_t^* = \Lambda_t^* / \Gamma_t^* = J_t^* \tau^*$	$\Pi_i^{*u} = \Lambda_i^* / \Gamma_i^{*u} = J_t^* \tau^*$
		$\Pi_i^{*c} = \Lambda_i^* / \Gamma_i^{*c} = J_t^* \tau^* / \bar{\gamma}_i^*$

average γ_i is complicated by the dependence of γ_i also on F_{3-i} and is described in section 3.3. In one case, different average γ_i for the two periods are obtained, corresponding to lack of heat conservation in the analogous heat regenerator. In Table 2, two forms of the parameter ratios between periods are given that differ in the treatment of this lack of conservation, which is described in section 3.4.

3.2 Heat Regenerator With Nonconstant σ. η_t for a heat transfer-alone regenerator in which σ varies linearly with temperature has been obtained for $\Lambda_t = \infty$ with $\Lambda_t^* = \Pi_t^* = 1$ [6], and by finite difference solution of the governing equations, Maclaine-cross [7]. Predictions of the error in η_t resulting from the use of $\sigma = \bar{\sigma}$ are presented in Fig. 3 [7, 14]. Overprediction is observed, which is small except near $\Gamma_t = 1$, with the peak increasing with the degree of σ variation and with Λ_t. However, decrease of Λ_t spreads the peak by displacing its maximum to lower Γ_t and raising its tail at high Γ_t.

These predictions of the effect of a linear variation in σ provide an estimate of the effect of nonlinear variation.

The analogous heat regenerators of a heat and mass regenerator for energy recovery or dehumidification usually have Γ_t much less or much greater than unity, so that the error from the use of $\sigma = \bar{\sigma}$ is estimated to be small, except when the degree of σ variation is high and Λ_t is low.

3.3 Average γ_i. Each average γ_i in an F_i regenerator corresponds to σ_c and thus $\bar{\sigma}$ in the analogous heat regenerator, and so is obtained by integrating γ_i with respect to F_i over the F_i range between entry air states. The dependence of γ_i also on F_{3-i} makes the average depend on the mode of regenerator operation, since this determines the extent to which the changes in F_i and F_{3-i} are simultaneous.

In previous analogy methods [5-7], average γ_i were calculated by integration with respect to specific humidity w. It follows from ([2], section 2.6) that this procedure corresponds to using particular F_i expressions, the nonlinearity of which depends on that of the integration path. Relations for average γ_i are given here that generalize the previous relations [6, 7] to any F_i expressions.

In single-blow operation, period times are sufficiently long for each matrix element to be brought into thermodynamic equilibrium with an air stream before being moved into the other air stream. The changes in the combined potentials are then separated in time because $\gamma_2 >> \gamma_1$, Fig. 2, provided that $J_t = J_w = J$ and J is not very small ($\Lambda > 1$), [4, 5, 15]. Therefore the average γ_i for such operation, in which

$$\Gamma_{ij} << 1, \qquad i, j = 1,2 \tag{11}$$

are given by

$$\bar{\gamma}_{1js} = \frac{\displaystyle\int_{F_{1e}}^{F_{1o}} \gamma_1(F_1, F_{2o})\, dF_1}{(F_{1o} - F_{1e})}, \qquad j = 1,2 \tag{12a}$$

and

$$\bar{\gamma}_{2js} = \frac{\displaystyle\int_{F_{2e}}^{F_{2o}} \gamma_2(F_2, F_{1e})\, dF_2}{(F_{2o} - F_{2e})}, \qquad j = 1,2 \tag{12b}$$

In dehumidifier operation

$$\Gamma_{1j} << 1 \quad \text{and} \quad \Gamma_{2j} >> 1, \qquad j = 1,2 \tag{13}$$

and the combined potential changes occur partly simultaneously. Consideration of a wave diagram for the matrix [6] leads to the following average γ_i

$$\bar{\gamma}_{1jd} = \frac{\displaystyle\int_{F_{1e}}^{F_{1o}} \int_{F_{2e}}^{F_{2o}} \gamma_1\, dF_1\, dF_2}{(F_{1o} - F_{1e})\,(F_{2o} - F_{2e})}, \qquad j = 1,2 \tag{14a}$$

and

$$\bar{\gamma}_{2jd} = \left(1 - \frac{1}{2}\Gamma_{1j}\right)\bar{\gamma}_{2js} + \frac{1}{2}\Gamma_{1j}\bar{\gamma}_{2(3-j)s}, \qquad j = 1,2 \tag{14b}$$

In energy recovery operation

$$\Gamma_{ij} >> 1, \quad i, j = 1,2 \tag{15}$$

and it follows from the analogy that air and matrix states lie close to a straight line between the entry air states on a t-w plot, Fig. 2. Therefore the γ_i need to be averaged along this line. It has been found adequate [7, 1] to use γ_i values at the midpoint of this line, giving

$$\bar{\gamma}_{ijr} = \gamma_{iM}, \quad \mathrm{i}, j = 1,2 \tag{16}$$

Maclaine-cross [7] evaluated the line integrals in equations (12) by integration with respect to specific humidity w, but did not evaluate similarly the area integral in equation (14a). Instead, two alternative approximations were used

$$\bar{\gamma}_{1jda} = \gamma_{1M}, \quad j = 1,2 \tag{17a}$$

and

$$\bar{\gamma}_{1jdb} = \frac{1}{2}\left(\bar{\gamma}_{1js} + \bar{\gamma}_{1(3-j)s}\right), \quad j = 1,2 \tag{17b}$$

Equation (17b) was recommended for entry air states far apart but close to the same F_2 line, and equation (17a) for all other cases ([7], p. 226).

3.4 Treatment of Lack of Conservation. For an F_i regenerator in energy recovery or dehumidifier operation, changes in the combined potentials occur simultaneously, section 3.3, so that the combined transferred substance is not conserved ([2], section 2.8). However, since average γ_i are used, there is lack of heat conservation in the analogous heat regenerator only when the average γ_i for the two periods differ. This occurs for the F_2 regenerator in dehumidifier operation, equations (14b).

Conservation in the analogous heat regenerator may be enforced by treating the $\bar{\sigma}$ ratio between periods as the result of the specific heats of the two fluid streams being different.

Table 3 Values of $\bar{\gamma}_i$ used in predictions by analogy methods, section 5, with entry air state pair B, Fig. 2.

Period		IP method	NL method
Dehumidifying	$\bar{\gamma}_1$	0.414	0.383
	$\bar{\gamma}_2$ at $\mu\kappa = 0.2$	16.99	15.20
Regenerating	$\bar{\gamma}_1$	0.414	0.383
	$\bar{\gamma}_2$ at $\mu\kappa = 0.2$	13.67	12.73

This treatment is denoted by superscript c in Table 2. Alternatively, the $\bar{\sigma}$ ratio between periods may be considered to represent a step change in matrix specific heat between periods, consistent with the inherent lack of conservation in the corresponding F_i regenerator mentioned above. In the absence of predictions for the effect of such a step change, it can be only omitted, and this treatment is denoted by superscript u in Table 2.

4 Analogy Methods

4.1 Energy Recovery Regenerator. For an energy recovery regenerator, the η_{ij} are determined using γ_{iM} values, section 3.3, and exit air states are determined using α_{iM} values, section 2.3. Thus a linear analogy method is used, with properties evaluated at the midstate between entry air states. Comparison of predictions with finite difference results has shown this application of the analogy method to be accurate within 0.1 percent of the span between entry air states, for $J_t = J_w$ [7, 1].

4.2 Regenerative Dehumidifier. The nonlinear analogy method for a regenerative dehumidifier presented previously [6, 7] is termed the intersection point (IP) method, after its procedure for exit air state determination, section 2.6. This method determines η_{ij} from γ_i averaged using nonlinear F_i expressions, section 3.3, determines exit air state using linear F_i expressions, and enforces conservation in the analogous heat regenerators, section 3.4.

The nonlinear analogy method for a regenerative dehumidifier presented here uses the same nonlinear F_i expressions, section 2.2, for determining both the η_{ij}, section 3.3, and exit air state, section 2.5, and is termed the nonlinear (NL) analogy method.

The NL method with conservation enforced and the IP method have been evaluated for a symmetric balanced silica gel dehumidifier with $J_t = J_w$ by comparison of predictions with finite difference results [10]. For optimum operation, that is with the period time giving maximum dehumidification, the error in exit dehumidified air state predicted by the IP method was about 1 percent of the span from entry state to intersection point state, *en* on Fig. 1, while that by the NL method was about 5 percent. This result is surprising in view of the use of linear F_i expressions in one step of the IP method. The result is explained by the consideration of the sources of error in the two methods in section 5.

4.3 Single-Blow Regenerator. It is not efficient to operate regenerators in the single-blow mode for energy recovery or dehumidification purposes, and this mode has been included in section 3.3 to clarify the presentation.

In single-blow heat and mass regenerators the profile of exit air state change, or breakthrough profile, is of primary interest. This profile is not predicted accurately by analogy to heat transfer alone with constant specific heat ratio because of the dependence of sorption properties on state [5, 15].

5 Sources of Error for Dehumidifier

5.1 Evaluation of Error. Errors in the analogy methods are evaluated by comparing predictions by the methods with results from finite difference solution of the governing equations using the computer program by Maclaine-cross [7]. The program utilizes extrapolation to zero grid size, and its error is estimated to be less than a tenth of that of the IP analogy method for $J_t = J_w$ [7].

A symmetric balanced silica gel dehumidifier with $J_t = J_w$ is considered using the average silica gel properties and the fitted F_i expressions described by Jurinak and Banks [10], except that in section 5.2 arbitrary functions u_i, equations (6), other than identity are considered. The fitted expressions are presented approximately in equations (8) above.

The IP method is applied using the relations for average γ_i given by equations (17*b*) and (14*b*), with the component line integrals evaluated by integration with respect to specific humidity w. Equation (17*b*) is chosen in preference to the alternative approximation to equation (14*a*), equation (17*a*), since the alternative gives less accurate prediction, though recommended for the entry air states used here (section 3.3 and Fig. 2). The NL method is applied using equations (14), with changes to equation (14*b*). Thus in equation (14*b*) for $\bar{\gamma}_2$, the factor 1/2 is replaced by 1 when the NL method is applied with conservation enforced, and by 0 without conservation enforced. However, η_2 is sensitive to $\bar{\gamma}_2$ only via Γ_2^* since $\Gamma_2 >> 1$, from analogy and [11]. Therefore the changes to equation (14*b*) affect only the results presented for the NL method with conservation enforced. The resulting values of $\bar{\gamma}_1$, and of $\bar{\gamma}_2$ at $\mu\kappa = 0.2$, are given in Table 3 for both analogy methods with an entry air state pair used.

The entry air state pairs shown in Fig. 2 are used, states A in considering *f-m* linearization error and states B in considering other sources of error. States B are one of the two entry state pairs used in [10], and the same predictions for the other pair have been carried out and found to give similar results.

5.2 *f-m* Linearization. Linearization of the F_i expressions between air and matrix states is necessary in transforming the governing conservation and rate equations to forms analogous to those for heat transfer alone ([2], section 2.5). The resulting error in η_i may be expected to increase with decrease in the number of transfer units Λ, and vary with the nonlinearity of the F_i expressions ([2], section 2.7). Errors in dehumidifier exit air state predicted by the NL method, Fig. 4, show this dependence, indicating that the varying component of the error results from *f-m* linearization.

Figure 4 shows results by the NL method using three different choices for the arbitrary function u_i in the F_i expressions, namely, identity, cubing, and near linearization in temperature, and using two numbers of transfer units. The identity function is seen to give the least average error, which is independent of Λ. The strong effect of Λ on the error for the other functions indicates that this error mainly results from *f-m* linearization.

The directions of F_i lines given on Fig. 4 show that the error apparently resulting from *f-m* linearization is much greater in η_2 than η_1. This result is consistent with the greater nonlinearity in F_2 expressions than F_1 expressions, equations (8), and the greater span of F_2 between the entry air states, A on Fig. 2.

The lack of effect of Λ on average error for the identity function indicates that the error resulting from $f-m$

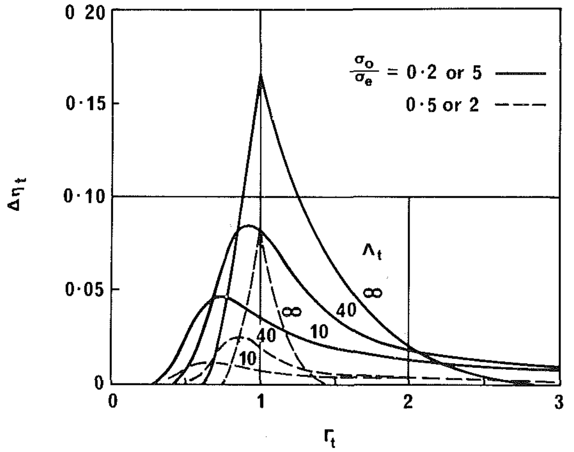

Fig. 3 η_t error from use of $\sigma = \bar{\sigma}$ when σ varies linearly with temperature, for symmetric balanced heat regenerator [7, 14]

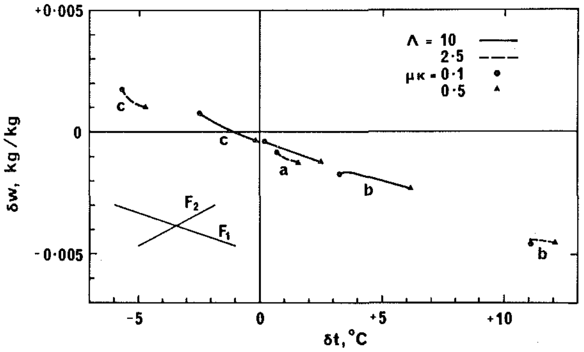

Fig. 4 Errors in exit state of dehumidified air stream predicted by NL method with conservation enforced, using (*a*) $F_i = v_i$, (*b*) $F_i = v_i^3$ and (*c*) $F_i = v_i^{1/m_i}$, with $v_i \equiv F_i$ in equations (8), for silica gel dehumidifier [10], $\mu\kappa$ range including optimum and entry air state pair A on Fig. 2

linearization is negligible for this function. This conclusion applies also to such error in predictions by the IP method, since the determination of average γ_i in it implicitly uses nonlinear F_i expressions, section 3.3, that necessarily have nonlinearity like that of the F_i expressions resulting from the identity function.

The results in Fig. 4 show that the convenient identity function is at least close to optimum for a silica gel dehumidifier. This function is used in the predictions presented subsequently and in [10].

5.3 Exit Air State Determination. The error in exit air state determination from the η_i by the NL method as a result of the approximate nature of the fitted F_i expressions has been estimated by Jurinak and Banks [10]. Results for $\Lambda = 20$ and a range of $\mu\kappa$ values including the optimum of 0.2 are shown in Fig. 5, together with estimates of the errors under these conditions caused by the procedure for exit air state determination in the IP method. The latter were obtained by using the fitted F_i expressions to obtain η_i values from the exit air state given by the finite difference solution, then substituting these values into equations (10). Thus the estimated errors presented for the procedure in the IP method include those for the procedure in the NL method, which are seen to be nearly invariant with $\mu\kappa$, facilitating comparison.

The IP method error in exit air state determination is seen to be a minimum at $\mu\kappa = 0.2$, corresponding to optimum dehumidifier operation. The exit air state is then closest to the intersection point, *n* on Fig. 1, in accord with conclusion of section 2.6.

Figure 5 shows that error in exit air state determination by the IP method is much greater than that by the NL method. The directions of F_i lines given on the figure show the error by the NL method to be mainly in η_1 and that by the IP method to be mainly in η_2.

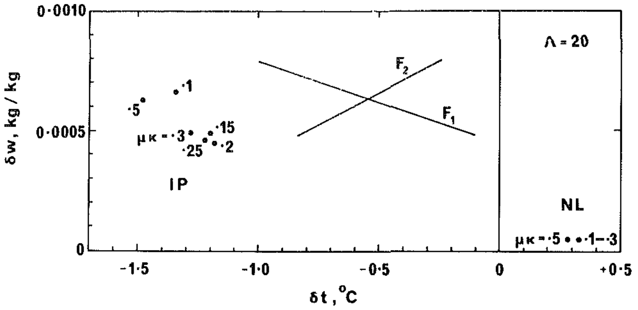

Fig. 5 Error in exit air state determination from the η_i by fitted F_i expressions [10], NL, and by equations (10), IP, for dehumidified air stream of silica gel dehumidifier [10], over $\mu\kappa$ range including optimum of 0.2, with entry air state pair B on Fig. 2

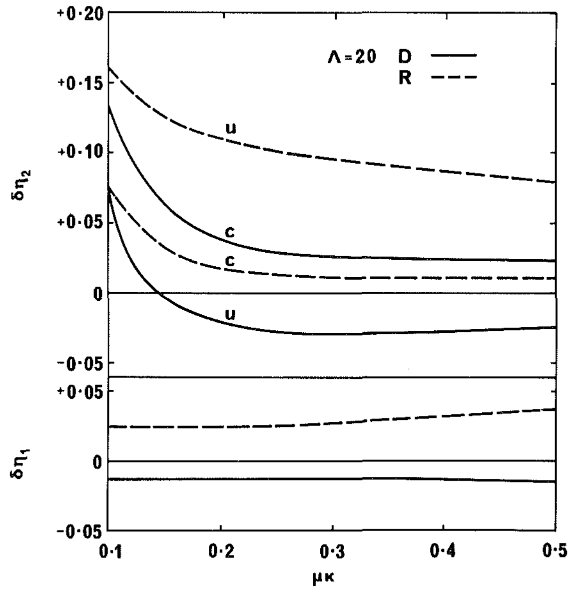

Fig. 6 Errors in η_i predicted by NL method, with conservation enforced (*c*) and without (*u*), for dehumidified (D) and regenerating (R) air streams of a silica gel dehumidifier [10] over $\mu\kappa$ range including optimum of 0.2, with entry air state pair B on Fig. 2

5.4 Lack of Conservation. Errors in the η_i predicted by the NL method are shown in Fig. 6 for the same operating conditions as for Fig. 5. The η_i values considered exact were obtained from the exit air states given by the finite difference solution using the F_i expressions. Results are shown for both dehumidifying (D) and regenerating (R) periods, with conservation enforced (c) and without (u), section 3.4. Both an η_i value predicted by the NL method and the associated η_i value considered exact are affected similarly by the approximate nature of the F_i expressions; therefore their difference $\delta\eta_i$ is affected negligibly.

Enforcement of conservation is seen to double the error in η_2 for the dehumidifying period at optimum operation ($\mu\kappa = 0.2$), but to decrease it much more for the regenerating period. The errors for both periods are seen to be similar after enforcement. Therefore, this procedure for treating lack of conservation improves the analogy more than omitting it. This conclusion applies for the IP method as well as the NL method, since the average γ_2 used in both methods are similar, Table 3. The causes of the error remaining after enforcement of conservation, and common to both methods, are now explored.

5.5 Averaging of γ_i. It is noted that the approximation in the fitted F_i expressions causes errors in the average γ_i for the NL method, since these are obtained using the expressions, section 3.3, [10]. However, the effect is negligible for the results shown in Fig. 6.

The assumption of constant σ in the analogous heat transfer alone regenerator, though γ_i varies in each F_i regenerator, leads to error in the prediction of η_i resulting from that of η_i in the analogous heat regenerator, section 3.2 and Fig. 3.

The ratio of γ_2 values between the entry air states is seen from Fig. 2, states B, to be near 10, though a smaller ratio, 6, occurs between entry and intersection point states in each air stream. For either period, $\bar{\gamma}_2 \cong 15$ giving for optimum dehumidifier operation, $\mu\kappa = 0.2$, $\Gamma_2 \cong 3$. It may be inferred from Fig. 3 that the variation in γ_2 causes overprediction in η_2 that accounts for much of the remaining error shown in Fig. 6, curves c, considering both the value of $\delta\eta_2$ at $\mu\kappa = 0.2$ and its variation with $\mu\kappa$. The greater remaining error for the dehumidifying period may be attributed to inaccurate correction for lack of conservation, section 5.1, and the effect of the unbalance assumed in this correction on the effect of the variation in γ_2 [7].

The ratio of γ_1 values between the entry air states is near 3, $\bar{\gamma}_1 = 0.4$, and $\Gamma_1 = 0.2$ for $\mu\kappa = 0.5$. Hence it is estimated from Fig. 3 that the effect of γ_1 variation on η_1 is negligible for the range of $\mu\kappa$ in Fig. 6. It follows that the errors in η_1 shown in Fig. 6 result from the relation for average γ_1 used, equation (14*a*). Since $\Gamma_1 << 1$, $\eta_1 \cong \Gamma_1 \propto \bar{\gamma}_1$, from analogy and [11], so that error in $\bar{\gamma}_1$ causes proportionate error in η_1. This argument indicates that $\bar{\gamma}_1$ is overestimated in the regenerating period and underestimated in the dehumidifying period. The effect of lack of conservation in an F_i regenerator is expected to be of opposite sign in the two periods ([2], section 2.8), like that of enforcement of conservation, Fig. 6. Therefore, the cause of the error in η_1 attributable to inaccuracy in the estimation of $\bar{\gamma}_1$ appears to be lack of conservation in an F_1 regenerator.

The value of $\bar{\gamma}_1$ used in the IP method is 8 percent greater than that used in the NL method, Table 3. The resulting increase in η_1 compensates in the dehumidifying period for the error in η_1 shown in Fig. 6. This compensation is fortuitous, since the different $\bar{\gamma}_1$ value used in the IP method is mainly the result of an arbitrary approximation, section 5.1.

6 Comparison of Methods for Dehumidifier

6.1 With Conservation Enforced. The greater accuracy of the IP method compared to the NL method with conservation enforced, section 4.2 and [10], despite the much greater error in exit air state determination in the former method, section 5.3, results from compensating errors. The underprediction of η_2 from this determination compensates for the overprediction that results mainly from neglect of the variation in γ_2, section 5.5. Also, the greater value of $\bar{\gamma}_1$ used in the IP method compensates for error in η_1 apparently due to lack of conservation in an F_1 regenerator, section 5.5.

6.2 Without Conservation Enforced. Enforcement of conservation increases η_2 in the dehumidifying period, Fig. 6, so that application of the NL method without this enforcement provides compensation in this period for the overprediction mainly resulting from neglect of γ_2 variation. As a result, the NL method without conservation enforced is nearly as accurate as the IP method for this period, which is of primary interest in air-conditioning system simulations. Equal accuracy would be achieved by the use of the same $\bar{\gamma}_1$ value in both methods.

6.3 Dehumidifier Simulation for Given η_i. A rapidly computed nonlinear model of a regenerative dehumidifier, suitable for inclusion in a computer simulation of an open-cycle cooling system installation, may be obtained by assigning values to the η_i and using F_i expressions to determine exit air states [1], and has been applied [8]. It follows from section 5.3 that such a model, which utilized the procedure for exit air state determination in the IP method, would be much less accurate.

6.4 Improvement of Methods. The IP method appears not amenable to improvement since its distinctive step is inherently very inaccurate. The method has given accurate prediction only because of fortuitous compensation of errors.

Less approximation in the fitted F_i expressions would reduce the error in exit air state determination from the η_i by the NL method, section 5.3.

Ways to improve the determination of η_i in the NL method follow from the discussion in section 5.5. The error in η_1 could be much reduced by an improved procedure for determining $\bar{\gamma}_1$, and that in η_2 by a correction for the effect of γ_2 variation. Maclaine-cross [14] envisages such a correction based on his work [7]. The improved procedure for determining $\bar{\gamma}_1$ needs to allow for lack of conservation in the F_1 regenerator, and further reduction in the error in η_2 would result from more accurate correction for such lack in the F_2 regenerator.

6.5 Matrix Materials Other Than Silica Gel. Errors in the IP and NL analogy methods have been evaluated here considering the regenerator matrix to be composed wholly of silica gel with average properties. Jurinak [16] has investigated the accuracy of the IP method for matrix materials with sorption properties very different from those of silica gel, including the effect of nonsorbent carrier material ([2], section 2.1), and found in general much greater error. This result confirms the conclusion above that the close accuracy of the IP method for a silica gel matrix is due to compensation of errors. The individual errors may be expected to vary differently with matrix properties, so that compensation is not expected for all matrix materials.

Rational ways for reduction of the errors in the NL method are apparent, so that this method is promising for application with matrix materials other than silica gel.

6.6 Extension to Unequal Transfer Coefficients. The reduction of either transfer coefficient reduces dehumidifier performance, thus moving an exit air state further from the nearby intersection point of F_i curves, Fig. 1. Such movement increases error in exit air state determination by the IP method, section 5.3. Therefore, the NL method is expected to be more accurate with unequal heat and mass transfer coefficients, particularly if improved as described in section 6.4.

7 Conclusions

The prediction of heat and mass regenerator performance by analogy from that of a similar regenerator transferring heat alone has been studied in view of the dependence of matrix sorption properties on state. Regenerators with equal overall transfer coefficients for heat and mass are considered, particularly air-conditioning regenerators with convective transfer controlling.

An analogy method using approximate nonlinear expressions for the combined potentials, such as those derived in Part 1, has been described. Application of the method in a general form has shown that the linear method previously presented is satisfactory for an energy recovery regenerator, while a nonlinear method is required for a regenerative dehumidifier.

The analogy method has two steps. First, the determination of the efficiencies of the two analogous heat transfer-alone regenerators superposed to represent the heat and mass regenerator. Second, the determination of exit air state from these efficiencies.

The previously presented nonlinear method for a dehumidifier has been seen to use linear combined potential expressions in the second step, resulting in significant error in this step. However, this error compensates for errors in the first step, resulting in close prediction for optimum operation of a silica gel dehumidifier. The error in the second step is much reduced for the nonlinear method described here, so that it is less accurate than the previous method, unless its second step is used alone as in a simple dehumidifier simulation model. However, ways to reduce errors in the first step are indicated, and also because of the different nature as well as magnitude of the errors in the second step for the two methods, the method described here promises to be more accurate for matrix materials other than silica gel, and for extension to regenerators with unequal overall transfer coefficients for heat and mass.

Acknowledgments

The computed results considered in section 5 were obtained by Dr. J. J. Jurinak at the Solar Engineering Laboratory, University of Wisconsin-Madison. These results include results presented and discussed otherwise by Jurinak and the author [10] and by Jurinak [16]. The author is grateful to Dr. Jurinak for providing these results, and for suggestions that aided the interpretation of these presented in this paper. Gratitude is also expressed to Dr. I. L. Maclaine-cross of the University of New South Wales, whose computer programs [7] are the foundation of those developed by Dr. Jurinak, for helpful comments.

References

1 Banks, P. J., "Prediction of Heat and Water Vapor Exchanger Performance from that of a Similar Heat Exchanger," *Compact Heat Exchangers—History, Technological Advancement and Mechanical Design Problems*, HTD-Vol. 10, edited by R. K. Shah, C. F. McDonald and C. P. Howard, ASME Winter Annual Meeting, Nov. 1980, ASME, New York, 1980, pp. 57-64.

2 Banks, P. J., "Prediction of Heat and Mass Regenerator Performance Using Nonlinear Analogy Method: Part 1—Basis," ASME JOURNAL OF HEAT TRANSFER, Vol. 107, February 1985, pp. 222-229.

3 Banks, P. J., "Coupled Equilibrium Heat and Single Adsorbate Transfer in Fluid Flow Through a Porous Medium—I Characteristic Potentials and Specific Capacity Ratios," *Chemical Engineering Science*, Vol. 27, No. 5, May 1972, pp. 1143-1155.

4 Close, D. J., and Banks, P. J., "Coupled Equilibrium Heat and Single Adsorbate Transfer in Fluid Flow Through a Porous Medium—II Predictions for a Silica Gel Air-Drier Using Characteristic Charts," *Chemical Engineering Science*, Vol. 27, No. 5, May 1972, pp. 1157-1169.

5 Banks, P. J., Close, D. J., and Maclaine-cross, I. L., "Coupled Heat and Mass Transfer in Fluid Through Porous Media—an Analogy with Heat Transfer," *Heat Transfer 1970* (Proceedings of the Fourth International Heat Transfer Conference, Versailles, Sept. 1970), Vol. VII, Elsevier, Amsterdam, 1970, paper CT 3.1, pp. 1-10.

6 Maclaine-cross, I. L., and Banks, P. J., "Coupled Heat and Mass Transfer in Regenerators—Prediction Using an Analogy with Heat Transfer," *International Journal of Heat and Mass Transfer*, Vol. 15, No. 6, June 1972, pp. 1225-1242.

7 Maclaine-cross, I. L., "A Theory of Combined Heat and Mass Transfer in Regenerators," Ph.D. thesis, Department of Mechanical Engineering, Monash University, Australia, 1974.

8 Jurinak, J. J., and Beckman, W. A., "A Comparison of the Performance of Open Cycle Air Conditioners Utilizing Rotary Desiccant Dehumidifiers," *Proceedings of 1980 Annual Meeting of American Section, International Solar Energy Society*, Phoenix, June 1980, pp. 215-219.

9 Nelson, J. S., Beckman, W. A., Mitchell, J. W., and Close, D. J., "Simulations of the Performance of Open Cycle Desiccant Systems Using Solar Energy," *Solar Energy*, Vol. 21, No. 4, Apr. 1978, pp. 273-278.

10 Jurinak, J. J., and Banks, P. J., "A Numerical Evaluation of Two Analogy Solutions for a Rotary Silica Gel Dehumidifier," *Heat Transfer in Porous Media*, HTD-Vol. 22, edited by J. V. Beck and L.-S. Yao, ASME Winter Annual Meeting, Nov. 1982, ASME, New York, 1982, pp. 57-68.

11 Kays, W. M., and London, A. L., "Heat Transfer in Periodic-flow-type Exchangers," *Compact Heat Exchangers*, 2nd ed., McGraw-Hill, New York, 1964, pp. 27-30.

12 Maclaine-cross, I. L., "Effect of Interstitial Fluid Heat Capacity on Regenerator Performance," ASME JOURNAL OF HEAT TRANSFER, Vol. 102, No. 3, Aug. 1980, pp. 572-574.

13 Banks, P. J., "Effect of Fluid Carryover on Regenerator Performance," ASME JOURNAL OF HEAT TRANSFER, Vol. 104, No. 1, Feb. 1982, pp. 215-217.

14 Maclaine-cross, I. L., personal communication, University of New South Wales, Australia, 1982.

15 Close, D. J., and Banks, P. J., "Coupled Heat and Mass Transfer in a Packed Bed with the Lewis Relation Not Satisfied," *Chemical Engineering Science*, Vol. 29, No. 5, May 1974, pp. 1147-1155.

16 Jurinak, J. J., "Open Cycle Solid Desiccant Cooling – Component Models and System Simulations," Ph.D. thesis, Department of Mechanical Engineering, University of Wisconsin – Madison, 1982.

Journal of Heat Transfer

Technical Notes

This section contains shorter technical papers. These shorter papers will be subjected to the same review process as that for full papers.

Diffusion-Driven Nonisothermal Evaporation

A. T. Prata[1] **and E. M. Sparrow**[2]

Nomenclature

c_p = specific heat of the mixture
c_{pj} = specific heat of component j
$\mathfrak{D}$ = binary diffusion coefficient
h = heat transfer coefficient
h_{fg} = latent heat of evaporation
K = mass transfer coefficient
k = thermal conductivity
M_j = molecular weight of component j
$\dot{m}$ = evaporation rate per unit area for liquid water
$\dot{m}_j$ = mass flux for component j
p = total pressure
T = temperature
T^* = reference temperature
T^+ = thermodynamic wet-bulb temperature
W_j = mass fraction of component j
$W_1{}^*$ = reference mass fraction of component 1
y = vertical coordinate
ρ = mixture density
ρ_j = density of component j
ϕ = relative humidity

Subscripts

i = gas–liquid interface
∞ = in the ambient
1 = vapor of evaporating liquid
2 = gas
$1i$ = component 1 at gas–liquid interface
1∞ = component 1 in the ambient

Introduction

The steady-state evaporation of a volatile liquid situated in a partially filled, open-topped container is termed the Stefan diffusion problem when the system is isothermal (e.g., [1]). Although the isothermal assumption obviates consideration of energy transfers in the Stefan problem, such transfers do take place and are necessary for the maintenance of steady-state evaporation. To maintain the evaporation, the energy inflow to the gas–liquid interface must precisely balance the latent heat requirements. In general, in real systems, which are necessarily nonisothermal, energy may be delivered to the interface through the liquid pool or through the gaseous mixture which occupies the space above the pool. The energy delivered through the gas is drawn from the ambient at the top of the container, while that delivered through the liquid flows from the ambient to the container wall and then into the liquid. The relative magnitude of these two energy supplies is governed by the thermal resistance encountered along the respective heat flow paths.

In the limiting case where the resistance for the heat flow from the ambient to the liquid via the container wall is negligibly small, the liquid temperature is virtually identical to the ambient temperature. Also, for this case, the gaseous mixture in the container takes on the ambient temperature. This is the condition for the Stefan diffusion problem.

If, however, the wall of the container is perfectly insulated, no energy will pass from the ambient through the container wall into the liquid. Therefore, the latent heat requirements have to be totally fulfilled by energy passing from the ambient through the gaseous mixture to the interface. Because of the finite thermal resistance of the gaseous mixture, the gas will be nonisothermal and the temperature of the interface will take on an equilibrium value lower than that of the ambient. In this situation, the liquid will be at a uniform temperature equal to that of the interface.

For given ambient conditions, the rate of evaporation will increase monotonically with the interface temperature. The highest value of the interface temperature (i.e., the ambient temperature) is attained in the Stefan model. It, therefore, provides the upper bound for the rate of evaporation. The lowest value of the interface temperature corresponds to the condition where the container wall is adiabatic. Therefore, this situation is the lower bound for the rate of evaporation.

In the present analysis, evaporation in an adiabatic-walled, open-topped container partially filled with a volatile liquid will be investigated. To compare the evaporation rates for this nonisothermal case with those of the Stefan diffusion model, calculations will be performed for the evaporation of liquid water into an ambient containing air.

Analysis

Consider a binary mixture of gases situated in an open-topped container partially filled with an evaporating liquid. One of the gases (subscript 1) is the vapor phase of the liquid, while the other gas (subscript 2) is insoluble in the liquid. In common with the Stefan model, the analysis will be made on a one-dimensional basis, where the spatial coordinate y is taken

---

[1,2] Department of Mechanical Engineering, University of Minnesota, Minneapolis, Minn. 55455

[2] Fellow ASME

Contributed by the Heat Transfer Division for publication in the JOURNAL OF HEAT TRANSFER. Manuscript received by the Heat Transfer Division March 6, 1984.

to be zero at the gas–liquid interface and increases in the upward direction perpendicular to the liquid surface. The top of the container is situated at $y = H$.

The gases form an ideal gas mixture, and the relevant thermophysical properties of the mixture (ρ, k, $\mathfrak{D}$, c_p) are taken to be constant, to be evaluated at a reference state as discussed later. The mass fractions W_1 and W_2 of the species are defined as

$$W_1 = \rho_1/\rho, \quad W_2 = \rho_2/\rho \tag{1}$$

and since $\rho = \rho_1 + \rho_2$

$$W_1 + W_2 = 1, \quad dW_1/dy = -dW_2/dy \tag{2}$$

The Conservation Equations and Their Solution. First, attention will be focused on the energy equation for the binary mixture. If the terms relevant to the problem under consideration are retained, then, from [2], p. 464, there follows

$$\rho c_p (DT/Dt) = k\nabla^2 T + \rho\mathfrak{D}(\nabla W_1 \cdot \nabla h_1 + \nabla W_2 \cdot \nabla h_2) \tag{3}$$

where h_1 and h_2 are the specific enthalpies of species 1 and 2, respectively. For a one-dimensional, steady-state situation, and utilizing equation (2) together with $dh_j/dy = c_{pj}(dT/dy)$, $j = 1, 2$, equation (3) can be written as

$$\rho c_p v (dT/dy) = k(d^2T/dy^2) + \rho\mathfrak{D}(c_{p1} - c_{p2})(dW_1/dy)(dT/dy) \tag{4}$$

The one-dimensional model requires that $v = v(y)$; any nonuniformities in v related to the no-slip boundary condition at the container wall have been shown to have a negligible effect on the rate of evaporation [3].

The mixture c_p in equation (4) may be eliminated by the relationship $c_p = W_1 c_{p1} + W_2 c_{p2}$, and the terms multiplying $c_{p1}(dT/dy)$ and $c_{p2}(dT/dy)$ in the resulting equation are seen to be the species mass fluxes as given by

$$\dot m_j = \rho_j v - \rho\mathfrak{D}(dW_j/dy) \quad j = 1,2 \tag{5}$$

Upon noting that $\dot m_2 = 0$ everywhere within the container, there follows

$$(\dot m_1 c_{p1}/k)(dT/dy) = (d^2T/dy^2) \tag{6}$$

where $\dot m_1$ is a constant throughout the gaseous mixture.

Now, the boundary conditions for the energy equation will be specified. At the gas–liquid interface, an energy balance yields

$$k(dT/dy)_i = \dot m_1 h_{fg} \tag{7}$$

where h_{fg} is the latent heat of evaporation for species 1, which is a function of the equilibrium temperature at the gas–liquid interface. For the second boundary condition, at the top of the container ($y = H$), the temperature is specified to be T_∞.

The integration of the energy equation (6), subject to the boundary conditions, gives the temperature distribution throughout the gaseous mixture

$$T(y) = (h_{fg}/c_{p1})[\exp(\dot m_1 c_{p1} y/k) - \exp(\dot m_1 c_{p1} H/k)] + T_\infty \tag{8}$$

The unknown $\dot m_1$, which appears in equation (8), will be determined by utilizing the solution of the mass transfer problem which will now be considered.

The species conservation equation for component 1 ([2], p. 482), when applied to the present problem, requires

$$v(dW_1/dy) = \mathfrak{D}(d^2W_1/dy^2) \tag{9}$$

By setting $\dot m_2 = 0$ in equation (5) and eliminating W_2 by means of equation (2), it follows that

$$v = -[\mathfrak{D}/(1 - W_1)](dW_1/dy) = \dot m_1/\rho \tag{10}$$

where equation (5) has been employed to obtain the right-hand term. Substitution of v from equation (10) into equation (9) yields

$$(\dot m_1/\rho\mathfrak{D})(dW_1/dy) = (d^2W_1/dy^2) \tag{11}$$

At the gas–liquid interface (subscript i), equation (10) yields

$$(dW_1/dy)_i = -(1 - W_{1i})(\dot m_1/\rho\mathfrak{D}) \tag{12}$$

where W_{1i} is the mass fraction of species 1 at the interface ($y = 0$). At the top of the container, W_1 is known and equal to $W_{1\infty}$.

The integration of equation (11), and the use of its boundary conditions, gives

$$W_1(y) = -(1 - W_{1i})[\exp(\dot m_1 y/\rho\mathfrak{D}) - \exp(\dot m_1 H/\rho\mathfrak{D})] + W_{1\infty} \tag{13}$$

Interface Temperature and Evaporation Rate. An expression for the equilibrium temperature at the gas–liquid interface is found by evaluating equation (8) at $y = 0$

$$T_i = (h_{fg}/c_{p1})[1 - \exp(\dot m_1 c_{p1} H/k)] + T_\infty \tag{14}$$

and similarly, the evaporation rate is extracted from equation (13) as

$$\dot m_1 = (\rho\mathfrak{D}/H)\ln[1 + (W_{1i} - W_{1\infty})/(1 - W_{1i})] \tag{15}$$

In solving for T_i and $\dot m_1$, the properties ρ, k, $\mathfrak{D}$, and c_{p1} are evaluated at a reference state defined as

$$T^* = ½(T_i + T_\infty), \quad W_1{}^* = ½(W_{1i} + W_{1\infty}) \tag{16}$$

and the total pressure p is constant throughout the container. The relevant properties k, $\mathfrak{D}$, and c_{p1} are table look-ups or the equivalent, and for ρ, the perfect gas law yields

$$\rho = pM/\mathcal{R}T^* \tag{17}$$

where $\mathcal{R}$ is the universal gas constant, and M is the mixture molecular weight at the reference state given by

$$M = M_1 M_2/[M_1 + (M_2 - M_1)W_1{}^*] \tag{18}$$

To begin the solution, a trial value of the interface temperature T_i is selected, and ρ_{1i} and h_{fg} are obtained from the liquid-vapor equilibrium data for the specific substance of interest. To find the corresponding W_{1i}, the definition

$$W_{1i} = \rho_{1i}/\rho \tag{19}$$

is combined with equation (17), after which M and $W_1{}^*$ are eliminated by using equations (18) and (16). Then, with this W_{1i} and with the given value of $W_{1\infty}$, the reference mass fraction $W_1{}^*$ follows from equation (16) and, in turn, M and ρ are calculated from equations (18) and (17), respectively.

At this point, all of the information needed to evaluate $\dot m_1$ from equation (15) is available. Next, $\dot m_1$ is substituted into equation (14) along with h_{fg} (which corresponds to the trial value of T_i), c_{p1}, and k. With these inputs, equation (14) provides an updated value of T_i. The updated value of T_i is used to initiate a new cycle of calculations, and thus to proceed iteratively to the solution.

Linearized Solution. In situations where the evaporation rate of the volatile liquid is very small, the series expansion $\exp(x) \cong 1 + x$, accurate for small values of x, can be used to obtain linear forms for $T(y)$ and $W_1(y)$ from equations (8) and (13). These linearized equations, when applied at the gas–liquid interface ($y = 0$), give

$$T_1 = -\dot m_1 h_{fg} H/k + T_\infty \tag{20}$$

$$\dot m_1 = (\rho\mathfrak{D}/H)(W_{1i} - W_{1\infty})/(1 - W_{1i}) \tag{21}$$

which can be solved using the same methodology as for equations (14) and (15). The linearized forms can also be derived from the energy and species conservation equations where, respectively, only the energy transported by conduction and the mass transported by diffusion are retained.

The conditions under which the linearization is valid will now be investigated, and for this purpose it is sufficient to analyze either the T_i or $\dot m_1$ solution. For the former, the nonlinearized solution (14) can be rewritten as

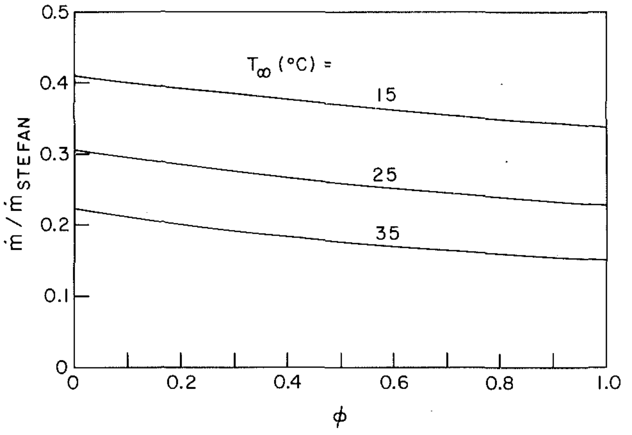

Fig. 1 Comparison of evaporation rates for nonisothermal and Stefan models

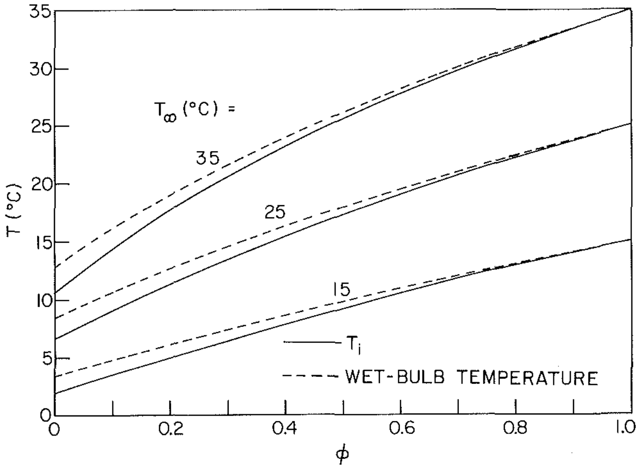

Fig. 2 Equilibrium temperature at the gas-liquid interface and thermodynamic wet-bulb temperature for various conditions at the top of the container

$$T_i = (h_{fg}/c_{p1})[1-\exp(\mathrm{Pe}_T)] + T_\infty \tag{22}$$

where $\mathrm{Pe}_T = \dot{m}_1 H c_{p1}/k$ is the heat transfer Peclet number. A numerical comparison of the $(T_i - T_\infty)/(h_{fg}/c_{p1})$ results from equations (20) and (22) shows that for $\mathrm{Pe}_T = 0.1$ and 0.01, the respective errors due to the linearization are 5 and 0.5 percent. Similarly, for values of the mass transfer Peclet number $\mathrm{Pe}_W = \dot{m}_1 H/\rho\mathfrak{D}$ equal to 0.1 and 0.01, the linearized-related errors in $\dot{m}_1$ are also 5 and 0.5 percent.

Application of the Solution

The foregoing nonisothermal evaporation model will now be applied to liquid water evaporating into ambient air. The water is situated in an open-topped container, and the walls of the container, including the bottom, are adiabatic. The ambient air is at one atmosphere pressure, and its relative humidity ϕ will be varied from 0 to 100 percent (the specification of ϕ is equivalent to the specification of $W_{1\infty}$ but conveys more physical content). In the calculations to be carried out, the temperature T_∞ at the top of the container will range from 15 to 35°C. The thermodynamic properties ρ_{1i} and h_{fg} needed in the calculations are obtained from [4]. Due to the negligible influence of the moisture on the thermal conductivity k [5], this quantity is evaluated as that for pure air from [6], p. 11. The diffusion coefficient $\mathfrak{D}$ was obtained from an empirical expression given in [7], p. 10, and the specific heat c_{p1} is taken from [8], p. 102. The equilibrium temperature T_i at the gas-liquid interface and the evaporation rate $\dot{m}_1$ (hereafter designated as $\dot{m}$) will be determined for each boundary condition pair (ϕ, T_∞) at the top of the container.

In Fig. 1, the evaporation rate obtained from the nonisothermal model is compared with that from the Stefan model via the ratio $\dot{m}/\dot{m}_{\mathrm{STEFAN}}$ which is plotted as a function of ϕ with T_∞ as the curve parameter. The figure shows that the ratio is always less than 1, as expected. For the range of parameters investigated here, the $\dot{m}$ values for the nonisothermal case range from 15 to 40 percent of the corresponding Stefan model. The magnitude of $\dot{m}/\dot{m}_{\mathrm{STEFAN}}$ is moderately affected by the relative humidity ϕ, and percentagewise, the influence of ϕ on $\dot{m}/\dot{m}_{\mathrm{STEFAN}}$ increases as T_∞ increases. Furthermore, the difference between $\dot{m}$ and $\dot{m}_{\mathrm{STEFAN}}$ is accentuated at higher ambient temperatures, a behavior which results from the greater difference between T_∞ and T_i at larger T_∞.

Figure 2 presents results for the interface temperature T_i for various conditions at the top of the container. To provide a basis for comparison, the adiabatic saturation temperature of the air T^+ (thermodynamic wet-bulb temperature), which corresponds to p, ϕ, and T_∞, is also plotted in the figure. As can be seen from Fig. 2, T_i is always less than the thermodynamic wet-bulb temperature. This behavior, which resembles the difference between the psychrometric wet-bulb temperature and the thermodynamic wet-bulb temperature ([9], p. 206), will now be explained.

An overall energy balance yields

$$h(T_\infty - T_i) = \rho K(W_{1i} - W_{1\infty})h_{fg} + \dot{m}c_{p1}(T_\infty - T_i) \tag{23}$$

where h and K are the heat and mass transfer coefficients, respectively. To determine under which circumstances the gas-liquid interface temperature T_i of equation (23) would be equal to the thermodynamic wet-bulb temperature T^+, it is convenient to work with a simplified but highly accurate expression for T^+. Such an expression can be derived by taking the density of the mixture to be that of dry air, and from any text on psychrometry (e.g., [9], p. 174)

$$c_p(T_\infty - T^+) = h_{fg}^+(W_{1i}^+ - W_{1\infty}) \tag{24}$$

where the subscript + refers to quantities evaluated at T^+. Now, comparing equations (23) and (24), the condition that yields $T_i = T^+$ emerges as

$$h/c_p\rho K = 1 + \dot{m}c_{p1}/c_p\rho K \tag{25}$$

It is relevant to determine the values of $h/c_p\rho K$ that correspond to $T_i < T^+$ and to $T_i > T^+$. To this end, the liquid-vapor equilibrium data for water may be used to establish the trendwise relationship between W_{1i} and T_i and between h_{fg} and T_i. With this information, it can be deduced from equations (23) and (24) that

$$h/c_p\rho K < 1 + \dot{m}c_{p1}/c_p\rho K, \quad \text{for} \quad T_i < T^+ \tag{26}$$

and

$$h/c_p\rho K > 1 + \dot{m}c_{p1}/c_p\rho K, \quad \text{for} \quad T_i > T^+ \tag{27}$$

The values of h and K from the present solution will now be determined in order to evaluate the ratio $h/c_p\rho K$ for comparison with expressions (25), (26), and (27). These quantities will be obtained from the defining equations

$$h = [\dot{m}h_{fg} + \dot{m}c_{p1}(T_\infty - T_i)]/(T_\infty - T_i) \tag{28}$$

and

$$K = \dot{m}/\rho(W_{1i} - W_{1\infty}) \tag{29}$$

By making use of the numerical results for the evaporation of water vapor into air, h and K were calculated from equations (28) and (29) and the ratio $h/c_p\rho K$ determined. The c_p which appears in the ratio is the specific heat of the mixture. It was evaluated at the reference state * by employing the relationship $c_p = W_1 c_{p1} + (1 - W_1)c_{p2}$, where c_{p1} and c_{p2} were taken from [8], p. 102 and p. 293, respectively.

Table 1 Values of $h/c_p\rho K$ for various conditions at the top of the container

	ϕ				
T_∞(°C)	0	0.25	0.5	0.75	$\rightarrow 1$
15	0.847	0.843	0.839	0.836	0.832
25	0.846	0.839	0.833	0.826	0.820
35	0.845	0.834	0.823	0.812	0.802

Table 1 shows the thus-obtained values of $h/c_p\rho K$ for various boundary conditions at the top of the container. All the values presented there are less than 1. Therefore, according to (26) (noticing that $\dot{m}c_{p1}/c_p\rho K$ is always positive), the equilibrium temperature at the gas–liquid interface should take on a value lower than T^+, thereby corroborating the results of Fig. 2.

Another feature of Fig. 2 is the sensitivity of the temperature depression $(T_\infty - T_i)$ to both T_∞ and ϕ. As expected, the depression decreases as ϕ increases for a fixed value of T_∞. For a fixed ϕ, the depression increases as T_∞ increases. For example, for $T_\infty = 35$°C and $\phi = 0$ prescribed at the top of the container, the difference between T_∞ and T_i is almost twice as large as the corresponding difference for $T_\infty = 15$°C and $\phi = 0$.

Acknowledgment

Support accorded to A. T. Prata by Universidade Federal de Santa Catarina and Conselho Nacional de Desenvolvimento Científico e Tecnológico (CNPq) of Brazil is gratefully acknowledged.

References

1 Burmeister, L. C., *Convective Heat Transfer*, John Wiley and Sons, New York, 1983.

2 Slattery, J. C., *Momentum, Energy and Mass Transfer in Continua* (2d ed.), Robert E. Krieger Publishing, Huntington, N.Y., 1981.

3 Nunez-Testa, G. A., "Evaporation in the Presence of Natural Convection and Nonuniform, Nonbuoyant Velocity Profiles," M.S. thesis, Department of Mechanical Engineering, University of Minnesota, Minneapolis, Minn., 1984.

4 Keenan, J. H., Keyes, F. G., Hill, P. G., and Moore, J. G., *Steam Tables*, John Wiley and Sons, New York, 1969.

5 Mason, E. A., and Monchick, L., "Survey of Equation of State and Transport Properties of Moist Gases," *Humidity and Moisture*, Vol. 3, edited by A. Wexler, Reinhold, New York, 1965, pp. 257–272.

6 *Tables of Thermodynamic and Transport Properties*, Pergamon Press, New York, 1960.

7 Sherwood, T. K., and Pigford, R. L., *Absorption and Extraction* (2d ed.), McGraw-Hill, New York, 1952.

8 Touloukian, Y. S., and Makita, T., *Specific Heat*, Vol. 6, Thermophysical Properties of Matter, IFI/Plenum, New York, 1970.

9 Threlkeld, J. L., *Thermal Environmental Engineering* (2d ed.), Prentice-Hall, Englewood Cliffs, N.J., 1970.

Vertical Circular Pin With Conjugated Natural Convection–Conduction Flow

Ming-Jer Huang(1), Chao-Kuang Chen(2), and J. W. Cleaver(3)

Nomenclature

f = dimensionless stream function
Gr_L = Grashof number, $g\,\beta(T_0 - T_\infty)L^3/\nu^2$
g = acceleration of gravity
h = local heat transfer coefficient
$\hat{h}$ = dimensionless local heat transfer coefficient, $hL/k\mathrm{Gr}_L^{1/4}$
k = fluid thermal conductivity
k_f = pin thermal conductivity
L = pin length
Nc = conjugated convection-conduction parameter, $2(kL/k_f r_0)\mathrm{Gr}_L^{1/4}$
Pr = Prandtl number
Q = overall heat transfer rate
q = local heat flux
r = radial coordinate
T = fluid temperature
T_0 = root temperature
T_f = pin surface temperature
T_∞ = ambient temperature
u,v = velocity components
x = axial coordinate
X = dimensionless axial coordinate, x/L

Greek Symbols

α = thermal diffusivity
β = thermal expansion coefficient
η = pseudosimilarity variable
θ = dimensionless temperature
θ_f = dimensionless pin temperature
θ_w = dimensionless surface temperature
ν = kinematic viscosity
λ = transverse curvature parameter, $2\sqrt{2}L/r_0\,\mathrm{Gr}_L^{1/4}$

Introduction

Recently, Sparrow and co-workers [1, 2] and Sunden [3] have studied the conjugated problems for a vertical plate fin. Huang and Chen [4] presented the problem of a vertical thin pin. Their conclusions are that the conventional fin model based on a uniform input value of the heat transfer coefficient leads to incorrect results. Even for natural convection flow, the local heat transfer coefficients are found not to decrease monotonically in the flow direction as is usual. Rather, the coefficient decreases at first, reaches its minimum, and then increases with increasing downstream distance [1].

The analysis of the present note focuses on the natural convection flow over a vertical circular pin. This type of pin fin is chosen so that one-dimensional condition in the longitudinal direction can be assumed and has a nonuniform temperature distribution. The temperature of the pin is strongly affected by the heat transfer coefficient, which is dependent on the ambient fluid flow. Hence, in order to determine the temperature of the pin, temperature must be coupled with the convective boundary layer equations and the energy equation of pin, thus making the attainment of results more complicated.

Analysis

Consider a vertical cylinder pin of radius r_0 which is extended from a wall at temperature T_0 and situated in an otherwise quiescent environment having temperature T_∞. Here if we assume $T_\infty < T_0$, the flow moves upward and the gravity g acts downward in the opposite direction to the flow. The coordinate system is illustrated in the inset of Fig. 1. By employing the Boussinesq approximation for the fluid properties, the natural convective boundary layer equations [5, 6] are

$$\frac{\partial(ru)}{\partial x} + \frac{\partial(rv)}{\partial r} = 0 \qquad (1)$$

$$u\frac{\partial u}{\partial x} + v\frac{\partial u}{\partial r} = g\beta(T - T_\infty) + \frac{\nu}{r}\frac{\partial}{\partial r}\left(r\frac{\partial u}{\partial r}\right) \qquad (2)$$

---

[1] Instructor; [2] Professor; Department of Mechanical Engineering, National Cheng Kung University, Tainan, Taiwan, Republic of China

[3] Senior Lecturer, Department of Mechanical Engineering, The University of Liverpool, Liverpool, England

Contributed by the Heat Transfer Division for publication in the JOURNAL OF HEAT TRANSFER. Manuscript received by the Heat Transfer Division January 23, 1984.

Table 1 Values of $h/c_p\rho K$ for various conditions at the top of the container

	ϕ				
T_∞(°C)	0	0.25	0.5	0.75	$\rightarrow 1$
15	0.847	0.843	0.839	0.836	0.832
25	0.846	0.839	0.833	0.826	0.820
35	0.845	0.834	0.823	0.812	0.802

Table 1 shows the thus-obtained values of $h/c_p\rho K$ for various boundary conditions at the top of the container. All the values presented there are less than 1. Therefore, according to (26) (noticing that $\dot{m}c_{p1}/c_p\rho K$ is always positive), the equilibrium temperature at the gas–liquid interface should take on a value lower than T^+, thereby corroborating the results of Fig. 2.

Another feature of Fig. 2 is the sensitivity of the temperature depression $(T_\infty - T_i)$ to both T_∞ and ϕ. As expected, the depression decreases as ϕ increases for a fixed value of T_∞. For a fixed ϕ, the depression increases as T_∞ increases. For example, for $T_\infty = 35$°C and $\phi = 0$ prescribed at the top of the container, the difference between T_∞ and T_i is almost twice as large as the corresponding difference for $T_\infty = 15$°C and $\phi = 0$.

Acknowledgment

Support accorded to A. T. Prata by Universidade Federal de Santa Catarina and Conselho Nacional de Desenvolvimento Científico e Tecnológico (CNPq) of Brazil is gratefully acknowledged.

References

1 Burmeister, L. C., *Convective Heat Transfer*, John Wiley and Sons, New York, 1983.

2 Slattery, J. C., *Momentum, Energy and Mass Transfer in Continua* (2d ed.), Robert E. Krieger Publishing, Huntington, N.Y., 1981.

3 Nunez-Testa, G. A., "Evaporation in the Presence of Natural Convection and Nonuniform, Nonbuoyant Velocity Profiles," M.S. thesis, Department of Mechanical Engineering, University of Minnesota, Minneapolis, Minn., 1984.

4 Keenan, J. H., Keyes, F. G., Hill, P. G., and Moore, J. G., *Steam Tables*, John Wiley and Sons, New York, 1969.

5 Mason, E. A., and Monchick, L., "Survey of Equation of State and Transport Properties of Moist Gases," *Humidity and Moisture*, Vol. 3, edited by A. Wexler, Reinhold, New York, 1965, pp. 257–272.

6 *Tables of Thermodynamic and Transport Properties*, Pergamon Press, New York, 1960.

7 Sherwood, T. K., and Pigford, R. L., *Absorption and Extraction* (2d ed.), McGraw-Hill, New York, 1952.

8 Touloukian, Y. S., and Makita, T., *Specific Heat*, Vol. 6, Thermophysical Properties of Matter, IFI/Plenum, New York, 1970.

9 Threlkeld, J. L., *Thermal Environmental Engineering* (2d ed.), Prentice-Hall, Englewood Cliffs, N.J., 1970.

Vertical Circular Pin With Conjugated Natural Convection–Conduction Flow

Ming-Jer Huang(1), **Chao-Kuang Chen**(2), **and J. W. Cleaver**(3)

Nomenclature

f = dimensionless stream function
Gr_L = Grashof number, $g\,\beta(T_0 - T_\infty)L^3/\nu^2$
g = acceleration of gravity
h = local heat transfer coefficient
$\hat{h}$ = dimensionless local heat transfer coefficient, $hL/k\mathrm{Gr}_L^{1/4}$
k = fluid thermal conductivity
k_f = pin thermal conductivity
L = pin length
Nc = conjugated convection-conduction parameter, $2(kL/k_f r_0)\mathrm{Gr}_L^{1/4}$
Pr = Prandtl number
Q = overall heat transfer rate
q = local heat flux
r = radial coordinate
T = fluid temperature
T_0 = root temperature
T_f = pin surface temperature
T_∞ = ambient temperature
u,v = velocity components
x = axial coordinate
X = dimensionless axial coordinate, x/L

Greek Symbols

α = thermal diffusivity
β = thermal expansion coefficient
η = pseudosimilarity variable
θ = dimensionless temperature
θ_f = dimensionless pin temperature
θ_w = dimensionless surface temperature
ν = kinematic viscosity
λ = transverse curvature parameter, $2\sqrt{2}L/r_0\,\mathrm{Gr}_L^{1/4}$

Introduction

Recently, Sparrow and co-workers [1, 2] and Sunden [3] have studied the conjugated problems for a vertical plate fin. Huang and Chen [4] presented the problem of a vertical thin pin. Their conclusions are that the conventional fin model based on a uniform input value of the heat transfer coefficient leads to incorrect results. Even for natural convection flow, the local heat transfer coefficients are found not to decrease monotonically in the flow direction as is usual. Rather, the coefficient decreases at first, reaches its minimum, and then increases with increasing downstream distance [1].

The analysis of the present note focuses on the natural convection flow over a vertical circular pin. This type of pin fin is chosen so that one-dimensional condition in the longitudinal direction can be assumed and has a nonuniform temperature distribution. The temperature of the pin is strongly affected by the heat transfer coefficient, which is dependent on the ambient fluid flow. Hence, in order to determine the temperature of the pin, temperature must be coupled with the convective boundary layer equations and the energy equation of pin, thus making the attainment of results more complicated.

Analysis

Consider a vertical cylinder pin of radius r_0 which is extended from a wall at temperature T_0 and situated in an otherwise quiescent environment having temperature T_∞. Here if we assume $T_\infty < T_0$, the flow moves upward and the gravity g acts downward in the opposite direction to the flow. The coordinate system is illustrated in the inset of Fig. 1. By employing the Boussinesq approximation for the fluid properties, the natural convective boundary layer equations [5, 6] are

$$\frac{\partial(ru)}{\partial x} + \frac{\partial(rv)}{\partial r} = 0 \tag{1}$$

$$u\frac{\partial u}{\partial x} + v\frac{\partial u}{\partial r} = g\beta(T - T_\infty) + \frac{\nu}{r}\frac{\partial}{\partial r}\left(r\frac{\partial u}{\partial r}\right) \tag{2}$$

---

[1] Instructor; [2] Professor; Department of Mechanical Engineering, National Cheng Kung University, Tainan, Taiwan, Republic of China

[3] Senior Lecturer, Department of Mechanical Engineering, The University of Liverpool, Liverpool, England

Contributed by the Heat Transfer Division for publication in the JOURNAL OF HEAT TRANSFER. Manuscript received by the Heat Transfer Division January 23, 1984.

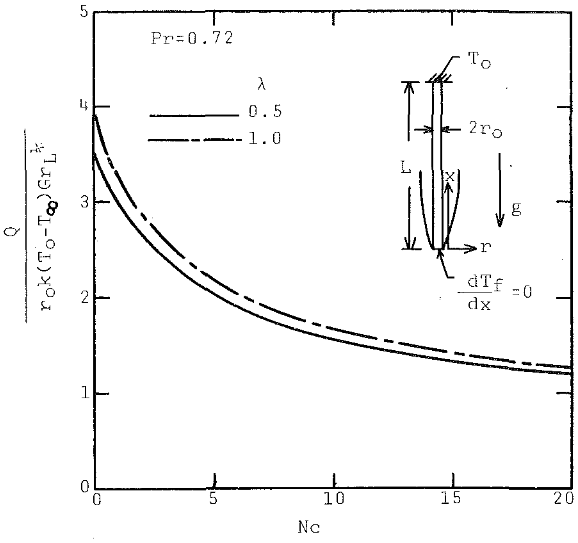

Fig. 1 Total heat transfer rate

$$u\frac{\partial T}{\partial x}+v\frac{\partial T}{\partial r}=\frac{\alpha}{r}\frac{\partial}{\partial r}\left(r\frac{\partial T}{\partial r}\right) \tag{3}$$

and the thin pin energy equation is

$$\frac{d^2(T_f-T_\infty)}{dx^2}=\frac{2h(x)}{k_f r_0}(T_f-T_\infty) \tag{4}$$

The equations (1-4) are subject to the following boundary conditions, respectively

$$\left.\begin{array}{lll} u=v=0, & T=T_w(x) & \text{at } r=r_0 \\ u\to 0, & T\to T_\infty & \text{at } r\to\infty \\ u=0, & T=T_\infty & \text{at } x=0, r>r_0 \\ T_f=T_0 & \text{at } x=L & \\ \frac{dT_f}{dx}=0 & \text{at } x=0 & \end{array}\right\} \tag{5}$$

Of particular interest is the thermal coupling between the pin and the convective boundary layer. The basic coupling is expressed by the requirement that the pin and fluid temperatures and heat fluxes be continuous for all x at the pin-fluid interface.

$$\left.\begin{array}{l} T_f(x)=T_w(x) \\ h(T_f-T_\infty)=-k\frac{\partial T}{\partial r}\Big|_{r=0} \end{array}\right\} \text{at } r=r_0, 0\leq x=L \tag{6}$$

Introducing dimensionless axial coordinate X and the pseudosimilarity variable η

$$X=\frac{x}{L},\quad \eta=\frac{r^2-r_0^2}{2\sqrt{2}Lr_0}(\mathrm{Gr}_L/X)^{1/4} \tag{7}$$

and the reduced stream function $f(X,\eta)$, the dimensionless temperature $\theta(X,\eta)$ and $\theta_f(X)$, are defined as, respectively

$$\left.\begin{array}{ll} f(X,\eta) & =\psi(x,r)[2\sqrt{2}\nu r_0 \mathrm{Gr}_L^{1/4}X^{1/4}] \\ \theta(X,\eta) & =(T-T_\infty)/(T_0-T_\infty) \\ \theta_f(X,\eta) & =(T_f-T_\infty)/(T_0-T_\infty) \end{array}\right\} \tag{8}$$

where the stream function $\psi(x, r)$ satisfies the continuity equation (1) with

$$ru=\frac{\partial\psi}{\partial r},\quad rv=-\frac{\partial\psi}{\partial x} \tag{9}$$

Combining equations (7) and (8) with equation (6) and substituting into equations (2-5), one obtains the transformed convective boundary layer equations as follows,

$$(1+\lambda\eta X^{1/4})f'''+(\lambda X^{1/4}+3f)f''-2f'^2+\theta =4X\left(f'\frac{\partial f'}{\partial X}-f''\frac{\partial f}{\partial X}\right) \tag{10}$$

$$\frac{1}{\mathrm{Pr}}(1+\lambda\eta X^{1/4})\theta''+\left(\frac{1}{\mathrm{Pr}}\lambda X^{1/4}+3f\right)\theta' =4X\left(f'\frac{\partial\theta}{\partial X}-\theta'\frac{\partial f}{\partial X}\right) \tag{11}$$

with

$$\begin{array}{l} f(X,0)=f'(X,0)=0,\quad \theta(X,0)=\theta_w(X) \\ f'(X,\infty)=\theta(X,\infty)=0 \end{array} \tag{12}$$

and the dimensionless energy equation of pin is

$$\frac{d^2\theta_f}{dX^2}=Nc\hat{h}\theta_f \tag{13}$$

with

$$\theta_f(X=1)=1,\quad \frac{d\theta_f(X=0)}{dX}=0 \tag{14}$$

In the foregoing equations, the standard symbols are defined in the Nomenclature and the transverse curvature parameter λ, the conjugated convective-conduction parameter Nc, and the dimensionless local heat transfer coefficient $\hat{h}(X)$ are given by

$$\left.\begin{array}{l} \lambda=2\sqrt{2}L/r_0\mathrm{Gr}_L^{1/4} \\ Nc=2KL\mathrm{Gr}_L^{1/4}/k_f r_0 \\ \hat{h}=\left[-\frac{\partial\theta}{\partial\eta}\Big/\theta_f\right]_{\eta=0}\Big/\sqrt{2}X^{1/4} \end{array}\right\} \tag{15}$$

Equations (10-14) are simultaneously solved by an efficient-implicit finite difference method [7] and direct inverse method. In order to assure the accuracy of present approach, the system can be reduced to the case of isothermal cylinder. The agreement between the results of Minkowycz and Sparrow [5] studied by the local nonsimilarity method and present work is excellent. Both the following results are calculated when $\lambda = 0.5$, $X = 1$, and $\mathrm{Pr} = 0.733$.

	$-\theta'(0)$	$f''(0)$
Present work	0.6127	0.6997
Minkowycz and Sparrow [5]	0.6156	0.7037

The complete descriptions of the method are available in [4]. Numerical results are presented for $\mathrm{Pr} = 0.72$ over a conjugated convection-conduction parameter of $Nc = 0.0$, 5.0, 20.0 and a transverse curvature parameter of $\lambda = 0.5$ and 1.0.

Results and Discussion

Numerical results of the overall rate of heat transfer Q from the pin can be obtained through the heat conducted from the wall into the pin base at $X = 1$ or from the integrating heat convection over the pin surface. The corresponding value of Q of these two methods is found to be in agreement. They may be expressed as

$$Q=k_f\pi r_0^2\frac{dT_f}{dx}\Big|_{x=L} \tag{16}$$

or

$$Q=2\pi r_0\int_0^L q\,dx \tag{17}$$

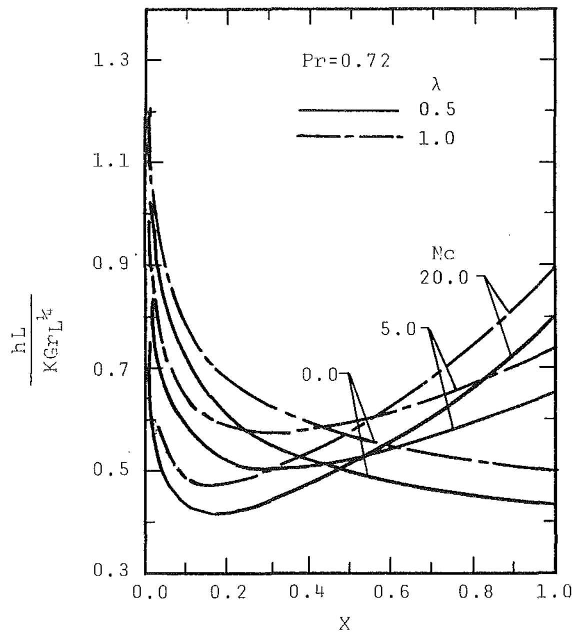

Fig. 2 Local heat transfer coefficients

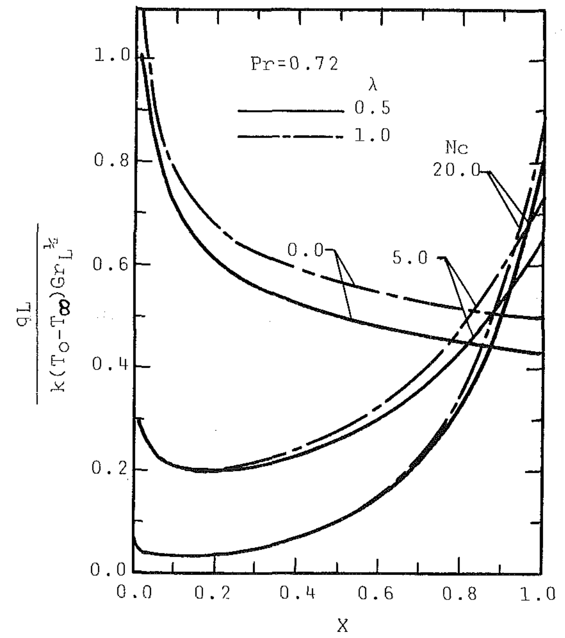

Fig. 3 Local heat fluxes

and the dimensionless form

$$\frac{Q}{r_0 k(T_0-T_\infty)\mathrm{Gr}_L{}^{1/4}} = \frac{2\pi}{Nc}\frac{d\theta_f}{dX}\bigg|_{X=1} \tag{18}$$

or

$$\frac{Q}{r_0 k(T_0-T_\infty)\mathrm{Gr}_L{}^{1/4}} = 2\pi\int_0^1 \frac{1}{\sqrt{2}X^{1/4}}\left[-\frac{\partial\theta}{\partial\eta}\right]_{\eta=0} dX \tag{19}$$

The results of overall heat transfer rate Q from the pin are presented as a function of the conjugated convection-conduction parameter Nc for two values of the transverse curvature parameter λ in Fig. 1. The downsloping trend of the curve indicates that the fin heat transfer increases as the fin conductance k_f increases.

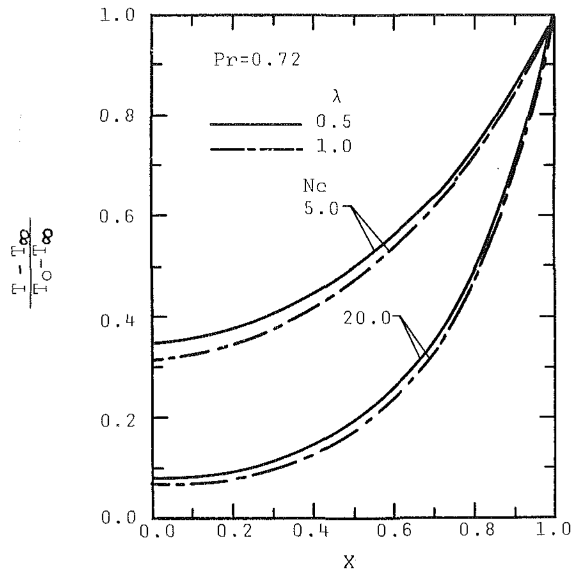

Fig. 4 Temperature distributions of pin

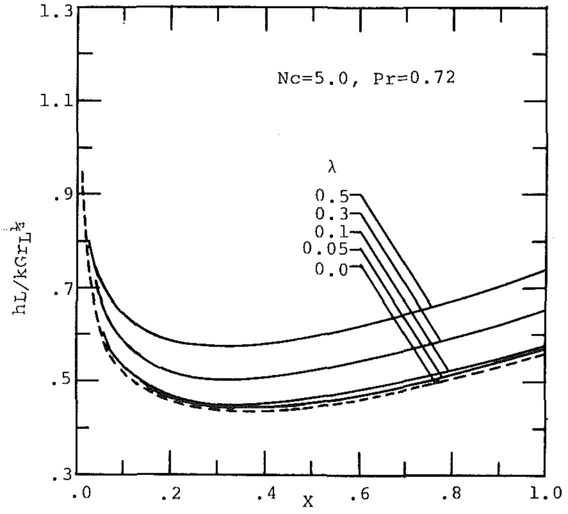

Fig. 5 Surface effect on the heat transfer coefficient

Figure 2 illustrates the distributions of the local natural convective heat transfer coefficient along the pin surface as a function of Nc for fixed $\lambda = 0.5$ and 1.0. The local heat transfer coefficient can be written as, in dimensionless form

$$\frac{hL}{k\mathrm{Gr}_L{}^{1/4}} = \frac{1}{\sqrt{2}X^{1/4}}\left[-\frac{\partial\theta}{\partial\eta}\Big/\theta_f\right]_{\eta=0} \tag{20}$$

Figure 2 contains three curves of $Nc = 0.0$, 5.0, and 20.0 for each transverse curvature parameter. The greater value of Nc indicates the smaller pin conductance. It is also shown that the greater variation of the response of the natural convective heat transfer coefficient, the greater the streamwise variation of the pin temperature for a given transverse curvature of cylinder.

As seen from Fig. 2, when Nc is near 0, h decreases monotonically from the tip to the root. But at higher value of Nc, the distribution of the heat transfer coefficient first decreases to some minimum value, and then increases steadily with X. The position of the minimum value approaches to the tip as Nc increases.

The foregoing phenomenon is the same as that of the natural convective flow over a vertical plate fin [1], which is attributed to enhanced buoyancy force associated with an increase in the wall-to-fluid temperature difference along the streamwise direction.

Similarly, the heat transfer coefficient increases as the transverse curvature of the pin increases.

The distributions of the dimensionless local convective heat flux at the pin surface are shown in Fig. 3 as a function of X, for Nc and λ, respectively. The local heat flux can be taken as

$$\frac{qL}{k(T_0 - T_\infty)\mathrm{Gr}_L^{1/4}} = \frac{1}{\sqrt{2}X^{1/4}}\left[-\frac{\partial\theta}{\partial\eta}\right]_{\eta=0} \qquad (21)$$

Figure 3 shows that for a given transverse curvature the total heat transfer rate, the area under the curve, increases as Nc decreases, which agrees with the prediction in Fig. 1.

Representative results for the pin temperature distibution are presented in Fig. 4 for two different transverse curvature cases. Each case contains the pin temperature distribution as a function of Nc. Figure 4 also shows the expected trend whereby the pin temperature decreases monotonically from the root to the tip. Figure 4 also confirms the assertions that the increasing value of Nc gives the increasing pin temperature variation.

To provide an understanding of what value of the surface curvature the cylinder pin and the plate fin can be essentially regarded as the same. As inspection of Fig. 5 reveals that for a given $Nc = 5.0$, the local heat transfer coefficient $\hat{h}$ increases with increasing surface curvature λ. The dotted line is the coefficient of the vertical flat plate fin (i.e., $\lambda = 0$). From the results presented in Fig. 5, the surface curvature effect on the local heat transfer coefficient, the maximum difference of the local heat transfer coefficient between the cylinder and the plate, is found to be less than 5 percent when $\lambda \leq 0.1$. Therefore, a cylinder pin can be reduced to a plate fin as $\lambda \leq 0.1$.

Conclusion

The present analysis of the laminar free convective flow over a vertical cylinder pin has been studied. The local heat transfer coefficient along the pin is simultaneously solved for the laminar free convective boundary layer equations of the fluid and the energy equation of the pin.

An efficient implicit finite difference technique is employed. The results show that the local heat transfer coefficient along the streamwise direction does not monotonically decrease but decreases at first, reaches its minimum value and then increases. This phenomenon is more obvious when the variation of the pin temperature is more nonuniform.

References

1 Sparrow, E. M., and Acharya, S., "A Natural Convection Fin With a Solution-Determined Nonmonotonically Varying Heat Transfer Coefficient," ASME JOURNAL OF HEAT TRANSFER, Vol. 103, 1981, pp. 218-225.

2 Sparrow, E. M., and Chyu, M. K., "Conjugated Forced Convection-Conduction Analysis of Heat Transfer in a Plate Fin," ASME JOURNAL OF HEAT TRANSFER, Vol. 104, 1982, pp. 204-206.

3 Sunden, B., "Conjugate Mixed Convection Heat Transfer From a Vertical Rectangular Fin," *Int. Comm. Heat Mass Transfer*, Vol. 10, 1983, pp. 267-276.

4 Huang, M. J., and Chen, C. K., "Vertical Circular Pin with Conjugate Forced Convection-Conduction Flow," ASME JOURNAL OF HEAT TRANSFER, Vol. 106, 1984, pp. 658-661.

5 Minkowycz, W. J., and Sparrow, E. M., "Local Nonsimilar Solutions for Natural Convection on a Vertical Cylinder," ASME JOURNAL OF HEAT TRANSFER, Vol. 96, 1978, pp. 178-183.

6 Cebeci, T., "Laminar-Free-Convective-Heat Transfer From the Outer Surface of a Vertical Slender Circular Cylinder," *Proc. Fifth Intl. Heat Transfer Conference*, Paper NC1.4, 1974, pp. 15-19.

7 Cebeci, T., and Bradshaw, P., Momentum Transfer in Boundary Layers, Hemisphere Publishing, Washington, D.C., 1977.

Quasi-Three-Dimensional Steady-State Analytic Solution for Melting or Freezing Around a Buried Pipe in a Semi-Infinite Medium

Guo-Ping Zhang[1], L. M. Jiji[2], and S. Weinbaum[2]

Nomenclature

a = pipe radius
C_p = specific heat of fluid
h_o = dimensionless pipe center position below free surface = $\tilde{h}_o/a$
h_i = dimensionless position of center of interface circle below free surface = $\tilde{h}_i/a$
i = $\sqrt{-1}$
k_1, k_2 = thermal conductivity of zone 1 and 2, respectively
k_a = thermal conductivity of fluid
L = latent heat of phase change medium
Pe^* = modified Peclet number, $\mathrm{Pe}^* = (k_a/k_2)\mathrm{Pe} = (k_a/k_2)(\rho C_p \bar{u} a/k_a)$
$\tilde{r}, \phi, \tilde{z}$ = interface cylindrical coordinates, Fig. 1
$\tilde{r}_p, \phi, \tilde{z}$ = pipe cylindrical coordinates, Fig. 1
r_i = dimensionless interface radius = $\tilde{r}_i/a$
R, α = cylindrical coordinates in complex plane, Fig. 2
R_o = $h_o + (h_o^2 - 1)^{1/2}$
R_i = interface radius in complex plane
T_o = free surface temperature
T_1, T_2 = temperature of zone 1 and 2, respectively
T_a = fluid bulk temperature, equal to surface temperature of pipe
T_{a_o} = fluid entrance temperature
T_f = freezing temperature
$\bar{u}$ = average velocity of fluid
u, v = Cartesian coordinates in complex plane, Fig. 2
W = $u + iv$, conformal transformation defined by equation (1)
$\tilde{x}, \tilde{y}, \tilde{z}$ = Cartesian coordinates, Fig. 1
x, y, z = dimensionless Cartesian coordinates, $x = \tilde{x}/a$, $y = \tilde{y}/a$, $z = \tilde{z}/a$
Z = $x + iy$, complex variable
$z_{\max}$ = dimensionless distance along pipe where $r_i = 1$
$\delta_i \equiv h_i - r_i$
θ_1 = dimensionless temperature of zone 1, $\theta_1 = (T_1 - T_o)/(T_f - T_o)$
θ_2 = dimensionless temperature of zone 2, $\theta_2 = (T_2 - T_a)/(T_f - T_a)$
θ_a = dimensionless fluid bulk temperature, $\theta_a = (k_2/k_1)(T_a - T_f)/(T_f - T_o)$
θ_{a_o} = $(k_2/k_1)(T_{a_o} - T_f)/(T_f - T_o)$
ρ, ρ_1 = density of fluid and phase change medium, respectively

---

[1] Graduate Student; [2] Herbert Kayser Professor, Department of Mechanical Engineering, The City College of The City University of New York, Mem. ASME

Contributed by the Heat Transfer Division for publication in the JOURNAL OF HEAT TRANSFER. Manuscript received by the Heat Transfer Division October 19, 1983.

attributed to enhanced buoyancy force associated with an increase in the wall-to-fluid temperature difference along the streamwise direction.

Similarly, the heat transfer coefficient increases as the transverse curvature of the pin increases.

The distributions of the dimensionless local convective heat flux at the pin surface are shown in Fig. 3 as a function of X, for Nc and λ, respectively. The local heat flux can be taken as

$$\frac{qL}{k(T_0-T_\infty)\mathrm{Gr}_L{}^{1/4}} = \frac{1}{\sqrt{2}X^{1/4}}\left[-\frac{\partial\theta}{\partial\eta}\right]_{\eta=0} \tag{21}$$

Figure 3 shows that for a given transverse curvature the total heat transfer rate, the area under the curve, increases as Nc decreases, which agrees with the prediction in Fig. 1.

Representative results for the pin temperature distibution are presented in Fig. 4 for two different transverse curvature cases. Each case contains the pin temperature distribution as a function of Nc. Figure 4 also shows the expected trend whereby the pin temperature decreases monotonically from the root to the tip. Figure 4 also confirms the assertions that the increasing value of Nc gives the increasing pin temperature variation.

To provide an understanding of what value of the surface curvature the cylinder pin and the plate fin can be essentially regarded as the same. As inspection of Fig. 5 reveals that for a given $Nc = 5.0$, the local heat transfer coefficient $\hat{h}$ increases with increasing surface curvature λ. The dotted line is the coefficient of the vertical flat plate fin (i.e., $\lambda = 0$). From the results presented in Fig. 5, the surface curvature effect on the local heat transfer coefficient, the maximum difference of the local heat transfer coefficient between the cylinder and the plate, is found to be less than 5 percent when $\lambda \leq 0.1$. Therefore, a cylinder pin can be reduced to a plate fin as $\lambda \leq 0.1$.

Conclusion

The present analysis of the laminar free convective flow over a vertical cylinder pin has been studied. The local heat transfer coefficient along the pin is simultaneously solved for the laminar free convective boundary layer equations of the fluid and the energy equation of the pin.

An efficient implicit finite difference technique is employed. The results show that the local heat transfer coefficient along the streamwise direction does not monotonically decrease but decreases at first, reaches its minimum value and then increases. This phenomenon is more obvious when the variation of the pin temperature is more nonuniform.

References

1 Sparrow, E. M., and Acharya, S., "A Natural Convection Fin With a Solution-Determined Nonmonotonically Varying Heat Transfer Coefficient," ASME JOURNAL OF HEAT TRANSFER, Vol. 103, 1981, pp. 218-225.

2 Sparrow, E. M., and Chyu, M. K., "Conjugated Forced Convection-Conduction Analysis of Heat Transfer in a Plate Fin," ASME JOURNAL OF HEAT TRANSFER, Vol. 104, 1982, pp. 204-206.

3 Sunden, B., "Conjugate Mixed Convection Heat Transfer From a Vertical Rectangular Fin," *Int. Comm. Heat Mass Transfer*, Vol. 10, 1983, pp. 267-276.

4 Huang, M. J., and Chen, C. K., "Vertical Circular Pin with Conjugate Forced Convection-Conduction Flow," ASME JOURNAL OF HEAT TRANSFER, Vol. 106, 1984, pp. 658-661.

5 Minkowycz, W. J., and Sparrow, E. M., "Local Nonsimilar Solutions for Natural Convection on a Vertical Cylinder," ASME JOURNAL OF HEAT TRANSFER, Vol. 96, 1978, pp. 178-183.

6 Cebeci, T., "Laminar-Free-Convective-Heat Transfer From the Outer Surface of a Vertical Slender Circular Cylinder," *Proc. Fifth Intl. Heat Transfer Conference*, Paper NC1.4, 1974, pp. 15-19.

7 Cebeci, T., and Bradshaw, P., Momentum Transfer in Boundary Layers, Hemisphere Publishing, Washington, D.C., 1977.

Quasi-Three-Dimensional Steady-State Analytic Solution for Melting or Freezing Around a Buried Pipe in a Semi-Infinite Medium

Guo-Ping Zhang[1], **L. M. Jiji**[2], **and S. Weinbaum**[2]

Nomenclature

a = pipe radius
C_p = specific heat of fluid
h_o = dimensionless pipe center position below free surface = $\tilde{h}_o/a$
h_i = dimensionless position of center of interface circle below free surface = $\tilde{h}_i/a$
i = $\sqrt{-1}$
k_1, k_2 = thermal conductivity of zone 1 and 2, respectively
k_a = thermal conductivity of fluid
L = latent heat of phase change medium
Pe^* = modified Peclet number, $\mathrm{Pe}^* = (k_a/k_2)\mathrm{Pe} = (k_a/k_2)(\rho C_p \bar{u} a/k_a)$
$\tilde{r}, \phi, \tilde{z}$ = interface cylindrical coordinates, Fig. 1
$\tilde{r}_p, \phi, \tilde{z}$ = pipe cylindrical coordinates, Fig. 1
r_i = dimensionless interface radius = $\tilde{r}_i/a$
R, α = cylindrical coordinates in complex plane, Fig. 2
R_o = $h_o + (h_o{}^2 - 1)^{1/2}$
R_i = interface radius in complex plane
T_o = free surface temperature
T_1, T_2 = temperature of zone 1 and 2, respectively
T_a = fluid bulk temperature, equal to surface temperature of pipe
T_{a_o} = fluid entrance temperature
T_f = freezing temperature
$\bar{u}$ = average velocity of fluid
u, v = Cartesian coordinates in complex plane, Fig. 2
W = $u + iv$, conformal transformation defined by equation (1)
$\tilde{x}, \tilde{y}, \tilde{z}$ = Cartesian coordinates, Fig. 1
x, y, z = dimensionless Cartesian coordinates, $x = \tilde{x}/a$, $y = \tilde{y}/a$, $z = \tilde{z}/a$
Z = $x + iy$, complex variable
$z_{\max}$ = dimensionless distance along pipe where $r_i = 1$
$\delta_i \equiv h_i - r_i$
θ_1 = dimensionless temperature of zone 1, $\theta_1 = (T_1 - T_o)/(T_f - T_o)$
θ_2 = dimensionless temperature of zone 2, $\theta_2 = (T_2 - T_a)/(T_f - T_a)$
θ_a = dimensionless fluid bulk temperature, $\theta_a = (k_2/k_1)(T_a - T_f)/(T_f - T_o)$
θ_{a_o} = $(k_2/k_1)(T_{a_o} - T_f)/(T_f - T_o)$
ρ, ρ_1 = density of fluid and phase change medium, respectively

---

[1] Graduate Student; [2] Herbert Kayser Professor, Department of Mechanical Engineering, The City College of The City University of New York, Mem. ASME

Contributed by the Heat Transfer Division for publication in the JOURNAL OF HEAT TRANSFER. Manuscript received by the Heat Transfer Division October 19, 1983.

Introduction

Interest in energy storage systems, pipeline liquid transport in permafrost regions, and cryosurgery has focused attention on the problem of melting or freezing outside fluid carrying pipes. A representative model for such problems is shown in Fig. 1. The free surface, $\tilde{y} = 0$, of the semi-infinite phase change material (PCM) is maintained at a uniform temperature T_o, which is below the freezing temperature T_f of the PCM. A thin-walled pipe of radius a is buried in the PCM at a distance $\tilde{h}_o$ below the surface $\tilde{y} = 0$. Fluid enters the pipe at $\tilde{z} = 0$ with a uniform temperature T_{a_o}, where $T_{a_o} > T_f$ and flows with a constant average velocity $\bar{u}$.

While the analysis accounts for the effects of planar surface, thermal interaction between the PCM and the fluid, the axial variation throughout the system, it is limited to steady-state conditions. The available steady-state solution to the corresponding two-dimensional buried pipe problem is utilized in a surprisingly simple scheme to obtain a closed-form analytic solution to this three-dimensional problem. The solution neglects axial conduction and free convection and assumes constant properties and locally uniform temperature along the pipe axis.

The approach used to solve this problem can be extended to treat the corresponding transient case. A brief discussion on this extension is presented at the end of the following section.

Analysis

Three zones are identified in the system under consideration in Fig. 1. Zones 1 and 2 are the frozen and thawed regions of the PCM, respectively. Here $T_o < T_f < T_{a_o}$. However, the mathematical formulation and solution are the same for the corresponding case of $T_o > T_f > T_{a_o}$. Zone 3 is the pipe interior in which the moving fluid interacts thermally with zone 2.

Two coordinate systems, $\tilde{x}$, $\tilde{y}$, $\tilde{z}$ and $\tilde{r}_p$, ϕ, $\tilde{z}$, are used to describe the problem mathematically (see Fig. 1). Another set of cylindrical coordinates ($\tilde{r}$, ϕ, $\tilde{z}$) is used to define the phase change interface. Since the interface at any axial distance $\tilde{z}$ is circular with a radius $\tilde{r}_i(\tilde{z})$, the origin of this system is at $\tilde{x} = \tilde{z} = 0$ and $\tilde{y} = -\tilde{h}_i(\tilde{z})$, which is the center of the circle $\tilde{r}_i(\tilde{z})$ in the $\tilde{x}\tilde{y}$-plane. Details of the mathematical formulation and solution are given in [1]. A brief summary will be presented here.

Based on the model described here, the governing equations for the temperature distribution in zones 1 and 2 are the two-dimensional Laplace's equations, subject to Dirichlet boundary conditions in the plane normal to the pipe axis. Using conformal mapping [2], the pipe surface and free surface as well as all isotherms, including the interface, are mapped into concentric circles in the complex W-plane. The bicircular transformation W is shown in Fig. 2 and is given by

$$W = \frac{R_o Z + (R_o h_o - 1)i}{(R_o - h_o) + Zi} \qquad (1)$$

where $h_o = \tilde{h}_o/a$, $R_o = h_o + (h_o^2 - 1)^{1/2}$, and $i = \sqrt{-1}$. The two dimensionless temperature fields θ_1 and θ_2 can be solved in terms of the local unknown dimensionless interface radius $R_i(z)$. Details of the solution for θ_1 and θ_2 are found in [2].

The three-dimensional character of the problem is attributed to the thermal interaction with the pipe wall, i.e., $\theta_a(z)$. The relationship between $R_i(z)$ and $\theta_a(z)$ is established by the interface energy equation

$$\frac{\partial\theta_1(R_i,\alpha,z)}{\partial R} + \theta_a(z)\,\frac{\partial\theta_2(R_i,\alpha,z)}{\partial R} = 0 \qquad (2)$$

where θ_a is dimensionless fluid bulk temperature in zone 3 and R is the radial coordinate in the complex plane.

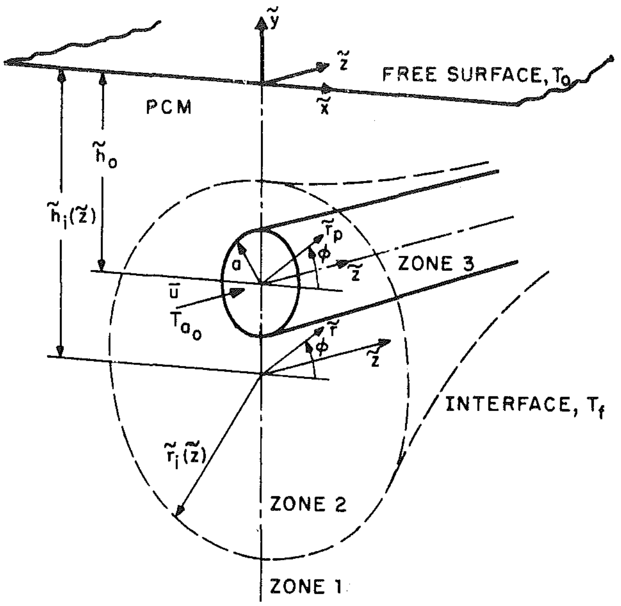

Fig. 1 Configuration and coordinate system

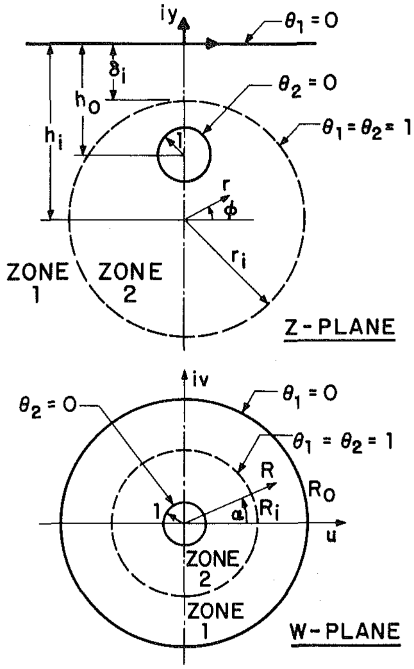

Fig. 2 Two-dimensional problem in physical and transformed planes

Conservation of energy for the fluid in the pipe is given by

$$-\frac{\pi \mathrm{Pe}^*}{\theta_a}\frac{d\theta_a}{dz} = \int_0^{2\pi} \frac{\partial\theta_2(1,\alpha,z)}{\partial R}\,d\alpha \qquad (3)$$

where Pe* is a modified Peclet number.

Substituting the solutions for θ_1 and θ_2 in the interface condition (2), an equation relating $\theta_a(z)$ to $R_i(z)$ is obtained. Another equation is obtained by substituting θ_2 into the fluid energy equation (3) and solving the resulting differential equation using the entrance condition $\theta_a(0) = \theta_{a_o}$. The two equations are then solved for $\theta_a(z)$ and $R_i(z)$. The solution for $\theta_a(z)$ is given by

$$\frac{1+\theta_a}{1+\theta_{a_o}} = \exp\left(-\frac{2}{\ln R_o}\,\frac{z}{\mathrm{Pe}^*}\right) \qquad (4)$$

Since the radius $r_i(z)$ and location of the origin $h_i(z)$ of the circular interface in the physical plane are geometrically

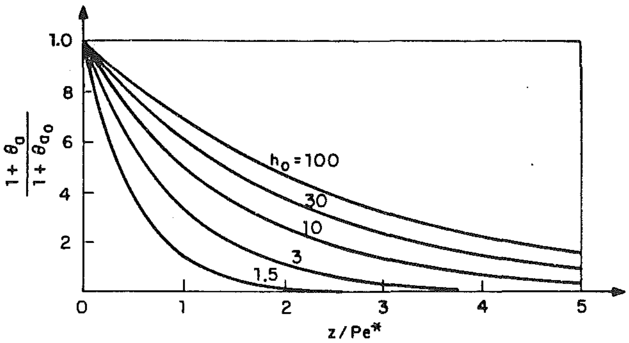

Fig. 3 Axial variation of fluid temperature in pipe

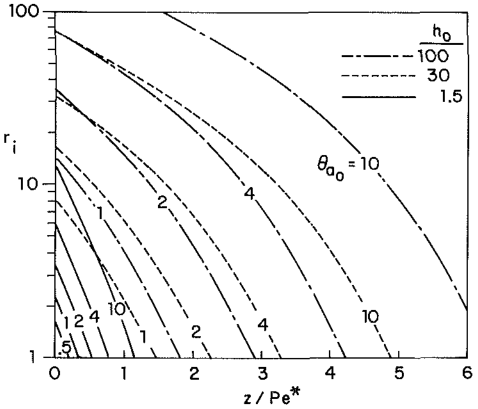

Fig. 4 Axial variation of interface radius

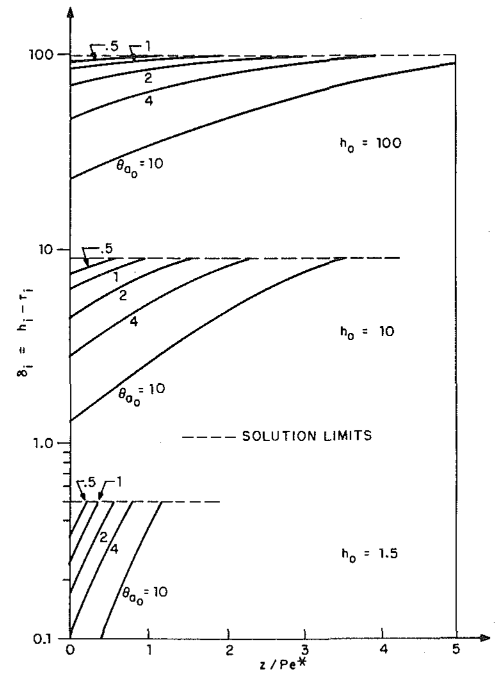

Fig. 5 Axial variation of interface depth below free surface

determined by $R_i(z)$ in transformation (1), the interface position $r_i(z)$ is given by

$$r_i(z) = \frac{(R_o^2 - 1)}{R_o} \frac{R_o^{\frac{1}{(1+\theta_{a_o})} \exp\left(\frac{2}{\ln R_o} \frac{z}{\mathrm{Pe}^*}\right)}}{R_o^{\frac{1}{(1+\theta_{a_o})} \exp\left(\frac{2}{\ln R_o} \frac{z}{\mathrm{Pe}^*}\right)} - 1} \tag{5}$$

and the depth of the interface below the planar surface $\delta_i(z) = h_i - r_i$ is given by

$$\delta_i(z) = h_o - R_o \frac{1 + R_o^{\frac{1}{(1+\theta_{a_o})} \exp\left(\frac{2}{\ln R_o} \frac{z}{\mathrm{Pe}^*}\right) - 2}}{1 + R_o^{\frac{1}{(1+\theta_{a_o})} \exp\left(\frac{2}{\ln R_o} \frac{z}{\mathrm{Pe}^*}\right)}} \tag{6}$$

The solution is valid up to a maximum axial distance $z_{\max}$ where the interface intersects the pipe. Noting that $\theta_a = 0$ at $z = z_{\max}$, equation (4) gives

$$\frac{z_{\max}}{\mathrm{Pe}^*} = \frac{1}{2}(\cosh^{-1} h_o) \ln(1 + \theta_{a_o}) \tag{7}$$

The relatively simple algebraic relationship between R_i and θ_a given by equation (2) does not carry over to the transient quasi-steady analysis even if one assumes that the isotherms are eccentric circles of the steady-state solution. In the transformed W-plane one would obtain concentric circles where the interface energy equation is given by

$$\frac{K_1(T_f - T_o)}{a^2 \rho_1 L} \left[\frac{\partial \theta_1(R_i, \alpha, z, t)}{\partial R} + \theta_a(z,t) \frac{\partial \theta_2(R_i, \alpha, z, t)}{\partial R} \right] = \frac{\partial R_i}{\partial t} \left| \frac{dZ}{dW} \right|^2 \tag{8}$$

Equation (8) can be solved relatively easily for two cases (*i*) the steady-state where equation (8) reduces to equation (2) when $\partial R_i / \partial t = 0$, and (*ii*) the transient two-dimensional approximation where θ_a is constant and equation (8) can be solved numerically for R_i as a function of time. The solution to equations (3) and (8) for the more general case where $\theta_a = \theta_a(z,t)$ is currently in progress. Finally it should be emphasized that the approximate solution procedure just outlined for the transient problem where the phase change starts at the pipe surface cannot be applied to the case where the interface commences at the free surface. In the latter case the interface cannot be even approximately described by eccentric circles.

Results

Examination of the closed-form analytic solution shows that the problem is characterized by three dimensionless parameters: h_o, θ_{a_o}, and Pe*. The effect of these parameters on the solution is presented in Figs. 3–5. Fluid temperature variation in the axial direction $\theta_a(z)$ is plotted in Fig. 3 for various values of h_o. As might be expected, the temperature gradient increases as the burial distance h_o is decreased. Figure 4 shows the radius of the cylindrical interface surface $r_i(z)$, which is seen to decrease axially. Furthermore, a decrease in h_o or θ_{a_o} causes r_i to decrease at a given axial distance z. The effects of h_o and θ_{a_o} on the distance between the planar surface and the uppermost position of the interface $\delta_i = h_i - r_i$ is presented in Fig. 5.

Acknowledgment

This study was sponsored by the National Science Foundation under Grant No. MEA 8209034.

References

1 Zhang, G. P., Jiji, L. M., and Weinbaum, S., "Three-Dimensional Steady-State Analytic Solution for Melting or Freezing Around a Buried Pipe in a Semi-Infinite Medium," ASME Paper No. 83-HT-20, presented at the 21st National Heat Transfer Conference, Seattle, July 24–27, 1983.

2 Lunardini, V. J., *Heat Transfer in Cold Climates*, Van Nostrand Reinhold, New York, 1981.

Heat Transfer Characteristics of a Continuous, Stretching Surface With Variable Temperature

L. J. Grubka[1,2] **and K. M. Bobba**[1]

Nomenclature

A = constant
B = constant
c = specific heat
F = dimensionless stream function defined by equation (4)
M = Kummer's function defined by equation (9)
Pr = Prandtl number, ν/α
q = local heat transfer rate per unit area, $-k(\partial T/\partial y)$
u = velocity component in the x-direction
v = velocity component in the y-direction
x = coordinate measuring distance in direction of surface motion
y = coordinate measuring distance normal to surface
α = thermal diffusivity
γ = temperature parameter
η = dimensionless similarity variable, $y(B/\nu)^{1/2}$
θ = dimensionless temperature, $T-T_\infty/T_w-T_\infty$
ν = kinematic viscosity
ξ = dimensionless function, $-\text{Pr}\exp(-\eta)$
ψ = stream function

Subscripts

w = continuous surface conditions
∞ = ambient conditions

Introduction

The continuous surface heat transfer problem has many practical applications in industrial manufacturing processes. Since the pioneering work of Sakiadis [1, 2], various aspects of the problem have been investigated by many authors. Most studies have been concerned with constant surface velocity and temperature (see, for example, Tsou et al. [3]) but for many practical applications the surface undergoes stretching and cooling or heating that cause surface velocity and temperature variations. Crane [4], Vleggaar [5], and Gupta and Gupta [6] have analyzed the stretching problem with constant surface temperature while Soundalgekar and Ramana Murty [7] investigated the constant surface velocity case with power law temperature variation. In the present paper the effect of power law surface temperature variation on the heat transfer characteristics of a continuous, linearly stretching surface is analyzed. A series solution to the energy equation in terms of Kummer's functions is developed for the specified problem. Several closed-form analytical solutions are also reported for specific conditions.

Analysis

The laminar velocity and thermal boundary layers on a continuous stretching surface with velocity $u_w = Bx$ and temperature $T_w = T_\infty + Ax^\gamma$ moving axially through a stationary incompressible fluid with constant physical properties and temperature T_∞ may be described using normal boundary layer approximations by the following continuity, momentum, and energy equations

$$\frac{\partial u}{\partial x} + \frac{\partial v}{\partial y} = 0 \tag{1}$$

$$u\frac{\partial u}{\partial x} + v\frac{\partial u}{\partial y} = \nu\frac{\partial^2 u}{\partial y^2} \tag{2}$$

$$u\frac{\partial T}{\partial x} + v\frac{\partial T}{\partial y} = \alpha\frac{\partial^2 T}{\partial y^2} \tag{3}$$

with the boundary conditions

$u = Bx,\ v = 0,\ T = T_\infty + Ax^\gamma$ at $y = 0$

$u \to 0,\ T \to T_\infty$ as $y \to \infty$

The x-axis runs along the continuous surface in the direction of motion, and the y-axis is perpendicular to it; u and v are the velocity components in the direction of x and y, respectively.

The solution of equation (1) may be written in terms of the stream function ψ defined by the relations

$$u = \frac{\partial\psi}{\partial y},\ v = \frac{-\partial\psi}{\partial x}$$

Introducing the usual similarity transformations and dimensionless temperature

$$\eta = y(B/\nu)^{1/2},\ F = \frac{\psi}{x(\nu B)^{1/2}},\ \theta = \frac{T-T_\infty}{T_w - T_\infty} \tag{4}$$

the momentum equation (2) and energy equation (3) can be written as

$$F''' + FF'' - (F')^2 = 0 \tag{5}$$

$$\theta'' + \text{Pr}F\theta' - \gamma\text{Pr}F'\theta = 0 \tag{6}$$

with the boundary conditions

$F(0) = 0,\ F'(0) = 1,\ \theta(0) = 1$

$F'(\infty) \to 0,\ \theta(\infty) \to 0$

where primes denote order of differentiation with respect to η. The solution of equation (5) was shown by Crane [4][3] to be

$F = 1 - e^{-\eta}$

Introducing a new variable ξ as

$\xi = -\text{Pr}e^{-\eta}$

and substituting the solution for F into equation (6) gives

$$\xi\frac{d^2\theta}{d\xi^2} + (1 - \text{Pr} - \xi)\frac{d\theta}{d\xi} + \gamma\theta = 0 \tag{7}$$

with the appropriate boundary conditions

$\theta(-\text{Pr}) = 1$

$\theta(0) \to 0$

It can be readily demonstrated that the solution of equation (7) in terms of Kummer's functions [8] is

$$\theta = \left(\frac{-\xi}{\text{Pr}}\right)^{\text{Pr}} \frac{M(\text{Pr}-\gamma, \text{Pr}+1, \xi)}{M(\text{Pr}-\gamma, \text{Pr}-1, -\text{Pr})} \tag{8}$$

where

$$M(a,b,z) = 1 + \sum_{n=1}^{\infty} \frac{a_n}{b_n}\frac{z^n}{n!}$$

---

[1] Owens-Corning Fiberglas Corporation, Technical Center, Granville, Ohio 43023

[2] Assoc. Mem. ASME

Contributed by the Heat Transfer Division for publication in the JOURNAL OF HEAT TRANSFER. Manuscript received by the Heat Transfer Division October 17, 1983.

[3] Crane's solution to the boundary layer equations also happens to be an exact solution to the Navier-Stokes equations.

Table 1 Temperature and wall gradient expressions for various Prandtl numbers and temperature parameter values

γ	Pr	θ	$\theta'(0)$
-2	Pr	$(1+\mathrm{Pr}-\mathrm{Pr}(e^{-\eta}))\exp(\mathrm{Pr}(1-\eta-e^{-\eta}))$	Pr
-1	Pr	$\exp(\mathrm{Pr}(1-\eta-e^{-\eta}))$	0
0	1	$\frac{e}{1-e}(\exp(-e^{-\eta})-1)$	$\frac{1}{1-e}$
Pr	γ	$e^{-\mathrm{Pr}(\eta)}$	$-\mathrm{Pr}$

Table 2 Wall temperature gradient as a function of Prandtl number and temperature parameter

	$\theta'(0)$					
γ \ Pr	.01	.72	1.0	3.0	10.0	100.0
-3	0.0201	2.2500	4.0000	-12.0000	-5.0000	-4.0816
-2	0.0100	0.7200	1.0000	3.0000	10.0000	100.0000
-1	0.0	0.0	0.0	0.0	0.0	0.0
0	-0.0099	-0.4631	-0.5820	-1.1652	-2.3080	-7.7657
1	-0.0197	-0.8086	-1.0000	-1.9237	-3.7207	-12.2940
2	-0.0294	-1.0885	-1.3333	-2.5097	-4.7969	-15.7120
3	-0.0390	-1.3270	-1.6154	-3.0000	-5.6934	-18.5516

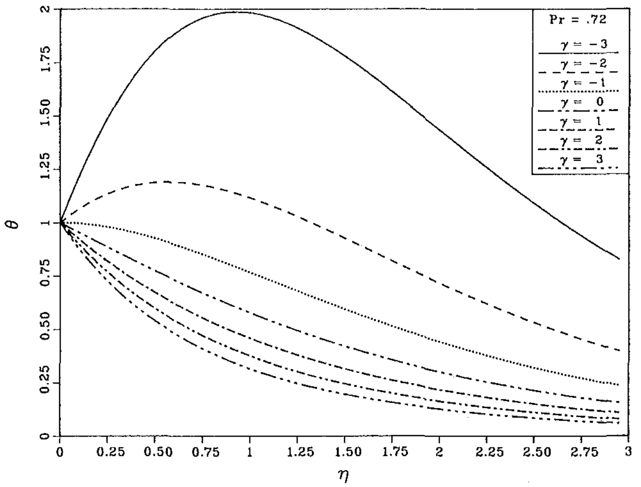

Fig. 1 Temperature profiles as a function of the similarity variable for various values of the temperature parameter at Pr = .72

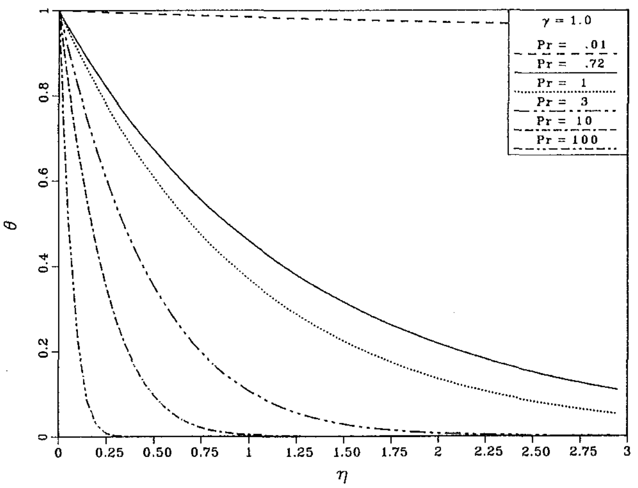

Fig. 2 Temperature profiles as a function of the similarity variable for various values of Prandtl number at γ = 1.0

$$a_n = a(a+1)(a+2)\ldots(a+n-1) \qquad (9)$$
$$b_n = b(b+1)(b+2)\ldots(b+n-1)$$

Rewriting equation (8) in terms of η

$$\theta = e^{-\mathrm{Pr}\cdot\eta}\,\frac{M(\mathrm{Pr}-\gamma,\mathrm{Pr}+1,-\mathrm{Pr}e^{-\eta})}{M(\mathrm{Pr}-\gamma,\mathrm{Pr}+1,-\mathrm{Pr})} \qquad (10)$$

Closed-form solutions can readily be developed from equation (10) for specific values of γ and Pr. Four such cases are reported in Table 1. The local dimensionless wall temperature gradient corresponding to equation (10) is

$$\theta'(0) = -\mathrm{Pr} + \frac{\mathrm{Pr}(\mathrm{Pr}-\gamma)}{(\mathrm{Pr}+1)}\,\frac{M(\mathrm{Pr}-\gamma+1,\mathrm{Pr}+2,-\mathrm{Pr})}{M(\mathrm{Pr}\text{-}\gamma,\mathrm{Pr}+1,-\mathrm{Pr})} \qquad (11)$$

and the local wall heat flux can be expressed as

$$q_w = -k\left(\frac{\partial T}{\partial y}\right)_w = -kA\,(B/\nu)^{1/2}\,\theta'(0)x^{\gamma}$$

Results and Discussion

Equations (10) and (11) were evaluated to determine the temperature distribution and the surface temperature gradient as a function of the temperature parameter γ and Prandtl number Pr. The results were checked by direct numerical integration of equation (6) and comparison with published results. Agreement was found to be excellent, with the exception of the work of Gupta and Gupta [6] where significant differences in wall temperature gradient at Pr not equal to 1 were found. There is some concern about their numerical results due to exhibiting incorrect Pr trends.

Temperature profiles were obtained for Pr of .01, .72, 1, 3, 10, and 100 with γ ranging between -3 and 3. Plots for the various parameter combinations are shown in Figs. 1 and 2. Both parameters are seen to have a significant effect on the temperature profiles. The Pr effects found for this problem are typical. For a given γ value, the smaller the Pr, the larger the thermal boundary layer thickness. To discuss the effect of γ, it is helpful to examine Table 2, which gives a tabulation of the wall temperature gradient. For $\gamma > -1$, the wall temperature gradient is negative, and heat flows from the continuous surface to the ambient. The magnitude of the temperature gradient increases as γ increases. When $\gamma = -1$, there is no heat transfer between the continuous surface and the ambient. For $-2 \leq \gamma < -1$, the sign of the temperature gradient changes and heat flows into the continuous surface from the ambient. The magnitude of the temperature gradient increases with decreasing γ. For $\gamma < -2$ and for Pr greater than certain values, the sign of the temperature gradient changes again and the heat flow is directed from the continuous surface. Temperature distributions for these γ and Pr values are found to have regions of temperature less than ambient. The temperature solutions, though satisfying equation (6), are physically unrealistic and calculations for these γ and Pr combinations are not reported.

The results for $\gamma \leq -1$ appear to be somewhat surprising. However, the studies by Sparrow and Gregg [9] and Levy [10], concerning boundary layer problems with specified power law wall temperature distributions, do indicate that this type of behavior is indeed characteristic. A more detailed discussion of some aspects of this behavior is given by Eckert and Drake [11] in regards to the wedge flow problems studied by Levy.

Conclusions

In this work, the heat transfer from a linearly stretching, continuous surface with a power law temperature distribution has been solved in terms of Kummer's functions. Several closed form temperature solutions for specified conditions are presented.

The heat transfer characteristics for this problem are found to be determined by the temperature parameter γ and Prandtl number Pr. The magnitude of γ affects the direction and quantity of heat flow. For $\gamma = -1$, there is no heat transfer occurring between the continuous surface and the ambient. Heat is transferred from the continuous surface to the fluid for $\gamma > -1$ and to the continuous surface for $-2 \leq \gamma < -1$. For $\gamma < -2$ and certain Pr values, unrealistic temperature distributions are encountered. Typical Pr effects on thermal boundary layer thickness, for a specified γ, are found.

Acknowledgment

The authors would like to thank the reviewer whose comments led to the discovery that Crane's solution to the boundary layer equations also represented an exact solution to the Navier–Stokes equations.

References

1 Sakiadis, B. C., "Boundary-Layer Behavior on Continuous Solid Surfaces: I. Boundary-Layer Equations for Two-Dimensional and Axisymmetric Flow," *AIChE Journal*, Vol. 7, No. 1, 1961, pp. 26–28.

2 Sakiadis, B. C., "Boundary-Layer Behavior on Continuous Solid Surface: II. Boundary-Layer On a Continuous Flat Surface," *AIChE Journal*, Vol. 7, No. 1, 1961, pp. 221–225.

3 Tsou, F. K., Sparrow, E. M., and Goldstein, R. J., "Flow and Heat Transfer in the Boundary Layer on a Continuous Moving Surface," *International Journal of Heat and Mass Transfer*, Vol. 10, 1967, pp. 219–235.

4 Crane, L. J., "Flow Past a Stretching Plane," *Z. Amgew. Math. Phys.*, Vol. 21, 1970, pp. 645–647.

5 Vleggaar, J., "Laminar Boundary-Layer Behavior on Continuous, Accelerating Surfaces," *Chemical Engineering Science*, Vol. 32, 1977, pp. 1517–1525.

6 Gupta, P. S., and Gupta, A. S., "Heat and Mass Transfer on a Stretching Sheet with Suction or Blowing," *Canadian Journal of Chemical Engineering*, Vol. 55, No. 6, 1977, pp. 744–746.

7 Soundalgekar, V. M., and Ramana Murty, T. V., "Heat Transfer Past a Continuous Moving Plate with Variable Temperature," *Warmeundstoffubertragung*, Vol. 14, 1980, pp. 91–93.

8 Abramowitz, M., and Stegun, L. A., *Handbook of Mathematical Functions*, National Bureau of Standards, AMS 55, Dec. 1972.

9 Sparrow, E. M., and Gregg, J. L., "Similar Solutions for Free Convection from a Nonisothermal Vertical Plate," ASME *Transactions*, Vol. 80, 1958, pp. 379–386.

10 Levy, S., "Heat Transfer to Constant-Property Laminar Boundary-Layer Flows with Power-Function Free-Stream Velocity and Wall Temperature," *Journal of the Aeronautical Sciences*, Vol. 19, 1952, pp. 341–348.

11 Eckert, E. R. G., and Drake, R. M., *Analysis of Heat and Mass Transfer*, McGraw-Hill, 1972, pp. 306–314.

Mixed Free and Forced Convection From a Short Vertical Cylinder Placed in a Laminar Horizontal Flow

M. F. Young[1,2] **and T. Ozel**[1]

Nomenclature

A = surface area
c_p = specific heat
d = diameter or differential
g = acceleration of gravity
Gr_L = Grashof number based on $L = g\beta(T_w - T_\infty)L^3/\nu^2$
$\bar{h}$ = average convective heat transfer coefficient
k = thermal conductivity
L = height
m = mass
$\bar{\mathrm{N}}\mathrm{u}_d$ = average Nusselt number based on $d = \bar{h}d/k$
$\dot{Q}$ = heat transfer rate
Re_d = Reynolds number based on $d = U_\infty d/\nu$
t = time
T = temperature
U_∞ = free-stream velocity
β = coefficient of thermal expansion
ϵ = emissivity
σ = Stefan–Boltzmann constant
ν = kinematic viscosity

Introduction

Mixed free- and forced-convection external flows arise when free-stream inertial and near-wall buoyant forces have strong effects on the resulting convective heat transport. Mixed convection is a fundamentally important heat transfer problem that occurs in a variety of technological and industrial applications. These applications include electronic devices cooled by fans, heat exchangers placed in low-velocity environments, nuclear reactors cooled during emergency shutdown, and solar central receivers exposed to wind currents.

Analytical studies of orthogonal mixed convection from vertical surfaces have been few, probably because of the complexities with treating a three-dimensional flow field. One of the first three-dimensional studies of laminar mixed convection from a vertically heated plate was conducted by R. J. Young and K. T. Yang [1]. Eichhorn and Hasan [2] reported numerical results for orthogonal mixed convection from vertical and horizontal wedges while Evans and Plumb [3] studied orthogonal laminar mixed convection from an isothermal vertical flat plate. Orthogonal laminar mixed convection from a vertical cylinder was studied by Yao and Chen [4]. Oosthuizen [5] also studied mixed convection from a vertical cylinder placed in a laminar horizontal flow and found that the numerical solution was inaccurate near the thermal leading edge. In a recent study, Yao [6] used a finite difference solution method to investigate the thermal leading edge region. It was found in [6] that buoyancy delays separation and significantly affects the heat transfer in the thermal leading edge region.

Few investigators have measured mixed convection heat transfer coefficients from vertical surfaces placed in a crossflow. Oosthuizen and Leung [7] measured orthogonal

---

[1] Department of Mechanical Engineering, University of California, Irvine, Calif. 92717

[2] Mem. ASME

Contributed by the Heat Transfer Division for publication in the JOURNAL OF HEAT TRANSFER. Manuscript received by the Heat Transfer Division November 15, 1983.

from the ambient. The magnitude of the temperature gradient increases with decreasing γ. For $\gamma < -2$ and for Pr greater than certain values, the sign of the temperature gradient changes again and the heat flow is directed from the continuous surface. Temperature distributions for these γ and Pr values are found to have regions of temperature less than ambient. The temperature solutions, though satisfying equation (6), are physically unrealistic and calculations for these γ and Pr combinations are not reported.

The results for $\gamma \leq -1$ appear to be somewhat surprising. However, the studies by Sparrow and Gregg [9] and Levy [10], concerning boundary layer problems with specified power law wall temperature distributions, do indicate that this type of behavior is indeed characteristic. A more detailed discussion of some aspects of this behavior is given by Eckert and Drake [11] in regards to the wedge flow problems studied by Levy.

Conclusions

In this work, the heat transfer from a linearly stretching, continuous surface with a power law temperature distribution has been solved in terms of Kummer's functions. Several closed form temperature solutions for specified conditions are presented.

The heat transfer characteristics for this problem are found to be determined by the temperature parameter γ and Prandtl number Pr. The magnitude of γ affects the direction and quantity of heat flow. For $\gamma = -1$, there is no heat transfer occurring between the continuous surface and the ambient. Heat is transferred from the continuous surface to the fluid for $\gamma > -1$ and to the continuous surface for $-2 \leq \gamma < -1$. For $\gamma < -2$ and certain Pr values, unrealistic temperature distributions are encountered. Typical Pr effects on thermal boundary layer thickness, for a specified γ, are found.

Acknowledgment

The authors would like to thank the reviewer whose comments led to the discovery that Crane's solution to the boundary layer equations also represented an exact solution to the Navier–Stokes equations.

References

1 Sakiadis, B. C., "Boundary-Layer Behavior on Continuous Solid Surfaces: I. Boundary-Layer Equations for Two-Dimensional and Axisymmetric Flow," *AIChE Journal*, Vol. 7, No. 1, 1961, pp. 26–28.

2 Sakiadis, B. C., "Boundary-Layer Behavior on Continuous Solid Surface: II. Boundary-Layer On a Continuous Flat Surface," *AIChE Journal*, Vol. 7, No. 1, 1961, pp. 221–225.

3 Tsou, F. K., Sparrow, E. M., and Goldstein, R. J., "Flow and Heat Transfer in the Boundary Layer on a Continuous Moving Surface," *International Journal of Heat and Mass Transfer*, Vol. 10, 1967, pp. 219–235.

4 Crane, L. J., "Flow Past a Stretching Plane," *Z. Amgew. Math. Phys.*, Vol. 21, 1970, pp. 645–647.

5 Vleggaar, J., "Laminar Boundary-Layer Behavior on Continuous, Accelerating Surfaces," *Chemical Engineering Science*, Vol. 32, 1977, pp. 1517–1525.

6 Gupta, P. S., and Gupta, A. S., "Heat and Mass Transfer on a Stretching Sheet with Suction or Blowing," *Canadian Journal of Chemical Engineering*, Vol. 55, No. 6, 1977, pp. 744–746.

7 Soundalgekar, V. M., and Ramana Murty, T. V., "Heat Transfer Past a Continuous Moving Plate with Variable Temperature," *Warme-undstoffubertragung*, Vol. 14, 1980, pp. 91–93.

8 Abramowitz, M., and Stegun, L. A., *Handbook of Mathematical Functions*, National Bureau of Standards, AMS 55, Dec. 1972.

9 Sparrow, E. M., and Gregg, J. L., "Similar Solutions for Free Convection from a Nonisothermal Vertical Plate," ASME *Transactions*, Vol. 80, 1958, pp. 379–386.

10 Levy, S., "Heat Transfer to Constant-Property Laminar Boundary-Layer Flows with Power-Function Free-Stream Velocity and Wall Temperature," *Journal of the Aeronautical Sciences*, Vol. 19, 1952, pp. 341–348.

11 Eckert, E. R. G., and Drake, R. M., *Analysis of Heat and Mass Transfer*, McGraw-Hill, 1972, pp. 306–314.

Mixed Free and Forced Convection From a Short Vertical Cylinder Placed in a Laminar Horizontal Flow

M. F. Young[1,2] **and T. Ozel**[1]

Nomenclature

A = surface area
c_p = specific heat
d = diameter or differential
g = acceleration of gravity
Gr_L = Grashof number based on $L = g\beta(T_w - T_\infty)L^3/\nu^2$
$\bar{h}$ = average convective heat transfer coefficient
k = thermal conductivity
L = height
m = mass
$\overline{\mathrm{Nu}}_d$ = average Nusselt number based on $d = \bar{h}d/k$
$\dot{Q}$ = heat transfer rate
Re_d = Reynolds number based on $d = U_\infty d/\nu$
t = time
T = temperature
U_∞ = free-stream velocity
β = coefficient of thermal expansion
ϵ = emissivity
σ = Stefan–Boltzmann constant
ν = kinematic viscosity

Introduction

Mixed free- and forced-convection external flows arise when free-stream inertial and near-wall buoyant forces have strong effects on the resulting convective heat transport. Mixed convection is a fundamentally important heat transfer problem that occurs in a variety of technological and industrial applications. These applications include electronic devices cooled by fans, heat exchangers placed in low-velocity environments, nuclear reactors cooled during emergency shutdown, and solar central receivers exposed to wind currents.

Analytical studies of orthogonal mixed convection from vertical surfaces have been few, probably because of the complexities with treating a three-dimensional flow field. One of the first three-dimensional studies of laminar mixed convection from a vertically heated plate was conducted by R. J. Young and K. T. Yang [1]. Eichhorn and Hasan [2] reported numerical results for orthogonal mixed convection from vertical and horizontal wedges while Evans and Plumb [3] studied orthogonal laminar mixed convection from an isothermal vertical flat plate. Orthogonal laminar mixed convection from a vertical cylinder was studied by Yao and Chen [4]. Oosthuizen [5] also studied mixed convection from a vertical cylinder placed in a laminar horizontal flow and found that the numerical solution was inaccurate near the thermal leading edge. In a recent study, Yao [6] used a finite difference solution method to investigate the thermal leading edge region. It was found in [6] that buoyancy delays separation and significantly affects the heat transfer in the thermal leading edge region.

Few investigators have measured mixed convection heat transfer coefficients from vertical surfaces placed in a crossflow. Oosthuizen and Leung [7] measured orthogonal

---

[1] Department of Mechanical Engineering, University of California, Irvine, Calif. 92717

[2] Mem. ASME

Contributed by the Heat Transfer Division for publication in the JOURNAL OF HEAT TRANSFER. Manuscript received by the Heat Transfer Division November 15, 1983.

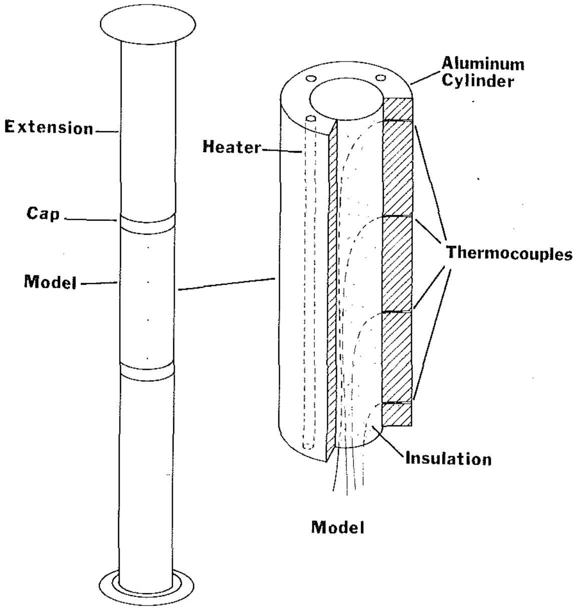

Fig. 1 Model configuration

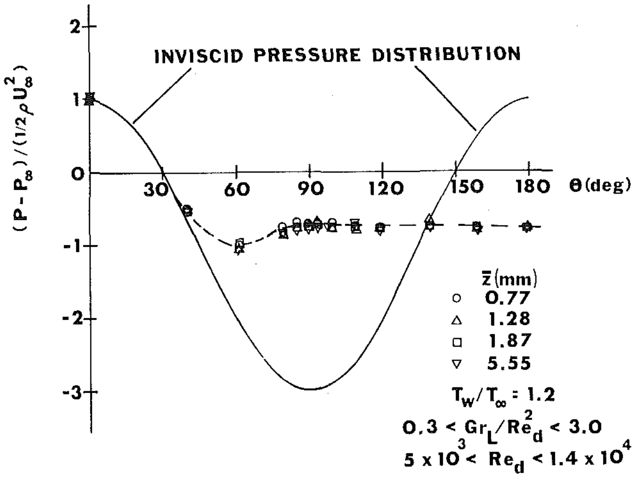

Fig. 2 Pressure distributions near the thermal leading edge

mixed convection heat transfer coefficients from vertical cylinders with height to diameter ratios between 8 and 16. Other studies include Wagner [8] (also reported in Clausing, Wagner, and Skarda [9]) Young and Ulrich [10], and Siebers et al. [11]. In [8] the mixed convection heat transfer coefficient was measured from a vertical cylinder, with a height to diameter ratio of 2, using a cryogenic wind tunnel. A cryogenic wind tunnel was also used in [10] to investigate mixed convection from vertically heated cylinders placed in a horizontal forced flow. In a recent study that was motivated by a need to estimate heat transfer losses from solar central receivers, Siebers et al. investigated orthogonal mixed convection from a large vertical flat plate.

In the present study, the effects of buoyancy on the heat transfer coefficient for a vertically heated cylinder placed in a crossflow are determined. The Grashof number Gr_L range investigated is about 10^6 to 10^8, while the Reynolds number Re_d is varied from about 500 to 30,000. The present study is an extension of the investigation in [10]. The range of the governing nondimensional buoyancy-inertia parameter for a cylinder, i.e., $(L/d)^4\ Re_d^2/Gr_L$, is greatly extended to include pure free convection. In addition, pressure distribution results will be presented.

Table 1 Model dimensions

Model	Height mm (in)	Diameter mm (in)	L/d	Blockage correction applied to the Reynolds number
1	63.5(2.5)	127 (5)	0.5	1.17
2	101.6 (4)	50.8 (2)	2	1.07
3	228.6 (9)	50.8 (2)	4.5	1.07

Wind Tunnel and Models

The experiments were conducted in a subsonic, recirculating ambient air wind tunnel with a 609.6 × 914.4 mm (2 × 3 ft) test section. The wind tunnel velocity can be varied continuously from about 0.3 to 40 m/s (1-130 ft/s). The mean velocity profile, at the location of the models, for all test velocities was uniform to within ±1 percent and the turbulence intensity was less than 0.10 percent.

Three models with height L to diameter d ratios of 0.5, 2, and 4.5 were tested in the present study. Cylinder heights and diameters are listed in Table 1. The models were hollow aluminum cylinders and were fitted with insulating ends. The models were attached on each end to an insulating section and mounted vertically in the wind tunnel. Consequently, the models were thermally finite and hydrodynamically infinite. Heater elements (nichrome wire) were inserted down axial holes which were drilled at several locations around the cylinder. Between 16 and 24 Type E (Chromel-Constantan) thermocouples were placed around each cylinder to measure the cylinder temperature. Thermocouples were also suspended at various interior centerline locations to measure end losses. After the thermocouples were installed, the interior of the cylinders were filled with liquid foam insulation and allowed to harden. A diagram of a model is shown in Fig. 1 (details are given in [12]).

Pressure Distribution Results

It was postulated by Yao [6] that when a vertically heated cylinder was placed in a horizontal forced flow, buoyancy would delay boundary layer separation in the vicinity of the thermal leading edge. Using a finite difference method, Yao found that slightly above the thermal leading edge the boundary layer separated at the rear stagnation line ($\theta = 180$ deg), rather than at about 85 deg that is the approximate separation location for a pure forced flow. Further up the cylinder, the separation point was found to move forward until a value of about $\theta = 104$ deg was attained. Forced convection was found to dominate after this, with the separation location fixed at about $\theta = 104$ deg.

In the present study, circumferential pressure distributions were measured near the thermal leading edge of a vertically heated cylinder placed in a horizontal flow. For these measurements the cylinder with an aspect ratio of 4.5 (see Table 1) was tested. Pressure taps were placed in four axial planes, 0.77, 1.28, 1.87, and 5.55 mm from the thermal leading edge. Each plane contained pressure taps at twelve circumferential locations between 0 and 180 deg. The pressure taps were 0.20-mm-i.d. surgical steel tubes that were connected to a scanning value by tygon tubing. The scanning value was then connected to a MKS Baratron pressure transducer, which has an accuracy of about ±0.08 percent of the scale reading. The output of the pressure transducer was fed directly to the data acquisition system (HP-9826 and HP-3497A). Construction details and calibration results can be found in [12].

The cylinder was first heated to the desired temperature (usually about 100-120°C). After steady state was reached, about 1 to 2 hrs, pressure readings were recorded by stepping through the 48 channels. Approximately 5 min were allowed for each pressure measurement. During the pressure

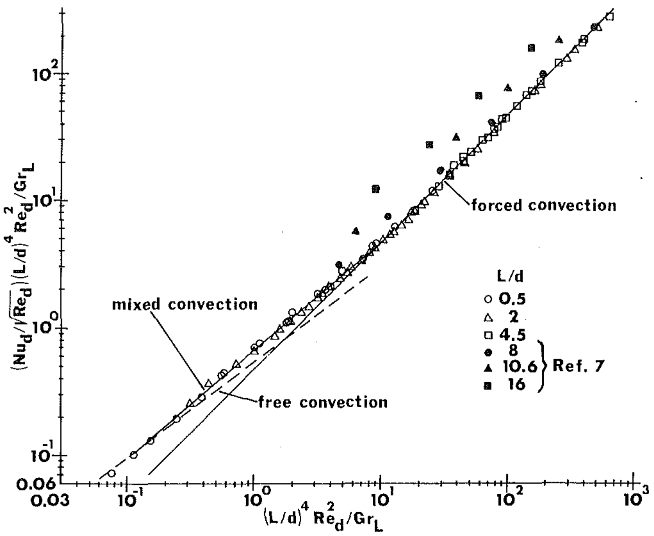

Fig. 3 Mixed convection heat transfer results for short vertical cylinders

measurements the free-stream velocity and temperature, as well as the cylinder temperatures, were recorded. The experiment was repeated for various free-stream velocities and hence various Richardson numbers. The Grashof number was held almost constant at about 10^8.

The pressure measurement results are shown in Fig. 2. For the Richardson number range investigated, no dependence on Richardson number is noted. Also shown is the inviscid pressure distribution. Separation occurs at about 85 deg for all axial distances from the leading edge. In the results of Yao, Fig. 3 in [6], the separation angle is plotted as a function of the nondimensional axial distance z for two Prandtl numbers, 10 and 0.733. Using the present nomenclature z, can be expressed as

$$z = (\tilde{z}/4)(L^3/d^4)(Re_d^2/\mathrm{Gr}_L) \qquad (1)$$

where $\tilde{z}$ is the distance from the thermal leading edge.

The smallest value of z simulated in the present study is $z = 0.10$. For this value of z and for a Prandtl number of about 0.7, the results of Yao indicate a separation angle of about 120 deg, whereas 85 deg was measured in the present study. Since smaller values of z could not be simulated, it is difficult to ascertain how much if any buoyancy delays separation in the thermal leading edge region. It is suspected, however, that because the thermal boundary layer is very thin in the vicinity of the thermal leading edge, the external forced convection boundary layer dominates.

Nondimensional Mixed Convection Parameters

A useful engineering plot of mixed convection heat transfer from a vertical cylinder would show the pure forced- and pure free-convection limits and the intermediate region where mixed convection is important. This plot would be similar to mixed convection from a vertical flat plate where $\mathrm{Nu}_x/\sqrt{\mathrm{Re}_x}$ is plotted versus $\mathrm{Gr}_x/\mathrm{Re}_x^2$ (see Lloyd and Sparrow [13]). A similar plot can be made for mixed convection from a vertical cylinder using the following nondimensional parameters. These nondimensional parameters can be found by manipulating the pure forced- and pure free-convection correlations. For example, for forced convection, the average Nusselt number based on the diameter of the cylinder can be written as (see [14])

$$\bar{\mathrm{Nu}}_{d,FC} = C_{FC}\sqrt{\mathrm{Re}_d} \qquad (2)$$

where C_{FC} is an experimental constant which includes the Prandtl number dependence. Equation (2) can be rearranged to give

$$\frac{\bar{\mathrm{Nu}}_{d,FC}}{\sqrt{\mathrm{Re}_d}}(L/d)^4\frac{\mathrm{Re}_d{}^2}{\mathrm{Gr}_L} = C_{FC}(L/d)^4\frac{\mathrm{Re}_d{}^2}{\mathrm{Gr}_L} \qquad (3)$$

The usefulness of rearranging equation (2) to include the nondimensional buoyancy parameter, $(L/d)^4\mathrm{Re}_d{}^2/\mathrm{Gr}_L$, on both sides of equation (3) will become evident when the pure free-convection correlation is also shown to take a similar form. Hence both the pure forced- and pure free-convection limits can be plotted on a single graph. The inverse of the nondimensional buoyancy parameter also arises if d^2/L is used as the characteristic length scale in the Richardson number, as originally suggested by Clausing [15] for the laminar-subcritical regime.

In a similar manner, the average Nusselt number based on the cylinder height for free convection from a vertical cylinder is given by

$$\bar{\mathrm{Nu}}_{L,NC} = C_{NC}\mathrm{Gr}_L{}^{1/4} \qquad (4)$$

Changing the length scale of the Nusselt number to the cylinder diameter and rearranging the resulting equation gives

$$\frac{\bar{\mathrm{Nu}}_{d,NC}}{\sqrt{\mathrm{Re}_d}}(L/d)^4\frac{\mathrm{Re}_d{}^2}{\mathrm{Gr}_L} = C_{NC}\left\{(L/d)^4\frac{\mathrm{Re}_d{}^2}{\mathrm{Gr}_L}\right\}^{1/4} \qquad (5)$$

If $C_{NC} = C_{FC}$, then the nondimensional buoyancy-inertia parameter would be unity, and free- and forced-convection effects would be equal. The free- and forced-convection constants, however, are not equal, e.g., for a Prandtl number equal to 0.72, $C_{FC} = 0.48$ (see [14]), and $C_{NC} = 0.523$ (see [16]). Note that C_{FC} is an experimentally determined coefficient whose value ranges by about ±10 percent from the value used above. Similarly, although C_{NC} is an exact result, its value is dependent on the relative thickness of the thermal boundary layer to the cylinder radius of curvature. Three-dimensional effects are significant in the present study and have been included in the calculation for C_{NC}.

The previously presented nondimensional parameters for mixed convection from a vertical cylinder, i.e.,

$$\frac{\bar{\mathrm{Nu}}_d}{\sqrt{\mathrm{Re}_d}}(L/d)^4\frac{\mathrm{Re}_d{}^2}{\mathrm{Gr}_L} \quad \text{and} \quad (L/d)^4\frac{\mathrm{Re}_d{}^2}{\mathrm{Gr}_L}$$

will be used to correlate the experimental heat transfer data.

Heat Transfer Data Reduction

The mixed convection heat transfer rate can be measured by performing an energy balance on the cylinder. The wind tunnel was operated at a particular velocity setting (between 0.3 and 10 m/s), and the cylinder heated. When the cylinder reached about 100°C, the heater was turned off, and the heat transfer tests were started. For the case when the heater power was zero, an energy balance on the cylinder gave

$$\dot{Q}_{\text{convection}} = -mc_p\frac{dT}{dt} - \epsilon\sigma A(T_w{}^4 - T_\infty{}^4) - \dot{Q}_{\text{end losses}} \qquad (6)$$

Note that in equation (6), the reasonable assumption was made that the wind tunnel walls were at T_∞. The cylinder emissivity was estimated from tabulated data to be 0.11. The radiation and end losses contributed about 7 and 1 percent, respectively, to equation (6). The cylinder and insulation temperatures were recorded by the data acquisition system. Consequently, by monitoring the rate of decay of the cylinder temperature, the free-stream temperature, and the insulation temperature, equation (6) could be solved for the mixed convection heat transfer rate. The Nusselt number could then be calculated at any time from

$$\bar{\mathrm{Nu}}_d = \dot{Q}_{\text{convection}}\{d/[Ak(T_w - T_\infty)]\} \qquad (7)$$

The measurement of the mixed convection heat transfer rate was compared to results when the heater power was not zero. The two methods agreed within ±3 percent. The latter

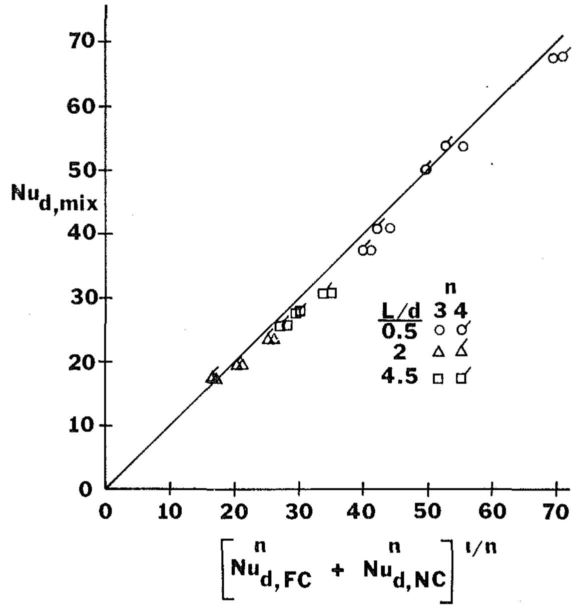

Fig. 4 Nusselt number calculations using the weighted sum method

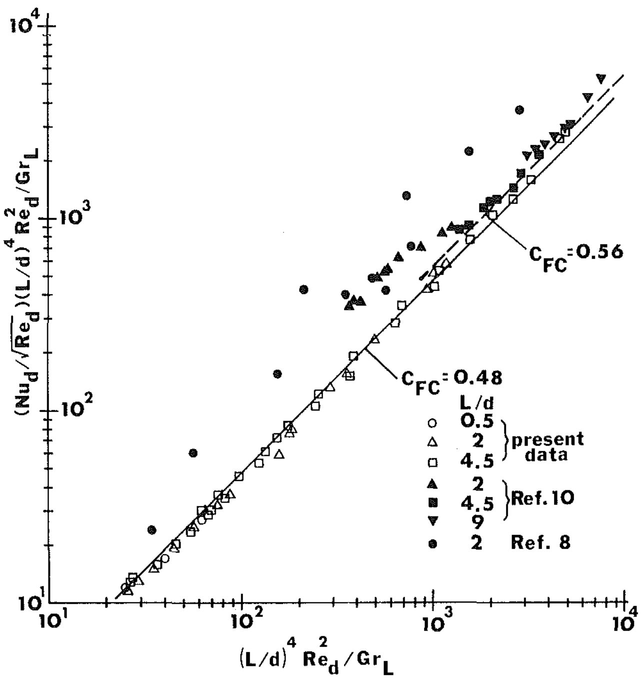

Fig. 5 Comparison of mixed convection heat transfer results

method was not used extensively, since its use required 1 to 2 hrs for the cylinder to reach steady state.

The cylinder temperatures were found to be uniform at any particular time during cool down, to within ±0.5°C. The mass of the cylinder was measured with a precision mass balance to within ±0.1 gm. An error analysis indicates that the measured mixed convection heat transfer coefficients are probably accurate to within ±5 percent.

Heat Transfer Results

Using the procedure outlined previously, the free- and forced-convection limits were checked. They were found to be in agreement with accepted correlations ([14] and [16]). The average Nusselt number results for the three models tested are shown in Fig. 3. The thermal boundary condition simulated, at a particular time, was that of a constant wall temperature. The results in Fig. 3 were corrected for model blockage effects using the ratio of the test section area to the mean flow areas as described in Perkins and Leppert [17]. The blockage corrections applied to the Reynolds numbers are listed in Table 1. The fluid properties used in the Nusselt, Reynolds, and Grashof numbers were evaluated at the film temperature, $T_f = (T_w + T_\infty)/2$, except for the coefficient of thermal expansion, which is, $\beta = 1/T_\infty$.

The solid line shown in Fig. 3 is the pure forced convection limit from [14]. The free-convection limit is also shown in Fig. 3 as a dotted line and is from [16]. The two lines intersect at a value of the abscissa of about 1.4. The data presented in Fig. 3 are for model aspect ratios of 0.5, 2, and 4.5. The overheat ratio T_w/T_∞ is about 1.2, and the Richardson number range investigated is about 0.003 to 40.

The present results indicate that force convection is dominant for $(L/d)^4 \mathrm{Re}_d^2/\mathrm{Gr}_L$ greater than about 10. Below this value of the abscissa to about 0.1, free convection adds between 5 to 25 percent to the heat transfer results. For values of $(L/d)^4 \mathrm{Re}_d^2/\mathrm{Gr}_L$ less than about 0.1, pure free convection dominates the heat transfer process. The data is seen to diverge smoothly from the forced convection limit and converge smoothly with the pure free-convection results. A least-squares curve fit to the data for values of the abscissa between 10 and 0.1 gives

$$\frac{\bar{\mathrm{Nu}}_{d,\mathrm{mix}}}{\sqrt{\mathrm{Re}_d}} = 0.67\left\{(L/d)^4 \frac{\mathrm{Re}_d^2}{\mathrm{Gr}_L}\right\}^{-0.15} \qquad (8)$$

Valid for:

$$400 < \mathrm{Re}_d < 2500$$
$$10^6 < \mathrm{Gr}_L < 10^7$$
$$0.5 < L/d < 4.5$$
$$\frac{T_w}{T_\infty} \simeq 1.2$$

Equation (8) represents the data to within ±5 percent. It should be noted that equation (8) is for thermally short and hydrodynamically infinite cylinders.

Also shown as darkened symbols in Fig. 3 are data from Oosthuizen and Leung [7]. These data appear to be mainly in the forced convection regime. The data for an L/d of 8 follow closely the present data, but for larger aspect ratios are considerably higher. The Grashof and Reynolds number ranges investigated in [7] are similar to those simulated in the present study, but the aspect ratio range is much larger. Large aspect ratio cylinders may operate in a different flow regime than short aspect ratio cylinders, e.g., in the transition or turbulent regime compared to laminar flow for short aspect ratio cylinders. This may explain why the data of [7] are higher than for the short cylinder data of the present study.

A convenient approximation for the mixed convection heat transfer coefficient when mixed convection data are not available is a weighted sum of the pure forced- and pure free-convection contributions. Such an approximation takes the form

$$\bar{\mathrm{Nu}}_{d,\mathrm{mix}} = \{\bar{\mathrm{Nu}}^n_{d,FC} + \bar{\mathrm{Nu}}^n_{d,NC}\}^{1/n} \qquad (9)$$

where n is a suitable exponent (see [18]). Equation (9) for $n=3$ and 4 is plotted in Fig. 4 versus experimentally determined values of $\bar{\mathrm{Nu}}_{d,\mathrm{mix}}$. The pure forced and pure free convection Nusselt numbers in equation (4) were calculated from correlating equations in [14] and [16], respectively. The straight line represents equality between the experimental results and equation (9). Most of the data plotted in Fig. 4, for $n=4$, deviate from the straight line by at most about 10 percent. Consequently, equation (9), for $n=4$, is probably a good approximation if mixed convection data are not available. For short vertical cylinders, however, equation (8) is recommended for use over equation (9).

An expanded plot for buoyancy values between 10^1 to 10^4, is shown in Fig. 5. Also shown in Fig. 5 are data from Wagner [8] and from Young and Ulrich [10]. The data from Wagner is considerably higher than the present data and that of [10], and may be due to flow regime and experimental setup differences. The data from [10] show transition from pure forced convection beginning at a value of the abscissa of about 1300. This is in contrast to the present results in Fig. 3, which show this transition occuring at about 10. This two order of magnitude increase in the transition point is probably due to a difference in flow regimes between the two studies. The results of [10] are for transitional to turbulent flow, while the present results are for laminar flow. In addition, the overheat ratios simulated in [10] were between 2 and 3 while the overheat ratio is about 1.2 in the present study. Consequently, flow regime differences are further accentuated because of the much larger overheat ratios investigated in [10]. Transition to turbulent flow will occur much sooner along the cylinder length for larger overheat ratios. Hence even for the same aspect ratio, Reynolds, and Grashof numbers, the cylinders investigated in [10] will be operated in entirely different flow regimes than the cylinders of the present study. Further studies are needed to separate the effects of flow regime and overheat ratio on the mixed free- and forced-convection heat transfer coefficient.

Concluding Remarks

Mixed free and forced convection are a fundamentally important heat transfer phenomena for which accurate experimental data are lacking. The purpose of the present study is to investigate mixed convection heat transfer from relatively short vertical cylinders placed in a crossflow. Data are obtained for the pure forced- and pure free- and the mixed-convection regimes. A nondimensional buoyancy-inertia parameter, similar to the Richardson number, and given by $(L/d)^4 \mathrm{Re}_d{}^2/\mathrm{Gr}_L$, is seen to correlate the data for vertical cylinders in all three regimes.

Mixed convection is found to be important in the region $0.1 < (L/d)^4 \mathrm{Re}_d{}^2/\mathrm{Gr}_L < 10$. For values of the nondimensional parameter greater than 10, pure forced convection dominates, while for values less than 0.1, the pure-free-convection limit is approached. A correlation is proposed for the calculation of the average mixed convection Nusselt number and represents the data to within ±5 percent.

References

1 Young, R. J., and Yang, K. T., "Effect of Small Crossflow and Surface Temperature Variation on Laminar Free Convection Along a Vertical Plate," *J. Applied Mechanics*, Vol. 39, 1963, pp. 252–256.

2 Eichhorn, R., and Hasan, M. M., "Mixed Convection About a Vertical Surface in Cross-Flow: A Similarity Solution," ASME JOURNAL OF HEAT TRANSFER, Vol. 102, 1980, pp. 775–777.

3 Evans, G. H., and Plumb, O. A., "Laminar Mixed Convection From a Vertical Heated Surface in a Crossflow," ASME JOURNAL OF HEAT TRANSFER, Vol. 104, 1982, pp. 554–558.

4 Yao, L. S., and Chen, F. F., "A Horizontal Flow Past a Partially Heated Infinite Vertical Cylinder," ASME JOURNAL OF HEAT TRANSFER, Vol. 103, 1981, pp. 546–551.

5 Oosthuizen, P. H., "Numerical Study of Combined Convective Heat Transfer From a Vertical Cylinder in a Horizontal Flow," *Proceedings of the 6th International Heat Transfer Conference*, Toronto, Canada, 1978, pp. MC-4 to MC-11.

6 Yao, L. S., "Buoyancy Effects on a Boundary Layer Along an Infinite Cylinder With a Step Change of Surface Temperature," ASME JOURNAL OF HEAT TRANSFER, Vol. 105, 1983, pp. 96–101.

7 Oosthuizen, P. H., and Leung, R. K., "Combined Convection Heat Transfer from Vertical Cylinders in a Horizontal Flow," Paper No. 78-WA/HT-45, ASME Winter Annual Meeting, 1978.

8 Wagner, K. C., "The Influences of Variable Properties in Combined Convection from a Vertical Cylinder in Crossflow," M.S. thesis, Department of Mechanical and Industrial Engineering, University of Illinois, Urbana-Champaign, 1982.

9 Clausing, A. M., Wagner, K. C., and Skarda, R. J., "An Experimental Investigation of Combined Convection From a Vertical Cylinder in a Crossflow," *Proceedings of the ASME-JSME Thermal Engineering Joint Conference*, Vol. 3, 1982, pp. 155–161.

10 Young, M. F., and Ulrich, T. R., "Mixed Convection Heat Transfer from a Vertical Heated Cylinder in a Crossflow," *International Journal of Heat and Mass Transfer*, Vol. 26, 1983, pp. 1889–1892.

11 Siebers, D. L., Schwind, R. G., and Moffat, R. J., "Experimental Mixed Convection Heat Transfer From a Large Vertical Surface in a Horizontal Flow," Sandia Report, SAND 83-8225, 1983.

12 Ozel, T., "Mixed Convection from a Vertically Heated Cylinder in Crossflow," M.S. thesis, University of California, Irvine, 1984.

13 Lloyd, J. R., and Sparrow, E. M., "Combined Forced and Free Convection Flow on Vertical Surfaces," *International Journal of Heat and Mass Transfer*, Vol. 16, 1973, pp. 1958–1964.

14 Incropera, F. P., and DeWitt, D. P., *Fundamentals of Heat Transfer*, John Wiley and Sons, 1981, p. 345.

15 Clausing, A. M., "Modeling Requirements for Determination of Convective Losses from Solar Receivers," *Proceedings of the American Section of Int. Solar Energy Society*, Philadelphia, Pa., Vol. 41, 1981, pp. 371–375.

16 Sparrow, E. M., and Gregg, J. L., "Laminar Free Convection from the Outer Surface of a Vertical Circular Cylinder," ASME *Transactions*, Vol. 78, 1956, pp. 1828–1829.

17 Perkins, H. C. and Leppert, G., "Forced Convection Heat Transfer from a Uniformly Heated Cylinder, ASME JOURNAL OF HEAT TRANSFER, Vol. 84, 1962, pp. 257–263.

18 *Heat Exchanger Design Handbook*, Vol. 2, Hemisphere, Washington, D.C., 1983.

The Behavior of a Toroidal Thermosyphon at High Graetz (and Grashof) Numbers

A. Ronen[1] and Y. Zvirin[1]

Nomenclature

a = minor radius of torus
c = specific heat
C_1 = constant (equation 13*a*)
C_3 = constant (equation 13*b*)
C_4 = constant (equation 13*c*)
f = friction coefficient
g = acceleration of gravity
G = complex function (equation 11)
Gz = Graetz number, equation (4)
h = average heat convection coefficient (cooled upper section)
k = thermal conductivity
N = parameter (equation 13*a*)
Nu = Nusselt number, $h \cdot 2a/k$
Pr = Prandtl number
q = heat flux input (heated lower section)
r = radial coordinate
R = major radius of torus
Re = Reynolds number
t = time
T = temperature
V = characteristic velocity, $[g\beta Raq/2\pi c\mu]^{1/2}$
w = dimensionless velocity, W/V
$\bar{w}$ = average velocity
W = axial velocity
β = thermal expansion coefficient
η = dimensionless radial coordinate, $(r/a)\sqrt{\mathrm{Gz}}$
θ = angular coordinate, along the torus axis
μ = dynamic viscosity
ρ = density
σ = stability parameter
τ = dimensionless time, $t/(2\pi R/V)$
ϕ = dimensionless temperature, $(T-T_w)/(qa/k)$

---

[1] Faculty of Mechanical Engineering, Technion—Israel Institute of Technology, Haifa 32000, Israel.

Contributed by the Heat Transfer Division for publication in the JOURNAL OF HEAT TRANSFER. Manuscript received by the Heat Transfer Division October 6, 1983.

is shown in Fig. 5. Also shown in Fig. 5 are data from Wagner [8] and from Young and Ulrich [10]. The data from Wagner is considerably higher than the present data and that of [10], and may be due to flow regime and experimental setup differences. The data from [10] show transition from pure forced convection beginning at a value of the abscissa of about 1300. This is in contrast to the present results in Fig. 3, which show this transition occuring at about 10. This two order of magnitude increase in the transition point is probably due to a difference in flow regimes between the two studies. The results of [10] are for transitional to turbulent flow, while the present results are for laminar flow. In addition, the overheat ratios simulated in [10] were between 2 and 3 while the overheat ratio is about 1.2 in the present study. Consequently, flow regime differences are further accentuated because of the much larger overheat ratios investigated in [10]. Transition to turbulent flow will occur much sooner along the cylinder length for larger overheat ratios. Hence even for the same aspect ratio, Reynolds, and Grashof numbers, the cylinders investigated in [10] will be operated in entirely different flow regimes than the cylinders of the present study. Further studies are needed to separate the effects of flow regime and overheat ratio on the mixed free- and forced-convection heat transfer coefficient.

Concluding Remarks

Mixed free and forced convection are a fundamentally important heat transfer phenomena for which accurate experimental data are lacking. The purpose of the present study is to investigate mixed convection heat transfer from relatively short vertical cylinders placed in a crossflow. Data are obtained for the pure forced- and pure free- and the mixed-convection regimes. A nondimensional buoyancy-inertia parameter, similar to the Richardson number, and given by $(L/d)^4 \mathrm{Re}_d{}^2/\mathrm{Gr}_L$, is seen to correlate the data for vertical cylinders in all three regimes.

Mixed convection is found to be important in the region $0.1 < (L/d)^4 \mathrm{Re}_d{}^2/\mathrm{Gr}_L < 10$. For values of the nondimensional parameter greater than 10, pure forced convection dominates, while for values less than 0.1, the pure-free-convection limit is approached. A correlation is proposed for the calculation of the average mixed convection Nusselt number and represents the data to within ±5 percent.

References

1 Young, R. J., and Yang, K. T., "Effect of Small Crossflow and Surface Temperature Variation on Laminar Free Convection Along a Vertical Plate," *J. Applied Mechanics*, Vol. 39, 1963, pp. 252–256.

2 Eichhorn, R., and Hasan, M. M., "Mixed Convection About a Vertical Surface in Cross-Flow: A Similarity Solution," ASME JOURNAL OF HEAT TRANSFER, Vol. 102, 1980, pp. 775–777.

3 Evans, G. H., and Plumb, O. A., "Laminar Mixed Convection From a Vertical Heated Surface in a Crossflow," ASME JOURNAL OF HEAT TRANSFER, Vol. 104, 1982, pp. 554–558.

4 Yao, L. S., and Chen, F. F., "A Horizontal Flow Past a Partially Heated Infinite Vertical Cylinder," ASME JOURNAL OF HEAT TRANSFER, Vol. 103, 1981, pp. 546–551.

5 Oosthuizen, P. H., "Numerical Study of Combined Convective Heat Transfer From a Vertical Cylinder in a Horizontal Flow," *Proceedings of the 6th International Heat Transfer Conference*, Toronto, Canada, 1978, pp. MC-4 to MC-11.

6 Yao, L. S., "Buoyancy Effects on a Boundary Layer Along an Infinite Cylinder With a Step Change of Surface Temperature," ASME JOURNAL OF HEAT TRANSFER, Vol. 105, 1983, pp. 96–101.

7 Oosthuizen, P. H., and Leung, R. K., "Combined Convection Heat Transfer from Vertical Cylinders in a Horizontal Flow," Paper No. 78-WA/HT-45, ASME Winter Annual Meeting, 1978.

8 Wagner, K. C., "The Influences of Variable Properties in Combined Convection from a Vertical Cylinder in Crossflow," M.S. thesis, Department of Mechanical and Industrial Engineering, University of Illinois, Urbana-Champaign, 1982.

9 Clausing, A. M., Wagner, K. C., and Skarda, R. J., "An Experimental Investigation of Combined Convection From a Vertical Cylinder in a Crossflow," *Proceedings of the ASME-JSME Thermal Engineering Joint Conference*, Vol. 3, 1982, pp. 155–161.

10 Young, M. F., and Ulrich, T. R., "Mixed Convection Heat Transfer from a Vertical Heated Cylinder in a Crossflow," *International Journal of Heat and Mass Transfer*, Vol. 26, 1983, pp. 1889–1892.

11 Siebers, D. L., Schwind, R. G., and Moffat, R. J., "Experimental Mixed Convection Heat Transfer From a Large Vertical Surface in a Horizontal Flow," Sandia Report, SAND 83-8225, 1983.

12 Ozel, T., "Mixed Convection from a Vertically Heated Cylinder in Crossflow," M.S. thesis, University of California, Irvine, 1984.

13 Lloyd, J. R., and Sparrow, E. M., "Combined Forced and Free Convection Flow on Vertical Surfaces," *International Journal of Heat and Mass Transfer*, Vol. 16, 1973, pp. 1958–1964.

14 Incropera, F. P., and DeWitt, D. P., *Fundamentals of Heat Transfer*, John Wiley and Sons, 1981, p. 345.

15 Clausing, A. M., "Modeling Requirements for Determination of Convective Losses from Solar Receivers," *Proceedings of the American Section of Int. Solar Energy Society*, Philadelphia, Pa., Vol. 41, 1981, pp. 371–375.

16 Sparrow, E. M., and Gregg, J. L., "Laminar Free Convection from the Outer Surface of a Vertical Circular Cylinder," ASME *Transactions*, Vol. 78, 1956, pp. 1828–1829.

17 Perkins, H. C. and Leppert, G., "Forced Convection Heat Transfer from a Uniformly Heated Cylinder, ASME JOURNAL OF HEAT TRANSFER, Vol. 84, 1962, pp. 257–263.

18 *Heat Exchanger Design Handbook*, Vol. 2, Hemisphere, Washington, D.C., 1983.

The Behavior of a Toroidal Thermosyphon at High Graetz (and Grashof) Numbers

A. Ronen[1] and Y. Zvirin[1]

Nomenclature

a = minor radius of torus
c = specific heat
C_1 = constant (equation 13*a*)
C_3 = constant (equation 13*b*)
C_4 = constant (equation 13*c*)
f = friction coefficient
g = acceleration of gravity
G = complex function (equation 11)
Gz = Graetz number, equation (4)
h = average heat convection coefficient (cooled upper section)
k = thermal conductivity
N = parameter (equation 13*a*)
Nu = Nusselt number, $h \cdot 2a/k$
Pr = Prandtl number
q = heat flux input (heated lower section)
r = radial coordinate
R = major radius of torus
Re = Reynolds number
t = time
T = temperature
V = characteristic velocity, $[g\beta Raq/2\pi c\mu]^{1/2}$
w = dimensionless velocity, W/V
$\bar{w}$ = average velocity
W = axial velocity
β = thermal expansion coefficient
η = dimensionless radial coordinate, $(r/a)\sqrt{\mathrm{Gz}}$
θ = angular coordinate, along the torus axis
μ = dynamic viscosity
ρ = density
σ = stability parameter
τ = dimensionless time, $t/(2\pi R/V)$
ϕ = dimensionless temperature, $(T-T_w)/(qa/k)$

---

[1] Faculty of Mechanical Engineering, Technion—Israel Institute of Technology, Haifa 32000, Israel.

Contributed by the Heat Transfer Division for publication in the JOURNAL OF HEAT TRANSFER. Manuscript received by the Heat Transfer Division October 6, 1983.

Subscripts

p = perturbation
ss = steady state
w = wall (cooled upper section) or at temperature T_w

1 Introduction

A two-dimensional study of heat transfer and fluid flow in a toroidal thermosyphon has recently been performed [1]. Temperature and velocity distributions in steady-state, as well as friction and heat transfer correlations, were obtained for a relatively narrow range of the problem parameter, i.e., the Graetz number Gz. No attempt was made to carry out a stability analysis, using the new correlations. The aim of the present work is to extend the results to higher values of Gz and to apply the two-dimensional friction and heat transfer correlations in a stability analysis of the problem.

The results show an interesting behavior of the velocity and temperature cross-sectional profiles for intermediate values of Gz $\approx$ 100: The peaks occur near the tube wall and not on the axis. For the stability analysis, comparison with available data, [3] shows good agreement.

2 Steady-State Solution

A toroidal natural circulation loop is considered, where the lower half is heated by a constant heat flux over the entire surface, and the upper section is cooled by maintaining a constant wall temperature. Laminar flow is treated, for which the governing momentum and energy equations and boundary conditions are given in the following nondimensional form[2], according to Mertol et al. [1]

$$\int_0^{2\pi} \phi \cos\theta \, d\theta + \frac{2}{\pi}\left(\frac{d^2 w}{d\eta^2} + \frac{1}{\eta}\frac{dw}{d\eta}\right) = 0 \qquad (1)$$

$$w\frac{\partial\phi}{\partial\theta} = \frac{2}{\pi}\left(\frac{\partial^2\phi}{\partial\eta^2} + \frac{1}{\eta}\frac{\partial\phi}{\partial\eta}\right) \qquad (2)$$

$$\left.\frac{dw}{d\eta}\right|_{\eta=0} = 0 \qquad (3a)$$

$$\left.\frac{\partial\phi}{\partial\eta}\right|_{\eta=0} = 0 \qquad (3b)$$

$$w(\mathrm{Gz}^{1/2}) = 0 \qquad (3c)$$

$$\phi(\mathrm{Gz}^{1/2},\theta) = 0 \qquad 0<\theta<\pi \qquad (3d)$$

$$\left.\frac{\partial\phi}{\partial\eta}\right|_{\eta=\mathrm{Gz}^{1/2}} = \mathrm{Gz}^{-1/2} \qquad \pi<\theta<2\pi \qquad (3e)$$

It has been assumed that the flow has a single velocity component w in the direction of the torus axis. The continuity equation yields, then, the result that $w = w(t, r)$. The momentum equation (1) was derived by integration around the loop so that the pressure term vanishes. The Boussinesq approximation was adopted, i.e., the density ρ is taken everywhere as a constant except for the buoyancy term, where ρ is assumed to be a linear function of temperature according to $\rho = \rho_w[1 - \beta(T - T_w)]$. The Graetz number that appears in the boundary conditions is the only parameter of the steady-state problem; it is defined by

$$\mathrm{Gz} = \frac{2\rho_w c a^2 V}{\pi k R} \qquad (4)$$

and is related to the Grashof number.

The equations were solved numerically by a finite difference scheme, using the successive overrelaxation method (S.O.R.). This enabled us to provide results for a wider range of Gz, extending thus the results of [1]. A grid of 40 × 20 points (in the axial and radial direction) was used; a finer mesh (60 × 30) yielded results within 0.5 percent. In the regions near $\theta = 0, \pi$ where the boundary conditions are discontinuous, the inaccuracies are larger (up to 20 percent).

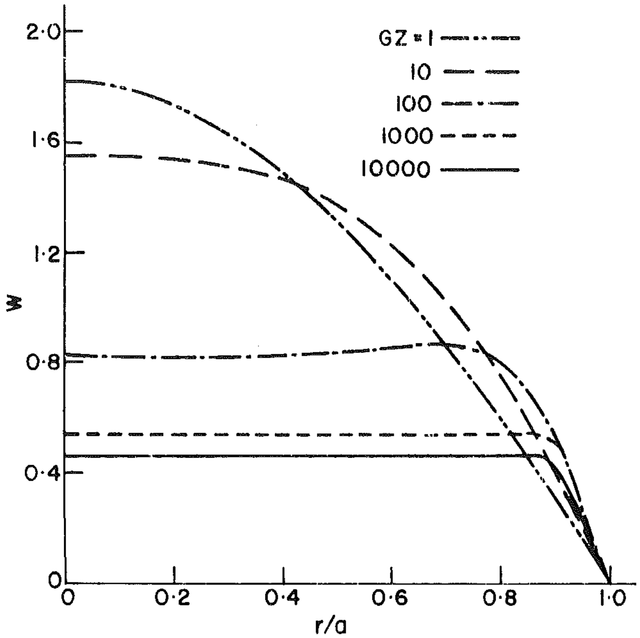

Fig. 1 Velocity distributions along the radius

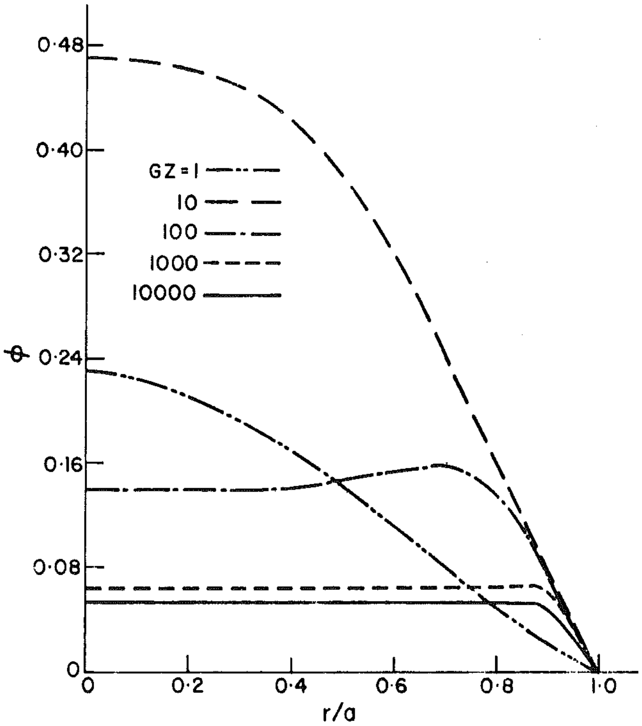

Fig. 2 Temperature distributions along the radius at $\theta = \pi/2$

The transverse velocity and temperature distributions are shown in Figs. 1 and 2 for various Graetz numbers. As mentioned above, w does not depend on the axial coordinate θ. The temperature ϕ depends on both η and θ, and Fig. 2 shows the profile at the middle of the cooled section, $\theta = \pi/2$. For low values of Gz the profiles are similar to those of simple forced laminar tube flow, i.e., parabolic distributions of velocity and temperature as functions of the radius. For high

---

[2] See also Nomenclature.

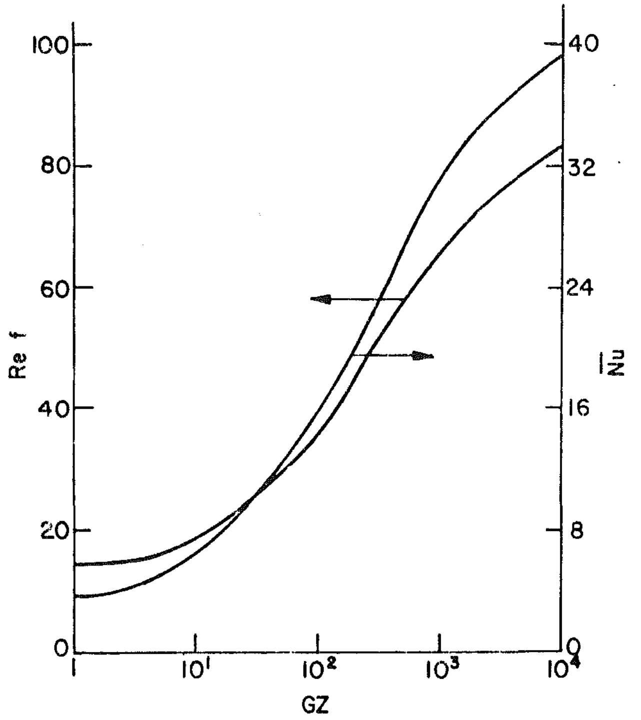

Fig. 3 Friction factor and cooled section mean Nusselt number as functions of the Graetz number

values of Gz the profiles become almost rectangular, while the gradients are concentrated in the boundary layer next to the tube wall. An interesting phenomenon occurs when Gz ≈ 100, whereby the maxima of velocity and temperature are found at $r \approx 0.8\,a$. It seems that for these values of Gz the buoyancy is stronger in the neighborhood of this location, which causes higher temperature and velocity. This phenomenon of maximal velocity and temperature not located on the axis of symmetry is well known in problems of natural convection in enclosures (see [4]). Detailed results for the temperature and velocity fields, including the variations of the wall and bulk temperature, are given in [2]. Figure 3 shows the results for the friction factor f and for the cooled section mean Nusselt number Nu as a function of the Graetz number Gz. The mean velocity $\bar{w}$ as a function of the Graetz number is shown in Fig. 4. The figure includes a comparison between the results obtained from the two-dimensional model described in this section and results of two one-dimensional models[3]: one with the correlations for the friction and heat transfer coefficients obtained in the two-dimensional model [1, 2] and the other with the laminar forced flow correlations f = 16/Re and Nu = 3.65. It can be seen that the agreement between the two-dimensional and the first one-dimensional model is quite good; the maximum deviations, at low Gz, are less than 7 percent. These discrepancies are mainly because the one-dimensional model uses the bulk temperature instead of the cross-sectional averaged temperature in the governing equations. Moreover, the inaccuracies of the models (as compared in [1, 2] with the data of [3]) may follow from the three-dimensional effects observed in thermosyphons (see [5]). The one-dimensional model with the forced flow correlations, however, yields reasonable results only at low Gz, while for Gz > 10 it is clearly erroneous. This indicates that the use of one-dimensional analyses in thermosyphonic loops is justified provided that the correct friction and heat transfer correlations are available. The sensitivity of one-dimensional models to the friction correlation has also been pointed out in [6].

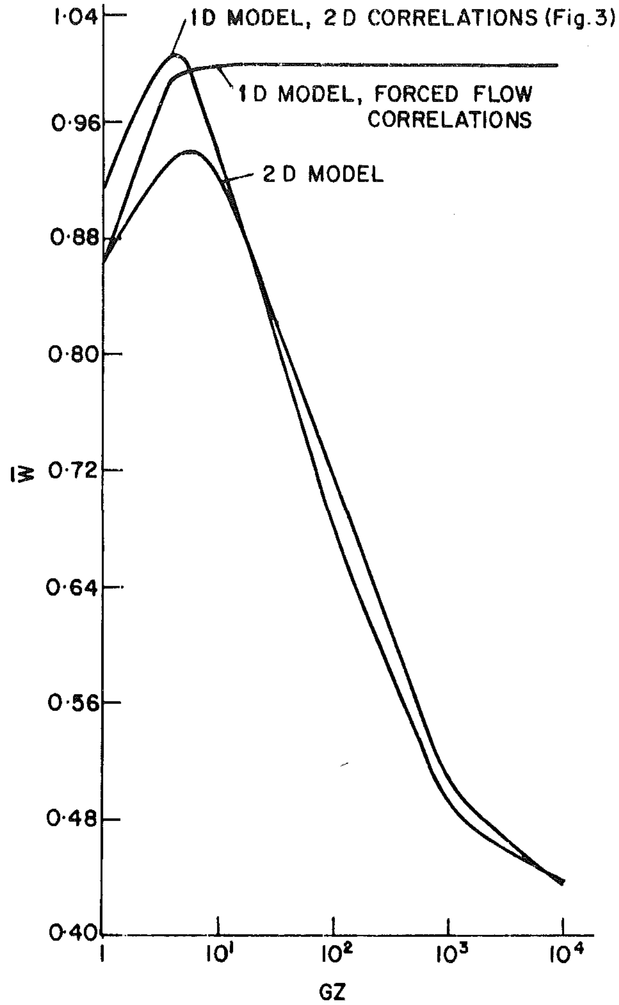

Fig. 4 Average velocity as a function of the Graetz number Gz, from two-dimensional and one-dimensional models

3 Stability Analysis

The analysis was performed by a one-dimensional model, applying the "small perturbations" method. The one-dimensional equations and boundary conditions of [3] were transformed to a nondimensional form, involving the parameters used in the two-dimensional model (Pr, Gz)

$$-\frac{1}{2\pi \mathrm{Pr}}\frac{\partial w}{\partial \tau}+\int_0^{2\pi}\phi\cos\theta\,d\theta-\mathrm{Re}\cdot f\cdot w\cdot\frac{1}{\pi \mathrm{Gz}}=0 \qquad (5)$$

$$\frac{1}{2\pi}\frac{\partial \phi}{\partial \tau}+w\frac{\partial \phi}{\partial \theta}=\begin{cases}-\dfrac{\mathrm{Nu}}{\mathrm{Gz}}\dfrac{2}{\pi}\phi & 0<\theta<\pi\\[2ex] \dfrac{4}{\pi \mathrm{Gz}} & \pi<\theta<2\pi\end{cases} \qquad (6)$$

$$\phi(0)=\phi(2\pi) \qquad (7a)$$

$$\phi(\pi^{+})=\phi(\pi^{-}) \qquad (7b)$$

The correlations for friction (f) and heat transfer (Nu), Fig. 3, are taken from the two-dimensional steady-state solution. A constant mean value of Nu (Gz) has been taken, enabling an analytical solution of the energy equation. A further assumption is that the steady-state correlations apply under the dynamic conditions related to the stability. This

---

[3] The steady-state, one-dimensional governing equations are those appearing in section 3, without the time derivatives.

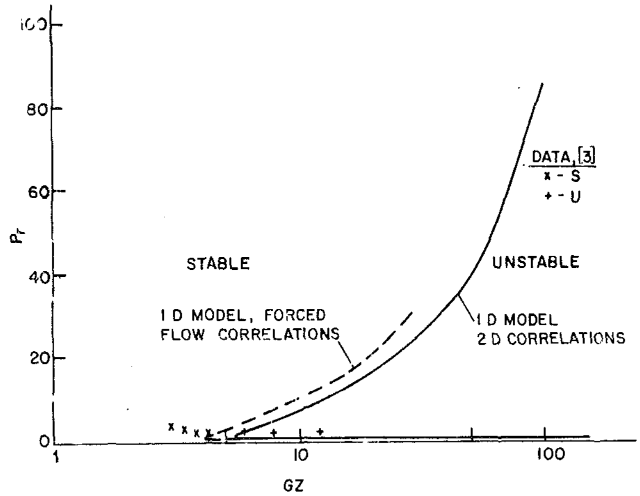

Fig. 5 Stability map obtained by one-dimensional models with correlations of natural and forced flows and comparison to experimental results of [3]

assumption is justified because we are interested only in the onset of the unstable motion.

In the analysis we assume that the velocity and temperature can be written as the steady-state solution with a small superimposed disturbance

$$w = w_{ss} + w_p e^{\sigma\tau} : \phi = \phi_{ss} + \phi_p e^{\sigma\tau} \tag{8}$$

where σ is the stability parameter. The flow system is unstable if there exists at least one eigenvalue σ, with a positive real part. Substitution of the temperature and velocity functions (8) into equations (5–7), dropping the terms that satisfy the steady-state equations and linearizing, yield the "perturbed momentum and energy equations"

$$-\frac{\sigma}{2\pi \mathrm{Pr}} w_p + \int_0^{2\pi} \phi_p \cos\theta \, d\theta - \mathrm{Re}\bullet f \bullet w_p \frac{1}{\pi \mathrm{Gz}} = 0 \tag{9}$$

$$\frac{\sigma}{2\pi}\phi_p + w_{ss}\frac{\partial \phi_p}{\partial \theta} + w_p \frac{\partial \phi_{ss}}{\partial \theta} = \begin{cases} -\dfrac{\mathrm{Nu}}{\mathrm{Gz}} \dfrac{2}{\pi} \phi_p & 0 < \theta < \pi \\ 0 & \pi < \theta < 2\pi \end{cases} \tag{10}$$

The energy equation can be solved analytically for ϕ_p in both ranges of θ with w_p as a parameter. Introduction of the resulting temperature distributions into the momentum equation yields the characteristic equation for σ. We are interested in constructing the stability map, or the marginal stability boundary in the plane of the system parameters Gz, Pr. For this we write $\sigma = R(\sigma) + i\mathrm{Im}(\sigma)$, insert $R(\sigma) = 0$ for marginal stability, and obtain the characteristic equation

$$\frac{1}{\mathrm{Pr}} = \frac{2\pi}{\sigma}\left[C_3 \frac{\dfrac{\sigma + 2\pi N}{2\pi w_{ss}}\left(1 + e^{-\frac{\sigma+2\pi N}{2w_{ss}}}\right)}{1 + \left(\dfrac{\sigma+2\pi N}{2w_{ss}}\right)^2} + \frac{C_1 N \bullet 2\pi}{\sigma w_{ss}} \frac{\dfrac{N}{w_{ss}}\left(1 + e^{-\frac{N\pi}{w_{ss}}}\right)}{1 + \left(\dfrac{N}{w_{ss}}\right)^2} - C_4 \frac{\dfrac{\sigma}{2\pi w_{ss}}}{1 + \left(\dfrac{\sigma}{2\pi w_{ss}}\right)^2}\left(e^{-\frac{\sigma}{2w_{ss}}} - e^{-\frac{\sigma}{w_{ss}}}\right) - \frac{1}{\pi \mathrm{Gz}}\mathrm{Re}\bullet f \right] \tag{11}$$

$$\equiv G(\mathrm{Gz}, \sigma)$$

The characteristic stability equation (11) is separated into the following real and imaginary parts

$$\frac{1}{\mathrm{Pr}} = R(G) \tag{12a}$$

$$\mathrm{Im}(G) = 0 \tag{12b}$$

where

$$N = \frac{2\mathrm{Nu}}{\pi \mathrm{Gz}} ; \; C_1 = \frac{4}{\mathrm{Gz}\bullet w_{ss}\left(1 - e^{-\frac{2\mathrm{Nu}}{w_{ss}\mathrm{Gz}}}\right)} \tag{13a}$$

$$C_3 = C_4 e^{-\frac{\sigma}{w_{ss}}} - \frac{8}{\sigma \mathrm{Gz} w_{ss}} - \frac{2\pi C_1 N}{\sigma w_{ss}} \tag{13b}$$

$$C_4 = \frac{e^{\frac{\sigma}{2w_{ss}}}}{\left(e^{-\frac{\sigma+\pi N}{w_{ss}}} - 1\right)}\left[\left(\frac{8}{\sigma \mathrm{Gz} w_{ss}} + \frac{2\pi C_1 N}{\sigma w_{ss}}\right) e^{-\frac{\sigma+2\pi N}{2w_{ss}}} - \frac{8}{\sigma \mathrm{Gz} w_{ss}} - \frac{C_1 N \, 2\pi}{\sigma w_{ss}} e^{-\frac{N\pi}{w_{ss}}}\right] \tag{13c}$$

The neutral stability margin is obtained from equations (12) in the following manner: for any value of Gz, equation (12*b*) is first solved for Im(σ). The result is introduced into (12*a*) and the corresponding value of Pr is calculated, yielding a point (Gz, Pr) on the marginal stability curve. If equation (12*b*) does not have any root, Im(σ), for any Gz, all cases for this value of the Graetz number are either stable or unstable. It is noted that in most cases, equation (12*b*) has two roots. The results have also been confirmed by using the Nyquist criterion.

The stability map is shown in Fig. 5, which also includes data points of [3]. The agreement is obviously very good. It is noted, however, that the experiments of [3] were carried out with water, at a narrow temperature range. The experimental confirmation of the analysis is therefore restricted to a neighborhood of a single point on the stability margin. The marginal stability curve obtained in [7] by a one-dimensional model with forced flow correlations is also shown in Fig. 5. Considerable differences are seen between the two one-dimensional models even at low values of Gz, where the agreement between the steady-state results was quite good (see Fig. 4). The lowest Gz for an unstable state is predicted to be 5.5 by the model with natural flow correlations and 4.0 by the other one-dimensional model, a deviation of 27 percent. Unfortunately, there is no datum point available in this region. The deviation between the upper branches of the stability boundaries obtained by the two models increase with the Graetz number.

Acknowledgment

The authors wish to thank Professor R. Greif and Dr. A. Mertol, Department of Mechanical Engineering, University of California, Berkeley, for their helpful comments.

References

1 Mertol, A., Greif, R., and Zvirin, Y., "Two-Dimensional Study of Heat Transfer and Fluid Flow in a Natural Convection Loop," ASME JOURNAL OF HEAT TRANSFER, Vol. 104, 1982, pp. 508–514.

2 Ronen, A., "Investigation of the Velocity and Temperature Fields in a Thermosyphonic Loop," (in Hebrew), M.Sc. thesis, Department of Mechanical Engineering, Technion, Israel, 1983.

3 Creveling, H. F., DePaz, J. F., Baladi, J. Y., and Schoenhals, R. J., "Stability Characteristics of Single Phase Free Convection Loop," *J. Fluid Mechanics*, Vol. 67, 1975, pp. 65–84.

4 MacGregor, R. K., and Emery, A. P., "Free Convection Through Vertical Plane Layers: Moderate and High Prandtl Number Fluids," ASME JOURNAL OF HEAT TRANSFER, Vol. 91, 1969, pp. 391-398.

5 Damerell, P. S., and Schoenhals, R. J., "Flow in a Toroidal Thermosyphon with Angular Displacement of Heated and Cooled Section," ASME JOURNAL OF HEAT TRANSFER, Vol. 101, 1979, pp. 672-676.

6 Hart, J. E., "A New Analysis of the Closed Loop Thermosyphon," *International Journal of Heat and Mass Transfer*, Vol. 27, 1984, pp. 125-136.

7 Zvirin, Y., "The Effect of Dissipation on Free Convection Loops," *International Journal of Heat and Mass Transfer*, Vol. 22, 1979, pp. 1539-1546.

Biot's Variational Method to Fluidized-Bed Coating on Thin Plates

V. Dharma Rao[1], P. K. Sarma[2], G. J. V. J. Raju[3]

Nomenclature

C = specific heat
h = heat transfer coefficient
h_{sf} = latent heat of fusion of the polymeric resin
H = heat flux variable defined in equation (7)
H^* = dimensionless heat flux variable, $\phi\alpha_c H/X_m^2 h(T_m - T_\infty)$
k = thermal conductivity
L = half-thickness of the object
t = time
T = temperature
x = position coordinate
x^* = dimensionless position coordinate, x/X_m
X = coating film thickness
X_m = maximum coating thickness for the case of constant object temperature, $k_c(T_{w_0} - T_m)/h(T_m - T_\infty)$
z = heat capacity ratio parameter, $(\rho_c C_c/\rho_w C_w)(k_c/hL)$

Greek Symbols

α = thermal diffusivity
θ_ω = dimensionless variable object temperature, $(T_w(t) - T_m)/(T\omega_0 - T_m)$
ρ = density
τ = dimensionless time, $\phi\alpha_c t/X_m^2$
ϕ = temperature ratio parameter, $(T_{\omega_0} - T_m)/(T_m - T_\infty)$
δ = x/x_m

Subscripts

c = coating film
w = object
∞ = fluidized bed

Introduction

The method of fluidized-bed coating of polymeric resins on metal objects has been extensively in use either to suppress corrosion or to provide adequate electrical insulation. Theory and practice regarding this process have been put forth in various references [1, 2, 3, 4, 5, 6]. In a recent paper El-Genk and Cronenberg [7] have summarized all the possible boundary conditions at the interface of wall-frozen crust and that of frozen crust-liquid. According to them, many problems pertaining to phase transformation should fall in one of the four cases (See Table 1 of [7]). The general classification is given as follows: (*i*) continuous growth of the frozen crust, (*ii*) asymptotic growth of the crust, and (*iii*) growth and decay of the crust, depending upon the combination of boundary conditions chosen. However, a possibility of asymptotic growth of the frozen crust with the fourth kind of boundary condition, viz., the convective condition at the interface of the frozen crust and the fluid and diabatic condition of equality of the heat fluxes at the interface of frozen layer and wall, is encountered in problems dealing with coating of polymeric resins on metal objects of finite size immersed in a levitated medium of the polymer powder. Thus the present note investigates this aspect precluded in [7]. Elmas [4], tackled this problem with the inclusion of an arbitrary exponential decay of the object temperature with time. A redundant coupling of the decay of the temperature of the metal object with respect to time with the equation of thermal diffusion and other governing equations depicting phase transformation does not yield realistic values. Hence the present note is intended to solve the problem of frozen crust of polymer considering the thin metal object as a lumped system making use of Biot's variational technique.

Analysis of the Problem

The configuration of the metal object chosen for coating is a thin plate of 2 L thickness with the thermal conductivity of the object being much greater than that of the resin. The plate, initially at a temperature T_{w_0} is immersed in the bulk of the fluidized medium of the resin powder and $T_{w_0} > T_m > T_\infty$.

The coating process is governed by the unsteady-state heat conduction equation in the region of the coating film as follows

$$k_c \frac{\partial^2 T}{\partial x^2} = \rho_c C_c \frac{\partial T}{\partial t} \tag{1}$$

which obeys the following boundary conditions

$$x = 0 \text{ [i.e., frozen crust-wall interface]}, T = T_w(t) \tag{2}$$

$$x = X(t) \text{ [i.e., frozen crust-fluidized medium interface]}, T = T_m \tag{3}$$

$$x = X(t), -k_c \frac{\partial T}{\partial x} = h(T_m - T_\infty) + \rho_c C_c (T_m - T_\infty) \frac{dX}{dt} \left[1 + \frac{h_{sf}}{C_c(T_m - T_\infty)}\right] \ldots \tag{4}$$

and the initial boundary condition being

$$t = 0, X = 0 \tag{5}$$

The active period of coating formation is stipulated by the condition $dX/dt = 0$. For the periods of time greater than the active coating duration, the enthalpy change of the plate is to be balanced by the convective cooling and the temperature on the coating film surface thereafter should assume time-variant behavior.

In case of powdered polymers used for coating objects, usually the ratio $h_{sf}/C_c(T_m - T_\infty)$ is by far less than unity. Thus in equation (4) the term $(\rho_c h_{sf}\, dX/dt)$ can be deleted. Further, lumped system analysis is accepted when Biot modulus $(hl^*/k_w) \leq 0.1$, where l^* is the characteristic dimension of the object [8]. Accepting that the same limit holds good in the present case, combination of the heat

---

[1,3] Department of Chemical Engineering.

[2] Department of Mechanical Engineering, Andhra University, Visakhapatnam, 530 003, India

Contributed by the Heat Transfer Division for publication in the JOURNAL OF HEAT TRANSFER. Manuscript received by the Heat Transfer Division April 20, 1984.

4 MacGregor, R. K., and Emery, A. P., "Free Convection Through Vertical Plane Layers: Moderate and High Prandtl Number Fluids," ASME JOURNAL OF HEAT TRANSFER, Vol. 91, 1969, pp. 391-398.
5 Damerell, P. S., and Schoenhals, R. J., "Flow in a Toroidal Thermosyphon with Angular Displacement of Heated and Cooled Section," ASME JOURNAL OF HEAT TRANSFER, Vol. 101, 1979, pp. 672-676.
6 Hart, J. E., "A New Analysis of the Closed Loop Thermosyphon," *International Journal of Heat and Mass Transfer*, Vol. 27, 1984, pp. 125-136.
7 Zvirin, Y., "The Effect of Dissipation on Free Convection Loops," *International Journal of Heat and Mass Transfer*, Vol. 22, 1979, pp. 1539-1546.

Biot's Variational Method to Fluidized-Bed Coating on Thin Plates

V. Dharma Rao[1], **P. K. Sarma**[2], **G. J. V. J. Raju**[3]

Nomenclature

C = specific heat
h = heat transfer coefficient
h_{sf} = latent heat of fusion of the polymeric resin
H = heat flux variable defined in equation (7)
H^* = dimensionless heat flux variable, $\phi\alpha_c H/X_m^2 h(T_m - T_\infty)$
k = thermal conductivity
L = half-thickness of the object
t = time
T = temperature
x = position coordinate
x^* = dimensionless position coordinate, x/X_m
X = coating film thickness
X_m = maximum coating thickness for the case of constant object temperature, $k_c(T_{w_0} - T_m)/h(T_m - T_\infty)$
z = heat capacity ratio parameter, $(\rho_c C_c/\rho_w C_w)(k_c/hL)$

Greek Symbols

α = thermal diffusivity
θ_ω = dimensionless variable object temperature, $(T_w(t) - T_m)/(T\omega_0 - T_m)$
ρ = density
τ = dimensionless time, $\phi\alpha_c t/X_m^2$
ϕ = temperature ratio parameter, $(T_{\omega_0} - T_m)/(T_m - T_\infty)$
δ = x/x_m

Subscripts

c = coating film
w = object
∞ = fluidized bed

Introduction

The method of fluidized-bed coating of polymeric resins on metal objects has been extensively in use either to suppress corrosion or to provide adequate electrical insulation. Theory and practice regarding this process have been put forth in various references [1, 2, 3, 4, 5, 6]. In a recent paper El-Genk and Cronenberg [7] have summarized all the possible boundary conditions at the interface of wall-frozen crust and that of frozen crust-liquid. According to them, many problems pertaining to phase transformation should fall in one of the four cases (See Table 1 of [7]). The general classification is given as follows: (*i*) continuous growth of the frozen crust, (*ii*) asymptotic growth of the crust, and (*iii*) growth and decay of the crust, depending upon the combination of boundary conditions chosen. However, a possibility of asymptotic growth of the frozen crust with the fourth kind of boundary condition, viz., the convective condition at the interface of the frozen crust and the fluid and diabatic condition of equality of the heat fluxes at the interface of frozen layer and wall, is encountered in problems dealing with coating of polymeric resins on metal objects of finite size immersed in a levitated medium of the polymer powder. Thus the present note investigates this aspect precluded in [7]. Elmas [4], tackled this problem with the inclusion of an arbitrary exponential decay of the object temperature with time. A redundant coupling of the decay of the temperature of the metal object with respect to time with the equation of thermal diffusion and other governing equations depicting phase transformation does not yield realistic values. Hence the present note is intended to solve the problem of frozen crust of polymer considering the thin metal object as a lumped system making use of Biot's variational technique.

Analysis of the Problem

The configuration of the metal object chosen for coating is a thin plate of 2 L thickness with the thermal conductivity of the object being much greater than that of the resin. The plate, initially at a temperature T_{w_0} is immersed in the bulk of the fluidized medium of the resin powder and $T_{w_0} > T_m > T_\infty$.

The coating process is governed by the unsteady-state heat conduction equation in the region of the coating film as follows

$$k_c \frac{\partial^2 T}{\partial x^2} = \rho_c C_c \frac{\partial T}{\partial t} \qquad (1)$$

which obeys the following boundary conditions

x = 0 [i.e., frozen crust-wall interface], $T = T_w(t)$ (2)

x = $X(t)$ [i.e., frozen crust-fluidized medium interface], $T = T_m$ (3)

$$x = X(t), -k_c \frac{\partial T}{\partial x} = h(T_m - T_\infty) + \rho_c C_c (T_m - T_\infty)\frac{dX}{dt}\left[1 + \frac{h_{sf}}{C_c(T_m - T_\infty)}\right] \ldots \qquad (4)$$

and the initial boundary condition being

t = $0, X = 0$ (5)

The active period of coating formation is stipulated by the condition $dX/dt = 0$. For the periods of time greater than the active coating duration, the enthalpy change of the plate is to be balanced by the convective cooling and the temperature on the coating film surface thereafter should assume time-variant behavior.

In case of powdered polymers used for coating objects, usually the ratio $h_{sf}/C_c(T_m - T_\infty)$ is by far less than unity. Thus in equation (4) the term $(\rho_c h_{sf}\, dX/dt)$ can be deleted. Further, lumped system analysis is accepted when Biot modulus $(hl^*/k_w) \leq 0.1$, where l^* is the characteristic dimension of the object [8]. Accepting that the same limit holds good in the present case, combination of the heat

---

[1,3] Department of Chemical Engineering.
[2] Department of Mechanical Engineering, Andhra University, Visakhapatnam, 530 003, India

Contributed by the Heat Transfer Division for publication in the JOURNAL OF HEAT TRANSFER. Manuscript received by the Heat Transfer Division April 20, 1984.

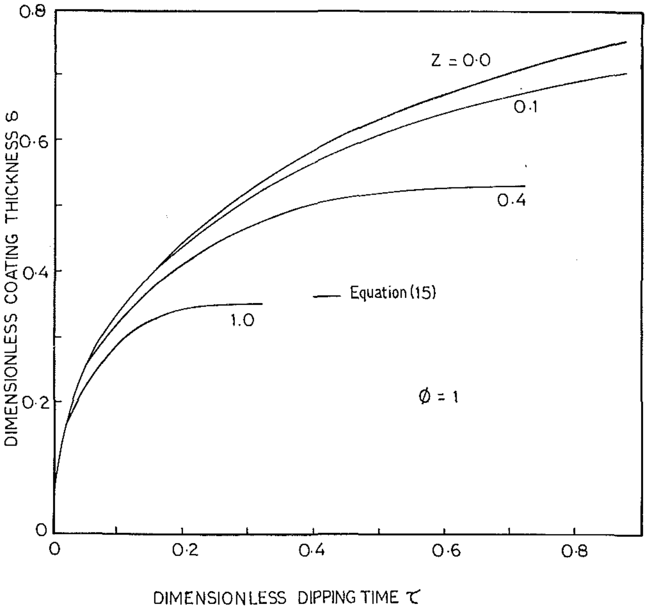

Fig. 1 Effect of the heat capacity ratio parameter z on the coating rate

balance at the object's surface ($x=0$) with equation (1) in integral form gives the following relation for the variable objective temperature, $T_w(t)$

$$\rho_w C_w L(T_{w_0} - T_w) = h(T_m - T_\infty)t + \rho_c C_c(T_m - T_\infty)X + \rho_c C_c \int_0^X (T - T_m)dx \tag{6}$$

Following Biot, a heat flux variable, H is defined such that

$$\left.\begin{aligned} \frac{\partial H}{\partial t} &= -k_c \frac{\partial T}{\partial x} \\ \text{and} \qquad \frac{\partial H}{\partial x} &= -\rho_c C_c (T - T_m) \end{aligned}\right\} \tag{7}$$

In terms of H equations (2–4) and equation (6) are transformed as below

$$\frac{\partial H}{\partial x}(0,t) = -\rho_c C_c (T_w - T_m) \tag{8}$$

$$\frac{\partial H}{\partial x}(X,t) = 0 \tag{9}$$

$$\frac{\partial H}{\partial t}(X,t) = h(T_m - T_\infty) + \rho_c C_c (T_m - T_\infty)\frac{dX}{dt} \tag{10}$$

$$H(0,t) = \rho_w C_w L (T_{w_0} - T_w) \tag{11}$$

A second degree equation for H is chosen subject to the boundary conditions equations (8–11). Thus the profile can be written as follows

$$H^* = \left(\tau + \delta + \frac{\phi\delta}{2}\theta_w\right) - \phi\theta_w x^* + \frac{\phi\theta_w}{2\delta} x^{*2} \tag{12}$$

where

$$\theta_w = (1 - z\tau - z\delta)\Big/\left(1 + \frac{z\phi}{2}\delta\right) \tag{13}$$

For the particular case, Biot's variational statement in dimensionless notation is expressed below

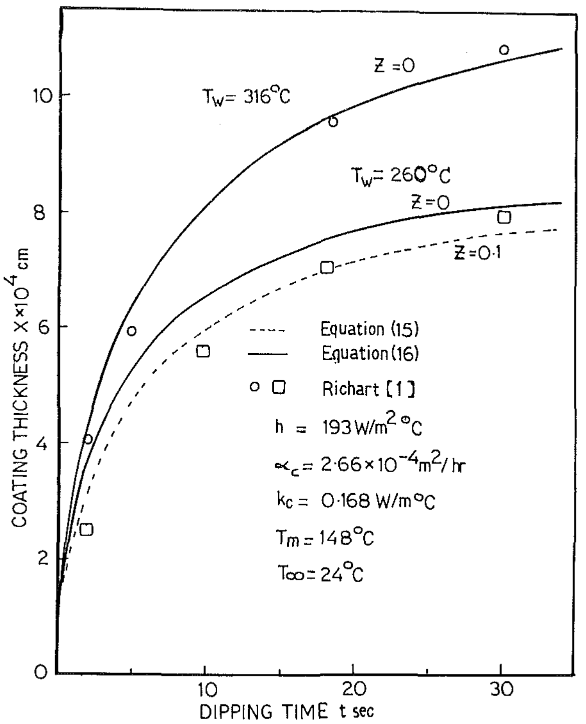

Fig. 2 Comparison of the present theory with experimental data of Richart [1]

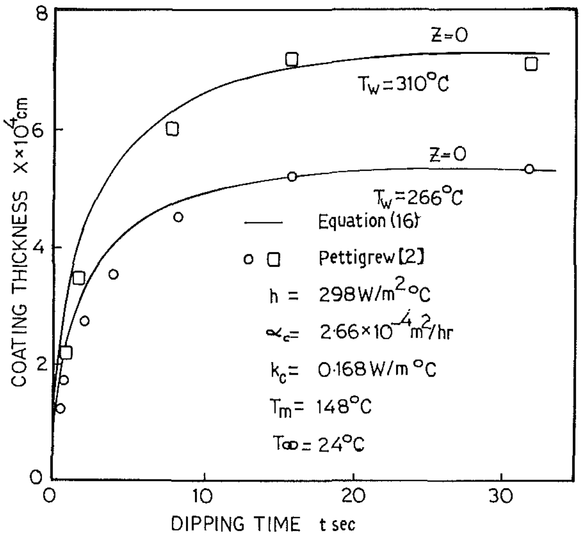

Fig. 3 Comparison of the present theory with experimental data of Pettigrew [2]

$$\int_0^\delta \left[\phi \frac{\partial H^*}{\partial \tau}\frac{\partial H^*}{\partial \delta} + \frac{\partial H^*}{\partial x^*}\frac{\partial}{\partial \delta}\left(\frac{\partial H^*}{\partial x^*}\right)\right]dx^* = \left.\frac{\partial H^*}{\partial x^*}\frac{\partial H^*}{\partial \delta}\right|_0^\delta \tag{14}$$

H^* from equation (12) is substituted in equation (14) to yield the following differential equation

$$\frac{d\delta}{d\tau} = \frac{60(\theta_w - \delta) + 20\phi(1-\delta)(\theta_w - F_1) + F_2F_3}{\delta[20(3 + \phi\theta_w - \phi F_1) + \phi\theta_w(20 + 8\phi\theta_w - 9\phi F_1) - \phi F_1 F_3]} \tag{15}$$

where

$$F_1 = z\delta(2+\phi-z\phi\tau)/(2+z\phi\delta)^2$$

$$F_2 = \phi z\delta^2/(2+z\phi\delta)$$

and

$$F_3 = 20+9\phi\theta_w-12\phi F_1$$

With the initial condition $\tau=0$, $\delta=0$, equation (15) is numerically solved for δ as a function of τ by employing the fourth-order Runge-Kutta method, and the results are plotted in Fig. 1 for various values of the dimensionless heat capacity ratio parameter z.

The value of $z=0$ signifies the infinite heat capacity of the metal object to that of the coating resin, which incidentally corresponds to the particular case of constant object temperature, i.e., $T_w(t)=T_{w_0}$ (see equation (13)). The case of constant object temperature was already solved numerically by Gutfinger and Chen [3]. For the case of $z=0$, equation (15) reduces to a simple integrable form yielding an explicit solution for the coating film history with respect to time, hither to not available, as follows

$$\tau=\frac{(15+10\phi+2\phi^2)}{5(3+\phi)}[-\ln(1-\delta)-\delta] \tag{16}$$

Obviously, the isothermal case of the wall excludes the influence of the heat capacity ratio parameter z. The present theory is compared with the experimental data of Richart [1] and Pettigrew [2] in Figs. 2 and 3, respectively. Unfortunately, the magnitude of z is not evident in the experimental results of [2, 3]. For this reason equation (16), a limiting solution of equation (15) with $z=0$, is used for comparison with the experimental data. However, in a particular situation where the deviation between equation (16) and the experimental data is considerable, results of equation (15) with a reasonably fair guess $z=0.1$, gives closer agreement between theory shown as dotted line in Fig. 2 with the data of Richart [1]. Thus, the deviation, if any, between the data and theory can be mainly attributed to the influence of z, not accounted for in equation (16).

In conclusion, the present note brings out the effect of heat capacity ratio parameter on the coating rate and an explicit solution in simple form for ready use by the coating technologist giving the limiting values of growth of the coating film with respect to time under isothermal conditions.

Acknowledgments

The authors thank Dr. M. Epstein, the reviewers for their constructive comments and The University Grants Commission New Delhi for financial support.

References

1 Richart, D. S., "A Report on the Fluidized-Bed Coating System, Part 2—Plastics for Coating and Their Selection," *Plastics Design Technology*, Vol. 2, 1962, pp. 26-34.

2 Pettigrew, C. K., "Fluidized-Bed Coating," *Modern Plastics*, Vol. 44, 1966, pp. 150-156.

3 Gutfinger, C., and Chen, W. H., "Heat Transfer with a Moving Boundary—Application to Fluidized-Bed Coating," *International Journal of Heat and Mass Transfer*, Vol. 12, 1969, pp. 1097-1108.

4 Elmas, M., "On Heat Transfer with Moving Boundary," *International Journal of Heat and Mass Transfer*, Vol. 13, 1970, pp. 1625-1627.

5 Abuaf, N., and Gutfinger, C., "Heat Transfer with a Moving Boundary—Application to Fluidized-Bed Coating of Thin Plates," *International Journal of Heat and Mass Transfer*, Vol. 16, 1973, pp. 213-216.

6 Dharma, Rao, V., Murthy, G. S., and Sarma, P. K., "A Note to Predict the Thickness of the Resin Coating with Time—A Moving Boundary Problem," *Chem. Eng. Sci.*, Vol. 32, 1977, pp. 671-673.

7 El-Genk, M. S., and Cronenberg, A. W., "Stefan—Like Problems in Finite Geometry," *AIChE Symposium Series*, Vol. 75, 1979, pp. 69-80.

8 Holman, J. P., *Heat Transfer*, McGraw-Hill, New York, 1968.

Limitations of the Single-Phase Model for Solid-Gas Heat Transfer in Packed Beds

C. R. B. Hoerger[1] **and W. F. Phillips**[2]

Introduction

Since the early work of Schumann [1], analysis of heat transfer in packed beds has led to the refinement of the original two-phase model into single-phase models. The differential equations of the two-phase models were formulated from separate energy balances for both the solid and fluid phases. The reduction of the two-phase model to a single-phase model is usually performed by neglecting the fluid heat capacity and assuming that the fluid temperature or its spatial derivative is the same as that for the solid [2-5].

Several authors have shown that the single-phase model is equivalent to the two-phase model for typical air-rock bed energy storage applications [2-8]. However, these studies have not set rigorous limits on the ranges of parameters for which the single-phase and two-phase models are equivalent. In addition, Phillips [8] has shown that the assumption of equality of gas and bed temperatures or their spatial derivatives is unnecessarily strict in the single-phase model development. This result indicates that the single-phase model may accurately describe heat transfer in packed beds with finite heat transfer coefficients. The present study examines the model parameters and determines the limits for which the two models are equivalent.

A convenient nondimensionalization and development of the single-phase model is presented by Phillips [8]. The equations of the model are

$$\frac{\partial T_b}{\partial \tau} - \left(M_k + \frac{1}{N_s}\right)\frac{\partial^2 T_b}{\partial \zeta^2} + \frac{\partial T_b}{\partial \zeta} = 0 \tag{1}$$

$$\left(M_k + \frac{1}{N_s}\right)\frac{\partial T_b}{\partial \zeta}(0,\tau) + T_i - T_b(0,\tau) = 0 \tag{2}$$

$$\frac{\partial T_b}{\partial \zeta}(1,\tau) = 0 \tag{3}$$

$$T_g = T_b - \frac{1}{N_s}\frac{\partial T_b}{\partial \zeta} \tag{4}$$

where the dimensionless variables are defined

$$\zeta = \frac{X}{H} \tag{5}$$

$$\tau = \frac{\dot{C}t}{C_s} \tag{6}$$

$$N_s = \frac{HA_c h_v}{\dot{C}} \tag{7}$$

$$M_k = \frac{A_c k}{\dot{C}H} \tag{8}$$

$$\lambda = \frac{(1-\gamma)A_c}{A_s} \tag{9}$$

Here T_b and T_g are the temperature of the bed and the gas,

---

[1] Graduate Student, Utah State University, and presently Adjunct Assistant Professor, Department of Mechanical Engineering, Montana State University, Bozeman, Montana 59717.

[2] Professor, Mechanical Engineering Department, Utah State University, Logan, Utah 84322.

Contributed by the Heat Transfer Division for publication in the JOURNAL OF HEAT TRANSFER. Manuscript received by the Heat Transfer Division June 22, 1983.

where

$$F_1 = z\delta(2+\phi-z\phi\tau)/(2+z\phi\delta)^2$$
$$F_2 = \phi z\delta^2/(2+z\phi\delta)$$

and

$$F_3 = 20+9\phi\theta_w-12\phi F_1$$

With the initial condition $\tau=0$, $\delta=0$, equation (15) is numerically solved for δ as a function of τ by employing the fourth-order Runge-Kutta method, and the results are plotted in Fig. 1 for various values of the dimensionless heat capacity ratio parameter z.

The value of $z=0$ signifies the infinite heat capacity of the metal object to that of the coating resin, which incidentally corresponds to the particular case of constant object temperature, i.e., $T_w(t)=T_{w_0}$ (see equation (13)). The case of constant object temperature was already solved numerically by Gutfinger and Chen [3]. For the case of $z=0$, equation (15) reduces to a simple integrable form yielding an explicit solution for the coating film history with respect to time, hither to not available, as follows

$$\tau=\frac{(15+10\phi+2\phi^2)}{5(3+\phi)}[-\ln(1-\delta)-\delta] \tag{16}$$

Obviously, the isothermal case of the wall excludes the influence of the heat capacity ratio parameter z. The present theory is compared with the experimental data of Richart [1] and Pettigrew [2] in Figs. 2 and 3, respectively. Unfortunately, the magnitude of z is not evident in the experimental results of [2, 3]. For this reason equation (16), a limiting solution of equation (15) with $z=0$, is used for comparison with the experimental data. However, in a particular situation where the deviation between equation (16) and the experimental data is considerable, results of equation (15) with a reasonably fair guess $z=0.1$, gives closer agreement between theory shown as dotted line in Fig. 2 with the data of Richart [1]. Thus, the deviation, if any, between the data and theory can be mainly attributed to the influence of z, not accounted for in equation (16).

In conclusion, the present note brings out the effect of heat capacity ratio parameter on the coating rate and an explicit solution in simple form for ready use by the coating technologist giving the limiting values of growth of the coating film with respect to time under isothermal conditions.

Acknowledgments

The authors thank Dr. M. Epstein, the reviewers for their constructive comments and The University Grants Commission New Delhi for financial support.

References

1 Richart, D. S., "A Report on the Fluidized-Bed Coating System, Part 2—Plastics for Coating and Their Selection," *Plastics Design Technology*, Vol. 2, 1962, pp. 26-34.

2 Pettigrew, C. K., "Fluidized-Bed Coating," *Modern Plastics*, Vol. 44, 1966, pp. 150-156.

3 Gutfinger, C., and Chen, W. H., "Heat Transfer with a Moving Boundary—Application to Fluidized-Bed Coating," *International Journal of Heat and Mass Transfer*, Vol. 12, 1969, pp. 1097-1108.

4 Elmas, M., "On Heat Transfer with Moving Boundary," *International Journal of Heat and Mass Transfer*, Vol. 13, 1970, pp. 1625-1627.

5 Abuaf, N., and Gutfinger, C., "Heat Transfer with a Moving Boundary—Application to Fluidized-Bed Coating of Thin Plates," *International Journal of Heat and Mass Transfer*, Vol. 16, 1973, pp. 213-216.

6 Dharma, Rao, V., Murthy, G. S., and Sarma, P. K., "A Note to Predict the Thickness of the Resin Coating with Time—A Moving Boundary Problem," *Chem. Eng. Sci.*, Vol. 32, 1977, pp. 671-673.

7 El-Genk, M. S., and Cronenberg, A. W., "Stefan—Like Problems in Finite Geometry," *AIChE Symposium Series*, Vol. 75, 1979, pp. 69-80.

8 Holman, J. P., *Heat Transfer*, McGraw-Hill, New York, 1968.

Limitations of the Single-Phase Model for Solid-Gas Heat Transfer in Packed Beds

C. R. B. Hoerger[1] **and W. F. Phillips**[2]

Introduction

Since the early work of Schumann [1], analysis of heat transfer in packed beds has led to the refinement of the original two-phase model into single-phase models. The differential equations of the two-phase models were formulated from separate energy balances for both the solid and fluid phases. The reduction of the two-phase model to a single-phase model is usually performed by neglecting the fluid heat capacity and assuming that the fluid temperature or its spatial derivative is the same as that for the solid [2-5].

Several authors have shown that the single-phase model is equivalent to the two-phase model for typical air-rock bed energy storage applications [2-8]. However, these studies have not set rigorous limits on the ranges of parameters for which the single-phase and two-phase models are equivalent. In addition, Phillips [8] has shown that the assumption of equality of gas and bed temperatures or their spatial derivatives is unnecessarily strict in the single-phase model development. This result indicates that the single-phase model may accurately describe heat transfer in packed beds with finite heat transfer coefficients. The present study examines the model parameters and determines the limits for which the two models are equivalent.

A convenient nondimensionalization and development of the single-phase model is presented by Phillips [8]. The equations of the model are

$$\frac{\partial T_b}{\partial \tau}-\left(M_k+\frac{1}{N_s}\right)\frac{\partial^2 T_b}{\partial \zeta^2}+\frac{\partial T_b}{\partial \zeta}=0 \tag{1}$$

$$\left(M_k+\frac{1}{N_s}\right)\frac{\partial T_b}{\partial \zeta}(0,\tau)+T_i-T_b(0,\tau)=0 \tag{2}$$

$$\frac{\partial T_b}{\partial \zeta}(1,\tau)=0 \tag{3}$$

$$T_g=T_b-\frac{1}{N_s}\frac{\partial T_b}{\partial \zeta} \tag{4}$$

where the dimensionless variables are defined

$$\zeta=\frac{X}{H} \tag{5}$$

$$\tau=\frac{\dot{C}t}{C_s} \tag{6}$$

$$N_s=\frac{HA_c h_v}{\dot{C}} \tag{7}$$

$$M_k=\frac{A_c k}{\dot{C}H} \tag{8}$$

$$\lambda=\frac{(1-\gamma)A_c}{A_s} \tag{9}$$

Here T_b and T_g are the temperature of the bed and the gas,

---

[1] Graduate Student, Utah State University, and presently Adjunct Assistant Professor, Department of Mechanical Engineering, Montana State University, Bozeman, Montana 59717.

[2] Professor, Mechanical Engineering Department, Utah State University, Logan, Utah 84322.

Contributed by the Heat Transfer Division for publication in the JOURNAL OF HEAT TRANSFER. Manuscript received by the Heat Transfer Division June 22, 1983.

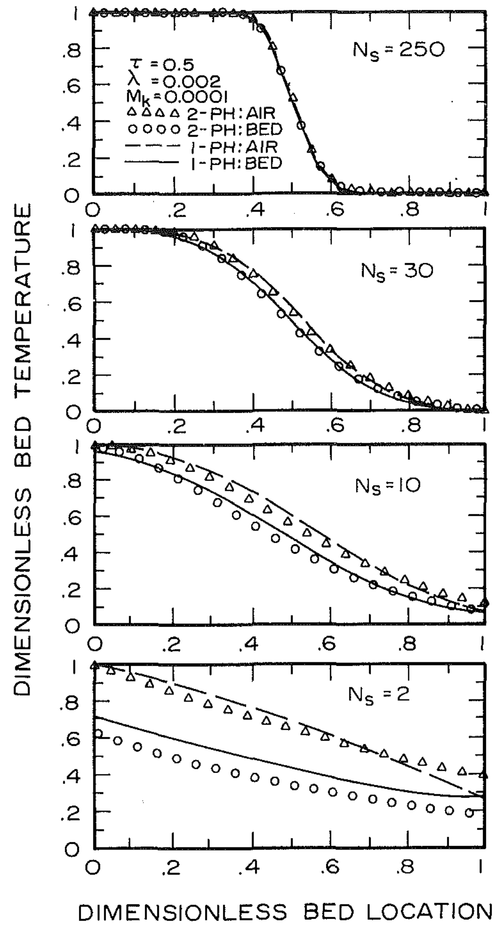

Fig. 1 Effect of N_S on single- and two-phase temperature profiles for M_k = 0.0001

respectively; C_s is the mass-specific heat product for the bed; H is the length of bed parallel to the flow direction; h_v is the reduced volumetric heat transfer coefficient; k is the thermal conductivity of the bed; t is time; A_c is the bed cross-sectional area perpendicular to the flow; X is the spatial coordinate in the direction of flow measured from the inlet; $\dot{C}$ is the mass flow rate-specific heat product for the gaseous phase; γ is the void fraction; T_i is the inlet gas temperature; and A_s is the total surface area of the bed packing material. For a discussion of the various parameters, assumptions, and model development see [2–6, 8]. The parameter λ does not appear in the single-phase model, but occurs in the two-phase model. Its effect on differences between the models will be considered below.

Although analytical solutions exist for simple inlet conditions, the models are usually solved numerically to allow for an arbitrarily specified inlet fluid temperature. In this study, the governing equations were solved using central differences to approximate both spatial and temporal derivatives. The number of spatial elements and the time step were determined by comparing the results to an analytical solution for the case of an infinitely long bed. The conditions of constant initial bed temperature and a step change in inlet gas temperature were used to calculate the bed and gas temperature profiles as a function of time. The resulting profiles for the two models were then compared to determine the range in the parameters M_k, N_s, and λ for which the single-phase model is accurate.

Results

To determine the range of N_s for which the single-phase model remains valid, N_s was reduced until there was substantial deviation between the single-phase and two-phase models. Temperature profiles for N_s = 250, 30, 10, and 2 are plotted in Fig. 1 for a bed with low thermal conductivity. Figure 1 shows that when N_s is large, the gas and bed temperatures are essentially the same and both models predict the same temperature profile. When N_s is reduced to 30, the air and bed temperatures are no longer equal; however, the single-phase model still agrees with the two-phase model. As N_s is reduced further, the temperature profiles predicted by the two models begin to deviate by N_s = 10 and show substantial deviation at N_s = 2, as shown in Fig. 1.

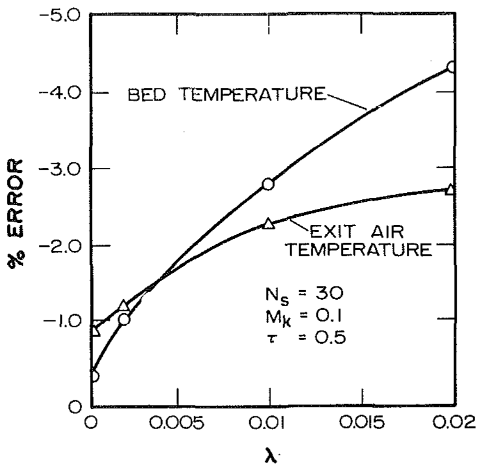

Fig. 2 Effect of λ on the agreement of the single-phase and two-phase models

Similar sets of temperature profiles were studied for M_k values of 0.0001, 0.01, and 0.1. For the cases with $N_s \geq 30$, the error between the two models was at most 1.0 percent in terms of average bed temperature, and less than 2.0 percent in predicted exit gas temperature. Even at N_s = 10, the maximum errors of the single-phase model were 1.3 and 5.2 percent for average bed and exit gas temperatures, respectively.

For a typical rock bed of 1 m^2 cross-section, 2 m height, with an air flow rate of 5 m^3/min, and 2.5 cm rocks, N_s would equal 37 and M_k would be about 0.0003. For such a bed, the air and rock temperatures would not be equal; however, the single-phase model would still accurately predict the temperature profiles.

The third parameter studied was λ, which appears only in the boundary conditions of the two-phase model [8]. Physically, λ represents the ratio of the heat transfer area at the bed entrance (normal to the flow) to the total heat transfer surface area in the bed. For a bed of packed spheres, it may be shown that

$$\lambda = \frac{1}{6}\left(\frac{d}{H}\right) \tag{10}$$

where d is the diameter of the spheres. Using this expression for the previous example, (H/d = 80) gives λ = 0.002. Assuming a minimum bed height of 10 dia would result in a λ of approximately 0.02. Thus the range in λ studied was from 0.0 to 0.02.

For M_k values of 0.0001 and 0.01, varying λ affected the average bed temperature and gas exit temperature by less than 1 percent of the temperature step. For an M_k value of 0.1, λ did have an effect on the temperature profiles. Figure 2 shows the error for the worst case, N_s = 30.

Over the range of parameters studied, varying λ resulted in at most 4.3 percent error in average bed temperatures calculated by the single-phase model. Variations in gas exit temperatures were less.

Discussion

The simplicity of the single-phase model results in several advantages over the two-phase model. Numerical solutions for the single-phase model converge more rapidly in terms of the number of spatial elements, especially at $M_k \geq 0.1$. The two-phase iteration matrix has two equations for each element – one for the bed and one for the gas – versus one for the single-phase model. Both of these advantages result in the single-phase model requiring much less computation time than the two-phase model. In addition, the single-phase model is more easily applied to convolution and other analytical methods because it is less complex mathematically.

These advantages of the single-phase model are likely to justify its use even in parameter ranges that cause it to be slightly in error. The results show that the single-phase model is accurate to within one percent for $M_k \leq 0.01$ and $N_s \geq 30$, regardless of the value of λ. Furthermore, for $N_s \geq 10$ and $M_k \leq 0.1$, the single-phase model yields results that are accurate to within about 5 percent of the two-phase model. Thus the suggested range of use for the single-phase model is $M_k \leq 0.1$ and $N_s \geq 10$, regardless of λ. This range covers a large portion of packed bed applications and does not require that the gas and bed temperatures be equal. Furthermore, equation (4) may be used to calculate the gas temperature profile from the bed temperature profile. Extrapolating to the case of highly conducting beds ($M_k > 0.1$), the single-phase model is likely to yield good results for small λ. Such cases were not studied, due to the excessively long execution times required for the two-phase model in this range.

References

1 Schumann, T. E. W., "Heat Transfer: A Liquid Flowing Through a Porous Prism," *Journal of Franklin Institute*, Vol. 208, 1929, pp. 405-416.

2 Loef, G. O. G., and Hawley, R. W., "Unsteady-State Heat Transfer between Air and Loose Solids," *Industrial Engineering Chemistry*, Vol. 40, 1948, pp. 1061-1070.

3 Vortmeyer, D., and Schaefer, R. J., "Equivalence of One- and Two-Phase Models for Heat Transfer Processes in Packed Beds: One Dimensional Theory," *Chemical Engineering Science*, Vol. 29, 1974, pp. 485-491.

4 Riaz, M., "Analytical Solutions for Single- and Two-Phase Models of Packed-Bed Thermal Storage Systems," ASME JOURNAL OF HEAT TRANSFER, Vol. 99, 1977, pp. 489-492.

5 Hughes, P. J., Klein, S. A., and Close, D. M., "Packed Bed Thermal Storage Models for Solar Air Heating and Cooling Systems," ASME JOURNAL OF HEAT TRANSFER, Vol. 98, 1976, pp. 336-338.

6 Jefferson, C. P., "Prediction of Breakthrough Curves in Packed Beds," *AIChE Journal*, Vol. 18, 1972, pp. 409-420.

7 Klein, S. A., Cooper, P. I., Beckman, W. A., and Duffie, J. A., "TRNSYS, A Transient Simulation Program," Engineering Experiment Station Report #38, University of Wisconsin, Madison, 1974.

8 Phillips, W. F., "Effects of Stratification on the Performance of Solar Air Heating Systems," *Solar Energy*, Vol. 26, 1981, pp. 175-180.

On the Two Regimes of Nucleate Boiling

J. H. Lienhard[1]

Nomenclature

g = acceleration of gravity
h_{fg} = latent heat of vaporization
MBT = the Moissis-Berenson transition
$q, q_{\max}, q_{\rm MB}$ = boiling heat flux; peak pool boiling heat flux; heat flux at the Moissis-Berenson transition
R = radius of a horizontal cylindrical heater
β = contact angle
ΔT = heater temperature minus saturation temperature of boiled liquid
θ = the angle of tilt of a plate away from the horizontal upward-facing position
ρ_f, ρ_g = saturated liquid and vapor densities
σ = surface tension

Introduction

Moissis and Berenson's [1] explanation of the transition from the isolated bubbles regime to that of slugs and columns, in 1963, was a very important contribution to our understanding of nucleate pool boiling. This explanation, which traces to an idea advanced by Zuber [2], is seldom quoted because observations of the nucleate boiling heat flux q as a function of wall superheat ΔT are fairly continuous through the MBT (or Moissis-Berenson Transition.) It does not demand attention the way the peak heat flux transition, $q_{\max}$, does.

Nishikawa et al. [3] recently observed q and ΔT on a flat plate oriented at an angle θ, that varied between 0 and 175 deg from a horizontal, upward-facing position. Their results are shown in Fig. 1. The orientation strongly influences q, when q is low, but has no perceptible influence when q is high. Their discussion suggests they are aware of some features of the MBT, but they make no reference to it. We shall show how these data reveal the MBT, and how viewing them in terms of the mechanics of the MBT teaches us about the influence of orientation on boiling.

Some Hydrodynamic Mechanisms in Nucleate Boiling

The MBT. The assumed mechanism of the transition is simple: as q increases, isolated bubbles rise with increasing frequency from each active site. When they become close enough together to touch one another, a vapor jet must replace the series of bubbles. The point where this occurs

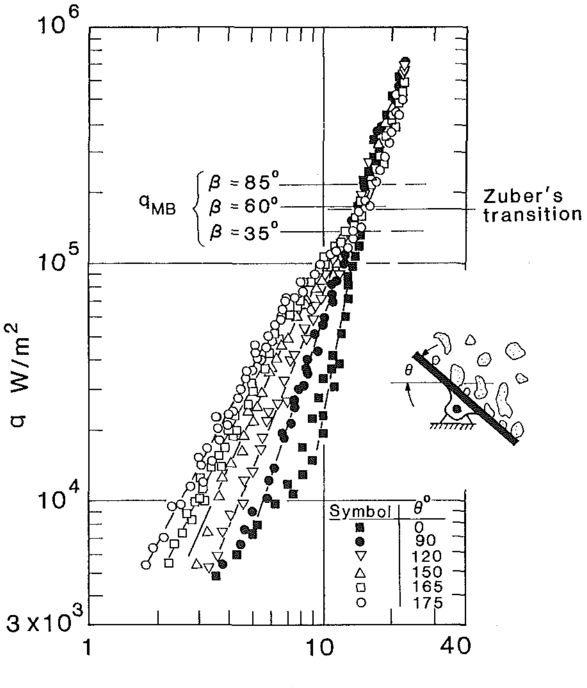

Fig. 1 The data of Nishikawa et al. and the predicted transition from isolated bubbles to slugs-and-columns

---

[1] Professor, Heat Transfer/Phase Change Laboratory, Mechanical Engineering Department, University of Houston, Houston, Texas 77004, Fellow ASME

Contributed by the Heat Transfer Division for publication in the JOURNAL OF HEAT TRANSFER. Manuscript received by the Heat Transfer division January 16, 1984.

Discussion

The simplicity of the single-phase model results in several advantages over the two-phase model. Numerical solutions for the single-phase model converge more rapidly in terms of the number of spatial elements, especially at $M_k \geq 0.1$. The two-phase iteration matrix has two equations for each element – one for the bed and one for the gas – versus one for the single-phase model. Both of these advantages result in the single-phase model requiring much less computation time than the two-phase model. In addition, the single-phase model is more easily applied to convolution and other analytical methods because it is less complex mathematically.

These advantages of the single-phase model are likely to justify its use even in parameter ranges that cause it to be slightly in error. The results show that the single-phase model is accurate to within one percent for $M_k \leq 0.01$ and $N_s \geq 30$, regardless of the value of λ. Furthermore, for $N_s \geq 10$ and $M_k \leq 0.1$, the single-phase model yields results that are accurate to within about 5 percent of the two-phase model. Thus the suggested range of use for the single-phase model is $M_k \leq 0.1$ and $N_s \geq 10$, regardless of λ. This range covers a large portion of packed bed applications and does not require that the gas and bed temperatures be equal. Furthermore, equation (4) may be used to calculate the gas temperature profile from the bed temperature profile. Extrapolating to the case of highly conducting beds ($M_k > 0.1$), the single-phase model is likely to yield good results for small λ. Such cases were not studied, due to the excessively long execution times required for the two-phase model in this range.

References

1 Schumann, T. E. W., "Heat Transfer: A Liquid Flowing Through a Porous Prism," *Journal of Franklin Institute*, Vol. 208, 1929, pp. 405-416.

2 Loef, G. O. G., and Hawley, R. W., "Unsteady-State Heat Transfer between Air and Loose Solids," *Industrial Engineering Chemistry*, Vol. 40, 1948, pp. 1061-1070.

3 Vortmeyer, D., and Schaefer, R. J., "Equivalence of One- and Two-Phase Models for Heat Transfer Processes in Packed Beds: One Dimensional Theory," *Chemical Engineering Science*, Vol. 29, 1974, pp. 485-491.

4 Riaz, M., "Analytical Solutions for Single- and Two-Phase Models of Packed-Bed Thermal Storage Systems," ASME JOURNAL OF HEAT TRANSFER, Vol. 99, 1977, pp. 489-492.

5 Hughes, P. J., Klein, S. A., and Close, D. M., "Packed Bed Thermal Storage Models for Solar Air Heating and Cooling Systems," ASME JOURNAL OF HEAT TRANSFER, Vol. 98, 1976, pp. 336-338.

6 Jefferson, C. P., "Prediction of Breakthrough Curves in Packed Beds," *AIChE Journal*, Vol. 18, 1972, pp. 409-420.

7 Klein, S. A., Cooper, P. I., Beckman, W. A., and Duffie, J. A., "TRNSYS, A Transient Simulation Program," Engineering Experiment Station Report #38, University of Wisconsin, Madison, 1974.

8 Phillips, W. F., "Effects of Stratification on the Performance of Solar Air Heating Systems," *Solar Energy*, Vol. 26, 1981, pp. 175-180.

On the Two Regimes of Nucleate Boiling

J. H. Lienhard[1]

Nomenclature

g = acceleration of gravity
h_{fg} = latent heat of vaporization
MBT = the Moissis–Berenson transition
$q, q_{\max}, q_{\mathrm{MB}}$ = boiling heat flux; peak pool boiling heat flux; heat flux at the Moissis–Berenson transition
R = radius of a horizontal cylindrical heater
β = contact angle
ΔT = heater temperature minus saturation temperature of boiled liquid
θ = the angle of tilt of a plate away from the horizontal upward-facing position
ρ_f, ρ_g = saturated liquid and vapor densities
σ = surface tension

Introduction

Moissis and Berenson's [1] explanation of the transition from the isolated bubbles regime to that of slugs and columns, in 1963, was a very important contribution to our understanding of nucleate pool boiling. This explanation, which traces to an idea advanced by Zuber [2], is seldom quoted because observations of the nucleate boiling heat flux q as a function of wall superheat ΔT are fairly continuous through the MBT (or Moissis-Berenson Transition.) It does not demand attention the way the peak heat flux transition, $q_{\max}$, does.

Nishikawa et al. [3] recently observed q and ΔT on a flat plate oriented at an angle θ, that varied between 0 and 175 deg from a horizontal, upward-facing position. Their results are shown in Fig. 1. The orientation strongly influences q, when q is low, but has no perceptible influence when q is high. Their discussion suggests they are aware of some features of the MBT, but they make no reference to it. We shall show how these data reveal the MBT, and how viewing them in terms of the mechanics of the MBT teaches us about the influence of orientation on boiling.

Some Hydrodynamic Mechanisms in Nucleate Boiling

The MBT. The assumed mechanism of the transition is simple: as q increases, isolated bubbles rise with increasing frequency from each active site. When they become close enough together to touch one another, a vapor jet must replace the series of bubbles. The point where this occurs

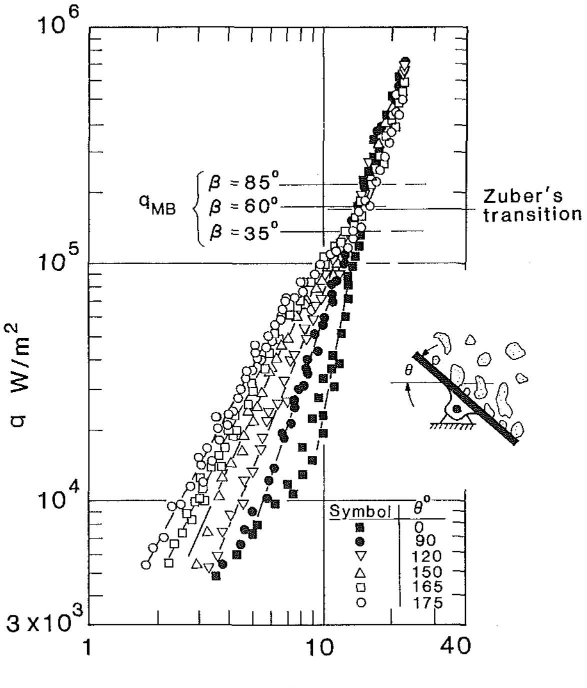

Fig. 1 The data of Nishikawa et al. and the predicted transition from isolated bubbles to slugs-and-columns

---

[1] Professor, Heat Transfer/Phase Change Laboratory, Mechanical Engineering Department, University of Houston, Houston, Texas 77004, Fellow ASME

Contributed by the Heat Transfer Division for publication in the JOURNAL OF HEAT TRANSFER. Manuscript received by the Heat Transfer division January 16, 1984.

depends on the departure diameter of the bubbles, and that in turn depends on the contact angle β. Thus the transitional heat flux $q_{\rm MB}$ obtained in [1] for a flat-plate heater was

$$q_{\rm MB} = 0.11 \rho_g h_{fg} (\sigma g/(\rho_f - \rho_g))^{1/4} \beta^{1/2} \text{ (flat plate)} \qquad (1)$$

A decade later, Lienhard and Bhattacharya [4] rederived the equation for a horizontal cylindrical heater of radius R and got

$$q_{\rm MB} \cong 0.000333 \rho_g h_{fg} \sqrt[4]{\frac{\sigma^3}{g(\rho_f - \rho_g)^3}} \frac{\beta^{3/2}}{R} \text{ (cylinder)} \qquad (2)$$

Both expressions were verified experimentally, but the transitions were blurred over modest ranges of q. Both depend on β, which is a nuisance variable in the problem, but the flat-plate prediction suffers far less, since q is proportional to $\beta^{1/2}$ instead of $\beta^{3/2}$.

Equation (1) is compared with the data from [3] in Fig. 1, based on g = earth-normal gravity. To make the comparison we had to guess β for this water-on-copper system. Despite the many analyses of nucleate boiling that involve β, useable values of β cannot be tabled, because it varies from one situation to another. However, values of 50 and 60 deg [5, 6] have been suggested for water boiling *in situ* on copper.

We checked this situation experimentally by dipping a tilted copper tube in water. With a patina of oxide, the otherwise clean surface gave β = 60 to 70 deg. Then we sanded the tube with fine emery paper and rinsed it in water without touching it. As we slowly immersed the dry copper in the water tank we obtained $\beta \cong$ 70 deg, but once it had been immersed, the clean sanded tube became wetted $- \beta = 0$. Photos of bubbles departing during nucleate boiling (see, e.g., [7]) do not ordinarily show wetting behavior. Indeed, most photos suggest that β = 50 to 70 deg is a reasonable *in situ* value. Therefore we used 60 deg in Fig. 1. An error of ±25 deg in β gives only ±21 percent variation of $q_{\rm MB}$ according to equation (1), as is noted in Fig. 1. That is within the "blur" of the observed transition.

Zuber's [2] prediction of the transition approaches equation (1) at low pressure, with one important difference. Instead of the factor $0.11\beta^{1/2}$ he got $1.53\pi/6$, which compared favorably with just the data of Gaertner and Westwater [8]. (This suggests that β was 53 deg for those data.) Zuber's result is also shown in Fig. 1.

Unfortunately, equations (1) and (2) show $q_{\rm MB} = fn(g)$. They are based on the notion that the bubble departure size is set by the force of gravity acting normal to the surface where the bubble grows. When θ is less than 90 deg, the mechanism is the same – it acts at an angle, but it should still set a comparable value of $q_{\rm MB}$. Beyond 90 deg, the component of g driving the bubble along the surface varies as $\sin\theta$. The mechanism of the MBT will differ in this range and the actual transition point will doubtless be shifted somewhat.

It thus seems clear that $q_{\rm MB}$ is where the Nishikawa et al. data lose their orientation dependence. We next ask what this says about nucleate boiling behavior.

Gravity and Orientation Dependence in the Isolated-Bubbles Regime. Many investigators of nucleate boiling have given correlations and/or predictions that suggest there is no influence of gravity on q [9–13]. While these results have provided valuable insights, they fail to explain what forces drive bubbles away from a heater. This is also true of the rationale in [3], where a successful prediction of q depends on measured values of bubble frequency which in turn is determined in an unknown way by gravity or other forces.

The correlations in [12] and [13], which suggested that q is proportional to $g^{1/2}$, will not only fail for $\theta \geq 90$ deg, but they are also inconsistent with the very suprising observed increase of q with increasing θ. (It is possible that vertical sidewalls – without endwalls – create a chimney effect as θ is increased, and that escaping vapor forms a density pump in this chimney.)

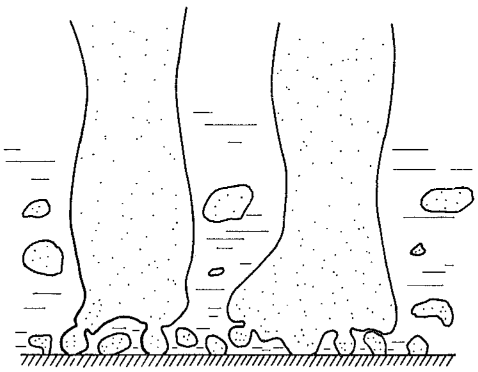

Fig. 2 Vapor removal in the slugs-and-columns regime. A "honeycomb" or "Swiss cheese" structure at the surface feeds relatively stationary columns that lead vapor away from the surface.

Let us summarize what we learn from [3]:

- The influence of orientation – and the related parameter of gravity – appears to vanish above the MBT.
- Orientation/gravity influences q in the isolated bubbles regime. (This might have been anticipated, but it is at variance with much that is reported in the literature.)
- Orientation/gravity does not influence q in what would appear to be the slugs-and-columns regime.

If our claim that the influence of orientation vanishes at the MBT is to be convincing, and if we know that the isolated bubble regime is susceptible to gravity, then it remains for us to show *a priori* that $q_{\text{slugs-and-columns}}$ should not depend on gravity or orientation. We turn to that next.

Gravity-Dependence in the Slugs-and-Columns Regime. Figure 2 shows how vapor leaves a heater in the slugs-and-columns regime. Bubbles nucleate at a large number of active sites in the liquid next to a heating surface. They almost immediately merge into one another, and then into liquid jets, only a short distance from the surface. This behavior was shown clearly in the photos by Semaria and by Gaertner, that Zuber [2] quoted when he first explained this action by which jets were formed out of bubbles.

When isolated bubbles rise through the liquid, gravity exerts its influence on the fluid motion by driving the bubbles. But when a standing array of jets (through which vapor flows) replaces the moving jets, gravity no longer has means to exert an influence.[2] We can see why this is true by looking at the prediction of $q_{\max}$.

The peak pool boiling heat flux for any large submerged heater (see e.g. [13]) is given by

$$q_{\max} = \rho_g h_{fg} u_c (A_j/A_h) \qquad (3)$$

where the ratio of the cross-sectional jet area A_j to the heater area A_h is gravity-independent (see, e.g., [14]); and where g enters the problem through the Helmholtz unstable vapor velocity in the jets u_c which varies as the square root of the susceptible wavelength in the wall of the jet. This wavelength in turn is proportional to the Taylor unstable wavelength, which sets the geometry of the jets and which varies as $\sqrt{g}$.

The details of this calculation have been worked out in different ways, but all lead to the conclusion that $q_{\max}$ for large heaters varies as $g^{1/4}$. This result is solidly substantiated by data when the comparisons are made correctly.

But while $q_{\max}$ is gravity-dependent, q must be gravity-independent in the region of slugs and columns because the standing jets provide stable escape paths. Without individual bubble action, gravity has no way of influencing the heat flux.

---

[2] We defer the $\theta \geq 90$ deg cases for a moment.

Reference [3] includes photographs showing that, as the plate is tilted beyond 90 deg, the jets bend over and slide up the plate as large amorphous slugs. This means that a modified hydrodynamic theory would be required to predict $q_{\max}$ in this region. Actually, such a mechanism has been proposed recently by Katto [15]. He suggested that $q_{\max}$ might occur as the result of Helmholtz instability, not in the large jets, but in small feeder jets (below the obvious jets) formed by the merging bubbles.

It is quite possible that such a hydrodynamic mechanism would dictate a higher $q_{\max}$ than is given by the conventional prediction, and that it can only come into play when the large jets are eliminated (as they are in subcooled boiling, or when the heater is tilted beyond 90 deg.) But this question aside, the nucleate boiling heat removal process beyond $\theta = 90$ deg remains one in which bubbles merge into large slugs. Thus gravity still cannot influence their motion or their departure size, and the altered direction of gravity still cannot influence q.

Deductions, Inferences, and Conclusions

1 We expect *a priori* that heat removal in the regime of isolated bubbles is gravity-dependent, and that it is gravity-independent in the regime of slugs and columns.

2 The effect of variations of orientation cannot be assumed identical to the effect of changes in g. However:

3 The transition between an orientation-dependent and an orientation-independent regime, observed in [3], is predicted by the Moissis-Berenson equation.

4 We therefore conclude that this loss of orientation-dependence reflects the MBT and can be predicted as $q_{\rm MB}$ for both the flat plate and other geometries.

5 Correct predictions of q in the isolated bubbles regime must show an influence of gravity.

6 Predictions of q involving individual bubble models cannot be carried beyond the isolated bubbles regime.

7 The data in [3] call for the development of new hydrodynamic models for $q_{\max}$ that are valid when large columnar vapor jet structures do not exist.

References

1 Moissis, R., and Berenson, P. J., "On the Hydrodynamic Transition in Nucleate Boiling," ASME JOURNAL OF HEAT TRANSFER, Vol. 85, No. 3, 1963, pp. 221–229.

2 Zuber, N., "Nucleate Boiling, the Region of Isolated Bubbles and the Similarity with Natural Convection," *International Journal of Heat and Mass Transfer*, Vol. 6, 1963, pp. 53–78.

3 Nishikawa, K., Fujita, Y., Uchida, S., and Ohta, H., "Effect of Heating Surface Orientation on Nucleate Boiling Heat Transfer," *Proc. ASME-JSME Thermal Engr. Joint Conf.*, Honolulu, Mar. 20–24, 1983, Vol. 1, ASME, New York, 1983, pp. 129–136.

4 Bhattacharya, A., and Lienhard, J. H., "Hydrodynamic Transition in Electrolysis," *J. Basic Engr.*, Vol. 94, No. 4, pp. 804–810.

5 Jakob, M., *Heat Transfer*, John Wiley and Sons, New York, 1949.

6 Chang, Y. P., and Snyder, N. W., "Heat Transfer in Saturated Boiling Heat Transfer," *Chem. Engr. Prog. Symp. Series*, Storrs, Conn., Vol. 56, No. 30, 1960, pp. 25–38.

7 Westwater, J. W., and Santangelo, J. G., "Photographic Study of Boiling," *Ind. Engr. Chem.*, Vol. 47, 1955, pp. 1605–1610.

8 Gaertner, R. F., and Westwater, J. W., "Population of Active Sites in Nucleate Boiling Heat Transfer," Paper No. 30, *Chem. Engr. Prog. Symp. Series*, Vol. 56, 1960, p. 39.

9 Yamagata, K., Kirano, K., Nishikawa, K., and Matsuoka, H., "Nucleate Boiling of Water on a Horizontal Heating Surface," *Mem. Fac. Engr. Kyushu Univ.*, Vol. 15, No. 1, 1955, pp. 98–163.

10 Tien, C. L., "A Hydrodynamic Model for Nucleate Pool Boiling," *International Journal of Heat and Mass Transfer*, Vol. 5, 1962, pp. 533–540.

11 Kurihara, H. M., and Myers, J. E., "The Effect of Superheat and Surface Roughness on Boiling Coefficients," *AIChE Journal*, Vol. 6, No. 1, 1960, pp. 83–91.

12 Rohsenow, W., "A Method of Correlating Heat Transfer Data for Surface Boiling of Liquids," ASME *Transaction*, Vol. 74, 1952, pp. 969–975.

13 Lienhard, J. H., "A Semi-Rational Nucleate Boiling Heat Flux Correlation," *International Journal of Heat and Mass Transfer*, Vol. 6, 1963, pp. 215–219.

14 Lienhard, J. H., and Dhir, V. K., "Extended Hydrodynamic Theory of the Peak and Minimum Pool Boiling Heat Fluxes," NASA CR-2270, July 1973.

15 Katto, Y., "Critical Heat Flux in Forced Convection," *Proc. ASME-JSME Thermal Engr. Joint Conf.*, Honolulu, Mar. 20–24, 1983, Vol. 3, ASME, New York 1983, pp. 1–10.

The Maximum Slope of Single-Blow Transient Testing for Compact Heat Exchanger Surfaces

Chung-Hsiung Li[1] and R. K. Shah[1]

Introduction and Purpose

The single-blow transient test technique is used for obtaining the dimensionless heat transfer characteristics of compact heat exchanger surfaces. The test section is a single-fluid exchanger (matrix) built from the heat transfer surface under investigation. Initially, matrix wall and fluid are at a uniform temperature. At time equals zero, a known monotonic increase (or decrease) is imposed on the inlet temperature of the test fluid, which is usually air. The temperature–time history of the fluid outlet temperature is then directly related to heat transfer that occurs in the matrix. A comparison of theoretical and experimental outlet temperature responses then permits the evaluation of the average heat transfer coefficient. Although any arbitrary variation in the inlet temperature can be imposed, the most commonly used is a step change in the inlet temperature. There are a number of data reduction methods available in the literature to compare the experimental and theoretical temperature responses at the test section outlet [1–3]. One of the most common data reduction methods is the maximum slope data reduction technique in which a maximum slope of the fluid outlet temperature response is determined and compared with the theory to determine core NTU (number of heat transfer units) and subsequently the Colburn factor $j(=\mathrm{St}\,\mathrm{Pr}^{2/3})$. This data reduction method and tabular results of maximum slope as a function of core NTU and longitudinal wall heat conduction parameter λ are presented in detail by Pucci et al. [1].

The theoretical results presented by Pucci et al. are based on the numerical analysis conducted during early 1960s when the computer capability was limited. Also, their tabular data do not cover the practical range of low NTU, intermediate values of λ, and the presented table is incomplete (maximum slope values are missing for some values of NTU and λ). The purpose of this technical note is to compute the theoretical solutions for a complete table of maximum slope for the practical ranges of NTU and λ with somewhat better accuracy. Also provide a comparison of the differences between the results of Pucci et al. and the present results.

Although the modern trend is to record the temperature–time history of the fluid outlet temperature on a mini/micro computer and perform the data reduction numerically by a curve matching method [4], there are a number of industries and universities still using the existing test facilities and the maximum slope data reduction method. Hence the completeness of the maximum slope as a function of NTU and λ is still needed.

Analysis

The dimensionless differential energy equations for the solid and fluid at a given instant of time for the single-blow problem are [1]

---

[1] Engineering Technologies Department, C-E Air Preheater Company, Wellsville, N.Y. 14895, Mem. ASME

[2] Harrison Radiator Division, General Motors Corporation, Lockport, N.Y. 14094, Fellow ASME

Contributed by the Heat Transfer Division for publication in the JOURNAL OF HEAT TRANSFER. Manuscript received by the Heat Transfer Division July 30, 1984.

Reference [3] includes photographs showing that, as the plate is tilted beyond 90 deg, the jets bend over and slide up the plate as large amorphous slugs. This means that a modified hydrodynamic theory would be required to predict $q_{\max}$ in this region. Actually, such a mechanism has been proposed recently by Katto [15]. He suggested that $q_{\max}$ might occur as the result of Helmholtz instability, not in the large jets, but in small feeder jets (below the obvious jets) formed by the merging bubbles.

It is quite possible that such a hydrodynamic mechanism would dictate a higher $q_{\max}$ than is given by the conventional prediction, and that it can only come into play when the large jets are eliminated (as they are in subcooled boiling, or when the heater is tilted beyond 90 deg.) But this question aside, the nucleate boiling heat removal process beyond $\theta = 90$ deg remains one in which bubbles merge into large slugs. Thus gravity still cannot influence their motion or their departure size, and the altered direction of gravity still cannot influence q.

Deductions, Inferences, and Conclusions

1 We expect *a priori* that heat removal in the regime of isolated bubbles is gravity-dependent, and that it is gravity-independent in the regime of slugs and columns.

2 The effect of variations of orientation cannot be assumed identical to the effect of changes in g. However:

3 The transition between an orientation-dependent and an orientation-independent regime, observed in [3], is predicted by the Moissis-Berenson equation.

4 We therefore conclude that this loss of orientation-dependence reflects the MBT and can be predicted as q_{MB} for both the flat plate and other geometries.

5 Correct predictions of q in the isolated bubbles regime must show an influence of gravity.

6 Predictions of q involving individual bubble models cannot be carried beyond the isolated bubbles regime.

7 The data in [3] call for the development of new hydrodynamic models for $q_{\max}$ that are valid when large columnar vapor jet structures do not exist.

References

1 Moissis, R., and Berenson, P. J., "On the Hydrodynamic Transition in Nucleate Boiling," ASME Journal of Heat Transfer, Vol. 85, No. 3, 1963, pp. 221–229.

2 Zuber, N., "Nucleate Boiling, the Region of Isolated Bubbles and the Similarity with Natural Convection," *International Journal of Heat and Mass Transfer*, Vol. 6, 1963, pp. 53–78.

3 Nishikawa, K., Fujita, Y., Uchida, S., and Ohta, H., "Effect of Heating Surface Orientation on Nucleate Boiling Heat Transfer," *Proc. ASME-JSME Thermal Engr. Joint Conf.*, Honolulu, Mar. 20–24, 1983, Vol. 1, ASME, New York, 1983, pp. 129–136.

4 Bhattacharya, A., and Lienhard, J. H., "Hydrodynamic Transition in Electrolysis," *J. Basic Engr.*, Vol. 94, No. 4, pp. 804–810.

5 Jakob, M., *Heat Transfer*, John Wiley and Sons, New York, 1949.

6 Chang, Y. P., and Snyder, N. W., "Heat Transfer in Saturated Boiling Heat Transfer," *Chem. Engr. Prog. Symp. Series*, Storrs, Conn., Vol. 56, No. 30, 1960, pp. 25–38.

7 Westwater, J. W., and Santangelo, J. G., "Photographic Study of Boiling," *Ind. Engr. Chem.*, Vol. 47, 1955, pp. 1605–1610.

8 Gaertner, R. F., and Westwater, J. W., "Population of Active Sites in Nucleate Boiling Heat Transfer," Paper No. 30, *Chem. Engr. Prog. Symp. Series*, Vol. 56, 1960, p. 39.

9 Yamagata, K., Kirano, K., Nishikawa, K., and Matsuoka, H., "Nucleate Boiling of Water on a Horizontal Heating Surface," *Mem. Fac. Engr. Kyushu Univ.*, Vol. 15, No. 1, 1955, pp. 98–163.

10 Tien, C. L., "A Hydrodynamic Model for Nucleate Pool Boiling," *International Journal of Heat and Mass Transfer*, Vol. 5, 1962, pp. 533–540.

11 Kurihara, H. M., and Myers, J. E., "The Effect of Superheat and Surface Roughness on Boiling Coefficients," *AIChE Journal*, Vol. 6, No. 1, 1960, pp. 83–91.

12 Rohsenow, W., "A Method of Correlating Heat Transfer Data for Surface Boiling of Liquids," ASME *Transaction*, Vol. 74, 1952, pp. 969–975.

13 Lienhard, J. H., "A Semi-Rational Nucleate Boiling Heat Flux Correlation," *International Journal of Heat and Mass Transfer*, Vol. 6, 1963, pp. 215–219.

14 Lienhard, J. H., and Dhir, V. K., "Extended Hydrodynamic Theory of the Peak and Minimum Pool Boiling Heat Fluxes," NASA CR-2270, July 1973.

15 Katto, Y., "Critical Heat Flux in Forced Convection," *Proc. ASME-JSME Thermal Engr. Joint Conf.*, Honolulu, Mar. 20–24, 1983, Vol. 3, ASME, New York 1983, pp. 1–10.

The Maximum Slope of Single-Blow Transient Testing for Compact Heat Exchanger Surfaces

Chung-Hsiung Li[1] **and R. K. Shah**[1]

Introduction and Purpose

The single-blow transient test technique is used for obtaining the dimensionless heat transfer characteristics of compact heat exchanger surfaces. The test section is a single-fluid exchanger (matrix) built from the heat transfer surface under investigation. Initially, matrix wall and fluid are at a uniform temperature. At time equals zero, a known monotonic increase (or decrease) is imposed on the inlet temperature of the test fluid, which is usually air. The temperature–time history of the fluid outlet temperature is then directly related to heat transfer that occurs in the matrix. A comparison of theoretical and experimental outlet temperature responses then permits the evaluation of the average heat transfer coefficient. Although any arbitrary variation in the inlet temperature can be imposed, the most commonly used is a step change in the inlet temperature. There are a number of data reduction methods available in the literature to compare the experimental and theoretical temperature responses at the test section outlet [1–3]. One of the most common data reduction methods is the maximum slope data reduction technique in which a maximum slope of the fluid outlet temperature response is determined and compared with the theory to determine core NTU (number of heat transfer units) and subsequently the Colburn factor $j(= \mathrm{St}\,\mathrm{Pr}^{2/3})$. This data reduction method and tabular results of maximum slope as a function of core NTU and longitudinal wall heat conduction parameter λ are presented in detail by Pucci et al. [1].

The theoretical results presented by Pucci et al. are based on the numerical analysis conducted during early 1960s when the computer capability was limited. Also, their tabular data do not cover the practical range of low NTU, intermediate values of λ, and the presented table is incomplete (maximum slope values are missing for some values of NTU and λ). The purpose of this technical note is to compute the theoretical solutions for a complete table of maximum slope for the practical ranges of NTU and λ with somewhat better accuracy. Also provide a comparison of the differences between the results of Pucci et al. and the present results.

Although the modern trend is to record the temperature–time history of the fluid outlet temperature on a mini/micro computer and perform the data reduction numerically by a curve matching method [4], there are a number of industries and universities still using the existing test facilities and the maximum slope data reduction method. Hence the completeness of the maximum slope as a function of NTU and λ is still needed.

Analysis

The dimensionless differential energy equations for the solid and fluid at a given instant of time for the single-blow problem are [1]

---

[1] Engineering Technologies Department, C-E Air Preheater Company, Wellsville, N.Y. 14895, Mem. ASME

[2] Harrison Radiator Division, General Motors Corporation, Lockport, N.Y. 14094, Fellow ASME

Contributed by the Heat Transfer Division for publication in the Journal of Heat Transfer. Manuscript received by the Heat Transfer Division July 30, 1984.

$$\frac{\partial T}{\partial \tau} = \lambda \mathrm{NTU} \frac{\partial^2 T}{\partial z^2} + (t - T) \quad \text{for solid} \tag{1}$$

and

$$\frac{\partial t}{\partial z} = T - t \quad \text{for fluid} \tag{2}$$

$$\tau \simeq \frac{hA}{W_s c_s} \theta, \; z = \frac{hA}{\dot{m} c_p} \frac{x}{L} = \mathrm{NTU} \frac{x}{L}, \; \lambda = \frac{k_s A_s}{\dot{m} c_p L} \tag{3}$$

Here T and t are solid and fluid temperatures at an instant of time; τ and z are dimensionless time and axial distance; h is the heat transfer coefficient; A is the total heat transfer surface area of the matrix; W_s is the mass of the matrix; c_s is the specific heat of matrix material; $\dot{m}$ is the mass flow rate of the test fluid; c_p is the specific heat of the fluid at constant pressure; x is the distance along the flow passage in the direction of flow; L is the total fluid flow length in the matrix; k_s is thermal conductivity of the matrix wall material; and A_s is the matrix wall (solid) cross-sectional area for longitudinal (in the x-direction) wall heat conduction. The major idealizations involved in deriving equations (1) and (2) are: fluid and solid physical properties are independent of temperature and time; fluid flow is steady; porous solid is homogeneous; the heat transfer coefficient is uniform and independent of temperature and time; the thermal conductivity of the solid is infinite perpendicular to the fluid flow direction and finite in the axial (parallel to fluid flow) direction; and axial heat conduction in the fluid is negligible. The initial and boundary conditions for the single-blow problem are:

1 The matrix is initially at a uniform temperature.

2 At time equals zero, the temperature of the entering fluid is changed instantaneously, a step change in the present case.

3 The matrix boundaries are adiabatic.

Equations (1) and (2) are complicated and no general analytical closed-form solution is available. The present solution is obtained by finite difference methods. Dividing the matrix into n elements in the flow direction and m time steps, equations (1) and (2) can be represented in the finite difference form as

$$\begin{aligned} &\frac{T_{i,j+1/2} - T_{i,j-1/2}}{\Delta\tau} \\ &= \frac{\lambda \mathrm{NTU}}{\Delta z^2} \left[\left(\frac{T_{i+1,j-1/2} + T_{i+1,j+1/2}}{2} - \frac{T_{i,j-1/2} + T_{i,j+1/2}}{2} \right) \right. \\ &\left. - \left(\frac{T_{i,j-1/2} + T_{i,j+1/2}}{2} - \frac{T_{i-1,j-1/2} + T_{i-1,j+1/2}}{2} \right) \right] \\ &+ \frac{t_{i-1/2,j} - t_{i+1/2,j}}{\Delta z} \end{aligned} \tag{3}$$

$$\begin{aligned} &\frac{t_{i+1/2,j} - t_{i-1/2,j}}{\Delta z} \\ &= \frac{T_{i,j-1/2} + T_{i,j+1/2}}{2} - \frac{t_{i-1/2,j} + t_{i+1/2,j}}{2} \end{aligned} \tag{4}$$

where i represents the matrix element and j the time step.

In order to obtain high accuracy in the maximum slope results, equations (3) and (4) were solved by two numerical methods: the Crank-Nicolson method for $\mathrm{NTU} \le 10$, which becomes more accurate with decreasing values of NTU; and the modified Gauss-Seidel method by Li [5] for $\mathrm{NTU} \ge 10$, which becomes more accurate with increasing values of NTU. In the modified Gauss-Seidel method, all the matrix elements are used to compute fluid and metal temperature distributions for each time step, in contrast to the single-element calculations performed in the Gauss-Seidel method. For the numerical computation, the matrix was divided into 50 elements ($n = 50$) and the time step was kept variable as follows: for $\mathrm{NTU} \ge 10$, $\Delta\tau = 0.5$ for $\lambda \le 0.04$, $\Delta\tau = 0.25$ for $0.04 < \lambda \le 0.5$, $\Delta\tau = 0.1$ for $\lambda > 0.5$; for $\mathrm{NTU} < 10$, $\Delta\tau = 1/(0.5 + 2\lambda/n^2\mathrm{NTU})$.

After finding the exit fluid temperature distribution with the initial fluid and matrix temperatures as zero and the value of the step function for the fluid temperature as unity, one can

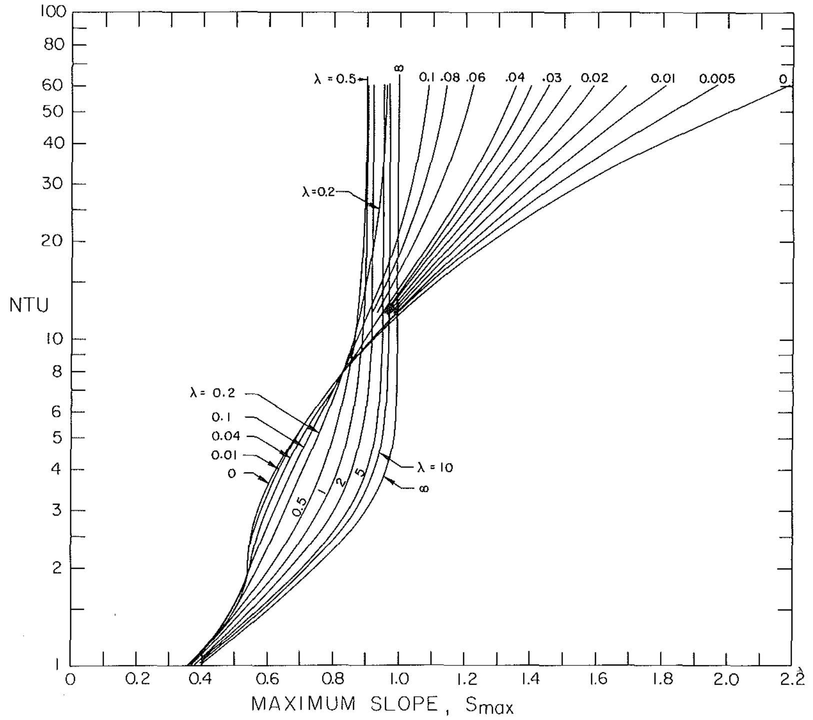

Fig. 1 Number of transfer units as a function of the maximum slope and longitudinal conduction parameter.

Table 1 Maximum slope as a function of number of transfer units and longitudinal conduction parameter

NTU	MAXIMUM SLOPE, S_{max}																		
	λ = 0	.005	.010	.015	.020	.025	.030	.035	.040	.060	.080	.100	.200	.500	1.00	2.00	5.00	10.00	∞
.5	.152	.149	.151	.151	.151	.151	.151	.151	.151	.151	.151	.152	.152	.152	.152	.152	.152	.153	.155
.6	.198	.194	.196	.196	.197	.197	.197	.197	.197	.197	.197	.197	.198	.198	.198	.198	.200	.201	.204
.7	.243	.239	.241	.242	.242	.242	.243	.243	.243	.243	.243	.243	.243	.243	.243	.244	.248	.250	.253
.8	.288	.282	.285	.286	.286	.287	.287	.287	.287	.287	.287	.287	.287	.288	.288	.290	.295	.298	.303
.9	.329	.323	.326	.327	.328	.328	.328	.328	.329	.329	.329	.329	.329	.329	.330	.335	.341	.345	.352
1.0	.368	.361	.364	.366	.366	.366	.367	.367	.367	.367	.367	.368	.368	.368	.370	.377	.386	.391	.400
1.1	.403	.395	.399	.400	.401	.401	.402	.402	.402	.402	.402	.402	.403	.403	.408	.417	.429	.435	.445
1.2	.434	.426	.430	.431	.432	.432	.432	.433	.433	.433	.433	.433	.434	.435	.443	.455	.469	.476	.488
1.3	.461	.453	.457	.458	.459	.459	.459	.460	.460	.460	.460	.460	.460	.464	.476	.490	.507	.515	.529
1.4	.483	.475	.479	.481	.481	.482	.482	.482	.482	.483	.483	.483	.483	.490	.506	.523	.542	.552	.568
1.5	.502	.495	.498	.500	.500	.501	.501	.501	.501	.502	.502	.502	.502	.515	.534	.554	.575	.586	.604
1.6	.517	.510	.514	.515	.515	.516	.516	.516	.516	.516	.517	.517	.519	.537	.559	.582	.606	.618	.637
1.8	.536	.532	.534	.534	.535	.535	.535	.535	.535	.535	.536	.537	.547	.575	.604	.632	.660	.674	.697
2.0	.541	.541	.541	.542	.542	.543	.543	.544	.544	.547	.550	.554	.570	.608	.642	.674	.706	.722	.748
2.2	.544	.545	.546	.547	.549	.550	.551	.553	.554	.559	.564	.569	.591	.635	.674	.710	.745	.763	.791
2.4	.549	.551	.553	.555	.557	.559	.561	.562	.564	.571	.577	.583	.609	.659	.701	.740	.778	.797	.827
2.6	.557	.559	.562	.564	.567	.569	.571	.573	.575	.583	.590	.597	.626	.679	.724	.765	.806	.826	.857
2.8	.566	.569	.572	.575	.577	.579	.582	.584	.586	.595	.603	.610	.641	.697	.744	.786	.828	.849	.882
3.0	.577	.579	.582	.585	.588	.590	.593	.595	.598	.607	.615	.623	.655	.712	.761	.804	.848	.869	.903
3.2	.587	.590	.593	.596	.599	.602	.604	.607	.609	.619	.627	.635	.667	.726	.775	.819	.864	.886	.920
3.4	.598	.601	.605	.608	.610	.613	.616	.618	.621	.630	.639	.647	.679	.738	.787	.832	.877	.899	.934
3.6	.609	.613	.616	.619	.622	.624	.627	.630	.632	.642	.650	.658	.691	.749	.798	.843	.888	.910	.946
3.8	.621	.624	.627	.630	.633	.636	.638	.641	.643	.653	.661	.669	.701	.759	.807	.852	.897	.920	.956
4.0	.632	.635	.639	.641	.644	.647	.649	.652	.654	.664	.672	.680	.711	.768	.816	.860	.905	.928	.964
4.5	.660	.663	.666	.669	.672	.674	.676	.679	.681	.690	.697	.704	.733	.786	.832	.875	.919	.942	.978
5.0	.688	.691	.693	.696	.698	.700	.702	.704	.706	.714	.721	.727	.753	.801	.844	.886	.929	.951	.987
5.5	.715	.717	.720	.722	.724	.725	.727	.729	.730	.736	.742	.747	.770	.813	.854	.893	.935	.956	.992
6.0	.741	.743	.745	.746	.748	.749	.750	.752	.753	.758	.762	.766	.785	.824	.861	.899	.939	.960	.995
6.5	.767	.768	.769	.770	.771	.772	.773	.774	.774	.778	.781	.784	.798	.832	.867	.903	.942	.963	.997
7.0	.792	.792	.793	.793	.794	.794	.794	.794	.795	.796	.798	.800	.810	.839	.872	.906	.944	.964	.998
7.5	.816	.816	.816	.815	.815	.815	.814	.814	.814	.814	.814	.814	.821	.846	.876	.909	.946	.965	.999
8.0	.840	.839	.838	.837	.836	.835	.834	.833	.832	.830	.829	.828	.830	.851	.879	.911	.947	.966	.999
9.0	.885	.883	.880	.877	.875	.872	.870	.868	.866	.860	.855	.852	.847	.860	.884	.914	.948	.967	1.000
10.0	.929	.921	.916	.912	.908	.904	.900	.898	.895	.885	.878	.872	.860	.866	.888	.916	.950	.969	1.000
11.0	.970	.961	.954	.948	.942	.936	.932	.927	.922	.909	.899	.891	.871	.871	.891	.917	.950	.970	1.000
12.0	1.010	.998	.989	.981	.973	.966	.960	.954	.948	.931	.917	.907	.881	.876	.893	.919	.951	.971	1.000
13.0	1.048	1.034	1.023	1.013	1.003	.995	.986	.978	.973	.951	.934	.921	.890	.879	.895	.920	.951	.969	1.000
14.0	1.086	1.068	1.055	1.042	1.031	1.021	1.010	1.002	.995	.968	.949	.934	.897	.882	.896	.920	.951	.970	1.000
15.0	1.121	1.101	1.086	1.070	1.058	1.045	1.034	1.024	1.014	.985	.962	.946	.903	.885	.898	.921	.952	.970	1.000
16.0	1.156	1.133	1.115	1.097	1.083	1.068	1.056	1.044	1.033	1.000	.975	.956	.909	.887	.899	.921	.952	.969	1.000
18.0	1.223	1.194	1.170	1.148	1.128	1.111	1.095	1.081	1.068	1.027	.997	.974	.918	.890	.900	.922	.952	.970	1.000
20.0	1.286	1.251	1.220	1.194	1.170	1.149	1.130	1.114	1.098	1.050	1.015	.989	.925	.892	.901	.923	.952	.969	1.000
22.0	1.347	1.304	1.267	1.236	1.208	1.183	1.162	1.142	1.125	1.070	1.031	1.002	.931	.894	.902	.923	.952	.970	1.000
24.0	1.404	1.355	1.312	1.274	1.243	1.215	1.190	1.168	1.148	1.087	1.044	1.013	.936	.896	.903	.923	.953	.970	1.000
26.0	1.460	1.402	1.353	1.311	1.275	1.244	1.216	1.191	1.170	1.103	1.056	1.022	.940	.897	.903	.924	.953	.970	1.000
28.0	1.513	1.447	1.392	1.345	1.305	1.270	1.240	1.213	1.189	1.117	1.066	1.030	.944	.898	.903	.924	.953	.970	1.000
30.0	1.565	1.491	1.428	1.377	1.333	1.295	1.261	1.233	1.207	1.129	1.076	1.038	.947	.899	.904	.924	.953	.970	1.000
32.0	1.615	1.532	1.463	1.406	1.358	1.317	1.282	1.251	1.223	1.140	1.084	1.044	.949	.899	.904	.924	.953	.970	1.000
34.0	1.663	1.571	1.495	1.434	1.382	1.338	1.300	1.267	1.238	1.150	1.091	1.050	.951	.900	.904	.924	.953	.970	1.000
36.0	1.711	1.609	1.527	1.460	1.405	1.358	1.317	1.282	1.251	1.159	1.098	1.055	.953	.900	.904	.924	.953	.970	1.000
38.0	1.756	1.645	1.557	1.485	1.426	1.376	1.333	1.296	1.264	1.168	1.104	1.060	.955	.901	.904	.924	.953	.970	1.000
40.0	1.801	1.681	1.585	1.508	1.445	1.392	1.348	1.309	1.275	1.175	1.110	1.064	.957	.901	.905	.924	.953	.970	1.000
45.0	1.908	1.763	1.650	1.562	1.490	1.431	1.381	1.338	1.301	1.192	1.122	1.073	.960	.902	.905	.924	.953	.970	1.000
50.0	2.010	1.839	1.709	1.609	1.529	1.464	1.409	1.362	1.322	1.206	1.131	1.080	.963	.902	.905	.924	.953	.970	1.000
55.0	2.107	1.909	1.763	1.652	1.564	1.493	1.433	1.384	1.341	1.218	1.140	1.086	.965	.903	.905	.924	.953	.970	1.000
60.0	2.199	1.973	1.811	1.689	1.594	1.518	1.455	1.402	1.357	1.228	1.146	1.091	.966	.903	.905	.924	.953	.970	1.000

find the dimensionless temperature slope S with respect to the time at the exit as

$$S_j = \frac{\Delta\left(\dfrac{t_{n+1,j}-t_{\text{initial}}}{t_{\text{inlet}}-t_{\text{initial}}}\right)}{\Delta\tau_j/\text{NTU}} \qquad (5)$$

where $t_{n+1,j}$ is the exit fluid temperature at the jth time step. The calculation is terminated when

$$S_j > S_{j-1} \text{ and } S_j > S_{j+1} \qquad (6)$$

Thus the maximum slope $S_{\max} = S_j$ is obtained at

$$\tau = \sum_1^j \Delta\tau_j.$$

Table 2 *Differences in the maximum slope values at NTU = 10 by the two methods employed*

λ	Crank-Nicolson Method	Ref. [5] Method	Average Value	± % Deviation from Mean Value
0.005	0.9241	0.9213	0.9227	0.15
0.010	0.9196	0.9162	0.9179	0.19
0.015	0.9151	0.9125	0.9138	0.14
0.020	0.9109	0.9083	0.9096	0.14
0.025	0.9070	0.9036	0.9053	0.19
0.030	0.9033	0.9002	0.9018	0.18
0.035	0.9000	0.8977	0.8989	0.13
0.040	0.8969	0.8948	0.8959	0.12
0.060	0.8866	0.8854	0.8860	0.07
0.080	0.8789	0.8779	0.8784	0.06
0.10	0.8732	0.8722	0.8727	0.06
0.20	0.8605	0.8597	0.8601	0.05
0.50	0.8665	0.8663	0.8664	0.01
1.00	0.8882	0.8881	0.8882	0.01
2.00	0.9160	0.9163	0.9162	0.01
5.00	0.9494	0.9498	0.9496	0.02
10.00	0.9678	0.9692	0.9685	0.07

Results and Discussion

The numerical results obtained for the dimensionless maximum slope are presented in Table 1 and Fig. 1 for the following extended ranges: $0.5 \leq \mathrm{NTU} \leq 60$ and $0.005 \leq \lambda \leq 10.0$. For the completeness of the table, the results for $\lambda = \infty$ are obtained from the closed form solution of the Mondt [6] and $\lambda = 0$ from Locke as reported by Pucci et al. [1]. As mentioned earlier, to obtain the highest accuracy, the results for $\mathrm{NTU} < 10$ are obtained by the Crank-Nicolson method, and for $\mathrm{NTU} > 10$ by the [5] method. The results for $\mathrm{NTU} = 10$ in this table are the arithmetic average of the results by these two methods. As compared in Table 2, the results by the two methods differ at the most by ±0.2 percent from the average value, and provides an idea on the accuracy of the present results.

A comparison of the maximum slope values of the present analysis and that of [1, 2] reveals that the present values of $S_{\max}$ are higher than those of [1, 2]: 0.1 to 1.5 percent higher for $\lambda = 0.005$ to 1.0, respectively, at $\mathrm{NTU} = 10$; and 0.4 to 2.3 percent higher for $\mathrm{NTU} = 30$. The present results obtained with a much finer step size and improved numerical techniques are believed to be up to 2 percent more accurate. It should be emphasized that because of the steep slope of NTU versus $S_{\max}$ curves in Fig. 1, a 1 percent error in $S_{\max}$ results in about 3 percent and higher error in NTU [1] in the exchanger design range. Therefore, the improvements in the results of Table 1 are highly desirable from the designer's viewpoint.

Summary

In order to determine the heat transfer characteristics of compact heat exchanger surfaces, the single-blow transient test technique is commonly used. The maximum slope of the temperature-time history of the test fluid at the downstream of the test core for a step change in the inlet fluid temperature uniquely represents the surface heat transfer characteristics. The numerical results for the dimensionless maximum slope as a function of the matrix number of heat transfer units and longitudinal conduction parameter for the matrix wall are obtained accurate to ±0.2 percent, and are presented in Table 1 and Fig. 1.

References

1 Pucci, P. F., Howard, C. P., and Piersall, C. H., Jr., "The Single-Blow Transient Testing Technique for Compact Heat Exchanger Surfaces," ASME *Journal of Engineering for Power*, Vol. 89, 1967, pp. 29–40.

2 Howard, C. P., "Heat Transfer and Flow Friction Characteristics of Skewed Passage and Glass-Ceramic Heat Transfer Surfaces," T.R. No. 59, Department of Mechanical Engineering, Stanford University, Stanford, Calif., 1963.

3 Wheeler, A. J., "Single-Blow Transient Testing of Matrix-Type Heat Exchanger Surfaces at Low Values of N_{tu}," T.R. No. 68, Mechanical Engineering Department, Stanford University, Stanford, Calif., 1968.

4 Mullisen, R. S., and Loehrke, R. I., "A Transient Heat Transfer Test for Computer-Based Data Reduction," ASME Paper No. 83-HT-65, 1983.

5 Li, C. H., "A Numerical Finite-Difference Method for Performance Evaluation of a Periodic-Flow Heat Exchanger," ASME JOURNAL OF HEAT TRANSFER, Vol. 105, 1983, pp. 611–617.

6 Mondt, J. R., "Effects of Longitudinal Thermal Conduction in the Solid on Apparent Convection Behavior with Data for Plate-Fin Surfaces," *International Developments in Heat Transfer*, Boulder, Colo., 1961-62, pp. 614–621.

ERRATA

Corrections to "On the Presentation of Performance Data for Enhanced Tubes Used in Shell-and-Tube Heat Exchangers," by W. J. Marner, A. E. Bergles, and J. M. Chenoweth, published in the May 1983 issue of the ASME JOURNAL OF HEAT TRANSFER, pp. 358–365.

Table 3 Parameters for tubeside and shellside flow

Parameters	Tubeside flow	Shellside crossflow	Shellside parallel flow
Envelope diameter	$\tilde{D}_i$	$\tilde{D}_o$	$\tilde{D}_o$
Tube length	L	L	L
Total number of tubes	--	N_t	N_t
Number of tube rows	--	N_r	--
Tube pitch	--	P	P
Tubefield layout angle	--	α	α
Flow area	$\tilde{A}_{fi} = \pi \tilde{D}_i^2/4$	$(\tilde{A}_f)_{oc} = (N_t/N_r)L(P-\tilde{D}_o)$	$(\tilde{A}_f)_{op} = A_{\text{shell}} - N_t \pi \tilde{D}_o^2/4$
Mass velocity	$\tilde{G}_i = W_i/\tilde{A}_{fi}$	$\tilde{G}_{oc} = W_o/(\tilde{A}_f)_{oc}$	$\tilde{G}_{op} = W_o/(\tilde{A}_f)_{op}$
Reynolds number	$\tilde{\text{Re}}_i = \tilde{G}_i \tilde{D}_i/\mu_i$	$\tilde{\text{Re}}_{oc} = \tilde{G}_{oc} \tilde{D}_o/\mu_o$	$\tilde{\text{Re}}_{op} = \tilde{G}_{op} \tilde{D}_o/\mu_o$
Fanning friction factor	$\tilde{f}_i = \rho_i \Delta p_i (\tilde{D}_i/L)/2\tilde{G}_i^2$	$\tilde{f}_{oc} = \rho_o (\Delta p_{oc}/N_r)/2\tilde{G}_{oc}^2$	$\tilde{f}_{op} = \rho_o \Delta p_{op} (\tilde{D}_o/L)/2\tilde{G}_{op}^2$
Prandtl number	$\text{Pr}_i = (C_p)_i \mu_i/k_i$	$\text{Pr}_o = (C_p)_o \mu_o/k_o$	$\text{Pr}_o = (C_p)_o \mu_o/k_o$
Grashof number	$\tilde{\text{Gr}}_i = \rho_i^2 g \beta_i \lvert T_{wi} - T_{bi} \rvert \tilde{D}_i^3/\mu_i^2$	$\tilde{\text{Gr}}_o = \rho_o^2 g \beta_o \lvert T_{wo} - T_{bo} \rvert \tilde{D}_o^3/\mu_o^2$	$\tilde{\text{Gr}}_o = \rho_o^2 g \beta_o \lvert T_{wo} - T_{bo} \rvert \tilde{D}_o^3/\mu_o^2$
Viscosity ratio (liquids)	μ_{bi}/μ_{wi}	μ_{bo}/μ_{wo}	μ_{bo}/μ_{wo}
Temperature ratio (gases)	T_{bi}/T_{wi}	T_{bo}/T_{wo}	T_{bo}/T_{wo}
Average wall temperature	T_{wi}	T_{wo}	T_{wo}
Surface area	$\tilde{A}_{si} = \pi \tilde{D}_i L$	$\tilde{A}_{so} = N_t \tilde{D}_o L$	$\tilde{A}_{so} = N_t \pi \tilde{D}_o L$
Nusselt number	$\tilde{\text{Nu}}_i = \tilde{h}_i \tilde{D}_i/k_i$	--	--
Colburn *j*-factor	--	$\tilde{j}_{oc} = (\tilde{h}_{oc}/(C_p)_o \tilde{G}_{oc}) \text{Pr}_o^{2/3}$	$\tilde{j}_{op} = (\tilde{h}_{op}/(C_p)_o \tilde{G}_{op}) \text{Pr}_o^{2/3}$
Actual flow area	A_{fi}	$(A_f)_{oc}$	$(A_f)_{op} = (\tilde{A}_f)_{op}$
Actual wetted perimeter	p_i	--	--
Actual surface area	$A_{si} = p_i L$	$A_{so} = N_t (A_o/L) L$	$A_{so} = N_t (A_o/L) L$